ISSN 0858-2114

International Agricultural Engineering Journal

Published by Asian Association for Agricultural Engineering (AAAE)

Vol.26, No.3, 2017

AAAE Secretariat

AAAE was formed for the general advancement of the agricultural engineering profession and its practice in all aspects, especially in Asia and the Pacific region. Since its establishment in 1990, AAAE has played an important role in promoting agricultural engineering worldwide by means of publishing the International Agricultural Engineering Journal (IAEJ), holding biannual academic conferences, exchanging visits among its members, etc. At present, AAAE has more than 260 members in the field of agricultural engineering from 30 countries and regions all over the world.

AAAE has kept developing since its headquarters were shifted to China in April 2010. During the previous seven years, the Secretariat was located in Chinese Academy of Agricultural Mechanization Sciences (2010). Led by AAAE former President Prof. Li Shujun and Secretary General Prof. Zhang Lanfang, the Association has expanded its impacts through holding academic events and working on IAEJ. In March, 2017, due to retirement of Prof. Zhang Lanfang, Prof. Cheng Yongqiang from China Agricultural University was nominated as the Secretary General of AAAE and Executive Editor-in-Chief of IAEJ. Thanks to the solid foundation the former Secretariat has laid, AAAE has grown to an influential platform to enhance communication, motivate knowledge sharing among experts in agricultural engineering all over the world.

The Secretariat is now located in College of Food Science and Nutritional Engineering, China Agricultural University with several staff members working for AAAE routine work. The AAAE Secretary General Prof. Cheng Yongqiang is an expert in food science and head of Department of Food Science and Engineering, and has been an active participant in international academic activities in agricultural engineering. He undertakes the administrative duties associated with AAAE in liaison with the President and the Executive Council. According to the AAAE Statutes, the Secretary General makes appropriate decisions in absence of the President in consultation with the Executive Council members.

College of Food Science and Nutritional Engineering of China Agricultural University will offer a good platform for future growth of the association, for its strength in academic researches and its intensive cooperation with universities, institutes and enterprises in China and abroad. Moreover, China Agricultural University as the origin of modern higher education of agriculture in China that integrates agronomy, life sciences, agricultural engineering and food sciences will provide strong support to the Association.

The Treasurer of AAAE is Ms. Zhou Rong. She is responsible for maintaining records of the income and expenditures of the Association, and providing an annual accounts statement during the General Body meeting of AAAE.

AAAE is one of the world's leading international academic societies in the agricultural engineering field. The AAAE Secretariat will continue to do a better job according to the working plan made by the AAAE President and approved by the AAAE Executive Council meeting. The AAAE Secretariat would like to work together and collaborate with all its members worldwide for the purpose of promoting the advancement of agricultural engineering to upgrade the quality of life of people.

Contact Information:
Secretariat of Asian Association for Agricultural Engineering (AAAE)
Mail Box No. 40, East campus of China Agricultural University, No. 17 Qinghua East Road, Haidian District, 100083 Beijing, China
Tel: +86-10-62737401 Fax:+86-10-62737401
Email: aaaese@aliyun.com iaejeditor@aliyun.com

SP 29/5/18

International Agricultural Engineering Journal

An International Journal on Research and Development in Agricultural Engineering
Published by the Asian Association for Agricultural Engineering (AAAE)

Editor-in-Chief:

Dr. Prof. Li Shujun, China National Machinery Industry Corporation, China.

Executive Editors-in-Chief:

Prof. Cheng Yongqiang, College of Food Science and Nutritional Engineering, China Agricultural University.

IAEJ International Editorial Board Members in 2017:

Prof. Billy A. Stout, Professor Emeritus, Texas A&M University, USA. Email: stouttamu@yahoo.com.

Prof. Vilas M. Salokhe, Kaziranga University, India. Email: vsalokhe@yahoo.com.

Prof. Ying Yibin, Zhejiang University, China. Email: ybying@zju.edu.cn.

Prof. Ma Haile, Jiangsu University, China. Email: mhl@ujs.edu.cn.

Prof. Rameshwar S. Kanwar, Iowa State University, USA. Email: rskanwar@iastate.edu.

Prof. A. Q. Mughal, Greenwich University. Email: draqmughal@gmail.com.

Prof. Peng Yankun, China Agricultural University, China. Email: ypeng@cau.edu.cn.

Prof. Li Dong, China Agricultural University, China. Email: dongli@cau.edu.cn.

Prof. Yin Lijun, China Agricultural University, China. Email: ljyin@cau.edu.cn.

Prof. Liu Donghong, Zhejiang University, China. Email: dhliu@zju.edu.cn.

Prof. Chen Kun, Chinese Academy of Agricultural Mechanization Sciences, China. Email: ahkunchen@126.com.

Prof. Xiu-Lun Wang, Mie University, Japan. Email: wang@bio.mie-u.ac.jp.

Prof. Zheng Xianzhe, Northeast Agricultural University, China. Email: zhengxz2008@gmail.com.

Prof. Ji Jiangtao, Henan University of Science and Technology, China. Email: jjt0907@163.com.

Dr. Zhongli Pan, Research Engineer of Western Regional Research Center, United States Department of Agriculture; Adjunct Professor of University of California, Davis, USA. Email: zlpan@ucdavis.edu.

Dr. Ajay Kumar Sharma, Director of Aravali Institute of Technical Studies; Associate Professor of Maharana Pratap University of Agriculture and Technology, India. Email: sharma_ajayk@yahoo.com.

Dr. Wang Yingkuan, Associate Professor of Chinese Academy of Agricultural Engineering. Email: wangyingkuan@gmail.com.

Dr. Hemantha P. W. Jayasuriya, Associate Professor of Sultan Qaboos University, Oman. Email: hemanthaj@hotmail.com.

Dr. B. Sahoo, Assistant Professor of Indian Institute of Technology, India. Email: bsahoo2003@yahoo.com.

Dr. S. Pathmarajah, Senior Lecturer of University of Peradeniya, Sri Lanka. Email: s_pathma@yahoo.com.

Dr. Sunil Jha, Senior Scientist of Indian Agricultural Research Institute, India. Email: skj_agengg@yahoo.co.in.

Dr. Parish Nalavade, Assistant Professor of Indian Institute of Technology, India. Email: parish.nalavade@yahoo.com.

Dr. Sagar Dhakal, Ph.D candidate of China Agricultural University, Nepal. Email: dhakal_sagar@hotmail.com.

© 2017 AAAE

Any statements or views expressed in the papers published in this journal are those of authors, and the Editor or Association will not be responsible for the accuracy of such statements or views.

Aims and Scope: The aim of this journal is to communicate advances in Agricultural Engineering, with particular reference to Asia, to practicing professionals in the field. The scope will include soil and water engineering, farm machinery, farm structures, post-harvest technology, biotechnology food processing and emerging technologies. Subjects of general interest to agricultural engineers such as ergonomics, energy, systems engineering, precision agriculture, protected cultivation, terramechanics, instrumentation, environment in agriculture and new materials are also included.

Publication Schedule: International Agricultural Engineering Journal is published in four issues per year.

Subscriptions: For academic institutions, the annual subscription is US$ 280 per calendar year. The journal copies will be mailed by sea mail.

Correspondence: All manuscripts and other correspondence should be directed to the Executive Editor-in-Chief, College of Food Science and Nutritional Engineering, China Agricultural University. E-mail: iaejeditor@aliyun.com

Any statements or views expressed in the papers published in this journal are those of author/s, and the Chief Editor, Assistant/Associate Editors or AAAE will not be responsible for the accuracy of such statements or views expressed in the published manuscripts.

INTERNATIONAL AGRICULTURAL ENGINEERING JOURNAL

Published by

ASIAN ASSOCIATION FOR AGRICULTURAL ENGINEERING (AAAE)

Vol. 26, No. 3, 2017

TABLE OF CONTENTS

Impact of tire compaction on hydro-thermal feature of sandy and loam soils
..... Wang Xianliang, Wang Qingjie, Li Hongwen, He Jin, Lu Caiyun, Niu Qi, Xu Qimeng, Zhang Yufan, Huang Xingyuan (1)

Hydrostatic driving system for self-propelled sprayer
..... Zou Fan, Kang Jingjing, Xiao Maohua, Song Xucheng, Ji Guojun (12)

Performance optimization of combine harvester inertia separation chamber based on BPNN
..... Dong Zhigui, Wang Fulin, Song Qingfeng, Wu Zhihui, Fang Kun (19)

Mechanism of reducing force and tillage performance analysis of bionic subsoiler based on discrete element method
..... Li Bo, Wang Xuewen, Xia Rui, Chen Jun, Yang Zhaojian (27)

Development of 3-DOF lifting platform for hilly orchards
..... Duan Zhenhua, Qiu Wei, Ding Weimin, Liu Yande, Ouyang Yuping, Huang Liang (37)

Quantification of mechanization index and its impact on crop productivity and socio-economic factors
..... Adnan Abbas, Yang Minli, Ehsan Elahi, Khurram Yousaf, Riaz Ahmad,Tahir Iqbal (49)

Strength analysis and optimal design of transmission system of sugarcane leaf stripping machine
..... Xu Minmin, Huang Wei, Mo Zhimin, Niu Sijie, Ruan Xiaofang, Lu Xuewen (55)

Parameters optimization of improved air-assisted orchard sprayer based on RSM and RBF neural network
..... Qu Feng, Zhang Mingming, Li Xi, Zhang Junxiong, Liu Jingyun (64)

Comparative experimental study on working performance of air-blowing and air-suction cotton-boll separation device
..... Chen Changlin, Kong Fanting, Shi Lei, Xie Qing, Zhang Yutong, Sun Yongfei, Huang Mingsen (75)

Vibration study of the gearbox of hydro-mechanical continuously variable transmission based on Mean Filter Method
..... Xiao Maohua, Zou Fan, Zhang Haijun, Xiao Dengsong, Lu Zhixiong, Zhang Cunyi (82)

Influence of different tillage methods on growth characteristics and maize yield after straw returning
..... Zhu Cunxi, Huang Xin, Wang Weiwei, Qi Haijun, Chen Liqing (88)

Experiment and simulation analysis on high-speed up-film transplanting mechanism
..... Jin Xin, Pang Jing, Ji Jiangtao, Du Xinwu, He Zhitao, Wang Shiguang (95)

Screening model and optimization of grains group by queuing theory on air-and-screen cleaning device
..... Tang Zhong, Li Yaoming, Zhao Huiming, Mei Rongjie, Hui Yi (103)

Design and simulation analysis of chain type sweet potato seedling recycling machine
..... Wei Lele, Lv Zhaoqin, Zheng Wenxiu, Lu Yao, Liu Zhengduo, Zhu Binbin, Cai Yuhu (112)

Design and dynamic response analysis of rope laying system of roped type rice direct seeding machine
..... Zhang Baofeng, Song Yuqiu, Wu Liyan, Xin Mingjin, Ren Wentao (120)

Pulsed vacuum drying kinetics of Goji berry (*Lycium barbarum* L.)
..... Yang Xuhai, Zhang Qian, Deng Lizhen, Xie Long, Fang Xiaoming, Gao Zhenjiang, Kan Za (130)

Optimal agricultural production decision model based on futures hedging
..... Yu Xing, Liu Guibo, Kun Wen (141)

Enhancement of lutein biosynthesis in *chlorella vulgaris-1068* under low temperature and luminosity stress conditions
..... Wang Wanqing, Chen Mingyang, Liu Jie, Hua Wei, Wu Shuang, Diao Mengjie, Cheng Yanling (151)

Effects of purple yam polysaccharides (PYPs) on the liver and brain in a D-galactose-induced model of aging in rats
..... Zhang Limei, Song Shuhui, Gan Jing, Satoru Nirasawa, Cheng Yongqiang (157)

Effects of drying modes followed rough rice harvesting on the texture and taste properties of rice
..... Zhang Qiang, Lan Haipeng, Zheng Xianzhe, Liu Nian (166)

Identification of vegetable pests using spectral clustering analysis
..... Xia Ji'an, Yang Yuwang, Cao Hongxin, Zhang Wenyu, Ge Sijun, Chen Guangwei (176)

Effect of fermentation by different strains on the soybean oligosaccharide content in douchi
..... Gan Jing, Wang Yongquan, Shi Lin, Cai Kun, Yin Lijun, Satoru Niarasawa, Cheng Yongqiang (184)

Counting method of wheat stripe rust spores based on shape factor and improved Harris corner detection
..... Jiao Lin, Niu Leilei, Lei Yu, He Dongjian, Yang Shuqin, Song Huaibo (193)

Preparation of antihypertensive peptides from broad bean by compound enzymatic hydrolysis
..... Tang Jie, Tian Yang, Chen Cunkun, Tao Sha, Meng Yue, Xue Wentong (200)

Bacterial diversity in home-made paocai brine of different ages by SMRT sequencing
..... Cao Jialu, Hou Qiangchuan, Yu Zhongjie, Xu Haiyan, Sun Zhihong, Zhang Liebing (213)

Experiment on mechanical properties of processing tomatoes and theoretical study of fruit-seedling separation
..... Du Xinwu, Ji Jiangtao, Lv Huangzhen, Wang Shiguang, Yang Xulong (221)

A multi-attribute decision model for performance assessment of eco-village construction in China
..... Zhang Biao, Fu Zetian, Zhang Lingxian, Liu Hailin (227)

A radio frequency based positioning and alarm device for rural nursing homes for the elderly
Li Hui, Hua Ruoxue, Li Wenjie, Li Xinxing (238)
Adhesive sweet pepper fruits segmentation method based on AHE and normalized cut
Niu Peiyun, Ye Haijian, Liu Chengqi, Lang Rui (248)
AgriCore: an agricultural application specific chip
Zhang Ganghong, Xiao Wan'ang, Gao Wanlin, Yu Lina, Zhang Guofeng, Zhong Zhen (255)
Application research on intelligent irrigation system based on frequency conversion technology and AGA in China
Huang Yeda, Xiao Yutian, Wei Wenqiang, Wu Yang, Zhai Qingzhi, Zhu Xinzhi, Yang Shuo (263)
Construction and specification of complex events from sensor network data in farmland
Li Xiang, Wei Xiaohong, Chen Xin, Tang Xianglu, Xie Taomin, Jia Lu (269)
Cultivating online: an analysis on an agricultural Q&A community
Li Xiang, Gu Liyang, Chen Xin, Liu Lei, Jia Lu (283)
Design and experiment of high-throughput maize ear analysis platform
Cui Xuelian, Ma Qin, Zhu Dehai, Guo Hao, Liu Zhe, Zhang Xiaodong, Yang Liangdi (292)
Design and implementation of IoT-based beef cattle breeding system
Hao Shangbo, Cai Saihua, Sun Ruizhi, Li Jiayao, and Cheng Chunming (302)
Design and implementation of a selenium-rich grape disease diagnosis expert system
Li Hui, Zhou Jing, Zhang Biao, Zhang Lingxian (310)
Design and realization of agricultural intelligent inspection robot Chen Zhichang, Gao Wanlin (320)
Design of an automatic pipettor for ISE based on soil nutrient detection
Zheng Jie, Zhang Miao, Wang Maohua, Pan Linpei, Li Yanhua, Yang Qingliang, Chen Ming (327)
Diseases warning system for spinach based on genetic-BP network algorithm
Zhang Lingxian, Gu Dongyue, Liu Chundi, Zou Chunyu, Li Xinxing (333)
Evaluation model for water environment of Eriocheir sinensis ponds based on AdaBoost classifier
Liu Yiran, Duan Qingling, Zhang Lu (340)
Farmer skill training system based on motion sensing technology and user behavior analysis
Cai Yifeng, Ma Qin, Wang Qing, Chen Hong, Lu Yi, Feng Tianwei, Zhang Ya (349)
High throughput measurement algorithm of maize ear 3D phenotype based on multi-view stereo vision
Ma Qin, Zhang Qinchuan, Zhu Dehai, Guo Hao, Yang Ling (356)
Image segmentation method of adherent corn ears based on improved watershed
Zhang Ya, Ma Qin, Zhu Dehai, Liu Zhe, Zhang Xiaodong, Zhang Fan (367)
Impacts of fertilization rate on soil quality in Taihu Lake watershed Xu Wenping, Gao Hongju (375)

Monitoring spike differentiation stages of winter wheat based on land surface temperature time series and Kalman Filter
..... Liu Junming, Pan Peizhu, Wang Pengxin, Cui Zhenzhen, Hu Xin (385)
Remote crop water requirement monitoring system based on multi-sensor
..... Wang Yongqian, Fan Lifeng, Huang Lan, Zhao Pengfei, Wang Ziyang, Wang Zhongyi (399)
Service modes of agricultural information based on network technology
..... Hu Hui, Gao Wanlin, Shi Kaite (410)
Short-term prediction model for ammonia nitrogen in aquaculture pond water based on optimized LSSVM
..... Chen Yingyi, Cheng Yanjun, Cheng Qianqian, Yu Huihui, Li Daoliang (416)
Detection method of moving object pig based on difference method and energy minimization
..... Li Yue, Sun Longqing, Zou Yuanbing, Li Yiyang (428)

Impact of tire compaction on hydro-thermal feature of sandy and loam soils

Wang Xianliang, Wang Qingjie*, Li Hongwen, He Jin, Lu Caiyun, Niu Qi, Xu Qimeng, Zhang Yufan, Huang Xingyuan

(College of Engineering, Beijing Key Laboratory of Optimized Design for Modern Agricultural Equipment, China Agriculture University, Beijing, 100083, China)

Abstract: In order to study the effect of soil compaction on soil hydro-thermal feature, field experiments were carried out on sandy and loam soils in Hebei Province. The experiments were performed in randomized complete block design with three replications. Effects of five different kinds of compaction frequencies (1, 3, 5, 7 and 9 times) and a control treatment of no compaction on soil volume water content, soil water storage, soil temperature and crop yield were analyzed. The results showed that soil compaction could increase soil bulk density under sandy and loam soils at 0-40 cm soil depth. From the entire growth cycle analysis, soil compaction treatment significantly increased the soil volume water content and water storage, the 9 passes maximum increase by 35.4%, 34.1% respectively, compared to control treatment on sandy soil; 3 passes treatment could increase the soil volume water content and water storage on loam soil, the maximum growth rate were 12.4%, 9.1% respectively, compared to control treatment, at 0-20 cm soil depth. Reversely, soil compaction could decrease volume water content and soil water storage on sandy and loam soil at 20-80 cm soil depth. During the whole growing season, soil compaction decreased soil temperature at 0-10 cm soil layer, the range of temperature reduction were 6.8%-19.3% on sandy soil, 6.7%-50.3% on loam soil, respectively. However, soil compaction treatment has no significant effect on soil temperature at 20 cm depth on flaxen and loamy soil. Soil compaction could decrease maize yield, caused a decline in maize yield of 0.3%, 1.0%, 5.6%, 6.1%, 9.3% in sandy soil, 0.6%, 3.6%, 6.9%, 12.0%, 17.1% in loam soil, respectively, with 1, 3, 5, 7 and 9 pass, compared to control treatment. Sb, we can take advantage of the soil hydro-thermal feature principle in farm production, such as adjusting the suppression device combination the climate, to keep the good moisture and temperature condition. And this study also can be helpful in the promotion of the soil hydro-thermal feature in compacted areas under different soil type in North China.

Keywords: tire, soil compaction, soil hydro-thermal feature, crop yield

Citation: Wang, X. L., Q. J. Wang, H. W. Li, J. He, C. Y. Lu, Q. Niu, Q. M. Xu, Y. F. Zhang, and X. Y. Huang. 2017. Impact of tire compaction on hydro-thermal feature of sandy and loam soils. International Agricultural Engineering Journal, 26(3): 1–11.

1 Introduction

The distribution of water and heat in soil is an important indicator of the energy cycle of soil material, which has important influence on soil comprehensive characteristics and crop growth. Research shows that the suitability of soil moisture and temperature is the most important environmental feature for crop growth. For instance, the unsuitable soil moisture and temperature significantly delayed crop growth, especially in seedling stage (Helms et al., 1996). At present, agricultural machinery in China increasingly developed into the large scale, and operations were up to 11 times from sowing to harvesting, which destroyed the soil structure and caused soil compaction (Botta et al., 2008; Wang et al., 2015). Soil compaction decreases porosity between soil particles, reduces soil macrospores, water movement and the energy exchange between the upper and lower layers, which ultimately affects crop growth (Botta et al., 2016;

Received date: 2017-07-03 **Accepted date:** 2017-07-20

* **Corresponding author:** Wang Qingjie, Associate Professor, College of Engineering, China Agricultural University, No.17, Qinghua East Road, Haidian District, Beijing 100083, China. Email: wangqingjie@cau.edu.cn.

Wang et al., 2016). Therefore, further study on the effect of soil compaction on soil temperature and moisture characteristics is of great significance to the sustainable development of soil.

Currently, studies on soil compaction mainly focused on effects of compaction on soil properties and crop growth. For example, Ewa A Czyz et al. (2004) studied effects of agricultural machinery rolling on soil bulk density and barley growth, the results showed that compaction could increase soil bulk density, reduce soil oxygen flux and reduce barley yield. Onã da Silva Freddi et al. (2007) studied on effects of soil compaction on root growth and maize yield, the results indicated that compaction could seriously inhibit the growth of maize roots and reduce the yield.

Studies on soil thermal and moisture regimes mainly focused on the effects of surface cover and irrigation on soil hydrothermal properties. For instance, Yin et al. (2014) studied on effects of no-tillage straw mulching mode and straw -plastic film dual mulch mode on soil temperature and moisture characteristics, the results showed that dual mulch mode could effectively increase the surface soil temperature and improve the water content of topsoil in the early stage, and provide good hydrothermal condition for maize growth. Chen et al. (2013) studied on effects of straw mulching quantity on the spatiotemporal variation of soil moisture in freezing season, results showed that straw mulching thickness of 10-15 cm could maximumly ease the freezing damage and enhance soil moisture. By studding effects of drip irrigation frequency on the growth of spring maize and distribution of soil water and heat in North China, Wang et al. (2008) found that high frequency irrigation could significantly promote the distribution of spring maize roots in the upper soil (0-40 cm) and suggested low frequency drip irrigation for spring maize in north China. In summary, researchers mainly studied soil compaction and soil temperature and moisture characteristics, while effects of soil compaction on soil moisture and temperature were not studied systematically.

In this paper, field experiments were conducted in the typical soil types of sandy and loam. By measuring soil moisture, water storage, temperature and maize yield, we studied the effects of soil compaction on soil thermal and moisture regimes and maize yield. The relationship between soil compaction and soil hydro-thermal feature under two soil types was shown clearly in this paper. This paper can provide some guidance for the further understanding of soil compaction.

2 Materials and method

2.1 Site and climatic conditions

Experiments were conducted in sandy and loam soil at two sites, respectively. Experiment 1 was conducted in Tillage Conservation and Observation Experimental Station of China Agricultural University (Site 1), which located in Dongchengfang town (39°28′N, 115°56′E) of Zhuozhou, Baoding City, Hebei Province. Experiment 2 was conducted in Nanbingshang Village (40°00′N, 113°40′E) (Site 2) of Dongwenshan, Laishui County, Hebei Province. The soil in site 1 and site 2 was classified as sandy soil and loam soil, and the mean field capacity of each site in 0 to 80 cm were11.3% and 18.6%, wilting water content were 1.2% and 8.1%, and thermal conductivity were 0.52 and 0.31 W m^{-1} k^{-1} respectively. The specific soil properties were shown in Table1. The average yields of maize in the past 5 years were 10015.5 and 11024.6 kg hm^{-2} respectively.

Table 1 Soil properties of the experiment field

Field	Agrotype	Mechanical composition, %			Bulk density, g/cm	Organic matter, g/kg	pH
		<0.002 mm	≥0.002-0.02 mm	≥0.02-2 mm			
1	Sandy	13.6	25.1	61.3	1.42	5.38	7.6
2	Loam	14.9	35.8	49.3	1.33	11.5	7.9

Two sites are characterized by a typical warm temperate of semi-humid continental monsoon climate. During the experimental period, the average temperature and total accumulated temperature were 11.6°C and 4198°C (with 178 frost-free days), respectively, and the annual rainfall was 450 mm. The temperature and rainfall of the two sites were shown in Figure 1. The planting system is double cropping of winter wheat and summer maize.

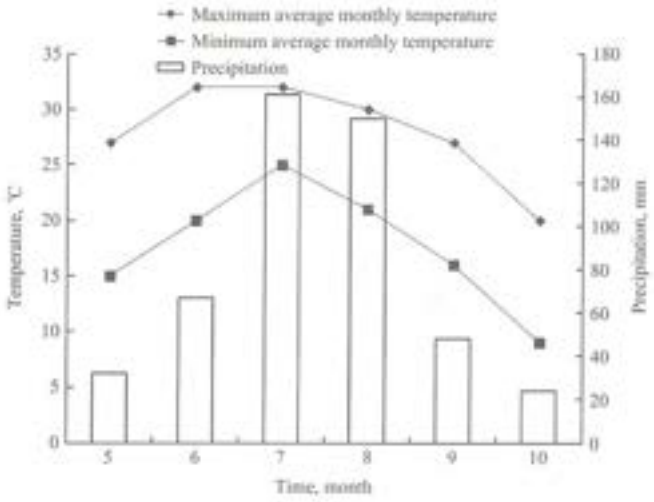

Figure 1 Temperature and rainfall during maize growth period in 2016

2.2 Agronomic measures

Site 1: The farming system was adopted as follow: wheat harvest—No-tillage maize planting—spraying—maize harvest—straw crushing and returning—No-tillage wheat planting from 2011.

Site 2: The farming system was adopted as follow: wheat harvest—No-tillage maize planting—spraying and weed controlling—maize harvest—partial straw crushing and returning—subsoil—wheat planting from 2013.

During the experimental period, the variety of maize was Zhengdan 958, the type of seeder was 2BMZH-3, the maize was uniformly planted with a spacing of 20 and 60 cm respectively, and fertilizers were applied at the following rates: 284 kg N ha^{-1}, 102 kg P_2O_5 ha^{-1} and 95 kg K_2O ha^{-1}. During the entire growing season of maize, there was no water treatment and plow pan phenomenon because the no-tillage treatment and subsoil treatment were applied in site 1 and site 2, respectively.

2.3 Experimental design

Select Lovol Lepopard 904 tractor as compaction equipment in the experiment, its weight was 4155 kg. The tire parameters were shown in Table 2.

Table 2 Parameters of compactness tractor

Specification	Standard type	Tire width, mm	Tire pressure, kPa	Wheelbase, mm
Front tires	12.4-24	315	85	1610
Rear tires	16.9-34	430	100	1608

Six treatments of different compaction time were designed: 0(C_0), 1(C_1), 3(C_3), 5(C_5), 7(C_7) and 9(C_9). No-compaction treatment 0 was control group, where the crop zone was permanent separated with machine compaction zone to avoid soil compaction caused by field management. Each treatment was tested three times, namely18 compaction experiments were set in total. The field experimental design of each treatment was shown in Figure 2, and each plot was 15 m wide by 20 m long.

Two weeks before the experiment, the field was completely subsoiled at a depth of 50 cm. In the experimental process of soil compaction, there was a 2 h interval among the each compaction of tractor.

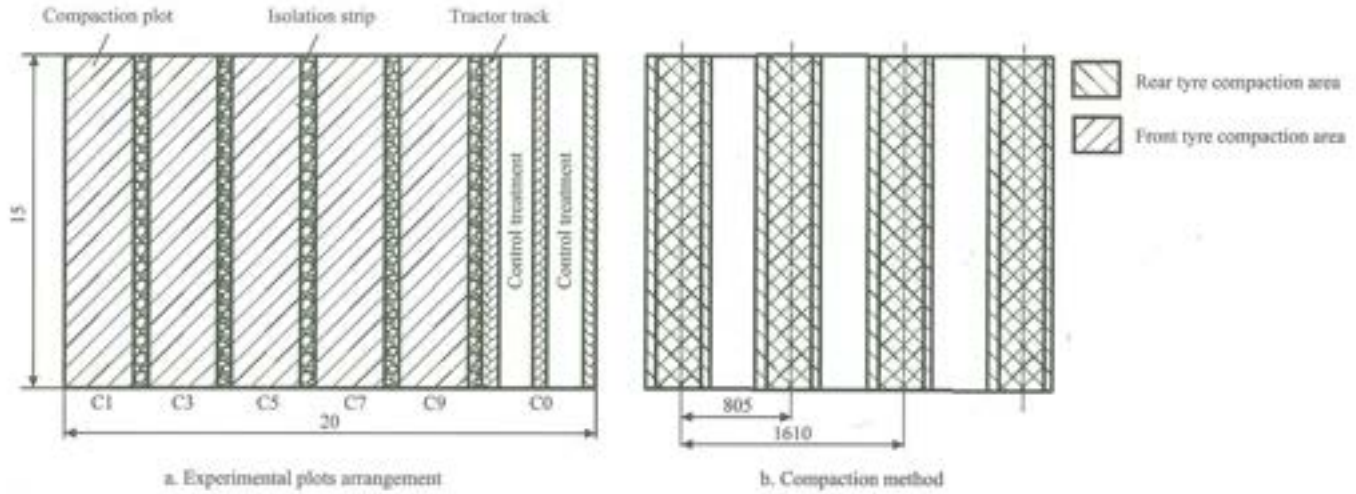

a. Experimental plots arrangement b. Compaction method

Figure 2 Field specific operation

2.4 Measurement

2.4.1 Soil bulk density

Soil bulk density was measured by drying method. Aiming at two kinds of soil in site 1 and site 2, all the undisturbed core samples were collected at the 0 to 10, 10 to 20, 20 to 30, 30 to 40 cm soil depths, which were taken by using a stainless steel core sampler (50.46 mm diameter by 50 mm length) and then stored in aluminum

boxes (100 cm^3). Every soil sample was taken on the tractor lane under different compaction frequencies randomly. Then the samples were dried at 108°C to a constant weight, weighed soil bulk density.

2.4.2 Soil water content monitoring of different depth in maize growing period

Soil water content was measured at four keys growing period including seeding stage, elongation stage, filling stage and maturation stage, and it was measured at 0 to 10, 10 to 20, 20 to 30, 30 to 40, 40 to 60, 60 to 80 cm soil depths respectively by using AZS-2 soil moisture measurement instrument.

Soil water storage was calculated as follow:

$$C = \sum(\Delta\theta_i \times h_i) \quad (1)$$

where, C is soil water storage, mm; $\Delta\theta_i$ is a layer of soil volume water content,%; h_i is the thickness of a layer soil, mm; i is soil layer.

2.4.3 Dynamic change of soil temperature

The soil temperature was recorded by HOBO soil temperature and moisture real-time system which consisted of data collector (4/15 channel), temperature sensor and solar energy panel. The temperature sensor probe was embedded in 10 cm and 20 cm under soil surface among the maize, and the stainless steel probe had a strong anticorrosion ability, which can be embedded in soil layer to monitor soil temperature in a longtime. The data was automatically collected and recorded every 30 minutes.

2.4.4 Maize yield

According to the principle of random sampling, select three 1 × 1 m^2 zones in each ploy, and record maize spike number, row number per maize spike and grain number per row in this zone. After threshing and drying to a constant weight, calculate the hundred-grain weight of maize, thus the yield can be calculated as:

$$Y = (H \times M \times W)/100000 \quad (2)$$

where, Y is maize yield, kg hm^{-2}; H is maize spike number per hectare; M is grain number; W is hundred-grain weight, g.

2.5 Data analysis

The experimental data was analyzed by Microsoft Excel 2003 software and IBM SPSS Statistics 20 software, significance test was performed by LSD method, and significance level was selected as 0.05.

3 Results

3.1 Soil bulk density

Table 3 shows the effects of different compaction times on soil bulk density in sandy soil and loam soil, respectively. As is shown in Table 3, soil bulk density of 0-40 cm increased with the soil depth increasing for each treatment. Soil compaction can significantly increase soil bulk density in 0-40 cm soil layer, compared with C_0 treatment, the average soil bulk density of sandy soil treated with C_1, C_3, C_5, C_7 and C_9 increased by 6.3%, 20.3%, 22.7%, 29.7%, 34.4%, respectively. The average soil bulk density of loam soil treated with C_1, C_3, C_5, C_7 and C_9 increased by 10.3%, 19%, 24.6%, 36.5%, 39.7%, respectively.

Table 3 Varieties of soil bulk density under different experiment treatment

Soil	Soil depth	Bulk density for treatment						LSD $P \leq 0.05$
		C_0	C_1	C_3	C_5	C_7	C_9	
Sandy	0-10	1.22	1.30	1.47	1.49	1.62	1.68	0.022
	10-20	1.25	1.33	1.51	1.53	1.66	1.72	0.017
	20-30	1.31	1.40	1.58	1.61	1.67	1.73	0.028
	30-40	1.33	1.41	1.59	1.63	1.69	1.75	0.047
	Average	1.28	1.36	1.54	1.57	1.66	1.72	0.032
Loam	0-10	1.18	1.39	1.47	1.49	1.68	1.69	0.021
	10-20	1.23	1.44	1.53	1.57	1.71	1.74	0.04
	20-30	1.29	1.34	1.50	1.61	1.73	1.79	0.012
	30-40	1.35	1.39	1.51	1.62	1.76	1.80	0.048
	Average	1.26	1.39	1.50	1.57	1.72	1.76	0.033

3.2 Soil moisture content

Figure 3 is the effect of soil compaction on soil volumetric moisture content during the critical growth period of summer maize under sandy and loamy soil. From Figure 3a, it can be seen that under the sandy soil condition, the volume moisture content of soil surface (0-20 cm) increased with the increase of soil compaction times. At seedling stage, the volumetric moisture content of soil treated with C_0 was 8.6%, 9.4%, 21.6%, 26.6%, 33.8% lower in comparison with C_1, C_3, C_5, C_7 and C_9, respectively; At elongating stage, it was 24.8%, 32.5%, 30.9%, 25.6% and 25.9% lower, respectively; at grain filling stage, it was lower than 9.1%, 11%, 8.5%, 8.3%, 8.4%, accordingly; at maturation stage, it was lower than

54.8%, 60.7%, 63.7%, 65.5%, 66.1%, accordingly. However, the average soil volumetric water content in 20~80 cm soil layer decreased with the increase of soil compaction times, at seedling stage, the volumetric moisture content of soil treated with C_0 was 20.3%, 32.4%, 51.7%, 60.2%, 69.9% higher in comparison with C_1, C_3, C_5, C_7 and C_9, respectively; at elongating stage, it was higher than 20.3%, 24.4%, 31.1%, 37.2%, 39.3%, accordingly; at grain filling stage, it was higher than 2.6%, 5.9%, 11.2%, 17.9%, 23.7%, accordingly; at maturation stage, it was higher than 48.3%, 83.6%, 103%, 165.4%, 215.9%, respectively.

Figure 3b shows that under the loam soil condition, the volumetric moisture content in the 0-20 cm soil layer from top to bottom is C_3, C_1, C_0, C_5, C_7, C_9 during the whole growth period, and the average volume moisture contents are 20.1%, 18.8%, 17.9%, 16.2%, 14%, 13.1%, respectively. However, soil compaction could decrease moisture content at 20-80 cm layer, the mean volumetric moisture content from C_0 to C_9 treatment, during the whole growth period were 23.1%, 20.8%, 19.6%, 17.7%, 16.5%, 15.8% respectively.

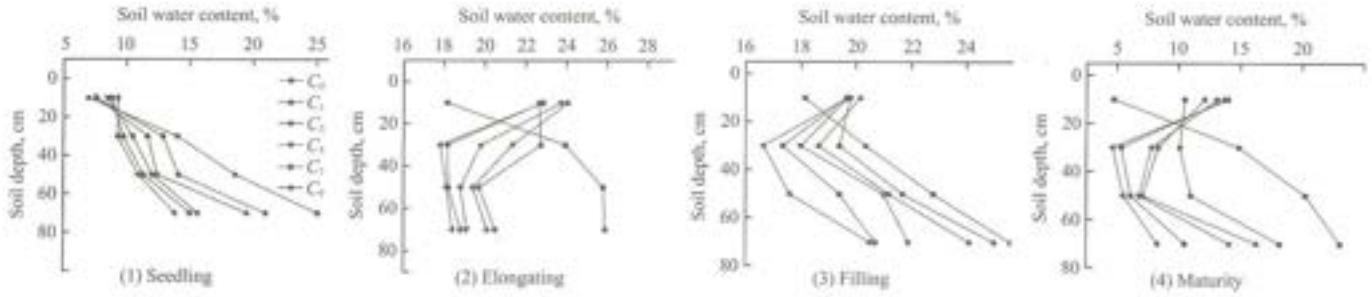

a. Sandy soil

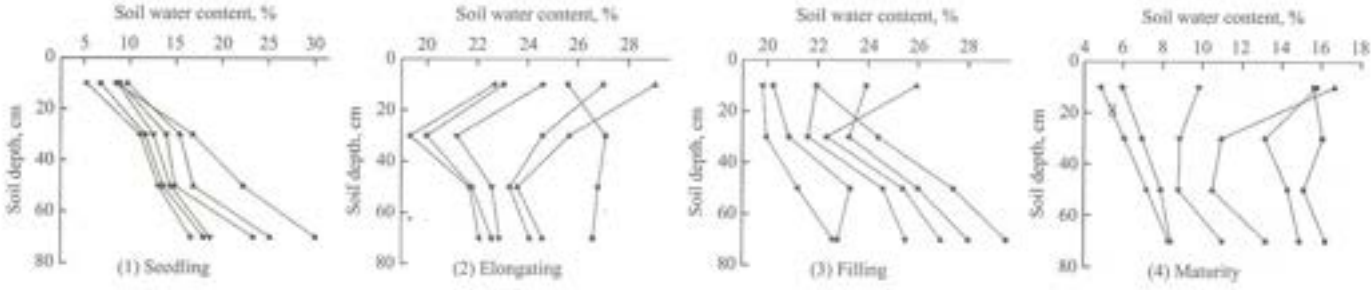

b. Loam soil

Figure 3 Effect of soil compaction on soil volumetric water content

3.3 Soil water storage

Table 4 shows the influence of soil compaction on soil water storage during the critical growth period of maize. Under the sandy soil condition, the effect of soil compaction on soil water storage displayed differences at four critical maize growing seasons. During seeding and maturity growth stage, C_3, C_5, C_7 and C_9 treatment could significantly increase soil water storage compared to C_0 and C_1 treatment at 0-20 cm depth. During elongating and filling stage, C_3 treatment has the maximum soil water storage compared to C_0, C_1, C_5, C_7 and C_9 treatment at 0-20 cm depth. Under the loam soil, during seeding and maturity growth stage, C_3 treatment has the maximum soil water storage, while C_0 has maximum soil water storage during elongating and filling stage at 0-20 cm depth. The soil compaction could decrease soil water storage during each four growth stage at 20-80 cm depth.

Under the sandy soil condition, the average water storage of soil, during the whole season, treated with C_0 in 0-20 cm soil layer was 20.7%, 24.9%, 26.2%, 26%, 27% lower than that of C_1, C_3, C_5, C_7 and C_9 soil, respectively; in 20-80 cm soil layer, it was 18.2%, 27.8%, 37.8%, 50.4%, 58.5% higher, respectively. Under the loam soil condition, C_0, C_1, C_3 treatment could significantly increase the average water storage in the 0-20 cm soil layer compared to C_5, C_7, C_9 treatment. And the C_3 treatment, which has maximum soil water storage, is 4.3% higher compared to C_0 treatment. C_9 treatment, which has minimum soil water storage, is 41.8% lower compared to C_0 treatment. In the 20-80 cm soil layer, the water storage of soil treated with C_0 was higher than C_1, C_3, C_5, C_7, C_9 by 11.4%, 17.6%, 31.1%, 41.0%, 47.6%, respectively.

Table 4 Effect of soil compaction on soil water storage under critical growth period of maize

Type	Depth, cm	Time	C_0	C_1	C_3	C_5	C_7	C_9
Sandy soil	0-20	Seedling	13.9^c	15.1^b	16.2^a	16.9^a	17.6^a	18.6^a
		Elongating	36.3^c	45.3^b	48.1^a	47.5^a	45.6^b	45.7^b
		Filling	36.3^c	39.6^a	40.3^a	39.4^a	39.3^a	39.2^a
		Maturity	9.5^c	21^b	24.2^b	26.2^a	27.5^a	28^a
	Average		24^c	30.3^b	32.0^b	32.5^a	32.5^a	32.9^a
	20-80	Seedling	107.6^a	91.2^b	82.8^c	72.8^d	68.6^e	64.8^f
		Elongating	149.4^a	128.6^b	123.3^b	116.3^c	110^d	108.2^d
		Filling	132.2^a	128.3^b	123.9^c	118.4^d	112.2^e	107.1^f
		Maturity	109.8^a	74.1^b	60.2^c	54.8^d	41^e	34.7^f
	Average		124.7^a	105.5^b	97.5^c	90.5^d	82.9^e	78.7^f
Loam soil	0-20	Seedling	17^b	17.8^b	20.4^a	17.3^b	13.6^c	10.6^d
		Elongating	52.5^c	52^c	52.1^c	49.2^d	46.1^e	45.4^e
		Filling	49.9^a	49.8^a	50.3^a	43.9^b	40.43^c	39.6^c
		Maturity	31.2^a	30.5^a	31.3^a	19.6^b	11.9^c	9.7^c
	Average		37.6^a	37.9^a	38.1^a	32.5^b	28^c	26.3^c
	20-80	Seedling	129^a	109.4^b	99.3^c	87.3^d	82.35^e	77.9^f
		Elongating	161.4^a	149.9^b	144.3^b	131.9^d	126.6^e	123.8^f
		Filling	158.6^a	150.8^b	145.5^c	140^d	131.7^e	125.6^f
		Maturity	95.1^a	83.3^b	68.4^c	56.3^d	45.3^e	41.4^f
	Average		136.0^a	123.1^b	114.6^c	103.8^d	96.5^e	92.1^f

Note: Values with different letters (horizontal) show significant differences among treatments (P<0.05).

3.4 Soil temperature

Figure 4 shows the effect of soil compaction on soil temperature in 0-20 cm soil layer aimed at two soil types, and the effect varies with depth and climate temperature. By Figure 4a, under the sandy soil, when the average temperature is higher than 22°C, the soil temperature of 0-10 cm depth decreases with the increase of soil compactness, soil temperature treated with C_0 was 6.8%, 7.7%, 10.9%, 17.1%, 19.3% higher in comparison with C_1, C_3, C_5, C_7, C_9 treatment, respectively; when the average temperature is lower than 22°C, the C_1, C_3, C_5 treatments have the higher temperature, while temperature of C_7, C_9 is lower, compared to controlled treatment C_0. And the average temperatures were 16.4°C, 17.3°C, 16.8°C, 16.6°C, 15.6°C, 15.3°C, accordingly. Figure 4b shows that in the whole growth period, the soil temperature of 20 cm depth from top to bottom was C_0, C_1, C_3, C_5, C_7, C_9 successively, and the average temperatures were 14.62°C, 14.33°C, 13.7°C, 13.21°C, 11.96°C, 10.92°C, respectively.

By Figure 4c, under the loam soil, when the average temperature is higher than 25°C, the soil temperature of 0-10 cm depth decreases with the increase of soil compactness, soil temperatures treated with C_0 were 6.7%, 11.4%, 21.5%, 35.1%, 50.3% higher in comparison with C_1, C_3, C_5, C_7, C_9 treatment, respectively; when the average temperature is lower than 25°C, the C_1, C_3 treatments have the higher temperature, while temperature of C_5, C_7, C_9 is lower, compared to the controlled treatment of C_0. The average soil temperatures from top to bottom C_1, C_3, C_0, C_5, C_7, C_9 were 17.2°C, 18.5°C, 17.8°C, 16.4°C, 14.7°C and 13.3°C, respectively. As shown in Figure 4d, the soil temperatures of 20 cm depth ranged from top to bottom were C_0, C_1, C_3, C_5, C_7, C_9, successively, and the average temperatures are 16.5°C, 16.2°C, 15.5°C, 15.1°C, 14.8°C, accordingly.

3.5 Maize yield

Table 5 shows the effects of soil compaction on maize yield under different soil types. Soil compaction can reduce maize yield, under loam soil condition, compared with C_0 treatment, maize yield dealt with C_1, C_3, C_5, C_7 and C_9 treatments decreased by 0.6%, 3.5%, 6.5%, 10.7%, 14.6%, respectively, their hundred-grain weight decreased by 0.2%, 1.3%, 3.2%, 5.1%, 13.6%, accordingly. Under sandy soil condition, compared with

C_0 treatment, maize yield dealt with C_1, C_3, C_5, C_7 and C_9 treatments decreased by 0.3%, 1.0%, 5.3%, 5.7%, 8.5% respectively, their hundred-grain weight decreased by 0.5%, 1.7%, 4.7%, 7.9%, 13.1%, accordingly.

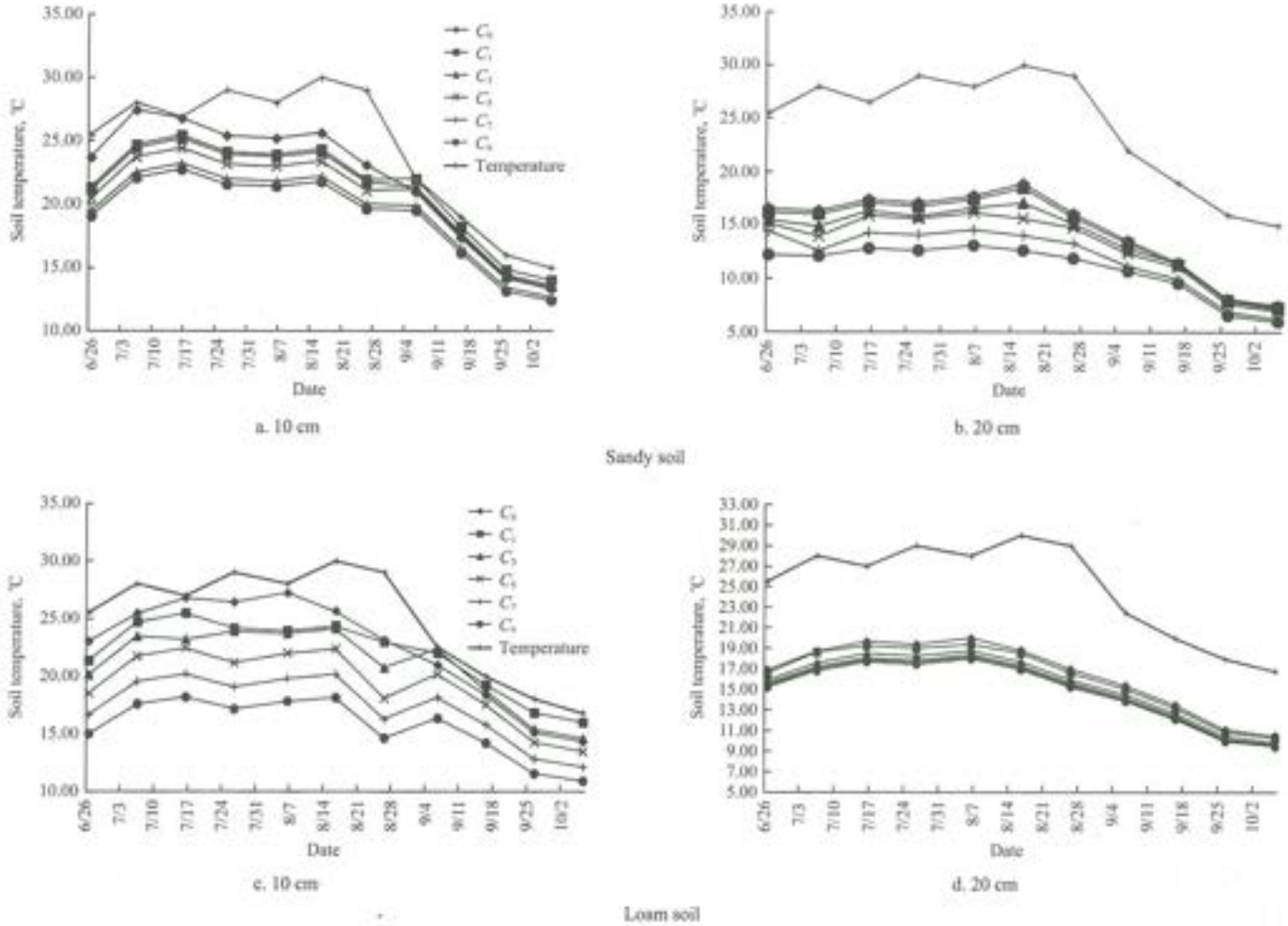

Figure 4 Effect of soil compaction on soil temperature during maize growth period

Table 5 Effect of soil compaction on maize yield

Soil type	Treatment	Grain number per ear	100-grain weight, g	Yield, kg hm^{-2}
Sandy	C_0	632.1^a	40.6^a	10023.2^a
	C_1	627.7^a	40.4^a	9993.1^a
	C_3	617.3^a	39.9^a	9924.0^a
	C_5	613.7^a	38.7^a	9491.7^b
	C_7	581.0^b	37.4^a	9446.9^b
	C_9	544.4^c	35.3^b	9170.4^c
Loam	C_0	645.1^a	45.3^a	11082.4^a
	C_1	638.1^a	45.2^a	11016.3^a
	C_3	625.7^b	44.7^a	10697.3^a
	C_5	618.5^b	43.9^a	10367.1^b
	C_7	584.3^c	43.1^a	9895.0^b
	C_9	549.0^d	39.9^b	9464.0^c

Note: The difference between the letters in each column indicates a significant difference under different soil types.

4 Discussion

4.1 Effect of soil compaction on soil bulk density

Soil bulk density is an important index to judge whether the soil is compacted by external forces and has a great significance to judge whether the soil is suitable for crop growth (Ewa et al., 2004). Patel et al (2011) found that the soil bulk density changes caused by tractor compaction 16 times were mainly concentrated in 0-20 cm soil layer, and the maximum soil bulk density appeared in 15-20 cm soil layer. Horn et al. (1998) found that the soil bulk density increased by 10 times soil compaction was mainly concentrated in 0-30 cm soil layer. The results showed that soil compaction 9 times can significantly increase the soil bulk density of 0-40 cm, and the main reason for the deviation of the results of Patel and Horn is that the soil texture is different, which leads to the different bearing capacities of the soil to the external force, and the different factors such as the weight of the compaction device, the grounding area caused by compaction device tire type. Soil moisture content is the

most important factor affecting soil compaction (Nidal et al., 2003), which could increase soil stress transmission coefficient (He et al., 2017), the soil stress could propagate to deeper soil and increase deep soil bulk density.

4.2 Effects of soil compaction on soil moisture

A large number of studies (Wang et al., 2000, Wang et al., 2014, Li et al., 2000, Li et al., 2002) have shown that soil infiltration, evaporation, soil organic matter content, soil aggregate content, bulk density and other soil parameters have a decisive effect on soil water content during the crop growth cycle. Under sandy soil condition, the soil moisture contents of 0-20 cm treated soil layer with C_0 treatment were 24.3%, 28.4%, 31.2%, 31.5%, 33.6%, less than C_1, C_3, C_5, C_7 and C_9 in the whole corn growing period. The main reason for the increase in soil moisture content is that soil compaction increases soil capillary space, while non capillary voids and water holding spaces decrease significantly. Porosity is the key factor affecting soil water infiltration, which results in the decrease of soil infiltration rate and the influence of soil moisture on deep movement during rainfall irrigation (Qin, 2003). The precipitation mainly concentrated on the surface, and increase the compaction of soil capillary porosity content, increase capillary force (Huang, 2000), reduce soil evaporation, increase soil field capacity (Botta et al., 2008, Li et al., 2000, Yang et al., 2006), to a certain extent, the soil moisture enhanced drought ability, this also explains that compaction can increase soil water storage in sandy soil of 0-20 cm. However, under loam soil condition, during the whole growth period of corn, the average volume moisture contents of 0-20 cm surface soil from large to small are C_3, C_1, C_0, C_5, C_7 and C_9, the main reason of the difference between two types of soil is that the soil micro aggregate composition and sensitivity to soil compaction (Lu et al., 2015), under the condition of loam soil, the multiple compaction of the tractor can cause serious soil compaction, destroy soil aggregates, reduce soil porosity (Botta et al., 2009), reduce soil water infiltration, and lead to water runoff and evaporation. It should be noted that although compaction can increase soil moisture content to a certain extent, compaction increases soil penetration resistance and increases soil wilting point, so the maximum available water content of compacted soil is reduced (Yang et al., 2006). During the whole growth period, the average soil water contents and storage capacities of 20-80 cm soil from large to small were C_0, C_1, C_3, C_5, C_7, C_9 under the condition of sandy soil and loam soil, the main reason may be that soil compaction prevents soil moisture from moving downward, leading to the difficulty of supplying deep soil moisture, and the absorption of deep soil moisture by maize roots, resulting in a decrease in soil moisture.

4.3 Effects of soil compaction on soil temperature

Soil temperature is one of the most important factors in the soil microbes and crop growth. The root and seedling growth were affected by soil temperature characteristics directly, moreover the atmosphere near the ground warm conditions also was affected by the soil moisture evaporation and migration directly or indirectly (Zhai et al., 2012; Cai et al., 2013). The climate played an important role for the topsoil temperature, when the average temperature is higher than 22°C, the temperature presented a decreasing order of C_0, C_1, C_3, C_5, C_7 and C_9, while the temperature is lower than 22°C, temperature presented a decreasing order of C_1, C_3, C_5, C_0, C_7 and C_9, under sandy soil condition. Under the loam soil condition, when the average temperature is higher than 25°C, temperature presented a decreasing order of C_0 to C_1, C_3, C_5, C_7 and C_9, while the temperature is lower than 25°C, temperature presented a decreasing order of C_1, C_3, C_0, C_5, C_7 and C_9. That is because of the soil compaction destroyed soil physical properties, furthermore blocked soil gas exchange with the atmosphere (Kuncoro et al., 2014). Figure 1 shows that the climate temperature in the early stage of corn growth is low, and gradually increasing, reached to the highest temperature in July. In August, the temperature began to decline, and the soil temperature also decreased. The results showed that when soil temperature declined from the peak, soil compaction increased daily minimum temperature; on the contrary, it will decrease daily minimum temperature (Botta et al., 2008). The soil is compacted, soil temperature was

blocked about temperature exchange between atmosphere and soil at maize early growing stage at 0-10 cm depth. So, that principle finally leads to the slowly change of soil temperature as atmosphere temperature variation. The main reason for the inconsistency between the two soils is that the loam is more cohesive and sensitive to soil compaction than the sand soil (Thomas et al., 2010). Therefore, C_5, C_7, C_9 treatments resulting in soil structure destroyed seriously, smaller soil heat capacity and higher thermal conductivity because of reducing soil pore under loam soil (Tetiana et al., 2013), consequently, the C_5, C_7, C_9 have lower temperatures than C_0. Under two soil types, the temperature was decreased with the increasing compactness during the whole corn growing season at 20 cm depth. Because of the cumulative effect, soil compaction has a negative effect on soil porosity and energy circulation (Shen et al., 2011, Wang et al., 2011). But the soil temperature differences between treatments are not significant at 20 cm depth, which is consistent with the results of Wang et al. (2008).

4.4 Effects of soil compaction on maize yield

The results showed that soil compaction could decrease maize yield, whether in sandy soil or loam soil. Under sandy condition, compared with C_0 treatment, C_1, C_3, C_5, C_7 and C_9 corn yield decreased by 0.3%, 1.0%, 5.3%, 5.7%, 8.5%; while under the loam soil condition, compared with C_0 treatment, C_1, C_3, C_5, C_7 and C_9 maize yield decreased by 0.6%, 3.5%, 6.5%, 10.7% and 14.6%. It was found that soil drought and crop accumulated temperature were the most important factors for affecting crop yield in two cropping areas a year (Zhang et al., 2013). Soil compaction could reduce differences between the maximum and minimum temperatures each day (Botta et al., 2008). That phenomenon could lead to lower soil temperature at the early stage of maize growth, thereby impairing the root growth and development of maize. And at later stage of maize growth, soil compaction also resulted in a small temperature difference between day and night, which is harmful to sugar accumulation, finally decrease the crop yield (Wu et al., 1998). Soil compaction could decrease soil water storage at 20-80 cm, which resulting in water supply deficiency maize growth needed at critical stage. And compaction hindered the soil water infiltration, which is not conducive to deep soil water supply (Wang et al., 2014). In summary, soil compaction affected the growth of maize yield seriously.

5 Conclusions

In this paper, the research of soil moisture, soil temperature and yield was conducted to study the effects of soil compaction on soil hydro-thermal feature and maize yield by field experiment. The following conclusions were drawn:

(1) Soil compaction could increase soil bulk density both under sandy and loam soils at 0-40 cm soil depth. Soil compaction could increase soil moisture content and soil water storage at 0-20 cm depth, and reduce soil moisture content and soil water storage in 20-80 cm soil layers both under sandy and loam soils.

(2) Soil compaction could reduce crop yields, and 5 passes compaction could significantly decrease maize yields both under sandy and loam soil conditions.

(3) The precipitation condition after compaction could significant decreased the variety of compaction frequency on deep soil (20-80 cm), water content and water storage.

The results show that the compaction has significant influence on soil hydro-thermal feature. Therefore, the results of this study are of guiding significance for the study of tire soil compaction in the double cropping area.

Acknowledgements

This work was supported by the National Key Research and Development Program (2016YFD0700301). We thank all the graduate students working at the Conservation Tillage Research Center, Ministry of Agriculture, providing their inputs to this work.

[References]

[1] Abu-Hamdeh, N. H. 2003. Compaction and subsoiling effects on corn growth and soil bulk density. *Soil Science Society of America Journal*, 67(4): 1213–1219.

[2] Botta, G. F., A.Tolon-Becerra, and D. Rivero. 2016. Compaction produced by combine harvest traffic: Effect on soil and soybean (Glycine max l.) yields under direct sowing

in Argentinean Pampas. *European Journal of Agronomy*, 74: 155–163.

[3] Botta, G. F., A. T. Becerra, and F. B. Tourn. 2009. Effect of the number of tractor passes on soil rut depth and compaction in two tillage regimes. *Soil and Tillage Research*, 103(2): 381–386.

[4] Botta, G. F., D. Rivero, M. Tourn, F. B.Melcon, O. Pozzolo, G. Nardon, and R.Balbuena. 2008. Soil compaction produced by tractor with radial and cross-ply tyres in two tillage regimes. *Soil and Tillage Research*, 101(1): 44–51.

[5] Cai, T. Y., Z. C. Chen, and H. J. Huang. 2013. Effects of different modes of cropping systems using straw mulch on the soil temperature and soil water on the Weibei highland region of China. *Journal of Agro-Environment Science*, 32(7): 1396–1404.

[6] Chen, J. F., X. Q. Zheng, Z. D. Qin, P. Liu, H. F. Zang, and F. Sun. 2013. Effects of maize straw mulch on spatiotemporal variation of soil profile moisture and temperature during freeze-thaw period. *Transactions of the Chinese Society of Agricultural Engineering*, 29(20): 102–110. (In Chinese with English abstract)

[7] Ewa A. Czyz. 2004. Effects of traffic on soil aeration, bulk density and growth of spring barley. *Soil and Tillage Research*, 79(2): 153–166.

[8] Freddi, O. S., C. J. Frederico, and N. B. Amauri. 2007. Effect soil compaction on root growth and maize yield. *Revista Brasileira De CiêNcia Do Solo*, 31: 627–636.

[9] He, T. F., Q. S. Ding, Y. N. Li, R. Y. He, J. L. Xue, and W. Qiu. 2017. Stress transmission coefficient: a soil stress transmission property for a loading process. *Soil and Tillage Research*, 166: 179–184.

[10] Huang, Y. C. 2000. Soil Science. *Beijing: China Agriculture Press*.

[11] Helms, T. C., E. Deckard, and R. J. Goos, and J. W, Enz. 1996. Soil moisture, temperature, and drying influence on soybean emergence. *Agronomy Journal*, 88(4): 662–667.

[12] Horn, R., H. Kretschmer, T. Baumgartl, K. Bohne, and A. Neupert. 1998. Soil mechanical properties of a partly reloosened (split plough system) and a conventionally tilled over consolidated gleyicluvisol derived from glacial till. *International Agrophysics*, 12(3): 143–154.

[13] Kuncoro, P. H., K. Koga, N. Satta, Y. Muto. 2014. A study on the effect of compaction on transport properties of soil as and water. II: soil pore structure indices. *Soil and Tillage Research*, 143(12): 180–187.

[14] Li, H. W., H. W. Gao, J. D. Chen, and W. Y. Li. 2000. Study on controlled traffic with conservation tillage. *Transactions of the Chinese Society of Agricultural Engineering*, 16(4): 73–77. (In Chinese with English abstract)

[15] Li, R. X., C. H. Lin, and H. W. Gao. 2002. The research of soil compaction caused by tractor. *Transaction of the Chinese Society for Agricultural Machinery*, 1(33): 126–129. (In Chinese with English abstract)

[16] Lu, Q. Q., E. H. Wang, and X. W. Chen. 2015. Effect of mechanical compaction on soil micro-aggregate composition and stability of black soil. *Transactions of the Chinese Society of Agricultural Engineering*, 31(11): 54–59. (In Chinese with English abstract)

[17] Patel, S. K., and M. Indra. 2011. Effect of multiple passes of tractor with varying normal load on subsoil compaction. *Journal of Terramechanics*, 48(4): 277–284.

[18] Qin, Y. D. 2003. Soil Physics. *Beijing: Higher Education Press*.

[19] Thomas, K., and L. Mathieu. 2010. Challenges in the development of analytical soil compaction models. *Soil and Tillage Research*, 111(1): 54–64.

[20] Shen, L.X., P. Wang, and L. L. Zhang. 2011. Effects of degradable film on soil temperature, moisture and growth of maize. *Transactions of the Chinese Society of Agricultural Engineering*, 27(6): 25–30. (In Chinese with English abstract)

[21] Tetiana, N. F., S. T. Mykola, L. A. Karim, B. Walter, and B. Rafic. 2013. Methods and results of experimental researches of thermal conductivity of soils. *Energy Procedia*, 42: 775–783.

[22] Wang, J. D., S. H. Gong, and J. Sui. 2008. Effects of drip irrigation frequency on the farmland soil water-heat distribution and spring maize growth in North China. *Transactions of the Chinese Society of Agricultural Engineering*, 24(2): 39–45. (In Chinese with English abstract)

[23] Wang, M., H. X. Wang, Q. F. Han, and R. Zhang. 2011. Effects of different mulching materials on soil water, temperature, and corn growth. *Acta Agronomica Sinica*, 37(7): 1249–1258.

[24] Wang, Q. J., C. Y. Lu, H. W. Li, J. He, K. S. Khoban, J. R. Rabi, and Z. H. Liang. 2014. The effects of no-tillage with subsoiling on soil properties and maize yield: 12-Year experiment on alkaline soils of Northeast China. *Soil and Tillage Research*, 137(3): 43–49.

[25] Wang, X. L., Q. J. Wang, H. L. Li, J. He, and W. Y. Li. 2015. Current research status of soil compaction by agricultural machinery. *Chinese Journal of Tropical Agriculture*, 35(6): 72–76.

[26] Wang, X. Y., H. W. Gao, and Y. X. Li. 2000. Effect of tractor wheel compaction on runoff and infiltration. *Agricultural Research in the Arid Areas*, 18(4): 57–60.

[27] Wang, X.L., Q. J. Wang, X. C. Zhang, K. Zheng, and H. Hu.

2016. The soil compaction forms and research status. *Journal of Agricultural Mechanization Research*, 53(9): 264–268.

[28] Wu, S., S. Y. Zhang, and Y. G. Shen. 1998. Influence of temperature difference between day and night on the growth characteristics in wheat. *Acta Agronomica Sinica*, 24(3): 333–337.

[29] Yang, J. L., G. L. Zhang, Y. G. Zhao, W. J. Zhao, Y. He, and X. L. Ruan. 2006. Effect of compaction on soil water characteristics. *Acta Pedologica Sinica*, 43(1): 33–38.

[30] Yin, T., W. Q. He, C. R. Yan, and S. Liu. 2014. Effects of plastic mulching on surface of no-till straw mulching on soil water and temperature. *Transactions of the Chinese Society of Agricultural Engineering*, 30(19): 78–87. (In Chinese with English abstract)

[31] Zhai, Z. F. 2012. Comprehensive Evaluation of Agricultural Water-Saving Technologies Adapting Climate Change. *Beijing: Chinese Academy of Agricultural Sciences*. (in Chinese with English abstract)

[32] Zhang, X.C., H. W. Li, J. He, Q. J. Wang, Z. Q. Zheng, and P. Jing. 2013. Effects of different tillage managements on characteristics of soil and crop in annual double cropping areas in Northern China. *Transaction of the Chinese Society for Agricultural Machinery*, S1: 4477–8271. (In Chinese with English abstract)

Hydrostatic driving system for self-propelled sprayer

Zou Fan[1], Kang Jingjing[1], Xiao Maohua[1*], Song Xucheng[1], Ji Guojun[2]

(1. *College of Engineering, Nanjing Agricultural University, Nanjing 210031, China;*
2. *Essen Agricultural Machinery Changzhou Co., Ltd., Changzhou 213200, China*)

Abstract: The aim of this paper is to design a transmission system based on HST hydraulic drive technology, which was designed for the traditional self-propelled sprayer when mechanical transmission is large, and it is prone to subsidence and slipping in the field, especially in paddy field. Firstly, the overall transmission scheme was designed on the basis of the overall layout in the medicine box, and the technical parameters were determined according to the working conditions and load analysis. Secondly, the simulation model of the self-propelled sprayer was constructed by AMESim software. Finally, according to the simulation results and the design of the program, the walking performance experiment was carried out on the experimental model of Essen. The experiment was carried out on the performance test of the HST and the speed control analysis. The stable output flow of the main pump is 78.8 L/min, the load stable speed and the load torque are 33.2 r/min, 772.6 N·m, respectively, compared with the traditional mechanical transmission. Left and right roll angles and front and rear pitch angles fluctuation ranges are small. The simulation and prototype experiments showed that the designed transmission system was stable and responsive, and it could meet the requirement of effectively reducing the weight.

Keywords: self-propelled sprayer, HST, transmission system, hydraulic drive, AMESim

Citation: Zou, F., J. J. Kang, M. H. Xiao, X. C. Song, and G. J. Ji. 2017. Hydrostatic driving system for self-propelled sprayer. International Agricultural Engineering Journal, 26(3): 12–18.

1 Introduction

Food is the first necessity of the people, and the high yield of major crops such as rice, soybeans and corn is very important to the livelihood of the people, thus controlling pests and diseases for crops is especially important. At present, the agricultural pest control is mainly used traction sprayers in China, the chassis from the ground to a small gap and high weight makes it difficult to spray on the growth of rice and other tall crops. However, the cultivation of rice in China is mostly located in the south, the soil has complex rheological and thixotropic characteristics. The operating conditions are more complex, and the large and medium-sized plant protection machinery is not suitable for a long time (Gu et al., 2000). Therefore, in order to improve the mechanization level of rice plant protection in China, it is of great significance to develop plant protection machinery driving system which adapts to various working conditions.

Hydrostatic Static Transmission (HST) is widely used in agricultural machinery because of its small size, light weight and easy operation (Gao et al., 2017), such as John Deere's 4730 sprayer (Zaman et al., 2011). HST technology has been applied to tractors (Batte et al., 2006) and combine harvesters in China (Sun et al., 2014), But compared with other countries, in China, there is a big gap among the same type of hydrostatic CVT transmission in quality (Zhang; 2014; Liu et al., 2016).

Compared with the traditional mechanical transmission, the driving mode of hydraulic full drive based on HST has the advantages of small quality when no-load, stable transmission performance, easy maintenance and other advantages (Huang and Su, 2010), can greatly reduce the quality of the spray machine, improve the sprayer in the field especially when the performance of the paddy field walking (Wang et al.,

Received date: 2017-05-31 **Accepted date:** 2017-08-02

* **Corresponding author: Xiao Maohua**, Associate Professor, Doctor. Department of Mechanical Engineering, Nanjing Agricultural University, Nanjing 210031, China. Email: zoufan1997@163.com.

2014). Therefore, a transmission scheme based on HST technology with small quality and stable transmission performance was designed in this paper. Simulation analysis and experimental verification were also carried out.

2 Layout of the machine and technical requirements

2.1 Layout of the machine

In this paper, the program was arranged in the medicine box whose gravity was always more stable. The layout of each part of the machine is shown in Figure 1.

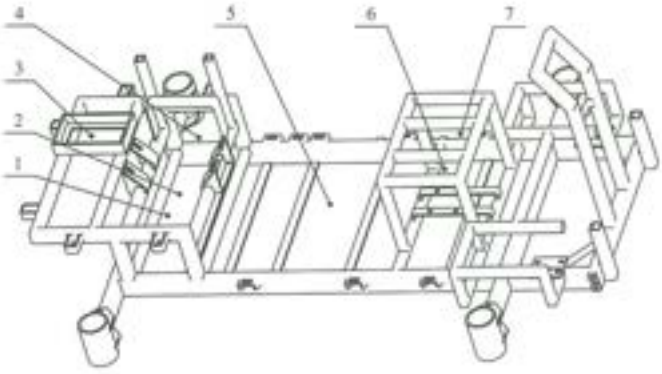

1. Driven hydraulic pump 2. Diesel tank 3. Hydraulic oil tank 4. Diesel engine 5. Medicine chest 6. Application of hydraulic pump 7. Chair

Figure 1 Layout scheme of the sprayer

The hydraulic layout scheme enabled the sprayer to operate smoothly in the complicated and changeable road conditions, and effectively reduced the risk of accidents such as rollover (Du et al., 2014).

2.2 Technical requirements

According to the characteristics of field operations (Ji et al., 1999) and the actual performance requirements of the sprayer, the main technical parameters required by the sprayer designed were shown in Table 1.

Table 1 Main technical parameters of sprayer

Project	Unit	Technical parameter
Machine quality	kg	900
Working pressure	MPa	0.4-1.0
Maximum spray amplitude	m	12
Ground clearance	mm	1100
Theoretical operation speed	Km h^{-1}	1-5
Barrel capacity	L	500
Maximum gradient	-	20

Considering the fact that the sprayer was mainly used in the field and on the road, the road condition was relatively simple, but the road conditions in the field were more complicated, so the horizontal bending condition, torsion, emergency braking and emergency turning condition, the four common conditions were mainly considered.

3 Analysis and design of Hydraulic Driving System of the sprayer

3.1 Load analysis of Hydraulic Driving? System

When climbing: $M_t=M+M_f+M_a$

When activated: $M_t=M+M_f+M_a$

Stable operation: $M_t=M+M_f$

When deceleration was stopped:

$$M_t=M+M_f-M_a \quad (1)$$

The M_t in the formula was the total load that the motor overcame, N·m; M was the working load torque, N·m; M_f was the torque of the rotating part to the motor shaft diameter, N·m; M_a was the inertia moment of the hydraulic pressure in the wheel and the motor at start and stop, N·m.

The maximum traction during travel was about:

$$F_t = G\cdot\sin\alpha + G\cdot f\cdot\cos\alpha \quad (2)$$

The maximum torque was:

$$M_z=F_t\cdot R/\eta X \quad (3)$$

where, ηX was the mechanical efficiency of the sprayer.

According to the calculated load value and the size of the motor, the working pressure of the hydraulic system was selected, and the economic factor and the specifications of the existing hydraulic component were taken into account (Zhi et al., 2010). By the maximum traction force of 5718.34 N, can be the primary working pressure of 19 MPa.

3.2 Design scheme of Hydraulic Driving System

Compared with the open system, closed system, although the structure is complex, needs to be designed a separate cooling device, while the fuel tank has small size, compact structure, the oil is not easy to be contaminated and stable performance, suitable for volume control circuit. Therefore, closed hydraulic circuit was used.

The hydraulic system used twin pumps, the main pump was an inclined plate axial plunger variable pump, and the auxiliary pump was one-way quantitative hydraulic pump. At the same time, a closed loop was formed by four variable motors.The speed change device

was manual servo valve. The overall scheme of the hydraulic driving system was shown in Figure 2.Among them, Changchai 3M78 diesel engine was chosen for this experiment as it uses the tunnel structure, the vibration is small, and the noise is low. The oil of the feeding, steering and servo control circuit was supplied by the auxiliary pump of the system through the priority valve, that is, the hydraulic power was provided by the auxiliary pump through the priority valve to the charge system, steering system, servo control system to provide hydraulic power. When there is no steering nor speed change, the auxiliary pump enters the priority valve through the oil inlet P, and then enters the oil supplying circuit from the oil outlet EF. When the turn occurred, the priority valve supplied hydraulic oil from the DF port to the steering loop first, and the steering loop hydraulic oil directly got into the oil supply loop to achieve oil supplying function. When the speed need to be changed, the auxiliary pump provided pressure oil to the manual servo valve 3, and then entered the pump servo hydraulic cylinder to control swashplate swinging, regulate pump or motor displacement, so as to achieve the sprayer drive at different speeds.

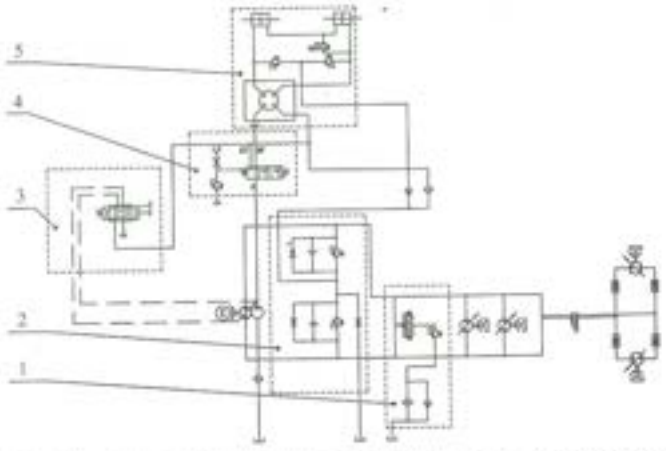

1. Cooling circuit 2. Fill oil circuit 3. Manual servo valve 4. Priority valve 5. Turn circuit

Figure 2 Schematic diagram of hydraulic system

As the pump and motor were integrated with a variety of valves, the structure was compact, easy to be arranged. Because of the closed circuit, the fuel tank was small in size, and the whole seal of the tank could reduce pollution. The variable pump and variable motor can be adjusted conveniently. Only one Joystick can realize forward, backward and stepless speed was changed. The closed loop system composed of pump and motor can also realize bidirectional reversible transmission. The four wheel synchronous drive was realized by the motor parallel loop, and the aim of locking the rear wheel, the four wheel steering and the two wheel steering switching were realized, and the walking performance of the sprayer was improved.

4 Modeling, simulation and verification on AMESim

4.1 Build simulation model

Based on the above design and analysis, the simulation model of the hydraulic transmission of the sprayer was built in the AMEsim software, as shown in Figure 3, the main simulation parameters were shown in Table 2.

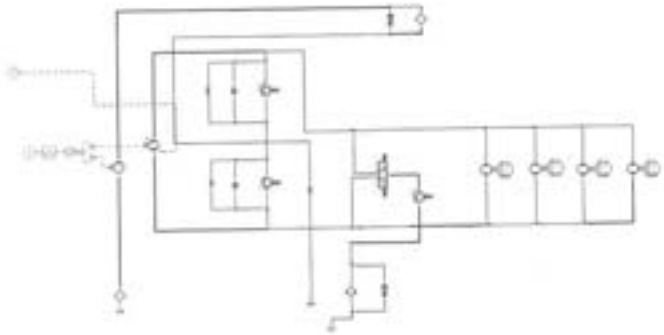

Figure 3 Simulation model of hydraulic transmission of sprayer

Table 2 Simulation parameters

Parameter	Unit	Value
Engine speed	r/min	3600
Displacement of hydraulic main pump	mL/r	21.8
Displacement of charge pump	mL/r	4.1
Motor displacement	Ml/r	380
Motor maximum speed	r/min	800
Load moment of inertia	kg m^2	35.34
Load torque	N·m	739.44
Safety valve	MPa	25

Since there was no twin pumps model in hydraulic press, the main pump and the auxiliary pump were separated and connected to the engine respectively. The signal source ⊙ sent a constant signal, which was converted to the speed output of the engine through a signal converter, and then it was connected to the speed input end of the two pumps. The equivalent rotation inertia, sliding friction and static friction can be set up by using load rotating dynamics model ⏀ instead of wheel. The manual servo valve was replaced with a signal source

to control the displacement of the variable pump or motor and the speed of the sprayer (Xin et al., 2010).

4.2 Simulation analysis

4.2.1 HST performance test simulation

The preferred sub model was assigned to each component, and the component parameters were entered according to Table 2, the simulation time was set to 15 s and the step was 0.01 (Yuan et al., 2013).

After the simulation is completed, the flow of the two-way hydraulic main pump and auxiliary pump, hydraulic motor flow and pressure, the speed and torque curve of the load were shown as the follows (Figures 4, 5, and 6).

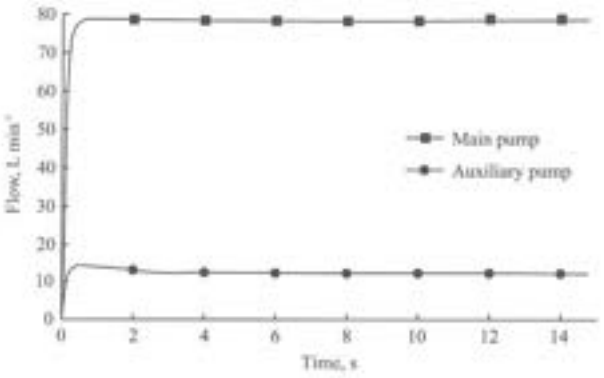

Figure 4 Flow rate of two-way hydraulic main pump and auxiliary pump

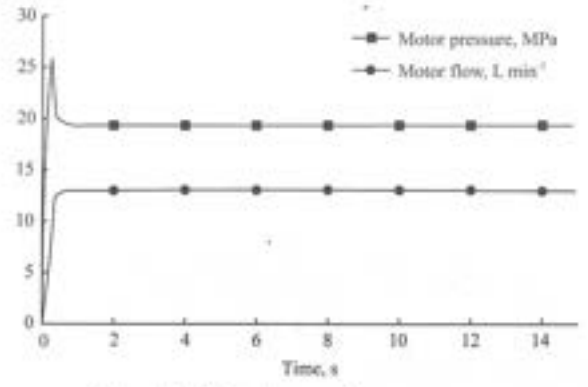

Figure 5 Motor flow and pressure curve

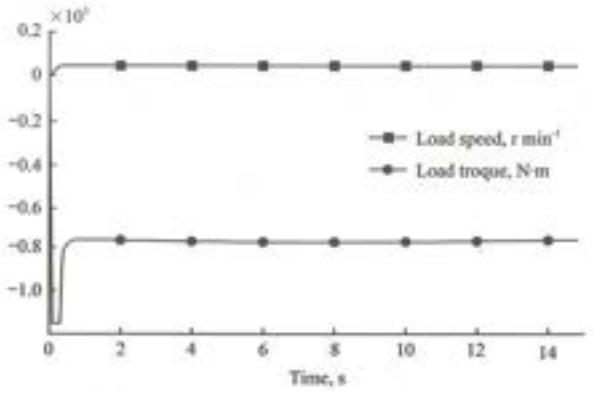

Figure 6 Speed and torque curve of load

As can be seen from Figure 4, the steady output flow of the hydraulic main pump was 78.8 r/min, which was slightly larger than the maximum output flow of the PY-21.8 hydraulic pump. However, considering the simulation of the hydraulic pump, the existence of hydraulic oil leaks was neglected. The result of simulation was in the error range. According to Figure 5 and Figure 6, the steady output flow and the pressure of the motor were within the normal range of operation. It can be seen from Figure 6 that the load stable speed and load torque were 33.2 r/min and 772.6 N·m respectively, and the speed of the load (motor speed) should be greater than 30.8 r/s when the sprayer was running at the fastest speed of 5 km/h, simultaneously, the load torque (motor torque) should be greater than 739.4 N·m, so the simulation results met the design requirements (Zhang et al., 2010).

4.2.2 Speed analysis

As mentioned above, the system changed the angle of the swashplate of the pump by manual servo valve to change the displacement of the hydraulic pump so as to achieve the purpose of speed regulation. As the AMESim hydraulic library did not have a manual servo valve model, the output parameters of the variable pump were changed by using the signal source to change the displacement of the main pump.

The main input parameters of the main pump are shown in Table 3.

Table 3 Variable pump control parameters

Initial value	Terminal value	Run time, s	Stage
0	+1	5	Accelerated start
+1	+1	10	Positive uniform
+1	−1	10	From positive to reverse
−1	−1	10	Reverse uniform
−1	+1	10	From reverse to positive

The simulation time was set to 60 s and the step was 0.01. Click the start, after the simulation was completed, we can get the main pump variable coefficient changes, hydraulic motor and flow, load speed, load torque curve, which were as the follows (Figures 7 to 10).

As can be seen from Figure 8, the flow and pressure of the motor were basically stable at all stages of the speed and coincide with the trend of the speed. When the displacement was close to zero, the motor flow and speed

were zero at a certain stage, which was also consistent with that the motor had critical speed characteristics consistent. In contrast to Figures 7, 9 and 10, the change of load speed and torque was consistent with the change of the main pump displacement to achieve the speed change, and the change was relatively stable. Therefore, the results can be seen that the performance of hydraulic transmission system is relatively stable and can adapt to the sprayer speed requirements.

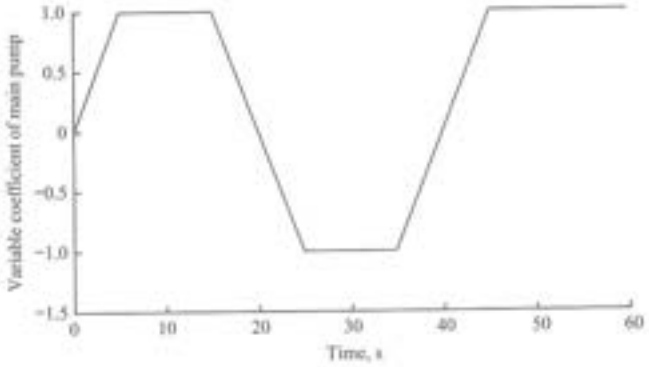

Figure 7 Variable coefficient curve of the main pump

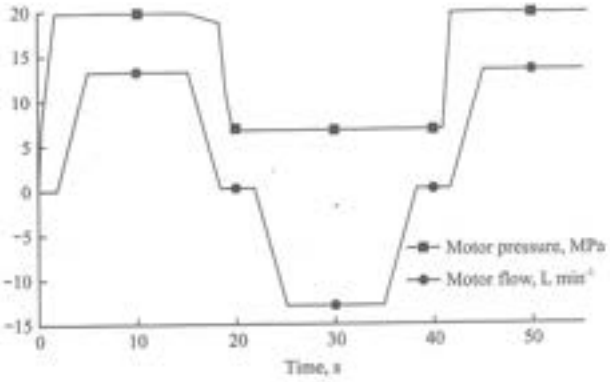

Figure 8 Motor flow and pressure curves

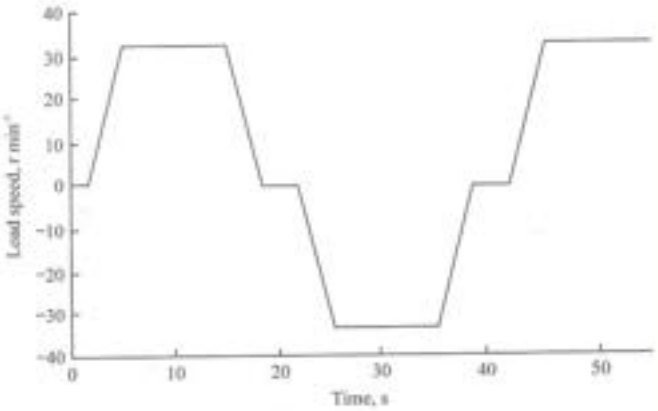

Figure 9 Load speed curve

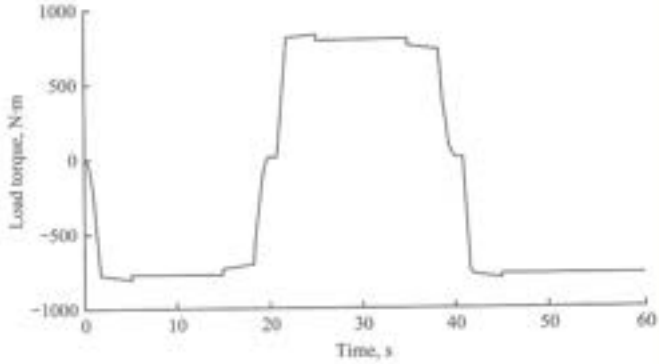

Figure 10 Load torque curve

5 Test verification

After the hydraulic system design was completed, the test prototype was produced in cooperation with Essen Agricultural Machinery Co., Ltd. The hydraulic system designed in the previous design was carried out on the test prototype of the Essen agricultural machine. Test prototype and test ramp were shown in Figure 11.

Figure 11 Test prototype and test ramp

Two typical working conditions, the running test of the rugged field work and the upper and lower ramp were tested. The dynamic monitoring data of two indexes, left and right roll angle and front and rear pitch angle, are mainly monitored to characterize the stability of the system and to test ride comfort. (The test instrument was

mounted in the middle of the machine).

Angle sensor real-time detection data analysis, and processing results were shown in Figure 12. When driving in rugged fields, the pitch angle fluctuates in the range of 10°, and the fluctuation range of the obstacle is 20° due to the large fluctuation of the road or the gravel. The whole sprayer is stable and reliable. The test ramp is about 20 degrees, and the surface of the ramp has certain fluctuations whose ups and downs are in the range of about 5 degrees. The design meets the requirements, which can adapt the needs of a variety of operating conditions.

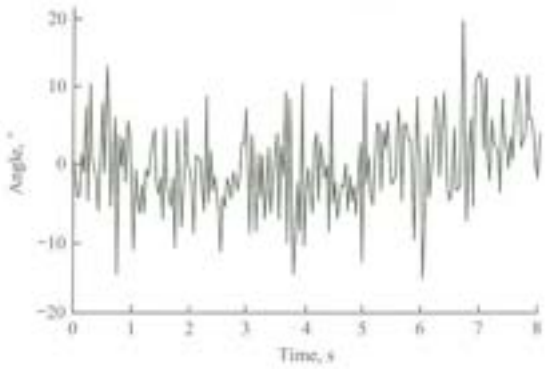

a. Rugged road front and rear pitch angle

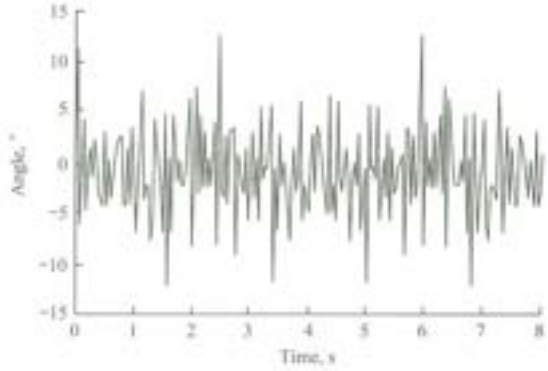

b. Rugged road around the roll angle

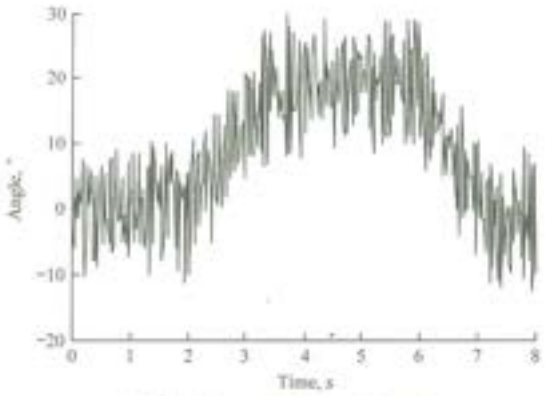

c. Uphill before and after the pitch angle

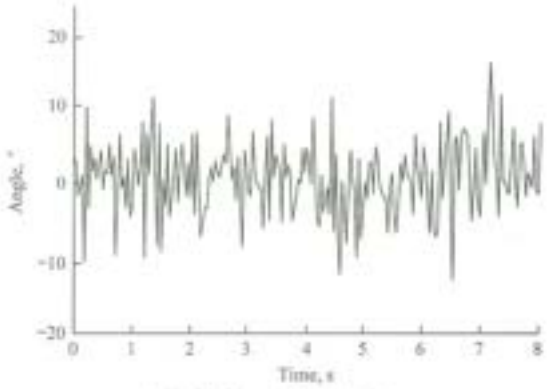

d. Uphill left and right roll angle

Figure 12 Rugged terrain and hillside test results

6 Conclusions

(1) Based on HST full hydraulic drive, the transmission system was designed for the self-propelled sprayer, and the functions of steering, speed and cooling were realized.

(2) Through building the mode and analyzing it in the AMEsim software, the simulation test and prototype test results showed that the design of hydraulic program was accurate, fast, stable, and met the operational requirements.

(3) The research will be helpful to optimize the hydraulic transmission system of the paddy field sprayer and reduce the weight of water field spray machine, which is of reference value for the application of agricultural plant protection machinery and HST technology in agriculture.

Acknowledgments

The research is funded partially by Central University of Basic Scientific Research Business Special Funds (KYZ201760), Jiangsu Province, Six Talent Summit Project (2015-ZBZZ-011) and Nanjing Agricultural University College of Technology Outstanding Young Talent Science and Technology Fund (YQ201605) and Nanjing Agricultural University Students Innovation Training (1630B16).

[References]

[1] Batte, M. T., and M. R. Ehsani. 2006. The economics of precision guidance with auto-boom control for farmer-owned agricultural sprayers. *Computers & Electronics in Agriculture*, 53(1): 28–44.

[2] Du, J., G. Zhang, T. Liu, and S. To. 2014. Improvement on

load performance of externally pressurized gas journal bearings by opening pressure-equalizing grooves. *Tribology International*, 73(5): 156–166.

[3] Gao, X., J. Guo, Z.Zhu, and S. Han. 2017. Design of Power Transmission System of High-clearance Self-propelled Sprayer. *Journal of Agricultural Mechanization Research*, 39(4): 247–268.

[4] Gu, D. X., G.R.Zhang, R. J. Zhang, and Y. Peng. 2000. Review on fifty-years biological control of insect pests in southern China. *Acta Entomologica Sinica*, 43(3): 327–335.

[5] Huang, K. J., and H. W. Su. 2010. Approaches to parametric element constructions and dynamic analyses of spur/helical gears including modifications and undercutting. *Finite Elements in Analysis & Design*, 46(12): 1106–1113.

[6] Ji, C. Y., Z. X. Lu, and J. Z. Pan. 1999. Analysis of bearing capacity and adhesion to solid surfaces of paddy soils. *Journal of Nanjing Agricultural University*, 22(4): 105–108. (In Chinese with English abstract)

[7] Liu, X. M., Y. Li, M. Li, J. Yuan, and Q. Fang. 2016. Design and Test of Smart-targeting Spraying System on Boom Sprayer. *Transactions of the Chinese Society for Agricultural Machinery*, 47(3): 37–44. (In Chinese with English abstract)

[8] Sun, S. M., J. G. Wang, and K. E. Jian. 2014. New HST optimal design and test in harvester. *Journal of Machine Design*, 2014(5): 34–38.

[9] Wang, X. N., X. K. He, A. Herbst, L. Jan, and J. Zheng. 2014. Development and performance test of spray drift test system for sprayer with bar. *Transactions of the Chinese Society of Agricultural Engineering*, 30(18): 55–62. (In Chinese with English abstract)

[10] Xin, F. U., M. Xu, and W. Wang. 2010. Hydraulic system design and simulation of the forging manipulator. *Journal of Mechanical Engineering*, 46(11): 49–54.

[11] Yuan, S. H., C. B.Yin, and S. H. Liu. 2013. Working properties of counterbalance valve based on AMESim Code. *Transactions of the Chinese Society for Agricultural Machinery*, 44(8): 273–280. (In Chinese with English abstract)

[12] Zaman, Q. U., T. J. Esau, A. W. Schumann, D. C. Percival, and Y. K. Chang. 2011. Original papers: Development of prototype automated variable rate sprayer for real-time spot-application of agrochemicals in wild blueberry fields. *Computers & Electronics in Agriculture*, 76(2): 175–182.

[13] Zhang, L. J. 2014. Design and performance analysis of Self-propelled Boom Sprayer. M.S. thesis, Jiangsu University.

[14] Zhang, T. T., M. Chen, and H. M. Chen. 2010. The designing and optimizing of fully hydraulic driving system of engineering machinery based on Matlab. *Journal of Machine Design*, 27(3): 58–61.

[15] Zhi, Y. H., X. P. Shi, Y. S. Liu, and Z. F. Yue. 2010. Dynamical optimization design on pipe diameter and pipeline support of the hydraulic pressured/fuel oil pipeline system. *Journal of Machine Design*, 27(3): 75–79.

Performance optimization of combine harvester inertia separation chamber based on BPNN

Dong Zhigui[1], Wang Fulin[1*], Song Qingfeng[2], Wu Zhihui[1], Fang Kun[1]

(1. *College of Engineering, Northeast Agricultural University, Harbin 150030, China;*
2. *He University, Shenyang 110163, China*)

Abstract: In order to overcome the flaws and limitation, and obtain the optimal performance of combine harvester inertia separation chamber, an BP neural network-based optimization method that using hyperbolic tangent function as transfer function was proposed. This method was built on the basic of BP neural network function fitting. In view of minimizing mathematic model of network output, basic ideas of the optimization method was illuminated, the computational formula of search direction of Newton type arithmetic and optimum step were given, and the first and two partial derivatives of the network's output versus its input were deduced. On this basis, the terminate rule and realization process of BP neural network-based optimization method were carried out. The optimization method was used to determine the optimal input process parameters of the combine harvest inertial separation chamber to give minimum optimum pressure loss of combine harvest inertial separation chamber. The optimization results are as follows: inlet gas velocity of inertia separation chamber was 9.8 m/s, clapboard length was 780 mm, height of inertia separation chamber was 1120 mm, length of inertia separation chamber was 2036.6360 mm, and minimum suction system pressure loss minimum value was 129.3533 Pa. The optimization result showed that, it is a stable and feasible arithmetic for similar optimization problems of agriculture engineering field.

Keywords: combine harvester, inertia separation chamber, BP neural network, optimization method, Newton type arithmetic, optimal step

Citation: Dong, Z. G., F. L. Wang, Q. F. Song, Z. H. Wu, and K. Fang. 2017. Performance optimization of combine harvester inertia separation chamber based on BPNN. International Agricultural Engineering Journal, 26(3): 19-26.

1 Introduction

The performance of combine harvester inertia separation chamber (4ZTL-1800, invented by academician Jiang Yiyuan) is affected by many factors, such as physical property of grain, mass and flux of grain, length and installation height of clapboard, length and dip of back wall, aperture and shape of baffle and so on. It is the traditional method that regression equation was used to confirm the effect of each factor to performance of inertia separation chamber and obtain the optimal performance combination (Jiang et al., 2000; Wang et al., 2007; Wang, 2006; Wang et al., 2005), but this method have many obvious flaws and limitation. Firstly, the error caused by approximate calculation affects the precision of regression model. Secondly, the regression equation built on the presumptive model has especial limitations. Thirdly, the variable substitution is difficult to be multivariable. Fourth, regression equation lacks the processing capacity to noise of sample itself. Therefore, in order to obtain the optimal performance of combine harvester inertia separation chamber, it is necessary to propose a new method to solve this optimization problem.

BP neural network model, which is one of the most important artificial neural network models, is a multi-layer forward neural network being most widely studied and used at present. Theories have proved that if a three-layer BP neural network has enough hidden layer nodes, it can simulate any complex nonlinear mapping(Hecht-Nielsen, 1992; Villiers and Barnard, 1993; Funahashi, 1989). In recent years, with the

Received date: 2017-01-12 **Accepted date:** 2017-07-14

* **Corresponding author: Wang Fulin**, PhD, Professor of College of Engineering, Northeast Agricultural University, Harbin 150030, Heilongjiang Province, China. Email: fulinwang1462@126.com, Tel: +86-451-55191462.

development of BP neural network algorithm, people began to study the BP neural network-based optimization method on the basis of BP neural network fitting. Although some studies were called BP neural network-based optimization researches, these so-called researches are actually considered as not really optimization since they obtained the optimal value by using orthogonal experimental design (Wang et al., 2014), numerical simulation (Merad et al., 2007; Gulati et al., 2010; Wang et al., 2009; Liu, 2010), or genetic algorithm (Zhou et al., 2012). The BP neural network-based optimization method is a kind of global search optimization method proposed by Liu et al. (2010), and this method can adjust the input values of BP neural network to obtain the optimal output values (globally optimal solution), which was built on the neural network fitting. However, the theoretical study of their article was not systematic, and the method had errors when solving constrained optimization problems since it could not guarantee solution within feasible region (Liu et al., 2010). Although Wang et al. (2010) proposed an unconstrained BP neural network-based optimization method and studied systematic, but the partial derivative of network's output versus its input is incorrect (Wang et al., 2010). Zhang et al. (2016) made utilization of the unipolar Sigmoid transfer function to construct the BP neural network model and studied the optimization method, in which a gradient direction of the network output versus input was selected as search direction, the number of initial search step was given in a form of constant, and the next iterative generation of search step number is inherited from the previous iteration in accordance with the principle of the transformation step adjustment (Zhang et al., 2016). Sometimes, this method cannot be used to obtain the optimal solution in essence, because the optimal iteration will terminate when a better point can't be obtained by using the gradient direction.

In order to overcome the above-mentioned flaws and limitations, and improve the optimization result, this paper proposes an BP neural network-based optimization method, which is applied to obtain an optimal performance of combine harvester inertia separation chamber. The BP neural network model is built by considering the hyperbolic tangent function as transfer function, and the search step was confirmed by using optimal step formula in optimization process. This paper can be divided into four parts. In the first part, the aim and significance of the research and the status quo is discussed. The second part mainly involves the BP neural network-based optimization method, including mathematics model, the basic idea, the partial derivative of network's output versus its input, termination criterion, and realization process of optimization method. In the third part, the minimum pressure loss of combine harvester inertia separation chamber is obtained by using the proposed method. And in the last part, the achievement and conclusion of this research is demonstrated.

2 BP neural network-based optimization method

2.1 Mathematical model

The minimum output problems of BP neural network are used as an example to illustrate the optimization method. If $F(X)$ expresses the relationship between input and output, a generalized mathematical model of unconstraint optimization based on BP neural network can be expressed as follows:

$$\begin{cases} \min Y = \min F(X) \\ X \in R^n \end{cases} \tag{1}$$

In Equation (1), X is a input vector and $X=(x_1, x_2, \ldots, x_q)^T$; R^n is a feasible region, and Y is the output of BP neural network. If the maximum output of BP neural network is desired, the objective function can be transformed to $\max F(X) = -\min[-F(X)]$.

2.2 Basic ideas

First, an initial feasible point $X(t)$ (t=0) is artificially selected or randomly generated, and the gradient with respect to $X(t)$ is computed. If the gradient of $X(t)$ satisfies the termination criterion, then, $X(t)$ is an optimal solution and its corresponding network output Y is the optimal solution. Otherwise, we searched for a new iterative point $X(t+1)$ being along the search direction of $X(t)$, and calculated the gradient with respect to $X(t+1)$. If the gradient of $X(t+1)$ point dissatisfied the termination criterion, the next iteration was continued from $X(t+1)$,

until the gradient of $X(t+1)$ point satisfied the termination criterion or was unable to obtain another better point. In this case, $X(t+1)$ value was the optimal input and its corresponding network output Y was the optimal output.

2.3 Method of generating search direction

$F(X)$ is a multivariate function, X^* is a minimal point of $F(X)$, and $X(t)$ is an approximate point of X^*. The Taylor expansion of $F(X)$ at $X(t)$ point was reserved and the quadratic term was obtained as follows

$$F(X) \approx \varphi(X) = F(X(t)) + \nabla F(X(t))(X - X(t)) + \frac{1}{2}(X - X(t))^{\mathrm{T}} \nabla^2 F(X(t))(X - X(t)) \quad (2)$$

where, $\nabla F(X(t))$ is the gradient and $\nabla^2 F(X(t))$ is the Hessian matrix of $F(X)$ with respect to $X(t)$.

By setting $X(t+1)$ as the minimal point and taking it as a next approximate point of X^*, we can obtain the Equation (3) according to the requirement of extremum

$$\nabla \varphi(X(t+1)) = 0 \quad (3)$$

thus,

$$\nabla F(X(t)) + \nabla^2 F(X(t))(X(t+1)) - X(t)) = 0 \quad (4)$$

then,

$$X(t+1) = X(t) - [\nabla^2 F(X(t))]^{-1} F(X(t)) \ (t=0,1,2,\ldots) \quad (5)$$

Equation (5) is the extremum iterative formula of Newton algorithm for multivariate function, and this method is quadratic convergence to quadratic function. Sometimes, the function values will increase when the Equation (5) was used on non-quadratic function. That is to say, $F(X(t+1)) > F(X(t))$. Therefore, mathematical programming approach was lead up to improve the aforementioned Newton algorithm, and the "damped Newton method" was proposed.

If we defined the $d(t)$ as follows

$$d(t) = -[\nabla^2 F(X(t))]^{-1} F(X(t)) \quad (6)$$

It be called Newton direction and can be regarded as search direction, and the iteration formula of damped Newton method was as follows

$$X(t+1) = X(t) + \lambda d(t) = X(t) - \lambda [\nabla^2 F(X(t))]^{-1} F(X(t)) \quad (7)$$

where, λ is the optimal step along Newton direction, or it can be called damped factor.

2.4 Optimal step

The optimum step size λ was defined as a step size which can obtain the minimum value of this search direction in optimization process, when the iteration point $X(t)$ is searching along search direction. That is

$$\min F(X(t+1)) = \min(F(X(t)) + \lambda d(t)) \quad (8)$$

The Taylor expansion of Equation (8) at $X(t)$ point was reserved the quadratic term and obtained

$$(F(X(t)) + \lambda d(t)) \approx F(X(t)) + \lambda (d(t))^{\mathrm{T}} \nabla F(X(t)) + \frac{1}{2}\lambda^2 (d(t))^{\mathrm{T}} \nabla^2 F(X(t)) d(t) \quad (9)$$

to deduce the partial derivative of Equation (9) with respect to λ and let it equals to 0, thus the optimal step λ of $d(t)$ direction was obtained (Chen, 2005)

$$(d(t))^{\mathrm{T}} \nabla F(X(t)) \quad (10)$$

Because the geometrical significance of $(d(t))^{\mathrm{T}} \nabla F(X(t))$ is a permanent negative, the optimal step λ is a positive value, that is to say, $\lambda > 0$.

2.5 The first-order and second-order partial derivatives of network's output versus input

The gradient vector of function $F(X)$ is

$$\nabla F(X) = \frac{\partial F(X)}{\partial X} = \left(\frac{\partial F}{\partial x_1}, \frac{\partial F}{\partial x_2}, \ldots, \frac{\partial F}{\partial x_n} \right) \quad (11)$$

Thus, as long as the partial derivative of function $F(X)$ is calculated, the gradient of function $F(X)$ can be obtained. The following is the procedure to derive the partial derivative of the network's output versus its input, with the hyperbolic tangent function used as network transfer function. Let x_i and x_l (i, l=1,2,$\cdots$, n) to be the i^{th} and the j^{th} variables of network,and y_k (k=1,2,...,q) to be the k^{th} output of network. The weight value linking the i^{th} neuron and the j^{th} neuron is expressed as w_{ij} (i=1, 2, ..., n; j=1, 2, ..., p). The weight linking the j^{th} neuron and the k^{th} neuron is expressed as v_{ij} (j=1, 2, ..., p; k=1, 2, ..., q). The arbitrary neuron's input value of hidden layer is denoted by I_{1j} (j=1, 2, ..., p) and the output value is denoted by s_{1j} (j=1, 2, ..., p). The arbitrary neuron's input of output layer is denoted by I_{2k} (k=1, 2, ..., q).

The first-order partial derivative of the network's output y_k versus the input x_i is

$$\frac{\partial y_k}{\partial x_i} = \frac{\partial y_k}{\partial I_{2k}} \cdot \sum_{j=1}^{p} \left(\frac{\partial I_{2k}}{\partial x_i} \right) = \frac{\partial y_k}{\partial I_{2k}} \cdot \sum_{j=1}^{p} \left(\frac{\partial I_{2k}}{\partial s_{1j}} \cdot \frac{\partial s_{1j}}{\partial I_{1j}} \cdot \frac{\partial I_{1j}}{\partial x_i} \right) \quad (12)$$

$$v_{jk} = \frac{\partial I_{2k}}{\partial s_{1j}} \quad (13)$$

$$w_{ij} = \frac{\partial I_j}{\partial x_i} \tag{14}$$

The hyperbolic tangent function is expressed as follows

$$f(x) = \frac{e^x - e^{-x}}{e^x + e^{-x}} \tag{15}$$

The first-order partial derivative of hyperbolic tangent function is

$$f'(x) = 1 - f^2(x) \tag{16}$$

We suppose that,

$$a_k = \frac{\partial y_k}{\partial I_{2k}} = 1 - y_k^2 \tag{17}$$

$$b_{jk} = \frac{\partial s_{1j}}{\partial I_{1j}} = 1 - s_{1j}^2 \tag{18}$$

thus,

$$\frac{\partial y_k}{\partial x_i} = a_k \sum_{j=1}^{p} (v_{jk} \cdot b_{jk} \cdot w_{ij}) \tag{19}$$

Hessian matrix $\nabla^2 F(X(t))$ is a square matrix which is formed by second-order partial derivatives of function $F(X)$ at $X(t)$ point. Thus, as long as the second-order partial derivative of function $F(X)$ is calculated, the Hessian matrix of function $F(X)$ can be obtained. According to the above result, the second-order partial derivative of network's output y_k versus input x_i and x_l is derived as follows

$$\frac{\partial^2 y_k}{\partial x_i \partial x_l} = \frac{\partial\left(\frac{\partial y_k}{\partial x_i}\right)}{\partial x_l} = \frac{\partial\left(\frac{\partial y_k}{\partial I_{2k}}\right)}{\partial x_l} \cdot \sum_{j=1}^{p} \frac{\partial I_{2k}}{\partial x_i} + \frac{\partial y_k}{\partial I_{2k}} \cdot \frac{\partial\left(\sum_{j=1}^{p} \frac{\partial I_{2k}}{\partial x_i}\right)}{\partial x_l} \tag{20}$$

$$\frac{\partial\left(\frac{\partial y_k}{\partial I_{2k}}\right)}{\partial x_l} = \left(\frac{\partial y_k}{\partial I_{2k}}\right)' \cdot \sum_{j=1}^{p} \frac{\partial I_{2k}}{\partial x_l} \tag{21}$$

$$\frac{\partial\left(\sum_{j=1}^{p} \frac{\partial I_{2k}}{\partial x_i}\right)}{\partial x_l} = \sum_{j=1}^{p} \left(\frac{\partial I_{2k}}{\partial s_{1j}} \cdot \frac{\partial I_{1j}}{\partial x_i} \cdot \left(\frac{\partial s_{1j}}{\partial I_{1j}}\right)' \cdot \frac{\partial I_{1j}}{\partial x_l}\right) \tag{22}$$

The second-order partial derivatives of hyperbolic tangent function was obtained by Equations (15) and (16)

$$f''(x) = -2f(x)(1 - f^2(x)) \tag{23}$$

We suppose that,

$$c_k = \left(\frac{\partial y_k}{\partial I_{2k}}\right)' = -2y_k(1 - y_k^2) \tag{24}$$

$$d_{jk} = \left(\frac{\partial s_{1j}}{\partial I_{1j}}\right)' = -2s_{1j}(1 - s_{1j}^2) \tag{25}$$

Based on Equations (12) to (25), it can be obtained:

$$\begin{aligned} \frac{\partial y_k}{\partial x_i \partial x_l} &= c_k \sum_{j=1}^{p} (v_{jk} b_{jk} w_{ij}) \sum_{j=1}^{p} (v_{jk} b_{jk} w_{lj}) \\ &+ a_k \sum_{j=1}^{p} (v_{jk} d_{jk} w_{ij} w_{lj}) \end{aligned} \tag{26}$$

2.6 Termination criterion

According to the fundamental of unconstraint optimization, it must be judge whether the iteration point $X(t)$ is convergence or not after every iteration, that is judge whether the iteration point $X(t)$ is the optimal point or not. If the gradient of iteration point $X(t)$ satisfied the Equation (27), $X(t)$ is the optimal input and the corresponding network output is the optimal output.

$$\|\nabla F(X(t))\| \le \varepsilon \quad t \in [0,1,2,\ldots] \tag{27}$$

where, ε is a pre-establish convergence precision.

2.7 The optimization method and realization process

The BP neural network-based optimization method and its realization process were as follows:

Step 1: Organize training samples and create BP neural network model, initialize network's weight and biases. Train BP neural network after preset expectation error of network, and save the network's weight and biases when the error meets the expected accuracy.

Step 2: Primary iteration point $X(t)(t=0)$ is artificially selected or randomly generated, and the convergence precision ε is given.

Step 3: The network's output Y of $X(t)$ point is calculated through propagation process, and the gradient $\nabla F(X(t))$ is calculated by using Equation (19).

Step 4: If the modulus of gradient of $X(t)$ point satisfied the Equation (27), the iteration will termination, $X(t)$ is the optimal input and its corresponding network output Y is the optimal output. Otherwise, go to Step 5.

Step 5: The second-order partial derivative of network output versus input at $X(t)$ point was calculated by using Equation (26), thus the Hessian matrix of function $F(X)$ can be obtained. Calculate search direction by using Equation (6) and the optimal step λ by using Equation (10). The new iteration point $X(t+1)$ was generated by using Equation (11), let $t=t+1$, go back Step 4.

3 Process parameters optimization of combine harvester inertial separation chamber

3.1 Experimental results of combine harvester inertial separation chamber

We used the BP optimization network to investigate how the main factors of combine harvester inertial separation chamber affect performance index. For this purpose, we chose 4 input parameters as inlet gas velocity (IGV), clapboard length (CL), height of the inertia separation chamber (HISC) and length of the inertia separation chamber (LISC), and used the pressure losses of the combine harvester inertial separation chamber suction system (PLSC) as output evaluation index. The actual experimental data used for training the network are shown in Table 1 (Wang, 2006).

Table 1 Training data for BP learning

No.	IGV x_1, m/s	CL x_2, mm	HISC x_3, m	LISC x_4, mm	PLSC y, Pa	No.	IGV x_1, m/s	CL x_2, mm	HISC x_3, m	LISC x_4, mm	PLSC y, Pa
1	15.2	1080	1060	2300	546.2	19	13.4	1180	1000	2100	370.3
2	15.2	1080	1060	1900	509.9	20	13.4	780	1000	2100	425.6
3	15.2	1080	940	2300	418.5	21	13.4	980	1120	2100	409.3
4	15.2	1080	940	1900	445.2	22	13.4	980	880	2100	409.5
5	15.2	880	1060	2300	459.6	23	13.4	980	1000	2500	349
6	15.2	880	1060	1900	462.9	24	13.4	980	1000	1700	408.7
7	15.2	880	940	2300	506.1	25	13.4	980	1000	2100	414.1
8	15.2	880	940	1900	570.7	26	13.4	980	1000	2100	417.1
9	11.6	1080	1060	2300	313.8	27	13.4	980	1000	2100	414.3
10	11.6	1080	1060	1900	318.4	28	13.4	980	1000	2100	415.3
11	11.6	1080	940	2300	222.8	29	13.4	980	1000	2100	418.1
12	11.6	1080	940	1900	274.1	30	13.4	980	1000	2100	415.4
13	11.6	880	1060	2300	248.8	31	13.4	980	1000	2100	416.5
14	11.6	880	1060	1900	286.6	32	13.4	980	1000	2100	418.6
15	11.6	880	940	2300	317.5	33	13.4	980	1000	2100	415.0
16	11.6	880	940	1900	417.4	34	13.4	980	1000	2100	414.8
17	16.9	980	1000	2100	587.4	35	13.4	980	1000	2100	415.0
18	9.8	980	1000	2100	206.3	36	13.4	980	1000	2100	414.8

The modeling performance of the BP network was compared with the modeling performance by quadratic polynomial regression. For this purpose, the experimental data in Table 1 was also processed with the Reda package of quadratic regression (Wang, 2006). The results are as follows:

$$y = 416.11 + 95.17x_1 - 13.38x_2 - 1.24x_3 - 15.81x_4 - 4.46x_1^2 + 3.84x_1x_2 + 5.97x_1x_3 + 7.95x_1x_4 - 4.55x_2^2 + 42.95x_2x_3 + 10.22x_2x_4 - 2.01x_3^2 + 14.81x_3x_4 - 9.84x_4^2 \quad (28)$$

3.2 Data modeling based on BP neural network

Then, the data in Table 1 was used to train the BP neural network. The structure of the 3-layer BP neural network was chosen as 4-7-1. In order to facilitate programming and avoid saturation, we normalized the input and output data to the interval $[a, b]$ by using

$$x_i' = a + (b-a)\frac{x_i - x_{\min}}{x_{\max} - x_{\min}} \quad (i = 1, 2, ..., P) \quad (29)$$

where, x_i is the input sample; x_i' is the input data after normalization, $x_i' \in [a, b]$; $x_{\max}$ and $x_{\min}$ are the maximum and minimum value of the input sample data x_i. The interval $[a, b]$ was chosen as [0.1, 0.8].

The inverse of Equation (29) is given by

$$x_i = x_{\min} + \frac{(x_i' - a)(x_{\max} - x_{\min})}{b - a} \quad (30)$$

The modeling performance of the BP neural network in comparison to the modeling performance of quadratic regression is shown in Figure 1.

The weight and threshold values of the BP neural network learned are as follows:

The weight values between input layer and hidden layer are:

$$W=\begin{bmatrix} 0.4316 & -2.6534 & 0.3417 & -2.6470 & -18.9214 & 0.0978 & -2.1184 \\ 0.3668 & 3.5621 & 0.5042 & -7.9271 & 13.6902 & 0.5170 & -4.1564 \\ -0.3792 & -5.3184 & -0.9534 & -10.0226 & -15.6125 & 0.1403 & -0.7887 \\ 0.2437 & 1.5327 & 0.8539 & -2.0686 & 7.8760 & -0.7006 & 5.7739 \end{bmatrix}$$

The weight values between hidden layer and output layer are:

$$V=[3.3197 \quad -2.2444 \quad 3.6579 \quad 0.9150 \quad 0.5033 \quad -2.5326 \quad -0.9313]^T$$

The biases of the hidden layer are:

$$\theta_1=[0.1679 \quad 0.1100 \quad 0.8493 \quad -6.2989 \quad -0.0245 \quad 0.4886 \quad -0.0336]^T$$

The biases of the output layer is:

$$\theta_2=[-0.9311]$$

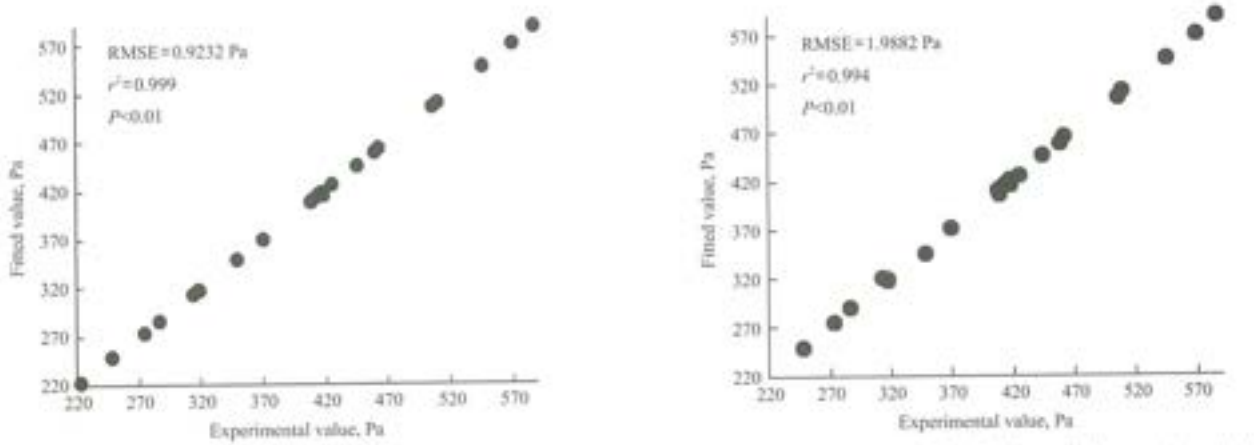

a. Experimental value and fitted value by BP neural network

b. Experimental value and fitted value by quadratic regression model

Figure 1 Comparison of experimental and fitted value using different models

The fitted value of BP. neural network model compared with experimental value was shown in Figure 1a, and the fitted value of quadratic regression model compared with experimental value was shown in Figure 1b. The R^2 is 0.999 (P<0.01) and the root-mean-square error (RMSE) is 0.9232 Pa in BP neural network fitting model, while the R^2 is 0.994 (P<0.01) and the RMSE is 1.9882 Pa in quadratic regression fitting model. Compared Figure 1a with Figure 1b, the fitting degree and precision of BP neural network model are better than those of regression model, and the relations of experimental factors with experimental object can be truly expressed while using the BP neural network model to fit the function.

With the given data, the minimum suction system pressure loss value appeared to be 206.3 Pa with data order number of 18. The corresponding parameters of the inertia separation chamber are as follows: inlet gas velocity of inertia separation chamber is 9.8 m/s, clapboard length is 980 mm, height of inertia separation chamber is 1000 mm, length of inertia separation chamber is 2100 mm.

3.3 Optimization of the process parameters of combine harvest inertia separation chamber

Then, we used the trained BP network to determine the input parameters that optimized the output according to the method discussed in Section 2. The method was initialized by randomly choosing an initial feasible point $X(0)$. This was followed by the iterations carried out until iteration terminal condition is satisfied.

The optimization results are as follows: inlet gas velocity of inertia separation chamber is 9.8 m/s, clapboard length is 780 mm, height of inertia separation chamber is 1120 mm, length of inertia separation chamber is 2036.64 mm, minimum suction system pressure loss minimum value is 129.35 Pa.

The regression equation of quadratic regression model (Equation 28) was optimized and the optimization results were obtained as follows (Wang, 2006; Wang et al., 2007): inlet gas velocity of inertia separation chamber is

9.8 m/s, clapboard length is 1180 mm, height of inertia separation chamber is 1120 mm, length of inertia separation chamber is 1700 mm, and minimum suction system pressure loss minimum value is 156.34 Pa.

4 Discussion and conclusions

4.1 Discussion

Compared the optimization result obtained by two method, all of the RMSE, R^2, and P value of fitting function obtained by BP neural network method are better than that obtained by quadratic regression model, and the optimal performance optimized by proposed method is better than that optimized by regression model. The performance optimization problem of combine harvester inertia separation chamber belongs to black box problem, good or bad of the optimization result obtained by this two method can't be judged because of the optimal solution of black box problem is indeterminacy. The optimized research on performance optimization of combine harvester inertia separation chamber was done by using the BP neural network-based optimization method or regression analysis method was established on the basic of function fitting. In theory, the fitting function with relatively small average error is closer to the real function of problem, and the accuracy of the obtained optimization results is higher.

4.2 Conclusions

An optimization method based on the BP neural network was proposed in this paper. The optimization method was mainly applied to solve the black box problem. The BP neural network was first trained by using the input-output data. The trained network represents the complex functional relationship between the input and the output. Then the inputs are determined and optimize the output by using the method discussed in this paper.

The optimization method was used to determine the optimal input process parameters of the combine harvest inertial separation chamber. We obtained the minimum optimum pressure loss of combine harvest inertial separation chamber of 129.3533, and the corresponding performance was as follows: inlet gas velocity of inertia separation chamber of 9.8 m/s, clapboard length of 780 mm, height of inertia separation chamber of 1120 mm, length of inertia separation chamber of 2036.6360 mm. The experiment was carried out in comparison with the modeling using second order polynomial regression. The optimization results were also more reliable since the modeling using BP network was superior to modeling using polynomial regression.

Acknowledgement

The research is supported by National Natural Science Foundation of China (Grant No. 31071331), Project in the National Science & Technology Pillar Program during the Twelfth Five-year Plan Period of China (Grant No. 2014BAD06B04-2-9), Agriculture Industry Research Special Funds for Public Welfare Projects of China (Grant No.201503116-04).

[References]

[1] Chen, B. L. 2005. Optimization theory and its algorithm (second edition). *Beijing: Tsinghua University Press*.

[2] Funahashi, K. I. 1989. On the approximate realization of continuous mappings by neural networks. *Neural Networks*, 2(3): 183–192.

[3] Gulati, T., M. Chakrabarti, A. Singh, M. Duvuuri, and R. Banerjee. 2010. Comparative study of response surface methodology, artificial neural network and genetic algorithms for optimization of soybean hydration. *Food Technology & Biotechnology*, 48(1): 11–18.

[4] Hecht-Nielsen, R. 1992. Theory of the back propagation neural network. *Neural Networks for Perception*, 1(1): 65–93.

[5] Jiang, E. C., and Y. Y. Jiang. 2000. Studies on the characteristics of air flow field surrounding the stripping rotor with triangle plate teeth. *Transactions of the CSAE*, 16(1): 59–62.

[6] Liu, G. L., F. L. Wang, and J. Q. Wang. 2010. The research on optimization of BPNN model and its application. *Mathematics in Practice and Theory*, 40(6): 161–166.

[7] Liu, L. 2010. Index tracking optimization method based on genetic neural network. *System Engineering Theory & Practice*, 30(1): 22–29.

[8] Merad, L., F. T. Bendimerad, S. M. Meriah, and S. A. Djennas. 2007. Neural networks for synthesis and optimization of antenna arrays. *Radio Engineering*, 16(1): 23–30.

[9] Wang, F. L., H. X. Zhu, and J. Q. Wang. 2010. An unconstrained BP neural network-based optimization method. *ICIC Express Letters*, 7(11): 1–9.

[10] Wang, L. J., E. C. Jiang, and Y. Y. Jiang. 2007. Effect of factors on pressure drop in the inertia separation chamber of stripper combine harvester with air suction. *Transactions of the CSAE*, 23(4): 84–87.

[11] Wang, L. J. 2006. Research on mechanism of the inertial separation of air-suction combine harvester threshing prior to cutting. PhD dissertation. *Harbin: Northeast Agricultural University*.

[12] Wang, L. J., Z. F. Sun, and E. C. Jiang. 2005. Study on the deposition chamber with air suction. *Journal of Northeast Agriculture University*, 36(3): 354–357.

[13] Wang, L. Y., P. Yu, and W. U. Mei. 2014. Optimization of aluminum alloy surface treatment process parameters based on BP network. *Corrosion & Protection*, 35(2): 179–184.

[14] Wang, X. M., B. Zhao, X. L. Wang, and Q. L. Zhang. 2009. Optimization of drilling and blasting parameters based on back-propagation neural network. *Journal of Central South University (Science and Technology)*, 40(5): 1411–1416.

[15] Villiers, J., and E. Barnard. 1993. Back propagation neural nets with one and two hidden layers. *IEEE Transactions on Neural Networks*, 4(1): 136–141.

[16] Zhang, L., F. L. Wang, T. Sun, and B. Xu. 2016. A constrained optimization method based on BP neural network. *Neural Computing & Applications*, 7(11): 1–9.

[17] Zhou, J., X. Z. Lu, R. Z. Shu, and J. Ling. 2012. BP neural network and genetic algorithm for the filling properties optimization of crankshaft. *Journal of Chongqing University*, 35(5): 52–56.

Mechanism of reducing force and tillage performance analysis of bionic subsoiler based on discrete element method

Li Bo[1*], Wang Xuewen[1], Xia Rui[1], Chen Jun[2], Yang Zhaojian[1]

(1. *Shanxi Key Laboratory of Fully Mechanized Coal Mining Equipment, Taiyuan University of Technology, Taiyuan 030024, China;*
2. *College of Mechanical and Electronic Engineering, Northwest A & F University, Yangling 712100, China*)

Abstract: Subsoiling is an important part in conservation tillage. However, the large tillage force of subsoilers is one of the existing problems for further promoting. This study compared the tillage forces of a bionic subsoiler and a standard arc-shaped subsoiler using experiments. The tillage velocity was 0.8 m/s and the tillage depth was 220, 260 and 300 mm, respectively. The discrete element model of soil-subsoiler interaction was established and the tillage process was simulated under the same condition with the test. The mechanism of reducing force and tillage performance of the bionic subsoiler were analyzed. Results showed that bionic subsoiler could reduce tillage force significantly and the force reducing rate was 26.81%, 19.97% and 10.99% under the depth of 220, 260 and 300 mm, respectively. The discrete element model could simulate the tillage process well. Soil particles pushed by arc-shaped subsoiler moving towards the center of the arc and the subsoiler's lifting effect on the soil were the two reasons of arc-shaped subsoiler's larger force. The tillage performance of these two subsoilers was almost the same.

Keywords: bionic subsoiler, reducing force, tillage performance, DEM, PFC^{3D}

Citation: Li, B., X. W. Wang, R. Xia, J. Chen, and Z. J. Yang. 2017. Mechanism of reducing force and tillage performance analysis of bionic subsoiler based on discrete element method. International Agricultural Engineering Journal, 26(3): 27–36.

1 Introduction

As the main conservation tillage component, subsoiler is used for loosing soil without disturbing the soil layer. During the working process, the subsoiler cuts and breaks the soil by the shank and the point. Therefore, the structure of the subsoiler has direct impacts on tillage force and the whole machine performance. However, the subsoiler has the problem of large energy consumption, which hindered further promoting of the deep loosing technology.

Different methods have been tried to achieve the purpose of reducing the resistance of tillage components. Some scholars reduced the tillage force by adding vibration on working parts. Shahgoli et al. (2010) studied the vibration subsoiler and found that the tillage force could be reduced from 25.8 kN to 9.3 kN as the vibration frequency changing between 1.9 Hz and 8.8 Hz comparing with the original subsoiler. Mouazen and Nemenyi (1999a; 1999b) and Mouazen (1999) predicted the tillage force of four kinds of subsoiler using the finite element method (FEM). Results showed that the subsoiler had the minimum tillage force as the shank had an angle of 75° combining with a rake angle of 15°, which achieved the required tillage performance. Mouazen and Ramon (2002) used a regression equation to analyze the tillage force under different moisture contents, bulk densities and working depths. Abo-Elnor (2004) studied the bulldozing plate and found that the width of bulldozing plate had great influence on the tillage force, which provided ideas for optimizing tillage machinery.

The structure of existing animals has adapted to the environment in the long process of evolution, and animal structures provide the basis for human bionic researches. Many applications have been tried in improving agricultural machinery using bionic methods (Ren et al., 2006). To improve the wear resistance of soil engaging tools, the texture of shell surface was applied by Tong et

Received date: 2017-02-09 **Accepted date:** 2017-06-26

* **Corresponding author: Li Bo,** Shanxi Key Laboratory of Fully Mechanized Coal Mining Equipment, Taiyuan University of Technology. Email: libo@tyut.edu.cn.

al. (2010). Less pressure was found on opener surface after applying the convex domes of beetles (Tong et al., 2009). The structure of mole claw was used to reduce the resistance of soil cutting tools (Ji et al., 2010; Zhang et al., 2016). The claw of animals good at burrowing (like pangolin, rat, rabbit, bear) had evolved into the structure suitable for interacting with soil. During the working process, the subsoiler can loose soil, break the plow pan, so as to improve the water storage capacity of soil and the growth condition of plants. Therefore, the application of the claw's structure in optimizing the subsoiler would solve the problem of large tillage force. Guo et al. (2010) compared the tillage performance of tillage tools' soil contacting line applying on the claw of rat, vole, mole cricket and rooster. Results showed that the soil contacting line and longitudinal/depth ratio were the two important factors affecting the tillage force. The curved tillage tools obtained better tillage performance compared with linear ones under the small longitudinal/depth ratio (less than 1); parabolic tillage tools could obtain good mechanical properties of tillage in a wide range of longitudinal/depth ratio; cycloid curve was suitable for designing tillage part with larger longitudinal/depth ratio (more than 2). Guo et al. (2003) also found that the best cutting performance occurred when the longitudinal/depth ratio was between 0.6 and 0.9. Zhu and Tong (2003) described the application of effective and energy-saving subsoiling technology, and predicted the bionic subsoiler development trend. The above studies provided the research foundation of bionic applications on subsoiler design. Bear is good at digging holes using its sharp and curved claw, the shape of which is suitable for designing subsoilers. Thus, this study analyzed a bionic subsoiler based on the bear claw for the purpose of reducing tillage force.

In recent years, the DEM has been widely used in agricultural engineering, mainly in optimizing agricultural machine and some basic soil engaging experiments (Li et al., 2014; Sun et al., 2009). Many scholars studied the soil-tool interaction using the DEM (Ucgul et al., 2017). Tsuji et al. (2012) used the bond model (Utili and Nova, 2008) to analyze the working process of bulldozing plate. The cohesive force between particles had significant influence on particles' motion and the bulldozing resistance increased as the bond strength increased. Momozu et al. (2002) simulated the soil breaking process under the effect of soil cutting tools. The discrete element model was established by adding bonds between particles to reflect the real process of loosing soil better. Shmulevich et al. (2007) used the method proposed by Asaf et al. (2007) to determine the parameters of soil particles. The tillage forces of four kinds of tools were compared and the soil movement was also analyzed. However, this particle model was established by two-dimensional disk, which had a certain gap with actual particles. Van der Linde (2007) analyzed the tillage force and working performance of vibration subsoilers under different frequencies using the DEM. The reasons of reducing force by vibration were also analyzed. Shmulevich (2010) analyzed applications of the DEM in studying the soil-tool interaction and pointed out the advantages and limitations by using this method.

Above studies showed that some scholars designed the bionic subsoiler and achieved good experimental results. However, the movement of soil particles during the soil-subsoiler interaction and the reasons of bionic subsoiler's reducing force have not been analyzed using DEM. In this study, the DEM was used to establish a soil-subsoiler interaction model. The purposes of this study were: 1). explaining the reasons of bionic subsoiler's reducing force comparing with the arc-shaped subsoiler (JB/T 9788-1999); 2). analyzing the tillage performance of the bionic subsoiler using DEM.

2 Methodology

2.1 Theoretical force analysis

The point of the subsoiler could be regarded as the horizontal low speed movement of a slope in the soil during the tillage. Soehne (1956) analyzed the interaction between the soil and the point. The forces applied on the soil block above the point are shown in Figure 1. Shear failure occurred in front of the point during the process of cutting soil. Gravity, acceleration force, friction were acted on the soil block above the point. For no stone and other debris in the soil, the cutting resistance could be neglected.

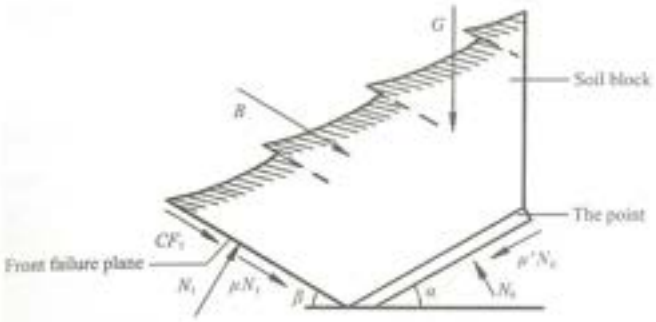

Figure 1 Force applied on the soil block

Through the above analysis of force, force balance equations of soil block above the point in horizontal and vertical direction could be listed as follows:

For horizontal direction:

$$N_0(\sin\alpha+\mu'\cos\alpha)-N_1(\sin\beta+\mu\cos\beta)-(CS'+B)\cos\beta=0 \quad (1)$$

For vertical direction:

$$N_0\cos\alpha-\mu'N_0\sin\alpha+N_1\cos\beta-(B+CS'+\mu N_1)\sin\beta-G=0 \quad (2)$$

where, N_0 is pressure from the soil block above the point (N); μ' is friction coefficient between soil and metal; α is rake angle (°); N_1 is pressure from the front failure surface (N); β is the angle between the front failure surface and horizontal direction (°); B is acceleration force of the soil block above the point (N); C is cohesion of soil (Pa); S' is the area of the front failure surface (m^2); μ is friction coefficient between soil particles, and G is the weight of soil above the point (kg).

The cutting ability is the main function of the shank. Figure 2 shows the force acting on the shank. Three main parts of force were acted on the shank: the force components caused by the normal force applied on the wedge edge, the force components caused by the tangential force applied on the wedge edge, and the force components caused by the tangential force applied on the side face. Therefore, the force of soil applied on the shank could be expressed as follows:

$$W=2\left(N_2\sin\frac{\varphi'}{2}+N_2\mu'\cos\frac{\varphi'}{2}+N_3\mu'\right) \quad (3)$$

where, W is the total force acted on the shank in the horizontal direction, N; φ' is the angle of the wedge edge, °; N_2 is the normal force acted on the wedge edge, N; and N_3 is the normal force acted on the side face, N.

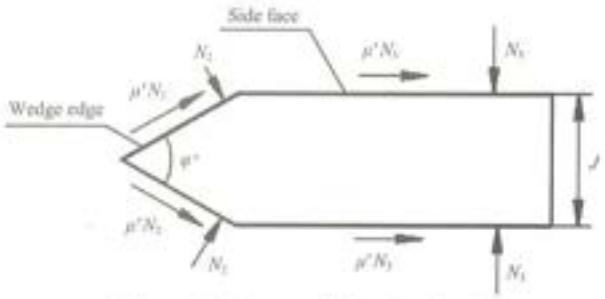

Figure 2 Force applied on the shank

2.2 Subsoilers used in the test

The bionic subsoiler tested in this study was designed based on the standard arc-shaped subsoiler and the curve of bear claw (Li et al., 2015).

Three subsoilers were tested, in which, S_1 is the bionic subsoiler shank with chisel-shaped point; S_2 is the bionic subsoiler; S_3 is the standard arc-shaped subsoiler. S_1 and S_2 had the same shank, while S_1 and S_3 had the same point. The soil bin test was completed in the agriculture machinery lab, i.e. Northwest A&F University, Yangling, Shaanxi, China. The soil type was sandy loam soil.

Figure 3 shows the bionic subsoiler S_2 and the standard arc-shaped subsoiler S_3. Figures 3b and 3d were the bionic point and the standard chisel point, respectively. S_1 was the subsoiler of S_2 replaced by the standard chisel point. The subsoiler was fixed on the working frame by a U shaped clip. Keep the working frame in horizontal position by adjusting the three point suspension device. By using the hydraulic lift system, the subsoiler work was set at the specified tillage depth and the velocity of 0.8 m/s. Make sure the data acquisition system work well before running the traction wagon. The working depth of the subsoiler was 220, 260 and 300 mm, respectively. The soil should be leveled and compacted after each test and make sure the rigidity maintain the same. Each test was repeated three times and the average value was taken as the final results.

2.3 Soil preparation and the test

(1) Soil watering

To achieve similar soil moisture with the field, soil in the soil bin needed to be watered by the watering system of the traction wagon. Two weeks of natural infiltration were required to avoid the moisture content of upper soil higher than the lower part. The soil moisture content was

monitored from the depth of 220 mm to 300 mm until it reached 19.0%.

a. Bionic subsoiler

b. Bionic point

c. Standard arc-shaped subsoiler

d. Standard chisel point

Figure 3 Bionic subsoiler and standard subsoiler

(2) Rotary tilling and soil leveling

The soil surface was not smooth enough when the soil reached the specified soil moisture. What's worse, some large clods were still existed. Therefore, the clods should be broken and the land should be leveled. The rotary cultivator was hung on the traction wagon to break the clods and a scraper plate was used to level the soil (Figure 4a).

(3) Soil compaction

The soil was relatively flat after rotary tillage, and the soil compaction was required to reach the soil compactness in the field. A rolling wheel of 1.2 t was hung on the traction wagon to compact the soil (Figure 4b).

(4) Soil rigidity measurement

Soil rigidity was measured after soil compaction to ensure the consistent soil compactness (Figure 4c). Probe test was carried out at 10 positions in the travelling direction of the subsoiler. The average value of 10 points was taken as the soil rigidity (460 kPa).

a. Rotary tillage

b. Soil compaction

c. Soil compaction test

Figure 4 Preparation of soil bin test

Subsoiler of S_1, S_2 and S_3 was hung on the traction wagon respectively (Figure 5). The travelling velocity of each subsoiler was 0.8 m/s. After each test, the soil should be leveled and compacted for next test. The horizontal resistance of each subsoiler was monitored by sensors during the test. The upper link sensor, hanging pin sensor and angle sensor transferred the measured data to the dynamic data collector. The draft force was the horizontal vector sum of these forces. The data collector sent the data through the antenna to a laptop which would finally deal with the data. The tillage length of each subsoiler was 22 m, and the tillage force was taken from the stable working area of 3 m to 18 m from the start position.

Figure 5 The four-wheel-drive soil bin traction wagon

2.4 The DEM parameters

The soil bin (1 m long, 0.5 m wide and 1 m high) with five walls was established by PFC^{3D}. The soil used in the test was a kind of sandy loam soil and the liquid bridge force between soil particles should be considered. Therefore, the parallel bonds were added to soil particle model using DEM. The DEM parameters of soil used in the simulation were adjusted by comparing the simulation results with the laboratory triaxial compression test. The soil used for the triaxial compression test was the same with the one used in the tillage test. Set the minimum radius of the soil particle to 0.6 mm and the ratio of maximum/minimum radius to 3:1. The soil porosity was same with the soil test (0.4). The DEM parameters for the simulation are listed in Table 1.

Table 1 Parameters for DEM simulation

Parameter	Value
Soil porosity	0.40
Friction factor	0.93
Soil particle density, kg/m^3	2760
Particle-particle contact normal stiffness, N/m	4×10^5
Particle-particle contact shear stiffness, N/m	3.5×10^5
The critical damping ratio in the normal direction	0.8
The critical damping ratio in the shear direction	0.6
The parallel-bond radius multiplier	1.0
The parallel-bond normal stiffness, Pa/m	4×10^8
The parallel-bond shear stiffness, Pa/m	4×10^8
The parallel-bond normal strength, Pa	4×10^5
The parallel-bond shear strength, Pa	4×10^5

Different structures of subsoiler would lead to different forms of soil movement. To analyze the soil movement clearly, two layers of green belt, 75 mm in thickness, were applied in the simulation (Figure 6). Only the color of these two layers was different from other soil particles, soil properties maintained the same. The working condition of the simulation was the same with the test.

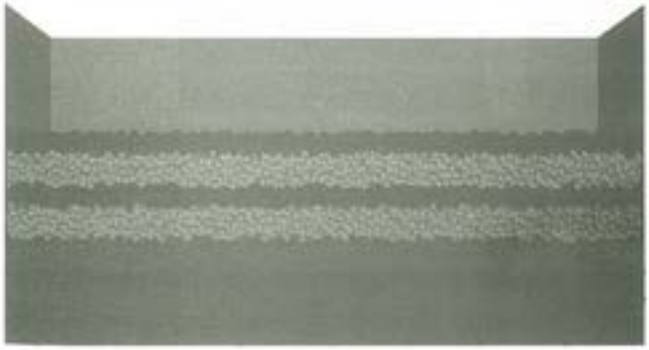

Figure 6 The initial state of the soil

3 Results and discussion

3.1 Tillage resistance

Figure 7 shows the horizontal resistance curve of S_1, S_2, S_3 during the stable state under the working depth of 260 mm. The tillage forces of S_1, S_2 and S_3 were F_{21}, F_{22}, and F_{23}, respectively. It showed that the tillage force fluctuated around the mean value. The tillage force had great volatility in the test, which was caused by the inhomogeneity of soil conditions and the clods in the soil bin. The green curve represented the force of standard arc-shaped subsoiler (S_3), which was relatively higher than other two and the fluctuation range was the maximum among these three curves. The bionic subsoiler (S_2) was the blue curve, which had the lowest tillage force and the smallest fluctuation, indicating the bionic subsoiler could effectively reduce tillage resistance and operate stably. The red curve fluctuated greatly and the tillage force was between the other two.

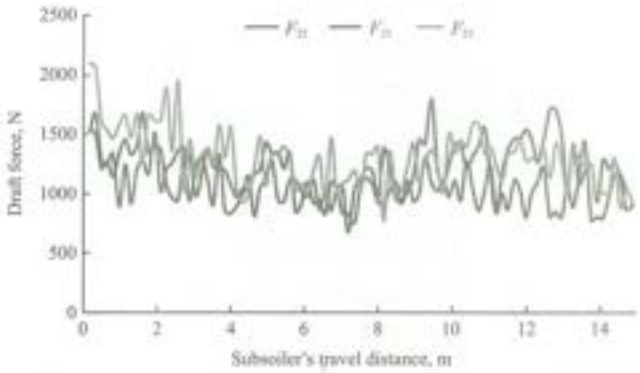

Figure 7 The horizontal resistance of three subsoilers in the test (depth is 260 mm)

The simulation and test results of three kinds of subsoiler under 0.8 m/s are listed in Table 2. The F_{11}, F_{12} and F_{13} were the simulation results of S_1, S_2 and S_3, respectively. The F_{21}, F_{22} and F_{23} were the tillage resistance of the test that corresponding to simulation. The ε was the force reducing rate of S_2 relative to S_3 in simulation; δ was the corresponding reducing rate in the test. θ_1, θ_2 and θ_3 were the simulation relative errors of S_1, S_2 and S_3 respectively, comparing with the test.

The S_3 had the largest tillage resistance, and S_2 had the smallest resistance at the velocity of 0.8 m/s under three depths (Table 2). The DEM simulation achieved the similar results. The relative errors were between 1.42% and 27.43%, which were in the allowable range,

indicating that the DEM could predict the tillage force of a subsoiler instead of doing experiments. The relative errors larger than 20% only happened at the depth of 220 mm for S_2, which required further analysis.

Table 2 The tillage resistance results of three subsoilers

Depth, mm	F_{11}, N	F_{12}, N	F_{13}, N	F_{21}, N	F_{22}, N	F_{23}, N	ε, %	δ, %	θ_1, %	θ_2, %	θ_3, %
220	1042	929	1055	869	729	996	11.94	26.81	19.91	27.43	5.92
260	1199	1124	1310	1234	1074	1342	14.20	19.97	2.84	4.66	2.38
300	1566	1521	1615	1544	1491	1675	5.82	10.99	1.42	2.01	3.58

3.2 Force reducing mechanism and tillage performance of the bionic subsoiler

3.2.1 Soil disturbance analysis

To compare the soil disturbances of bionic subsoiler and the standard arc-shaped one working at different stages, the soil was cut in the travelling direction (Figure 8). Based on the travelling stage of the subsoiler, three distances of 250, 350 and 600 mm from the start position were selected, respectively. In the first stage, the point and parts of the shank entered into the soil bin; in the second stage, the inner baseline of two subsoilers entered into the soil bin; in the third stage, two subsoilers worked in the stable stage. The velocity field, the contact force field and the parallel bond field were all compared in these three stages.

The soil in front part of the subsoiler was lifted when the subsoiler entered into the soil bin (Figures 8a and 8d). More soil disturbance and fluctuation were observed as the subsoiler entering into the soil (Figures 8b and 8e). In the stable stage, soil around the point suffered more disturbance than other areas (Figures 8c and 8f), which meant the point of the subsoiler had the function of breaking plow pan. These two subsoilers were similar in soil disturbance.

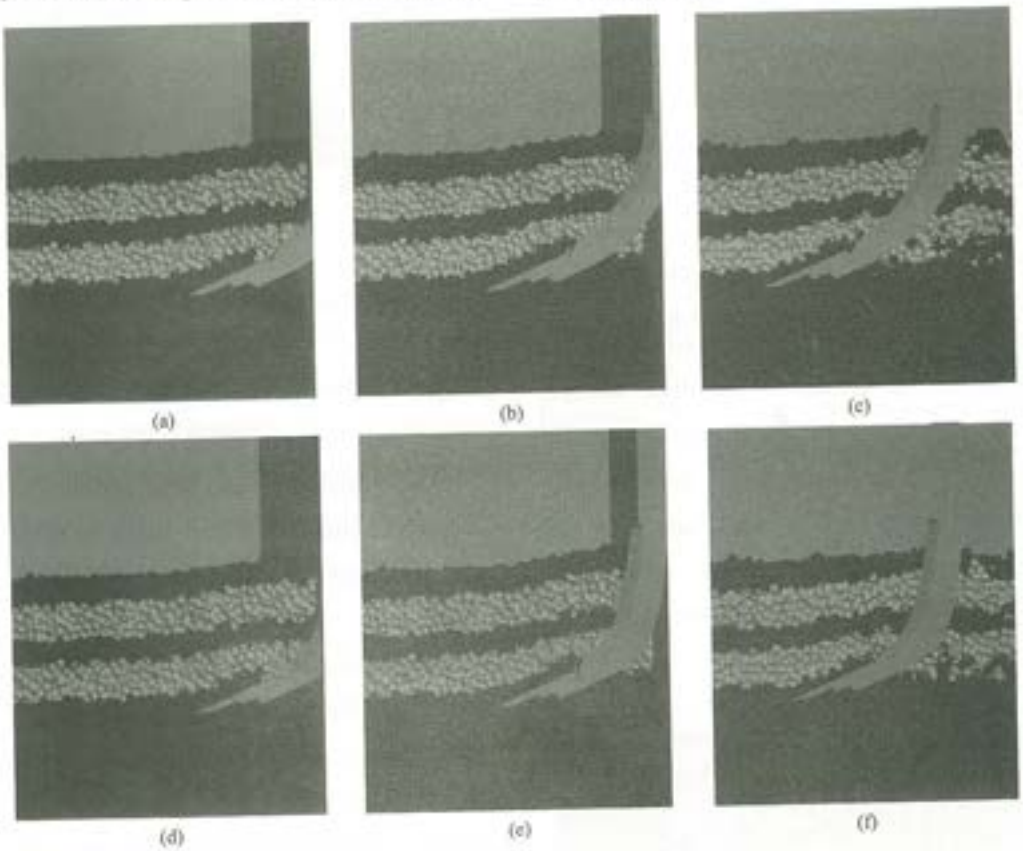

Figure 8 Dynamic behaviors of soil particles

(a)-(c) Standard arc-shaped subsoiler; (d)-(f) Bionic subsoiler

3.2.2 Velocity field analysis

The velocity field of the disturbed soil particles could be reflected by different colors during the simulation. Figure 9 is the velocity contour. The direction of each particle's velocity could be reflected by the arrow while the length of the arrow showed the magnitude.

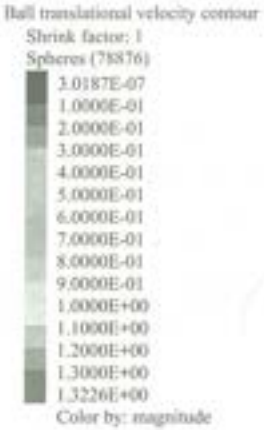

Figure 9 Velocity contour

As the subsoiler travelling into the soil bin, the disturbed area increased gradually until the whole subsoiler entered into the soil (Figure 10). Soil particles started to move under the effect of the point in the first stage (Figures 10a and 10d). The difference was obvious in the second stage. Soil particles pushed by the arc-shaped subsoiler moving towards the center of the arc. This would lead to the accumulation of soil and hindered the subsoiler travelling forward (Figure 10b). While soil moved in the direction of inclining upward under the effect of bionic subsoiler (Figure 10e). During the stable stage (Figures 10c and 10f), more soil was thrown behind the arc-shaped subsoiler with relatively higher velocity compared with the bionic subsoiler. It could be explained that arc-shaped subsoiler had more lifting effect on the soil. However, large lifting effect was useless for improving the tillage performance and would increase the tillage resistance and the surface roughness. For the purpose of tillage was loosening the soil and the plow pan without disturbing land layers. In addition, the rough soil surface was helpless for the subsequent field work.

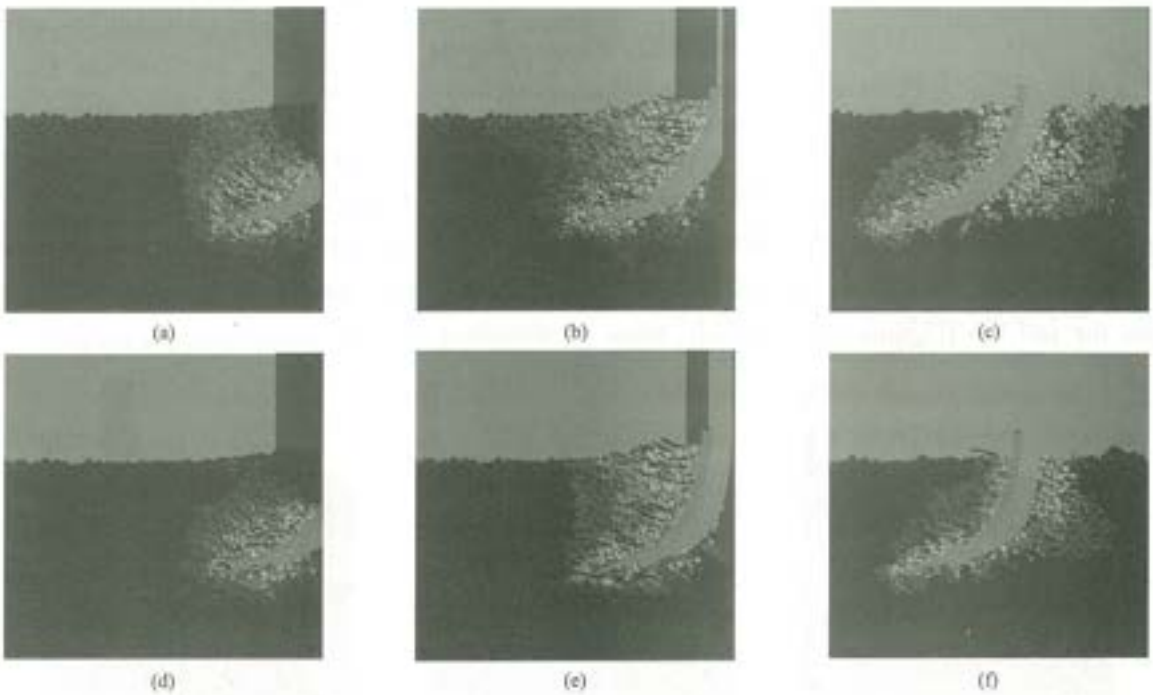

Figure 10 Velocity field

(a)-(c) standard arc-shaped subsoiler; (d)-(f) bionic subsoiler

3.2.3 Contact force field

Contact force between particles was formed at the contact point in PFC^{3D} (Itasca 2015). The contact force field was composed by the force chain whose size reflected the magnitude of force. The force chain would break when the force acting on soil particles exceeded the contact force. In this study, the contact force field was obtained from the 42 mm thick slice containing the subsoiler (Figure 11), so that the force chain around the subsoiler could be reflected.

Figure 11 showed that the contact force mainly concentrated at the contact surface of the subsoiler. For these two subsoilers, the point suffered larger concentrated force than other parts. From the analysis of three stages, the stress concentration areas were basically the same: the upper surface of the point and the edge of the shank. The force chains between soil particles were broken after tillage (Figures 11c and 11f). There was almost no difference in breaking the force chain, which showed that these two subsoilers had similar tillage performance.

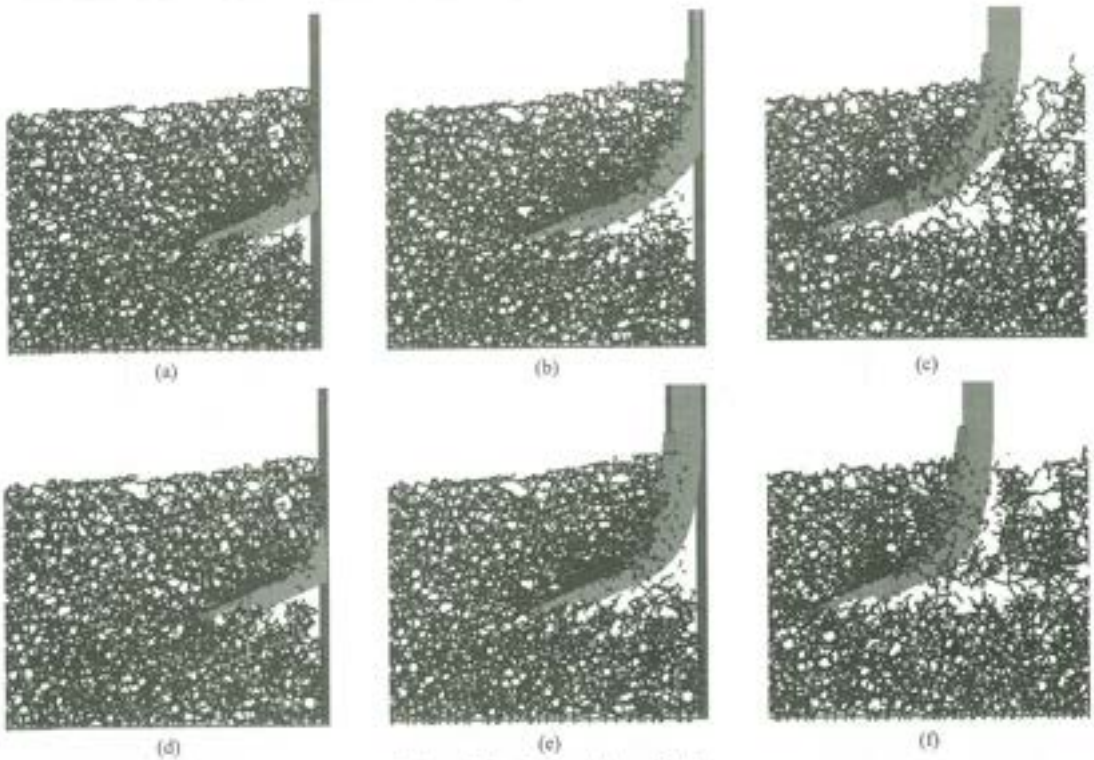

Figure 11 Contact force field

(a)-(c) Standard arc-shaped subsoiler; (d)-(f) Bionic subsoiler

3.2.4 Parallel bond field

Parallel bonds were the cylindrical areas between two contact soil particles to bear the force and torque. Parallel bonds around the point were broken as the subsoiler entered into the soil bin (Figures 12a and 12d). More bonds were destroyed as the subsoiler moving forward (Figures 12b and 12e). The bond chains behind the subsoiler became sparse for the contact soil particles were disturbed. Two subsoilers had the similar effect on disturbing the soil.

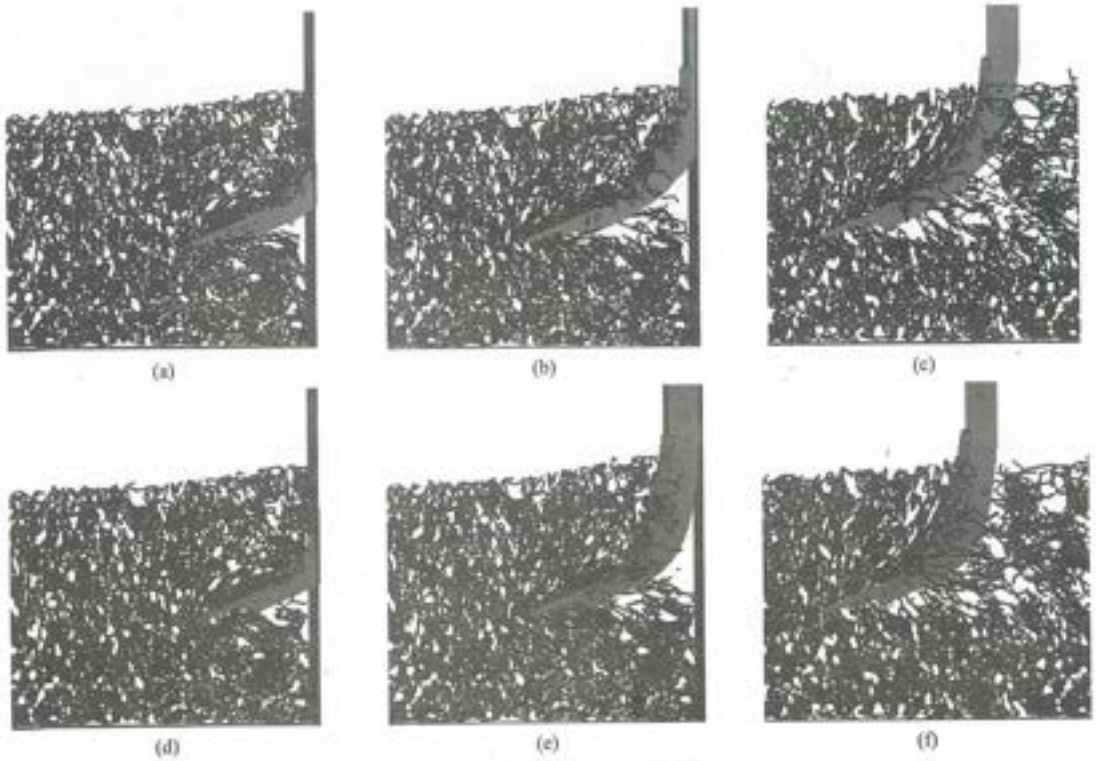

Figure 12 Parallel bond field

(a)-(c) Standard arc-shaped subsoiler; (d)-(f) Bionic subsoiler

In summary, two subsoilers were similar in tillage performance after comparing them in soil movement, velocity field, force field and parallel bond field.

4 Conclusions

This study compared the bionic subsoiler and the standard arc-shaped subsoiler by the DEM simulation and soil bin test. Results showed that the bionic subsoiler could reduce the tillage force significantly. By comparing these two subsoilers in soil movement, velocity field, contact force field and parallel bond field, the mechanism of reducing tillage force and the tillage performance were analyzed. Results showed that soil particles moving towards the center of the arc and the high lifting effect were the reasons of arc-shaped subsoiler's large tillage force. The bionic subsoiler had the similar tillage performance in disturbing the soil and breaking the contacts with the standard arc-shaped subsoiler. This study explained the reasons of reducing force using the bionic subsoiler and provided the theoretical basis for designing subsoilers. It should be noticed that the above conclusions were drawn for a specific soil (sandy loam soil) in the given soil moisture content. For different conditions, further research is required.

Acknowledgment

The project was supported by the Open Research Fund of Shanxi Key Laboratory of Fully Mechanized Coal Mining Equipment (No. mkzczb201602), Youth Foundation of Taiyuan University of Technology (No. 1205-04020203).

[References]

[1] Abo-Elnor, M., R. Hamilton, and J. T. Boyle. 2004. Simulation of soil-blade interaction for sandy soil using advanced 3D finite element analysis. *Soil & Tillage Research*, 75(1): 61–73.

[2] Asaf, Z., D. Rubinstein, and I. Shmulevich. 2007. Determination of discrete element model parameters required for soil tillage. *Soil & Tillage Research*, 92(1-2): 227–242.

[3] Guo, Z. J., D. Y. Zhou, and Z. L. Zhou. 2010. Simulation research on mechanical performances of several kinds of cultivating components with different soil-engaging surfaces. *Journal of Mechnical Engineering*, 46(15): 71–75.

[4] Guo, Z. J., and Z. L. Zhou. 2003. 2D Finite element analysis for the cutting performance of bionic curved cutting tools. *Chinese Journal of Mechanical Engineering*, 39(9): 106–109.

[5] Itasca. 2015. PFC3D-Particle flow code in three dimensions, theory and background. Itasca Consulting Group, Inc., Minneapolis, MN, USA.

[6] JB/T 9788-1999. 2000. Subsoiler and share shaft. Machinery Industry Standard of the People's Republic of China.

[7] Ji, W. F., D. H. Chen, H. L. Jia, and J. Tong. 2010. Experimental investigation into soil-cutting performance of the claws of mole rat (*Scaptochirus moschatus*). *Journal of Bionic Engineering*, 7(3): S166–S171.

[8] Li, B., F. Y. Liu, J. Y. Mu, J. Chen, and W. T. Han. 2014. Distinct element method analysis and field experiment of soil resistance applied on the subsoiler. *International Journal of Agricultural and Biological Engineering*, 7(1): 54–59.

[9] Li, B., F. Y. Liu, R. Xia, and J. Chen. 2015. Distinct element method analysis and experiment of a biomimetic subsoiler. *International Agricultural Engineering Journal*, 24(1): 47–54.

[10] Momozu, M., A. Oida, M. Yamazaki, and A. J. Koolen. 2002. Simulation of a soil loosening process by means of the modified distinct element method. *Journal of Terramechanics*, 39(4): 207–220.

[11] Mouazen, A. M., and M. Nemenyi. 1999a. Finite element analysis of subsoiler cutting in non-homogeneous sandy loam soil. *Soil & Tillage Research*, 51(1-2): 1–15.

[12] Mouazen, A. M., and M. Nemenyi. 1999b. Tillage tool design by the finite element method: part 1. finite element modelling of soil plastic behaviour. *Journal of Agricultural Engineering Research*, 72(1): 37–51.

[13] Mouazen A. M., M. Nemenyi, H. Schwanghart., and M. Rempfer. 1999. Tillage tool design by the finite element method: part 2. experimental validation of the finite element results with soil bin test. *Journal of Agricultural Engineering Research*, 72(1): 53–58.

[14] Mouazen, A. M., and H. Ramon. 2002. A numerical-statistical hybrid modelling scheme for evaluation of draught requirements of a subsoiler cutting a sandy loam soil, as affected by moisture content, bulk density and depth. *Soil & Tillage Research*, 63(3-4): 155–165.

[15] Ren, L. Q., Z. W. Han, J. Q. Li, and J. Tong. 2006. Experimental investigation of bionic rough curved soil cutting blade surface to reduce soil adhesion and friction. *Soil & Tillage Research*, 85(1-2): 1–12.

[16] Shahgoli, G., J. Fielke, J. Desbiolles, and C. Saunders. 2010. Optimising oscillation frequency in oscillatory tillage. *Soil & Tillage Research*, 106(2): 202–210.

[17] Shmulevich, I. 2010. State of the art modeling of soil-tillage interaction using discrete element method. *Soil & Tillage*

Research, 111(1): 41–53.

[18] Shmulevich, I., Z. Asaf, and D. Rubinstein. 2007. Interaction between soil and a wide cutting blade using the discrete element method. *Soil & Tillage Research*, 97(1): 37–50.

[19] Soehne, W. 1956. Some principles of soil mechanics as applied to agricultural engineering. *Grundlagen der Landtechnik*, 7: 11–27.

[20] Sun, P., F. Gao, W. Li, S. Z. Yao, and Y. T. Gong. 2009. Discrete element simulation of cone penetration process. *Transactions of the CSAM*, 40(1): 184–188.

[21] Tsuji, T., Y. Nakagawa, N. Matsumoto, Y. Kadono, T. Takayama, and T. Tanaka. 2012. 3-D DEM simulation of cohesive soil-pushing behavior by bulldozer blade. *Journal of Terramechanics*, 49(1): 37–47.

[22] Tong, J., B. Z. Moayad, Y. H. Ma, J. Y. Sun, D. H. Chen, H. L. Jia, and L. Q. Ren. 2009. Effects of biomimetic surface designs on furrow opener performance. *Journal of Bionic Engineering*, 6(3): 280–289.

[23] Tong, J., M. A. Mohammad, J. B. Zhang, Y. H. Ma, B. J. Rong, D. H. Chen, and C. Menon. 2010. DEM numerical simulation of abrasive wear characteristics of a bioinspired ridged surface. *Journal of Bionic Engineering*, 7(2): 175–181.

[24] Ucgul, M., C. Saunders, and J. M. Fielke. 2017. Discrete element modelling of tillage forces and soil movement of a one-third scale mouldboard plough. *Biosystems Engineering*, 155: 44–54.

[25] Utili, S., and R. Nova. 2008. DEM analysis of bonded granular geomaterials. *International Journal for Numerical and Analytical Methods in Geomechanics*, 32(17): 1997–2031.

[26] Van der Linde, J. 2007. Discrete element modeling of a vibratory subsoiler. M.S. Thesis. Department of Mechanical and Mechatronic Engineering, University of Stellenbosch, Matieland, South Africa.

[27] Zhang, Z. J., H. L. Jia, and J. Y. Sun. 2016. Review of application of biomimetics for designing soil-engaging tillage implements in Northeast China. *International Journal of Agricultural and Biological Engineering*, 9(4): 12–21.

[28] Zhu, F. W., and J. Tong. 2003. Development of high-efficient and energy-saving bionic bubsoiling techniques. *Journal of Jilin University (Engineering and Technology Edition)*, 33(2): 95–99.

Development of 3-DOF lifting platform for hilly orchards

Duan Zhenhua[1,2], Qiu Wei[1,2], Ding Weimin[1,2*], Liu Yande[2], Ouyang Yuping[2], Huang Liang[1]

(1. *College of Engineering, Nanjing Agricultural University, Nanjing 210031, China;*
2. *Co-Innovation Center of the Intelligent Management and Equipment for Orchard on the Hilly Land in South China, Nanchang, 330013, China*)

Abstract: In order to improve the mechanization degree of operations such as picking, pruning, and bagging in hilly orchards, and solve the problems of insufficient operating capabilities and low operating range of current orchard lifting machinery in complex terrains, a 3-DOF lifting platform for hilly orchards was developed. The main structure and operating parameters such as operating height, operating radius, and operating range were determined by the geometric parameters of fruit trees and theoretical analysis. To evaluate the performance of the platform, experiments of the prototype including operating parameters experiment, operating effect on fruit trees experiment, leveling experiment and tilting stability experiment were carried out. The experimental results indicated that lifting, rotating and leveling actions were smooth at low speed, the maximum operating height was 1.2 m, and at a maximum operating radius of 1.42 m, the lifting device could rotate 360° with an operating range of 3.6 m^2. In addition, the leveling error was less than 0.4°, which is negligible and the leveling device can be considered to have a relatively high accuracy. The maximum tilting angle when the platform was at any parked position, equipped with different loads and at various operating heights, was 19.3° to 30°, which were consistent with the design requirements. The maximum tilting angle could also adapt to slope conditions of 5° to 20° in hilly orchards. The proposed 3-DOF lifting platform for hilly orchards has a better tilting stability performance compared to contemporary machinery. This study can provide reference for future design of lifting machinery in hilly orchards based on the characteristics of terrain and fruit tree planting.

Keywords: 3-DOF lifting platform, orchard mechanization, hilly land, lifting platform, operating parameters, leveling, experiments

Citation: Duan, Z. H., W. Qiu, W. M. Ding, Y. D. Liu, Y. P. Ouyang, and L. Huang. 2017. Development of 3-DOF lifting platform for hilly orchards. International Agricultural Engineering Journal, 26(3): 37–48.

1 Introduction

Mechanization of orchard activities is not only important for the development of the fruit industry, but is also an important part of agricultural production mechanization (Chang et al., 2013; Hong et al., 2010). In recent years, with the rapid development of the orchard industry, more large-scale and standardized orchards are built in China. These orchards have certain requirements on the shape of fruit trees, and have a larger row spacing and plant spacing. This promotes the use of adaptable multi-functional orchard management machinery, and provides a push for orchard mechanized operations at the same time (Wang et al., 2013; Li et al., 2012). This mechanization also increases the efficiency in traditional orchard production processes such as picking, pruning, bagging, etc. which were mostly carried out using ladders, stepping on stools and other modes of artificial climbing operation, which were not only labor intensive, but also had greater security risks.

Because of proper planning, flatness, and maneuverability of machinery in orchards in European and American countries were better, which resulted in the earlier adoption of orchard lifting platforms in these countries. This also led lifting platforms to mainly use the wheel travel mechanism, which were suitable for operating in plain terrain (Liu et al., 2015). British Genie

Received date: 2017-03-29 **Accepted date:** 2017-07-03

* **Corresponding author: Ding Weimin**, Ph.D., Professor of Department College of Engineering, Nanjing Agricultural University, Nanjing 210031, China. Email: wmding@njau.edu.cn, Tel: 025-5860 6502.

developed Gr12, Gr15 and Gr20 models of electric wheel type lifting platform and Seymour developed Windegger picking devices wheel lifting platform (Tang et al., 2006); American Nelson developed tree squirrel pruning and picking tower for orchards; Australia Crendon developed lifting platform for picking the mango and avocado; Japan Shikoku Agricultural Experiment Station developed crawler chassis self walking type picking vehicle (Wang et al., 2014). In recent years, many research institutions and companies have also developed a few lifting platforms for orchards in China. Xinjiang Institute of Mechanization developed a multi-functional orchard machine (Liu et al., 2009); Beijing Agricultural Machinery Test and Accreditation Station developed a small multi-function remote control power platform (Wang, 2011); Hebei Agricultural University developed a crawler multifunctional orchard operating platform (Sun, 2012; Wang, 2013); Shandong Agricultural University developed a hanging operating platform for hilly orchards (Wang, 2013); Hunan Agricultural University developed a lifting platform in citrus orchards (Liu, 2013), etc. Although these current machineries make the lifting operation possible, most of them do not have the ability to work in hilly orchards, and cannot adapt to the rugged terrain conditions. The scissor structure that was mainly used in these machineries could only lift in the vertical direction. In addition, limited by the size of the worktable, the operating range in the horizontal plane was generally small, usually between 0.64 m^2 and 1.5 m^2. As a result, these lifting platforms had to move frequently to change the operating position for some fruit trees with larger crown. This not only made the operation tedious, but also increased the risk on hilly lands.

Considering the structure, working principle, and problems associated with the current lifting platforms used in orchards, this study developed a 3-DOF lifting platform for hilly orchards to realize operations under complex terrain conditions and improve the overall production efficiency.

2 Design requirements and structural principle

2.1 Design requirements

Barring a few exceptions, a large scale and centralized planting pattern when adopted in hilly orchards, has certain requirements on row spacing, plant spacing and fruit tree shape. Thus, the orchard lifting platform should be adapted to the planting environment of the hilly land and the orchard management practices, and in line with the operating requirements of picking, pruning, bagging, etc. which are stated as follows. The operating height and operating radius should be adapted to the height and crown of different fruit trees, and at the same time have a larger operating range. The manned worktable should have sufficient carrying capacity to transfer fruits, branches, leaves, etc. conveniently. In addition, the lifting platform should be usable on sloping fields with slope angle ranging from 5° to 20° with the manned worktable being horizontally leveled.

2.2 Main structure

The proposed 3-DOF lifting platform mainly consists of manned worktable, lifting device, power device, walking device and leveling device, as is shown in Figure 1. The lifting device is mainly composed of a folding-arm, slewing bearing, lifting hydraulic cylinder, hydraulic pump station and an electromagnetic valve group. The leveling device consists of leveling cylinder and leveling turbo-worm. The walking device adopts an agricultural crawler chassis, which has the advantages of compact structure, large ground connect area, small turning radius, and the ability to cross a ditch ridge (Zhang et al., 2014; Zhao et al., 2014; Cao et al., 2007). The parameters of the lifting platform are summarized in Table 1.

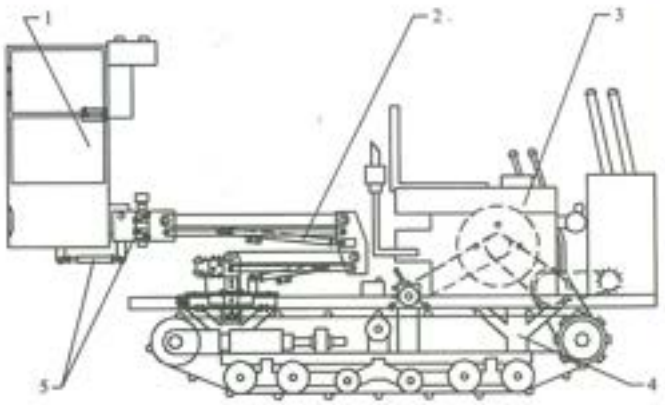

1. Manned worktable 2. Lifting device 3. Power device 4. Walking device 5. Leveling device

Figure 1 Diagram of 3-DOF lifting platform for hilly orchards

Table 1 Parameters of 3-DOF lifting platform for hilly orchards

Parameters	Value
Dimensions (L×W×H), mm	2730×1500×1900
Dimensions of manned worktable (L×W×H), mm	500×1000×1000
Weight, kg	1531.5
Maximum load, kg	150
Power, kW	16.2
Angle of rotating, °	360
Angle of leveling, °	±25

2.3 Working principle

When the lifting platform is moving in an orchard, the driver can control the joystick to realize forward, backward, and turning movements using different gears. The operator standing on the manned worktable can also reach a proper operating position by controlling the lifting device to lift and rotate. Additionally, the manned worktable can be leveled by the leveling device based on a bubble level (LJD13060C) when the ground is uneven.

The leveling principle: taking into account, the effect of different operating heights and different operating radii on the manned worktable level, the leveling cylinder and the leveling turbo-worm are put into operation to level the worktable through movements in all four directions.

As is shown in Figure 2, coordinate systems $oxyz$, $o_1x_1y_1z_1$, and $o_2x_2y_2z_2$ are set up ,on the basis of the horizontal ground, the lifting platform and the manned worktable, respectively. When the lifting platform is parked at any location with an angle α'' to the slope, which in turn has an angle α and α' with the x axis and y axis, respectively, the lifting device makes a rotational angle ω, with the lower-arm and upper-arm having angles θ_1 and θ_2 in the horizontal direction post lifting. The operating position of the manned worktable is can be determined by the angles α, α', α'', ω, θ_1 and θ_2. Under the coordinate system $o_2x_2y_2z_2$, the manned worktable has dip angle β and γ in the horizontal and vertical direction, respectively. The operator can control the leveling device to level at different operating positions using a bubble level installed on the control box.

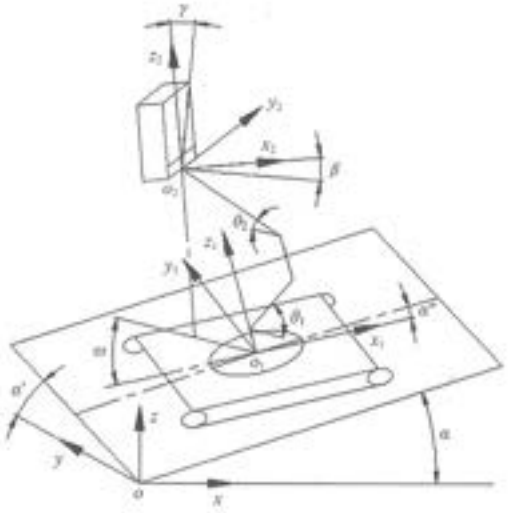

Figure 2 Schematic diagram of the leveling principle

3 Design of key parts

3.1 Lifting device design

3.1.1 Determination of operating height and radius

Figure 3 shows the relationship between the operation parameters of the lifting platform and the geometric parameters of fruit trees, from where the operating height and radius were determined using row spacing ($2s$), tree height (H), and tree crown (d). Where in this figure, h is the operating height, m; R is the operation radius, m; H is the tree height, m; H_1 is the trunk height, m; d is the diameter of tree crown, m; s is half of row spacing, m; h_1 is the height from the ground without lifting, m; h_2 is the average operating height of operator, m; θ_1 is lifting angle of lower-arm, (°); θ_2 is lifting angle of upper-arm, (°); l_1 is the length of lower-arm, mm; l_2 is the length of upper-arm, mm; l_3 is the length of mounting distance on the middle-arm between lower-arm and upper-arm in the horizontal direction, mm; l_4 is the length of leveling device, mm; and l_5 is the length of manned worktable, 500 mm.

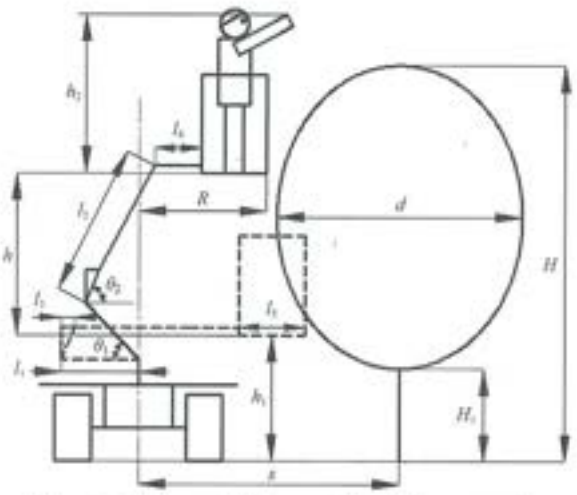

Figure 3 Schematic diagram of the lifting operation

The operating height and radius need to satisfy Equations (1) and (2), respectively:

$$h = H - h_1 - h_2 \quad (1)$$

$$R = s - 0.5d \quad (2)$$

Accurate data of geometric parameters of fruit trees were collected by visiting orchards in hilly areas in Jiangxi Province and summarizing the results of previous studies (Qiu et al., 2012; Liu et al., 2014; Ding et al., 2013; Zhou at al., 2015; Qiu et al., 2016). It could be summarized that row spacing varied from 4 m to 6 m, plant spacing varied from 2 m to 4 m, tree height varied from 3 m to 3.8 m, tree crown varied from 1.5 m to 3 m, trunk varied from 0.4 m to 1 m, and the angle of slope varied from 5° to 20°. It had been known that h_1 was 0.9 m and h_2 was 1.7 m. Substituting these values in Equations (1) and (2) and solving them shows that the operating height and radius should be from 0.4 m to 1.2 m and from 1.3 m to 1.5 m, respectively. Therefore, the effective operating height and radius of lifting platform were chosen as 1.2 m (maximum value) and 1.4 m (average value).

3.1.2 Lifting mechanism

The lifting mechanism was developed as a folding-arm system with the advantages being a larger range and more operational flexibility compared to other lifting forms such as the scissors mechanism (Miao et al., 2013). As is shown in Figure 4, both ends of the upper-arm cylinder and lower-arm cylinder were connected with the middle-arm and upper-arm, base and lower-arm, respectively. The upper-arm linkage and lower-arm linkage ensured that the manned worktable was always parallel with the base, which was fixed on the slewing bearing. In addition, the base was also connected to the solenoid valve group and the central swivel joint.

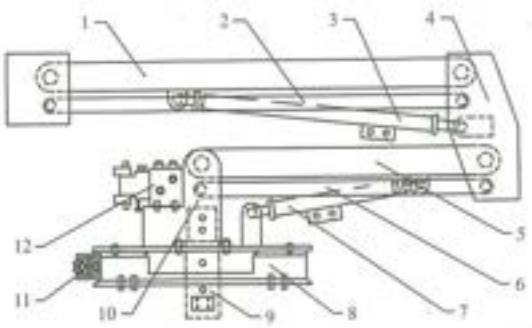

1. Upper-arm 2. Upper-arm linkage 3. Upper-arm cylinder 4. Middle-arm 5. Lower-arm 6. Lower-arm linkage 7. Lower-arm cylinder 8. Slewing bearing 9. Central swivel joint 10. Base 11. Rotating hydraulic motor 12. Solenoid valve group

Figure 4 Structural schematic of the lifting device

As per the geometric relationship in the lifting mechanism (Figure 3), the operating height and radius satisfy the following equations:

$$h = l_1 \sin\theta_1 + l_2 \sin\theta_2 \quad (3)$$

$$R = l_2 \cos\theta_2 + l_3 + l_4 + l_5 - l_1 \cos\theta_1 \quad (4)$$

Considering the mounting space and based on the design values of operating height (1.2 m) and radius (1.4 m), l_1 was set to 590 mm, l_2 was set to 900 mm, l_3 was set to 80 mm, and l_4 was set to 320 mm. Subsequently, the mounting distances and cylinder displacement of lower-arm cylinder and upper-arm cylinder were set to 380 mm and 160 mm, 510 mm and 230 mm, respectively and at the same time, the maximum θ_1 and θ_2 were 47° and 62°, respectively.

3.2 Manned worktable and leveling device design

As is shown in Figure 5, one side of the guardrails of the manned worktable could be opened for operator to get in conveniently through a bolt. The worktable had enough space for some portable tools and was connected to the upper-arm through the leveling device. The operating box with buttons for lifting, rotating, and leveling was fixed on the front of the worktable.

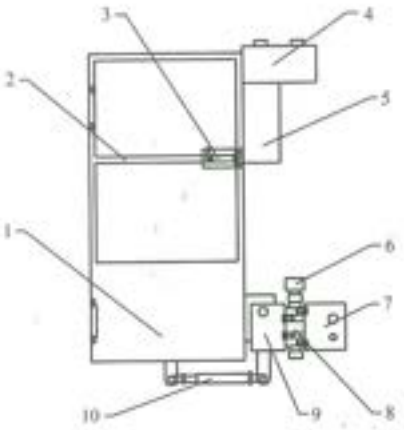

1. Manned worktable 2. Guardrail 3. Bolt 4. Operating box 5. Control box 6. Leveling hydraulic motor 7. Connection plate of left and right leveling 8. Leveling turbo-worm 9. Connection plate of front and back leveling 10. Leveling cylinder

Figure 5 Structural schematic of the manned worktable

The leveling turbo-worm was driven by the leveling hydraulic motor which could theoretically rotate the manned worktable by 360°, and satisfied the design parameters for left and right leveling operations (±25°). On the other hand, when the leveling cylinder telescoped, the manned worktable could rotate around the hinge point between itself and the leveling device to realize front and

back leveling operations. The relationship between leveling angle and displacement of the leveling cylinder is shown in Figure 6 when the manned worktable is leveled to the front, where α_0 is the leveling angle, (°); $A(A_0)$ is the hinge point between manned worktable and leveling device; $B(B_0)$ is the hinge point of leveling cylinder; $C_0(C)$ is the hinge points of leveling cylinder; D_0 (D) is the points of intersection of $A(A_0)$ and $C_0(C)$ in the horizontal and vertical direction, respectively; a is the horizontal distance, mm; b is the vertical distance, mm; c is the horizontal distance of $A(A_0)$ and $B(B_0)$; l_0 is the mounting distance of leveling cylinder, mm; and Δl is the displacement of leveling cylinder, mm.

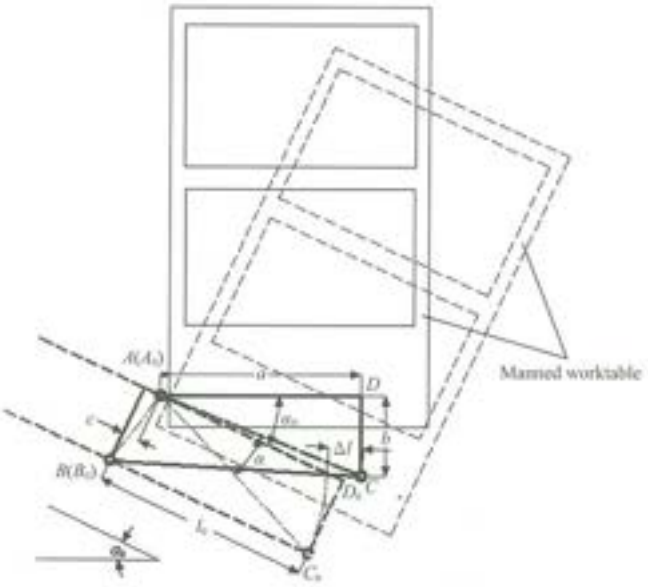

Figure 6 Schematic diagram of relationship between leveling angle and displacement of leveling cylinder

The relationship can be expressed by the following equation as per geometric positions:

$$\Delta l = \sqrt{X^2 + Y^2 - 2XY\cos(\arccos\frac{X^2 + Y^2 - l_0^2}{2XY} + \alpha_0)} - l_0 \quad (5)$$

where, $X^2 = a^2 + b^2$, and $Y^2 = b^2 + c^2$.

Considering the design requirements of the leveling range, the values of a, b, c, and l_0 were set to 430 mm, 180 mm, 35 mm, and 465 mm, respectively. When α_0 was 25°, substituting the values in Equation (5) and solving it, gave $\Delta l = 71$ mm. Meanwhile, it was known that the displacement of the leveling cylinder should be greater than $2\Delta l$, and it was chosen to be 150 mm.

3.3 Operating range

Taking into account the operating characteristics of the 3-DOF lifting platform, the operating range could be divided into two parts, one was the vertical operating range because of the lifting operation, and another was the horizontal operating range because of the rotating operation. The schematic diagram of the lifting track in the vertical direction shows the operating range of the manned worktable through lifting, and boundaries of the track can be obtained by the graphical method (Wang et al., 2011; Feng et al., 2010), as is shown in Figure 7, where O is the supporting point of the lifting device; OA_j is the base; A_jB_j is the lower-arm; B_jC_j is the middle-arm; D_jE_j is the upper-arm; E_jF_j is the leveling device; F_jG_j is the mounting distance of worktable and leveling device in the vertical direction, m; G_jH_j and $G_j'H_j'$ are the worktable bottom, and $j = 1, 2, 3$.

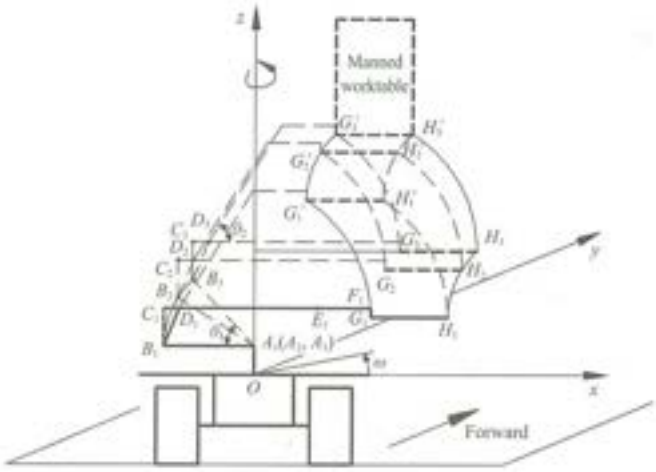

Figure 7 Schematic diagram of lifting track in the vertical direction

When the lifting device was in operation, the manned worktable had three special positions which formed three tracks based on the substitute points of the worktable bottom. When the upper-arm (D_1E_1) was lifted by θ_2, $G_1H_1H_1'G_1'$ was the operating track of the worktable; when lower-arm (A_2B_2) was lifted by $5\theta_1/8$ and upper-arm (D_2E_2) by θ_2, $G_2H_2H_2'G_2'$ was the operating track; when lower-arm (A_3B_3) and upper-arm (D_3E_3) were lifted by θ_1 and θ_2, respectively, $G_3H_3H_3'G_3'$ was the operating track. Obviously, track G_1H_1, G_1G_1', $G_1'G_3'$, $G_3'H_3'$, $H_3'H_3$, and H_3H_1 were the boundaries of the operating ranges in the vertical plane. The maximum operating height were at points G_3' and H_3', and the maximum and minimum operating radius were at points H_3 and G_1'. When the lifting device was rotating by ω at

any operating height, the track could form a torus, which was the operating range of the worktable in the horizontal plane.

Setting the point A_1 as the origin, the right direction of the lifting platform as the x axis, the forward direction as the y axis, and the upward direction from the ground as the z axis, the coordinate system A_1xyz was built. Then, the track G_1H_1, G_1G_1', $G_1'G_3'$, $G_3'H_3'$, $H_3'H_3$, and H_3H_1 in the space coordinate system could be expressed by the following equations:

Track G_1H_1 ($\theta_1 = 0°$, $\theta_2 = 0°$, $0° \le \omega \le 360°$):

$$\begin{cases} \sqrt{x^2+y^2} = l_2 + l_3 - l_1 + l_4 + l_{GH} \\ x = (l_2 + l_3 - l_1 + l_4 + l_{GH})\cos\omega \\ y = (l_2 + l_3 - l_1 + l_4 + l_{GH})\sin\omega \\ z = l_{BC} - l_{FG} \end{cases} \quad (6)$$

Track G_1G_1' ($\theta_1 = 0°$, $0° \le \theta_2 \le 62°$, $0° \le \omega \le 360°$):

$$\begin{cases} (\sqrt{x^2+y^2} + l_1 - l_3 - l_4)^2 + (z - l_{BC} + l_{FG})^2 = l_2^2 \\ \sqrt{x^2+y^2} = l_3 + l_4 - l_1 + l_2\cos\theta_2 \\ x = (l_3 + l_4 - l_1 + l_2\cos\theta_2)\cos\omega \\ y = (l_3 + l_4 - l_1 + l_2\cos\theta_2)\sin\omega \\ z = l_{BC} - l_{FG} + l_2\sin\theta_2 \end{cases} \quad (7)$$

where, l_1 is 0.59 m; l_2 is 0.9 m; l_3 is 0.08 m; l_4 is 0.32 m; l_5 is 0.5 m; l_{GH} is from 0 m to 0.5 m; l_{BC} is 0.25 m; and l_{FG} is 0.02 m. Substituting the values and solving the Equations (6) and (7):

Track G_1H_1 ($\theta_1 = 0°$, $\theta_2 = 0°$, $0° \le \omega \le 360°$):

$$\begin{cases} \sqrt{x^2+y^2} = 0.71 + l_{GH} \\ x = (0.71 + l_{GH})\cos\omega \\ y = (0.71 + l_{GH})\sin\omega \\ z = 0.23 \end{cases}, \ 0 \le l_{GH} \le 0.5m \quad (8)$$

Track G_1G_1' ($\theta_1 = 0°$, $0° \le \theta_2 \le 62°$, $0° \le \omega \le 360°$):

$$\begin{cases} (\sqrt{x^2+y^2} + 0.19)^2 + (z - 0.23)^2 = 0.81 \\ \sqrt{x^2+y^2} = -0.19 + 0.9\cos\theta_2 \\ x = (-0.19 + 0.9\cos\theta_2)\cos\omega \\ y = (-0.19 + 0.9\cos\theta_2)\sin\omega \\ z = 0.23 + 0.9\sin\theta_2 \end{cases} \quad (9)$$

Similarly, track $G_1'G_3'$, $G_3'H_3'$, $H_3'H_3$, H_3H_1 could be expressed as:

Track $G_1'G_3'$ ($0° \le \theta_1 \le 47°$, $\theta_2 = 62°$, $0° \le \omega \le 360°$):

$$\begin{cases} (\sqrt{x^2+y^2} - 0.82)^2 + (z - 1.02)^2 = 0.35 \\ \sqrt{x^2+y^2} = 0.82 - 0.59\cos\theta_1 \\ x = (0.82 - 0.59\cos\theta_1)\cos\omega \\ y = (0.82 - 0.59\cos\theta_1)\sin\omega \\ z = 1.02 + 0.59\sin\theta_1 \end{cases} \quad (10)$$

Track $G_3'H_3'$ ($\theta_1 = 47°$, $\theta_2 = 62°$, $0° \le \omega \le 360°$):

$$\begin{cases} \sqrt{x^2+y^2} = 0.42 + l_{GH} \\ x = (0.42 + l_{GH})\cos\omega \\ y = (0.42 + l_{GH})\sin\omega \\ z = 1.43 \end{cases}, 0 \le l_{GH} \le 0.5\ m \quad (11)$$

Track $H_3'H_3$ ($\theta_1 = 47°$, $0° \le \theta_2 \le 62°$, $0° \le \omega \le 360°$)

$$\begin{cases} (\sqrt{x^2+y^2} - 0.5)^2 + (z - 0.66)^2 = 0.81 \\ \sqrt{x^2+y^2} = 0.5 + 0.9\cos\theta_2 \\ x = (0.5 + 0.9\cos\theta_2)\cos\omega \\ y = (0.5 + 0.9\cos\theta_2)\sin\omega \\ z = 0.66 + 0.9\sin\theta_2 \end{cases} \quad (12)$$

Track H_3H_1 ($0° \le \theta_1 \le 47°$, $\theta_2 = 0°$, $0° \le \omega \le 360°$):

$$\begin{cases} (\sqrt{x^2+y^2} - 1.8)^2 + (z - 0.23)^2 = 0.35 \\ \sqrt{x^2+y^2} = 1.8 - 0.59\cos\theta_1 \\ x = (1.8 - 0.59\cos\theta_1)\cos\omega \\ y = (1.8 - 0.59\cos\theta_1)\sin\omega \\ z = 0.23 + 0.59\sin\theta_1 \end{cases} \quad (13)$$

The lifting operation range around the fruit trees on both sides of the vertical plane is shown in Figure 8a, and its value is set as S. The operating range for the rotating operation at maximum radius is set as S', as is shown in Figure 8b.

S and S' can be calculated from the Equations (14) and (15):

$$\begin{aligned} S &= S_{G_1G_1'H_1'H_1} + S_{G_1'G_3'H_3'H_1'} + S_{H_1H_1'H_3'H_3} \\ &= l_3 l_2'\sin\theta_{2\max} + l_3 l_1'\sin\theta_{1\max} + \\ &\quad 4l_1'l_2'\sin\frac{\theta_{1\max}}{2}\sin\frac{\theta_{2\max}}{2}\sin\frac{\theta_{1\max}+\theta_{2\max}}{2} \end{aligned} \quad (14)$$

$$S' = \pi[R_{\max}^2 - (R_{\max} - l_5)^2] \quad (15)$$

where, l_1' is equal to the length of lower-arm, m; l_2' is equal to the length of upper-arm, m; $\theta_{1\max}$ is the maximum lifting angle of lower-arm, (°); $\theta_{2\max}$ is the maximum lifting angle of upper-arm, (°); and $R_{\max}$ is the maximum operating radius, m.

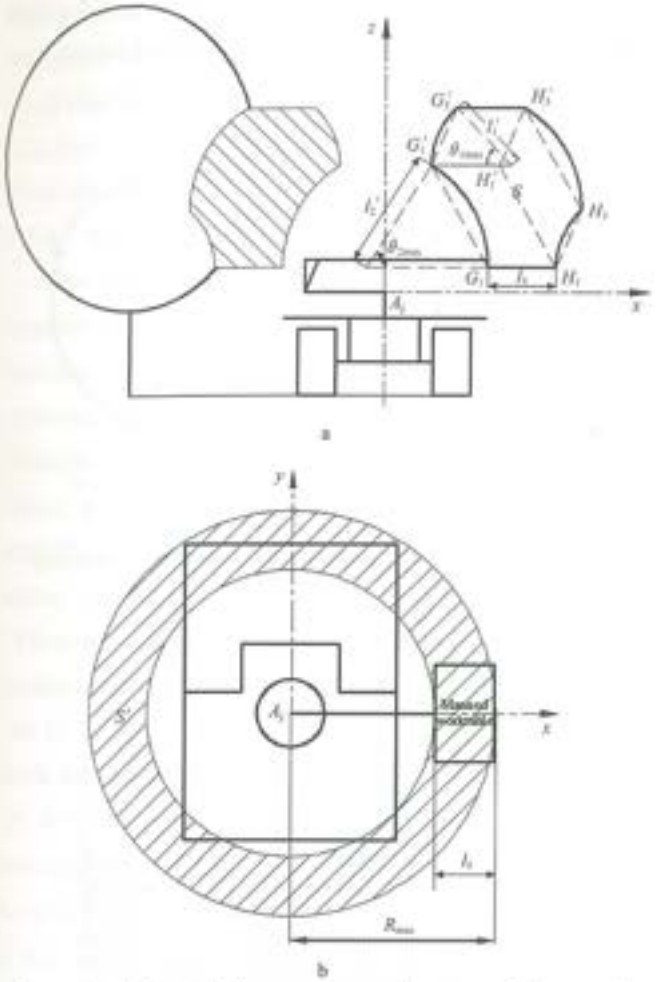

Figure 8 Schematic diagram of operating range of the manned worktable

Substituting the values in Equations (14) and (15) and solving them yields an operating range for lifting and rotating of about 1.9 m^2 and 3.6 m^2. Compared to other machines, this lifting platform, thus, has a larger operating range.

3.4 Hydraulic system design

The hydraulic system was powered by the engine which was connected to the gear pump through the belt transmission. A clutch was fixed to the gear pump to switch the power transmission on and off. As is shown in Figure 9, the gear pump supplied oil to every hydraulic element. A two position four-way solenoid directional valve was always open and set to control the gear pump unloading. As the hydraulic system only comprised three kinds of action - lifting, rotating, and leveling and no other special actions, double action hydraulic cylinder and double action quantitative hydraulic motor were selected. The work flow was adjusted by one-way throttle valve. When lifting platform was operational in the orchards, the system needed to start and stop frequently to change the operating position of the manned worktable; however, in order to keep the stability of the operation, hydraulic locks were adopted on the branches of the lifting cylinders to realize static locking.

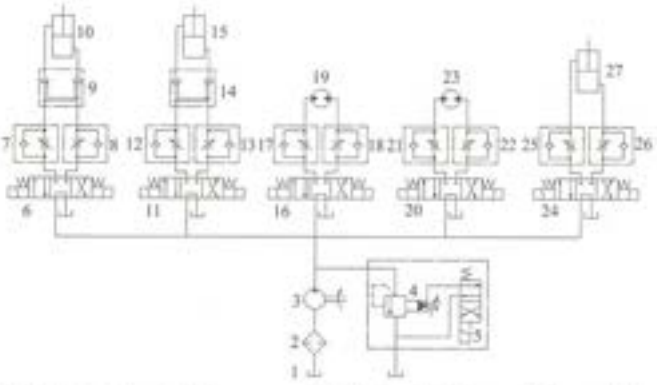

1. Tank 2. Filter 3. Gear pump 4. Piloted relief valve 5. Two position four-way solenoid directional valve 6, 11, 16, 20, 24. Three position four-way solenoid directional valve 7, 8, 12, 13, 17, 18, 21, 22, 25, 26. Throttle valve 9,14. Hydraulic lock 10,15. Lifting cylinder 19. Rotating hydraulic motor 23. Leveling hydraulic motor 27. Leveling cylinder

Figure 9 Schematic diagram of the hydraulic system

Considering the type of equipment (Wang et al., 2016), the maximum working pressure was set to 16 MPa. The outer diameter and inner diameter of the leveling cylinder were selected as 50 mm and 35 mm as per the requirements of 1.25 times the maximum load. The rotating speed of lifting device and leveling turbo-worm needed to be slower for the operator to work comfortably; hence, they were set from 0.5 r/min to 1 r/min. In addition, the working parameters of other elements and different component selections are shown in Table 2.

Table 2 Model of hydraulic and drive components

Project	Model
Lower-arm cylinder	50×35×160
Upper-arm cylinder	50×35×230
Leveling cylinder	50×35×150
Leveling turbo-worm	SE3
Slewing bearing	SE12
Rotating hydraulic motor	BM1-160-H
Leveling hydraulic motor	HMM-50
Gear pump	CBT-E304
Hydraulic lock	YS6-03A
Solenoid relief valve	DBW-10B-2B2
Solenoid directional valve	DSG-02-3C2

4 Materials and methods

4.1 Experimental conditions

In accordance with the design parameters of a 3-DOF

lifting platform, the prototype was developed as is shown in Figure 10. It has been known that the rated speed of the engine is 2200 r/min, and the lifting platform is able to work in the middle throttle. Experiments including operating parameters experiment, operating effect on fruit trees experiment, leveling and tilting stability experiment were carried out to analyze the performance of the 3-DOF lifting platform for hilly orchards. The experiments were conducted in October and November 2016 on the field of College of Engineering, Nanjing Agricultural University.

Figure 10 Prototype of 3-DOF lifting platform for hilly orchards

4.2 Experimental methods

4.2.1 Operating parameters experiment

Operating parameters experiment used parameters such as the speed of lifting operation, rotating operation, and leveling operation, and test of maximum operating height and radius. This can be referenced from the "Scissors elevating platforms - Testing method" (JB/T 9229.3-1999).

4.2.2 Operating effect on fruit trees experiment

Three fruit trees with different growth parameters (tree height, trunk height, and tree crown) were selected, and marked 1, 2, and 3. The canopies were divided into three vertical layers, which were marked as a, b, and c, and every layer was divided into a_k, b_k, and c_k (k=1, 2, 3, 4, 5). A total of 16 markers within the top point (T) of the tree were set as experimental positions (Figure 11), and label papers were pasted on the leaves at the corresponding positions. The position of the parked lifting platform was 2 m or 2.5 m away from the fruit tree.

The experimental points were marked with Y (Yes) or N (No) depending on whether the operator could reach them or not without any tools when lifting and rotating as is shown in Figure 12.

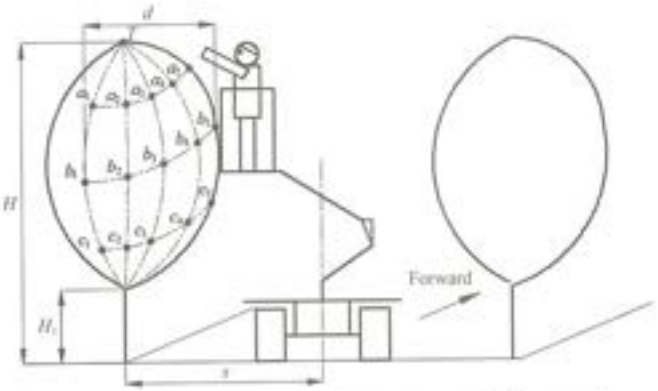

Figure 11 Schematic diagram of experiment of the operating range

Figure 12 Field experiment in progress

4.2.3 Leveling experiment

When the 3-DOF lifting platform was parked on the slope, different operating positions of the manned worktable resulted in different tilt angles and directions. As a result, there were different leveling actions including front, back, left and right. A tilting table was used to simulate different angles of slopes where the lifting platform was parked on and was fixed by safety rope. The operating height was 0.8 m and the tilt angles of the tilting table were 6° and 18°. The lifting device was rotated counterclockwise to 0°, 0°-90°, 90°, 90°-180°, 180°, 180°-270°, 270°, 270°-360°. Thus, the manned worktable was leveled using the bubble level in X and Y

direction. The error in the leveling operation could be measured by a digital inclinometer. In addition, the right hand side of the manned worktable was set as the positive direction of the X axis and the front as the positive direction of the Y axis.

4.2.4 Tilting stability experiment

The tilting stability was one of the most important features of the 3-DOF lifting platform, because different parking positions with different operating heights, different operating radii and different loads resulted in different tilting angles, and could make working on the lifting platform safe or unsafe on a slope. The tilting stability performance was characterized by the maximum tilting angle that could be measured. Using the "Tri-wheel vehicles and low-speed goods vehicles-Test method of maximum stable side-inclination" (GB/T 19133-2015), the operating environment was simulated with the following parameters: 8 parking positions with 0°, 45°, 90°, 135°, 180°, 225°, 270°, and 315° between the forward direction and the slope direction; 4 operating heights of 0 m, 0.4 m, 0.8 m, and 1.2 m; and 4 loadings of 0 kg, 50 kg, 100 kg, and 150 kg. Due to the manned worktable along the slope being always the most easily tilting position no matter where the lifting platform was parked, the experiment positions were set as is shown in Figure 13. The maximum angle of tilting test table is 30°, the length of table is 4 m, the width is 5 m, and the start-stop mode is the electric control.

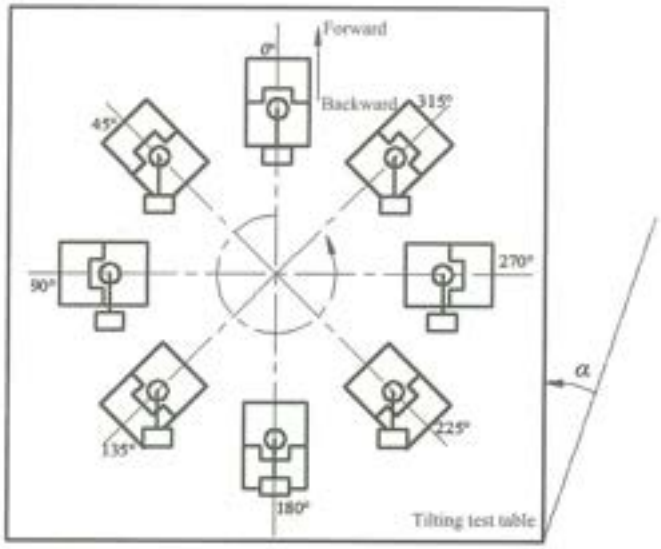

Figure 13 Schematic diagram of experimental positions

5 Results and discussion

5.1 Operating parameters

The experimental results are shown in Tables 3 and 4. Lifting, rotating and leveling had lower operating speeds which satisfied the design requirements, and the lifting speed was less than 0.4 m/s. Meanwhile, operating with full load always led to slower speeds. The maximum operating height was 1.2 m, and the height from the ground was 2.1 m at the same time. When the operating height was above 0.62 m, the lifting device could rotate 360° with a maximum radius of 1.42 m, for which the operating range was about 3.6 m^2. However, at operating height of less than 0.62 m, it could only rotate 180° because of space limitations.

Table 3 Speed of lifting, rotating and leveling

Load, kg	Lifting, m·s^{-1}		Falling, m·s^{-1}		Rotating, r·min^{-1}		Leveling, rad·s^{-1}			
	Upper-arm	Lower-arm	Upper-arm	Lower-arm	Left	Right	Front	Back	Left	Right
0	0.065	0.063	0.085	0.056	0.58	0.58	0.071	0.065	0.074	0.067
150	0.056	0.056	0.068	0.067	0.57	0.56	0.055	0.052	0.069	0.065

Table 4 Parameters of operating height and radius

Project	Maximum operating height/m	Maximum height from the ground/m	Rotating in 360°	
			Maximum operating radius, m	Operating height, m
Parameters	1.2	2.1	1.42	0.62

5.2 Operating effect on fruit trees

Growth parameters of fruit trees selected are shown in Table 5. Due to the shape of the fruit trees being approximately ellipsoidal, the layer b had a larger crown than layer a and c. The markers b_1, b_5, c_1 and c_5 were the most difficult positions for the operator to reach. In addition, the lifting platform could only move in a small range to adjust the boundaries of the crown. The layer c had a lower distance from the ground, so other operator could stand on the ground to finish the operations for

markers c_1 and c_5. When the distance from the lifting platform to the fruit trees was 2 m, the operating effect was better than when the distance was 2.5 m. Overall, the operating range could almost cover entire canopies. Thus, the 3-DOF lifting platform had a good operating effect on fruit trees when the distance between them was 2 m.

Table 5 Operating effect on fruit trees

No.	Growth parameters			Distance, m	Operating effect															
	Tree height, m	Trunk height, m	Tree crown, m		T	a_1	a_2	a_3	a_4	a_5	b_1	b_2	b_3	b_4	b_5	c_1	c_2	c_3	c_4	c_5
1	3.24	0.62	2.3	2	Y	Y	Y	Y	Y	Y	Y	Y	Y	Y	N	N	Y	Y	Y	N
				2.5	Y	N	Y	Y	Y	N	N	Y	Y	Y	N	N	Y	Y	Y	N
2	3.35	0.65	2.8	2	Y	Y	Y	Y	Y	Y	N	Y	Y	Y	N	N	Y	Y	Y	N
				2.5	N	N	Y	Y	Y	N	N	Y	Y	Y	N	N	Y	Y	Y	N
3	3.46	0.72	2.7	2	Y	Y	Y	Y	Y	Y	Y	Y	Y	Y	N	Y	Y	Y	Y	Y
				2.5	Y	N	Y	Y	Y	N	N	Y	Y	Y	N	N	Y	Y	Y	N

5.3 Leveling error

It can be seen from Table 6 that different rotating positions of the manned worktable had different leveling actions. Irrespective of the angle of slope being 6° or 18°, the leveling errors for the leveling actions were all less than 0.4°, which is negligible. Thus, using a leveling cylinder and leveling turbo-worm to keep the manned worktable horizontal according to the bubble level can be considered to have a relatively high accuracy.

5.4 Maximum tilting angle

The experimental results in Table 7 indicate that the maximum tilting angle decreased with an increase in load, for the same parked position and operating height. Moreover, the maximum tilting angle decreased and then increased with an increase in operating height. The angles of different parked positions, for different operating heights and different loads were from 19.3° to 30°, but some of the experimental angles were above 30° which were out of the measured range of the tilting table. Thus, the experiment results satisfied the design requirements, and the proposed 3-DOF lifting platform has a better tilting stability and can adapt to slope conditions of 5° to 20° in hilly orchards.

Table 6 Leveling error

Angle of slope, (°)	Rotating positions, (°)	Leveling actions	Dip angles, (°)		Leveling error, (°)	
			X axis	Y axis	X axis	Y axis
6	0	Front	0	−6	–	0.2
	0-90	Right, Front	−3.2	−5.7	0.2	0.1
	90	Right, Front	−7.3	−1.4	0.4	0.1
	90-180	Right, Back	−1.9	4.6	0.1	0.2
	180	Back	0	6	–	0.3
	180-270	Left, Back	4.1	4.3	0.4	0.3
	270	Left, Front	7.6	−1.3	0.3	0.2
	270-360	Left, Front	1.6	−2.1	0.2	0.2
18	0	Front	0	−18	–	0.3
	0-90	Right, Front	−13.5	−14.2	0.2	0.3
	90	Right, Front	−18.6	−2.7	0.3	0.1
	90-180	Right, Back	−11.5	12.3	0.2	0.2
	180	Back	0	18	–	0.2
	180-270	Left, Back	10.7	14.8	0.1	0.3
	270	Left, Front	18.8	−1.3	0.3	0.1
	270-360	Left, Front	12.5	−14.1	0.2	0.4

Table 7 Maximum tilting angle experimental value

Parking Position, (°)	Maximum tilting angle of different loads at various operating heights, (°)															
	0 kg				50 kg				100 kg				150 kg			
	0 m	0.4 m	0.8 m	1.2 m	0 m	0.4 m	0.8 m	1.2 m	0 m	0.4 m	0.8 m	1.2 m	0 m	0.4 m	0.8 m	1.2 m
0	>30	>30	29.2	>30	>30	27.4	25.7	26.1	27.4	23.9	22.6	23.7	26.1	20.4	19.3	21.4
45	>30	>30	>30	>30	>30	>30	27.8	28.1	>30	26.3	24.1	25.2	26.7	23.1	22.8	23.3
90	>30	>30	>30	>30	29.5	29.1	28.2	28.5	28.8	27.4	24.9	25.6	27.8	25.3	23.8	24.5
135	*	>30	>30	>30	*	>30	>30	>30	*	>30	>30	>30	*	28.8	27.2	28.1
180	*	*	>30	>30	*	*	>30	>30	*	*	>30	>30	*	*	28.4	29.8
225	*	>30	>30	>30	*	27.8	26.3	26.8	*	26.5	25.3	25.7	*	25.2	23.9	24.6
270	*	>30	29.4	>30	*	27.1	25.7	26.2	*	24.9	24.1	24.3	*	22.5	20.7	21.9
315	>30	>30	>30	>30	>30	>30	29.2	>30	>30	>30	25.4	26.1	27.6	24.5	21.2	22.1

Note: * means the position where the manned worktable can not reach.

6 Conclusions

A 3-DOF lifting platform was developed to improve the level of mechanization of processes such as picking, pruning, and bagging in hilly orchards and to solve the problem of lack of equipment for such processes. The lifting device which was one of the most important parts, was developed using a folding-arm mechanism. In addition, a leveling device was designed to keep the manned worktable horizontal on different terrains. The structural parameters and operating parameters were determined based on design requirements and the geometric parameters of fruit trees that were collected by visiting orchards on hilly lands. Subsequently, experiments were carried out to evaluate the performance of the proposed lifting platform.

The experimental results indicated that the operations of lifting, rotating and leveling were slow and smooth, the maximum operating height was 1.2 m, the lifting device could rotate 360° at a maximum operating radius of 1.42 m when operating height was above 0.62 m, and as a result, the operating range was about 3.6 m^2 at the same time. It was also confirmed that operator standing on the manned worktable could reach almost any position on the fruit trees. Compared to other current mechanical devices, the proposed 3-DOF lifting platform has the advantages of having a larger operating range, more operational flexibility and being more efficient when parked.

Furthermore, the error in any leveling action was less than 0.4°, which is negligible and the leveling device can thus be considered to have a relatively high accuracy. The maximum tilting angle at different parked positions, different operating heights and different loads was from 19.3° to 30°, which was as per the design requirements and could be adapted to slope conditions with an angle ranging from 5° to 20° in hilly orchards. The proposed 3-DOF lifting platform for hilly orchards, thus, had a better tilting stability performance compared to current machinery.

Acknowledgements

This study was supported by Co-Innovation Center of the Intelligent Management and Equipment for Orchard on the Hilly Land in South China (JX2014XCHJ02).

[References]

[1] Cao, F. Y., Z. L. Zhou, and H. S. Jia. 2007. Research summarization on simulation of turning performance of tracked vehicle. *Transactions of the Chinese Society for Agricultural Machinery*, 38(1): 185–188. (In Chinese with English abstract)

[2] Chang, Y. H., X. L. Lv, , Lv Xiaolan, J. Lin, X. Y. Xue, and Z. H. Wang. 2013. Present state and thinking about development of orchard mechanization in China. *Journal of Chinese Agricultural Mechanization*, 34(6): 21–25. (In Chinese with English abstract)

[3] Ding, S. M., X. M. Fu, X. Y. Xue, L. F. Zhou, and X. L. Lv. 2013. Design of power chassis for low self-propelled orchard sprayer. *Transactions of the Chinese Society for Agricultural Machinery*, 44(Supp.1): 101–106. (In Chinese with English abstract)

[4] Feng, Q. C., C. Ji, J. X. Zhang, and W. Li. 2010. Optimization design and kinematic analysis of cucumber-harvesting-robot manipulator. *Transactions of the Chinese Society for Agricultural Machinery*, 41(Supp.1): 244–248. (In Chinese with English abstract)

[5] GB/T 19133-2015 Tri-wheel vehicles and low-speed goods vehicles-Test method of maximum stable side-inclination. National Standards of the People's Republic of China.

[6] Hong, T. S., Z. Yang, S. R. Song, Y. Q. Zhu, X. J. Yue, and J. Su. 2010. Mechanization of citrus production. *Transactions of the Chinese Society for Agricultural Machinery*, 41(12): 105–110. (In Chinese with English abstract)

[7] JB/T 9229.3-1999 Scissors elevating platforms-Testing method. Machinery Industry Standards of the People's Republic of China

[8] Liu, D. W. 2013. Design and experimental research on lifting platform in citrus orchard. Changsha: Hunan Agricultural University.

[9] Liu, X. N., H. T. Zhu, and H. T. Ba. 2009. Development of a Faun LG1 type multifunctional orchard operating machine. *Xinjiang Agricultural Mechanization*, 2(1): 42–44. (In Chinese with English abstract)

[10] Liu, D. W., F. P. Xie, X. Li, X. L. Wang, and T. Mei. 2014. Citrus canopy shape and picking platform mechanical adaptability relationship with the inexact research. *Acta Agriculturae Universitatis Jiangxiensis*, 36(5): 1091–1095. (In Chinese with English abstract)

[11] Li, Q., Y. P. Song, D. S. Gao, X. C. Li, and H. R. Su. 2012. Status and development of orchard machinery in China. *Agricultural Equipment & Vehicle Engineering*, 247(2): 1–3.

[12] Liu, D. W., F. P. Xie, X. Li, and X. L. Wang. 2015. Design and experiment of small lifting platform in orchard. *Transactions of the CSAE*, 31(3): 113–121. (In Chinese with English abstract)

[13] Miao, M., H. Yuan, X. G. Song, Z. C. Shen, and W. Zhao. 2013. Folding-boom aerial working vehicle tracking and control. *Chinese Journal of Construction Machinery*, 11(4): 320–323. (In Chinese with English abstract)

[14] Qiu, W., W. M. Ding, X. C. Wang, Y. Gong, and X. X. Zhang. 2012. 3WZ-700 self-propelled air-blowing orchard sprayer. *Transactions of the Chinese Society for Agricultural Machinery*, 43(4): 26–30. (In Chinese with English abstract)

[15] Qiu, W.,C. D. Sun, X. L. Lv, Y. L. Chen, and W. M. Ding. 2016. Effects of spraying mode and application rate on pesticide deposition on fruit trees. *International Agricultural Engineering Journal*, 25(3): 182–196.

[16] Sun Z. J. 2012. Design and research of crawler multifunctional orchard operating Platform. Baoding: Hebei Agricultural University.

[17] Tang J. W., W. P. Liu, D. G. Liu, and G. Cheng. 2006. An analysis of steering track for tracked vehicle at inaccurate steering. *Acta Armamentarii*, 27(5): 779–783.

[18] Wang X. L., F. P. Xie, D. W. Liu, X. Li, and W. Lu. 2014. Citrus canopy shape and picking platform mechanical adaptability relationship with the inexact research. *Journal of Hunan Agricultural University Natural Sciences*, (5): 548–551. (In Chinese with English abstract)

[19] Wang, Z. 2011. Small multi-function remote control power platform. *Agricultural Equipment & Technology*, (3): 39.

[20] Wang, Y., Q. H. Yang, G. J. Bao, Y. Yi, and L. B. Zhang. 2011. Optimization design and experiment of fruit and vegetable picking manipulator. *Transactions of the Chinese Society for Agricultural Machinery*, 42(7): 192–195. (In Chinese with English abstract)

[21] Wang, P. F. 2013. The control system design and research of orchard operating platform. Baoding: Hebei Agricultural University.

[22] Wang, H. B., F. Z. Liu, D. X. Wang, H. Zhai, and Y. P. Du. 2013. Review on research, development and application of orchard machinery in China. *Journal of Fruit Science*, 30(1): 165–170.

[23] Wang, J. C. 2013. Design on hanging operating platform for hilly orchards. Tai'an: Shandong Agricultural University.

[24] Wang, B. S., W. Z. Wang, M. M. Wang, D. F. Zhong, and J. Chen. 2016. Design and experiment of full hydraulic drive high clearance tracked vehicle. *Transactions of the Chinese Society for Agricultural Machinery*, 47(Supp.1): 471–476. (In Chinese with English abstract)

[25] Zhang, X. H., Z. Y. Jiang, G. Q. F, and L. L. Cao. 2014. Self-propelled crawler directional air-blowing orchard sprayer. *Transactions of the Chinese Society for Agricultural Machinery*, 45(8): 117–122. (In Chinese with English abstract)

[26] Zhao, J. Z., F. C. Wang, B. Yu, and D. C. Wang. 2014. Research on all-terrain profiling crawler power chassis. *Transactions of the Chinese Society for Agricultural Machinery*, 45(9): 20–24. (In Chinese with English abstract)

[27] Zhou, L. F., X. M. Fu, W. M. Ding, S. M. Ding, J. Chen, and Z. J. Chen. 2015. Design and experiment of combined disc air-assisted orchard sprayer. *Transactions of the CSAE*, 31(10): 64–71. (In Chinese with English abstract)

Quantification of mechanization index and its impact on crop productivity and socio-economic factors

Adnan Abbas[1], Yang Minli[1,2*], Ehsan Elahi[3], Khurram Yousaf[4], Riaz Ahmad[1], Tahir Iqbal[5]

(1. *College of Engineering, China Agricultural University, Beijing 100083, China;*
2. *China Research Center for Agricultural Mechanization Development, China Agricultural University, Beijing 100083, China;*
3. *College of Economics and Management, China Agricultural University, Beijing 100083, China;*
4. *College of Engineering, Nanjing Agricultural University, Nanjing 210095, China;*
5. *School of Renewable Energy and Clean Power, North China Electric Power University, Beijing 102206, China*)

Abstract: In this study mechanization index (MI) was assessed, its influence on corn productivity in correspondence with socioeconomic factors of Pakistani farmers were further analyzed through inter correlation and linear regression analysis. An overall MI ensued 0.60 per hectare with an average corn yield 142.7 mon/ha. Furthermore, results revealed that large farmers had higher MI and corn yield as compared to the small and medium ones and it varied from 0.85 to 0.34 with negative fluctuation in farm size. Moreover, farmers specific and socioeconomic variables (such as farmers education, farming experience, dependency burden, ownership status of machines and external support towards agriculture machinery) were used to observe their influence on MI. Education level, owned and subsidized agriculture machinery have a significant effect while farming experience and dependency burden found an egative effect on MI. So, improving the farmers educational level through literacy campaign and long-term investment for creating support services infrastructure is require to increase the MI at corn farms of Pakistan.

Keywords: mechanization index, corn, productivity, socio-economic factors

Citation: Abbas, A., M. L. Yang, E. Elahi , K. Yousaf, R. Ahmad, and T. Iqbal. 2017. Quantification of mechanization index and its impact on crop productivity and socio-economic factors. International Agricultural Engineering Journal, 26(3): 49–54.

1 Introduction

Agriculture has always played an imperative role in the economy of Pakistan. Irrespective of hasty urbanization and economic discrepancy, it still provides 42% employment of the total labors and contributes 19.8% to gross domestic product (GDP) (GOP, 2016). Machinery, tools and their implements are crucial to agriculture. Moreover, an inclusive narration of the application of these inputs generally entitled as mechanization (Bagheri and Bordbar, 2014).

Mechanization is considered as a set of technological expertise to ensure enhancement of productivity by introducing timely field operations, and quality of grain (Kepner et al., 2003). As productivity is positively correlated with potential unit farm power (mechanization) (Singh, 2006), hence, increasing demand of productivity signpost the requirement of efficient mechanization in developing countries. More specifically, the efficient utilization of farm power with better management of agriculture machinery is assertive for sustainable production in Pakistan (Rehman et al., 2016, Iqbal et al., 2015). In order to maximize the efficiency of mechanization, the farming system should be first characterized, especially to identify possible resource constraints and to capture the diversity of farming systems (Zangeneh et al., 2015).

Numerous studies have been conducted in different

Received date: 2017-06-30 **Accepted date:** 2017-08-08

* **Corresponding Author: Yang Minli**, Professor, College of Engineering, China Agricultural University, Beijing 100083, China. China Research Center for Agricultural Mechanization Development, China Agricultural University, Beijing 100083, China. Email: qyang@cau.edu.cn, dr_adnan219@yahoo.com.

regions of the world for mechanization assessment in reference with the intensity of power or energy availability (Zangenehet al., 2015; Ramirez et al., 2007; Hormozi et al., 2012; Singh, 2006). However, thequality of mechanization with the intensity of farm power is not suitable, as it doesn't have time dimensions (Sundaram et al., 2012). Moreover, as the majority of the farmers in developing country like Pakistan use tractors for agriculture as well as non-agriculture commodities, therefore, quantification of mechanization based on mechanical tractive farm power to total farm power, does not bring to light the actual use scenario.

The mechanization should incorporate the relevance and utility of using equipment for different field operations at the individual farm level (McNulty and Grace, 2009). So, mechanization index (MI) based on the ratio of energy used by machinery to the total energy used by human, animal, and machinery at corn farms, were suggested for estimation and future planning (Singh, 2006).

Furthermore, investigating the status of MI in selected area, along with potential agricultural productivity and other socioeconomic indicators, will lead to an improvement in the sustainability of the agricultural system (Zhangeneh et al., 2010). Industrialization of the country and economic development of farmer has a direct relation with mechanization (Singh, 2006), which implies that mechanization status is location-specific and dynamic. Hence, formulation of mechanization needs the quantification, its impact on productivity and economic factors (Hormozi et al., 2012).

More specifically, country's significant dependency on agriculture and indeed development in mechanization for macro level planning has lead this study to assess the MI at crop (corn) production level in Pakistan. The particular objectives are avaluation of MI (based on energy), influencing factors (socioeconomic) and effect of MI on crop yield, which is lacking in the proceeding studies.

2 Material and methods

2.1 Study area and data acquisition

Corn, being an important industrial commodity, accounts 2.2% to value addition and 0.4% to GDP of Pakistan (GOP, 2016). Due to conventional farming ways and less involvement of innovative technology, the country is facing productivity problems (Rehman et al., 2015). So, for assessment of mechanization index (MI), its impact on crop yield and to study the possible potential constraints that affects MI, this research was performed in three (main) corn producing districts (Figure 1) of Punjab (main corn producer province), Pakistan during Kharif production season of corn in 2015.

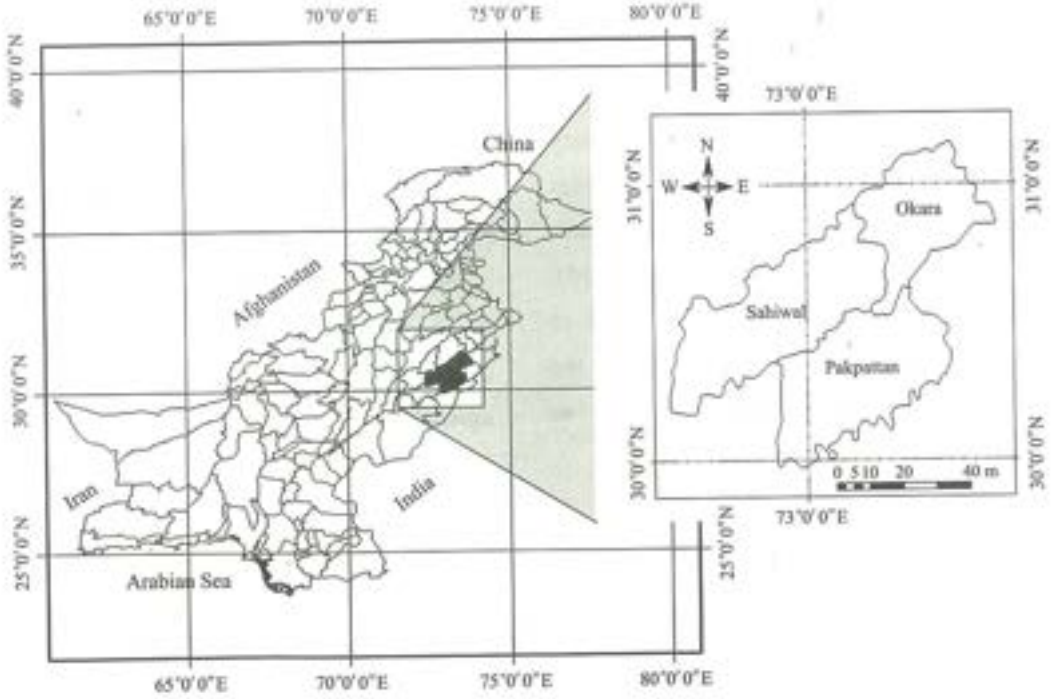

Figure 1 Study area

Face to face questionnaire method has been adopted to acquire the data, from a total of 160 farmers by direct communication with the respondents (corn farmers). Majority of the farmers in Pakistan are small farmers (81%) cultivating 39% of area, although large farmers are less in numbers (7%) while cultivating 40% of area (GOP, 2004). So, to gain more realistic results and a clear picture of MI, data were collected from different farm categories such as small (0-<5 ha), medium (5-<10 ha) and large farmers (10->10 ha). The questionnaire consisted of per acre (lately changed to per hectare) data in quest concerning working hours of inputs-output (human labor, animals, machinery, diesel fuel and crop yield) consumed in field practices such as field preparation, seeding, fertilization, irrigation, plant protection, harvesting (cobs picking), post harvesting (cutting of corn stalks and residue) and threshing. The main key factors that influence successful mechanization include socioeconomic, supporting infrastructure and technical skills (Olaoye and Rotimi, 2010). So, a questionnaire was also delved down into information on socio-economic characteristics of the farmers such as level of education, farming experience, dependency burden, ownership status and supporting infrastructure.

2.2 Technical details

MI is the ratio of machine energy (fuel energy and machinery energy) to the sum of machine energy, animal energy and human energy as suggested by Nowacki (1978). A higher value of MI is the affirmation that most of the work has been done by machine.

$$MI = \frac{Mech._E}{(Mech._E + An._E + Hu._E)} \quad (1)$$

where, MI is MI based on energy; $Mech._E$ is the machine energy (MJ/ha); $An._E$ animal energy (MJ/ha); $Hu._E$ human energy (MJ ha^{-1}).

The energy associated with fuel, human and animal working hours were estimated directly by multiplying their equivalences (Table 1), however, the machine energy was calculated using Equation (2).

$$Mech._E = \frac{(W_m \times E_{eq} \times t_m)}{T_{em}} \quad (2)$$

where, $Mech._E$ is the machine energy (MJ/ha); W_m is the mass of machine (kg); E_{eq} is the energy equivalent for machinery (Table 1); t_m is the time that machine used per unit area (h/ha); T_{em} is the economic life of machine (h).

Table 1 Energy equivalents used for MI in corn production

Inputs, unit		Energy equivalents, MJ per unit	References
1. Labor, h			
	Male	1.96	Nassiri and Singh, 2009
	Female	1.57	Nassiri and Singh, 2009
2. Animal	Bullock (medium)	10.1	Nassiri and Singh, 2009
3. Machinery, kg			
	Tractor	138	Elhami et al., 2016
	Plow + Disk	180	Elhami et al., 2016
	Boundaries (Ridger)	160	Elhami et al., 2016
	Leveler	149	Elhami et al., 2016
	Sprayer	129	Elhami et al., 2016
	Rotary Hoes	148	Elhami et al., 2016
	Thrashing (h)	62.7	Elhami et al., 2016
4. Diesel		47.8	Elhami et al., 2016

2.3 Analytical technique

Collected data were analyzed using descriptive statistics and quantitative classification. Lately, the influence of various socioeconomic factors on MI and MI on crop (corn) yield has been examined by employing multi-regressive technique and inter-correlation respectively. MI articulated as a function of socioeconomic attributes and subsidized supporting parameters as depicted in Equation (3).

$$MI = f(x_1, x_2, x_3, \ldots, x_n) \quad (3)$$

where, x_1, x_2, x_3, ..., x_n are the selected attributes e.g., farmer's education level (completed years of schooling), farming experience (years), dependency burden (number of dependent family members), ownership status of agriculture machines (1=owner, 0= otherwise), and subsidy/external support on agriculture machinery (1=availed, 0= otherwise), hereafter, x_1, x_2, x_3, x_4 and x_5, respectively.

Generally, the relationship between attribute's matrix (hereafter X) and the dependent variable vector (Y) (here MI) is acute for significant model selection. To assess this relationship between Y and X, a multi-regressive approach (Equation (4)) is used.

$$Y = \beta_0 + X\beta + \varepsilon \quad (4)$$

where, $X = \begin{bmatrix} x_{11} & \cdots & x_{1k} \\ \vdots & \ddots & \vdots \\ x_{T1} & \cdots & x_{Tk} \end{bmatrix}$, $\beta = \begin{bmatrix} \beta_1 \\ \vdots \\ \beta_T \end{bmatrix}$, $\varepsilon = \begin{bmatrix} \varepsilon_1 \\ \vdots \\ \varepsilon_T \end{bmatrix}$, β_0 is the intercept; β is the regression coefficient; ε is the

remaining unexplained noise (error); k is the number of selected attributes, and T the number of respondents.

The primary purpose under consideration in this study was to find the set of variables (a subset of X) that resulted in the minimum residual errors. Primarily, the sum of the squared errors

$$(SSE = g(\beta_n) = \sum_{t=1}^{T}\left(y_t - \left(\beta_0 + \sum_{n=1}^{k}\beta_n x_{nt}\right)\right)^2)$$ is employed

in the standard regression analysis as a measure of fitting. Moreover, several models resulted from the selected attributes X and MI were investigated using multi-regression method. They were developed using different combinations of the MI and attributes X under some constraints. The model having the minimum g (β_n), a variance inflation factor (VIF) less than 5 for the attributes, and a t-test of statistical significance was considered to be the optimum model among the different combinations that were considered.

3 Results and discussion

To deal with the specific objectives, the study involved descriptive and influential analysis. The descriptive statistics entailed mean and percentage (Table 2).

Table 2 Summary of descriptive statistics

Variables	Definition of variables	Average value
Education (Continues)	Number of schooling years	6.74
Farming experience (Continues)	Number of years	19.05
Dependency burden (Continues)	(Number of dependent persons in family)	6.74
Ownership of agricultural machinery (Dummy)	1= Owner; 0= Otherwise	0.34
Subsidy on agricultural implements (Dummy)	1= Availed; 0= Otherwise	0.13
Small farmers (Continues)	Percentage	43.75
Medium farmers (Continues)	Percentage	35.38
Large farmers (Continues)	Percentage	21.88
Corn yield (Continues)	Yield per hectare	142.7
MI (Continues)	MI per hectare	0.6

Note: SE refers to standard error and all parameters are significant at 1%.

Table 2 presented that the average level of education, agriculture farming experience and dependency burden of respondent were observed 6.74, 19.05 and 6.74 respectively. The average farmers having owned agricultural machinery were observed 0.34, while farmers availing subsidy were stated 0.13. Smaller farmers contributed higher in the sample, as 43.75%, followed by medium 35.38%, the large farmers were the least one (21.88%). An overall of MI (based on Equation (1)) was found 0.60 for corn production with an average yield 142.7 mon ha^{-1} in the target region.

3.1 Mechanization index and its impact on crop productivity

A notable relationship of MI and corn productivity per hectare was found as is shown in Figure 2. A significant variation is found between MI and productivity in the perspective of farm size. Comparative to medium and small farmers the MI of the large farmer is 1.4 and 2.5 times higher, respectively. Similarly, corn yield of the large farmer is respectively 17% and 48% higher than medium and small farmers. This implies that the MI and crop productivity dependent on the farm size. Perhaps, the large farmers may have more capital and resources to utilize at their farm which leads toward higher MI and production per hectare. Small farmers found constraints in the use of machinery due to the smaller size of fields and limited capital resources. Our result is in the same trend of recent studies, for instance, Singh and De (1999), and Alam and Singh (2003) also reported the large farmers used to advance technology for example tractors and had higher crop productivity comparative to other group of farmers.

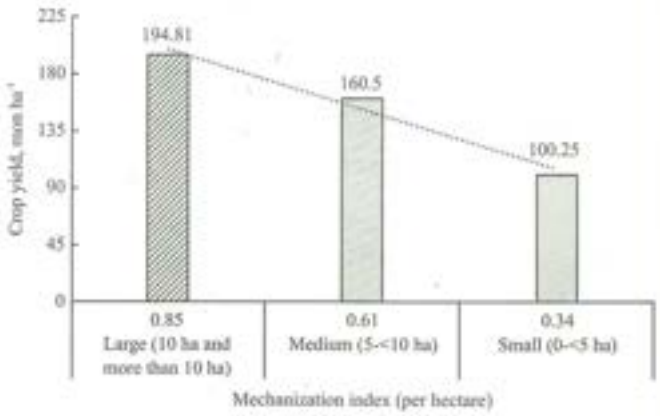

Figure 2 Effect of MI on crop yield

3.2 Effects of socioeconomic and external support on mechanization index

Equation (5) revealed the results of influential analysis of external support with socioeconomics and farmer's characteristics on MI. Outcomes depicted that education, ownership, and agriculture machinery subsidy have a significant effect on MI. While experience and

dependency burden have a negative effect on MI.

$$MI = 0.015x_1 - 0.006x_2 + 0.192x_3 - 0.037x_4 + 0.046x_5 + 0.803 \quad (5)$$

Furthermore, we categorized farm MI on the base of farmer's characteristics such as, ownership of agricultural machinery, education, experience, dependency burden and supporting infrastructure (subsidized agriculture machine). We found astonishing results that, the MI of machinery owners is 0.3 times higher than their counter part. On another hand, the MI decreased with the increase of the experience in farming because the majority of farmers in this study are old farmers with more experience. Despite the old farmers are living with more experience, however, they are less likely to adopt or reluctant to use innovative or new technologies, particularly in the developing countries. Our results are in the same line with Owombo et al. (2012), where they also found a negative relationship between farm MI and experience. Moreover, we found that with increasing number of schooling years the farm MI significantly increases. Specifically, those farmers with more than 10 years of schooling have higher MI than farmers having schooling years less than 10 years. Naqvi and ashfaq (2014) also found the similar results, with a higher level of farmer's education, farmers are more prone to adopt advanced technology and consequently achieved the optimum level of crop productivity. Furthermore, our findings revealed a negative correlation between MI and dependency burden, varied from 0.67-0.33 with the increase in dependent persons from 3->6 respectively, because affordability towards agriculture machinery decreases with increasing financial burden. Results further depicted that MI of farmers availed subsidy is higher than that of non-availed ones, therefore a long-term investment for creating support services infrastructure is required and government must take sustainable measures to boost up mechanization.

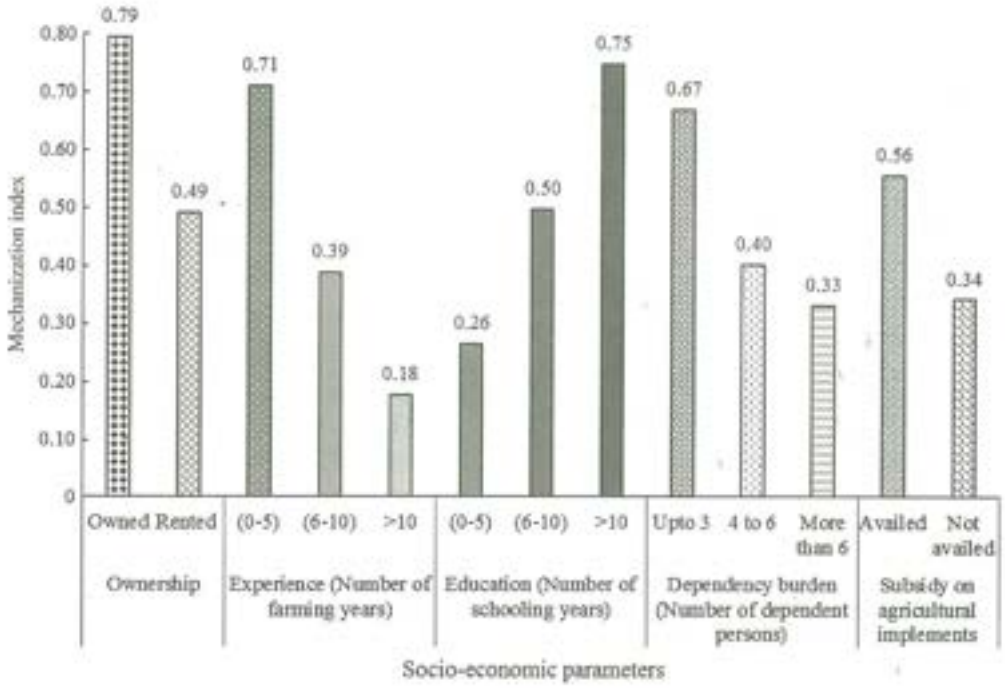

Figure 3 Effect of socioeconomic parameters on MI

4 Conclusions

In this study MI at corn production systems of Pakistan were assessed, hereupon, its impact on corn productivity was appraised through inter correlation analysis and furthermore, the correspondence of socioeconomic factors with MI was examined through linear regression. The intention was to provide an index that could facilitate mechanization planners and policy makers to assess and formulate future strategies. For this purpose, a cross sectional data of 160 corn growers were collected from three main corn producing districts (Sahiwal, Okara, Pakpattan) of Punjab, Pakistan. Assessment confided that average MI at crop (corn) level

was 0.60 per hectare with an average corn yield 142.7 mon/ha and it varied from 0.85 to 0.34 with negative fluctuation in farm size. It is proclaimed that the farmers having higher crop yields (194.81 mon/ha) have adopted higher levels of mechanization (0.85 per ha) to ensure timeliness operations. The analysis has further revealed as a consequence of socioeconomic influence on MI, owned and subsidized agricultural machinery have a significant effect on MI. The literacy rate was also found significant, while farming experience and dependency burden has negative effect on MI. An insufficient level of MI has been perceived, therefore, long-term investment for creating support services infrastructure is required. The Government must take endurable measures to encourage mechanization.

[References]

[1] Alam, A., and G. Singh. 2003. Status and future needs of farm mechanization and agro-processing in India. Technical Bulletin No. CIAE/2003/96, Central Institute of Agricultural Engineering, Nabi Bagh, Berasia Road, Bhopal.

[2] Bagheri, N., and M. Bordbar. 2014. Factor analysis of agriculture mechanization challenges in Iran. *Agricultural Engineering International: CIGR Journal*, 16(1): 167–172.

[3] Elhami, B., A. Akram, and M. Khanali. 2016. Optimization of energy consumption and environmental impacts of chickpea production using data envelopment analysis (DEA) and multi objective genetic algorithm (MOGA) approaches. *Information Processing in Agriculture*, 3(3): 190–205.

[4] Government of Pakistan (GOP). 2016. Pakistan Economic Survey 2015-2016. Economic Advisor's Wing, Finance Division, Islamabad, Pakistan.

[5] Government of Pakistan. 2004. Agricultural Census, Pakistan Bureau of Statistics. Islamabad.

[6] Hormozi, A. M., M. A. Asoodar, and A. Abdeshahi. 2012. Impact of mechanization on technical efficiency: A case study of rice farmers in Iran. *Procedia Economics and Finance*, 1: 176 – 185.

[7] Iqbal, A. M., A. Iqbal, S. Afzal, N. Akbar, N. R. Abbas, and Z.H. Khan. 2015. In Pakistan, agricultural mechanization status and future prospects. *American-Eurasian Journal of Agricultural & Environmental Sciences*, 15(1): 122–128.

[8] Kepner, R. A., R. Bainer, and E. L. Berger. 2003. Principles of Farm Machinery (9th Eds). New Delhi: CBS Publishers and Distributors.

[9] Naqvi, A. A. S., and M. Ashfaq. 2014. Estimation of technical efficiency and its determinants in the hybrid maize production in district Chiniot: a cobb Douglas model approach. *Pakistan Journal of Agricultural Sciences*, 51(1): 181–185.

[10] Nassiri, M. S., and S. Singh. 2009. Study on energy use efficiency for paddy crop using data envelopment analysis (DEA) technique. *Applied Energy*, 86(7-8): 1320–1325.

[11] Nowacki, T. 1978. Methodology used by ECE countries in forecasting mechanization developments. United Nations Economic Commission for Europe, AGRI/MECH Report No. 74.

[12] McNulty, B. P., and P. M. Grace. 2009. Agricultural mechanization and automation. Paris: EOLSS publishers.

[13] Olaoye, J. O., and O. A. Rotimi. 2010. Measurement of agricultural mechanization index and analysis of productivity of farm settlements in south Nigeria. *Agricultural Engineering International: CIGR Journal*, 12(1): 125–134.

[14] Owombo, P. T., A. A. Akinola, O. O. Ayodele, and G. F. Koledoye. 2012. Economic Impact of Agricultural Mechanization Adoption: Evidence from Maize Farmers in Ondo State, Nigeria. *Journal of Agriculture and Biodiversity Research*, 1(2): 25–32.

[15] Sundaram, P.K., S.S. Singh, S.C. Sharma and A. Rahman. 2012. Prospect of farm mechanization, page 279-292, ICAR-RCER, PATNA publishers India.

[16] Ramírez, A. A., A. Oida, H. Nakashima, J. Miyasaka, and K. Ohdoi. 2007. Mechanization index and machinery energy ratio assessment by means of an artificial neural network: A Mexican case study. *Agricultural Engineering International: CIGR Journal*, 9: 1–21.

[17] Rehman, A., L. Jingdong, B. Shahzad, A. A. Chandio, I. Hussain, G. Nabi, and S. M. Iqbal. 2015. Economic perspectives of major field crops of Pakistan. *Pacific Science Review B: Humanities and Social Sciences*, 1(3): 145–158.

[18] Rehman, U. T., M. U. Khan, M. Tayyab, M. W. Akram, and M. Faheem. 2016. Current status and overview of farm mechanization in Pakistan -A review. *Agricultural Engineering International: CIGR Journal*, 18(2): 83–93.

[19] Singh, G. 2006. Estimation of a mechanization index and its impact on production and economic factors— a case study in India. *Biosystems Engineering*, 93(1): 99–106.

[20] Singh, G., and D. De. 1999. Quantification of a mechanization indicator for Indian agriculture. *Applied Engineering in Agriculture*, 15(3): 197–204.

[21] Zangeneh, M., M. Omid, and A. Akram. 2010. Assessment of agricultural mechanization status of potato production by means of Artificial Neural Network model. *Australian Journal of Crop Science*, 4(5): 372–377.

[22] Zangeneh, M., M. Omid., and A. Akram. 2015. Integrated assessment and modeling of agricultural mechanization in potato production of Iran by Artificial Neural Networks. *Agricultural Research*, 4(3): 283–302.

Strength analysis and optimal design of transmission system of sugarcane leaf stripping machine

Xu Minmin, Huang Wei*, Mo Zhimin, Niu Sijie, Ruan Xiaofang, Lu Xuewen

(*College of Mechanical Engineering, Guangxi University, Nanning 530004, China*)

Abstract: In order to find out the causes of crackles grown on rubber wheels and improve the reliability of the sugarcane leaf stripping machine, strength analysis and optimal design were studied on the transmission system. With the introduction of the structure, working process and strength problem, multi-body dynamics was carried out based on virtual prototype model of the sugarcane leaf stripper. Dynamics simulation showed that the relatively large forces on rubber wheels were the major reason for crackles. Experiments were used to verify the accuracy of the model and the result. In order to reduce the forces on cracked rubber wheels, optimal design was carried out based on orthogonal test with taking front distance, front spring's stiffness and preload, rear distance, rear spring's stiffness and preload as variables, taking maximum absolute value and mean value of the forces as observations. Range analysis showed that preload of rear spring and stiffness of front spring had significant effect on the maximum absolute value of the force on front under wheel, while stiffness of rear spring and preload of front spring affected that on rear upper wheel significantly. The optimal results showed that when the six selected variables were chosen as 15 mm, 10 N/mm, 40 N, 18 mm, 15 N/mm and 45 N respectively, the maximum absolute value of forces on four rubber wheels had reduced 29.63%, 32.16%, 46.68% and 2.5% compared with initial parameters. At the same time, the mean value had reduced 43.73%, 29.33%, 45.63% and 58.04%. The optimal design has obvious effect and provides strong evidence for improving the machine.

Keywords: sugarcane leaf stripping machine, crackle, multi-body dynamics, orthogonal test, optimal design

Citation: Xu, M. M., W. Huang, Z. M. Mo, S. J. Niu, X. F. Ruan, and X. W. Lu. 2017. Strength analysis and optimal design of transmission system of sugarcane leaf stripping machine. International Agricultural Engineering Journal, 26(3): 55–63.

1 Introduction

Guangxi is Chinese largest sugarcane planting area and sugar producing area (Ma et al., 2012; Zhan, 2013). Both planting size and sugar yield account for more than 60% of China. The industrial scale ranks the first in China, which benefits 20 million farmers (Zhan, 2013). However, most of the sugarcane planting regions in Guangxi are narrow hilly topography (Huang et al., 2009). At present, in these areas, mechanization lags behind and large combine harvester is difficult to be widely used. Sectional type of harvest, cutting sugarcane and peeling leaf separately, is the main way to take (Zhan, 2013; Shen et al., 2014). In face of so huge a scale, the problems of harvesting sugarcane and stripping leaf fast and efficiently need to be solved urgently.

The sugarcane harvester consists of cut-section and whole-stalk sugarcane harvester. Whole-stalk type contains joint type and sectional type. Cut-section harvester is commonly used in sugar industry developed countries, such as America, Australia and Brazil, while whole-stalk harvester is widely used in our country, especially sectional type (Zhan, 2013). With the promotion of agricultural mechanization, more and more sugarcane harvesting and leaf stripping machinery have been invented and used (Huang et al., 2008; Yao et al., 2007; Li et al., 2008), and the relevant theoretical and practical research were carried out as well.

In the aspect of whole-stalk joint sugarcane harvester, researches mainly focused on analysis and improvement of sugarcane cutter and lifting mechanism (Li et al.,

Received date: 2016-11-30 Accepted date: 2017-07-18

* Corresponding author: Huang Wei, Ph.D., Professor, College of Mechanical Engineering, Guangxi University, Nanning, 530004, China. Email: buaahw@126.com, Tel: 13977186436.

2016), feeding system (Shen et al., 2014) and breaking tails mechanism (Ma et al., 2012; Luo et al., 2013).

In the aspect of stripping leaf, Shang et al. (2000) studied the stripping principle with computer image technology. Wang et al. (2007) established the dynamics model of stripping leaf and studied the relationship between stripping quality and influencing factors. Liu et al. (2007) explored the mechanics properties of crop stalks, as well as the damage process in cutting sugarcane stalk with smooth-edge blade. Mou et al. (2014) researched the elastic dentations in the process of sugarcane leaf sheath stripping with analysis and experiment. Meng et al. (2003) analyzed the design and property of the cleaning element with virtual experiments.

By referring to the previous research experience, a new type of sugarcane leaf stripper was developed, which is different from the machine depends on the hitting of flexible element. The machine works through the rational arrangement of cutting tools and feeding mechanism. Experimental results showed that the stripping effect was improved. However, because of the long working hours and poor working environment, the issues of poor reliability occurred.

In order to find out the causes of crackles grown on rubber wheels and improve the reliability of the sugarcane leaf stripping machine, strength analysis and optimal design were carried out on the transmission system. Strength analysis aimed at finding out the reason for the crackles on rubber wheels. Optimal design was expected to seek out the better parameters' combination to reduce force on the rubber wheels and improve the reliability of the machine.

2 Materials and methods

2.1 Sugarcane leaf stripping machine

Based on the majority of sugarcane leaf stripping machine on the market, the fulfilling of the stripping depends on the hitting of the leaf stripping element (Meng et al., 2003). But the machine in the paper works through the rational arrangement of cutting tools and feeding mechanism. The structure of the machine is shown in Figure 1.

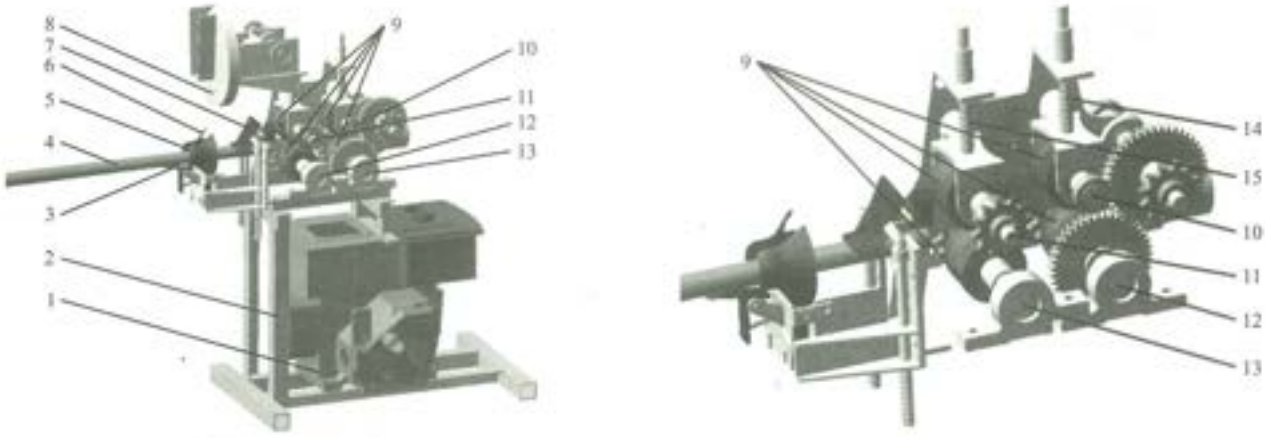

1. Engine 2. Machine frame 3. Front knife 4. Sugarcane 5. Left knife 6. Right knife 7. Back knife 8. Circular saw 9. Rubber wheel 10. Rear upper shaft 11. Front upper shaft 12. Front under shaft 13. Rear under shaft 14. Rear spring 15. Front spring

Figure 1 Structure of the sugarcane leaf stripping machine

2.1.1 Working process

The using process of the leaf stripping machine consists of truncation, feeding, and transmission, as shown in Figure 2. When the machine works, the tail of the sugarcane was cut off by the circular saw at first. And then give the sugarcane an initial force to make it enter the drive mechanism through knife tools in every direction. At last, the sugarcane moved forward under the driving of the rubber wheel. And at the same time, the leaf of the sugarcane was cut off by the combined knife tools.

After the above 3 processes, the leaf on the sugarcane was stripped by the combined tools.

2.1.2 Strength problem

According to the experimental test, stripping effect of the machine was better, as well as lower impurity rate and acceptable structural strength of the frame (Yang et al., 2016; Xu et al., 2016). However, after using for a period

of time, different degrees of wear and crackle appeared on the surface of the front under wheel and rear upper wheel. Figure 3 shows different degrees of wear and extrusion crackles. Besides, it found that the crackle on rear upper wheel was more serious.

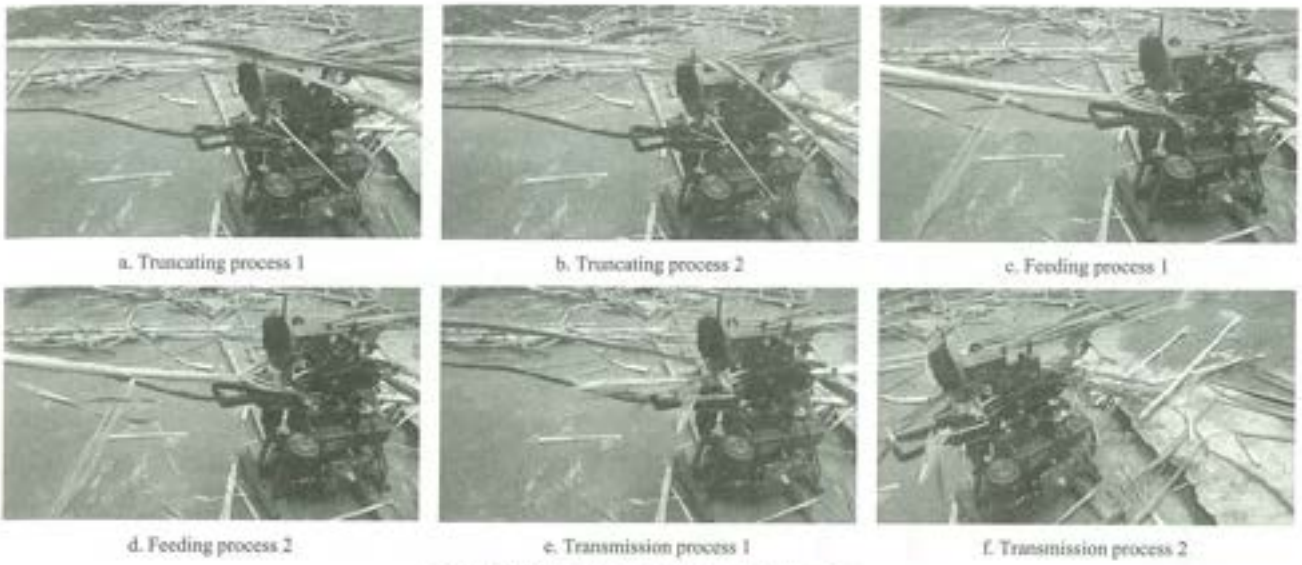

a. Truncating process 1 b. Truncating process 2 c. Feeding process 1

d. Feeding process 2 e. Transmission process 1 f. Transmission process 2

Figure 2 Structural analysis of the machine

a. Crackle on front under wheel b. Crackle on rear upper wheel

Figure 3 Crackles on rubber wheels

2.2 Strength analysis

In this part, strength analysis was carried out with dynamics simulation, aiming at finding out the internal mechanical cause of the crackles.

2.2.1 Dynamics analysis

Virtual prototype model of the sugarcane leaf stripper was built according to the design drawings. According to the above working process in Figure 2, giving the sugarcane two initial forces to make it entered the drive mechanism. The two initial forces, as shown in Figure 4, point to the direction of front and up respectively. The upward force was used to balance the gravity of sugarcane, which was set as 5 N lasting for 0.2 s. At the same time, the effect of the forward force made the sugarcane move forward. The original value was set as 60 N lasting for 0.2 s, which was gotten from practical experience.

Under the effect of the two forces, the sugarcane entered the drive mechanism along the forward direction, as similar as the practical experiments.

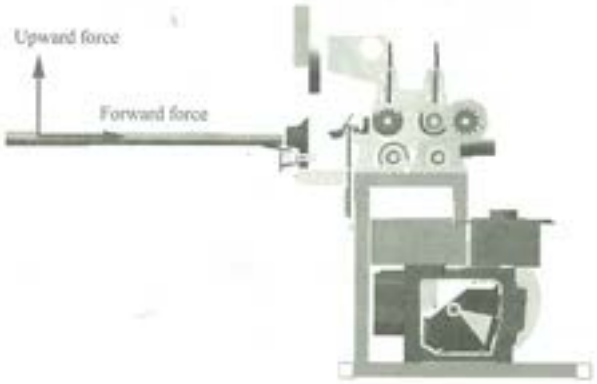

Figure 4 Virtual prototype model

Setting the motion speed as 2000 r/min, the sugarcane moved forward under the driving of the rubber wheel. A series of the parameters used in the simulation experiment were set through practical experience, as is shown in

Table 1, including the characteristic of the sugarcane. The front spring, rear spring, front bracket, rear bracket and the distances are shown in Figure 5.

Table 1 Settings of parameters

Parameters	Value
Minimum diameter of sugarcane, mm	20 mm
Maximum diameter of sugarcane, mm	30 mm
Effective length of sugarcane, mm	1500 mm
Density of the sugarcane, kg/m^3	1.1×10^3 kg/m^3
Poisson ratio of the sugarcane	0.33
Elastic modulus of the sugarcane, MPa	1.1×10^4 MPa
Distance between front upper and under wheel, mm	15 mm
Stiffness of the front spring, N/mm	20 N/mm
Preload of front spring, N	40 N
Distance between rear upper and under wheel, mm	15 mm
Stiffness of the rear spring, N/mm	20 N/mm
Preload of rear spring, N	40 N

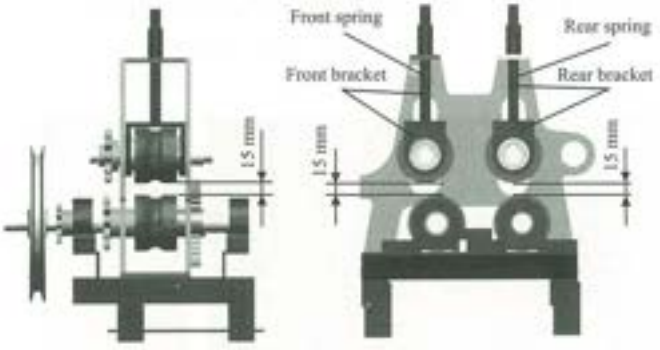

Figure 5 Interpretation of the structural parameters

2.2.2 Mechanical analysis of rubber wheels

Through dynamics simulation, contact state and forces on the four rubber wheels were obtained, as shown in Figure 6. After calculation, it found that, to front couple of rubber wheels, the mean value of under wheel's force (371.04 N) is bigger than the upper (143.91 N). There is some different in the rear couple of wheels. The force of under wheel is not constant. But the maximum absolute value of the upper wheel reaches 3411.05 N. The high force is the internal mechanical cause of the crackles.

2.3 Experimental verification

2.3.1 High-speed photography

An experiment was carried out to verify the accuracy of the above analysis with high-speed photography (Cui et al., 2013). From the experiment, in the process of entering the driving mechanism, contact was taken place firstly between sugarcane and front under rubber wheel (Figure 7 b), and then the upper wheel (Figure 7 c-d). On the contrary, sugarcane reached the rear upper wheel firstly (Figure 7 e). It was in agreement with dynamics simulation.

2.3.2 Displacement test

In order to verify the accuracy of the analysis, an experiment was carried on with DH5981 dynamic analyzer and displacement transducers. The settings of the experiment are shown in Table 2. The connection of experimental equipment and tested data curve was displayed in Figure 8.

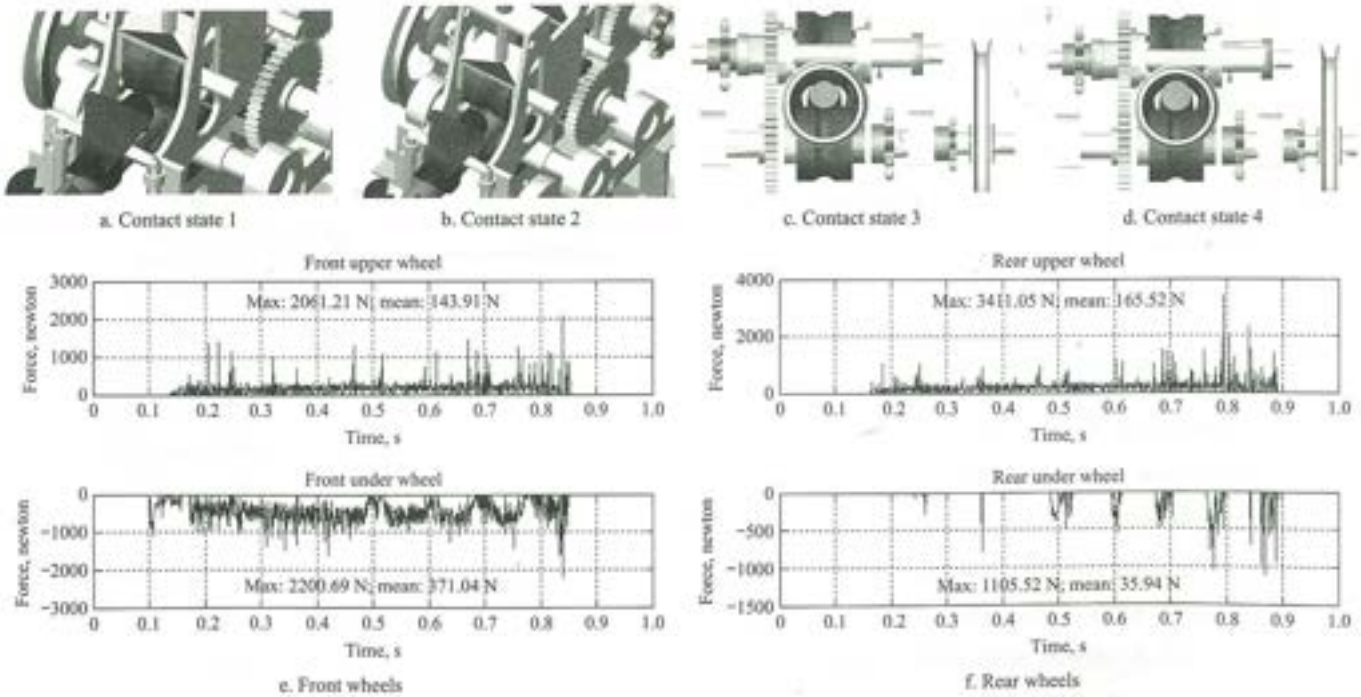

Figure 6 Contact state and forces on rubber wheels

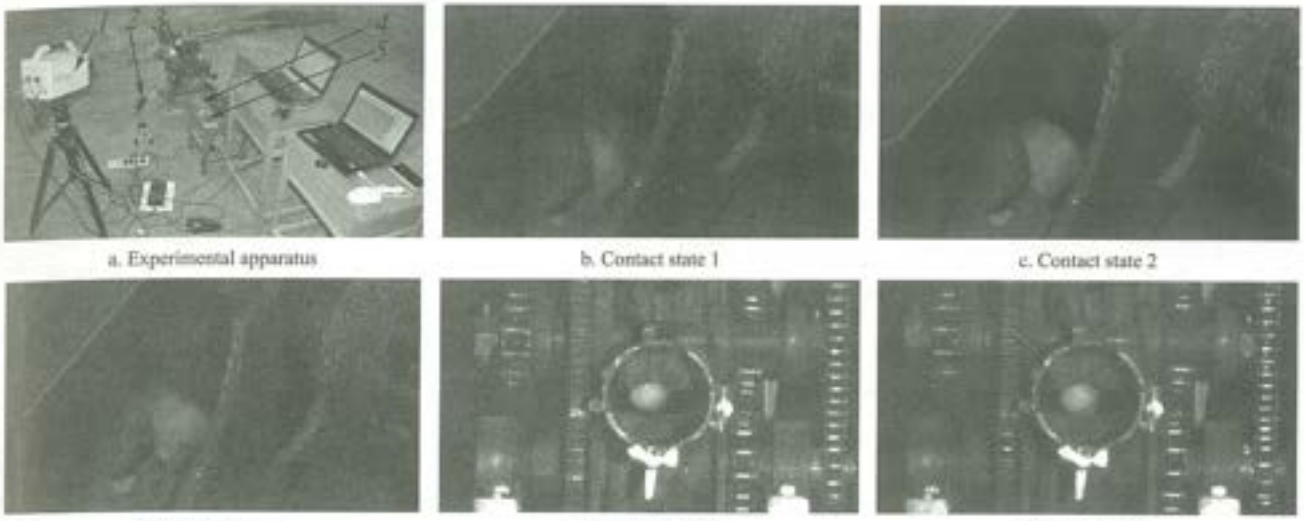

a. Experimental apparatus b. Contact state 1 c. Contact state 2

d. Contact state 3 e. Contact state 4 f. Contact state 5

1. High-speed camera FASTCAM SA-X2 2. Spotlight 3. Sugarcane leaf stripping machine 4 .DH5981 dynamic analyzer 5. DH5901 vibration analyzer

Figure 7 Result of high-speed photography

Table 2 Settings of parameters

Parameters	Value
Test instrument	DH5981
Channel number	Using 2
Connection mode of displacement transducers	Half-bridge connection
Sensor power supply voltage, V	2 V
Sensor sensitivity, mm	0.01 mm

a. Experimental apparatus

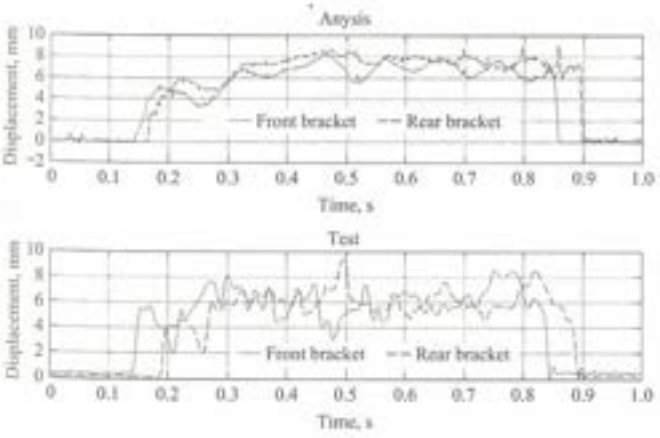

b. Result of analysis and test

1. Contact displacement sensor 2. DH5981dynamic analyzer

Figure 8 Displacement test

From the simulation and the experimental test, it found that the total time of striping leaf is about 1 s. The sugarcane entered the drive mechanism before 0.2 s, and then front upper and rear upper rubber wheel rose successively. The sugarcane is transmitted stably between 0.2 s and 0.8 s. Because of the changing diameter, the displacement of the front bracket and rear bracket rise up and down. Even though there are some concrete change differences between analysis and test, the general trend, range of motion and beginning and ending time displayed better consistency, which verified the accuracy of the simulation and the model.

2.4 Optimal design based on the orthogonal test

In view of the previous research, the contact force exerted on the rubber wheels was the major reason for the crackles. Consequently, optimal design was expected to reduce the force on the rubber wheels. The smaller force is, the longer life will be. In this part, selecting six parameters as variables, an orthogonal test (Wang, 1986) was carried out to find out the better parameters combination to reduce the force on the cracked rubber wheels.

As shown in multi-body dynamics analysis, the structure parameters mainly contain distance between front upper and under wheel (x_1 mm), stiffness of the front spring (x_2 N/mm), preload of front spring (x_3 N), distance between rear upper and under wheel (x_4 mm), stiffness of the rear spring (x_5 N/mm), preload of rear spring (x_6 N). The original value and the change value of the six variables were shown in Table 3.

According to the simulations, maximum absolute

value and mean value the forces, the most important digital features, were chosen as the observed objects. In the result data, y_1, y_3, y_5, y_7 were used to stand the maximum absolute value of the force on front upper wheel, front under wheel, rear upper wheel, rear under wheel respectively. At the same time, y_2, y_4, y_6, y_8 stand the mean value of them. The data of the oethogonal test was shown in Table 4.

Table 3 Value of the six variables

Variable	Original value	Change value
x_1	15	12, 13.5, 15, 16.5, 18
x_2	20	10, 15, 20, 25, 30
x_3	40	30, 35, 40, 45, 50
x_4	15	12, 13.5, 15, 16.5, 18
x_5	20	10, 15, 20, 25, 30
x_6	40	30, 35, 40, 45, 50

Table 4 Data of the orthogonal test

Num	x_1	x_2	x_3	x_4	x_5	x_6	y_1	y_2	y_3	y_4	y_5	y_6	y_7	y_8
0	15	20	40	15	20	40	2061.12	143.91	2200.69	371.04	3411.05	165.52	1105.52	35.94
1	12	10	30	12	10	30	1733.33	101.12	1903.24	306.36	1601.59	110.95	1478.77	25.09
2	12	15	35	13.5	15	35	1505.99	141.05	2986.40	360.50	1909.34	137.35	872.79	28.12
3	12	20	40	15	20	40	2044.24	184.87	1681.07	405.95	3313.48	156.83	1115.81	31.74
4	12	25	45	16.5	25	45	1905.43	217.13	2372.12	440.59	2201.75	153.08	1292.73	36.02
5	12	30	50	18	30	50	2904.11	268.10	2408.17	483.49	2473.58	147.87	2103.76	28.37
6	13.5	10	35	15	25	50	1395.72	103.14	1455.53	311.67	2072.70	191.86	1352.98	55.20
7	13.5	15	40	16.5	30	30	2353.17	135.98	2390.32	349.58	2850.42	165.99	1041.69	38.75
8	13.5	20	45	18	10	35	3309.55	155.33	1445.65	322.22	1528.94	66.38	1047.58	6.87
9	13.5	25	50	12	15	40	1443.65	200.55	1786.98	431.69	1945.54	157.35	1576.07	37.77
10	13.5	30	30	13.5	20	45	1953.95	211.07	2562.42	441.23	1936.76	181.46	1539.66	45.10
11	15	10	40	18	15	45	1450.40	80.98	1492.92	262.23	1819.19	89.99	1077.89	15.08
12	15	15	45	12	20	50	1786.13	129.62	2011.75	373.84	3166.00	226.89	1657.65	68.25
13	15	20	50	13.5	25	30	1762.79	150.83	1785.84	380.63	2447.49	208.40	1595.81	57.03
14	15	25	30	15	30	35	1373.29	154.11	2980.03	387.20	1591.67	200.36	1708.79	64.64
15	15	30	35	16.5	10	40	1837.23	179.25	1785.84	345.10	2265.17	88.01	1247.10	13.65
16	16.5	10	45	13.5	30	40	2129.91	88.94	1800.41	324.25	2103.34	252.43	1671.78	102.79
17	16.5	15	50	15	10	45	1550.17	95.48	1918.85	291.47	1835.50	98.82	1074.65	17.90
18	16.5	20	30	16.5	15	50	1262.83	97.41	1823.62	304.03	1136.23	109.62	1080.42	23.36
19	16.5	25	35	18	20	30	1189.52	121.56	2188.56	324.21	1368.94	98.53	1619.29	17.73
20	16.5	30	40	12	25	35	1742.76	155.88	1788.51	397.09	2493.23	237.07	2103.23	92.46
21	18	10	50	16.5	20	35	1499.70	63.39	2929.35	282.21	2768.34	115.54	1941.24	31.37
22	18	15	30	18	25	40	2164.10	69.72	1855.76	274.90	2492.16	117.60	1289.94	25.52
23	18	20	35	12	30	45	1378.70	97.65	1744.64	340.14	2115.14	282.74	1195.20	131.78
24	18	25	40	13.5	10	50	1447.99	96.29	1716.48	298.48	1792.31	114.25	1162.95	21.85
25	18	30	45	15	15	30	2774.40	122.69	2615.58	325.00	1878.59	119.82	1019.75	21.12

3 Results and discussion

The original design values were shown in the zeroth group. The varying curves of the maximum absolute value and mean value the forces are shown in Figure 9.

In Figure 9, the maximum absolute value had larger fluctuations, while mean value changed little. Consequently, the lower maximum absolute value was the primary consideration.

3.1 Range analysis

According to the mathematical statistics principle, the range analysis results were shown in Table 5 and Figure 10. Cracked rubber wheels were analyzed emphatically.

Range analysis showed that preload of rear spring and stiffness of front spring had significant effect on the maximum absolute value of the force on front under wheel, while stiffness of rear spring and preload of front spring affected that on rear upper wheel significantly.

3.2 Optimal results

According to orthogonal test and comprehensive equilibrium method (Yang et al., 2011), taking into account of the maximum absolute value and mean value, the most optimal set of the structure parameter was the 11th group: 15 mm, 10 N/mm, 40 N, 18 mm, 15 N/mm, 45 N. Compared with initial parameters, the maximum absolute value of the contact force reduced 29.63%, 32.16%, 46.68% and 2.50% respectively, reaching the best. At the same time, the mean values had reached the best combination, reduced 43.73%, 29.33%, 45.63% and 58.04%.

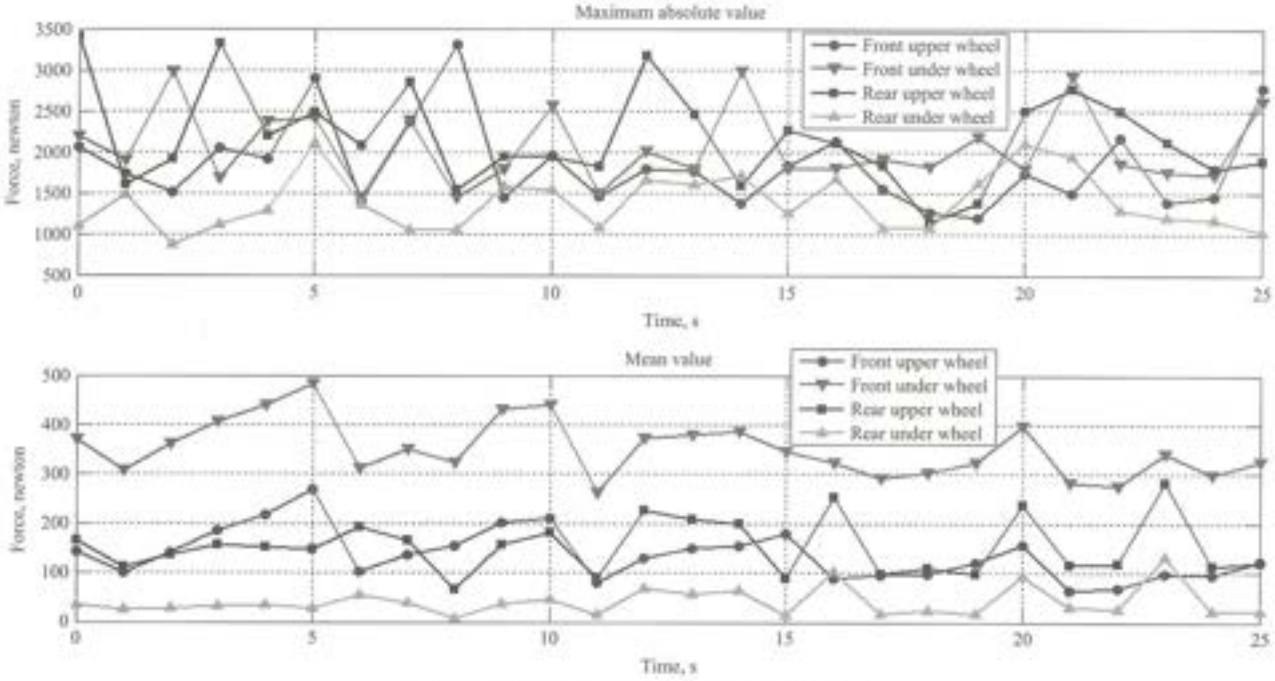

Figure 9 Varying curves of observed objects

Table 5 Chart of range analysis

	Factor	k_1^M	k_2^M	k_3^M	k_4^M	k_5^M	Range	Rank
Front under wheel	A	2270.20	1928.18	2011.28	1903.99	2172.36	366.21	6
	B	1916.29	2232.62	1696.16	2208.83	2232.10	536.46	2
	C	2225.01	2032.19	1813.86	2049.10	2165.84	411.15	5
	D	1847.02	2170.31	2130.21	2260.25	1878.21	413.23	4
	E	1754.01	2141.10	2274.63	1851.55	2264.71	520.62	3
	F	2176.71	2425.99	1782.01	2018.19	1883.11	643.98	1
Rear upper wheel	A	2299.95	2066.87	2257.90	1787.45	2209.31	512.50	4
	B	2073.03	2450.68	2108.26	1780.04	2209.47	670.64	3
	C	1751.68	1946.26	2453.73	2175.72	2294.09	702.05	2
	D	2264.30	2037.85	2138.39	2244.38	1936.56	327.74	6
	E	1804.70	1737.78	2510.70	2341.47	2226.83	772.92	1
	F	2029.41	2058.30	2423.94	1981.67	2128.16	442.27	5

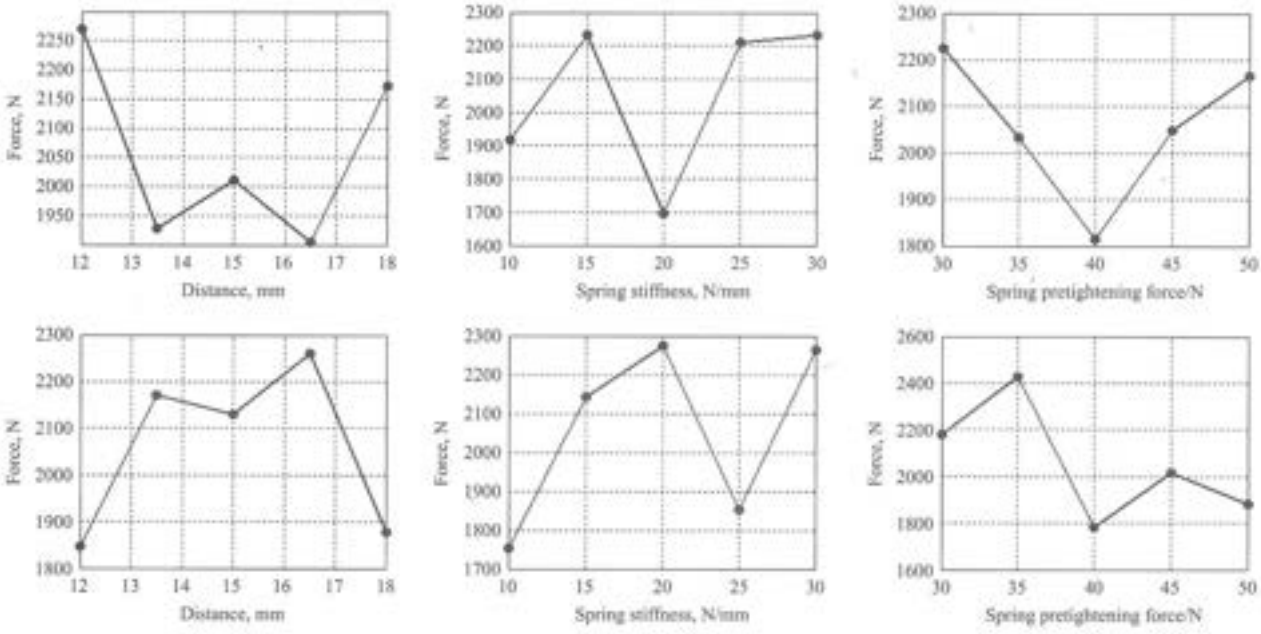

a. Range analysis of front under wheel

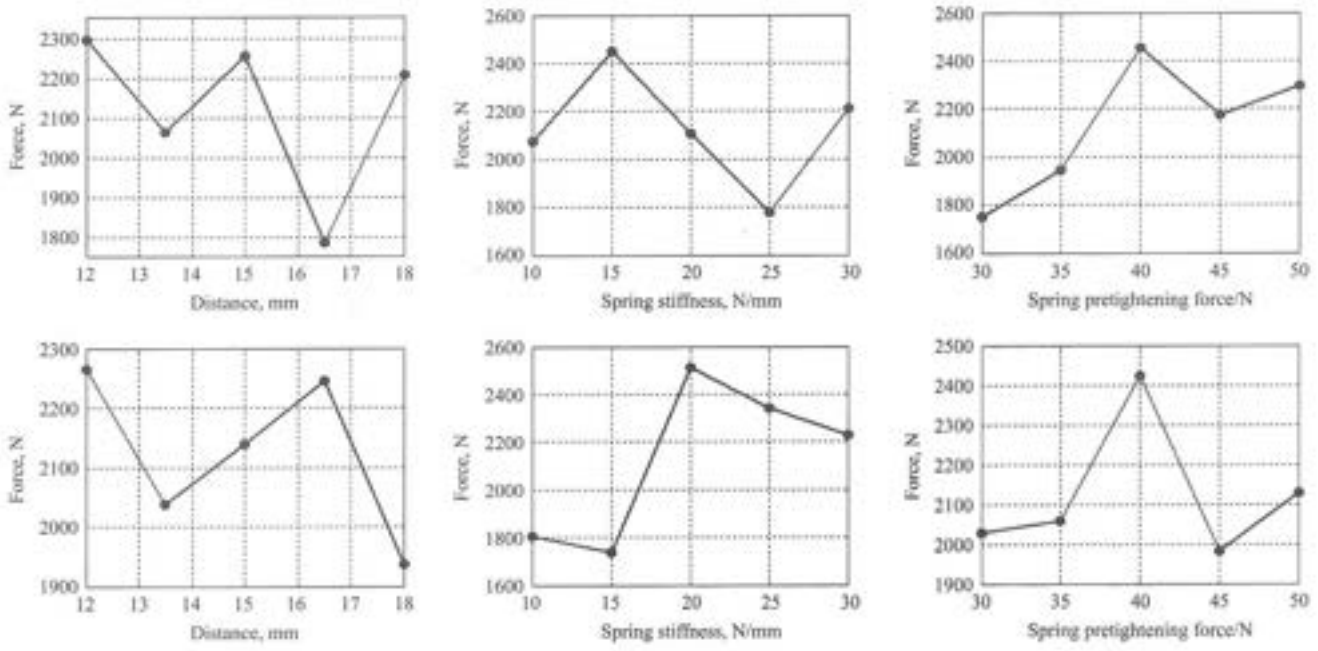

b. Range analysis of rear upper wheel

Figure 10 Range analysis

The structure of the prototype was adjusted according to the optimal design. Tested by experiment, the stripping effect and impurity rate satisfies the design requirement. Working for a period of time, there were no crackles. Consequently, fatigue life of rubber wheels will be longer than before. However, the life after optimization needs further research and experiment.

4 Conclusions

According to the full text, the following conclusions were obtained.

(1) The crackles on the rubber wheels were caused by the high contact force between sugarcane and wheels. What's more, the maximum absolute value of the forces on the cracked rubber wheel were relatively large, reaching 3411.05 N.

(2) Range analysis showed that preload of rear spring and stiffness of front spring affected the force of front under wheel significantly, while stiffness of rear spring and preload of front spring had significant influence on rear upper wheel.

(3) The optimal design showed that when the six variables were chosen as 15 mm, 10 N/mm, 40 N, 18 mm, 15 N/mm, 45 N respectively, the maximum absolute value of the force on four wheels had reduced 29.63%, 32.16%, 46.68% and 2.50% compared with the original value. The optimal design has obvious effect and provides strong evidence for improving the machine.

[References]

[1] Ma, F. L., H. M . Jiang, S. P. Li, Z. W. Xu, B. X. Yang, and Z. D. Fan. 2012. Design and experiment on cleaning leaves and breaking tails mechanics of whole-stalk sugarcane harvester. *Transactions of the Chinese Society for Agricultural Machinery*, 43(6): 73–78. (In Chinese with English abstract)

[2] Zhan, N. Y. 2013. Comparative study on the research and application of domestic and overseas sugarcane leaf stripping machine. *Light Industry Science and Technology*, (5): 39–43.

[3] Huang, H., M. Li, and G. R Deng. 2008. Development status and suggestions of sugarcane leaf stripping machine in China. *China Tropical Agriculture*, (6): 32–34.

[4] Shen, Z. H., S. P. Li, F. L. Ma, and J. L. Gao. 2014. Simulation and Experiment on Feed Ability of Small Sugarcane Harvester. *Transactions of the Chinese Society for Agricultural Machinery*, 45(11): 117–123. (In Chinese with English abstract)

[5] Yao, W. 2007. Brief discussion and thinking about the development of China sugarcane cleaner technologies. *Journal of Agricultural Mechanization Research*, 29(10): 232–234.

[6] Li, M., H. Huang, G. R. Deng, and Y. G. Deng. 2008. Research status and development of sugarcane leaf harvesting machine. *Farm Machinery*, (1): 24–26.

[7] Li, S. P., X. Deng, C. F. Ye, H. B. Wang, and Z. H. Shen. 2016. Analysis and improvement of transportation performance of sugarcane cutter spiral lifting mechanism.

Transactions of the Chinese Society of Agricultural Engineering, 32(5): 21–28. (In Chinese with English abstract)

[8] Li, S. P., X. Deng, J. Q. Zhong, J. M. Song, and H. B. Wang. 2016. Structure Improvement and Simulation Test of Sugarcane Harvester Feeding System. *Transactions of the Chinese Society for Agricultural Machinery*, 47(5): 91–98. (In Chinese with English abstract)

[9] Luo, J. C., Y. Y. Ou, Q. T. Liu, X. W. Mou, Y. J Lin, and G. X. Peng. 2013. Tail-breaking Mechanism of Whole Stalk Sugarcane Combine Harvester. *Transactions of the Chinese Society for Agricultural Machinery*, 44(4): 89–94. (In Chinese with English abstract)

[10] Shang, H. Q., and Y. G. Qu. 2000. Application of computer image technology on principle of sugarcane detrashing. *Journal of South China Agricultural University*, 21(4): 81–84

[11] Wang, G. J., Y. H. Qiao, and Y. Lv. 2007. Study on Sugarcane Leaf Detrashing. *Journal of Shandong Agricultural University (Natural Science)*, 38(3): 461–464.

[12] Liu, Q.T., Y. G. Ou, S. L. Qing, and W. Z. Wang. 2007. Study progress on mechanics properties of crop stalks. *Transactions of the Chinese Society for Agricultural Machinery*, 38(7): 172–176. (In Chinese with English abstract)

[13] Liu, Q.T., Y. G. Ou, S. L. Qing, and C. H. Song. 2007. Cutting force test of sugarcane stalk. *Transactions of the Chinese Society of Agricultural Engineering*, 23(7): 90–94. (In Chinese with English abstract)

[14] Liu, Q.T., Y. G. Ou, S. L. Qing, and S. X. Huang. 2007. High-speed photography analysis on the damage process in cutting sugarcane stalk with smooth-edge blade. *Transactions of the Chinese Society for Agricultural Machinery*, 38(10): 31–35. (In Chinese with English abstract)

[15] Mou, X.W. 2015. Study on Dynamic Hitting Force of Elastic Dentation for Sugarcane Stalk and Mechanism of Leaf Sheath Stripping. *Transactions of the Chinese Society for Agricultural Machinery*, 46(3):103–109. (In Chinese with English abstract)

[16] Meng, Y. M., S. P. Li, S. Z. Liu, F. L. Ma, and F. Lin. 2003. Research on the effect mechanism of front angle of sugarcane cleaning element in brush shape. *China Mechanical Engineering*, 14(11): 901–904. (In Chinese with English abstract)

[17] Yang, C. L., M. M. Xu, M. J. Hu, W. Huang, F. L. Ma, and X. W. Lu. 2016. Structural Analysis and Experimental Study of New Type Sugarcane Leaf Stripper's Frame. *Journal of Agricultural Mechanization Research*, 38(12): 179–182.

[18] Xu, M. M., C. L. Yang, Y. X. Duan, Y. K. Wang, W. Huang, and F. L. Ma. 2016. Fatigue life prediction based on rain-flow counting method. *Machine Design and Research*, 32(5): 184–187.

[19] Cui, T., J. Liu, and L. Yang. 2013. Experiment and simulation of rolling friction characteristic of corn seed based on high-speed photography. *Transactions of the Chinese Society of Agricultural Engineering*, 29(15): 34–41. (In Chinese with English abstract)

[20] Wang, R. X. 1986. Mathematical statistics. *Xi'an: Xi'an Jiaotong University Press.*

[21] Yang, K. J., and C. Q. Tang. 2012. Optimization of structure crashworthiness for a passenger car in high-speed rear-end impact. *China Mechanical Engineering*, 25(5): 616–620.

Parameters optimization of improved air-assisted orchard sprayer based on RSM and RBF neural network

Qu Feng, Zhang Mingming, Li Xi, Zhang Junxiong*, Liu Jingyun

(*College of Engineering, China Agricultural University, Beijing 100083, China*)

Abstract: As traditional axial-flow air-assisted orchard sprayer is lack of guidance for the air-assisted spray, it causes droplets easily drift into the air or fall on the ground, which wastes lots of pesticides and cannot satisfy the desired prevention and cure effects. In order to improve spraying performance of the traditional sprayer, linear guide plates were installed above the upper air outlet of the sprayer. Orthogonal tests with mixed levels based on Box-Behnken method were designed. Length and angle of guide plate, air velocity of air outlet, and pressure of pump were opted as the experimental factors. In addition, droplet coverage rate was taken as an evaluation index of spraying. Combined Response Surface Method (RSM) with Computational Fluid Dynamics (CFD), wind field of the improved prayer was simulated, and influences of the simulation wind field on test results were analyzed. RSM model and Radical Basis Function (RBF) Neural Network model were respectively adopted to approximate the relationships and establish the approximate models between the experimental factors and the experimental data. Experimental factors were analyzed and optimized based on different approximate models, and the model of RBF Neural Network was proved to be the better one in the verification tests at different sample heights. In verification tests, at the height of 150 cm, droplet coverage rate and forecast error were 55.06% and 3.5%; at the height of 200 cm, they were 28.13% and 5.2%; at the height of 250 cm, they were 17.01% and 9.2%. The results will provide references for parameters optimization of the improved air-assisted orchard sprayer.

Keywords: air-assisted sprayer, response surface method, approximate model, parameter optimization

Citation: Qu, F., M. M. Zhang, X. Li, J. X. Zhang, and J. Y. Liu. 2017. Parameters optimization of improved air-assisted orchard sprayer based on RSM and RBF neural network. International Agricultural Engineering Journal, 26(3): 64–74.

1 Introduction

Air-assisted sprayer plays an important role in orchard spraying and improvements of its spraying performance have been widely studied and applied for recent years. Researches on spraying characteristics, influence factors, parameters optimization and experimental verification using characters of gas-liquid two-field flow field based on CFD have achieved some results. Most of them were focused on establishing airflow field models (Endalew et al., 2010; Salcedo et al., 2015) and finding out laws of droplet deposition (Qi et al., 2010; Wang et al., 2015) which proved method based on CFD is able to provide effective references. However, because of restricted accuracy of models and complicated atomization principles, method based on CFD cannot completely simulate the real spraying situation. Effects of air-assisted spraying can be affected by multiple factors, such as mass concentration of pesticide (Qiu et al., 2015), wind velocity of fan (Sun et al., 2015; Song et al., 2011), sprayer structure (Song et al., 2013) and so on. Most researches had just considered a single factor during tests and neglected interactions between deferent factors, which can hardly explain the actual influences on spraying effects of each factor. Although combinations of air-assisted sprayer and electrostatic sprayer (Zhou et al., 2016; Wang et al., 2015), automatic target sprayer (Jiang et al., 2016), disc sprayer (Zhou et al., 2015) or directional sprayer (Zhang et al., 2014; Zhang et al., 2016) have provided new methods for improving air-assisted orchard sprayer, there still seldom have studies on wind

Received date: 2017-03-22 **Accepted date:** 2017-08-13

* **Corresponding author: Zhang Junxiong,** Ph.D., Associate Professor of College of Engineering, China Agricultural University, 100083, Beijing, China. Email: cau2007@cau.edu.cn. Tel: (86)10-62737726.

field guidance for circle arranged nozzles of axial-flow sprayer, especially lack units or methods which are able to guide upper airflow of sprayer. Droplets are easy to drift into the air or fall on the ground which leads to huge waste of pesticides is still an urgent problem.

This paper selected the general used axial-flow air-assisted orchard sprayer (Gu et al., 2014) as the study object, whose air intake is axial set and air outlet is circle arranged. A linear guide plate was installed above the upper air outlet of the sprayer to guide wind field of fan. And orthogonal tests with mixed levels based on Box-Behnken method were designed to find out the influences on spraying effects of different factors. The results will provide references for parameters optimization of the improved air-assisted orchard sprayer.

2 Devices and methods

2.1 Test devices

For fruit trees such as apple, pear, peach, pomelo and so on, canopy height about 1.5-2.5 m, bottom height of canopy is about 0.5-1.0 m, row spacing of trees is about 4 m. And spray range of traditional axial-flow air-assisted orchard sprayer covers a sector whose center is the axis of fan, schematic of the range is shown as α which is equal to 240° in Figure 1. There are no crops in the sector area above sprayer during spraying, causing droplets easily drift into the air or fall on the ground, which wastes lots of pesticides and cannot satisfy the desired prevention and cure effects. In order to solve this problem, an improved air-assisted orchard sprayer was designed. Two linear guide plates whose cross section was C shape were symmetrically installed above the upper air outlet of the sprayer to change its flow direction, which was aimed at improving spraying performances.

An improved self-propelled air-assisted orchard sprayer was selected as test devices in this study, and structure of the sprayer is shown in Figure 2. Diameter of the axial-flow fan is 580 mm and its maximum revolving speed is 2700 r/min. At the maximum speed, air velocity of its outlet is 25 m/s+/-0.5 m/s and air volume is 14722 m^3/h. In order to study the influences of guide plate length on spraying quality, two guide plates with different sizes which were 38 cm and 88 cm were designed according to the canopy sizes of different fruit trees. Angle between guide plate and horizontal direction was adjustable from 0 to 90°. Guide plates were installed above the upper air outlet of the fan and the height from ground is about 1 m. Ten orange nozzles (D2) which produced by Tee Jet company were installed around air outlet of the axial-flow fan. The nozzles were all equipped with drip-proof and rotary tip, and their parameters are list as follow: spray angle is 74°, working pressure is 0.5-1.5 MPa, flow is 0.41-0.63 L/min. Both movement and spraying of the sprayer can be remote controlled.

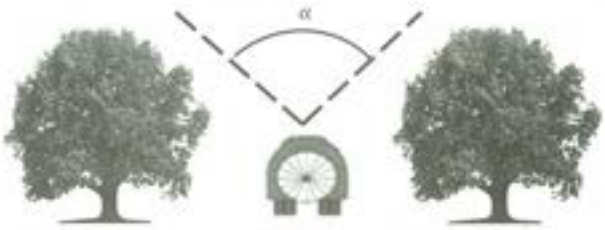

Figure 1 Schematic of spray range

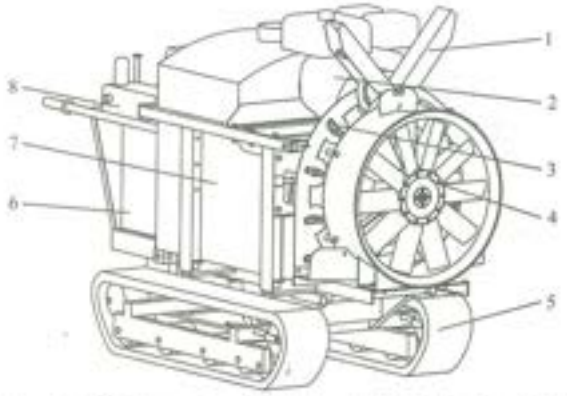

1. Guide plate 2. Fan engine 3. Nozzle 4. Axial-flow fan 5. Moving mechanism 6. Control cabinet 7. Pesticide tank 8. Plungerpump

Figure 2 Structure of self-propelled air-assisted orchard sprayer

2.2 Test design and methods

Operation quality of the improved sprayer was measured based on occupation standard of 'The Operation Quality of Air-assisted Orchard Sprayer' (NY/T992-2006). As structure of axial-flow fan and installation position of nozzles are both symmetrical, tests and simulation based on one side is acceptable and adequate. Instead of real crops, 300 cm height poles were designed as simulated targets according to situation of crops cultivation and structure size of sprayer. Within heights from 150 to 250 cm, three test units were uniformly set as 150, 200 and 250 cm. Every unit had been placed four pieces of water sensitive paper which

produced by Syngenta company and its sizes is 2×3 cm. In each unit, two water sensitive papers are horizontally placed, and others are vertically placed. As is shown in Figure 3, all poles were set in a line which was 200 cm far away from the center line of the sprayer, and distance between each pole was 300 cm.

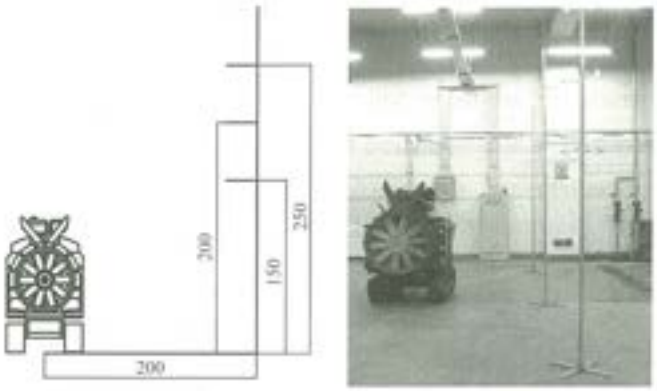

a. Schematic of pole b. Testing site

Figure 3 Spraying test

Orthogonal tests with mixed levels based on Box-Behnken method were designed. Length and angle of guide plate, air velocity of air outlet, and pressure of pump were opted as experimental factors. Levels of each factor are presented in Table 1. In addition, droplet coverage rate was taken as the evaluation index of spraying. There are totally 34 group tests, and the average droplet coverage rate of water sensitive papers at the same height was adapted as final result in every group.

Table 1 Factors and levels table

Levels	Factors			
	A: Angle of guide plate, °	B: Air velocity of fan, m/s	C: Pressure of pump, MPa	D: Length of guide plate, cm
+1	55	25	1.5	88
0	35	20	1.0	-
−1	15	15	0.5	38

When sprayer pass through sampling area, droplets will deposit on water sensitive papers caused by drag force of air flow and become blue spots. After field tests, using industrial camera (Mercury 20) produced by IMAVISION company to collect images of water sensitive papers. As droplet coverage rate is defined as ratio of blue area to total area of water sensitive paper, it is easily to figure out the results by image processing techniques using MATLAB. Images with different droplet coverage rate were shown in Figure 4. Meteorological parameters of tests were also recorded and presented as follows: temperature ranged from 10°C to 17°C, maximum relative humidity was 60%, average wind velocity was under 1.5 m/s and travel speed of sprayer was 0.76 m/s.

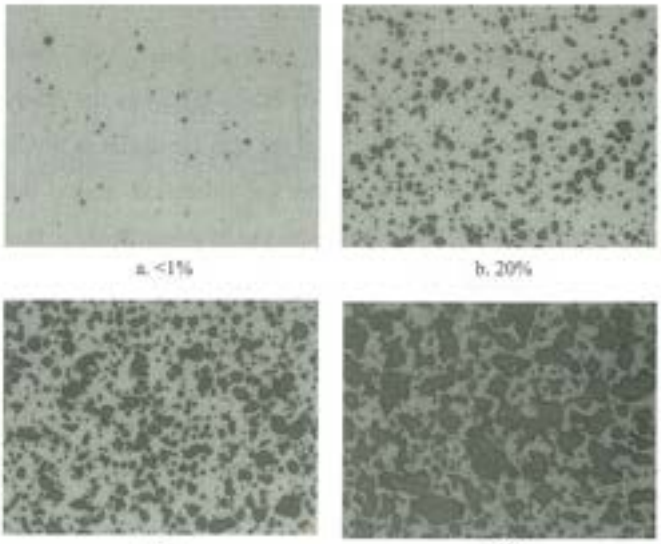

a. <1% b. 20%

c. 40% d. 60%

Figure 4 Images with different droplet coverage rates

3 Results and analysis

3.1 Test results

From the test results presented in Table 2, it is easily to find out that droplet coverage rate decrease with sampling height increase, which is probably caused by changing of airflow filed around the axial-flow fan. In order to confirm this presume, according to methods of reference article (Qi et al., 2010; Wang et al., 2015), airflow filed around the axial-flow fan was simulated using Fluent software. In the simulation, the boundary conditions were set as follow: (1) temperature was 15°C; (2) relative humidity was 45%; (3) gas viscosity was 1.789×10^{-5} Pa·s; (4) the half arc on the left side was set as velocity inlet, which was the airflow inlet; (5) upside and right side of the axial-flow fan were set as free outlet; (6) the left side of the simulation field were set as the symmetry; (7) the other boundaries were set as no-slip wall conditions. Speed fields of different airflow in test areas were figured out through k-ε turbulence model, which are shown in Figure 5. And results indicated that distribution characteristics of different speed fields which are 15, 20 and 25 m/s were similar to each other, only the magnitude were different. So there just gives out partial simulation results which presented in Table 2.

Table 2 Test results

No.	Factors				Droplet coverage rate at different heights, %		
	A: Angle of guide plate, °	B: Air velocity of fan, m/s	C: Pressure of pump, MPa	D: Length of guide plate, cm	150 cm	200 cm	250 cm
1	15	15	1.00	38	18.49	2.38	0.52
2	55	15	1.00	38	30.71	17.80	2.58
3	15	25	1.00	38	10.48	3.17	0.45
4	55	25	1.00	38	11.47	12.71	5.27
5	15	20	0.50	38	11.95	1.86	0.46
6	55	20	0.50	38	28.85	16.80	7.09
7	15	20	1.50	38	20.72	3.66	1.55
8	55	20	1.50	38	33.19	29.62	12.42
9	35	15	0.50	38	36.54	18.10	3.01
10	35	25	0.50	38	30.18	12.67	6.18
11	35	15	1.50	38	58.93	20.75	10.00
12	35	25	1.50	38	25.59	26.56	12.22
13	35	20	1.00	38	22.35	25.27	9.91
14	35	20	1.00	38	22.42	17.13	9.13
15	35	20	1.00	38	24.48	21.52	8.66
16	35	20	1.00	38	20.32	13.83	10.68
17	35	20	1.00	38	22.88	18.74	10.22
18	15	15	1.00	88	12.05	3.29	1.89
19	55	15	1.00	88	38.98	22.43	6.94
20	15	25	1.00	88	36.89	3.39	0.01
21	55	25	1.00	88	32.03	21.11	4.02
22	15	20	0.50	88	27.96	6.57	2.50
23	55	20	0.50	88	48.00	15.28	10.47
24	15	20	1.50	88	26.17	7.28	3.23
25	55	20	1.50	88	38.55	22.57	10.04
26	35	15	0.50	88	47.19	21.31	14.71
27	35	25	0.50	88	48.99	11.48	3.34
28	35	15	1.50	88	44.17	20.08	7.51
29	35	25	1.50	88	38.10	24.37	5.40
30	35	20	1.00	88	36.84	22.19	12.43
31	35	20	1.00	88	40.35	25.60	12.24
32	35	20	1.00	88	32.32	20.06	6.92
33	35	20	1.00	88	36.85	25.78	12.95
34	35	20	1.00	88	39.67	26.01	7.69

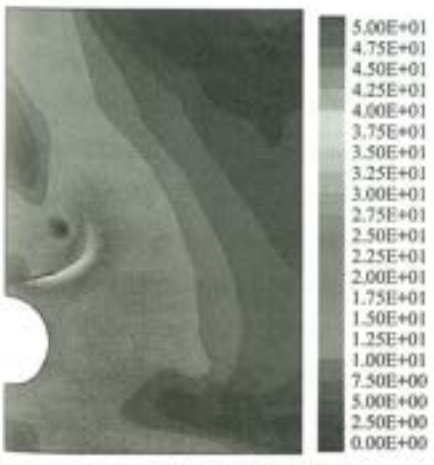

a. A=15°, D=38 cm, v=20 m/s

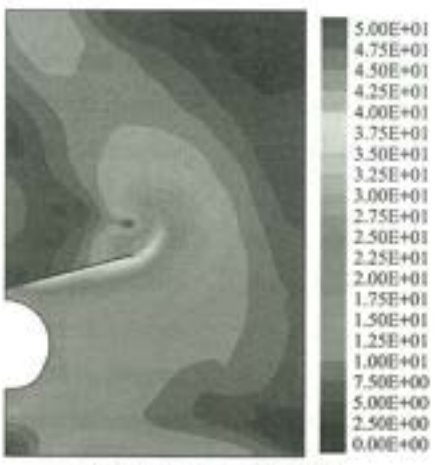

b. A=15°, D=88 cm, v=20 m/s

c. A=35°, D=38 cm, v=20 m/s

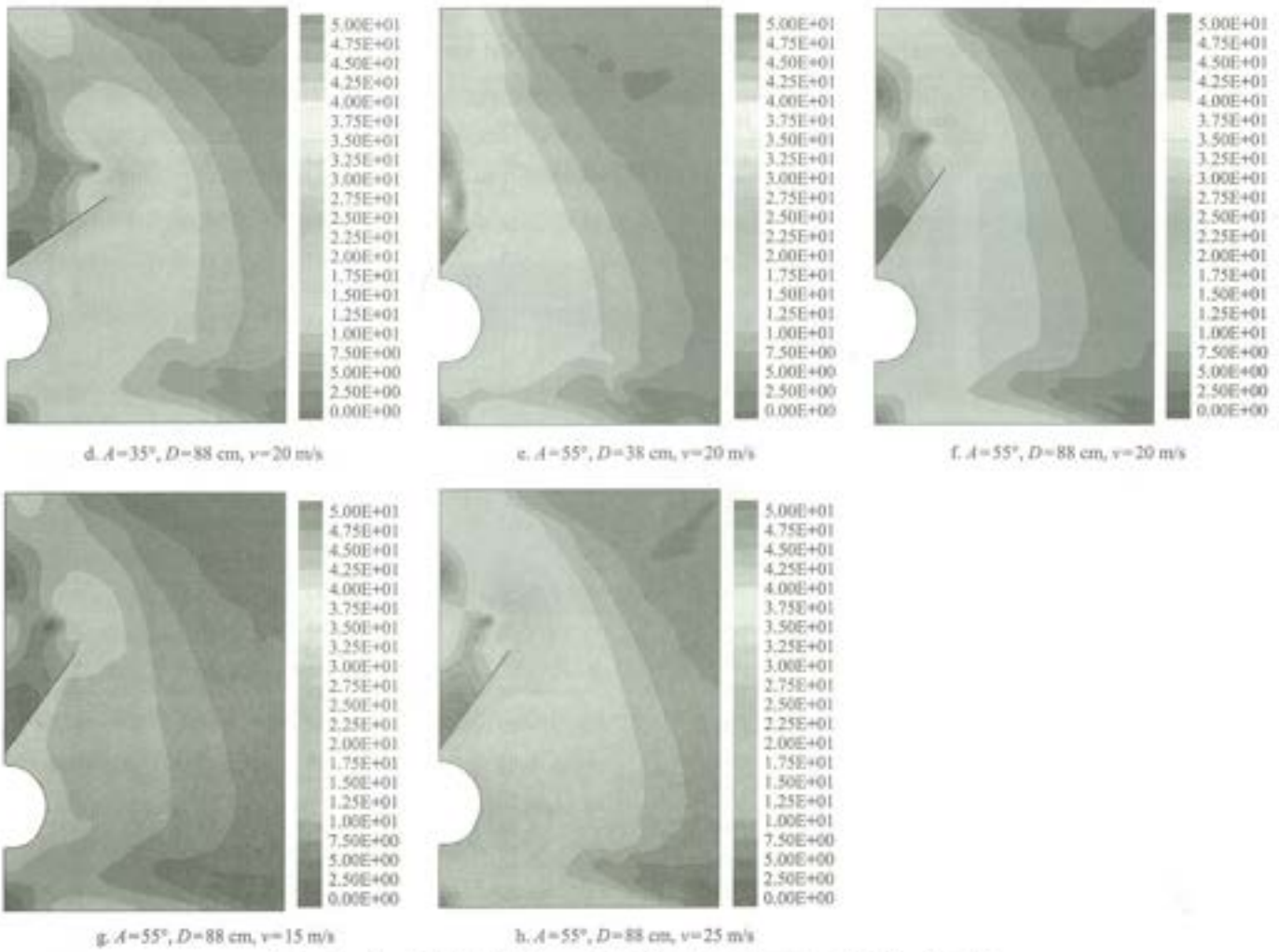

d. A=35°, D=88 cm, v=20 m/s e. A=55°, D=38 cm, v=20 m/s f. A=55°, D=88 cm, v=20 m/s

g. A=55°, D=88 cm, v=15 m/s h. A=55°, D=88 cm, v=25 m/s

Figure 5 Speed field of air flow with different lengths and angles of guide plate

3.2 Analysis of variance (ANOVA)

In consideration of quadratic influences between different factors, it is necessary to analyze the variances of data presented in Table 2. Analysis results had indicated the response relationships between parameters of prayer and different sampling heights which presented in Table 3. Significant degrees of each factor influenced on droplet coverage rate were figured by F test, and the smaller P value is, the more significant influence on droplet coverage rate is. In the vertical plane which was 200 cm away from the center line of axial-flow fan and according to Table 3, it is easily to conclude that: (1) at height of 150 cm, factors of significant influences whose P value is bigger than 0.05 on droplet coverage rate are A, B, D, AB, BC, BD, CD, A^2, C^2, and the other factors are not significant whose P value is smaller than 0.05; (2) at height of 200 cm, significant factors are A, C, D, BC, A^2, B^2; (3) at height of 250 cm, significant factors are A, C, BD, CD, A^2, B^2.

3.3 Influences of each factor on droplet coverage rate

According to P value in Table 3, at height of 150 cm, the sequence of factors, according to significant degree of influences on droplet coverage rate, was D, A, Band C. As pressure of pump had less influence on droplet coverage rate, the droplet coverage rate at this height can be seemed as influencing by interaction of D, A and B. When D was equal to 38 cm and C was at average level which was equal to 1.0 MPa, response surface figure of interaction A with B was shown in Figure 6a. When D was equal to 88 cm and C was at average level, response surface figure of interaction A with B was shown in Figure 6b. Both of them indicated that: (1) with increasing of guide plate angle, droplet coverage rate increased at first and then decreased; (2) when guide plate length was 38 cm, droplet coverage rate decreased with air velocity increasing; (3) when guide plate length was 88 cm, droplet coverage rate increased a little at high air velocity.

Table 3 ANOVA table

Variables	Droplet coverage rate at 150 cm height				Droplet coverage rate at 200 cm height				Droplet coverage rate at 250 cm height			
	SS	DF	F value	P value	SS	DF	F value	P value	SS	DF	F value	P value
Models	37.060	13	19.030	<0.0001	45.570	13	24.120	<0.0001	29.980	13	19.620	<0.0001
A	5.770	1	38.500	<0.0001	24.500	1	168.610	<0.0001	10.480	1	89.190	<0.0001
B	1.390	1	9.270	0.0064	0.120	1	0.840	0.3690	0.420	1	3.590	0.0728
C	0.034	1	0.230	0.6379	2.390	1	16.430	0.0006	0.730	1	6.190	0.0218
D	10.140	1	67.690	<0.0001	0.880	1	6.020	0.0234	0.230	1	1.960	0.1765
AB	2.290	1	15.280	0.0009	0.140	1	0.960	0.3381	0.240	1	2.000	0.1727
AC	0.200	1	1.310	0.2666	0.280	1	1.940	0.1793	0.000	1	0.000	0.9917
AD	0.021	1	0.140	0.7125	0.170	1	1.170	0.2913	0.022	1	0.190	0.6674
BC	0.890	1	5.950	0.0241	1.110	1	7.620	0.0121	0.170	1	1.460	0.2406
BD	4.060	1	27.130	<0.0001	0.009	1	0.060	0.8088	2.280	1	19.370	0.0003
CD	1.340	1	8.920	0.0073	0.120	1	0.840	0.3707	1.160	1	9.900	0.0051
A^2	6.180	1	41.260	<0.0001	14.700	1	101.140	<0.0001	10.160	1	86.440	<0.0001
B^2	0.270	1	1.780	0.1966	0.740	1	5.060	0.0359	3.380	1	28.750	<0.0001
C^2	5.050	1	33.690	<0.0001	0.010	1	0.072	0.7910	0.260	1	2.170	0.1559
Residual	3.000	20			2.910	20			2.350	20		
Lack of Fit	2.620	12	4.650	0.0184	1.610	12	0.830	0.6261	1.420	12	1.020	0.5060
Error	0.380	8			1.290	8			0.930	8		
Total	40.050	33			48.480	33			32.330	33		

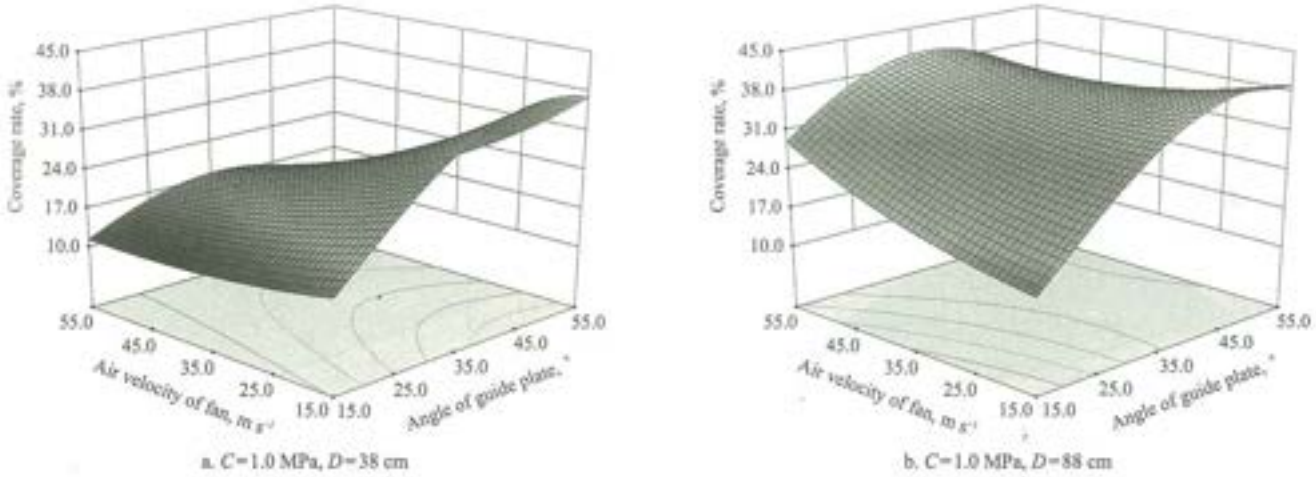

a. C=1.0 MPa, D=38 cm b. C=1.0 MPa, D=88 cm

Figure 6 Influences of interaction factors on droplet coverage at 150 cm height

Combined with simulation results of Figure 5, it can be concluded that: (1) when guide plate angle was small, droplets fell down to the ground by drag force of air flow and caused low droplet coverage rate; (2) when guide plate angle was too big, droplets drifted upward targets of poles and also caused low droplet coverage rate; (3) when guide plate length increased, airflow field got closer to sampling targets of poles, which was similar to reduce distance between poles and sprayer, so droplet coverage rate increased a little with air velocity increased.

At height of 200 cm, the sequence of factors, according to significant degree of influences on droplet coverage rate, was A, C, D and B. As length of guide plate had less influence on droplet coverage rate, average of guide plate length was selected to analyze the results. According to interaction analysis of different factors, the other factors were correspondingly selected at average level calculated by the software of Design-Expert 8.0.6, and response surface figures were shown in Figure 7. According to the figures, it can be found that: (1) with air velocity increasing, droplet coverage rate change a little, which indicated air velocity of fan had less influence on droplet coverage rate and is in accordance with Table 2; (2) at the height of 200 cm, with increasing of guide plate angle, droplet coverage rate increased at first and then decreased which is same as at height of 150 cm; (3) droplet coverage rate increased with pump pressure increasing, which caused by increasing of spraying flow.

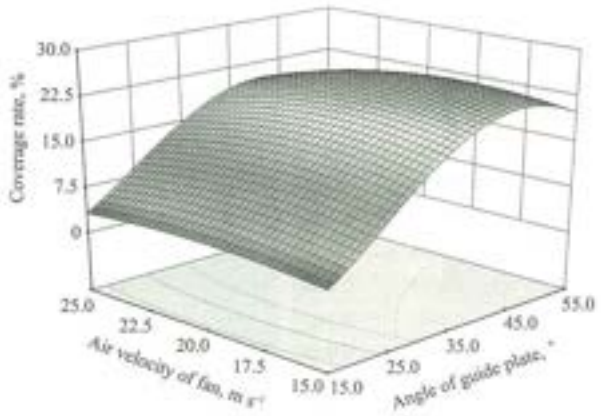

a. C=1.0 MPa, D=Average

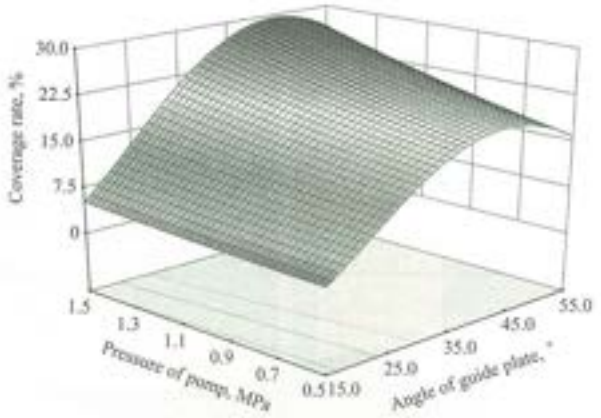

b. B=20 m/s, D=Average

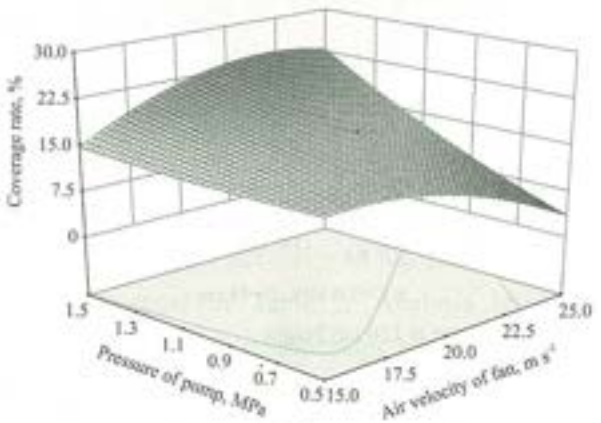

c. A=35°, D=Average

Figure 7 Influences of interaction factors on droplet coverage at 200 cm height

At the height of 250 cm, the sequence of factors, according to significant degree of influences on droplet coverage rate, was A, C, B and D. Also, guide plate length was selected as average value, and according to interaction analysis of different factors, the other factors were correspondingly selected at average level, response surface figures were shown in Figure 8. According to the figures, we can find that: (1) at the height of 250 cm, the factor of most significant influence on droplet coverage rate was guide plate angle which is same as height of 150 cm and 200 cm; (2) droplet coverage rate increased with pump pressure increasing, which also caused by increasing of spraying flow; (3) with increasing of air velocity, droplet coverage rate increased at first and then decreased, which was caused by straight movement more than deposition movement of droplets.

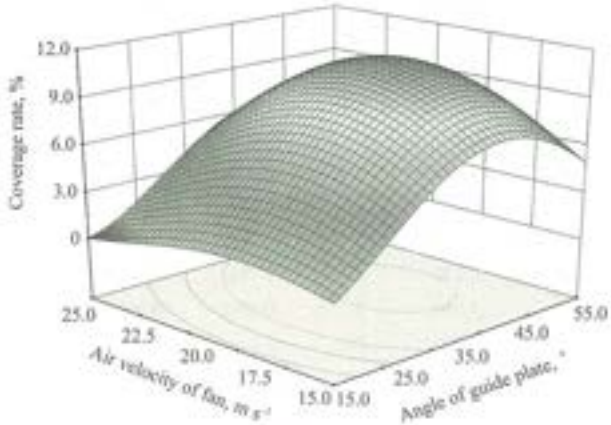

a. C=1.0 MPa, D=Average

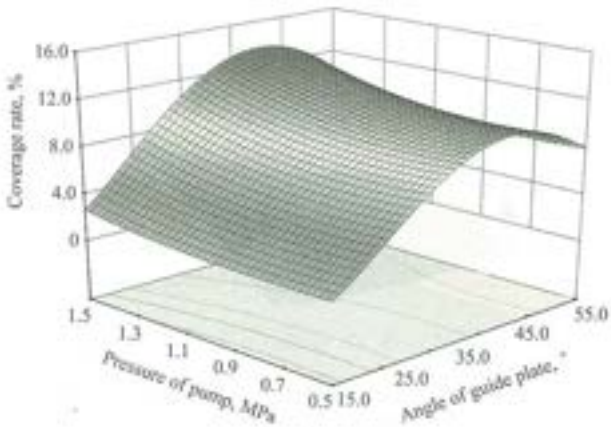

b. B=20 m/s, D=Average

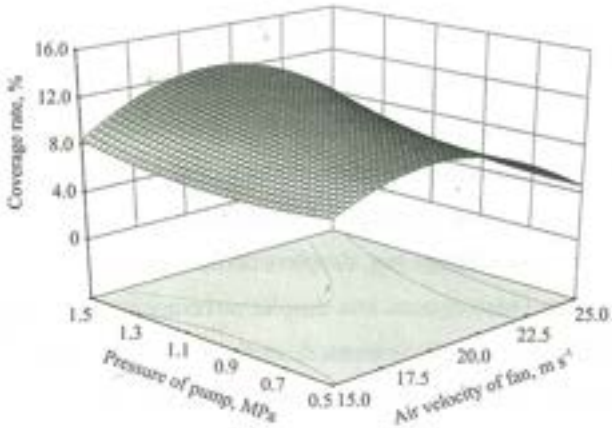

c. A=35°, D=Average

Figure 8 Influences of interaction factors on droplet coverage at 250 cm height

Above all, as the influence of main factors on droplet coverage rate changed with heights of pole, it is necessary to adjust operating parameters of sprayer at different

heights in order to satisfy the desired prevention and cure effects.

4 Approximate models of factors

From the previous analysis, it is necessary to adjust and optimize operating parameters of sprayer at different heights in order to realize optimal spraying effects. However, because of complicated atomization principles, it is unrealistic to establish a completely accurate model of spraying performance, equivalent model with reliable accuracy is enough.

In the optimization design, approximate model approximates the relationships between input and output variables through using mathematics, which is able to solve two kinds of problems in practical projects: 1) unable to establish explicit mathematical optimization model because of complicated structure; 2) established model is too complex to solve. The basic thought of approximate model is to establish a model which has enough accuracy and simple calculation based on limited test data. There are some common approximate models, such as RSM model, Kriging model, Multivariate Adaptive Regression Spline (MARS) model, and Radial Basis Function (RBF) Neural Network model (Han et al., 2012).

4.1 RSM model

Quadratic regression fitting models were established through software Design-Expert 8.0.6 based on analysis results of response surface method, which were able to explain the relationships between droplet coverage rate and spraying parameters when the distance between center line of sprayer and sampling poles was 2 m. By guaranteeing the models are significant and unfit terms are insignificant as premises, insignificant terms were rejected according to P value in Table 3, RSM models were figured out and presented as Equations (1)-(3):

$$R_1 = 5.49 + 0.60 \times A - 0.29 \times B + 0.046 \times C + 0.55 \times D - 0.54 \times AB - 0.33 \times BC + 0.50 \times BD - 0.29 \times CD - 0.85 \times A^2 + 0.78 \times C^2 \quad (1)$$

$$R_2 = 4.64 + 1.24 \times A - 0.088 \times B + 0.39 \times C + 0.16 \times D + 0.37 \times BC - 1.32 \times A^2 - 0.29 \times B^2 \quad (2)$$

$$R_3 = 3.23 + 0.81 \times A - 0.16 \times B + 0.21 \times C + 0.082 \times D - 0.38 \times BD - 0.27 \times CD - 1.09 \times A^2 - 0.62 \times B^2 \quad (3)$$

where, A is angle of guide plate, °; B is air velocity of fan, m/s; C is pressure of pump, MPa; D is length of guide plate, cm; R_1, R_2, R_3 respectively represents droplet coverage rate at heights of 150, 200 and 250 cm, and unit of them is %.

Determination coefficients R^2 of optimized models were respectively calculated as 91.31%, 92.49%, 90.61% at the heights of 150, 200 and 250 cm, which indicated that the models could fit about more than 90% response variables with high correlation and low error between predicted and test values. Furthermore, maximums of droplet coverage rate at different heights were set as object function, and variation range of its variables were the same as Table 1. Based on RSM models, optimization spraying parameters at different heights were calculated out and presented in Table 4.

Table 4 Predicted value of RSM model

Height, cm	A: Angle of guide plate, °	B: Air velocity of fan, m/s	C:Pressure of pump, MPa	D: Length of guide plate, cm	Droplet coverage rate, %
150	39.97	24.95	0.51	88	57.04
200	45.57	20.23	1.47	88	29.81
250	44.88	20.73	1.49	38	15.40

4.2 RBF Neural Network model

RBF Neural Network is a local approximate network with three layers. The first layer is input layer consisting of sensing units, and is used to connect input variables with neural network. The second layer is hidden layer used to translating input space to hidden space as non-linear transformations. It should be pointed out that RBF is usually a non-negative and non-linear function, which is radial symmetry and attenuation around central point. The third layer is linear output layer used to output response values of corresponding input variables. RBF Neural Network has many advantages such as simple structure, fast convergence rate of learning and could approximate any continuous functions with arbitrary precision (Shi, 2009; Wang et al., 2015).

As parameters optimization of improved air-assisted

orchard sprayer is a multi-objective optimization problem, multi-objective optimization algorithm was adopted to calculate the final results. RBF Neural Network models were established through software Isight according to data in Table 3, and approximate models of droplet coverage rate at different heights were figured out and presented as Equation (4):

$$\begin{cases} \max R_1' = f_1(A,B,C,D) \\ \max R_2' = f_2(A,B,C,D) \\ \max R_3' = f_3(A,B,C,D) \end{cases} \quad (4)$$

where A, B, C, D are same as Equations (1)-(3); R'_1, R'_2, R'_3 respectively represents droplet coverage rate at heights of 150, 200 and 250 cm, and units of them are %.

Determination coefficients R^2 of optimized models were respectively calculated as 95.76%, 97.19%, and 97.54% at heights of 150, 200 and 250 cm, which indicated that the models could fit about more than 95% response variables. It is easily to find that determination coefficients of RBF Neural Network models are all higher than RSM models, because RSM is limited at quadratic polynomial which has bounded capabilities of fitting test data. However, RBF Neural Network adapts global non-linear fitting which has higher precision.

Furthermore, maximums of droplet coverage rate at different heights were set as object function, and variation range of its variables were same as Table 1. Using software through NSGA-II multi-objective genetic algorithm, population size was set as 10, evolutional generation was set as 20, cross-over rate was set as 0.4, and mutation probability was set as 0.02, optimization spraying parameters at different heights were calculated out and presented in Table 5.

Table 5 Predicted value of RBF neural network model

Height, cm	A: Angle of guide plate, °	B: Air velocity of fan, m/s	C: Pressure of pump, MPa	D: Length of guide plate, cm	Droplet coverage rate, %
150	32.82	24.48	0.50	88	57.06
200	44.64	21.42	1.50	38	29.67
250	43.20	21.72	1.49	38	15.58

4.3 Verification of models

To verify the precision of modes, tests were repeated for three times based on optimized operation parameters presented in Tables 4 and 5. Averages of droplet coverage rate at different heights were selected as final results presented in Table 6. According to Table 6, both of RSM model and RBF neural network model are able to fit the droplet coverage rate at different sample heights. Meanwhile, the precision of RBF Neural Network is better than RSM, which causes by restriction fitting ability of quadratic regression RSM model. Therefore, RBF Neural Network model was selected as reference to optimize parameters of sprayer.

Table 6 Comparison of predicted and test value with different models

Height, cm	RSM Model			RBFNN Model		
	Predicted value, %	Test value, %	Relative error, %	Predicted value, %	Test value, %	Relative error, %
150	57.04	60.58	6.2	57.06	55.06	3.5
200	29.81	27.16	8.9	29.67	28.13	5.2
250	15.40	17.22	11.8	15.58	17.01	9.2

5 Conclusions

(1) Based on RSM, length and angle of guide plate, air velocity of air outlet, and pressure of pump were opted as influence factors. In addition, droplet coverage rate was taken as response index of spraying. And orthogonal tests with mixed levels based on Box-Behnken method were designed and carried out. Furthermore, influences of the improved sprayer operating parameters on spraying effects were found out as follow: in the vertical plane which was 200 cm away from the center line of axial-flow fan, at height of 150 cm, the sequence of factors according to significant degree of influences on droplet coverage rate was length of guide plate, angle of guide plate, air velocity of fan, and pressure of pump; at height of 200 cm, the sequence was angle of guide plate, pressure of pump, length of guide plate, and air velocity of fan; at height of 250 cm, the sequence was angle of guide plate, pressure of pump, air velocity of fan, and length of guide plate.

(2) RSM model and RBF Neural Network model were

respectively adopted to approximate the relationships and establish the approximate models between experimental factors and experimental data. In verification tests, at height of 150 cm, droplet coverage rate and forecast error were 55.06% and 3.5%; at height of 200 cm, they were 28.13% and 5.2%; at height of 250 cm, they were 17.01% and 9.2%. The results showed that both of the two approximate models are able to fit the droplet coverage rate at different sample heights. Meanwhile, the model of RBF Neural Network was proved better, which causes by restriction fitting ability of quadratic regression RSM model.

(3) Based on RBF Neural Network model, optimization operating parameters of improved air-assisted orchard sprayer were figured out as follow: at height of 150 cm, length of guide plate was 88 cm, angle of guide plate was 32.82°, air velocity of air outlet was 24.48 m/s, and pressure of pump was 0.5 MPa; at height of 200 cm, length of guide plate was 38 cm, angle of guide plate was 44.64°, air velocity of air outlet was 21.42 m/s, and pressure of pump was 1.5 MPa; at height of 250 cm, length of guide plate was 88 cm, angle of guide plate was 43.20°, air velocity of air outlet was 21.72 m/s, and pressure of pump was 1.49 MPa. The results indicated that it was necessary to adjust operating parameters of sprayer at different heights in order to realize optimal spraying effects for canopies at different heights.

Acknowledgements

This work was partially financed by the National Key Research and Development Plan: High Efficient Ground and Aerial Spraying Technology and Intelligent Equipment (Grant No. 2016YFD0200700).

[References]

[1] Endalew, A. M., C. Debaer, N. Rutten, J. Vercammen, M. A. Delele, H. Ramon, B. M. Nicolaï, and P. Verboven. 2010. A new integrated CFD modelling approach towards air-assisted orchard spraying. Part I. Model development and effect of wind speed and direction on sprayer airflow. *Computers and Electronics in Agriculture*, 71(2): 128–136.

[2] Gu, J. B., W. M. Ding, W. Qiu, and C. D. Sun. 2014. Current research situation and development trend of equipment and technology for orchard spraying. *Journal of Fruit Science*, 31(6): 1154–1157.

[3] Han, D., and J. R. Zheng. 2012. A Survey of metamodeling techniques in engineering optimization. *Journal of East China University of Science and Technology: Natural Science Edition*, 38(6): 762–768.

[4] Jiang, H. H., P. Bai, L. M. Liu, X. F. Dong, J. L. Song, and X. H. Zhang. 2016. Caterpillar self-propelled and air-assisted orchard sprayer with automatic target spray system. *Transactions of the Chinese Society for Agricultural Machinery*, 47(S1): 189–195. (In Chinese with English abstract)

[5] Qi, L. J., Y. Q. Zhao, J. Wang, R. H. Ji, and L. Mang. 2010. CFD simulation and experiment verification of droplet dispersion of air-assisted orchard sprayer. *Transactions of the Chinese Society for Agricultural Machinery*, 41(2): 62–67. (In Chinese with English abstract)

[6] Qiu, W., J. B. Gu, W. M. Ding, X. L. Lv, C. D. Sun, and J. Lu. 2015. Experiment on control effect of different pesticide concentration using air-assisted sprayer. *Transactions of the Chinese Society for Agricultural Machinery*, 46(1): 94–99. (In Chinese with English abstract)

[7] Salcedo, R., R. Granell, G. Palau, A. Vallet, C. Garceră, P. Chueca, and E. Moltó. 2015. Design and validation of a 2D CFD model of the airflow produced by an airblast sprayer during pesticide treatments of citrus. *Computers and Electronics in Agriculture*, 116(C): 150–161.

[8] Shi, Z. Z. 2009. Neural Network. *Beijing: Higher Education Press*.

[9] Song, S. R., T. S. Hong, D. Z. Sun, Y. Q. Zhu, and C. Luo. 2011. Effect of fan power supply frequency on deposition of air-assisted sprayer. *Transactions of the Chinese Society of Agricultural Engineering*, 27(1): 153–159. (In Chinese with English abstract)

[10] Song, S. R., H. B. Xia, H. S. Liu, T. S. Hong, D. Z. Sun, and Y. H. Lu. 2013. Numerical simulation and experiment of structural optimization for air-blast sprayer. *Transactions of the Chinese Society for Agricultural Machinery*, 44(6): 73–78, 55. (In Chinese with English abstract).

[11] Sun, C. D., W. Qiu, W. M. Ding, and J. B. Gu. 2015. Parameter optimization and experiment of air-assisted spraying on pear trees. *Transactions of the Chinese Society of Agricultural Engineering*, 31(24): 30–38. (In Chinese with English abstract)

[12] Wang, J. X., L. J. Qi, and Q. J. Xia. 2015. CFD simulation and validation of trajectory and deposition behavior of droplets around target affected by air flow field in greenhouse. *Transactions of the Chinese Society of Agricultural Engineering*, 31(11): 46–53. (In Chinese with English abstract)

[13] Wang, Z. T., Y. H. Zhang, Q. M. Dong, X. Y. Wang, and J. L.

Wen. 2015. Experiment of wind-blowing electrostatically charged spray. *Journal of Jiangsu University: Natural Science Edition*, 36(4): 425–430. (In Chinese with English abstract)

[14] Wang, W. J., J. Pei, S. Q. Yuan, J. F. Zhang, C. Z. Xu, and F. Zhang. 2015. Optimization of impeller meridional shape based on radial basis Neural Network. *Transactions of the Chinese Society of Agricultural Engineering*, 46(6): 78–83. (In Chinese with English abstract)

[15] Zhang, X. H., Z. Y. Jiang, G. Q. Fan, and L. L. Cao. 2014. Self-propelled crawler directional air-blowing orchard sprayer. *Transactions of the Chinese Society of Agricultural Engineering*, 45(8): 117–122, 247. (In Chinese with English abstract)

[16] Zhang, X. H., L. J. Wang, C. L. Hou, Y. L. Li, and H. M. Feng. 2016. Development and experiment of air-assisted vineyard sprayer. *Journal of Chinese Agricultural Mechanization*, 37(7): 57–61, 74. (In Chinese with English abstract)

[17] Zhou, L. F., L. Zhang, X. Y. Xue, W. M. Ding, Z. Sun, Q. Q. Zhou, and L. F. Cui. 2016. Design and experiment of 3WQ-400 double air-assisted electrostatic orchard sprayer. *Transactions of the Chinese Society of Agricultural Engineering*, 32(16): 45–53. (In Chinese with English abstract)

[18] Zhou, L. F., X. M. Fu, W. M. Ding, S. M. Ding, J. Chen, and Z. J. Chen. 2015. Design and experiment of combined disc air-assisted orchard sprayer. *Transactions of the Chinese Society of Agricultural Engineering*, 31(10): 64–71. (In Chinese with English abstract)

Comparative experimental study on working performance of air-blowing and air-suction cotton-boll separation device

Chen Changlin, Kong Fanting, Shi Lei*, Xie Qing, Zhang Yutong, Sun Yongfei, Huang Mingsen

(Nanjing Research Institute for Agricultural Mechanization, Ministry of Agriculture, Nanjing 210014, China)

Abstract: Some cotton bolls, cotton stalks, cotton leaves and other impurities are always collected with cotton during cotton mechanization harvesting. And then all of them are put into the postposition cleaning device. Cotton-boll separation device is added on stripper cotton harvester during cotton mechanization harvesting due to the immature cotton bolls, which can easily dye the cotton and cause the decline of cotton quality. In order to improve separating efficiency, decrease immature cotton bolls dying the cotton, and solve other problems, two kinds of cotton-boll separation device, i.e., air-suction separation device and air-blowing separation device were developed based on their main elementary structures, working principle and the difference between suspending velocities of different materials. The inner airflow velocities and pressures distributions of two kinds of cotton-boll separation devices were numerically simulated by using ANSYS Fluent software, and then the simulation results were analyzed. The suspending velocities of different materials and performances of cotton-boll separation device experiments were carried out and the simulation results were compared with the experiment results. The experimental results showed that: the average error between simulation and experimental results were less than 5%, which is valuable and has great meaning in the research of cotton mechanization harvesting. Air-suction cotton-boll separation device is better than air-blowing cotton-boll separation device. The airflow of air-suction cotton-boll separation device get together in the stable zone of negative pressure formed during cotton conveying process. The suspending velocity of cotton was low enough to separate seed cotton from cotton fluid cluster. Air-suction cotton-boll separation device can improve more than 20% of cotton-boll separating rate and reduce 5% of cotton loss rate than air-blowing cotton-boll separation device.

Keywords: cotton, boll, air-blowing, air-suction, experiment

Citation: Chen, C. L., F. T. Kong, L. Shi, Q. Xie, Y. T. Zhang, F. Y. Sun, and M. S. Huang. 2017. Comparative experimental study on working performance of air-blowing and air-suction cotton-boll separation device. International Agricultural Engineering Journal, 26(3): 75–81.

1 Introduction

Cotton is one of the most important economic crops in China and is also an important raw material in the textile industry. In recent years, shortage of labor issue is becoming increasingly acute that seriously restricts the development of cotton industry in China. Promoting the mechanization of cotton harvesting has become the inevitable tendency of cotton industry sustainable development. The perennial planting area of cotton is 4222.33 thousand hectares and the mechanization harvesting area is 661.16 thousand hectares (Ye et al., 2011), but mechanization harvesting rate just is 15.7% (Ding et al., 2012).

Manual picking was widely adopted by the cotton farmer due to the lack of suitable cotton harvester. The reduced number of cotton picking worker leads to a higher labor cost and lower cotton price in recent years. An amount of cotton has been left in the field and the economy of the cotton declines very seriously. The cost of stripper cotton harvester remarkably decreased with the constant innovation, it means that the market of

Received date: 2017-06-12 **Accepted date:** 2017-07-07

* **Corresponding author**: **Chen Changlin**, Nanjing Research Institute for Agricultural Mechanization. Tel.: 86-025-58619528, Email: njscel@163.com.

stripper cotton harvester has a great potential for development. While only a small amount of stripper cotton harvester are used in South America and the horizontal spindle type cotton harvester were widely used in the main cotton field of American and other countries. Researchers have studied different methods for designing and optimizing a new field cleaning device with improved cleaning performance and processing capacity (Barker et al., 1991; Baker et al., 1999; Baker et al., 2000; Whitelock et al., 2007; Lu, 2013). There are little breakthroughs in the study of machine-mounted seed cotton pre-treatment apparatus.

EMA-SA-0030 type stripper cotton harvester, developed by Auros Company in Argentina, was introduced by Nanjing Research Institute for Agricultural Mechanization, Ministry of Agriculture in 2009. The practical experiment proved that cotton trash content which has been processed by its machine-mounted seed cotton pre-treatment apparatus was too high to meet the need of the cotton harvesting in China. This research group has improved machine-mounted seed cotton pre-treatment apparatus and also developed two kinds of cotton-boll separation devices on the basic of the problems found during the pre-experiments (Huang et al., 2016; Price et al., 1996). Cotton-boll separation device is key part of stripper cotton harvester and one of innovative subjects. Optimization and improvement of this device is convenient for improving efficiency of following cleaning work (Tian et al., 2017), collecting the bolls and increasing income of cotton farmer (Krifa et al., 2013).

2 Working principle of cotton-boll separation device

2.1 Suspending velocity of material

Suspending velocity is one of main material aerodynamics characteristic (Brashears et al., 1995), which is the important basic design parameter for pneumatic conveying, pneumatic separation and other devices (Carlos et al., 2009). Not only the airflow, but also the gravities and disturbance resistances affected cotton-impurity mixtures when the cottons were moving in pipeline.

Material and the airflow can be uniform and in a straight line with the same speed while the material's resultant force is zero and material is in equilibrium. That means the velocity of airflow is the suspending velocity of material. The material will downward at a finite speed when air force is less than the force keep material upward. The resistance force of material will increase with the increasing descent velocity.

When the length of pipeline is under ideal condition, there is always a moment that velocity of material is in equilibrium. At that time the velocity is called "settlement velocity of material". Settlement velocity has different meanings with suspending velocity although they are equal in number. So they are uniformly called "critical speed of material". The theoretical value of material's acting force affected by airflow can be calculated with following formula derivation.

$$P = k\rho A v^2 \tag{1}$$

where, k is the aerodynamic drag factor which is affected by material shape, surface properties and Reynolds number; ρ is air density, kg/m^3; A is the maximum cross-section area of material in direction of perpendicular to relative velocity, m^2; and v is relative speed between material and airflow, m/s.

The kinematic equation used to calculate material which is affected by vertical airflow field is:

$$m\frac{d_v}{d_t} = P - G \tag{2}$$

where, m is materials quality, kg; G is material suffered gravity, N.

By the knowledge of hydromechanics we can know that: when material is affected by vertical airflow field and keeps in equilibrium,

If the material is in the state of suspend: $\frac{d_v}{d_t} = 0$

If the material is in the state of moving upward: $\frac{d_v}{d_t} > 0$

If the material is in the state of moving downward: $\frac{d_v}{d_t} < 0$

Cotton-boll separation device separate the boll from cotton by use of difference suspend velocities between

closed boll, light impurities and other materials.

2.2 Elementary structure and working principle of cotton-boll separation device

Air-blowing cotton-boll separation device and seed cotton convey device is shown as Figure 1, which mainly consist of centrifugal fan, accelerating duct, cotton picked roller, air-lock valve for cotton gather, feeding duct and so on, where A, B, C, D, E, F represent wind pressures and wind speed measurement areas. Parameters of air-blowing cotton-boll separation device is shown in Table 1. Working principle of air-blowing cotton-boll separation device refers to separating the boll from cotton cluster using different masses of seed cotton and boll. Wind-force was produced by high-speed centrifugal fan and further speeded up by accelerating duct over work. That can push the cotton with cotton picked roller and diffuse rapidly. Under the push of flow power, light cotton kept moving upwards until entering into the following seed cotton pretreatment device. Heavy boll being along the baseplate moved over backwards under the resultant force of gravity, inertia force and airflow thrust. The wind pressure damped when passed the baseplate. Some bolls fell down to air-lock valve because their gravities were larger than the wind thrust that achieves a separation.

Air-blowing cotton-boll separation type was also called air-assisted separation type which usually can be seen in heavy impurity separator of cotton processing line (Gillum et al., 2001) and achieves the function of soil block, carpolite and other heavy impurities separating (Whitelock et al., 2007).

2.3 Elementary structure and working principle of air-suction cotton-boll separation device

Air-suction cotton-boll separation device which includes centrifugal fan, Accelerating duct, cotton picked roller, opening boll collecting and transfer part, feeding duct and other parts is shown as Figure 2 and their mainly parameters are shown in Table 2, where A, B, C, D, E, F represent wind pressure and wind speed measurement area. The working principle of air-suction cotton-boll separation is based on the theory of gas-solid two-phase flow. The cotton becomes loose, diffusion and layering under the push of cotton picked roller. Wind-force was produced by high-speed centrifugal fan and further speeded up by accelerating duct over work. Then negative pressure which exerted a strong pull on seed cotton was formed at diffusion zone. Because of obviously different suspend velocities of seed cotton and boll, two different materials can be separated.

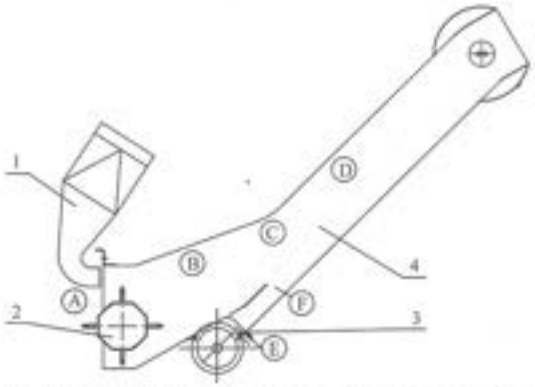

1. Accelerating duct 2. Cotton picked roller 3. Air-lock valve 4. Feeding duct

Figure 1 Air-blowing cotton-boll separation device

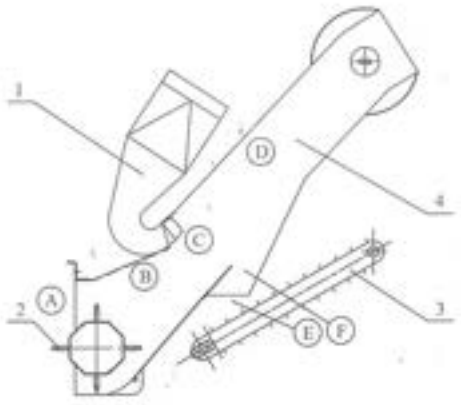

1. Accelerating duct 2. Cotton picked roller 3.Opening boll convey 4. Feeding duct

Figure 2 Air-suction cotton-boll separation device

Table 1 Parameters of air-blowing cotton-boll separation device

Name	Units	Targeted value
Diameter of cotton picked roller	mm	250
Linear speed of cotton picked roller	m/s	2-2.2
Lifting difference in height of cotton boll	mm	>270
Flow of fan	m^3/h	>10000
Feed quantity of seed cotton	kg/s	0.5-0.8

Table 2 Parameters of air-suction cotton-boll separation device

Name	Units	Targeted value
Diameter of cotton picked roller	mm	250
Linear speed of cotton picked roller	m/s	2.2-2.5
Lifting difference in height of cotton boll	mm	>320
Flow of fan	m^3/h	>10000
Feed quantity of seed cotton	kg/s	0.5-0.8

3 Simulation analysis based on ANSYS

3-D solid models of two kinds of cotton-boll separation devices have been designed by using ProE software. Inner airflow velocities and pressures distribution of cotton-boll separation device under the action of strong airflow have been simulated respectively by ANSYS Fluent software. Based on proper grid partition and parameters, i.e., relative pressure of all the exits of zero and inlet velocity of 40 m/s, and other boundary conditions, the results of simulation analysis can be obtained.

3.1 Simulation analysis results of air-blowing cotton-boll separation device

Simulation analysis results of air-blowing cotton-boll separation device are shown as Figure 3 and Figure 4.

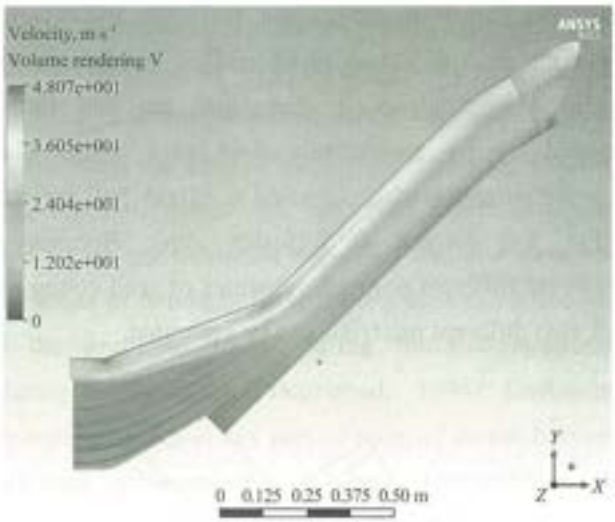

Figure 3 Velocity distribution of air-blowing cotton-boll separation device

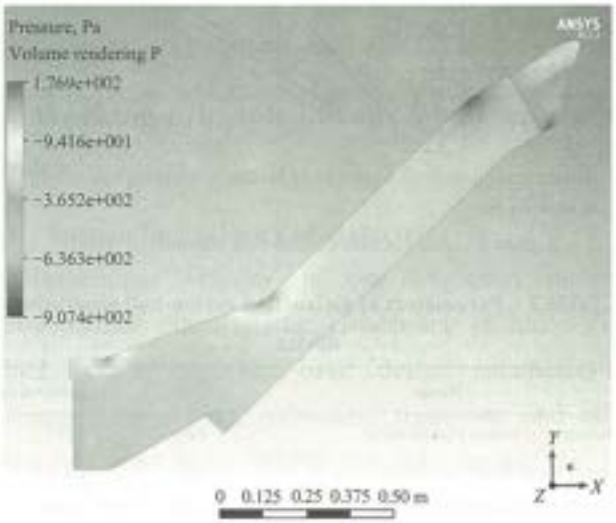

Figure 4 Pressure distribution of air-blowing cotton-boll separation device

By analyzing the simulation diagram that can be get to know: flow velocities of air-blowing cotton-boll separation device from top to bottom taper off in the same section, flow spread quickly and difficult to aggregated along the direction of feeding duct.Pressure has sudden changed in some bending positions and it would easily arose the vortex, which would generated interference and had the impact on movement direction of seed cotton.

3.2 Simulation analysis results of air-suction cotton-boll separation device

Simulation analysis results of air-suction cotton-boll separation device as is shown in Figures 5 and 6.

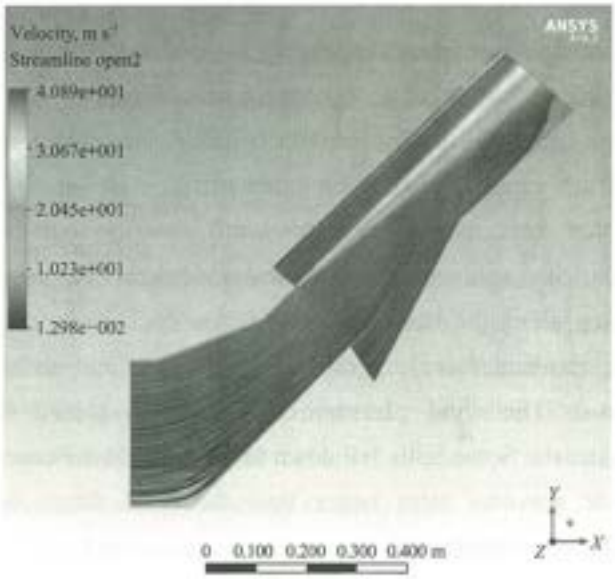

Figure 5 Velocity distribution of air-suction cotton-boll separation device

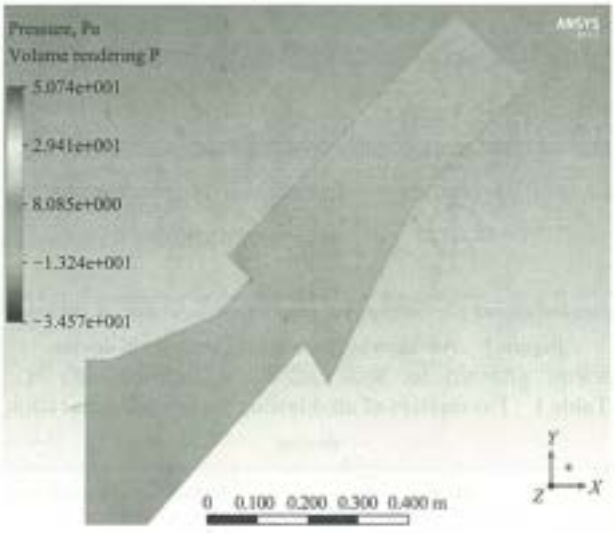

Figure 6 Pressure distribution of air-suction cotton-boll separation device

The internal flow velocity of air-suction cotton-boll separation device was faster than the internal flow

velocity of air-blowing cotton-boll separation device. The flow obviously stratified and got together. Meanwhile, air-suction cotton-boll separation device had more negative pressure, thus achieving the cotton-boll separation and seed cotton transfer easier.

4 Experimental verification

4.1 Experiment of suspending velocity

The cotton fluid units always contain seed cottons, cotton stalks, cotton bolls, cotton leaves and other materials which were harvested by stripper cotton harvester. Suspending velocities of different materials can be respectively measured by using suspending velocity test-bed, and the experiment results were shown in Table 3.

Table 3 Suspending velocities of materials

Material	Suspending velocity, m/s
Single seed cotton	2.9-3.6
Seed cotton per boll	4.1-5.0
Lateral branch	6.2-6.7
Main stem	8.2-10.3
Bracteole	4.9-7.0
Closed boll	11.0-13.2
Ajar boll	6.2-7.8
"ginned cotton" control group	1.6-2.9

As the experimental results shown in Figure 7, the ascending sequences of different materials' suspending velocities are: closed boll>main stem>ajar boll>bracteole>lateral branch>seed cotton per boll> ginned cotton. Although it is found that suspending velocity of the same kinds of material is also affected by moisture content, their own sizes and other factors in the experiment. There are obvious difference suspend velocities between closed boll and light impurities, it means that they can be easily separated by airflow acting force under the same experimental condition.

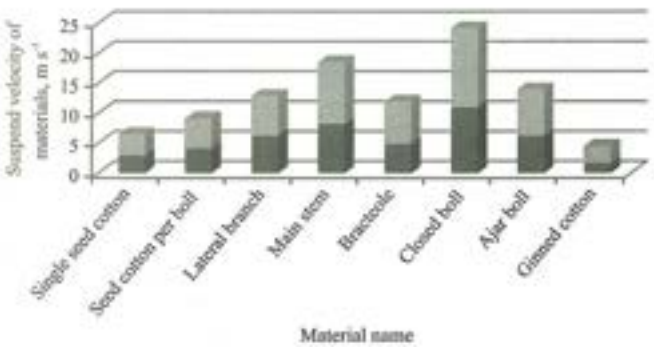

Figure 7 Interval distribution of suspending velocities

4.2 Experimenting of cotton-boll separation device

Two kinds of cotton-boll separation devices were respectively driven by high speed centrifugal fan which shaft power is 40 kW. The rated speed is 3800 r/min, the measured air volume is 13000 m^3/h and the wind pressure is 3.7 kPa. In the experiment, high speed airflow was produced by centrifugal fan and entered into cotton-boll separation device from the front of device. A, B, C, D, E, F and other experimental points had been set in the device.

Pressure measuring equipment was GM520 type barometer which was manufactured by Benetech Technologies Co Ltd. Its ranges are –35-35 kPa and accuracy is 0.001 kPa. Wind speed measuring equipment was AVM-07 type anemograph which was manufactured by TES Electrical Electronic Corp. Its ranges are 0-45 m/s and accuracy is 0.01 m/s. Wind speeds and wind pressures distribution had been measured and their change rules were researched. The experiment results were shown as Table 4 and Table 5.

Table 4 Wind speeds and wind pressures of air-blowing cotton-boll separating device

Item	Parameters of each measuring point					
	A	B	C	D	E	F
Wind pressure, kPa	–0.34	0.36	0.3	0.21	–0.03	–0.15
Wind speed, m/s	12	42	36	28	9	11

Table 5 Wind speeds and wind pressures of air-suction cotton-boll separating device

Item	Parameters of each measuring point					
	A	B	C	D	E	F
Wind pressure, kPa	–0.07	–0.09	–0.14	0.51	–0.09	–0.18
Wind speed, m/s	2.35	2.5	5.5	44	9	13

The error between simulation and experimental results of air-blowing cotton-boll separation device was about 4.7%. The error between simulation and experimental results of air-suction cotton-boll separation device was about 3.5%. It can be assumed that the simulation model was reasonable and requirement of practical inspection could be fulfilled. Through the comparison of wind speeds and wind pressures value between two kinds of cotton-boll separating devices, it can be found that, wind speeds of all experimental points which had been set in air-blowing cotton-boll separating

device were greater than the suspending velocities of the testing materials which cannot separate the cotton and boll easily. The wind speed at experimental point C, which was set in air-suction cotton-boll separating device, was between the suspending velocities of cotton and impurities that make it easy to separate the cotton and boll.

The quantitative mixture composed of picking cotton with machinery and cotton boll that was feeding in the front of device when ran the performance tests. The percentage of the mass of bolls in separated cotton to feed quantity in the front of device that cotton-boll separating rate. And the percentage of the mass of cotton drop out with bolls at experimental point E to the total amount of falling materials that is cotton loss rate. Prototype structure of air-suction cotton-boll separation device was shown in Figure 8.

1. Accelerating duct 2. Opening boll convey 3. Feeding duct

Figure 8 Prototype structure of air-suction cotton-boll separation device

The cotton-boll separating rate was 76% and loss rate of seed cotton was 5% by using air-blowing cotton-boll separation device. The results showed that: part of boll and seed cottons were lifted up with cotton picked roller, which was too late to disperse and then pushed to the following feeding duct directly. The flow direction, speed and pressure at the bottom of device were instantaneously affected by the undispersed fluid cluster. Some cottons discharging from boll exit with boll that caused the cotton loss.

Cotton-boll separating rate was 99% and loss rate of seed cotton was 0 by using air-suction cotton-boll separation device. The results showed that, the cotton fluid cluster can be dispersed and layered sufficiently and a stable zone of negative pressure was formed at separating zoon and boll exit.

5 Conclusion and discussion

Based on the simulation analysis of software ANSYS and combined experimental results of two kinds of cotton-boll separation devices, the conclusions can be drawn as follows:

(a) Average error between simulation and experimental results was less than 5%. It could be assumed that the simulation model is reasonable and requirement of practical inspection can be fulfilled.

(b) Flow velocity of air-blowing cotton-boll separation device from top to bottom taper off in the same section, flow spread quickly and difficult to aggregate along the direction of feeding duct. Pressure has sudden changes in some bending positions and easily arises the vortex, which would generate interference and have the impact on movement direction of seed cotton. Simulation and experimental results both verificated that the boll could not be easily separated from cotton cluster unit by using air-blowing cotton-boll separation device.

(c) A stable zone of negative pressure was formed at boll exit and separating zoon that facilitated to separate seed cotton from cotton fluid cluster, reduced seed cotton loss and improved the recycling efficiency of seed cotton.

(d) The combination property of air-suction cotton-boll separation device is obviously better than air-blowing cotton-boll separation device. Air-suction separation device improved more than 20% of cotton-boll separating rate and reduced 5% of cotton loss rate than air-blowing separation device

[References]

[1] Barker, G. L., R. V. Baker, and J. W. Laird. 1991. *GINQUAL: a cotton processing quality model. Agricultural Systems*, 35(1): 1–20.

[2] Baker, R. V., and A. D. Brashears. 1999. Effects of multiple lint cleaning on the value and quality of stripper harvested cotton. *World Journal of Surgery*, 26(3): 335–341.

[3] Baker, R. V., and A. D. Brashears. 2000. Combined effects of field cleaning and lint cleaning on stripper harvested cotton. In *Proceedings Beltwide Cotton Conferences, San Antonio, USA*, 2000: 1616–1621.

[4] Brashears, A. D., and K. D. Hake. 1995. Comparing picking and stripping on the Texas highplains. In *Proc. Beltwide Cotton Conf., San Antonio, TX*.1995: 652–654.

[5] Carlos, B. A., and D. B. Kevin. 2009. Harvesting and seed cotton cleaning of a cotton cultivar with a fragile seed coat. *Engineering and Ginning*, 13(2): 158–165.

[6] Ding, Z. F., W. X. Wang, S. N. Jia, and Y. G. Wang. 2012. Separation system design of all-harvest cotton picker. *Machinery Design and Manufacture*, 3(3): 25–26.

[7] Gillum, M. N., C. B. Armijo, and D. D. Mc Alister. 2001. Optimization the speed of the cleaning cylinder on the Batt-Less lint cleaner. *Journal of Electronic Packaging*, 44(3): 487–492.

[8] Huang, M. S., S. Lei, Y. T. Zhang, C. L. Chen,Y. F. Sun, Q. Xie, and T. F. Kong. 2016. *Optimization experiments of machine-mounted seed cotton pre-treatment apparatus for cotton stripper harvester*. *Transactions of the Chinese Society of Agricultural Engineering*. 32(21): 21–29. (In Chinese with English abstract)

[9] Krifa, M., and G. Holt. 2013. Impacts of gin and mill cleaning on medium-long staple stripper-harvested cotton. *Transactions of the ASABE*, 56(1): 203–215.

[10] Lu, W. D. 2013. The problem met in extending machine pickup cotton technology and its countermeasures. *China Fiber Inspection*, 2013(9): 31–31. (In Chinese with English abstract)

[11] Price, J. B., and R. V. Baker. 1996. Cleaning experiences with stripper-harvested cottons. In *Beltwide Cotton Conferences*.

[12] Tian, J , X. Zhang, W. Zhang, H. Dong, X Jiu., and Y Yu. 2017. Leaf adhesiveness affects damage to fiber strength during seed cotton cleaning of machine-harvested cotton. *Industrial Crops and Products*, 2017(107): 211–216.

[13] Whitelock, D. P., C. B. Armijo, G. R. Gamble, and S. E. Hughs. 2007. *Survey of seed-cotton and lint cleaning equipment in U.S. roller gins*. *Journal of Cotton Science*, 29(11): 128–140.

[14] Ye, W., and H. X. Zhang. 2011. Simulation research on cotton harvester about positive wind power conveying system based on Floworks. *Journal of Jiamusi University (Natural Science Edition)*. (29)3: 252–255.

Vibration study of the gearbox of hydro-mechanical continuously variable transmission based on Mean Filter Method

Xiao Maohua*, Zou Fan, Zhang Haijun, Xiao Dengsong, Lu Zhixiong, Zhang Cunyi

(College of Engineering, Nanjing Agricultural University, Nanjing 210031, China)

Abstract: Hydro-mechanical continuously variable transmission (HMCVT) is an important drive assembly part of high-horsepower tractors. Its loading ability changes violently under various conditions. Additionally, starting shifting or barking of hydraulics will cause more violent vibration, which may greatly influence the lifetime of the gearbox. Therefore, effective test and analysis of the vibration of different parts will play an important role in ensuring the system's reliable operation. A Mean Filtering Method was used in this paper to calculate and analyze the vibration of the gearbox's important parts. The vibration signal data was filtered by Mean Filtering Method, and was changed from Time Domain Waveform into Frequency Domain Waveform by Fourier Transform Method. The filtering effect can be shown clearly by comparing the two different frequency range charts with or without filtering. Root-mean-square vibration speed in each point was sought by Matlab. Vibration intensity level in each part then was judged according to rotating machinery vibration standard (SHS 01003-2004). Combined with the construction and transmission route of the HMCVT, a prioritization scheme that changed two output semi-axes into one output axis using layer-stepping type and casting type gearbox body was proposed, and the control system on the body surface was installed.

Keywords: vibration, HMCVT, high-horsepower tractors, Mean Filter Method

Citation: Xiao, M. H., F. Zou, H. J. Zhang, D. S. Xiao, Z. X. Lu, and C. Y. Zhang. 2017. Vibration study of the gearbox of hydro-mechanical continuously variable transmission based on Mean Filter Method. International Agricultural Engineering Journal, 26(3): 82–87.

1 Introduction

Hydro-mechanical continuously variable transmission (HMCVT) is an important drive assembly part of high-horsepower tractors, and its loading changes due to different working conditions (Ji et al., 2009). The drive system vibrates violently, which influences greatly on transmission's service life, with pure hydraulic starting, shifting and braking. Although in the ideal working condition, forced vibration due to the engine's periodic speed fluctuations maybe coused, since the transmission is delivering power with its engine. Therefore, by testing, analyzing and improving every single part's vibration, it plays a great role in ensuring the transmission body's reliability service.

The study on HMCVT was relatively late in China, and up to now, there is no commercialized HMCVT products in the market. Liu (1998), a professor in Beijing Institute of Technology, is a predecessor of researching on HMCVT in China. The analysis on hydrodynamic mechanical transmission system in Liu's book built a systematical research of HMCVT (Liu et al., 1998). Hu et al. (2008) had come up with a two-stage scheme which had been applied to high-speed tracked vehicle. And also, a three-stage scheme was invented by Zhang et al. (2007); Ji et al. (2009), Zhang et al. (2011) and Tian et al. (2011), who are from Jilin University, mainly focused on HMCVT's application in engineering vehicles. Ni (2013); Wang et al. (2014); Shi et al. (2011) in Nanjing Agricultural University had come up with a four-stage transmission scheme, which helped to do the theoretical analysis and experimental research on transmission's shifting and efficiency characteristics. They even created

Received date: 2017-03-21 **Accepted date:** 2017-07-16

* **Corresponding author: Xiao Maohua**, Ph.D., Associate Professor of College of Engineering, Nanjing Agricultural University, Nanjing, 210031, China. Email: xiaomaohua@njau.edu.cn, Tel: 025-58606623, Fax: 025-58606580.

the sample prototype (Lu et al., 2009; Tao et al., 2013). The paper, vibration and noise analysis of transmission (Dong et al., 2000), analyzed the reasons for some abnormal vibration and noises of a transmission. It tested and analyzed the sample prototype's vibration and noise signal under different conditions by arranging four experimental points in the transmission body. At the same time, by creating a model of transmission shell, it did a modal analysis on the front side of transmission shell and calculated each wheel gear's gear-mesh frequency, with which to estimate how the results influence the peaks in vibration and noise-based power spectrum. The final analysis result revealed that it would decrease vibration and reduce noise if we changed the original cast iron materials of transmission shell into pressure-casting aluminum. Furthermore, with the creation of three-dimensional transmission body, Li et al. (2009) had got an idea that if the outer casting vibrated slightly, the thickness of the outer casting could be redesigned. Besides, it got more amplitude in inside ribs and partitions, thus some parts of the body can be reinforced on.

Ashwani Kumar et al. (2014) studied a truck's free vibration of transmission shell, which was made of FG260. The author concluded that the inherent frequency variation of the gear box side connection bolt based on the constrained boundary condition was 2954-1002 Hz. Also Shawki et al. (2013) studied vehicle transmission using the method of analyzing vibration. They analyzed the vehicle transmission and calculated its radiate efficiency. Tuma et al. (2009) did a research on a truck's noise and vibration. He found that heavy vibration frequency was between 500-2500 Hz by analyzing and fourier transforming the experimental results. Kumar et al. (2015) also did research on the vibration of different materials. The simulation results showed that its fixed frequency was 1002-3784 Hz.

The listed researches have solved the problems about vibration of HMCVT by changing the materials or shape of its body without considering its manufacturing technique and the effects of drive system on body vibration. The vibration of some important parts of the gearbox with a method called Mean Filter Method was analyzed in this paper. Firstly, 20 important positions were chosen as the testing points on the body surface to see their vibration signals under different situations. Secondly, the signals were filtered and their time domain waveform were changed into frequency domain waveform through Fourier transform. Then, root-mean-square vibration speed in each point was calculated through filtering with Matlab 9.0. According to (SHS 01003-2004), the root-mean-square vibration speed which varies from frequency 10 to 100 Hz was used as a symbol to represent the measured parameters of mechanical vibration. When the experimental data were shown on table and bar chart, it can be seen clearly that vibrates on gearbox body was greatest, and then on its bearing parts. The vibration on cover and bracket were smallest. Combining with the construction and transmission rout of HMCVT, a prioritization scheme which changed two output semi-axises into one semi-axis was put forward. The gearbox body was designed as layer-stepping type and casting type, and also the control system was installed on the body surface.

2 Mean Filter Method

According to the Rotating Machinery Vibration Standard (SHS 01003-2004), the root-mean-square vibration speed which varies from frequency 10 to 1000 Hz can be used as a symbol to represent the measured parameters of mechanical vibration. The test data which were not in the measurement range should be filtered firstly. Then the collected data should be calculated to root-mean-square, which will be the final experimental data.

In order to reduce noise of the collected signal as much as possible, Mean Filter Method was used in this paper. The time domain waveform of the signal was transformed into frequency domain waveform by Fourier transform. Then, the filtering effect was compared with the filtered frequency domain map before filtering, thus showing the filtering effect. Root-mean-square speed of each point was analyzed by Matlab 9.0 listed below:

```
s=csvread('D:\111\k_a. csv');
data1=s(:, 2);
a=1;
```

```
b=[1/20, 1/20, 1/20, 1/20, 1/20, 1/20, 1/20, 1/20, 1/20,
1/20, 1/20, 1/20, . .
1/20, 1/20, 1/20, 1/20, 1/20, 1/20, 1/20, 1/20];
data2=filter(b, a, data1);
fs=1/0. 000061;
n=0:length(data2)-1;
t=n/fs;
N=length(data2);
result = sqrt(sum(data2. ^2)/length(data2))
y1=fft(data1);
figure;
subplot(2, 1, 1);
plot((0:N/2-1)*fs/N, abs(y1(1:1:N/2))*2/N);
xlabel('frequency/Hz');
ylabel('velocity amplitude/mm/s');
title('Wave before filtering');
%frequency domain after filtering
y2=fft(data2);
subplot(2, 1, 2);
plot((0:N/2-1)*fs/N, abs(y2(1:1:N/2))*2/N);
xlabel('frequency/Hz');
ylabel('velocity amplitude/mm/s');
title('filtered frequency domain waveform');
```

3 Experiment and analysis

3.1 Distribution of the vibration test points

Twenty different important parts of the HMCVT body were picked up as the test points which were mainly distributed near each bearing holes, body cover and side walls. They were distributed evenly on X, Y, and Z axis directions. Among all of these, the first one to the eighth points were distributed mainly on Z axis direction, the ninth to the sixteenth points were distributed mainly on X axis direction and the rest points were on Y axis direction. Figure 1 shows all the points distribution. They were all representative points for the body, the cover and the bracket.

3.2 Experiment and results analysis

3.2.1 Test method

The vibration equipment used in this test was VIBXPERT-II, which was produced by the Germany Pulu Fu company. The instrument has 102400 lines and its specific parameters are as follows:

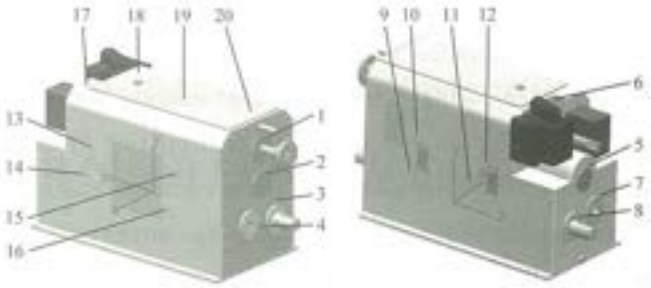

Figure 1 Distribution of the vibration test points

Frequency range: 0.8 Hz-40 KHz

Dynamic (measured / total): 96 dB/136 dB

Sampling frequency: <= 131 KHz / channel

Speed range: RPM 10-200 000 rpm / ±1‰ / ±1 rpm

Displacement: 6000 μm (p-p) / ±1%

Speed: 6000 mm/s (p-p) / ±1%

Acceleration: 6000 m/s^2 (p-p) / ±1%

Frequency FFT measurement range: Fmin: 0.5 Hz - 10 Hz, Fmax: 200 Hz-51.2 KHz

The engine named WP6T180E21 was equipped in the HMCVT prototype. Its rated power was 132.5 kW, and rotating range speed was between 750-2200 r/min. To ensure the integrity of the experimental data, a number of gears (corresponding to different speeds) were tested. There were three speeds selected for testing, which were named HM1 (750 r/min), HM2 (1300 r/min), and HM3 (2000 r/min). The vibration at twenty test points were tested at the three different input speeds. The tractor would work under a big load in both paddy fields and dry lands which were complicated working environment. Therefore, the magnetic powder brake was used and the preliminary loading of the driver output shaft was set to 300 N·m while testing in the section HM2.

The engine speed and the set point were set in the test firstly, then the frequency range of the vibration measurement was adjusted between 10 to 1000 Hz. The sample period T was 0.000061 s, and the frequency f=1/T=1/0.000061=16384 Hz=16.384 kHz. To ensure the accuracy of the test, many test points were selected. Vibrations at the same point, the same level and the same speed sampled were measured at least 3 times. So, 16384 data were acquisited in every data collection, and a total of 540 groups of data were acquisited in each test. The input speed of the engine in the testing experiment was set at the beginning of the test. Then the speed of every

set points can be measured and saved in form of .csv while the HMCVT experiment table worked smoothly. Finally, the saved data were transferred to PC and analyzed after all the experiments had been finished.

3.2.2 Data processing and analysis

By using the Mean Filter Method mentioned above, root-mean-square vibration speed after filtering of each point was calculated. Figure 2 showed the frequency domain contrast figure before and after filtering. It can be found that the data larger than 1000 Hz were filtered out after filtering in the figure below. So, the effective data was obtained.

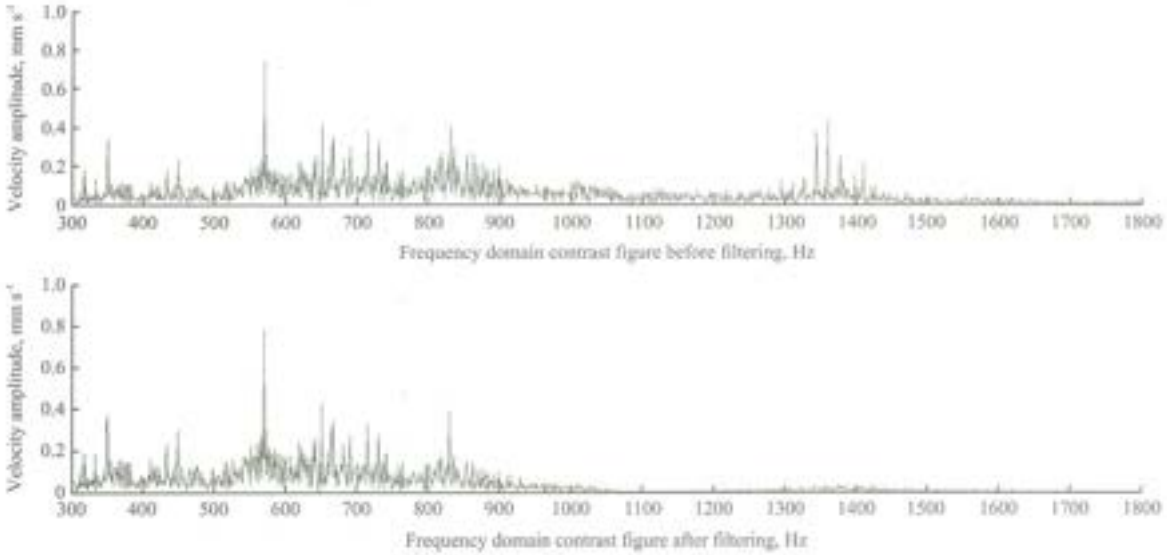

Figure 2 Frequency domain contrast figure before and after filtering

The relationship between time and vibration speed in each point under disparate input speed was measured in three different gears of HM1, HM2 and HM3. In order to judge the vibration intensity in each point, the input speed should be converted to root mean square speed RMS value. Then they were judged whether qualified according to the mechanical rotating vibration standard (SHS 01003-2004). A total of 20 points were selected in the vibration test and each point in the same rank and the same input speed was tested 3 times. The data capacity of each set was 16384 and twenty-seven sets of data were collected in the same point. The speed RMS value of each point can be obtained in various sections under disparate input speed by using Matlab function "result =sqrt(sum(data. ^2)/length(data))". Among them three speed RMS values were available in the same section under the same rotational speed. Then the arithmetic average of the three speed RMS values and the numerical value were obtained as speed RMS value of that point.

The vibration severity of each point under high band was analyzed because of a large amount of data. There were four pointsshould be analyzed in each X, Y, and Z axis direction. Point 13, 14, 15 and 16 were in X axis direction, in HM3. Their speed RMS values were listed in Table 1 and the comparison graph of root mean square value in the point 13, 14, 15, 16 was shown in Figure 3. With the same idea, point 17, 18, 19 and 20 were in Y axis direction, in HM3. Their speed RMS values were listed in Table 2 and the comparison graph of root mean square value was shown in Figure 4. Point 5, 6, 7 and 8 were in Z axis direction, in HM3. Their speed RMS values were listed in Table 3 and the comparison graph of root mean square value was shown in bar chart in Figure 5.

Table 1 Speed rms value of the test point 13, 14, 15, 16

Speed rms, mm/s / r/min	Position			
	13	14	15	16
750	2.9063	3.4828	3.9008	2.3412
1300	3.9585	3.1637	4.3687	3.1617
2000	4.1278	3.2859	4.4786	2.3768

Table 2 Speed rms value of the test point 17, 18, 19, 20

Speed rms, mm/s / r/min	Position			
	17	18	19	20
750	1.4712	1.6028	2.2856	2.4524
1300	1.413	1.5636	2.4976	2.3826
2000	1.2628	1.3315	2.4678	2.3317

Table 3 Speed rms value of the test point 5, 6, 7, 8

Speed rms, mm/s / r/min	Position			
	17	18	19	20
750	0.8154	2.833	0.6552	0.7775
1300	1.0425	3.3001	0.6831	0.8486
2000	0.9903	3.445	0.6614	0.9147

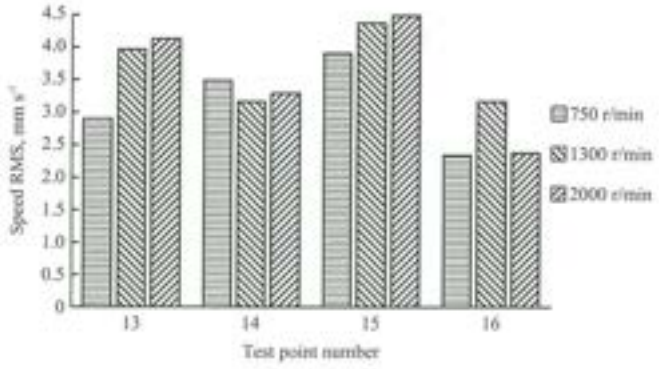

Figure 3 Comparison graph of root mean square value in the point 13, 14, 15, 16

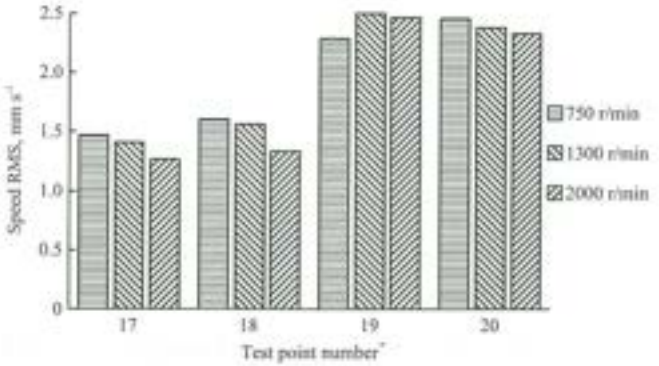

Figure 4 Comparison graph of root mean square value in the point 17, 18, 19, 20

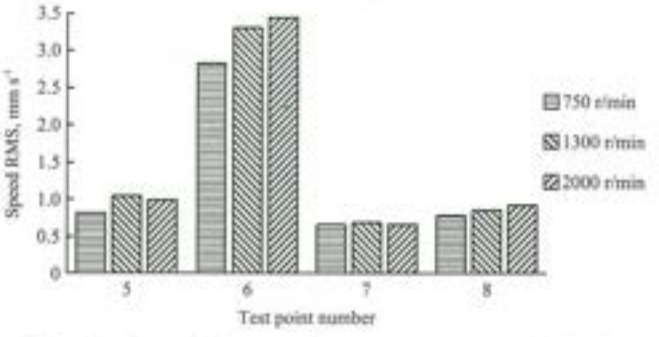

Figure 5 Comparison graph of root mean square value in the point 5, 6, 7, 8

By analyzing Figures 3, 4 and 5, most parts of the gearbox body vibrated in excellent or good situation, while just a few ones vibrated greatly and it should be improved. It also could be found that, the gearbox showed the most severe vibration, while the bearing parts showed medium vibration. Vibration in the cover and the bracket were very small. The vibration velocity at the input and output points of the test points near the shaft bearings were relatively large, while the values of the remaining sections were relatively small. The reason of the vibration speed trend could be concluded by comparing the test results, the construction and transmission route of HMCVT.

Firstly, the HMCVT applied in this research was dual planetary bus bar. The engine input power through input axle, then the power flow was divided into mechanical drive and hydraulic drive, which finally run together by the bus bar. At the same time, the dual planetary was connected by two semi-axises. It supported the whole bus bar and resisted the impact force which was produced in the process of distributaries and confluence with a sliding axle which was fixed on the gearbox body.

Secondly, the gearbox output axis was constituted by two semi-axises. It was output through the two semi-axises firstly, and then output through a long axis. In this way, it expanded the number of the gear pair. Moreover, the existing errors made a larger axial float which may be the reason of more vibration.

Thirdly, the input axle was connected to the engine with a coupling, and the output axle was also connected to magnetic powder brake with the coupling. The different loads offered by magnetic powder brake and the impact force will also cause vibration. So, much serious vibration appeared near the bearing holes.

Fourthly, the bracket of the gearbox was fixed to the rack with the bolt. The amount of the vibration resources was limited near the body cover. Therefore, the vibration speed in the cover and bracket were relatively small.

Finally, the errors produced by the wheel gears manufacturing, the technology assembly, the slight stability and so on may also cause vibration to a certain extent.

4 Conclusion

The vibration speed in the important parts of HMCVT was analyzed under the existing experiment platform. According to the analysis results on the vibration speed of the gear box under the different bands and engine speeds, it was found that vibration on gearbox body were the greatest, and then on its bearing parts. The vibration on

cover and bracket were the smallest. Also, the existing gearbox body was unitary, and its wheel gears and axles were too huge and complex to assemble. It was not easy for the transmission to be installed, disassembled and maintained.

Acknowledgments

The research is funded partially by the National Key Research and Development Program of China (2016YFD0701103), Jiangsu Provincial Natural Science Foundation of China (BK20140727), Jiangsu Province Science and Technology Support Program (BE2014134), Science and Technology Foundation of Outstanding Young Talents of Nanjing Agricultural University (YQ201605), the Fundamental Research Funds for the Central Universities fund (KYZ201760), and the six major talent summit in Jiangsu province (2015-zbzz-011).

[References]

[1] Dong, X. L. 2012. Analysis of gearbox vibration and noise. *Mechanical Management and Development*, 6(1): 53–54.

[2] Hu, J. B., C. Wei, J. Y. Du, and Y. Y. Zhang. 2008. Research on speed ratio tracking control system of hydraulic mechanical continuously variable transmission. *Journal of Beijing Institute of Technology*, 28(6): 481–485.

[3] Ji, X. B. 2009. Characteristic analysis and application simulation of hydraulic mechanical continuously variable transmission. M.S. thesis. *Jilin: Jilin University.*

[4] Kumar, A., H. Jaiswal, A. Pandey, and P. P. Patil. 2014. Free vibration analysis of truck transmission housing based on FEA. *Procedia Materials Science*, 6(1-2): 1588–1592.

[5] Kumar, A., A. Dwivedi, H. Jaiswal, and P. P. Patil. 2015. Material based vibration characteristic analysis of heavy vehicle transmission gearbox casing using Finite Element Analysis (FEA), *Advances in Intelligent Systems and Computing*, 308(3): 527–533.

[6] Li, J., C. L. Xiang, and H. Liu. 2009. Numerical simulation analysis of vibration characteristics of transmission box. *Chinese Journal of Construction Machinery*, 7(2): 142–145.

[7] Liu, X. J. 1998. Analysis of vehicle transmission system. *Beijing: National Defence Industry Press*

[8] Lu, T., Z. L. Zhou, and M. Z. Zhang. 2009. Hydraulic mechanical stepless transmission bench test manual control. *Journal of Henan University of Science and Technology*, 30(6): 35–37.

[9] Ni, X. D. 2013. Study on tractor hydraulic mechanical multi section stepless gearbox transmission characteristics of double bus. PhD. Thesis. *Nanjing: Nanjing Agricultural University.*

[10] Abouel-Seoud, S. S., S. M, Eid, A. A. Abdel-Hamid, and A, S. Abdallah. 2013. Analytical technique for predicting passenger car gearbox structure noise using vibration response analysis. *British Journal of Applied Science & Technology*, 3(4): 860–883.

[11] Shi, J. L. 2011. Study on the design of non-pole transmission and variable pump control performance of non-road vehicle. M.S. thesis. *Nanjing: Nanjing Agricultural University.*

[12] Tao, H. L. 2013. Research on simulation and change quality of hydraulic mechanical continuously variable transmission system. M.S. thesis. *Nanjing: Nanjing Agricultural University*

[13] Tian, C. Y. 2011. Research on the control strategy of the hydraulic mechanical continuously variable transmission.M.S. thesis. *Jilin: Jilin University.*

[14] Tuma, J. 2009. Gearbox noise and vibration prediction and control. *International Journal of Acoustics and Vibration*, 14(2): 99–108.

[15] Wang, G. M. 2014. Research on the characteristics, control and fault diagnosis of the tractor hydraulic machinery. PhD. Thesis. *Nanjing: Nanjing Agricultural University.*

[16] Wei, C., S. H. Yuan, J. B, Hu, and W. Q. Song. 2011. Theoretical and experimental research on the speed ratio control of differential hydraulic mechanical continuously variable transmission. *Journal of Mechanical Engineering*, 47(16): 101–105.

[17] Zhang, X. S. 2011. Research on the smooth change and control strategy of hydraulic mechanical continuously variable transmission. M.S. thesis. *Jilin: Jilin University.*

[18] Zhang, Y. C., S. H. Yuan, C. B. Jing, and J. B. Hu 2007. Research on energy storage technology of hydraulic mechanical stepless transmission system. *Machine Tools and Hydraulic*, 35(2): 146–150.

Influence of different tillage methods on growth characteristics and maize yield after straw returning

Zhu Cunxi, Huang Xin, Wang Weiwei, Qi Haijun, Chen Liqing*

(College of Engineering, Anhui Agricultural University, Anhui 230036, China)

Abstract: In order to study the influence of different tillage methods on production process and growth characteristics of Anhui summer maize of double cropping system after total returning of wheat straw, a comparative analysis was made to analyze and compare four tillage methods in this paper. Through comparative analysis on treatment of preceding wheat straw, maize seeding and harvesting, the indexes of pulverization rate, straw scattering in homogeneity, anti-blockage and crop characteristics were applied to show the production process and growth characteristics of summer maize. Study results showed that, under tillage method A (wheat combine harvester fixed with pulverize and no-till planting of maize), pulverization of preceding wheat straw had significant scattering effects with good performance in anti-blockage; maize grew well at early stage and its yield was improved during harvesting period. The plant height increased by 4.9%; stem diameter increased by 11.75% and yield increased by 7.63% on average.

Keywords: total returning of wheat straw, tillage methods, summer maize, growth characteristics

Citation: Zhu, C. X., X. Huang, W. W. Wang, H. J. Qi, and L. Q. Chen 2017. Influence of different tillage methods on growth characteristics and maize yield after total straw returning. 2017. International Agricultural Engineering Journal, 26(3): 88–94.

1 Introduction

Mechanized total returning of wheat straw can fully utilize straw and increase organic matters in soil, thus improve soil structure by loosening soil, increase porosity, reduce soil bulk density, and increase yield by improving the activity of microorganism and growth of root system. Besides, it can avoid environmental pollution caused by straw burning and benefit the development of ecological agriculture and environment-friendly agriculture. Therefore, the technology of straw returning as an important technology in environment-friendly agriculture is one of the new and key technologies promoted and implemented by Chinese government (Dalal et al., 1986; Zhao et al., 2003; Hu, 2000; Li et al., 2014; Li et al., 2015; Pan et al., 2013).

Compared with tedious traditional methods of crop harvesting including moving away straw, turning up soil and seeding of next season, straw returning can simplify farming stages and save time and cost. Straw returning can also increase the soil surface straw and reduce the evenness of soil surface. The changes in traditional farming will bring about changes in soil condition, seeding method, growth status and yield. Wang pointed out that straw returning effectively increased water-soluble organic carbon (WSOC) in soil by 23%-68% and soil microbial biomass carbon (MBC) by 21%-40% (Wang et al., 2013); the study of Zhao showed that deep ploughing + straw returning can increase soil respiration rate of winter wheat and summer maize by 41.9% and 21%, and can increase dry matter accumulation and improve the growth of root system (Zhao et al., 2014); the study of Yang pointed out that straw returning significantly increased the enzymatic activity of unease and sucrose (Yang et al., 2013). The experts above studied the advantages of straw returning and its influence on growth characteristics of next season crops; however, there are no in-depth discussions on the systematic influence of different mechanized tillage methods on growth

Received date: 2017-06-25 **Accepted date:** 2017-08-29

* **Corresponding author: Chen Liqing,** College of Engineering, Anhui Agricultural University, Anhui 230036, China. Email: clq79111@126.com.

characteristics and yield.

In this paper, through analysis of different tillage methods and crop yield under total returning of wheat straw in Anhui, an easy, applicable and cost-saving tillage method for total returning of wheat straw was found out, with the aim to provide reference to the mechanized planting model in the wheat-maize rotation system.

2 Materials and method

2.1 Information of test fields

The test was carried out in a 50 mu test field of Anhui Agricultural University in Xiaoxinji Village, Mengcheng county, Anhui province in 2015 and 2016. Mengcheng county is located in the south of the Huanghuaihai Plain, in warm temperate zone and has a semi-humid monsoon climate. It is a region mainly affected by tropic oceanic air mass and polar continental air mass, with temperate and humid climate and four distinctive seasons. The annual average temperature here is 14.7°C, the average temperature in January the coldest month is –0.1°C; the average temperature in July the hottest month is 27.5°C. The area is affected by distinctive alternations of monsoon, with frequent south wind in the summer and north wind in the winter. The mean annual precipitation there is 822 mm; rainfall frequently occurs from June to August; frost-free season lasts for 216 days, annual sunshine hours are 1400-2200 h. The climate is very suitable for growing wheat and corn. The soil in the experiment was Shajiang Black Soil. The soil status after total returning of straw of double crops for two consecutive years is shown in Table 1.

Table 1 Physicochemical properties of soil under different treatment methods

No.	Treatment method	Soil depth, cm	PH	Organic matters, g/kg	Available K, mg/kg	Available P, mg/kg	Total N, g/kg
The first year	Total returning of straw	0-10	6.5	22.69	166	30.22	1.34
		10-20	6.0	19.51	138	16.42	1.45
The second year	Total returning of straw	0-10	7.2	23.71	218	32.44	1.64
		10-20	5.9	20.32	194	18.59	1.23

2.2 Test conditions

The variety "Wanmai 52" were planted on October 1, 2014 and October 10, 2015 (10 kg per mu), and "Jinqiu 963" were planted on June 14, 2015 and June 16, 2016 respectively (5000 seedlings per mu). The maize straw of the two years was pulverized and returned to field by a tractor suspended with a pulverizer. In order to ensure the reliability of the comparative test, the same method was used in middle stage of field management of wheat and maize.

2.3 Test design

Four plots A, B, C, D with equal areas (Figure 2) were selected from the test field (10 mu=6666.7m^2) for four tillage methods in terms of machine in wheat harvesting, treatment method of wheat straw, use of maize seeder, and method of maize harvesting, as is shown in Figure 1.

Figure 1 Test design of different tillage methods

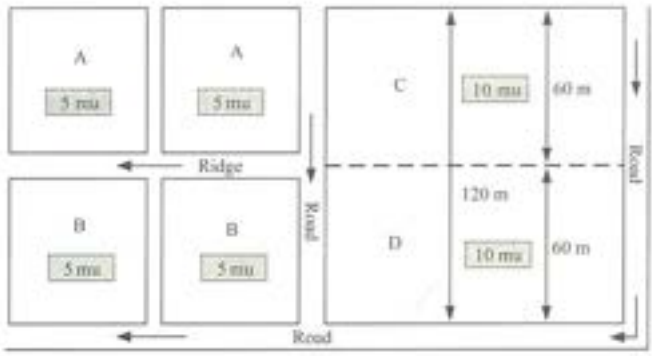

Figure 2 Division of test fields

2.4 Evaluation indexes

In order to scientifically and precisely analyze the differences in working efficiency, growth status of maize, maize yield and tillage economy under different tillage methods, based on the testing indexes of working quality for agricultural machinery formulated by China Agricultural Machinery Testing Center,and according to GB/T 24675.6-2009, *Conservation tillage machinery - smashed straw machine,* -the requirements (GB/T 24675.6-2009, 2009),the indexes of straw pulverization rate, straw scattering in homogeneity, anti-blockage, growth properties of crops and maize yield were selected to comprehensively evaluate different tillage methods in total returning of straw.

2.4.1 Wheat straw pulverization rate and straw scattering in homogeneity

In the four plots of A, B, C, D, a 1m×1m metal frame was used to choose five sampling points, and 20 samples were obtained in all. All straw on ground surface in the range of metal frame of each sampling point was weighed, M (kg); then straw longer than 10 cm after pulverization was chosen and the weight of the straw m (kg), was obtained, and

(1) Straw pulverization rate is: $\eta = (1-\frac{m}{M})\times 100\%$;

where, η is pulverization rate; m is mass of straw longer than 10 cm, kg; M is total straw mass in sampling area, kg.

(2) Straw scattering in homogeneity is

$$F_b = \frac{1}{\overline{M}}\sqrt{\frac{\sum_{i=1}^{5}(M_{zi}-\overline{M})^2}{5}}\times 100\%;$$

where, $\overline{M}$ is the average straw mass in each sampling point of test area, kg; M_{zi} is the total straw mass of sampling point i, kg; F_b is straw scattering in homogeneity, %.

2.4.2 Anti-blockage of seeder

According to property detection and literature of non-tillage seeders by China Agricultural Machinery Testing Center (Sidhu et al., 2007; Luo et al., 2006; Wang et al., 2002), the degrees of blockage within 60 cm of working distance were categorized. The status of straw congestion that hinders machine operation is serious blockage; the status of straw congestion that doesn't need to stop machine is common blockage; the status of straw congestion that can allow automatic flowing between furrow openers is slight blockage; without the status of straw congestion and smooth operation is no blockage.

2.4.3 Determination of plant characters

An analysis was made on plant height and stem diameter of maize seedlings (three-leaf stage) and (ten-leaf stage) under different tillage methods. The 100 maize seedlings were selected randomly in the four plots A, B, C and D to test their plant height and stem diameter. The maximum distance from soil surface to the top leaf in natural hanging status of the maize seedlings is plant height H, cm. The average diameter of maize stem measured on the ground surface by vernier caliper is stem diameter B, mm.

2.4.4 Yield measuring

Two days before maize harvesting, five continuous rows of 3 m long maize seedlings were randomly selected from plots A, B, C and D for ear plucking, threshing and weighing. Some kernels were selected in the samples and put in a drying box at 105°C for drying until the mass became stable. Then the maize yield was calculated based on 14% moisture content.

3 Test results

3.1 Wheat straw pulverization rate and scattering in homogeneity

Then pulverization and scattering status of wheat straw were measured on the plots under the four tillage methods, and the test data are shown in Table 2.

3.2 Anti-blockage test

The seeder walked at a constant speed at first high-speed gear. The stubble height was 20 cm; straw

coverage rate was higher than 50% and even reached 90% in some area; the straw qualification rate after pulverization was above 85%; straw mulching quantity was 1.05 kg/m^2. The seeder walked on the field with straw moisture content <15% back and forth for three times. The data of seeder are shown in Table 3.

3.3 Characters of maize plants

The influences of different tillage methods on plant height and stem diameter of maize seedlings (three-leaf stage) and (ten-leaf stage) are shown in Table 4.

3.4 Maize yield measurement

From September 28, 2015 to October 1, 2016, the maize in the test field were harvested and the number of maize seedlings and maize yield were measured, maize yields under different tillage methods were obtained, as is shown in Table 5.

Table 2 Test data of unqualified pulverization

Tillage methods	Mass	Test data in 2015			Test data in 2016		
		Mean value, kg	Pulverization rate, %	Straw scattering inhomogeneity, %	Mean value, kg	Pulverization rate, %	Straw scattering inhomogeneity, %
Method A	M (kg)	0.400±0.03	0.884	0.122	0.424±0.05	0.901	0.120
	m (kg)	0.046±0.02			0.042±0.01		
Method B	M (kg)	0.384±0.06	0.881	0.110	0.414±0.08	0.884	0.105
	m (kg)	0.044±0.03			0.048±0.02		
Method C	M (kg)	0.357±0.03	0.847	0.094	0.248±0.03	0.885	0.086
	m (kg)	0.055±0.07			0.029±0.02		
Method D	M (kg)	0.430±0.08	0.876	0.115	0.237±0.09	0.824	0.105
	m (kg)	0.050±0.02			0.042±0.01		

Table 3 Records of anti-blockage of seeder

Tillage methods (maize seeding)	Test data in 2015			Test data in 2016		
	1st test	2nd test	3rd test	1st test	2nd test	3rd test
A	No blockage	No blockage	No blockage	A slight blockage	No blockage	No blockage
B	Two slight blockages	A slight blockage	No blockage	A slight blockage	A slight blockage	A serious blockage
C	A slight blockage	No blockage	A slight blockage	No blockage	Three slight blockages	A slight blockage
D	A serious blockage	No blockage	Two slight blockages	A slight blockage	A slight blockage	Two slight blockages

Table 4 Plant height and stem diameter of maize seedlings under different tillage methodsin 2015 and 2016

Tillage methods	(Three-leaf stage, 2015)		(Ten-leaf stage, 2015)		(Three-leaf stage, 2016)		(Three-leafstage, 2016)	
	Plant height/cm	Stem diameter/cm	Plant height/cm	Stem diameter/cm	Plant height/cm	Stem diameter/cm	Plant height/cm	Stem diameter/cm
A	23.08±0.12	0.63±0.05	64.58±0.10	2.72±0.06	24.38±0.22	0.79±0.01	64.50±0.14	2.88±0.03
B	22.75±0.18	0,60±0.03	61.64±0.15	2.15±0.07	22.95±0.17	0.64±0.02	62.84±0.25	2.35±0.06
C	22.65±0.11	0.68±0.01	63.08±0.09	2.36±0.04	23.20±0.15	0.69±0.01	63.42±0.16	2.42±0.04
D	21.36±0.09	0.59±0.05	60.26±0.15	2.12±0.03	21.64±0.17	0.60±0.03	59.76±0.25	2.16±0.05

Table 5 Maize yield under different tillage methods

Tillage methods	Maize yield measured in 2015			Maize yield measured in 2016		
	Number of maize seedlings in one test area on average	Maize yield in one test area on average, kg	Yield per mu on average, kg (2015)	Number of maize seedlings in one test area on average	Maize yield in one test area on average, kg	Yield per mu on average, kg (2016)
A	54.4±0.30	8.55±0.16	791.67	57.4±0.36	8.66±0.25	801.54
B	57.0±0.44	7.72±0.21	715.00	57.2±0.43	7.64±0.21	707.66
C	56.2±0.57	8.30±0.32	768.89	56.8±0.65	8.39±0.34	776.42
D	54.8±0.43	8.21±0.15	760.19	54.4±0.36	8.19±0.20	758.50

4 Analysis and discussion

Based on test data of the two years, a comparative analysis was made on mechanized working status, maize characters and maize yield under different tillage methods.

4.1 Analysis on pulverization of preceding wheat straw stalks

Wheat straw pulverization rate and straw scattering inhomogeneity under different tillage methods are shown

in Figures 3 and 4.

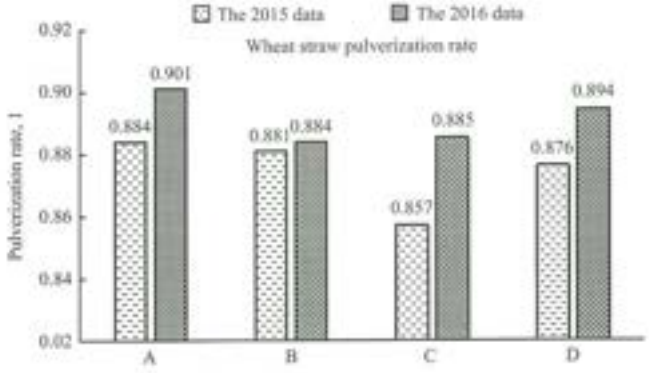

Figure 3 Status of preceding wheat straw pulverization under different tillage methods

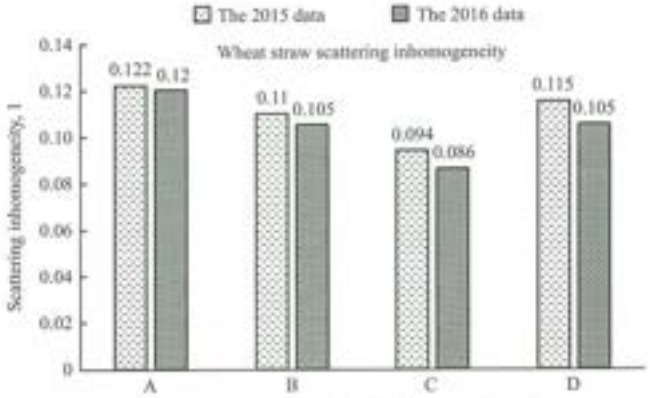

Figure 4 Scattering status of pulverized preceding wheat straw under different tillage methods

The two-year experiment data showed that, under tillage methods A and D, the wheat straw pulverization rate and straw scattering inhomogeneity were better than that under tillage methods B and C, and pulverization rate of wheat straw was increased by 12.3%, straw scattering homogeneity increased by 19.65%.showing that, combine harvester fixed with pulverizer could achieve obvious wheat straw pulverization effects, meanwhile, it can reduce utilization of the machine and thus alleviate machine compaction on soil.

4.2 Anti-blockage analysis

During seeding, the smooth functioning of the seeder can affect the working efficiency as well as seeding quality. Therefore, the two years of test data showed that, compared with tillage method C and method D, the working performance of the maize seeder was improved under method A and method B respectively. The result further verified the conclusion that the pulverization effects of preceding wheat straw were better under tillage methods A and D. Second, compared with method D and method B, the seeder had better performance in anti-blockage under methods A and C, showing good seeding effects for the non-tillage seeder under the same treatment conditions of the preceding wheat straw.

4.3 Analysis on plant height and stem diameter of maize

Test data analysis showed that, the seedlings grew well before the ten-leaf stage under method A, and plant height increased by 3.13% compared with method B, 2.14% compared with method C, and 8.91% compared with method D on average; the stem diameter increased by 10.37% compared with method B, 4.76% compared with method C and 15.22% compared with method D on average, as is shown in Figures 5 and 6. The possible reason might be the high pulverization rate and good straw scattering homogeneity of wheat straw under method A, besides, soil moisture were well preserved and no blockage occurred in seeding. The smooth seeding process resulted in good growth of maize seedlings.

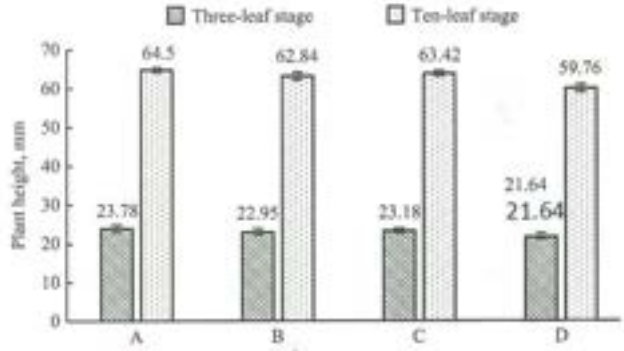

Figure 5 Statistics of maize plant height under different tillage methods

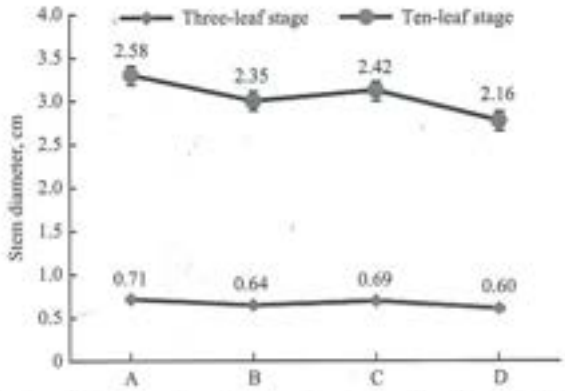

Figure 6 Statistics of maize stem diameter under different tillage methods

4.4 Maize yield analysis

The maize yield under tillage method A increased by 11.99% compared with tillage method B, and increased

by 3.10% and 4.91% compared with tillage methods C and D respectively. Under the same field management method, different tillage methods may have different impacts on maize yield. High maize yield can be achieved under tillage method A, one reason is the good growth status of maize seedlings at early stage, and the other reason might be the straw treatment method and seeding method. High straw treatment quality can achieve good decomposition effects and increase nutritional elements in the soil. No blockage occurrence during seeding also ensured the basic number of seedlings per mu and achieved high yield.

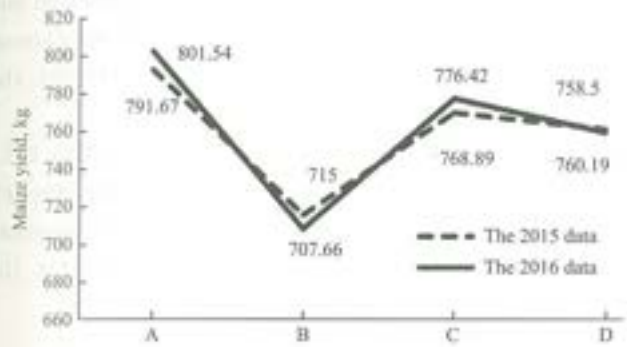

Figure 7 Statistics of maize yield under different tillage methods

5 Conclusions

1) Tests showed that, under tillage methods A and D, combine harvester fixed with pulverizer had better straw returning effects than combine harvester without pulverizer and tractor suspended with stubble cleaner under tillage methods B and C, and pulverization rate of wheat straw was increased by 12.3%, straw scattering homogeneity increased by 19.65%.

2) Tests showed that after total returning of preceding wheat straw, the seedlings grew well before the ten-leaf stage under method A, and plant height increased by 3.13% compared with method B, 2.14% compared with method C, and 8.91% compared with method Don average; the stem diameter increased by 10.37% compared with method B, 4.76% compared with method C and 15.22% compared with method Donaverage. It was consistent with the conclusions of Zhu et al. (2013) that, under the condition of total returning of preceding wheat straw, the growth of maize seedlings was obviously better than that of maize seedlings without wheat straw returning and returning to field for the second time.

3) Tests also showed that after total returning of preceding wheat straw, the maize yield under tillage method A increased by 11.99% compared with tillage method B; increased by 3.10% compared with tillage method C and increased by 4.91% compared with tillage method D.

4) Taking into consideration the indexes such as treatment effects of preceding wheat straw, anti-blockage in seeding, plant characteristics at seedling stage and maize yield, the test data of two consecutive years showed that, in the wheat and maize planting area in Anhui province, the tillage method A (harvesting wheat by applying combine harvester fixed with pulverizer + maize non-tillage seeder + combine harvesting of maize) had better performances after total returning of preceding wheat straw.

Acknowledgements

This research was supported by Special Fund of Ministry of Agriculture of China for Public Welfare Projects (No:201503136) and Natural Science Foundation of Anhui Province (No: 1604a0702035) and Graduate innovation fund of Anhui Agricultural University (No:2017yjs-42)

[References]

[1] Dalal, R. C., and R. J. Mayer. 1986. Long-term trends in fertility of soils under continuous cultivation and cereal cropping in southern Queensland. IV. Loss of organic carbon from different density functions. *Australian Journal of Soil Research*, 24(2): 281–292.

[2] GB/T 24675.6-2009 2009. Conservation tillage machinery - Smashed straw machine.

[3] Hu, D. 2000. The utilizing status and prospects of the crop straw resources in China. *Resource Development & Market*, 16(1): 19–20. (In Chinese with English abstract)

[4] Li, W., Y. Q. Qiao, H. Chen, C. F. Cao, S. Z. Du, and Z. Zhu. 2014. Effects of combined straw and N application on the physicochemical properties of lime concretion black soil and crop yields. *Acta Ecologica Sinica*, 34(17): 5052–5061.

[5] Li, X. S., N. Wu, L. Liu, Y. P. Peng, X. Xu, H. F. Han, T. Y. Ning, and Z. J. Li. 2015. Effects of different straw recycling and tillage methods on soil respiration and microbialactivity. *Chinese Journal of Applied Ecology*, 26(6): 1765–1771. (In Chinese with English abstract)

[6] Liu, T. 2004. A Study of measurement on-board ship of fuel

consumption for emission control. Dalian Maritime University.

[7] Luo, H. Q., H. W. Gao, A. D. Liu, W. G. Yang, and Q. J. Wang. 2006. Study on ridge-till and no-till corn planter. *Transactions of the Chinese Society for Agricultural Machinery*, 2006(04): 45–47. (In Chinese with English abstract)

[8] Pan, J. L., W. A. Dai, Z. H. Shang, and R. Y. Guo. 2013. Review of research progress on the influence and mechanism of field straw residue incorporation on soil organic matter and nitrogen availability. *Chinese Journal of Eco-Agriculture*, 21(5): 526–535. (In Chinese with English abstract)

[9] Sidhu, H. S., M.S ingh, E. Humphreys, B. Singh, S. S. Dhillon, J. Blackwell, V. Bector, M. Singh, and S, Singh. 2007. The happy seeder enables direct drilling of wheat into rice stubble. *Australian Journal of Experimental Agriculture*, 47(7): 844–854.

[10] Wang, D. D., L. Zhou, S. Q. Huang, C. F. Li, and C. G. Cao. 2013. Short-term effects of tillage practices and wheat-straw returned to the field on topsoil labile organic carbon fractions and yields in Central China. *Journal of Agro-Environment Science*, 17(1): 127–131.

[11] Wang, Q. J., J. He, and H. W. Li. 2012. Design and experiment on furrowing and anti-blocking unit for no-till planter. *Transactions of the Chinese Society of Agricultural Engineering*, 28(01): 27–31. (In Chinese with English abstract)

[12] Yang, M. F., L. Q. Zhu, X. Z. Han, K. J. Gu, N. J. Hu, Z. W. Zhang, and X. M. Bian. 2013. Effects of tillage and crop residues incorporation on soil nutrient, microbial biomass and enzyme activity under rice-wheat rotation. *Journal of Soil and Water Conservation*, 27(2): 272–275.

[13] Zhao, J. S., X. D. Zhang, X. Yuan, and J. Wang. 2003. Characteristics and environmental significance of soil dissolved organic matter. *Chinese Journal of Applied Ecology*, 14(1): 126–130.

[14] Zhao, Y. L., Z. W. Xue, H. B. Guo, X. Y. Mu, and C. H. Li. 2014. Effects of tillage and crop residue management on soil respiration and its mechanism. *Transactions of the Chinese Society of Agricultural Engineering*, 30(19): 155–165. (In Chinese with English abstract)

[15] Zhu, L. J., B. Q. Li, L. L. Shi, T. T. Zhou, W. N. Xiao, Z. L. Chen, and X. Ge. 2013. Preliminary study on the effect of wheat straw returning on growth and yield of complant. *Chinese Agricultural Science Bulletin*, 29(9): 123–128. (In Chinese with English abstract)

Experiment and simulation analysis on high-speed up-film transplanting mechanism

Jin Xin[1], Pang Jing[1], Ji Jiangtao[1*], Du Xinwu[1], He Zhitao[1], Wang Shiguang[2]

(1. *College of Agricultural Equipment Engineering, Henan University of Science and Technology, Luoyang 471003, China;*
2. *Chinese Academy of Agricultural Mechanization Sciences, Beijing 100083, China*)

Abstract: Planting mechanism is a key component on transplanter to plant pot seedlings into soil. It is aimed at planting seedlings stably at high speed, and rising up quickly without taking out any seedlings. In order to adapt to transplanting with mulch film, the film should be perforated and the planting mechanism should ascend quickly to avoid film tearing. In this paper, an analysis on the ideal movement trajectory of pot seedlings and planting mechanism during the high-speed planting process was made, and a seven-rod planting mechanism was proposed, and also a 3D simulation model of the mechanism is established. Transmission ratio, length of the two cranks, phase difference of the cranks, angle of planting mouth were adopted as the test factors; trajectory characteristics were selected as assessment indexes in this study, and an orthogonal simulation test of factor effects was done and the influence rule of key parameter changes of planting mechanism on planting trajectory was found out, the following optimized parameter combination was obtained: L_1=30 mm, L_2=184 mm, L_3=34 mm, L_4=110 mm, L_5=13 mm, L_6=146 mm, L_7=71 mm, L_8=64 mm, L_9=240 mm, L_{10}=255 mm; φ_1=70°, φ_3=229°, β=86°, γ=93°, ω=π rad/s, v_x=500 mm/s. When the planting frequency was 70/min, the penetration depth of the planter was 50 mm; and the lengths of approximate straight-line segments of the planting trajectory in earth and elevating trajectory were 76 mm; and the hole size was a bit bigger than that of the penetration unit. Field experiment results show that: when advancing velocity was 0.57 m/s, transplanting efficiency was 66/min, perpendicularity of the seedlings was 93.6%, seedling leakage rate was 6.8%; qualification rate of row spacing was 100%, showing that the condition could meet the requirement of high-speed up-film transplanting.

Keywords: up-film transplanting, planting mechanism, simulation analysis, orthogonal test

Citation: Jin X., J. Pang, J. T. Ji, X. W. Du, Z. T. He, and S. G. Wang. 2017. Experiment and simulation analysis on high-speed up-film transplanting mechanism. International Agricultural Engineering Journal, 26(3): 95–102.

1 Introduction

During the transplanting process, the unit that plant single pot seedling into the soil is called planting mechanism, and the ground-breaking planting method widely utilized at present applies the method of ditching (He, 2014; Hu, 2011). Plastic film mulching has significant advantages in heat preservation, moisture preservation, nutrition maintenance, lighting effect increasing and prevention of disease, insect and weed, besides, it can achieve precocity and yield increase. With the application of plastic film mulching technology, there are new demands on the penetration method of transplanter's planting mechanism (Wang et al., 2015; Feng et al., 2002). At present, the planting mechanisms suitable for up-film transplanting are planetary rotary arm type, parallelogram type, multi-link type, turbine type, dibble type and duckbilled type (Zhang et al., 2011; Zhou et al., 2003). These devices may tear film or take away seedlings at high working speed because of restrictions in planting trajectory; therefore, the planting efficiency and quality may be reduced. For this reason, the planting mechanisms stated above are not applied in large-scale promotion.

The moving trajectory of parallelogram planting mechanism with duckbilled planting device may have curtate cycloid, cycloid and trochoid influenced by characteristic parameter λ. A study showed that, λ>1 is the

Received date: 2017-07-08 **Accepted date:** 2017-09-07

* **Corresponding author: Ji Jiangtao,** Professor, College of Agricultural Equipment Engineering, Henan University of Science and Technology, Luoyang 471003, China. Email: jjt0907@163.com.

necessary condition for normal working of the planting mechanism; when $\lambda>1$, the moving trajectory of the duckbilled planting device may form the shape of a retaining ring (Chen et al., 2013), thus can meet the necessary conditions of the parallelogram planting mechanism, but in the same time increase the stir of soil and enlarge the size of the hole made by the duckbilled device.

The main working units of turbine type planting mechanism are turbine and spades, which are evenly distributed on the outershell of the turbine. It works by rolling the tractor-driven turbine through friction with the soil; in the meantime, the spades on the tip circle penetrate into the film and perforate on the soil (Jin et al., 2016). The moving trajectory of the spades is trochoid, and the trajectory doesn't have approximate straight-line segments with that of the penetration and moving up process required by up-film transplanting.

The planetary rotary-arm type planting mechanism is mainly composed of planet wheel, planet carrier and planting device (Liu et al., 2017). Compared with connecting rod mechanism, it can plant seedlings with stability at high speed, but the trajectory of planting device doesn't have any perpendicular stage during the penetration and moving up process, so the hole may be enlarged and seedlings may be easily taken out.

The multi-link planting mechanism uses the combination of cranks and connecting rods to realize the trajectory of planting device. It has the advantages of simple structure and diversified trajectories (Chen et al., 2011; Jin et al., 2012). By learning from the research results on theory of mechanism, a seven-rod planting mechanism based on the ideal moving trajectory of up-film high speed transplanting and planting device was designed in this paper, and the modeling, simulation and test analysis on the mechanism was done, the influence rule of key parameters on trajectory was found out, and finally the optimal parameter combination was obtained. The penetration and moving up trajectories of the planting point were almost perpendicular and the there were a long part of trajectory overlapping straight-line segment.

2 Analysis on the process of up-film planting

2.1 Analysis on the moving trajectory of pot seedlings

The movement of pot seedlings can be divided into two stages: seedling dropping and seedling planting.

(1) Seedling dropping is the moving process of pot seedlings from the dropping drum to reaching the planting device. Suppose that the initial speed of pot seedlings at upright direction is zero, the main forces on the seedlings are gravity and air resistance.

Thus, the force on pot seedlings at upright direction is:

$$F=mg-ksv_y \tag{1}$$

where, m is the mass of pot seedling; g is gravity acceleration; k is air resistance coefficient, which is generally 2.937(Li et al., 2012; Wang et al., 2009); s is the area of resistance at upright direction, namely, the frontal projected area of seedling leaves; v_y is the instantaneous speed of seedling at upright direction at time point t.

The speed of pot seedling at upright direction during seedling dropping is:

$$v_y=(g-ksv_y/m)\cdot t \tag{2}$$

Displacement of pot seedling at upright direction during seedling dropping is:

$$S_y=\int_0^t(\mathrm{g}-ksv_y/\mathrm{m})dt \tag{3}$$

The displacement of pot seedling at horizontal direction during seedling dropping is:

$$S_x=v_x t-\int_0^t(v_x-ks_1v_x/\mathrm{m}t)dt \tag{4}$$

where, v_x is the advancing velocity of the machine; s_1 is the area of resistance of pot seedling at advancing direction, namely, the projected area of seedling leaves at advancing direction.

(2) Seedling planting is the process from the touching point between pot seedling and the planting device to the lowest point of the planting device.

In the moving process of the pot seedlings and planting device, the ideal moving trajectory of pot seedlings is the perpendicular line to the ground, namely, the absolute speed of pot seedling at advancing direction is zero, and the ideal moving trajectory of pot seedling in planting is shown in Figure 1.

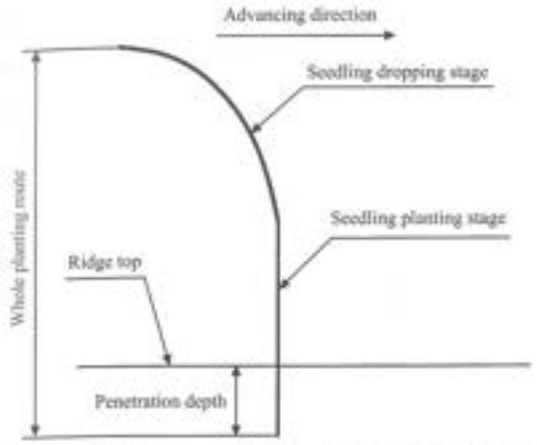

Figure 1 Ideal moving trajectory of pot seedling planting

2.2 Moving trajectory of the duckbilled planting device

The planting device first catches the dropped pot seedling and perforates on the film, then plants the seedling into soil. The trajectory of the duckbilled planting device from the lowest point to seedling catching point next time can be divided into two sections. To avoid the influence on the perpendicularity of pot seedlings and reduce horizontal film break, there should be a vertical lifting section for the duckbilled planting device; and the section ends when the lowest point of duckbilled planting device reaches the top of the pot seedlings; there is a free lifting section from the end of vertical lifting to the point of catching the next seedling, and this section doesn't have any strict demands on the trajectory of duckbilled planting device, except that it should keep upright when it reaches the point of catching the next seedling and keep the speed and acceleration as low as possible.

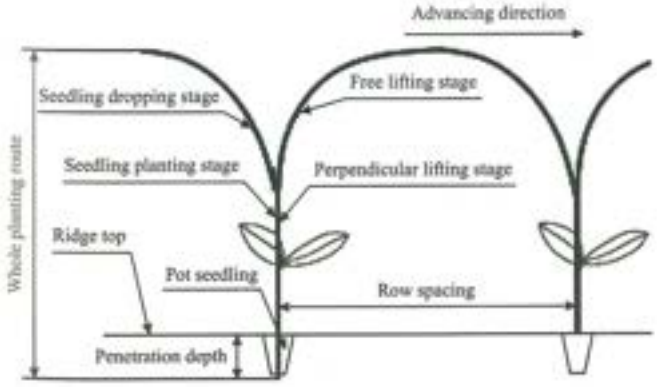

Figure 2 Ideal moving trajectory of the planting device

The analysis above can divide the moving trajectory of duckbilled planting device into four stages (as is shown in Figure 2): seedling dropping, planting, perpendicular lifting and free lifting. When the stages of planting and perpendicular lifting overlap each other, better planting effects can be achieved with the minimum degree of film break. At the top of the trajectory, there should be a relatively even section, which is good for catch seedlings steadily.

3 Simulation and modeling of planting mechanism

The planting mechanism is a double-crank seven-rod mechanism, whose movement is shown in Figure 3. Crank *AB* and crank *CD* are the two driving links with the same rotation direction and the same rotary speed. Rod *BG* and crank *AB* are hinged at point *B*, rod *DF* and rod *EF* are hinged at point *F*, rod *BG* and rod *EF* are fixed at point *E* and *EF* is perpendicular to *BG*, rocking bar *LI* and body frame are hinged at point *L*, and rod *GI* is hinged with rod *BG* and rocking bar *LI* at points *G* and *I* respectively. The duckbilled planting device is simplified as rod *JK*, and point *K* is the planting point of the device (namely the end point), *JK* is fixed on the rod *GI* through rod *HJ* (*H* is the midpoint of *GI* and *HJ* is perpendicular to *GI*). When the machine advances forward, the driving force is transmitted through gearbox to the cranks *AB* and *CD* of the seven-rod planting device, and the multi-link drives the duckbilled planting device to catch and plant seedlings.

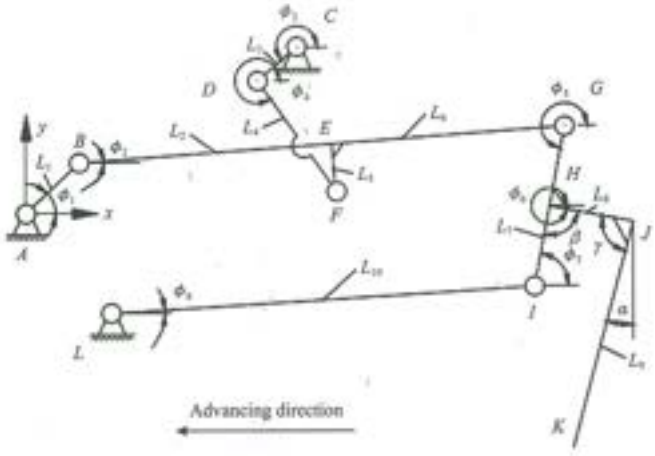

Figure 3 Motion diagram of the seven-rod planting mechanism

Where, L_i (i=1, 2 …, 10) is rod length, mm; φ_i (i=1, 2 …, 8) is the starting phase angle of the corresponding rod, (°); α is the initial angle of the duckbilled planting device, (°); ω represents the angular velocity of the two cranks, rad/s; γ represents the angle between the central axis of the duckbilled planting device and the fixed rod HJ, (°).

Based on the motion diagram, the software ADAMS-2013 was used for virtual modeling of motion, as is shown in Figure 4. In the figure, the hinge points of each rod are revolving pairs, which hinge rods *AB*, *CD* and *LI* together on the body frame. The body frame and the ground are combined by moving pairs. Then render rod AB and rod CD with rotational speed by the order of rotational joint motion, and render the body frame with translational speed by the point motion order.

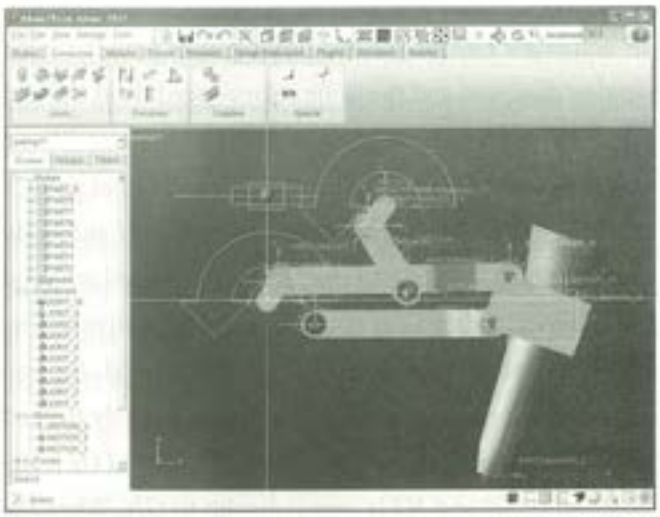

Figure 4 Simulation model of the seven-rod planting mechanism

4 Simulation test analysis of the planting mechanism

4.1 Test factors and evaluation indices

The motion diagram of the planting mechanism shows that, the lengths of crank *AB* and crank *CD* determine the swing scope of the machine at the advancing direction and height of moving trajectory of the duckbilled planting device; the phase difference of the two cranks φ_{AC} may influence the speed matching of motion at vertical and horizontal directions and then influence the shape of the trajectory; the initial angle α of the duckbilled planting device determines its penetration posture and seedling picking status; therefore, L_1, length of crank *AB*, and L_3, length of crank *CD*, phase difference of the two cranks φ_{AC} and initial angle of the duckbilled planting device α were selected as the influencing factors on planting trajectory for the simulation test analysis.

Taking trajectory characteristics as evaluation factors, the trajectory characteristics of up-film planting mechanism are the overall height of the trajectory, height difference between the overlapping vertical section and the trajectory of seeding catching stage. Trajectory evaluation parameters $\sum\Delta H$ was introduced and the following equation can be obtained:

$$\sum\Delta H=\Delta H_1+\Delta H_2+\Delta H_3 \quad (5)$$

where, ΔH_1 is the absolute difference between overall height of the trajectory and the standard value of trajectory height, mm; ΔH_2 is the absolute difference between height of the vertical section and standard value of the vertical section, mm; ΔH_3 is the absolute difference between the height of trajectory in seedling catching and the standard value of the height of trajectory in seedling catching, mm.

4.2 Orthogonal experiment

Four-factor and three-level virtual orthogonal experiment was adopted and the factor level coding is shown in Table 1.

Table 1 Coding of factors and levels

Levels	Factors			
	L_1, mm	L_3, mm	φ_{AC}, (°)	α, (°)
1	27	28	159	15
2	30	31	169	20
3	33	34	179	25

The orthogonal experiment and the results are shown in Table 2. The overall height is the gage length from the lowest point to the highest point of the trajectory; the height of the vertical section is the trajectory length of the stage when the distance of penetration and moving up trajectory of duckbilled planting device is less than 10 mm; height difference of seedling catching stage is the part above the height of the seedling.

The trajectory curve of some test points is shown in Figure 5.

The height of seedling pots was among 30-40 mm, therefore, the penetration depth should be more than 50 mm; the seedling height was among 100−120 mm, so the highest point of the planting trajectory should be 120 mm higher than the ridge top. Since the total height of pot seedlings was lower than 160 mm, the height of planting trajectory should be a little bit higher, and 170 mm was an ideal height; since seedling height was 160 mm, the trajectory height at vertical direction should be higher than 160 mm; duckbilled planting device should catch the seedlings at the same height, therefore, the height

difference of trajectory at seedling catching stage was almost zero. The smaller the trajectory evaluation parameter is, the more approximate was the trajectory to the ideal trajectory.

Table 2 Orthogonal experiment scheme and result

Test No.	Factors				Overall height of trajectory, mm	Characteristic parameters of the trajectory and height of perpendicular overlapping section, mm	Height difference of seedling catching stage, mm	Evaluation parameters of the trajectory, mm
	L_3, mm	L_4, mm	φ_{6C}, (°)	α, (°)				
1	1	1	1	1	146	60	15	139
2	1	2	2	2	169	69	26	118
3	1	3	3	3	185	70	41	146
4	2	1	2	3	163	60	15	122
5	2	2	3	1	211	88	83	196
6	2	3	1	2	184	115	19	78
7	3	1	3	2	207	90	80	187
8	3	2	1	3	180	85	21	106
9	3	3	2	1	236	115	87	198

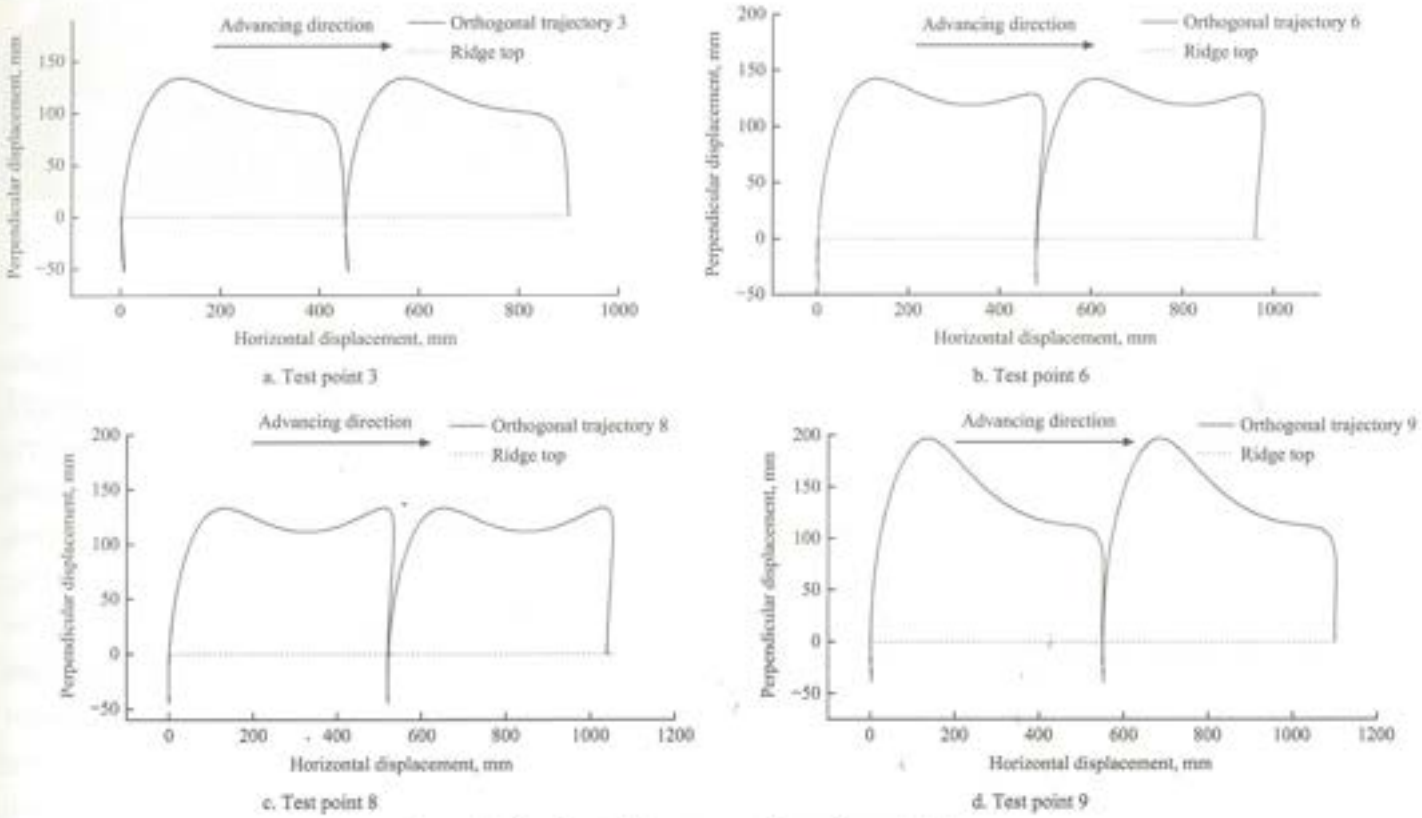

a. Test point 3 b. Test point 6 c. Test point 8 d. Test point 9

Figure 5 Planting trajectory curve in the orthogonal test

Test result showed that trajectory evaluation parameter of the simulation test point 6 was the minimum; the planting trajectory was the most similar to ideal trajectory. The comparatively better parameter combination is: L_1= 30 mm, L_2=184mm, L_3=34 mm, L_4=110 mm, L_5=13 mm, L_6=146 mm, L_7=71 mm, L_8=64 mm, L_9=240 mm, L_{10}= 255 mm; φ_1=70°, φ_2=1°, φ_3=229°, φ_4=300°, φ_5=251°, φ_6=338°, φ_7=71°, φ_8=3°, α=20°.

4.3 Discussion

When the planting frequency was 60/min, the static trajectory, the speed at vertical direction and hole size under optimal parameter combination are shown in Figures 6 to 8.

Figure 6 shows that, the width of the static trajectory is 180 mm, the top of the trajectory is relatively smooth and even and good for catching seedlings.

Figure 7 shows that, the speed of the duckbilled planting device at vertical direction is among the range of 0.9-0.75 m/s. When the initial speed of the duckbilled planting device in penetration was 0.75 m/s, and the speed at vertical direction reduced sharply to let pot seedlings drop to the bottom of the duckbilled planting device. In this way,

the pot seedlings can be easily planted into soil when the duckbilled planting device reached the lowest point.

Figure 8 shows that, the hole made by the nozzle is a little bit larger than the nozzle itself, thus it can effectively reduce damages on mulching film.

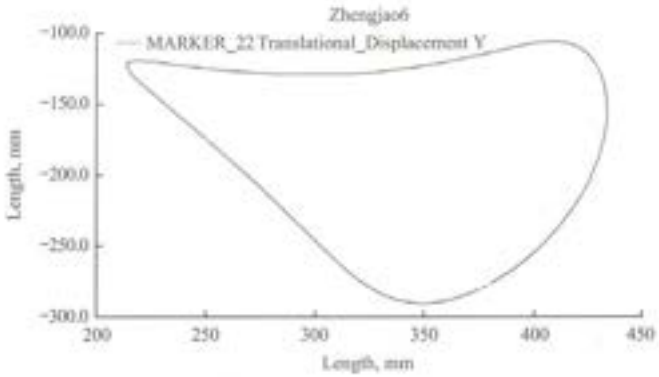

Figure 6 Static trajectory curve of the duckbilled planting device

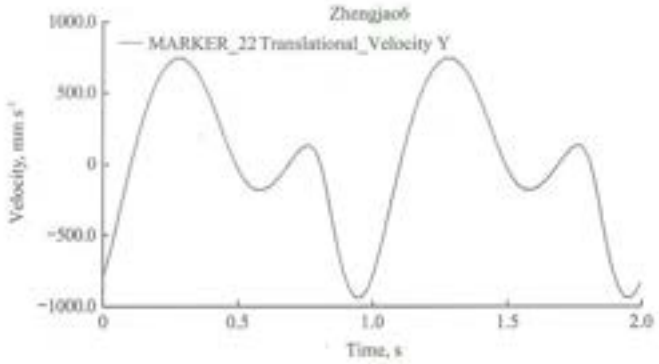

Figure 7 Speed curve of the duckbilled planting device at vertical direction

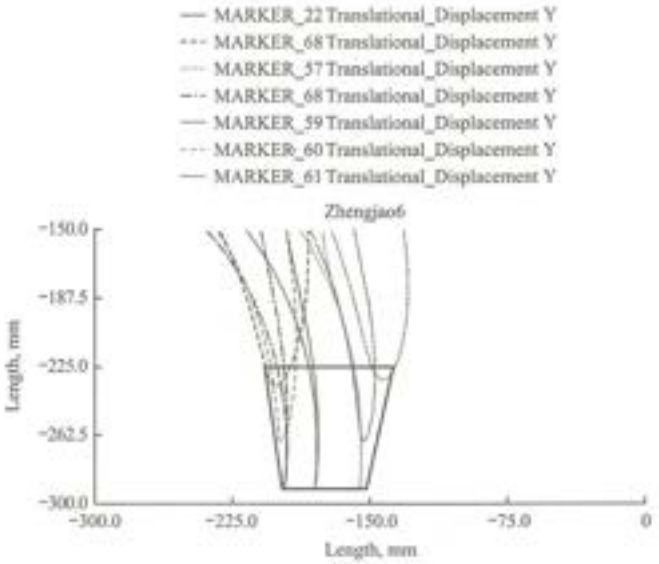

Figure 8 Hole size

5 Field test

5.1 Test conditions

Test materials: tobacco pot seedlings were selected as planting objects in the test. The seedling age was about 40 days; the seedling cultivation substrate was made up of peat, perlite and vermiculite, whose volume ratio was 3:1:1; the substrate was in a cone shape, with diameter of 10 mm at the bottom and diameter of 20 mm at the top, height of 40 mm. The average height of pot seedlings was 151.6 mm, average width of seedling leaf was 99.2 mm. 150 pot seedlings were prepared in the test.

Test equipment: a sample transplanter with a seven-rod planting mechanism (Figure 9); a tape with measuring range of 100 m, a vernier caliper with precision of 0.01 mm, a timer and a protractor.

Figure 9 Test of the seven-rod planting mechanism

5.2 Evaluation indices

(1) Seedling perpendicularity

Seedling perpendicularity refers to the standing status of seedlings after transplanting, which is represented by α, the angle between seedling stalk and the ground. The standing status of seedling can be defined as: $\alpha \leq 45°$ is lodging status, $\alpha > 45°$ is qualified status, and $\alpha \geq 70°$ is excellent standing status.

Lodging rate: $F=A_1/M\times100\%$

Qualification rate of perpendicularity: $H=A_2/M\times100\%$

Excellence rate of perpendicularity: $Y=A_3/M\times100\%$

where, A_1 is number of lodged seedlings; A_2 is number of seedlings in qualified status; A_3 is number of seedlings in excellent status; M is total number of seedlings.

(2) Seedling exposure rate

Seedling exposure refers to the status of planted seedlings with insufficient covering soil, when the root system or pot is totally exposed on soil.

Seedling exposure rate: $L=A_4/M\times100\%$

where, A_4 is number of exposed seedlings; M is total number of measured seedlings

(3) Qualification rate of row spacing

Qualification rate of row spacing is an important index that indicates planting uniformity. Qualified seedling distance can be defined as:

$$0.5Xr<Xi\leq1.5Xr$$

where, Xi is measured seedling distance; Xr is rated seedling distance

5.3 Test method

A transplanter with a seven-rod planting mechanism dragged by a Dongfanghong 300 tractor was used for transplanting in the test. The test area was 50 m, and preparation area was 15 m; the transplanting effects of tobacco pot seedling were tested when the tractor was set at second gear (0.375 m/s), third gear (0.577 m/s) and fourth gear (0.789 m/s) respectively. The test site and seven-rod planting device are shown in Figure 9.

5.4 Results and analysis

After film-covering and ridge-forming, three groups of field transplanting tests were conducted, and the test results are shown in Table 3.

Table 3 Test results

Traction gear	Measured advancing velocity, m/s	Planting efficiency, seedling, min	Perpendicularity qualification rate, %	Seedling exposure rate, %	Qualification rate of row spacing, %
Second gear	0.36	42	100	0	100
Third gear	0.57	66	93.6	6.8	100
Fourth gear	0.75	87	83.4	23.5	100

The results of field transplanting test show that, under traction speed of the second and third gear of the tractor, the seven-rod transplanting mechanism had the qualification rate of perpendicularity of over 90% with low seedling exposure rate and good working performance; under the traction speed of the fourth gear, more lodged seedlings were caused, and the qualification rate of perpendicularity reduced to 83.4%, and could not satisfy the agronomic requirements of transplanting (≥90%). Therefore, when the advancing speed was around 0.57 m/s, namely when planting frequency was 66 seedlings/min, the seven-rod planting mechanism can accomplish the high-speed up-film transplanting work.

6 Conclusions

(1) The seven-rod planting mechanism was proposed and a 3D simulation model of the mechanism was established. The orthogonal simulation test obtained a better combination of key parameters for the planting mechanism: when the planting frequency was 70/min, the penetration depth of the planter was 50 mm, and the length of similar straight-line segment of the planting trajectory in earth and elevating trajectory was 76 mm, the hole size was similar to that of the penetration unit.

(2) Field experiment results of the seven-rod planting mechanism show that: when advancing velocity was 0.57 m/s, transplanting efficiency was 66/min, qualification rate of upright pot seedlings was 93.6%, seedling leakage rate was 6.8%, qualification rate of row spacing was 100%, showing that the condition could meet the requirement of high-speed up-film transplanting.

Acknowledgements

This project was supported by the National Key Research and Development Program of China Sub-project (No. 2017YFD0700801), National Natural Science Foundation of China (Grant No.51505130), the Research Project of Science and Technology of Henan Province (No.172102110021).

[References]

[1] Chen, J. N., B. H. Wang, and G. Y. Ren. 2010. Kinematics modeling and parameters analysis of seven-linkage vegetableseedling transplanting mechanism. *Transactions of the Chinese Society for Agricultural Machinery*, 41(12): 48–53.

[2] Chen, J. N., B. H. Wang, and X. Zhang. 2011. Kinematics modeling and characteristic analysis of multi-linkagetransplanting mechanism of pot seeding transplanter with zero speed. *Transactions of the Chinese Society of AgriculturalEngineering*, 27(9): 7–12.

[3] Feng, J., G. Qin, and W. T. Song. 2002. The kinematic analysis and design criteria of the dibble-type transplanters. *Transactions of the Chinese Society for Agricultural Machinery*, 33(5): 48–50.

[4] He, J. Y. 2014. Design and experiments research ofseedling feeder mechanism of the plug seedlings auto-transplanter.Master's diss. Zhen Jiang: Jiangsu University. (accessed July, 2017)

[5] Hu, M. J. 2011. Hole plate seedling transplanting key technology research. M.A. thesis. Nan Jing: Nanjing Agricultural University.

[6] Jin, X., S. J. Li, X. J. Yang, and H. Yan. 2012. Motion Analysis and Parameter Optimization for Pot Seedling Planting Mechanism Based on Up-film Transplanting, *Transactions of the Chinese Society ofAgricultural Machinery*, 43(S1): 29–34.

[7] Jin, X., X. W. Du, C. H. Yang, and J. T. Jiang. 2016. Design and Experiment on Crank-chute Planting Mechanism of Transplanting Machine. *Transactions of the Chinese Society ofAgricultural Machinery*, 47(5): 32–40.

[8] Li, Q. Y., J. W. Zha, and M. X. Ding. 2003. Experimental study onslideway parting-bowl-wheel transplanter. *Transactions ofthe Chinese Society of Agricultural Engineering*, 19(5): 98–103.

[9] Liu, J. D., W. B. Cao, D. Y. Tian, and H. Z. Zhao. 2017. Kinematic analysis and test on transplanting mechanism with effective zero-speed transplanting on mulch film. *Journal of Mechanical Engineering*, 53(7): 76–84.

[10] Wang, M. M., J. N. Song, and C. L. Liu. 2015. Design and experiment of crank rocker type clamp seedlings mechanism of vegetable transplanter. *Transactions of the Chinese Society of Agricultural Engineering*, 31(14): 49–57.

[11] Wang, W. M., W. G. Dou, and C. N. Wang. 2009. Parameter analysis of the planting process of 2ZT-2 beettransplanter. *Transactions of the Chinese Society ofAgricultural Machinery*, 40(1): 69–73.

[12] Zhang, Z. L., J. L. Wang, and W. Z. Zhang. 2011. Kinematic analysis and performance experiment of cantilever cupvegetable transplanter. *Transactions of the Chinese Society of Agricultural Engineering*, 27(11): 21–25.

[13] Zhou, D. Y., Y. J. Sun, and C. L. Ma. 2003. Design and analysis of a supporting-seeding mechanism with cam and combined rocker. *Transactions of the Chinese Society for Agricultural Machinery*, 34(5): 26–30.

Screening model and optimization of grains group by queuing theory on air-and-screen cleaning device

Tang Zhong*, Li Yaoming, Zhao Huiming, Mei Rongjie, Hui Yi

(*School of Agricultural Equipment Engineering, Jiangsu University, Zhenjiang 212013, China*)

Abstract: In order to develop screening models of grains group on air-and-screen cleaning device, the grains group separating through sieve process and state transition were analyzed by stochastic queuing theory. The models of accumulation grains thickness, grains group separating through sieve hole and losing grain rate of cleaning sieve were developed by stochastic queuing theory. The optimal sieve holes were predicted by controlling the minimum of operating costs and grain losing costs of cleaning sieve. Grains distribution under the cleaning sieve was obtained by performing a cleaning test to verify the predictive value of grain separation and loss process models. The results showed that when the separating capability of one sieve hole was 1.5 Grains per second (Abbreviated as: Gs/s) with grains group feed rate 36.0 Gs/s, the cleaning loss rate of losing grain model was 0.037 Gs/s (grains losing ratio was 0.103%); and the cleaning loss rate of cleaning experiment was found to be 0.042 Gs/s (grains losing ratio was 0.117%) with the relative error 11.97% to model predictive value. The rate of grains group separating through sieve holes and losing grain on cleaning sieve were demonstrating supported by cleaning experimentally of air-and-screen cleaning device. The modeling of grains group separating through sieve hole and losing grain ratio were useful for designing the structural and variable components of the air-and-screen cleaning device.

Keywords: Grains group, queuing theory, cleaning process, sieve hole, cleaning sieve

Citation: Tang, Z., Y. M. Li, H. M. Zhao, R. J. Mei, and Y. Hui. 2017. Screening model and optimization of grains group by queuing theory on air-and-screen cleaning device. International Agricultural Engineering Journal, 26(3): 103–111.

1 Introduction

Separating grains from the mixture material on cleaning device was an important step for combine harvester. But the more cleaning efficiency and the lesser grain losses ratio demanded much bigger cleaning device (Tang et al., 2013). From an economic point of view, grain losses in cleaning process resulted in a direct loss of income for the farmer (Craessaerts et al., 2010). Energy consumption by huge and complex cleaning device also resulted in a higher harvesting costs (Liao et al., 2015). So, minimizing grain loss and simplifying structure size were the design requirements of cleaning device. The mixture ingredients separating through cylinder concave were grains, chaff and shredded leaves, short straw. The function of cleaning device was separating grains from the mixture material.

Improvements in modern combine harvesters including new threshing and separation devices have resulted in higher crop yield prompting many researchers to carry out studies to design new cleaning device prototypes (Shen et al., 2016). Structure and parameter design of new cleaning device was based on agricultural machinery manual, past experience, paper data or foreign prototypes (Gu et al., 2014; Cui et al., 2015). But the grain yield, water content of straw and stem characteristics were difference from the state being years ago. So the design theory and design parameters of cleaning device applied to cleaning Chinese crops should be developed. For improving cleaning efficiency and minimizing cleaning loss, many researchers investigated the influence of different cleaning device settings such as fan speed, screen lip angle, oscillating frequency and amplitude (Su et al., 2016).

Several mathematical models using empirical,

Received date: 2017-05-30 **Accepted date:** 2017-9-03

* **Corresponding author: Tang Zhong,** Ph.D., Associate Researcher of Jiangsu University, School of Agricultural Equipment Engineering, Jiangsu University, Zhenjiang, 212013, Jiangsu, China. Email: tangzhong2012@126.com.

statistical, and physical approaches have been developed in the last decades (Craessaerts et al., 2008). Physical interpretation of cleaning and grain segregation along sieve length was used to describe the cleaning process by Miu et al. (2003); Zhao et al. (2010) simulated the cleaning process of particle flow on vibrating plate based on the soft-ball dry contact model. Ren et al. (2015) established a cleaning results relationship curve affected by airflow velocity in cleaning shoes. Based on experimental data and modeling analysis, non-optimum working regimes can be distinguished from the optimum. Above cleaning investigation was macroscopic method taking cleaning process as an overall without intuitive process model. More physical insight into the cleaning process could be gained by developing physical and statistical models.

A disadvantage was that the coefficients in these mathematical functions were influenced by crop properties, adjustments, and design parameters. Some researches tried to create a deeper insight into certain aspects of the cleaning process, but the common drawback of most standard modeling was that most of these mathematical models were regression models or simulation models. The general applicability of a regression model was very limited. Li et al. (2013) presented mathematical investigation of particulate motion on an inclined screening chute using the Discrete Element Method (DEM). After that, Jiao et al. (2008) developed a two-dimensional DEM emulator, and investigated three typical penetrating behaviors in cleaning process by the emulator. Li et al. (2014) simulated discrete grain separating process on sieve based on the DEM software to improve efficiency and reduce grain loss. Above investigation methods were discrete motion of particles. These EDEM cleaning simulation could display characteristics parameters of single grain. In EDEM cleaning simulation process, the grains group behavior was obviously. But there was not widely accepted cleaning theory and model (Craessaerts et al., 2007a, 2007b; Liu et al., 2015; Joernsgaard and Halmoe., 2003).

In this paper, the separation and loss model of grains group were developed by the queuing theory. The numbers of sieve holes was optimized using the queuing separating model, and rice grain cleaning tests were performed to verify the queuing separation model. These models of grains group separating through sieve holes and losing grain rate of cleaning sieve could be used to optimize the structure of the cleaning device and monitor the grain loss in harvesting.

2 Materials and methods

2.1 Air-and-screen cleaning device

Air-and-screen cleaning device was an important component of combine harvesters. Cleaning device on a combine harvester consists of mixture inlet, oscillating pan, cleaning sieve, collecting pan, fan and boom cleaning sieves and fan. The structure of air-and-screen cleaning device was shown in Figure 1.

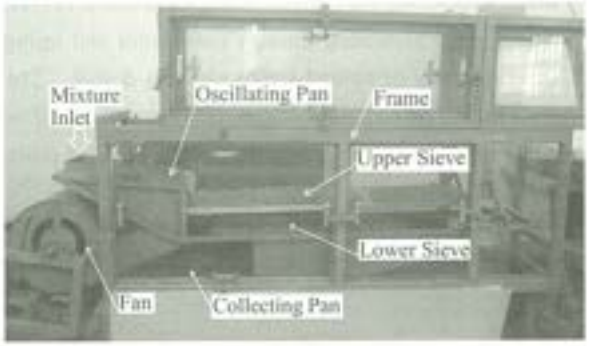

1. Mixture inlet 2. Oscillating pan 3. Upper cleaning sieve 4. Frame 5. Boom 6. Fan 7. Collecting pan 8. Lower cleaning sieve

Figure 1 Structure of air-and-screen cleaning device test bench

The structure size of upper cleaning sieve was approximately 650 mm long, 200 mm wide, with sieve holes diameter of 8-12 mm. Mixture material was fed onto upper cleaning sieve from oscillating pan. Then grains were separating from the mixture material on upper cleaning sieve. The fan speed, sieve holes diameter, oscillating frequency and oscillating amplitude of this air-and-screen cleaning device could be changed or replaced. The screening process of this air-and-screen cleaning device was coupled simulation using a commercial Computational Fluid Dynamics code (CFD® 2015) and a commercial three-dimensional DEM code (EDEM® 2.5,) (Tang et al., 2015; Li et al., 2012). Preliminary findings were based on a fan speed of 800 rpm, sieve holes diameter at 8 mm.

A variable-frequency motor was used to drive the cleaning device. Mechanical oscillations of the cleaning

sieve resulted in the transport of all materials along the sieve length. When the cleaning device was loaded with grains, chaff, shredded leaves and short straw, the reciprocating oscillation carries out the upper sieve. This was done by the up and down action of the grain, which pushes it into the sieve hole. The reciprocating oscillation of the upper and lower sieve includes the sieve, boom, four-bar linkage and crank mechanism. The structure and diagrams of oscillating sieve was shown in Figure 2. The motion analysis of oscillating sieve was also introduced by Li et al. (2012).

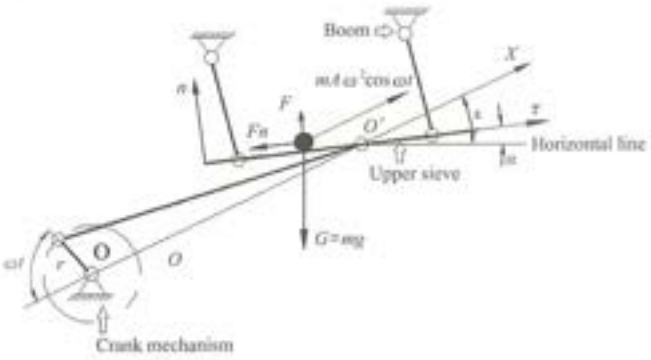

Note: ω was the rotation velocity of crank mechanism, rad/s; t was working time, s; r was the crank radius, mm; O was coordinate origin; G was gravity, N; n was the direction perpendicular to the sieve surface; Fn was friction between grain and sieve; A was the amplitude of oscillating sieve, mm; O' was endpoint of bar linkage; X was the direction of x-axis; F was the comprehensive force, N; ε was angle of horizon line and x-axis; r was angle of horizon line and sieve surface.

Figure 2 Mechanism diagrams of oscillating sieve

According to Figure 2 when the upper sieve was reciprocating moving with the rotation of crank mechanism, the grain started moving on the upper sieve. There was relatively motion between upper sieve and grains. So, the motion rule of grains group was different from the upper sieve. The motion of oscillating sieve was promoting the grains group separating through sieve holes.

2.2 Statistical analysis

Analysis of variance to discriminate significant differences between the group mean values was performed on all subjects. The data was presented as mean result (M) ± standard deviation (SD). The mean of the data was analysed statistically, using a factorial design with the SPSS software (version 13.0, SPSS Inc., CA, USA). The mean results were compared by least significant difference (LSD) post-hoc test at the 5% significance level (p<0.05).

2.3 Ingredients of mixture material

Ingredients of mixture material separating through cylinder grid concave seriously affected the cleaning results. The ingredient of cleaning mixture material on oscillating sieve was well correlated with cleaning loss. It has been a well-known fact that crop properties (like moisture, grain/straw ratio) vary within different fields. There was a need for homogenous units and uniformly cultivated. The cleaning mixture includes grain, chaff and straw (rice varieties: Wu japonica rice 13#). The morphological characteristics of cleaning mixture material were shown in Figure 3.

a. Grains group b. Chaff c. Short straw

Figure 3 Sample morphological of rice cleaning mixture

The rice grain was spherical or ellipsoid, about long 6 mm with a radius of 1.6 mm. The short straw was cylindrical, about 30 mm long with a diameter of 4 mm diameter. And the mass ratio of the mixture was short straw 9%, chaff 13%, and grain 78%. Moisture content of straw and chaff was 49.09% (SD = 6.04) and 36.74% (SD = 4.29) respectively. Moisture content of grains group was 22.56% (SD = 2.02). The average mass of grains per 1000 was 28.5 g (SD = 3.46) (Number of test groups was 10).

2.4 Grains group separating of queuing theory

The cleaning results can be expressed in terms of cleaning loss, cleaning efficiency, and grain purity ratio on collecting pan. The cleaning results were influenced by two categories: promoting grains group into the sieve holes, and hindering the grains group separating through the sieve holes. These separating behaviors helped to shorten cleaning time and helped to maintain homogenous through grain quality. Grains group separating through sieve hole and some grains loss blown outside sieve tail was random.

2.4.1 Characteristic factor of queuing separation

In the cleaning process of cleaning device, there were

continuous and large amounts of grains on oscillating sieve. Based on the research results of grains movement on oscillating sieve (Li et al., 2012), the grains group separating through sieve process and screening model were analyzed by stochastic queuing theory. The following assumptions have been made:

(a) The amount of grain getting into the sieve hole was independent and undisturbed within the same time.

(b) The probability of grain getting into the sieve hole was random.

(c) Two or more than two grains getting through the sieve hole was impossible within the same hole.

2.4.2 Modeling of queuing separation

Based on stochastic probabilistic model, Kendall presented the Kendall Symbol' $M/M/S/d/\infty/R$' of queuing theory (Kendall, 1953). The state transition diagram of $M/M/S/d/\infty/R$ was shown in Figure 4. Let the feeding rate of cleaning grain group was λ, and the separating service capability of one sieve hole was μ.

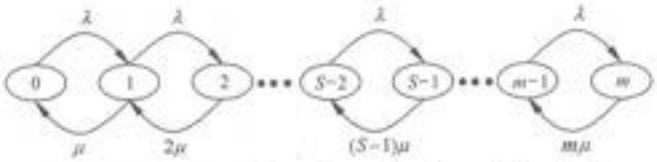

Figure 4 State transition of separating through sieve hole

According to Figure 4, the state transition separations was {0, 1, 2, ...m}, the state of grains group separating through sieve hole of "0," where the sieve was idle. The state of "k ($1 \le k \le S$)" means that the number of separating grain number was k (the numbers of idle sieve holes was S-k.). E.g. when the state transition of grains group was at state of "1", the state of "1" would change to the state of "0" ("1"→ "0"). The separating service capability of one sieve hole was μ. If the grains group separated through sieve hole at the state of "k", there would be several sieves separating grains, changing the state of "k" to "k–1"("k"→"k–1"). If the sieve was at stable rate, and there was no loss, the capability of grain group spreading was greater than the rate of feed. Let the probability of grain separating through sieve hole state "i" was Pi, the expectations number of feeding grain $E(\lambda_i)$ and the expectations number of separating grain through the sieve hole $E(\mu i)$ could be described as follows:

$$E(\lambda_i) = \lambda_{(i-1)} P_{(i-1)} + \mu_{(i+1)} P_{(i+1)} \quad (1)$$

$$E(\mu_i) = \mu_i P_i + \lambda_i P_i \quad (2)$$

If the state of grains group separating through sieve hole was a stable state (the losing grain was 0), the equation of sieve stable state could be described as follows:

$$\mu_i P_i + \lambda_i P_i = \lambda_{(i-1)} P_{(i-1)} + \mu_{(i+1)} P_{(i+1)}, \ 2 \le i \le S-1 \quad (3)$$

When the grains group separating through sieve hole, the state was "0"; there were $\mu P_1 = \lambda P_0$ and $(S\mu)Ps = \lambda P_{(S-1)}$. According to Equation (1) to Equation (3), the probability of every state of grains group separating through sieve hole could be described as follows:

$$P_i = \frac{\lambda_{(i-1)}}{\mu_i} P_{(i-1)} = \frac{\lambda^S}{\mu(2\mu)\cdots(S-1)\mu(S\mu)} P_0 \quad (4)$$

If there were k grains in one column of sieve holes with the maximum number of sieve holes S, the probability P_k (the derivation process was described by Lu (1984)) of grain separating through sieve hole could be described as follows:

$$P_k = \frac{1}{k!}\left(\frac{\lambda}{\mu}\right)^k P_0, \ k \le S \quad (5)$$

$$P_k = \frac{1}{S^{(k-2)} S!}\left(\frac{\lambda}{\mu}\right)^k P_0, \ k > S \quad (6)$$

2.4.3 Indicators of queuing separation

Models of queuing separation need to be solved in order to evaluate the quality and efficiency of grain group separating through sieve holes, and to obtain the optimal parameter combination. The feeding rate of grain group was λ, with $1/\lambda$ being the interval between two feeding grains. The separating service capability of one sieve hole was μ, and then $1/\mu$ was the interval between two separating grains.

Due to $\sum_{k=0}^{\infty} P_k = 1$, then

$$\sum_{k=0}^{s} P_k + \sum_{k=s+1}^{m} P_k = 1 \quad (7)$$

By substituting Equation (5) and Equation (6) into Equation (7), Equation (7) could be solved as:

$$\sum_{k=0}^{s} P_k + \sum_{k=S+1}^{m} P_k = P_0 \sum_{k=0}^{s} \frac{1}{k!}\left(\frac{\lambda}{\mu}\right)^k + \frac{P_0}{S!}\left(\frac{\lambda}{\mu}\right)^S \frac{1}{1-\rho} = 1 \quad (8)$$

$$\rho = \frac{\lambda}{S\mu} \tag{9}$$

where, ρ was the intensity coefficients of grain group separating through sieve hole. The Equation (8) could be solved as P_0:

$$P_0 = [\sum_{k=0}^{S} \frac{(S\rho)^k}{k!} + \frac{S^S}{S!}\frac{\rho(\rho^S - \rho^m)}{1-\rho}]^{-1} \tag{10}$$

According to Equation (9) and Equation (10), the grains group state transition of separating through sieve hole could be described as follows:

(a) If ρ<1, grains group on oscillating sieve were waiting for separating through sieve holes, the state of grains group separating through sieve hole was stable state.

(b) If ρ=1, grains group on oscillating sieve were waiting for separating through sieve holes was zero, the state of grains group separating through the sieve holes was saturation.

(c) If ρ>1, grains group on oscillating sieve were waiting for separating through sieve holes was increasing, the state of grains group separating through the sieve holes was congested. Grains group not separating through sieve holes would be losing.

Using the same method (Bauerlen, 2006; Mecitc, 2006), the accumulation grains group thickness L_q (the derivation process was described by Lu (1984)) on oscillating sieve waiting to separating through sieve holes could be solved as:

$$L_q = \frac{(S\rho)^S \rho P_0}{S!(1-\rho)^2}[1 - \rho^{(m-S)} - (m-S)\rho^{(m-S)}(1-\rho)] \tag{11}$$

The losing grains rate of oscillating sieve P_m (the derivation process was described by Lu (1984)) which was not separating through sieve holes could be solved as:

$$P_m = \frac{S^s}{S!}\rho^m P_0 \tag{12}$$

2.4.4 Sieve holes number optimization

By increasing the number of sieve holes, the separating capability was improved. Utilizing the separation model optimizes the number of the sieve holes. In order to optimize the number of sieve holes, two aspects were taken into consideration: cost and grain loss. Let the cleaning objective function of oscillating sieve was Z, then cleaning objective function of oscillating sieve could be described as follows:

$$Z = C_s \times S + C_w \times L_q \tag{13}$$

where, C_S was operating costs, due to the number of sieve openings S, which were equipment wear, equipment maintenance, labor costs, etc. C_W was the grain losing costs, due to the accumulation grain thickness L_q, the grain was losing in separating the sieve holes.

According to Equation (13), the accumulation grain thickness $L_q(S)$ was a function of sieve holes number S. Objective function of oscillating sieve $Z(S)$ was only a function of sieve holes number S. Because Equation (13) was not a continuous function, objective function $Z(S)$ could be solved by the Marginal Analysis.

If the objective function $Z(S)$ was minimum $Z(S^*)$, the $Z(S^*)$ could be described as follows:

$$\begin{cases} Z(S^*) \le Z(S^*+1) \\ Z(S^*) \le ZS^* - 1 \end{cases} \tag{14}$$

By substituting Equation (13) into Equation (14), the Equation (14) could be solved as:

$$\begin{cases} C_s \times S^* + C_w L_q(S^*) \le C_s \times (S^*-1) + C_w L_q(S^*-1) \\ C_s \times S^* + C_w L_q(S^*) \le C_s \times (S^*+1) + C_w L_q(S^*+1) \end{cases} \tag{15}$$

Let $L_q(+1)=L_q(S^*)=L_q(S\text{-}+1)$ and $L_q(-1)=L_q(S^*-1)-L_q(S^*)$. The Equation (14) could be solved as:

$$L_q(+1) \le \frac{C_s}{C_w} \le L_q(-1) \tag{16}$$

3 Results and Discussion

In order to calculate the indications of cleaning capability and cleaning loss, let feeding rate of grains group λ was 4.5-225 grains per second (Abbreviated as: Gs/s). Because grain proportion 78% of mixture and average mass 28.5 g of grains per 1000 grains, the feeding rate of cleaning mixture material was 0.16-8.22 kg/s. Let the separating service capability of one sieve hole μ was 1.5 Gs/s, the maximum number of sieve holes S was 30; the sectional grains number of waiting separating on oscillating sieve d was 90. The cleaning losing grains rate Pm which was not separated through the sieve hole was calculated by Equation (12). The intensity coefficients ρ of grains group separating through

sieve holes could be calculated by Equation (10). The cleaning capability indicators with cleaning loss were shown in Table 1.

Table 1 Cleaning capability indicators by queuing model

No.	Feeding rate λ Gs/s	Cleaning grain intensity coefficient ρ	Grain loss rate P_m Gs/s
1	4.5	0.1	0
2	9.0	0.2	0
3	13.5	0.3	0
4	18.0	0.4	0
5	22.5	0.5	0
6	27.0	0.6	0
7	31.5	0.7	0
8	36.0	0.8	0.01
9	40.5	0.9	0.21
10	54.0	1.2	1.67
11	67.5	1.5	33.33
12	90.0	2.0	50.00
13	225.0	5.0	80.00

According to Table 1, the feeding rate increased with the grain intensity. Due to the increasing of grain feeding rate, the grain doesn't have the opportunity to separating through the sieve holes. The accumulation grains group thickness on oscillating sieve pan increased. If the feeding rate was less than 40.5 Gs/s, the cleaning grain intensity coefficient ρ was less than 1. If ρ<1, grains group on oscillating sieve were waiting for separating through sieve holes, the state of grains group separating through sieve hole was stable state. When the feeding rate was 54 Gs/s (the grain intensity was 1.2 in Table 1), the cleaning loss rate was 1.67 Gs/s. If the feeding rate was more than 54 Gs/s, then cleaning grain intensity coefficient was ρ>1. If ρ>1, grains group on oscillating sieve were waiting for separating through sieve holes was increasing, the state of grains group separating through the sieve holes was congested. Grains group not separating through sieve holes would be losing. So, the feeding rate was more than 54 Gs/s, the sieve holes would be congested. In order to decrease the cleaning loss rate, increasing the number of sieve holes would increase the opportunity for grain separation. If the number of sieve holes were unlimited, the structure and institutions of cleaning device would be huge. If the holes were too little, cleaning loss would be much greater. Based on minimum of operating costs and grain losing costs, the optimal numbers model was developed shown in Equation (16).

The cleaning separation and loss process models were developed by the Kendall Symbol of queuing theory in this paper. According to the stochastic queuing theory cleaning modeling, in ideal conditions as the short straw would remain on sieve pan, where the grain would separating through the sieve and into the grain bin. The grains group run outside sieve tail was reported as grain loss. The losing grain rate of oscillating sieve was shown in Equation (12), using the stochastic queuing theory model. Many probability models were applied to design and optimize cleaning device, but grains group cleaning loss model and state transition model was not reported.

For each feeding rate value, an optimal interval $[L_q(+1)\ ,\ L_q(-1)]$ could be obtained by Equation (15). Because C_S/C_W was a known value, and C_S/C_W could be any value. If C_S/C_W being different values, objective function $Z(S)$ was different. But the relative size was certain. The C_S/C_W value was based on the operating costs and losing costs. The value of C_S/C_W was a variable, and any value was the same results for the design of oscillating sieve. In this paper, let C_S/C_W being 0.8.

The C_S/C_W value indicated that the optimal number of sieve holes could be calculated by Equation (16). The results of optimal sieve holes, with different feed rate were shown in Table 2.

Table 2 Optional variable of sieve holes by queuing model

No.	Feed rate λ Gs/s	Cleaning grain intensity coefficient ρ	Optimal interval $[L_q(+1), L_q(-1)]$	Objective value Z	Optimal sieve hole S^*
1	4.5	0.1	[0.26 , 1.17]	21.77	5
2	9.0	0.2	[0.68 , 2.60]	37.36	8
3	13.5	0.3	[0.44 , 1.14]	51.99	12
4	18.0	0.4	[0.66 , 1.59]	66.38	15
5	22.5	0.5	[0.43 , 0.88]	80.58	19
6	27.0	0.6	[0.56, 1.09]	94.23	22
7	31.5	0.7	[0.68 , 1.26]	143.94	25
8	36.0	0.8	[0.78 , 1.36]	162.60	28
9	40.5	0.9	[0.52 , 0.84]	134.82	32
10	54.0	1.2	[0.77 , 1.07]	172.32	40
11	67.5	1.5	[0.75 , 0.94]	291.95	47
12	90.0	2.0	[0.79 , 0.91]	892.07	53
13	225.0	5.0	[0.61 , 0.86]	1968.89	59

Based on the Equation (13), the objective function $Z(S)$ could be obtained. The objective function $Z(S)$ was index, which could be used to solved Optimal sieve hole S^* by Equation (14). According to Table 2, when the cleaning grain intensity coefficient ρ was less than 1, the

state of grains group separating through sieve hole was stable state. Then the optimal interval $[L_q(+1), L_q(-1)]$ was [0.52, 0.84]. If the oscillating sieve needs to be a stable state (the losing grain was minimum), the capability of separating grains group were more than that of the feeding rate (shown in Table 2). As feeding rate increases, the need for sieve holes increases. The optimal numbers of sieve holes at each feeding rate was shown in Table 2.

The cleaning grains group feeding rate was 4.5 Gs/s (mixture material feeding rate was 0.16 kg/s) at each column (Continue to feed 3 minutes). Then the total cleaning grains group feeding rate was 49.5 Gs/s (mixture material feeding rate was 1.81 kg/s), there were 11 sieve holes of each sieve columns. The cleaning loss rate of feeding rate 4.5 to 225 Gs/s were test. Based on the optimal sieve hole, the cleaning loss rate predictive and test results with optimal number of sieve holes were shown in Table 3.

Table 3 Grain loss rate of each column sieve hole

Sieve holes S^*	Feeding rate λ Gs/s	Sieve cleaning loss rate Gs/s	
		Predictive value	Test results M±SD
5	4.5	0.021	0.034±0.014
8	9	0.059	0.045±0.018
12	13.5	0.031	0.042±0.012
15	18	0.038	0.045±0.016
19	22.5	0.028	0.058±0.018
22	27	0.032	0.054±0.014
25	31.5	0.034	0.046±0.012
28	36	0.037	0.042±0.013
32	40.5	0.029	0.046±0.012
40	54.0	0.031	0.074±0.006
47	67.5	0.061	0.182±0.048
53	90	0.159	0.364±0.116
59	225	0.607	0.864±0.102

According to Table 3, when the feeding rate was 36.0 Gs/s, the grain intensity was 0.8 (shown in Table 2), while the cleaning loss rate was 0.042 Gs/s. Because grains group feeding rate was 36 Gs/s with 3 seconds. The total losing grains divided by total feeding grains, then grains losing ratio was 0.117%. When the feeding rate was 36.0 Gs/s, the optimum number of sieve holes was 28 (shown in Table 2). This resulted in the sieve loss being 0.042 Gs/s (grains losing ratio was 0.117%), when compared to the calculated results 0.037 Gs/s (grains losing ratio was 0.103%), and the error being 11.97%. When compared to the test results in Table 3, the results of modeling agree well with that of experiments. This shows that the separation modeling of material motion on oscillating sieve of air-and-screen cleaning device was feasible.

Where the grain loss was less than 0.042 Gs/s (grains losing ratio was 0.117%), the total grain loss was 1.32 Gs/s (the width of oscillating sieve was 0.6 meter). According to estimates (Craessaerts et al., 2010), even in optimum settings, it was very difficult to reduce total cleaning loss below 1%-2% (Craessaerts et al., 2007a, 2007b). However, total grain cleaning losses in Germany remained 4%-6%. Spengler stated that if total losses could be diminished to 5%, this would offer an increasing in turnover of 20 k$ per year, for each combine (Spengler et al., 2003).

The cleaning efficiency and capability of air-and-screen cleaning device was typically expressed in terms of cleaning loss. From the experimental and model results, there was some deviation between some model predictive data and experimental data. These models also can be seen as a tool for researchers and designers who want to simulate and optimize the cleaning process. These modeling of queuing and separating through oscillating sieve could be used to investigate the losses sensor installed at the tail of oscillating sieve to predict the grain losing. The predicting of grain cleaning loss by separation and loss process model of air-and-screen cleaning device was very useful, and it could be applied to other crops such as barley, corn, oats, and rapeseed.

5 Conclusions

For developing screening model of grains group on air-and-screen cleaning device, the accumulation grain thickness on oscillating sieve, losing grains rate of oscillating sieve, state transition of separating through sieve hole, intensity coefficients of grain group separating through sieve hole were developed by queuing theory. Based on minimum of operating costs and grain losing costs, the optimal numbers model was developed.

(1) If oscillating sieve needs to be a stable state, the capabilities of separating grains group were more than that of the feeding rate. If intensity coefficients ρ more

than 1, grains group on oscillating sieve were waiting for separating through sieve holes. The state of grains group separating through the sieve holes was congested.

(2) When the feed rate was 36.0 Gs/s, the separating service capability of one sieve hole was 1.5 Gs/s, the maximum number of sieve holes was 30, and then the cleaning loss rate at each sieve column is 0.042 Gs/s (grains losing ratio was 0.117%). Then compared to the calculated results 0.037 Gs/s (grains losing ratio was 0.103%), and the error being 11.97%.

Acknowledgement

This research work was supported by China Postdoctoral Science Foundation Fund (2015M581742), Natural Science Foundation of Jiangsu Province (BK20170553), Jiangsu Province Post-doctoral Research Aid Program (1501111B), Research proposal of Jiangsu University (16A342), and A Project Funded by the Priority Academic Program Development of Jiangsu Higher Education Institutions (PAPD).

[References]

[1] Bauerlen, E. F. 2006. On the waiting time of arriving aircrafts and the capacity of airports with one or two runways. *European Journal of Operational Research*, 43(12): 56–62.

[2] Craessaerts, G., W. Saeys, B. Missotten, and J. De Baerdemaeker. 2007a. A genetic input selection methodology for identification of the cleaning process on a combine harvester, part I: selection of relevant input variables for identification of the sieve losses. *Biosystems Engineering*, 98(1): 166–175.

[3] Craessaerts, G., W. Saeys, B. Missotten, and J. De Baerdemaeker. 2007b. A genetic input selection methodology for identification of the cleaning process on a combine harvester, part II: selection of relevant input variables for identification of material other than grain (MOG) content in the grain bin. *Biosystems Engineering*, 98(1): 297–303.

[4] Craessaerts, G., W. Saeys, B. Missotten, and J. DeBaerdemaeker. 2008. Identification of the cleaning process on combine harvesters Part I: A fuzzy model for prediction of the material other than grain content (MOG) in the grain bin. *Biosystems Engineering*, 101(1): 42–49.

[5] Craessaerts, G., W. Saeys, B. Missotten, and J. DeBaerdemaeke. 2010. Identification of the cleaning process on combine harvesters, Part II: A fuzzy model for prediction of the sieve losses. *Biosystems Engineering*, 106(2): 97–102.

[6] Cui, J. W., Z. D. Han, and Z. R. Zhang. 2015. Experiments and Analysis about Airflow Distribution over Oscillating Sieve of Grain Combine Harvester. *Agricultural Engineering*, 5(2): 1–5.

[7] Gu, F. W., Z. C. Hu, and M. Z. Cao. 2014. Design of 4LZ–1.0Q type lightweight- simplified combine harvester of rice and wheat with hilly and mountainous area. *Journal of Chinese Agricultural Mechanization*, 35(2): 148–154.

[8] Jiao, H. G., P. Liu, and J. Ma. 2008. Development and application of screen simulation program by using particle discrete element method. *Journal of henan polytechnic university (natural science)*, 27(1): 711–715.

[9] Joernsgaard, B., and S. Halmoe. 2003. Intra-field yield variation over crops and years. *European Journal of Agronomy*, 19(1): 23–33.

[10] Kendall, D. G. 1953. Stochastic Processes Occurring in the Theory of Queues and Their Analysis by the Method of the Imbedded Markov Chain. *Annals of Mathematical Statistics*, 24(3): 338–354.

[11] Li, H. C., Y. M. Li, and F. Gao. 2012. CFD–DEM simulation of material motion in air-and-screen cleaning device. *Computers and Electronics in Agriculture*, 88(1): 111–119.

[12] Li, H. C., Y. M. Li, Z. Tang, and L. Z. Xu. 2013. Numerical Simulation of Material Motion on Vibrating Screen of Air-and-screen Cleaning Device Based on CFD–DEM. *Transactions of the Chinese Society for Agricultural Machinery*, 43(2): 79–84.

[13] Li, S. B., P. S. Diao, and F. H. Li. 2014. The Performance Decision Research of Air-and-screen Cleaning Unit Based on SWOT–FAHP. *Journal of Agricultural Mechanization Research*, 45(5): 88–93.

[14] Liao, Q. X., X. Y. Wan, and H. T. Li. 2015. Design and experiment on cyclone separating cleaning system for rape combine harvester. *Transactions of the Chinese Society of Agricultural Engineering*, 31(14): 24–31.

[15] Liu, Z. H., Y. P. Zheng, and Z. M. Wang. 2015. Design on Air-flowing Cleaning Unit of Micro Rice-Wheat Combine Harvester. *Transactions of the Chinese Society of Agricultural Machinery*, 46(7): 102–108.

[16] Lu F. S. 1984. Queuing theory and its application, *Science and Technology of Hunan Province*.

[17] Mecitc, G. 2006. Integrated modeling of information and physical flows in transportation system. *Transportation Research Part C*, 14(1): 139–156.

[18] Miu, P. I. 2003. Stochastic modeling of separation process on combine cleaning shoe. International Conference on Crop Harvesting and Processing. *American Society of Agricultural and Biological Engineers*: 65(1): 19–26.

[19] Ren, S. G., F. P. Xie, and X. S. Wang. 2015. Gas-solid two-phase separation operation mechanism for 4LZ-0.8 rice

combine harvester cleaning device. *Transactions of the Chinese Society of Agricultural Engineering (Transactions of the CSAE)*, 31(12): 16–22.

[20] Shen, Y. F., M. L. Wu, and C. Y. Guan. 2016. Study Status and Developmental Strategies of Cleaning Device of Small Combine Harvester. *Journal of Agricultural Mechanization Research*, (10): 263–267.

[21] Spengler, A., S. Mehne, and A. Feiffer. 2003. Combine harvesting at large scale enterprises in Europe. In *Proc Electronic of the International Conference on Crop Harvesting and Processing*. Louisville, Ky., 16-20 Nov.

[22] Su, T. S., Z. D. Han, and J. W. Cui. 2016. Research status and development trend of cleaning unit of cereal combine harvesters. *Journal of Agricultural Mechanization Research*, 38(2): 6–11.

[23] Tang, Q., C. Y. Wu, and J. Wu. 2015. Research on the DEM–CFD Simulations of Grain Cleaning. *Journal of Agricultural Mechanization Research*, 43(1): 35–38.

[24] Tang Z., Y. M. Li, and C. H. Wang. 2013. Experiments on variable-mass threshing of rice in the tangential-longitudinal-flow combine harvester. *Journal of Agricultural Science and Technology*, 15(2): 1319–1334.

[25] Zhao, L. L., C. S. Liu, and J. X. Yan. 2010. Numerical Simulation of Particles Flow on the Vibrating Screen Plate Using a 3D Discrete Element Method. *Journal of China University of Mining and Technology*, 39(2): 414–419.

Abbreviations used:

Kendall Symbol 'M/M/S/d/∞/R'(*Poisson Distribution* of feeding grain method (*M*)/ Negative *Exponential Distribution* of grain separating through the sieve hole (*M*)/ maximum sieve hole number (*S*)/ sectional grain number of waiting separating grain on sieve (*d*)/ unlimited amount of feeding grain (∞)/ the rule of separating through the sieve of losing or waiting method (R)); SD (standard deviation).

Parameters: ω (rotation velocity of crank mechanism); t (working time); r (the crank radius); O (coordinate origin); G (gravity); n (direction perpendicular to the sieve surface); F_n (friction between grain and sieve); A (amplitude of oscillating sieve); O' (endpoint of bar linkage); X (direction of x-axis); F (comprehensive force); ε (angle of horizon line and x-axis); τ (angle of horizon line and sieve surface); λ (feed rate of cleaning mixture); μ (separating service capability of one sieve hole); i (grain separating through the sieve state); P_i (probability of grain separating through sieve hole); S (grains in one column with the maximum number of sieve hole); ρ (intensity coefficients of grain separating).

Design and simulation analysis of chain type sweet potato seedling recycling machine

Wei Lele[1], Lv Zhaoqin[1,2*], Zheng Wenxiu[1], Lu Yao[1], Liu Zhengduo[1], Zhu Binbin[1], Cai Yuhu[1]

(1. *College of Mechanical and Electronic Engineering, Shandong Agricultural University, Tai'an 271018, China*; 2. *Shandong Provincial Key Laboratory of Horticultural Machinery and Equipment, Tai'an 271018, China*)

Abstract: In this paper, a kind of chain type sweet potato seedling recycling machine is proposed. And the 3D design and virtual assembly of the recycling machine are completed with Solidworks software. The machine size is 2300 mm× 1500 mm×1200 mm. The parametric design of eccentricity and eccentric shaft speed which influence the cutter speed were completed by ADAMS. The simulation results showed that the eccentric shaft speed had greater influence on the cutting speed than eccentricity. If the potato seedlings were cut off in one time, the rotational speed range of the eccentric shaft need to stay in 450-550 r/min. Through the cutting chart calculated by MATLAB, the speed of the machine in line with the cutting speed was 4.2-6.3 km/h which meets the machine operating speed requirements. This design has the following characteristics: the copying shovel of machine is in the bottom of ditch when the machine is in work; the longer potato seedlings can be cut off by the side cutting cutter, which reduces the probability of discontinuity; with the help of the tension mechanism of double-row conveyor chain mechanism, it can effectively prevent the phenomenon of dropping and plug during the process of the seedling transportation. The knife board at the bottom of the potato seedling cutter solves the problem of high rate of injuring potato and high stubble height.

Keywords: potato seedling, recycling, reciprocating cutter, ADAMS, MATLAB

Citation: Wei, L. L., Z. Q. Lv, W. X. Zheng, Y. Lu, Z. D. Liu, B. B. Zhu, and Y. H. Cai. 2017. Design and simulation analysis of chain type sweet potato seedling recycling machine. International Agricultural Engineering Journal, 26(3): 112–119.

1 Introduction

1.1 Environmental conditions

According to a large number of statistical data ridging is mainly applied in sweet potato cultivation in China. The distance of ridges is 600-900 mm and the height of ridge is 250-300 mm in general. The seedling length is up to 1.5-2.5 m. Some can even grow to 4 m. Seedling vine grow vigorously and intertwined between the ridges and the seedling has fibrous roots. The sweet potato seedling will cover the entire field during the maturity period. With the toughness of seedlings, there is a certain degree of difficulty in the process of recycling.

Received date: 2016-12-26 **Accepted date:** 2017-08-23

* **Corresponding author: Lv Zhaoqin,** Professor, College of Mechanical and Electronic Engineering, Shandong Agricultural University, Tai'an, 271018, China. Email:lzqsdau2003@126.com.

Sweet potato is widely recognized as a multipurpose crop. It is not only an important food, animal feed and raw material for industrial production, but also a new energy source and a high-quality anti-cancer health care product. In recent years, China's sweet potato planting area has exceeded 600 million hectares. The total output is about 120 million tons that accounts for about 86% of the world's sweet potato total output. However, the mechanization of sweet potato production is in low level development, especially in the stage of getting rid of seedlings that needs more human labor. The low level of mechanization greatly limits the initiative of farmers. The existing sweet potato seedling machine are converted from the potato or corn machinery that is not suited to the ridge agronomic characteristics and result in low rate of mechanical killing seedlings and high rate of injury. Therefore, the implementation of mechanized seedling

has become an inevitable trend.

1.2 Research status at home and abroad

Foreign sweet potato stem and leaf harvesting machinery development started earlier and has entered a stable development period. There have been many mature products in the market such as Japan's self-walking type sweet potato vine machine, South Korea's small vine machine, the United States of roll vine machine and Holland's pulling vine machine. In recent years, the foreign sweet potato seedling machinery development has entered the joint harvest stage. The mechanical and electrical integration and hydraulic technology have been applied to the seedling processor to reduce mechanical vibration and noise. The production efficiency and stability have been greatly improved and it can complete crushing and collecting work at the same time. However, the price is higher. To some degree, due to the low purchasing power of farmers and the low input and output of agriculture, this limits the farmers' ability to use machine produced by other countries. At present, the domestic seedling processing machine is mainly concentrated on the small and medium-sized machines development and has small-scale promotion, which is far behind the wheat, corn and other joint harvesting machinery level. There are mainly 4UJH-type sweet potato equipment jointly developed by Zhengzhou City, Henan Province Agricultural Machinery Extension Station and Machinery Manufacturing Co. Ltd which is used with tractors and can complete seedling cutting, crushing, field and other operations at once; two rear-wheel drive sweet potato vine machine with four small wheel developed by Xuzhou Jiangsu Sweet Potato Research Center and agricultural machine enterprises which is in the probationary stage; a large double-line of killing vine machine behaved well developed by Jiangsu Province, Lianyungang City Tianyuan Agricultural Research Institute; the 4UL-80-type potato seedling machine developed by Anhui Province, Fuyang City, Anhui Province, which can complete cutting seedlings, cutting roots, collecting seedling work at one time; Shandong Laoling Tiancheng Construction Machinery Co. Ltd. also launched a development of sweet potato seedling processing machinery; Tengzhou Golden potato Wang Agricultural Machinery Development Co. Ltd. developed a 4US-1 seedling machine. The existing sweet potato seedling machine mostly learns from the potato mechanical structure. Because of the differences in growth characteristics between sweet potatoes and potatoes, there are poor effects of existing sweet potato seedling machine. It is prone to have low rate of seedling, high damaged rate, long stubble, low passing rate, poor seedling utilization and damage caused by crushing seedling. At present, there is no good operation for dealing with seedling. Therefore, an economical and suitable sweet potato seedling machine is of great significance for mechanization and sustainable development of sweet potatoes.

2 Structure design and principles

2.1 Overall structure

The chain-type sweet potato seedling recycling machine is composed of frame assembly, suspension bracket, gear box assembly, contoured picking mechanism, reciprocating cutter mechanism, potato seedling clamping conveyor mechanism, cutting cutter mechanism, transmission device and wheel assembly. Machine structure is shown in Figure 1.

2.2 Working principles

The machine is moving along the ridge direction and it is single ridge operation. The tractor provides the power, which is input to the gear box assembly by the universal drive shaft. After changing direction and speed, the gearbox input the power to the reciprocating cutter mechanism, the chain holding conveyor and auxiliary of potato seedlings harvest (cutting cutter and seeding roller). The copying shovel mechanism installed in the front of the machine raises the seedling of the ridge base and feeds seedlings to the front-stage V-type feed port of holding conveyance mechanism with the auxiliary device of the potato seedling harvesting. When the potato seedlings are raised up by the copying shovel mechanism, the reciprocating cutter under the machine cut the main stem of potato seedlings. The potato seedlings are sent to the rear part of machine with the help of gripping chain and put in the field ridge bottom.

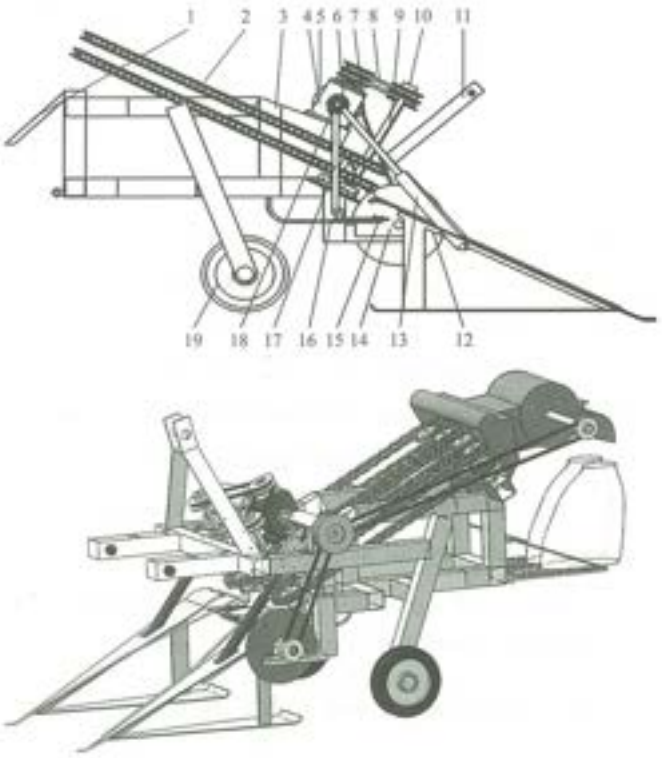

1. Seedling guide plate 2. Gripping chain 3. Frame 4. Gear box 5. Pulley of cutter plate 6. Gear for seedling roller 7. Belt of cutter plate 8. Sprocket belt 9. Sprocket shaft 10. Sprocket pulley 11. Hanger 12. Copying shovel 13. Seeding roller 14 Cutter plate 15. Reciprocating cutter 16. Cutter blade 17.Off center shaft of cutter 18. Gear off center shaft 19. Wheel

Figure 1 Schematic diagram of chain sweet potato seedling recycling machine

2.3 Technical parameters

Table 1 Main technical parameters of the chain sweet potato seedling recycling machine

Number	Parameters	Values
1	Machine size (length×width×height, mm)	2300×1500×1200
2	Raw	Single row
3	Matched power, kW	20.5
4	Operating speed, km/h	4-6
5	Work breadth, mm	750
6	Productivity, hm^2/h	0.3-0.4
7	Stubble height, mm	≤30

3 Design and simulation of main components

3.1 Auxiliary device of harvester

Copying shovel, dripping roller and cutting cutter all belong to the auxiliary devices of sweet potato harvester (Figure 2). Its role is to cooperate with the potato seedling cutting and transportation equipment to improve operation efficiency. During the working process, the spade tip is below the surface of ground. And the coping shovel with rope roller work together and its role is to raise potato seedling of ridge bottom for cutting off the potato seedling stems easily. The picking shovel is hinged with the frame so that it can always be in contact with the floor. The two shovels also welded on the carrier support bar to prevent potato seedlings creep down between the two shovels. The dripping roller is counter rotating, which makes the potato seedlings move the middle of the conveyor chain that facilitates clamping conveyor of potato seedling. The cutting cutter plate is designed to cut off long potato seedlings and prevents seedlings from wrapping up on the frame that affects the machine's normal operation continuity. The cutter plate is driven by the belt pulley. Cutter line speed is selected as 5 m/s and the cutter's diameter is 300 mm.

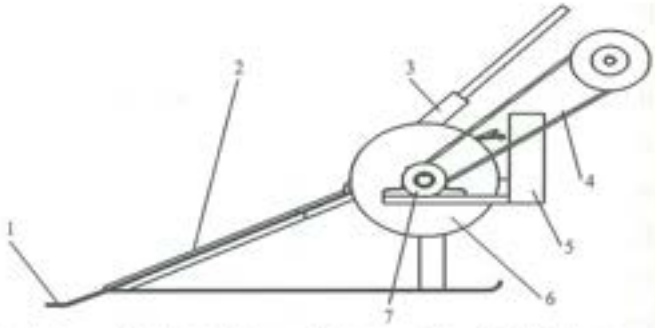

1. Picking spade's tip 2. Picking spade 3. Rope roller 4. V-Belt of cutter 5. Frame 6. Cutter plate 7. Cutter support

Figure 2 Side-mounted cutter head (anti-wrap mechanism)

3.2 Cutting and conveying mechanism

The sweet potato seedling cutting and conveying mechanism is the main part of the sweet potato seedling recycling machine. It is composed of reciprocating cutter, potato seedling clamping conveyor chain, chain wheel and cutter blades. The main function is to cut off the main stems of potato seedlings and transport the seedling to the back of the machine and put the seedling in the bottom of the ridge ditch.

3.2.1 Clamping conveyor

The clamping conveyor (Figure 3) consists of conveyor chain, sprocket, power train device and tension device. Clamping chain is double row layout, which makes the transport action more reliable. Chain length is 2400 mm and the layout angle is 27°, the front shape of chain is the V-shaped openings. The V-shaped opening in the front of the chain makes the feeding of potato seedlings more convenient. According to the transport seedling volume, the distance H between the clamping chains can be changed under the conditions of chain

tension mechanism, which can make the holding of seedling more reliable. When the conveyor chain works, its speed should be greater than the machine forward speed, which ensures the smooth delivery of potato seedlings. The clamping conveyor speed ratio K=1.2. The chain line speed can be obtained by the following equations:

$$v=v_h/\cos\alpha \quad (1)$$

$$v_h=K\cdot v_1 \quad (2)$$

where, v is the mean clamping chain speed, m/s; v_1 is the mean machine forward speed, m/s; K is the mean clamping conveyor speed ratio; α is the mean angle between the chain and the ground; V_h is the mean chain of horizontal speed.

The chain speed decomposition diagram is shown in Figure 4.

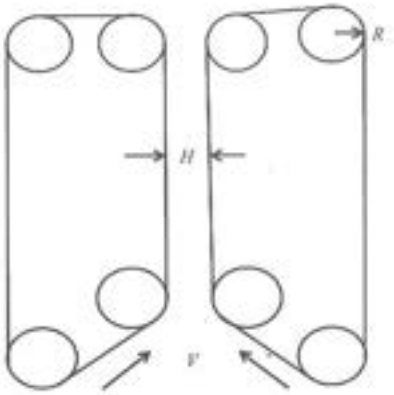

Figure 3 Schematic diagram of clamping conveyor

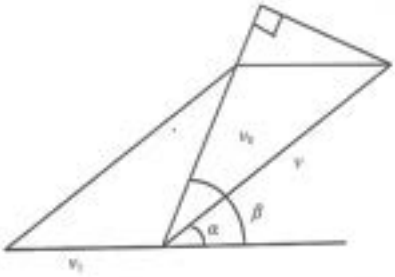

Figure 4 Chain speed decomposition diagram

The conveying speed v_0 of the potato seedling holding is determined by the following equation

$$\vec{v}_0=\vec{v}_1+\vec{v} \quad (3)$$

where, v_1 is mean the machine forward speed, m/s; v is mean the clamping chain speed, m/s; v_0 is mean the Holding speed of sweet potato seedling, m/s.

3.2.2 Reciprocating cutter mechanism

Reciprocating cutter mechanism consists of moving knife, fixed knife, cutting tool holder and eccentric shaft. And fixed knife is fixed on the cutting tool holder by the bolt and there is a chute on moving knife, which is fit with eccentric shaft. And through this joint, it changes the circular motion of eccentric shaft into reciprocating linear motion of movable knife. At present, the ideal blade shape is triangular or trapezoidal. Because of wearing, the blade edge length of the triangular blade is shortened, and trapezoidal blade edge length will not be reduced. So the machine uses the shape of-trapezoid blade. The two types of blade's situation after wearing are shown in Figure 6.

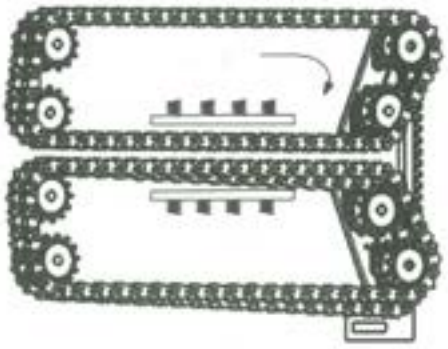

Figure 5 Clamp chain structure

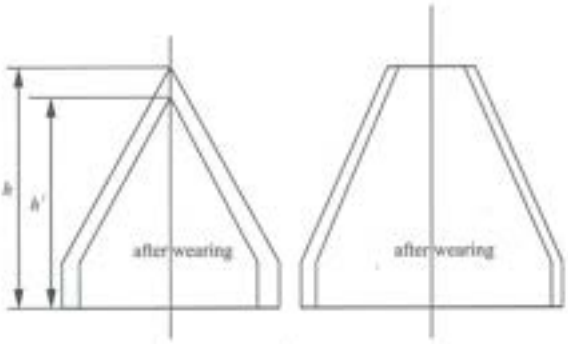

Figure 6 Comparison of blade wear

This design uses standard Ⅱ cutting knife (According to national standards, cutters can be divided into three categories, and this is one of them). According the standards, its dimensions are h = 55 mm, b = 24 mm, a = 76.2 mm and e = 17 mm. In the Figure 7, a, b, e, f, g, h are the width of the blade, the average width of the blade, the width of the front end of the blade, the actual cutting stroke begins displacement, the actual cutting stroke ends displacement and blade width

In general, the greater the slip angle is, the stronger cutting ability of the cutting knife is and the cutting is easier. However, the range of sliding angle must meet the clamping or bite conditions of seedling. Through literature, if the potato seedling is cut off at once, the speed of knife needs to be above 0.8 m/s (Luan et al.,

2014). Taking the difference between the field work and the experimental environment and the tear of tool into account, the cutting speed of the harvester machine is generally 1.2 m/s.

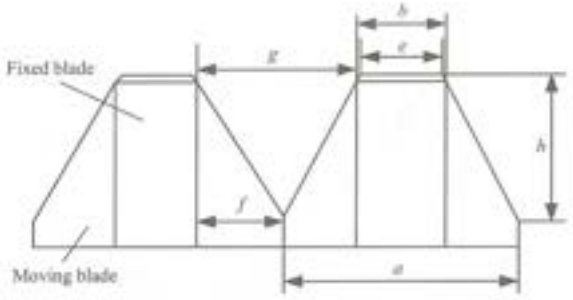

Figure 7 Structural parameters of blade

The reciprocating cutter's cutting effect of harvesting machine is closely related with the relationship of cutting speed and machine's speed. This relationship is usually described by the cutter distance H (the distance of the machine in a cutting cycle) (Yang et al., 2016). The knife and machine speed ratio λ is also a method to describe the cutting effect. When the machine operating speed is in a certain case, the low cutter speeds will lead to leakage phenomenon of cutting, and the machine operating results are not satisfactory. However, if knife speed is too fast, it will lead to repeatedly cutting phenomenon of potato seedlings, which results in energy waste. Therefore, the correct matching of the machine operating speed and the cutting speed is the basis for realizing the reasonable cutting of the potato seedling. The moving blade's displacement x, velocity v and acceleration a in reciprocating motion can be obtained by the following equation:

$$\begin{aligned} x &= \sqrt{(r+1)^2 - h^2} - r\cos\omega t - l + \frac{h^2}{2l} + \frac{rh}{l}\sin\omega t + \\ &\quad \frac{r^2}{2l}\sin^2\omega t + \cdots\cdots \\ v &= r\omega(\sin\omega t + \frac{h}{l}\cos\omega t + \frac{r}{2l}\sin 2\omega t + \cdots\cdots) \\ a &= r\omega^2(\cos\omega t - \frac{h}{l}\sin\omega t + \frac{r}{l}\cos 2\omega t + \cdots\cdots) \end{aligned} \quad (4)$$

There is the case of ignoring r/l and h in some mechanism. The design of the reciprocating cutter in this paper can ignore the impact of these three parameters.

The average speed V_p (m/s) of the cutter is obtained by dividing the integral of one of the reciprocating motion of the lateral speed by the required time and is expressed by the following equation:

$$v_p = \frac{2s \times n}{60} \quad (5)$$

$$H = v_m \times t = 30v_m / t \quad (6)$$

$$\lambda = v_p / v_m \quad (7)$$

where, S is the mean stroke of cutter, m; n is the mean number of reciprocating motion of the cutter per minute; v_m is the mean machine advancing speed, m/s; v_p is the mean cutting speed, m/s; t is mean the time for the cutter to complete a cutting cycle, s; H is mean the cutting distance, m; λ is mean the knife and machine speed ratio.

3.2.3 Kinematics simulation of reciprocating cutter mechanism based on ADAMS2013

The reciprocating cutter is driven by the eccentric shaft. The two parameters of affecting the speed of cutter are the eccentricity e and eccentric shaft speed n. First of all, under the conditions of the eccentric shaft rotation speed unchanged (n = 500 r/min), the eccentricity of e influence ability on the cutter speed was analyzed. Get some value within the eccentricity e±20% range. The ADAMS simulation results are shown in the following Figure 8.

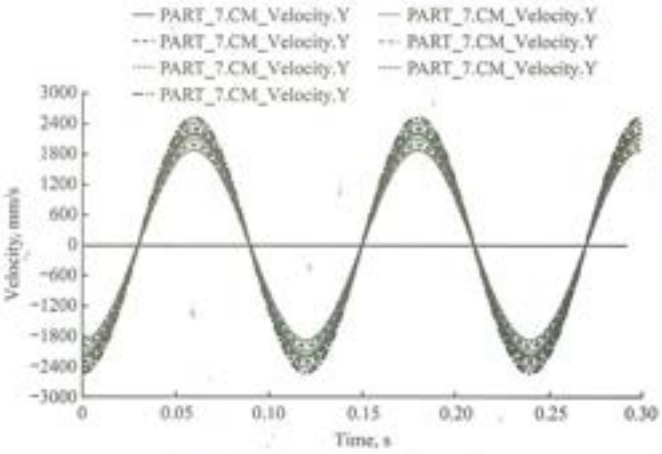

Figure 8 Tool speed-time graph

Although the change of eccentricity e can affect the cutting speed, the eccentricity e can also affect the size of displacement of the moving knife, since a single blade has a certain size. If the eccentricity e is too small, the shear action can't be completed; if choosing a larger eccentricity e, the arrangement of the machine shaft will become a new problem. Moreover, through the velocity-time simulation result, the velocity is less sensitive to the change of eccentricity e. Through the

choice of gear, different tractor engine speed can be obtained. Considering that the tractor engine speed can be changed with different operating speeds in work, so getting different cutting blade speed through changing the tractor engine speed had more practical significance and greater operation ability.

The result of the simulation of the different eccentric shaft speed is shown in the figure below.

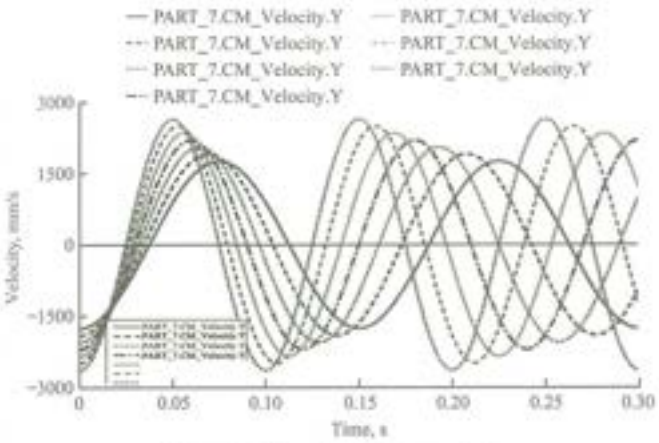

Figure 9 Tool speed-time graph

Figure 9 shows the simulation results in the range 500±100 r/min of eccentric shaft's rotation speed. It can be seen that the change of the shaft speed had a great influence on the cutting speed. Taking into account that the bigger shaft speed, the greater the vibration of the machine, and the part life and the cutting effect can also be affected. So the speed 500 r/min of the spindle speed was selected and the cutting speed at this time was above 1.2 m/s, which means that in a certain period, the speed of the cutter is greater than 1.2 m/s. Through the simulation analysis, when the speed of the eccentric shaft is 450-550 r/min, the potato stem can be cut off once.

By comparing the two simulation results, the effect of eccentricity on the speed of cutter is eliminated.

3.2.4 Draw the reciprocating cutting tool drawing based on the MATLAB7.0

The cutting effect of the reciprocating cutter is related to the blade and machine speed ratio λ. λ value is too large, the machine re-cut area is large; λ value is too small, leakage cut area is bigger and the stubble cutting height is irregular. The following Figure 10 shows the machine cutting plot in MATLAB when λ is 0.7, 1, 1.4. By plotting the cutting plot, it can be seen that the value of λ has a great influence on the cutting quality. For getting a better quality of work, the optimal value of the knife speed ratio λ need to be 0.8-1.2. By the presetting speed of the cutter linear velocity, the machine speed is calculated that is 4.2 to 6.3 km/h, which is within the selected machine operating speed range

Through the cutting chart of reciprocating cutter (Figure 10), it can be seen that in order to achieve better cutting quality, λ value range is generally 0.8-1.2. The following figure is the cutting plot in MATLAB. The relationship between the cutting effect of the reciprocating cutter and the λ speed ratio with the knife is obvious. If the λ value is too large, the re-cut area is too large; λ value is too small, the cut crop height is untidy and leakage cut area is too large. Through analysis, it is clear that the value of λ has a great influence on the cutting quality. And by plotting the cutting plot, it is possible to determine the optimum speed ratio λ, typically λ = 0.8 to 1.2. It can be calculated that the speed of the machine from the preselected line speed of 1.17-1.75 m/s. And the range 4.2-6.3 km/h is within the six selected machine operating speed ranges.

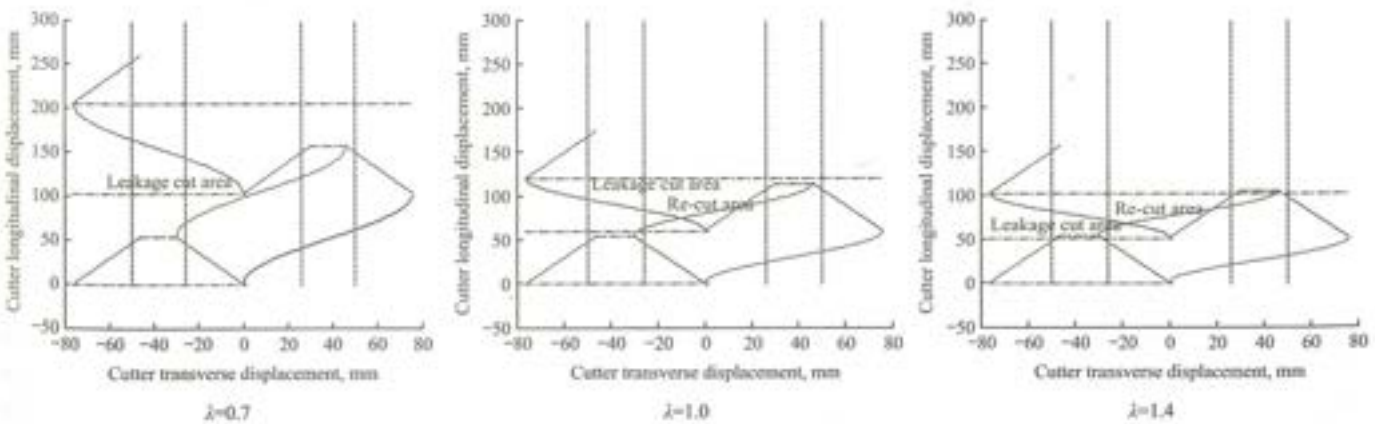

Figure 10 Reciprocating cutter cutting engineering drawing

4 Discussions

(1) In the two factors of influencing the moving knife's speed, the eccentricity was eliminated by analysis of ADAMS and the method of changing the speed of the moving knife by adjusting the speed of the spindle speed was obtained.

(2) Recycling mode of operation can improve the efficiency of potato seedling. Although the advantage of the recycling mode is not obvious for small plots of sweet potato planting, it puts forward new ideas for large-scale sweet potato planting operations in the future.

(3) Cutting cutter plate can cut longer potato seedlings and avoid potato wrapped around the rack, improve the work fluency and efficiency.

(4) The picking height of picking mechanical device should be higher than the height of ridge. It not only improves convenience in cutting seedling for the cutter, but also reduces the damage rate of sweet potatoes. For the method of reducing stubble height of potato seedlings, the design program is that adjust the rack height by human observation to ensure the smaller stubble height before the work of machine. This approach cannot adjust rack height based on ridge at any time and the cutting knife may come into the soil where the potato ridge is higher, which can cause damage to the cutter. Such defects can be solved by installing hydraulic control systems and monitoring devices, which can achieve adjustment of rack height at any time to ensure a small stubble height.

5 Conclusions

1) The existing problem that it is not suitable for sweet potato planting characteristic in seedling processing machinery was solved by the chain type of sweet potato recycling machine.

2) Three-dimensional design and virtual assembly of the chain type of sweet potato seedling recycling machine were carried out by Solidworks.

3) The parameters eccentricity e and eccentric shaft speed which influence the cutter speed are parametric design in ADAMS. The simulation results showed that the eccentric shaft rotation speed had a great influence on the cutting speed and the eccentricity e had little influence on the cutting speed. The speed of the eccentric shaft 450-550 r/min was also obtained when the seedling can be cut off at once.

4) Through MATLAB, the cutting plot is obtained. And the speed of the machine in line with the speed of the machine 4.2-6.3 km/h was got and can meet the machine operating speed requirements.

Acknowledgement

This work is supported by Foundation of Modern Agricultural Technology System Innovation Team Expert in Shandong Province (NO.SDAIT10-22-10).

[References]

[1] Ge, M., H. G. Jia, and B. Liu. 2011. Contact-impact analysis with clearance hinge in flexible multi-body system. *Yichang: Proceeding of the IEEE International Conference on Electrical and Control Engineering, 3406–3409.*

[2] Hou, J. L., T. Jiang, and Y. Q. Wu. 2014. Design and experiment of wheat straw cutting reciprocating test bench. *Transactions of the Chinese Society of Agricultural Machinery*, 2014(45): 101–105. (In Chinese with English abstract)

[3] Hu, L. L., G. P. Wang, and X. Y. Ling. 2015. Mechanical properties of sweet potato vine and stalk during harvest. *Transaction of the Chinese Society of Agricultural Engineering*, 31(9): 45–49. (In Chinese with English abstract)

[4] Hu, L. L., L. J. Tian, and F. L. Ji. 2011. Analysis and discussion on the restriction causations for harvesting mechanization of sweet potato in China. *Chinese Agricultural Mechanization*, 2011(3): 16–18. (In Chinese with English abstract)

[5] Hu L. L., L. J. Tian, and F. L. Ji. 2014. Research on the working mode of sweet potato production mechanization. *Journal of Chinese Agricultural Mechanization*, 35(5): 165–168. (In Chinese with English abstract)

[6] Hu, L. L., Z. C. Hu, and Y. Z. Xie. 2011. Study on the route of mechanization of sweet potato (ipomoea batatas lam.) production technology in China. *Chinese Agricultural Mechanization*, 2011(6): 20–25. (In Chinese with English abstract)

[7] Liu, Z. L., X. D. Zhang, and X. Zhang. 2012. Analysis process of grabing corn seed of vertical disc air- suction metering device. *Journal of Agricultural Mechanization Research*, 2012(7): 73–77. (In Chinese with English abstract)

[8] Luan, G. D., Q. W. Sun, and Y. Y. Wang. 2014. Design and test of clamping and collection device of 2 ridges and 4 lines peanut combine harvester. *Journal of Agricultural Mechanization Research*, 2014(1): 132–135. (In Chinese with English abstract)

[9] Ma, B., L. L.Hu, and L. Y. Xu. 2013. Status about sweet potato planting and its production machinery in China. *Journal of Chinese Agricultural Mechanization*, 34(1): 42–46. (In Chinese with English abstract)

[10] Ma, J. F., J. H. Cheng, and J. Wang. 2012. The development of sweet potato industry at home and abroad. *Journal of Jiangsu Agricultural Sciences*, 40(12): 1–5. (In Chinese with English abstract)

[11] Pfeiffer, F., and C. Glocker. 2000. Contacts in multibody systems. *Applied Mathematics and Mechanics*, 64(5): 773–782.

[12] Shen, C., X. W. Li, and B. Zhang. 2016. Bench experiment and analysis on ramie stalk cutting. *Transactions of the Chinese Society of Agricultural Engineering*, 32(01): 68–76. (In Chinese with English abstract)

[13] Shi, Z. H., L. L. Hu, and N. Wu. 2015. Potato and sweet potato planting and its harvest machinery. *Journal of Agricultural Mechanization Research*, 2015(4): 263–268. (In Chinese with English abstract)

[14] Song, Z. H., H. L. Song, and Y. F. Yan. 2016. Optimizing design on knife section of reciprocating cutter bars for harvesting cotton stalk. *Transactions of the Chinese Society of Agricultural Engineering*, 32(6): 42–49. (In Chinese with English abstract)

[15] Xia, P., S. Yin, and L. Q. Chen. 2007. Numerical simulation of cutting pattern of a reciprocating cutter. *Transactions of the Chinese Society of Agricultural Engineering*, 38(3): 65–68. (In Chinese with English abstract)

[16] Xu, X. Y., W. Q. Zhang, and H. M. Yang. 2011. Design and kinematic analysis of double-acting cutting device of walk-type pasture reaper. *Transactions of the CSAE*, 27(7): 156–161. (In Chinese with English abstract)

[17] Yang, R. B., H. G. Yang, and S. Q. Shang. 2016. Design and test of poking roller shoving type potato harvester. *Transactions of the Chinese Society of Agricultural Machinery*, 47(7): 119–126. (In Chinese with English abstract)

[18] Yang, R. B., Y. B. Fan, and S. Q. Shang. 2016. Design and experiment of twice-receiving device on 4HBL-2 peanut combine. *Transactions of the Chinese Society of Agricultural Machinery*, 47(9): 114–120. (In Chinese with English abstract)

[19] Yang, S. C., Y. W. She, and S. M. Yang. 2005a. Computation numerical value about three regions' area in cutting graph by using MATLAB. *Journal of Agricultural Mechanization Research*, 2005(5): 66–67. (In Chinese with English abstract)

[20] Yang, S. C., Y. W. She, and S. M. Yang. 2005b. The influence from the speed of harvester to triangle area on incise diagram. *Journal of Agricultural Mechanization Research*, 2005(3): 114–116. (In Chinese with English abstract)

[21] Zhang, Y. N., Y. Y. Shi, and X. C. Wang. 2016. Design on flexible clamping-conveying mechanism of orderly harvester for stems-leafy vegetable. *Journal of Chinese Agricultural Mechanization*, 37(9): 48–51. (In Chinese with English abstract)

[22] Zhang, Z. L., Z. D. Han, and S. J. Li. 2016. Simulation and test on straw cutting and clamping device of corn combine harvester for stalk and ears. *Transactions of the Chinese Society of Agricultural Machinery*, 2016(47): 215–221. (In Chinese with English abstract)

Design and dynamic response analysis of rope laying system of roped type rice direct seeding machine

Zhang Baofeng, Song Yuqiu, Wu Liyan, Xin Mingjin, Ren Wentao*

(*College of Engineering, Shenyang Agricultural University, Shenyang 110161, China*)

Abstract: Rope laying mechanism is one of the important parts of roped type rice direct seeding machine. In order to solve the problems of breakage and loosening of seed rope during rope laying of the roped type rice direct seeding machine, a kind of rope laying mechanism composed of a rope disk, guiding wheels and a furrow opener was designed in this paper. The mechanism lays the rope by applying the friction between the rope and the soil. A simulation test of the rope laying system was carried out based on the Adams/Cable module for the first time to study the effect of wrap angle and the relative positions of the guide wheel on rope laying tension. The results showed that the smaller the wrap angle of the guiding wheel was, the less the rope tension would become. The validity of the simulation was proved by rope laying experiments and force analysis on the seed rope and the wheels. The minimal rope laying tension was obtained when the wrap angle of the bottom guiding wheel was 45°. Step response test showed that the rope laying system could satisfy the characteristics of first-order inertia process, and its amplification coefficient was 1.148, time constant was 0.174 s. Dynamic response analysis proved that the designed rope laying system could meet the design requirements and provide theoretical basis for design of roped type rice direct seeding machine and other related machinery.

Keywords: direct seeding of rice; rope laying system; simulation test; dynamic response

Citation: Zhang, B. F., Y. Q. Song, L. Y. Wu, M. J. Xin, and W. T. Ren. 2017. Design and dynamic response analysis of rope laying system of roped type rice direct seeding machine. International Agricultural Engineering Journal, 26(3): 120–129.

1 Introduction

Roped type direct seeding technology was first applied in western countries and it was mainly aimed at small seed crops such as vegetables (Lerink, et al., 2005; Henrik, 2006; Deppermann, et al., 2011; Deppermann et al., 2013). It was brought to Asia in 1961 and Nippon Company in Japan and Kon in Korea studied this technology (Kon, 1982; Park, 1986). The roped type rice direct seeding technology was first proposed by Ren (2005), and some related experimental researches were carried out and proved it is practical, seeds saving and more economical than normal direct seeding (Lv et al., 2008; Lv, 2008; Ren et al., 2009; Lv et al., 2010; Han, 2016; Zhang, et al., 2017; Lv, 2017). After developing several generations of sample machine, the roped type rice direct seeding machine mainly includes the following sections: ditching system, rope laying system, compacting system and soil covering system. As one of the key steps in roped type direct seeding, the rope laying system mainly guides seed rope disk to ditch stably based on the preset trajectory. In the process of rope laying, the rope should have good consistency and not easy to break and loosen, because the reliability of the rope laying system determines seeding quality. Zhang et al. (2006) designed a manual roped type rice direct seeding machine which rope laying device is driven by storage battery powered electric motor which is a kind of active rope laying system. The roped type rice direct seeding machine designed by Wang and Shang (2012) guided the seed rope to the field through a rope pipe. Song et al. (2014) designed a kind of automatic rope laying device, which can realize automatic rope laying by joint work of guiding pipe, rope pressing wheels and ditch pressing wheels. The mechanism can solve the problem of rope pressing by manpower and raise the rope laying efficiency, and has high demand on the

Received date: 2017-07-13 **Accepted date:** 2017-09-10
Corresponding author: Ren Wentao, Ph.D., professor, College of Engineering, Shenyang Agricultural University, 110866, China. Email: rwtsyau@sina.com

quality of tillage land. Zhu (2017) put forward a kind of seed rope and a plant method by putting the finished seed rope into the furrow and covered it with soil.

In conclusion, there are many researches on the related technologies and equipment of roped type rice direct seeding; however, there are few researches on dynamic response characteristics of rope laying system. Moreover, there are no researches on the effect of guiding angle and the relative position of guiding wheel on the rope laying tension. For the present roped type rice direct seeding machine, a direct connection was applied generally between the rope disk and rotating shaft, therefore, unstable friction occurs during seeding. In seed rope laying process, if the damping of the system is too high, the rope tension will be increased; besides, the inappropriate rope guiding mechanism may also lead to high tension on the rope. When rope tension increases to an ultimate value, the rope will break. Normally, rope breakage takes place at the start of working. Besides, if the damping of the system is too small, when the seeding machine stops, the rope disk may continue rotating for a period influenced by inertia, and the rope would be too long and become very loose so that it may affect seeding. To solve the existing problems of the rope system, a simulation test was made on the rope laying system of the seeder and rope tension under different guiding angles and penetration angles based on the Adams/Cable module and manually operated roped type rice direct seeding machine (Guo et al., 2016; Zhang et al., 2017). After verification tests on the module, the optimal parameters of the rope were determined. After step response test on the rope laying system, the rope laying system were determined to test if they could meet the design requirement (Kang, 2016). The study can offer reference to function improvement for roped type rice direct seeding machine.

2 Design of rope laying system and static force analysis of seed rope

The rope laying system can be divided into two types in terms of power sources: active rope laying system and passive rope laying system. However, there are cases when the seed rope is too long or too short and affect seeding, therefore, the rope laying method was changed to passive rope laying in newly designed machine (Ren, et al.,2014; Lv, 2017). Aiming at solving the problems in rope laying at present, the rope laying system proposed in this paper has the following design requirements: 1) the system should be simple enough and the maximum tension in the rope laying process should be as small as possible and less than the limit tension of the rope; 2) After the seeding machine stops, the rope length should be not more than 15 cm. The seed rope needs to have good continuity, should not broke and slacken. In this paper, a two-stage rope guiding mechanism was adopted in the system, it was mainly composed of a rope disk, guiding wheels a and b, as is shown in Figure 1. The rope reached ditch through guiding wheels a and b. After covering with soil, there was friction between the rope and soil. When the seeder walked ahead, influenced by the friction, the rope disk rotated and laid the rope.

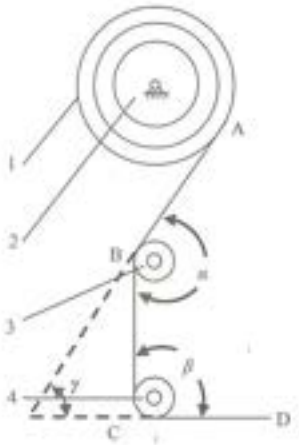

1. Seed rope 2. Rope disk 3. Guiding wheel a 4. Guiding wheel b

Figure 1 Structure of the rope laying system

The force analysis on seed rope and guiding wheel a was shown in Figure 2. A small section of seed rope *ds* on the wheel was randomly selected, and force analysis was done by microelement method. The width of the center angle of *ds* is $d\theta$, and the tensions at the two ends were T and $T + dT$, the elasticity between the rope and the wheel is dN, the sliding friction is df, and the weight of the rope is small and can be ignored, and the gravity on *ds* is not taken into consideration. Based on balance of forces, and:

$$(T+dT)\cos\frac{d\theta}{2} = T\cos\frac{d\theta}{2} + df \tag{1}$$

Since θ is very small, thus $\cos\frac{d\theta}{2} \approx 1$, and substitute it into Equation (1) and:

$$dT = df$$

Integrate two sides of the equation and get:

$$\int_0^\theta dT = \int_0^\theta df \tag{2}$$

That is:

$$T_{BC} - T_{AB} = \int_0^\theta df = f_1 \tag{3}$$

$$f_1 = \mu \cdot N \tag{4}$$

$$N = (T_1 + T_2) \cdot \sin\frac{\theta}{2} \tag{5}$$

Equations (3), (4) and (5) show that, the smaller θ is, the smaller the friction between seed rope and guiding wheel would be. When the angle of the guide rope is constant, the larger the diameter of the guide wheel is, the bigger the arc length of guiding wheel of the rope round. Therefore, the sliding friction will increase. Besides, the rotational inertia of bigger guiding wheel is bigger, and needs to be driven by larger friction. Therefore, the diameter of the guide rope wheel designed in this paper is 15 mm. The vertical distance of guiding wheels a and b is the height of furrow opener curve, which is 100 mm. The guiding wheels a and b were placed on the same vertical line in the initial design, and the position parameters were optimized by experiment.

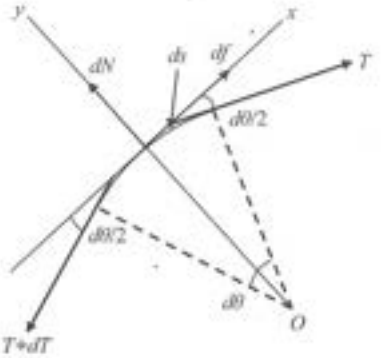

Figure 2 Force analysis of seed rope

3 Materials and method

3.1 Simulation test of rope laying based on Adams/Cable

3.1.1 Establishment of the test model

The simulation of the rope laying systems was carried out with Adams/Cable and the seed rope was simplified as a uniform cable. Since the rope weight per unit length was very small, and there was no need to study the swaying status of the rope, the "simplified" method in rope generation method was adopted in the simulation. In order to simplify the calculation model, only a two-dimensional force analysis was made on the rope laying system, and the axial translation of rope disk was not taken into consideration. In building the rope laying model, two fixed pulleys were used to represent guiding wheels a and b; two dummy balls represented the starting and end points of the rope laying mechanism, which were set at the center points of the two dummy balls.

The full-load diameter of the rope disk was 240 mm, no-load diameter of 80 mm, and the changing length of the radius of 80 mm. Since the diameter of the rope disk would decrease in laying rope, in order to simulate this change, a certain horizontal velocity v_0 was exerted on the dummy ball, and the rope laying speed was controlled by applying the winch order. A horizontal constant force F was exerted on the dummy ball at the end point to simulate the friction between the soil and seed rope. The simplified model of rope laying system is shown in Figure 3.

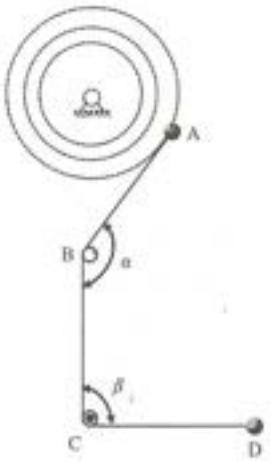

Note: A. Starting point of rope laying; B. Guiding wheel a; C. Guiding wheel b; D. Pulling end.

Figure 3 Model of rope laying system

3.1.2 Test method

In seeding, there are two types of motion between guiding wheels and seed rope: sliding and rolling, therefore, "Fixed" pully type was adopted to simulate the sliding movement between the seed rope and guiding wheels, and "revolute" pully type was adopted to simulate the rolling movement between seed rope and guiding wheels. Simulation parameters are shown in Table 1. Taking rope laying speed, type of guiding wheels as test variables, pulling force on rope as the test index, six groups of tests were carried out and each group of tests were repeated for five times.

Table 1 Parameter settings of seed rope laying simulation

Constraints and driving settings		Parameter settings of seed rope and guiding wheels	
Related components	Constraint type (parameters)	Friction coefficient	0.3
Rope laying end and ground	Horizontal sliding pairs	Critical contact velocity, mm/s	5
Pulling end and ground	Horizontal sliding pairs	Contact rigidity	1E4
Gravity	Closed	Type of guiding wheels	Fixed, Revolute
Rope laying speed, mm/s	300, 500, 700	Carrier of guiding wheels	Ground
Pulling force, N	10	Rope type	Simplified
Speed of rope laying end, mm/s	10	Simulation time, s	15

Note: In order to get the changing trend of the forces on the rope, the rope laying speed in the simulation test is higher than the speed of radius reduction of rope disk in practical work.

3.2 Test of tension in rope laying

3.2.1 Test materials

Test instruments and equipment are as following: (1) Rope tension collection system: a) QLYS-type tension sensor and QL-BSQ-8-type transmitter with measuring range of 0-50 kg, precision of 0.1%, the input voltage is direct current 24 V, which are produced by Qi Li sensor systems engineering co. LTD in Bengbu; b) 24 V power pack; c) JKU12 Data Acquisition Card which produced by Labjack company in USA; d) software program of a dual channel storage oscilloscope; (2) Testing device of pulling speed: ultrasonic distance measuring sensor US-100 which was produced by Yongye electronic technology co. LTD in Shenzhen; b) Arduino development board; c) SD card Module; (3) Testbed for rope laying system; (4) Rope disk; (5) Computer. The distance measuring range of the ultrasonic sensor is 0.024.5 m, input voltage is 2.4-5.5 V, quiescent current is 2 mA, working temperature is –20°C-70°C with temperature compensation function.

The design of rope laying system testbed: the testbed is composed of a body frame and moveable guiding wheels. The size of the testbed is 400×400×1500 mm. The rope disk is fixed at the top of the testbed through wheels and axles, and the guiding wheels a and b can move horizontally.

3.2.2 Test method

In order to test the impact of rope laying speed and angle on rope tension, rope guiding angle α and rope laying speed v were adopted as test variables, rope tension T was adopted as test index for a single-factor test, the test system and test scheme are shown in Figure 4. Refer to Figure 1, the position of guiding wheels a and b was adjusted to keep α was 180°, 165°, 150°, 140°, 135° respectively and β should be kept at 90°. When α = 180°, only the guiding wheel b was used for rope guiding. One end of the rope was connected in series with the tension sensor, the other end was connected with the ultrasonic sensor. After setting the initial position, a vertical baffle was placed at 2.4 m from the initial position for ultrasonic positioning. The rope laying speed was measured indirectly by the ultrasonic sensor; the sampling frequency of rope tension test system was 200 Hz. Since the rope was pulled by hands, the traction speed cannot be controlled with precision, therefore for each test, a period with stable speed was selected for rope tension analysis, and each test was repeated three times.

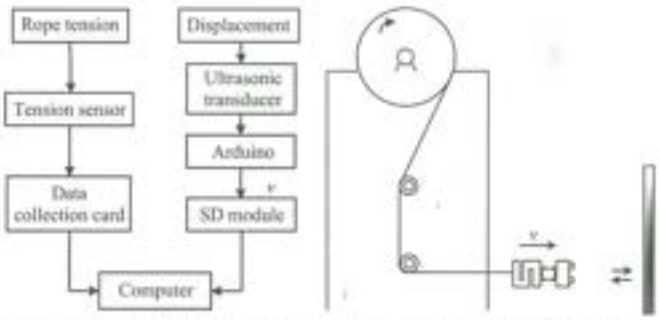

a. Seed rope tension test system diagram b. Connection diagram of the system

Figure 4 Seed rope tension test system diagram and connection diagram

Data processing: data processing was done by Excel 2007, then SPSS19 was used for statistical analysis, and Duncan method was used for significance testing, with significance level α=0.05.

3.3 Optimization test of rope laying system

3.3.1 Test model

Test model is the same with that in the rope laying simulation test.

3.3.2 Test plan

Figure 1 shows that:

$$\alpha+\beta=\pi+\gamma \tag{6}$$

The radius of the rope disk changed slowly in seeding, thus γ was regarded as a constant value in a short period of

time, namely section AB on the seed rope kept its position and the sum of α and β was a constant value. The test scheme and parameter settings are shown in Table 2 and Table 3, where, α varies within the range of 60°-180° along with the movement of guiding wheel b.

Table 2 Test scheme

Test variables		Test indexes
γ	45°, 60°, 75°, 90°	T_{AB}
α	60°-180°	

Table 3 Parameter setting of rope laying simulation test

Constraints and driving settings		Parameter settings of seed rope and guiding wheels	
Related components	Constraint type (parameters)	Friction coefficient	0.3
Rope laying end and ground	Fixed	Critical contact speed, mm/s	5
Rope laying speed, mm/s	100	Contact rigidity	1E4
Guiding wheel b and the ground	Horizontal sliding pairs	Type of guiding wheels	Fixed
Moving speed of guiding wheel b, mm/s	15	Carrier of guiding wheels	Ground
Pulling end and ground	Horizontal sliding pairs	Rope type	Simplified
Pulling force, N	10	Simulation time, s	15

3.4 Dynamic response analysis test of the rope laying system

3.4.1 Test materials

Instruments and equipment: (1) rope tension collecting system: (the same with the above). (2) Testing system of rotating speed; a) Hall sensor; b) Arduino development board; c) SD Module; d) Button magnet, diameter d = 6 mm; (3) Test bed for rope laying system; (4) Rope disk; (5) 1 kg weight; (6) Computer.

3.4.2 Test method

In this paper, step response characteristics were applied to study the rope laying system. The step response curve of the inertial element is an ascending curve of exponential function (Yang et al., 2016; Kang et al., 2016), which can be expressed by:

$$y(t) = Kx_0(1 - e^{-t/T_c}) \quad (7)$$

Pretreatment of input signal: the input signal is a step function: $x(t)=x_0\times 1(t)$. Therefore, a weight of 1 kg was used in the test to give a constant excitation $F_0(t)$ to the system under the influence of gravitational force as system input.

Output signal collection: the output signal of the rope laying system is rope laying speed, namely, the rotating speed of rope disk, $\omega(t)$. The test used Hall sensor to measure the rotating speed of rope disk. The sensor moved in a circular motion (R=100) at one end face of the rope disk, with the same center with the rope disk. The circumference was divided into 24 equal parts, and a button magnet with a diameter of 6 mm was put on each knot, as is shown in Figure 5b. Then a Hall sensor was installed on the corresponding position on the testbed to receive electromagnetic signals and transmit the signals into the Arduino motherboard. Based on the equation $\omega(t) = \frac{\pi}{12t}$, the instantaneous angular velocity could be obtained, and signals of rotating speed were recorded into PC. The block diagram of signals of rotating speed and the connection diagram are shown in Figures 5a and 5c.

a. Block diagram of rotating speed signals

b. Rotating speed collection system for rope disk

c. Rope laying test system

Figure 5 Dynamic response measurement system of seed rope

4 Results and discussion

4.1 Results and discussion of the rope laying simulation test

In the simulation test, in order to find out the position parameters of the guiding wheels at minimum rope tension, the pulling force at the rope end point was 10 N, and when the force on the starting point approximated to 10 N, the energy loss became less under such condition. Suppose that the minimum force that drives rotating of the rope disk was a constant, then the seeder could lead to minimum rope tension under such condition. The simulation results are shown in Figure 6. When there was sliding movement between the rope and guiding wheels, the tension on each section on the rope changed, and the section CD had the maximum tension, which was equal to the pulling force of

10 N; the tension of section BC was 6.4 N; the tension on the section AB was the minimum, but the tension on section AB increased linearly, and when the simulation came to an end, the tension on section AB was near to that of section BC, as is shown in Figure 6a. When there was only rolling between the seed rope and guiding wheels, each section on the rope was the same and equal to the pulling force, as is shown in Figure 6b, namely the pulling forces from both sides of the pulley were equal to each other. The reason was that, the starting point A of the rope had a horizontal-left speed, when α increased gradually, the wrap angle of guiding wheel a decreased gradually, and the friction between the rope and the guiding wheels also reduced, resulting in gradual increase of rope tension on section AB, but the wrap angle of guiding wheel b didn't change with time, so the tension on sections BC and CD kept constant. By ignoring the weight of seed rope, rope disk and guiding wheels, the rope laying speed didn't influence rope tension, since the sliding friction between the seed rope and guiding wheels was irrelevant to speed.

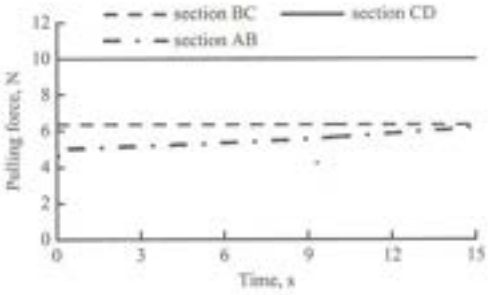

a. Tension on each section in sliding movement between seed rope and guiding wheels

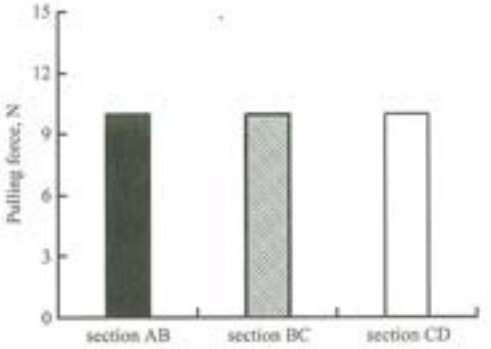

b. Tension on each section in rolling movement between seed rope and guiding wheels

Figure 6 Simulation results on rope tension

4.2 Results and discussion of the rope tension test

In order to test the validity of the rope tension test, a rope tension test was done on the solid model of the rope laying system. The measured tension was the tension on the section CD in Figure 1. The decrease of the tension on section CD in the rope tension test and the increase of tension on section AB in the simulation test are the same kind of conclusion. The results of rope tension test are shown in Figure 7. When α=180°, the tension value was the lowest. With the decrease of α, rope tension increased, showing that with the increase of wrap angle α of the guiding wheel a, the rope tension also increased in rope laying. The variance analysis showed that, $T_{a1}$was significantly lower than T_{a5} (P<0.05), which was in line with the simulation test. Figure 7b shows the influence of rope laying speed on rope tension, where, Tv_5 is the maximum. But the variance analysis shows that, the differences among Tv_1, Tv_2, Tv_3, Tv_4, Tv_5 were insignificant, showing that the influence of rope laying speed on rope tension was also insignificant. This is in line with the influence trend of the rope laying speed on rope tension. The simulation test of rope laying based on Adams/Cable was proved to be effective.

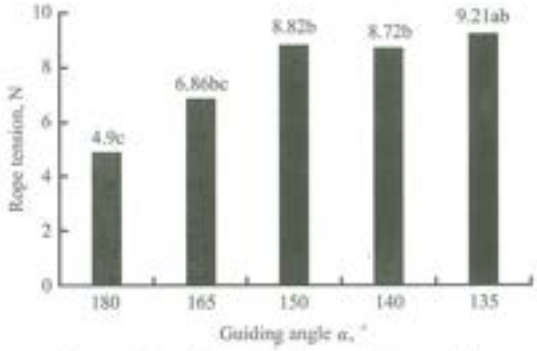

a. Rope tension at different guiding angles in rope laying

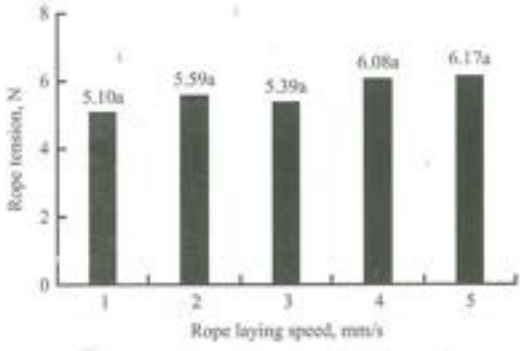

b. Rope tension at different rope laying speed

Figure 7 Results of seed rope tension test

4.3 Results and discussion of the rope laying structure optimization test

Based on the analysis above, the influence of the value of α and β on the friction between seed rope and guiding wheel is: the larger the angle between the seed ropes on

both sides of the guiding wheel, the smaller the friction is. Another simulation test of rope laying system was performed to optimize the position relationship of guiding wheels and the seed rope with a minimum friction between them. As is shown in Figure 8, with different γ angles, the tensions of section AB had the same shapes of curves, which went up with the increase of the wrap angle of guiding wheel a, and the tension of section AB reduced before an increase. This illustrates that when γ keeps constant, there was an optimum position to reach the maximum tension of section AB of the rope in simulation, in other words, the rope tension was the minimum in working. Besides, with the increase of the angle γ, the maximum value of AB section of the rope was also increasing gradually.

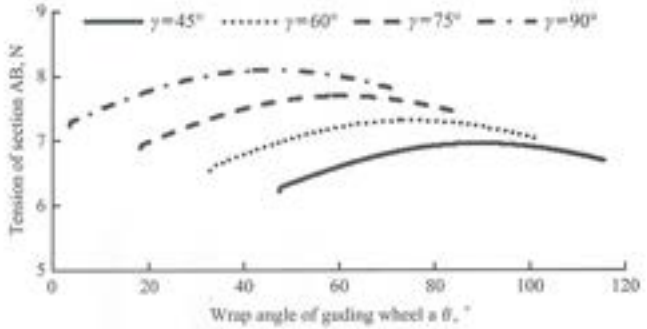

Figure 8 Comparison of simulation test results

θ_{a1} - θ_{a4}, θ_{b1} - θ_{b4} were used to represent γ=45°, γ=60°, γ=75°, γ=90°, which were the wrap angles of guiding wheel a when the section AB of the seed rope had the maximum tension, and:

$$\begin{cases} \theta_{a1} = 89.12° \\ \theta_{a2} = 74.80° \\ \theta_{a3} = 60.29° \\ \theta_{a4} = 45.25° \end{cases}$$

Substitute them into Equation (6) and get:

$$\begin{cases} \theta_{b1} = 45.88° \\ \theta_{b2} = 45.20° \\ \theta_{b3} = 44.71° \\ \theta_{b4} = 44.75° \end{cases}$$

For different γ angles, when section AB of the seed rope had the maximum tension, the wrap angles θ_a were different for the guiding wheel a, but the wrap angles of guiding wheel b were almost the same, at about 45°, showing that in the simulation test, for any values of γ angle, when the wrap angle θ_b of the guiding wheel b was about 45°, the AB section of the seed rope had the maximum tension. After rounding off the value, the following can be got:

$$\theta_b = 45°$$

Namely,

$$\beta = 180° - \theta_b = 135°$$

At this time the rope tension was the minimum, based on the optimized result of the curve of the furrow opener blade (Zhang et al., 2017), the overall structure of the rope-guided furrow opener is shown in Figure 9.

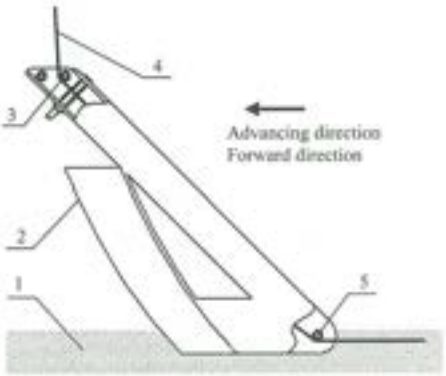

1. Soil 2. Blade of furrow opener 3. Guiding wheel a 4. Seed rope 5. Guiding wheel b

Figure 9 Structural diagram of rope-guided furrow opener

4.4 Results and discussion of the dynamic response test

4.4.1 Establishment of the transfer function model of the rope laying system

Set system input as rope tension of AB section in Figure 1, and system output as rotating speed of the rope disk, the rope disk diameter R reduced with seeding, thus the rotary inertia of the rope disk J would also change with time. According to moment of momentum theorem, the differential equation of the rope laying system was obtained:

$$F(t)R(t) = c\omega(t) + J(t)\dot{\omega}(t) \quad (8)$$

where, F(t) is the tension of AB section of the rope, N; $\omega(t)$ is the rotating speed of the rope disk, rad/s; R is radius of rope disk, m; J is rotary inertia of the system, kg·m^2; c is the equivalent coefficient of friction of the system, Nm/rad·s^{-1}.

Equations (8) show that, the differential equation is first order differential equation with variable coefficient, which is corresponding with linear time-variant system (Yang, 2016). Considering that the radius and weight of the rope disk would not change greatly, therefore the

model was simplified to first order differential equation with constant coefficients:

$$F(t)R = c\omega(t) + J\dot{\omega}(t) \tag{9}$$

Then the Laplacian transformation was applied on Equation (9) and the transfer function of the rope laying system that taking rope tension as input and rotating speed of rope disk as output was obtained:

$$G(s) = \frac{W(s)}{F(s)} = \frac{R}{c + Js} \tag{10}$$

Let $K = \frac{R}{c}$, $T_c = \frac{J}{c}$, and Equation (10) can be changed to:

$$G(s) = \frac{W(s)}{F(s)} = \frac{K}{1 + T_c s} \tag{11}$$

Equation (11) shows that, the rope laying system was in line with the first-order inertia link, K was amplification coefficient of the system and T_c was the time constant.

4.4.2 Determination of system parameters

The step response curve of the rope laying system is shown in Figure 10a, by applying the fitting tool Matlab/cftool (Xie, et al., 2012; Lin, et al., 2016), and taking Equation (7) as the theoretical regression equation, and the fitting result was obtained, as is shown in Figure 10b. Therefore, the step response equation of the rope laying system is:

$$y = 1.148x_0\left(1 - e^{-\frac{t}{0.174}}\right) \tag{12}$$

where, the confidence interval was 95%, regression coefficient R^2=0.92, showing a high fitting degree, namely K=1.148, T_c=0.174, thus the transfer function of the system is:

$$G(s) = \frac{W(s)}{F(s)} = \frac{1.148}{1 + 0.174s} \tag{13}$$

When the rope disk was fully loaded, it has greater rotary inertia, therefore, if the fully-loaded rope disk can meet design requirements, the rope laying system can also meet the design requirements, so checking calculation was done according to the size of the rope disk when it was fully loaded. According to rope tension, and:

$$T_{max} = \text{MAX}\{T_{AB}, T_{BC}, T_{CD}\} < [T] \tag{14}$$

where, T_{max} was the maximum tension of the seed rope, N; T_{AB}: tension of AB on the rope, N; T_{BC}: tension of BC on the rope, N; T_{CD}: tension of CD on the rope, N; $[T]$: maximum permissible stress of the rope, N.

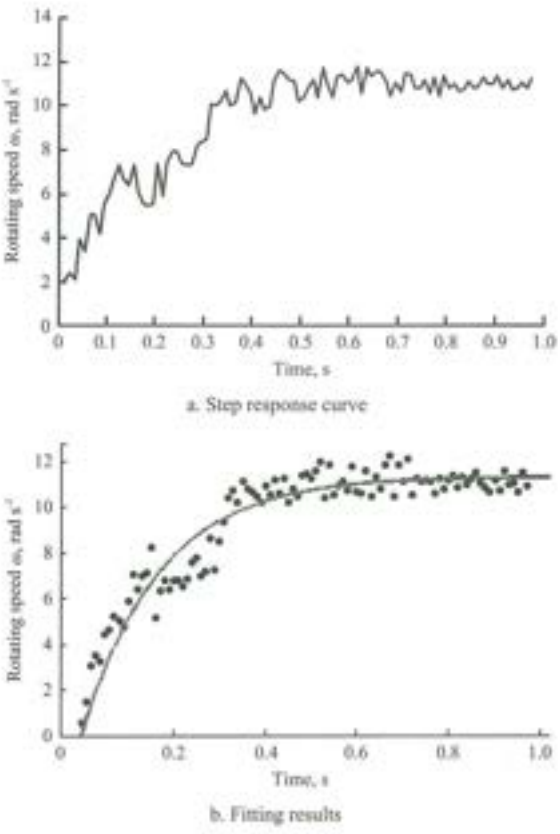

a. Step response curve

b. Fitting results

Figure 10 Result of the step response test

The seed rope pulling test shows that when it broke, the rope tension was influenced by the twist number in unit length, and the variation range was 27-43 N. It can be obtained by the simulation test that:

$$\text{MAX}\{T_{AB}, T_{BC}, T_{CD}\} = T_{CD} = T_{AB} + f_1 + f_2 \tag{15}$$

where, f_1, f_2 are the frictions between the seed rope and guiding wheel a and b respectively, N. The average advancing velocity of the manpower roped type rice direct seeding machine was set as v_0=0.8 m/s, and the angular velocity $\omega = v_0/R$=6.67 rad/s. The Laplace transform of the transfer function showed that, the rope tension of section AB of the rope at this time was about 5.8 N. Besides, the frictional resistance on the rope made by the optimized guiding wheel was about 2 N, and T_{max}=5.8+2=7.8 N < $[T]$, showing that no rope breakage would occur and the system could meet the design demand.

After the seeder stopped going forward, it can be regarded that the seed falling length could meet the law of uniformly retarded motion.

$$x = \frac{1}{2}v_0 t \tag{16}$$

where, x is length of the falling rope, m; v_0 is the advancing speed of the seeder, m/s; t is the time for rope disk to stop working, s.

The rope laying system demands that the rope falling length x should not exceed 15 cm after the seeder stops moving forward, and substitute it into Equation (16) and get t=0.375 s, showing that within 0.375 s after the seeder stopped moving forward, the rope disk stopped working, and could meet the design requirements. And the time constant of the rope laying system T_c=0.174<t. In conclusion, the rope laying system can meet the design requirements.

5 Conclusions

1) In this paper, a kind of rope laying device composed of a rope disk, guiding wheels a and b was designed, and the device could realize synchronous rope laying by the friction between soil and the seed rope in soil.

2) Based on Adams/cable module, a simulation test was made on the rope laying system. The simulation results and theoretical analysis proved the significant influence of position of guiding wheels on rope tension, and the smaller the wrap angle of the guiding wheel is, the smaller the frictional resistance is, and the more rope tension was reduced in rope laying; rope laying speed had no influence on rope tension proving the effectiveness of the simulation analysis.

3) By applying the simulation analysis result and taking the rope guiding angle and wrap angle of the guiding wheel as test variables, the position relationship between rope disk and guiding wheels when the rope tension was the minimum during rope laying was obtained. When the angle γ between seed rope and the horizontal direction kept constant, the rope tension was the smallest when the wrap angle of the guiding wheel b was 45°, and on this basis, the position of guiding wheel b was adjusted to ensure the wrap angle was 45° in rope laying.

4) Through analytical method, the transfer function model of the rope laying system was determined as the first-order inertia mode. Through the step response test, the amplification coefficient of the transfer function of the system was determined as 1.148 and the time constant was 0.174. After considering design requirements and checking, the time for rope disk in stopping working Tc was less than the the required time t in design, the maximum tension of the rope T_{max} was less than the rope limit tension[T], indicating that the system could meet the design requirements.

The symbols in this paper are as follows:

α: the angle between sections AB and BC on the rope, degree;

β: angle between section BC and horizontal direction, degree;

γ: angle between section AB on the seed rope and vertical direction, degree;

F: external force in rope laying simulation, N;

v: rope laying speed, mm/s;

$T_{\alpha i}$: tension of section AB on the rope when dealing with the i-th α, N;

T_{vi}: tension of section AB on the rope when dealing with the i-th$v$, N;

T_{max}: the maximum tension of the seed rope, N;

T_{AB}: tension of section AB on the rope, N;

T_{BC}: tension of section BC on the rope, N;

T_{CD}: tension of section CD on the rope, N;

[T]: maximum permissible stress of the rope, N;

$\omega(t)$: rotating speed of the rope disk, rad/s;

K: amplification coefficient;

T_c: time constant of the system;

f_i: friction between the i-th rotary pipe and rope, N;

μ: coefficient of dynamic friction;

θ: wrap angle of the guiding wheel, degree;

θ_{ai}: wrap angle of the guiding wheel at the i-th γ treatment when the tension of AB section reaches maximum, degree;

θ_{bi}: wrap angle of the guiding pipe b at the i-th treatment when the tension of AB section reaches maximum, degree;

x: length of falling rope, m;

v_0: advancing velocity of the seeder, m/s;

t_s: time of stopping the rope disk, s;

R: radius of rope disk, m;

J: rotary inertia of the system, kg*m^2;

c: equivalent friction coefficient of the rope laying system, Nm/rad·s^{-1}.

[References]

[1] Deppermann, K. L., B. J. Forinash, T. Frey, and M. Mcnabnay. 2011. Seed tape planter. WO Patent 2011/119391 A1, filed 2011-03-16, and issued 2011-09-29.

[2] Deppermann, K. L., J. F. Brian, F. Travis, and M. Marcus. 2013. US Patent 2013/0152836 A1, filed and issued 2013-7-20.

[3] Guo, W., S. Li, and L. Ma. 2016. ADAMS 2013 Advanced application tutorial with Examples. *Beijing: China Machine Press*.

[4] Henrik, A. P. 2007. A germinating unit as well as a seed tape including several of such germinating units successively arranged. WO Patent 2007/065436A1, filed 2006-12-30, and issued 2007-06-14.

[5] Han, S. 2016. Improved design and Experimental Study on rice seed rope direct sowing machine. D.S. thesis, Shenyang Agricultural University.

[6] Kang, J., S. Li, X. Yang, L. Liu, and R. Zhu. 2016. Virtual simulation and power test of rotary ditcher based on multi-body dynamics. *International Agricultural Engineering Journal*, 4(25): 57–64.

[7] Kon, Y. 1986. Perforated seed tape. NZ Patent 201634A, filed and issued 1986-05-09.

[8] Lerink, P., and J. Wondergen. 2005. Device for planting seed(ling) tape. WO Patent 2005/72508 A1, filed 2005-01-26, and issued 2005-08-11.

[9] Lv, P. 2017. Design and study on walking rice rope direct seeding machine. M.S. thesis, Shenyang Agricultural University.

[10] Lv, X. 2008. Design and study on rice rope direct seeding machine. D.S. thesis, Shenyang Agricultural University.

[11] Lv, X., X. Cheng, and W. Ren. 2010. Design the key working part s of rice rope direct seeding machine. *Journal of Gansu Agricultural University*, 2010(3): 122–125, 130.

[12] Lv, X., X. Lv, and W. Ren. 2008. Analysis and research for the technology of rice direct sowing with seed rope. *Journal of Agricultural Mechanization Research*, 2008(01): 212–215.

[13] Park, D. C. 1986. Germinating tape of grass seed. KR Patent 890001102Y1, filed and issued 1986-09-17

[14] Ren, W., X. Li, H. Cui, and W. Liu. 2005. Effect of the technique of rice direct sowing with seeds twisted in paper rope on rice yield character. *Journal of Shenyang Agricultural University*, 36(3): 265–270.

[15] Ren, W., X. Lv, A. Kong, B. Zhang, H. Cui, and Y. Yang. 2009. Development of the taped type rice direct seeding machine. *Journal of Shenyang Agricultural University*, 40(1): 62–66.

[16] Ren, W., Y. Song, M. Xin, L. Wu, and H. Cui. 2014. Crop seed rope direct sowing machine.CN Patent CN103858566A, filed 2014-03-18, and issued 2014-6-18.

[17] Song, Y., W. Ren, M. Xin, and L. Wu. 2014. Automatic seed rope laying device. CN Patent CN 103858565 B, filed 2014-03-18, and issued 2014-06-18.

[18] Xie, Z., G. Li, H. Liu, P. Wu, and Z. Zheng. 2012. Matlab from zero to advanced. *Beijing: Beihang University Press*.

[19] Wang, J., and S. Shang. 2012. Development of plot precision planter based on seed tape planting method. *Transactions of the Chinese Society of Agricultural Engineering*, 28(65-71).

[20] Yang P., Weng S., and Z. Wang. 2016. Principles of Automatic Control. *Beijing: China Electric Power Press*.

[21] Zhang, Y. 2006. Study on development principle and testing for seed rope direct sowing machine of rice. M.S.thesis, Shenyang Agricultural University.

[22] Zhang, B., M. Xin, Y. Song, L. Wu, and W. Ren. 2017. Design of a manually operated rice seed rope planter. *International Agricultural Engineering Journal*, 26(1): 104–111.

Pulsed vacuum drying kinetics of Goji berry (*Lycium barbarum* L.)

Yang Xuhai[1], Zhang Qian[1], Deng Lizhen[2], Xie Long[2],
Fang Xiaoming[3], Gao Zhenjiang[2], Kan Za[1*]

(1. *College of Mechanical and Electric Engineering, Shihezi University, Shihezi 832001, China;*
2. *College of Engineering, China Agricultural University, P.O. Box 194, No. 17 Qinghua East Road, Beijing 100083, China;*
3. *Bee Research Institute of Chinese Academy of Agricultural Sciences, Beijing 100093, China*)

Abstract: In order to explore a more efficient and safer drying technology for Goji berry processing, pulsed vacuum drying was applied for Gojiberry dehydratation. The drying kinetics of Goji berry were investigated in a pulsed vacuum dryer under different normal atmosphere holding time (2, 4, 6, 8, and 10 min), vacuum holding time (5, 10, 15, 20, and 25 min), and drying temperatures (50°C, 55°C, 60°C, 65°C, and 70°C). It was found that all the three parameters, namely drying temperature, normal atmosphere holding time, and vacuum holding time had significant effect on drying time. Drying temperature had the most obvious effect among the three parameters. The calculated moisture diffusion coefficient of Goji berry increased from 1.95×10^{-9} to 5.43×10^{-9} m^2/s as the drying temperature increased from 50°C to 70°C. The activation energy (Ea) was 46.54 kJ/mol calculated by the Arrhenius equation. Considering the drying behavior and dried product quality, pulsed vacuum drying at 60°C with 15 min and 2 min as the normal atmosphere and vacuum holding time, respectively, was proposed as the most favorable drying conditions for Goji berry drying. The findings of current work contribute to a better understanding of the drying characteristics of Goji berry under pulsed vacuum drying, which can enhance the drying process of Goji berry.

Keywords: pulsed vacuum drying, Goji berry, moisture diffusion coefficient, activation energy

Citation: Yang, X. H., Q. Zhang, L. Z. Deng, L. Xie, X. M. Fang, Z. J. Gao, and Z. Kan. 2017. Pulsed vacuum drying kinetics of Goji berry (*Lycium barbarum* L.). International Agricultural Engineering Journal, 26(3): 130–140.

1 Introduction

Goji berry (*Lycium barbarum* L.) is one of the most popular herbs in China, commonly known as wolfberry in the western world. It is a good source of health-promoting compounds such as carotenoids, polysaccharides and flavonoid compounds that show preventive effect against cardiovascular disease and cancer (Lin et al., 2014). Nowadays, Goji berry is widely consumed as traditional medicine or functional food in China.

Fresh Goji berry, having relatively high moisture contentgenerally about 80% (wet basis, w.b.), is very sensitive to microbial spoilage and not suitable for long-term storage after being harvested. It is reported that the storage time of Goji berry is only 2-3 days at normal temperature condition or 7 days at refrigerated conditions (Li et al., 2011). Therefore, fresh Goji berry should either be consumed or processed into various products. Drying is the most frequently used technology for Goji berry processing. It can be processed into raisins for longer shelf-life by reducing the moisture content to a low level, so as toprevent the growth and reproduction of microorganisms which cause decay, and to hinder the moisture-mediated deteriorative reactions (Xie et al., 2017a; Bai et al., 2013b; Ju et al., 2016b). The Goji berry raisins can be consumed either directly as traditional Chinese medicine, function food or as ingredients in biscuits, breads and porridges.

Currently the natural open sun drying is widely used to dry Goji berry and other agricultural products, due to the low investments and operation simplicity. Although this drying practice can be used for large quantities of products with no-cost energy, it exhibits several drawbacks. One of them is the great exposure to

Received date: 2017-05-18 **Accepted date:** 2017-08-04

* **Corresponding authors: Kan Za,** Professor, College of Mechanical and Electric Engineering, Shihezi University, Shihezi 832001, China. Email address: kanza_shz@163.com.

environmental contamination, such as bacterial pollution, dust and sand, insects, rodents, and birds (Xiao et al., 2015). In addition, it is strongly dependent on weather conditions and the rewetting or rotting problem of Goji berry becomes serious under rainy weather (Xiao, 2010b). Furthermore, chemical pretreatments are often used to improve the drying rate of Goji berry, by dipping them into an alkaline emulsion for several minutes to reduce the wax layer covering on the berry surface (Xiao et al., 2017; Wang et al., 2017a and b). However, this method can cause many water soluble nutrition lost by leaking out into the solutions during the dipping pretreatment (Bai et al., 2013a; Xiao et al., 2017). Also the chemical dipping method has an adverse impact on Goji berry appearance and easily to trigger food safety issues due to chemical reagent residues on Goji berry surface (Xie et al., 2017a and b). For example, it was observed that the polysaccharide content of dried Goji berry decreased from 9.77% to 9.23% after one min dipping pretreatment with 3% alkali solution at drying pretreatment (Wu et al., 2015). Therefore, in order to improve the quality of dried Goji berry, the traditional natural open sun drying method and the chemical dipping pretreatment should be replaced by more efficient, safe and controllable industrial drying methods.

With high sugar content and compact tissue of Goji berry pulp and a wax coating covered on the Goji berry skin (Li et al., 2006), drying of Goji berry is more difficult than traditional fruits and vegetables (Hashemi et al., 2009). So, there has been substantial interest to develop new drying methods for Goji berry's drying and several studies have also been conducted. Convective drying is a popular and cost-effective method for drying of agri-food products, but hot air drying is time consuming and low energy efficiency, in particular during the falling-rate period (Zielinska and Markowski, 2016; Ju et al., 2016c). In addition, long time exposure to high temperatures may result in substantial deterioration of food quality, such as loss of nutrients and color, structural changes, severe shrinkage, reduced rehydration capacity (Zielinska et al., 2016). In order to shorten the drying time and improve the quality of dried product, Wu et al. (2015) applied multi-stage varying temperatures hot air drying to dry Goji berry. It was observed that the drying time was decreased extensively from above 48 to 15 h as the drying air temperature increased from 40°C to 60°C while high drying temperature had a negative effect on product quality such as color and polysaccharide content.

Zheng et al. (2012) also observed that drying air temperature was the decisive parameter on the drying rate of Goji berry, and the products' quality was affected by the drying temperature, velocity and humidity in the process of hot air drying. Microwave drying is a promising approach in food and bioproducts processing as it is a rapid, more uniform and energy efficient way compared to the conventional hot-air drying (Zhang et al., 2006). Zhao et al. (2013) investigated the influence of different microwave power density on drying kinetics of polysaccharide extract of Goji berry. The results showed that drying rate increased with the increase of the microwave power density. In addition, Zhang et al. (2010) explored the effect of freeze drying parameters on drying energy consumption, drying time and product quality, such as Goji berry polysaccharide. It was found that freeze drying obtained better quality products compared with hot air drying as freeze drying can minimize nutrition loss in dried products due to the low temperature used in drying process. However, freeze drying is one of the most expensive processes because of the slow drying rate and high energy consumption, and large capital investments, which hinder the application of this drying technology (Duan et al., 2016).

Pulsed vacuum drying (PVD) is an innovative drying technology. During the drying process of PVD, the chamber pressure is alternating between vacuum and normal atmosphere condition, which breaks the balance condition of water vapor partial pressure between material surface and the drying medium, by thus enhancing drying rate extensively (Chua and Chou, 2004). Meanwhile, as the PVD process occurs at lower pressure, the boiling point of the water is depressed; therefore moisture evaporation can take place at lower temperature (Thorat et al., 2012). Compared to the conventional atmospheric drying, PVD can not only enhance the drying rate but preserve the quality of the dried product as

well (Xie et al., 2017a; 2017b). It is a very feasible drying technology for heat-sensitive biomaterials as the oxygen deficient environment during PVD process prevents oxidative reactions. It was found that sharp decline of pressure inside the vacuum drier could form partial water vapor pressure and lead to a porous structure inside the products (Haddad et al., 2004). Maache et al. (2001) found that pulsed vacuum drying could form the capillary structure in the material and accelerate the diffusion of water during the drying of scleroglucan. Chua and Chou (2004)explored the effects of pressure cycle time, pressure amplitude and drying temperature on material drying kinetics, product color and pore structure inside material during pulsedvacuum drying. Experimental results showed that the PVD technology can not only enhance drying kinetics but also the drying quality attributes of carrots and potato cues such as its color. Fang et al. (2016) found that pulsed vacuum drying can enhance drying process and quality of lotus pollen. Xie et al. (2017a and b) investigated the effect of far-infrared radiation heating assisted pulsed vacuum drying on drying kinetics and quality of Goji berry. It was observed that porous and fissured microstructure was formed on the surface, which can enhance drying kinetics and rehydration process. Xie et al. (2017c) explored the application of PVD on drying kinetics and quality of rhizoma dioscoreae slices and found that pulsed vacuum environment was helpful in inhibiting browning and puffed structure was formed which was benefit for enhancing rehydration capacity. Deng et al. (2017) observed that PVD resulted in higher rehydration ratio, water holding capacity, red pigment and ascorbic acid content, brighter colour, lower non-enzyme browning index and comparable antioxidant capacity of red pepper compared to samples dried by infrared assisted hot air drying and hot air drying at the same drying temperature. However up to date, rare information is available in the literature about the PVD drying characteristics of Goji berry. Therefore, in current work, the effects of different drying temperatures, normal atmosphere pulse time and vacuum pulse time on drying characteristics and quality of Goji berry were investigated in order to explore a new feasible drying technology for Goji berry.

2 Material and methods

2.1 Material

Fresh Goji berry was purchased from Kuitun city Xinjiang Uygur Autonomous Region, China. Fresh red uniform and surface intact fresh Goji berry was selected as testing material, which was free from rotting and insect damage. The short axis diameter and long axis diameter of Goji berry were 9.71×10^{-3} m and 17.55×10^{-3} m, respectively. The average weight of Goji berry was 1.12±0.08 g per granule and the initial moisture content was 80.00%±0.09% in wet basis, which was determined by vacuum drying at 70°C for 24 h following the AOAC method no.934.06 (AOAC, 1990). Soluble solid was about 24°Brix determined by anAbberefractometer (AR4 Series, A. Kruss Optonic, Hamburg, Germany). The weight of fresh Goji berry was controlled between 200-300 g and spread in a single layer on a silica gel plate. Prior to experiments fresh wolfberries were preserved on plate (free from squeezing) and stored in a refrigerator at 3°C±1°C and 90% relative humidity.

2.2 Pulsed vacuum drying equipment

The schematic diagram of equipment used for pulsed vacuum drying is shown in Figure 1. This apparatus basically consists of vacuum system (mainly including water ring vacuum pump, vacuum pipelines and drying chamber), heating system (including heating water box, temperature sensor, circulating water and heating plate) and control system. The vacuum system can reach to the lowest pressure of 3 kPa in drying chamber. An 8-bit microcontroller (PIC 16F877A, Microchip Technology Inc, Chandler, United States) was used to control the time of ambient pressure duration and vacuum pressure duration according to the different drying requirements. The air flowing into the drying chamber through electromagnetic valve is at temperature of 30°C–35°C and humidity of 20%-30% with the flow rate of 0-60 m/s. The drying temperature can be controlled in the range of room temperature to 80°C. The control system is used to set and control the vacuum holding time and normal atmosphere holding time. A Proportional-Integral-Derivative (PID) controller (Omron, model E5CN, Tokyo, Japan) with accuracy of ±0.1°C was

used to control the temperature of water tank and pressure in the drying chamber. All the experiments were started when the drying temperature reached to the setting value and was stable with setting vacuum holding time and normal atmosphere holding time.

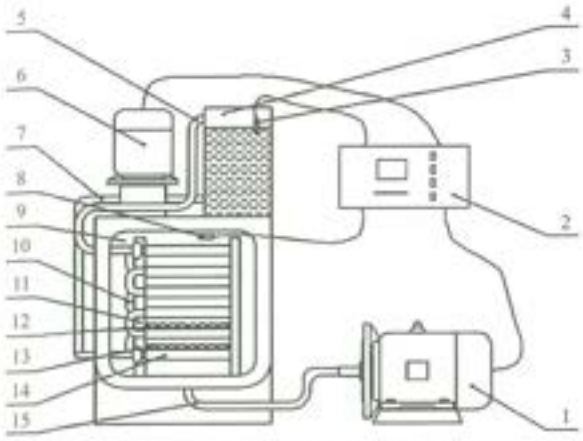

1. Vacuum pump 2. Control box 3. Water level sensor 4. Water tank 5. Outlet pipe 6. Hot water pump 7. Inlet pipe 8. Pressure sensor 9. Drying chamber 10. Circulating pipe 11. Heating plate bracket 12. Material tray 13. Material 14. Heating plate 15. Intake pipe

Figure 1 Schematic diagram of equipment used for pulsed vacuum drying

2.3 Experimental method

Prior to the experiments, the wolfberries were taken out from refrigerator to recover its temperature to the room temperature about 20°C. It was washed with tap water and drained with a towel, then spread in a single layer on a silica gel plate. To investigate the effects of drying temperature, normal atmosphere pulse time and vacuum pulse time on PVD drying characteristics and quality of Goji berry, experiments were performed according to Table 1.

Table 1 Schedule of pulsed vacuum drying experiment

No.	Drying temperature, ℃	Vacuum holding time, min	Normal atmosphere time, min
1	60	5	4
2	60	10	4
3	60	15	4
4	60	20	4
5	60	25	4
6	60	15	2
7	60	15	6
8	60	15	8
9	60	15	10
10	50	15	2
11	55	15	2
12	65	15	2
13	70	15	2

During the experiments, the weight loss was measured by an electronic balance (YP, Jingke, Shanghai, China) with the accuracy of ±0.01 g at one hour intervals. Drying process was stopped till the final moisture content of the samples decrease to 13.4%-13.7% (w.b.). After drying, the dried samples were cooled at the environment temperature, then were put in polyethylene bags and stored in drying dish for measuring other parameters. All the drying experiments were conducted in triplicate and samples were packed using vacuum packaging machine (DZQ400/2D, Tianyueyuan Instrument Co. Ltd., Beijing, China).

2.4 Calculation method of relevant parameters

2.4.1 Drying kinetics

The moisture ratio (MR) of wolfberries during drying experiments was calculated using Equation (1) (Wang et al., 2015; Borah et al., 2015).

$$MR = \frac{M_t - M_e}{M_0 - M_e} \quad (1)$$

where, M_0 is the initial moisture content and unit is g/g; M_e is the equilibrium moisture content (g/g); M_t is the moisture content at time t (g/g).

The values of the equilibrium moisture content M_e are relatively small compared to M_t or M_0. Thus Equation (1) can be written in a more simplified form as follows (Dai et al., 2015; Ju et al., 2016a):

$$MR = \frac{M_t}{M_0} \quad (2)$$

The drying rate of wolfberries during drying experiments can be given by Equation (3) (Zhang et al., 2012; Xiao et al., 2012).

$$DR = \frac{M_{t_1} - M_{t_2}}{t_2 - t_1} \quad (3)$$

where, M_{t1} and M_{t2} is moisture content in dry basis of wolfberries at time t_1 and t_2, respectively.

Drying curves of wolfberries were fitted with the Weibull model Equation (4) (Bai et al., 2013b; Zhang et al., 2015b; Corzo et al., 2008) .

$$MR = \exp\left[-\left(\frac{t}{\beta}\right)^{\alpha}\right] \quad (4)$$

where, t is the drying time; α is the shape parameter of the Weibull model, and β is the scale parameter of the model.

2.4.2 Moisture effective diffusion coefficient

Fick's second law of diffusion has been used to describe the drying process during the falling rate period. However, the drying process of PVD probably includes the period of rising drying rate. Weibull model can be used to estimate the moisture diffusion coefficient during the drying process without considering the characteristics of moisture migration (Dai et al., 2015). Equation (5) is the calculation formula of D_{cal}.

$$D_{cal} = \frac{r^2}{\beta} \tag{5}$$

where, D_{cal} is the calculated moisture diffusivity (m^2/s); r is the volume equivalent radius of Goji berry samples, with a value of 5.91×10^{-3} m.

The relationship between the calculated moisture diffusion coefficient (D_{cal}) and the moisture effective diffusion coefficient (D_{eff}) is expressed as follows (Zhang et al., 2015a; Fang et al., 2016; Ju et al., 2016b):

$$D_{eff} = \frac{D_{cal}}{R_g} \tag{6}$$

where, R_g is the physical dimension constant.

2.4.3 Activation energy

The relationship of moisture effective coefficient and drying activation energy can be described by Arrhenius equation, as shown in Equation (7) (Bai et al., 2013a; Xiao et al., 2010a; 2010c).

$$D_{eff} = D_0 \exp\left[-\frac{E_a}{R(T+273.15)}\right] \tag{7}$$

where, D_{eff} is the moisture effective diffusion coefficient during drying, m^2/s; D_0 is the constant diffusivity basis, m^2/s; E_a is the activation energy, kJ/mol; R is the universal gas constant with 8.314 J/(mol·K) as its value; T is the drying air temperature, °C.

Equation (7) can be transfigured into Equation (8) by taking the natural logarithm of both sides.

$$\ln D_{eff} = \ln D_0 - \frac{E_a}{R(T+273.15)} \tag{8}$$

Equation (6) is introduced into Equation (8) can obtain Equation (9).

$$\ln D_{cal} = \ln R_g + \ln D_0 - \frac{E_a}{R(T+273.15)} \tag{9}$$

The logarithm form of calculated moisture diffusion coefficient $\ln D_{cal}$ and the reciprocal of the temperature ($1/(T+273.15)$) showed a linear relationship and the slope $-Ea/R$ can be gained by linear regression. Then Ea can be calculated by putting $-Ea/R$ into Equation (9), as is shown in Equation (10).

$$E_a = -kR \tag{10}$$

3 Results and discussion

3.1 Effects of different vacuum holding time on drying kinetics

The effects of different vacuum holding time (5, 10, 15, 20 and 25 min) on the drying kinetics of wolfberries with 60°C and 4 min as its constant drying temperature and normal atmosphere holding time, respectively, were shown in Figures 2 and 3. Figure 2 illustrated that moisture ratio decreased with increasing drying time under different vacuum holding time. The drying time needed for moisture content of wolfberries decreased to 13.4%-13.6% was 480, 494, 374, 440, and 486 min for the vacuum holding time of 5, 10, 15, 20, 25 min, respectively. Obviously, drying time was the shortest under 15 min vacuum holding time which was shortened by 22.08%, 24.3%, 15% and 23.05% compared to vacuum holding time of 5, 10, 20 and 25 min, respectively. Therefore, vacuum holding time had significant influence on drying time and the 15 min was the optimized vacuum holding time.

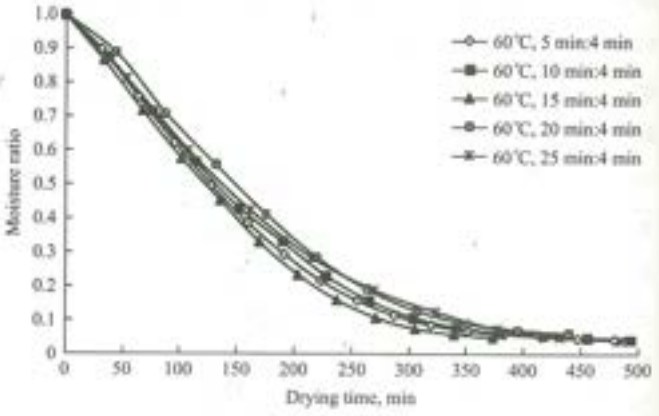

Figure 2 Moisture ratio curves vs drying time of Goji berry under different vacuum holding time

The drying rate curves of Goji berry under drying conditions of vacuum holding time of PVD were shown in Figure 3. It was observed that the PVD process of Goji berries can be divided into three stages: an accelerating period, a constant rate period, and a decelerating period.

Similar result was reported by Zhan and Liao (2014) for onion. During the acceleration period, which was short, heat was absorbed by material to increase its temperature to enhance moisture transfer gradually and at the meantime the samples' texture became soft due to the rising temperature. For this period, drying rate increased gradually and moisture loss came to the highest point. During the decelerating period, moisture loss decreased slowly and a short constant drying rate process appeared. This phenomenon occurred maybe due to the fact that the internal moisture diffusion rate is faster than moisture evaporation from material surface to environment outside so that drying rate is kept stable. Deceleration drying period is governed by internal moisture transfer so that drying rate decreased gradually. From Figure 3, it can be also found that drying rate was fastest under 15 min vacuum holding time.

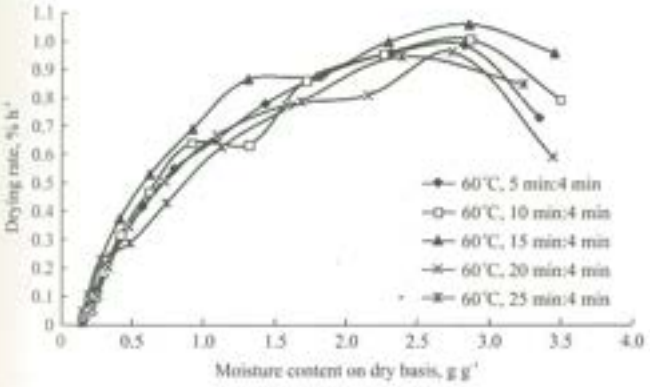

Figure 3 Drying rate curves of Goji berry under different vacuum holding time

3.2 Effects of different normal atmosphere holding time on drying kinetics

The effects of different normal atmosphere holding time (2, 4, 6, 8, and 10 min) on the PVD drying kinetics of wolfberries with 60°C and 4 min as the constant drying temperature and vacuum holding time, respectively, were shown in Figures 4 and 5. Figure 4 illustrated that moisture ratio decreased with increasing drying time under different normal atmosphere holding time. The drying time needed for moisture content of wolfberries reaching final moisture content was 424, 544, 440, 473 and 470 min for the normal atmosphere holding time of 2, 4, 6, 8, 10 min, respectively. The variation of moisture ration was decreased successively at the same time.

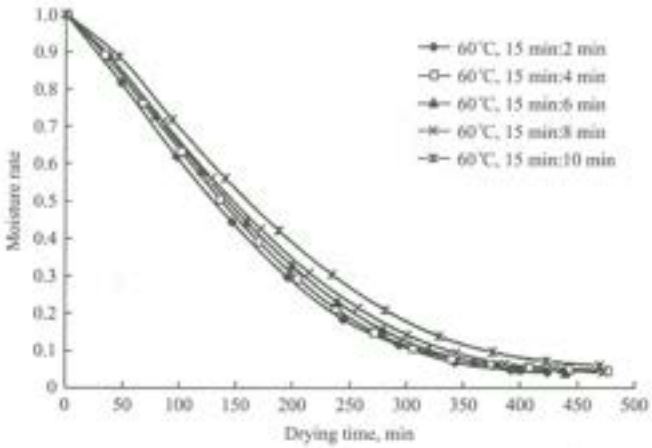

Figure 4 Moisture ratio curves vs drying time of Goji berry under different normal atmosphere holding time

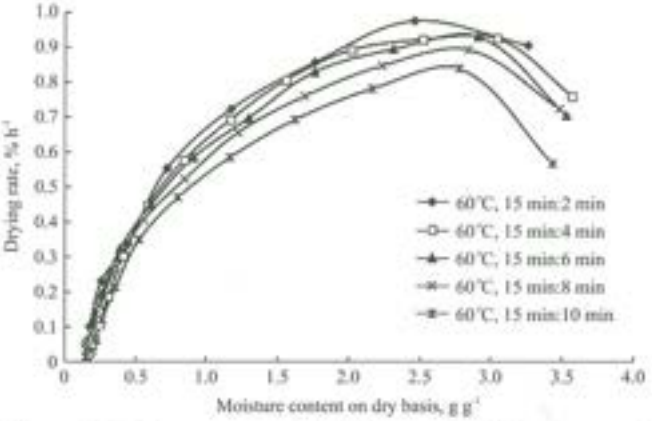

Figure 5 Drying rate curves of Goji berry under different normal atmosphere holding time

Figure 5 illustrated that vacuum pulse drying rate under different normal atmosphere had two stages: an accelerating period and a decelerating period which was comparatively longer than the accelerating period. This result was highlighted also by Gu et al. (2014) for green radish. This is probably due to the fact that the free water is relatively easier to remove in soft wolfberries during initial drying process, while for the deceleration drying period, non-free water was the main moisture content which is relatively harder to lose. In addition, from Figure 5, it was also found that when the normal atmosphere holding time was 2 min, the drying rate was fastest and the drying time was shortest.

3.3 Effects of different drying temperatures on drying kinetics

The effects of different drying temperatures (50°C, 55°C, 60°C, 65°C, and 70°C) on the drying kinetics of wolfberries with 15 and 2 min as the constant vacuum holding time and normal atmosphere holding time,

respectively were shown in Figures 6 and 7. Figure 6 showed that water diffusion increased with increasing temperature, which meant high drying rate and efficiency. This is in agreement with the results observed by Limpaiboon (2011) for pumpkin; Ihns et al. (2011) for apricot; and Mariem et al. (2014) for tomato. Besides, combining quality property of Goji berry itself and low temperature of vacuum pulse drying, the drying temperature 60°C was selected as optimal drying temperature to ensure relatively fast drying, as well as good quality, nutrition and pharmacological value.

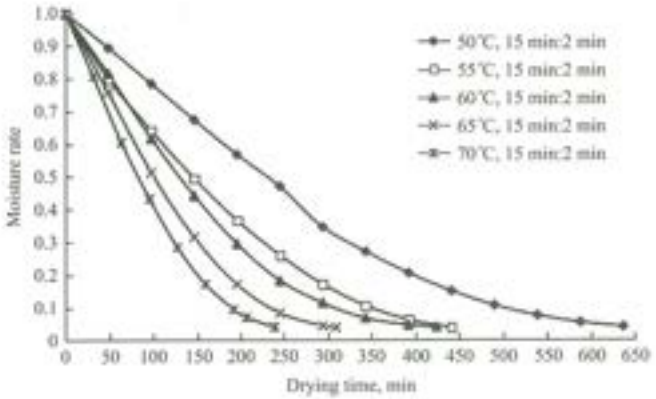

Figure 6 Moisture ratio curves vs drying time of Goji berry under different drying temperatures

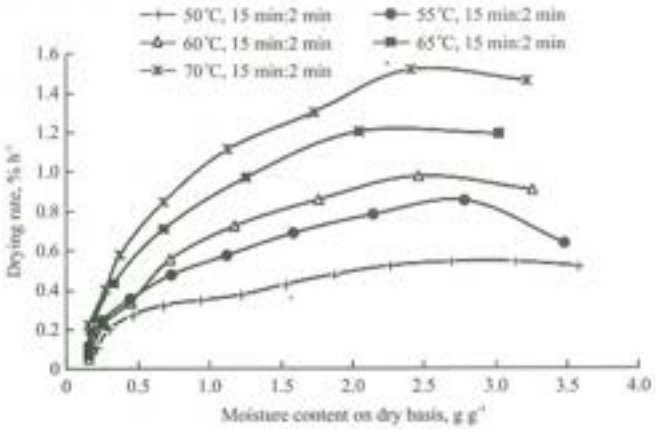

Figure 7 Drying rate curves of Goji berry under different drying temperatures

Figure 7 illustrated that temperature influenced drying of wolfberries significantly. Acceleration and deceleration period were obvious at drying temperatures of 70°C and 55°C, although the acceleration period was short. While when the samples were dried at 60°C and 65°C, the acceleration stage was not apparent and the whole drying process was in the deceleration process. When dried at 50°C, the drying rate was slowest and the whole drying process was basically a constant speed process. Therefore, by comprehensive analysis, 60°C was selected as suitable drying temperature.

3.4 Calculation of moisture effective diffusion coefficient and activation energy

The curves of ln(MR) versus time under different vacuum holding time, normal atmosphere holding time and drying temperatures are shown in Figures 8, 9, and 10, respectively. By linear regression, the calculated moisture diffusion coefficient of the Goji berry was calculated as shown in Table 2. Table 2 illustrated that the moisture diffusion coefficient increased obviously with increasing drying temperature. In addition, drying temperature had a more significant effect on D_{cal} than the vacuum holding and normal atmosphere holding time as both of which had little influence on D_{cal}.

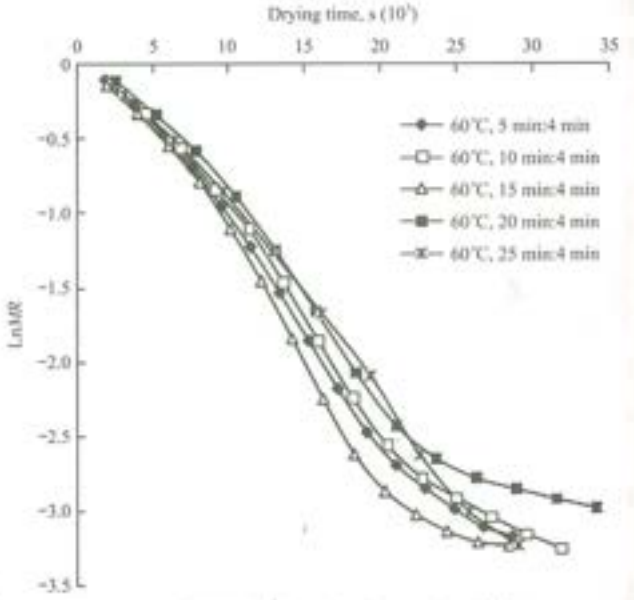

Figure 8 Curves of lnMR vs drying time under different vacuum holding time

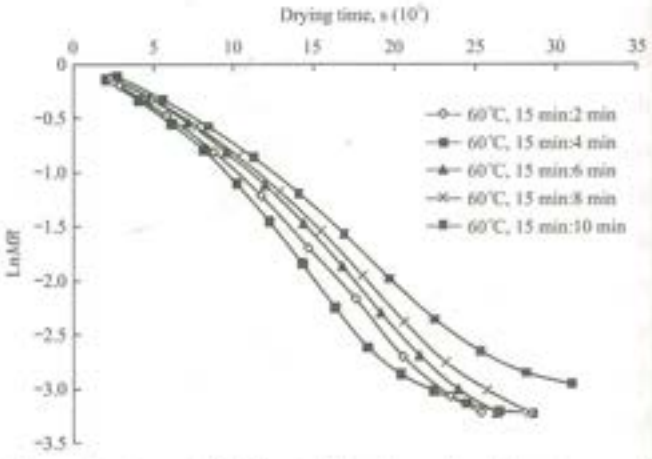

Figure 9 Curves of lnMR vs drying time under different normal atmosphere holding time

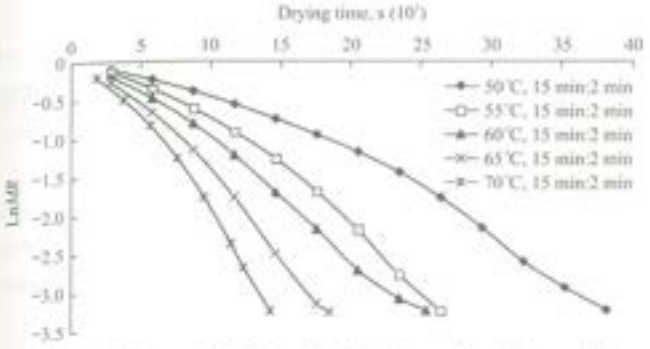

Figure 10 Curves of lnMR vs drying time under different drying temperatures

Table 2 Calculated moisture diffusion coefficient (D_{cal}) of Goji berry subjected to different drying condition

No.	Drying condition	Linear regression fitting equation	D_{cal} ($\times 10^{-9}$ m^2/s)	R^2
1	60°C, 5 min:4 min	$Ln MR=-(t/8967)^{1.003}$	3.8952	0.9804
2	60°C, 10 min:4 min	$Ln MR=-(t/9084)^{1.009}$	3.8450	0.9724
3	60°C, 15 min:4 min	$Ln MR=-(t/8106)^{1.023}$	4.3089	0.9655
4	60°C, 20 min:4 min	$Ln MR=-(t/9664)^{0.9509}$	3.6142	0.9540
5	60°C, 25 min:4 min	$Ln MR=-(t/10540)^{1.195}$	3.3139	0.9950
6	60°C, 15 min:2 min	$Ln MR=-(t/9739)^{1.265}$	3.5864	0.9950
7	60°C, 15 min:6 min	$Ln MR=-(t/10640)^{1.341}$	3.2827	0.9953
8	60°C, 15 min:8 min	$Ln MR=-(t/10930)^{1.282}$	3.1956	0.9933
9	60°C, 15 min:10 min	$Ln MR=-(t/11680)^{1.198}$	2.9904	0.9858
10	50°C, 15 min:2 min	$Ln MR=-(t/17930)^{1.362}$	1.9480	0.9968
11	55°C, 15 min:2 min	$Ln MR=-(t/12360)^{1.549}$	2.8259	0.9988
12	65°C, 15 min:2 min	$Ln MR=-(t/7741)^{1.275}$	4.5121	0.9982
13	70°C, 15 min:2 min	$Ln MR=-(t/6431)^{1.470}$	5.4312	0.9990

The activation energy value of wolfberries subjected to pulsed vacuum drying by linear regression equation was determined to be 46.54 kJ/mol, which means that removing one kg water content from Goji berry using PVD needs at least 2585.6 kJ energy to trigger moisture transfer.

In order to compare the activation energy of Goji berry and other agricultural products, the drying activation energies of many bioproducts are listed in Table 3. From Table 3, it was found that the activation energy of Goji berry is higher than the activation energy of squash seed, apricot, corn kernel and apple slice, but lower than the activation energy of zizyphus jujube mill. This result indicated that the energy required for removal of the equivalent water from Goji berry was more than that of squash seed, apricot, corn kernel and apple slice and less than that of zizyphus jujube mill. The drying activation energy of the material is closely related to the shape, size and constituent of the material (Xiao et al., 2010a; Wang et al., 2015). The ratio of volume and surface area of squash seed and corn kernel are smaller than that of Goji berry, so they are easier to be dried. The sugar content of zizyphus jujube mill is higher than Goji berry, and sugar has a strong adsorption to water. Therefore, the activation energy of zizyphus jujube mill is relatively higher.

Table 3 Activation energies of Goji berry and other related products

Products	Ea, kJ/mol	References
Goji berry	46.54	Present work
Squash seed	31.94-34.49	Chayjan et al. (2013)
Apricot	29.35-33.78	Mirzaee et al. (2009)
Corn kernel	10.39-15.56	Voc'a et al. (2007)
Apple slice	22.66-30.92	Meisami et al. (2010)
Zizyphus jujube mill	74.2	Motevali et al. (2012)

4 Conclusion

To evaluate the feasibility of using PVD to dry Goji berry, the effects of normal atmosphere holding time (2, 4, 6, 8, 10 min), vacuum holding time (5, 10, 15, 20, 25 min), and drying temperatures (50°C, 55°C, 60°C, 65°C, 70°C) on the PVD drying kinetics of Goji berry were investigated. It was found that all three parameters had significant effect on the drying process of Goji berry. The D_{cal} values of Goji berry dried by PVD at various conditions ranged from 1.95×10^{-9} to 5.43×10^{-9} m^2/s, calculated using the Weibull model. The drying activation energy (E_a) of Goji berry dried by PVD was 46.54 kJ/mol, which indicated that removing one kg water content from Goji berry using PVD needs at least 2585.6 kJ energy to trigger moisture transfer. The findings of current work contribute to a better understanding of the drying characteristics of Goji berry under PVD and indicate it is a promising drying technology for Goji berry.

Acknowledgements

This research is supported by the National Natural Science Foundation of China (No.31760471, 31501548), the National Key Research and Development Program of China (No. 2017YFD0400905) and the Chinese Transformation Fund of Agricultural Scientific and Technological Achievements (No.2014GB2G410112).

[References]

[1] AOAC. 1990. Official methods of analysis (15th edition). Association of Official Analytical Chemists, Washington, DC, USA.

[2] Bai, J. W., D. W. Sun, H. W. Xiao, A. S. Mujumdar, and Z. J. Gao. 2013a. Novel high-humidity hot air impingement blanching (HHAIB) pretreatment enhances drying kinetics and color attributes of seedless grapes. *Innovative Food Science and Emerging Technologies*, 20(5): 230–237.

[3] Bai, J. W., J. L. Wang, H. W. Xiao, H. Y. Ju, Y. H. Liu, and Z. J. Gao. 2013b. Weibull distribution for modeling drying of grapes and its application. *Transactions of the Chinese Society of Agricultural Engineering*, 29(16): 278–285. (in Chinese with English abstract)

[4] Borah, A., K. Hazarika, and S. M. Khayer. 2015. Drying kinetics of whole and sliced turmeric rhizomes (*Curcuma longa* L.) in a solar conduction dryer. *Information Processing in Agriculture*, 2(2): 85–92.

[5] Chayjan, R. A., K. Salari, Q. Abedi, and A. A. Sabziparvar. 2013. Modeling moisture diffusivity, activation energy and specific energy consumption of squash seeds in a semi fluidized and fluidized bed drying. *Journal of Food Science and Technology*, 50(4): 667–677.

[6] Chua, K.J., and S.K. Chou. 2004. On the experimental study of a pressure regulatory system for bioproducts dehydration. *Journal of Food Engineering*, 62(2): 151–158.

[7] Corzo, O., N. Bracho, and A. Pereira. 2008. Weibull distribution for modeling air drying of coroba slices. *LWT - Food Science and Technology*, 41(10): 2023–2028.

[8] Dai, J. W., J. Q. Rao, D. Wang, L. Xie, H. W. Xiao, Y. H. Liu, and Z. J. Gao. 2015. Process-based drying temperature and humidity integration control enhances drying kinetics of apricot halves. *Drying Technology*, 33(3): 365–376.

[9] Deng, L. Z., X. H. Yang, A. S. Mujumdar, J. H. Zhao, D. Wang, Q. Zhang, J. Wang, Z. J. Gao, and H. W. Xiao. 2017. Red pepper (*Capsicum annuum* L.) drying: effects of different drying methods on drying kinetics, physicochemical properties, antioxidant capacity, and microstructure. *Drying Technology*. (Accessed on August 2, 2017)

[10] Duan, X., X. Yang, G. Ren, Y. Pang, L. Liu, and Y. Liu. 2016. Technical aspects in freeze-drying of foods. *Drying Technology*, 34(11): 1271–1285.

[11] Fang, X. M., X. Zhang, J. Wang, Q. Zhang, H. W. Xiao, Y. Liu, H. Ju, S. Liang, and Z. J. Gao. 2016. Vacuum pulsed drying characteristics and quality of lotus pollen. *Transactions of the Chinese Society of Agricultural Engineering*, 32(10): 287–295 (in Chinese with English abstract).

[12] Gu, W. R., Y. Li, and S. G. Lou. 2014. Study on kinetics modeling of thin-layer vacuum drying of green radish. *Packaging and Food Machinery*, 32(5): 18–21.

[13] Haddad, J., F. Juhel, and N. Louka. 2004. A study of dehydration of fish using successive pressure drops (DDS) and controlled instantaneous pressure drop (DIC). *Drying Technology*, 22(3): 457–478.

[14] Hashemi, G., D. Mowla, and M. Kazemeini. 2009. Moisture diffusivity and shrinkage of broad beans during bulk drying in an inert medium fluidized bed dryer assisted by dielectric heating. *Journal of Food Engineering*, 92(3): 331–338.

[15] Ihns, R., L.M. Diamante, G. P. Savage, and L. Vanhanen. 2011. Effect of temperature on the drying characteristics, colour, antioxidant and beta-carotene contents of two apricot varieties. International *Journal of Food Science & Technology*, 46(2): 275–283.

[16] Ju, H. Y., H. El-Mashad, X. M. Fang, Z. L. Pan, H. W. Xiao, Y. H. Liu, and Z. J. Gao. 2016a. Drying characteristics and modeling of yam slices under different relative humidity conditions. *Drying Technology*, 34(3): 296–306.

[17] Ju, H. Y., Q. Zhang, A. S. Mujumdar, X. M. Fang, H. W. Xiao, and Z. J. Gao. 2016b. Hot airdrying kinetics of yam slices under step change in relative humidity. *International Journal of Food Engineering*, 12(8): 783–792.

[18] Ju, H. Y., Q. Zhang, X. Guo, H.W. Xiao, X. M. Fang, Y. Liu, H. Zhao, and Z. J. Gao. 2016c. Control method of relative humidity of carrot hot air drying based on detecting material's temperature. *Transactions of the Chinese Society of Agricultural Engineering*, 32(4): 269–276 (in Chinese with English abstract).

[19] Limpaiboon, K. 2011. Effects of temperature and slice thickness on drying kinetics of pumpkin slices. *Walailak Journal of Science & Technology*, 8(2): 159–166.

[20] Lin, D. B, H. He, H. Ji, J. Willis, L. Willard, Y. Jiang, D. M. Medeiros, L. Wark, J. Han, Y. Z. Liu, and B. Lu. 2014. Wolfberries potentiate mitophagy and enhance mitochondrial biogenesis leading to prevention of hepatic steatosis in obese mice: The role of AMP - activated protein kinase α2 subunit. *Molecular Nutrition & Food Research*, *58*(5): 1005–1015.

[21] Li, W. Q., Z. B. Zhang, and J. J. Li. 2006. Plant epicuticular wax drought resistance as well as its molecular biology. *Journal of Plant Physiology and Molecular Biology*, 32(5): 505–512.

[22] Li, Y.C., Y. Bi, Y. Wang, L. Yuan, and Y. Yin. 2011. Effects of film packaging on major storage characters of fresh wolfberry fruit during room and low temperature storage. *Science and Technology of Food Industry*, 32(2): 302–304.

[23] Maache, Z., S. Rezzoug, and K. Allaf. 2001. Kinetics of drying and hydration of the scleroglucan polymer. *Drying Technology*, 19(8): 1961–1974.

[24] Mariem, S. B., S. B. Mabrouk, S. B. Mariem, and S. B. Mabrouk. 2014. Drying characteristics of tomato slices and

mathematical modeling. *International Journal of Energy Engineering*, 4(2A): 17–24.

[25] Meisami-Asl, E., S. Rafiee, and A. Keyhani. 2010. Drying of apple slices (var. Golab) and effect on moisture diffusivity and activation energy. *Plant Omics*, 3(3): 97–102.

[26] Mirzaee, E., S. Rafiee, and A. Keyhani. 2009. Determining of moisture diffusivity and activation energy in drying of apricots. *Research in Agricultural Engineering*, 55(3): 114–120.

[27] Motevali, A., A. Abbaszadeh, and S. Minaei. 2012. Effective moisture diffusivity, activation energy and energy consumption in thin-layer drying of jujube (*Zizyphus jujube* Mill). *Journal of Agricultural Science & Technology*, 14(3): 523–532.

[28] Thorat, I. D., D. Mohapatra, R. F. Sutar, S. S. Kapdi, and D. D. Jagtap. 2012. Mathematical modeling and experimental study on thin-layer vacuum drying of ginger (*Zingiber Officinale* R.) slices. *Food and Bioprocess Technology*, 5(4): 1379–1383.

[29] Voc'a, N., T. Krička, A. Matin, V. Jannusic, and Z. Jukic. 2007. Activation energy of water release rate from corn kernel during convective drying. *Agriculturae Conspectus Scientificus*, 72(3): 199–204.

[30] Wang, D., J. W. Dai, H. Y. Ju, L. Xie, H. W. Xiao, Y. H. Liu, and Z. J. Gao. 2015. Drying kinetics of American ginseng slices in thin-layer air impingement dryer. *International Journal of Food Engineering*, 11(5): 701–711.

[31] Wang, J., X. H. Yang, A. S. Mujumdar, D. Wang, J. H. Zhao, X. M. Fang, Q. Zhang, L. Xie, Z. J. Gao, and H. W. Xiao. 2017a. Effects of various blanching methods on weight loss, enzymes inactivation, phytochemical contents, antioxidant capacity, ultrastructure and drying kinetics of red bell pepper (*Capsicum annuum* L.). *LWT-Food Science and Technology*, 77(4): 337–347

[32] Wang, J., X. M. Fang, A. S. Mujumdar, J. Y. Qian, Q. Zhang, X. H. Yang, Y. H. Liu, Z. J. Gao, and H. W. Xiao. 2017b. Effect of high-humidity hot air impingement blanching (HHAIB) pretreatment on drying characteristic and quality attributes of red pepper (*Capsicum annuum* L.). *Food Chemistry*, 220(8): 145–152.

[33] Wu, Z. H., W.L. Li, L. J. Zhao, J. F. Shi, and Q. Liu. 2015. Drying characteristics and product quality of Lycium barbarum under stages-varying temperatures drying process. *Transactions of the Chinese Society of Agricultural Engineering*, 31(11): 287–293 (in Chinese with English abstract).

[34] Xiao, H. W., C. L. Pang, L. H. Wang, J. W. Bai, W.X. Yang, and Z. J. Gao. 2010a. Drying kinetics and quality of Monukka seedless grapes dried in an air-impingement jet dryer. *Biosystems Engineering*, 105(2): 233–240.

[35] Xiao, H. W., H. Lin, X. D. Yao, Z. L. Du, Z. Lou, and Z. J. Gao. 2009. Effects of different pretreatments on drying kinetics and quality of sweet potato bars undergoing air impingement drying. *International Journal of Food Engineering*, 5(5): 64–67

[36] Xiao, H. W., J. W. Bai, D. W. Sun, and Z. J. Gao. 2014. The application of superheated steam impingement blanching (SSIB) in agricultural products processing-a review.*Journal of Food Engineering*, 132(1): 39–47.

[37] Xiao, H. W., J. W. Bai, L. Xie, D. W. Sun, and Z. J. Gao. 2015. Thin-layer air impingement drying enhances drying rate of American ginseng (*Panax quinquefolium* L.) slices with quality attributes considered. *Food and Bioproducts Processing*, 94(2): 581–591.

[38] Xiao, H. W., S. X. Zhang, J.W. Bai, X. M. Fang, Z. J. Zhang, and Z. J. Gao. 2010b. Air impingement drying characteristics of apricots. *Transactions of the Chinese Society of Agricultural Engineering*, 26(7): 318–323 (in Chinese with English abstract).

[39] Xiao, H. W., X. D. Yao, H. Lin, W. X. Yang, J. S. Meng, and Z. J. Gao. 2012. Effect of SSB (superheated steam blanching) time and drying temperature on hot air impingement drying kinetics and quality attributes of yam slices. *Journal of Food Process Engineering*, 35(3): 370–390.

[40] Xiao, H. W., Z. Pan, L. Z. Deng, H. M. El-Mashad, X. H. Yang, A. S. Mujumdar, Z. J. Gao, and Q. Zhang. 2017. Recent developments and trends in thermal blanching-a comprehensive review. *Information Processing in Agriculture*, 4(2): 101–127.

[41] Xiao, H. W., Z. J. Gao, H. Lin, and W. X. Yang. 2010c. Air impingement drying characteristics and quality of carrot cubes. *Journal of Food Process Engineering*, 33(5): 899–918.

[42] Xie, L., A. S. Mujumdar, X. M. Fang, J. Wang, J. W. Dai, Z. L. Du, H. W. Xiao, Y. Liu, and Z. J. Gao. 2017a. Far-infrared radiation heating assisted pulsed vacuum drying (FIR-PVD) of Wolfberry: effects on drying kinetics and quality attributes. *Food and Bioproducts Processing*, 102(2): 320–331.

[43] Xie, L., A. S. Mujumdar, Q. Zhang, J. Wang, S. Liu, L. Z. Deng, D. Wang, H. W. Xiao, Y. H. Liu, and Z. J. Gao. 2017b. Effects of pulsed vacuum drying on infrared radiation heating (PVD-FIR) and electronic panel contact heating (PVD-EPC) on drying kinetics, colour and volatile compounds of wolfberry. *Drying Technology*, 35(11): 1312–1326.

[44] Xie, Y., Z. J. Gao, Y. Liu, and H. W. Xiao. 2017c. Pulsed vacuum drying of rhizoma dioscoreae slices. *LWT-Food Science and Technology*, 80(7):237–249.

[45] Zhan, D., and C. H. Liao. 2014. Study on the dynamics of onion vacuum drying. *Contemporary Chemical Industry*, 12(6): 2535–2538.

[46] Zhang, M., J. Tang, A.S. Mujumdar, and S. Wang. 2006.

Trends in microwave-related drying of fruits and vegetables. *Trends in Food Science & Technology*, 17(10): 524–534.

[47] Zhang, Q., H.W. Xiao, X.H. Yang, J.W. Bai, Z. Lou, and Z. J. Gao. 2012. Effects of pretreatment on air impingement drying characteristics and product color for line pepper. *Transactions of the Chinese Society of Agricultural Engineering*, 28(1): 276–281. (in Chinese with English abstract)

[48] Zhang, W. P., H. W. Xiao, Z. J. Gao, Z. A. Zheng, H. Y. Ju, P. Zhang, and X. M. Fang. 2015a. Improving quality of Poria cocos using infrared radiation combined with air impingement drying. *Transactions of the Chinese Society of Agricultural Engineering*, 31(10): 269–276. (in Chinese with English abstract)

[49] Zhang, W. P., Z. J. Gao, H. W. Xiao, Z. A. Zheng, H. Y. Ju, and L. Xie. 2015b. Drying characteristics of poria cocos with different drying methods based on Weibull distribution. *Transactions of the Chinese Society of Agricultural Engineering*, 31(5): 317–324. (in Chinese with English abstract)

[50] Zhang, X. D., J. M. Cheng, and L. Liu. 2010. Optimization of procedure parameters in freeze drying of lycium barbarum polysaccharide. *Journal of Nanjing TCM University*, 26(1): 50–52.

[51] Zhao, Q., L. Y. Zhang, and Z. M. Qiu. 2013. Study on microwave-vacuum drying of lycium barbarum polysaccharide extracts and analysis of its quality. *Science and Technology of Food Industry*, 34(23): 266–270.

[52] Zheng, S., M. B. Li, and S. Mu. 2012. Study and experiment on Chinese wolfberry drying dynamic characteristics in the condition of hot air convection. *Journal of Food Industry*, 33(9): 143–146.

[53] Zielinska, M., and M. Markowski. 2016. The influence of microwave-assisted drying techniques on the rehydration behavior of blueberries (*Vaccinium corymbosum* L.). *Food Chemistry*, 196(4): 1188–1196.

[54] Zielinska, M., P. Sadowski, and W. Błaszczak. 2016. Combined hot air convective drying and microwave-vacuum drying of blueberries (*Vaccinium corymbosum* L.): drying kinetics and quality characteristics. *Drying Technology*, 34(6): 665–684.

Optimal agricultural production decision model based on futures hedging

Yu Xing[1*], Liu Guibo[2], Kun Wen[3]

(1. *School of Mathematics & Finance, Hunan university of Humanities, Science and Technology, Loudi 417000, China;*
2. *School of Business Administration & Tourism Management, Yunnan University, Kunming 650504 China;*
3. *Jiangxi Administrative Institute, Jiangxi, 330000, China*)

Abstract: Considering the influence of natural factor on the agricultural production, this paper proposes futures hedging models to solve the optimal production decision-making problems for the risk-averse farmers in cases of basis risk existing or not. Theoretical results show that the marginal cost corresponding to the optimal production equals to the current futures price and the futures position is full-hedge when the natural factor is not accounted for. When the natural factor is not accounted for, the marginal cost corresponding to the optimal production is less than the current value of the futures, and the optimal futures position is less than the optimal expected output (under-hedge) in the case of basis risk not existing. In the case of basis risk and natural factor existing, the marginal cost corresponding to the optimal production is less than the mean value of the spot price. Furthermore, for the prudent farmer, if the spot price is assumed to be a linear function of the futures price and the linear coefficient is smaller than 1, the futures is still under-hedge. In the empirical analysis, the price is assumed to be related to the natural state and the farmer's preference is characterized by a negative exponential utility, this paper deduces the expression of the farmer's utility, then analyzes the influence of decision variable on utility. The empirical results show that using futures for hedging is gainful to improve the farmer's utility. However, the farmer is suggested not to enhance the futures position blindly, but to choose the futures with small basis volatility for hedging.

Keywords: Optimal production decision; futures hedging; risk-averse; negative exponential utility function

Citation: Yu, X., G. B. Liu, and W. Kun. 2017. Optimal agricultural production decision model based on futures hedging. International Agricultural Engineering Journal, 26(3): 141–150.

1 Introduction

Small farmers are the main part of China's agricultural production, and also the main contribution force to realize the grain security strategy of our country. Therefore, it is of great significance to improve the production efficiency of small farmers to improve the grain production in China. However, Donovan (2015) pointed out that "small farmers" in the "big market" in a weak position, it is difficult to resist all aspects of risk. When prices of agricultural products decline, farmers have to face with lower prices. While, when the output of agricultural products is surplus and the supply exceeds demand, the agricultural products which farmers get may be wasted in vain. Therefore, in agricultural production, farmers are faced with price risk and demand risk. To reduce these two risks, scholars have put forward some solutions. For example, generally implemented in the practice of protection price mechanism is one of the commonly used methods for farmers to cope with risks. For farmers, this is the most direct and most acceptable contract mechanism, which is also beneficial to farmers. The minimum purchase price not only can help farmers reduce their faces two wholesale market price volatility risk, allowing farmers to concentrate on production, can also help to reduce transaction costs, make the supply chain is more stable. In the long run, the protective pricing mechanism plays a positive role in promoting the development of the order agriculture market. However, the defect of this model is mainly the high default rate of

Received date: 2017-06-07 **Accepted date:** 2017-06-26
* **Corresponding author: Yu Xing,** Associate Professor of Hunan University of Humanities, Science and Technology. Email: hnyuxing@163.com.

the company. According to the survey, in all orders agricultural default event, the leading enterprise default rate reaches 70% (Ma and Xu, 2008). Therefore, scholars have studied how to use game theory to control the behavior of breach of order in agriculture. Bogetoft (2002) presented coordination, incentives, and transaction costs as elements of a design order. Ye and Lin (2012) used revenue sharing contract mechanism to coordinate the supply chain. However, the mechanism of information sharing is also asymmetric. To solve this problem, Lin and Ye (2014) introduced a revenue sharing contract mechanism based on Nash negotiation to coordinate the interests between the company and the farmers. Palsule (2013) put forward a game model of revenue sharing contract, in which supply chain revenue depended on revenue sharing factor. Feng et al. (2014) studied the reliability income sharing mechanism in the N echelon supply chain contract. Although these studies have solved the problem of how to balance and distribute the benefits between farmers and firms to a certain extent, the whole order chain is still in a zero sum game. Risk and income shift between farmers and companies. Therefore, some scholars have proposed methods to transfer part of the risk through the way of government subsidies. Huang et al. (2017) constructed the three stage game model of government, retailers and agricultural enterprises under the subsidy mechanism provided by the government. Subsidies are also widely adopted in large agricultural countries. In China, the government has issued a number of documents on the issue of subsidies for agriculture, rural areas and farmers. But the form of direct subsidy also brings such problems as "cheating subsidies" and "abuse of subsidies", which is not conducive to the healthy development of agriculture. Moreover, direct subsidies may also be difficult to achieve the function of subsidies. Shang (2011) pointed out from economic analysis point of view, in grain subsidy, beneficiary was not grain producers, but food consumers. Castiblanco et al. (2015) studied the subsidy policies of petroleum palm oil and biofuels in Columbia, and found that subsidies were not an effective way to achieve government goals. Based on the above analysis, it can be concluded that farmers are faced with price, demand and natural factor risk in production. The existing order agriculture has problems of a higher default rate and asymmetric information. Government subsidies through external intervention cannot fundamentally solve the problem, then farmers should be innovative with external methods to defuse the risks faced by themselves.

Hedging risk with derivatives such as options and futures is a common method of risk management for decision makers. Ritchken and Tapiero (1986) first introduced option mechanism in inventory research to hedge the fluctuation of product price and quantity fluctuation. Xu (2010) pointed out that under the stochastic output and stochastic demand, the option contract can make the supplier avoid the risk of low demand and low price, and make the manufacturer avoid the risk of high price and low demand. Zhao et al. (2010) proposed a supply chain coordination mechanism based on option and income sharing contract. Li and Li (2001) made a preliminary study on the application of option pricing in evaluating venture capital and guiding the application of contracted agricultural contracts. Shang et al. (2013) took the update time of the demand forecast information as the decision variable, introduce the option ordering, gave the quantity flexibility, and established the two stage productions and order model. But options markets are not well developed in some countries (such as developing countries), and options, especially options based on agricultural products, are rare. At present, there is no formal option for agricultural products in China. There are also many scholars using futures hedging to study production decision problem. The Sandmo (1971) proved that risk averse producers reducing output in the face of uncertain prices to cope with uncertainty risks. When there is a futures market, Holthausen (1979) further studies producer optimal decision problem under the condition of price uncertainty. It is found that futures hedging can improve the firm's output. This also shows that futures hedging can transfer market risks, make up for the shortage of the spot market and optimize the allocation of market resources. Wong (2013) assumes that commodity prices and money forward markets are independent and unbiased, and establishes an exchange rate and commodity futures hedging model to study the

optimal production level of firms. Wong (2014) establishes optimal production decision and futures hedging model to hedge the price risk under different delivery methods. Broll (2015) considered the risk on the basis of futures, futures hedging decision problems based on the concept of relying on production. Yang (2011) sets up a market equilibrium model before and after the introduction of futures trading, and examines the conditions for the management of default risk under the "order + futures' model" by model solving and numerical analysis. Although these studies consider the problem of derivative hedging in production decisions, ignoring an important exogenous factor in agricultural production, that is, the influence of natural factors. Natural factors have a great influence on agricultural production. As we know, when farmers are in a bad year, the actual output ratio is expected to yield low. When a good harvest comes, output will increase more than expected. The price of agricultural products is affected by the output to a certain extent, which shows that both the price and the actual output are affected by natural factors. In addition, considering that the development of our country's agricultural futures market is more perfect, there is still a lack of agricultural products option market. Therefore, considering the influence of natural factors, this paper studies how to hedge the price risk faced by farmers by using futures hedging.

Under two frameworks of with or without basis risk, this paper proposes futures hedging model for the risk aversion farmers. In the model, we study the problems of optimal production and the effects of the futures basis risk on the production decision by a comparative analysis. Since the specific form of the utility function is not limited, the results of the study have general applicability. Then, we discuss the effects of risk aversion, futures basis risk and natural factors on the negative exponential utility function. The outline of this paper is as follows. In Section 2, we present the optimal production decision model and give some assumptions. And then, we study the optimal production decision under different cases. In Section 3, a simulation example is given to illustrate the application of the proposed model and analyze sensitivities of the parameters. Finally, we conclude this paper in Section 4.

2 Optimal production decision model

For ease of expression, we call a single farmer or a union of farmers as "the farmer". In this section, we assume that the farmer is risk aversion and present models under different basis risk cases. Then, the uniqueness and existence of the solution of the model are proved, and the conditions of the optimal expected quantity of production and the position of the futures position are given. To begin, we propose some assumptions as follows.

2.1 Basic assumptions and symbolic description

Hypothesis 1. Suppose the futures delivery date is the harvest time of the agricultural products. Let $\tilde{P}$ be the market purchasing price of agricultural products at harvest, and $\tilde{f}$ be the corresponding futures delivery price.

Hypothesis 2. Assume that the futures market is unbiased (i.e. the expected value of the stochastic price on the futures delivery date equals the current value. That is, $E(\tilde{f}) = f_0$; If there is no basis of futures price, then the prices of futures and spot are the same on the delivery date, say, $\tilde{p} = \tilde{f}$. We also assume that futures contracts can be traded infinitely.

Hypothesis 3. Suppose farmers have sufficient margin futures. In futures hedging, sufficient margin should be reserved. Otherwise, there will be market to market risk. In fact, farmers can eliminate the insufficient margin concerns by the government. This paper does not consider loaning futures transaction fees.

Hypothesis 4. Assume that the peasant household is risk averse, then its utility function satisfies $U'(\Pi)>0$, $U''(\Pi)<0$, where Π represents the stochastic income of the farmer. In order to avoid the demand risk, it is assumed that the farmer has signed the contract of production and marketing with the company. The contract stipulates that the company will buy all the output of the farmers at the market price, and the specific expected output is determined by the farmers.

Hypothesis 5. At the beginning of the production, the farmer expects the output to be q, and decides to put

in production costs according to projected output. The production cost of farmer is related to and expected to yield, which satisfies $C'(q)>0$, $C''(q)>0$. Similar to Ye et al. (2012), we assume that production costs can be written as $C(q)=c_0+c_1q+c_2q^2$, where c_0 is the fixed costs, that is, not to produce, but also to pay costs, such as the farmer's daily consumption, farm tools and so on; $c_1q>0$ is the inputs for the cultivation of agricultural products, such as seeds, fertilizers, pesticides, etc; $c_2>0$ is the cost factor of effort for the farmer, and $c_2q^2>0$ represents the effort costs of farmers to produce agricultural products, including the time and energy spent in production.

Hypothesis 6. Natural random factor $\tilde{s}$ represents the impact of weather on unit projected output. $\tilde{s}<0$ indicates adverse conditions resulting in lower actual output than expected output; $\tilde{s}>0$ represents favorable natural conditions that make actual output higher than projected output. $\tilde{s}=0$ means that natural conditions have little impact, and actual output is comparable to projected output. Thus, the actual yield of the farmer is equal to $(1+\tilde{s})q$. The most extreme natural conditions lead the farmer no gains. So, $\tilde{s}>-1$. Assume that even if a farmer meets a bumper harvest, the actual harvest is at most double the expected output, i.e. $\tilde{s}<1$, and suppose that $E(\tilde{s})=0$.

2.2 The basic model

The farmer needs to determine the optimal expected output q_0^* at the beginning of production, the farmer prepares the production according to the expected output and sells the futures corresponding to the agricultural products in the futures market. Denote futures position as X_0. In the basic model, the effects of natural factors are not taken into account. Under condition of no basis of futures price based on the above assumptions, random gains of the farmer at the end of production are given by

$$\Pi_0 = q_0 \tilde{p} - C(q_0) + (f_0 - \tilde{f})X_0 \tag{1}$$

The optimal decision problem of the farmer is described as

$$(P_0)\max_{q_0, X_0} EU(\Pi_0)$$

Because the farmer is risk averse, whose utility function satisfies $U'(\Pi)>0$, $U''(\Pi)<0$, therefore, the optimal decision of the farmer is unique. Under the objective of maximizing the expected utility function, the corresponding first-order conditions are expressed as follows:

$$EU'(\Pi_0^*)(\tilde{p} - C'(q_0^*)) = 0 \tag{2}$$

$$EU'(\Pi_0^*)(f_0 - \tilde{f}) = 0 \tag{3}$$

Adding Equation (2) to Equation (3), it yields $EU'(\Pi_0^*)(f_0 - C'(q_0^*)) = 0$, then we have

$$C'(q_0^*) = f_0 \tag{4}$$

Then the optimal production decision can be obtained according to the cost function of $q_0^* = \frac{f_0 - \alpha_1}{2\alpha_2}$. Furthermore, based on Equation (3) and the unbiased futures market, it follows that

$$Cov(U'(\Pi_0^*), \tilde{f}) = 0$$

Then, we have

$$EU''(\Pi_0^*)(q_0^* - X_0^*) = 0$$

That is, $X_0^* = q_0^*$, the optimal futures position is fully hedged.

From the above analysis, it is not difficult to find that when the output is not affected by natural factors based on independent and no basis when farmers futures price optimal production decision and risk aversion. From the discussion above, we can find that when the output does not be affected by the natural factors, and if the futures is unbiased, the optimal production decision is free of risk aversion. The conclusion is general. Generally speaking, natural factors have great impacts on agricultural production. In the following, we will discuss the optimal production decision taking natural factors account for.

2.3 The optimal production decision when there is no basis

Consider the natural factors described in Hypothesis 6, and we assume that the natural factors are independent on the price. If there is no basis, note the output as q_1, the futures position is X_1, then the random profit of the farmer at the end of production is

$$\Pi_1 = (1+\tilde{s})q_1 \tilde{p} - C(q_1) + (f_0 - \tilde{f})X_1 \tag{5}$$

The optimal decision problem of farmers is described as follows

$$(P_1)\max_{q_1, X_1} EU(\Pi_1)$$

Proposition 1 If the risk averse farmer intends to hedge price risk with unbiased futures hedging, and the futures market has no basis, then the optimal production of the farmer is $q_1^* < \frac{f_0 - c_1}{2c_2}$. Furthermore, when the farmer is prudent (Kim, 1993), the optimal futures position is under-hedged, that is $X_1^* < q_1^*$. Where referring to Kim, when the position of the futures is smaller than the spot position, it is called as "under-hedged". When the position of the futures equals to the spot position, it is called as "full-hedged". And when the position of the futures is larger than the spot position, it is called as "over-hedged".

Proof: The first-order conditions of model (P_1) are as follows

$$EU'(\Pi_1^*)[(1+\tilde{s})\tilde{p} - C'(q_1^*)] = 0 \tag{6}$$

$$EU'(\Pi^*)(f_0 - \tilde{f}) = 0 \tag{7}$$

From Eq. (6) and Eq.(7), since there is no basis and the mean of $\tilde{s}$ is zero, we have

$$E[U'(\Pi_1^*)\tilde{s}\tilde{p}] = Cov(U'(\Pi_1^*)\tilde{p},\ \tilde{s}) \tag{8}$$

According to the definition of covariance, we have

$$E[U'(\Pi_1^*)\tilde{s}\tilde{p}] + EU'(\Pi_1^*)[f_0 - C'(q_1)] = 0 \tag{9}$$

Therefore, the sign of $E[U'(\Pi_1^*)\tilde{s}\tilde{p}]$ and $\frac{\partial E[U'(\Pi_1)|\ \tilde{s}=s]}{\partial s}|_{q_1=q_1^*, X_1=X_1^*}$ are the same.

Furthermore,

$$\frac{\partial E[U'(\Pi_1)|\ \tilde{s}=s]}{\partial s}|_{q_1=q_1^*, X_1=X_1^*} = E[U''(\Pi_1^*)q_1^*\tilde{p}^2]$$

Then from the condition of $U''(\Pi_1)<0$, it follows that the sign of $\frac{\partial E[U'(\Pi_1)|\ \tilde{s}=s]}{\partial s}|_{q_1=q_1^*, X_1=X_1^*}$ is negative.

Furthermore, the sign of $E[U'(\Pi_1^*)\tilde{s}\tilde{p}]$ is positive. Based on Equation (8) and $U'(\Pi)>0$, it yields

$$C'(q_1^*) < f_0 \tag{10}$$

According to Equation (10) and the cost function, we get the optimal output is $q_1^* < \frac{f_0 - c_1}{2c_2}$. By comparing the basic model, it finds that because of the effect of the natural factors, the firm will decrease its expected output. Therefore, if the farmer takes the natural factors into account for, it is suggested to reduce production scale appropriately.

Let X_1^* be the optimal futures position. Then, we have

$$\frac{\partial EU(\Pi_1)}{\partial X_1}|_{X_1=X_1^*} = 0 \tag{11}$$

The derivative function of the expected utility at the optimal output is

$$\frac{\partial EU(\Pi)}{\partial X_1}|_{X_1=q_1^*} = E[U'(\Pi_1^\Delta)(f_0 - \tilde{f})]$$

Since the futures market is unbiased, we have

$$\frac{\partial EU(\Pi_1)}{\partial X_1}|_{X_1=q_1^*} = -Cov(U'(\Pi_1^\Delta),\ \tilde{f})$$

where, $\Pi_1^\Delta = \tilde{s}q_1^*\tilde{p} - C'(q_1^*) + f_0 q_1^*$.

Since

$$\frac{\partial E[U(\Pi_1^\Delta)|\ \tilde{f}=f]}{\partial f} = E[U''(\Pi_1^\Delta)\tilde{s}q_1^*] = q_1^* Cov(U''(\Pi_1^\Delta,\tilde{s}))$$

and the sign $Cov(U''(\Pi_1^\Delta),\tilde{s})$ and $E(U'''(\Pi_1^\Delta)q_1\tilde{p})$ are the same. Besides, the farmer is prudent, then $E[U'''(\Pi_1^\Delta)q\tilde{p}] > 0$. Furthermore, we have

$$\frac{\partial EU(\Pi_1)}{\partial X_1}|_{X_1=q_1^*} < 0$$

According to the concavity of the utility function, it follows that $X_1^* < q_1^*$. So, the optimal futures position is under-hedged. Comparing the basic model, we suggest the farmer whose products are highly affected by weather to reduce the futures position.

2.4 The optimal production model when futures basis exists

Generally speaking, although the trend of futures price and spot price the same, there is still the basis. Referring to Benninga (1984), we assume that the relation of spot price and the futures price is

$$\tilde{p} = \alpha + \beta\ \tilde{f} + \theta \tag{12}$$

where the mean of θ is zero, and the variance of θ is finite.

Proposition 2 If the risk averse farmer intends to hedge price risk by using futures hedging, when the relation of spot price and the futures price is described in

Equation (12), the optimal production of the farmer is $q_2^* < \frac{\alpha + \beta f_0 - c_1}{2c_2}$. Furthermore, if the farmer is prudent and $\beta<1$, the optimal futures position is over-hedged, i.e., $X_2^*<q_2^*$.

Proof: According to Eqs.(5) and (12), the profit of the farmer can be expressed by

$$\Pi_2 = (1+\tilde{s})q_2(\alpha + \beta\tilde{f} + \theta) - C(q_2) + (f_0 - \tilde{f})X_2 \quad (13)$$

Then, the first-order conditions of the objective function are

$$EU'(\Pi_2^*)[(1+\tilde{s})(\alpha + \beta\tilde{f} + \theta) - C'(q_2^*)] = 0 \quad (14)$$

$$EU'(\Pi_2^*)(f_0 - \tilde{f}) = 0 \quad (15)$$

Adding Eqs. (14) and (15), we have

$$\begin{aligned}&[\alpha + \beta f_0 - C'(q_2)]EU'(\Pi_2) + EU'(\Pi_2\theta) + \\ &E[U'(\Pi_2)(\alpha + \beta\tilde{f} + \theta)\tilde{s}] = 0\end{aligned} \quad (16)$$

Since $EU'(\Pi_2)<0$, and the signs of the second term of Equation (16) and $EU'(\Pi_2)$ are the same, then $EU'(\Pi_2\theta)<0$. Similarly, the signs of the third term of Equation (16) and $EU''(\Pi_2)q_2(\alpha + \beta\tilde{f} + \theta)^2 < 0$ are the same, we have

$$E[U'(\Pi_1)(\alpha + \beta\tilde{f} + \theta)\tilde{s}] < 0$$

According to concavity of utility function and Equation (16), it follows that

$$C'(q_2^*) < \alpha + \beta f_0 \quad (17)$$

Based on Equation (12), we have $\overline{p} = \alpha + \beta\overline{f}$. Furthermore, due to the unbiased futures market, we have $\overline{p} = \alpha + \beta f_0$. Then, $C'(q_2^*) < \overline{p}$. Subsisting the cost function into Equation (17), we can find that the optimal production satisfies $q_2^* < \frac{\alpha + \beta f_0 - c_1}{2c_2}$.

The proof is similar to Proposition 1. One the one hand, at the optimal position, we have $\frac{\partial EU(\Pi_2)}{\partial X_2}|_{X_2=X_2^*} = 0$. On the other hand,

$$\frac{\partial EU(\Pi_2)}{\partial X_2}|_{X_2=q_2^*} = -Cov(U'(\Pi_2^\Delta), \tilde{f}) \quad (18)$$

where, $\Pi_2^\Delta = [(1+\tilde{s})(\alpha + \beta\tilde{f} + \theta) + f_0 - \tilde{f}]q_2^* - C(q_2^*)$.

Because the sign of $Cov(U'(\Pi_2^\Delta), \tilde{f})$ and $\frac{\partial E(U'(\Pi_2^\Delta)|\tilde{f}=f)}{\partial f} = EU''(\Pi_2^\Delta)(\beta-1)q_2^* + EU''(\Pi_2^\Delta)\tilde{s}$ are the same, when the farmer is prudent, the sign of $EU''(\Pi_2^\Delta)\tilde{s}$ and $EU'''(\Pi_2^\Delta)q_2^*(\alpha + \beta\tilde{f} + \theta) > 0$ are the same. Then, when $\beta<1$, $\frac{\partial EU(\Pi_2)}{\partial X_2}|_{X_2=q_2^*} < 0$. Thus, according to the concavity of utility function, we have $X_2^*<q_2^*$, i.e., the futures position is under-hedged. Comparing Propositions 1 and 2, we can find that, due to the effect of natural factors on the output and the effect of futures price basis, the farmer will reduce futures positions to meet risks.

3 Numerical simulation

We assume that the farmer exhibits constant absolute risk aversion (CARA). Namely, the farmer possesses the negative exponential utility function. Furthermore, in the theoretical section, the farmer is risk aversion, whose utility function satisfies $U'(\cdot)>0$, $U''(\cdot)<0$, and the negative exponential utility function just satisfies the conditions of $U(\Pi) = -e^{-\lambda\Pi}$, $\lambda>0$ is the risk aversion coefficient of the farmer. Larger λ means more risk aversion. In general, natural factors affect the actual output of agricultural products, while the output of agricultural products indirectly affects prices. When the output decreases, the corresponding price increases generally, whereas the price of agricultural products decreases. In this section, we assume that there are three natural states: $\tilde{s} = \frac{1}{a}, 0, \frac{1}{b}$, where $a<-1$, $b>1$. $\tilde{s} = \frac{1}{a}$ means that farmers suffer from adverse weather impacts, the actual output is decreases by $\frac{1}{a}$ of the actual output. Assume that the probability of the adverse wealth is p_1. Similarly, $\tilde{s} = \frac{1}{b}$ represents a favorable natural factor that increases actual output over projected output of $\frac{1}{b}$. The probability of the good natural factors is p_2; $\tilde{s} = 0$ means that the natural factors have no effect on the actual output. The probability of the normal natural factors is $1 - p_1 - p_2$. Prices are indirectly influenced by natural

factors. We suppose that when $\tilde{s}=0$, then $\tilde{p}=\bar{p}$; When $\tilde{s}=\frac{1}{a}$, $\tilde{p}=(1-1/a)\bar{p}$; And when $\tilde{s}=\frac{1}{b}$, $\tilde{p}=(1-1/b)\bar{p}$. Substituting the relations into Equation (13), we have the expected utility of the farmer is

$$EU(\Pi_2)=\exp\{-\lambda[(f_0+\alpha/\beta)X-C(q)]+\frac{\lambda^2X^2\sigma^2}{2\beta^2}\}\cdot$$
$$\{p_1\exp(-\lambda((1+1/a)q-X/\beta)(1-1/a)\bar{p})+$$
$$(1-p_1-p_2)\exp(-\lambda(q-X/\beta)\bar{p}+$$
$$p_1\exp(-\lambda((1+1/b)q-X/\beta)(1-1/b)\bar{p})\} \quad (19)$$

To analyze the effect of parameters on the target function, we take the following set of parameters:

$\bar{p}=f_0=6$, $\sigma=1$, $p_1=p_2=1/3$, $a=-2$, $b=2$, $\alpha=1$, $\beta=5/6$.

The methodology to solve the hedging problems can be summarized as follows:

Step 1. Simulate the price dynamics of spot and the futures based on the given parameters.

Step 2. Submit the prices and the parameters into Equation (19) to get the relationship between the utility function of farmers and the futures position and the production quantity.

Step 3. Find the maximum mean of $-e^{-\lambda\Pi}$, and determine the corresponding decision variables.

Figures 1 and 2 respectively describe the affects of futures position and production volume on utility function.

From Figures 1-2, it is not difficult to find that the utility function increases with the increase of the farmer's expected output; with the increase of the futures position, the utility function of farmers increases first and then decreases. From Figure 1, we can also find that when the futures position is set at 0 (That is, without futures hedging), the utility of the farmer is smaller than the use of futures hedging. This shows that futures hedging can improve the utility of a risk averse farmer. As seen from Figure 2, the futures position is not expected to be too large when the production is expected to be small. This is consistent with the conclusion that the futures position is under-hedged. When the expected output increases, the futures position is more, and the utility is larger. Although futures hedging is beneficial to improve the utility of the farmer, it is suggested the farmer appropriately to expand the production scale according to his own production capacity, rather than blindly increase the futures positions.

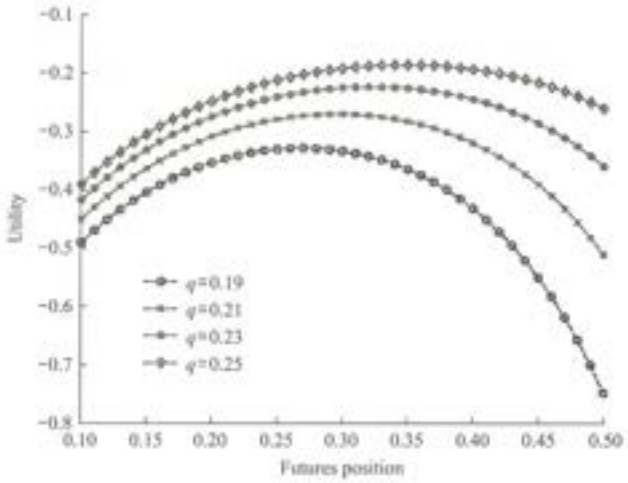

Figure 1 Relation between utility function and futures position

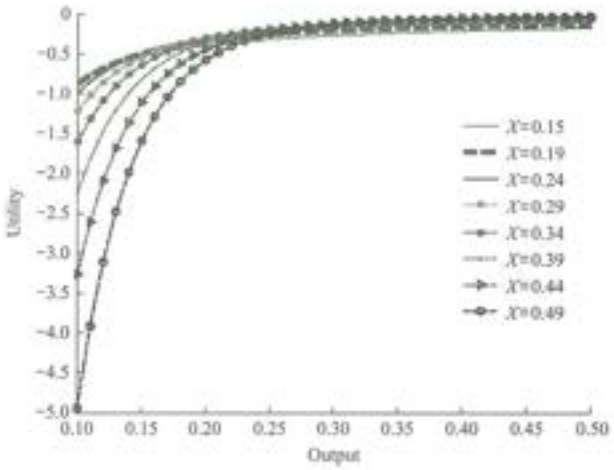

Figure 2 Relation between utility function and output

Figure 3 shows the maximum effectiveness of different risk aversion coefficients when the farmer uses futures hedging. In general, for the same variety of agricultural products, the corresponding futures has basis. If the corresponding agricultural products future does not exist, the farmer often can choose to cross futures hedging, and for cross futures, the basis may be greater. Therefore, take the risk aversion coefficient with 2 as an example to analyze the impact on the farmer's maximum utility as Figure 4.

We can see from Figure 3, with the increase of the farmer's risk aversion coefficient, the maximum utility increases. This shows that the greater the risk aversion coefficient of the farmer the more favorable to use of futures hedging. From Figure 4, as the basis of increased volatility, the maximum utility of the farmer reduces, it

means that volatility is not conducive to improving farmer's utility. Therefore, the farmer should choose futures with smaller basis volatility to hedge risk.

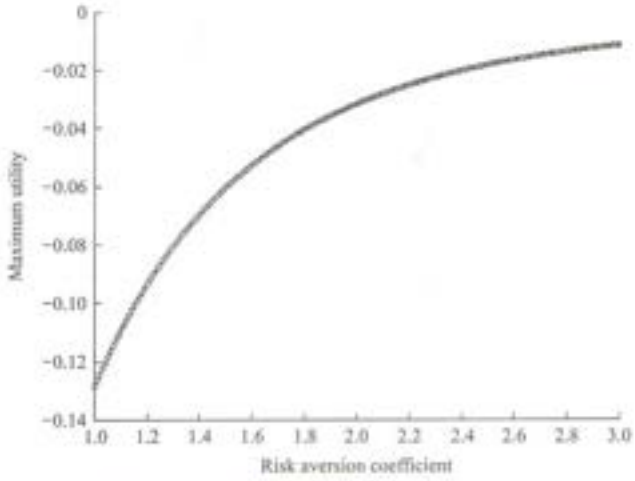

Figure 3 Relationship between maximum utility function and risk aversion coefficient

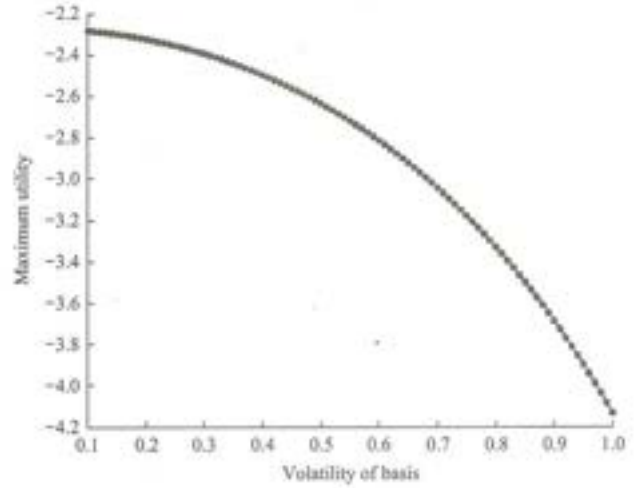

Figure 4 Relationship between maximum utility function and volatility of futures basis

The natural conditions (such as weather, etc.) have great influence on agricultural production. Figures 5-7 show the maximum utility of farmers under different conditions of bad, normal and good weather:

As can be seen from Figures 5-7, the maximum utility of farmers is affected by the probability of bad, normal, and good weather, wherein the greater the probability of good weather, the greater the maximum utility of farmers; Although the probability of bad weather and normal weather is not related to the maximum utility, by observing extreme conditions, it can be found that, when the probability of bad weather or normal weather is very small (close to 0), the maximum utility of the farmer is almost larger, while the probability is very large (near 1), and the utility of farmers is relatively smaller. That is, higher probability of bad weather or normal weather is not conducive to improving the maximum utility of the farmer.

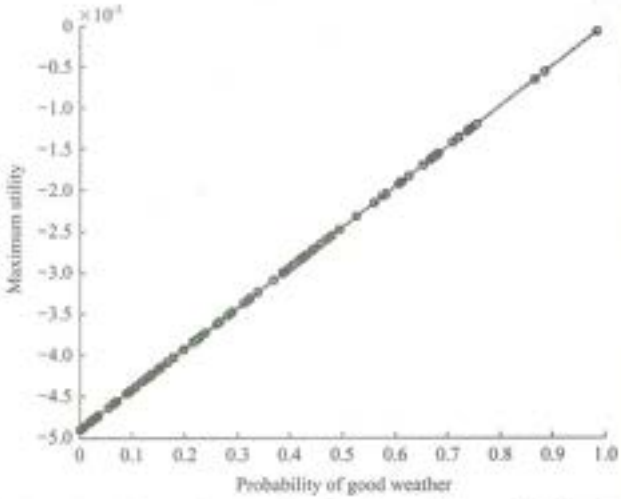

Figure 5 The maximum utility function and the probability of good weather

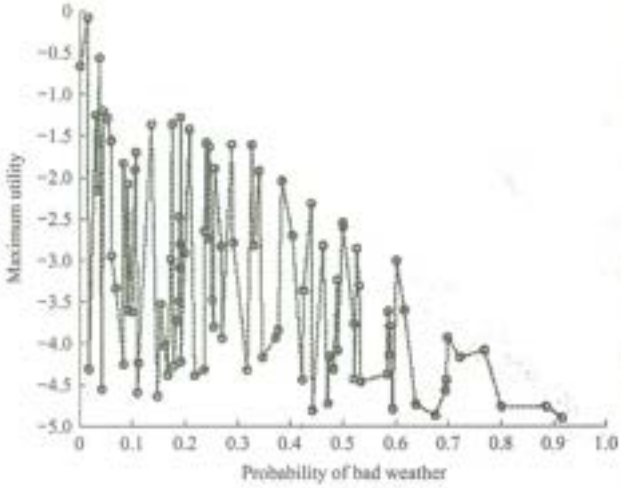

Figure 6 The maximum utility function and the probability of bad weather

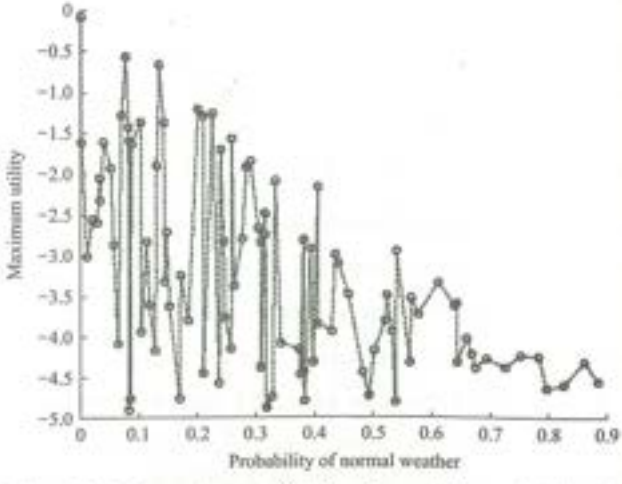

Figure 7 The maximum utility function and the probability of normal weather

4 Conclusion

This study focuses on the risk management of a risk averse farmer, and puts forward the optimal production decisions and futures hedging methods in three different situations. Theoretical research results show that: In the absence of natural factors and futures prices under the condition of no basis, the marginal cost corresponding to the most favorable output of a farmer is equal to the current price of futures, and the optimal futures position is fully hedged; In consideration of the natural factors and the futures price basis does not exist, the marginal cost of the most favorable output of farmers is less than the current price of futures, and the optimal futures position is under-hedged; When the natural factors are taken account for and there exists futures basis, if coefficient between the spot price and futures price is less than 1, the marginal cost of the most favorable output of the farmer is less than the average price of the spot, and the optimal futures position is still under-hedged. Through comparative study, we find that because of the influence of natural factors on actual output, farmers tend to reduce expected output and futures positions to meet risks. Taking negative exponential utility function as an example, the empirical results obtained by futures hedging can improve the farmer especially the greater risk aversion utility, volatility is not conducive to the basis of futures hedging. Probability analysis of different natural conditions occurs that good weather is conducive to the improvement of household utility. We suggest the farmer not blindly to increase futures positions, should be appropriate to select the basis volatility smaller futures for hedging. In this paper, we assume that the farmer's futures margin reserve capital adequacy, which can avoid the marking to market risk. A future research direction is to analyze the impact of the deposit of the opportunity cost of peasant's production decision.

Acknowledgments

This paper is supported by Hunan Provincial Natural Science Foundation of China (No.2016JJ6046) and Hunan Provincial Social Science Foundation of China (16YBA220).

[References]

[1] Benningga, S., R. Eldor, and I. Zilcha. 1984. The optimal hedge ratio in unbiased futures market. *Journal of Futures Market*, 4(2): 155–159.

[2] Bogetoft, P., and H. Olsen. 2002. Ten rules of thumb in contract design: lessons from Danish agriculture. *European Review of Agricultural Economics*, 29(2): 185–204.

[3] Broll, U., P. Welzel, and K .P. Wong. 2015. Futures hedging with basis risk and expectation dependence. *International Review of Economics*, 62(3): 213–221.

[4] Castiblanco, C., A. Moreno, and A. Etter. 2015. Impact of policies and subsidies in agribusiness: The case of oil palm and biofuels in Colombia. *Energy Economics*, 49(5): 676–686.

[5] Donovan, J. 2015. Guides for value chain development: a comparative review. *Journal of Agribusiness in Developing and Emerging Economies*, 5(1): 2–23.

[6] Feng, X. H., I. Moonb, and K. Ryuc. 2014. Revenue-sharing contracts in an N-stage supply chain with reliability considerations. *International Journal of Production Economics*, 147(1): 20–29.

[7] Holthausen, D. M. 1979. Hedging and the competitive firm under price uncertainty. *American Economic Review*, 69(5): 989–995.

[8] Huang, J. H., F. Ye, and Q. Lin. 2017. Government subsidy mechanism in agricultural supply chain considering capital constrain under random yield. *Chinese Journal of Management*, 14(2): 277–285.

[9] Kimbal, M. S. 1993. Standard risk aversion. *Econometrica*, 61(3): 589–611.

[10] Li, D. S., and D. F. Li. 2001. Option pricing model, risk investment decision and order agriculture. *Journal of Agrotechnical Economics*, (5): 1–4.

[11] Lin, Q., and F. Ye. 2014. Coordination for "company + farmer" contract-farming supply chain under Nash negotiation model. *Systems Engineering-Theory & Practice*, 34(7): 1669–1778.

[12] Ma, J. J., and X. G. Xu. 2008. Market structure and performance analysis of order agriculture. *Issues in Agricultural Economy*, 2008(3): 35–41.

[13] Omkar, D, and D. Palsule. 2013. Supply chain coordination using revenue-dependent revenue sharing contracts. *Omega*, 41(4): 780–796.

[14] Ritchken, P., and C. Tapiero. 1986. Contingent claims contracting for purchasing decision in inventory management. *Operation Research*, 34(6): 864–870.

[15] Sandmo, A. 1971. On the theory of the competitive firm under price uncertainty. American Economic Review, 61(1): 65–73.

[16] Shang, W. B. 2011. Evolution, problems and countermeasures

of China's subsidy policy for agriculture. *Asian Agricultural Research*, 3(12):14–18.

[17] Shang, W. F., M. Qi, and Q. Chen. 2013. Supply chain coordination by flexible option contracts with instant demand forecast information updating. *Chinese Journal of Management*, 10(12): 1847–1854.

[18] Wong, K. P. 2013. International trade and hedging under joint price and exchange rate uncertainty. *International Review of Economics & Finance*, 27(2): 160–170.

[19] Wong, K. P. 2014. Production and hedging in futures markets with multiple delivery specifications. *Decisions in Economics and Finance*, 37(2): 413–421.

[20] Xu, H. 2010. Managing production and procurement through option contracts in supply chains with random yield. *International Journal of Production Economics*, 126(2): 306–313.

[21] Yang, F. 2011. Empirical analysis on the contract breaking risk for using the futures market to manage agricultural orders. *Journal of Agrotechnical Economics*, (5): 97–104.

[22] Ye, F., and Q. Lin. 2012. Revenue sharing contract mechanisms of risk-averse supply chains. *Journal of Industrial Engineering and Engineering Management*, 26(1): 113–118.

[23] Ye, F., Q. Lin, and R. J. Mo. 2012. Contract-farming supply chain coordination mechanism based on B-S model. *Journal of Management Sciences in China*, 15(1): 66–76.

[24] Zhao, Y., S. Wang, and T. C. Cheng. 2010. Coordination of supply chains by option contracts: A cooperative game theory approach. *European Journal of Operational Research*, 207(2): 668–675.

Enhancement of lutein biosynthesis in *chlorella vulgaris-1068* under low temperature and luminosity stress conditions

Wang Wanqing[1,2], Chen Mingyang[1], Liu Jie[1], Hua Wei[1,2], Wu Shuang[1,2], Diao Mengjie[1], Cheng Yanling[1,2*]

(1. *Biochemical Engineering College, Beijing Union University, Beijing 100023, China;*
2. *Beijing Key Laboratory of Biomass Waste Resource Utilization, Beijing 100023, China*)

Abstract: Lutein, a high-value primary carotenoid with a broad range of applications in food, feed, nutraceutical, and pharmaceutical industries, has been widely studied in recent years. The green microalgae *Chlorella vulgaris-1068*(*C.v-1068*) screened by our lab showed both a high content in this carotenoid and a high growth rate and has a good profile for lutein production. This work studies the variety of environmental stimulants which enhance cellular accumulation of lutein from *C.v-1068*. The lutein accumulation and its biosynthesis pathway genes expression were analyzed under low temperature and high luminosity. We find that both cold and high light stresses can induce lutein biosynthesis in *C.v-1068*. In addition, during dark to light transition also leads to higher lutein productivity and the maximal lutein content (2.86 mg/g DW) was attained after six days dark-cultivated then exposed to 1000 μ photons m^{-2} s^{-1} for two days treatment. Consistently, the transcript levels of lutein biosynthesis genes *PSY* and *ZDS* were largely enhanced by cold, high light and dark to light transition treatments. And except *PSY* and *ZDS*, 1000 μ photons m^{-2} s^{-1} luminosity stress also highly increased expression of *PDS* as compared with low irradiance condition.

Keywords: lutein, microalgae, cold and luminosity stress, gene expression

Citation: Wang, W. Q., M. Y. Chen, J. Liu., W. Hua., S. Wu., M. J. Diao, and Y. L. Cheng. 2017. Enhancement of lutein biosynthesis in *chlorella vulgaris-1068* under low temperature and luminosity stress conditions. International Agricultural Engineering Journal, 26(3): 151–156.

1 Introduction

Carotenoids are an important group of natural pigments that are synthesized by all photosynthetic organisms as well as some non-photosynthetic bacteria and fungi (Goodwin, 1980). Lutein, as primary carotenoids, plays essential roles in photosynthesis, nutrition and protection against photooxidative damage in higher plants (Boussiba, 2000; Dweyer et al., 2001; Olmedilla et al., 2003; Stahl et al., 2005). In recent years, additional applications for lutein, especially in the field of human health, have been found. Lutein is known to play a critical function in prevention of certain cancers and chronic diseases (Nkondjock et al., 2005). Currently the commercial source of lutein is French marigold (*Tagetespatula*) (Campo et al., 2007). However, mass plantation of marigold occupies a large land area and is easily influenced by season and climate. Therefore, there is an increasing interest in microalgae as an alternative source of this carotenoid. *ChlorellaVulgaris-1068* screened by our lab is a strain that produces a high yield of lutein, which is proposed as potential source of lutein. Nevertheless, its lutein values are not high enough to be economically feasible on an industrial scale. To further improve lutein accumulation and productivity, the mechanism for molecular regulation of lutein levels is needed to be understood.

The lutein biosynthesis pathway in *ChlorellaVulgaris-1068* is similar to that of higher plants and is highly conserved in all carotene genic organisms (Liang et al.,

Received date: 2017-06-07 **Accepted date:** 2017-06-26
***Corresponding author: Cheng Yanling,** Professor of Biochemical Engineering College, Beijing Union University, Beijing 100023, China. Email: cheng1012cn@aliyun.com.

2006; Sieiro et al., 2003). The process starts with the condensation of two geranyl pyrophosphate (GGPP) molecules to form the first carotene, phytoene, catalyzed by phytoene synthase (PSY) (Figure 1). Then, four double bonds are introduced into the phytoene by phytoene desaturases (PDS) and ζ-carotene desaturases (ZDS) to produce pro-lycopene, which is isomerized by a specific isomerase to all-*tans* lycopene. The cyclation of lycopene by lycopene ε-cyclase (LYCE) and lycopene β-cyclase (LYCB) introduces ε- and β-ionone end groups, respectively, yielding α- and β-carotenes (Harjes et al., 2008). α-carotene is modified to lutein by hydroxylation of one β- and one ε-ring, catalyzed by two heme-containing cytochrome, β-carotene hydroxylase (BHY) and ε-carotene hydroxylase (EHY), respectively. Although the biosynthesis pathway is well known by us, the regulatory mechanisms that control lutein biosynthesis are poorly understood.

In this study, we provide biochemical and molecular evidence to demonstrate: (1) the effect of some environmental factors on lutein production in *ChlorellaVulgaris-1068*; (2) the molecular mechanism for environmental regulation of lutein biosynthesis.

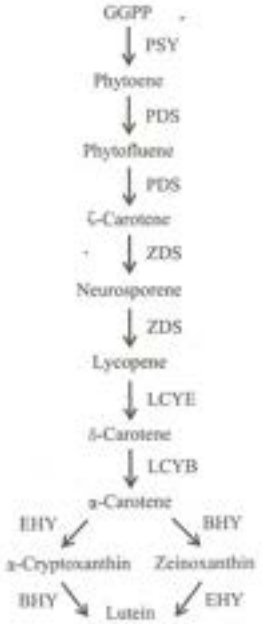

Figure 1 Schematic diagram of the lutein biosynthetic pathway and enzymes in plants and microalgae.

2 Materials and methods

2.1 Microalgae strain and culture conditions

The microalgae used in this study was *ChlorellaVulgaris-1068*, purchased from the Freshwater Culture Collection of the Institute of Hydrobiology, the Chinese Academy of Science, Wuhan, China.

2.2 Cultivation and stress conditions

2.2.1 Medium

C.v-1068 was cultivated in an algae culture medium, which composition per liter of distilled water is: 400 mg NH_4Cl, 100 mg $MgSO_4 \cdot 7H_2O$, 50 mg $CaCl_2 \cdot 2H_2O$, 108 mg K_2HPO_4, 56 mg KH_2PO_4, 2420 mg Tris (hydroxymethyl) aminomethane, 1 mL Glacial acetic acid, 1 mL trace elements solution consisted of 50 g Na_2EDTA, 22 g $ZnSO_4 \cdot 7H_2O$ (/L), 11.4 g H_3BO_3, 5.06 g $MnCl_2 \cdot 4H_2O$, 4.99 g $FeSO_4 \cdot 7H_2O$, 1.61 g $CoCl_2 \cdot 6H_2O$, 1.57 g $CuSO_4 \cdot 5H_2O$, 1.10 g $(NH_4)_6Mo_7O_{24} \cdot 4H_2O$, and 16 g KOH.*C.v-1068* strain was grown in 1 L Erlenmeyer flasks and continuously shaken at 80 r/min, 25°C in an incubator, illuminated with LED lamp at 150 μmol photons m^{-2} s^{-1} (μE) for 12 h per day.

2.2.2 Stressed phase: effect of temperature and illumination

C.v-1068 was grown in the algae medium for two weeks for biomass growth, and then the temperature and irradiances were changed. The temperature was decreased to 15°C and 4°C and the two high irradiances, 1000 μE and 2000 μE were treated. The experiments were carried out for three days.

2.2.3 Photoperiod effect

Two weeks' growth *C.v-1068* were transferred to various time periods of darkness, two days, four days or six days, then separately exposed to 150 μE for 6 d, 4 d and 2 d to induce lutein biosynthesis.

2.3 Harvesting

The microalgae were harvested by decantation prior to centrifugation at 10,000 rpm, at 15°C for 15 min (Beckman, Avanti J-251), then freeze-dried and ground and dry weight using glass fiber filters (GF/C, 47 mm, Whatman) at 80°C overnight.

2.4 Lutein extraction and HPLC analysis

Cells of *C.v-1068* were harvested by centrifugation and washed twice with distilled water. The pigment was extracted with 80% of acetone (v/v) according to leon et al (2005). Then the sample was centrifuged (2862×g, 5 min), and the supernatant was obtained for HPLC

analysis.

Lutein extracts were analyzed by HPLC (Agilent 1260series) as described by Wang, et al. (2010) equipped with a quaternary pump, automatic injector, degasser, column heater, ultraviolet detector and a data acquisition system. The extracts were separated with C18 column (Shim-packVP-ODS, 5 μm, 4.6 mm×250 mm) and the eluted compounds were analyzed at 445 nm. Mobile phase was the mixture of methanol and acetonitrile in a binary isocratic elution, keeping the ratio of 90:10 for 15 min. Flow rate was 1.0 mL/min and the column temperature was set to 20°C. The solvents were of HPLC-grade and filtered in 0.20 μm organic membranes before use. Samples were also filtered before injection.

2.5 Ribonucleic acid (RNA) extraction and quantitative real-time PCR (qRT-PCR)

The microalgae total RNA was extracted by RNA extraction kit (Tiangen). The first-strand cDNA was synthesized by reverse transcriptase (Invitrogen). Real-time PCR was performed with the SYBR Premix ExTaq kit (Takara) in a 15 mL reaction system following the manufacturer's instructions. Three biological replicates were performed for each sample, and the expression levels were normalized to those of *CBLP*, which encodes a G-protein β-subunit-like polypeptide. All primers sequences are listed in Table 1.

Table 1 Nucleotide sequences of primer pairs used for PCR amplification

Primer	Sequence(5'→3')
PSY-F	ATTCAGGGACATGATTGGG
qPSY-R	CCCTTGTACGCTTTGTCAAC
qZDS-F	AGCTCGACTTCCGCTTCTAC
qZDS-R	CACCTTGTCGGTGAAGGAC
qLYCE-F	AGGGCTGCTCATCCAGAG
qLYCE-R	AGATGCACGAGGAGGAGTG
qLYCB-F	CCTTTGAGCTGGACACCAT
qLYCB-R	CTTCAGGTCAGGGAAGTCAAC
qPDS-F	TGCTGGAGCTGGTCTTTGCA
qPDS-R	CGCACTCGGGCACCGTCTTG
qCBLP-F	CGCCACCAGTCCTCCATCAAGA
qCBLP-F	CTAGGCGCGGCTGGGCATTTAC

3 Results and discussion

3.1 Cold stress induces lutein biosynthesis in *Chlorella vulgaris-1068*

Temperature is one of the most important environmental factors affecting many biosynthetic pathways, including lutein biosynthesis (Hayman et al., 1974). To assess the influence of temperature on lutein level of *C.v-1068*, two-week-old normal cultured cells were transferred to cold stress, and the cellular lutein contents were recorded after three days. We found that lutein accumulation increased by about 40% with temperature down to 4°C and the maximum cellular lutein content (2.27 mg/g DW) was obtained at 15°C in the early deceleration phase of growth (Figure 2). These data indicate that temperature plays an important role in lutein biosynthesis of *C.v-1068*, and it maybe control the concentration of enzymes to regulate lutein level in algae cell.

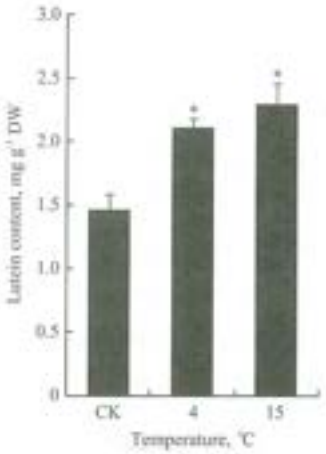

Figure 2 Effect of temperature on lutein accumulation in *Chlorella vulgaris-1068* 2-w-old normal cultured cells were grown at the indicated temperature and 25°C as a control (CK), the rest of culture conditions being the standard ones described in methods. Lutein content data are the mean values of three independent measurements recorded after 3 days. Asterisks indicate significant differences of 4°C and 15°C compared with CK based on Student's t test, $P<0.05$ (*)

3.2 Higher irradiance promotes lutein accumulation in*C.v-1068*

Lutein production and accumulation are reported to be positively affected by light irradiation in algae (Boussiba and Vanshak, 1991). We investigated lutein accumulation in *C.v-1068* bath cultures at different irradiances. Similar to cold treatment, 2-w-old normal cultured cells were transferred to light intensities of 1000 μmol photons m^{-2} s^{-1} or higher irradiance for three days. Lutein content in the culture was enhanced by 1.5-fold as irradiance increased from 150 to 1000 μE, decreasing at higher irradiance value (Figure 3). The

maximum cellular lutein content (2.32 mg g^{-1} DW) was reached at 1000 μE.

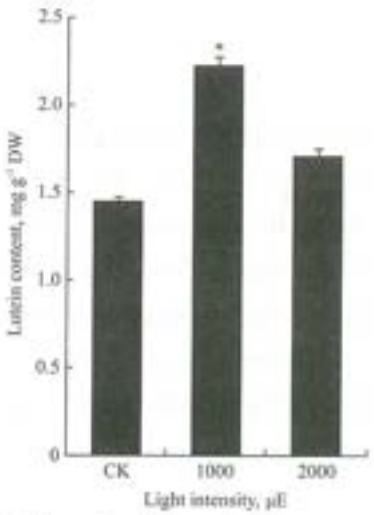

Figure 3 Effect of irradiance on lutein accumulation in *Chlorella vulgaris-1068*

Lutein contents of 2-w-old normal cultured cells transferred to high light (1000 μmol m^{-1} s^{-1}, 2000 μmol m^{-1} s^{-1}) for 3 days and 150 μmol photons m^{-2} s^{-1} as a control (CK). Error bars indicate the standard deviations of three independent measurements. Asterisks indicate significant differences of 1000 μE compared with CK based on Student's t test, $P<0.05$ (*).

3.3 Dark to light transition boost lutein biosynthesis in*C.v-1068*

Reactive oxygen species (ROS), generated by excess photooxidation caused by high light irradiance, has been found to play a crucial role upon lutein synthesis (Fernández et al., 2010). In darkness, the algae cells accumulate excess free protochlorophyllide (pchlide). When upon light illumination, excess pchlide may generate ROS or free radicals to enhance lutein biosynthesis and protect cell from ROS damage (Wagner et al., 2004). To investigate the influence of ROS on lutein level of *C.v-1068*, 2-w-old algae cells grown in different periods of darkness were illuminated with high intensity white light (1000 μE), and the lutein contents were menstruated after an additional two days. We found that the lutein accumulation increased by about 62% after four days or longer of dark treatment and the maximum cellular lutein content (2.61 mg/g DW) was obtained after six days treatment (Figure 4). We thus conclude that lutein holds a protection role conveyed by its antioxidant features.

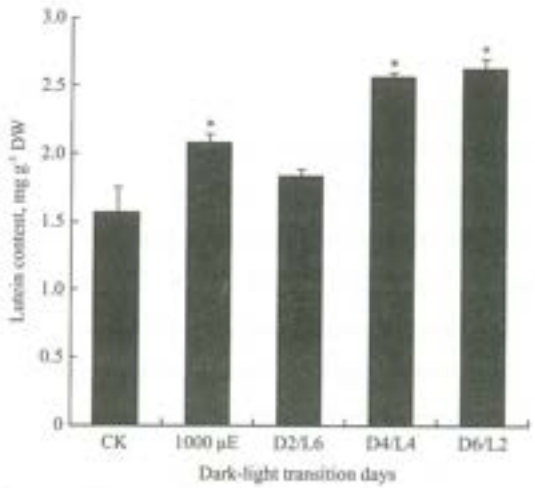

Figure 4 Effect of photoperiod on lutein accumulation in *Chlorella vulgaris-1068*

Two weeks' growth *C.v-1068* were transferred to various time periods of darkness, 2d, 4d or 6d, then separately exposed to 150 μE for 6 d, 4 d and 2 d to detect lutein contents. Cells cultivated at 150 μmol photons m^{-2} s^{-1} (μE) for 12h per day as a control (CK). Lutein content data are the mean values of three independent measurements. Asterisks indicate significant differences of 1000 μE, D4/L4 and D6/L2 compared with CK based on Student's t test, $P<0.05$ (*).

3.4 Effect of cold and irradiance on the expression of *C.v-1068* gene

To establish how the cold and luminosity stress affect the lutein biosynthesis, we analyzed the relative gene expression by quantitative RT-PCR (qRT-PCR). Cells of *C.v-1068* were grown at low irradiance and suitable temperature (as indicated in materials and methods) for two weeks. Then cells were kept in darkness for 18 h, in order to make the transcript levels come down to basal values. After this dark period, cells were subjected to either high irradiance or cold temperature. As shown in Figure 5a, under low temperature, the relative transcript levels of *PSY* and *ZDS* increased significantly, attaining 1.5-fold higher values than basal ones after 48 h. Similarly, high irradiance also had a strong effect on transcript levels of *PSY*, *ZDS* and *PDS*, which increased more than 2-flod higher as compared to basal level after 48 h (Figure 5b). To assess how expressions of lutein biosynthetic genes were regulated during dark to light transition, four days dark-grown cells was transferred to high light. Real-time RT-PCR analysis shown that the

PSY and *ZDS* transcript level were also largely elevated after light treatment for 48 h (Figure 5c). These findings indeed support the important role of environment in regulating lutein biosynthesis.

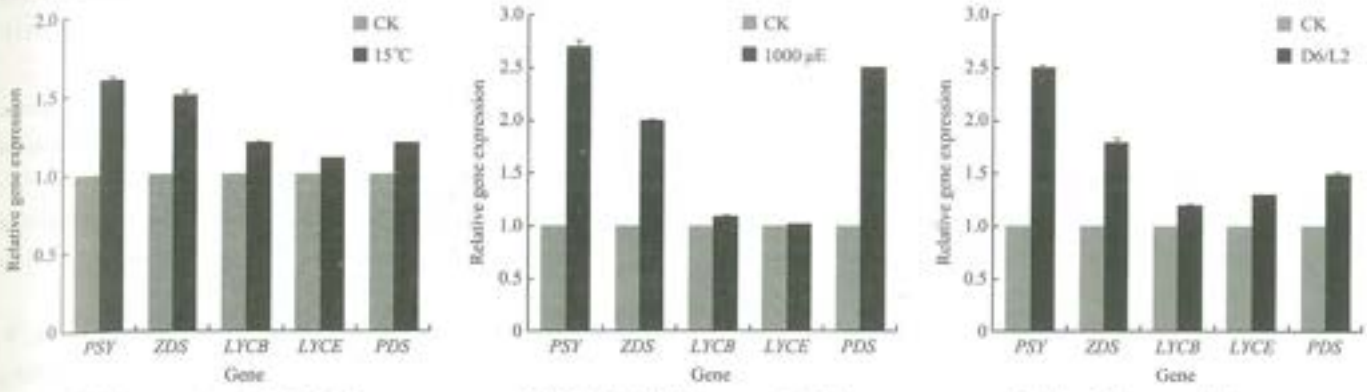

a. Cold stress treatment (15°C) for 2 days

b. 1000 μE high light treatment for 2 days

c. Six-day-darkness growth algae were transferred to 1000 μE high light for 2 days

Figure 5 Effect of temperature, irradiance and photoperiod on the mRNA levels of *PSY, ZDS, LYCB, LYCE, PDS*

Relative expression levels are normalized to the housekeeping control gene CFBLP. Error bars indicate the standard deviations of three independent measurements.

4 Conclusions

Microalgae as a new source of safe antioxidants has been the focus of extensive research. The microbial production of lutein has significant market and industrial potential. In this paper, we study the variety of environmental stimulants which can enhance volumetric production and cellular accumulation of lutein in green microalgae *C.v-1068*. Both cold and high light stresses can highly induce lutein biosynthesis and the transcript levels of lutein biosynthesis genes *PSY* and *ZDS* were consistently enhanced by cold, high light and dark to light transition treatments. Though manipulation of external stimulants can allow lutein production to be scaled-up for commercialization, the lutein synthesis also needs to be explored to the fullest extent. Modern technology, such as the use of recombinant DNA, coupled with the isolation of some of the vital genes involved in lutein biosynthesis have encouraged research into lutein production. Maybe the *PSY* and *ZDS* genes will be the suitable candidate factors.

Acknowledgements

This work was supported by grants from the science and technology foundation of Beijing municipal education committee and the opening foundation of Beijing key laboratory of biomass waste resource utilization to WW. We gracefully acknowledge financial support of Scientific Research Project from Facing Characteristic Discipline of Beijing Union University KYDE40201704. WW and YC conceived the research; WW and YC designed the experiments; WW, MC, JL and MD performed the research; WW, WH and YC analyzed data; and WW wrote the paper.

[References]

[1] Boussiba, S., and A. Vonshak. 1991. Astaxanthin accumulation in the green alga Haematococcuspluvialis. *Plant & Cell Physiology*, 32(7): 1077–1082.

[2] Boussiba, S. 2000. Carotenogenesis in the green alga *Haematococcuspluvialis*: Cellular physiology and stress response. *Physiologia Plantarum*, 108(7): 111–117.

[3] Del Campo, J.A., M. Garcia-Gonzalez., and M.G. Guerrero. 2007. Outdoor cultivation of microalgae for carotenoid production: Current state and perspectives. *Applied Microbiology & Biotechnology*, 74(7): 1163–1174.

[4] Dweyer, J.H., M. Navab, K.M. Dwyer, K. Hassan, P. Sun, A. Shircore, S. Hama-Levy, G. Hough, X. Wang, T. Drake, N.B. Merz, and A.M. Fogelman. 2001. Oxygenated carotenoid lutein and the progression of early atherosclerosis. *Circulation*, 103(24): 2922–2927.

[5] Fernández-Sevilla, J.M., F.G. Acién-Fernández, and E. Molina-Grima. 2010. Biotechnological production of lutein and its applications. *Applied Microbiology & Biotechnology*, 86(1): 27–40.

[6] Goodwin, T.W. 1980. The biochemistry of the carotenoids.*Plants*, 1.

[7] Harjes, C.E., T.R. Rocheford, L. Bai, T.P. Brutnell, C.B. Kandianis, S.G. Sowinski, A.E. Stapleton, R. Vallabhaneni, M. Williams, and E.T. Wurtzel. 2008. Natural genetic variation in lycopene epsilon cyclase tapped for maize biofortification. *Science*, 319(5861): 330–33.

[8] Hayman, E.P., H. Yokoyama, C.O. Chichester, and K.L. Simpson. 1974. Carotenoid biosynthesis in Rhodotorulaglutinis. *Journal of Bacteriology*, 120(3): 1339–1343.

[9] León, R., M. Vila, D. Herranz, and C. Vilches. 2005. Production of phytoene by herbicide-treated microalga Dunaliellabardawil in two phase systems. *Biotechnology & Bioengineering*, 92(6): 695–701.

[10] Liang, C., F. Zhao, W. Wei, Z. Wen, and S. Qin. 2006. Carotenoid biosynthesis in cyanobacteria: structural and evolutionary scenarios based on comparative genomics. *International Journal of Biological Sciences*, 1(4): 197–207.

[11] Nkondjock, A., P. Ghadirian, K.C. Johnson, and D. Krewski. 2005. Dietary intake of lycopene is associated with reduced pancreatic cancer risk. *Journal of Nutrition*, 135(3): 592–597.

[12] Olmedilla, B., F. Granado, I. Blanco, and M. Vaquero. 2003. Lutein, but not α-tocopherol, supplementation improves visual function in patients with age-related cataracts: a 2-y double blind, placebo-controlled study. *Nutrition*, 19(1): 21–25.

[13] Siciro, C., M. Poza, T. Miguel, and T. G. Villa. 2003. Genetic basis of microbial carotenogenesis. *International Microbiology*, 6(1): 11–16.

[14] Stahl, W., and H. Sies. 2005. Bioactivity and protective effects of natural carotenoids. *Biochimica Et Biophysica Acta Molecular Basis of Disease*, 1740(2): 101–107.

[15] Wagner, D., D. Przybyla, R. Op den Camp, C. Kim, F. Landgraf, K.P. Lee, M. Würsch, C. Laloi, M. Nater, E. Hideg, and K. Apel. 2004. The genetic basis of singlet oxygen-induced stress responses of Arabidopsis thaliana. *Science*, 306(5699): 1183–1185.

[16] Wang, Y. Y., X. Q. Wang, Z. Z. Wang, and D. Ji. 2010. Separation of carotenoids in chlorella sp by HPLC. *Progress in Modern Biomedicine*, 10(8): 1546–1549.

Effects of purple yam polysaccharides (PYPs) on the liver and brain in a D-galactose-induced model of aging in rats

Zhang Limei[1,2], Song Shuhui[3], Gan Jing[1], Satoru Nirasawa[4], Cheng Yongqiang[1*]

(1. *Beijing Key Laboratory of Functional Food from Plant Resources, College of Food Science and Nutritional Engineering, China Agricultural University, Beijing 100083, China;*
2. *New Era Health Industry (Group) Co. Ltd., Beijing 102206, China;*
3. *National Engineering Research Center for Vegetables, Beijing, 100080, China;*
4. *Japan International Research Center for Agricultural Sciences, Tsukuba 305-8686, Japan*)

Abstract: Purple yam polysaccharides (PYPs) are natural polysaccharides extracted from purple yams, a Chinese yam with bright purple flesh used as a traditional Chinese medicine (TCM) and functional food. This study aimed to verify the anti-aging activity of PYPs and explore their mechanism of action at the molecular level. Purple yam powder water extracts were precipitated with ethanol at a final concentration of 80% (v/v). PYPs were obtained after the precipitate lyophilized. A model of aging in rats by injecting D-galactose for 45 d with the simultaneous administration of PYPs (20, 100, and 500 mg/kg bw) was constructed. The results showed that PYPs administration reduced damage to the liver and brain cells of rats and attenuated the production of malondialdehyde (MDA) induced by D-galactose. In addition, PYPs administration significantly restored the activities of superoxide dismutase, catalase, glutathione, and glutathione peroxidase and the total anti-oxidant capacity. The expression levels of the p16 and p21 genes in the liver and brain tissues of rats treated with PYPs were also found to be significantly down-regulated compared with their expression in the D-galactose group. Based on these results, the conclusions can be drawn that PYPs protect against the oxidative damage caused by D-galactose and can delay the process of senescence by affecting the p16/p21 pathway, and PYPs could be a beneficial ingredient for inclusion in healthcare products.
Keywords: purple yam polysaccharides, D-galactose, p16/p21 genes, aging

Citation: Zhang, L. M., S. H. Song, J. Gan, S. Nirasawa, and Y. Q. Cheng. 2017. Effects of purple yam polysaccharides (PYPs) on the liver and brain in a D-galactose-induced model of aging in rats. International Agricultural Engineering Journal, 26(3): 157–165.

1 Introduction

The Chinese yam (*Rhizoma dioscoreae, Dioscorea opposita*) has been used as a TCM for more than 2000 years for treating diabetes (Zhang et al., 2011; Marie et al., 2006), diarrhea (Park et al., 2013; Huang et al., 2012), pneumopathy (Yang et al., 2015), and other ailments (Han et al., 2014; Liu et al., 2007; Chiu et al. 2013). Chinese yam polysaccharides are the main functional components of this medicine and in the past decade, a number of studies on these polysaccharides have reported that the results showed the Chinese yam polysaccharides have anti-aging effects (Hsuet et al. 2009; Ju et al. 2014). The purple yam (*Dioscorea alata* L) is a type of Chinese yam with purple flesh and is considered to have a greater nutritional value than other Chinese yams due to its anthocyanin content (Kumi 1991a; Kumi 1991b; Lubag 2008). However, as a novel functional raw material, there are few studies on purple yam that focused on the breeding of this plant and analyzing its nutritional composition, such as the levels of anthocyanin, saponin, and polysaccharides. So far, no specific research has been conducted on the extraction and function of PYPs.

D-galactose (D-gal) is a reducing sugar that can disturb the body's metabolic process, cause cognitive declines, reduce the activity of anti-oxidant systems, and even cause cell senescence if fed to rats in excessive

Received date: 2017-05-09 **Accepted date:** 2017-07-20
* **Corresponding author:** Cheng Yongqiang, Beijing Key Laboratory of Functional Food from Plant Resources, College of Food Science and Nutritional Engineering, China Agricultural University, Beijing 100083, China, Email: anthony.nolan@ucd.ie.

amounts. A great deal of research has been performed on D-gal-induced models of aging in rats to evaluate antioxidant capacities (Jin 2012), memory repair (Wang 2016), cognitive improvements (Otilia 2014; Wang 2010), protection against the effects of aging (Mao 2010) and other topics.

Currently, more and more researchers are focusing their studies on the molecular mechanism of senescence to evaluate the anti-aging activities of compounds and identify materials that may be valuable in preventing age-related diseases (Flachsbart 2010; Murielle 2009; Ryu 2008). In recent years, studies have shown that there are senescence-associated genes (SAGs) in the human body, which can lead to senescence when overexpressed (Yoon 2004; Park 2011). P16 and p21 are two of the most important senescence genes. A large number of studies have indicated that the main pathways of cellular senescence induced by oxidative stress involve the expression of p16 and p53/p21 (Lim 2011; H. Christian Reinhardt 2012). Therefore, p16 and p53/p21 likely play key roles in regulating pathways leading to cellular senescence.

In this paper, the D-gal-induced model of aging in rats was established. The activity of anti-oxidant enzymes and the expression of p16 and p21 mRNA were then measured and the histological changes in liver and brain tissues of aging rats were observed to evaluate the anti-aging effects of PYPs.

2 Material and methods

2.1 Preparation of PYPs

Purple yam rhizomes (*Dioscorea alata* L), which is a tuber of Dioscorea opposite Thunb of Dioscorea plants, are mainly produced in Jiangxi, Fujian, Guangxi provinces of China. In this study, the purple yam rhizomes were purchased from *Wanzai Huiming Organic Agriculture Science and Technology Co., LTD.* in Jiangxi province of China.

The rhizomes were washed with water, then sliced and freeze-dried and crushed to obtain the lyophilized purple yam powder. The powder (100 g) was soaked in 80% ethanol (8 times the volume of the powder) and stirred for 2 h at ambient temperature to remove some of the colored and organic materials. The extraction mixture was then centrifuged, and the supernatant was discarded. Crude PYPs were extracted from the precipitate under the following optimized extraction conditions: ratio of water to raw materials, 20:1; extraction temperature, 80°C; extraction time, 2 h; extractions were performed twice. Then, the solution was centrifuged at 8000 r/min for 30 min and concentrated with a rotary evaporator at 55°C under a vacuum. After this step, ethanol was added at a final concentration of 80% (v/v), and the solution was kept at 4°C overnight. The crude PYPs samples were obtained via centrifugation (8000 r/min, 30 min), and the precipitate was lyophilized.

2.2 Chemicals

The following chemicals were of analytical grade and were obtained commercially: D-galatose (dissolved in 0.9% saline at a concentration of 400 mg/mL; Beijing Chemical-Reagent Company, Beijing, China); Trizol (Invitrogen, USA), DNase I, 6×Loading Buffer (Fermentas (MBI), USA), M-MLV, dNTP, 2×Ex TaqMix (Takara, Dalian, China), and Eva_green (Biotium, USA). Assay kits for measuring superoxide dismutase (SOD), glutathione (GSH), glutathione peroxidase (GSH-Px), total antioxidant capacity (T-AOC), and malondialdehyde (MDA) were purchased from Jiancheng Institute of Biotechnology, Nanjing, China.

2.3 Animals and models

A D-galactose-induced model of aging in rats was established as previously described (Fu, 2011). Fifty healthy male SD rats (average weight, 150±2.4 g; provided by the experimental animal center, Academy of Military Medical Sciences, Permit No. scxk (Army) 2012004) were randomly divided into five groups: a control group (Cont), a D-gal-treated group (D-gal), a low-dosage group (PYP-L, 20 mg/kg bw), a medium-dosage group (PYP-M, 100 mg/kg bw), and a high-dosage group (PYP-H, 500 mg/kg bw). The Cont group was injected with normal saline daily for 45 d, while the other groups were injected with D-gal (400 mg/kg bw) over the same period. In this period, the low, medium and high-dosage group was administrated with PYPs, while the Cont group and the D-gal group were administrated with normal saline. All groups were

housed in an air-conditioned animal facility maintained at a constant temperature of 23°C±1°C, a relative humidity of 60%±5%, and with a 12 h day/night cycle. After 45 d, all the rats were sacrificed, and the liver and brain tissues were collected.

2.4 Biochemical assays

The liver and brain tissue samples were ground (1:10 w/v) in a cold saline solution (0.86% NaCl). Homogenates was centrifuged at 3000 g for 10 min at 4°C, and the supernatant was collected for the detection of antioxidant enzymes. The T-AOC, the SOD, GPx and CAT activities and the GSH and MDA contents were measured using commercial kits according to the manufacture's protocol.

2.5 Histological analysis

Liver and brain tissue samples were rinsed with distilled water and fixed with 10% neutral buffered formalin. They were then dehydrated in an increasing series of ethanol, cleared in xylene and embedded in paraffin wax. Slices (4 μm thick) where collected and stained with hematoxylin-eosin (HE). Histological assessments were performed using a Leica camera (Germany).

2.6 RNA isolation and real-time PCR

Total RNA was extracted separately from liver and brain tissue using a Trizol solution following the manufacturer's protocol, and the samples were preserved at −70°C. Total RNA was quantified via denaturing agarose gel electrophoresis (1.5% agarose gel). A 40-μL reaction system was used for the reverse transcription, which contained 4 μg RNA, 4 μL reverse transcription primer T18 (50 μM), 8 μL5×first-strand buffer (250 mM Tris-HCl, 375 mM KCl, 15 mM $MgCl_2$), 2 μL dNTP mix (10 mM), 1 μLRNase inhibitor (20 Uμ/L, MBI), 2 μLM-MuLV (MBI), and DEPC water. The reaction mixture was incubated at 42°C for 60 min and then heated at 70°C for 10 min to spot the reaction.

Quantitative RT-PCR reactions were conducted in a volume of 25 μL using an ABI-2720 PCR system (ABI). Each reaction contained 1.0 μL template (cDNA), 10 mM forward/reverse primer (0.75 μL), 12.5 μL 2xEx TaqMix, 0.75 μLEVA green, and 10 μLddH_2O. All primers are shown in Table 1. All PCR reactions were performed under the same conditions: an initial denaturation at 95°C for 5 min, a denaturation at 95°C for 30 s, annealing at 60°C for 30 s, extension at 72°C for 30 s, and termination of the reaction at 4°C.

Table 1 PCR primers

Primer	Sequence, 5' to 3'	Base number	Length of product bp
Actin (forward)	GAAGTGTGACGTTGACATCCG	21	282
Actin (reverse)	GCCTAGAAGCATTTGCGGTG	20	282
p16 (forward)	CTACTCTCCTCCGCTGGGAA	20	116
p16 (reverse)	GGCCTAACTTAGCGCTGCTT	20	116
p21 (forward)	CTGGTGGCGTAGGCAAGA	18	201
p21 (reverse)	AGCCCTCCCCAGTTCTCAT	19	201

2.7 Statistical analysis

All data are expressed as the means ± standard deviation (SD), and analyses were performed using Turkey test in SPSS 19.0 (SPSS China, Shanghai, China). Significant between groups was determined using $p<0.05$ confidence limits.

3 Results and discussion

3.1 Histological observations

Typical histological images are shown in Figure 1. Compared with the Cont group, liver cells from the D-gal group were characterized by a column cells decrease, nuclear condensation, enhanced staining, and obvious cellular fatty degeneration. However, these characteristics were improved in PYP-treated rats, especially in the PYP-M and PYP-H groups, with the cells showing a tight and orderly organization and a no fatty degeneration. These results indicate that PYPs can prevent the liver damage induced by D-galactose.

The images of the CA1 region of the hippocampus in the Cont rats showed a normal appearance: 3-4 layers of pyramidal neurons arranged closely and neatly, all with a clearly visible nucleus, nucleolus, and cytoplasm. However, this arrangement of neurons became loose and disorganized following D-gal-induced injury: the structure of neurons was changed and some neurons died or even disappeared. PYP-treatment group appeared to obviously stimulate the recovery of neuronal damage caused by D-gal. As can be observed in Figure 1, the neurons in the samples from the PYP-M and PYP-H groups generally appeared normal.

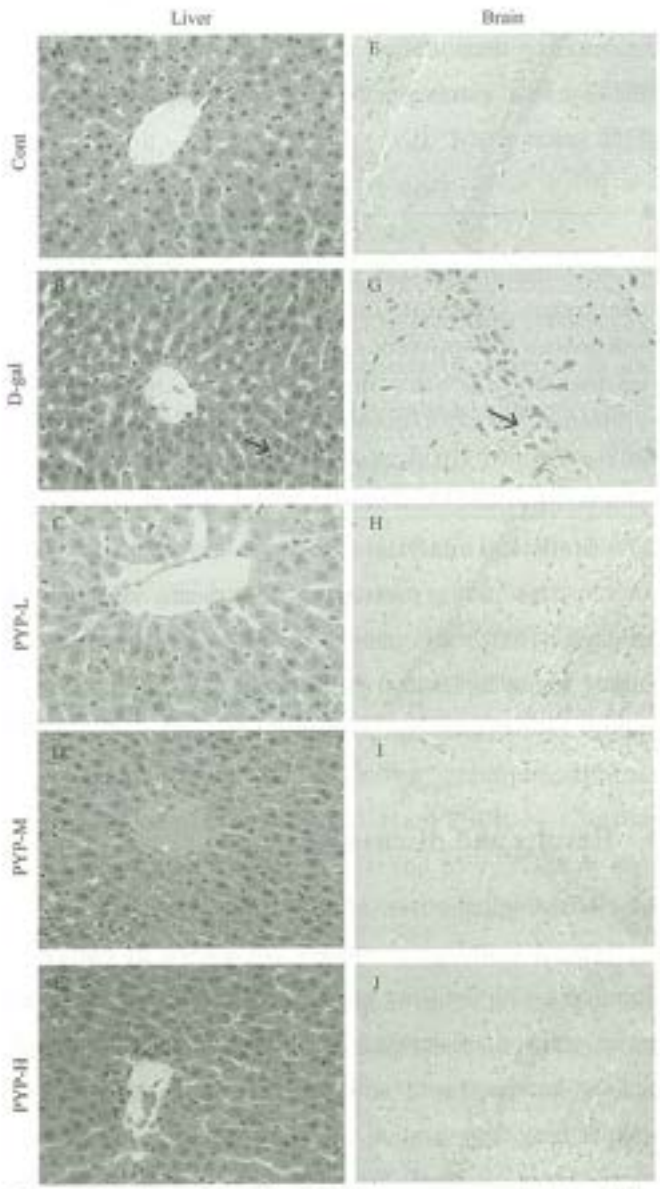

B: Liver of D-gal rats. Tissue is marked by the appearance of obvious cellular fatty degeneration (black arrow), which vanishes in D (PYP-M, 100 mg/kg bw) and E (PYP-H, 500 mg/kg bw). G: CA1 region of the hippocampus of a D-gal rat brain. Pyramidal cell morphology is changed entirely, with cell deformation and death (black arrow). H (PYP-L, 20 mg/kg bw), I (PYP-M, 100 mg/kg bw), and J (PYP-H, 500 mg/kg bw) showed relatively normal pyramidal cell morphologies.

Figure 1 Effects of PYPs on the histological characteristics of liver and brain tissues of rats

3.2 Antioxidant enzyme activities and GSH and MDA contents in the liver and brain

Many studies have shown that bioactive polysaccharides have antioxidant properties that can enhance the activity of the body's antioxidant enzyme system. GSH, GPx, T-AOC, CAT, and SOD are the main antioxidant enzymes and can effectively scavenge ROS in the body. As is shown in Figure 2, compared with the activities in the Cont group, the antioxidant enzyme activities were obviously reduced in the D-gal group, while PYP treatment counteracted this D-gal-induced decline in antioxidant capacity and even significantly increased GPx activity (p<0.01), T-AOC (p<0.01) and the GSH content (p<0.05) in the liver of rats. PYP treatment also protected the antioxidant enzyme system in the brains of rats, but this influence was significantly weaker than that observed in the liver.

MDA is a by-product of the membrane lipid peroxidation caused by free radicals and is widely used as a biomarker of oxidative stress. The results in Figure 2f show that D-gal treatment led to higher MDA levels in the liver and brain compared with levels in the Cont group. However, the MDA content was decreased compared with levels in the D-gal group after PYP treatment.

3.3 Expression of p16, p21 mRNA in rat liver and brain tissues

Compared with their expressions in the Cont group, p16 and p21 mRNA expression in the D-gal group was significantly increased (p<0.01) in rat liver and brain tissues, indicating that the D-gal-induced aging model was successful. As Figure 3a and b show, the mRNA expression of p16 and p21 in the PYP-treated groups was nearly the same as that in the Cont group, with the low-, medium- and high-dose PYP-treated groups showing significantly lower expression levels than were observed in the D-gal group (p<0.01). This indicates that PYPs function to delay age-associated effects by reducing the expression of the senescence-associated genes p16, p21.

4 Discussion

An increasing number of studies have demonstrated that rats receiving subcutaneous injections of D-gal (50-500 mg/kg) for 6-8 weeks showed a loss of neurons, oxidative damage and mitochondrial dysfunction, resulting in cognitive dysfunction, memory impairment and other signs of aging, which are processes that are similar to those that normally occur in aging brains (Gong, 2016; Gong, 2015; Zhou, 2013). This study proved that long-term injections of D-gal can successfully establish an animal model of aging.

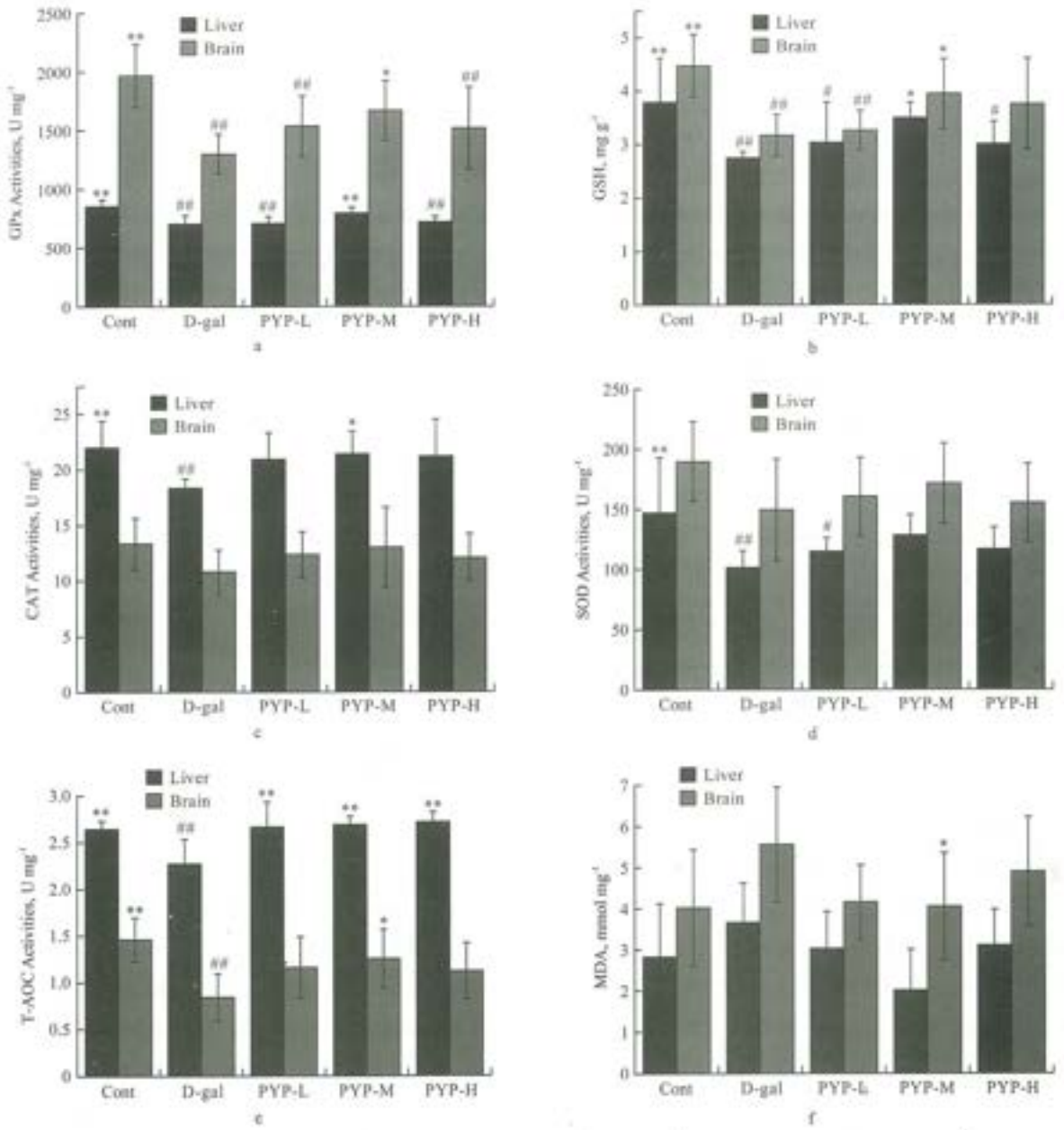

Note: Values are expressed as the means ±S.D. ($n=10$). $^{\#}p<0.05$ compared with the Cont group, $^{\#\#}p<0.01$ compared with the Cont group, $^{*}p<0.05$ compared with the D-gal group, $^{**}p<0.01$ compared with the D-gal group.

Figure 2 Effect of PYPs on the activities of antioxidant enzymes and the GSH and MDA content in liver and brain samples from rats

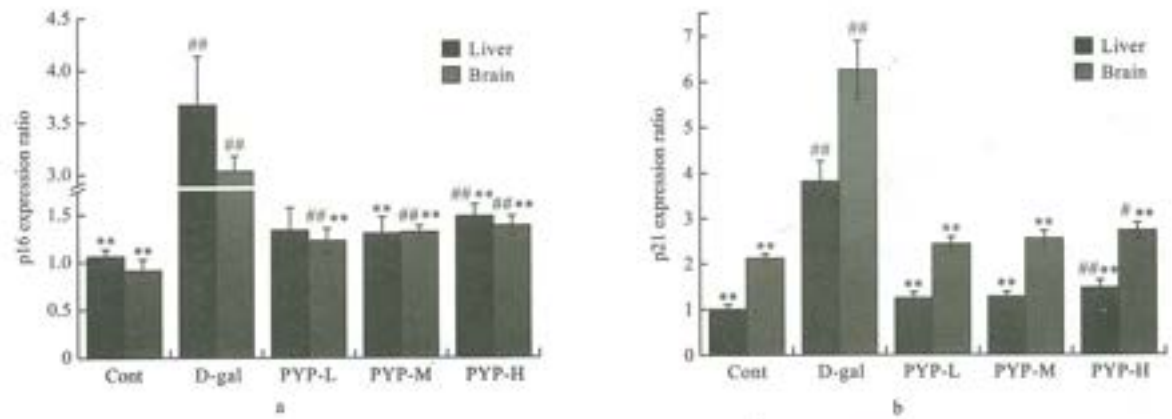

Note: Values are expressed as the means ±S.D. ($n=10$). $^{\#}p<0.05$ compared with the Cont group, $^{\#\#}p<0.01$ compared with the Cont group, $^{*}p<0.05$ compared with the D-gal group, $^{**}p<0.01$ compared with the D-gal group.

Figure 3 Effect of PYP treatment on p16 and p21 mRNA expression in the liver and brain tissues of rats

After 45 d of treatment, the rats in Cont group and the PYP-treated groups showed normal dietary habits, were lively, and had good skin elasticity, while the D-Gal group showed weakness, slowed activity, a dull hair color, and even depilation. Moreover, the antioxidant indices of D-gal-treated rats were significantly different than those of the control group, which shows that the D-gal-induced aging model was successful.

The overproduction of free radical and the chain reactions they can cause are essential factors leading to age-related effects in the body. Excessive free radicals can attack the lipids and proteins located in the inner mitochondrial membrane, resulting in mitochondrial dysfunction, cell damage, aging and disease.

SOD, GSH-Px, GSH and CAT exist in the body as an endogenous antioxidant defense system. GSH is a tripeptide and is involved in a number of crucial cellular functions, such as free-radical scavenging, metal binding and detoxification. GSH-Px is an enzyme specialized for protecting glutathione from peroxide reactions, and it plays a significant role in maintaining cell membrane integrity. In this study, the GSH content and GSH-Px activity were shown to be simultaneously and significantly increased, relative to the levels in the D-gal group, in the liver and brain tissues of PYP-treated rats, particularly in the PYP-M group, and both reach 80% of the levels in control group. These data indicated that PYPs has enhancing effects on the activity of antioxidant enzymes in removing ROS and resisting oxidative damage and oxidative stress. In addition, PYPs can recover the activities of CAT and SOD in D-gal-induced aging rats. MDA is an important product of lipid peroxidation, and it is a sensitive indicator that can reflect the level of free radicals and the extent of oxidative damage occurring under conditions of oxidative stress. The MDA content was sharply increased in the liver and brain tissues of the D-gal group, which demonstrates that the excessive intake of galactose leads to a disruption of lipid metabolism. MDA levels were reduced in the PYP-treated groups. All the results above suggest that PYPs can delay the aging-induced effects of oxidative stress in the liver and brain by improving the ability of the body to scavenge oxygen free radicals.

Recent research has found that aging is controlled by specific genes, such as the p16 gene (Shen, 2006). P16 is a significant Ink4 (inhibitor of CDK4) protein and can inhibit the effect of the cyclin-D1 CDK6 and cyclin-D1 CDK4 complex. Excessive p16 expression is considered a signal of cell senility. Although a few researchers suggest that the abnormal expression of some aging-related genes are just a small component of the factors that influence cell senescence, numerous experiments have confirmed that the overexpression of p16 or p53/p21 can specifically cause cell senescence (Victor, 2010; Brigitte, 2008; Wang, 2014; Tozawa, 2007; Feng, 2008; Guterres, 2013). The expression of p16, based on an immunohistochemical evaluation, is consistent with a good prognosis of some cancers, and the expression of the p16 gene can be used as a predictor for the aging-related diseases (Yang, 2014; Su, 2014; Tsygankov, 2009). In this study, the expression of the p16 gene was significantly upregulated in the liver and brain tissues of the D-gal group compared with its expression in the control group ($p< 0.01$) and was maintained at a level close to that of control group by PYPs treatment. This suggests that the capacity of PYPs to delay senility is related to a decrease in p16 gene expression.

P21 is another important biomarker of cell senescence, and the expression of p21 is significantly increased in aging cells. P21 is an important member of the cell cycle inhibiting group of proteins, which can inhibit the activity of the cyclin-dependent kinase (CDK) complex, regulating the relationship between the cell cycle and DNA repair. Many of the studies on p21 have mainly focused on the function of p21 in relation to tumor cells, and all the results showed that the expression level of p21 can influence many types of cancer (Koo 2015). Currently, p21 expression is used as an indicator in the diagnosis and prognosis of tumors (Masson, 2015; Varshney, 2015; Jawanjal, 2015). P21-induced cellular senescence is also related to reactive oxygen species (ROS). It has been found that p21 can increase the level of ROS in normal fibroblasts and p53-negative tumor cells, while ROS inhibitors can delay p21-induced senescence (Yang 2014). PYPs significantly reduced the overexpression of the p16 and p21 genes induced by

D-galatose ($p<0.01$), suggesting that PYPs function in delaying cellular senescence by reducing the expression of senescence genes.

5 Conclusions

In this paper, D-gal-induced model of aging in rats was successfully established and these rats with PYPs were treated. The results showed that PYPs can improve the activity of antioxidant enzymes in the body, helping to prevent or repair the damage caused by D-gal in the livers and brains of rats. Furthermore, PYPs can alter the expression levels of the senescence genes p16 and p21 in livers and brains of aging rats. These results suggest that PYPs can play an important role in preventing the aging-related effects caused by oxidative stress and that they could be a new type of raw material for use in health foods, acting as a potential functional antioxidant.

Funding

This study was supported by China Agriculture Research System - Green Manure.

Acknowledgements

The authors gratefully acknowledge Mr. Zou Haiming, Ms. Tang Xiaoyan and Ms. Zhang Biqian (National Engineering Research Center for Vegetables) for the help of rats feeding and management.

[References]

[1] Chiu, C. S., J. S. Deng, H. Y. Chang, Y. C. Chen, M. M. Lee, W. C. Hou, C. Y. Lee, and G. J. Huang. 2013. Antioxidant and anti-inflammatory properties of Taiwanese yam (Dioscorea japonica Thunb. var. pseudojaponica (Hayata) Yamam.) and its reference compounds. *Food Chemistry*, 141(2): 1087–1096.

[2] Feng, Q. H., G. Deftereos, S. E. Hawes, J. E. Stem, and J. B. Willner. 2008. DNA hypermethylation, Her-2/neu overexpression and p53 mutations in ovarian carcinoma. *Gnecologic Oncology*, 111(2): 320–329.

[3] Flachsbart, F., A. Franke, R. Kleindorp, A. Caliebe, H. Blanché, S, Schreiber, and A. Nebel. 2010. Investigation of genetic susceptibilityfactors for human longevity-A targeted nonsynonymous SNP study. *Mutation Research*, 694(1-2): 13–19.

[4] Fu, C. W., T. J. Wang, Y. Wang, X. H. Chen, J. Jiao, F. Ma, M. Zhong, and K. S. Bi. 2011. Metabonomics study of the protective effects of green tea polyphenols on aging rats induced by d-galactose. *Journal of Pharmaceutical and Biomedical Analysis*, 55(5):1067–1074.

[5] Gong, Y. S., J. Guo, K. Hu, Y. Q. Gao, and B. J. Xie. 2016. Ameliorative effect of lotus seedpod proanthocyanidins on cognitive impairment and brain aging induced by d-galactose. *Experimental Gerontology*, 74:21–28.

[6] Gould, V. E., M. S. Schmitt, V. B. Reddy,P. Bitterman, A. Alonso, and P. Gattuso. 2010. Human papillomavirus and p16 expression in inverted papillomas of the urinary bladder. *Cancer Letters*, 292(2): 171–175.

[7] Guterres, F. A., G. R. Martine, M. E. Roch, and S. M. Winnischofer. 2013. Simvastatin rises reactive oxygen species levels and induces senescence in human melanoma cells by activation of p53/p21 pathway. *Experimental Cell Research*, 319(19): 2977–2988.

[8] Han, C. H., Y. F. Lin, Y. S. Lin, T. L. Lee, W. J. Huang, S. Y. Lin, and W. C. Hou. 2014. Effects of yam tuber protein, dioscorin, on attenuating oxidative status and learning dysfunction in d-galactose-induced BALB/c mice. *Food and Chemical Toxicology*, 65(1): 356–363.

[9] Hsu, C. K., J. Y. Yeh, and J. H. Wei. 2011. Protective effects of the crude extracts from yam (Dioscorea alata) peel on tert-butylhydroperoxide-induced oxidative stress in mouse liver cells. *Food Chemistry*, 126(2): 429–434.

[10] Huang, C. H., J. Y. Cheng, M. C. Deng, C. H. Chou, and T. R. Jan. 2012. Prebiotic effect of diosgenin, an immunoactive steroidal sapogenin of the Chinese yam. *Food Chemistry*, 132(1): 428–432.

[11] Jawanjal, P., S. Salhan, I. Dhawan, and G. Rath. 2015. Comparative analysis of p53 and p21 proteins in normal cervix and HPV associated precancerous and cancerous lesions of cervix. *Journal of the Anatomical Society of India*, 64(1): 3–11.

[12] Jin, S. L., and Y. G. Yin. 2012. In vivo antioxidant activity of total flavonoids from indocalamus leaves in aging mice caused by D-galactose. *Food and Chemical Toxicology*, 50(10): 3814–3818.

[13] Josue, A., A. Lubag, A. C. Laurena, and E. M. Tecson-Mendoza. 2008. Antioxidants of Purple and White Greater Yam (*Dioscorea alata* L.) Varieties from the Philippines. *Philippine Journal of Science*, 137(1): 61–67.

[14] Ju, Y., Y. Xue, J. L. Huang, Q. Z. Zhai, and X. H. Wang. 2014. Antioxidant Chinese yam polysaccharides and its pro-proliferative effect on endometrial epithelial cells. *International Journal of Biological Macromolecules*, 66(5): 81–85.

[15] Koo, B. H., Y. Kim, J. C. Yang, and D. S. Kim. 2015. Distinct roles of transforming growth factor-β signaling and

transforming growth factor-β receptor inhibitor SB431542 in the regulation of p21 expression. *European Journal of Pharmacology*, 764: 413–423.

[16] Lim, J. S., S. H. Park, and K. L. Jang. 2011. All-trans retinoic acid induces cellular senescence by up-regulating levels of p16 and p21 via promoter hypomethylation. *Biochemical and Biophysical Research Communications*, 412(3): 500–505.

[17] Liu, Y. W., H. F. Shang, C. K. Wang, F. L. Hsu, and W. C. Hou. 2007. Immunomodulatory activity of dioscorin, the storage protein of yam (Dioscorea alata cv. Tainong No. 1) tuber. *Food and Chemical Toxicology*, 45(11): 2312–2318.

[18] Mao, G. X., H. B. Deng, L. G. Yuan, D. D. Li, Y. Y. Li, and Z. Wang. 2010. Protective role of Salidroside against aging in a mouse model induced by D-galactose. *Biomedical and Environmental Sciences*, 23(2): 161–166.

[19] Masson, A. O., R. Hess, K. Brien, K. L. Bertram, P. Tailor, E. Irvine, G. Ren, and R. J. Krawetz. 2015. Increased levels of p21 (CIP1/WAF1) correlate with decreased chondrogenic differentiation potential in synovial membrane progenitor cells. *Mechanisms of Ageing and Development*, 149: 31–40.

[20] McAnuff-Harding, M. A., F. O. Omoruyi, and H. N. Asemota. 2006. Intestinal disaccharidases and some renal enzymes in streptozotocin-induced diabetic rats fed sapogenin extract from bitter yam (Dioscorea polygonoides). *Life Sciences*, 78(22): 2595–2600.

[21] Mimeault, M., and S. K. Batra. 2009. Recent insights into the molecular mechanisms involved in aging and the malignant transformation of adult stem/progenitor cells and their therapeutic implications. *Ageing Research Reviews*, 8(2): 94–112.

[22] Otilia, J. F., D. Banji, and K. Ch. 2014.Curcumin and besperidin improve cognition by suppressing mitochondrial dysfunction and apoptosis induced by D-galactose in rat brain. *Food and Chemical Toxicology*, 74: 51–59.

[23] Park, J. M., Y. J. Kim, J. S. Kim, Y. M. Han, N. Kangwan, K. B. Hahm, T. S. Kim, O. Kwon, and E. H. Kim. 2013. Anti-inflammatory and carbonic anhydrase restoring actions of yam powder (Dioscorea spp) contribute to the prevention of cysteamine-induced duodenal ulcer in a rat model. *Nutrition Research*, 33(8): 677–685.

[24] Park, S. H., J. S. Lim, and K. L. Jang. 2011. All-trans retinoic acid induces cellular senescence via upregulation of p16, p21, and p27. *Cancer Letters*, 310(2): 232–239.

[25] Reinhardt, H. C., and B. Schumacher. 2012. The p53 network: cellular and systemic DNA damage responses in aging and cancer. *Trends in Genetics*, 28(3): 128–136.

[26] Ryu, E., H. Su, J. Kang, J. H. Woo, J. J. Park, J. Lee, J. S. Seo. 2008. Identification of senescence-associatedgenes in human bone marrow mesenchymal stem cells. *Biochemical and Biophysical Research Communications*, 371(3): 431–436.

[27] Samama, B., S. Christiane, and B. Nelly. 2008. P16 expression in relation to human papillomavirus in liquid-based cervical smears. *Gynecologic Oncology*, 109(2): 285–290.

[28] Shen, W., L. Li, X. J. Wu, Y. R. Zhou, Q. J. Pan, H. Chen, and J. X. Deng. 2006. Accelerated somatic cell senescence and changes in p16 (INK4a) expression after exogenous DNA transfection. *Hereditas*, 28(11): 1383–1388.

[29] Su, C. Y., Y. C. Chang, Y. C. Chan, T. C. Lin, M. S. Huang, C. J. Yang, and M. Hsiao. 2014. MTAP is an independent prognosis marker and the concordant loss of MTAP and p16 expression predicts short survival in non-small cell lung cancer patients. *European Journal of Surgical Oncology (EJSO)*, 40(9): 1143–1150.

[30] Tozawa, E., Y. Ajioka, H. Watanabe, K. Nishikura, G. Mukai, T. Suda, T. Kanoh, and K. Hatakeyama. 2007. Mucin expression, p53 overexpression, and peritumoral lymphocytic infiltration of advanced colorectal carcinoma with mucus component: Is mucinous carcinoma a distinct histological entity? *Pathology Research and Practice*, 203(8): 567–574.

[31] Tsygankov, D., Y. Liu, H. K. Sanoff, N. E. Sharpless, and T. C. Elston. 2009. A quantitative mod el for age-dependent expression of the P16INK4a tumor suppressor. *Proceedings of the National Academy of Sciences of the United States of America*, 106(39): 16562–16567.

[32] Varshney, M., A. Chandra, R. Jain, R. Ahmad, V. Bihari, C. K. Chandran, M. K. R. Mudiam, S. Patnaik, and S. K. Goel. 2015. Occupational health hazards of trichloroethylene among workers in relation to altered mRNA expression of cell cycle regulating genes (p53, p21, bax and bcl-2) and PPARA. *Toxicology Reports*, 108: 748–757.

[33] Wang, C. H., Z. Chen, Q. Q. Ge, J. H. Hu, and F. Li. 2014. Up-regulation of p21WAF1/CIP1 by miRNAs and its implications in bladder cancer cells. *FEBS*, 588(24): 4654–4664.

[34] Wang, P. P., H. X. Sun, C. J. Liu, M. H. Hu, X. Q. He, S. Yue, Z. Z. Jiao, and L. Xiang. 2016. Racemic oleracein E increases the survival rate and attenuates memory impairment in D-galactose/NaNO2-induced senescent mice. *Phytomedicine*, 23(5): 460–467.

[35] Wang, C. Q., and G. Q. Yang. 2010. Betacyanins from Portulaca oleracea L. ameliorate cognition deficits and attenuate oxidative damage induced by D-galactose in the brains of senescent mice. *Phytomedicine*, 17(7): 527–532.

[36] Yang, C. H., C. C. Wu, W. T. Chen, C. Y. Chai, and S. F. Yang. 2014. Expressions of p16 and p27 in urothelial carcinoma and their prognostic value. *Kaohsiung Journal of Medical Sciences*, 30(9): 453–458.

[37] Yang, M. Y., L. Luna, J. G. Sørbø, I. Alseth, and R. F. Johansen. 2014. Human OXR1 maintains mitochondrial

DNA integrity and counteracts hydrogen peroxide-induced oxidative stress by regulating antioxidant pathways involving p21. *Free Radical Biology and Medicine*, 77(5): 41–48.

[38] Yang, W. F., Y. Wang, X. P. Li, and P. Yu. 2015. Purification and structural characterization of Chinese yam polysaccharide and its activities. *Carbohydrate Polymers*, 117(5): 1021–1027.

[39] Yoon, I. K., H. K. Kim, Y. K. Kim, I. H. Song, W. Kim, S. Kim, S. H. Baek, J. H. Kim, and J. R. Kim. 2004. Exploration of replicative senescence-associated genes in human dermal fibroblasts by cDNA microarray technology. *Experimental Gerontology*, 39(9): 1369–1378.

[40] Yoshida, K., T. Kondo, K. Kameda, S. Kawakishi. A. J .M. Lubag, E. M. T. Mendoza, and T. Goto. 1991. Structures of alatanin A, B and C isolated from edible purple yam Dioscorea alata. *Tetrahedron Letters*, 32(40): 5575–5578.

[41] Yoshida, K., T. Kondo, and T. Goto. 1991. Unusually stable monoacylated anthocyanin from purple yam dioscorea alata. *Tetrahedron Letters*, 32(40): 5579–5580.

[42] Yu, Y. H., F. L. Bai, W. F. Wang, Y. N. Liu, Q. Y. Yuan, S. Qu, T. Zhang, G. Tian, S. Li, D. Li, and G. Ren. 2015. Fibroblast growth factor 21 protects mouse brain against d-galactose induced aging via suppression of oxidative stress response and advanced glycation end products formation. *Pharmacology Biochemistry and Behavior*, 133(1): 122–131.

[43] Zhang, L., B. Bai, X. H. Liu, Y. Wang, M. J. Li, and D. B. Zhao. 2011. α-Glucosidase inhibitors from Chinese Yam (Dioscorea opposita Thunb.). *Food Chemistry*, 126(1): 203–206.

[44] Zhou, X. X., Q. Yang, Y. H. Xie, J. Y. Sun, P. C. Qiu, C. Wei, and S. W. Wang. 2013. Protective effect of tetrahydroxystilbene glucoside against d-galactose induced aging process in mice. *Phytochemistry Letters*, 6(3): 372–378.

Effects of drying modes followed rough rice harvesting on the texture and taste properties of rice

Zhang Qiang[1,2], Lan Haipeng[3], Zheng Xianzhe[4], Liu Nian[1,2*]

(1. *College of Engineering, Huazhong Agricultural University, Wuhan 430070, China;*
2. *Key Laboratory of Agricultural Equipment in Mid-lower Yangtze River, Ministry of Agriculture, Wuhan 430070, China;*
3. *College of Mechanic and Electrical Engineering, Tarim University, Alar 843300, China;*
4. *College of Engineering, Northeast Agricultural University, Harbin 150030, China*)

Abstract: The effects of two drying modes, including timely drying operation and stacked drying operation followed by rough rice harvesting of different dates, on the texture and taste characteristics of cooked rice were studied. The heated-air temperatures of 40°C, 50°C, and 60°C were respectively used to dry rough rice. Results indicated that harvesting date, drying mode and drying temperature had significant effects on the texture and taste characteristics of cooked rice. At the drying temperatures of 40°C, 50°C, and 60°C, the hardness, adhesiveness, springiness and stickiness of cooked rice from rough rice harvested pre-frosting period and timely dried, were higher than those processed by delay drying treatment. The optimum value of smell, color, appearance, palatability and flavor of the processed rice can be obtained from rough rice dried in time and harvested at the second harvesting date. The taste value of cooked rice harvested before frosting firstly increased and then decreased with the extension of the harvesting date. It also decreased with the increase of stacking time. These results suggested that a drying treatment in time could contribute to a high taste of the rough rice.

Keywords: Rough rice, harvesting date, dried in time, stacked drying, texture, taste

Citation: Zhang, Q., H. P. Lan, X. Z. Zheng, and N. Liu. 2017. Effects of drying modes followed rough rice harvesting on the texture and taste properties of rice. International Agricultural Engineering Journal, 26(3): 166–175.

1 Introduction

Taste value is a crucial index to evaluate rice quality and depends on many factors such as variety, cultivation, harvesting, drying, processing and storage (Pearce et al., 2001; Sunthonvit et al., 2005; Wiset et al., 2005; Anderson and Guraya, 2006; Bello et al., 2006; Aquerreta et al., 2007). Most of researchers strongly focused on the effects of these factors on taste quality of rice. Moisture content of rough rice is generally in range of 20%–30% (w.b.) after harvesting. To meet the requirements for safe storage, drying treatment is a necessary processing for the post-harvesting of rough rice to reach the safe moisture content of 14.5% (w.b.) (Sablani et al., 2009; Golmohammadi, 2015). At present, the main drying mode of rough rice is to dry after a period of stacking. Phenomena, such as hot flashes and mildew, are usually found in the stacking period because of the respiration of rough rice with high moisture, which may affect the taste attributes of cooked rice (Champagne et al., 2004). Taste attributes of rice determine its consumers acceptance (Zheng et al., 2011). Therefore, it is necessary for rough rice to dry in time after harvesting to keep the rice fresh and maintain its taste attributes.

The post-harvesting conditions, such as harvesting dates and drying modes, have obvious effects on the quality of post-drying rough rice. Harvesting date obviously influences texture attributes and taste quality of cooked rice (Asano et al., 2000; Chae and Jun, 2002). Asano et al. (1999) found that taste value of rice decreased with the delaying of harvesting date. Champagne et al. (2005) studied the impacts of harvesting date on the sensory and physicochemical properties of rice, and found that the early harvested rice

Received date: 2017-06-16 **Accepted date:** 2017-09-01

* **Corresponding author:** Liu Nian, PhD, lecturer, College of Engineering, Huazhong Agricultural University. Email: newlion@mail.hzau.edu.cn.

was harder and more cohesive than that harvested in delay period when cooked. The post-harvest treatment method of rough rice plays a key role in maintaining the rice quality and generally includes drying method, drying temperature, moisture content and storage time (Meeso et al., 2004; Madamba and Yabes, 2005; Madhiyanon and Soponronnarit, 2005; Rordprapat et al., 2005; Iguaz et al., 2006; Dong et al., 2010; Takuma et al., 2013). Meullenet et al. (1999) investigated that the hardness of rice subjected to delayed drying decreased. Champagne et al. (2004) observed that after a period of storage, the taste of rough rice declined with high moisture during the drying process. Wongpornchai et al. (2004) suggested that harvested rough rice followed by dried immediately under low drying temperature may keep the aroma quality. Concentration of the aroma compound in rice may decline due to the energy consumption and thermal generation caused by respiratory activity of rough rice kernels with high moisture content during stacked storage. The rough rice dried after a period of stacking decreased the taste attributes of cooked rice. Timely drying refers to a drying operation after the harvesting of rough rice in 8 hours. Timely drying mode may avoid the deterioration of the taste quality due to stacking. However, systematic studies considering effects of drying modes and harvesting date on texture attributes and taste quality of rice are limited, which constraints the taste value of high quality rough rice.

Based on the above-mentioned reviews, it is necessary to study the effect of proper harvesting date and drying modes on the texture attributes and taste quality of rough rice and obtain the optimum process parameters considering drying mode, drying temperature and harvesting date for the drying treatment of post-harvesting rough rice.

2 Materials and methods

2.1 Rough rice sample

Considering the differences of factors, such as varieties and climate, the rough rice annual mature date is slightly different. In this study, harvesting dates of rough rice at the rice proper maturity period were chosen from 25th September to 11th October in 2016. Fresh rough rice (variety Chaochan 4) with a moisture content of 19.0%-24.0% (w.b.) was collected from the Rice Research Center at the Northeast Agricultural University (Harbin, China). At the beginning of the proper maturity stage, rough rice was collected every four days for four times. The previous three samples were obtained before frosting and the last one was obtained after frosting. After harvested, part of the samples were dried immediately and the rest samples were sealed in plastic bags, then stored at room temperatures of 20°C-22°C in relative humidity of 55%-65% for 3 days or 6 days, respectively and dried in stacked. The ratio of "part" and "the rest" was one to two. In order to maintain the taste quality at the same level, all rough rice samples were stored in cool and dry room before drying. These operations were completed in 2 h after rough rice was harvested. After sampling, the samples were re-sealed to prevent water loss in rough rice. The moisture content of rough rice was measured by using AOAC (1995b) official method (oven dry method, 135°C, 3 h) (Zhang et al., 2014).

2.2 Experimental procedure

Thin-layer drying experiments were performed using perforated trays in a drying chamber, as shown in Figure 1, in which the drying temperature was controlled by an auto-controller. The drying temperature was measured by using a temperature sensor (accuracy ±0.5°C; MF 54, Shanghai Pudong Sanliao Electronic Co., Shanghai, China). The surface velocity of heated air was measured using a thermal anemometer (accuracy ±0.2%; Testo 425, Testo AG, Lenzkirch, Germany). The anemometer probe was fixed to the bottom of the drying tray during rough rice drying. The relative humidity in the range of 70%–75% for all drying methods was measured using a temperature and humidity sensor (accuracy ±3%; HMP45A, Vaisala, Helsinki, Finland). The drying temperatures were fixed at 40°C, 50°C, and 60°C. Surface velocity of heated air was fixed at 0.5 m s^{-1}. The rough rice obtained at four harvesting times was dried in time and in stacking respectively. The harvesting dates, drying modes and drying temperatures are shown in Table 1. Each of the rough rice samples containing 100 g was spread in a perforated tray. When the sample weight reached the corresponding value for moisture content of

14%-15% (w.b.), rough rice was sealed in a plastic bag and stored at room temperatures of 20°C-22°C. All drying experiments were repeated three times and average value was reported. The drying rough rice sample was milled using a miller (THU-35B type, Satake Co., Tokyo, Japan) and sealed in plastic bags for further analysis.

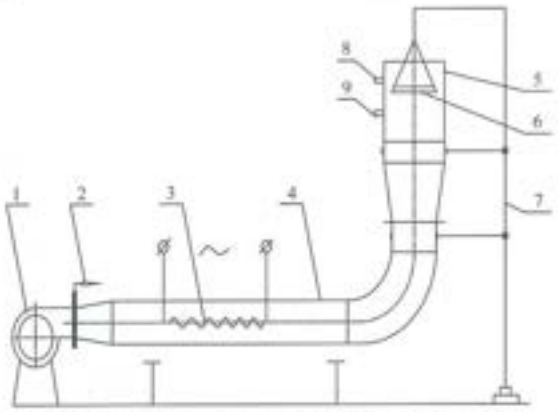

1. Fan 2. Wind rate control board 3. Heating apparatus 4. Air duct 5. Drying cylinder 6. Dried screen 7. Scaffold 8. Anemometer probe 9. Temperature sensor

Figure 1 Schematic diagram of thin-layer drying of paddy rice

Table 1 Drying modes and drying temperatures for the different drying experiments

Harvesting dates	Drying modes	Drying temperatures, °C
The first harvest	Drying in time	40, 50, 60
The first harvest	Drying in stacked three days	40, 50, 60
The first harvest	Drying in stacked six days	40, 50, 60
The second harvest	Drying in time	40, 50, 60
The second harvest	Drying in stacked three days	40, 50, 60
The second harvest	Drying in stacked six days	40, 50, 60
The third harvest	Drying in time	40, 50, 60
The third harvest	Drying in stacked three days	40, 50, 60
The fourth harvest	Drying in time	40, 50, 60
The fourth harvest	Drying in stacked three days	40, 50, 60

2.3 Instrumental texture analysis

Texture profile analysis of each rice sample was measured using a Stable Micro System TA-XT2 texture analyzer (Texture Technologies Co., Surrey, UK) with a 2.5 mm cylindrical probe. The speeds of pre-test, test and post-test were respectively 1.0, 0.5, 0.5 mm/s, and deformation ratio was 90%. The force–time curve was recorded and analyzed by the software in TA-XT2 texture analyzer, which presented the texture characteristics of the cooked rice including hardness ($H1$), adhesiveness ($A3$), cohesiveness ($A2/A1$), springiness ($D2/D1$), stickiness ($H2$), gumminess and chewiness. Gumminess was obtained by Hardness×Cohesiveness and chewiness was obtained by Gumminess×Springiness based on the standard calculations of curve attributes of texture profile analysis. Measurements were performed in six replicates and averages were reported for each sample as presented in Tables 2-4.

2.4 Taste evaluation method

Ten professionally trained panelists employed at the National Rice Quality Test Center (Harbin, China) developed a taste profile of cooked rice samples according to GB/T15682-1995 method (rice taste standard from the Ministry of Agriculture, P. R. China). During panel tests, the cooked rice taste (100 points) was evaluated in terms of smell (25 points), appearance (10 points), color (10 points), palatability (30 points) and flavor (25 points). Preparation and taste evaluation of cooked rice referred to Zheng and Lan (2007). The taste values of cooked rice subjected to different drying modes are shown in Figures 2-7.

2.5 Data analysis

All analyses were performed in triplicate. Both texture and taste data were analyzed using ANOVA to perform the significance of all drying modes and temperatures for the objective variables. Both texture and taste data were analyzed using ANOVA. The results of ANOVA were obtained by using SPSS software (Ver. 8.2, SPSS Institute, INC., Cary, NC). The results of variance analysis at $p<0.05$ level were retained.

3 Results and discussion

3.1 Effects of drying modes and drying temperatures on the texture attributes of cooked rice

The texture attributes in Tables 2-4 may describe the effects of drying modes and drying temperatures on the texture attributes of cooked rice. The results of variance analysis were retained at $p<0.05$ level.

Table 2 shows the texture attributes of cooked rice after drying at 40°C. As can be seen in Table 2, drying modes and drying temperatures have significant effects on the texture attributes of cooked rice. Hardness of cooked rice is the force required to bite through the sample using the molars. The hardness of cooked rice from the rough rice harvested before frosting had significant difference ($p<0.05$). No significant effect of

drying modes on the hardness of cooked rice at the fourth harvesting date was found (p>0.05). There was significant difference in the adhesiveness of cooked rice obtained before frosting (p<0.05). Adhesiveness difference of cooked rice at the fourth harvesting date was non-significant (p>0.05). Adhesiveness is the degree to which the kernels adhere to contacting substances. The difference in the springiness of cooked rice obtained before frosting was significant (p<0.05). No significant effect of drying modes on the springiness of the fourth harvested cooked rice was appeared (p>0.05). Springiness of cooked rice is the degree of recovery to its original shape after partial compression. Cohesiveness index is defined as the degree to which the grains deform rather than crumble, crack, or break when biting with the molars. In this research, no significant effects of drying modes on the cohesiveness of cooked rice at the four harvesting dates were found (p>0.05). Gumminess of cooked rice at the four harvesting dates had significant difference (p<0.05). Gumminess of cooked rice is the degree to which the kernels adhere to each other. The difference in the chewiness of cooked rice before frosting was significant (p<0.05). Chewiness difference of cooked rice at the fourth harvesting date was non-significant (p>0.05). Chewiness refers to the amount of work taking to chew the samples. There was significant difference in the stickiness of cooked rice obtained before frosting (p<0.05). The stickiness difference of the fourth harvested cooked rice was non-significant (p>0.05). Stickiness is the degree of binding between kernels from stretched to original state. At pre-frost season, the hardness, adhesiveness, springiness and stickiness of cooked rice obtained from rough rice by drying timely, were significantly higher than those of cooked rice obtained from rough rice by delay drying treatment (p<0.05).

Table 2 Texture attributes value of rice subject to various drying modes at 40°C

Drying modes	Hardness, g	Adhesiveness	Springiness	Cohesiveness, g.s	Gumminess	Chewiness	Stickiness
1	3533±115^a	−696±63^a	0.67±0.07^a	0.459±0.025^a	1678±89^a	1135±143^a	0.266±0.015^a
2	3260±103^b	−627±58^b	0.57±0.15^b	0.474±0.024^a	1486±97^b	932±121^b	0.246±0.017^b
3	3196±143^c	−563±48^c	0.52±0.11^c	0.481±0.033^a	1543±73^c	1044±122^c	0.233±0.021^c
4	3716±126^a	−683±61^a	0.79±0.13^a	0.451±0.035^a	1487±107^a	924±139^a	0.284±0.035^a
5	3628±139^b	−524±57^b	0.69±0.10^b	0.457±0.042^a	1452±93^b	903±113^b	0.277±0.018^b
6	3124±139^c	−504±43^c	0.62±0.09^c	0.460±0.034^a	1543±88^c	1222±134^c	0.245±0.027^c
7	3594±118^a	−737±39^a	0.67±0.08^a	0.458±0.028^a	1803±76^a	1247±148^a	0.270±0.026^a
8	3263±151^b	−539±51^b	0.55±0.12^b	0.465±0.031^a	1520±70^b	839±120^b	0.245±0.016^b
9	3588±122^a	−589±60^a	0.66±0.08^a	0.479±0.029^a	1721±81^a	1169±134^a	0.265±0.031^a
10	3671±145^a	−620±58^a	0.61±0.09^a	0.506±0.037^a	1866±104^b	1168±128^a	0.286±0.019^a

Notes: 1-3 represent the first harvest, among which, 1 represents drying in time, 2 represents drying in stacked three days, 3 represents drying in stacked six days; 4-6 represent the second harvest, among which, 4 represents drying in time, 5 represents drying in stacked three days, 6 represents drying in stacked six days; 7-8 represent the third harvest, among which, 7 represents drying in time, 8 represents drying in stacked three days; 9-10 represent the fourth harvest, among which, 9 represents drying in time, 10 represents drying in stacked three days. Data expressed as mean ±SD of triplicate determinations. Means within rows followed by the same letter are not significant different at p<0.05.

Table 3 illustrates the texture attributes of cooked rice after drying at 50°C. As can be seen in Table 3, drying modes have significant effects on the cooked rice texture attributes at 50°C. The texture attributes, in terms of hardness, adhesiveness, springiness, gumminess, chewiness and stickiness, of cooked rice harvested before frosting had significant difference (p<0.05). No significant effect of drying modes on the hardness, adhesiveness, springiness, gumminess, chewiness and stickiness of cooked rice at the fourth harvesting date was found (p>0.05). There was no significant difference of cohesiveness at four harvesting dates (p>0.05). The hardness, adhesiveness, springiness, gumminess, and stickiness of cooked rice harvested before frosting with timely drying, were significantly higher than those of cooked rice obtained from rough rice by delay drying treatment (p<0.05).

Table 4 represents the texture attributes of cooked rice after drying at 60°C. As can be shown in Table 4, drying modes have significant effects on the cooked rice texture attributes at 60°C. The differences of two modes in the hardness, adhesiveness, springiness, gumminess,

chewiness and stickiness of cooked rice obtained before frosting were significant (p<0.05). However, no significant effects of drying modes on the hardness, adhesiveness, springiness, gumminess, chewiness and stickiness of cooked rice at the fourth harvesting date were found (p>0.05). The cohesiveness differences of the four times harvested cooked rice were not significant (p> 0.05). The hardness, adhesiveness, springiness, gumminess, and stickiness of the cooked rice harvested before frosting decreased with the stacked time, and this decrement was significant between the rice with two drying modes (p<0.05). In this research, it was found that hardness, adhesiveness and springiness of the cooked rice also decreased with increase of the drying temperature in the same drying modes. This result agrees with previous studies by Kunze et al. (2008).

Table 3 Texture attributes value of rice subject to various drying modes at 50°C

Drying modes	Hardness, g	Adhesiveness	Springiness	Cohesiveness, g.s	Gumminess	Chewiness	Stickiness
1	3460±423^a	-686±67^a	0.65±0.09^a	0.439±0.035^a	1810±83^a	1211±113^a	0.301±0.012^a
2	3325±312^b	-624±62^b	0.52±0.12^b	0.446±0.025^a	1948±78^b	826±137^b	0.281±0.025^b
3	2989±334^c	-556±47^c	0.44±0.15^c	0.451±0.027^a	1623±98^c	1383±143^c	0.267±0.013^c
4	3588±116^a	-660±58^a	0.72±0.11^a	0.512±0.024^a	2043±96^a	1396±126^a	0.32±0.025^a
5	3453±222^b	-582±57^b	0.66±0.13^b	0.518±0.036^a	1757±89^b	907±129^b	0.304±0.019^b
6	3183±115^c	-516±55^c	0.57±0.12^c	0.531±0.043^a	1575±107^c	1104±143^c	0.279±0.018^c
7	3637±334^a	-682±68^a	0.63±0.09^a	0.472±0.037^a	1738±94^a	1384±128^a	0.281±0.025^a
8	3280±328^b	-577±71^b	0.49±0.08^b	0.482±0.033^a	1936±87^b	726±112^b	0.255±0.017^b
9	3572±238^a	-558±52^a	0.66±0.13^a	0.469±0.041^a	1956±106^a	900±137^a	0.279±0.025^a
10	3531±211^a	-606±67^a	0.59±0.12^a	0.462±0.029^a	1875±86^a	855±118^a	0.288±0.029^a

Notes: 1-3 represent the first harvest, among which, 1 represents drying in time, 2 represents drying in stacked three days, 3 represents drying in stacked six days; 4-6 represent the second harvest, among which, 4 represents drying in time, 5 represents drying in stacked three days, 6 represents drying in stacked six days; 7-8 represent the third harvest, among which, 7 represents drying in time, 8 represents drying in stacked three days; 9-10 represent the fourth harvest, among which, 9 represents drying in time, 10 represents drying in stacked three days. Data expressed as mean ± SD of triplicate determinations. Means within rows followed by the same letter are not significant different at p<0.05.

Table 4 Texture attributes value of rice subject to various drying modes at 60°C

Drying modes	Hardness, g	Adhesiveness	Springiness	Cohesiveness, g.s	Gumminess	Chewiness	Stickiness
1	3356±367^a	-601±80^a	0.61±0.09^a	0.431±0.035^a	2381±125^a	1748±133^a	0.355±0.015^a
2	3135±249^b	-526±74^b	0.47±0.12^b	0.426±0.025^a	2147±124^b	1517±154^b	0.321±0.011^b
3	2876±163^c	-437±68^c	0.42±0.15^c	0.403±0.027^a	2043±136^c	1596±138^a	0.319±0.023^c
4	3457±324^a	-630±85^a	0.67±0.11^a	0.483±0.024^a	1948±98^a	1383±147^a	0.301±0.011^a
5	3278±226^b	-552±88^b	0.61±0.13^b	0.468±0.036^a	1941±129^b	1522±120^b	0.281±0.021^b
6	3109±165^c	-456±81^c	0.53±0.12^c	0.456±0.043^a	1704±148^c	1465±151^c	0.263±0.024^c
7	3226±278^a	-582±63^a	0.57±0.09^a	0.462±0.037^a	2118±111^a	1527±163^a	0.305±0.025^a
8	2959±254^b	-427±59^b	0.45±0.08^b	0.451±0.033^a	1913±138^b	1056±149^b	0.286±0.027^b
9	3219±289^a	-528±71^a	0.56±0.13^a	0.469±0.041^a	1876±125^a	953±144^a	0.277±0.017^a
10	3368±193^a	-506±76^a	0.49±0.12^a	0.463±0.029^a	1796±121^a	861±123^a	0.259±0.019^a

Notes: 1-3 represent the first harvest, among which, 1 represents drying in time, 2 represents drying in stacked three days, 3 represents drying in stacked six days; 4-6 represent the second harvest, among which, 4 represents drying in time, 5 represents drying in stacked three days, 6 represents drying in stacked six days; 7-8 represent the third harvest, among which, 7 represents drying in time, 8 represents drying in stacked three days; 9-10 represent the fourth harvest, among which, 9 represents drying in time, 10 represents drying in stacked three days. Data expressed as mean ± SD of triplicate determinations. Means within rows followed by the same letter are not significant different at p<0.05.

3.2 Effects of drying modes and drying temperatures on the taste value of cooked rice

The taste characteristics of cooked rice, including smell, color, appearance, palatability and flavor attributes, were evaluated by the taste evaluation protocol. The analysis results of texture attributes may explain the effect of drying modes and drying temperatures on the taste characteristics of cooked rice, as illustrated in Figures 2-4, the data expressed as mean ± SD of triplicate determinations.

The results in Figure 2 indicate the effects of drying modes on the taste qualities of cooked rice after drying at 40°C. Smell and flavor values of cooked rice obtained before frosting had significant difference (p<0.05), but were non-significant for one harvested at the fourth time (p>0.05). The smell value of cooked rice is the panelists'

sense for the special odors of cooked rice by olfactory perception. Flavor refers to the taste impression of cooked rice and is mainly determined by the senses of taste and smell. Before frosting, stacking time shows negative effects on the smell value and flavor value. Rough rice has unique aroma, which decays with stacking time, resulting in the decrease of the smell value of cooked rice (Wongpornchai et al., 2004). The flavor value of cooked rice had positive correlation with hardness and stickiness, with the result that the flavor value of cooked rice from rough rice dried timely was higher than that from delay drying treatment (Zheng et al., 2011). The difference in the taste properties of cooked rice, including color, appearance and palatability, was non-significant (p>0.05). The color value of the cooked rice refers to the panelists' sense and is determined by visual perception. Whiteness is the color of cooked rice favored by consumers (Jinorose et al., 2010). The color of cooked rice declined with stacking time. The appearance of cooked rice is the overall observation in terms of shape, integrity and transparency. Palatability of cooked rice refers to the acceptable or agreeable degree to the palate or taste of cooked rice, which decreased with the increase of stacking time. The cooked rice with fine palatability had the characteristics of high hardness, stickiness, springiness and adhesiveness. The optimum value of smell, flavor, color, appearance and palatability appeared at the second harvesting date followed by drying in time.

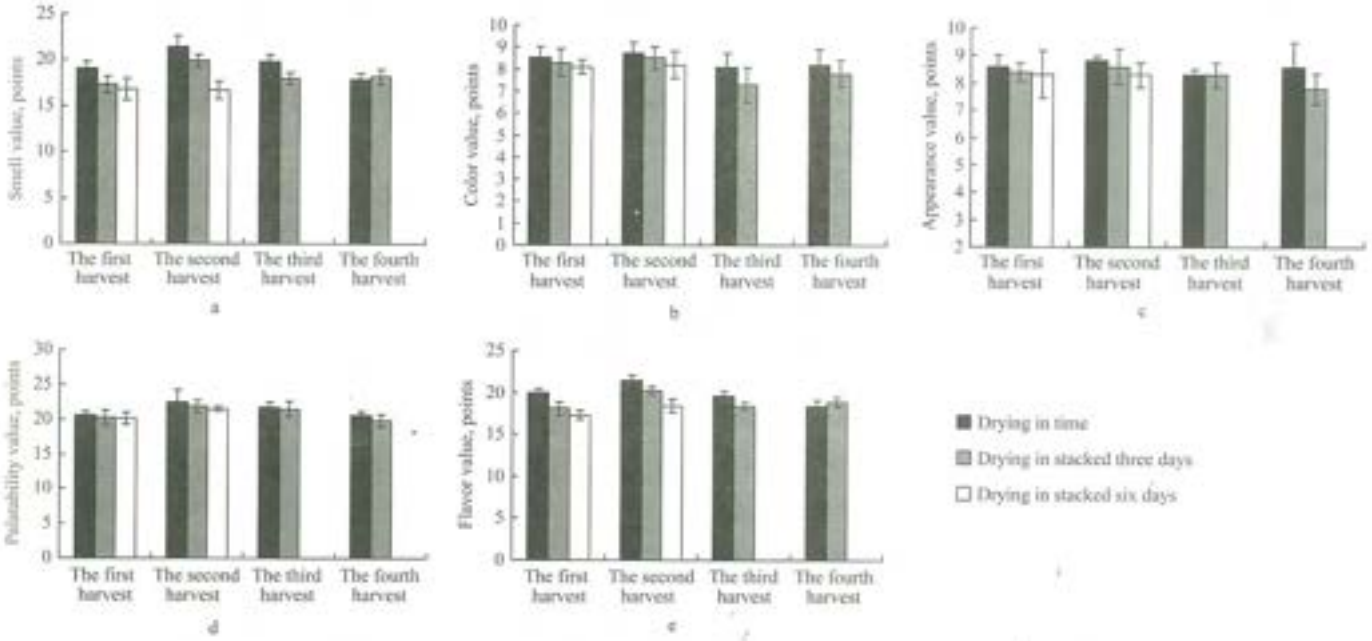

Figure 2 Taste characteristics value of rice at 40°C for different drying modes in 2016 harvesting time

The effects of drying modes on the taste qualities of cooked rice after drying at 50°C are shown in Figure 3. The smell and flavor values of cooked rice harvested before frosting had significant difference (p<0.05). No significant effect of drying modes on the smell and flavor value of cooked rice at the fourth harvesting date was found (p>0.05). The results show that stacked time has a significant negative effect on the smell and flavor value of cooked rice before frosting. The smell value of cooked rice has positive correlation with its stickiness. The flavor value of cooked rice has positive correlation with its hardness and stickiness. Therefore, the smell value of the cooked rice also decreased with decrease of the stacked time due to the decrease of hardness and stickiness (Zheng et al., 2011). The flavor value had a significant positive correlation with hardness and stickiness (Zheng et al., 2011). There was no significant difference of color, appearance and palatability value at the four harvesting dates (p>0.05). The color, appearance and palatability value of cooked rice had positive correlation with stacked time. The cooked rice had fine color and palatability value with the characteristics of high hardness, stickiness, springiness and adhesiveness. The optimum value of smell, color, appearance, palatability and flavor was obtained at the second harvesting time by drying in time.

Figure 4 shows the effect of drying modes on taste qualities of the cooked rice after drying at 60°C. Smell and flavor values of cooked rice harvested before frosting had significant difference ($p<0.05$). Smell and flavor values of cooked rice at the fourth harvesting date were non-significant ($p>0.05$). No significant effect of drying modes on the color, appearance and palatability value of cooked rice at the four harvesting dates was found ($p>0.05$). The change reason of taste qualities of the cooked rice after drying at 60°C was the same as that drying at 50°C. The optimum value of smell, color, appearance, palatability and flavor was found at the second harvesting time by drying in time. In this research, it is revealed that smell, color, appearance, palatability and flavor values of the cooked rice also decreased with the increase of drying temperature in the same drying mode. This result agrees with what was reported by other researchers (Zheng et al., 2011; Kunze, 2008).

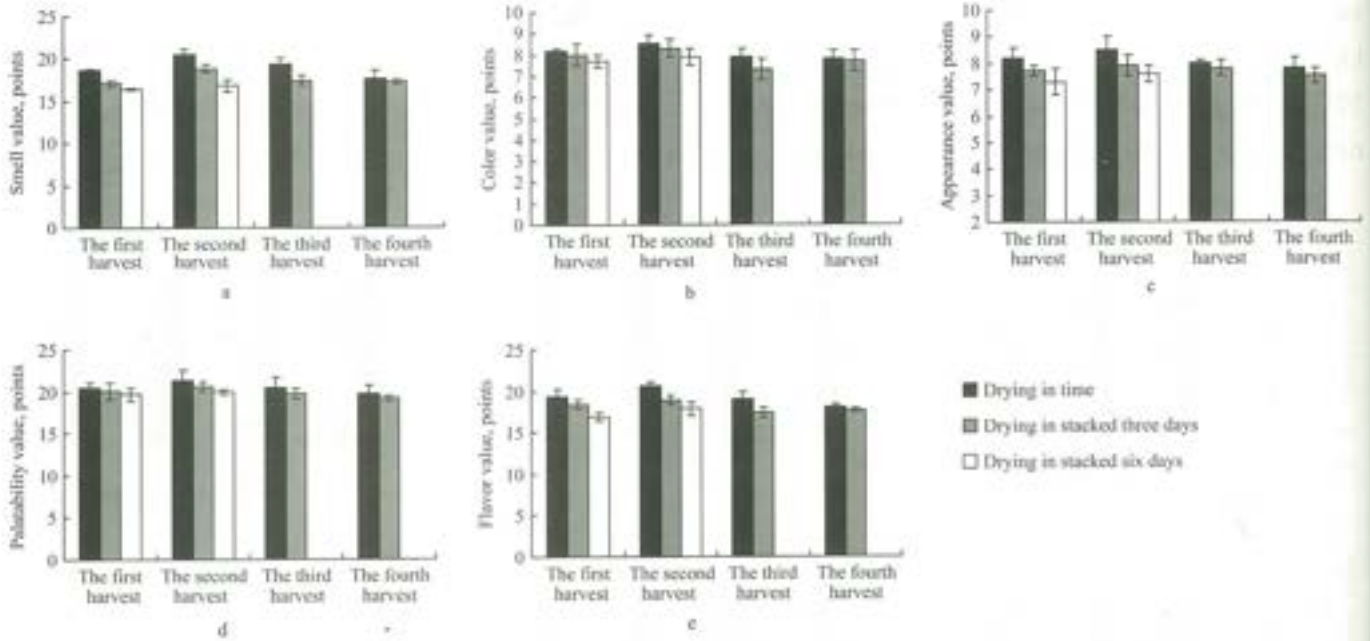

Figure 3 Taste characteristics value of rice at 50°C for different drying modes in 2016 harvesting time

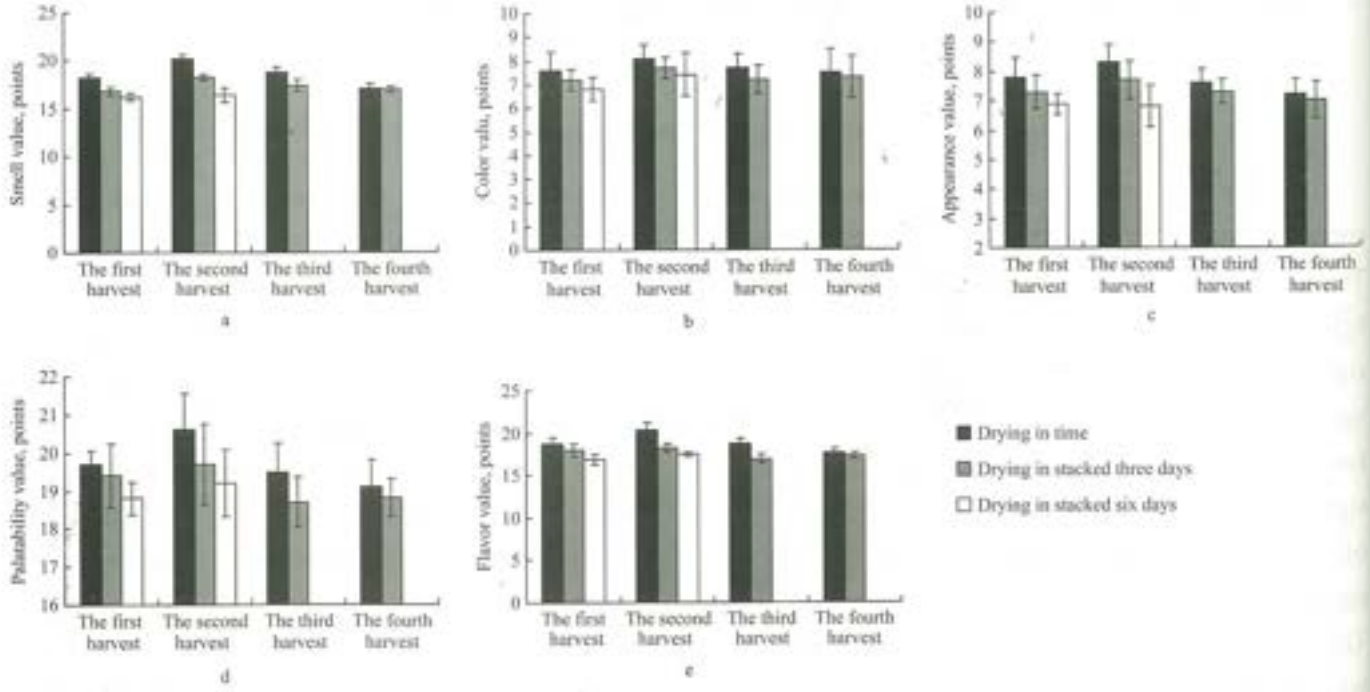

Figure 4 Taste characteristics value of rice at 60°C for different drying modes in 2016 harvesting time

3.3 Comprehensive analysis of taste value for cooked rice

The results of texture attributes in Figures 5-7 may explain the effect of drying modes and drying temperatures on the taste qualities of cooked rice. In Figures 5-7, the data expressed mean ±SD of triplicate determinations.

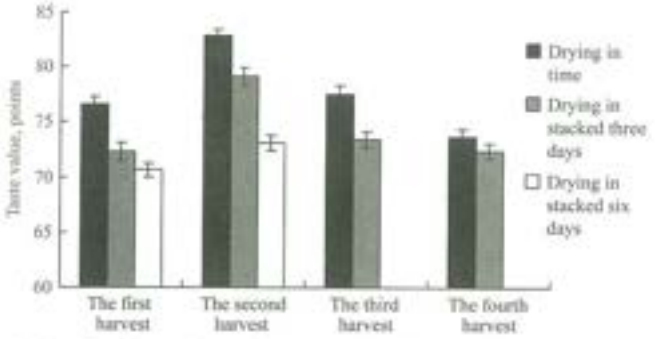

Figure 5 Comprehensive evaluation of taste value at 40°C for different drying modes in 2016 harvesting time

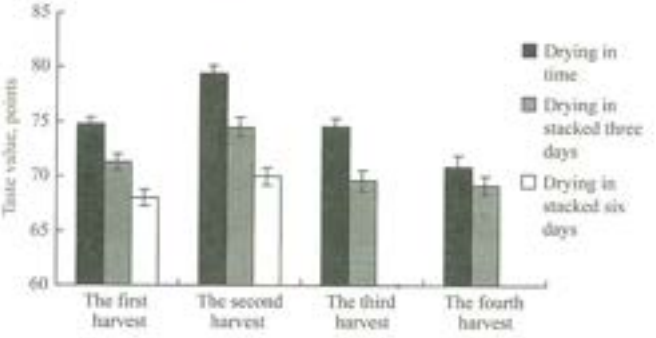

Figure 6 Comprehensive evaluation of taste value at 50°C for different drying modes in 2016 harvesting time. Data expressed mean ±SD of triplicate determinations.

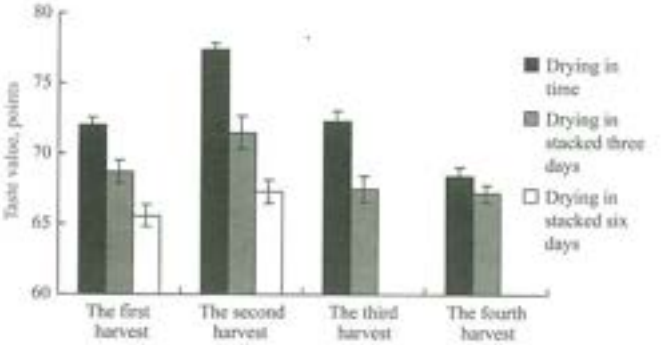

Figure 7 Comprehensive evaluation of taste value at 60°C for different drying modes in 2016 harvesting time

The results in Figure 5 present the effects of drying modes on the taste qualities of cooked rice after drying at 40°C. The differences in the taste attributes of cooked rice harvested before frosting were significant ($p<0.01$). There was no significant difference in taste attributes of cooked rice at the fourth harvesting date ($p>0.05$). For the rough rice harvested before frosting date, the taste attributes of cooked rice treated by drying timely were higher than those treated by delay drying treatment, which decreased with the increase of stacking time. The highest taste value of the cooked rice was the rough rice harvested at the 8th day after proper mature date followed by drying in time.

The results in Figures 6-7 present the effects of drying modes on the taste qualities of cooked rice after drying at 50°C and 60°C. The results showed that the changing trend of taste attributes of cooked rice after drying at 50°C and 60°C was in accordance with that of cooked rice after drying temperatures at 40°C. The increase of drying temperatures caused the decrease of taste attributes of cooked rice at the same drying modes as shown in Figures 5-7.

The taste value is in high level for the rough rice harvested in pre-frost season and followed by the drying timely treatment. The hardness, adhesiveness, springiness and stickiness of cooked rice obtained from rough rice harvested at pre-frost season dried timely, are higher than those by delay drying treatment. The highest values of hardness, adhesiveness, springiness and stickiness for the cooked rice were obtained at the 8th day of mature period and dried in time. The smell, flavor and palatability of cooked rice obtained from rough rice harvested at pre-frost season followed by dried timely, are higher than those dried by delay drying treatment. The highest values of smell, flavor and palatability for the cooked rice were obtained at the 8th day of mature period dried in time. The flavor value of cooked rice has positive correlation with hardness and stickiness (Zheng et al., 2011). The drying timely mode improves the flavor of cooked rice. The palatability of cooked rice has positive correlation with springiness, adhesiveness and stickiness (Zheng et al., 2011). The drying timely mode improves the palatability of cooked rice. The results explain the influence of texture attributes on the taste quality of cooked rice. The relationship between the texture attributes and the taste characteristics explains the reasons that rough rice harvested in time and dried timely can improve the taste quality of cooked rice.

4 Conclusions

The effects of harvesting dates, drying modes and drying temperatures on the texture and taste attributes of cooked rice are significant. The impacts of harvesting dates, drying temperatures and drying modes on the texture of cooked rice are the key reasons resulting in variations in taste. Stacking time has a negative effect on hardness, adhesiveness, springiness, stickiness, smell, flavor and palatability of rough rice. Therefore, drying in time is helpful in improving the taste properties of cooked rice. The highest taste value for the cooked rice is obtained under the optimal mode of harvesting at the 8th day of mature period and drying in time. The analysis results show the influence of texture attributes on the taste quality of cooked rice. The relationship between the texture attributes and the taste characteristics explains the mechanism that harvesting in time and timely drying mode can improve the taste quality of rice.

Acknowledgments

The authors express their acknowledgment to the Fundamental Research Funds for the Central Universities (2662015QD043, 2662015QD013), Opening Subject for Key Laboratory of Modern Agriculture, Tarim University (TDNG20160102) and Industrial Science and Technology Project of Xinjiang Production and Construction Corps (2015AB039) for the financial support and all of the people who assisted in this writing.

[References]

[1] Anderson, A. K., and H. S. Guraya. 2006. Effects of microwave heat-moisture treatment on properties of waxy and non-waxy rice starches. *Food Chemistry*, 97(2): 318–323.

[2] Aquerreta, J., A. Iguaz, C. Arroqui, and P. Virseda. 2007. Effect of high temperature intermittent drying and tempering on rough rice quality. *Journal of Food Engineering*, 80(2): 611–618.

[3] Asano, H., F. Hirano, K. Isobe, and H. Sakurai. 2000. Effect of harvest time on the protein composition (glutelin, prolamin, albumin) and amylose content in paddy rice cultivated by Aigamo duck farming system. *Japanese Journal of Crop Science*, 69(3): 320–323.

[4] Asano, H., K. Isobe, and Y. Tsuboki. 1999. Effect of harvest time on the quality and palatability of paddy rice cultivated by aigamo duck farming system. *Japanese Journal of Crop Science*, 68(3): 375–378.

[5] Bello, M., R. Baeza, and M. P. Tolaba. 2006. Quality characteristics of milled and cooked rice affected by hydrothermal treatment. *Journal of Food Engineering*, 72(2): 124–133.

[6] Chae, J. C., and D. Jun. 2002. Effect of harvest date on yield and quality of rice. *Korea Journal of Crop Science*, 47(3): 254–258.

[7] Champagne, E. T., J. F. Thompson, K. L. Bett-Garber, R. Mutters, J. A. Miller, and E. Tan. 2004. Impact of storage of freshly harvested paddy rice on milled white rice flavor. *Cereal Chemistry*, 81(4): 444–449.

[8] Champagne, E. T., K. L. Bett-Garber, J. Thompson, R. Mutters, C. C. Grimm, and A. M. McClung. 2005. Effects of drain and harvest dates on rice sensory and physicochemical properties. *Cereal Chemistry*, 82(4): 369–374.

[9] Dong, R. J., Z. H. Lu, Z. Q. Liu, S. Koide, and W. Cao. 2010. Effect of drying and tempering on rice fissuring analyzed by integrating intra-kernel moisture distribution. *Journal of Food Engineering*, 97(2): 161–167.

[10] Golmohammadi, M. 2015. On the characteristics of thin layer drying models for intermittent drying of rough rice. *Chemical Engineering Communications*, 202 (8): 1024–1035.

[11] Iguaz, A., M. Rodriguez, and P. Virseda. 2006. Influence of handing and processing of rough rice on fissures and head rice yields. *Journal of Food Engineering*, 77(4): 803–809.

[12] Jinorose, M., S. Prachayawarakorn, and S. Soponronnarit. 2010. Development of a computer vision system and novel evaluation criteria to characterize color and appearance of rice. *Drying Technology*, 28(9): 1118–1124.

[13] Kunze, O. R. 2008. Effect of drying on grain quality-Moisture readsorption causes fissured rice grains. *Agricultural Engineering International: CIGR Journal*, 46(1): 1–17.

[14] Madamba, P. S., and R. P. Yabes. 2005. Determination of the optimum intermittent drying conditions for rough rice (*Oryza sativa*, L.). *LWT-Food Science Technology*, 38(2): 157–165.

[15] Madhiyanon, T., and S. Soponronnarit. 2005. High temperature spouted bed paddy drying with varied downcomer air flows and moisture contents: Effects on drying kinetics, critical moisture content, and milling quality. *Drying Technology*, 23(3): 473–495.

[16] Meeso, N., A. Nathakaranakule, T. Madhiyanon, and S. Soponronnarit. 2004. Influence of FIR irradiation on paddy moisture reduction and milling quality after fluidized bed drying. *Journal of Food Engineering*, 65(2): 293–301.

[17] Meullenet, J. F. C., B. P. Marks, K. Griffin, M. J. Daniels. 1999. Effects of rough rice drying and storage conditions on

sensory profiles of cooked rice. *Cereal Chemistry*, 76(4): 483–486.

[18] Pearce, M. D., B. P. Marks, and J. F. Meullenet. 2001. Effects of postharvest parameters on functional changes during rough rice storage. *Cereal Chemistry*, 78(3): 354–357.

[19] Rordprapat, W., A. Nathakaranakule, W. Tia, and S. Soponronnarit. 2005. Comparative study of fluidized bed paddy drying using hot air and superheated steam. *Journal of Food Engineering*, 71(1): 28–36.

[20] Sablani, S. S., L. Bruno, S. Kasapis, and R. M. Symaladevi , 2009. Thermal transitions of rice: Development of a state diagram. *Journal of Food Engineering*, 90(1): 110–118.

[21] Sunthonvit, N., G. Srzednicki, and J. Craske. 2005. Effects of high-temperature drying on the flavor components in Thai fragrant rice. *Drying Technology*, 23(7): 1407–1418.

[22] Takuma, G., I. Asako, U. Toshitaka, T. Fumihiko, and H. Daisuke. 2013. Optimization of drying condition for brown rice with low moisture content. *Journal Faculty of Agriculture Kyushu University*, 52(1): 381–385.

[23] Wiset, L., G. Srzednicki, M. Wootton, R. H. Driscoll, and A. B. Blakeney. 2005. Effects of high-temperature drying on physicochemical properties of various cultivars of rice. *Drying Technology*, 23(9-11): 2227–2237.

[24] Wongpornchai, S., K. Dumri, S. Jongkaewwattana, and B. Siri. 2004. Effects of drying methods and storage time on the aroma and milling quality of rice (*Oryza sativa* L.) cv. Khao Dawk Mali 105. *Food Chemistry*, 87(3): 407–414.

[25] Zhang, Q., F. G. Jia, C. H. Liu, J. K. Sun, and X. Z. Zheng. 2014. Rapid detection of aflatoxin B_1 in paddy rice as analytical quality assessment by near infrared spectroscopy. *International Journal of Agricultural and Biological Engineering*, 7(4): 127–133.

[26] Zheng, X. Z., C. H. Liu, Z. Y. Chen, N. Y. Ding, and C. J. Jin. 2011. Effect of drying conditions on the texture and taste characteristics of rough rice. *Drying Technology*, 29(11): 1297–1305.

[27] Zheng, X. Z., and Y. B. Lan. 2007. Effects of drying temperature and moisture content on rice taste quality. *Agricultural Engineering International: CIGR Journal*, 9: 1–9.

Identification of vegetable pests using spectral clustering analysis

Xia Ji'an[1], Yang Yuwang[1*], Cao Hongxin[2], Zhang Wenyu[2],
Ge Sijun[2], Chen Guangwei[3]

(1. *School of Computer Science and Engineering, Nanjing University of Science and Technology, 210094 China*;
2. *Institute of Agricultural Information, Jiangsu Academy of Agricultural Sciences, 210014 China*;
3. *Purdue University-West Lafayette, IN. 47906, USA*)

Abstract: The broad bean, an annual leguminous plant, is widely planted in China as a food source. During its growing period, the leaves and pods of the broad bean are often damaged by pests, which reduces yield and even results in crop death. Information on crop growth can be obtained quickly and comprehensively by collecting green crop reflectance spectra followed by using cluster analysis to identify the spectra of infected crops. In this study, a spectral acquisition device was designed to collect visible-near infrared reflectance spectra for three types of broad bean leaf samples in a darkroom with supplemental lighting. The tested samples included healthy leaves, leaves with slight insect infestation, and leaves with strong insect infestation, 30 spectra were sampled from each type. Principal component analysis (PCA) was used to conduct dimension reduction of the spectrum dataset. Hierarchical cluster analysis of the sampled spectra was conducted using the single-link, complete-link, and average-link methods and the sum of squares of deviations (Ward's method). Our results showed that hierarchical clustering effectively identified the three types of spectral samples. Ward's method had the highest identification rate of sample spectra, followed by the single-link and average-link methods, whereas the complete-link method exhibited the poorest performance. The single-link method required the least amount of time, followed by the complete-link and average-link methods, whereas Ward's method required the most time.

Keywords: broad bean, pest identification, spectrum technology, clustering analysis

Citation: Xia, J. A., Y. W. Yang, H. X. Cao, W. Y. Zhang, S. J. Ge, and G. W. Chen. 2017. Identification of vegetable pests using spectral clustering analysis. International Agricultural Engineering Journal, 26(3): 176–183.

1 Introduction

In China, broad bean crops cover an area of approximately 3.2 million acres, with an annual output around 6.6 billion pounds. Broad beans are used as both food and nectar plants. Their flowers, leaves, and stems are used as an auxiliary treatment for constipation, hypertension, and edema, which give the crop a high economic and pharmaceutical value. Major pests that feed on broad beans include the broad bean weevil, aphid, and vegetable leaf miner; of these, the broad bean weevil is the most common. The adult bean weevil mainly infects bean pollen and tender leaves, and the larva parasitizes the pod and eats the bean. If infestation is not detected quickly and preventive measures are not implemented, significant decreases in crop output may occur.

Precision agriculture (PA) offers a fast and accurate method of obtaining information on crops that suffer from pest infestation, allowing strategic management during the crop growing period (Gebbers et al., 2010). Pest control in modern agriculture utilizes computer-based intelligent equipment, remote sensing technology, and real-time monitoring methods to distinguish healthy and infested plants and the degree of crop damage. By comparing the spectral features of infested and healthy crops, differences in crop spectral reflectance within characteristic bands may be detected.

The spectrum analysis has a long history; the application of modern near-infrared spectrum technology

Received date: 2016-10-10 **Accepted date:** 2017-08-22

*** Corresponding Author: Yang Yuwang**, Professor of Computer Science and Engineering College, Nanjing University of Science and Technology, Nanjing, 210094, China. Email: yuwangyang@njust.edu.cn; Tel: +8613512503829.

began with quality analyses of agricultural products. Birth and Norris et al. (1957, 1958) used near-infrared spectrum analysis to examine the quality of eggs, fruits, and vegetables. Recently, analytical methods based on spectrum technology have been widely studied and applied in agriculture. Niewitetzld et al. (2010) built a model for the automatic and optimal selection of rape seeds using infrared spectrum technology. Sankaran et al. (2011) used visible-near infrared spectrum analysis to build an identification model to determine the degree of huanglongbing infection in citrus. Lin et al. (2014) selected spectra with wavelengths from 550 to 650 nm with image information to analyze cabbage leaves damaged by diamondback moths. Anna et al. (2014) used Fourier-transform infrared spectroscopy in three sample groups of coast live oak to determine its resistance to phytophthora ramorum prior to infection. Naresh et al. (2013) studied different spectral indices to analyze cotton pests and obtained 69%-74% accuracy. Zhang et al. (2012) studied spectral and digital images of crop leaf area index (LAI), and the results showed that the spectral method was more stable than the digital image method using LAI measurements.

Cluster analysis is an unsupervised multivariate statistical method. Based on characteristics of the data, it can analyze relationships between close and distant objects using similarity or difference indices. Cluster analysis has been widely applied in agriculture in recent years. Jan et al. (2015) applied cluster analysis via advanced machine learning to detect biotic stress. Li et al. (2012) used Fourier-transform infrared spectroscopy and a cluster analysis to study the characteristics of broad bean diseases and pests. Gumienna et al. (2016) used PCA alongside the nonlinear iterative partial least squares (NIPALS) algorithm to detect the bioethanol production efficiency of 258 different corn types, and the result showed that the ethanol yield of the fermentation process depended on the variety of the grain. Cheilane et al. (2016) used hierarchical classification to analyze the mineral components of breadfruit. Jin et al. (2016) used PCA and hierarchical clustering to study the oxidation resistance and color of 110 different herb teas, compared them with eight types of green tea.

At present, pattern recognition and data mining of crop spectra and images is a major focus of precision agriculture. Through cluster analysis of the spectra of specific crops, which can provide data and theoretical support for further research and application of cluster analysis in agriculture, we can effectively recognize and classify crop pests and diseases.

2 Materials and methods

2.1 Plant and pest materials

Three types of broad bean leaves were selected as the experimental subjects: healthy leaves, leaves slightly infested by pests, and leaves strongly infested by pests (Figure 1). Thirty sample spectra of each type were collected, such there were 90 experimental samples in total. Leaves and broad bean weevils were collected from the experiment field at the Jiangsu Academy of Agricultural Sciences on May 1, 2016.

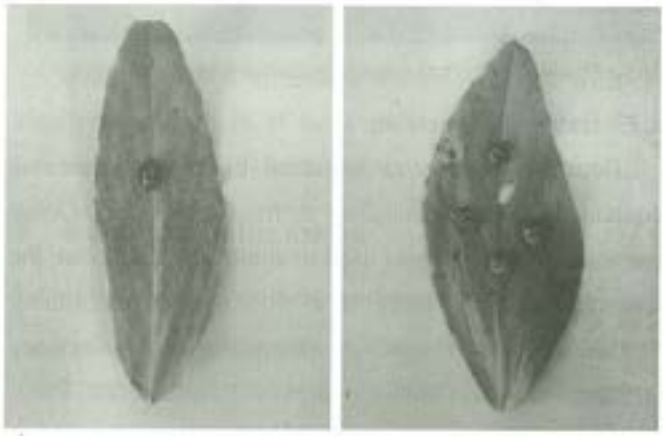

Figure 1 Experimental samples

2.2 Spectral acquisition

An Ocean Optics portable fiber optic spectrometer (USB4000) with an acquisition band from 200 to 1100 nm and an optical resolution of 1.5 nm was used to acquire crop spectra. Reflected light was transmitted to the spectrometer through probes and fiber optics (Figure 2), and the spectrometer transferred the collected spectral data to a laptop for download and analysis. It is difficult to ensure a stable and continuous source of sunlight during long experiments. For this reason, and because stray natural light can affect spectral collection, the experiment was conducted in a darkroom environment, using a 25 W UVB halogen tungsten lamp as the light source. A round $BaSO_4$ test whiteboard was used to

balance the spectra and adjust the integration time. During spectral acquisition, the distance between the fiber optics probe and the center of the sample surface was 3.5 cm. To minimize the impact of the incident angle of the light source on the reflectance spectrum, we set angles between the light source and the sample at 45°, 90°, and 135° for reflectance spectrum measurements; the average value of the spectra from all three directions was considered the reflectance spectrum value for the sample.

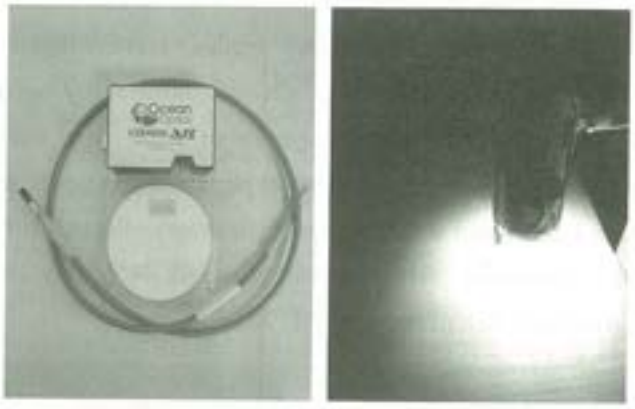

Figure 2 Spectral acquisition device and environment

2.3 Data preprocessing

Because the spectra collected by the spectrometer contained noise and baseline drifts, the Savitzky–Golay convolution method was used to smooth and de-noise the spectra. Savitzky–Golay is a filtering and smoothing technology widely used in absorption and reflectance spectrum analysis (Ruffin et al., 1999; Turton et al., 1992; Luo et al., 2005).

$$X_i^* = \frac{\sum_{j=-r}^{r} X_{i+j} W_j}{\sum_{j=-r}^{r} W_j} \quad (1)$$

The 5-point convolution smoothing method was applied to collect spectrum data considering the weighting factors of the Savitzky–Golay coefficient window:

$$X_i^* = \frac{-3X_{i-2} + 12X_{i-1} + 17X_i + 12X_{i+1} - 3X_{i+2}}{35} \quad (2)$$

Through the data pre-proceeding, the reflectance spectra of the three kinds of samples is shown in Figure 3. Chlorophyll plays a crucial role in the absorption of light by green plants. Because chlorophyll tends to strongly absorb spectra from a band range of 200 to 450 nm, spectra within this band have a low average reflectance, generally within 10%. Because wavelengths around 550 nm are considered within the range of significant spectrum reflection for chlorophyll, the reflectance spectrum curve for spectral bands from 490 to 600 nm displays a wave peak and medium reflectivity (approximately 8%-28%) within this range. Between the visible light waveband and the near-infrared waveband (i.e., around 760 nm), reflectivity increases sharply (45%-55%) and forms a red edge, which is the most significant feature in the reflectance spectrum curve for green plants. Because pests have complicated chemical components with differing optical power absorption, the pest spectrum does not follow any rule, and further research is required to analyze the spectral characteristics of certain pests.

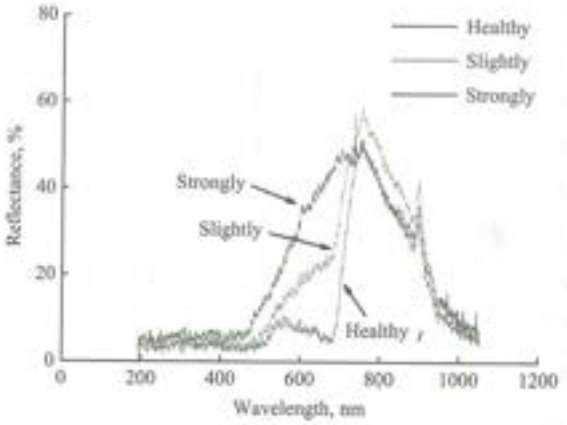

Figure 3 Reflectance spectra of the three sample types

2.4 Cluster analysis

Cluster analysis is a multivariate method of classification that uses individual characteristics to ensure that individuals within the same class will have maximum homogeneity while different classes will exhibit maximum heterogeneity. Hierarchical clustering is the most widely used method of cluster analysis and is known for its stable clustering results and straightforward process (Praisler et al., 2015). It can also be applied in high-dimensional data clustering and therefore is widely used in precise agriculture research (Mratinic et al., 2012; Balan et al., 2015; Justyna et al., 2016).

This study used hierarchical clustering to conduct cluster analyses of crop spectra. Hierarchical clustering uses the distance coefficient as its classification statistic, which requires consideration of two core factors: (I)

similarity measurement between samples and (II) similarity measurement between classes. Many methods can be used to measure the similarity between samples (Li et al., 2010; Kavitha et al., 2013). Zong et al. (2014) used Euclidean distance, cosine angle, and correlation methods to measure similarity between pest spectra of brassica chinensis, showing that Euclidean distance performed best in identifying pest spectra. There are various methods of measuring similarity between classes; the proper method should be chosen based on the nature and characteristics of the clustering object.

Table 1 Distance measurement of hierarchical clustering

Similarity measurement of hierarchical clustering			
Similarity measurement between samples		Similarity measurement between classes	
1	Similarity distance	1	Single-Link
2	Cosine angle	2	Complete-Link
3	Correlation coefficient	3	Average-Link
4	Relative error distance	4	Centroid-Link
5	Maximum dissimilarity coefficient	5	Sum of Squares of Deviations (WARD)

Four methods of the single-link were selected, namely, complete-link, average-link methods and Ward's method to measure the similarity between classes. Then the hierarchical cluster analyses of the spectra of three types of crops were conducted and the clustering results were analyzed.

(I) Single-link method

Assuming that d_{ij} is the similarity distance between sample i and sample j, and D_{pq} is the distance between class G_p and class G_q, then Formula (3) can be used to calculate the distance between different classes:

$$D_{pq} = \underset{i \in G_p, j \in G_q}{Min} d_{ij} \tag{3}$$

The single-link method defines interclass distance as the distance between the most similar samples in two classes.

(II) Complete-link method

By adopting the assumption in Formula (3), Formula (4) can be used to calculate the distance between Class G_p and Class G_q:

$$D_{pq} = \underset{i \in G_p, j \in G_q}{Max} d_{ij} \tag{4}$$

The complete-link method defines interclass distance as the longest similarity distance between two samples from two classes.

(III) Average-link method

By adopting the assumption in Formula (3), n_p and n_q refer to the sample quantity; Formula (5) can then be used to calculate interclass distance using the average-link method:

$$D_{pq} = \frac{1}{n_p n_q} \underset{i \in G_p, j \in G_q}{Max} d_{ij} \tag{5}$$

The average-link method uses the average value of distances between samples as the measurement between classes.

(IV) Ward's method

Assuming that n samples must be divided into k classes denoted by G_1, $G_2 \ldots G_k$, n_t refers to the sample quantity in Class G_t. $\bar{X}^{(t)}$ is the center of gravity of G_t, and $X_i^{(t)}$ is the i^{th} sample in i. The total sum of squares of deviations for k classes is

$$W = \sum_{t=1}^{k} \sum_{i=1}^{n_t} (X_i^{(t)} - \bar{X}^{(t)})'(X_i^{(t)} - \bar{X}^{(t)}) \tag{6}$$

Ward's method combines the two classes with the smallest variation in W until all samples are combined into one class.

3 Results and discussion

3.1 Hierarchical clustering of pest spectra

Matlab 2012b was used to implement the hierarchical clustering algorithm. Using the Euclidean distance for distance measurements between samples, and using four different interclass measurement methods for the hierarchical cluster analysis of the three types of samples, we obtained four different tree diagrams (Figures 4).

These tree diagrams showed that all four clustering methods first calculated the Euclidean distance between samples, then categorized samples with the smallest Euclidean distance into one class, and finally calculated the distance between new classes and other samples. Because different methods were used to calculate interclass distance, the final clustering results were different. The advantage of the hierarchical clustering method is that the principle is simple; thus, we can observe in detail the process by which small classes are aggregated into large classes, and the similarity between samples can be seen in the similarity distance.

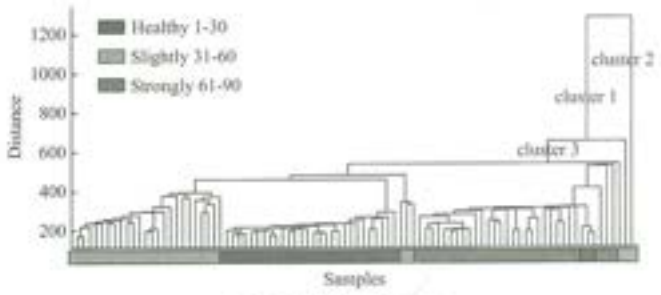

a. Single-link tree diagram

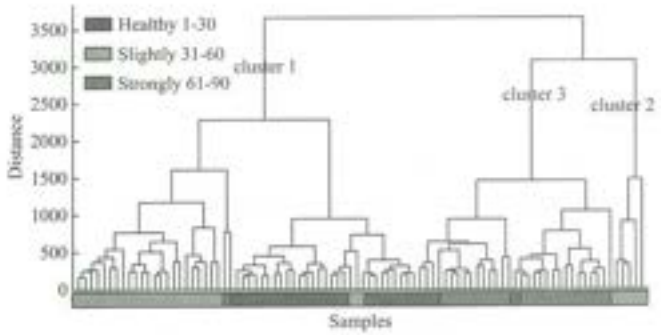

b. Complete-link tree diagram

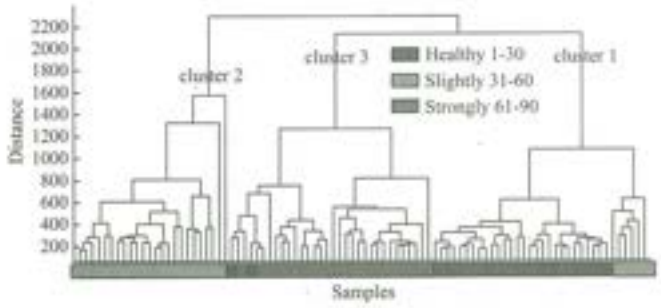

c. Average-link tree diagram

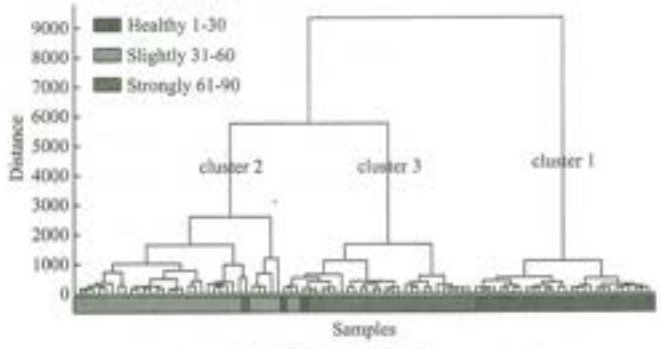

d. WARD tree diagram

Figure 4 Hierarchical clustering results of broad bean pests' spectra

3.2 Cluster analysis of pest spectra

Because the pest spectral clustering contained high-dimensional data clustering, PCA was used to conduct dimension reduction processing of the spectral data, which can effectively evaluate the effects of hierarchical clustering.

PCA transforms multiple variables into a smaller number of comprehensive factors. Through linear transformation, PCA can transform the original data into a set of main feature components that are linearly independent in dimension and can be used to extract data and reduce the dimensions of high-dimensional data (Maurizio et al., 2009).

PCA determines the final data dimension by calculating the contribution rate of the feature components. Generally speaking, corresponding values with contribution rates higher than 70% can be used as the data dimension (Jolliffe et al., 2016). We used Matlab 2012b to run the PCA algorithm and applied dimension reduction processing to the original spectral data. Table 2 lists the corresponding relationships between different eigenvectors and dimensions in the spectral matrix. We chose two-dimensional spectral data, and the contribution rate of the eigenvectors was 99.78%.

Table 2 Contribution rate of eigenvectors

	Principal component analysis of pest spectra				
Data dimension	1	2	3	4	5
Contribution rate	0.9436	0.9978	0.9989	0.9990	0.9992

Through PCA of the sample spectra, the high-dimensional spectral data were reduced to a lower dimension for expression and analysis. It showed that the distribution diagram of the three samples in two-dimensional space following PCA in Figure 5.

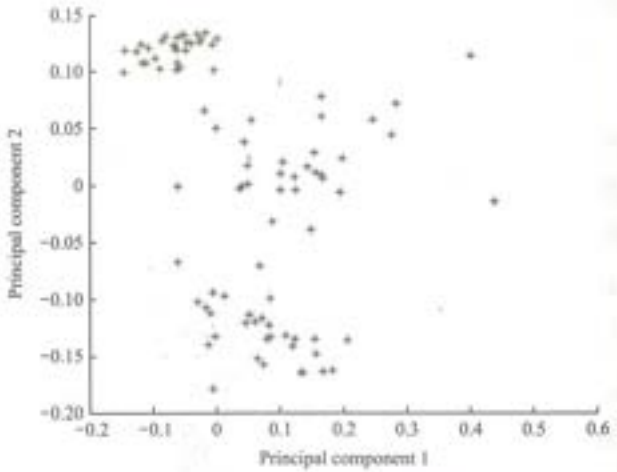

Figure 5 Pest spectral distribution

Using PCA to reduce the dimension of the high-dimensional pest spectral data, we demonstrated the distribution of sample spectra in low-dimensional space. Figure 6 shows the hierarchical clustering results of pests' spectra by using different interclass measurement methods. In the new two-dimensional space, when we

used different interclass measurement methods, the hierarchical clustering results were different. At the boundary of the three types of samples, the clustering results were clear distinction.

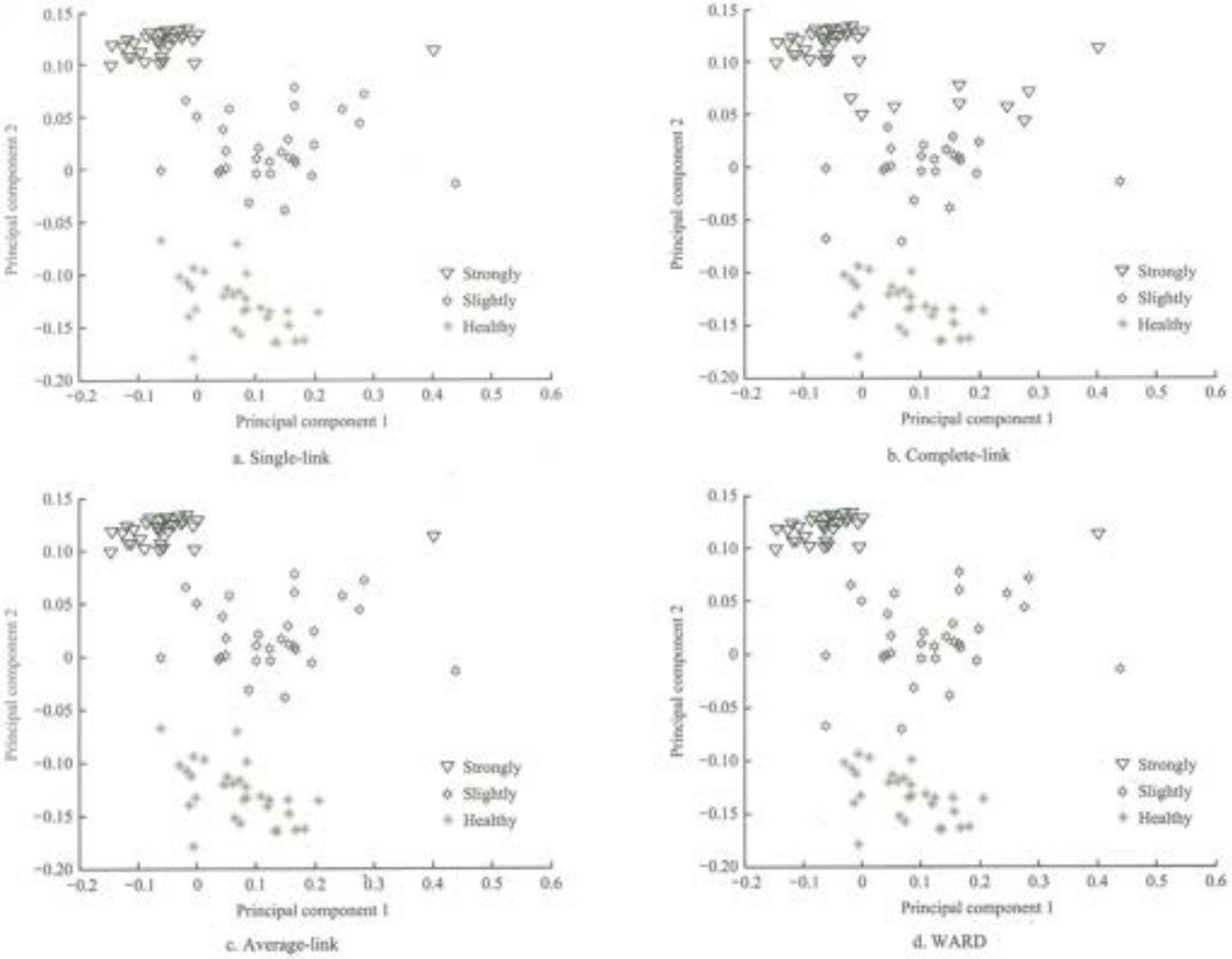

Figure 6 Principal component analysis results for four methods of analyzing pest spectral

Four different hierarchical clustering methods were used to conduct cluster analysis of three types of pest spectra; the statistical results were shown in Table 3.

Table 3 Recognition rate of hierarchical clustering

Model	Recognition rate		
	Healthy	Slightly	Strongly
Samples	30	30	30
Single	32 (93.3%)	29 (96.6%)	29 (96.6%)
Complete	30 (100%)	23 (76.6%)	37 (76.6%)
Average	32 (93.3%)	29 (96.6%)	29 (96.6%)
WARD	30 (100%)	31 (96.6%)	29 (96.6%)

In accordance with the clustering result in the experiment, the clustering effects of the four kinds of similar distance are summarized, in which, the single-link distance's identification rates of the three types of samples are 93.3%, 96.6% and 96.6% respectively; the complete-link distance's identification rates of the three types of samples are 100%, 76.6% and 76.6% respectively. The identification rates of average-link distance are 93.3%, 96.6% and 96.6% respectively. The identification rates of WARD distance are 100%, and 96.6% and 96.6%, respectively.

It can be seen from the results that the WARD distance is the best for the identification of the pests' sample spectrum, followed by single and average distance, the identification rate of complete distance is the worst.

We executed each of the four hierarchical clustering methods 50 times and calculated the average time required by each method. We used an AMD A8 processor with a frequency of 3.6 GHz in Windows 7 and 8 GB of RAM memory. The time consumed for each clustering method was 0.52 s (Single), 0.61 s (Complete), 0.55 s (Average), and 0.65 s (WARD), respectively.

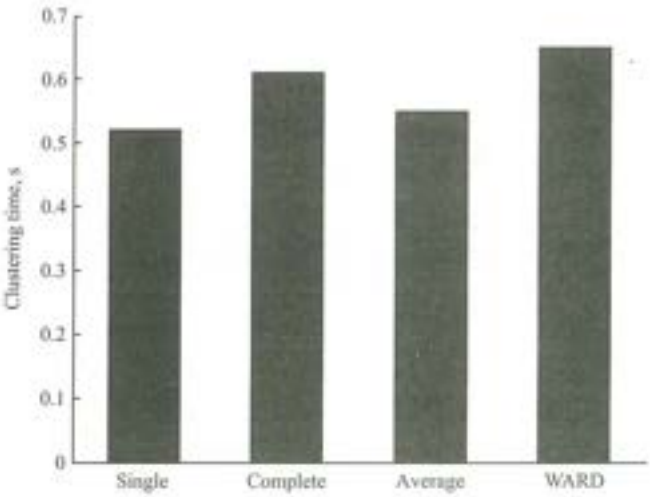

Figure 7 Clustering time consumption

4 Conclusion

The quality of crop spectral acquisition was affected by various factors, such as the light source, acquisition distance, incident light angle, pest density, and integration time of the spectrometer. To improve the accuracy of spectral acquisition, the experiment was conducted multiple times in a darkroom environment; the spectra were acquired from different angles, with the average result used as the experimental data. However, guaranteed accuracy of the acquired spectral data was not possible under these conditions. Consequently, we recommend finding a more reliable method of obtaining crop pest spectral information in a fast and accurate manner.

Some currently used clustering methods, such as K-means and fuzzy C-means, require predefined cluster numbers, and the clustering center is randomly chosen during the process, which tends to yield unstable clustering results. Hierarchical clustering avoids defining the clustering number by using a similarity matrix during clustering yet generates the same result. The direct observation of the sample clustering process and the results obtained by combining the clustering results through tree diagrams and PCA results is beneficial to research on crop spectral analysis.

Because there are many types of crops and pests that have different characteristic reflectance spectra, it is necessary to determine the appropriate cluster analysis method. This study used hierarchical clustering and PCA to analyze crop and pest spectra. In future research, hierarchical cluster analysis can be widely used to analyze and identify crop disease and pest spectra to improve the detection of diseases and pests for precision agriculture.

Acknowledgements

The research is funded by the National Natural Science Foundation of China (No. 61671244, 61640020). The Agricultural Innovation Program of Jiangsu, China (No. CX(13)3054, CX(14) 2114 and CX(16)1006). The Key Research and Development Program of Jiangsu, (No. BE2016368-1).

[References]

[1] Anna, O. C., L. E. Rodriguez-Saona, B. A. Mcpherson, D. L. Wood, and P. Bonello. 2014. Identification of Quercus agrifoli (coast live oak) resistant to the invasive pathogen phytophthora ramorum in native stands using Fourier-transform infrared(FT-IR) spectroscopy. *Frontiers in Plant Science*, 5(521): 1–9.

[2] Balan, A. V., E. Toma, C. Dobre, and E. Soare. 2015. Organic farming patterns analysis based on clustering methods.*Agriculture & Agricultural Science Procedia*, 6: 639–646.

[3] Birth, G. S., and K. H.Norris. 1958. An instrument using light transmittance for nondestructive measurement of fruit maturity. *Food Technology*, 12(11): 592–594.

[4] Cheilane, T., S. A. R Soares, A. F. S Queiroz, A. M. P. D. Santos, and S. L. C. Ferreira. 2016. Determination and evaluation of the mineral composition of breadfruit (Artocarpus altilis) using multivariate analysis technique. *Microchemical Journal*, 128: 84–88.

[5] Gebbers, R., and V. I. Adamchuk. 2010. Precision agriculture and food security. *Science*, 327(5967): 828–831.

[6] Gumienna, M., A. Szwengiel, M. Lasik, K. Szambelan, D. Majchrzychi, J. Adamczyk, J. Nowak, and Z. Czarnecki. 2016. Effect of corn grain variety on the bioethanol production efficiency. *Fuel*, 164: 386–392.

[7] Jan, B., A. K. Mahlein, T. Rumpf, C. Römer, and L. Plümer. 2015. A review of advanced machine learning methods for the detection of biotic stress in precision crop protection. *Precision Agriculture*, 16(3): 239–260.

[8] Jin, L., X. B. Li, D. Q. Tian, X. P. Fang, Y. M. Yu, H. Q. Zhu, Y. Y. Ge, G. Y. Ma, W. Y. Wang, W. F. Xiao, and M. Li. 2016. Antioxidant properties and color parameters of herbal teas in China. *Industrial Crops and Products*, 87: 198–209.

[9] Jolliffe, I. T., and J. Cadima. 2016. Principal component analysis: a review and recent developments. *Philosophical*

Transaction of the Royal Society A-Mathematical Physical and Engineering Sciences, 374(2065): 1–16.

[10] Justyna, B. C., G. Malgorzata, and S. Piotr. 2016. Monitoring of essential and heavy metals in green tea from different geographical origins. *Environmental Monitoring and Assessment*, 188(3): 1–11.

[11] Kavitha, K. A., P. Mintu, and K. Lubna. 2013. Comparative analysis of similarity measures in document clustering. *The 2013 International Conference on Green Computing, Communication and Conservation of Energy, (ICGCE)*, 857–860. Beijing, China, 20-23 August.

[12] Li, L. B., and H. Y. Deng. 2010. Research of similarity measurements in the clustering analysis. *The Second International Conference on Information Technology and Computer Science*, 3-6. Kiev, Ukraine., 24-25 July.

[13] Li, Z. Y., G. Liu, L. Li, Q. H. Ou, and X. Zhao. 2012. FTIR spectroscopic study of broad bean diseased leaves. *Spectroscopy and Spectral Analysis*, 13(11): 1217–1220.

[14] Lin, L. B., H. N. Li, P. F. Cao, F. Qin, and S. Yang. 2015. The characteristic analysis of spectral image for cabbage leaves damaged by diamondback moth pests. *The International Conference on Photonics and Optical Engineering (icPOE 2015)*, 9449, 1–6. Xi'an, China, 13-15 Oct.

[15] Luo, J. W., K. Ying, and J. Bai. 2005. Savitzky–Golay smoothing and differentiation filter for even number data. *Signal Processing*, 85(7): 1429–1434.

[16] Maurizio, V., and S. Gilbert. 2009. Clustering and disjoint principal component analysis. *Computational Statistics and Data Analysis*, 53(8): 3194–3208.

[17] Mratinic, E., F. A. Milica, and R. Jovkovic. 2012. Analysis of wild sweet cherry (prunus avium L.) germplasm diversity in south-east Serbia. *Genetika*, 44(2): 259–268.

[18] Naresh, K., N. Ram, M. L. Khichar, R. K Saini, and B. Biswas. 2013. Effect of different growing environments on population dynamics of sucking pests in relation to various spectral indices in cotton. *Journal of the Indian Society of Remote Sensing*, 41(2): 309–317.

[19] Niewitetzki, O., P. Tillmann, H. C. Becker, and C. Möllers. 2010. A new Near-Infrared reflectance spectroscopy method for high-throughput analysis of oleic acid and linolenic acid content of single seeds in oilseed rape (brassica napus L.). *Journal of Agricultural and Food Chemistry*, 58(1): 94–100.

[20] Norris, K. H., and J. Rowan. 1957. Use of the automatic green rot detector to improve the quality of liquid. *Food Technology*, 11: 374–377.

[21] Praisler, M., S. C. Ghinita, A. Stoica, and L. Dumitriu. 2015. Hierarchical Cluster Analysis: a reliable tool allowing more detailed (regional) traceability investigations. *19th International Conference on System Theory, Control and Computing (ICSTCC)*, 157–161. Cheile Gradistei, Romania., 14-16 October.

[22] Ruffin, C., and R. L. King. 1999. The analysis of hyperspectral data using Savitzky-Golay Filtering-Theoretical Basis (Part1). *IEEE 1999 International Geoscience and Remote Sensing Symposium*, 2: 756–758.

[23] Chao, W. L., H. H. Su, S. Y. Chien, W. Hsu, and J. J. Ding. 2011. Visible-near infrared spectroscopy for detection of Huanglongbing in citrus orchards. *Computers and Electronics in Agriculture*, 77(2): 127–134.

[24] Turton, B. C. H. 1992. Novel variant of the Savitzky-Golay filter for spectroscopic applications. *Measurement Science & Technology*, 3(9): 858–863.

[25] Zhang, R. X., J. L. Ba, Y. Ma, S. Q. Wang, J. Zhang, and W. D. Li. 2012. A comparative study on wheat leaf area index by different measurement methods. *First International Conference on Agro-Geoinformatics*. 1-5. Shanghai, China, 2-4 Aug.

[26] Zong, J. X., Y. W. Yang, L. Wang, W. Zhao, and M. He. 2014. Detection of vegetable pests identification based on spectrum. *International Agricultural Engineering Journal*, 1(23): 47–55.

Effect of fermentation by different strains on the soybean oligosaccharide content in douchi

Gan Jing[1], Wang Yongquan[1], Shi Lin[1], Cai Kun[1], Yin Lijun[1], Satoru Niarasawa[2], Cheng Yongqiang[1*]

(1. *Beijing Key Laboratory of Functional Food from Plant Resources, College of Food Science and Nutritional Engineering, China Agricultural University, Beijing 100083, China;*
2. *Japan International Research Center for Agricultural Sciences, Tsukuba, 305-8686, Japan*)

Abstract: Douchi, a popular soybean food in China, has many prominent physiological activities. In the current research, the content changes of stachyose and raffinose during the douche processing, fermented by Aspergillus orgzae, Rhizopus oligosporus, Actinomucor elegans and Bacillus subtilis respectively were investigated. The results showed that the α-galactosidase activity of the fermented soybeans played the main role in the degradation of raffinose and stachyose during the primary fermentation, and the highest enzymatic activity reached 412.36 U/g dry weight of *A. oryzae*, 357.51 U/g dry weight of *R. oligosporus*, and 288.37 U/g dry weight of *A. elegans*. In the *B. subtilis*- fermented douchi, the main enzyme was invertase (30.05 mg/g dry weight). During the post-fermentation, the α-galactosidase activity of the fermented soybeans decreased dramatically, but the invertase activity increased. A trace amount of α-galactosidase in the *B. subtilis*-fermented douchi was detected. The sucrose content and the total amount of fructose and glucose in different douchi samples were 10.69 and 36.85 mg/g dry weight of *A. oryzae*, 7.69 and 16.23 mg/g dry weight of *R. oligosporus*, 6.05 and 14.79 mg/g dry weight of *A. elegans*, and 2.44 and 4.87 mg/g dry weight of *B. subtilis*, respectively. Our study revealed the key factors that control the soybean oligosaccharide content during fermentation, which will provide an experimental basis for producing douchi with appropriate oligosaccharide contents.

Keywords: α-galactosidase, douchi, fermentation, soybean oligosaccharides

Citation: Gan, J., Y. Q. Wang, L. Shi, K. Cai, L. J. Yin, S. Niarasawa, and Y. Q. Cheng . 2017. Effect of fermentation by different strains on the soybean oligosaccharide content in douchi. International Agricultural Engineering Journal, 26(3): 184–192.

1 Introduction

Gastrointestinal diseases, such as diarrhea, gastritis, and colon cancer, have become common not only in the elderly, but also in children, because of changes in people's lifestyle and dietary habits (De Looze et al., 1998; Stone et al., 1990) Antibiotics, probiotics, prebiotics, and synbiotics are usually used to treat or prevent gastrointestinal problems (Collins and Gibson, 1999; Rolfe, 2000; Ziemer and Gibson, 1998). Hence, prebiotics from food sources have become an attractive therapeutic approach for preventing and treating gastrointestinal problems. Prebiotics are factors that promote the growth of bifidobacteria in human intestine. They are always in the form of oligosaccharides, which are not digested in the gastrointestinal tract. Prebiotic oligosaccharides include fructooligosaccharides, inulin, galactooligosaccharides, and soybean oligosaccharides. Soybean oligosaccharides are a general name for soluble sugars in soybean and leguminous seeds that primarily account for 7%-10% of all carbohydrates. Stachyose and raffinose account for 2-10 g/100 g soybean dry weight (Guillon and Champ, 2002).

Soybean oligosaccharides were always thought to be a cause of flatulence, because of the lack of an enzyme that metabolizes alpha-D-galactose glucoside in body, which leads to the production of carbon dioxide, hydrogen, and

Received date: 2016-11-27 **Accepted date:** 2017-07-17

* **Corresponding author:** Cheng Yongqiang, Beijing Key Laboratory of Functional Food from Plant Resources, College of Food Science and Nutritional Engineering, China Agricultural University, Beijing 100083, China. Email: chengyq@cau.edu.cn.

methane following fermentation (Murphy et al., 1972; Reddy et al., 1980). While stachyose and raffinose were once considered to be causes of flatulence, Edwin et al. (1981) demonstrated that they are not. These compounds did not produce any negative effects when administered in a beverage (3 g/100 mL) daily for 2 weeks (Hideo, 1994). Additionally, a study of 51 women that ate 45 g of white navy beans daily revealed that 76.5% of the women did not experience diarrhea (Song et al., 2008). These oligosaccharides can be used as probiotics when consumed in the form of 3 g of α-oligosaccharides daily for long periods, and they do not produce any negative effects. A previous study showed that regardless of the soybean variety, the degree of flatulence was so low that it was widely considered to be acceptable when the oligosaccharide contents in soybeans were 1.9, 2.6, and 3.5 g/100 g (Veenstra et al., 2010). A previous study observed that the optimal added quantity of oligosaccharides in bottle-fed infants was 4 g/L. Furthermore, the addition of oligosaccharides improved the diversity and the proportion of bifidobacteria in the gut(Holscher et al., 2012). Another study demonstrated that there were no significant differences in the number of adverse reactions in the gut between infants who consumed milk with added oligosaccharides compared with those who consumed milk alone (Mansilha, 2011). Thus, consuming a certain amount of stachyose and raffinose does not induce flatulence, and it can regulate and improve the intestinal flora of humans.

Soybean and its products have been appreciated by people as healthy foods because of their nutritional and medicinal attributes. Specifically, long-term intake of soybean foods can prevent several diseases such as type II diabetes and cancers. Douchi, a popular soybean food in China, is fermented by different microorganisms, which have many prominent physiological activities and special flavors (Dajanta et al., 2011) Many studies have reported that douchi can decrease blood pressure and moderate blood glucose levels (Chen et al., 2007; Hiroyuki et al., 2001; Mccue et al., 2005) . After the fermentation of douchi, the contents of some active ingredients increase while inhibitory factors decrease (Cho et al., 2011; Tsai et al., 2007; Chung et al., 2011). Previous studies showed that douchi possesses anti-diabetic and anti-tumor properties, and a douchi extract exhibited significant antioxidant activities and anti-α-glucosidase activity. Douchi can be divided into different types, depending upon whether it is fermented by *Aspergillus*, *Rhizopus*, *Mucor*, *Neurospora*, or bacteria. It is accepted widely that many nutrients in douchi, such as soy isoflavone, soluble sugar, angiotensin-converting-enzyme inhibitors, vitamin B, folic acid, and short-chain fatty acids, are generated or improved after fermentation (Nakajima et al., 2005; Zhang et al., 2005).

Microorganisms and fermentation are important for improving the nutrition of soybean products; however, the changes of soybean oligosaccharides in douchi during fermentation have not yet been investigated. In this study, we analyzed the stachyose and raffinose contents in 10 douchi samples collected from various parts of China. The contents of stachyose, raffinose, fructose, glucose, and sucrose, as well as the α-galactosidase activity, of douchi prepared using four microbes (*Aspergillus oryzae*, *Rhizopus oligosporus*, *Actinomucor elegans*, or *Bacillus subtilis*) were analyzed at different fermentation time. The objective of the study was to observe the changes of oligosaccharides during fermentation, as well as the factors that are responsible for such changes.

2 Materials and methods

2.1 Materials

Ten douchi samples were purchased from douchi manufacturers in different parts of China (Table 1,). Stachyose, raffinose, fructose, glucose, and sugar standards were purchased from Sigma-Aldrich (St. Louis, MO, USA). The other chemicals used in the study were of analytical grade.

2.2 Microorganisms and culture conditions

Four microbes were used: *A. oryzae*, *R. oligosporus*, *A. elegans*, and *B. subtilis*. The mold strains were cultivated and activated in potato dextrose agar culture medium at 28°C, which was made by combining wheat bran and deionized water (1:1.4) and autoclaving at 121°C for 20 min. After 72 h of cultivation, the spore concentration in each inoculum reached 1×10^7/mL. *Bacillus subtilis* was cultivated and activated in De Man,

Rogosa, and Sharpe broth at 37°C for 24 h.

2.3 Production and preparation of douchi

Fifty grams of black soybeans was washed and soaked in 200 mL of deionized water for 8 h, and then the soybeans were drained, placed into a 500 mL triangular flask, and autoclaved at 121°C for 20 min. After cooling, the soybeans were inoculated with the different strains at a 1:1 (w/v) ratio. Salt was added to douchi to a concentration of 6% (g/mL), and then douchi made by the mold strains was fermented at 28°C, while douchi made by *B. subtilis* was fermented at 37°C. Samples were removed daily until the 10th day of fermentation. Douchi was freeze-dried and stored at 4°C until use.

The pre-fermentation procedure was conducted as follows. Soybeans were inoculated with 1% (w/v) of the microbial inocula (10^7 spores/mL) as a pure culture fermentation starter. Soybeans fermented by *A. oryzae*, *R. oligosporus*, and *A. elegans* were cultured at 28°C for 16, 32, and 48 h, while those fermented by *B. subtilis* were cultured at 37°C for 16, 32, and 48 h. After the primary fermentation, salt was added to soybeans to a concentration of 6% (mL/g), and then the mold and bacterial strains were cultured at 40°C and 37°C, respectively, for 1 to 10 days to produce douchi.

2.4 Determination of oligosaccharides in douchi

Briefly, freeze-dried douchi was crushed and sieved through a 100-mesh screen. After degreasing in a hexane solution, 1.5 g of douchi powder was mixed with 15 mL of 80% ethanol at 70°C for 1 h in a shaking water bath, and then it was subjected to three rounds of centrifugation at 8,000 *g* for 20 min in a refrigerated centrifuge at 0°C to 5°C to remove the insoluble fraction; the soluble supernatant was collected after each round of centrifugation. Each supernatant was rotary evaporated to 2 mL and diluted with water to 5 mL; all the supernatants were filtered through a 0.45 μm filter using a Membranes-aquo system. The filtrate was analyzed using high-performance liquid chromatography with an evaporative light scattering detector using an amino column (4.6 mm × 250 mm, 5 μm, Prevail Carbohydrates ES). The mobile phases were 30% water and 70% acetonitrile. The temperatures of the column and drift tube were 30°C and 82.3°C, respectively. The oligosaccharides were identified based on their retention times after comparison with corresponding standards purchased from Sigma-Aldrich.

2.5 Determination of the fructose, glucose, and sugar in douchi

The fructose, glucose, and sugar in the aforementioned filtrates were analyzed using high-performance liquid chromatography with a refractive index detector using an amino column (4.6 mm × 250 mm, 5 μm, Sugar-D). The mobile phase was 30% water and 70% acetonitrile. The temperature of the column was 30°C. Fructose, glucose, and sugar were identified based on their retention times after comparison with corresponding standards purchased from Sigma-Aldrich.

2.6 Determination of α-galactosidase activity of douchi

The α-galactosidase activity was analyzed by a microplate spectrophotometer at 605 nm, after modifying the method described by Alazzeh et al. (2009) The fermented douchi (2 g) was dissolved in 40 mL of acetate buffer and ground for 1 min. α-galactosidase was extracted by magnetic stirrers at room temperature for 40 min, and then the solution was subjected to three rounds of centrifugation at 8000 r/min at 4°C for 20 min to remove the insoluble fraction; the soluble superanatant was collected after each round of centrifugation. Each supernatant (10 μL) was added to 80 μl of acetate acid buffer and 10 μL of *p*-nitrophenol glucopyranoside in 96-well plates. Additionally, 10 μL of crude enzyme was added to 80 μL of acetate acid buffer and 100 μL of a sodium carbonate solution as a control. Then, two experimental replicates were shaken in a water bath at 40°C for 10 min, and then 100 μL of a sodium carbonate solution was added rapidly to terminate the reaction, while 10 μL of *p*-nitrophenol glucopyranoside was added to the control. The α-galactosidase activity was based on the optical density value according to the *p*-nitrophenol standard curve.

2. 7 Determination of sucrose-metabolizing enzymatic activity of douchi

The sucrose-metabolizing enzymatic activity was determined according to the method described by Yanase

with modifications (Yanase et al., 1991). Two grams of fermented douchi was mixed with 40 mL of sodium acetate buffer (0.2 mol/L, pH 4.6), ground for 40 min, and then it was subjected to three rounds of centrifugation at 8000 r/min for 20 min at 4°C to remove the insoluble fraction; the soluble supernatant was collected after each round of centrifugation. The sucrose-metabolizing enzymatic activity was determined based on the reducing sugars released from the sample.

2.8 Statistical analysis

All data analyses were performed using Origin 8.0 software, and structural formulas were generated by ChemDraw 7.0. All experiments were performed at least twice.

3 Results and discussion

3.1 Stachyose and raffinose contents in commercial douchi samples

Ten douchi samples were collected from various parts of China. Their stachyose and raffinose contents, brand names, origins, and type of strains used for their preparation are listed in Table 1. Among these samples, the stachyose and raffinose contents of douchi fermented by *B. subtilis* were significantly higher than those of the others. Thus, the stachyose and raffinose contents differed because of the use of different fermentation strains. However, the stachyose and raffinose contents even differed when the same strain was used. These differences most probably arose from variations in processing techniques.

Table 1 Contents of raffinose and stachyose in commercial douchi samples

Sample No.	Brands	Origins	Tape of strains	Raffinose, mg/g	Stachyose, mg/g
1	YC	Sichuan	Hair mold	0.653	1.998
2	TC	Sichuan	Hair mold	0	2.583
3	CN	Sichuan	Hair mold	0.437	1.47
4	SDC	Sichuan	Bacterial	2.012	2.183
5	WYZ	Shandong	Aspergillus	0.208	1.825
6	TH	Yunnan	Aspergillus	0.198	1.798
7	LJ	Hunan	Aspergillus	1.258	0
8	YPX	Hunan	Aspergillus	0.611	1.923
9	LYP	Hunan	Aspergillus	0.298	1.753
10	YJ	Guangdong	Aspergillus	0.292	1.592

3.2 Determination of oligosaccharides in douchi

The oligosaccharide contents in douchi during the fermentation are shown in Figure 1. Generally, the stachyose and raffinose contents at the beginning of the fermentation were 44.1 and 26.0 mg/g dry weight, respectively. After soaking and boiling, the oligosaccharide contents decreased slightly. During fermentation, the stachyose and raffinose in soybeans are hydrolyzed by microorganisms (Mital and Steinkraus, 1975; Prashanth and Mulimani, 2005). Aworh found that the stachyose and raffinose contents decreased by 83.9% and 50%, respectively, after douchi was fermented by *R. oligosporus*. The stachyose and raffinose in cowpea were eliminated after 15 h of fermentation by *Rhizopus microspores*. However, changing trends of the stachyose and raffinose contents in douchi fermented by different microorganisms have not been reported until now. As can be seen in Figure 1, before fermentation, the stachyose and raffinose contents were 20.39 and 24.56 mg/g dried weight, respectively, whereas at the end of the pre-fermentation, the contents were 5.23 and 6.03 mg/g dry weight of *A. oryzae*, 6.48 and 6.59 mg/g dry weight of *R. oligosporus*, 11.75 and 10.72 mg/g dry weight of *A. elegans*, and 12.81 and 8.64 mg/g dry weight of *B. subtilis*, respectively. The results showed that the hydrolysis of stachyose and raffinose at 16-32 h was higher than that at 0-16 h and 32-48 h; this is because of the enzymatic activity in the fermentation (date not shown). At the beginning of the fermentation, protease, α-D-galactose glucoside enzyme, α-D-glycosidase, and amylase in the soybeans were secreted, and the microorganisms used the resulting nutrients, including proteins, glucose, fructose, sucrose, and oligosaccharides, as carbon sources, but α-galactosidase was not the dominant enzyme. With increasing fermentation time, the enzymatic activity increased until maximum activity was observed at 32 h. This was the result of the oligosaccharides becoming the main carbon source at 16-32 h, when starch and other carbon sources had been degraded, and the stachyose and raffinose contents in douchi declined significantly when fermented by *A. oryzae*, *R. oligosporus*, or *B. subtilis*. At 32-48 h, the stachyose and raffinose contents stabilized because of an increase in secondary metabolites, which may affect microbial growth.

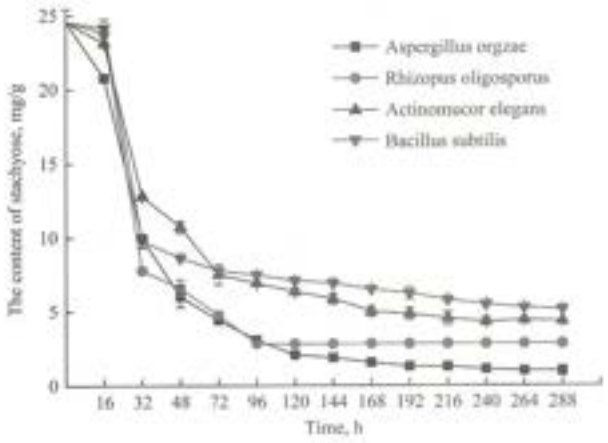

a

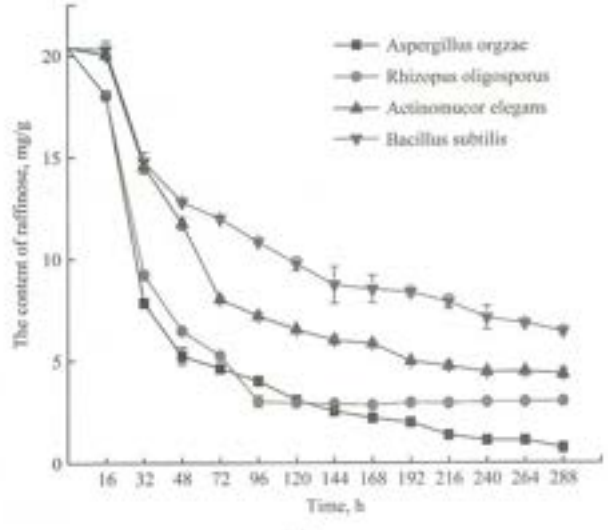

b

Figure 1 Effects of different microorganisms on the contents of stachyose (a) and raffinose (b) in douchi during fermentation

During the post-fermentation, salt was added to the soybeans at a concentration of 6%, and stachyose and raffinose contents of douchi decreased to 0.73 and 0.98 mg/g dry weight of *A. oryzae*, 3.01 and 2.83 mg/g dry weight of *R. oligosporus*, 6.42 and 5.14 mg/g dry weight of *A. elegans*, and 11.75 and 10.72 mg/g dry weight of *B. subtilis*, respectively. The downward trends decreased slightly during processing, which may be associated with the oxygen level, temperature, and salt concentration. When the fermentation began, the oxygen level declined sharply and the temperature increased in the culture medium. Salt can destroy the charge balance on the surface of cells, which resulted in a decrease in enzymatic activity. Meantime, short-chain fatty acids and organic acids were produced during the fermentation; thus, the total acid content in douchi increased, and the pH of the culture medium decreased, which restrained the growth of *B. subtilis*. Zhang et al. (2007) reported that organic acids are mainly produced during post-fermentation. The change in the pH affects the dissociation of charged groups and microstructures on the cell surface, thus affecting the ratio of absorbed nutrients and secreted metabolic substances. This phenomenon is consistent with the observations of Sims et al.

The decreases in the stachyose and raffinose contents during the fermentation are shown in Table 2, and all the microorganisms showed the ability to hydrolyze raffinose and stachyose. Among the four stains, *A. oryzae* showed higher hydrolytic activities than the others, especially during the pre-fermentation. In contrast, the decreases in the stachyose and raffinose contents in douchi fermented with *B. subtilis* were significantly lower than those of the others.

Table 2 Decrease of raffinose and stachyose content in douchi during the pre-fermentation and total fermentation

Microorganism	Stage	Decrease ratio of Raffinose, %	Decrease ratio of Stachyose, %
Aspergillus orgzae	Pre-fermentation	74.35	75.44
	Total-fermentation	96.41	96.01
Rhizopus oligosporus	Pre-fermentation	68.22	73.17
	Total-fermentation	85.24	88.48
Actinomucor elegans	Pre-fermentation	42.37	56.35
	Total-fermentation	78.67	82.33
Bacillus subtilis	Pre-fermentation	37.17	64.82
	Total-fermentation	68.46	79.07

3.3 Contents of sucrose, glucose, and fructose during fermentation

Soybean oligosaccharides include raffinose (4%), stachyose (1%), and sucrose (5%). Stachyose is a tetrasaccharide, which comprises two α-D-galactose units, one α-D-glucose unit, and one β-D-fructose unit. However, raffinose is a trisaccharide, which comprises galactose, glucose, and fructose, in which the galactose and sucrose moieties are linked by α-(1,2) galactosidase. Stachyose, raffinose, and galactose are non-reducing sugars. Raffinose and stachyose can be hydrolyzed into galactose and sucrose, and the sucrose can be hydrolyzed into glucose and fructose, but glucose and fructose are the reducing sugars. Figure 2 shows the sucrose content during the fermentation, and Figure 3 shows the glucose and fructose contents during fermentation.

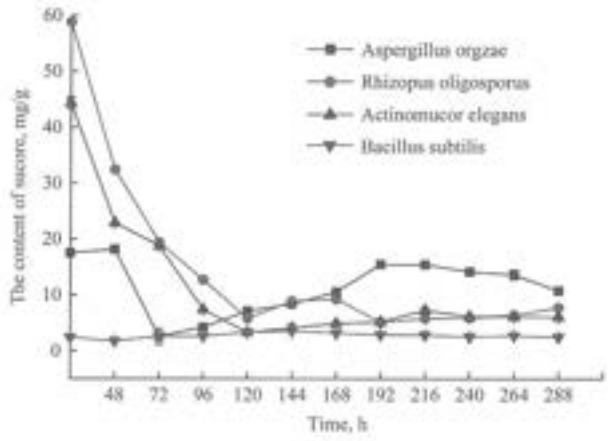

Figure 2 Effects of microorganisms on the sucrose content of douchi during fermentation

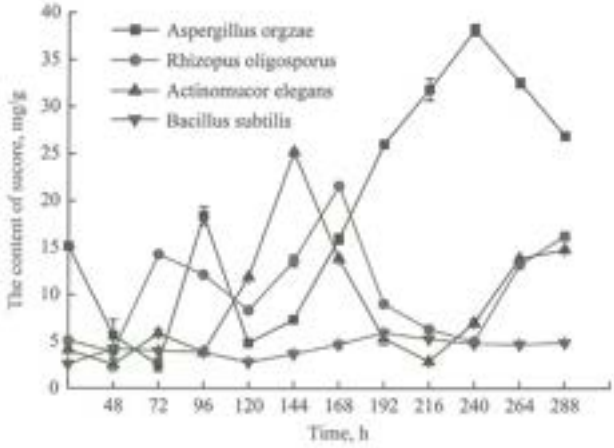

Figure 3 Effects of microorganisms on the glucose and fructose contents of douchi during fermentation

During the pre-fermentation, the sucrose content of douchi fermented by *A. oryzae* increased slightly, while the total fructose and glucose contents decreased significantly. Meanwhile, the sucrose, total fructose, and glucose contents of douchi fermented by *R. oligosporus* or *A. elegans* decreased. In contrast, in douchi fermented by *B. subtilis*, the sucrose content declined slightly, while the total fructose and glucose contents were steady. During the post-fermentation, the sucrose content of douchi fermented by *A. oryzae*, *R. oligosporus*, or *A. elegans* showed a similar trend, which declined rapidly at the beginning, rose slightly later, and then stabilized. In contrast, the sucrose content in douchi fermented by *B. subtilis* increased initially, followed by an additional slight increase and a subsequent stabilization. The total fructose and glucose contents in douchi fermented by *B. subtilis* decreased until 120 h (Figure 3), and this was followed by a relatively low increase and then a subsequent stabilization.

3.4 α-galactosidase activities of douchi during fermentation

α-galactosidase is distributed widely in microorganisms. It hydrolyzes a variety of simple α-D-galactosides and more complex polysaccharides. Figure 4 shows the results of the α-galactosidase production by the four microorganisms.

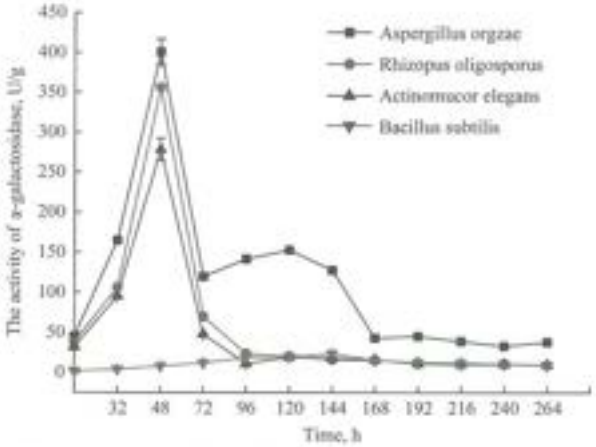

Figure 4 Production of α-galactosidase by *A. orgzae*, *R. oligosporus*, *A. elegans*, and *B. subtilis* in douchi

Aspergillus oryzae was the best strain for α-galactosidase production, as it gave the highest enzyme activity (412.36 U/g). This contrasts with earlier reports, which showed that *R. oligosporus* and *A. elegans* yielded the highest α-galactosidase production. Maximum α-galactosidase activities of 210 and 215 U/g were produced with *R. oligosporus* and *A. elegans* in 48 h(Han et al., 2003). Another study showed that *A. oryzae* is the best fungus for α-galactosidase production in soymilk (Shankar and Verappa, 2010). Ouoba et al. (2004) reported that *B. subtilis* is less effective for α-galactosidase production. During the post- fermentation, the α-galactosidase activity produced by the three molds declined dramatically, and this might be associated with the salt added to medium, as well as the negative effects of increased temperature and an exhaustion of oxygen, which inhibited their growth. These results are in accordance with a previous study, Sun., 2008 demonstrated that molds cannot grow well during post-fermentation, while fungi, yeast, and lactic acid bacteria can. Another study reported that the number of mold colonies decreased from 7.08×10^{10} colony-forming units/g to 4×10^{10} colony-forming units/g during post-fermentation (Hu et al., 2012). Fungi favor a moist

environment for their growth, and the initial moisture content is a critical factor for growth and enzyme production. A lower moisture easily reduces substrate stability and swelling, while higher moisture levels can cause particles to agglomerate, thereby resulting in a gas transfer limitation and competition with bacteria (Gowthaman et al., 2001). During the post-fermentation, enzyme production did not increase, which might be due to increased competition for carbon sources and nutrients. This could lead to nutrient exhaustion, which could result in reduced enzyme production.

3.5 Invertase activities of douchi during fermentation

Invertase can hydrolyze sucrose into D-glucose and D-sucrose because it can aid raffinose and stachyose degradation by hydrolyzing α-1, 2-glucosidic bonds. The results showed that *B. subtilis* was the best strain for invertase production during the pre-fermentation, as it yielded the highest enzymatic activity (30.1 U/g). *Aspergillus oryzae* (2.6 U/g), *R. oligosporus* (1.8 U/g), and *A. elegans* (1.2 U/g) were less effective for enzyme production. During the post-fermentation, the invertase activity of *A. oryzae* increased to 7.48 U/g initially, and then it decreased to 3.66 U/g; however, the invertase activities of the other strains decreased during the fermentation.

During the preparation of enzyme-ripened douchi, it is reasonable to expect that the hydrolytic enzymes that leach from microorganisms may catalyze the hydrolysis of sugar components in the douchi substrate. It was reported that *A. oryzae* produces α-galactosidase in addition to β-glucosidase, protease, amylase, and lipase (Hernaiz and Crout, 2000). α-galactosidase may catalyze the hydrolysis of α-1,6-linked α-galactoside residues. Thus, the catalytic action of α-galactosidase may lead to the reduced stachyose and raffinose contents in douchi during fermentation. During the pre-fermentation, stachyose and raffinose contents declined significantly as the activity of α-galactosidase increased. The sucrose from these oligosaccharides was hydrolyzed into glucose and fructose by invertase, which was due to the high rate of microbial growth at the beginning of the fermentation. However, in the *B. subtilis*-fermented douchi, the α-galactosidase activity was lower than that of the other strains, while the invertase activity was the highest; thus, the fructose and glucose contents increased during the fermentation. During the post-fermentation, the stachyose and raffinose contents of douchi fermented by *A. oryzae*, *R. oligosporus*, or *A. elegans* decreased steadily, and this was associated with environmental changes, such as temperature and pH. In contrast, the α-galactosidase activity in the *B. subtilis*-fermented douchi increased at the beginning of the fermentation and then decreased. These differences occurred because the growth of the molds was inhibited during the fermentation.

4 Conclusions

This study determined the stachyose and raffinose contents in commercial douchi. The stachyose and raffinose contents in the *B. subtilis*-fermented douchi were higher than those of the others. Moreover, the effects of fermentation by *A. oryzae*, *R. oligosporus*, *A. elegans*, or *B. subtilis* on stachyose and raffinose metabolism in douchi were also investigated. The degradation of raffinose and stachyose during the pre-fermentation was higher than that during the post-fermentation, and the highest degradation rate was observed in douchi fermented with *A. oryzae*. Higher α-galactosidase activity during the fermentation was associated with a higher oligosaccharide degradation rate, and *B. subtilis* yielded the high degradation rate during the post-fermentation.

Acknowledgements

This work was supported by the grants from National Science Foundation of China (31571791, 31771964) , the National Key-technologies R&D Project (2016YFD0400402) during the 13th 5-year Plan of the People's Republic of China and the China Agriculture Research System- Green Manure .

[References]

[1] Alazzeh, A. Y., S. A. Ibrahim, D. Song, A. Shahbazi, and A. A. AbuGhazaleh. 2009. Carbohydrate and protein sources influence the induction of α- and β-galactosidases in Lactobacillus reuteri. *Food Chemistry*, 117(4): 654–659.

[2] Chen, J., Y. Q. Cheng, K. Yamaki, and L. T. Li. 2007. Anti-α-glucosidase activity of Chinese traditionally

fermented soybean (douchi). *Food Chemistry*, 103(4): 1091–1096.

[3] Collins, M. D., and G. R. Gibson. 1999. Probiotics, prebiotics, and synbiotics: approaches for modulating the microbial ecology of the gut. *The American Journal of Clinical Nutrition*, 69: 1052s–7s.

[4] Cho, K. M., J. H. Lee, H. D. Yun, B. Y. Ahn, H. Kim, and W. T. Seo. 2011. Changes of phytochemical constituents (isoflavones, flavanols, and phenolic acidsduring cheonggukjang soybeans fermentation using potential probiotics Bacillus subtilis CS90. *Journal of Food Composition and Analysis*, 24(3): 402–410.

[5] Chung, I. M., S. H. Seo, J. K. Ahn, and S. H. Kim. 2011. Effect of processing fermentation, and aging treatment to content and profile of phenolic compounds in soybean seed, soy paste. *Food Chemistry*, 127(3): 960–967

[6] Dajanta, K., A. Apichartsrangkoon, and E. Chukeatirote. 2011. Volatile profiles of thua nao, a Thai fermented soy product. *Food Chemistry*, 125(2): 464–470.

[7] De Looze, D., M. Van Laere, M. De Muynck, R. Beke, and A. Elewaut. 1998. Constipation and other chronic gastrointestinal problems in spinal cord injury patients. *Spinal Cord*, 36(1): 63–66.

[8] Fleming, S. E. 1981. A study of relationships between flatus potential and carbohydrate distribution in legume seeds. *Journal of Food Science*, 46(3): 794–798.

[9] Gowthaman, M. K., C. Krishna, and M. Moo-Young. 2001. Fungal solid state fermentation, -an overview. *Applied Mycology & Biotechnology*, 1: 305–352.

[10] Guillon, F., and M. M. Champ. 2002. Carbohydrate fractions of legumes: uses in human nutrition and potential for health. *British Journal of Nutrition*, 88 Suppl 3 (S3): S293–306.

[11] Han, B. Z., Y. Ma, F. M. Rombouts, and N. Mjr. 2003. Effects of temperature and relative humidity on growth and enzyme production by Actinomucor elegans and Rhizopus oligosporus during sufu pehtze preparation. *Food Chemistry*, 81(1): 27–34.

[12] Hernaiz, M. J., and D. H. Crout. 2000. Immobilization stabilization on Eupergit C of the β-galactosidase from B, circulans and an α-galactosidase from Aspergillus oryzae. *Enzyme and Microbial Technology*, 27(1-2): 26–32.

[13] Hideo, T. 1994. Health effects of oligosaccharides. *Food Technology*, 48(10): 61–65.

[14] Hiroyuki, F., Y. Tomohide, and O. Kazunori. 2001. Efficacy and safety of Touchi extract, an α-glucosidase inhibitor derived from fermented soybeans, in non-insulin-dependent diabetic mellitus. *The Journal of Nutritional Biochemistry*, 12(6): 351–356.

[15] Holscher, H. D., K. L. Faust, L. A. Czerkies, R. Litov, E. E. Ziegler, H. Lessin, T. Hatch, S. M. Sun, and K. A. Tappenden. 2012. Effects of prebiotic-containing infant formula on gastrointestinal tolerance and fecal microbiota in a randomized controlled trial. *Journal of Parenteral and Enteral Nutrition*, 36(1 Suppl): 95S–105S.

[16] Hu, H. P., J. X. Hao, Y. Q. Cheng, L. J. Yin, Y. L. Ma, Y. Z. Wei, and L. T. Li. 2012. Effect of fermented rice culture on the microbiological, biochemical and sensory characteristics of low-salt douchi, a traditional Chinese fermented soybean condiment. *International Journal of Food Science & Technology*, 47(4): 689–695.

[17] Mansilha, H. F. 2011. *Nascer e Crescer - Revista do Hospital de Crianças Maria Pia*, 20(1): 35–37.

[18] Marcotte, S. M. Tosh, E. R. Farnworth, and A. J. Wright. 2010. Effect of pulse consumption on perceived flatulence and gastrointestinal function in healthy males. *Food Research International*, 43(2): 553–559.

[19] Mccue, P., Y. I. Kwon, and K. Shetty. 2005. Anti-diabetic and antihypertensive potential of sprouted and solid-state bioprocessed soybean. *Asia Pacific Journal of Clinical Nutrition*, 14(2): 145–152.

[20] Mital, B., and K. Steinkraus. 1975. Utilization of oligosaccharides by lactic acid bacteria during fermentation of soy milk. *Journal of Food Science*, 40(1): 114–118.

[21] Murphy, E. L., H. Horsley, and H. K. Burr. 1972. Fractionation of dry bean extracts which increase carbon dioxide egestion in human flatus. *Journal of Agricultural & Food Chemistry*, 20(4): 813–817.

[22] Nakajima, N., N. Nozaki, K. Ishihara, A. Ishikawa, and H. Tsuji. 2005. Analysis of isoflavone content in tempeh, a fermented soybean, and preparation of a new isoflavone-enriched tempeh. *Journal of Bioscience and Bioengineering*, 100(6): 685–687.

[23] Ouoba, L. I. I., B. Diawara, W. K. Amoa-Awua, A. S.Traoré, and P. L. Møller. 2004. Genotyping of starter cultures of Bacillus subtilis and Bacillus pumilus for fermentation of African locust bean (Parkia biglobosa) to produce Soumbala. *International Journal of Food Microbiology*, 90(2): 197–205.

[24] Prashanth, S. J., and V. H. Mulimani. 2005. Soymilk oligosaccharide hydrolysis by Aspergillus oryzae α-galactosidase immobilized in calcium alginate. *Process Biochemistry*, 40(3-4): 1199–1205.

[25] Reddy, N. R., D. K. Salunkhe, and R. P. Sharma. 1980. Flatulence in rats following ingestion of cooked and germinated black gram and a fermented product of black gram and rice blend. *Journal of Food Science*, 45(5): 1161–1164.

[26] Rolfe, R. D. 2000. The role of probiotic cultures in control of gastrointestinal health. *The Journal of Nutrition*, 130: 396s–402s.

[27] Shankar, K., and H. M. Verappa. 2010. Production of

α-Galactosidase by Aspergillus oryzae through solid-state fermentation and its application in soymilk Galactooligosaccharide hydrolysis. *Brazilian Archives of Biology and Technology,* 1(53): 211–218.

[28] Sims, I. M., J. L. Ryan, and S. H. Kim. 2014. In vitro fermentation of prebiotic oligosaccharides by Bifidobacterium lactis HN019 and Lactobacillus spp. *Anaerobe,* 25(1): 11–17.

[29] Song, Y. S., J. Frias, C. Martinezvillaluenga, C. Vidalvaldeverde, and D. M. Egonzalez. 2008. Immunoreactivity reduction of soybean meal by fermentation, effect on amino acid composition and antigenicity of commercial soy products. *Food Chemistry,* 108(2): 571–581.

[30] Stone, J. M., M. Nino-Murcia, V. A. Wolfe, and I. Perkash. 1990. Chronic gastrointestinal problems in spinal cord injury patients: a prospective analysis. *The American Journal of Gastroenterology,* 85(9): 1114–1119.

[31] Sun, S. 2008. The changing of microorganisms in douchi during post-fermentation. *China Food Additives*, 2008(2): 139–143.

[32] Tsai, Y. H., H. F. Kung, S. C. Chang, T. M. Lee, and C. I. Wei. 2007. Histamine formation by histamine-forming bacteria in douchi, a Chinese traditional fermented soybean product. *Food Chemistry,* 103(4): 1305–1311.

[33] Veenstra, J. M., A. M. Duncan, C. N. Cryne, B. R. Deschambault, J. I. Boye, M. Benali, M.

[34] Yanase, H., H. Fukushi, N. Ueda, Y. Maeda, A. Toyoda, and K. Tonomura. 1991. Cloning, sequencing and characterization of the intracellular invertase gene from zymomonas-mobilis. *Agricultural and Biological Chemistry,* 55(5): 1383–1390.

[35] Zhang, J. H., E. Tatsumi, C. H. Ding, and L. T. Li. 2006. Angiotensin I-converting enzyme inhibitory peptides in douchi, a Chinese traditional fermented soybean product. *Food Chemistry,* 98(3): 551–557.

[36] Zhang, J. H., E. Tatsumi, J. F. Fan, and L. T. Li. 2007. Chemical components of Aspergillus-type Douchi, a Chinese traditional fermented soybean product, change during the fermentation process. *International Journal of Food Science & Technology,* 42(3): 263–268.

[37] Ziemer, C. J., and G. R. Gibson. 1998. An overview of probiotics, prebiotics and synbiotics in the functional food concept: perspectives and future strategies. *International Dairy Journal,* 8(5): 473–479.

Counting method of wheat stripe rust spores based on shape factor and improved Harris corner detection

Jiao Lin[1,2], Niu Leilei[1,2], Lei Yu[1,2], He Dongjian[1,2], Yang Shuqin[1,2], Song Huaibo[1,2*]

(1. *College of Mechanical and Electronic Engineering, Northwest A&F University, Yangling, Shaanxi 712100, China*;
2. *Key Laboratory of Agricultural Internet of Things, Ministry of Agriculture, Yangling, Shaanxi 712100, China*)

Abstract: Wheat stripe rust is one of the most serious diseases which affect the yield and quality of wheat in China. It is an important guarantee to predict wheat stripe rust accurately for the quality and high yield of wheat. This can be realized by automatically monitoring the number of stripe rust spores in the air and analyzing the stripe rust combined with other data. Due to the problem of time consumption and low accuracy of traditional microscopic observation and molecular biological counting methods, an automatic counting method for adhesive spores was proposed. Firstly, the K-means clustering algorithm was applied to extract target object from complex background in the spore image, and mathematical morphology algorithm was carried out. Secondly, the geometric shape factor was applied to estimate whether the spores were adhered or not. The optimal geometric factor threshold was chosen and adhesive spores were tested by using an improved Harris algorithm to get much robust and accurate detection of corners. Finally, 30 wheat stripe rust images were randomly selected to verify the feasibility of the method, and compared with the average area method. The experimental results demonstrated that the average accuracy rate based on the improved Harris corner detection method was 91%, which was 26% higher than that of the average area method. The results showed that the improved Harris corner point detection algorithm could achieve a higher accuracy for the counting of wheat stripe rust spores.

Keywords: wheat stripe rust, adhesive spores, K-means, shape factor, Harris corner detection

Citation: Lin, J., L. L. Niu, Y. Lei, D. J. He, S. Q. Yang, and H. B. Song. 2017. Counting method of wheat stripe rust spores based on shape factor and improved Harris corner detection. International Agricultural Engineering Journal, 26(3): 193–199.

1 Introduction

Grain problem is one of the primary issues puzzling the global development. Wheat stripe rust is widespread and serious in China, which seriously restricts the overall economic and social benefits of Chinese grain industry (Li et al., 2002; Shang, 2008). It is important to prevent the occurrence of the disease and ensure wheat yield (Luo et al., 2008). And the number of wheat stripe rust spores in air is vital parameter to monitor whether wheat stripe rust happened or not. The prediction of wheat strip rust disease has a wide range of practical applications and has received increased attention.

Presently, the counts of the stripe rust spores are mostly carried out using microscopic observation or molecular biology counting (eg, Real-time Polymerase Chain Reaction PCR) in laboratory. The amount of slant spores of cephalosporium acremonium was measured through photoelectric turbidimetry by Zhang Ping (2002). The number of exact spores of slant was measured by plate colony-counting, and then the suspension was prepared into different concentrations of diluents. Finally, the absorbance values which were measured by spectrophotometer were substituted into the regression equation to calculate the number of unknown slant spores. The accuracy of microscope counting method is low and the cost of biological methods is high, and the turbidimetric operation is also complex. Besides, the three methods are time-consumption and laborious, so it is difficult to achieve real-time processing. Applying image processing technology to recognize and count wheat stripe rust spores can overcome the

Received date: 2017-05-15 **Accepted date:** 2017-08-17

* **Corresponding author: Song Huaibo,** College of Mechanical and Electronic Engineering, Northwest A&F University. Email: songyangfeifei@163.com.

above-mentioned shortcomings and realize an automatic counting.

So far, there are little relevant studies and reports on spores recognition and counting by applying microscopic image processing technology, especially in the field of segmentation of adhesion targets. Lin et al. (2003) proposed an approach by applying computer image recognition technology to the automatic counting of poplar disease spores, and the recognition rate reached 98%, but the adherent spores were not considered. Huang et al. (2003) and Hu (2011) introduced morphological characteristics to the study of the identification of silkworm microbial disease, and the recognition rate was about 88%. Jin (2008) obtained the total number of bacteria in food by micro-image technology and BP-neural network technology, and the rapid detection system of total bacteria in food was established, but the method was time-consumption. Lee et al. (2013) realized the automatic counting and labeling of wheat stripe summer spores by taking K-means clustering and watershed segmentation algorithms into the images which were obtained from microscopic photographic techniques. However, the counting of multiple adhesive spores was ignored. Hu et al. (2015) presented the approaches and processing which can deal with the area counting of bunt smut winter spores of imported wheat, but the count would be severely reduced for multiple spore adhesion problems. Qi et al. (2015) proposed a method of automatic detection and counting of P.oryzae spores by applying improved watershed algorithm based on distance transformation and Gaussian filtering. However, the identification rate of adherent spores was only 75%.

In this study, after processing spore images through K-means clustering and morphological algorithm, the geometric shape factor was applied in estimating whether the spores were adhered or not. Then, the quantities of adherent spores were reached by measuring angular points by applying the improved Harris corners detection. Finally, the spores were identified and counted automatically.

2 Materials and equipment

In this study, the wheat stripe rust spores were grown in the laboratory of the College of Plant Protection, Northwest A&F University and mixed with the clear mineral oil at a volume of 1:10, and then the mixture was dropped onto the slides. Olympus biological electron microscope (BX63, UCMOS 14000 KPA Pro series true color high resolution with intelligent CCD microscope digital camera) was applied to capture spore images which were saved as 4096×3288 pixel size, JPEG format. The image acquisition device is shown in Figure 1.

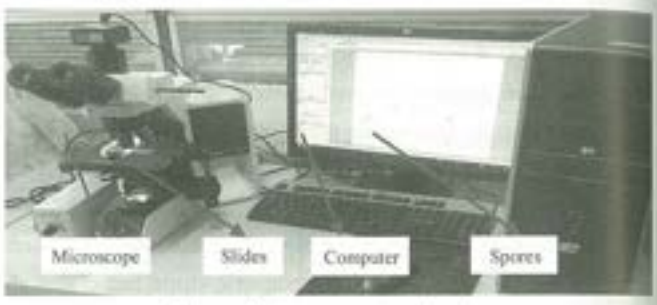

Figure 1 Image capture device

The image processing device is a desktop computer, which is configured as: CPU: Pentium (R) Dual-Core E5400 2.70 GHz; RAM: 3 G. All algorithmic programs run on MATLAB 2014a software.

3 Segmentation and counting of spores

3.1 Segmentation of spore images based on K-means algorithm

$L^*a^*b^*$ color space is based on XYZ color space, and it is considered as an intermediate mode which can convert RGB color space to $L^*a^*b^*$color space. RGB color space to XYZ color space conversion is presented in Equation (1), and the XYZ color space to $L^*a^*b^*$ color space conversion is shown in Equation (2).

$$\begin{cases} X = 0.49 \times R + 0.31 \times G + 0.2 \times B \\ Y = 0.177 \times R + 0.812 \times G + 0.011 \times B \\ Z = 0.01 \times G + 0.99 \times B \end{cases} \quad (1)$$

$$\begin{cases} L^* = 116 \times f(Y) - 16 \\ a^* = 500 \times [f(\frac{X}{0.982}) - f(Y)] \\ b^* = 200 \times [f(Y) - f(\frac{Z}{1.183})] \end{cases} \quad (2)$$

In Equation (2), $f(t)$ is a function which can be described as follow.

$$f(t) = \begin{cases} t^{1/3} & t > 0.008856 \\ 7.787 \times t + 0.138 & t \le 0.008856 \end{cases}$$

where, L^* is the brightness, a^* ranges from red to green, b^* ranges from blue to yellow. The values of a^* is $-128a$~$+127$a. $+127a$ represents red, $-128a$ represents green. The value of b^* is $-128b$~$+127b$. $+127b$ represents yellow, and $-128b$ represents blue. All colors are composed of these three interactive changed values.

K-means clustering algorithm is an indirect clustering algorithm based on the similarity measurement between samples, which belongs to the unsupervised learning algorithm, and its characteristics are fast processing speed, more intuitive and easy to implement. The algorithm improves the similarity between the same objects by applying iteration, and decreases gradually between the heterogeneous objects (Wang et al, 2009; Li et al, 2012; Rekik et al, 2007; Yusoff et al, 2013). The target is clustered into the k categories hypothetically, and the steps of K-means clustering algorithm are as follows:

Step 1: Select k categories initial clustering centers respectively: $\boldsymbol{Z}_1(1)$, $\boldsymbol{Z}_2(1)$,..., $\boldsymbol{Z}_k(1)$, where k is the number of categories of clusters;

Step 2: Apply the following method to classify samples $\{\mathbf{Z}\}$ in the N^{th} iteration: for i,j=1,2,...,k, $i\neq j$, if the relationship of inequality $\|\mathbf{Z}-\mathbf{Z}_j(n)\|<\|\mathbf{Z}-\mathbf{Z}_i(n)\|$ is satisfied, the expression $\mathbf{Z}\in S_j(n)$ is right;

Step 3: Define the samples obtained from Step 2 as new clustering centers $\mathbf{Z}_j(n+1)$ which makes the values of $\sum_{j=1}^{k}\sum_{Z\in S_j(n)}\left\|Z-Z_j(n+1)\right\|^2$ minimum.

Step 4: For any j=1, 2,..., k, if the relationship $Z_j(n+1)=\mathbf{Z}_j(n)$ is met, the iterative process is completed; Otherwise, $n=n+1$, and jump to Step (2) and continue.

In this study, the original images were compressed to the size of 1024×822 pixels to improve the speed of the algorithm, and converted from *RGB* color space to $L^*a^*b^*$ color space. The image could be divided into spores and background (only need to extract the spore target areas, clustering number k=2) by applying the K-means algorithm, and then the spore targets would be separated from the image.

The image was processed by using K-means algorithm, and the results were shown in Figure 2. Figure 2a was an original image where there were adhesive spores with many complex impurities. Figure 2b was the background sub-image, and Figure 2c was the spore sub-image. It could be seen from these images that the active spores had been separated from the background and impurities, and the spores were well extracted.

a. Original image b. Background sub-image c. Spore sub-image

Figure 2 Results of K-means clustering

3.2 Pre-processing of spores' images

The image segmentation using threshold (value was 0) was implemented in Figure 2c, and the result was shown in Figure 3a where existed holes and noise spots. In order to deal with the above problems, the open operation using 'disk' structure elements with a radius of 3 pixels was carried out to remove noise and got more smooth contour lines in Figure 3a, and then area filling was carried out to remove holes, as was shown in Figure 3b. It could be found that the holes and noises had been removed.

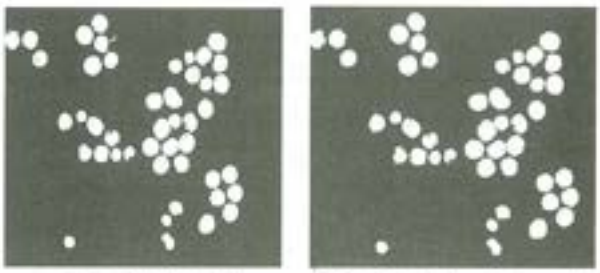

a. Segmentation result b. Morphological processing result

Figure 3 Results of pre-processing

3.3 Detection of adhesive spores based on shape factor

The shape factor is a characteristic description of target, and it can be extracted effectively according to the calculation and statistics of a certain type of specific shape factor. There are single and adhesive spores in preliminary processing spore images, which could be distinguished by using shape factors. The principle—the boundary profile of the adhesive spores is more complex than single spore's—can be applied to judge the types of spores. The shape factor (*SF*) can be reached through the operation of essential attributes of original shape. The *SF* is defined as follow:

$$SF=4\pi S/C^2 \quad (3)$$

where, S is the pixel values of connected domain area; C is the pixel values of connected domain perimeters (Li et al, 2015).

As is shown in Equation (3), SF ranges from 0 to 1. The highest value of the shape factor is one if the target to be detected is a standard circle. Graph boundary would become complex because of many adhesive spores. And the value of SF will be reduced accordingly, thus it can be applied in differentiating adhesive spores. As were shown in Figure 3, Figure 3a was a single spore, and its shape factor was 0.8469; Figure 3b was adhesive spores, and its shape factor was 0.5526. It could be concluded that SF can be applied to distinguish single and the adhesive spores preferably.

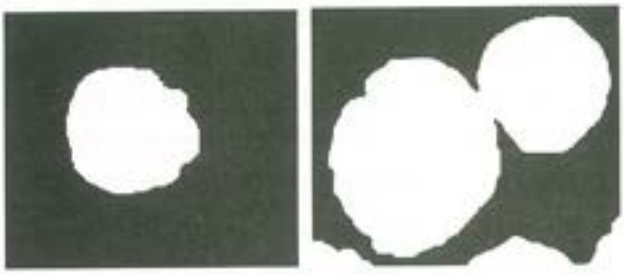

a. Single spore b. Adhesive spores

Figure 3 Geometric shape factor

Finally, the threshold SF_0 and maximum area S_{max} were obtained through comparing the results of experiments, and they could be the basis to determine whether there were adhesive spores or not. That is to say that this area is considered as an adhesive region if the regional data satisfy the inequalities of $SF_i<SF_0$, $S_i>S_{max}$. The parameters SF_0=0.7 and S_{max}=6600 were selected by the comparison of many tests.

3.4 Corner detection of spores based on improved Harris algorithm

Corner point refers to the point of abrupt change on the edge of image, and can also be regarded as the point of intersection of two-side boundary. It contains feature points of two main directions in the neighborhood. And the corner points have characteristic with rotation invariance and scale invariance (Liu et al, 2013; Panchal et al, 2016).

Suppose $I(x,y)$ is the spores image to be detected, and a whole process of the Harris corner detection algorithm is as follows:

Step1: Calculate the gradient I_x and I_y of $I(x, y)$ at the x and y directions respectively, as are shown in Equation (4).

$$I_x=\frac{\partial I}{\partial x}=I\otimes\begin{bmatrix}-1 & 0 & 1\end{bmatrix},\ I_y=\frac{\partial I}{\partial y}=I\otimes\begin{bmatrix}-1 & 0 & 1\end{bmatrix}^{\mathrm{T}} \quad (4)$$

Step2: Calculate the product of all gradients, as is shown in Equation (5).

$$I_x^2=I_x\cdot I_x;\ I_y^2=I_y\cdot I_y;\ I_{xy}=I_x\cdot I_y \quad (5)$$

Step3: All product terms in the above Equation (5) are carried out Gauss weighting with Gaussian function w, and then generate matrix **M** which contains the elements of A, B, and C; as are shown in Equation (6):

$$\begin{cases}A=g\left(I_x^2\right)=I_x^2\otimes\omega;\\ B=g\left(I_y^2\right)=I_y^2\otimes\omega;\\ C=g\left(I_{xy}\right)=I_{xy}\otimes\omega;\\ M=\begin{bmatrix}A & C\\ C & B\end{bmatrix}\end{cases} \quad (6)$$

Step4: Count the Harris response values of all pixels, and limit the threshold;

$$R=\{R:\det M-\alpha(traceM)^2<t\} \quad (7)$$

in Equation (7), t is the threshold value, and R is the response value. If R is less than the threshold t, R will be set to zero.

Step5: Reach the maximum value of the 5*5 neighborhood by non-maximal suppression method, and the maximum is the corner point of the image.

Due to the strong detection sensitivity, the effect of Harris corner detection algorithm in actual operation is not ideal, and excessive false corners are always detected, as is shown in Figure 4a. The number of corners which are detected will be less with the decrease of sensitivity.

In order to obtain robust corner detection results, the Harris corner algorithm is improved. Suppose that eigenvalues of a got matrix **M** satisfy the inequations $\lambda_1\geq\lambda_2\geq0$, the relationship between trace and determinant of matrix **M** is as follows:

$$\begin{cases}\det M=\prod_i\lambda_i\\ traceM=\sum_i\lambda_i\end{cases} \quad (8)$$

When the relationship of $\lambda_1=\lambda$; $\lambda_2=k\lambda(0\leq k\leq1)$ are satisfied, there is the Equation (9).

$$R=\lambda_1\lambda_2-\alpha(\lambda_1+\lambda_2)^2=\lambda^2(k-\alpha(1+k)^2) \quad (9)$$

When the value of R is not less than 0, there will be the inequations $0 \le \alpha \le \frac{k}{(1+k)^2} \le 0.25$. Suppose the value of k is smaller, the relation $R \approx \lambda^2(k-\alpha), \alpha < k$ can be obtained.

It can be concluded that with the increases of α value, the response value detected could be reduced, and the sensitivity of corner detection would be cut down, the number of corner points also would be lowered accordingly, thus the robustness of corner detection was improved. Parameter value α=0.23 was chosen after many tests in this study.

The result by using improved Harris corner detection method was shown in Figure 4b. It can be seen that the false corners points other than the adhesive points had been well suppressed by setting the sensitivity parameter to suppress non-maximum of the corner points, so that the number of detection would conform to the actual number of corner points. The number of spores could be the final count because there is a direct quantitative relationship between the number of corner points obtained and the number of spores. Therefore, this method can be applied to spore counting.

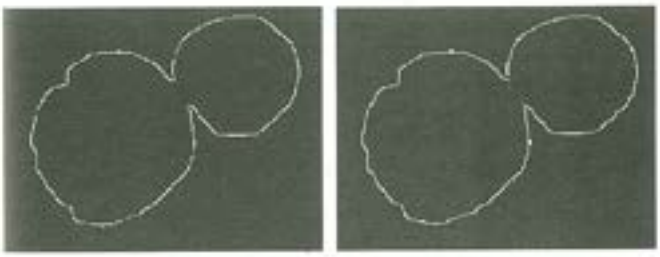

a. Detected corner points b. Detected corner points

Figure 4 Corner points detection

4 Results and analysis

4.1 Results

There were some spore images which were tested, as were shown as follows.

a. Detected image b. Detected image c. Detected image

Figure 5 Original spore images

Thirty images which contain 622 wheat stripe rust spores were tested by using the above algorithm. The test results of 20 images which basically include no more than three adhesive spores were shown in Table 1, and the test results of 10 images which include more than three adhesive spores were shown in Table 2. The average area method was regarded as the comparison algorithm, and the parameter—average area was calculated and chosen by contrast. In addition, the different magnification of the microscopic image has different parameters. For 200 times spore micrograph, the parameter 400 pixels was selected, and for 400 times image, the parameter was 800 pixels. The counting results were shown as Table 1 and Table 2.

Table 1 Test results of spore count of wheat stripe rust (Three and below spores adhesion)

No.	Spores number	Mean area		Improved Harris angular points detection	
		Test number	Accuracy, %	Test number	Accuracy, %
1	6	3	50	6	100
2	38	33	92	38	100
3	52	48	92	51	98
4	21	16	76	22	95
5	7	5	71	8	98
6	10	6	60	9	88
7	5	4	80	5	100
8	9	8	88	9	100
9	20	33	35	19	95
10	16	23	69	16	100
11	20	13	65	18	89
12	12	19	41	12	100
13	12	21	25	13	92
14	13	21	38	12	92
15	22	17	77	20	90
16	43	39	91	45	95
17	18	13	72	18	100
18	23	17	73	23	100
19	21	18	85	21	100
20	53	64	79	52	98
Statistics	421	—	68	—	97

As was shown in Table 1, for no more than three adhesive spores, the counting accuracy which applied to improved algorithm was between 89% and 100%, and the average accuracy rate was 97%, which had been increased by 29% than the average area method. It could be found in Table 2 for more than three adhesive spores that the counting accuracy of the improved algorithm was between 38% and 96%, and an average accuracy rate was

78% which had been raised 21% than the average area method. In general, according to the statistical data of Table 1 and Table 2, the average accuracy rate of the improved Harris corner detection for wheat stripe rust spores was 91% which increased 26% than the average area method. Consequently, it proved that the test method based on improved Harris algorithm could be applied to the counting of the spores of wheat stripe rust exactly.

Table 2 Test results of spore count of wheat stripe rust (More than three spores adhesion)

No.	Spores number	Mean area		Improved Harris angular points detection	
		Test number	Accuracy,%	Test number	Accuracy,%
1	14	28	50	18	72
2	22	29	68	33	50
3	15	24	40	16	93
4	15	22	53	17	87
5	25	32	68	20	80
6	28	35	75	31	90
7	26	26	100	42	40
8	26	45	26	27	96
9	13	20	46	14	92
10	17	27	41	14	82
Statistics	201	—	57	—	78

4.2 Analysis

(1) It can be seen from the above data that the improved algorithm can perform well, and satisfy the requirements by agricultural applications.

(2) The *SF* was effective to describe a single spore and adherent spores.

(3) The improved Harris algorithm was applied to detect corner points of adhesive spores, and the accuracy rate was lower, as were shown in Figure 6. The numbers of detected corner points were more than the actual, because the edge of the image was not smooth enough and the result was influenced by impurities.

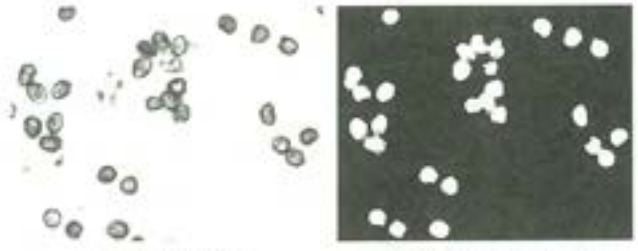

a. Original image b. Results of corner detection

Figure 6 Improved Harris corner detection

5 Conclusions

In order to realize rapid and automatic counting of spores, the counting algorithm based on image K-means clustering algorithm and improved Harris corner detection method was proposed. Using the above methods, the following conclusions could be conducted:

(1) The proposed method could achieve accurate count of wheat stripe rust spores. And the average accuracy of the proposed algorithm was 91%, which was increase by 26% than average area method. Thus, the algorithm is feasible for the counting of wheat stripe rust spores.

(2) The shape factor was used to distinguish adhesive spores, and the results indicated that the shape factor could be applied to judge adhesive spores effectively.

(3) The proposed method can not only be applied in wheat stripe rust spores, but also in the segmentation of adhesive targets, as fruits, cells and particles.

(4) Given that it was limited by the condition of the equipment, like impurities on the spores or slide glass, it was still difficult to achieve high accuracy detection of adhesive spores. In addition, how to improve the accuracy of counting for more than three spores adhesions will still need further study in future.

[References]

[1] Gao, H. S. 2008. Wheat stripe rust and its control. Beijing: Jindun Publishing House.

[2] Hu, X. A., J. Z. Deng, Z. B. Yuan, J. Jin, and W. S. Lin. 2015. Acquisition and processing of the wheat micro-image of winter spores. *Guangdong Agricultural Sciences*, 2015(12): 163–167. (In Chinese with English abstract)

[3] Hu, X. Y. 2011. Research on image recognition method of silkworm microparticles based on machine vision. Ph.D. thesis: Wuhan University of Technology, Wuhan.

[4] Huang, H. H., and J. R. Cai. 2003. Improvement of computer vision technology in detecting pebrine in silkworm. *Journal of Jiangsu University (Natural Science Edition)*, 24(02): 43–46. (In Chinese with English abstract)

[5] Jin, S. L., Y. J. Li, and Y. G. Yin. 2008. Rapid detection of total number of bacteria in food using digital micro-image identification technique. *Transactions of the Chinese Society of Agricultural Engineering*, 24(04): 177–180. (In Chinese with English abstract)

[6] Li, L., T. S. Hong, X. Y. Zeng, and J. B. Zheng. 2012. Citrus red mite image target identification based on K-means clustering. *Transactions of the Chinese Society for Agricultural Machinery*, 28(23): 147–153. (In Chinese with

English abstract)

[7] Li, W. Y., M. Li, J. P. Qian, C. H. Sun, S. F. Du, and M. X. Chen. 2015. Segmentation method for touching pest images based on shape factor and separation points location. *Transactions of the Chinese Society for Agricultural Machinery*, 31(05): 175–180. (In Chinese with English abstract)

[8] Li, X. L., Z. H. Ma, Z. Y. Sun, and H. G. Wang. 2013. Automatic counting of summer spores simulated capture of wheat stripe rust based on image processing. *Transactions of the Chinese Society of Agricultural Engineering*, 29(02): 199–206. (In Chinese with English abstract)

[9] Li, Z. Q., and S. M. Zeng. 2002. Wheat rust in China. Beijing: China Agricultural Press.

[10] Lin, X. Y., W. Y. Liu, X. D. Chen, and M. Y. Cao. 2003. Spore image reorganization of polar disease. *Chinese Journal of Scientific Instrument*, 24(4S2): 364–366. (In Chinese with English abstract)

[11] Liu, B. C., J. Zhao, and Q. Sun. 2013. Improved Harris corner detection method based on edge. *Chinese Journal of Liquid Crystals & Displays*, 28(6): 939–942. (In Chinese with English abstract)

[12] Luo, J. H., W. J. Huang, and C. L. Wei. 2008. Establishment of pre-warning system for crop diseases and insect pests. *Transactions of the Chinese Society of Agricultural Engineering*, 24(12): 127–131. (In Chinese with English abstract)

[13] Panchal, T., H. Patel, and A. Panchal. 2016. License plate detection using Harris Corner and character segmentation by integrated approach from an image. *Procedia Computer Science*, 79: 419–425.

[14] Qi, L., Y. Jiang, Z. H. Li, X. Ma, Z. X. Zheng, and W. J. Wang. 2015. Automatic detection and counting method for spores of rice blast based on micro-image processing. *Transactions of the Chinese Society of Agricultural Engineering* (In Chinese with English abstract), 31(12): 186–193.

[15] Rekik, A., M. Zribi, and M. Benjelloun. 2007. A K-means clustering algorithm initialization for unsupervised statistical satellite image segmentation. *IEEE International Conference on E-Learning in Industrial Electronics*, 2007: 11–16.

[16] Wang, S. Z., D. J. He, and W. Li. 2009. Plant leaf disease recognition based on kernel K-means clustering algorithm. *Transactions of the Chinese Society for Agricultural Machinery*, 40(3): 152–155. (In Chinese with English abstract)

[17] Yusoff, I. A., N. A. Mat Isa, and K. Hasikin. 2013. Automated two-dimensional K-means clustering algorithm for unsupervised image segmentation. United Kingdom: Pergamon Press.

[18] Zhang, P. 2002. Count of the number of spores of cephalosporium acremonium by photoelectric turbidimetric method. *Journals of China Pharmaceutical*, 11(11): 33. (In Chinese with English abstract)

Preparation of antihypertensive peptides from broad bean by compound enzymatic hydrolysis

Tang Jie, Tian Yang, Chen Cunkun, Tao Sha, Meng Yue, Xue Wentong*

(College of Food Science and Nutritional Engineering, China Agricultural University, Beijing 100083, China)

Abstract: Antihypertensive peptides prepared from broad bean by compound enzymatic hydrolysis were studied, assessing the impact of amino acid composition on potential antihypertensive activity. Broad bean protein concentrate (BPC) was prepared using ultrasonic assisting with alkali-solution and acid-isolation extraction method. And its amino acid composition and hydrophobic value were determined. It was proved that broad bean protein was a good source for antihypertensive peptides preparation as it had high proportion of hydrophobic amino acids, aromatic amino acids and proline, which were related to antihypertensive activity. Four enzymes of Protamex, Flavourzyme, Alcalase and Neutrase were studied to hydrolyze BPC. And the condition of compound enzymes Neutrase and Protamex under pH-spontaneous was selected as the optimum hydrolysis condition. The final degree of hydrolysis (DH) was 26.53%. All sample solution was diluted to 10 mg mL^{-1} when determined the angiotensin-converting enzyme (ACE) inhibition. And the ACE-inhibition of hydrolyzate was 54.31%. After fractionation by Sephadex G-15, 3 fractions were collected. Fraction P3 showed the strongest ACE inhibitory activity, which was 65.93%. P3 was further fractionated by semi-preparative RP-HPLC and 14 fractions were collected. Fraction F9 showed the strongest ACE inhibitory activity, which was 81.17%. Amino acid sequences of fraction F9 in RP-HPLC were analyzed by using LC-MS/MS. Five potential antihypertensive peptides were identified, they are DSTLIMQLLR, SAEYVRLY, LDWYKGPT, IYAPHWN, EGSLLLPHYNSR respectively. This study obtained broad bean hydrolysates with potential ACE-inhibitory activities, which can be used to obtain new added value functional ingredients from broad bean meal.

Keywords: antihypertensive peptides, broad bean, compound enzymatic hydrolysis, RP-HPLC, Sephadex G-15

Citation: Tang, J., Y. Tian, C. K. Chen, S. Tao, Y. Meng, and W. T. Xue. 2017. Preparation of antihypertensive peptides from broad bean by compound enzymatic hydrolysis. International Agricultural Engineering Journal, 26(3): 200–212.

1 Introduction

Broad bean (*Vicia Faba L.*) is widely planted in more than 40 countries in the world. It is the world's sixth largest bean crop (McCurdy and Knipfel 1990). China is the world's largest broad bean production country, which produces around 40% of the world's supply of broad beans. Broad bean is a kind of legume foods with high content of protein and starch, low content of fattiness. Since its first use encompasses starch extraction, the remaining bulk product, rich in protein and fibre, is usually applied in animal feeding and only a small portion is further processed into various types of broad bean protein products for human consumption, e.g. broad bean protein concentrate. The BPC has many good characters, such as high nutritional value, suitable amino acid constitution and good equilibrium of the essential amino acid (Tan *et al.* 2010). As a low added value co-product, it needs to be upgraded by protein extraction or hydrolysis. Hydrolysis may generate functional ingredients with high added value, since the resulting hydrolysate frequently exhibit bioactive properties such as antioxidant or antihypertensive properties (Pena-Ramos and Xiong 2002).

Hypertension is one of the most serious chronic diseases threatening human health (Sun and Zhang 2005). Present prevention and control measure of hypertension is taking chemical-based medicines, such as captopril, enalapril and lisinopril. Clinical results showed these medicines had good effect of lowering blood pressure,

Received date: 2017-06-26 **Accepted date:** 2017-08-23

* **Corresponding author: Xue Wentong,** Professor, College of Food Science and Nutritional Engineering, China Agricultural University, Beijing 100083, China. Email: xwt@cau.edu.cn.

but frequently caused side effects like coughing and ngioneurotic ed (Koklu *et al.* 2005, Guazzi and Arena 2010). Human body blood pressure is mainly regulated by Renin-Angiotensin System (RAS) and Kallikrein-Kinin System (KKS). ACE is the rate-limiting enzyme for this system (Nakagomi *et al.* 2000). ACE-inhibitory peptides prepared from food resources have drawn researchers' attention for their high antihypertensive activity, non-toxic side effects and high absorption. These peptides have strong targeting function so that they have obvious hypotensive effect on hypertensive patients, and have no deteriorated effect on hypotension (Yin *et al.* 2008, Wang *et al.* 2012).

In the current study of antihypertensive peptides prepared from legume resources, the preparation and antihypertensive activity of soy peptides are most extensively investigated. Peptides prepared from peas, green beans, black beans also have been researched generally. Native antihypertensive peptides from five soybean-based infant formulas were separated by ultra-filtration. The highest ACE-inhibitory activity in fractions was observed from 3 to 5 kDa and below 3 kDa (Puchalska *et al.* 2014). Soybean peptide fractions isolated from Korean fermented soybean paste were extracted and separated, peptide His-His-Leu (HHL) proved to have antihypertensive activity in vivo (Shin *et al.* 2001). The ACE-inhibitory activity of the extracts of bean and viscous material from the fermented black soybeans varied with extraction solvents and starter organism. But it increased as the fermentation period was extended (Juan *et al.* 2010). Pea protein isolate was hydrolyzed with alcalase, separated with cationic solid-phase extraction (SPE) and RP-HPLC. Major peptides identified as IR, KF, and EF proved to have higher potency against ACE than against renin (Li and Aluko 2010). However, very few studies have investigated broad bean proteins for the presence of ACE-inhibitory peptides as well as for the isolation and structural characterization of the most active peptides.

In the preparation of biological active peptides, protein should be hydrolyzed by chemicals, enzymes or fermentation. Chemical hydrolysis includes acid hydrolysis and alkaline hydrolysis. Amino acids are easily destroyed by chemicals and the environment is also polluted by waste liquid (Fife *et al.* 2002). Enzymatic hydrolysis is most widely used at present. Proteases prepared from microbial, plant or animal have been used in preparation of antihypertensive peptides. Compared with microbial protease, plant and animal protease are less origin and expensive. So, microbial protease is widely used in actual production. In this paper, we chose four kinds of microbial proteases which had good enzymolysis activeness. And compound enzymatic hydrolysis under pH-controlled condition and pH-spontaneous condition was studied in the hydrolysis of BPC. The hydrolyzates were separated to obtain the highest ACE-inhibitory activity fraction using the chromatographic methods including gel filtration and reversed phase high-performance liquid chromatography, and the sequences of peptides were assayed by LC-MS/MS.

2 Materials and methods

2.1 Materials

The broad bean variety Chenghudabai was obtained from Sichuan Academy of Agricultural Sciences (Sichuan, China). The commercial enzymes Protamex, Flavourzyme, Alcalase, Neutrase were purchased from sigma-Aldrich (Steinheim, Germany).

2.2 Preparation of BPC

Broad bean was defatted after peeling and milling. BPC was prepared from defatted broad bean powder. Proteins were dissolved in water in the ratio of powder to water of 1:12 by alkalization to pH 12 with 2.5 N NaOH(Wolf 1970). After extraction under ultrasonic condition for 30 min, the extract was clarified by centrifugation at 5000 r min^{-1} for 15 min, and then, protein was precipitated by acidification to pH 4.2 with 2 N HCl and the insoluble fraction was collected by centrifugation at 5000 r min^{-1} for 20 min. The precipitate was freeze dried and stored at 4℃ for further utilization. BPC was done in duplicate for each condition.

2.3 Determination of total protein, water, ash and starch

Total protein content was determined by the Kjeldahl Method (AOAC 2016). Water content was determined by

the direct drying method. Drying temperature was 105°C, and drying time was 4 h. Ash content was determined by combustion method. Starch content was determined by enzymatic hydrolysis method.

2.4 Determination of amino acid composition and hydrophobic value in broad bean protein

Tryptophan content was determined by alkaline hydrolysis method. 1.5 mL 4 N NaOH was added to 74.05 mg of sample material. They were hydrolyzed for 20 h under the condition of 110°C with no oxygen. After cooling down, the sample was acidized to pH 4 to pH 5 by adding 1140 μL 6 N HCl and diluted to 50 mL. Sample volumes of 20 μL were injected into the Agilent 1200 HPLC system mounted with the reversed phase column Innoval C18 (250×4.6 mm, 5 μm particle size) and eluted at 25°C, with a flow rate of 1 mL/min (Farvin et al. 2010). The mobile phase was methanol-sodium acetate buffer (5:95). Detection wavelength was set at 280 nm.

The other amino acids were determined by acidic hydrolysis method. Ten mL 6 N HCl was added to 66.78 mg of sample material. They were hydrolyzed for 24 h under the condition of 110°C, with no oxygen. After cooling down, the sample was diluted to 50 mL. One mL of this solution was transferred and blown to dry with nitrogen. Five mL 0.02 N HCl was added to re-dissolve the sample. Sample solution was filtered and analyzed by the L-8900 automatic amino acid analyzer (Hitachi Co. Ltd., Japan). The hydrophobic value was calculated according to the following Equations (1)-(2).

$$\Delta Q = \frac{AA_i / M_i}{\sum AA_i / M_i} \times \Delta f_i \quad (1)$$

$$Q = \sum \Delta Q_i \quad (2)$$

where, AA_i = amino acids content/100 g protein (g); Q = hydrophobic value of protein; M_i = molecular weight of amino acid (g/mol); Δf_i = hydrophobic value of amino-acid side chains (KJ/mol); $\Sigma AA_i/M_i$ = the total number of moles of amino acids in 100 g protein (mol).

2.5 Measurement of ACE-inhibitory effect

The ACE-inhibitory effect was measured using the modified RP-HPLC method (Cushman and Cheung 1971). HHL was dissolved in 0.1 M borax-borate buffer (pH 8.3) containing 0.3 mol/L NaCl to form 5 mM solution for further utilization. ACE working solution was diluted to 0.025 U. Sample solution was diluted to 10 mg/mL with buffer solution. All sample solution was diluted to 10 mg/mL when determined the ACE-inhibition. The experiment was performed according to Table 1.

Table 1 Determination of ACE inhibition activity in vitro

Reagent, μL	A, Sample	B, Control	C, Blank
1 M HCl	0	0	100
0.025 U ACE	160	160	160
Sample	30	0	30
0.1 M borax-borate buffer	0	30	0
37°C incubated for 10 min			
5 mM HHL	50	50	50
37°C reacted for 30 min			
1 M HCl	100	100	0
Sample	0	30	0
0.1 M borax-borate buffer	30	0	30

Note: Cooled down to room temperature, 10 μL product was filtrated through a 0.45-μm membrane, hippuric acid content was determined with RP-HPLC, ACE-inhibitory effect was determined

Hippuric acid content was determined with RP-HPLC (Wang et al., 2011). Samples were eluted at 25°C with a flow rate of 0.8 mL/min. The mobile phase was acetonitrile-water (25:75) which contains 0.1% TFA. Detection wavelength was set at 228 nm. Column temperature was 25°C. The activity of each sample was tested in triplicate. The formula applied to calculate the percentage of ACE-inhibitory activity was as:

ACE-inhibitory activity (%) =100×(C−A)/(C−B)

The letter in the formula stands for the peak area value of each group.

2.6 Enzymatic hydrolysis

2.6.1 Single enzymatic hydrolysis

Single enzymatic hydrolysis was studied under pH-controlled and pH-spontaneous conditions. Substrate concentration was 5%. Enzyme concentration was 16000 U/g protein. Firstly, single enzymatic hydrolysis was studied under their optimum reaction conditions, as shown in Table 2. Concrete operations as follows: Distilled water was added to 5 g broad bean powder to form 5% sample solution. After mixing well, it was stirred constantly in 90°C water bath for 15 min and then cooled to optimum temperature of enzyme. At the same time, 80000 U enzyme solution was preheated for 10 min by water bath which was at the optimum temperature of enzyme. After both being adjusted to optimum pH,

sample solution and enzyme solution were mixed well and put in water bath constant temperature vibrator to hydrolyze. At the 0, 15, 30, 45, 60, 75, 90, 120, 150, 180, 240, 300, 360, 420, 450 min of the hydrolysis, pH of the solution and the volume amount of 1 mol/L NaOH solution added to make the solution back to the initial pH were recorded. At the end of the reaction, solution was put in boiling water bath for 10 min to inactive the enzyme, and then clarified by centrifugation at 5000 r min^{-1} for 20 min after cooling down to room temperature. The supernatant was dehydrated using freeze drying method and stored in 4°C refrigerator for further utilization.

Table 2 Optimum reaction conditions of Protamex/ Flavourzyme/Alcalase/Neutrase

Enzyme	Optimum reaction condition	
	pH	Temperature, °C
Protamex	7.0	58
Flavourzyme	6.3	55
Alcalase	8.5	55
Neutrase	7.0	50

For the hydrolysis under pH-spontaneous condition, pH of the solution was recorded at 0, 15, 30, 45, 60, 75, 90, 120, 150, 180, 240, 300, 360, 420, 450 min. NaOH was not added to make the pH back to original state until the reaction ended. The other operations were the same as the pH-controlled condition.

2.6.2 Compound enzymatic hydrolysis

Two enzymes were selected based on the results of single enzymatic hydrolysis test. Compound enzymatic hydrolysis was studied according to the following two processes (Table 3).

Table 3 Process of double-enzyme compound hydrolysis

Type	Compound enzymes	Temperature, °C	pH	Enzyme concentration, U/g protein	Incubation time, min
1	enzyme$_1$-enzyme$_2$	T_1 - T_2	pH_1-pH_2	enzyme$_1$ & enzyme$_2$ are both 16000	0-t_1-end
2	enzyme$_2$-enzyme$_1$	T_2 - T_1	pH_2-pH_1		

Notes: t_1 = incubation time of the first enzyme (Under controlled pH condition, t_1 = 210 min; Under not controlled pH condition, t_1 = 90 min).

Substrate concentration was 5%. Enzyme concentration was 16000 U/g protein. Timing started and pH was recorded after adjusting the sample solution and the first enzyme solution to the optimum condition. The volume amount of 1 mol/L NaOH solution added to make the solution back to the initial pH was also recorded. The mixture was heated by boiling water bath for 10 min to end the first period of enzyme hydrolysis. After adjusting the mixture to optimum condition for the second enzyme, same amount of second enzyme was added and timing started. NaOH solution was not added to restore the pH until the pH change was not obvious any more. The solution was put in boiling water bath for 10 min to inactive the enzyme, and then clarified by centrifugation at 5000 r/min for 20 min after cooling down to room temperature. The supernatant was freeze dried and stored in 4°C refrigerator for further utilization.

2.7 Determinations of degree of hydrolysis

The DH was determined using the modified pH-Stat method (Adlernissen, 1979). As the pH level of solution was not steady during enzymatic hydrolysis, DH was determined based on the quantity of the alkali liquor added to make the solution back to the initial pH level. The % DH was calculated according to the following Equations (4)-(6).

$$DH = \frac{B \times N_b}{\alpha \times M_p \times h_{tot}} \times 100\% \quad (4)$$

$$\alpha = \frac{10^{(pH-pK)}}{1+10^{(pH-pK)}} \quad (5)$$

$$pK = 7.8 + \frac{2400(298-T)}{298T} \quad (6)$$

where, B = volume of alkali liquor, L; N_b = concentration of alkali liquor, mol/L; α = dissociation degree of α-NH_3^+; pH = pH value of reaction system; pK = mean dissociation constant of released α-NH_3^+ in reaction; M_p = total protein content in substrate, g; h_{tot} = total number of peptide bonds per protein equivalent (7.92 specific to broad bean protein). Absorbance of the eluent was monitored at 280 nm.

2.8 Fractionation by Sephadex G-15

The freeze dried hydrolyzates were dissolved in ultrapure water to a concentration of 50 mg/mL. Two mL sample solution was eluted on Sephadex G-15 at speed of 1.87 mL/min using eluent of ultrapure water. Absorbance of the eluent was monitored at 280 nm. Three peaks were detected and collected respectively.

2.9 Fractionation by semi-preparative HPLC

Fraction that had the highest ACE-inhibitory activity

was selected from fractions separated by Sephadex G-15 column. Semi-preparative HPLC was used for further isolation. Sample dissolved in ultrapure water containing 0.1% TFA to form 20 mg/mL solution and filtrated through a 0.45-μm membrane. Fractions were collected and freeze dried for ACE-inhibitory activity determination. Separation was performed on an Agilent Varian Prostar 218LC HPLC system with an Innoval C18 column (250×21.2 mm, 10 μm) at a flow rate of 10 mL/min. The compounds were separated using a linear elution gradient of (A) acetonitrile containing 0.1% TFA (v/v) and (B) ultrapure water containing 0.1% TFA (v/v) as follows: gradient of 10% to 50% A from 0 to 50 min; 10% A from 50.1 to 60 min. Detecting wavelength was at 280 nm.

2.10 Characterization and sequencing of peptides by LC–MS/MS

LC–MS/MS analysis was performed for identification of the amino acid sequences of peptides with the highest ACE-inhibitory activity. Sample was firstly separated on an ultimate 3000 HPLC system (Thermo Scientific, NY, USA) with a Waters C18 column (250×4.6 mm, 5 μm particle size) at a flow rate of 0.7 mL min^{-1}. The compounds were separated using a linear elution gradient of (A) 0.1% aqueous formic acid (v/v) and (B) acetonitrile-water (80:20) containing 0.08% formic acid (v/v) as follows: gradient of 5% to 35% B from 0 to 30 min; 95% B at 32 min; isocratic at 95% B from 32 to 37 min; 5% B at 39 min; isocratic at 5% B from 39 to 45 min. Fractions were collected and analyzed on a C18 column (120×0.15 mm, 1.9 μm particle size) with a C18 trap column(20×0.1 mm, 3 μm particle size) at a flow rate of 600 nL min^{-1}. The compounds were separated using a linear elution gradient of (A) 0.1% aqueous formic acid (v/v) and (B) acetonitrile-water (80:20) containing 0.08% formic acid (v/v) as follows: gradient of 6% to 9% B from 0 to 8 min; 14% B at 24 min; 30% B at 60 min; 40% B at 75 min; isocratic at 95% B from 78 to 85 min; 6% B at 86 min; isocratic at 6% B from 86 to 90 min. MS/MS analysis was carried out in the positive ion mode. For full MS condition, automatic gain control (AGC) target was $3E^6$, and maximum interval time (IT) was 80 ms. AGC target of dd-MS^2 was $5E^4$, and maximum IT was 45 ms. Spectra were obtained over a scan range from the mass to charge ratio (m/z) 300 to 1400. MS/MS data were acquired and analyzed by Proteome Discoverer software (Version 2.1, Thermo Scientific, NY, US).

2.11 Statistical analysis

Data were analyzed with SPSS (Version 20.0, IBM Inc., NY, US). Statistical differences between different treatments were assessed using analysis of variance, followed by Tukey's HSD post-hoc test ($p<0.05$). Data were expressed as means of at least two replicates.

3 Results and discussion

3.1 Characterization of broad bean powder and BPC

As is shown in Table 4, protein content of BPC was 2.2 times that of broad bean powder, and starch content of BPC was only 1/40 that of broad bean powder, which indicated the method of ultrasonic-assisted alkali-solution and acid-isolation could enrich protein and remove most starch in broad beans. In this way, the influence of other substances could be avoided in the further fractionation of peptides.

Table 4 Main components of broad bean powder and BPC

Content	Broad bean powder	BPC
Protein,%	34.4	75.70
Water, g/100 g	10.6	7.87
Starch, g/100 g	30.2	0.76
Ash, g/100 g	6.7	24.20

BPC contained 20 kinds of essential amino acids (Table 5). 40% of these amino acids were hydrophobic amino acids (Met, Try, Phe, Val, Leu, Ile, Pro and Ala), aromatic amino acids (Tyr, Phe and Try) and Proline. It was reported that the structure-function relationship of ACE-inhibitory peptides and found ACE-inhibitory activity of peptides was often related to hydrophobicity which was associated the composition and content of hydrophobic amino acids(Gu and Wu, 2013). Hydrophobic amino acids, aromatic amino acids and Pro took a great proportion in broad bean protein. So, peptides hydrolyzed from broad bean protein could have high ACE-inhibitory activity.

ACE-inhibition of BPC was about 14.4%, which was 6.8 times that of broad bean powder (Table 6). The reason for this great difference could be that protein in broad

bean powder had complete quaternary structure. But, in the process of crude protein production, more amino acid residues and branch chains were exposed. These exposed groups could improve ACE-inhibitory activity of BPC.

Table 5 Amino acid composition and hydrophobic value in broad bean protein

Amino acid	Hydrophobic value, KJ/mol	Protein, g/100 g
Trp	12.54	0.6702
Ile	12.41	3.5560
Tyr	12.00	2.7541
Phe	11.08	3.8591
Pro	10.87	3.0680
Leu	10.12	6.3704
Val	7.06	3.8051
Lys	6.27	5.4759
Met	5.43	0.7289
Cys	4.20	0.6072
Ala	3.05	3.0437
Arg	3.05	6.2149
Glu	2.30	14.4473
Asp	2.25	8.4657
His	2.09	1.7343
Thr	1.84	2.5504
Ser	0.17	3.6178
Gly	0	2.8368

Table 6 ACE-inhibition of broad bean powder and BPC

	Broad bean powder	BPC
ACE inhibition, %	2.13±0.16	14.4±1.2

3.2 Hydrolysis

3.2.1 Changes in degree of hydrolysis of BPC under pH-controlled condition

BPC was hydrolyzed with Protamex, Flavourzyme, Alcalase and Neutrase respectively. PH condition was controlled and the DH was measured (Figure 1). At the early beginning of the reactions, DH all increased quickly. As reactions processed, changes of DH became smaller and smaller. DH of BPC treated with Protamex reached 13.19% at 15 min of reaction. It reached 18.66% at 90 min and then its changes gradually slowed down until reaction ended at 210 min with final DH of 19.91%. DH of BPC treated with Flavourzyme increased quickly and reached 12.28% at 45 min. Then, it increased slowly until ended at 14.03% at 300 min. Its DH change rate and hydrolysis efficiency were lower compared to Protamex. The DH change rate was the highest when BPC was treated with Alcalase. DH had reached 16.03% at 30 min. At 480 min, the final DH of Alcalase was 22.49%, which was higher than that of the other three enzymes. In the hydrolysis of BPC treated with Neutrase, DH increased most quickly and reached 11.00% in the first 15 min. Its final DH was 21.00% at 210 min. The final DH of Protamex, Flavourzyme, Alcalase and Neutrase were 19.91%, 14.03%, 22.49% and 21.00% respectively. And their reaction time was 210, 300, 450 and 240 min. To increase production efficiency, 210 min was chosen as the reaction time. At 210 min, DH of BPC of the four enzymes in an increasing order as: Flavourzyme, Protamex, Neutrase, Alcalase. So, Alcalase and Neutrase were selected for the compound enzymatic hydrolysis test. And 210 min was the time to add the second enzyme in hydrolysis reaction.

BPC was hydrolyzed with compound enzymes Neutrase and Alcalase added in different order under pH-controlled condition and the DH was measured (Figure 2). In the first type of compound enzymatic hydrolysis, Neutrase was added firstly. The DH reached 12% at 15 min and finally reached 22.57% as the first stage of hydrolysis ended at 210 min. At 15 min after adding Alcalase for the second stage of hydrolysis, DH reached 28.24% which was much higher than the DH of BPC treated with only Neutrase. This might be because specific recognition sites of Alcalase and Neutrase do not coincide, or there are active sites which can be reacted by the second enzyme on the peptides produced in first stage (Rui et al., 2012). The DH reached 33.48% at 450 min and finally reached 33.83% which was 1.6 times the final DH of BPC treated with only Neutrase, and 1.5 times the one treated with only Alcalase. In the second type of compound enzymatic hydrolysis, Alcalase was added firstly. DH reached 22.94% at 210 min and finally reached 28.60% at 390 min after adding Neutrase. The final DH was 1.36 times the final DH of BPC treated with only Neutrase, and 1.27 times the one treated with only Alcalase. Final DH of the first type was higher than that of the second type. It might be because Alcalase hydrolysis could inhibit Neutrase hydrolysis more than the other way around. So, the first type of compound enzymatic hydrolysis was chosen for further study.

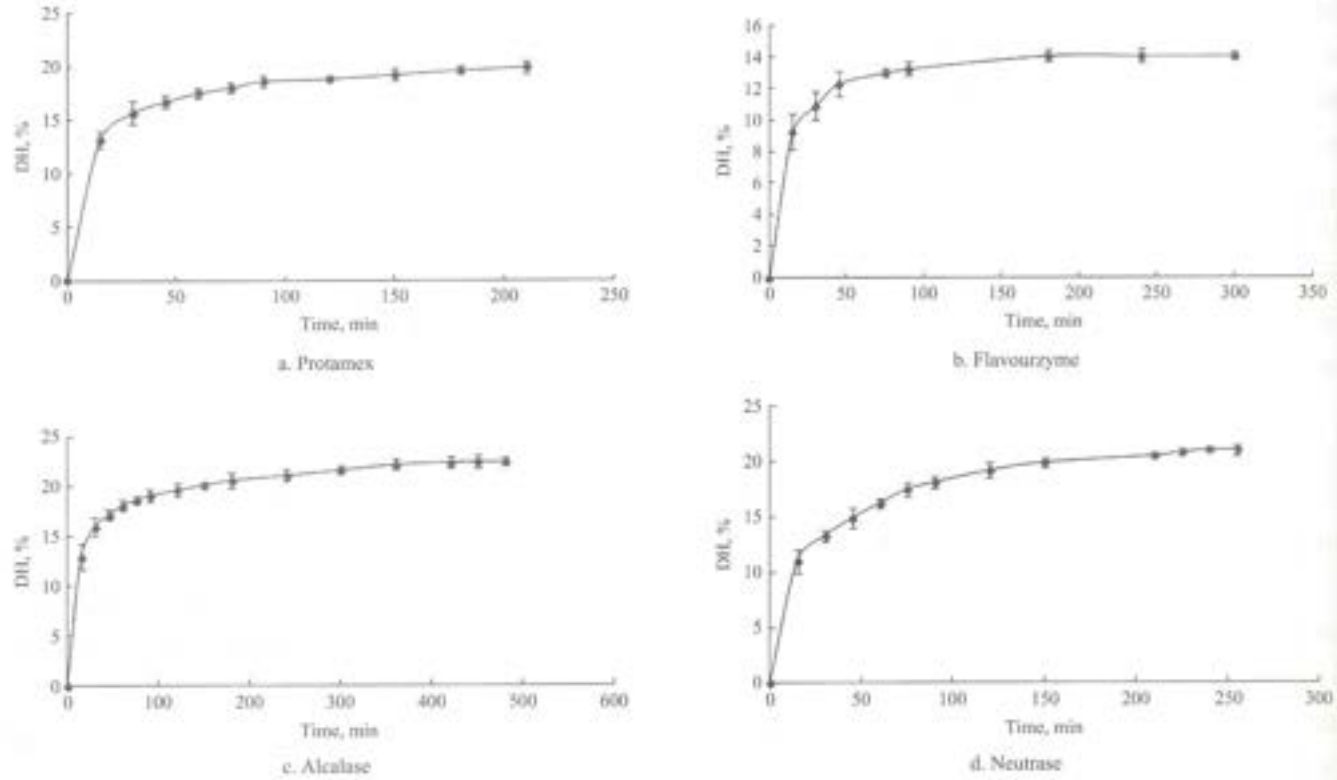

Figure 1 Changes in degree of hydrolysis of BPC treated with Protamex/Flavourzyme/Alcalase/Neutrase under pH-controlled condition

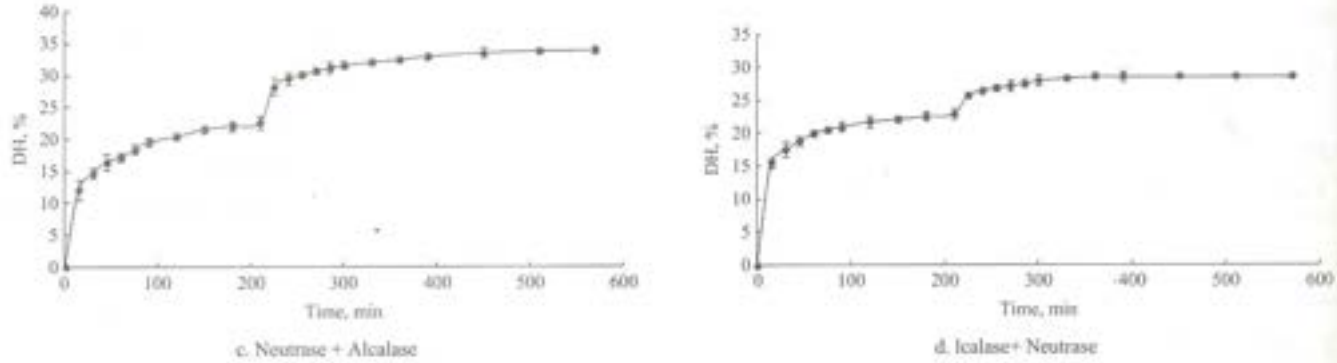

Figure 2 Changes in degree of hydrolysis of BPC treated with Neutrase + Alcalase / Alcalase+ Neutrase under pH-controlled condition

3.2.2 Changes in pH of hydrolyzates of BPC under pH-spontaneous condition

Under pH-controlled condition, enzymes could maintain highly active in solution of optimum range of pH. But, large amount of alkali salt was added to control pH. This made it harder to purify the peptides in the further study. Alkali salt was not added in the reaction under pH-spontaneous condition and DH could be lower than that of pH-controlled reaction.

BPC was hydrolyzed with Protamex, Flavourzyme, Alcalase and Neutrase respectively under pH-spontaneous condition, and the pH of hydrolysates was measured (Figure 3). At the beginning of Protamex hydrolysis, pH decreased greatly from 7 to 5.97 at 5 min. The decline rate of pH gradually decreased from 10 min to 45 min. The pH was 5.76 at 45 min and decreased to 5.74 by the end of reaction at 90 min. The final DH was 18.81% which was 94% of that of Protamex hydrolysis under pH-controlled condition (Table 7). In the hydrolysis process of Flavourzyme, pH decreased quickly from 6.3 to 5.81 at 5 min. Then, it decreased slowly to 5.65 at 30 min and almost unchanged till the end at 90 min. The final DH was 10.53% which was 75% of that of Flavourzyme hydrolysis under pH-controlled condition. This proved Flavourzyme was more relying on pH condition than Protamex. In the hydrolysis process of Alcalase, pH decreased quickly from 8.47 to 6.57 at 5 min. Then, it decreased slowly to 6.2 at 75 min and almost unchanged till the end at 180 min. The final DH was 18.53% which was 82% of that of Alcalase

hydrolysis under pH-controlled condition. Like the other three enzyme hydrolysis, in the hydrolysis process of Neutrase, pH decreased quickly from 7 to 6.23 at 5 min. Then, it decreased slowly to 5.93 at 60 min and almost unchanged till the end at 120 min. The final DH was 19.43% which was 92% of that of Neutrase hydrolysis under pH-controlled condition. PH-dependence of the four enzymes in an increasing order as: Protamex, Neutrase, Alcalase , Flavourzyme. Under pH-spontaneous condition, DH of the four enzymes in an increasing order as: Flavourzyme, Alcalase, Neutrase, Protamex. So, Neutrase and Protamex were selected for the compound enzymatic hydrolysis test.

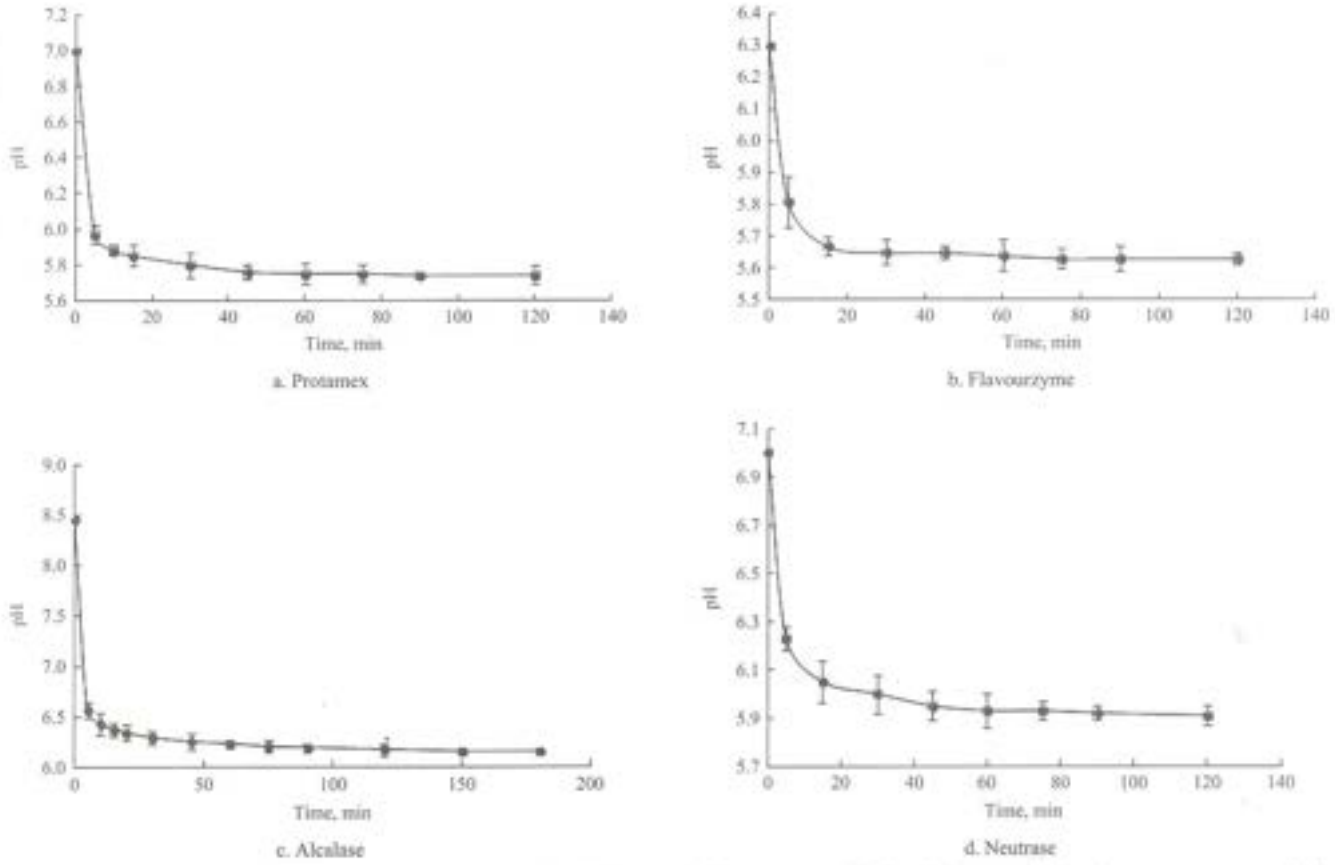

Figure 3 Changes in pH of hydrolyzates of BPC treated with Protamex/Flavourzyme/Alcalase/Neutrase under pH-spontaneous condition

Table 7 Degree of hydrolysis of BPC treated with single protease under pH-spontaneous condition

Enzyme	DH, %
Protamex	18.81
Flavourzyme	10.53
Alcalase	18.53
Neutrase	18.53

BPC was hydrolyzed with compound enzymes Neutrase and Protamex under pH-spontaneous condition and the pH of hydrolyzates was measured (Figure 4). In the first type of compound enzymatic hydrolysis, Neutrase was added firstly. The DH reached 17.10% as the first stage of hydrolysis ended at 60 min. At 5 min after adding the second enzyme Protamex, pH decreased quickly from 7.08 to 6.90. The decrease range was only 17% of the one treated with only Protamex. This might be because specific recognition sites of Protamex were destructed greatly by Neutrase hydrolysis(Rui et al., 2012). The pH decreased slowly from 65 min to 90 min. The final DH was 26.53% at 150 min (Table 8). In the second type of compound enzymatic hydrolysis, Protamex was added firstly. DH was 17.66% at 60 min by the end of first stage. In the second enzyme hydrolysis, pH decreased only 0.17 and DH only increased 1.51%, which meant that hydrolysis effect of the second enzyme was very limited. The final DH of the second type of compound enzymatic hydrolysis under pH-spontaneous condition was 19.17%, which was higher than the DH of only Protamex, but lower than the DH of only Neutrase. It was also lower than the DH of the first type of compound enzyme under pH-spontaneous condition. So,

the first type of compound enzyme was selected.

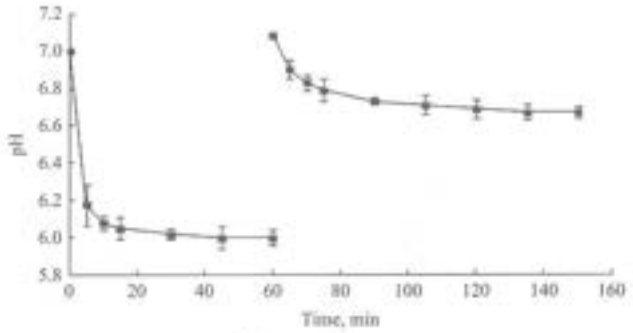

a. Neutrase +Protamex

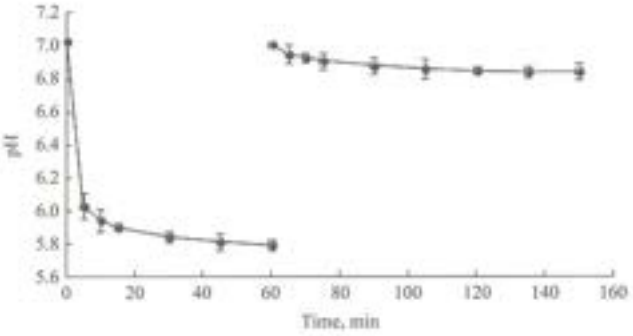

b. Protamex + Neutrase

Figure 4 Changes in pH of hydrolyzate of BPC treated with Neutrase +Protamex / Protamex + Neutrase under pH-spontaneous condition

Table 8 Degree of hydrolysis of BPC treated with compound enzymatic hydrolysis under pH-spontaneous condition

Compound enzyme	DH, %
Neutrase + Protamex	26.53%
Protamex + Neutrase	19.17%

3.2.3 Analysis of hydrolysates treated with double-enzyme hydrolysis under pH-controller and pH-spontaneous condition

As is shown in Table 9, the protein content of hydrolysates of compound enzyme Neutrase and Alcalase under pH-controlled condition was lower than that of hydrolysates of compound enzyme Neutrase and Protamex under pH-spontaneous condition. This might be because protein content was determined by Kjeldahl Method and it was calculated on basis of nitrogen content. During enzymatic hydrolysis, peptide bonds were cut off and combined with a water molecule, forming carboxyl group and amino group. So, when amino acid number stayed same, total quality of peptides increased for combining with water molecules. And protein content of higher hydrolytic degree sample was lower when calculating the nitrogen content of sample of the same quality. In the hydrolysis of compound enzyme Neutrase and Alcalase under pH-controlled condition, DH was higher, which meant more proteins were hydrolyzed to peptides. So, its protein content was lower.

The ash content of hydrolysates under pH-controlled condition was 1.3 times that of hydrolysates under pH-spontaneous condition and 1.4 times that of BPC. This was because much more alkali salt was added in the reaction under pH-controlled condition. And an amount of alkali salt was also added in the reaction under pH-spontaneous condition to calculate DH using pH-stat method and adjust optimum pH before adding enzymes. So, the second process in Table 9 should be selected to simplify the further fractionation process.

Table 9 Main components of hydrolysates of two hydrolysis process

Process	Protein, g/100 g	Ash, g/100 g
Neutrase + Alcalase under pH-controlled condition	49.9	34.3
Neutrase + Protamex under pH-spontaneous condition	66.7	26.0
BPC	75.7	24.2

Figure 5 shows the ACE-inhibitory activity of hydrolysates treated with double-enzyme hydrolysis under pH-controlled and pH-spontaneous condition. The ACE-inhibitory activity of hydrolysates treated with Neutrase and Protamex under pH-spontaneous condition was 54.3% which was 3.76 times that of BPC. The ACE-inhibitory activity of hydrolysates treated with Neutrase and Alcalase under pH-controlled condition was 63.20% which was 4.39 times that of BPC. This indicated that compound enzymatic hydrolysis was an effective way to produce ACE inhibition peptides.

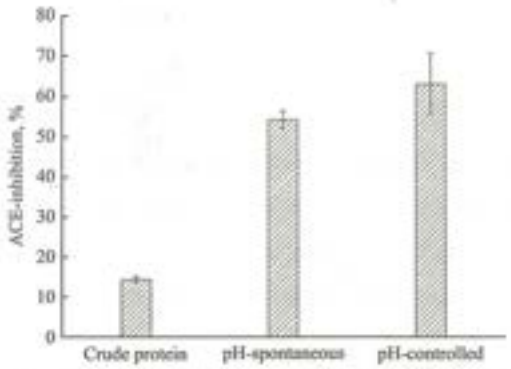

Figure 5 ACE-inhibitory activity of hydrolysates treated with double-enzyme hydrolysis under pH-controlled and pH-spontaneous condition

ACE-inhibitory activity of hydrolysates treated with compound enzymes was significantly higher than that of BPC (Table 10). The ACE-inhibitory activity of hydrolysates treated with Neutrase and Alcalase under pH-controlled condition was higher than that of hydrolysates treated with Neutrase and Protamex under pH-spontaneous condition, but the difference was not significant. It was reported that the tripeptide with C-terminal of aromatic amino acid and N-terminal of hydrophobic amino acid had higher ACE-inhibitory activity (Wu et al., 2006). So, ACE-inhibitory activity is associated with amino acid variety and branched chain type. But enzyme species and enzymatic hydrolysis processes are often different, branched chains and residues produced in hydrolysis are different correspondingly. So, although DH of hydrolysates treated with Neutrase and Alcalase under pH-controlled condition was higher than that of hydrolysates treated with Neutrase and Protamex under pH-spontaneous condition, the difference of ACE-inhibitory activity was not significant.

Table 10 Significance analysis of ACE-inhibitory activity of hydrolysates treated with double-enzyme hydrolysis under pH-controlled and pH-spontaneous condition

(I) VAR00001	(J) VAR00001	Mean difference (I-J)	Standard error	Significance	95% confidence interval	
					Lower limit	Upper limit
1	2	-39.90000*	3.68661	0.000	-48.9208	-30.8792
	3	-48.80000*	3.68661	0.000	-57.8208	-39.7792
2	1	39.90000*	3.68661	0.000	30.8792	48.9208
	3	-8.90000	3.68661	0.052	-17.9208	0.1208
3	1	48.80000*	3.68661	0.000	39.7792	57.8208
	2	8.90000	3.68661	0.052	-0.1208	17.9208

Notes: * at 0.05 significance level. 1. BPC, 2. Neutrase + Protamex hydrolysates under pH-spontaneous condition, 3. Neutrase + Alcalase hydrolysates under pH-controlled condition.

In addition, there were more differences in the operations of the three processes. First, alkali salt solution should be added continually in the pH-controlled process, which increased the difficulty of the experimental operations. Second, the alkali salt added in the hydrolysis process should be removed in the further fractionation stage, which would increase time and economic cost. Third, pH-controlled process required more time than pH-spontaneous process under the condition of same substrate amount and enzyme concentration.

So, the process of compound enzymes Neutrase and Protamex under pH-spontaneous condition was selected to hydrolyze BPC. The first stage of hydrolysis ended at 60 min and the second stage ended at 150 min with the DH of 26.53%. The hydrolysates were freeze dried for further fractionation.

3.3 Fractionation by Sephadex G-15 and semi-preparative HPLC

After fractionation by Sephadex G-15, three fractions were collected. ACE-inhibitory activity increased as molecular weight of fractions decreased. Fraction P3 which had the highest ACE-inhibitory activity was selected for further study (Figure 6).

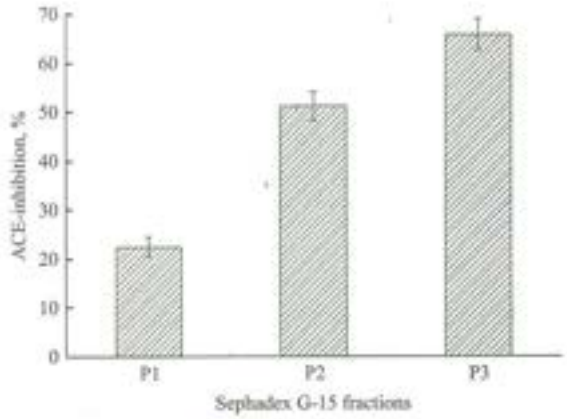

Figure 6 ACE inhibition of Sephadex G-15 fractions

Fraction P3 that had the highest ACE-inhibitory activity was selected from fractions separated by Sephadex G-15 column. Then it was separated by semi-preparative HPLC (Figure 7). Fourteen main components were collected. Hydrophobicity of components increased over elution time. And fraction F9 had the highest ACE-inhibitory activity of 81.17%. F9 was collected by repeating injection and freeze dried for

determination of amino acid sequences. ACE-inhibitory activity of peptides was often related to hydrophobicity, composition and content of hydrophobic amino acids(Farvin et al., 2016). But as shown in Figure 10, ACE-inhibitory activity did not increase over elution time, which indicated that hydrophobicity of amino acids did not affect ACE-inhibitory activity. So, amino acid sequences of peptides should be determined to analyze the structure-function relationship of ACE-inhibitory peptides.

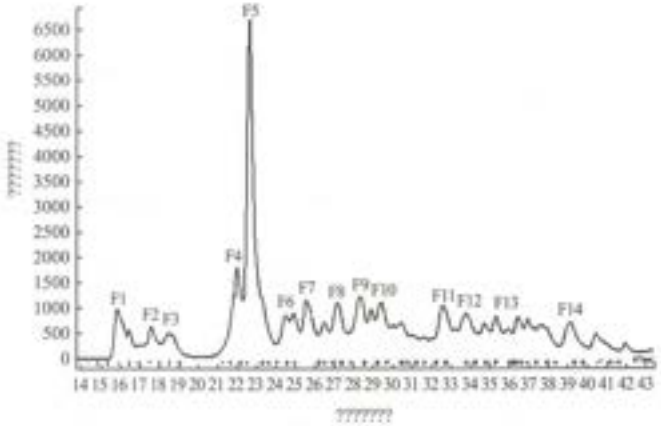

a. Chromatography of fraction P3 separated by semi-preparation RP-HPLC

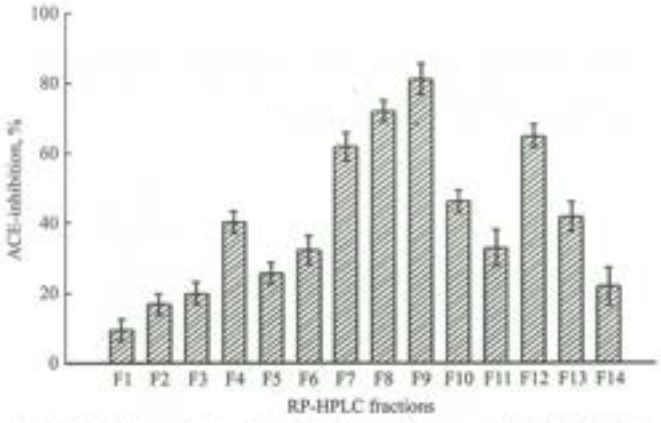

b. ACE-inhibitory activity of each fraction in chromatography of RP-HPLC

Figure 7 Fractionation by semi-preparative HPLC and ACE-inhibitory activity assay

3.4 Characterization and sequencing of peptides by LC–MS/MS

Fraction F9 which had the highest ACE-inhibition was analyzed by LC-MS/MS. Amino acid sequences were deduced by analyzing ESI-MS chromatograms of the major peptides (Table 11). By comparing the data base of Proteome Discoverer, the amino acid sequences of five peptides were selected, namely, DSTLIMQLLR, SAEYVRLY, LDWYKGPT, IYAPHWN, EGSLLLPHYNSR. These showed a marked hydrophobic character being rich in amino acids as leucine (L), proline (P) and isoleucine (I). It was reported that ACE showed preference for competitive inhibitors that contain a hydrophobic amino acid at the third position from the C-terminal (Fang et al., 2008, Lau et al., 2013). This is in accordance with the amino acid sequence of peptides identified. It was established that a tyrosine residue (Y) at the amino terminus was a common motif of the peptides with the most potent vasodilator activity when assayed in mesenteric arteries of rats (Garcia-Redondo et al., 2010).

Table 11 Predominant peptide sequences identified by LC-MS/MS

Mass obs. $[M+H]^+$	Retention time, min	MS(2) fragments	Putative sequence
1189.66	67.00	600.38, 773.47, 355.07, 286.10 *a.m.o*	DSTLIMQLLR
1000.51	39.21	131.08, 159.08, 713.39 *a.m.o*	SAEYVRLY
979.49	42.00	159.09, 207.11, 302.11, 402.23 *a.m.o*	LDWYKGPT
900.43	36.37	136.07, 249.16, 456.20 *a.m.o*	IYAPHWN
1385.71	36.58	773.36, 694.30, 487.15, 263.10 *a.m.o*	EGSLLLPHYNSR

4 Conclusions

The results obtained in the present study suggest that method of ultrasonic-assisted alkali-solution and acid-isolation could enrich protein and remove most starch of broad beans. The analysis of amino acid composition and hydrophobicity indicated that BPC had high proportion of hydrophobic amino acids, aromatic amino acids and Proline, which made it good resource of antihypertensive peptides. The process of compound enzymes Neutrase and Protamex under pH-spontaneous condition was selected to hydrolyze BPC. The first stage of hydrolysis ended at 60 min and the second stage ended at 150 min with the DH of 26.53%. The ACE-inhibition of hydrolyzates was 54.31%. Three fractions were collected by fractionation on Sephadex G-15 using eluent of ultrapure water at speed of 1.87 mL min^{-1} and fraction P3 proved to have the highest ACE-inhibition, which was 65.93%. P3 was further fractionated by semi-preparative RP-HPLC and 14 fractions were collected. Fraction F9 proved to have the highest ACE-inhibition, which was 81.17%. Amino acid sequences of fraction F9 in RP-HPLC were analyzed by LC-MS/MS. The result showed F9 mainly consisted of five peptides, namely.

DSTLIMQLLR, SAEYVRLY, LDWYKGPT, IYAPHWN, EGSLLLPHYNSR. These results suggested that broad bean peptide hydrolysates had potential antihypertensive activity and could be developed into new functional ingredients with this enzymatic food grade preparation. However, further studies need to be performed in future using other models to reinforce and confirm the results obtained.

Acknowledgments

The authors gratefully acknowledge the financial support by the China Agriculture Research System (CARS-09), Ministry of Agriculture, China.

[References]

[1] Adlernissen, J. 1979. Determination of the degree of hydrolysis of food protein hydrolysates by trinitrobenzenesulfonic acid. *Journal of Agricultural and Food Chemistry*, 27(6): 1256–1262.

[2] Aoac. 2016. Official methods of analysis. Washington, DC: Association of Official Analytical Chemists.

[3] Cushman, D. W., and H. S. Cheung. 1971. Spectrophotometric assay and properties of angiotensin-converting enzyme of rabbit lung. *Biochemical Pharmacology*, 20(7): 1637.

[4] Fang, H., M. Luo, Y. Sheng, Z. X. Li, Y. Q. Wu, and C. Liu. 2008. The antihypertensive effect of peptides: A novel alternative to drugs? *Peptides*, 29(6): 1062–1071.

[5] Farvin, K. H. S., L. L. Andersen, J. Otte, H. H. Nielsen, F. Jessen, and C. Jacobsen. 2016. Antioxidant activity of cod (gadus morhua) protein hydrolysates: Fractionation and characterisation of peptide fractions. *Food Chemistry*, 204: 409–419.

[6] Farvin, K. H. S., C. P. Baron, N. S. Nielsen, J. Otte, and C. Jacobsen. 2010. Antioxidant activity of yoghurt peptides: Part 2-characterisation of peptide fractions. *Food Chemistry*, 123(4): 1090–1097.

[7] Fife, T. H., R. Singh, and R. Bembi. 2002. Intramolecular general base catalyzed ester hydrolysis. The hydrolysis of 2-aminobenzoate esters. *Journal of Organic Chemistry*, 67(10): 3179–3183.

[8] Garcia-Redondo, A. B., F. R. Roque, M. Miguel, R. Lopez-Fandino, and M. Salaices. 2010. Vascular effects of egg white-derived peptides in resistance arteries from rats. Structure-activity relationships. *Journal of the Science of Food and Agriculture*, 90(12): 1988–1993.

[9] Gu, Y. C., and J. P. Wu. 2013. Lc-ms/ms coupled with qsar modeling in characterising of angiotensin i-converting enzyme inhibitory peptides from soybean proteins. *Food Chemistry*, 141(3): 2682–2690.

[10] Guazzi, M., and R. Arena. 2010. Pulmonary hypertension with left- sided heart disease. *Nature Reviews Cardiology* 7(11): 648–659.

[11] Juan, M. Y., C. H. Wu, and C. C. Chou. 2010. Fermentation with bacillus spp. As a bioprocess to enhance anthocyanin content, the angiotensin converting enzyme inhibitory effect, and the reducing activity of black soybeans. *Food Microbiology*, 27(7): 918–923.

[12] Koklu, S., O. Yuksel, M. Arhan, S. Coban, O. Basar, O. F. Yolcu, E. Ucar, M. Ibis, I. Ertugrul, and B. Sahin. 2005. Report of 24 left-sided portal hypertension cases: A single-center prospective cohort study. *Digestive Diseases and Sciences*, 50(5): 976–982.

[13] Lau, C. C., N. Abdullah, A. S. Shuib. 2013. Novel angiotensin i-converting enzyme inhibitory peptides derived from an edible mushroom, pleurotus cystidiosus ok miller identified by lc-ms/ms. Bmc Complementary and Alternative Medicine 13.

[14] Li, H. A., R. F. Aluko. 2010. Identification and inhibitory properties of multifunctional peptides from pea protein hydrolysate. *Journal of Agricultural and Food Chemistry*, 58(21): 11471–11476.

[15] Mccurdy, S. M., and J. E. Knipfel. 1990. Investigation of faba bean protein recovery and application to pilot scale processing. *Journal of Food Science*, 55(4): 1093–1094.

[16] Nakagomi, K., R. Yamada, H. Ebisu, Y. Sadakane, T. Akizawa, T. Tanimura. 2000. Isolation of acein-2, a novel angiotensin-i-converting enzyme inhibitory peptide derived from a tryptic hydrolysate of human plasma. *Febs Letters*, 467(2-3): 235–238.

[17] Pena-Ramos, E. A., Y. L. Xiong. 2002. Antioxidant activity of soy protein hydrolysates in a liposomal system. *Journal of Food Science*, 67(8): 2952–2956.

[18] Puchalska, P., M. C. Garcia, and M. L. Marina. 2014. Identification of native angiotensin-i converting enzyme inhibitory peptides in commercial soybean based infant formulas using hplc-q-tof-ms. *Food Chemistry*, 157(2014): 62–69.

[19] Rui, X., J. I. Boye, B. K. Simpson, S. O. Prasher. 2012. Angiotensin i-converting enzyme inhibitory properties of phaseolus vulgaris bean hydrolysates: Effects of different thermal and enzymatic digestion treatments. *Food Research International*, 49(2): 739–746.

[20] Shin, Z. I., R. Yu, S. A. Park, D. K. Chung, C. W. Ahn, H. S. Nam, K. S. Kim, and H. J. Lee. 2001. His-his-leu, an angiotensin i converting enzyme inhibitory peptide derived from korean soybean paste, exerts antihypertensive activity in

vivo. *Journal of Agricultural and Food Chemistry,* 49(6): 3004–3009.

[21] Sun, Z. J., and Z. E. Zhang. 2005. Historic perspectives and recent advances in major animal models of hypertension. *Acta Pharmacologica Sinica,* 26(3): 295–301.

[22] Tan, B., H. Z. Tan, X. H. Tian, and M. Liu. 2010. Eight underexploited broad beans from china: (i) chemicophysical, thermal properties and microstructure. *Journal of Food Processing and Preservation,* 34(5): 777–794.

[23] Wang, C. Y., J. Q. Tian, Q. Wang. 2011. Ace inhibitory and antihypertensive properties of apricot almond meal hydrolysate. *European Food Research and Technology,* 232(3): 549–556.

[24] Wang, S. J., J. Blazek, E. Gilbert, and L. Copeland. 2012. New insights on the mechanism of acid degradation of pea starch. *Carbohydrate Polymers,* 87(3): 1941–1949.

[25] Wolf, W. J. 1970. Soybean proteins - their functional, chemical, and physical properties. *Journal of Agricultural and Food Chemistry,* 18(6): 969–976.

[26] Wu, J. P., R. E. Aluko, and S. Nakai. 2006. Structural requirements of angiotensin i-converting enzyme inhibitory peptides: Quantitative structure-activity relationship study of di- and tripeptides. *Journal of Agricultural and Food Chemistry,* 54(3): 732–738.

[27] Yin, S. W., C. H. Tang, J. S. Cao, E. K. Hu, Q. B. Wen, and X. Q. Yang. 2008. Effects of limited enzymatic hydrolysis with trypsin on the functional properties of hemp (cannabis sativa l.) protein isolate. *Food Chemistry,* 106(3): 1004–1013.

Bacterial diversity in home-made paocai brine of different ages by SMRT sequencing

Cao Jialu[1], Hou Qiangchuan[2], Yu Zhongjie[2], Xu Haiyan[2], Sun Zhihong[2], Zhang Liebing[1*]

(1. *College of Food Science and Nutritional Engineering, China Agricultural University, Beijing 100083, China;*
2. *Key Laboratory of Dairy Biotechnology and Engineering, Inner Mongolia Agricultural University, Hohhot 010018, China*)

Abstract: Paocai is a traditional and popular fermented vegetable food in southwestern China where nearly every household has at least one paocai jar. Paocai brine (fermentation medium of paocai) is often reused for a long time, and some local residents believe the longer age of the brine, the better paocai brine. In order to verify this view, we compared the bacterial diversity in 22 home-made paocai brine (HMPB) samples of different ages (all over 10 years) via a metagenomic approach involving single-molecule, real-time (SMRT) sequencing of the full-length 16S rRNA gene. Our results revealed no significant differences in bacterial diversity and the dominant taxa were observed between HMPB samples within different age groups. But HMPB with longer age may have more metabolic pathways, indicating richer flavor of the HMPB. In general, our results suggested that the not the longer time of HMPB used, the better bacterial profiles of it.

Keywords: home-made paocai brine, bacterial diversity, age

Citation: Cao, J. L., Q. C. Hou, Z. J. Yu, H. Y. Xu, Z. H. Sun, and L. B. Zhang. 2017. Bacterial diversity in home-made paocai brine of different ages by SMRT sequencing. International Agricultural Engineering Journal, 26(3): 213–220.

1 Introduction

Fermented foods are consumed worldwide as they are important constituents of the human daily diet. In East Asia, fermented plant products are the most popular fermented food frequently consumed by people in different regions. Paocai is one of the traditional fermented vegetables in southwest China, which may date back to the third century B.C. (Liu et al., 2011). Usually, mixed, seasonal vegetable and various spices are fermented in brine with 6%-8% salt concentration (Yu et al., 2012), but it is not a sterile process and no specific inoculant is used. That is to say paocai fermentation mainly depends on the microorganisms present on the raw materials. Regarding home-made paocai, the fermentation brine is always reused and kept in the paocai jar for a long time. The microbial community of aged, home-made paocai brine (HMPB) is relatively stable and gives a particular flavor to paocai products (Xia, 2014). Some residents in southwest China have the belief that the longer the time the paocai brine is used, the better paocai brine.

The fermentation condition of paocai (e.g. room temperature and moderate salt concentration) favors the growth of lactic acid bacteria (LAB) resulting in the abundance of LAB in paocai at the end of fermentation (Chen et al., 2014). As LAB is widely considered beneficial to human health, LAB as well as the microbial community of paocai have been studied. *Lactobacillus* is the dominant genus (Yu et al., 2012) and *Pediococcus*, *Leuconostoc* and *Weissella* are often found in paocai (Chen et al., 2014). Physicochemical properties of paocai brine also impact the paocai microbial community. For instance, our previous work shows the higher acidity of paocai brine, the low bacterial diversity and the higher relative abundance of LAB (Cao et al., 2017); low salt concentration can accelerate the ripening period of paocai fermentation (Xiong et al., 2016; Zhang et al., 2016).

Received date: 2017-07-21 **Accepted date:** 2017-10-10

* **Corresponding author: Zhang Liebing,** Ph.D., Associate Professor of College of Food Science and Nutritional Engineering, China Agricultural University, 100083 China. Email: liebzhang@gmail.com.

Bacterial succession in the spontaneous or starter culture fermentation process of paocai has already been shown by culture-dependent methods (Xiong et al., 2012; Xiong et al., 2014). Additionally, some LAB strains from paocai have been identified and verified to have certain probiotic effects (Cao et al., 2015; Li et al., 2014). However, limited information is known about the difference in bacterial compositions and diversity of HMPB of different ages.

The Pacific Biosciences (PacBio) single-molecule, real-time (SMRT) sequencing technology can analyze the bacterial profiles of paocai brine samples based on the full-length 16S rRNA gene (Cao et al., 2017), which favors diversity analysis and affords the researcher a relatively unbiased view of microbial communities at different taxonomic levels. This study aimed to identify and compare the bacterial compositions and diversity in HMPB of different ages in order to verify whether the longer age of the brine, the better paocai brine from the view of bacterial profiles. We also compared the predicted functions of bacterial communities in different age groups of paocai brine samples.

2 Materials and methods

2.1 Samples

A total of twenty-two aged (10 + years), HMPB samples with salt concentration of 6%-8% obtained from rural families in Chongqing, China were analyzed in this work. Four paocai brine samples were sequenced in this work and the full-length 16S rRNA gene sequences of eighteen paocai brine samples were extracted from our previous projects (mgp20682 and mgp81213) in MG-RAST databases (see details in Table 2). The samples were divided into three groups based on their ages: Y10 (10-19 years), Y20 (20-29 years), and Y30 (≥30 years). The information of the samples is provided in Table 1.

Basic physicochemical properties (pH, titratable acidity (TA), and salt concentration) of the samples were measured as previously described (Cao et al., 2017).

2.2 DNA extraction

The procedures of pretreatment of paocai brine, DNA extraction, and quality examination were conducted as described previously (Cao et al., 2017). All extracted DNA samples were stored at –20°C until further analysis.

Table 1 Information about home-made paocai brine samples[a]

Sample[b]	Age, year	pH	TA, g/kg[c,**]	Salt concentration, %
Y10-01	10	3.46	12.44	7.32
Y10-02	10	4.21	8.91	7.58
Y10-03	>10	3.46	12.24	7.21
Y10-04	>10	3.30	12.11	6.80
Y10-05	>10	3.50	12.19	6.66
Y10-06	>10	3.28	15.47	7.41
Y10-07	>15	3.80	10.36	7.70
Y10-08	17	3.41	8.22	7.04
Y10-09	18	3.71	10.70	7.21
Mean		3.57±0.29	11.40±2.16	7.21±0.34
Y20-01	20	3.65	14.19	6.67
Y20-02	20	3.32	15.07	7.23
Y20-03	>20	3.45	13.57	6.51
Y20-04	>20	3.50	11.32	8.02
Y20-05	>20	3.32	13.82	6.79
Y20-06	>20	3.31	15.08	6.59
Y20-07	>20	3.47	12.58	7.84
Mean		3.43±0.12	13.66±1.35	7.09±0.62
Y30-01	30	3.20	22.98	6.20
Y30-02	>30	3.26	16.19	7.68
Y30-03	>30	3.38	13.83	8.07
Y30-04	>30	3.26	14.92	7.59
Y30-05	40	3.43	16.67	6.02
Y30-06	58	3.33	15.24	6.05
Mean		3.31±0.08	16.64±3.26	6.94±0.94

Note: [a] The main components of home-made paocai brine samples were chili, ginger, radish and cowpea. [b] Y10: sample of age of 10-19 years; Y20: sample of age of 20-29 years; Y30: sample of age ≥30 years. [c] Titratable acidity expressed in grams of acid per kg of sample by multiplying a factor (0.090) appropriate to lactic acid. **: $P<0.01$.

2.3 PCR amplification and SMRT sequencing

The extracted genome was first amplified as previously described (Cao et al., 2017). The sequencing of amplicons was performed on a PacBio RS II instrument (Pacific Biosciences, USA) using P6-C4 chemistry.

2.4 Bioinformatics processing

The quality control for PCR amplifications and sequence preprocessing was conducted as previously described (Mosher et al., 2013). Sequences were further processed following the analysis pipeline as described before (Cao et al., 2017). The alpha (Shannon, Simpson, Chao1 and observed species index) and beta (the principal coordinate analysis, PCoA) diversity were evaluated.

2.5 Functional prediction

The metagenomes of paocai brine samples were predicted by the processed, full-length 16S rRNA gene sequences in PICRUSt (phylogenetic investigation of

communities by reconstruction of unobserved states, http://picrust.github.io/picrust/) (Langille et al., 2013). Amino acid sequences were translated from the predicted metagenome and aligned against the proteins/domains in the Kyoto Encyclopedia of Genes and Genomes (KEGG) databases. Each protein was assigned to the KEGG orthologue group (KO) and KEGG pathway (Hou et al., 2016).

2.6 Statistical analysis

Statistical difference was tested using the R Package, Version 3.1.2 (https://www.r-project.org/). *P*-values below 0.05 between sample groups were considered statistically significant. The graph presentations were generated by the R Package, Version 3.1.2, and the Prism 7 (GraphPad Software, Inc., La Jolla, CA, USA). Significantly differentiating KEGG pathways were identified according to the final reporter score calculated from the aggregated Z-score of individual KOs with the cut-off level of ≥1.6 (90% confidence according to normal distribution). Whether the significantly differentiating pathways were enriched in the Y10, Y20, or Y30 group was further determined by comparing the number of individual KOs that was enriched in each group.

2.7 Nucleotide sequence accession numbers

The sequence data reported in this study have been deposited in the MG-RAST database (Project No. mgp8012).

3 Results and discussion

3.1 Physicochemical properties of home-made brine samples

Salt concentration and raw materials impact the microbial profiles of fermented vegetable products (Jung et al., 2014). Accordingly, we selected samples with common salt concentration (6%-8%) of paocai brine and whose main materials were chili, ginger, radish and cowpea to minimize their effects on the bacterial profile. The dominant microorganisms, LAB, in paocai are sensitive to salt concentration, which further affects the production of organic acids that increase the acidity of paocai brine (Zhang et al., 2016). As shown in Table 1, the pH of paocai brine samples ranged from 3.20 to 4.21, and TA values were in the range of 8.22-22.98 g/kg. However, there was no significant correlation ($P > 0.05$) between TA and salt concentration in the samples examined, which is not consistent with our previous findings. The Kruskal-Wallis test verified that there was significant difference ($P < 0.01$) in TA among the three sample groups (TA of group Y20 and Y30 were significant higher ($P < 0.05$) than that of group Y10. This is probably due to the accumulation of more organic acid in paocai brine with age.

3.2 Sequence depth

The details of the sequencing results of individual samples in each group are shown in Table 2. The SMRT sequencing of the 16S-PCR amplicons generated a total of 134,875 raw sequence reads from the 22 HMPB samples, which were further classified into 12,764 operational taxonomic units (OTUs) under 98.65% threshold identity after quality control. Although the individual rarefaction curves (not shown) for the samples failed to reach the saturation phase, the Shannon diversity curve of most samples did reach plateau (Figure 1a). This indicated that potential phylotypes would likely to be detected along with extra sequencing, but bacterial diversity of most samples has been captured, namely the sequence depth was adequate in this study.

3.3 Bacterial diversity

The rank-abundance curve visually represents species diversity (richness and evenness) of an individual sample. The length and shape of the curve differ depending on the diversity of the sampled community and on the underlying species-abundance distribution (Lynch and Neufeld, 2015). The wider the curve, the more abundant the species composition would become. A steep gradient indicates low evenness as the high-ranking species have much higher abundances than the low-ranking species, or vice versa. As revealed in Figure 1b, although species richness and evenness differed among samples, it is clear that most samples were rich in bacterial diversity.

The α diversity is the diversity in species at individual regions or ecosystems. The bacterial α diversity of each sample was evaluated by the Shannon, Simpson, Chao 1 and observed species index (Table 2). No significant differences ($P>0.05$) were observed in the diversity estimation indicators, suggesting that the age of the aged

(10+ years) HMPB did not significantly affect the α bacterial diversity in this study. PCoA was applied to analyse the β diversity which is used to compare diversity among various communities by distance calculation between two different samples and reflect differences in microbial communities (Fang et al., 2015). The PCoA plot based on unweighted UniFrac distance of the 22 samples examined is shown in Figure 2a. The first and second principle components accounted for 10.33% and 9.53% of the variance, respectively. Although a few samples from groups Y10, Y20 and Y30 separated from each other, some overlaps existed between sample clusters from different groups. Results of the multivariate ANOVA (Figure 2b, $P>0.05$) also confirmed the differences in bacterial structure between sample groups was not significant.

Table 2 Sequence abundance and bacterial diversity in home-made paocai brine samples

Sample [a]	No. of Reads	No. of OTUs [b]	Shannon	Simpson	Chao 1	Observed species	Project number
Y10-01	4986	1171	7.07	0.95	3578.45	709.82	mgp 81213
Y10-02	3907	535	6.47	0.97	1043.07	418.49	mgp 81213
Y10-03	4660	1011	5.30	0.88	4504.61	611.93	This work
Y10-04	6399	705	6.28	0.96	976.60	416.03	mgp 81213
Y10-05	2614	890	7.97	0.98	3345.50	889.00	mgp 81213
Y10-06	7044	577	5.90	0.95	732.56	332.93	mgp 81213
Y10-07	5767	985	6.28	0.94	1950.96	561.80	mgp 81213
Y10-08	2697	624	7.07	0.98	1756.58	610.09	mgp 81213
Y10-09	4064	1266	8.04	0.99	3548.43	904.73	mgp 81213
Mean	4682±1541	863±266	6.71±0.92	0.95±0.03	2381.86±1382.54	606.09±202.46	
Y20-01	7642	928	6.70	0.97	1209.36	485.10	mgp20682
Y20-02	9435	707	5.85	0.95	752.32	343.32	mgp20682
Y20-03	8474	807	6.16	0.95	943.80	404.96	mgp20682
Y20-04	4312	564	6.50	0.96	872.91	429.86	mgp20682
Y20-05	7014	650	6.03	0.96	854.22	364.41	This work
Y20-06	7950	1006	6.77	0.97	1241.62	511.90	mgp20682
Y20-07	4977	769	4.19	0.79	3784.94	436.70	This work
Mean	7115±1855	776±154	6.03±0.88	0.94±0.06	1379.88±1076.25	425.18±60.65	
Y30-01	8088	1444	6.08	0.93	3312.34	573.70	mgp20682
Y30-02	3120	565	6.35	0.95	1755.74	497.97	mgp20682
Y30-03	10470	1650	6.82	0.95	2256.92	600.82	This work
Y30-04	6120	1024	6.82	0.97	2031.11	554.33	mgp20682
Y30-05	5881	686	6.42	0.96	1021.15	425.68	mgp20682
Y30-06	9254	1252	6.51	0.96	1642.29	528.33	mgp20682
Mean	7156±2655	1104±426	6.50±0.29	0.95±0.01	2003.26±766.15	530.14±62.33	

Note: [a] Y10: sample of age of 10-19 years; Y20: sample of age of 20-29 years; Y30: sample of age ≥30 years. [b] OUTs: Operational taxonomic units.

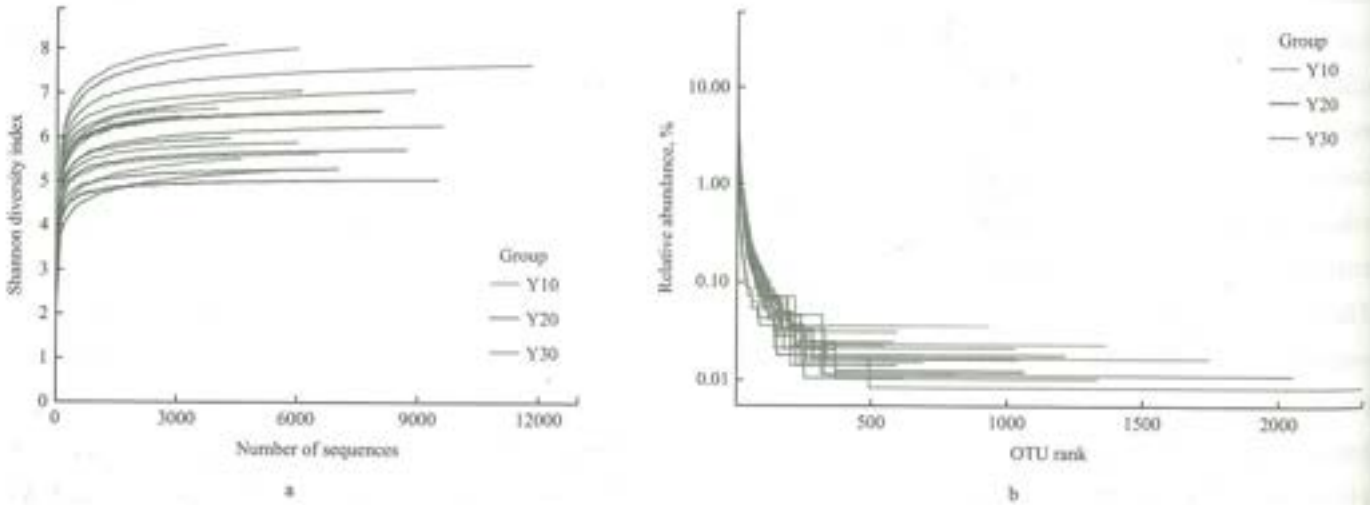

Figure 1 Shannon diversity curves (a) and rank-abundance curves (b)

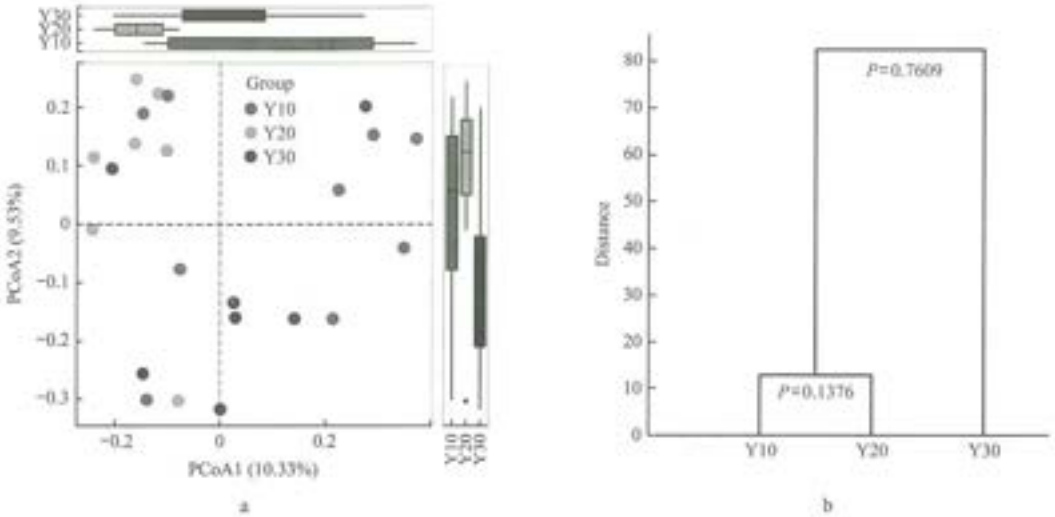

a b

Figure 2 Principal coordinate analysis (PCoA) plots (a) and group clustering calculated with multivariate ANOVA (b) based on unweighted UniFrac distances from paocai brine samples of different age groups

3.4 Comparison of bacterial compositions between sample groups

The sequence reads were assigned to 15 bacterial phyla, 232 genera and 378 species, phyla Firmicutes and Proteobacteria, genus *Lactobacillus* (*Lb.*), and species *Lb. acetotolerans* and *Lb. brevis* were the dominant taxa in paocai brine samples (Figure 3). Other prevalent genera and species with average relative abundance over 1% are also shown in Figure 3. It is obvious that there were large variations in the relative abundance of the predominant taxa in individual sample. The results of the Kruskal-Wallis test demonstrated that there was no significant difference between different groups in these taxa (P>0.05). Opportunistic pathogen bacteria *Enterobacter cloacae*, *Kluyvera cryocrescens*, and *Serratia marcescens*, were detected in all groups. Samples Y10-01, Y20-07, Y30-01, and Y30-03 were dominated by non-LAB bacteria. In particular, Y30-01 harbored high relative abundance of the uncommon aerobic bacteria *Stenotrophomonas (Ste.) geniculate* (22.76%) and *Ste. maltophilia* (21.63%), whose relative abundance was extremely low in the other samples (not visible in Figure 3b). Moreover, *Ste. maltophilia* is a multiple-drug-resistant organism which can cause various infections in humans (Brooke, 2012), indicating the safety risk of sample Y30-01. The high abundance of health threats or undesired bacteria in some samples may be related to poor management of HMPB in some local households. These results also indicated that not the longer age of HMPB, the better bacterial profiles in it. Daily maintenance of the paocai jar and brine, such as examination of air tightness and regular utensil cleaning, is essential to keep the HMPB in a good condition. Regarding the health and safety aspects, once odd flavor or spoilage occurs in the brine, measures should be promptly taken (e.g. add spirits or use new brine).

3.5 Differential KEGG genes and pathways of bacterial community in HMPB groups of different age

When Y10 compared with Y20 group, the KOs detected in the two groups were assigned to 221 KEGG pathway, 31 pathways of which had Z value greater than 1.6; Y20 group contained most (19) enriched pathways, while only one enriched pathway in the Y10 group. When Y10 compared with Y30 group, the KOs of the two groups were assigned to 219 KEGG pathways, 30 pathways of which had Z value greater than 1.6; Y30 group also had 19 enriched pathways while Y10 group had only one. When Y20 compared Y30 group, the KOs of the two groups was also assigned to 219 KEGG pathways, 24 pathways of which had Z value greater than 1.6; Y20 group has three enriched pathways, and Y30 group had one. As shown in Table 3, the enriched pathways in the Y10 group were less than the other two groups and only D-alanine metabolism pathway was enriched in Y10 group. There were 16 pathways in both Y20 and Y30 groups more abundant than Y10 groups, which were arginine and proline metabolism, flagellum assembly, tricarboxylic acid cycle, biotin metabolism, butyric acid metabolism, lipopolysaccharide biosynthesis, sulfur repeat system, porphyrin and chlorophyll metabolism, fluorobenzoate degradation,

nitrotoluene degradation, bacterial secretion system, valine, leucine and isoleucine biosynthesis, geranium degradation, two-component system, bacterial chemotaxis and glyoxylic acid, and dicarboxylic acid metabolism.

Although the bacterial α and β diversity of Y10, Y20 and Y30 groups were not significantly different, so as the relative abundance of dominant bacteria (P<0.05), there were some differences in pathways between the age groups. By comparing the enriched pathways in the three groups, Y30 and Y20 groups had more enriched metabolic pathways than Y10 group, such as glycine, serine and threonine metabolism, arginine and proline metabolism, glyoxylic acid and dicarboxylic acid metabolism, butyric acid metabolism, tricarboxylic acid cycle, valine, leucine and isoleucine biosynthesis. These carbohydrate and amino acid metabolic pathways are likely to have an impact on the flavor of HMPB as organic acids and amino acids are essential taste compounds in the brine. These results indicated that it is likely both the longer age of HMPB samples and more carbohydrate metabolic pathways in Y20 and Y30 groups contributed to higher TA compared with Y10 group.

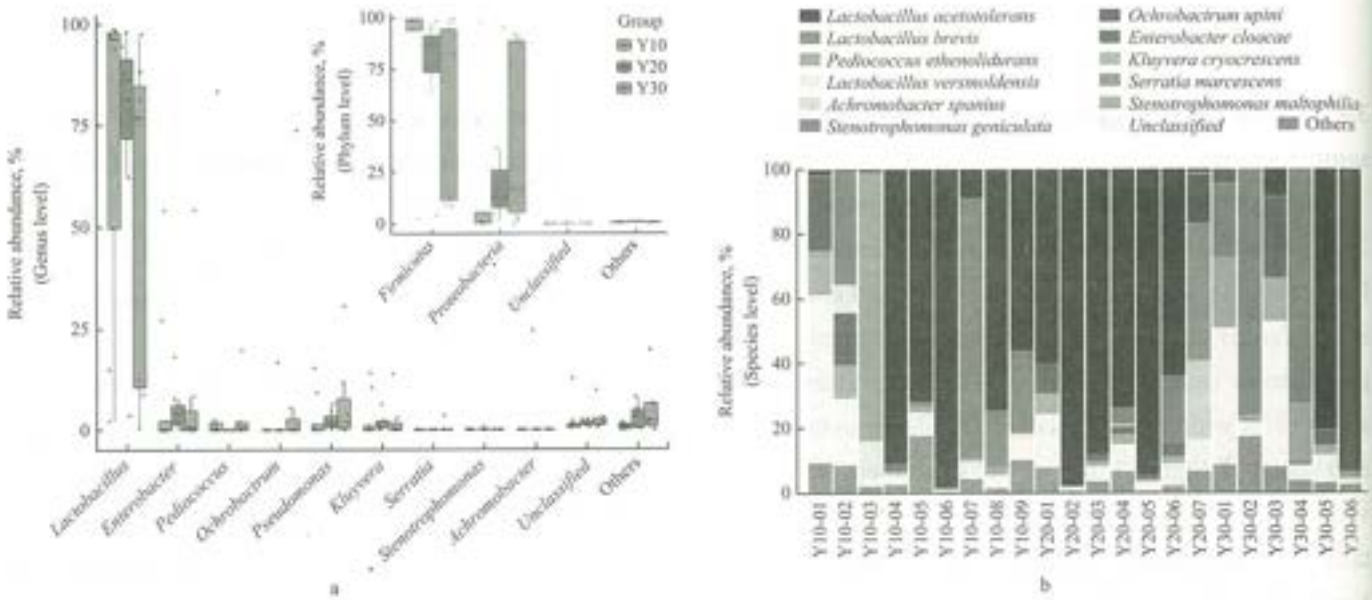

Figure 3 Bacterial compositions of different age groups of home-made paocai brine at (a) phylum and genus level, and (b) species level

Table 3 Significant differential KEGG pathway in Y10, Y20, or Y30 groups of paocai brine samples

Group	KEGG pathways	Z score	KO proportion, %	Differential pathway
				Pathways that were enriched in Y10 group
	ko00473	2.03	80.00	D-Alanine metabolism |Metabolism of other amino acids |Metabolism
				Pathways that were enriched in Y20 group
	ko00650	2.84	20.00	Butanoate metabolism |Carbohydrate metabolism |Metabolism
	ko00780	2.10	18.75	Biotin metabolism |Metabolism of cofactors and vitamins |Metabolism
	ko04122	2.51	17.65	Sulfur relay system |Folding, sorting and degradation |Genetic Information Processing
	ko00330	2.56	17.58	Arginine and proline metabolism |Amino acid metabolism |Metabolism
	ko00020	2.51	17.07	Citrate cycle (TCA cycle) |Carbohydrate metabolism |Metabolism
	ko00195	4.82	15.38	Photosynthesis |Energy metabolism |Metabolism
	ko03070	7.30	12.68	Bacterial secretion system |Membrane transport |Environmental Information Processing
Y10 vs Y20	ko00630	3.18	12.68	Glyoxylate and dicarboxylate metabolism |Carbohydrate metabolism |Metabolism
	ko02020	7.95	12.42	Two-component system |Signal transduction |Environmental Information Processing
	ko00910	2.41	7.50	Nitrogen metabolism |Energy metabolism |Metabolism
	ko00540	3.01	6.06	Lipopolysaccharide biosynthesis |Glycan biosynthesis and metabolism |Metabolism
	ko00860	3.28	5.19	Porphyrin and chlorophyll metabolism |Metabolism of cofactors and vitamins |Metabolism
	ko02030	4.58	3.85	Bacterial chemotaxis |Cell motility |Cellular Processes
	ko02040	5.44	0.00	Flagellar assembly |Cell motility |Cellular Processes
	ko00633	3.10	0.00	Nitrotoluene degradation |Xenobiotics biodegradation and metabolism |Metabolism
	ko00281	2.75	0.00	Geraniol degradation |Metabolism of terpenoids and polyketides |Metabolism
	ko00290	2.69	0.00	Valine, leucine and isoleucine biosynthesis |Amino acid metabolism |Metabolism
	ko00364	1.92	0.00	Fluorobenzoate degradation |Xenobiotics biodegradation and metabolism |Metabolism

Group	KEGG pathways	Z score	KO proportion, %	Differential pathway
				Pathways that were enriched in Y10 group
	ko00473	2.20	80.00	D-Alanine metabolism |Metabolism of other amino acids |Metabolism
				Pathways that were enriched in Y30 group
	ko00260	2.00	18.03	Glycine, serine and threonine metabolism |Amino acid metabolism |Metabolism
	ko04122	2.61	17.65	Sulfur relay system |Folding, sorting and degradation |Genetic Information Processing
	ko00720	1.84	16.42	Carbon fixation pathways in prokaryotes |Energy metabolism |Metabolism
	ko00330	3.07	15.22	Arginine and proline metabolism |Amino acid metabolism |Metabolism
	ko00630	3.65	14.08	Glyoxylate and dicarboxylate metabolism |Carbohydrate metabolism |Metabolism
	ko00650	3.05	13.56	Butanoate metabolism |Carbohydrate metabolism |Metabolism
	ko03070	7.72	11.27	Bacterial secretion system |Membrane transport |Environmental Information Processing
Y10 vs Y30	ko00860	3.31	10.39	Porphyrin and chlorophyll metabolism |Metabolism of cofactors and vitamins |Metabolism
	ko02020	7.22	10.09	Two-component system |Signal transduction |Environmental Information Processing
	ko00020	3.08	9.76	Citrate cycle (TCA cycle) |Carbohydrate metabolism |Metabolism
	ko00364	1.61	8.33	Fluorobenzoate degradation |Xenobiotics biodegradation and metabolism |Metabolism
	ko00290	2.93	6.67	Valine, leucine and isoleucine biosynthesis |Amino acid metabolism |Metabolism
	ko00540	3.89	6.06	Lipopolysaccharide biosynthesis |Glycan biosynthesis and metabolism |Metabolism
	ko02030	5.06	3.85	Bacterial chemotaxis |Cell motility |Cellular Processes
	ko02040	5.56	0.00	Flagellar assembly |Cell motility |Cellular Processes
	ko00281	2.83	0.00	Geraniol degradation |Metabolism of terpenoids and polyketides |Metabolism
	ko00633	2.43	0.00	Nitrotoluene degradation |Xenobiotics biodegradation and metabolism |Metabolism
	ko00780	2.20	0.00	Biotin metabolism |Metabolism of cofactors and vitamins |Metabolism
				Pathways that were enriched in Y20 group
	ko02060	5.88	91.30	Phosphotransferase system (PTS) |Membrane transport |Environmental Information Processing
Y20 vs Y30	ko00195	5.04	84.62	Photosynthesis |Energy metabolism |Metabolism
	ko00051	2.38	83.08	Fructose and mannose metabolism |Carbohydrate metabolism |Metabolism
				Pathways that were enriched in Y30 group
	ko02040	5.28	16.67	Flagellar assembly |Cell motility |Cellular Processes

Note: the table only includes pathways that have a high (≥80%) or a low (≤20%) proportion of KO of gene abundance, indicating that these pathways are either enriched in the former or latter sample group, respectively.

4 Conclusion

To our knowledge, this is the first report on the comparison of bacterial diversity in home-made paocai brine of different age (10+ years) based on SMRT sequencing. Our results revealed that for aged, home-made paocai brine, the bacterial diversity or compositions may not be classified by age. But home-made paocai brine with longer age likely have more bacterial metabolic pathways which may affect the paocai flavour.

Acknowledgement

This work was supported by the Earmarked Fund for Modern Agro-industry Technology Research System [grant numbers CARS-37].

[References]

[1] Brooke, J. S. 2012. Stenotrophomonas maltophilia: an emerging global opportunistic pathogen. *Clinical Microbiology Reviews*, 25 (1): 2–41.

[2] Cao, J., J. Yang, Q. Hou, H. Xu, Y. Zheng, H. Zhang, and L. Zhang. 2017. Assessment of bacterial profiles in aged, home-made Sichuan paocai brine with varying titratable acidity by PacBio SMRT sequencing technology. *Food Control*, 78: 14–23.

[3] Cao, Z., H. Pan, H. Tong, D. Gu, S. Li, Y. Xu, C. Ge, and Q. Lin. 2015. In vitro evaluation of probiotic potential of *Pediococcus pentosaceus* L1 isolated from paocai - a Chinese fermented vegetable. *Annals of Microbiology*, 66(3): (3): 963–971.

[4] Chen, G., W. Yu, Q. Zhang, P. Song, B. Zhang, Z. Liu, J. You, and H. Li. 2014. Research of Sichuan Paocai and Lactic Acid Bacteria. *Advance Journal of Food Science and Technology*, 6(1): 1–5.

[5] Fang, R., Y. Dong, F. Chen, and Q. Chen. 2015. Bacterial Diversity Analysis during the Fermentation Processing of Traditional Chinese Yellow Rice Wine Revealed by 16S rDNA 454 Pyrosequencing. *Journal of Food Science*, 80(10): M2265–M2271.

[6] Hou, Q., L. Y. Kwok, Y. Zheng, L. Wang, Z. Guo, J. Zhang, W. Huang, Y. Wang, L. Leng, H. Li, and H. Zhang. 2016. Differential fecal microbiota are retained in broiler chicken lines divergently selected for fatness traits. *Scientific Reports*,

6: 37376.

[7] Jung, J. Y., S. H. Lee, and C. O. Jeon. 2014. Kimchi microflora: history, current status, and perspectives for industrial kimchi production. *Applied Microbiology and Biotechnology*, 98(6): 2385–2393.

[8] Langille, M. G., J. Zaneveld, J. G. Caporaso, D. McDonald, D. Knights, J. A. Reyes, J. C. Clemente, D. E. Burkepile, R. L. Vega Thurber, R. Knight, R. G. Beiko, and C. Huttenhower. 2013. Predictive functional profiling of microbial communities using 16S rRNA marker gene sequences. *Nature Biotechnology*, 31(9): 814–21.

[9] Li, M., Di. Yang, L. Mei, L. Yuan, A. Xie, and J. Yuan. 2014. Screening and characterization of purine nucleoside degrading lactic acid bacteria isolated from Chinese sauerkraut and evaluation of the serum uric acid lowering effect in hyperuricemic rats. *PloS one*, 9(9): e105577.

[10] Liu, S., Y. Han, and Z. Zhou. 2011. Lactic acid bacteria in traditional fermented Chinese foods. *Food Research International*, 44(3): 643–651.

[11] Lynch, M. D., and J. D. Neufeld. 2015. Ecology and exploration of the rare biosphere. *Nature Reviews Microbiology*, 13(4): 217–29.

[12] Mosher, J. J., E. L. Bernberg, O. Shevchenko, J. Kan, and L. A. Kaplan. 2013. Efficacy of a 3rd generation high-throughput sequencing platform for analyses of 16S rRNA genes from environmental samples. *Journal of microbiological methods*, 95(2): 175–181.

[13] Xia, J. 2014. Dynamic Changes of Lactic Acid Bacteria Flora during the Fermentation. Master, Sichuan Agricultural University.

[14] Xiong, T., Q. Guan, S. Song, M. Hao, and M. Xie. 2012. Dynamic changes of lactic acid bacteria flora during Chinese sauerkraut fermentation. *Food Control*, 26(1): 178–181.

[15] Xiong, T., J. Li, F. Liang, Y. Wang, Q. Guan, and M. Xie. 2016. Effects of salt concentration on Chinese sauerkraut fermentation. *LWT - Food Science and Technology*, 69: 169–174.

[16] Xiong, T., F. Peng, Y. Liu, Y. Deng, X. Wang, and M. Xie. 2014. Fermentation of Chinese sauerkraut in pure culture and binary co-culture with Leuconostoc mesenteroides and *Lactobacillus plantarum*. *LWT-Food Science and Technology*, 59(2): 713–717.

[17] Yu, J., W. Gao, M. Qing, Z. Sun, W. Wang, W. Liu, L. Pan, T. Sun, H. Wang, N. Bai, and H. Zhang. 2012. Identification and characterization of lactic acid bacteria isolated from traditional pickles in Sichuan, China. *Journal of General and Applied Microbiology*, 58(3): 163–172.

[18] Zhang, Q., G. Chen, W. Shen, Y. Wang, W. Zhang, and Y. Chi. 2016. Microbial safety and sensory quality of instant low-salt Chinese paocai. *Food Control*, 59: 575–580.

Experiment on mechanical properties of processing tomatoes and theoretical study of fruit-seedling separation

Du Xinwu[1], Ji Jiangtao[1*], Lv Huangzhen[2], Wang Shiguang[2], Yang Xulong[1]

(1. *College of Agricultural Equipment Engineering, Henan University of Science and Technology, Luoyang, 471003, China;*
2. *Chinese Academy of Agricultural Mechanization Sciences, Beijing 100083, China*)

Abstract: The working object of fruit-seedling separation mechanism is tomato vines after harvesting. In order to optimize the parameters of a fruit-seedling separation mechanism, in this paper, the physical and biological characteristics of tomato variety liger 87-5 were tested and obtained that the equatorial diameter of the tomatoes was among 27-51 mm, the vertical diameter was among 28-45 mm, and fruit weight was among 19-104 g. Since the pericarp hardness of tomatoes is related to fruit size and maturity, after pericarp hardness testing of the tomatoes, the transverse damage force of liger 87-5 was among 24.2-67.1 N, and vertical damage force was among 28.6-75.3 N, the average value of pericarp hardness was 2.86 kg/cm^2. The biological force between fruit and seedling should be overcome in separation, and test results showed that when the fruit angle was 90°, the maximum separating biological force was 15.8 N, the average transverse damage force of fruit was 46.9 N, and the vertical damage force was 55.2 N. The study can provide a theoretical basis for the design of fruit-seedling separation machinery.

Keywords: processing tomatoes; fruit-seedling separation; fruit damage force; fruit-seedling separation force

Citation: Du, X. W., J. T. Ji, H. Z. Lv, S. G. Wang, and X. L. Yang. 2017. Experiment on mechanical properties of processing tomatoes and theoretical study of fruit-seedling separation. International Agricultural Engineering Journal, 26(3): 221–226.

1 Introduction

The processing tomato variety liger 87-5 in China was selected in this study, because it has excellent growing, anti-crack, and anti-pressure properties, also tolerant to storage, outstanding in stress resistance and disease resistance. In all, it is a fine variety for mechanized harvesting (Liu et al., 2016 and Wang et al., 2015). Liger 87-5 variety is widely cultivated, since it has practical significance as the research object. Fruit-seedling separation is a key point in the mechanized harvesting of liger 87-5 (Li et al., 2012 and Wang et al., 2015). In order to ensure smooth fruit-seedling separation, the design of mechanical structure should take pericarp hardness of the fruit into consideration to minimize fruit damage rate; at the same time, it should improve the fruit-seedling separation rate.

Received date: 2017-08-13 **Accepted date:** 2017-10-08

* **Corresponding author: Ji Jiangtao**, Professor, College of Agricultural Engineering, Henan University of Science and Technology. Email: jjt0907@163.com.

Related parameters of the biophysical characteristics of tomatoes were measured, and the measured data served as a reference for analyzing the mechanical process of fruit-seedling separation. During the separation process, in order to overcome the biological forces between the plant and the fruit, the tomatoes are subjected to the mechanical energy provided by the mechanical parts of the separation device, and finally fall off from the vine. The mechanical force of the fruit-seedling separation device and the biophysical properties of tomatoes as well as some other factors directly affect the fruit-seedling separation effect (Zhu et al., 2013).

2 Materials and method

In this paper, processing tomato variety liger 87-5 was selected as test variety, and the tomato cultivation base of Tianshan Agricultural Development Co., Ltd. located in Hutubi County of Xinjiang Changji Hui Autonomous Prefecture was selected as test field. One hundred seedlings of tomatoes were randomly selected from the test site for organization of the biophysical data. The whole plant of liger 87-5 was among 0.79-8.3 kg, and the

number of fruits per plant was between 21 and 122. Fruit weight was between 0.54 5.6 kg. Tomato fruit-seedling separation only deals with tomato vines which are harvested by a circular cutting machine (Qin, 2015). In the separation process, plant weight and number of fruits may affect the separation process, but the impact is not obvious. In the process of separation, it is necessary to consider the pericarp hardness of tomato fruit to optimize the design parameters of tomato fruit-seedling separation device (Liang, 2013). Since damage force of tomato fruit is an important index for tomato pericarp hardness, 200 tomatoes were randomly selected, and the fruit damage data are summarized in Table 1.

In the process of fruit-seedling separation, the effects of biomechanical factors were mainly taken into consideration.

The measurement items and instruments are:

(1) Vertical diameter, transverse: vernier caliper, the measuring range is 200 mm, the accuracy is 0.02 mm.

(2) Single fruit weight: electronic scale, the range is 5 kg, the accuracy is 1 g.

(3) Separation angle: angle ruler, the accuracy is 1 degree.

(4) Separation force: digital push pull HP-100, the range is 100N, the accuracy is 0.1N.

(5) Hardness: GY-4 digital hardness, the range is 1-50 kg, the accuracy is 0.5%.

The data of separation force are summarized in Table 2.

Table 1 Damage force data for tomato fruits

	Maximum value	Minimum value	Mean value (After removal of the maximum and the minimum values)
Transverse diameter, mm	52.6	27.3	43.3
Vertical diameter, mm	65	28.9	52.1
Single fruit weight, g	111	23	66.8
Transverse damage force, N	67.1	24.2	46.9
Vertical damage force, N	75.3	28.6	55.2

Table 2 Tomato fruit-seedling separation force

Mean value of transverse diameter, mm	Mean value of vertical diameter, mm	Mean value of fruit weight, g	Mean value of pericarp hardness, kg/cm^2	Angle, °	Separation force		
					Maximum value, N	Minimum value, N	Mean value, N
41.9	51.1	65.8	2.91	30	6.9	2.1	4.5
42.7	51.5	67.0	2.75	45	10.6	3.7	6.2
42.9	50.7	66.5	2.93	60	12.5	3.9	8.1
43.1	52.2	66.9	2.86	90	21.2	9.3	15.8

In measuring the data above, tomato vines were randomly selected from the test field to ensure the objectivity of the test. In measuring the damage force of tomato fruit, 200 tomatoes were divided into two groups for measuring transverse diameter and vertical diameter. The tomato fruits were placed on a steel plate of 10 mm in thickness, and they were pressed from above until they were broken; then the thrust on the gauge thrust was recorded in this process. One hundred sets of data were measured in each direction, the maximum and minimum values were removed and only the average was taken. In measuring the biological force in fruit-seedling separation, 40 tomato seedlings were randomly selected and divided into four groups of 10 seedlings. Then the biological force of the seedlings was measured at different angles respectively. In the test, 10 tomatoes with different shapes and different degrees of maturity were selected on the plant, and a total of 400 sets of data were obtained. In measuring biological force, first the fruit stems were pulled apart from an inclined angle, and the thrust on the force gauge was recorded; in measuring hardness, the tomato fruits were put on a steel plate of 10 mm in thickness, by holding the fruit by hand, the probe was inserted slowly into the fruit perpendicularly to the pericarp, and then the force on the hardness gauge was recorded.

3 Results and analysis

The double-power rotary and vibrating tomato fruit-seedling separation mechanism separates tomato fruit

from seedlings through its inertial vibrating working parts. Soviet experts obtained the fourth status below in Figure 1 through analysis of the tomato fruit separation process with a high-speed photography (Tan, 2012):

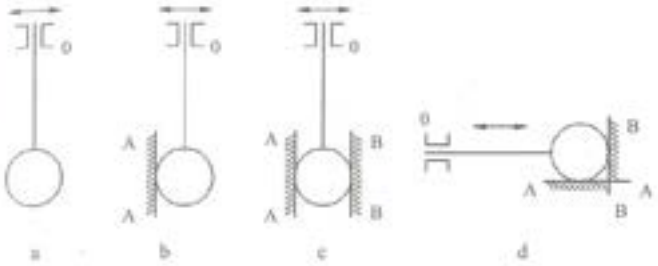

Figure 1 Four kinds of status in the process of fruit-seedling separation

3.1 Minimum impulse in fruit damage

Based on the analysis of the Soviet experts on the conveyor belt-vibrating sieve separation mechanism, in this paper, the roller-vibrating fruit-seedling separation mechanism was analyzed. First, the tomato seedlings with fruits were fed into the fruit-seedling separation device (Cao et al., 2009; Xiao, 2013). Assuming that the fruits collide with the vibration rod at an initial speed v_2, and the angle between its moving trajectory and coordinate axis was α; the vibration rod is in simple harmonic vibration at an initial speed of v_2, since the drum rotating speed is very low relative to vibration of the vibration rod, the rotating speed of the roller can be ignored; meanwhile, the slight movement relative to the coordinate system in theoretical analysis can also be ignored. The X axis was set to overlap with the center line through the fruit and vibrating rod, and the impact point is the coordinate origin O. When the fruits were fed into the separation mechanism, they collided with the vibrating rod, which was at maximum instantaneous speed. Under such circumstance, the collision could bring the greatest damage to the fruit. As the collision lasted for a very short period of time, it is assumed that the speed of the vibrating rod was not affected. When the fruit enters into the separation device, the vibration rod and tomato fruit collide, as is shown in Figure 2.

In such case, it is assumed that the positive pressure N was the same with the OX axis. Thus, the projection change of fruit velocity on this axis is the same as that of the collision of two semi-elastic objects along a straight line, namely:

$$u_{2x} = e(v_1 - v_{2x}) + v_1 \quad (1)$$

where, e is coefficient of restitution; u_{2x} is the projection of fruit velocity on X axis after collision, m/s; v_1 is the speed of a vibrating rod, m/s; v_{2x} is the projection of fruit velocity on X axis before collision, m/s.

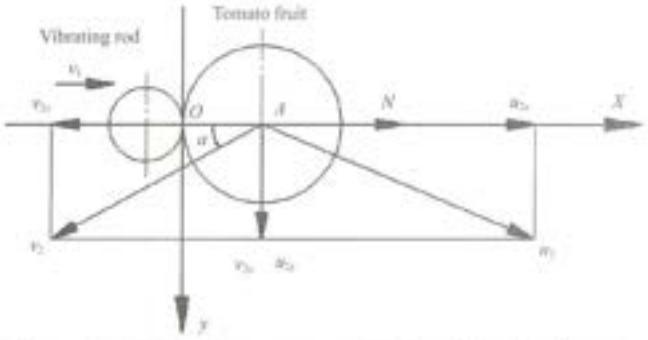

Figure 2 Collision between tomato fruits and the vibration rod

The velocity of Y axis is:

$$u_{2y} = v_{2y} = v_2 \sin\alpha \quad (2)$$

where, u_{2y} is the projection of fruit velocity on Y axis after collision, m/s; v_{2y} is the projection of fruit velocity on Y axis before collision, m/s; α is the angle between v_2 and X axis, rad.

The impulse on fruit at this time is:

$$I = m(u_{2x} - v_{2x}) = m(1+e)(v_1 + v_2\cos\alpha) \quad (3)$$

At this time, there are two kinds of possibilities for tomato breakage: first, the fruit might have been broken by the large impulse from the vibration rod; second, the fruits were crashed by the accelerated falling of the vibration rod, when the impulse is less than the direct blow to the fruit, so the impulse I_m by the vibration rod is the limiting value, namely the coefficient of restitution remains unchanged within the limiting value of impulse.

$$I_m = m(1+e)v_m = m(1+e)\sqrt{2gH_m} \quad (4)$$

where, H_m is the falling height of the fruit to the support surface, m. The fruit may be broken if the height is increased.

According to tests and experiments in mechanical harvesting, liger 87-5 with $H_m \geq 1000$ mm may easily get damaged by the vibration separation device of tomato harvesters, when vibration $H = 650$ mm in working. The most unfavorable condition for tomato fruit damage is the maximum speed of vibration rod in collision of fruit and the rod, namely, $v_1 = A\omega$, angle $\alpha = 0$, $v_1 = v_2$, and:

$$v_1 \leq \sqrt{0.5gH_m} \quad (5)$$

Put H_m=650 m into the Equation (5) and get

$v_1 \le \sqrt{0.5\times 9.8\times 0.65} = 1.78$ m/s.

Then put the maximum height H_m=1000 into the Equation (5) and get $v_1 \le \sqrt{0.5\times 9.8\times 1} = 2.21$ m/s

When A=0.05 m, the minimum angular frequency of vibration of the fruit separation device should be:

$$\omega_{min} \le \frac{v_1}{A} = \frac{1.78}{0.05} = 35.6 \text{ s}^{-1}$$

The maximum angular frequency is:

$$\omega_{max} \le \frac{2.21}{0.05} = 44.2 \text{ s}^{-1}$$

The minimum impulse for fruit damage obtained by the analysis above was 18.5 N·s. Such case of collision between the tomato fruit and the vibration rod was rare in the process of fruit-seedling separation. It was found that this was the main reason for fruit damage.

3.2 Minimum impulse in fruit-seedling separation

In the process of fruit-seedling separation, the separation force was the smallest when the fruit was in a free suspension status (Hao, 2015). At this time, the minimum impulse was provided by the fruit-seedling separation device. The analysis of tomato fruit separation process is shown in Figure 3.

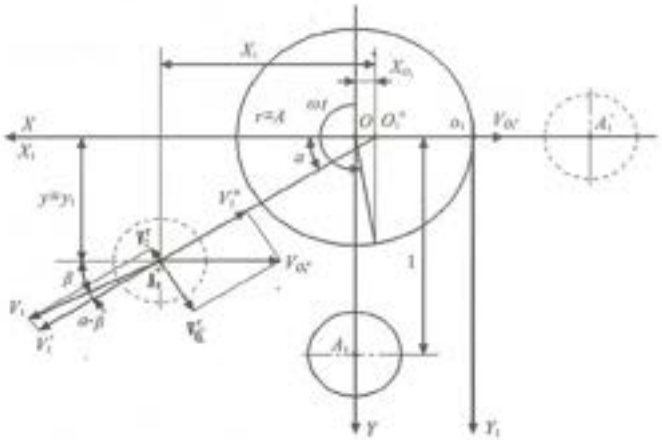

Figure 3 Modeling diagram of tomato fruit-seedling separation process

A fixed coordinate system XOY and transport motion coordinate system $X_1O_1Y_1$ were set. Set O_1 as the pendulum suspension point, and let O_1 represent the motion rule of the working surface, and get:

$$x_{o1} = A\sin\omega t \tag{6}$$

where, A is amplitude of oscillation, mm.

The equation of fruit gravity center is:

$$x = x_{o1} + x_1 \tag{7}$$

$$y = y_{o1} + y_1 \tag{7}$$

where, x_1 and y_1 are the coordinates of fruit gravity in the transport motion coordinate system. In an assumed case, y_{o1}=0, namely $y = y_1$.

When the pendulum vibration starting point deviates from the vertical angle $\varphi \ge 90°$, namely, it is in the horizontal position, then the velocity of the suspension point is:

$$\dot{x}_{o1} = A\omega\cos\omega t \tag{9}$$

The impulse at time of collision is:

$$I = m(v_1'' - v_1') \tag{10}$$

where, m is fruit weight, kg.

v_1' is the projection of fruit velocity on pendulum suspension line at the instant before collision, m/s;

v_1'' is the projection of suspension point on pendulum suspension line, m/s; Figure 3 shows that:

$$v_1' = v_1\cos(\alpha - \beta) \tag{11}$$

where, v_1 is the fruit velocity at the instant before collision, m/s; β is the angle between velocity vector v_1 and OX.

The modulus of velocity is:

$$v_1 = \sqrt{x^2 + y^2} = \sqrt{(A\omega)^2 + (gt_1)^2} \tag{12}$$

The direction of velocity vector was determined as:

$$\beta = arctg(\frac{dy}{dx}) = arctg(\frac{gt_1}{A\omega}) \tag{13}$$

And get:

$$v_1' = \sqrt{(A\omega)^2 + (gt_1)^2}\cdot \cos\{arctg[\frac{gt_1^2}{2(A\omega t_1 - 1 - A\sin\omega t_1)}] - arctg(\frac{gt_1}{A\omega})\} \tag{14}$$

Suppose that the connection of the suspension points is inelastic, the final velocity of the fruit is:

$$v_1'' = \dot{x}_{o1}\cos\alpha = A\omega\cos\omega t_1\cos[arctg(\frac{gt_1}{2(A\omega t_1 - 1 - A\sin\omega t_1)})] \tag{15}$$

Due to the short time of impulse occurrence, then suppose that the value and direction of the speed vectors v_1' and v_1'' in collision stay unchanged, then:

$$I = m[A\omega\cos\omega t_1\cos A' - \sqrt{(A\omega)^2 - (gt_1)^2}\cos(A' - B')] \tag{16}$$

where, $A' = arctg[\frac{gt_1^2}{2(A\omega t_1 - 1 - A\sin\omega t_1)}]$,

$B' = arctg(\frac{gt_1}{A\omega})$.

When the initial position $\varphi>90°$, namely, when the pendulum was in horizontal status, collisions may occur. At this time the minimum value of the impulse is:

$$I_{min}=2mA\omega \quad (17)$$

The results show that when the $A\omega = 1.78$ m/s, $A = 0.05$ m, $l = 0.05$-0.1 m, and the fruit weight $G = 0.066$ kg, the minimum separation impulse is 2.3 N·s.

At this time, the tomato fruits were in free suspension, which is the best status for tomato fruit-seedling separation. In the process of tomato fruit-seedling separation, normally, the tomato fruits are connected with the stems; there are few cases of free suspension; also there are few cases of firm grasp by the stem. In the test study, the status of tomato fruit is changing, due to the high frame of stem and leaf layer, the fruit position changes in the vibration process, and results in the situation stated above. Related test studies showed that the most appropriate feeding amount of tomato fruit is dependent on the variety, plant growth, the number of leaves, the biological force of fruit connection, and other factors.

2.2 Field test verification

In order to verify the theoretical conclusions of section 3, an experiment was carried out in Tianshan Agricultural Development Co., Ltd. located in Hutubi County of Xinjiang Changji Hui Autonomous Prefecture. According to the "Operating quality for tomato harvesters" (NYT 1824-2009), the no-load test was made after the prototype was installed, and test results and analysis results were contrast. Based on test results, the initial design parameters were adjust. The test table is shown in Figure 4.

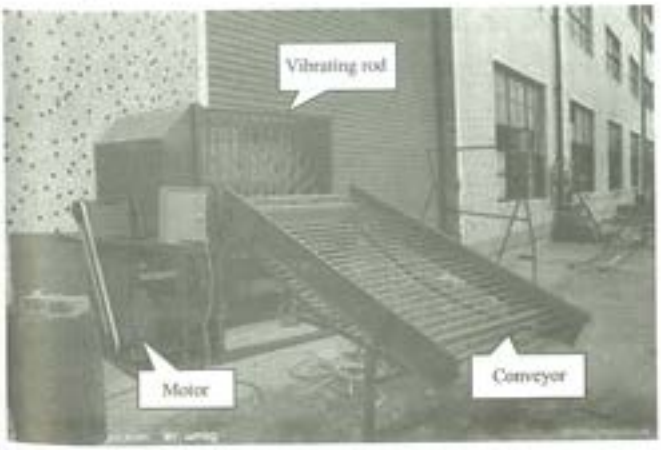

Figure 4 Test table of fruit-seedling separation

The experiments show that the separation rate of the separation device is more than 97%, and the breakage rate is less than 4%. The results show that the separation mechanism designed according to the theoretical model has good separation effect.

4 Conclusions

In this paper, the biophysical and mechanical properties of tomato seedlings were collected and analyzed by tests and modeling. The following results were obtained by the test: the average pericarp hardness of liger 87-5 was 286 kg/cm^2; the mean transverse damage force of fruit was 46.9 N, the mean value of vertical damage was 55.2 N, and the maximum biological force in separation was 15.8 N at 90°. The process of fruit-seedling separation of tomato fruits in vibration was analyzed theoretically, and the minimum impulse value of 18.5 N·s for damage, and the minimum impulse value of 2.3 N·s for separation were obtained. The results may provide the theoretical basis for the design and manufacturing of the fruit-seedling separation device in the future.

Acknowledgements

This research is supported by the Henan science and technology open cooperation project (No. 172102110016), and the Henan University of Science and Technology founds for Young Scholars (No. 2015QN004).

[References]

[1] Cao, J., W. Xu, X. Peng, and T. Yang. 2009. Design of the nearside divider of the tomato vine turning machine. *Journal of Shihezi University (Natural Science)*, 27: 261–264.

[2] Hao, Z. 2015. Experimental Study and design of dual-power rotary vibration type tomato separation. Beijing, China: Chinese Academy of Agricultural Mechanization Sciences.

[3] Li, C., Z.Kan, H.Tan,R. Sun,R. Liang, andY. Feng.2012. Movement process analysis on processing tomato fruit separation device. *Transactions of the Chinese Society for Agricultural Machinery*, 43(4): 66–69.

[4] Liang, R. 2013. Processing tomato fruit seedling separation device of hydraulic vibration system design study. Shihezi, China: Shihezi University.

[5] Liu, F., J. Zhu, J. Zhou, and C. Wang. 2016. Comparative study on nutritional quality of tomato varieties in Xinjiang. *Xinjiang Agricultural Sciences*, 53: 225–231.

[6] Qin, J. 2015. The separation mechanism of fruit processing tomato seedling based on double eccentric vibration generator.

Shihezi, China: Shihezi University.

[7] Tan, H. 2012. The experimental study of processing tomato separation device. Shihezi, China: Shihezi University.

[8] Wang, L., R.Liang, J.Qin,Z. Kan,C. Li, andX. Zhu.2015. Experiment of restitution coefficient of processing tomato seeds in collision models. *Transactions of the Chinese Society of Agricultural Engineering*, 2015(1): 23–28.

[9] Wang, L., B. Ran, Z. Kan, and C. Li. 2015. Experiment of restitution coefficient of processing tomato seeds in collision models. *Journal of Jiangsu University (Natural Science Edition)*, 36: 48–52, 69.

[10] Xiao, B. 2013. Research of the rotary roller-type fruit-stem separation device for processing tomato. Shihezi, China: Shihezi University.

[11] Zhu, X., C. Li, Z. Kan, J. Qin, and Y. Feng. 2013. Analysis of present development of fruit-seedling separation technology in tomato processing. *Journal of Hebei University of Science and Technology*, 34: 399–402.

A multi-attribute decision model for performance assessment of eco-village construction in China

Zhang Biao[1,2], Fu Zetian[1,2], Zhang Lingxian[1,3*], Liu Hailin[4]

(1. *China Agricultural University, Beijing 100083, China;*
2. *Beijing Laboratory of Food Quality and Safety, Beijing 100083, China;*
3. *Key Laboratory of Agricultural Informationization Standardization (Beijing), Ministry of Agriculture, 100083, China;*
4. *The General Office, the Government of Henan Province, Zhengzhou, 450003, China*)

Abstract: The eco-village is an idealized model for the establishment of internationally sustainable human settlements. To evaluate the performance of eco-village construction in China, this paper presents an evaluation index system of eco-village construction. It includes the six secondary indices, such as economic development, environmental hygiene, pollution control, resource protection and utilization, sustainable development and public participation, and 15 tertiary indices, and a method of eco-village construction utilizing multi-attribute decision models (MADM) of the Catastrophe Progression Method (CPM) and Analytical Hierarchy Process AHP method were constructed based on Capacity Index (CI) for comprehensive performance assessment. The comprehensive assessment result shows that the evaluation index system for eco-village construction can successfully assess and ensure village-level sustainability is attained in China, and can provide a beneficial reference framework for eco-villages elsewhere.

Keywords: eco-village construction, evaluation index system, performance assessment, multi-attribute decision models, sustainable rural development

Citation: Zhang, B., Z. T. Fu, L. X. Zhang, and H. L. Liu. 2017. A multi-attribute decision model for performance assessment of eco-village construction in China. International Agricultural Engineering Journal, 26(3): 227–237.

1 Introduction

The eco-village movement is a worldwide phenomenon that has arisen in response to the effects of the modern lifestyle on both our social and ecological environments. This movement is of particular interest and potential relevance in the United States, the country with by far the highest per capita consumption of resources (Kirby, 2003). Planning for the eco-village at Ithaca (EVI) began in 1991 as a group of individuals and families began meeting to plan a demonstration community that would challenge the existing social mode and offer a new model for sustainable development. The goal of the constructed eco-village at Ithaca is to create a "socially harmonious, economically viable and ecologically sustainable settlement that will demonstrate that human beings can live cooperatively with each other and with the natural environment" (Kirby, 2003).

The "eco-village" is a critical concept for the international establishment of sustainable human settlements (Dichristian, 1996), addressing it from an integrated perspective in trying to find sustainable solutions that can be managed locally, where farmers can take active part in research and in finding options to improve their livelihoods. The eco-village concept lies close to the UN Millennium Project (Sanchez et al., 2007) and aims at making a contribution to this program. Eco-construction refers to the application of ecological principles to the development of human ecosystems in order to achieve sustainability. It consists of three components: ecological engineering, ecological institutional reestablishment and ecological cultural remolding.

Received date: 2017-06-25 **Accepted date:** 2017-08-15

* **Corresponding author: Zhang Lingxian,** Professor, Ph.D. China Agricultural University, Beijing 100083, China. Email: zhanglx@cau.edu.cn.

In the 1990s', developed countries began to establish and study eco-villages due to the issues arising from over-expanded populations in cities, the exhaustion of non-renewable resources and deteriorating eco-environment. The eco-villages of European and North American countries are mainly designed for urban residents who are willing to live in the suburbs, containing advanced "green" houses and eco-technologies. In Japan, the eco-villages also present a solution for reviving rural areas (Liu et al., 2005). Since 1980, a vigorous campaign for demonstrating eco-construction has appeared in China and many eco-polis, eco-counties, eco-villages as well as eco-families have sprung up all over the country (Hu and Wang, 1998).

In fact, the eco-village is a form of ecological system composed of society, economy and nature. It is important to develop a framework of evaluation at the ecological level for eco-village construction in order to promote the sustainable development of rural areas. At a national level, an ecological level evaluation should establish an eco-environmental evaluation index system, and assess the ecological condition of certain regions from the perspective of ecological improvement and environmental protection, in order to bring about unified eco-environment programming and legal management. At the same time, the ecological level evaluation has been the main content of the management regulation of national environmental examining. Currently, there are imminent demands for ecological evaluations of ecological demonstration zones, ecological city and eco-village construction in China. An eco-village is an idealized model to achieve the sustainable rural development. To assess the performance of rural ecological planning, construction and management, the index and method of eco-village evaluation becomes the primary source of evidence. However, research of eco-village construction both in China and overseas are now at an exploratory stage given that there is no perfect evaluation system and method of eco-village construction.

Therefore, this paper promotes an evaluation index system of eco-village construction, based on the concept definition, characteristic analysis of an eco-village and the national criterion for the eco-village construction issued by Ministry of Environmental Protection of China (MEPC). Synchronously, the aim of the present study was to develop multi-attribute decision models (MADM) that assessed the sustainable developmental performance of eco-village construction utilizing the Analytical Hierarchy Process (AHP) and Catastrophe Progression Method (CPM) based on Capacity Index (CI). The remainder of this paper is organized as follows: Section 2 sets out the concept of eco-villages and the survey of eco-village construction. Section 3 puts forward and explains an evaluation index system and evaluation method of eco-village construction utilizing the AHP and CPM based on CI. Section 4 describes the application of the evaluation method of eco-village construction, and presents the results of the case analysis. In Section 5 the conclusions are provided.

2 The background in the eco-village construction

2.1 The concept of eco-villages

2.1.1 The origin of eco-villages

Early in the 1990s, some developed countries had reflected on environmental degradation, excessive consumption of non-renewable resources, habitat pollution and destruction and unsustainable life styles. In June 1996, the U.N. convened the second Conference on Human Settlements (HABITAT II) to discuss that how people should maintain sustainable settlements on the earth, protect the environment and the future generations, thereby stimulating subsequent research and development of the eco-village concept, and giving rise to an burgeoning world-wide eco-village movement sprang in both developed and developing countries .

The work of Robert C. Gilman was important in giving definition to the eco-village movement and shaping the direction of the Global Eco-village Network. In 1991, the Gilman co-authored Eco-Villages and Sustainable Communities, a seminal study of eco-villages for Gaia Trust. Also in 1991, Gilman, who was publisher

of the magazine In Context, wrote an article entitled "The Eco-village Challenge" that set out a definition of an eco-village as a: "human-scale, full-featured settlement, in which human activities are harmlessly integrated into the natural world, in a way that is supportive of healthy human development and can be successfully continued into the indefinite future". This was to become the standard definition on which the eco-village movement was founded and is still considered by many to be the most authoritative (Gilman, 1991). Through his investigation on the Ithaca eco-villages, Kirby (2003) found that "human beings can live cooperatively with each other and with the natural environment". Hence the eco-villages model encompasses complex sets of relations, including those between human beings and the natural landscape, artificial landscape, within the community itself, contact between individuals and contact between generations.

The research also showed that the eco-villages were not simply about advocating the maintenance of a natural landscape without any changes in the actions of human beings, but emphasized in eco-village construction the need for material recycling, economic development and ecological balance promoting social progress, natural harmony and stability. Economic development is main driver of the whole ecological system, and social progress implies improvement of settlement environment, enhancement of management level and population quality.

From the late 1970s, the national scholars had advocated the concepts of ecological balance and ecosystem to guide agricultural research, and gradually perfected the basic ideas and practical implementation of Chinese Ecological Agriculture. The concept of the eco-village in China emerged in the context of ecological agriculture in rural areas. At present, eco-village is generally considered as part of an agricultural ecosystem in China, which makes full use of natural resource and accelerates material recycling and energy conversation in natural or administrative villages in order to achieve ecological balance, economic development and social benefit together in the agricultural ecological system. In the practice there have been numerous eco-village modes such as "planting-breeding-processing", "four-in-one", "biogas utilization" and so on, which indicated that the development of ecological agriculture was integrally part of the construction and operation of the eco-villages. Furthermore, a rural area is not only an agricultural ecosystem but also a compound system combining both the agricultural and human ecosystems. In American and European eco-villages , the ethos was more inclined to the religious spiritualization, attaching importance to the landscape of the of rural area, aesthetic values and life-styles, to the heterogeneity of appearance and utilization of natural resources of the buildings to conserve energy and water, environmental greening and re-cyclable material (Yang, 2000). Hence there are a great of differences in the value orientations between the concept eco-villages in China and elsewhere in western countries, which shows that the content of 21st century. Eco-villages should contain not only ecological agriculture but also ecological dwelling houses, a pleasant rural landscape, and good social relationships (Su et al., 2004).

Sustainable development, especially from the viewpoint of harmonizing and planning the city zone and rural area as a whole, is now at the core of 21st century developmental thinking in China. In spite of the process of integration of town and country accelerating and rural infrastructure changing fundamentally, the construction of the eco-village still remains the primary developmental orientation of 21st century villages, which can not only accelerate the process of integration of town and country but also show clearly the developmental direction to better integrate them. Whereas, the eco-village is a historical and developmental concept arising out of different requirements in different periods, the content of the eco-village is more and more extensive (Su et al., 2004).

2.1.2 The definition of eco-village

There is, at this time, no generally agreed definition of an eco-village. This paper argues that the eco-village is an ideal model for the rural areas to accomplish sustainable development, which is an ecosystem making

full use of natural resource in a natural village or an administrative area, enhancing material recycling and energy transformation to achieve the synchronous and synergistic development of ecological, economic and social benefits. Eco-village development utilizes ecological economic theory and system engineering methods to change production and consumption behaviour and approaches to decision making and administration to draw on all useful potential resources in rural areas within the carrying capacity of the rural ecosystem (Li et al., 2007).

The basic conditions to be satisfied in the eco-village construction are: a) planning according to the general demands of regional environmental planning with a scientific program, rational layout, tidy rural surroundings, green areas surrounding the houses and roadside, sanitary water and atmosphere; b) villagers are able to follow the rules and regulations of environmental protection consciously aware of the its need and of avoiding possibilities of environment pollution; c)local economic development accords with national industrial policy and environmental protection policy; d) display and signage of rural regulations and environmental publicity to advocate the ecological civilization.

2.2 The survey of eco-village construction

Eco-construction as a scientific concept was explicitly put forward in 1987. It originated from the Chinese cultural tradition of agriculture in the very early ancient period and has been spontaneously applied all over the country for several thousands of years in China (Dumreicher, 2008). It refers to the application of ecological principles to develop human settlement in harmony with its environment. Eco-construction consists of three components: eco-engineering construction, eco-institutional construction and eco-cultural construction. Eco-construction presents a conceptual framework for China to achieve strugglingly local or regional sustainable development (Wang, 1990). As China started to redirect its steps towards the profound transition from planned to market economy in the early 1980s, a vigorous campaign for Ecological Demonstrative Rebuilding for Sustainable Settlements (EDRS) took place and many projects of ecopolis, eco-counties, eco-villages, as well as eco-families, were initiated and carried out across the country, these EDRS projects were aimed at applying the principles of ecology to the practice of local development and to explore further the specific operational approaches to achieve local sustainability (Wang and Hu, 1994; Zhang et al., 2007).

The first application of the concept of eco-village is in the report "eco-village and sustainable society" wrote by Robert Gilman from Danish. In 1991, an eco-village organization, the Gaia investment trust fund, was set up in Denmark. From then eco-villages began to spread gradually across the globe, where experts in agriculture, ecology and architecture collaborated spontaneously in rural areas, and gave attention to protecting problems of the economic, ecological and cultural heritage in order to advocate establishing a sustainable developmental society. Across the world, there are many well-known eco-villages, such as Bramfeld in Germany, the Eco-Tribe village in Netherlands, Tuggelite eco-village in Sweden, Earthaven eco-village in USA and Gaia eco-village in Argentina (Yang, 2000).

Chinese eco-villages developed initially in the late 1970s and early 1980s. As the rural areas relied mainly on agricultural production in China, the eco-village developed gradually following by the construction of ecological agriculture. "The eco-village is an agricultural ecosystem, which make full use of natural resource in a natural village or an administrative area, and accelerate material recycling and energy transformation to achieve synchronous development of ecology, economy and social benefit", is a viewpoint that Chinese scholars approve generally. For example, Liu Minying village in the Daxing district of Beijing city was voted one of the "500 best global environmental protection" by the United Nations Environment Programme in 1986, and awarded the title of "the first village of ecological agriculture in China" (Zhang and Ouyang, 2007). The early construction of eco-villages in China paid more attention to the practical model and methods of production, such as the organic agricultural methods, planting and breeding

projects, material and energy re-cylcing projects and the diagnosis of the agricultural ecosystem. Hence Chinese eco-village planning, in contrast to many foreign urban and suburban eco-villages, just focused on the establishment of organic agriculture, merely referring incidentally to the program of village spatial arrangement, land resource protection and settlement design. At present, the concept of eco-village in China is narrowly limited not only to the rural areas in the scope but also to the agricultural economic system in the eco-village construction (Yang 2000).

3 The evaluation methodology for eco-village construction

MADM evaluate alternatives to determine the best or better rated one according to decision-making goals. MADM are based on a hierarchical decomposition of the problem, where the target goal is decomposed into sub-concepts (represented by aggregate attributes) and finally to a finite set of (measurable) basic attributes. Basic-level descriptions of alternatives are gradually aggregated into the values of higher level attributes, until a final evaluation of each alternative is eventually obtained at the target (root) attribute (Bohanec et al., 2008). Many methodologies exist for MADM (Aguarón and Moreno-Jiménez, 2003; Korhonen and Voutilainen, 2006). In ecological modeling problems, these are often used to represent and combine indicators, evaluate alternatives and provide decision support in general. In some recent applications, MADM methods were used for decision support in land-use planning (Ananda et al., 2008), sustainable agriculture, eco-industrial development (Fang, Côté, Qin, 2007), and economic and ecological assessment of genetically modified crops (Bohanec et al., 2008).

Any environmental or ecological evaluation methodology should be objective, comprehensive and feasible. The central aim of evaluation of eco-villages is to improve their overall sustainable development. Therefore, this paper takes overall sustainable development as the main objective in evaluating the eco-village. The comprehensive capacity of sustainable development of an eco-village is influenced by many factors, and hence the evaluation system is multivariate, requiring a range of indices with appropriate weights in their construction. Therefore, this paper proposes an evaluation index system and evaluation method of eco-village construction utilizing the AHP and CPM method.

3.1 The evaluation index system of eco-village construction

In general, the improvement of ecological environmental evaluation index indicates that the research on sustainable development has evolved gradually from the exploration of individual, single attribute or single subject to the investigation of multi-dimensional, multi-level, multi-subjects system of society, economy and ecological environment, while the evaluation methods have changed from the traditional statistical analysis of the society and economy and environmental monitoring to the comprehensive evaluation of the multiple methods, multi-scale integration. As every system with the ecological environmental function is a complex composed of the multiple variables, there could be therefore a large and complicated index system on the description and evaluation of sustainability constitute, which could possess the function of description, evaluation, explanation, early warning and decision-making. It should reflect the developing speed and trends of every eco-environmental function and system in the time dimension, the integral distribution functions in the space dimension, the function strength and dimension in quantity, the function structure in layers. Of course, the evaluation system for an eco-village mainly embodies the condition of its rural economy, environment, ecology and society in the context of the degree of sustainability of its development (Li et al., 2007).

Based on the national criterion for the eco-village construction issued by MEPC, this paper presents the evaluation index system for the eco-village construction, which includes the 6 types (secondary indices) of the economic development, environmental hygiene, pollution control, resource protection and utilization, sustainable

development and public participation, and 15 tertiary indices (Table 1).

Table 1 The evaluation index system for the eco-village construction

Primary index	Secondary index	Tertiary index
Comprehensive capacity of sustainable development for an eco-village	Economic development	Per capita annual net income of rural residenter
	Environmental hygiene	Rate of health living drinking water
		Coverage rate of household sanitary toilets
	Pollution control	Pointing clean-up & deposit rates of living wastes (or Sound treatment rate for living wastes)
		Cleansing rate for living sewage
		Eligibility rate for the discharge of industrial pollutants
	Resource protection and utilization	Penetration rate of clean energy
		Recovery rate of plastic film
		Comprehensive utilization rate of crop straw
		Comprehensive utilization rate of wastes from large-scale integrated livestock and poultry
	Sustainable development	Coverage rate of vegetation
		Percentage of non-pollution, green, organic agricultural products base
		Average amount of fertilizer and pesticides application
		Content of farmland soil organic matter
	Public participation	Satisfaction degree of the villagers to environmental protection

Notes: The "village" referred in the national criterion for the eco-village construction issued by MEPC means the administrative village established according to the state institutions concerned.

3.2 Performance assessment model based on CPM

Catastrophe progression method is used to decompose the general objective of evaluation into a multi-level structure, and calculate from bottom to top by normalization formula to obtain the membership function (the evaluation result). The evaluation objective is divided into multiple levels, arranged in a hierarchy tree, and the original data only requires knowing the bottom index data. Relatively important indicators from the same layer are put in front, avoiding the weight determination and reducing the subjectivity.

3.2.1 Common catastrophe types

After constructing the index system of hierarchy structure, it is necessary to change the hierarchical structure model into mutation progression model according to the theory of catastrophe progression. The type of mutation model is determined according to the control variables and the number of dimensions (Table 2). The control variables of the general catastrophe system are not more than four, and four common catastrophe types are fold, cusp, swallowtail, and butterfly.

Table 2 Four common catastrophe types

Catastrophe type	Dimensions of control variation	Potential function	Bifurcation set	Normalization formula
Fold catastrophe	1	$f(x)=x^3+ux$	$u=-3x^2$	$x_u=\sqrt{u}$
Cusp catastrophe	2	$f(x)=x^4+ux^2+vx$	$u=-6x^2,\ v=8x^3$	$x_u=\sqrt{u},\ x_v=\sqrt[3]{v}$
Swallowtail catastrophe	3	$f(x)=\frac{1}{5}x^5+\frac{1}{3}ux^3+\frac{1}{2}vx^2+wx$	$u=-6x^2,\ v=8x^3,\ w=-3x^4$	$x_u=\sqrt{u},\ x_v=\sqrt[3]{v},\ x_w=\sqrt[4]{w}$
Butterfly catastrophe	4	$f(x)=\frac{1}{6}x^6+\frac{1}{4}ux^4+\frac{1}{3}vx^3+\frac{1}{2}wx^2+tx$	$u=-10x^2,\ v=20x^3,\ w=-15x^4,\ t=4x^5$	$x_u=\sqrt{u},\ x_v=\sqrt[3]{v},\ x_w=\sqrt[4]{w},\ x_t=\sqrt[5]{w}$

3.2.2 Establishment of the catastrophe progression model

First of all, the hierarchical structure model is established by using the weight value of the analytic hierarchy process to adjust the order of the original index. Because the number of control variables per layer is not more than four, the 6 secondary indexes could be divided into 3 groups according to index category. The index system changed from the 3 to 4 level index. The catastrophe progression model for evaluation value of the comprehensive capacity of sustainable development for eco-village is shown in Figure 1.

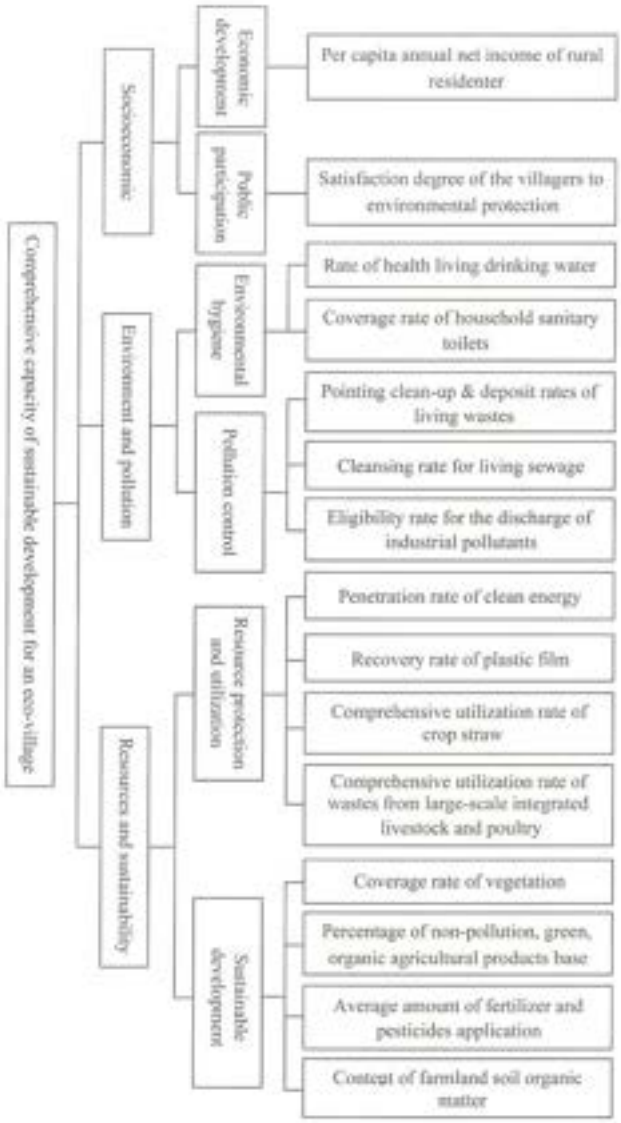

Figure 1 Catastrophe progression model

3.2.3 Normalization formula evaluation and standard index

Because the range of the original data and the measurement units are different, they cannot be directly compared. According to the requirements of catastrophe theory, before using the normalization formula, it is necessary to convert the original data of the control variables into the larger dimensionless values in the range of [0, 1]. The subordination degree concept of fuzzy had been used to dimensionless for data. The positive-type index is standardized using Equation (1), which indicates that performance assessment value is the greater with the increase of index value, such as rate of health living drinking water, coverage rate of vegetation. The negative-type index is normalized by using Equation (2), which indicates that performance assessment value is the lower with the increase of index value, such as Average amount of fertilizer and pesticides application.

$$x = \frac{x_i - x_{\min}}{x_{\max} - x_{\min}} \tag{1}$$

$$x = \frac{x_{\max} - x_i}{x_{\max} - x_{\min}} \tag{2}$$

After normalization, the catastrophe progression of control variables of the last level will be obtained and used as the control variable for the next level index depending on the principle of 'complementary' or 'non-complementary', until reaching the top of the catastrophe progression (namely evaluation results G). If there is a strong interaction between the control variables of the same index, the control variables of the object are called 'complementary type', or 'non-complementary type'. For complementary indicators, the value is obtained according to the principle of the average value (Equation (3)). The minimax principle (also called the minimum value principle) had been used for non-complementary indicators (Equation (4)).

$$x_b = average(x_{c1}, x_{c2}, \ldots x_{cn}) \tag{3}$$

$$x_b = \min(x_{c1}, x_{c2}, \ldots x_{cn}) \tag{4}$$

Finally, the average interval method was used to classify the level of evaluation of the comprehensive capacity of sustainable development for eco-village, and the results were divided into 4 grades (Table 3).

Table 3 The classification standard of results for CPM

Level	Index value	Performance situation
I	0.76-1	Very good comprehensive capacity of sustainable development
II	0.51-0.75	Better comprehensive capacity of sustainable development
III	0.26-0.50	General comprehensive capacity of sustainable development
IV	≤0.25	Poor comprehensive capacity of sustainable development

3.3 Performance assessment model based on AHP

3.3.1 Constructing the hierarchical structural model

From the primary strategic goal layer to the lowest level indicator layer, there exists a distinct three-level hierarchical structure in the evaluation system for eco-village construction. The top level is the general strategic goal of the hierarchical structure, namely the overall objective layer (A) with only one key element of the comprehensive capacity of sustainable development for eco-village. The intermediate level is the criterion

layer (C) with six intermediate elements, such as economic development, environmental hygiene, pollution control, resource protection and utilization, sustainable development and public participation, by which the key elements of the index layer influenced on the general goal of the comprehensive capacity of sustainable development for eco-village. The lowest level, namely the evaluation index layer of eco-village construction, is composed of fifteen key elements. There exists a specific logic in the relationships between neighboring levels; each pair of the elements in three layers are compared to establish the fraction relationship and determine the synthesized priorities for the key elements of index layer with respect to the general goal, using hierarchical or network structure methods.

3.3.2 The classification standard of results for AHP

In ecological evaluation for eco-village construction based on sustainable rural development, we adopt the evaluation standard of the comprehensive capacity of sustainable development. By taking various statistical yearbooks, bulletins and other relative data and national and international corresponding index standards into account, we designed a four-stage classification standard with the critical value and values of upper and lower limit of the index of comprehensive capacity of sustainable development for eco-village (Li et al., 2007) (Table 4).

Table 4 The classification standard of results for AHP

Level	Index value	Performance situation
I	76-100	Very good comprehensive capacity of sustainable development
II	51-75	Better comprehensive capacity of sustainable development
III	26-50	General comprehensive capacity of sustainable development
IV	≤25	Poor comprehensive capacity of sustainable development

Data resource: Li et al., 2007.

3.3.3 Weight calculation and consistency test

Based on the analytical methodology above, questionnaires were designed in light of the hierarchical structural model for evaluating the sustainability of eco-village construction in China. Data were collected through a questionnaire that had been sent to 180 persons invited to take part in the consultation, including the field experts, farmer representatives and government managers from the environmental sectors in China, of which 131 completed questionnaires were received, providing a 72.8% response. These questionnaires represent the attitudes of three social positions or ranks with regard to the eco-village construction in China. Each questionnaire consisted of three parts: 1) information related to the definition and categorization of the eco-village construction in China, and technique concerning the completion of the questionnaires; 2) effective scoring information by using the scale; and 3) paired comparison matrices information. In part 2, the key elements of evaluation index layer that affect comprehensive capacity of sustainable development for eco-village were assessed using on a scale from 1 to 9. In part 3, the reviewer was required to compare each criterion element (the key elements of evaluation index layer) against the others to constitute paired comparison matrices for the A-C layer and C-P layers. From to the collected questionnaires, we could systematically calculate the action forces and weight of different key elements of the evaluation index layer effects on the general objective of comprehensive capacity of sustainable development for eco-village.

A comparison matrix for the A-C layer was constructed, by which we could reckon the weight of the criterion layer to the general objective in Table 5. The comparison matrix of A-C layer would be considered consistent (and accepted) with a CR lower than 0.1. Similarly, we could obtain the weight of the evaluation index layer P_1 to economic development C_1, the weight of the evaluation index layer P_2-P_3 to environmental hygiene C_2, the weight of the evaluation index layer P_4-P_6 to pollution control C_3, the weight of the evaluation index layer P_7-P_{10} to resource protection and utilization C_4, the weight of the evaluation index layer P_{11}-P_{14} to sustainable development C_5, the weight of the evaluation index layer P_{15} to public participation C_6 (wholly passed the consistency test, and accepted).

From Table 5, it can be seen that the weights of the criterion layer to the general objective are 0.3910, 0.1645, 0.2373, 0.0692, 0.0610 and 0.0769 for economic development, environmental hygiene, pollution control, resource protection and utilization, sustainable

development and public participation respectively. The economic development has the maximum weight, pollution control the second, sustainable development the minimum.

Table 5 The weight calculated for the evaluation index system of eco-village construction in China

Evaluation index	Economic development	Environmental hygiene	Pollution control	Resource protection and utilization	Sustainable development	Public participation	Weight of total countable series of layers
	0.3910	0.1645	0.2373	0.0692	0.0610	0.0769	
Per capita annual net income of rural residenter	1.0000						0.3910
Rate of health living drinking water		0.6340					0.1043
Coverage rate of household sanitary toilets		0.3660					0.0602
Pointing clean-up & deposit rates of living wastes			0.3775				0.0896
Cleansing rate for living sewage			0.1526				0.0362
Eligibility rate for the discharge of industrial pollutants			0.4699				0.1115
Penetration rate of clean energy				0.0882			0.0061
Recovery rate of plastic film				0.1569			0.0109
Comprehensive utilization rate of crop straw				0.2717			0.0188
Comprehensive utilization rate of wastes from large-scale integrated livestock and poultry				0.4832			0.0334
Coverage rate of vegetation					0.5355		0.0371
Percentage of non-pollution, green, organic agricultural products base					0.1093		0.0076
Average amount of fertilizer and pesticides application					0.1300		0.0090
Content of farmland soil organic matter					0.2252		0.0156
Satisfaction degree of the villagers to environmental protection						1.0000	0.0769
Total	1.00	1.00	1.00	1.00	1.00	1.00	1.00

Table 5 accordingly showed the weight of the 15 indices of the evaluation index layer to the general objective of comprehensive capacity of sustainable development, of which, the largest influence is per capita annual net income of rural residents (0.391), the eligibility rate for the discharge of industrial pollutants influences second important (0.1115) and the least influence is the penetration rate of clean energy (0.0061).

4 An empirical analysis

This paper made an environmental evaluation for eco-village construction based on sustainable rural development. The data used are collected from field survey conducted in China with the help of the rural eco-environmental protection report in 2007 of the MEPC legislative research project 'science popularization action on eco-environmental protection in vast rural areas'. Stratified random sampling was used to select the villages (Chen et al., 2014). First, we divided all provinces into three regions, including eastern, central and western, according to geographical position and resources, as well as the diverse economic development in these regions. Then, we randomly selected three provinces in each region and one village in each province for field surveys. As a result, the survey samples included 9 villages in different provinces (see Figure 2). The villages in China's eastern area were Qianwei village in Shanghai, Beizha village in Zhejiang and Mohe village in Heilongjiang. The central region villages were Dongzu village in Hebei, Baimiao village in Henan and Yongfeng village in Shanxi. Baimei village in Guizhou, Tawan village in Ningxia and Xinmin village in Yunnan were located in the western region villages.

The survey data were analyzed by using the CPM and AHP models constructed above. The results were showed in Figure 3 and Table 7. The results of CPM shows that Yongfeng village in Shanxi had a top evaluation value of the comprehensive capacity of sustainable development for eco-village, but Baimiao village in Henan had a minimum value despite the same region. From other point of view, the level of the comprehensive capacity of sustainable development in villages in a order from good to poor were good (Qianwei, Beizha and Yongfeng Tawan), better (Mohe, Dongzu and Baimei), general (Xinmin) and poor (Baimiao). As for the results of AHP, the evaluation data shows that Yongfeng village in eastern

region had a top evaluation value of the comprehensive capacity of sustainable development for eco-village (consistenting with results of CPM), and Xinmin village in central region had a minimum value. According to the classification criteria of index value, 9 villages can be divided into 2 groups, such as good (Qianwei, Beizha, Yongfeng and Tawan) and general (Mohe, Dongzu, Baimiao, Baimeiand Xinmin).

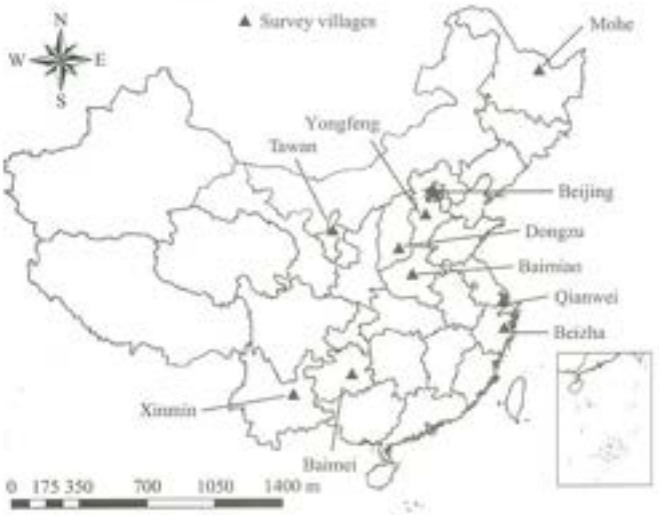

Figure 2 Location of villages in survey

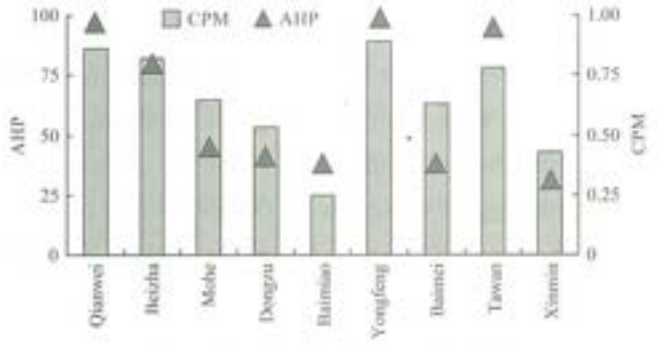

Figure 3 Results of CPM and AHP

Table 7 The evaluation results of the comprehensive capacity of sustainable development for eco-village

Regions	Villages	CPM		AHP	
		Value	Level	Value	Level
Eastern	Qianwei	0.86	I	97	I
	Beizha	0.82	I	80	I
	Mohe	0.65	II	45	III
	Mean	0.77	I	74.0	I
Central	Dongzu	0.53	II	41	III
	Baimiao	0.25	IV	38	III
	Yongfeng	0.89	I	99	I
	Mean	0.68	II	67.7	II
Western	Baimei	0.63	II	38	III
	Tawan	0.78	I	95	I
	Xinmin	0.43	III	31	III
	Mean	0.66	II	64.1	II

Furthermore, evaluation values of AHP have a greater different among villages than CPM. Six of the nine villages have the same level of the comprehensive capacity of sustainable development by AHP and CPM. The results (mean in three regions) of CPM and AHP together showed that the differences of the comprehensive capacity of sustainable development for eco-village of three regions are quite clear, and villages in the eastern region are greatest, in the central region come second and in the western region are lowest.

5 Conclusion

This paper makes the concept and characteristic analysis of an eco-village systematic, and puts forwards an evaluation index system of eco-village characteristics based on the national criterion for eco-village construction issued by MEPC. Besides, the CPM and AHP method were constructed based on CI to carry out a multivariate comprehensive assessment to be made of the overall sustainability of an eco-village. Finally, it is used to presented case study evaluations for 9 villages in China.

The results show that an eco-village evaluation index system can describe their likely relative levels of overall sustainability and provides a conceptual basis and methodological support for planning national eco-villages and solving rural eco-environmental problems in developing countries. These findings indicated that a multi-attribute decision model of CPM and AHP based on index system were effectively applied to evaluate performance of eco-village construction.

Through the performance assessment, the success of eco-village construction in China appears to be critically based on the following actions(Hu and Wang, 1998): 1) ecologically planning and designing village development; 2) implementing ecological engineering in environmental protection and the comprehensive utilization of local resources; 3) establishing social institutions to manage man-environment relations; 4) remaking local culture in its dimensions of behavior, psychology, intelligence and consciousness.

Acknowledgments

This research was made possible through financial support from the Beijing Social Science Foundation (No.

16YJA007) and the earmarked fund for Beijing Innovation Consortium of Agriculture Research System (BAIC07-2017).

[References]

[1] Aguarón, J., and J. M. Moreno-Jiménez. 2003. The geometric consistency index: Approximated thresholds. *European Journal of Operational Research*, 147(1): 137–145.

[2] Alphonce, C. B. 1997. Application of the analytic hierarchy process in agriculture in developing countries. *Agricultural Systems*, 53(1): 97–112.

[3] Ananda, J., and G. Herath. 2008. Multi-attribute preference modelling and regional land-use planning. *Ecological Economics*, 65(2): 325–335.

[4] Bohanec, M., A. Messéan, S. Scatasta, F. Angevin, B. Griffiths, H. P. Krogh, M. Žnidaršič, and S. Džeroski. 2008. A qualitative multi-attribute model for economic and ecological assessment of genetically modified crops. *Ecological Modelling*, 215(1): 247–261.

[5] Chen, H., J. Wang, and J. Huang. 2014. Policy support, social capital, and farmers' adaptation to drought in China. *Global Environmental Change*, 24: 193–202.

[6] Dichristian, M. 1996. The village green. *Environmental Popular Science*, 248(1): 60–64.

[7] Dumreicher, H. 2008. Chinese villages and their sustainable future: The European Union-China-Research Project "SUCCESS". *Journal of Environmental Management*, 87(2): 204–215.

[8] Fang, Y. P., C. P. Raymond, and R. Qin. 2007. Industrial sustainability in China: practice and prospects for eco-industrial development. *Journal of Environmental Management*, 83(3): 315–328.

[9] Gilman, R. 1991. The Eco-village Challenge. *Living Together*, 29(2): 10–11.

[10] Hu, D., and R. S. Wang. 1998. Exploring eco-construction for local sustainability: An eco-village case study in China. *Ecological Engineering*, 11(1-4): 167–176.

[11] Kirby, A. 2003. Redefining social and environmental relations at the ecovillage at Ithaca: A case study. *Journal of Environmental Psychology*, 23(3): 323–332.

[12] Korhonen, P., and R. Voutilainen. 2006. Finding the most preferred alliance structure between banks and insurance companies. *European Journal of Operational Research*, 175(2): 1285–1299.

[13] Li, F., X. S. Liu, Hu, D., Wang, R.S., 2007. Evaluation method and index system of eco-city development: a case study in Dafeng City of Jiangsu Province, China. *Chinese Journal of Applied Ecology*, 18(9): 2006–2012.

[14] Liu, C., J. L. Zhang, and W. L. Wu. 2005. The development of eco-village in developed countries and its enlightenment to China. *Ecological Economy*, 2: 43–46.

[15] Marianna, G., F. M. Laia, B. Alessandra, and T. Simona. 2011. Multi-criteria analysis for improving strategic environmental assessment of water programmes. A case study in semi-arid region of Brazil. *Journal of Environmental Management*, 92(3): 665–675.

[16] Sanchez, P., C. Palm, J. Sachs, G. Denning, R. Flor, R. Harawa, B. Jama, T. Kiflemariam, B. Konecky, R. Kozar, E. Lelerai, A. Malik, V. Modi, P. Mutuo, A. Niang, H. Okoth, F. Place, S. E. Sachs, A. Said, D. Siriri, A. Teklehaimanot, K. Wang, J. Wangila, and C. Zamba. 2007. The African Millennium Villages, *Proceedings of the National Academy of Sciences of the United States of America*, 104(43), 16775–16780.

[17] Su, C., W. L. Wu, and X. H. Yu. 2004. Research on typical ecology-village planning in the mountain area of the Beijing's suburbs. *Journal of Beijing Agricultural College*, 19(4): 51–54.

[18] Wang, R. 1990. *Human ecology in China*. Beijing: China Science and Technology Press.

[19] Wang, R., and D. Hu. 1994. Form economic prosperity to ecological sustainability: a theoretical and practical concern of sustainable development in China. *Journal of Environmental Sciences*, 4(4): 389–401.

[20] Yang, J. P. 2000. Review of global eco-village campaign. *Ecological Economy*, 4: 46–48.

[21] Zhang, D.Y., and W. Ouyang. 2007. The theory and practice of eco-village planning. *Journal* of *Beijing Construction Engineering Academy*, 1: 26–30.

[22] Zhang, L. X., Q. Liu, H. W. Nigel, and Z. T. Fu. 2007. An environmental accounting framework applied to green space ecosystem planning for small towns in China as a case study. *Ecological Economics*, 60(3): 533–542.

A radio frequency based positioning and alarm device for rural nursing homes for the elderly

Li Hui[1,3], Hua Ruoxue[1], Li Wenjie[2], Li Xinxing[1,3*]

(1. *College of Information and Electrical Engineering, China Agricultural University, Beijing 100083, China;*
2. *College of Engineering, China Agricultural University, Beijing 100083, China;*
3. *Key Laboratory of Agricultural Informationization Standardization (Beijing), Ministry of Agriculture, 100083, China*)

Abstract: In order to solve the problem of poor management in rural nursing homes in China, this paper studies the positioning equipment's precise range, reliability, anti-interference ability and scope of application using the wireless sensing theory, GPS positioning technology, RFID technology, sensor technology and GSM wireless communication technology. Based on this, a kind of practical wireless intelligent positioning equipment is developed for the remote monitoring and real-time positioning in the daily life of the nursing home to facilitate finding the elderly in great need of emergency services and improve equipment efficiency. It can monitor the elderly's heart rate in real time and call for help in time in case of heart rate abnormalities to reduce the waiting time for rescue. It has accurate positioning both indoors and outdoors, easy to carry with low cost. And it can meet the needs of future elderly nursing services, not only facilitating the nursing staff's management, but also protecting the safety of the elderly.

Keywords: rural nursing homes, wireless Sensor, heart rate monitoring, remote monitoring

Citation: Li, H., R. X. Hua, W. J. Li, and X. X. Li. 2017. A radio frequency based positioning and alarm device for rural nursing homes for the elderly. International Agricultural Engineering Journal, 26(3): 238–247.

1 Introduction

Population aging is an inevitable phenomenon in the process of population development. According to the United Nations Population Organization, it indicates to be an aging society in a country or region if the proportion of the population over 60 years of age (including 60 years old) reaches 10% of the total population, or the proportion of the elderly population over 65 years (including 65 years old) accounts for 7% of the total population (Bao, 2010; United Nations). China has entered into the aging society early in the year of 1999 (Kou, 2012). According to the results of the sixth census, the total population of China is 1.37 billion, of which the population of people aged 60 and above is 178 million, accounting for 13.26% and 2.93% higher than the fifth census. The population aged 65 and above is 1.2 billion, accounting for 8.9% and 1.9% higher compared to the fifth census. At the same time, the degree of rural population aging in China has reached 15.4%, 2.14% higher than the national average of 13.26%, and higher than the urban aging level (Creedy and Guest, 2008; Wang, 2012; Office of the National Committee on ageing).

On the one hand, the development of urban population aging in China has shown a trend of being empty nest. In 2007, China's empty nest elderly family accounted for 25% of the total elderly family with the number of 23.4 million. It is estimated that by 2030, the proportion of our country's empty nest elderly family may reach 90%, when our elderly families will be completely 'empty nest' (Li, 2007). On the other hand, the policy of reform and opening up has provided large-scale rural migration opportunities to the rural labor force, which leads to the growing of the rural "left-behind population" (Yin and Huang, 2011). The relocation of the labor force of the township has made the rural areas faced with enormous pension pressure and severe challenges since it has the

Received date: 2017-06-28 **Accepted date:** 2017-08-20

* **Corresponding author: Li Xinxing,** Ph.D., Associate Professor of College of Information and Electrical Engineering, China Agricultural University, Beijing, China. Email: lxxcau@cau.edu.cn. Tel: +86-10-62737653.

level of aging far more than the city's (Yu, 2012; Liu, 2013).

The urban and rural differences in economic fundamentals and system of organization result in the different development of urban and rural pension situation. At present, the old-age service agencies and facilities are relatively sound in some large cities, while there are many problems and difficulties in operation and management in rural areas, due to many reasons such as system construction, economic level, historical legacy and etc., in which the most serious is the security risks (Cuddihy et al., 2003).

In recent years, many universities and research institutions have carried out various human-centered research work aiming at improving the quality of the elderly life with the support of the government and society in the western developed countries, especially in the United States and Japan. Compared with the western developed countries, the majority of the current domestic research for the elderly still remains in a passive level featuring as medical care and the overall technology level lags behind, because of our research in intelligent monitoring technology started relatively late and lacked enough investment (Pan, 2013; Wang and Liu, 2012).

Considering the aging trend and poor management of nursing home in China, this paper designs a kind of wireless intelligent positioning device with the functions of indoor and outdoor positioning, heart rate real-time monitoring, one-button call and autonomous alarm, etc., through the research of intelligent monitoring at home and abroad. It has combined the RFID technology, GPS positioning technology, sensor technology and communication and network technology to conduct remote monitoring and real-time positioning for the daily life of the elderly in the nursing home. It is in line with the needs of future nursing services and has a broad market prospect since it can not only facilitate the management of nursing homes, but also protect the safety of the elderly.

2 Principle

2.1 Overall hardware module

2.1.1 Microprocessor module

Microprocessor is the core of the system hardware. Considering the performance, price and other parameters, the IAP15W4K48S4LQFP48 chip was adopted with its schematic diagram shown in Figure 1. It works at 28 MHz with the program space of 48 KB and SRAM space of 4 KB, and it is featured as low power consumption, high cost effective, high performance, multi-I/O port, being easy to use, small size and being easy to extend and so on. It is very suitable for the development of handheld and mobile terminal equipment.

With the combination of industrial computer and mobile terminal, it has fulfilled real-time and accurate supervision of the elderly personal safety through real-time positioning indoor and outdoor, intelligent rounds, special room overtime alarm and heart rate information monitoring.

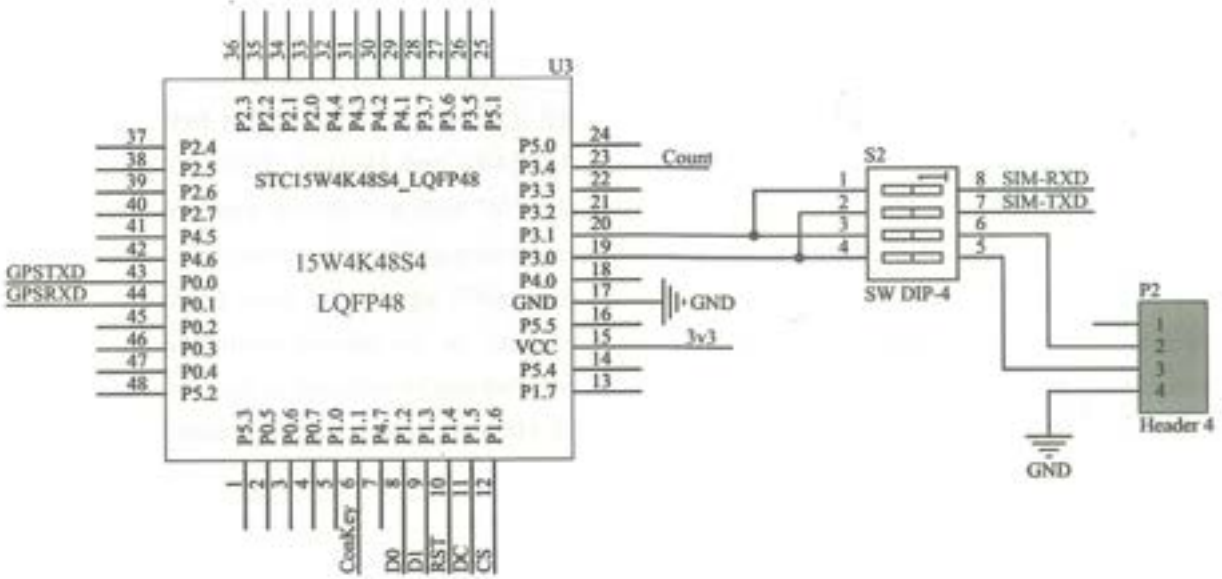

Figure 1 Schematic diagram of the microprocessor

2.1.2 Radio Frequency Identification Module

It uses the MFRC522 in the system, the schematic diagram shown in Figure 2. It is a kind of chip applied in 13.56 MHz non-contact communication of highly integrated level, the internal transmitter part of which can drive the reader antenna and ISO 14443A/MIFARE card to communicate with the answering machine, with no other circuit needed. The receiver section provides a robust and efficient demodulation and decoding circuit for handling ISO14443A-compatible transponder signals. The digital section handles with the ISO14443A frames and error detection (parity & CRC). In addition, it also supports the fast CRYPTO1 encryption algorithm to validate the MIFARE family of products. The MFRC522 supports MIFARE-family higher speed non-contact communication, two-way data transfer rate up to 424 kbit/s. It is also possible to select one of modes such as SPI, I2C or serial UART (similar to RS232) according to different user requirements, which is helpful to reduce the connection, the PCB board size and cost (Wang et al., 2014; Zhu et al., 2012; Guo et al., 2011).

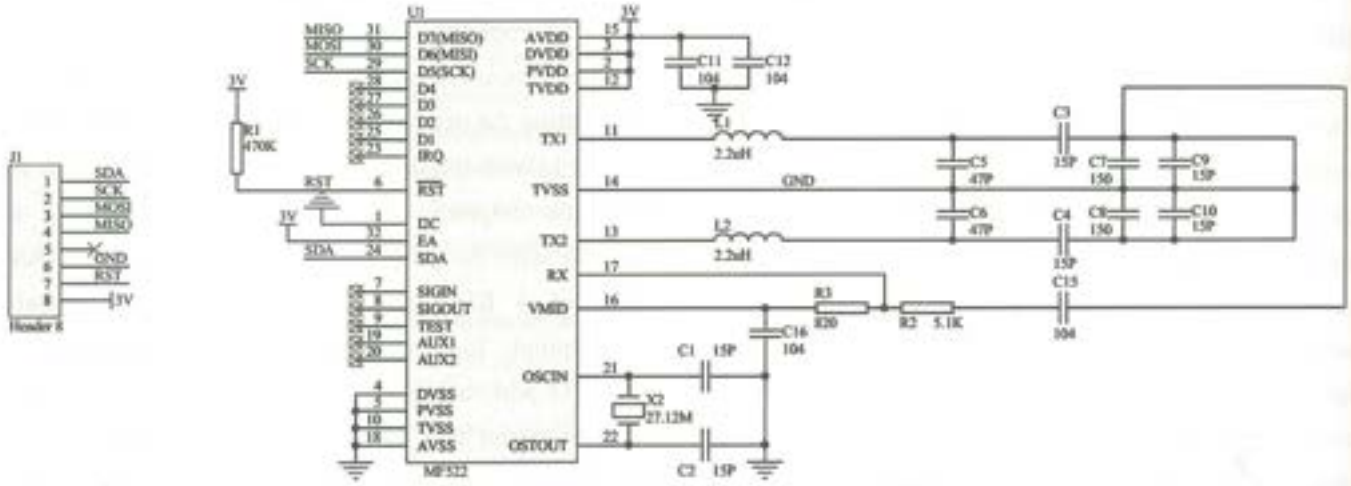

Figure 2 The schematic diagram of MFRC522

The electrical part of the radio frequency card within the mobile terminal consists of only one antenna and an ASIC. The antenna is only a few sets of winding coil, very suitable for packaging. The ASIC consists of a high-speed (106KB baud rate) RF interface, a control unit and an 8 Kbit EEPROM.

The reader has a set of fixed frequency of electromagnetic waves to the mobile terminal. The mobile terminal has an LC series resonant circuit whose frequency is the same as that of the reader. Under the excitation of the electromagnetic wave, the LC resonant circuit resonates so that there generates charge in the capacitor. The other end of the capacitor is connected to a one-way conduction electronic pump, which transfers the charge within the capacitor to another capacitor for storage. When the accumulated charge reaches 2 V, the capacitor can be used as power supply to provide operating voltage for other circuits, which helps to send out the data in the card or access to the reader data.

One can be identified as the only user by the radio frequency identification module since each RF card has unique information.

2.1.3 GPS positioning module

The system uses U-BLOX NEO-M8N-0-01, a high-precision GPS positioning module, its schematic diagram shown in Figure 3. The U-BLOX M8 can simultaneously acquire and track different GNSS (Global Navigation Satellite) systems, that is, parallelly receive GPS (QZSS) and GLONASS or BeiDou, or both receive GLONASS and BeiDou. This platform is specifically suited for high-performance applications that require the highest availability and accuracy even in the environment where GPS signals are poor (especially in the urban canyons). As the optimal positioning of the GPS/SBAS operation can be achieved in the clear sky conditions, the M8 platform is also equipped with a built-in intelligent automatic switching function. It can be automatically switch to a single GNSS operating mode according to the visibility and reliability of the GNSS satellites (Zhou et al., 2012).

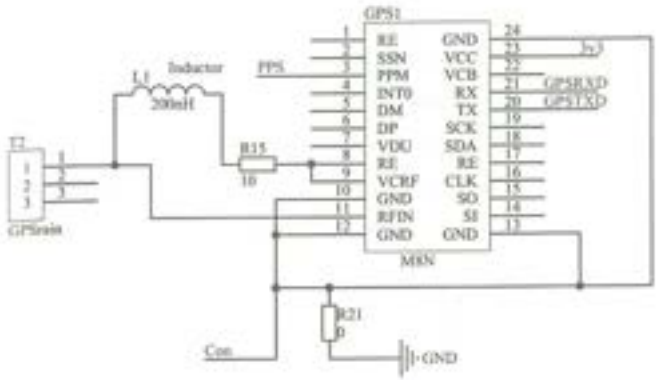

Figure 3 Schematic diagram of positioning module

U-BLOX M8 also offers long offline A-GNSS (GPS and GLONASS) function. With the U-BLOX's AssistNOW A-GNSS service, the offline support data can be valid for up to 35 days.

It is a comprehensive consideration of power and efficiency to select this chip, because it has a high rate of regeneration and supports both of the Beidou and GPS signals with low power consumption, fast positioning speed, high positioning accuracy.

2.1.4 GSM communication module

The system uses SIMcom's SIM800c module, the schematic diagram is shown in Figure 4. The module can support four bands of GSM/GPRS, namely, GSM850, EGSM900, DCS1800 and PCS1900MHz. The reason of selection of this chip is that it has low power consumption, high compatibility, small size and so on so as to meet the requirements of power consumption and communication. Meanwhile, it also meets the requirements of the wearable equipment. The positioning information and the heart rate module data are sent out to the industrial computer directly via SMS through the GPRS network. After receiving, the computer processes the information and data by the microprocessor module to timely determine the location coordinates and supervise the heart rate information in order to ensure the elderly personal safety (Chen et al., 2015; Sheng et al., 2012).

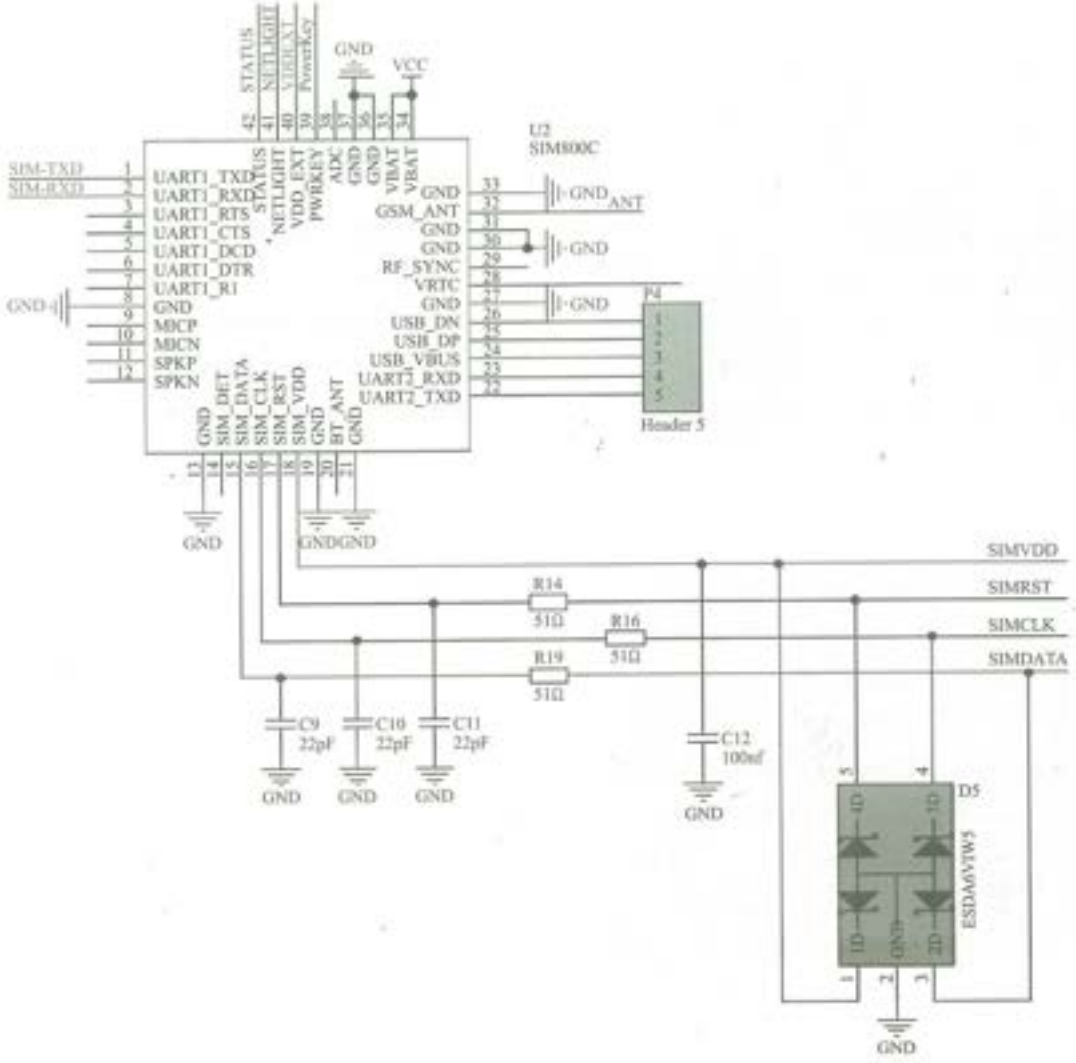

Figure 4 Schematic diagram of communication module

2.1.5 Heart rate sensor

The photoelectric heart rate sensor, son1303, can be placed in various parts of the human body to test human heart rate and pulse. The use of reflective photoelectric sensor, combined with the son3130 op amp, ensures a more flexible measurement, the scope of application including wearable electronic products and pulse measuring instruments of new test methods. The sensor integrates a high-tech nano-coating environment to filter unwanted light sources and reduce misjudgment from interferences of other sources. The SON1303 uses green light of 570 nm luminous wavelength, with higher reflectivity and sensitivity compared with the infrared light. And meanwhile, it improves the S/N ratio with higher accuracy.

The 3D simulation diagram of the mobile terminal and heart rate sensor circuit board are shown in Figures 5 and 6. The heart rate sensor is mounted on the back of the mobile terminal.

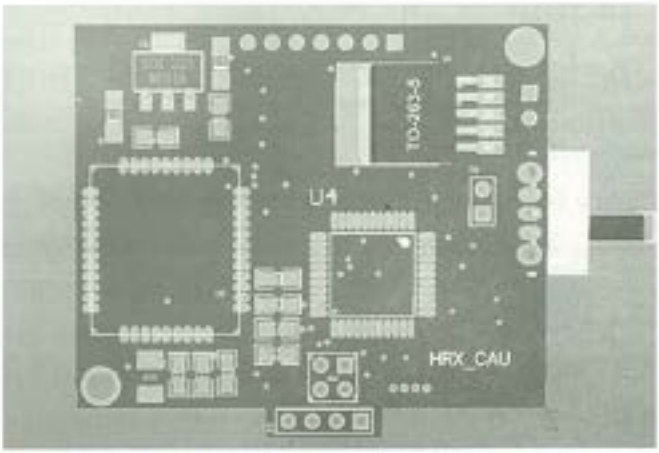

Figure 5 Circuit board of the mobile terminal (back)

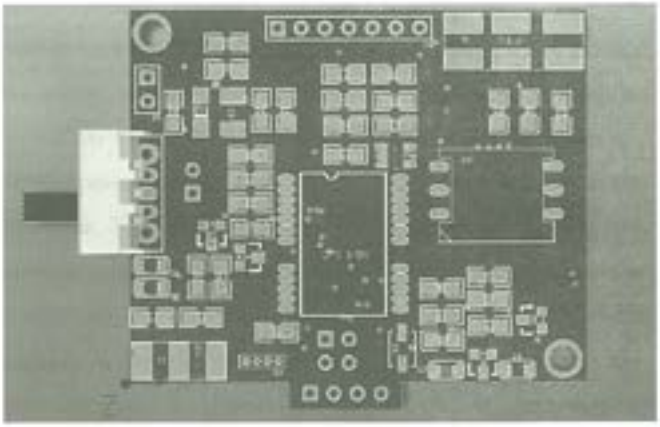

Figure 6 Circuit board of the mobile terminal (front)

2.2 Workflow

The system workflow chart is divided into three parts: the mobile terminal to collect data (Figure 7), the wireless network with two-way transmission of data, and the industrial control computer's analysis and processing data (Figure 8). The RFID detection model is shown in Figure 9 and the system communication model is shown in Figure 10.

After the mobile terminal system is powered on, the modules are initialized, and the GSM module initiates the connection to the server. After the connection is successful, the information is sent to the microprocessor through the serial port. The GPS module initiates communication to the satellite, and sends the relevant information to the microprocessor through the serial port. The heart rate sensor sends the user's heart rate data back to the microprocessor in real time. The microprocessor waits for instructions and instantly sends AT command to the GSM module if it finds there are heart rate monitoring data abnormalities or the elderly takes the initiative to press the call button in the process. Then the GSM communicates with the industrial control computer or calls the emergency contact in the form of text messages or telephone through the wireless network as well as promptly notifies the relevant medical staff. The GPS module sends the positioning information to the microprocessor in real time, which will detect if the positioning data is abnormal, so as to determine whether the elderly have security risks (Home telemedicine monitoring and consulting intelligent systems, 2001; Maybank and Tan, 2000; Naylor and Attwood, 2003). If it finds the elderly's location information is abnormal, the microprocessor immediately sends the AT command to the GSM module, which will inform the relevant medical staff by SMS and telephone, thus to ensure the health and environmental safety of the elderly.

After the industrial computer system is powered on, the modules are initialized. The GSM module initiates the connection to the server. After the connection is successful, the information is sent to the microprocessor through the serial port and displayed on the LCD screen. The RFID radio module starts and waits for the user to enter the recognition area. When the user enters the recognition area, the RFID radio module identifies the user information, informs the microprocessor through the

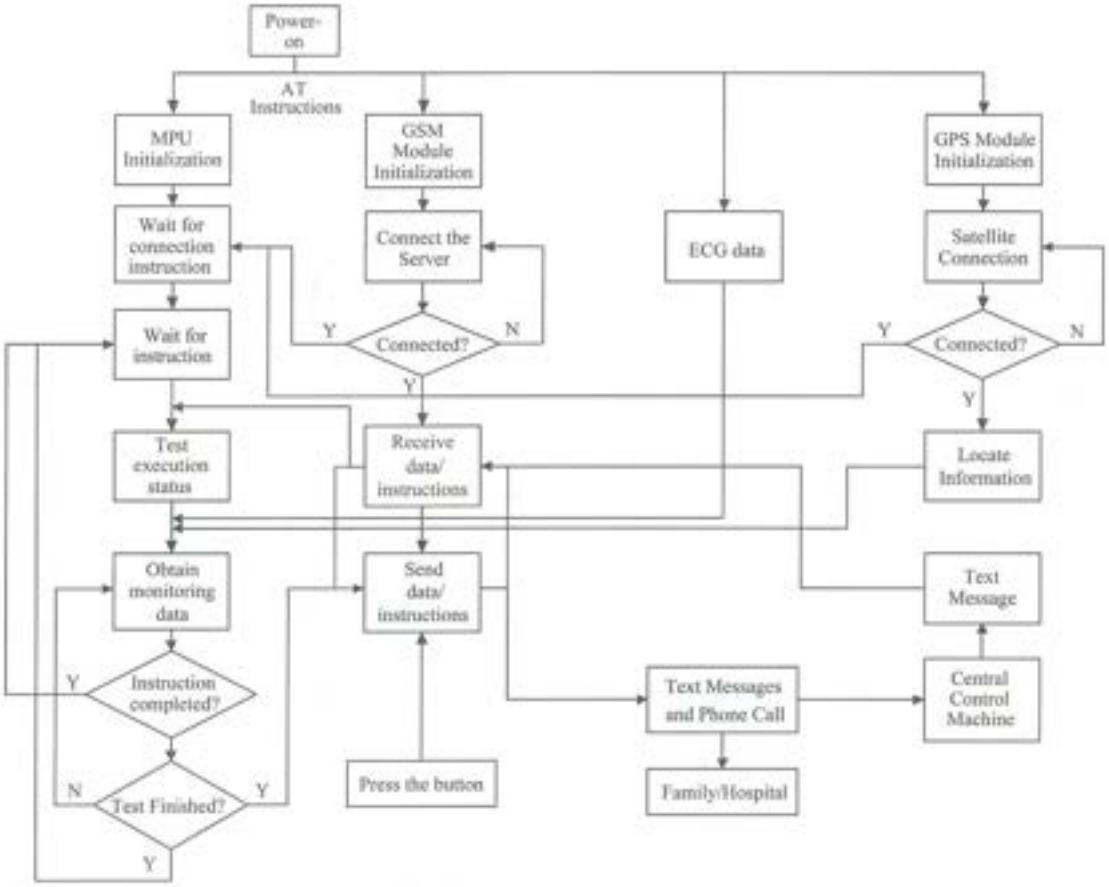

Figure 7 Working flow chart of the mobile terminal

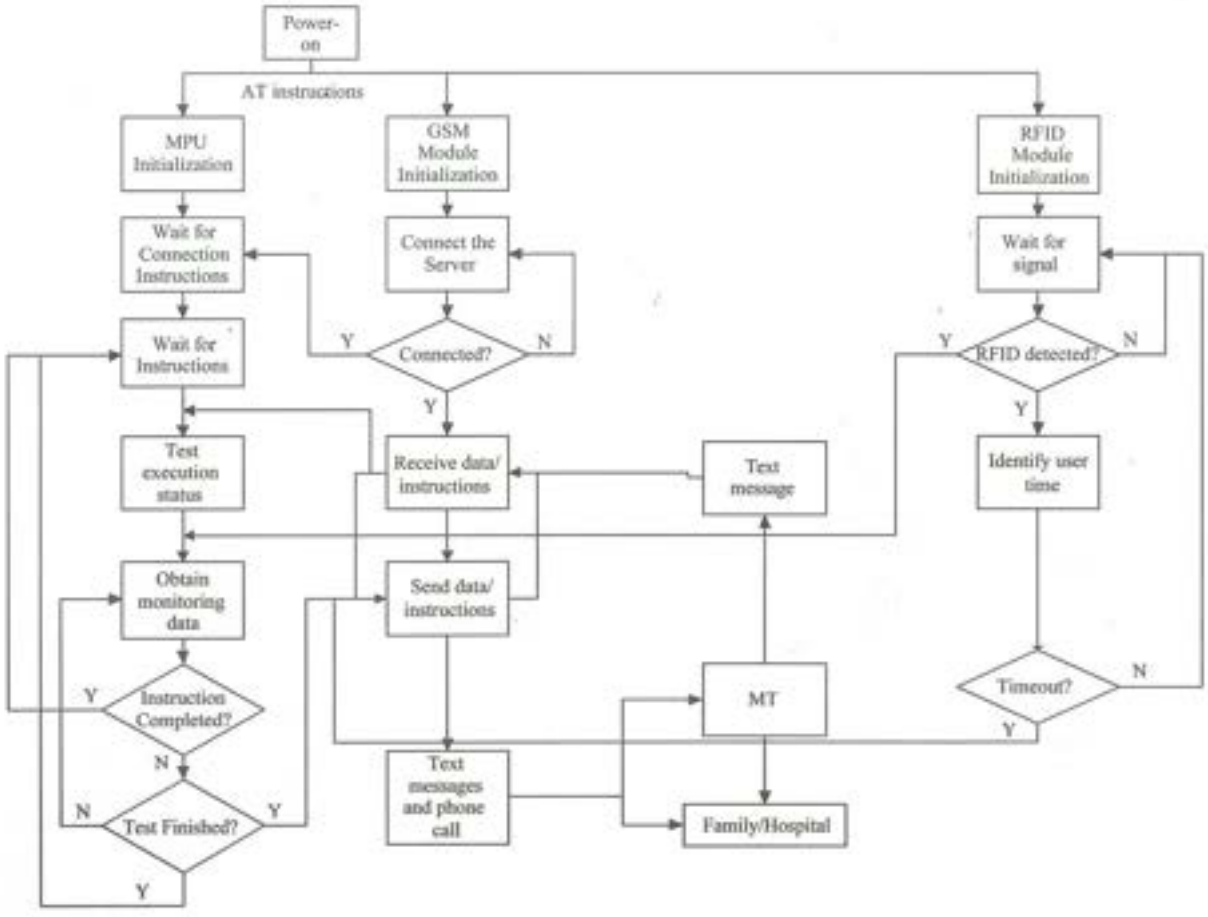

Figure 8 Working flow chart of the industrial control computer

serial port to record information and data such as time. The industrial computers have different time sets according to their locations. Taking the bathroom for example, the elderly toilet time should not be more than half an hour, so the timing in the computer at the toilet door is set at 30 minutes. It begins from the elderly entering into the bathroom, and if he/she does not leave the bathroom within 30 minutes, the computer will send an AT commands to the GSM module through the serial port in the form of SMS and telephone calls to inform the relevant health care workers, so as to ensure timely and effective protection of the elderly's personal safety.

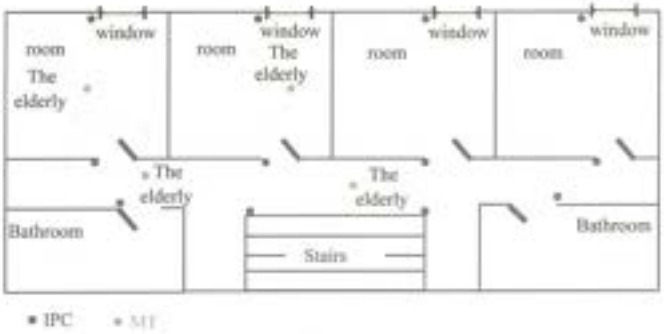

Figure 9 Diagrammatic sketch of the RFID monitoring

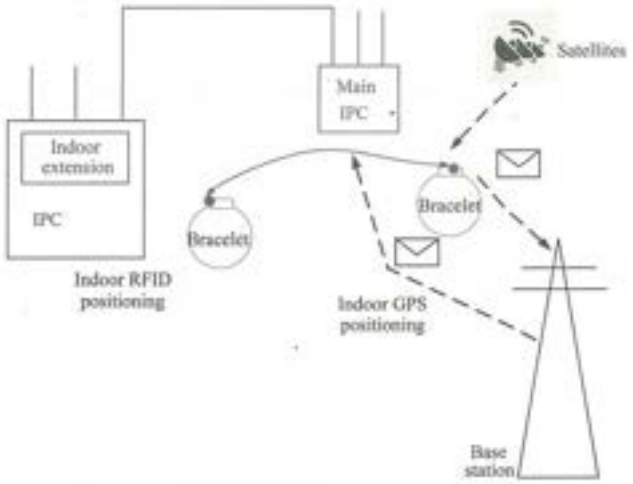

Figure 10 Diagrammatic sketch of the system communication

3 Test and Analysis

3.1 Test results

After the completion of the laboratory test, the performances of the mobile terminals and industrial computers were verified in Quyang County, Taiyuan, Shanxi Province. The computers were installed both at the living room door side and the bathroom door side, and the mobile terminal was put on for field testing and verification.

The GPS data are shown in Table 1.

Table 1 The latitude and longitude of GPS positioning data

Times	1	2	3	4
Latitude (N)	38°26'57918"	38°26'57911"	38°26'57902"	38°26'57874"
Longitude (E)	112°43'02524"	112°43'02470"	112°43'02424"	112°43'02354"
Times	5	6	7	8
Latitude (N)	38°26'57837"	38°26'57814"	38°26'57764"	38°26'57732"
Longitude (E)	112°43'02266"	112°43'02205"	112°43'02106"	112°43'02034"
Times	9	10	11	12
Latitude (N)	38°26'57708"	38°26'57700"	38°26'57806"	38°26'57821"
Longitude (E)	112°43'01979"	112°43'01941"	112°43'01932	112°43'01948"
Times	13	14	15	
Latitude (N)	38°26'57833"	38°26'57837"	38°26'57840"	
Longitude (E)	112°43'01963"	112°43'01966"	112°43'01962"	

According to the GPS test results of the latitude and longitude of the original data, a scatter plot is shown in Figure 11.

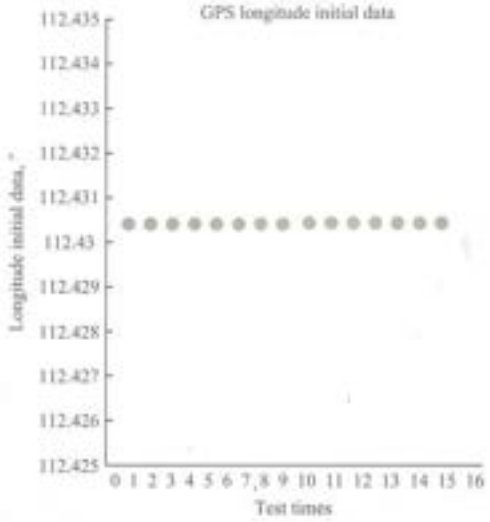

Figure 11 Scatter plots of the original data of GPS longitude

The functions including the indoor RFID near field communication, real-time heart rate monitoring and its accuracy, as well as the intelligent alarm have been validated. The field test is illustrated in Figures 12 to 18.

Figure 12 The mobile terminal (back)

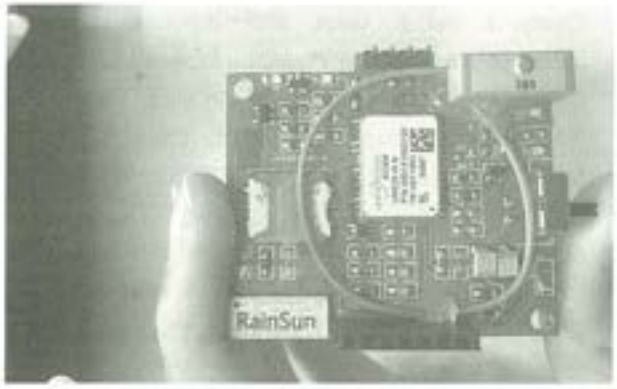

Figure 13 Mobile terminal (front without liquid crystal display)

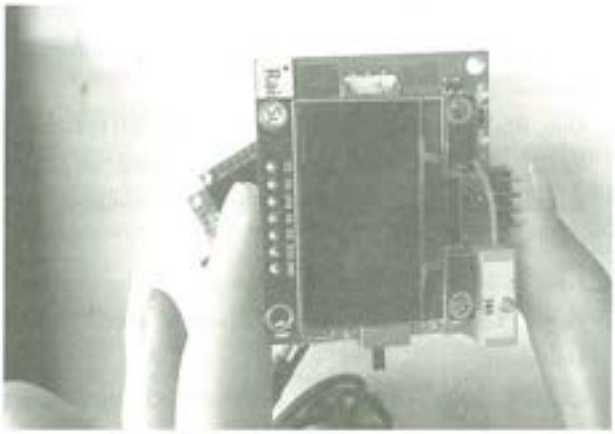

Figure 14 Mobile terminal (front with liquid crystal display)

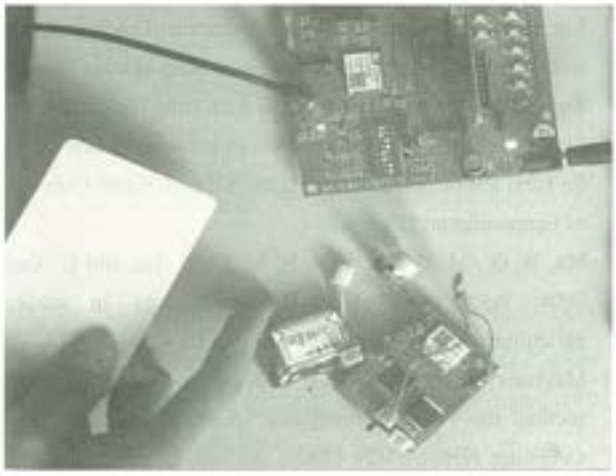

Figure 15 Industrial control computer and mobile terminal

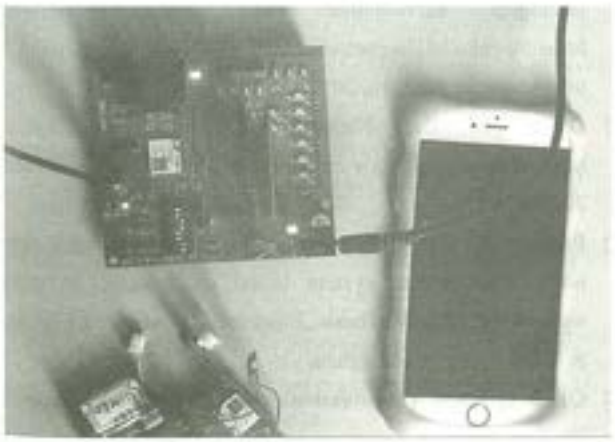

Figure 16 Indoor test of RFID and message sending

Figure 17 Real time monitoring of heart rate

Figure 18 Alarm test for abnormal heart rate

3.2 Performance analysis

3.2.1 Functional testing

The heart rate detection sensor works properly. The RFID radio frequency identification works normally and in a reliable status. The GSM accesses to message and dials normally. The GPS outdoor positioning data have slightly offset. The microprocessor has a quick instruction and analysis of data.

3.2.2 Performance testing

The heart rate sensor can detect the correct and effective heart rate data in the arm, ear and face. When the abnormal heart rate is detected, the mobile terminal immediately sends out the alarm message. The RFID effectively identifies the card number corresponding to the specific user and completes the indoor auxiliary positioning.

3.2.3 Performance analysis

- Both the design of the GSM module antenna and the block of indoor environment on the signal will affect the time of the module connected to the network.
- The design of the power circuit, the capacity of the battery pack and the working mode of each module will affect the working hours of the battery pack, to a certain extent, leading to the long-term work inconvenience.
- The design of the circuit board, antenna design, the

indoor and outdoor environmental interference and the signal strength of the satellite and communication base station, will have impact on the communication network and GPS positioning accuracy.

4 Conclusions

The following conclusions have been achieved through the laboratory pre-test and the actual test in rural areas.

Compared with domestic and foreign research results, the common chips and techniques selected in this paper can to a large extent reduce the cost of production, so that it will not constitute a lot of economic pressure for the rural nursing homes. The device has quick and accurate response, being easy to install, and can be used off the PC.

The device is repairable and rechargeable, equipped with the most common Micro USB charging port. It is small size, light weight, easy for the elderly to carry and use, hardly affecting the daily activities of the elderly.

It can be found from the actual test that the device does have the functions of indoor and outdoor positioning, real-time heart rate monitoring, one call for help and emergency alarm. The GPS positioning data is accurate with low cost, and the heart rate monitoring in real time is effective, so there will be a good promotion prospect in the future.

Acknowledgments

This research work has been supported by the National Science and Technology Support Program (2014BAL07B04).

[References]

[1] Bao, Y. X. 2010. Research on the influence of population aging on regional economic development. Phd thesis. Shandong Normal University.

[2] Chen, D. R. 2012. Circuit design for terminal of intelligent nursing home system. Master's thesis. Electronic University of Science &Technology of Hangzhou.

[3] Chen, X. W., J. Wang, and R. Q. Shen. 2015. Wireless electronic nose based on GPRS and its application on Mangos. *Transactions of the Chinese Society for Agricultural Machinery*, 46(4): 238–245.

[4] Creedy, J. and R. Guest. 2008. Population ageing and intertemporal consumption. *Population Economics*, 2008(2): 67.

[5] Cuddihy, P., M. Ganesh, and C. Graiehen. 2003. Remote monitoring and Adaptive models for Caregiver Peace of Mind. *December 4- 6, 2003: Proceedings of 2003 International Conference on Aging, Disability and Independence*.

[6] Elderly, elderly disabled and technology. 1994. Proceedings of the DVG-DGXIII workshop Brussels 17-18 January 1994.

[7] Elshayeb, S. A., K. B. Hasnan, and C. Y. Yen. 2009. RFID technology and Zigbee networking in improving supply chain traceability. *23-25 November 2009: International Conference on Instrumentation, Communications, Information Technology, and Biomedical Engineering*.

[8] Guo, R., Y. Li, Y. C. Wang, and J. W. Liu. 2011. Design of RFID equipment management system based on ZigBee technology. *Measurement and Control Technology*, 30(5): 89–93.

[9] Kou, J. 2012. Ethical examination of the phenomenon of empty nest for the elderly. Master's thesis. Nanhua University.

[10] Li, A. Q. 2007. An empirical study on the living conditions and social support of empty nest elderly in urban China: a case study of Xuzhou City. *Social Work*, 2007(3): 43–45.

[11] Liu, J. 2011. Research and implementation of communication technology for hospital interior positioning system based on ZigBee. Master's thesis. Shanghai Jiao Tong University.

[12] Liu, Y. J. 2013. Demand analysis of home aged care service for rural left behind elderly. Master's thesis. Hebei University of Economics and Business.

[13] Ma, B. Q., M. Q. Liu, B. J. Ji, M. Li, K. Lu, and C. Yuan. 2008. Application of ZigBee technology in accurate agriculture. *Acta Agriculturae Jiangxi*, 10(42): 126–129.

[14] Maybank, S., and T. Tan. 2000. Introduction of special section on visual surveillance. *International Journal of Computer Vision*, 37(2): 173.

[15] Naylor, M, and C. Attwood. 2003. Annotated digital video for intelligent surveillance and optimized retrieval. https://wenku.baidu.com/view/650ce8d226fff705cc170a34.html (Accessed June, 16, 2017)

[16] Office of the National Committee on ageing. http://www.cncaprc.gov.cn/info/13492.html. (accessed May. 20, 2017)

[17] Pan, Y. Y. 2013. Design and implementation of nursing home management system based on Internet of things technology. Master's thesis. Electronic University of Science & Technology of Hangzhou.

[18] Qi, Q. Q. 2009. Transmission design and reliability study of ZigBee communication network in community hospital system. Master's thesis. Beijing: Beijing University of Posts

and Telecommunication.

[19] Sheng, P., Y. Y. Guo, and P. P. Li. 2012. Intelligent measurement and control system of facility agriculture based on ZigBee and 3G. *Transactions of the Chinese Society for Agricultural Machinery*, 43(12): 229–233.

[20] United Nations. 1983. Vienna International Plan of Action on Ageing. New York.

[21] Wang, L., X. Y. Zou, S. Y. Liu, M. X. Shen, H. C. Zhu, and R. J. Zhu. 2014. Development of handheld terminal for sheep breeding information management based on RFID and Zigbee. *Transactions of the Chinese Society for Agricultural Machinery*, 45(9): 247–253.

[22] Wang, Y. M. 2012. Rural endowment problem and Countermeasures in the background of population aging in China. Master's thesis. Liaoning University.

[23] Wang, Z., and Z. B. Liu. 2012. Design and implementation of nursing home management system based on Internet of things. *Computer and Modernization*, 2012(6): 76–80. Yang J. 2001. Home telemedicine monitoring and consulting intelligent systems. Chinese Patent. CN 1291749 A, filed November 16, 2000, and issued April 18, 2001.

[24] Yin, P. J., and W. L. Huang. 2011. The status quo and trends of rural left behind elderly. *Jiangxi Social Science*, 31(2): 195–199.

[25] Yu, W. 2012. Study on the pension of the left behind elderly in rural areas. Master's thesis. Huazhong University of Science and Technology.

[26] Zhou, J. J., X. Wang, R. Zhang Rui, G. Liu, W. Ma, and Q. C. Feng. 2012. GPS/DR integrated navigation positioning method for agricultural machinery. *Transactions of the Chinese Society for Agricultural Machinery*, 43(Z1): 262–265.

[27] Zhu, W. X., C. Y. Dai, and P. Huang. 2012. Environmental control system based on IOT for nursery pig house. *Transactions of the Chinese Society of Agricultural Engineering (Transactions of the CSAE)*, 28(11): 177–182.

Adhesive sweet pepper fruits segmentation method based on AHE and normalized cut

Niu Peiyun[1], Ye Haijian[2*], Liu Chengqi[3], Lang Rui[4]

(College of Information and Electronics Engineering, China Agricultural University, Beijing 100083, China)

Abstract: As for vegetables in China, sweet pepper is the second-widest planted next only to Chinese cabbage and exported a lot to Japan, Southeast Asia and other countries. The visual recognition system of fruits is a necessary part in sweet pepper harvesting robot. In the meantime, the segmentation of adhesive pepper fruits is also inevitable in the quantitative analysis of the severity of sweet pepper diseases. However, few studies had research on this problem. So in order to get well recognition and segmentation for adhesive sweet pepper fruits in natural conditions, a method is proposed that combines adaptive histogram equalization (AHE) method and normalized cut (Ncut) method. Firstly, original image in RGB color space is processed by R channel subtracting G channel and then using mathematical morphological operation to segment the images to get close-up adhesive sweet pepper fruits and remove the tiny noise parts. Then use AHE algorithm to enhance the local details in the fruit surface, especially the edges of the adhesive part. Finally, based on the reinforced image, edges on the overlapped area are extracted from the image through the Ncut method. To prove its validity of this method, 19 adhesive sweet pepper fruits images under natural environment have been tested. Experiment result shows that, for adhesive sweet peppers in normal natural conditions, the mean segmentation error of this method is 5.4%. The mean contact ratio between segmented fruit image and original fruit image is 93.91%. Furthermore, our method maximized the utilization of the original contour information to build the new edge. The results demonstrate that out method has certain reference significance to detection of sweet pepper fruits and segmentation of other fruits of irregular shape under natural conditions.

Keywords: image segmentation, normalized cut, sweet pepper recognition, overlapped objects segmentation, graph theory, boundary segmentation

Citation: Niu, P. Y., H. J. Ye, C. Q. Liu, and R. Lang. 2017. Adhesive sweet pepper fruits segmentation method based on AHE and normalized cut. International Agricultural Engineering Journal, 26(3): 248–254.

1 Introduction

China is a great nation in term of vegetable cultivation. Quantity and per capita availability both rank first in the world. Planting area of sweet pepper is second-widest next only to Chinese cabbage in China and the fruits are exported a lot to Japan, Southeast Asia and many other countries. Harvesting robot technology is an integral part of modernization of agriculture. Therefore, it's strongly necessary to study the automatically harvesting robot of sweet peppers.

As to the visual system of harvesting robot, accurate detection and segmentation of the close-up fruit is the key to fruit picking successfully. However, it's quite common that sweet peppers are adhesive or overlapped with each other and the fruit is usually sheltered from other noises such as stems and leaves in nature environment . The shape of the sweet pepper fruit is irregular which means cannot be fitted with circle, ellipse or square. And more of these, the surface of the fruits has gully lines which means the surface is not flat or convex like surface of apple and citrus. Hence acquisition and segmentation of accurate sweet pepper fruits target in natural conditions are difficult points in development of the sweet pepper harvesting robot.

Harvesting robot have obtained some achievements in crops such as apple, kiwi fruit, cucumber and tomato, studies on sweet pepper are not so much yet. It the

Received date: 2017-06-30 **Accepted date:** 2017-08-23

* **Corresponding author: Ye Haijian,** Professor, College of Information and Electronics Engineering, China Agricultural University, Beijing 100083, China. Email: hjye@cau.edu.cn.

meantime, segmentation in image of adhesive crops have made some progress. A method of a sliding comparison window local segmentation algorithm is proposed, it can segment various type of surface defects (Rong and Rao, 2017). Using principal component analysis, three color channels are selected from the R, G, B, H, S, and V channels, then an adaptive channel selection Chan-Vese algorithm is proposed, reducing the number of iterations (Hu et al., 2017). The fusion of K-means and Ncut algorithm can solve the problem of accurate segmentation of the overlapped mature apples, which is proved to be better than Hough algorithm in the same condition (Wang, 2016). Many fruits have the shape like a circle or a ellipse so there are many researchers tried to segment the fruits by fitting the edge with a circle or ellipse. The edge of the fruit was get first, then circle is used to fit the edge of apple to separate the adhesive fruits, the center of the single apple is determined by applying max-min distance method on overlapped apples, after that the radius is equal to the minimum distances of every single pixel on the edge to the center of the contour. Finally, the overlapped apples would be separated by fitting circle on the image with the calculated center and radius (Shen, 2016). Snake model can used to segment the fruit from the background and with corner detection method, the corner in the edge would be detected therefore to locate the overlapped place in apples (Xu and Li, 2015). In grape harvesting, the color of grape stem is complex and contour is irregular rising the difficulty to locate the picking position. To locate the picking position, a new method is raised which combined the cluster image segmentation and minimum distance constraint algorithm. The new method solved this problem successfully (Luo et al., 2015). A method which combined the K-means and convex theory algorithm is posed to separate the overlapped apples, which reduced the complexity and improved the effectiveness (Song et al., 2015). Fast normalized cross correlation can improve the recognition efficiency when applying to the overlapped apples for pattern matching (Zhao et al., 2015). There's another way to improve the performance in segmentation in overlapped fruit, using binocular stereo vision system to get anaglyph which extend two-dimensional image to three-dimensional space, the edge error was restrained to 5.47%, that's pretty good effect (Peng et al., 2012). Because of the kiwi fruit's physical property, Hough transformation is applied to fit the fruits as ellipse in natural condition to get the adhesive fruits separated (Cui et al., 2012). A fusion algorithm of adaptive PCNN and maximum entropy approach gets pretty good result in image segmentation (Zhang Xinwei and Yi Kechuan., 2015). The length-width ratio is another concerned feature in overlapped crops. Using pose information of adhesive grains skeletal adhesion point improved the performance of grains segmentation. This method was proved to have better adaptability in complex serious adhesive grains (Niu et al., 2014). Boundary curvature estimation is applied to pick up the pits which mean catastrophe points, then with these feature points, the fruits would be fitted. Because of the characteristics of intensity inhomogeneity, noise, and blurred edges in crop lesion color images, an improved CV model and an efficient termination criterion in level-set for wheat leaf lesion segmentation is proposed, and get pretty good result (Hu et al., 2017). In natural condition, fruit detection and segmentation are not easy because of the uneven lightness distribution, the leaves blocking, stem division and much more other noises. By a sliding comparison window, local segmentation algorithm can successfully segment various types of surface disease and not affected by other noises (Rong and Rao et al., 2017). The pseudo canny edges can be divided into three categories and in this way different texture features can be constructed, this is a remarkably effective segmentation algorithm. In addition, segmentation algorithms for protein and cells adhesion have reference value to crops adhesion. Harris corner detection and polygon fitted were applied to get concave corners on the adhesion protein, then separation lines were constructed by concave points match to divide single protein (Zhao et al., 2017). Another method to segment overlapped protein is fusion of bottleneck detection and Dijkstra algorithm, this way can only divide one part into two parts, multicellular division needs to be determined and segmented repeatedly. Cells outlines can be distributed into two classes, strong outline and weak outline. Annular

dynamic contour search algorithm was applied to locate the weak outline so as to divide the overlapped cells.

Above all, few researchers study on sweet peppers in image segmentation, it's difficult to segment the adhesive sweet pepper fruits because the shape of the fruit is irregular, the surface is uneven and easy to be disturbed by illumination. Most methods applied on apple, citrus are not really suitable for sweet peppers, such as Hough transformation, least square method and so on. The intensity variation on the edge is not prominent because of the gully lines and shadows on the surface, further increasing the difficulty of detection and segmentation on adhesive sweet pepper fruits. This article raised a new method to solve these problems well, this method combined adaptive histogram equalization method and normalize cut method to segment adhesive sweet peppers in natural conditions. Firstly, image sample of RGB color space is calculated by R channel subtracting G channel and then segment to get close-up adhesive sweet pepper fruits by mathematical morphological operation and remove the tiny noise parts. Then, use AHE algorithm to enhance the details in the fruit especially the intensity variation of edge in the adhesive part. Finally, based on the reinforced image, edge on the overlapping area extracted from the fruit through the Ncut method, the foreground fruit is segmented completely.

2 Materials and method

2.1 Detailed enhancement on sweet pepper fruits

This article adopts methods including R channel subtracting G channel to get the initial fruit segmented image. Mathematical morphological operation, void filling, denoising and such steps to get the basic fruit image. The process is shown in Figure 1.

Figure 1 The initial extraction system interface of sweet peppers

As is shown in Figure 2, the fruits are still in adhesion at this point.

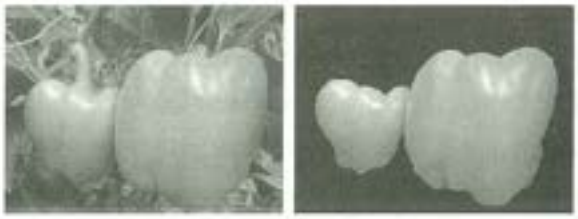

Figure 2 The initial extraction effect of sweet peppers

2.1.1 Introduction to adaptive histogram equalization algorithm

Histogram equalization algorithm is available to enhance the contrast of image, it can be divided into direct contrast enhancement and indirect contrast enhancement. Histogram equalization algorithm is to stretch the gradation histogram in the original image from a relatively intensive gray space to the whole gray scope, so to get a detail enhanced image. However, conventional histogram equalization algorithm have shortcoming in some situation, when there is too bright or too dark region in the original image, conventional histogram wouldn't play an effective role and would even cause distortion in these conditions. Furthermore, conventional histogram equalization has some other flaws such as it may cause gray scale decrease, detail lost after the transformation and image distortion influenced by noisy points.

Adaptive histogram equalization (AHE) is a computer image processing method to promote the image contrast. Different from the conventional histogram equalization algorithm, AHE adopts local processing method to equalize the histogram, which means by calculating the histogram in a local window, AHE redistributes the gray level to enhance the image to get more distinct details in a local window, in this way, the new image wouldn't be influenced by regions of no interest. The main idea of this algorithm is to equalize the histogram of a pixel and a small rectangular area around this pixel, the way redefining the gray value of a pixel is same with conventional histogram equalization method.

The global histogram equalization effect is shown in Figure 3a, while the effect of adaptive histogram equalization is shown in Figure 3b. As demonstrated in the figure, the edge contrast in Figure 3b is much more obvious than in Figure 3a.

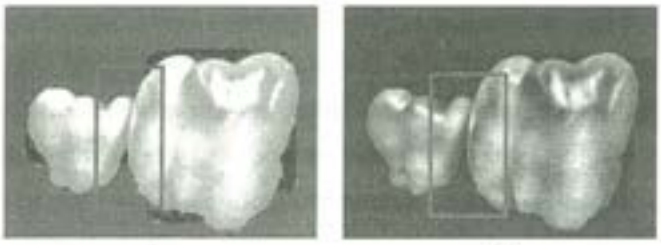

a b

Figure 3 Effects of different histogram equalization methods

The Equation of local region contrast enhancement is shown as follows:

$$\hat{x}_{i,j} = m_{i,j} + k(x_{i,j} - m_{i,j}) \quad (1)$$

The parameters $x_{i,j}$ and $\hat{x}_{i,j}$ respectively represent the gray value before transformation and after. And $m_{i,j}$ is the average gray value in the rectangular frame.

2.2 Segmentation in adhesive sweet pepper fruits

2.2.1 Introduction to normalized cut algorithm

Normalized cut (Ncut) algorithm is used to segment adhesive fruits after getting the detail enhanced image.

Ncut algorithm is proposed by Sin in 2000, it's a global optimization method based on graph theory. Technology based on graph theory has always been a hot topic. Graph theory describes a image as a weighted undirected graph, regarding the pixels as nodes in the graph, the relevance between the pixels as edges. Object segmentation is carried out in the rule of nodes clustering, in this way, conventional image segmentation problem is converted into an optimization problem in graph theory.

The Equation of Ncut is shown as the following:

$$Ncut(A,B) = \frac{cut(A,B)}{assoc(A,V)} + \frac{cut(A,B)}{assoc(B,V)} \quad (2)$$

$$assoc(A,V) = \sum_{u \in A, v \in V} w(u,v) \quad (3)$$

The result value of the Equation (2) is between-class similarity, the lower the between-class similarity is, the better the segmentation result. Equation (3) is to calculate the sum of weight between Part A and the whole graph nodes V.

$$Nassoc(A,B) = \frac{assoc(A,A)}{assoc(A,V)} + \frac{assoc(B,B)}{assoc(B,V)} \quad (4)$$

Within-class similarity is solved in Equation (4), the higher the within-class similarity is, the better the result.

The Equation can also be written as:

$$\begin{aligned} Ncut(A,B) &= \frac{cut(A,B)}{assoc(A,V)} + \frac{cut(A,B)}{assoc(B,V)} \\ &= \frac{assoc(A,V) - assoc(A,A)}{assoc(A,V)} + \frac{assoc(B,V) - assoc(B,B)}{assoc(B,V)} \\ &= 2 - \left(\frac{assoc(A,A)}{assoc(A,V)} + \frac{assoc(B,B)}{assoc(B,V)}\right) \\ &= 2 - Nassoc(A,B) \end{aligned} \quad (5)$$

It can be seen that Ncut algorithm not only ensure the lowest inter class similarity, in the meantime, it guarantees highest between class similarity, so the effect of Ncut is global optimized in pixel perspective.

The algorithm is calculated as following:

First, according to the graph theory, transform the original graph into an undirected weighted graph $G = (V, E)$, then calculate the weight matrix W and D.

Second, based on feature system Equation $(D-W)y = \lambda Dy$, determine the feature values and corresponding feature vectors.

Finally, cluster the feature vectors using cluster algorithm.

As shown in figure 4 is the contour result extracted by Ncut algorithm from the enhanced image. The goal of Ncut is to cluster the pixels in order to get global optimized result with lowest within-class similarity and highest between-class similarity. The contour on the adhesive part is recognized successfully, showing that Ncut have a nice effect in recognizing the edge on overlapped or adhesive parts.

Figure 4 Effect on edge of the adhesive fruits using Ncut method

The following figure shows the segment result under our method. Figures 5a and 5b is the result using sobel operator on adhesive sweet pepper fruits image to detect the edge directly without Ncut algorithm. Figures 5c and 5d are the result using Ncut algorithm. It can be observed that our method not only divides off the adhesive sweet peppers, but also keeps the original edge basically. There are many researchers using Hough transformation to fit apples, citrus, kiwi fruits with circles and ellipses to

divide the overlapped and adhesive fruits, but the flaw in this way is obvious, irregular shape cannot be fitted with regular form, and the fitted shape didn't use the original image edge information comprehensively.

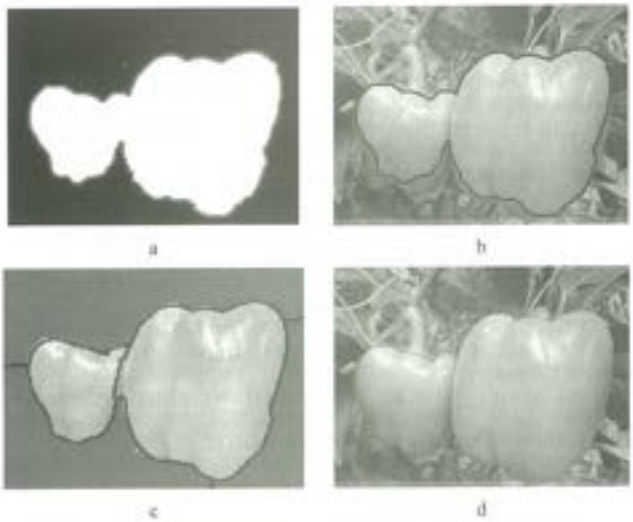

Figure 5 Final effect on edge of the adhesive fruits using Ncut method

Figure 6 shows the experiment results. The result without AHE algorithm in Figure 6a have more deviation than result with AHE algorithm in Figure 6b, indicating the effectiveness of AHE method and dedicating that AHE algorithm having certain significance to other detail enhancement study.

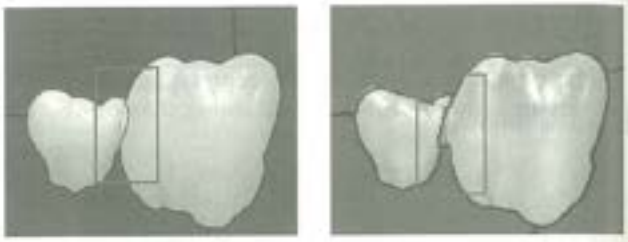

Figure 6 Effect of AHE method on segmentation

3 Results and discussion

Nineteen samples were tested in this paper, the segmentation results are shown in the following table.

Table 1 Segmentation results with our method and reasons

Sample number	Real area in image (pixel)	Segmented area with our method (pixel)	Overlapped ratio (percent)	reason	Error segmentation ratio (percent)
1	16036	13931	86.33		
2	41844	42847	100.00		1.4
3	13880	10225	73.66	Stem and leaf block	
4	9562	9613	99.12		
5	20657	18952	91.72		
6	2106	2034	96.65		
7	2654	2700	97.91		
8	3762	4577	82.10	Overlapped widespread	
9	28102	27596	98.11		
10	39125	38988	99.64		
11	6013	5676	94.39		
12	9026	8923	98.85		
13	10852	11365	95.49	Large scale shaded surface	
14	9302	9288	99.84		
15	28330	27765	98.01		8.6
16	9704	8303	85.56	Large scale shaded surface	
17	24732	23484	94.95		
18	9056	9003	99.41		
19	7326	7336	99.86	Blurred edge	

Note: Error segmentation means the ratio of error segmentation part from background to the complete real fruit part.

4 Conclusion

Compared with other crops like apple, tomato, citrus and kiwi fruit, sweet pepper fruit is more difficult to detect and segment from the image because of the irregular shape and uneven textured surface, so the studies on detection and segmentation of sweet pepper fruit in method of computer visual are few. Segmentation of adhesive multiple sweet pepper fruits has become one of the research key points and difficulties in sweet pepper

harvesting robot. This paper proposes a fusion method of AHE and Ncut method to segment the overlapped sweet pepper fruits, some progress has been made in automatic detection and segmentation of adhesive sweet pepper fruits in natural environment. Experimental results show that:

1) The uneven surface and illumination leads to partial shading in sweet pepper fruits, so the contour on the adhesive part is easy to be confounded with the fruit itself. To get a better detection of gray scale variation through Ncut method, this paper adopts AHE algorithm to enhance the details in the fruit surface especially to enhance the edge on the adhesive region. Compared with the result in conventional histogram equalization algorithm combining with Ncut, our method gets a better result which is more close to the actual situation, showing our method have certain significance in segmenting overlapped irregular objects in natural complex conditions.

2) The shape of sweet pepper fruit is irregular, so it's inefficient to use corner detection method and concave points match method in dividing the adhesive peppers. Ncut method, which is based on graph theory of global optimization, can segment the adhesive fruits on the basis of the original outline. It can be concluded that Ncut is feasible, supplying some ideas to further study on segmentation of multiple adhesive fruits of irregular shapes.

Algorithm in this paper basically solves the problem of segmentation of multiple adhesive sweet pepper fruits in natural condition. However, in natural environment, there are situations that multiple fruits overlap seriously. In these situations, our method is not very effective and needs to optimize from the perspective of detail enhancement. The fruit involved in our paper is mainly yellow peppers and red peppers, not including green peppers yet. How to enlarge generalization of this method still need further study.

Acknowledgements

My deepest gratitude goes first and foremost to Professor Ye Haijian, my supervisor, without his specific guidance and support, I wouldn't harvest in my study so much. Second, I would like to express my heartfelt thanks to my senior fellow apprentice Lang Rui and Liu Chengqi, they guide me into the world of computer vision, they give me a lot of help in life and study. This work was supported by the project of agricultural science and technology cooperation (201704070). My special thanks should go to Wang Dandan and her professor Song Huaibo, I do agree with their work which gave me inspiration on my work.

This study is supported by transformation and popularization project of agricultural scientific and technological achievements in Tianjin - "Integrated application of core information technology for early warning, diagnosis and prevention of greenhouse vegetable diseases" (201704070).

[References]

[1] Hu, Q. X., J. Tian, and D. J. He. 2017. Wheat leaf lesion color image segmentation with improved multichannel selection based on the Chan-Vese model. *Computers and Electronics in Agriculture*, 135: 260–268.

[2] Rong, D., X. Q Rao, and Y. B. Ying. 2017. Computer vision detection of surface defect on oranges by means of a sliding comparison window local segmentation algorithm. *Computers and Electronics in Agriculture*, 137: 59–68.

[3] Wang, D. D. 2013. Recognition and localization method of apple target under conditions of overlapping and occlusion. Master's thesis, Northwest A&F University.

[4] Shen, T. 2016. Research on fast dynamic recognition and location of overlapping fruit for apple harvesting robot. Master's thesis, Jiangsu University.

[5] Xu Y, Li Y, Song H, He D. 2015. Segmentation method based on the Snake model and the Angle point detection, the double fruit overlaps the apple target. *Computers and Electronics in Agriculture*, 31(01): 196–203.

[6] Luo Lufeng, Zou Xiangjun et al. 2015. Automatic positioning of picking points of grape picking robot in natural environment. *Transactions of the CSAE, (02):* 14–21. (In Chinese with English abstract)

[7] Song, H. B., and C. D. Zhang, J. P. Pan, X. Yin, and Y. B. Zhuang. 2013. Overlapping apple target segmentation and reconstruction algorithm based on convex hull. *Transactions of the CSAE*, (03): 163–168. (In Chinese with English abstract)

[8] Zhao, D. A., T. Shen, Y. Chen, and W. K. Jia. 2015. Apple pickers quickly track and identify overlapping fruits. *Transactions of the CSAE*, 2015(02): 22–28. (In Chinese with

English abstract)

[9] Peng, H., P. F. Wu, R. F. Zhai, S. M. Liu, L. L. Wu, and X. Jing. 2012. Image segmentation algorithm for overlapping fruits based on disparity map. *Transactions of the Chinese Society of Agricultural Machinery*, (06): 167–173. (In Chinese with English abstract)

[10] Zhang Xinwei, Yi Kechuan et al. 2015. The image segmentation of adhesive corn seed based on pulsed coupled neural network. *Journal of China Agricultural University*, (03): 208–215.

[11] Niu, J., X. Z. Pu, and K. Qian. 2014. Image segmentation method of adhesive grain Image segmentation method of adhesive grain using skeleton information. *Transactions of the Chinese Society of Agricultural Machinery*, *2014*(09): 280–284, 290. (In Chinese with English abstract)

[12] Cui, Y. J., S. Su, Z. H. Lv, P. P. Li, and X. Ding. 2012. The method of separating the fruit from the fruit by the Hough transform. *Journal of Agricultural Mechanization Research* (12): 166–169.

[13] Zhao, F. J., L. Li, and H. M. Xin. 2017. Study on the algorithm of protein point segmentation in gel images. *Computer Engineering and Applications*, 2017(05): 212–215.

AgriCore: an agricultural application specific chip

Zhang Ganghong[1,3], Xiao Wan'ang[2,4], Gao Wanlin[1,3*], Yu Lina[2,4], Zhang Guofeng[1,3], Zhong Zhen[1,3]

(1. *College of Information and Electrical Engineering, China Agriculture University, Beijing 100083, China;*
2. *Institute of Semiconductors, Chinese Academy of Sciences, Beijing 100083, China;*
3. *Key Laboratory of Agricultural Informationization Standardization, Ministry of Agriculture, Beijing 100083, China;*
4. *University of Chinese Academy of Sciences, Beijing 100049, China*)

Abstract: As key executers of agricultural Internet of Things (IoT), the main control chip and abundance of applications are subjected to a wide variety of high energy-efficiency regulation. Designing application specific System-on-Chip (SoC) architecture underlying this regulation is critical for improving sensor data collection in the field of agricultural IoT. Targeting domain specific knowledge requires methods that can control all devices connected with both high performance and low power consumption. However, current agricultural IoT using chips directly from industry has hitherto been limited either by random selection and narrow functions, or by not considering environments. A SoC system of agricultural specific processor compatible with standard 8051 microcontroller instructions set was designed in this paper. The system uses a top-down approach, and Verilog HDL language to complete the design of memory cell, logic operation unit and other units in the chip integrated all logical circuits into the same function, and verify it on Xilinx FPGA. Part of the typical circuits has been tested through the implementation of the software simulation and verification of the peripheral circuits, and the test results show that the designed SoC system can be as expected to execute instructions and a FPGA development board debugging, and meet the design requirements. This relatively reasonable design can be manufactured using IP merge methods.

Keywords: SoC, agricultural IoT, FPGA, lower power consumption, 8051

Citation: Zhang, G. H., W. A. Xiao, W. L. Gao, Yu Lina, G. F. Zhang, and Z. Zhong. 2017. AgriCore: an agricultural application specific chip. International Agricultural Engineering Journal, 26(3): 255–262.

1 Introduction

Main control chip or Microcontroller Unit (MCU) has played a crucial role since the advent of agricultural informationization and agricultural Internet-of-Things (IoT). Whatever smart greenhouse or all kinds of sensors (Zhang et al., 2002) served for agricultural areas, when acquiring parameter data or other application data, the key executer will be the main control chip. The chips are likely involved in nearly all signal processing functions of the data collection devices as well as being altered in application specific units in the field of precision agriculture (Gebbers et al., 2010). A chip is manufactured from a silicon wafer, which is first cut to size and then etched with circuits and electronic devices. In the past several decades, all kinds of chips have achieved great success for improving the progress of human society. For example, the three types of mainstream chip are based upon ARM (Advanced RISC Machine), x86 and MIPS (millions of instructions per second) instruction set. Especially, as one of the most popular chips based on ARM architecture (Gong et al., 2013) has been widely used in many areas. However, these chips are mainly designed for industrial and consumer areas (Haight et al., 2016; Georgakopoulos et al., 2016; Wang et al., 2017; Ambrosin et al., 2016; Potyrailo et al., 2016; Cass et al., 2017), and few researchers have focused on agricultural areas. With the ever-increasing demand of agricultural

Received date: 2017-07-05 **Accepted date:** 2017-08-23
*** Corresponding author: Gao Wanlin,** PhD, Professor, Research interests: agricultural informationization and application specific chip. Address: College of Information and Electrical Engineering, China Agriculture University, Beijing 100083 P.R. China. Tel: +86-010-62736755, Email: cau_szmtyjs@163.com.

IoT (Baranwal et al., 2016; Zou et al., 2017; Jin et al., 2015) and smart agriculture, the application specific chips (Bhongade et al., 2015; Cilardo et al., 2016; Knag et al., 2015) need to be designed to speed up the process of agricultural informationization.

In agricultural information areas, the application chips are mainly divided into two categories: one is for addressing problems in computer vision, image processing, speech recognition, UAV and robotics that can be hard to realize due to limited hardware capabilities, and the other is for application sensors, such as, CO_2, moisture, temperature and light intensity that mostly installed in smart greenhouses. Targeting more popular sensors requires methods that can acquire environment parameters with both high performance and low power consumption. This paper designs a SoC system (Menon et al., 2017) of agricultural specific processor compatible with standard 8051 microcontroller instructions set (Zheng et al., 2012; Chen et al., 2013; Hui et al., 2009). The system uses a top-down approach, and uses Verilog hardware description language (HDL) to complete the design of memory cell, logic operation unit and other units in the chip intergrated all the logical circuits with the same function, and verify it on Xilinx FPGA (Salim et al., 2006). Part of the typical circuits has been tested through the implementation of the software simulation and verification of the peripheral circuits, and the test results show that the designed SoC system can be as expected to execute instructions and a FPGA development board debugging, and meet the design requirements manufactured using IP merge methods.

2 Materials and method

2.1 Design flow

As one of the main drivers of the semiconductor technology in the past many years, System-on-Chip (SoC) contains digital, analog, mixed-signal, and other radio-frequency functions, integrated and employed intellectual property (IP) reuse to improve design productivity in an attempt to save costs and development time. Recently, designs of multi-million gate level with multiple third party IP cores have become commonplace. Efficient SoC designs based on IP reuse are implemented with hierarchical top-down design flows with previous designs done as IP used in the current design. In this paper, the design cycle as the diagram of SoC design flow is shown in Figure 1.

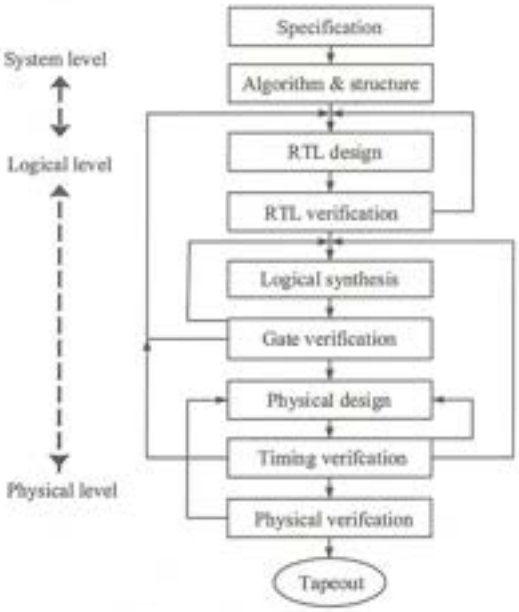

Figure 1 SoC design flow

There are three main stages: system level, logical level and physical level. Firstly, for system specification, designers should consider to refine architecture, algorithms; decompose into blocks; meet requirements and specifications; divide user interface, testing issues and applications. Furthermore, for logical implementation, register-transfer-language level (RTL) coding, IP integration, logical synthesis, verification and validation are inevitable. At the physical design phase, static and dynamic power consumption must be analyzed and power supply switches must be carefully placed, consequently, physical implementation will be acquired. Of course, the major bottlenecks are in the test and verification area. The system level and layout level links to RTL design play also an important role in a fluent design flow.

In accordance with the above design steps, in this paper presents an agricultural application specific chip named AgriCore that will provide services for agricultural informationization.

2.2 System structure and chip features

For sensor interface applied in agriculture, analog devices provide solutions to meet a wide range of automotive sensing challenges and improve vehicle

performance. The AgriCore instruction set is 100% compatible with the standard 8051 instruction set. It is particularly useful to designers who need the full ASIC top-level set of signals. The main on-chip modules are connected to the AgriCore by extending SFR (Special Function Registers) bus. The on-chip memory (including ROM and program and data RAM) is connected to the core via memory bus. The system structure is shown in Figure 2.

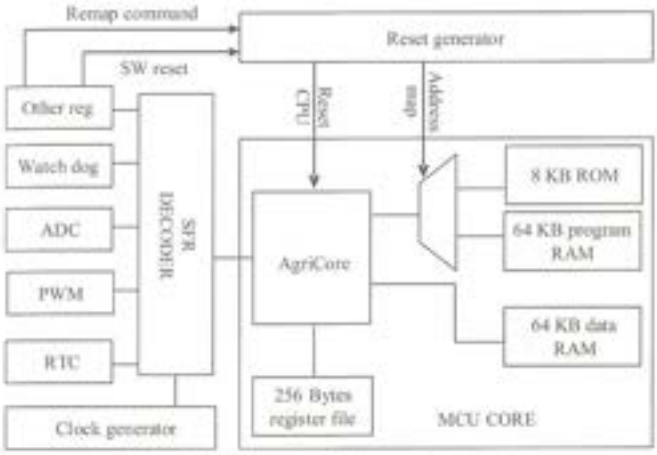

Figure 2 Diagram of the system structure

Features:

1) Compatibale with 8051 core;

2) Running frequency up to 120 MHz;

3) Configure phase locked loop (PLL);

4) ROM 8 KB;

5) 64 KB program RAM;

6) 64 KB data RAM;

7) Virtual Serial Peripheral interface SPI host interface to connect Flash chip;

8) 32 GPIO;

9) Three Timers;

10) Serial port of Universal Asynchronous Receiver/ Transmitter (UART);

11) 4 configurable PWM output;

12) 8 channel analog-to-digital converter (ADC);

13) Watchdog;

14) Real Time Clock;

15) The alternative to using external crystal (8 MHz) or internal LC oscillator (32 MHz) as a clock source;

16) Support a single 3.3 V power supply (built in LDO);

17) LQFP100 package.

2.3 IP cores reuse

For SoC design, the ideas of reuse and integration that will make SoC design and verification become simple. Well-specified cores interacting via clean and well-defined interfaces connected to the AgriCore in this paper played a critical role for improving the application. Figure 3 shows that the distribution of IP cores friendly intergrated into AgriCore and the base architecture is almost identical to the standard 8051, thus maintaining instruction-level compatibility. There are five IP cores existed the system: 1) S018ROSC_32MA: Mixed Signal 1.8V/3.3V Enhanced process Ring Oscillator 32 MHz single power supply: 1.8 V; 2) S018PLLGS_T500: Mixed Signal 1.8V/3.3V Enhanced process Clock Generator PLL, output freq. 25 M~500 MHz, with single power supply. Size: 621 um×265 um; 3) SP018_PX32K: Crystal Oscillator compatible with SP018, SP018W, SP018N; 4) S018AD2H: Mixed Signal 1.8V/3.3V Enhanced process 8-Channel 10bit 50K SAR ADC; 5) S018VREG18_ 150MCAP: This voltage regulator can provide up to 150 mA stable current with 1.8V +/-10% output voltage.

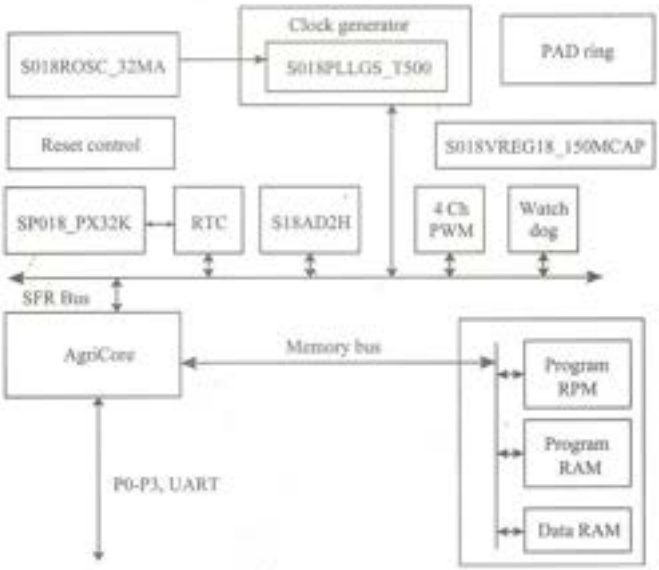

Figure 3 Diagram of IP core distribution

2.4 SFR registers

Standard 8051 has a fixed number of Special Function Registers (SFRs) defined. In AgriCore these fixed SFRs are all available; in addition, user can even add their own SFR in their design using this expansion port. For example, user can add more I/O port if the 4 I/O ports provided in AgriCore is insufficient. When compared to

memory mapped I/O devices, this method provides a much faster I/O access.

Special Function Registers (SFRs) are used by the 8051 as a quick method of accessing hardware. The standard 8051 has many SFRs for controlling the serial port, timers and I/O ports. In the AgriCore these registers are contained internal to the model. The designer can map in extra special function registers to the SFR space of the AgriCore, to control on-chip user specified hardware. The new SFRs must not conflict with the addresses of previously defined SFRs. Only the lowest 7 bits of the SFR address are brought out from the AgriCore, since by definition an SFR memory map occupies only addresses 0x80 to 0xFF. The Figures 4 and 5 are shown the waveforms of each module accessed through SFR bus.

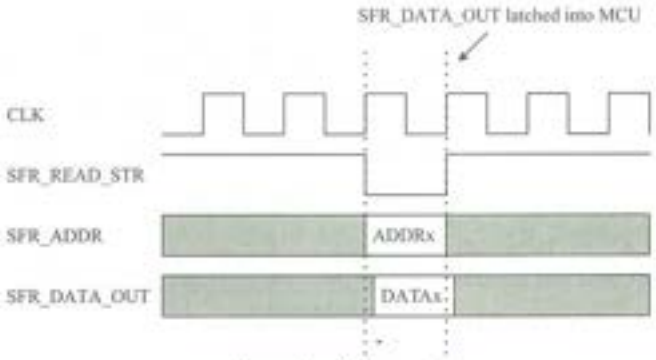

Figure 4 SFR read

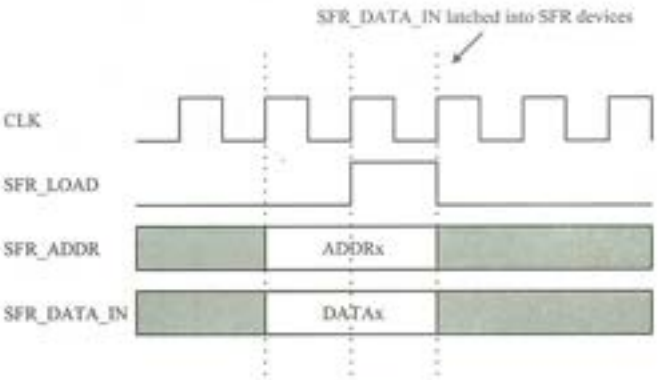

Figure 5 SFR write

2.5 Memory bus

The memory bus is the set of wires that is used to carry memory addresses and data to and from the system RAM. Alternatively, if the address on the program memory bus is checked when BusMon (0) is high, a record of program flow can be obtained. Similarly, a break point circuit can also be designed to detect if the program execution hit the breakpoint. The Figures 6 and 7 are shown the waveforms for accessing RAM/ROM through the Memory Bus module.

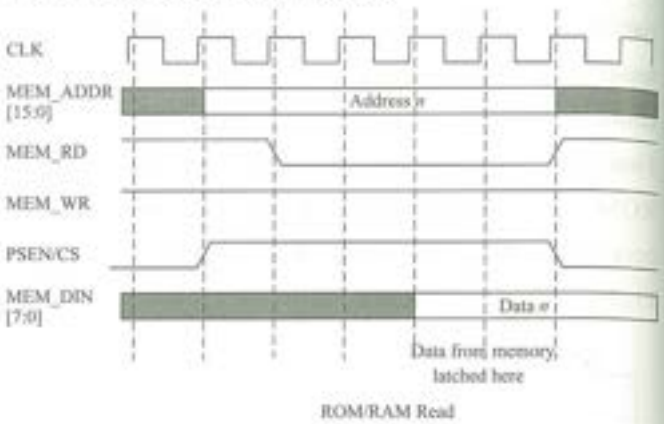

Figure 6 Memory bus read

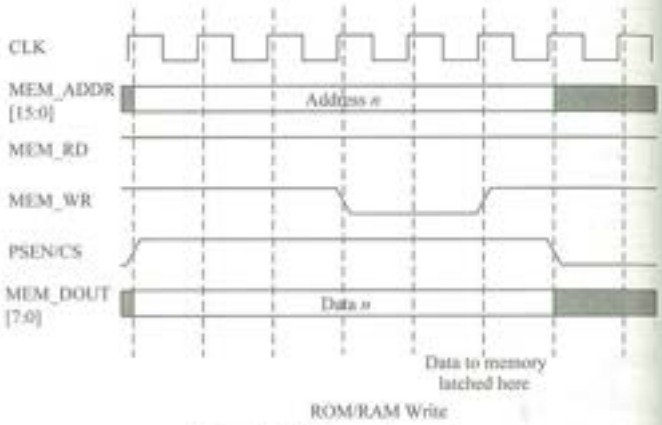

Figure 7 Memory bus write

2.6 Memory address mapping

One design goal of the AgriCore was to be able to use slow access time RAMs and ROMs with a fast processor. The standard 8051 performs two program memory fetches per machine cycle, but usually only uses the first one. In contrast, the AgriCore only does an extra program memory fetch during a jump. This means that for equivalent processing power, the AgriCore can use slower memories than the standard 8051. The memory bus of AgriCore can access three address ranges: startup ROM, program RAM, and data RAM. The 8KB startup ROM and program RAM using the address space, when the chip is powered on, AgriCore accesses the ROM space and executes the bootstrap program. At this time, 64KB program RAM space is mapped to the data RAM space to enable the software to be downloaded. At the end of the boot, AgriCore closes the ROM access space by configuring address mapping register and sets the address of program RAM and data RAM to a normal mapping relationship mode.

The extended SFR register address 0xEA is the address mapping control register REMAP [0]. When REMAP = 0, ROM is placed at the 0 address; when REMAP = 1, program RAM is placed at the 0 address. After the system reset, the value of REMAP returns to 0. When CPU is configured to be 1 through SFR bus, CPU subsystem reset will automatically trigger that enables CPU to start running from the 0x00 address of the REMAP.

Additionally, the chip uses free SFR address space to control major peripherals, such as Watchdog, ADC, etc.

2.7 Clock structure

The system has two clock sources: the 8MHz quartz oscillator and the resistance-capacitance (RC) oscillator. The quartz oscillator requires an external crystal. The internal RC oscillator eliminates the need for external crystals, but has relatively low clock accuracy. The selection of the two clock sources is controlled by the pin CLKSEL: the CLKSEL=1, using a crystal oscillator; the CLKSEL=0, using an internal RC oscillator. The internal RC oscillator generated about 32 MHz clock, and through frequency division using divide-by-2 produced about 8 MHz clock provided for PLL and directly drove core logic. In order to produce accurate baud rates in the UART boot mode, the external crystal oscillator should use the 11.0592 MHz frequency. The diagram clock structure is shown in Figure 8.

Although AgriCore has a machine cycle which is shorter than 12 cycles, in order to obtain compatibility with standard 8051 timers, the register is increased every 12 clock cycles when enabled in timer mode operation. And in counter mode operation, the register is incremented in response to falling edge at its corresponding external input pin, Timer 0, Timer 1, or Timer 2.

When the system started, the PLL is closed; if enable PLL to work, need to use the software register to generate required system clock.

Clock controller in the Clock Switch internal circuit is shown in Figure 9.

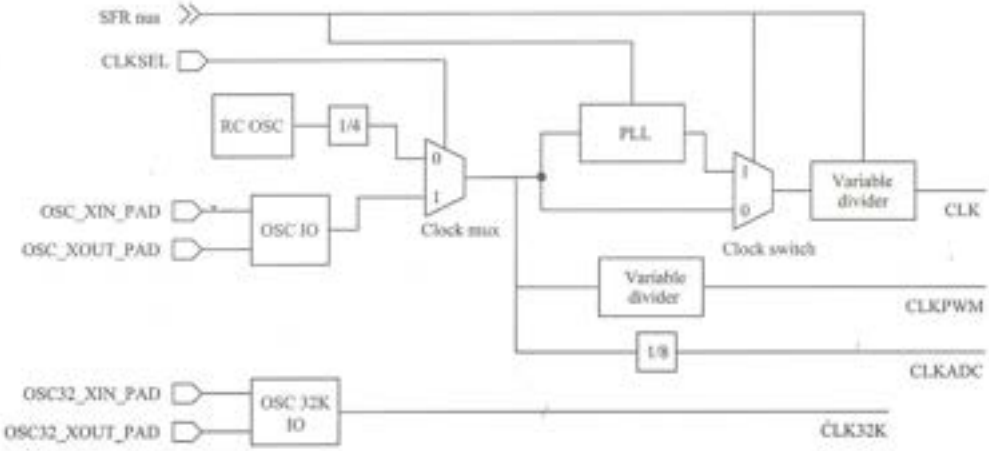

Figure 8 Clock structure

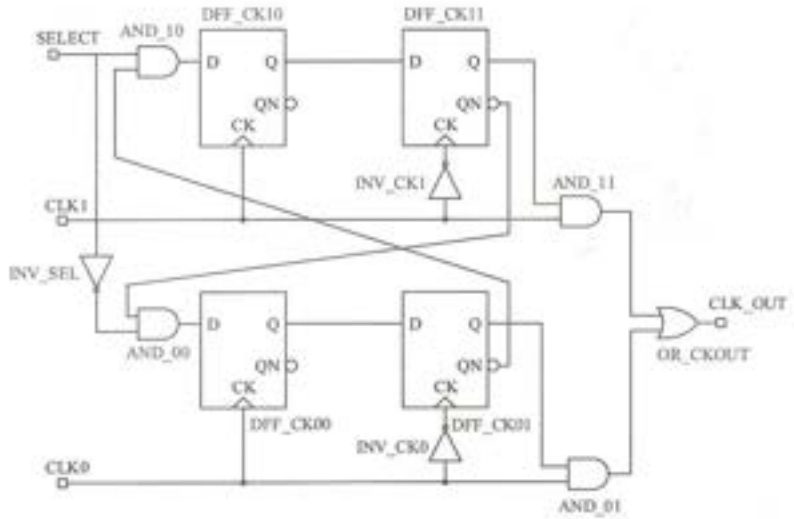

Figure 9 Clock Switch internal circuit

The SFR register used by the clock controller is listed below in Table 1.

Table 1 The SFR register used by the clock controller

SFR Address	Register	Reset Value	Descriptions
0xE9	SW_RESET	0x00	[0] – When write 1 to this bit, global chip reset will be triggered.
0xF1	CLKCFG	0x00	[7] - read only, CLKSEL pin status, 0 - uses internal 8MHz clock, 1 - uses external 11.0592MHz crystal clock [6] - PLL_SEL: 0 - uses the OSC clock as the main clock; 1 - uses the PLL output clock as the master clock [5:3] - PWM clock frequency division control: 0 - no divider 1 - 2 frequency division 2 - 4 frequency division ... 7 - 14 frequency division [2:0] - master clock frequency division control
0xF2	PLLCFG	0x17	[7] PLL_EN: 0 – PLL power down; 1 – PLL open [6:0] PLL frequency control：PLL output frequency = (Fosc * (2+PLLCFG))/8

2.8 Verification and testing

2.8.1 Verification in FPGA

On this board, the AgriCore is implemented inside a Xilinx FPGA. Since there is considerable spare capacity within the FPGA, used prototype the final on-chip logic within the FPGA also, allowing the full SoC to be prototyped in one FPGA and run at speed. To debug the embedded software, a simple software monitor has been developed. Figure 10 shows FPGA verification.

Figure 10 FPGA Verification

2.8.2 Flash read and write testing

The startup process of the chip is controlled by the program in the on-chip ROM. For AgriCore, the ROM program supports three functions:

Function 1: when connected to the PC through serial port, download the code to the program part of RAM, and jump to execute program.

Function 2: when connected to the PC through serial port, burn the code into the SPI Flash of the chip.

Function 3: without connecting to the PC, directly read the code from the outside SPI Flash, and put it into the program part of RAM, and jump to execute program.

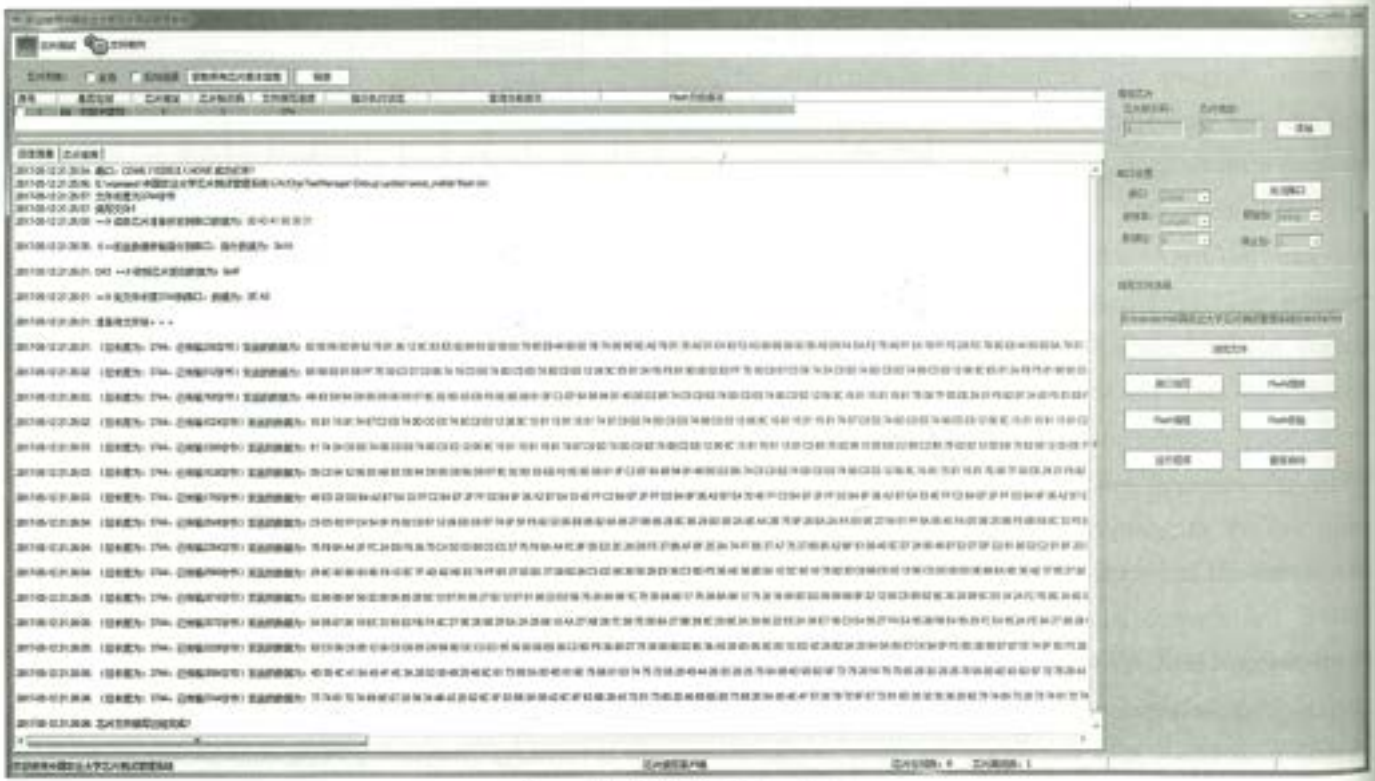

Figure 11 FLASH write and read

When the chip started, the chip will send the query string to the serial port, and if received the response from PC within a second, then finish Function 1 and Function 2 by an interactive command; if there is no response within one second, the Function 3 will be implemented and chip into the self-starting process. Figure 11 shows the process of embedded software written and read.

3 Results and discussion

The cell-based layout of based-AgriCore chip is shown in Figure 12. Through Synopsys software, the power of consumption of the chip is estimated as following Table 2. The total chip size is: the width is 4219.92, the height is 4219.92; and area is 17807724.81 μm^2.

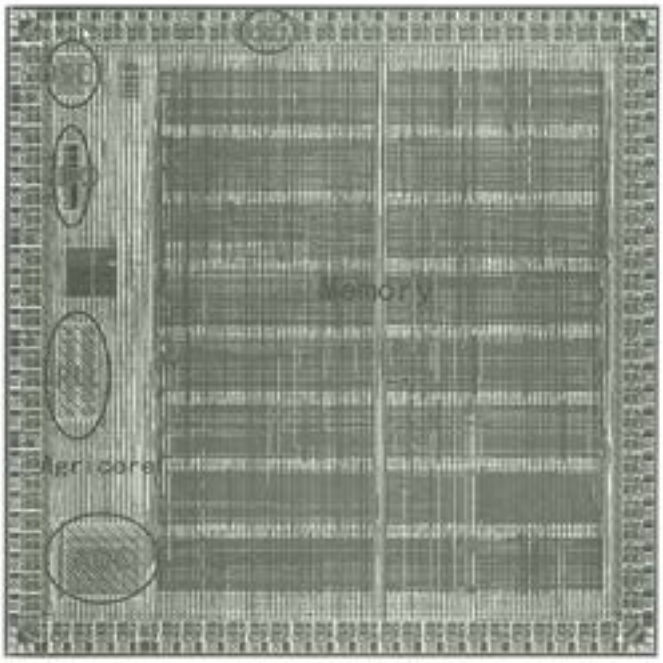

Figure 12 Snapshot of the layout

Table 2 Statistics for power consumption

units	Power, mW	(%)
Total Dynamic Power	15.2003	(100%)
Cell Internal Power	13.9765 mW	(92%)
Net Switching	1.2238 mW	(8%)
Dynamic Power	1	
Cell Leakage Power	0. 8050	

When applied in agricultural IoT areas for acquiring parameter values of soil moisture or air temperature, a smart sensor node based on AgriCore including four basic modules such as a power module, a sensing module, a processing module and a RF module which is shown in Figure 13. Sensing module mainly included sensor and ADC component, is connected to the processing module. The processing module can manage procedures through AgriCore to read data from sensor, and operate flash to store data. It also manages RF module which makes the sensor node join in the wireless sensor network. Of course, by this method, many applications can be implemented in different sensor nodes with relative interfaces.

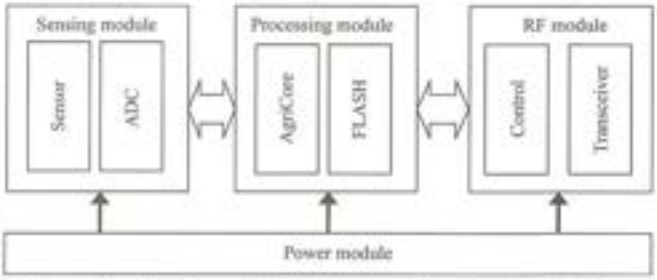

Figure 13 Modules of a smart sensor node based on AgriCore

4 Conclusions

The design methods of AgriCore SoC using chip development technology and the details of its implementation for rapid application in smart sensors of agricultural information areas were presented in this paper. The theoretical and empirical work in this paper demonstrates that SoC design method is an effective alternative to traditional methods to design a chip. In today's ARM-oriented MCU development environment, 8-bit devices might look old and a bit long, but in fact simple is the best. When coupled with modern process technologies and advanced mixed-signal peripherals, 8-bit performance on most control tasks can match or exceed many other CPU architectures, while providing improvements in speed, design time, size and integration. With the enhanced peripherals, these 8-bit machines can also offer a cost-effective solution that might preclude the need to move to a higher bus-width device, thus saving development time and money. The instruction execution in AgriCore is, on average, three times faster than standard part at the same clock frequency. In AgriCore, the Serial Transmission Clock is produced by the SerialClk and the transmission and reception of data are handled by SerialIn and SerialOut respectively. A tapeout schedule of the AgriCore chip is submitted.

Acknowledgements

The authors would like to thank their colleagues for their support of this work. The detailed comments from the anonymous reviewers were gratefully acknowledged. This work was supported by National Spark Program Key Project (Grant #: 2015GA600002) and Chinese Universities Scientific Fund (Grant #: 2017XD003).

[References]

[1] Ambrosin, M., A. Anzanpour, M. Conti, T. Dargahi, S. R. Moosavi, A. Rahmani, and P. Liljeberg. 2016. On the feasibility of attribute-based encryption on Internet of Things devices. *IEEE Micro*, 36(6): 25–35.

[2] Baranwal, T., Nitika, Pateriya P. K. 2016. Development of IoT based smart security and monitoring devices for agriculture. *2016 6th International Conference - Cloud System and Big Data Engineering*. January 14-15 2016, Noida, India.

[3] Bhongade, S., and P. Rusia. 2015. Digital implementation of PID controller using FPGA for temperature control. *Journal of Periodontal Research*, 20(1): 86–90.

[4] Cass S. 2017. A chip to protect the internet of things. *IEEE Spectrum*, 54(1): 20–21.

[5] Chen, Y. L., L. K. Zheng, and Z. Y. Li. 2013. Design and verification for data interface 8051_USB IP core. *Applied Mechanics & Materials*, 324: 387–390.

[6] Cilardo, A., and E. Fusella. 2016. Design automation for application-specific on-chip interconnects: a survey. *Integration the VLSI Journal*, 52(2016): 102–121.

[7] Gebbers, R., and V. I. Adamchuk. 2010. Precision agriculture and food security. *Science*, 327(5967): 828.

[8] Georgakopoulos, D., and P. P. Jayaraman. 2016. Internet of things: from internet scale sensing to smart services. *Computing*, 98(10): 1041–1058.

[9] Gong, A. P., X. Wu, Z. J. Qiu, and Y. He. 2013. A handheld device for leaf area measurement. *Computers & Electronics in Agriculture*, 98(7): 74–80.

[10] Haight, R., W. Haensch, and D. Friedman. 2016. Solar-powering the Internet of Things. *Science*, 353(6295): 124–125.

[11] Hui, X. U., J. H. Wang, and W. Wang. 2009. Design and implementation of 8051 IP core based on FPGA. *Computer Technology & Development*, 19(3): 42–45.

[12] Jin, L., M. Guo, and L. Gao. 2015. Application and innovation strategy of agricultural Internet of Things. *Transactions of the Chinese Society of Agricultural Engineering*, 2015(S2). (In Chinese with English abstract)

[13] Knag, P., J. K. Kim, T. Chen, and Z. Zhang. 2015. A sparse coding neural network ASIC with on-chip learning for feature extraction and encoding. *IEEE Journal of Solid-State Circuits*, 50(4): 1070–1079.

[14] Menon, S. M., R. S. Yavatkar, Dolev E., Valluru, S., and R. Rachakonda. 2013. Apparatus, system and method for a common unified debug architecture for integrated circuits and SoCs. US20130339790.

[15] Potyrailo, R. A. 2016. Multivariable sensors for ubiquitous monitoring of gases in the era of Internet of Things and industrial Internet. *Chemical Reviews*, 116(19): 11877.

[16] Salim, A. J., M. Othman, and M. A. M. Ali. Integration of 8051 with DSP in Xilinx FPGA. *IEEE International Conference on Semiconductor Electronics. IEEE*, 2006: 562–566.

[17] Wang, Y. P. E., X. Lin, A. Adhikary, A. Grovlen, Y. T. Sui, Y. Blankenship, J. Bergman, and H. S. Razaghi. 2017. A Primer on 3GPP Narrowband Internet of Things. *IEEE Communications Magazine*, 55(3): 117–123.

[18] Zhang, N., M. Wang, and N. Wang. 2002. Precision agriculture - a worldwide overview. *Computers & Electronics in Agriculture*, 36(2): 113–132.

[19] Zheng, W., J. P. Xu, D. G. Zhong, and Z. J. Xiao. 2012. Design and verification of 8051 interruption system with Verilog. Computer & Digital Engineering, 40(1): 59–62.

[20] Zou, Y., and L. Quan. 2017. A new service-oriented grid-based method for AIoT application and implementation. Modern Physics Letters, 31(19–21).

Application research on intelligent irrigation system based on frequency conversion technology and AGA in China

Huang Yeda[1], Xiao Yutian[1], Wei Wenqiang[1], Wu Yang[2], Zhai Qingzhi[1*], Zhu Xinzhi[3], Yang Shuo[3]

(1. *College of Information and Electrical Engineering, China Agricultural University, Beijing 100083, China*;
2. *State Grid Beijing Electric Power Company, Beijing 100031, China*;
3. *State Grid Hebei Electric Power Company, Hebei 050000, China*)

Abstract: Affected by the difference of natural environment, regional economic development and other factors, there are some problems in Chinese irrigation, including low water efficiency of irrigation and water shortage. What's more, most water pump motors are running under the mode of constant speed and constant frequency, which not only worsen this situation, but also make a great deal of waste of electricity and reduce the efficiency of electricity and water. To solve the problems above, this paper built an intelligent irrigation system by using information feedback technology and frequency conversion technology: first, according to the feedback information, the system can use adaptive genetic algorithm to get the optimal irrigation water allocation scheme of the current state in real time; second, the special frequency conversion technology, designed on the basis of the characteristics of irrigation, enable water pump motors to adjust the output water flow according to the optimal irrigation allocation scheme. Take the typical three-level canal system as an example which has rainfall during irrigation, this paper established an intelligent irrigation system and simulates its irrigation process, it is found that the system can reduce the total water consumption and improve the utilization efficiency of irrigation water and electricity. Therefore, construction and promote the intelligent irrigation system will be one of the way to develop Chinese irrigation.

Keywords: irrigation technology, intelligent irrigation system, frequency conversion technology, AGA

Citation: Huang, Y. D., Y. T. Xiao, W. Q. Wei, Y. Wu, Q. Z. Zhai, X. Z. Zhu, and S. Yang. 2017. Application research on intelligent irrigation system based on frequency conversion technology and AGA in China. International Agricultural Engineering Journal, 26(3): 263–268.

1 Introduction

Agriculture is one of the pillar industries in China. Large irrigation area, which accounts for 33.22% (Editorial Committee of Chinese Yearbook of Agriculture, 2013) of the total irrigation area, plays an important role in the development of economic and agricultural production in China. However, large irrigation areas have been constructed for a long time, there exist the following problems: 1) water efficiency of irrigation is as low as 0.5 (Fang, 2013), which is far from the world's advanced level of 0.7 to 0.9; 2) Scientific irrigation strategy is lack, resulting the water shortage of 30 billion cubic meters annually in China; 3) pump motor are running at constant frequency mode, which makes the pump motor output constant power and flow. As a result, the pump motor can't fit the scientific water distribution scheme, which will cause the waste of power and water, and it also requires pump motor to have a great capacity, which will improve standards of transformers and other electrical equipment.

Irrigation water is transported and distributed by pump motor, and the consumption of power and water are the same trend. Therefore, the irrigation mode, consisted of unscientific water distribution scheme and constant frequency mode of pump motor, will not only waste a lot of water, but also caused a huge power consumption. It is

Received date: 2017-06-29 **Accepted date:** 2017-08-26

* **Corresponding author: Zhai Qingzhi,** Master, Professor of College of Information and Electrical Engineering, China Agricultural University, 100083, China. Email: zhaiqz@cau.edu.cn.

a double reduction of resources efficiency. So it is necessary to make a scientific reformation in large irrigation area.

2 Intelligent irrigation system

There is a lack of scientific irrigation strategy of water in Chinese Large irrigation area. Mostly, time point and duration of water distribution time in the irrigation area are controlled by the operators according to their experience. Not only is it difficult to make efficient use of water resources, but also there may be a deviation between the amount of irrigation water and crop water demand. In addition, most pump motors are running at constant frequency mode, which makes the pump motor output constant power and flow, It can't match the real time water requirement of farmland, resulting in waste of water and electricity.

With the further development of frequency conversion technology, setting an intelligent irrigation system based on AGA and frequency conversion technology has become a technical choice to improve irrigation benefits.

2.1 Structure of the system

As shown in Figure 1, the steps of technical reconstruction in the large irrigation area can be divided into: 1) install CPU near the pump motor and transform the original motor with frequency conversion technology; 2) consummate the canal valves and configure various sensors.

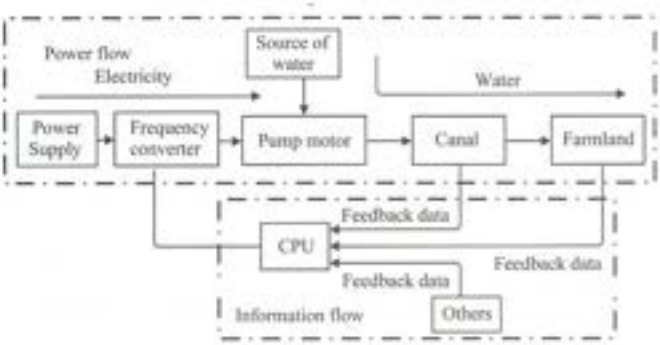

Figure 1 Intelligent irrigation system

When the Intelligent irrigation system is running, sensors can collect parameters of farmland and canal which can reflect water requirement of farmland. These parameters will be transmitted to CPU, and CPU adjusts irrigation strategy according to the feedback parameter. Then CPU adjusts frequency converter according to the new irrigation strategy. Pump motor will run at the control under the output signal of frequency converter, which can use irrigation water accurately and improve the water efficiency of irrigation and the utilization rate of energy.

2.2 Technology of the system

During the irrigation, irrigation strategies and water distribution scheme is needed, and they can be calculated by using adaptive genetic algorithm (AGA). According to the optimal water distribution scheme, the power and flow output of pump motor needs to be variable In order to realize water saving and electricity saving, the frequency conversion technology can meet this requirement.

Therefore, the intelligent irrigation system mainly uses the AGA and the frequency conversion technology.

2.2.1 Adaptive genetic algorithm (AGA)

Scientific irrigation strategy can scientifically and reasonably plan the water flow and water distribution time of each canal in the irrigation area according to the actual water demand of farmland, it can also shorten the whole irrigation period and reduce the leakage loss of the canals (Kang and Cai, 1996) which will increase water efficiency of irrigation. In order to find the optimal irrigation strategies and water distribution scheme quickly and accurately, an improved adaptive genetic algorithm (IAGA) (Xuan and Cheng, 2000) is used to optimize the model.

During the calculation, the superiority of adaptive genetic algorithm is that its fitness function, mutation rate and crossover rate can be changed according to the ratio of feasible solution in the process of calculation. The superiority makes the algorithm can avoid premature convergence in the early stage, move closer to the feasible solution domain quickly, and eventually converge to the optimal solution in the later stage. The specific operation is to introduce an adaptive penalty coefficient into the fitness function and introduce the Sigmoid function into the calculation function of mutation rate and crossover rate.

2.2.2 Frequency conversion technology

Before using frequency conversion technology, CPU

and frequency converter are needed to be installed near the pump motor. CPU regulates the output voltage and frequency of the converter according to the current parameters. Thereby, the speed and the torque of the pump motor are controlled, then the water quantity of the farmland irrigation is controlled, so as to realize the effect of water saving and electricity saving.

There are two running models of frequency converter, including the model of fixed-voltage altering-current and the model of fixed-current altering-voltage. The power-saving effect of the former model is between 35.4% to 66.7% (Li, 2003), the latter model is between 37.3% to 82.6% (Li et al., 2003).

2.3 Factors affecting the operation of the system

The intelligent irrigation system can adjust the irrigation strategy and the water distribution scheme in real time by collecting different kinds of information, which can react to water requirement of farmland, so as to obtain the optimal water distribution scheme for the current irrigation area.

Factors, including water flow, pressure, soil moisture, weather, crop types, and canal topology, can react water requirements of crop. If the above-mentioned factors change during the irrigation period, then the optimal water distribution scheme and the actual optimal water flow will change. What's more, these feedback parameters need to be added into calculation in order to adjust the effluent of the water pump motor accurately.

3 Case study

3.1 Model of a canal system

Set up a three-level irrigation canal system which is shown in Figure 2, The head of the main canal connects with the water source; the end of the main canal is divided into the North Main Canal and the South Main Canal; the main canal, the north canal and south canal are respectively connected with some branch canals; in order to simplify the calculation and expression, the branch canals, which are connected to the main canal, is equivalent to be connected to a virtual main canal; sum up the flow of virtual main canal, the north canal and south canal, and it is equal to the flow of main canal.

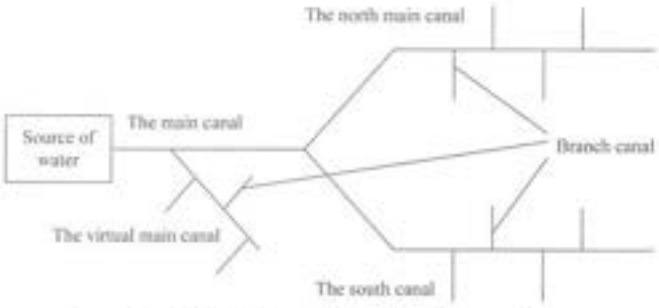

Figure 2 Model of three-level irrigation canal system

Objective function, which is aimed to minimize the total water leakage loss in the whole irrigation area, is established as follow:

$$\left.\begin{aligned} &Min \quad S = S_{bu} + S_{bd} + S_{nu} + S_{nd} + S_{xu} + S_{xd} \\ &S_x = \sum_{i=1}^{T} f\left(A_x, m_x, q_{xi}, l_x, t_x\right)\left(x = bu, nu, xu\right) \\ &S_y = \sum_{j=1}^{P_y} f\left(A_{yj}, m_{yj}, q_{yj}, l_{yj}, t_{yj}\right)\left(y = bd, nd, xd\right) \\ &S = f\left(A, m, q, l, t\right) = \frac{\left[A \cdot l \cdot q^{(1-m)} \cdot t\right]}{100} \end{aligned}\right\} \quad (1)$$

where, *bu*, *bd*, *nu*, *nd*, *xu*, *xd* is the code of the north main canal and its branch canals, the south main canal and its branch canals and the virtual main canal and its branch canals; S is mean water leakage loss during irrigation period, m^3; A, m, l, t respectively means the canal bed permeability coefficient and index, canal length and water distribution time; i is mean serial number of water distribution period; q_{xi} means the actual flow when the distribution period is i; j is mean the serial number of branch canal; P is mean the quantities of branch canal.

When AGA is used during the calculation, its fitness function is constructed by addition, shown by Equation (2):

$$F(x, c(p)) = 1/[f(x) + c(p) \cdot P(x)] \quad (2)$$

where, $f(x)$ is mean the objective function, as shown in the Equation (1); $P(x)$ is mean the penalty item, which is established according to the constraints; $c(p)$ is mean the adaptive penalty coefficient(Gan and Peng, 2009; Wang and Xiu, 2012; Tessema and Yen; Houck and Joines, 1994); p is mean the proportion of feasible solutions in the current generation.

When setting crossover rate and mutation rate, Sigmoid function (Ouyang et al., 2003; Wang and Cao, 2002; Sha et al., 2004) can be used which has a good

balance in the linear and nonlinear behavior. According to the Sigmoid curve, the value of crossover rate and mutation rate of individual is adjusted nonlinearly between the average fitness of the population and the maximum fitness of the individual.

3.2 Parameter setting

AGA is used to optimize the actual water distribution. The design flow of the main canal, the north main canal and south main canal were 27, 14 and 8 m^3/s; the values of permeability coefficient A and water permeability index m of all canals are 1.9 and 0.4 (Wang and Xiong, 1993). The water demand of farmland is 0.09 m^3 in the irrigation area, and each water distribution period is 12 hours. The value of parameters of branch canal of the main canal, the north main canal and the South main canal is equal to that in document (Wu, 2016). The population of genetic algorithm is set at 80. The upper and lower bounds of crossover rate are 0.8 and 0.6, and that of mutation rate are 0.05 and 0.005. The termination condition of the algorithm is that the number of iterations is 20000.

3.3 Result analysis

3.3.1 Results of routine operation of the system

After optimization, the water flow of branch canals of the main canal is shown in Figure 3a, where the ordinate corresponds to the canal number of branch canal as well as the width of the shaded rectangle is the length of the water distribution time and the height of the rectangle corresponds to the value of flow; the water flow of the main canal is shown in Figure 3b, where the vertical coordinate is the water flow volume of the head of the main canal and the shadow area is the total water input of irrigation area.

Figure 3b shows that, after irrigation water distribution optimization, the water flow of main canal is smooth and even can be kept constant in some continuous water period, which reduce the adjustment times. The water flow of canals is close to their design flow, the time to finish the irrigation target is short. Therefore, the optimized water distribution scheme calculated by AGA is useful.

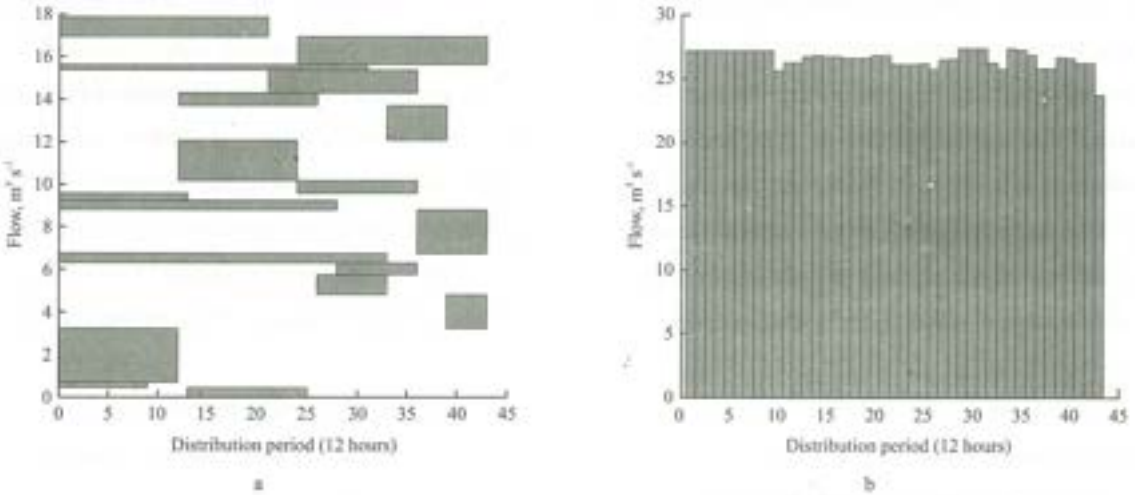

Figure 3 Distribution flow of the main canal and its branch canal

3.3.2 Results of operation of the system when considering precipitation

When an irrigation task is being finished in accordance with the original optimal water distribution scheme, any changes of feedback information will result in a deviation between the original water distribution scheme and the actual irrigation demand in a certain extent. Therefore, when irrigation feedback information changes, AGA must be used again to ensure the real-time water distribution scheme is optimal. The concrete steps are as follows: 1) Update the parameters of the new irrigation status according to the changed feedback information of the irrigation area; 2) Using AGA to reconstruct a new the water distribution scheme, which is optimal to now.

Meteorological factors have great effect to the water distribution scheme, which is mainly reflected in the rainfall. For example, it is d that there is raining in the north main canal irrigation area, which is cited from the second chapter.

Before rainfall, the water distribution scheme of the North main canal is shown in Figure 4, and the water distribution period is 43 (each period is 12 hours).

Suppose that rainfall occurs during the number 26 and 27 water distribution period. The total rainfall is 20 millimeters and is evenly distributed over time. At this time, using AGA again to calculate the water distribution scheme of the branch canals which do not finished their water distribution plan. Similarly, the minimum water loss is the objective function, and the parameters such as crossover rate, mutation rate, algorithm iteration number are the same. The fitness function is:

$$F_{fit} = 1 \Big/ \left\{ (S_u + S_d) \cdot \left[\sum_{i=1}^{T} \left(|Q_u - q_{ui}| \right) \right] \right\} \tag{3}$$

where, S_u and S_d respectively means the water leakage loss of main canal and its branch canal, (m^3); T is mean the total water distribution time, 12 hours; $|Q_u - q_{ui}|$ means the deviation between the actual water flow of the main canal and its designed flow during the water distribution period of number i, m^3/s; $\sum_{i=1}^{T}\left(|Q_u - q_{ui}|\right)$ means the penalty term of fitness function, which is the sum of all the deviation between the actual water flow of the main canal and its designed flow during the water distribution process. An individual with smaller water leakage loss has a greater fitness value. That means this individual has a greater probability of being retained, and to be participated in the operation of crossover and mutation.

The optimized calculation results are shown in Figure 5.

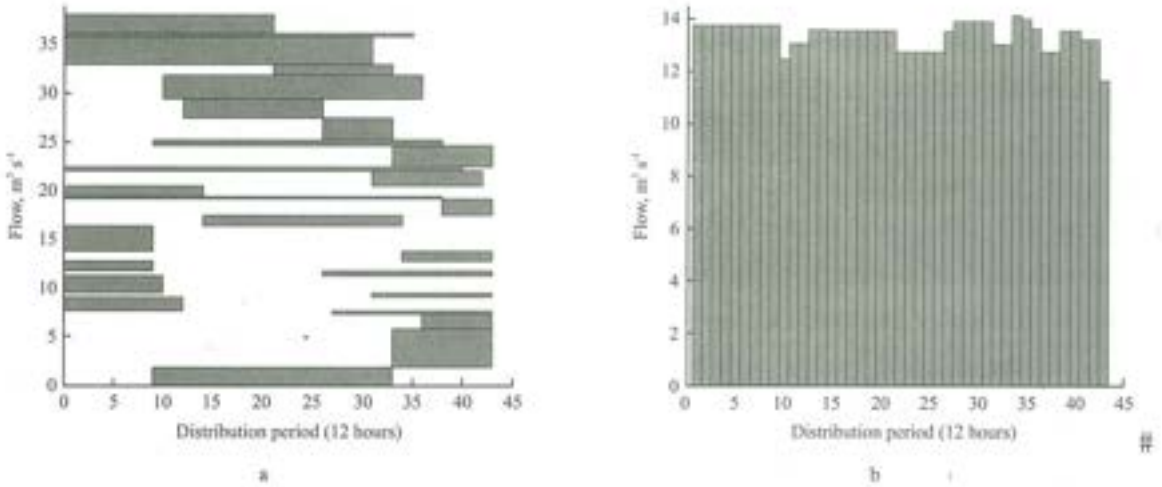

Figure 4 Distribution flow of the north main canal and its branch canal

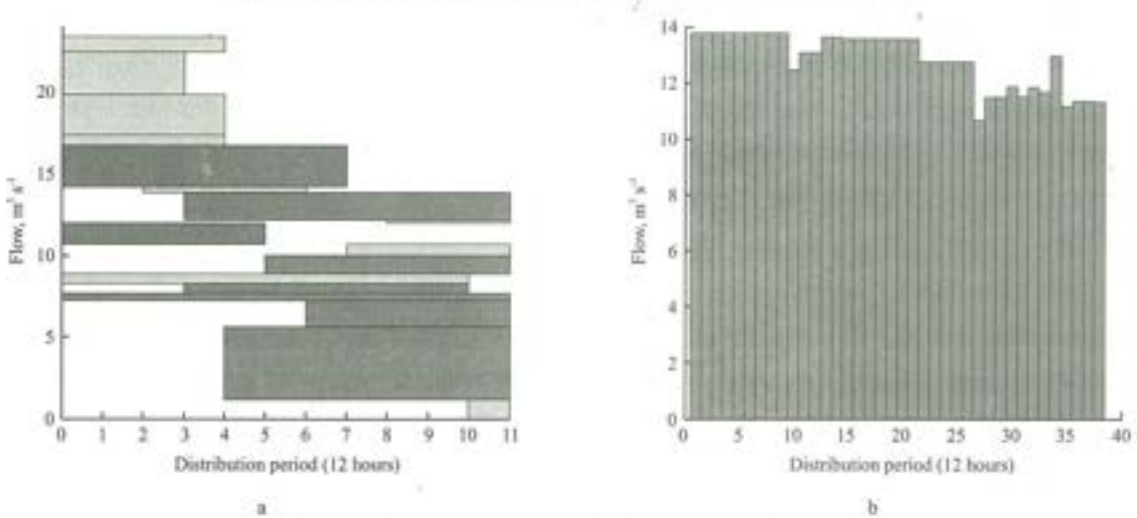

Figure 5 Distribution flow of the north main canal and its branch canal

Compared with Figure 4, after using AGA to calculate the water distribution scheme of the branch canals which do not finished their water distribution plan, It is easy to find that there exist differences of water flow

and water distribution time of the North main canal between the new scheme and the original one. Obviously, the total water distribution time is shortened from 43 water distribution periods to 38, and the total water delivery volume is reduced as well.

Therefore, when the precipitation occurs, intelligent irrigation system can restrict a new optimal water distribution scheme, which can improve the efficiency of water distribution. And the frequency conversion technology which is used in intelligent irrigation system enables pump motor to output variable flow, which is fitted to the actual need of farmland.

4 Conclusion

In the intelligent irrigation system, adaptive genetic algorithm can be used to achieve the scientific irrigation strategy according to the farmland parameters as well as the canal topology. And the application of frequency conversation technology allows pump motor to output flow which can be changed according to the optimal water distribution scheme. Meanwhile, the intelligent irrigation system can collect the feedback parameters reflecting water demand of farmland in real time, and adjust the irrigation strategy according to the feedback parameters, so that the irrigation system can work under the most optimal irrigation strategy.

In addition, the irrigation system mentioned above has perfect feedback system and gate system, if the feedback system and the gate system are not complete, the effect of water saving and energy saving will be more obvious.

In summary, intelligent irrigation system will be one of the effective ways to improve the efficiency of irrigation in China.

Acknowledgements

The Number of support project is SGTYHT/14-JS-188. This paper was completed by Huang-Yeda under the direction of professor Zhai Qingzhi. Meanwhile, engineer Zhu Xinzhi, Wu Yang, Yang Shuo and my teammate Xiao Yutian, Wei Wenqiang also have offered a great help, thanks for their work.

[References]

[1] Editorial Committee of Chinese Yearbook of Agriculture. 2013. China Agriculture Yearbook (2013). Beijing: China Agriculture Press.

[2] Fang, S. B. 2013. Research on the influencing factors of water efficiency of irrigation. Master's dissertation. Jiangsu: Yangzhou University, 2013.

[3] Kang, S. Z., and H. J. Cai. 1996. *Agricultural Water Management Science*. Beijing: China Agriculture Press.

[4] Xuan, G. N., and R. W. Cheng. 2000. *Genetic algorithm and engineering design*. Beijing: Science Press.

[5] Li, H. F. 2003. Design of a frequency conversion control system used for water-saving irrigation. *Transactions of the Chinese Society of Agricultural Machinery*, 34(5): 109–112.

[6] Li, Z. Q., G. S. Fan, and X. D. Lang. 2003. Application of frequency control technique to surface irrigation under low-pressure pipeline of water delivery. *Transactions of the Chinese Society of Agricultural Engineering*, 19(2): 89–92.

[7] Gan, M., and H. Peng. 2009. A new adaptive penalty function based algorithm for solving constrained optimization problems. *Information and Control*, 38(1): 24–28.

[8] Wang, Y. J., and N. H. Xiu. 2012. Nonlinear Optimization Theory and Methods. Beijing: Science Press.

[9] Tessema, B, and G. G. Yen. 2006. A self-adaptive penalty function based algorithm for constrained optimization. Evolutionary Computation, 2006. CEC 2006. IEEE Congress on. IEEE, 2006: 246–253.

[10] Houck, C. R., and J. A. Joines. 1994. On the use of non-stationary penalty functions to solve nonlinear constrained optimization problems with GA. *Proceedings of the First IEEE Conference on IEEE, June 27-29, 1994.*

[11] Ouyang, S., J. H. Wang, Y. S. Geng, Z. X. Song, and D. G. Chen. 2003. A new improved genetic algorithm. *Computer Engineering and Applications*, 39(11): 13–15.

[12] Wang, X. P., and L. M. Cao. 2002. *Genetic algorithms: theory, applications, and software implementation*. Xi'an: Xi'An Jiaotong University Press.

[13] Sha, Z. M., Y. Q. Hao, Y. S. Hao, and Y. H. Yang. 2004. A new adaptive genetic algorithm and its application in optimizing phasor measurement units placement in electric power system. *Transactions of China Electrotechnical Society*, 19(8): 107–112. (In Chinese with English abstract)

[14] Wang, Z. N., and Y. Z. Xiong. 1993. Optimal models for water allocation in irrigation canal system. *Journal of Northwest A & F University (Natural Science Edition)*. 1993 (2): 66–69. (In Chinese with English abstract)

[15] Wu, Y. 2016. *Research on irrigation area water consumption model and algorithm based on frequency conversion control*. Beijing: China Agricultural University.

Construction and specification of complex events from sensor network data in farmland

Li Xiang, Wei Xiaohong, Chen Xin*, Tang Xianglu, Xie Taomin, Jia Lu

(*College of Information and Electrical Engineering, China Agricultural University, Beijing 100083, China*)

Abstract: An important task of expert systems for precision farming is to recognizing composite situations in farmland to control intelligent devices to precision farming. In the existing expert systems, knowledges of composite situations are constructed to threshold inequation or production rules. However, threshold inequations could model only simple situations and production rules are complicated and lack readability. Complex event processing (CEP) is a helpful online pattern recognition technology. With CEP, composite situations can be detected according to pre-specified complex event patterns. In this paper, a novel model for complex events from sensor network in farmland is proposed, and a relevant event specification language is defined based on XML syntax. The model considers various influencing factors to judge and construct farmland complex events in a comprehensive manner. Especially, it supports mathematical, temporal and spatial logical relationships among constituent events of complex events. Spatial logic is necessary to model complex events from distributed sensors, but it is not supported by traditional complex event models. Data for 1 year from 27 sensors deployed in a 10 meters by 10 meters square farmland are collected. By analyzing the sensor data, five kinds of typical composite situations, i.e. rain, dry, irrigation, seepage and sensor damage, are constructed with the complex event model and specified with the specification language. Tests indicate false positives and omissions rate of our constructed complex evets are significantly lower than threshold control, the readability is better than production rules and complexity of specification is significantly lower than the widely-used model in SASE+.

Keywords: complex event processing, precision farming, expert system, sensor network, internet of things

Citation: Li, X., X. H. Wei, X. Chen, X. L. Tang, T. M. Xie, and L. Jia. 2017. Construction and specification of complex events from sensor network data in farmland. International Agricultural Engineering Journal, 26(3): 269–282.

1 Introduction

With wide use of intelligent agricultural expert systems in precision farming, the concept of "intelligent" is discussed more frequently. A necessary ability of an intelligent agricultural expert system is that it can recognize and respond to more composite situations in time. Nowadays, with the development of Internet of Things technology, more sensors are deployed in farmland to sense mass of status of air, soil and plants. Composite situations should be more precisely recognized from several dimensionalities of data from the mass of sensors deployed in different places, than from a single sensor. For example, rain is a composite situation. When it is rainy, a rain sensor in weather station can sense the rain and soil humidity sensor can sense the change of abnormal high humidity of soil. However, abnormal high humidity from a single sensor is not enough, for it may imply the sensor damage, instead of rain.

For this demand, traditional threshold control methods are not suitable, because only simple situations can be modeled. Many expert systems based on production inference were developed (Liu, 2007; Janssen et al., 2010). Although composite situations can be modeled in production rules, the specifications of these rules are complicated and lack of readabilities.

Complex event processing (CEP) is a helpful pattern recognition technology. Each composite situation can be

Received date: 2017-07-06 **Accepted date:** 2017-08-21

* **Corresponding author: Xin Chen,** Associate Professor of College of Information and Electrical Engineering, China Agricultural University, 100083 P. R. China. Email: chxin@cau.edu.cn. Tel: +86-135-0100-5205.

modeled as a complex event, which describes necessary data from sensors and temporal and spatial relationships among these data for recognition of the composite situation. CEP algorithms are used to online recognize and detect composite situations from atomic data depending on the pre-specified complex event patterns in real-time. Precise construction and specification of complex events with an effective complex event model is the key to precise recognition of composite situations.

In the recent decade, complex event models, real-time event detection algorithms and applications in different areas are developed (Buchmann et al., 2009). In 1990s, CEP was used in database management systems, in which semantic graph (Chakravarthy et al, 1994), Petri net (Gatziu, 1992) and finite state automata (Gehani, 1992) were the three most widely used models to construct database complex events. The models have supported mathematical logic and simple temporal logic, but their structures were too abstract and their readabilities are poor for users. In the late 2000s, it was found that CEP is effective to process event flow, so the technology got paid attention again. SQL-like models were developed (Wu, 2006). Then a regular SQL-like model was defined in SASE+ system, special operators like Kleene closure are defined (Diao et al., 2007). The model of SASE+ is still one of the most popular model now. A sliding window was added to the model (Krämer, 2009). Another popular model is defined in Esper system (EsperTech, 2016). It is also a SQL-like model. In addition, a XML-based complex event model is proposed in (Zang et al., 2007). Some new complex logic operators to specify composite situations are defined in IBM Amit system (Magid et al., 2010). The models above can describe very composite situation and have suitable readabilities. However, these models have not considered spatial logic relationships among constituent events, so they are lengthy when specifying complex events from sensor network distributed deployed in farmland.

In recent years, CEP is viewed as one of the leading technologies of Internet of Things (Haller et al., 2008). Event models and process algorithms are widely studied (Fengjuan et al., 2013; Jun et al., 2014). However, the advanced technology is rarely used in agriculture. Precisely model and specification language of complex events of internet of things in farmland are insufficient.

In this paper, a novel complex event model for farmland complex events is proposed and meanwhile a relevant event specification language is defined based on XML syntax. Five kinds of typical composite situations, i.e. rain, dry, irrigation, seepage and sensor damage, are constructed to complex events by analyzing data from actual sensor network in farmland and specified with the specification language. Tests indicate false positives and omissions rate of our constructed complex evets are significantly lower than threshold control, the readability is better than production rules and complexity of specification is significantly lower than the widely-used model in SASE+.

2 Complex event processing

An event is variations of some states in the physical world. It is usually "complex", i.e. several or dozens of states and variations of states need to be considered, so it is called complex event. Conversely, a variation of a single state is called an atomic event. A complex event could be specified in a pattern, which describes how the above-mentioned states and variations (i.e. atomic events) determine whether the complex event occurs and information of the occurrence. When a system is monitoring huge number of states in physical world, a number of atomic events can be detected and continually converged into an atomic event flow. From the flow, a complex event processing algorithm is used to detect complex events according to pre-specified complex event patterns.

There are two hot research topics in complex event processing area: 1) how to model complex events and 2) how to efficiently detect complex events from atomic event flow. This paper focuses on the first topic. A model of a complex event includes constituent atomic events and their relationships which can be described with mathematical logic, temporal logic and spatial logic functions. For example, $(((E_1 \Delta E_2);\ E_3);\ (E_2 \Delta E_4))$ is a complex event, in which E_1, E_2, E_3, E_4 are atomic events and linked with two logical operators: "Δ" and ";", respectively denoting mathematical logic function "and" and temporal logic function "sequence". With ";

2.1 Complex event model

A complex event model with spatial logic is proposed and a specification language to describe complex event models is defined. In the model, an event is formal represented as $E=(i, a)$, $a=\{d, t, r, p, o\}$. a is an attribute set, In that, $d=[t_0,t_1]$ and t denote time period and time point of the event occurrence; r and p denote spatial region and spatial position of it; o denotes other attributes of the event.

Figure 1 illustrates hierarchical structure of complex event model. A complex event consists of constituent events. Whether the complex event occurs or not is determined by constituent events. Attributes of the complex event is calculated with attributes of next level of events. Four sets determine occurrence and attributes of a complex event: *ES*, *IS*, *FJ*, and *FC*.

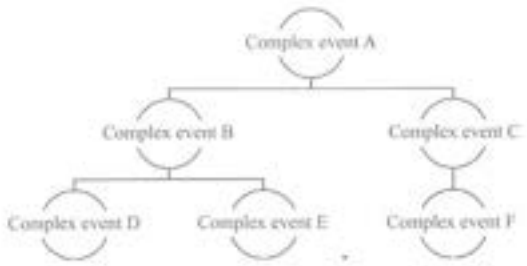

Figure 1 Hierarchical structure of complex event model

ES is constituent events set. For example, in Figure 2, $ES_A=\{B, C\}$.

IS is occurrence consumption strategies set, that determines which occurrences of constituent will be used or removed. Different consumption strategies can be chosen for different constituent events.

$$IS=(IS_C, IS_R, IS_W) \tag{1}$$

IS_C – chosen strategy of occurrences of constituent events used to assemble the complex event. Four common chosen strategies are: *recent* – choosing newest occurrences of constituent events; *chronicle* – choosing earliest occurrences of constituent events in the time window; *continuous* – choosing all occurrences of constituent events and assemble several occurrences of the complex event with different combinations; and *cumulative* – choosing all occurrences of constituent events and assemble only one occurrence.

IS_R – determines which occurrences will be removed from the constituent event occurrences flow after the detection of the complex event. Usually only newest occurrences are usable to detect complex event, so unusable occurrences should be removed because of store space limitation. Four common remove strategies are: *reserve* – not removing any occurrences; *removeone* – removing all occurrences in IS_C; *removeearly* – removing all occurrences in IS_C and removing all occurrences occurred early than them; and *removeall* – removing all occurrences in the time window.

ISw – determines the length of the sliding window of the constituent event occurrences flow. New occurrences will be added to the window continually and occurrences out of the window will be removed. Two common window strategies are: *timewindow* – occurrences occurred in a period keeping in the windows; and *lengthwindow* – a certain number of occurrences keeping in the window. Here which occurrences can be remained in the window is determined by both IS_R strategy and IS_W strategy.

FJ is a function to judge whether the complex event occurs.

$$FJ(\{e.a \mid \forall e \in IS_C(ins(E_{i1}),ins(E_{i2}),...,ins(E_{in}))\}) = \begin{cases} \text{true, complex event occurs} \\ \text{false, complex event not occurs} \end{cases}, E_i \in ES \tag{2}$$

$$\begin{cases} FJ = FJ_{occr} \,\&\, FJ_{d,t} \,\&\, FJ_{r,p} \,\&\, FJ_o \\ FJ_{occr} \equiv CJ(e_{i1},...,CJ_1(e_{j1},...),...) \\ FJ_{d,t} \equiv TJ(e_{i1}.t,e_{i1}.d,...,TJ_1(e_{j1}.t,e_{j2}.d,...),...) \\ FJ_{r,p} \equiv SJ(e_{i1}.p,e_{i1}.r,...,SJ_1(e_{j1}.p,e_{j2}.r,...),...) \\ FJ_o \equiv OJ(e_{i1}.o,...,OJ_1(e_{j1}.o,...),...) \end{cases} \tag{3}$$

FJ_{occr} defines rules to judge whether necessary constituent events occur. $FJ_{d,t}$ judges whether temporal relationships among constituent events in IS_C meet requirements by calculating d and t of them. $FJ_{r,p}$ is the judgement function for spatial relationships with arguments r and p, and FJ_o is for other relationships with arguments o.

e_E – an occurrence of event E.

$ins(E)$ – occurrences flow of an event E.

$e_E.x$ – attribute x of e_E.

CJ, *TJ*, *SJ* and *OJ* – occurrence, temporal, spatial and other judgement operators. All defined operators are listed in Table 1.

Table 1 Defined occurrence (*CJ*), temporal (*TJ*), spatial (*SJ*) and other judgement operators (*OJ*)

Category	Operator	Implication
CJ	$con(e_A, e_B, \ldots)$ or $e_A \wedge e_B \wedge \ldots$	All of events *A*, *B*, … occur
	$dis(e_A, e_B, \ldots)$ or $e_A \vee e_B \vee \ldots$	One of events *A*, *B*, … occurs
	$any(e_A, e_B, \ldots, n)$	Any *n* events of *A*, *B*, …, occur
	$not(e_A, e_B, \ldots)$	None of events *A*, *B*, … occur
	$count(e_A, n)$	Event A occurs for *n* times
TJ	$sync(e_A.t, e_B.t, \ldots, \rho)$	Events *A*, *B*, … occur in the same period ρ
	$between(e_A.t, e_B.t, e_C.t)$	Event *B* occurs between *A* and *C* occur.
	$sequence(e_A.t, e_B.t, \ldots)$	Event *A*, *B*, … occur in the order
	$after(e_A.t, e_B.t)$	An event *B* occurs after an event *A*
	$in(e_A.d, e_B.d)$	*d* of an event *A* is in *d* of and event *B*, i.e. $in_{align}(e_A, e_B) = e_A.t_0 \geq e_B.t_0 \,\&\, e_A.t_1 \leq e_B.t_1$ Values of subscript *align*: *begin* - $e_A.t_0 = e_B.t_0$ *end* - $e_A.t_1 = e_B.t_1$ *both* - $e_A.t_0 = e_B.t_0 \,\&\, e_A.t_1 = e_B.t_1$ *none* - $e_A.t_0 > e_B.t_0 \,\&\, e_A.t_1 < e_B.t_1$
	$follow(e_A.d, e_B.d)$	An event *B* occurs following an event *A*, i.e. $follow_{align}(e_A, e_B) = e_A.t_0 < e_B.t_0 \,\&\, e_A.t_1 < e_B.t_1$ Values of subscript *align*: *separate* - $e_A.t_1 < e_B.t_0$ *overlap* - $e_A.t_1 > e_B.t_0$ *tangency* - $e_A.t_1 = e_B.t_0$
SJ	$some(e_A.p, e_B.p)$	Event *A* occurs in the same point with event *B*
	$split(e_A.p, e_B.p)$	Event *A* occurs in the different point with event *B*
	$inside(e_A.p, e_B.r)$	Event *A* occurs in the region of event *B*
	$outside(e_A.p, e_B.r)$	Event *A* occurs out of the region of event *B*
	$disjoint(e_A.r, e_B.r)$	Region of e_A is disjoint with region of e_B
	$circumscribe(e_A.r, e_B.r)$	Region of e_A circumscribes region of e_B
	$overlap(e_A.r, e_B.r)$	Region of e_A overlaps with region of e_B
	$inscribe(e_A.r, e_B.r)$	Region of e_B inscribes with region of e_A
	$contain(e_A.r, e_B.r)$	Region of e_A contains region of e_B
	$equal(e_A.r, e_B.r)$	Region of e_A is the same as region of e_B
OJ	Other relationships to judge occurrence of the complex event with attributes of constituent events	

FC is a function to calculate attribute set *a* with attribute sets of constituent events.

$$e_E.a = FC(\{e.a \mid \forall e \in IS_U(ins(E_{i1}), ins(E_{i2}), \ldots, ins(E_{in}))\}), E_{ij} \in ES \quad (4)$$

$$\begin{cases} FC \equiv (FC_{d,t}, FC_{r,p}, FC_o) \\ FC_{d,t} \equiv TC(e_{i1}.t, e_{i1}.d, \ldots, TC_1(e_{j1}.t, e_{j2}.d, \ldots), \ldots) \\ FC_{r,p} \equiv SC(e_{i1}.p, e_{i1}.r, \ldots, SC_1(e_{j1}.p, e_{j2}.r, \ldots), \ldots) \\ FC_o \equiv OC(e_{i1}.o, \ldots, OC_1(e_{j1}.o, \ldots), \ldots) \end{cases} \quad (5)$$

$FC_{d,t}$ is the function to calculate the time period (*d*) and time point (*t*) of an occurrence of the complex event. $FC_{r,p}$ is used to calculate the spatial region (*r*) and spatial point (*p*). FC_o is used to calculate other attributes (*o*). *TC*, *SC* and *OC* are respectively temporal, spatial and other calculation operators. All defined operators are listed in Table 2.

Table 2 Defined temporal (*TC*), spatial (*SC*) and other calculation operators (*OC*)

Category	Operator	Implication
TC	$nc(e_A.t, e_B.t, \ldots)$	Calculate the time point of complex event *E* by numerical calculation of time points of constituent events *A*, *B*, …
	$continue(e_A.t, e_B.t, \ldots)$	Time period (*d*) of complex event *E* is the minimum period that contains all time points (*t*) of constituent events *A*, *B*, …, i.e. $e_E.d = [\min_t e_i.t, \max_t e_i.t]$
	$intervalunion(e_A.d, e_B.d, \ldots)$	The union of all time periods of constituent events *A*, *B*, …, i.e. $e_E.d = e_A.d \cup e_B.d \cup \ldots$
	$interalintersection(e_A.d, e_B.d, \ldots)$	The intersection of all time periods of constituent events *A*, *B*, …, i.e. $e_E.d = e_A.d \cap e_B.d \cap \ldots$
	$interaldifference(e_A.d, e_B.d)$	The relative complement of *d* of e_B with respect to *d* of e_A. $e_E.d = e_A.d \setminus e_B.d$
	$interalcontinue(e_A.d, e_B.d)$	Time period (*d*) of complex event *E* is the minimum period that contains all time periods (*d*) of constituent events *A*, *B*, …, i.e. $e_E.d = [\min_t e_i.t_0, \max_t e_i.t_1]$
SC	$centroid(e_A.r)$	The centroid of the region (*r*).
	$polygon(e_A.p, e_B.p, \ldots)$ or $polygon(e_A.r, e_B.r, \ldots)$	Spatial area (*r*) of complex event *E* is the minimum polygon that covers all spatial points (*p*) or all regions of constituent events *A*, *B*, …
	$circle(e_A.p, e_B.p, \ldots)$ or $circle(e_A.r, e_B.r, \ldots)$	Spatial area (*r*) of complex event *E* is the minimum circle (in 2D space) or ball (in 3D space) that covers all spatial points (*p*) or all regions of constituent events *A*, *B*, …
	$areaunion(e_A.r, e_B.r, \ldots)$	The union of all spatial areas of constituent events *A*, *B*, …, i.e. $e_E.r = e_A.r \cup e_B.r \cup \ldots$
	$areaintersection(e_A.r, e_B.r, \ldots)$	The intersection of all spatial of constituent events *A*, *B*, …, i.e. $e_E.r = e_A.r \cap e_B.r \cap \ldots$
	$areadifference(e_A.r, e_B.r)$	The relative complement of *r* of e_B with respect to *r* of e_A. $e_E.r = e_A.r \setminus e_B.r$
	$areapolygon(e_A.r, e_B.r, \ldots)$	Spatial area (*r*) of complex event *E* is the minimum polygon that contains all spatial areas (*r*) of constituent events *A*, *B*, …
	$areacircle(e_A.r, e_B.r, \ldots)$	Spatial area (*r*) of complex event *E* is the minimum circle (in 2D space) or ball (in 3D space) that contains all spatial areas (*r*) of constituent events *A*, *B*, …
OC	Other relationships to calculate *a* of the complex event with attributes of constituent events.	

2.1 Complex event specification language

A complex event specification language based on XML syntax is designed to describe complex events.

For atomic event, identification, sources and attributes will be specified, and for complex event, identification, *ES*, *IS*, *FJ*, and *FC* will be specified, as Table 3.

For a constituent event, a judgement function and a calculation function, the syntax is as Table 4.

Table 3 Syntaxes for specifying atomic event and complex event

Atomic event

```
<atom> // an atomic event
  <id>atomevent1</id>//identification
  <sources>
    <src>sensor1</src>//a source
    ...
  </source>
  <attributes>// attributes
     <attr id="o1" type="x" var="true| false"> o1 </attr>
    //an attribute, type is d | t | r | p | o
    ...
  </attributes>
  <jfunc> //a judgement function
    ...
  </jfunc>
</atom>
```

Complex event

```
<ce> // a complex event
  <id>complexevent1</id>//identification
  <otherattrs> ... </otherattrs>//other attributes
  <eventset>//constituent event set ES
   <event>...</event>//a constituent event and its occurrence consumption strategies
    ...
  </eventset>
  <judgefunction logic="conjunction|disjunction">   //judgement functions
    ...
  </judgefunction>
  <calculationfunction>//calculation functions
    ...
  </calculationfunction >
</ce>
```

Table 4 Syntaxes for specifying a constituent event, a judgement function and a calculation function

Constituent event

```
<event>
  <evn>...</evn>//id of the constituent event
  <chosenstrategy>recent | chronicle | continuous | cumulative</chosenstrategy>//ISc, with 4 options
  <removestrategy>reserve | removeone | removeearly | removeall </removestrategy>//ISk, with 4 options
  <timewindow>time1</timewindow>//time window
  <lengthwindow>10</lengthwindow>//length window
</event>
```

Judgement function

```
<judgefunction logic="conjunction|disjunction">
  <variables>//variables for judgement
    <var id="v1">//a variable
      <evn>e1</evn>//constituent event "e1"
      <occ>1</occ>// occurrence serial
      <attr>o1</ attr >// an attribute "o1"
    </var>
    ...
  </variables>
  <jfunc>f1(${v1},${v2},...)</jfunc>
  <jfunc>f2(${v1},${v2},...)</jfunc>
  ...
</judgefunction>
```

Calculation function

```
<calculationfunction>
  <variables>//variables for calculation
    <var id="v1">//a variable
      <evn>e1</evn>//constituent event "e1"
      <occ>1</occ>// occurrence serial
      <attr>o1</ attr >// an attribute "o1"
    </var>
    ...
  </variables>
  <cfunc attr="d|t|r|p|...">
    f(${v1},${v2},...)
  </cfunc>
</calculationfunction>
```

3 Construction and specification of complex events in farmland

3.1 Data

Data are collected from a 10×10 m^2 farmland in Shangzhuang, Beijing. The farmland is empty, no plants, except for grass. Nine monitoring points are assigned in the farmland, illustrated in Figure 2a. In each monitoring point, three sensors are deployed to sense soil temperature and moisture respectively in 10 cm, 20 cm and 40 cm deep, illustrated in Figure 2b. One weather station is deployed in north of the farmland to sense air temperature, humidity, rain, wind direction, etc. Frequencies of data sensing of soil sensors and weather station are the same - once per hour. The data was continued to collect in near one whole year, from May 2015 to May 2016. The soil moisture data sensed by sensors in the 10 cm in nine monitoring points and rainfall data sensed by the weather station from May 2015 to May 2016 are illustrated in Figure 3.

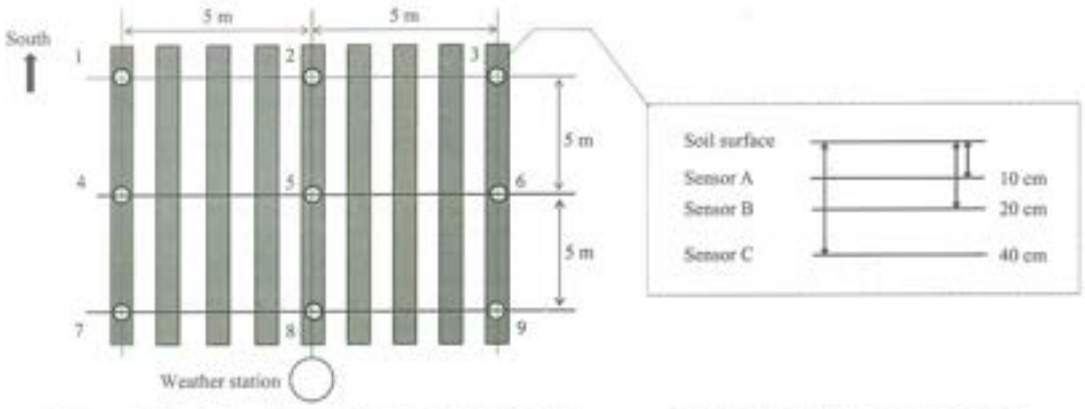

a. Nine monitoring points and one weather station in the 10 meters by 10 meters square farmland

b. Three levels of sensors deployed in each monitoring point

Figure 2 Setup of soil temperature and moisture data collection

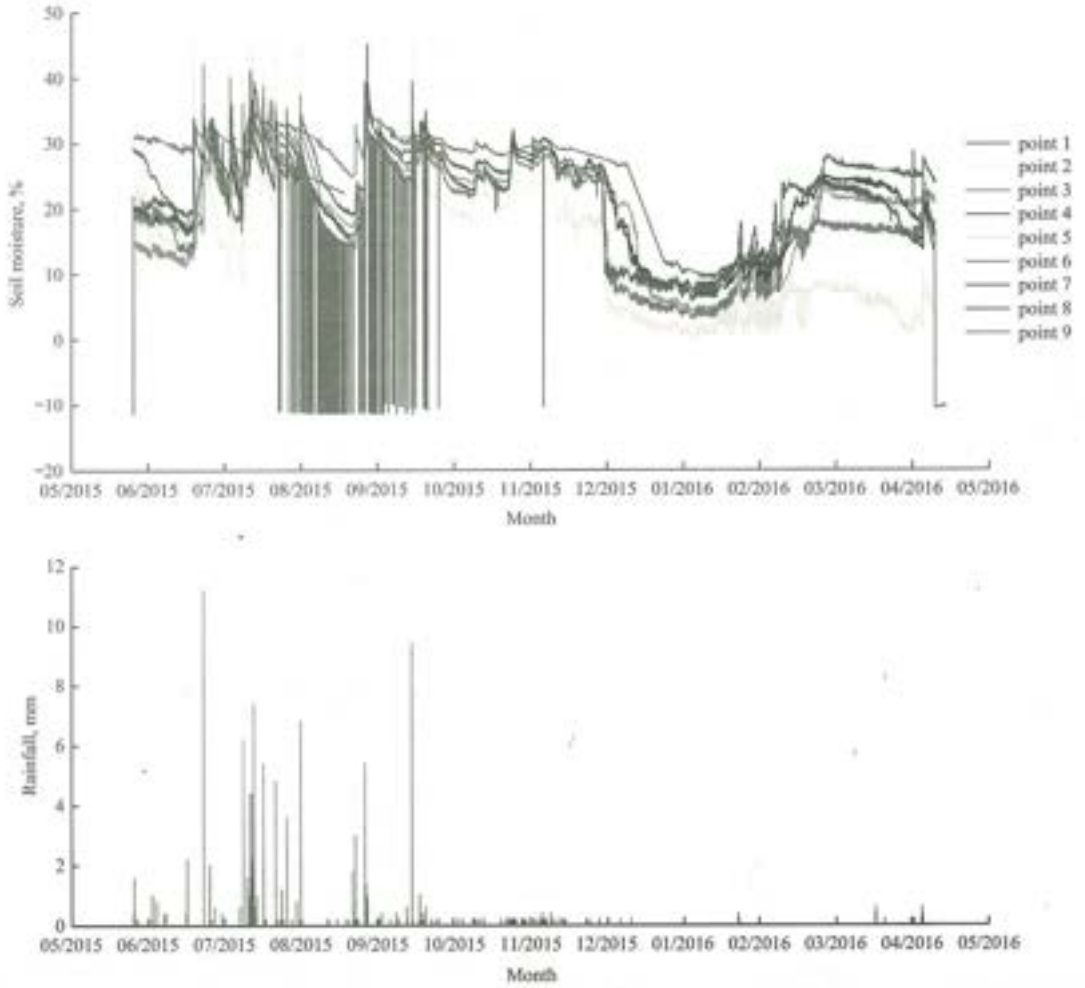

Figure 3 Soil moisture data sensed by sensors in 10 cm at 9 monitoring points and rainfall data sensed by the weather station from May 2015 to May 2016

3.2 Atomic events

For single sensor, five kinds of sensor data can be considered. The basic atomic event is "update data event", denoted as ***u***, which occurs when the sensor updates a piece of data.

"Higher event" and "lower event", respectively denoted as ***h*** and ***l***, which are defined by data from single sensor at only one time point, imply the value of the sensor is respectively higher and lower than a threshold. For example, soil moisture is impossible higher than 100%, so "higher than 100%" is a higher event.

The other two kinds of atomic events are more or less "complex", because they involve data from single sensor at two time points. In order to reduce the complexity of

complex events, the two kinds of frequently-used "complex" events are regarded as atomic events. They are "increase event" and "decrease event", denoted as "*i*" and "*d*". "increase event" implies that the increase of the sensor value from the previous time point to the latter time point is higher than a threshold. "decrease event" implies that the decrease is higher than a threshold. For example, "increase 20% between two time points" is an increase event.

Thresholds for atomic events are determined by statistics. Considering mathematical expectations (*mean*) and standard deviations (*std*) of all data from a sensor, we suggest that thresholds of higher event and lower event should be respectively *mean*+3·*std* and *mean*–3·*std*, and thresholds of increase event and decrease event should be 1·*std*. For example, for 10cm senor at point 1, *mean* and *std* of all soil moisture data are respectively 20.12% and 8.11%. Thus, the suggested thresholds of higher event and lower event are respectively *mean*+3·*std*=44.45% and *mean*–3·*std* = –4.21%. Because *mean*–3·*std*<0%, the threshold of lower event should be 0%. The thresholds of increase event and decrease event should be 1·*std*=8.11%.

An example of higher event is illustrated in Appendix I.

3.3 Complex events

"Sensor damage event"

The first kind of considered complex events is "sensor damage". Only after filtering "sensor damage" events, other complex events can be recognized correctly.

Figure 4 illustrates the data of the 10 cm sensors at seven points. Four sensor damage events occur at 7th point. From the figure, obvious characteristic of a sensor damage event can be found. Firstly, each sensor damage event can be detected with a higher event (h_i), a lower event (l_i), an increase event (i_i) or a decrease event (d_i), but it is not enough. In the broken blue circle in Figure 4, increase and decrease events of 10 cm sensors at all points, which imply there is a rain or irrigation event, but not sensor damage event. Thus, it implies a sensor damage event that h_i, l_i, i_i or d_i occurs at only one sensor while those atomic events have not occurred at other sensors at the same time point.

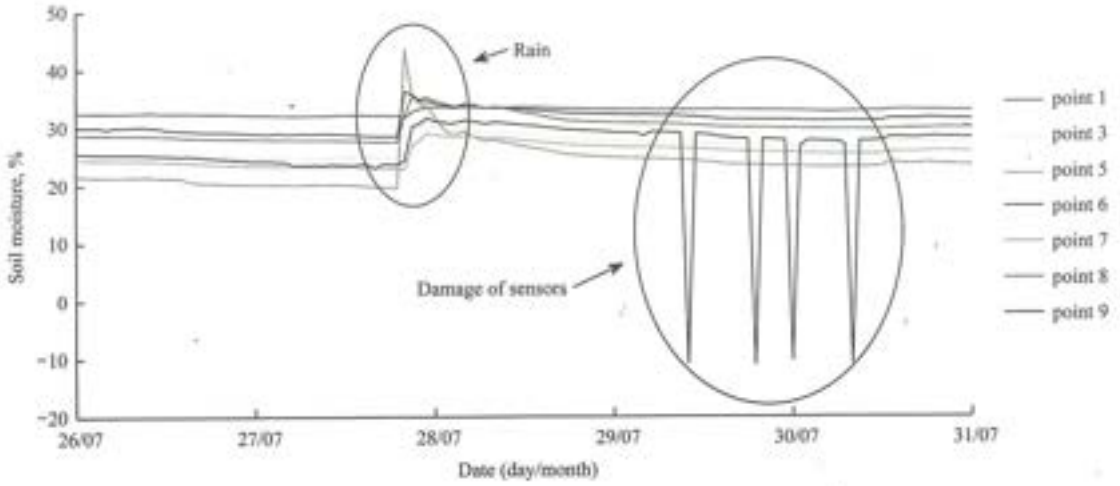

Figure 4 Four sensor damage events of the 10 cm sensor at 9th point

To construct the complex event of sensor damage, above-mentioned four kinds atomic events are constituent events. Only the newest one occurrence of each atomic event needs to be considered, so their IS_C strategies are *recent* and *ISw* strategies are *lengthwindow* with one length window. After detection of the complex event, all occurrences can be removed from the flow, so IS_R strategies are *removeall*. *FJ* functions of the complex event are as follow:

$$\begin{cases} FJ_{occr} = dis(h_{i1}, l_{i1}, i_{i1}, d_{i1}) \wedge not(h_{i2}, h_{i3}, ..., l_{i2}, l_{i3}, ..., \\ \qquad i_{i2}, i_{i3}, ..., d_{i2}, d_{i3}, ...) \\ FJ_{d_t} = sync(u_{i1}.t, u_{i2}.t, u_{i3}.t, ..., 2) \\ FJ_{r_p} = inside(u_{i1}.p, u_{i2}.r) \wedge inside(u_{i1}.p, u_{i3}.r) \wedge ... \end{cases} \quad (6)$$

Here *i*1 is the identification of the sensor which h_{i1}, l_{i1}, i_{i1} or d_{i1} occurs, and *i*2, *i*3,… are identifications of other sensors. FJ_{d_t} limits that the occurrence time of the update events of all considered sensors should be in two update periods of sensors. FJ_{r_p} limits that position of other

considered sensors should be in the region of event $i1$.

Considering FC of the complex event, attributes t, d, r, and p are equal to the corresponding attributes of h_{i1}, l_{i1}, i_{i1} or d_{i1}.

As an example, the specification of the sensor damage event with our specification language is illustrated in Appendix II.

Another kind of sensor damage event should be also considered: a sensor has not updated data for a long time. For the complex event, more than one occurrence states of update event of one sensor are detected. FJ function is:

$$FJ_{occr}=count(not(u_i),3) \quad (7)$$

implying update event of sensor i has not occurs for three data update periods. Attributes t, d, r, and p are equal to the corresponding attributes of the last occurrence of u_i. Considering consumption strategies (IS), three occurrences of u_i are used, so length of sliding window (IS_W) is 3.

"Rain event"

Figure 5 illustrates two rain events on July 23 and 28. The weather station has a rain sensor, so rain can be detected with higher events (h_{ws}) and increase events (i_{ws}) of the sensor. It is not enough, because of the errors or damage of the sensor. When it is rainy, higher events (h_i) and increase events (i_i) of soil sensors in 10 cm occur which can be used to assist detection of the rain. Thus, FJ functions of rain event are:

$$\begin{cases} FJ_{occr} = dis(h_{ws}, i_{ws}) \wedge any(h_1, h_2, ..., i_1, i_2, ..., 3) \\ FJ_{dJ} = sync(h_{ws}.t, i_{ws}.t, e_{i1}.t, e_{i2}.t, e_{i3}.t, 2) \end{cases} \quad (8)$$

Here, e_{i1}, e_{i2}, and e_{i3} are three actual occurrences of h_1, h_2, ..., i_1, i_2, ... It is rainy when h_{ws} or i_{ws} occurs and any three higher or increase events of soil sensors occur. All of these events should occur in two data update periods.

Considering that FC functions of a rain event (re), time attributes t and d of it are equal to the corresponding attributes of h_{ws} or i_{ws}. The region (r) of it should contain all region of constituent events and the position (p) should be the centroid of r. Thus, region and the position of the complex event is:

$$\begin{cases} re.r = polygon(h_{ws}.r, i_{ws}.r, e_{i1}.r, e_{i2}.r, e_{i3}.r) \\ re.p = centroid(re.r) \end{cases} \quad (9)$$

Considering consumption strategies (IS), only the newest one occurrence of each atomic event needs to be considered, so their IS_C strategies are *recent* and length of the windows of all constituent events are 1. After detection of the complex event, all occurrences can be removed from the flow, so IS_R strategies are *removeall*.

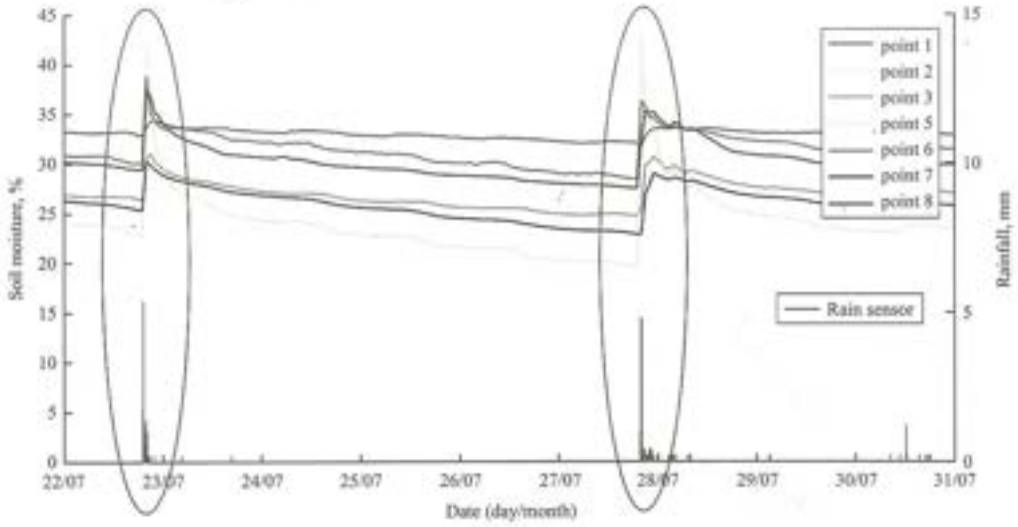

Figure 5 Two rain events on July 23 and July 28

"Irrigation event"

Figure 6 illustrates an irrigation event on November 7. When irrigation, higher events (h_i) or increase events (i_i) in 10 cm, 20 cm and even 40 cm. To ensure effect of irrigation, h_i or i_i in 20 cm are chosen. Meanwhile, to distinguish it from rain events, irrigation events usually occur in it is not rainy. Thus, FJ functions of the irrigation event are:

$$\begin{cases} FJ_{occr} = any(h_1, h_2, ..., i_1, i_2, ..., 3) \\ FJ_{dJ} = sync(e_{i1}.t, e_{i2}.t, e_{i3}.t, 1) \\ \qquad \wedge between(\min(e_{i1}.t, e_{i2}.t, e_{i3}.t), \\ \qquad not(re), \max(e_{i1}.t, e_{i2}.t, e_{i3}.t)) \end{cases} \quad (10)$$

Here, re is a rain event, and e_{i1}, e_{i2}, and e_{i3} are 3 actual occurrences of h_1, h_2, ..., i_1, i_2, ... An irrigation event occurs when any three higher or increase events of 20 cm soil sensors occur, all of these events of soil sensors should occur in the same data update period, and it is not rainy in the period.

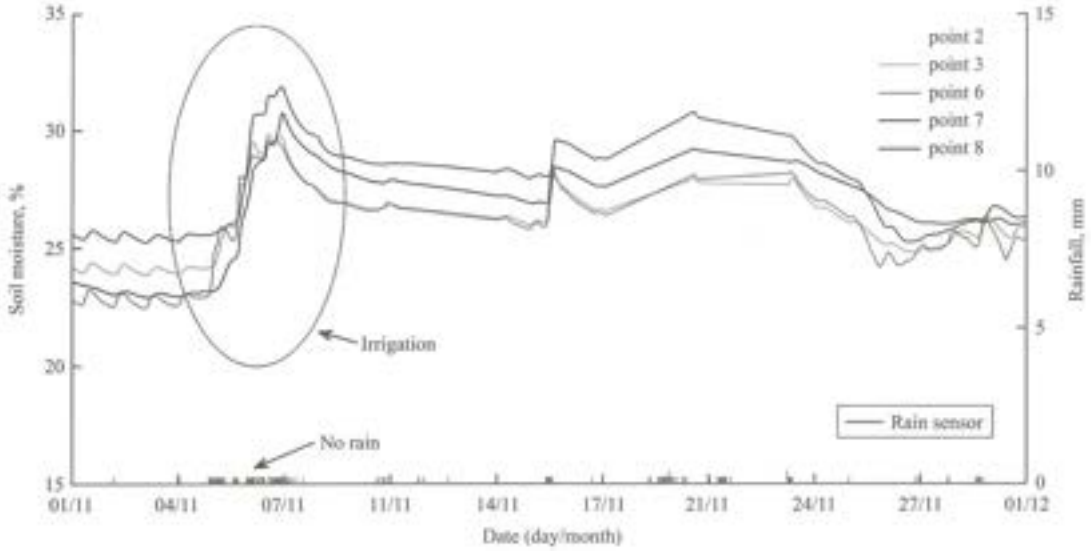

Figure 6 An irrigation event on Nov 07

Considering FC functions of an irrigation event (ie), time attributes t and d are equal to the corresponding attributes of the first constituent event h_i or i_i. Its region (r) contains all regions of constituent events and its position (p) is the centroid of its region (r), i.e.

$$\begin{cases} ie.r = polygon(e_{i1}.r, e_{i2}.r, e_{i3}.r) \\ ie.p = centroid(re.r) \end{cases} \tag{11}$$

IS_C, ISw and IS_R strategies are the same as rain event.

"Dry event"

Figure 7 illustrates some dry events in December 2015. When soil is dry, lower events (l_i) of more than three nearby sensors occur for three data update periods at the same time. FJ functions of dry event are:

$$\begin{cases} FJ_{occr} = any(count(l_1,3), count(l_2,3), ..., 3) \\ FJ_{d,t} = sync(l_{i1}^1.t, l_{i2}^1.t, l_3^1.t, 1) \\ FJ_{r,p} = overlap(l_{i1}^1.r, l_{i2}^1.r) \wedge overlap(l_{i1}^1.r, l_{i3}^1.r) \\ \qquad \wedge overlap(l_{i2}^1.r, l_{i3}^1.r) \end{cases} \tag{12}$$

Here, $FJ_{d,t}$ describes that the first occurrence of the three constituent events, denoted as l_{i1}^1, l_{i1}^2, and l_{i1}^3, should occur in one data update period, $FJ_{r,p}$ describes sensors $i1$, $i2$, $i3$ are neighbors.

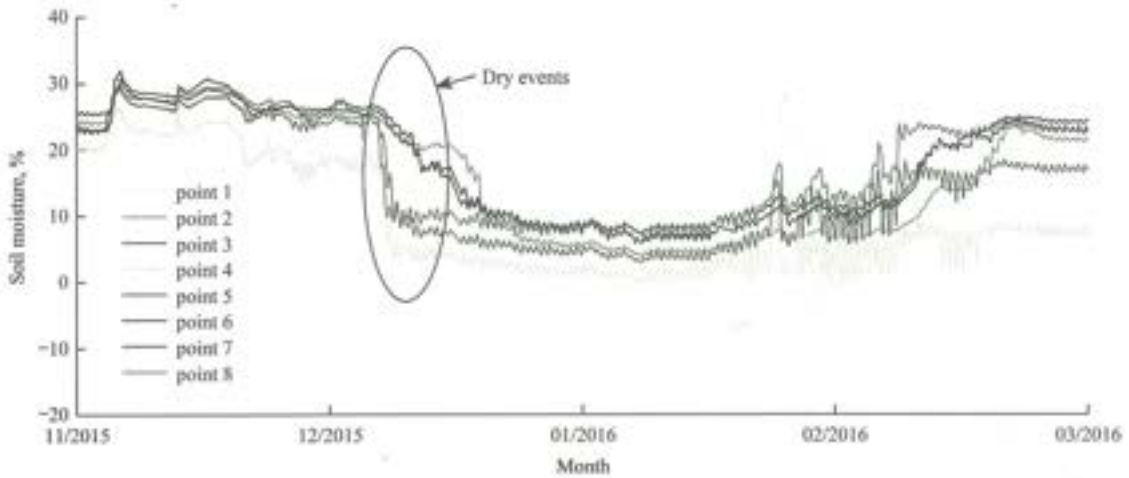

Figure 7 Dry events in December 2015

Considering FC functions of a dry event (de), time attributes t and d are equal to the corresponding attributes of the first constituent event l_i. The region (r) of it contains all regions of constituent events and position (p)

of it is the centroid of the region (r) of ie, i.e.

$$\begin{cases} re.r = polygon(I_{i1}^1.r, I_{i1}^2.r, I_{i1}^3.r) \\ re.p = centroid(re.r) \end{cases} \quad (13)$$

Considering consumption strategies (IS), all occurrences of constituent events in the window should be used to detect the complex event, so IS_C is *cumulative*. All occurrences in the window should be remained to detect other dry events, so IS_R is *reserve*. Meanwhile, three occurrences of each constituent events are needed, so length of the sliding windows of them are 3.

"Seepage event"

Seepage from a point to nearby points in the farmland usually implies leak of the irrigation device at the point. An example the dynamic process is illustrated in Figure 8. When a seepage event occurs, an increase event (i_{center}) and a series of higher events (h_{center}) occur at the nearest position from the leak point and then increase events and higher events occur at nearby positions followed. Thus, FJ functions are:

$$\begin{cases} FJ_{occr} = any(h_1, h_2, h_3, ..., 3) \\ FJ_{d,t} = after(h_{i1}.t, i_{i2}.t) \wedge after(h_{i1}.t, i_{i3}.t) \\ FJ_{r,p} = inside(h_{i2}.p, h_{i1}.r) \wedge inside(h_{i3}.p, h_{i1}.r) \end{cases} \quad (14)$$

Here, when any three higher events occur, the detection starts. Three actual occurrences are denoted as h_{i1}, h_{i2} and h_{i3}. $FJ_{d,t}$ limits that higher events of sensor $i2$ and $i3$ will follow an occurrence of higher event of sensor $i1$, meanwhile $FJ_{r,p}$ limits that $i2$ and $i3$ is in the region of $i1$, implying sensor $i1$ is the nearest from the leak device and $i2$ and $i3$ are nearby. Compared with irrigation event, in irrigation event more than three higher events occur in the same data update period, but in seepage event, h_{i2} and h_{i3} occurs later than h_{i1}.

Figure 8 An example of seepage

Considering FC functions, attributes t, d, r, and p are equal to the corresponding attributes of h_{i1} of the nearest sensor.

Considering consumption strategies (IS), all occurrences of constituent events in the window should be used to detect the complex event, so IS_C is *cumulative*. All occurrences in the window should be remained to detect other dry events, so IS_R is *reserve*. Meanwhile, IS_W is time window, and the seepage speed determines length of the sliding window.

4 Comparison and discussion

4.1 Comparison with threshold inequation

In this section, the complex events with widely-used threshold controls are compared. In threshold control for devices in farmland, an action is triggered by some threshold inequations, i.e. a situation that the value or the change becomes more or lower than a threshold, similar with our atomic events. However, it is too simple to model composite situations, leading to higher rates of false positives and omissions than complex event processing.

Figure 9 illustrates four composite situations should be detected, including two sensor damages, one rain and one no rain. With the constructions of complex events in farmland, the three complex events will be correctly detected and the one no rain situation is correctly ignored.

However, with threshold control, if rains are detected only by using rain sensor in weather station, we can set the threshold as 0.2 mm. From the data in Figure 9, two rains will be detected, in that the first one is false positive. If composite situations are detected only by using a single soil sensor, 4 kinds of composite situations cannot be distinguished: sensor damage, rain, irrigation and seepage. Assuming the change of moisture from a sensor over 5% is threshold to detect a rain, from the data in Figure 9, three rains are detected, but only the second is correct, and the other two detections are actually sensor damages.

In fact, our complex event model is compatible with threshold control, because the 4 kinds of atomic events are similar with 4 kinds of over-threshold situations. Based on that, more composite situations can be constructed with mathematical logic, temporal logic and spatial logic in our model. Thus, our complex event model and constructions of several complex events are

more effective for describe composite situations in farmland.

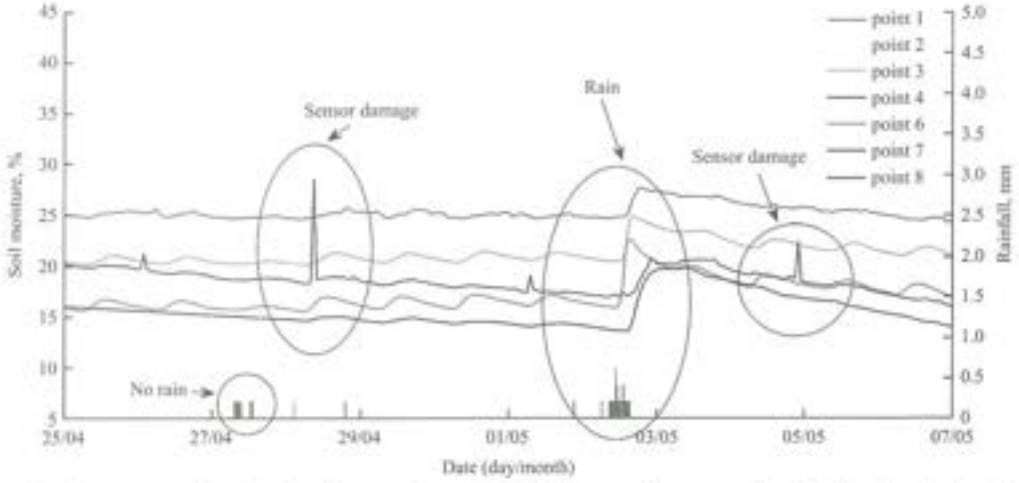

Figure 9 Four composite situations: 1) no rain on Apr. 27, 2) sensor damage on Apr. 28, 3) rain on May 02, and 4) another sensor damage on May 05

4.2 Comparison with production rules

/*Our Model */

$$Rain:\{ES:\{h_{ss},i_{ss},h_1,h_2,...,i_1,i_2,...\}$$

$$IS:IS_U=recent,IS_C=removeall,IS_W=lengthwindow(1)$$

$$FJ:\begin{cases}FJ_{occur}=dis(h_{ss},i_{ss})\wedge any(h_1,h_2,...,i_1,i_2,...,3)\\FJ_{d,t}=sync(h_{ss}.t,i_{ss}.t,e_{11}.t,e_{12}.t,e_{13}.t,2)\end{cases}$$

$$FC:\begin{cases}re.t=h_{ss}.t \text{ or } i_{ss}.t, re.d=h_{ss}.d \text{ or } i_{ss}.d\\re.r=polygon(h_{ss}.r,i_{ss}.r,e_{11}.r,e_{12}.r,e_{13}.r)\\re.p=centroid(re.r)\end{cases} \quad (16)$$

$$\text{Assertions}:\begin{cases}P_1:h_{ss}.occur=true\\P_2:i_{ss}.occur=true\\P_3:h_{ss}\ or\ i_{ss}\ \text{occur}\\P_4:h_1.occur=true\\P_5:h_2.occur=true\\...\\P_{21}:i_9.occur=true\\P_{22}:h_1,h_2,h_3\ \text{occur}\\P_{23}:h_1,h_2,h_4\ \text{occur}\\...\\P_{837}:i_7,i_8,i_9\ \text{occur}\\P_{838}:m_1=true\\P_{839}:m_2=true\\P_{840}:|h_{ss}.t-i_{ss}.t|\le 2\\P_{841}:|h_{ss}.t-e_{11}.t|\le 2\\...\\P_{849}:|e_{12}.t-e_{13}.t|\le 2\\P_{850}:m_3=ture\\P_{851}:re.occur\end{cases}$$

$$\text{Rules}:\begin{cases}R_1:P_1\vee P_2\rightarrow P_3\\R_2:P_4\wedge P_5\wedge P_6\rightarrow P_{22}\\R_3:P_4\wedge P_5\wedge P_7\rightarrow P_{23}\\...\\R_{817}:P_{19}\wedge P_{20}\wedge P_{21}\rightarrow P_{837}\\R_{818}:(P_{22}\vee...\vee P_{837})\rightarrow P_{838}\\R_{819}:P_3\wedge P_{838}\rightarrow P_{839}\\R_{820}:P_{840}\wedge P_{841}...\wedge P_{849}\rightarrow P_{850}\\R_{821}:P_{839}\wedge P_{850}\rightarrow P_{851}\end{cases} \quad (17)$$

Rain complex event is constructed with our model and production rules respectively in (16) and (17). From the comparison, readability of production rules is poor. Too many temporary symbols, assertions and rules are defined and there are so many complicated chain triggering relationships. It is difficult for users to check and eliminate loops, conflicts, redundancies, implications and even correctness of them. Conversely, construction with our model is far better readable.

4.3 Comparison with SASE+, Esper and Zang models

/*SASE+Model*/

$$PATTERN:$$

$$\{(SCAN\ h_{ss}\vee SCAN\ i_{ss})\wedge(SCAN*h_1[],SCAN*l_1[],SCAN*h_2[],SCAN*l_2[],...)\},$$

$$WHERE:$$

$$\{h_1.length+l_1.length+h_2.length+l_2.length+...\ge 3,\ |h_1.t-h_2.t|\le 2,\ |h_1.t-h_3.t|\le 2,\ |h_1.t-h_4.t|\le 2,...\ |h_2.t-h_3.t|\le 2,\ |h_2.t-h_4.t|\le 2,\ |h_2.t-h_5.t|\le 2,...\ |h_3.t-h_4.t|\le 2,\ |h_3.t-h_5.t|\le 2,\ |h_3.t-h_6.t|\le 2,...\ ...\}, \quad (18)$$

WITHIN: 1

RETURN:

$\{h_{ss}.t,\ i_{ss}.t,$

$h_{ss}.d,\ i_{ss}.d,$

$r = f_1(h_{ss}.r,\ h_{ss}.r,\ h_{i1}.r,\ h_{i2}.r,\ h_{i3}.r)$

$p = f_2(r)\}$

Rain complex event is constructed with the most popular SASE+ model in (18). From the comparison, the construction with SASE+ is far more complex and has poor readability than that with our model.

Firstly, SASE+ model does not support *any* semantics, so we have to define a inequation with lengths of occurrences sets of all constituent events. It is not intuitive. Conversely, in our model, the relationship is constructed as $any(h_1, h_2,\ldots, i_1, i_2,\ldots,3)$, which is more easily understood.

Secondly, because in SASE+ model, temporal logic relationships have to be described in mathematical equations inequation. The values of i and j in the inequation $|h_i.t - h_j.t| \leq 2$ are all permutations of 1 to N, if there are N atomic events. Conversely, in our model, the relationship is constructed with a simple temporal operator $sync(h_{ss}.t,\ i_{ss}.t,\ e_{i1}.t,\ e_{i2}.t,\ e_{i3}.t,\ 2)$. Details of the semantics of *sync* are processed by the CEP algorithm, and do not need explicit specification.

Thirdly, SASE+ model cannot support spatial logic, so the functions (f_1 and f_2) to calculate p and r of the rain event should be defined explicitly. f_1 is a function to find a minimum polygon that covers regions of all constituent events. f_2 is a function to find the centroid of the irregular polygon. Both of them involve too difficult geometries and their formulas will be very complicated to general users. Conversely, in our model, details are also hidden, and only two operators *polygon* and *centroid* are needed.

The model with three popular complex event models is compared: SASE+ (2007), Esper (2016) and Zang (2007). The results are listed in Table 5. All models support mathematical logic and temporal logic. However, besides our model, others cannot support spatial logic and personalized occurrence consumption strategies for different constituent events. Meanwhile, readability of our model and language is better than the models of SASE+ and Esper.

Table 5 Comparison with other complex event models. "s" denotes supported, and "u" denotes unsupported

Functions	This paper	SASE+	Esper	Zang
Mathematical logic	s	s	s	s
Temporal logic	s	s (partial)	s (partial)	s
Spatial logic	s	u	u	u
Personalized occurrence consumption strategies	s	u	u	u
Custom attributes	s	s (partial)	s	s
Readability	good	not too bad	bad	good

5 Conclusion

A novel model is proposed for complex events from sensor network distributed deployed in farmland. A relevant XML-based specification language is also defined. The model is suitable to construct farmland complex events because various influencing factors of judgement and construction are considered in a comprehensive manner. Especially, the model supports to describe mathematical logic, temporal logic and spatial logic relationships among constituent events. Spatial logic is not supported by other traditional complex event models. By analyzing data from actual farmland sensor network, five kinds of atomic events and five kinds of common complex events i.e. sensor damage, rain, irrigation, dry and seepage are constructed with the model and specified with the language. Tests indicate that our event model and language are more effective to construct farmland complex events and have better readability than threshold control, production rules and complex event models in other CEP algorithms. In the future, more complex events can be constructed with the event model.

Acknowledgements

This research is financially supported by the National Natural Science Foundation of China (No. 61601471) and Beijing Natural Science Foundation (No. 4164090).

[References]

[1] Buchmann, A., and B. Koldehofe. 2009. Complex event processing. *IT-Information Technology Methoden und innovative Anwendungen der Informatik und Informationstechnik*, 51(5): 241–242.

[2] Chakravarthy, S., and D. Mishra. 1994. Snoop: an expressive event specification language for active databases. *Data & Knowledge Engineering*, 14(1): 1–26.

[3] Diao, Y., N. Immerman, and D. Gyllstrom. 2007. SASE+: an agile language for kleene closure over event streams. UMass Technical Report.

[4] EsperTech. 2016. Esper: event series analysis and complex event processing for Java. EsperTech Inc. http://www.espertech.com/products/esper.php.(accessed in July, 2017)

[5] Gatziu, S., and K. R. Dittrich. 1992. SAMOS: an active object-oriented database system. *IEEE Data Engineering Bulletin*, 15(1-4): 23–26.

[6] Gehani, N. H., H. V. Jagadish, and O. Shmueli. 1992. Event specification in an active object-oriented database. *ACM SIGMOD Record*, 21(2): 81–90.

[7] Haller, S., S. Karnouskos, and C. Schroth. 2008: The internet of things in an enterprise context. *September, 2008: Future Internet Symposium. Springer, Berlin, Heidelberg.*

[8] Janssen, J. A. E. B., M. S. Krol, R. M. J. Schielen, A. Y. Hoekstra, and J. L. de Kok. 2010. Assessment of uncertainties in expert knowledge, illustrated in fuzzy rule-based models. *Ecological Modelling*, 221(9): 1245–1251.

[9] Jun, C., and C. Chi. 2014. Design of complex event-processing IDS in internet of things. *January, 2014: Measuring Technology and Mechatronics Automation (ICMTMA), 2014 Sixth International Conference of IEEE.*

[10] Krämer, J., and B. Seeger. 2009. Semantics and implementation of continuous sliding window queries over data streams. *ACM Transactions on Database Systems (TODS)*, 34(1): 4.

[11] Liu, Y. 2007. Research on some key technologies of agricultural IOT data processing based on the process of agricultural production. PhD Diss. Beijing: Beijing University of Posts and Telecommunications.

[12] Magid, Y., G. Sharon, S. Arcushin, I. Ben-Harrush, and E. Rabinovich. 2010. Industry experience with the ibm active middleware technology (amit) complex event processing engine. *July, 2010: Proceedings of the Fourth ACM International Conference on Distributed Event-Based Systems.*

[13] Wu, E., Y. Diao, and S. Rizvi. 2006. High-performance complex event processing over streams. June, 2006: Proceedings of the 2006 ACM SIGMOD International Conference on Management of Data.

[14] Wang, F. J., X. M. Zhang, Y. H. Wang, and K. N. Cao. 2013. The research on complex event processing method of internet of things. *January, 2013: Measuring Technology and Mechatronics Automation (ICMTMA). IEEE Fifth International Conference.*

[15] Zang, C., and Y. Fan. 2007. Complex event processing of real time enterprises based on smart items. *Chinese Journal of Mechanical Engineering*, 43(2): 22–32. (In Chinese with English abstract)

Appendix I

A higher atomic event

```
<atom>
    <id>h1</id>
    <sources>
        <src>sensor1</src>
    </sources>
    <attributes>
        <attr id="dx" type="d_x" var="false">5</attr>
        <attr id="dy" type="d_y" var="false">5</attr>
        <attr id="px" type="d_x" var="false">0</attr>
        <attr id="py" type="d_y" var="false">0</attr>
        <attr id="t" type="t" var="true" />
        <attr id="p" type="p" var="true" />
        <attr id="value" type="o" var="true" />
    </attributes>
    <jfunc>value>44.45%</jfunc>
</atom>
```

Appendix II

Sensor damage complex event

```
<ce>
    <id>sensordamage</id>
    <otherattrs />
    <eventset>
        <event>
            <evn>h1</evn>
            <chosenstrategy>recent </chosenstrategy>
            <removestrategy>removeall</removestrategy>
            <lengthwindow>1</lengthwindow>
        </event>
        …
    </eventset>
    <judgefunction logic="conjunction">
        <variables>
            <var id="h1">
                <evn>h1|h2|…</evn>
                <occ>1</occ>
            </var>
            <var id="u1t">
                <evn>u1|u2|…</evn>
                <occ>1</occ>
                <attr>t</attr>
            </var>
            …
        </variables>
        <jfunc>con(dis(h1,l1),not(h2,l2,h3,l3…)</jfunc>
        <jfunc>sync(u1t,u2t,u3t,…,2)</jfunc>
        <jfunc>inside(u1p,u2r)</jfunc>
        <jfunc>inside(u1p,u3r)</jfunc>
        …
    </judgefunction>
    <calculationfunction>
        <variables>
            <var id="h1d">
                <evn>h1</evn>
                <occ>1</occ>
                <attr>d</attr>
            </var>
            …
        </variables>
        <cfunc attr="d">h1d</cfunc>
        <cfunc attr="t">h1t</cfunc>
        <cfunc attr="p">h1p</cfunc>
        <cfunc attr="r">h1r</cfunc>
    </calculationfunction>
</ce>
```

Cultivating online: an analysis on an agricultural Q&A community

Li Xiang[1], Gu Liyang[1], Chen Xin[1], Liu Lei[2], Jia Lu[1*]

(1. *College of Information and Electrical Engineering, China Agricultural University, Beijing 100083, China;*
2. *Shandong Laodao Network Technology Co. LTD., Shandong 261000, China*)

Abstract: The "wisdom of the crowd" phenomenon has revolutionized content generation, discovery and curation in the Internet age. Online question & answer (Q&A) communities are nowadays enlightening over a billion people with crowdsourced knowledges. While previous analyses often focus on general Q&A sites like Quora and Yahoo answers, in this article, we conduct an in-depth analysis on an online Q&A site named "Nong Guan Jia" (meaning farm butler) that is exclusive for agricultural knowledges. Based on datasets containing over seven thousand questions and over 66 thousand answers, and detailed user information of over two thousand experts and over four thousand farmers, we characterize its knowledge repository and user activities, demonstrate positive reinforcement between user activity and popularity, propose a graph model that reveals user relationships and high-level structures, and successfully apply our findings to build machine-learnt classifiers to identify potential active and popular experts. Our analyses provide valuable information for maintaining the community prosperity and therefore assist the development of agricultural knowledge sharing.

Keywords: online Q&A community, user behavior, graph model, prediction

Citation: Li, X., L. Y. Gu, X. Chen, L. Liu, and L. Jia. 2017. Cultivating online: an analysis on an agricultural Q&A community. International Agricultural Engineering Journal, 26(3): 283–291.

1 Introduction

In China, with the development of agricultural industry and information technology, the number of online e-commerce platform about agriculture is exploding, reaching more than 30,000 till the present moment. Meanwhile, online question & answer (Q&A) communities, embodying the "wisdom of the crowd", are nowadays a major Internet phenomenon that educate over a billion users. While previous studies often focus on general Q&A sites, in this article, we choose Farm-Butler, an online Q&A site that is exclusive for agricultural knowledge as our research object.

Given the user scale, dynamics, and decentralization of the contents provided by individual users and the gradually shifting interests of the users, two fundamental questions for maintaining and growing such Q&A sites are that, at the questioner's perspective, how to improve the response rate of their questions so as to achieve smooth user questioning experiences, and that, at the replier's perspective, how to collect more rewards that will encourage them to maintain their activity level. In this paper, we seek to combine these two tasks so as to promote the community prosperity and to assist the development of agricultural knowledge sharing.

Our analysis of Farm-Butler mainly consists of three parts. First, we reveal, quantitatively, the scale and the characteristics of Farm-Butler by examining the question repository and user activities, and demonstrate a positive reinforcement between user activity and popularity. Then, we propose a graph model based on the Q&A activities, which captures both the direct user relationships and the higher-order social structures. Finally, applying our findings, we develop two machine-learned classifiers that can successfully identify experts who will reply a lot of questions and who will receive a large amount of donations, respectively.

Received date: 2017-06-19 **Accepted date:** 2017-08-17

* **Corresponding author: JIA Lu,** Ph.D., Associate Professor of College of Information and Electrical Engineering, China Agricultural University, Beijing 100083, China. Email: ljia@cau.edu.cn.

We summarize our contributions as follows:

• We collect four datasets that contain the complete view of Farm-Butler, with detailed statistics for 7,870 questions, 66,558 answers, 4,378 farmers, and 2,774 experts (Section 2).

• We provide a characterization on Farm-Butler. Our analyses include (i) the repository scale, (ii) the statistical properties of the question popularity, (iii) the questioning activity and the collected attention of the farmers, (iv) the reply activity and expert popularity of the experts, and (v) the user location distributions (Section 3).

• We propose a directed graph model to analyze the user relationships. The model contains in total 5,318 users (Section 4).

• We build machine-learned classifiers to predict with high accuracies the experts that will be active and gain great popularity (Section 5).

2 Farm-Butler dataset

2.1 An overview of Farm-Butler

Farm-Butler is an online Q&A site like Quora and Yahoo Answers but is exclusive for agricultural knowledge. Similar to general Q&A sites, the platform allows the users to raise questions that other users can answer directly. All users in Farm-Butler can browse the information and give the thumbs up or the thumbs down to the answers they find useful or wrong. In addition, Farm-Butler provides a feature of donation wherein users can donate to other users, in real money, to show the support for their efforts.

Compared with the general Q&A sites, it's more difficult for a questioner in Farm-Butler to act as a replier in the meantime, due to the exclusiveness and limitation of agricultural knowledge. For this reason, Farm-Butler has manually labeled the user status as either expert or farmer, based on the following rules:

(i) Farmers: the users that have raised at least one question,

(ii) Experts: the users that have replied at least one question.

2.2 Dataset

For our analysis, we have collected four datasets named the question dataset, the answer dataset, the farmer dataset and the expert dataset, respectively. The former two datasets represent a sample of the whole Q&A repository. They were collected on the 1st and the 15th of each month for the year of 2016. The latter two datasets include the complete user information since they join the community.

More specifically, the question dataset contains, for each question, the question identification (ID), the time when it was raised, the province and the city of the questioner, and when and who have replied. The answer dataset contains, for each answer, the answer ID, the question id of the associated question, the replier ID, and the reply time.

The farmer dataset contains, for each farmer, the farmer ID, the farmer's name, the province and the city of the farmer, the number of questions he has raised, and the number of replies received by all his questions. The expert dataset contains similar information, and in addition, for each expert, the number of ups, the number of downs, and the number of donations. The basic statistics of our datasets are introduced in Table 1.

Table 1 Farm-Butler scale

Type	Number	Type	Time dimension
#question	7,870	question time	1st and 15th of Jan 2016 – Dec 2016
#answer	66,558	reply time	1st and 15th of Jan 2016 – Dec 2016
#farmer	4,378	time	Jan 2016 – Dec 2016
#expert	2,774	time	Jan 2016 – Dec 2016

3 Farm-Butler characteristics

In this section, we first introduce the scale of Farm-Butler. Then we provide a characterization on its question repository and the user activities.

3.1 Farm-Butler scale

Table 1 introduces the scale of Farm-Butler derived from our datasets. During our observation period of 36 days extending one year, 7,870 questions were raised and 66,558 answers were made, achieving an average of 218 questions per day and 8 answers per question. Altogether, 4,378 farmers and 2,774 experts are involved, resulting an average of 24 answers per expert.

3.2 Question characteristics

In this section, we first discuss the temporal and spatial distribution of the questions. Then, we study the replies of the questions to examining their popularity.

3.2.1 Question injection

Figure 1 shows the number of questions injected on the 1st and 15th of each month in 2016. We find that Farm-Butler is growing dramatically from February to June, and users are most active during the summer time, i.e., from May to August. We believe this is the harvest time for most farmers and therefore they urgently need helps and advices from the experts.

To take a closer look, Figure 2 depicts the number of questions injected at different time of the day (in hour). We find that questions are mostly raised during the daytime, without a specific preference for the exact hour. This phenomenon is different from the patterns that have been observed in other online communities, such as YouTube and Twitch (Figueiredo et al., 2011; Jia et al., 2016). One possible reason is that most farmers do not follow a nine-to-five work as people in the urban areas do and therefore they have plenty of time to go online during the daytime.

3.2.2 Question location

Question location directly measures the usage of Farm-Butler in different areas. Figure 3 shows the number of questions from different provinces and autonomous regions in China. We find that Shandong Province is the top province in terms of number of questions, accounting for 14% of the total question repository. The other top nine provinces or autonomous regions account for more than 56% of the questions, while the remaining locations account for 30%.

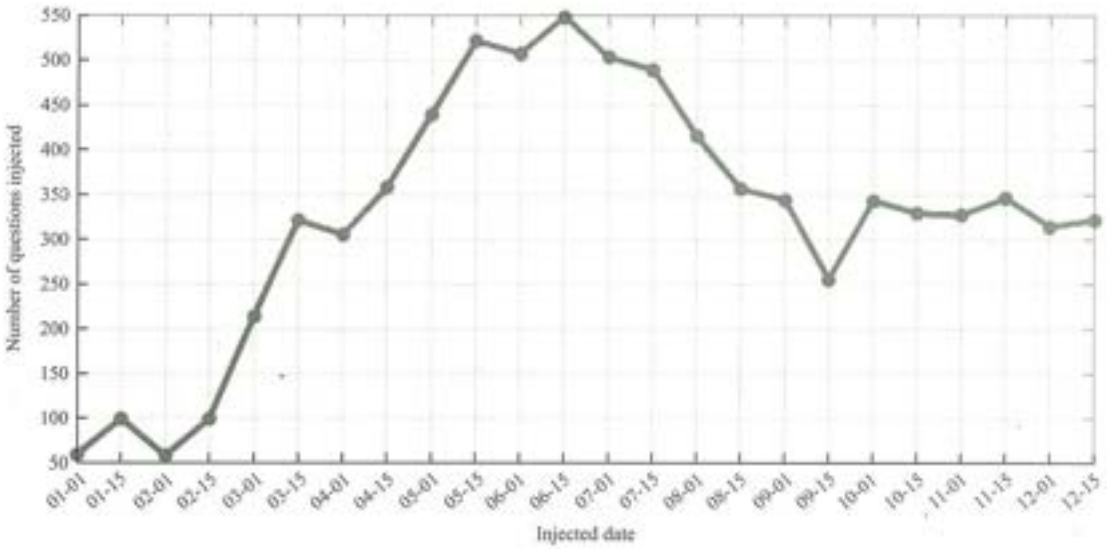

Figure 1 Number of questions injected over time

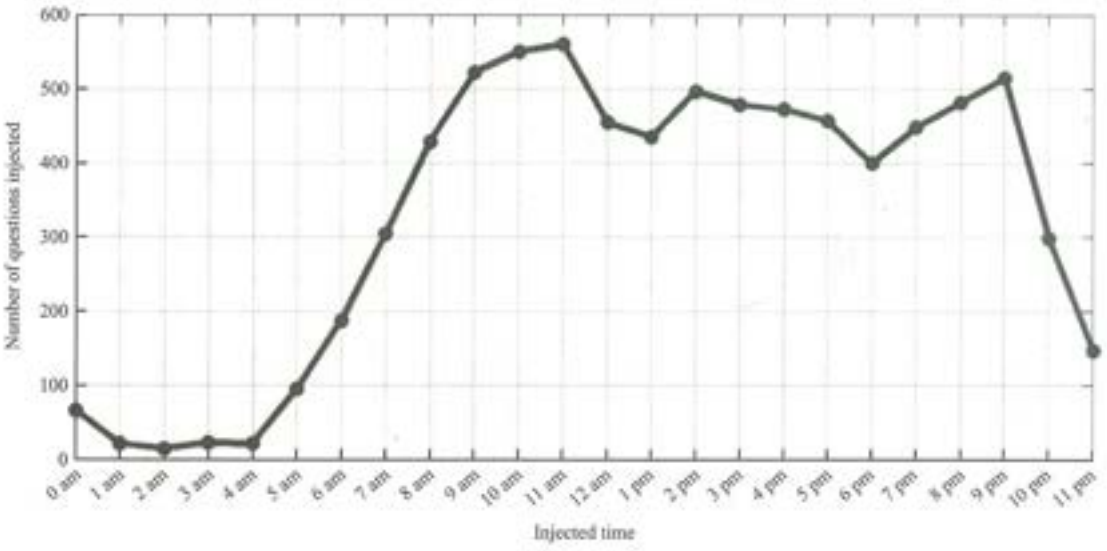

Figure 2 Number of questions injected at different time of a day

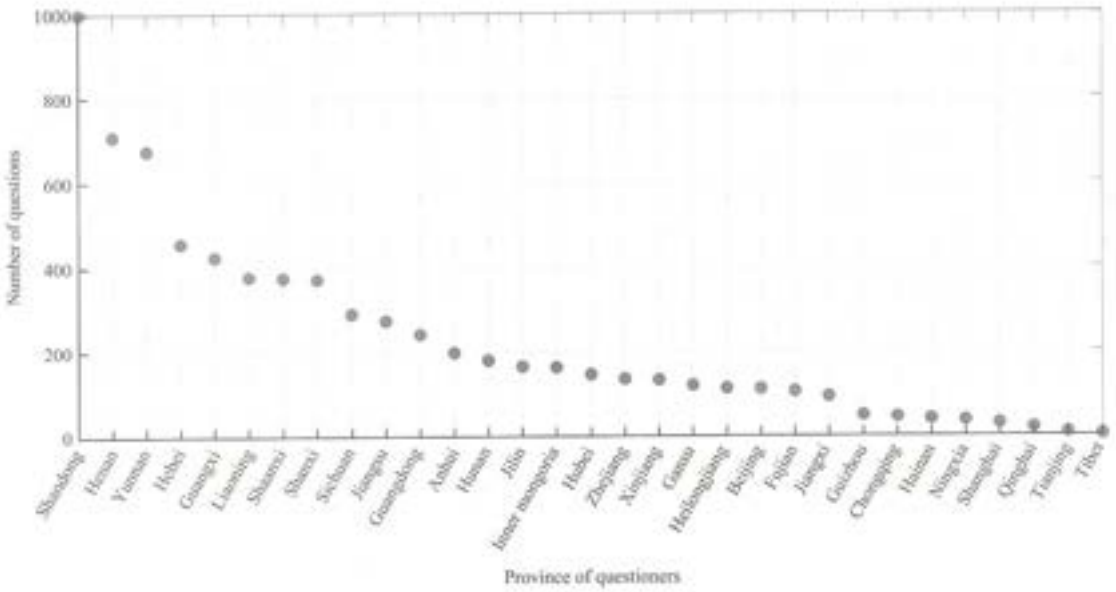

Figure 3 Geographic distribution of the questions

3.2.3 Question popularity

In any online Q&A site, question popularity provides important knowledge for the activity level of the experts, the potential workload for maintaining the site, and the community prosperity. Here, we measure the question popularity in the terms of the number of expert's replies to the question.

It is shown in in Figure 4 the complementary cumulative distribution function (CCDF) of the number of replies collected by each question. The question popularity is highly skewed, with a small number of questions attracting a large number of replies. When it is plotted on a log-log scale, we observe a curve that is close to a straight line with a negative slope, indicating that the number of replies can be well described as a power-law distribution.

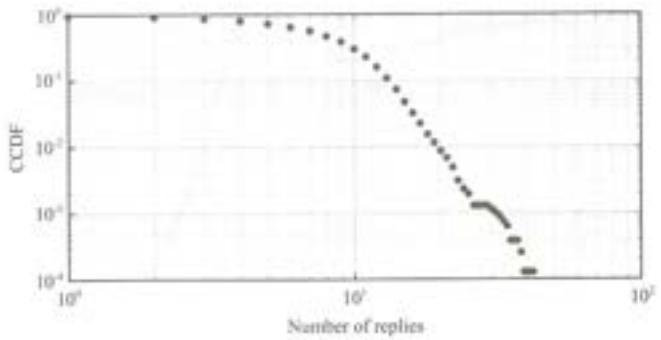

Figure 4 CCDF of the number of replies of the questions

3.3 User activities

In this section, we first analyze the activity and the popularity of the farmers and experts. Then, we study the location distribution of the users.

3.3.1 Questioning activity and the collected attention

In Farm-Butler, 4,378 users have raised at least one question and we name them farmers. The farmers on average have questioned 18.18 problems and have collected 247,789 replies, resulting in an average of 56.60 replies per question. The detailed statistics are shown in Table 2.

Table 2 Basic statistics of the farmers

	Number of questions	Number of replies
Minimum	1	0
1st quartile	4	1
Median	9	5
Mean	18.18	56.60
3rd quartile	21	15
Maximum	2,215	66,565

Questioning activity. Figure 5 plots the number of questions raised by the farmers, with the farmers ranked in the decreasing order by the number of questions. Surprisingly, the number of questions does not follow a Zipf distribution, indicating that the activity level in Farm-Butler is not as highly skewed as often observed in other online communities (Ding et al., 2011). We conjecture that the high response rate of questions in Farm-Butler promotes users to raise more questions and hence reduce the disparity. Among these farmers, the most active 20% of the farmers contribute 62.64% of the questions.

Collected attention. We measure the attention that a

farmer collected by the number of replies received by all the questions he raised. Figure 6 plots the CCDF of the number of replies received by the farmers. We find that 66.95% farmers have received fewer than 10 answers while around 1% farmers have received more than 1,000 answers for their questions. The disparities in the attentions they get are highly likely due to the differences in the number of questions they raised.

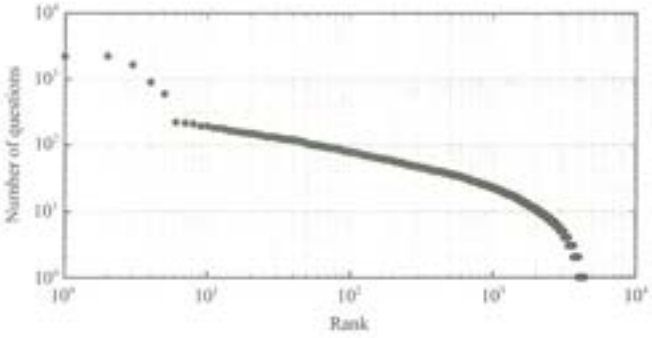

Figure 5 Number of questions of the farmers, ordered in the decreasing order

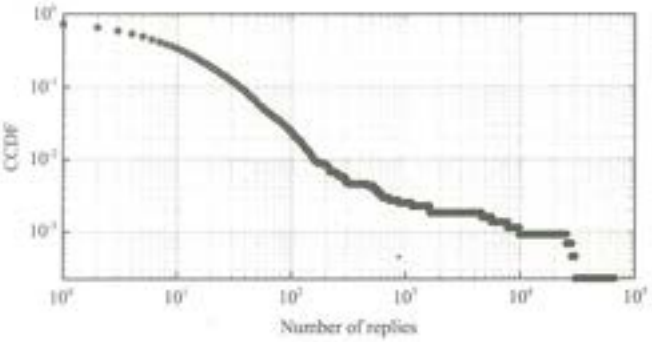

Figure 6 CCDF of the number of the replies collected by the farmers

3.3.2 Reply activity and expert popularity

In total, 2,774 users have replied at least one question and are labeled as experts by the community. We use the number of replies of the experts to measure their activity level. On average, each expert has replied 431 questions.

Reply activity. As shown in Figure 7, for experts in Farm-Butler, their levels are highly skewed: while 88.79% of experts have replied fewer than 100 questions, 2.81% of experts have replied more than 1,000 questions.

Expert popularity. Farm-Butler designed two features for the users to evaluate the answers made by the experts. They can give the thumbs ups or downs to the replies they find of high quality and they can donate to the experts in real money. In total, 1,369 experts have received at least one up, with a maximum number of ups, downs, and donations of 17,426, 2,542 and 27,146, respectively. To take a closer look, Figure 8 shows the number of ups, downs, donations, received by each expert, with the expert ranked in the decreasing order. We find that the expert popularity is high skewed.

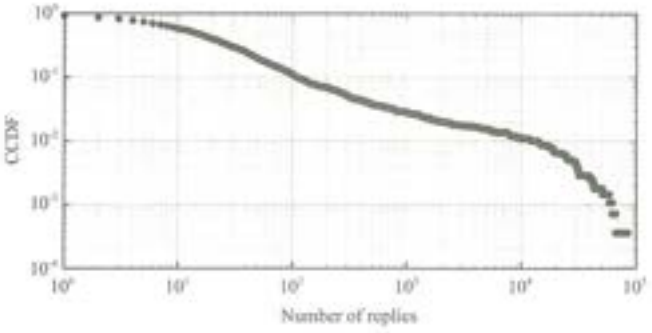

Figure 7 CCDF of the number of replies of the experts

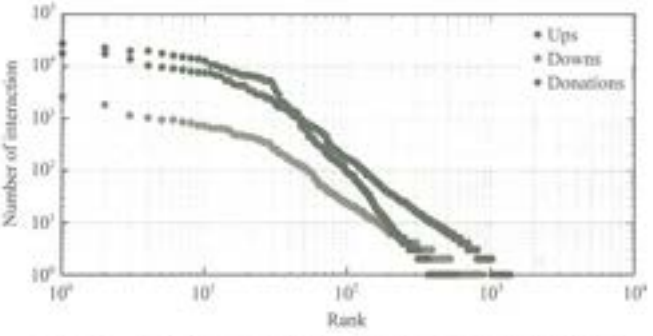

Figure 8 The number of ups, the number of downs, and the number of donations received by each expert, ranked in the decreasing order

Table 3 shows the spearman ranking correlation coefficients (SRCCs) and Pearson correlation coefficients (PCCs) between the number of ups, the number of downs, and the number of donations. We observe high correlations between any two of the three measures, and the SRCC between the number of downs and the number of donations reaches 0.9472. The high correlation between these features will later be leveraged for our prediction tasks.

Table 3 Correlations between number of ups, n_u, number of downs, n_d, and number of donations, n_e

	n_u vs. n_d	n_u vs. n_e	n_d vs. n_e
SRCC	0.8734	0.8401	0.9472
PCC	0.6602	0.5461	0.5102

3.3.3 User locations

Figure 9 and Figure 10 show the location distribution of farmers and experts, respectively. Similar to the

location distribution of the questions (as show in Figure 3), the top ten areas are identical in terms of the number of questions, farmers and experts, indicating the using level of farmers and experts in Farm-Butler is similar.

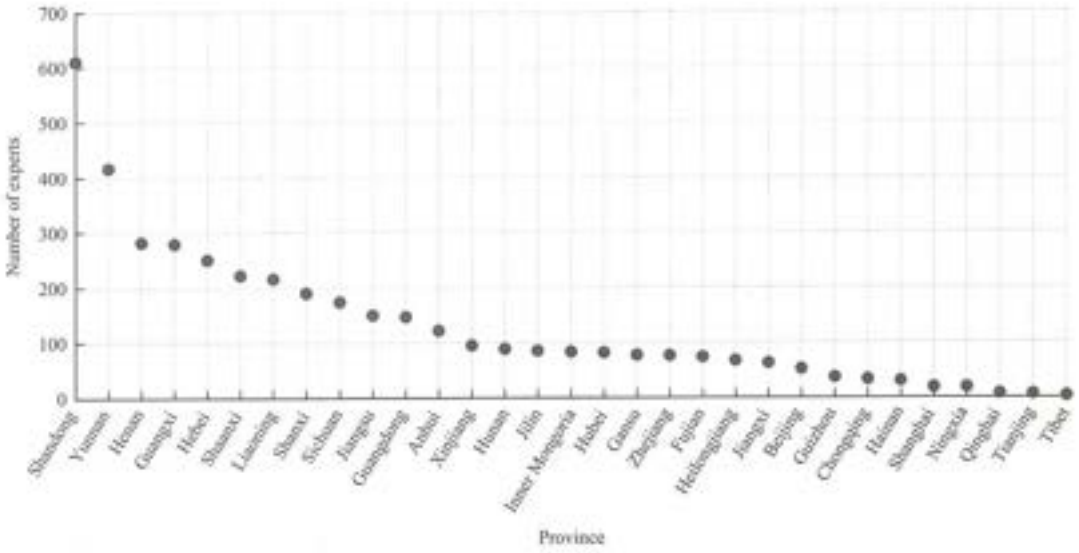

Figure 9 Geographic distribution of the farmers

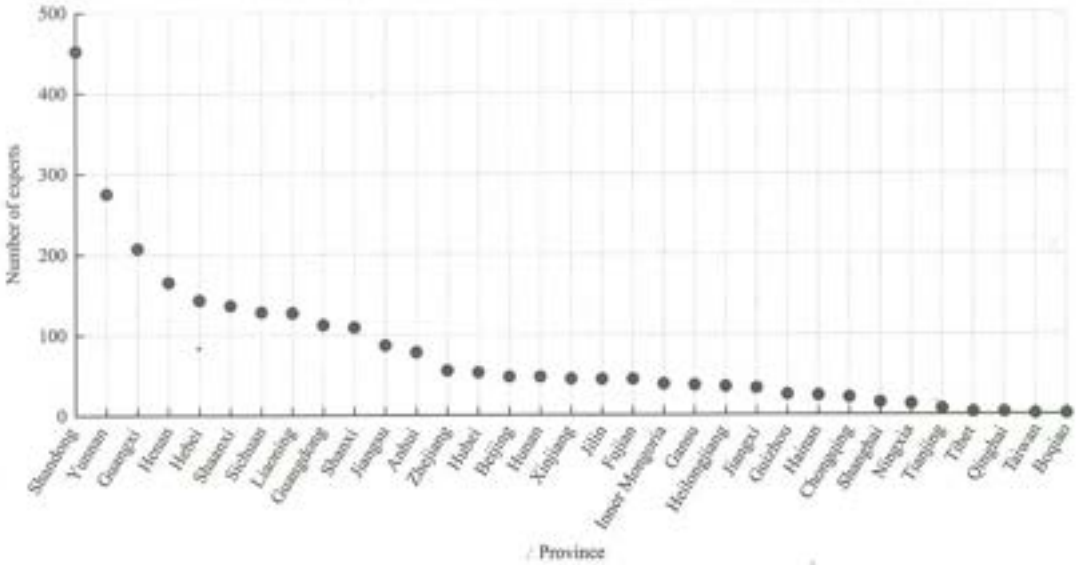

Figure 10 Geographic distribution of the experts

4 Graph model

To analyze user relationships in Farm-Butler, in this section we propose a graph model, named reply graph, based on expert's reply activities. In the reply graph, a vertex represents a user, and an edge directed from one vertex to another represents a user replies another user's questions. The edge weight indicates the number of questions in which the two users are involved. This graph model captures both the direct user relationships and higher-order social structures.

4.1 Edge weight distribution

Figure 11 shows the cumulative distribution function (CDF) of the edge weight of the reply graph. We find that, 82.68% of the edges have a weight of 1, indicating that most user pairs have only encountered once. Nevertheless, 305 edges have a weight of more than 5, and 158 edges have a weight of more than 10, showing that a modest number of user pairs have engaged repeatedly.

4.2 Degree distribution

Since the reply graph is directed, vertices have both in-degree (the number of respondents to the questions raised by the user) and out-degree (the number of cases wherein the users act as a respondent).

Figure 12 shows the CCDF of the in-degree and the out-degree for the experts and the farmers, respectively.

All the farms have out-degree of zero, as they have never answered others' questions. When plotted on a log-log scale, for the in-degree of the farmers and experts, we see a heavy tail resembling a power-law distribution. Surprisingly, there is very little variation between the in-degree distribution of farmers and experts, indicating that experts are also accustomed to raise questions in Farm-Butler. It is assumed that part of the experts are also farmers - they learn from the community and at the same time help others when they can.

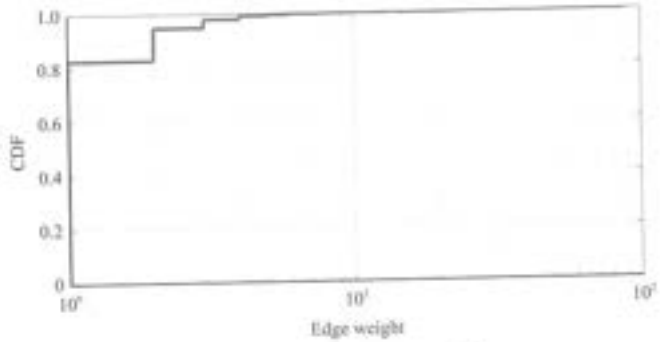

Figure 11 CDF of edge weight

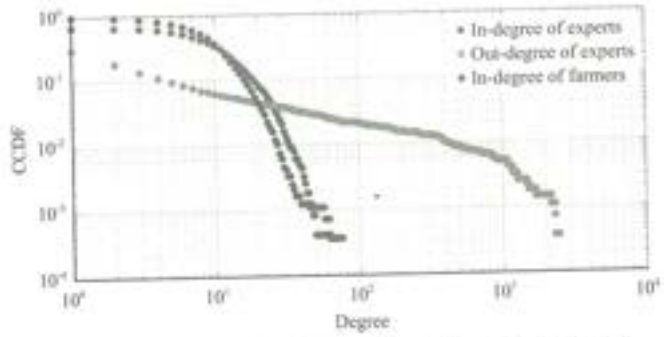

Figure 12 CCDF of in-degree and out-degree distributions

4.3 Clustering coefficient

The clustering coefficient (Watts and Strogatz, 1998) in social networks measures the fraction of users whose friends are themselves friends (Myers et al., 2014). Here, we examine the clustering coefficient of vertices in the Farm-Butler reply graph. Figure 13 plots the mean of the clustering coefficient against the vertex degree. We find that for small degrees (1-50), the average clustering coefficient stays stale, with minor fluctuations. When node degree further increases, the average clustering coefficient drops dramatically (notice the log scale for the axis), showing that with more "friends", it is more difficult to keep them close. Similar phenomenon has been observed in many other online social networks (Myers et al., 2014).

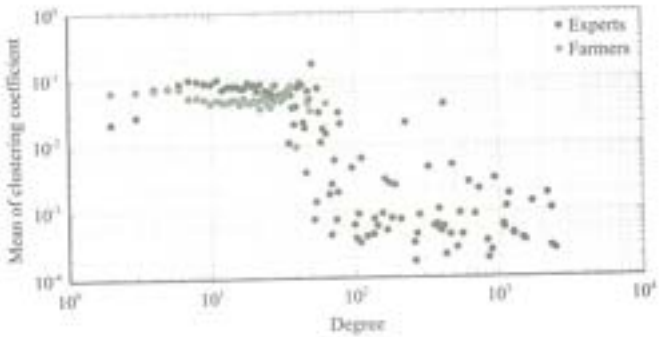

Figure 13 Clustering coefficient versus node degree

5 Predicting priority experts

Having gained several valuable insights on the characteristics of Farm-Butler and Farm-Butler users, we are now in a position to apply these findings by building machine-learned classifiers to predict experts that will be top active and gain great popularity. Successfully identifying these experts provides valuable information for maintaining and for boosting the community prosperity.

Classification tasks and methodology. More specifically, we have two classification tasks, one is to predict whether an expert will be one of the top experts in terms of the number of replies he responds, the other is to predict whether an expert will be one of the top experts in terms of the number of donations it received.

To this end, we have collected information on all the 2,774 experts that have replied questions during our observation period. At the end of this observation, we find that 311 experts have replied more than 100 questions, being the top 11% active experts, and 96 experts have received more than 100 donations, being the top 3.5% active experts. For the two classification tasks, we prepare two datasets, labeling the top 11% and top 3.5% experts as positive examples and the rest as negative examples, respectively.

Classification algorithm. We experimented with two classification algorithms-support vector machines, and random forests, and found the latter to work best. Hence all results reported here were obtained using random forests (Breiman, 2001). For each experiment, we run 5-fold cross validation and report the Area Under the receiver operating characteristic (ROC) Curve (AUC). We use balanced training and test sets containing equal numbers of positive and negative example, so random guesting results in an AUC of 50%.

Features. Based on previous analysis, we extract two groups of features including the user characteristic (u), and the reply graph properties (g). All these features have been extensively studied in Sections 3 and 4, and are summarized in Table 4. For the classification task of predicting the expert activity, we remove the number of replies in the user characteristic feature group. Similarly, for the classification task of predicting the expert popularity, we remove the number of donations in the user characteristic feature group.

Table 4 Classification features

Feature group	Description
User characteristic (u)	Number of replies, ups, downs, and donations
Reply graph properties (g)	Degree (in and out), clustering coefficient, and PageRank score of the experts

Results. Results for the two classification tasks are shown in Table 5 and Table 6, respectively. In order to understand which features are important for the prediction, we have progressively increased the group of features used in the classifier. We have a number of interesting findings as follows.

Table 5 Classification results of predicting replies

Features	AUC
u	90.83%
g	86.80%
u+g	93.37%

Table 6 Classification results of predicting donations

Features	AUC
u	94.44%
g	92.78%
u+g	95.00%

First, for the two tasks, using only the user characteristics achieves an AUC of 90.83% and 94.44% (remarkably better than random guessing). It indicates that the correlation between user characteristics is high, confirming our observation of high correlation between the number of ups, the number of downs, and the number of donations as introduced in section 3.3.3.

Secondly, the AUC of the two classification tasks reach 86.80% and 92.78% using only the reply graph properties. This result shows that the reply graph model we proposed provide valuable information for the two prediction tasks.

Thirdly, the best performance is achieved when combining all feature groups: the classifiers achieve an AUC of 93.97% and an AUC of 95.00% respectively for the two prediction tasks.

6 Related work

Related work is summarized within each research topic our work covers as follows.

Q&A in social networks. It refers to people asking questions on social networking sites. Morris et al. (2010) have explored how users leverage general-purpose online social networks for information seeking. Paul et al. (2011) conduct a study of question asking and answering behavior on Twitter and found that most popular question types were rhetorical and factual. Researchers evaluate the role of tie strength in question answers, finding that stronger ties (close friends) provide a subtle increase in information gain (Panovich et al., 2012). Users also can ask their friends questions by updating status in Facebook (Morris et al., 2010). These studies analyze users' behavior and the social network characteristic.

Community based Q&A. Researchers have studied community Q&A sites like Yahoo! Answers (Adamic et al., 2008), Live Q&A (Rodrigues et al., 2008) and MSN QnA (Hseih et al., 2009). For Live Q&A and Yahoo! Answers, Rodrigues et al. (2008) provide an in-depth analysis of the question labeling practices, finding that community tagging is related to higher levels of social interactions amongst users. Some studies explore the use of machine learning techniques to automatically classify questions as conversational or informational (Harper et al., 2009). Others estimate the quality of user's questions and answers (Paul et al., 2011; Shah and Pomerantz, 2010). In addition, some studies aim to develop algorithms to identify users with high capacity. For example, Pal et al. (2012) analyze the changes in experts' behavioral patterns over time, and using unsupervised machine learning methods to distinguish experts from one another.

Different from these work, we choose Farm-Butler, an online Q&A site that is exclusive for agricultural knowledge as our research object, focus on the experts' activity and popularity by investigating the question repository and the user activities.

7 Conclusion

In this paper, we conducted an analysis on an online Q&A site named Farm-Butler that is exclusive for

agricultural knowledge. Based on statistics on over 7 thousand questions, over 6 thousand answers, and over 5 thousand users, we first investigated the question repository and the user activities in Farm-Butler, and then we propose a graph model to analyze the user relationships. Finally, we applied our findings to build two machine-learned classifiers to predict active and popular experts.

Among our results, we find that Farm-Butler exhibits certain characteristics that are often observed in online social networks, for example, the highly-skewed content popularity. In addition, we find a number of fascinating distinctions in Farm-Butler. First, the users are most active during the summer time and the questions are mostly raised during the daytime. Secondly, on average, each farmer has raised 18.18 questions whereas each expert has replied 431 questions, indicating that the experts are more active than the farmer. Thirdly, in the graph model, the in-degree distribution of the farmers and the experts are similar, indicating that experts not only help others but also learn from the community. We leave a further analysis on the motivations of users taking different roles as our future work.

Acknowledgements

This work was partially supported by the National Science Foundation for Young Scholars of China (NSFYSC) No. 61502500 and Beijing Natural Science Foundation (BNSF) No. 4164090.

[References]

[1] Adamic, L. A., J. Zhang, E. Bakshy, and M. S. Ackerman. 2008. Knowledge sharing and yahoo answers: everyone knows something. *April 21-25, 2008:* In *Proc. 17th International Conference on World Wide Web*, 665–674. Beijing, China.

[2] Breiman, L. 2001. Random Forests. *Machine Learning*, 45(1): 5–32.

[3] Ding, Y., Y. Du, Y. Hu, Z. Liu, L. Wang, K. Ross, and A. Ghose. 2011. Broadcast yourself: understanding YouTube uploaders. *November 2-4, 2011: Proceeding of the 2011 ACM SIGCOMM on Internet Measurement Conference*, 361–370. Berlin, Germany.

[4] Figueiredo F., F. Benevenuto, and J. M. Almeida. 2011. The tube over time: characterizing popularity growth of youtube videos. February 9-12, 2011: *Proceeding of the 4th ACM International conf. on Web Search and Data Mining*, 745–754. Hong Kong, China.

[5] Harper, F. M., D. Moy, and J. A. Konstan. 2009. Facts or friends?: distinguishing informational and conversational questions in social Q&A sites. April, 4-9, 2009: *Proceeding of the SIGCHI Conference on Human Factors in Computing Systems*, 759–768. Boston, MA, USA.

[6] Hseih, G., and S. Counts. 2009. Mimir: a market-based real-time question and answer service. April 4-9, 2009: *Proceeding of the SIGCHI Conference on Human Factors in Computing Systems*, 769–778. Boston, MA, USA.

[7] Jia, A. L., S. Shen, D. H. Epema, and A. Iosup. 2016. When game becomes life: The creators and spectators of online game replays and live streaming. *ACM Transaction on Multimedia Computing, Communications, and Applications*, 12(4): 47.

[8] Morris, M. R., J. Teevan, and K. Panovich. 2010. What do people ask their social networks and why? A survey study of status message Q&A behavior. April 10-15, 2010, *Proceeding of the SIGCHI Conference on Human Factors in Computing Systems*, 1739–1748. Atlanta, GA, USA.

[9] Myers, S. A., A. Sharma, P. Gupta, and J. Lin. 2014. Information network or social network?: the structure of the twitter follow graph. April 7-11, 2014: *Proceeding of the 23rd International Conference on World Wide Web*, 493–498. Seoul, South Korea.

[10] Pal, A., S. Chang, and J. A. Konstan. 2012. Evolution of experts in question answering communities. *June 4-8, 2012: Proceeding of the 6th International AAAI Conference on Weblogs and Social Media*, 274–281. Dublin, Ireland.

[11] Panovich, K., R. Miller, and D. Kargerk. 2012. Tie strength in question & answer on social network sites. February 11-15, 2012: *Proceeding of the ACM 2012 Conference on Computer Supported Cooperative Work*, 1057–1066. Seattle, Washington, USA.

[12] Paul, S. A., L. Hong, and E. H. Chi. 2011. Is Twitter a good place for asking questions? a characterization study. July17-21, 2011: *Proceeding of the 5th International Conference on Weblogs and Social Media*, 578–581. Barcelona, Catalonia, Spain.

[13] Rodrigues, E. M., N. Milic-Frayling, and B. Fortuna. 2008. Social tagging behaviour in community-driven question answering. In *IEEE/WIC/ACM International Conf. on Web Intelligence and Intelligent Agent Technology*, vol. 3, 112–119. Sydney, Australia, 9-12 December.

[14] Shah, C., and J. Pomerantz. 2010. Evaluating and predicting answer quality in community QA. *July 19-23, 2010: Proceeding of the 33rd International ACM SIGIR Conference on Research and Development in Information Retrieval*, 411–418. Geneva, Switzerland.

[15] Watts, D. J., and S. H. Strogatz. 1998. Collective dynamics of 'small-world' networks. *Nature*, 393(6684): 440.

Design and experiment of high-throughput maize ear analysis platform

Cui Xuelian[1], Ma Qin[1,2*], Zhu Dehai[1,2], Guo Hao[1], Liu Zhe[1], Zhang Xiaodong[1], Yang Liangdi[3]

(1. *College of Information and Electrical Engineering, China Agricultural University, Beijing 100083 China;*
2. *Key Laboratory of Agricultural Information Acquisition Technology, Ministry of Agriculture, Beijing 100083, China;*
3. *Guangzhou Intelligent Equipment Research Institute, Guangzhou 519060, China*)

Abstract: At present, the most maize ear analysis platforms usually acquire the holographic images of ear by maize rotation shot, image mosaic or 3D reconstruction. There are problems such as high cost, complex computation, long time consuming about the above ear analysis platforms. Aiming at the above problems, the high-throughput maize ear analysis platform was constructed in this paper. The pipelining platform was composed of ear separation module (structure large batch ears to single ear vertically aligned), first level measurement module (acquire two-dimensional image and measure), second level measurement module (acquire multi-angle snap shot on freely falling ear and 3D measure) and recycling screening module (recover and screen ears). The 2D phenotypic traits (ear length, ear diameter, etc.) computed from the first level module were combined with the 3D visual measurement (ear row number, row grains, lack of grain yield, etc.) to restructure the 3D trait information of the ear in the second level measurement module. In the second level measurement module, drop snap shot method is used to acquire all-dimensional information of maize ear. And the 3D depth information of maize ear was computed and computational complexity was reduced greatly under the absence of additional fixed points. Finally, taking the hybrid maize as test object, the pipelining platform didn't need to carry out multiple images continuous scanning and stitching and reduced the computational complexity greatly. And the single channel measurement speed can reach 40 spike per minute. The accuracy of 2D parameters is more than 97.5%. The accuracy of 3D parameters, such as row number, the error is less two grains. This platform provides the basic data for the automated, high-throughput pipelines for maize ear analysis.

Keywords: maize ear, analysis platform, high throughput, holographic phenotypic trait

Citation: Cui, X. L., Q. Ma, D. H. Zhu, H. Guo, Z. Liu, X. D. Zhang, and L. D. Yang. 2017. Design and experiment of high-throughput maize ear analysis platform. International Agricultural Engineering Journal, 26(3): 292–301.

1 Introduction

Maize is one of the most important crops in the world (Huang, 2010) and its planting area is third only to the wheat and rice. A lot of researches show that the maize ear analysis has an important meaning for maize new variety breeding, genetic study, and cultivar identification (Chen, 2012; Li et al., 2010; Panigrahi et al., 1995). So maize variety test is the main means for acquiring the phenotypic traits (Yang et al., 2010). The traditional manual measurement is inefficient and restricts the development of maize seed industry for the complex phenotypic traits of maize (Ma et al., 2012; Zhou et al., 2015). In recent years, the automatic analysis platform of maize ear has played a huge role in modern seed industry (Bi et al., 2011). For the maize ear's irregular shape (space rotating body) and uneven growth, the phenotypic trait (ear row number, bare tip rate, lack of grain yield, ear length, etc.) acquisition device of ear needs to meet the high-throughput and all-dimensional requirements. In order to enhance the efficiency and accuracy of maize variety test, many scholars have researched the high-throughput method to acquire the all-dimensional phenotypic traits and achieved some research results (Liu,

Received date: 2017-07-01 **Accepted date:** 2017-08-17

*** Corresponding author: Ma Qin,** Ph.D., Associate Professor of College of Information and Electrical Engineering, China Agricultural University, 100083 China. Email: sockline@163.com.

Niu, et al., 2013; Qi et al., 2011; Wiendahl and Rybarczyk, 2003; Chang, 2009; Hausmann et al., 2009).

Wang et al. (2013, 2015) proposed an automatic and rapid 3D reconstruction method of maize ear based on the computer vision. In this paper, the maize ear was rotated in a proper angle interval to acquire the images in different view. And the point cloud of maize ear surface with binocular stereovision was calculated. The final 3D shape of maize ear was reconstructed by the point cloud of different views after removing error treatment. He also used the panoramic photography to make image fusion and create the ear panoramas by rotating maize sequence images. But the processing time is longer. Li et al. (2014) used two uniformly rotating rollers and line scan camera to acquire all-dimensional information of maize ear. But the hardware equipment is complex and time-consuming. In addition, Liu, Yang, et al. (2013), and Liu and Chen (2014) have proposed an implementation of the maize rotation shot method. And flat mirror imaging method (Bi et al., 2011) and transparent partition method are used to automatically acquire the holographic images of ear program. In addition, some foreign researchers (Alley et al., 2012; Brumback et al., 2016; Davis, 2016) developed a number of high-throughput ear sorting device can provide reference for this article. Such as Davis et al. (2016) proposed an optical robotic sorting apparatus for identifying and ting the maize ear. And the robotic sorter sorts at a rate of approximately 90 picks per minute.

In conclusion, the most maize ear analysis platforms usually acquire the holographic images of ear by maize rotation shot, image mosaic or 3D reconstruction. There are problems such as high cost, complex hardware devices, complex computation, long time consuming about the above ear analysis platforms, which can't meet the requirements of high-throughput maize varieties test. In foreign countries, most of the corn ear images are acquired from the pipeline. Aiming at the above problems, the low-cost, high-throughput maize ear analysis platform with 2D and 3D phenotypic measurements was constructed for acquiring all-dimensional phenotypic traits and reducing complex computation in this paper. This platform was composed of ear separation module (structure large batch ears to single ear vertically aligned), first level measurement module (acquire two-dimensional image and measure), second level measurement module (acquire multi-angle snap shot on freely falling ear and 3D measure) and recycling screening module (recover and screen ears). The pipelining platform will play important significance for achieving high-throughput assessment and accuracy breeding.

2 Materials and method

2.1 Comparison of all-dimensional imaging method

In order to better meet the high-throughput and low-cost requirements of the maize ear analysis platform, this paper makes a comparative analysis of the following three kinds of commonly used maize ear all-dimensional imaging method.

With regard to the maize rotation shot method, it can accurately collect the image of the all-dimensional information. And in the control of the rotational speed and scanning speed, the collected images can be ignored distortion. Then, the rotation shot takes a long time, resulting in an increase in the average measurement time of the ear. Such as the single ear measurement time in Liu, Yang, et al. (2013) is 30 seconds, and the time in Liu and Chen (2014) is 102 seconds, in Wang et al. (2013) is about 40 seconds. It can be seen that the use of this method can not meet the needs of high-throughput maize ear analysis measurement. The maize rotation shot method prototype is shown in Figure 1.

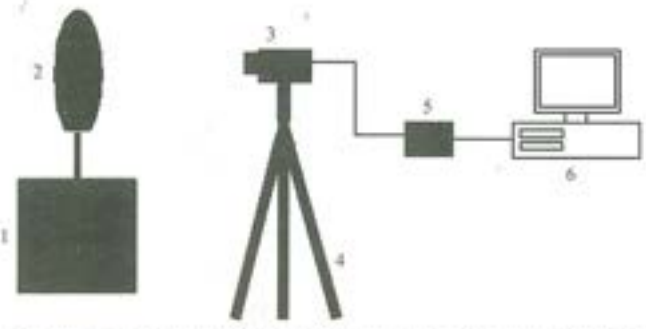

1. Rotating test platform 2. Sample maize ear 3. Binocular camera 4. Tripod 5. Image grabber 6. Computer

Figure 1 Prototype of the maize rotation shot method

With regard to the flat mirror imaging method, the size and location of the mirror is very important. In order to obtain the all-dimensional information, the ear can only take standing posture, which the ear need to be inserted in the fixed position of the thimble. As a result,

the mechanical design complexity of the equipment is greatly improved and the degree of automation is low. Also, the maize ear is damaged. The flat mirror imaging method prototype is shown in Figure 2.

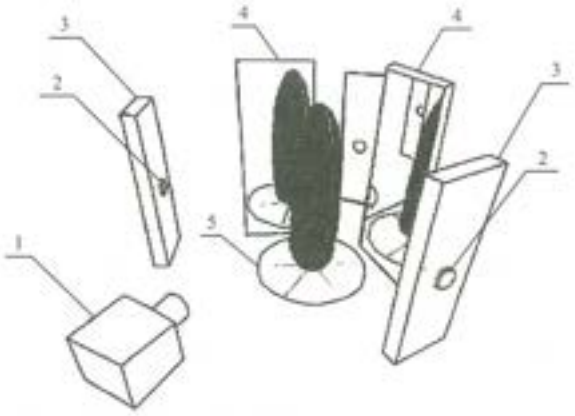

1. Image acquisition unit 2. Boundary light source 3. Boundary light source 4. The flat mirror 5. Tray

Figure 2 Prototype of the e flat mirror imaging method

For the transparent partition method, our paper has made the following analysis on the feasibility of this method.

First of all, the glass plate was selected as the transparent partition, and then made a measurement. In this device, the maize ear was placed on the transparent glass plate, and the upper and lower sides of the camera on both sides of the ear to collect.the images. After the acquisition is complete, if the two sides of the information is not enough to reflect the 360° all-dimensional information, you can add the camera to two at the top, and the camera below the ear does not change. The three cameras are captured an image at an angle of 120° from three directions. After a large number of experimental analysis, the acquisition method has the following problems:

1. The environmental illumination arrangement is high, especially when multiple cameras are used for collection. If the location of the illumination is not appropriate, there will be a large area of light spot in the imaging results due to the specular reflection, which will affect the image processing result.

2. Durability is not good. After several maize ear measurements, it is easy to adhere to silk and dust on the glass plate. Or the ear may scratch the glass plate, causing a decrease in the transmittance of the glass plate. And this resulted in the accuracy of the measurement reduced.

3. A long time is needed to place the ear in stable state.

In order to improve the above scheme, prevent the occurrence of a large area of light spot and debris deposition, we used a 0.1 mm transparent organic nylon rope net to replace the transparent glass plate. The prototype of the transparent net test device picture is shown in Figure 3.

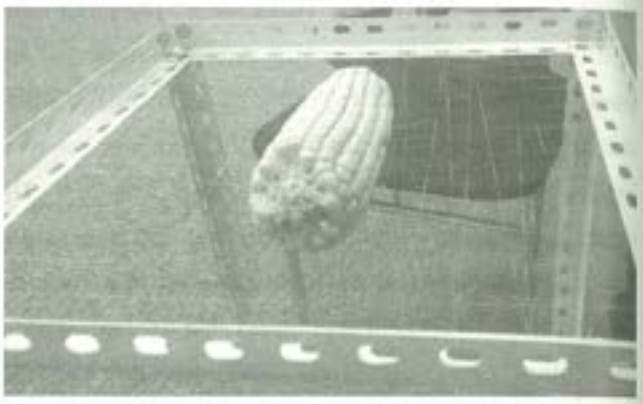

Figure 3 Prototype of the transparent net test device

With this method, the light layout requirement is lower, and there is no need to worry about the large area of light spot. And it doesn't pile up the silk and dust due to the long time use. However, depending on the tension and endurance of the silk thread, the different quality of the ear will cause different degrees of sedimentation. This resulted in the 2D calibration difficult to predict the error. And compared with the glass plate program, the assembly is more difficult. And this did not solve the complexity of the mechanical device and time-consuming issues. This can't meet the needs of high-throughput maize ear analysis accurately.

At present, the use of image processing methods have been able to achieve real-time processing requirements, such as Lie and Lei (2008) completed the automatic emerged corn plant spacing measurement of real-time crop row image reconstruction, Pearson (2009) completed a real-time detection and separation of grains with slight color differences or small defects. Besides, Xu and Zhao (2010) used machine-vision technology to grade strawberries, achieved the automation function. Therefore, the maize ear analysis platform should be able to meet the demands of disposable batch feeding and getting all-dimensional information of maize ear. In addition, it should be fast

and accurate as possible. So the pipelining platform was composed of ear separation module (structure large batch ears to single ear vertically aligned), first level measurement module (acquire two-dimensional image and measure), second level measurement module (acquire multi-angle snap shot on freely falling ear and 3D measure) and recycling screening module (recover and screen maize ears). The design line diagram of entire platform is shown in Figure 4. The prototype of the entire test platform picture is shown in Figure 5.

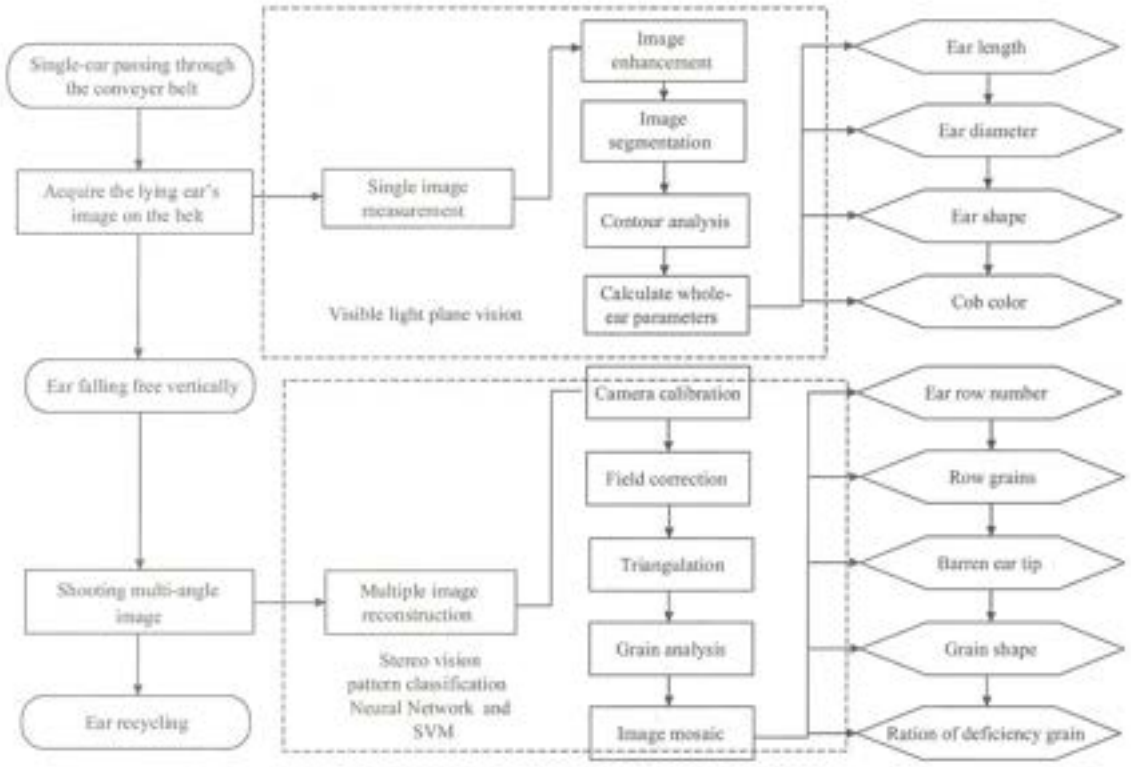

Figure 4 Design line diagram of high-throughput maize ear analysis platform

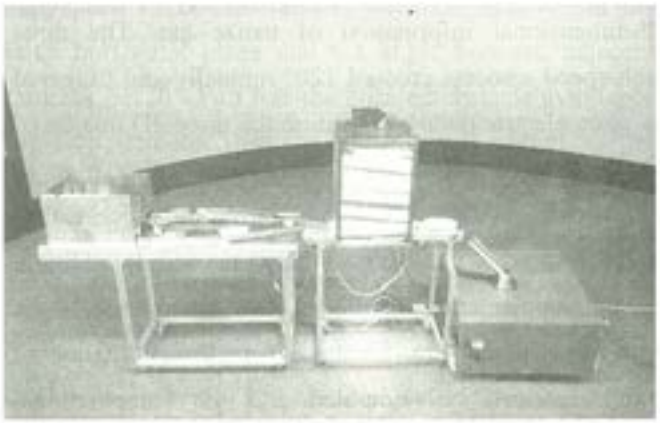

Figure 5 Prototype of high-throughput maize ear analysis platform

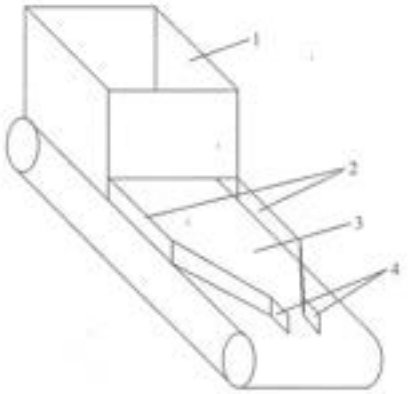

1. Feed inlet 2. Protecting sidewall 3. Wide conveyor belt 4. Folding sidewall

Figure 6 Design of ear separation module

2.2 Ear separation module

Ear separation module is designed to implement the requirement of structuring large batch ears to single ear vertically aligned. When the whole bag maize ears are poured into feed inlet, the inlet of conveyor belt will stir maize ears into the vertical face one by one and enter next module automatically. The design of ear separation module is shown in Figure 6.

As shown in Figure 6, part 1 is the ear feed inlet with size of 700 mm × 420 mm × 350 mm. The whole bag ears are put into the part 1. And the height of transversal trough in front of feed inlet can only allow a lying ear to pass through. So the device can separate the overlapping ears. Part 2 in Figure 6 is the protecting sidewall, which can prevent the ears from dropping to outside of conveyor belt. Part 3 of figure 6 is the wide conveyor belt and the

speed is adjustable, which is responsible for transmitting maize ears. Part 4 is the folding sidewall and its function is to arrange various directions ears to single ear vertically aligned. The width of folding sidewall is 80 mm that only allows one lying ear to pass through vertically. And its furling angle is small to prevent blockage caused by ears piles up here.

2.3 The first level measurement module

The first level measurement module is designed to measure the 2D characterization of the ear. It is composed of a narrow conveyor belt, which only allows single-ear pass vertically. There is a camera fixed above the narrow conveyor belt. Okopnik and Falate (2014) used the DFRobot RB-DFR-49 infrared sensor to detect the passage of corn seeds on the conveyor belt. Therefore, we use the photoelectric door sensor to detect the maize ear. When ear goes through the photoelectric door, the system will capture the 2D image of ear and calculate the essential parameters. And the capturing process is completed in the black box, which is filled light by the light source inside. Then use the color classification algorithm to extract the contours of maize ear, and the ear length and ear diameter are calculated by the minimum enclosing rectangle of the contour. And use the super blue feature extraction algorithm to extract the bare tip of maize ear. The 2D phenotypic traits (ear length, ear diameter, etc.) computed from the first level module were combined with the 3D visual measurement to restore the 3D trait information of the ear in the second level measurement module. The design of the first level measurement module is shown in Figure 7.

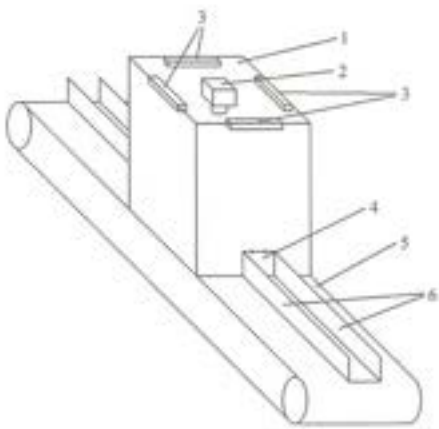

1. Collection black box 2. CCD camera 3. Strip light source 4. Mobile gate 5. Narrow conveyor belt 6. Protecting sidewall

Figure 7 Design of first level measurement module

As is shown in Figure 7, the first level measurement module is composed of two parts: black box and conveyor belt. Part 1 of Figure 7 is the collection black box (460 mm × 420 mm × 670 mm). Part 2 is the charge coupled device (CCD) camera, which is used to acquire the maize ear passing through the black box. Part 3 is the strip light source installed at the top of the black box. In order to achieve no-shadow transparent, four sides of top surface are equipped one strip light source for each. Part 4 is the mobile gate (160 mm × 80 mm), and two sides of the black box are equipped one mobile gate for each. The maize ears pass in and out the black box by passing through mobile gate. The mobile gate is closed when the ear is located in the shotting center to prevent the shotting environment from suffering ambient light. Part 5 is the narrow conveyor belt and its speed is adjustable, which is responsible for transmitting maize ears. Part 6 is the protecting sidewall and its role is to control ears pass through the first level measurement module with vertically position.

2.4 The second level measurement module

After leaving the first level measurement module, the ears will free fall into the second level measurement module. Drop snap shot method is used to acquire all-dimensional information of maize ear. The three high-speed cameras crossed 120° mutually and triggered by photoelectric door will capture the three 2D images of dropping ear to acquire all-dimensional information of ear. The ear falls down very fast during the process, thus the high speed of camera's shutter is needed. In addition, enough supplemental lighting is essential because of the high speed of camera. So the 3D depth information of maize ear can be computed and the computational complexity can be reduced greatly under the absence of additional fixed points.

This paper selects the industrial camera model DH-SV2001GC network interface digital camera with a resolution of 200w pixels. Due to the high-speed industrial cameras installed in the middle of the black box, the movement speed of the corn ear is faster, and the shutter time needs to be adjusted to eliminate the smearing phenomenon. After the experiment to determine the shutter speed is 800 μs.

The first and second level measurement modules are the core parts to realize the main platform in the above design. The design of two-level measurement modules is shown in Figure 8.

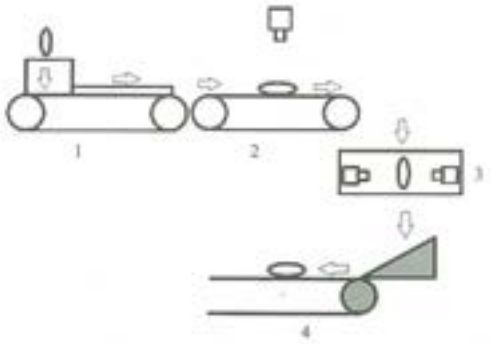

1. Ear separation module 2. The first level measurement module 3. The second level measurement module 4. Recovery screening module

Figure 8 Design of two-level measurement modules

The design of second level measurement module and recovery screening module are shown in Figure 9. As shown in Figure 9, part 1 is the maize ear and part 2 is the cohesion part between the first level measurement module and the second level measurement module. Part 3 is one vertical cylindrical catheter with 75 mm diameter and 200 mm height, which is designed to adjust the direction of ear to make ear drop vertically. Part 4 is the collection black box of image acquisition. Part 5 is the high-speed CCD camera, and three cameras are in the same horizontal plane and the angle between adjacent cameras is 120°. Part 6 is the infrared obstacle avoidance flip-flop detector, which can transmit signal to the controlled camera for acquiring image while ears passing through. Part 7 is the ring high light led source, which is used to supplement light for the black box. Part 8 and 9 are parts of recovery screening module. Part 8 is sponge slope guideway, which is designed to buffer dropping ears and channel to conveyor belt 9.

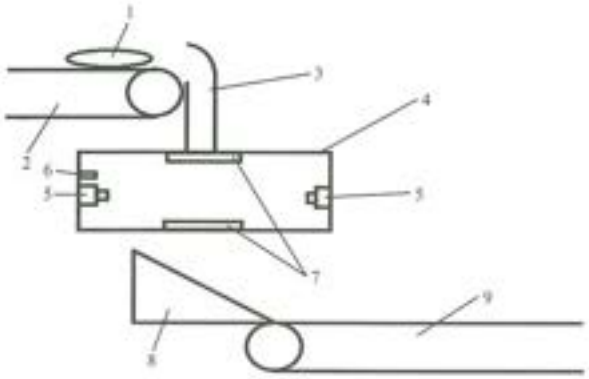

1. Maize ear 2. Cohesion department between two-level device 3. Vertical cylindrical catheter 4. Collection black box 5. CCD camera 6. Infrared obstacle avoidance flip-flop detector 7. Ring high-light led source 8. Sponge slope guideway 9. conveyor belt

Figure 9 Design of the second level measurement module and recovery screening module

The detailed design of the second level measurement module is shown in Figure 10. In order to solve the problem that maize ear could stuck inside the catheter when passing through, the catheter is designed to slow down the degree of curve.

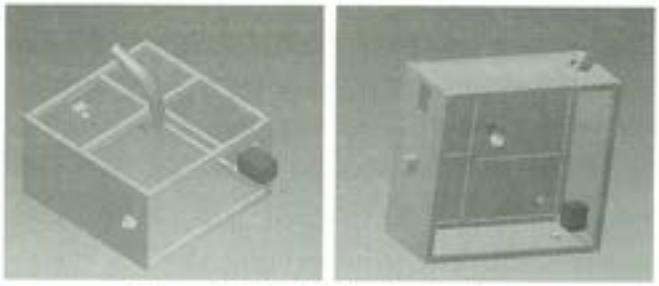

Figure 10 Detailed design of catheter

2.5 Recovery screening module

Ears will drop into recovery screening module after leaving the second level measurement module. Ears will be recovered or classified by parameters, which are calculated in previous modules.

In conclusion, the measurement module will receive the shape and size parameters of the conveyed ear when the second level device operates. And these parameters are transmitted from the first level measurement module. The detected ear will go into the cylindrical duct and finally leave from the catheter with vertical drop. When the infrared obstacle avoidance trigger of the black box detects the ear dropping, it will control three industrial high-speed CCD cameras to capture the images from three views at the same time. Then the computer will calculate the 3D parameters (ear row number, row grains, ration of deficiency grain, etc.) of maize ear according to parallax of three views and parameters obtained from the first level measurement module. The design in this paper has the following advantages:

1. High-speed and high-throughput.

2. The image calculation depth is 2.5D enough without 3D measurement.

3. Measure parameters are obtained from the three views. So it is unnecessary to use so much time to execute 3D reconstruction.

3 Results and discussion

3.1 Construction of experimental platform

In this section, taking the hybrid maize as test object, the high-throughput maize ear analysis platform is tested and evaluated. The most important parts of experimental platform are the camera and light sources.

The first level measurement device needs one camera and four light sources, and the four strip light sources are placed at the top of collection black box. The shooting height of CCD camera is about 450 mm .Under this height, the acquiring image is more accurate and the distortion is smaller. In addition, the conveyor belt is about 80 mm and just allows one single maize ear to pass through vertically. The physical map of first level measurement device is shown in Figure 11.

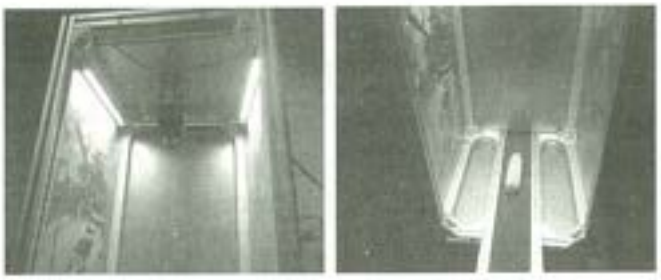

Figure 11 Physical map of the first level device

Then the second level measurement device needs three cameras and eight light sources. And eight strip light sources are placed in the black box, four sources arranged in a ring on the upper side, the others arranged in a ring on the lower side. The lighting directions should point to the intersection of three CCD cameras' measuring sight. The lighting strength of eight strip lights is so stronger to ensure the camera can get enough light to acquire the shape and texture features of maize ear during the short exposure time. Comparing the imaging effects of various conditions, the shooting distance of cameras is determined as 400 mm and the falling distance of maize ear is determined as 300 mm (leave the cylindrical catheter). Based on the above design, the physical map of second level detection module is shown in Figure 12.

After a lot of verification experiments, the pipelining platform can support high precise and efficient maize ear analysis as a practical tool and technical references. The images of maize ear acquired by the device are shown in Figure 13.

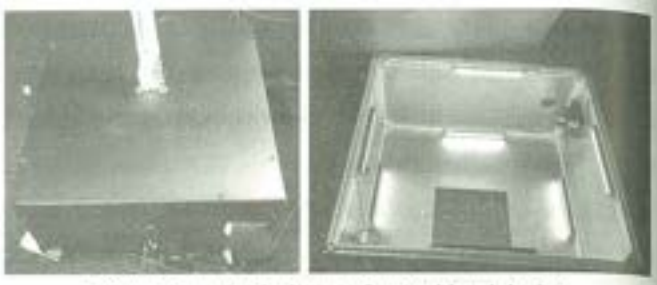

Figure 12 Physical map of second level device

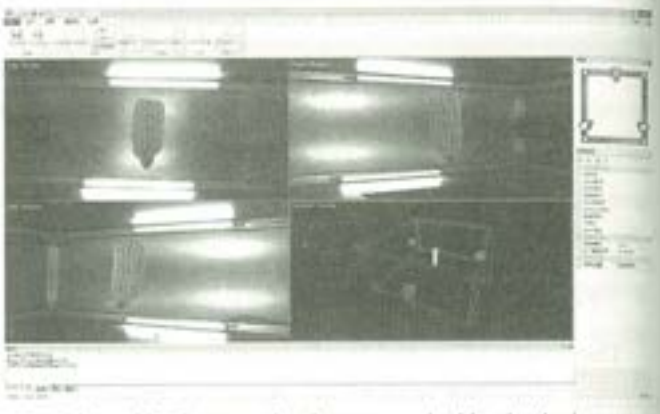

Figure 13 Images of maize ear acquired by the device

3.2 Experimental result analysis

In the stage of the two-dimensional characteristic measurement of the ear, it is mainly for the easy to extract on the single-sided image, and the measurement accuracy of the higher indicators. The parameters measured by the first level measurement module include ear length, ear dimeter, volume, and bare tip positioning and calculation. For the maize ear's irregular shape (space rotating body), some of the phenotypic parameters of the ear need to collect holographic images to calculate accurately. Therefore, it is necessary to measure the phenotype parameters in 3D mode. The parameters measured by the second level measurement module include ear row number, row grains, lack of grain yield and ration of deficiency grain.

In order to verify the measurement precision of length indicators calculated by the first level detection module, 50 maize ears are selected to do precision test with ear length and ear diameter. The test methods are as follows:

1. Randomly select 50 maize ears as the test samples.

2. Acquire image of every maize ear by the first level detection module.

3. Calculate the ear length and ear diameter by every ear image.

4. Measure actual ear length and diameter by vernier caliper.

5. Do data and error analysis.

The error analysis for ear length and ear diameter is shown in Table 1, Figure 14 and Figure 15.

Table 1 Error analysis for ear length and ear diameter

Test parameter	Average error	Maximum error	Minimum error	Standard deviation
Ear length	1.59%	5.77%	0.13%	0.0123
Ear diameter	2.45%	4.04%	0.41%	0.0105

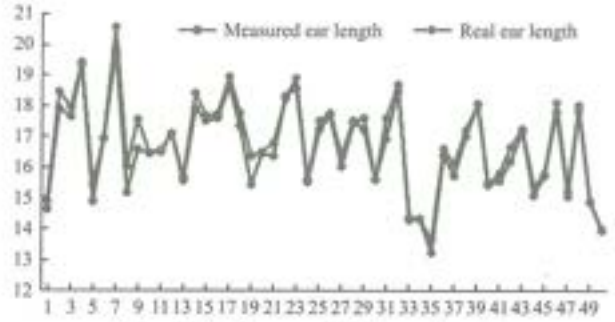

Figure 14 Error analysis for ear length

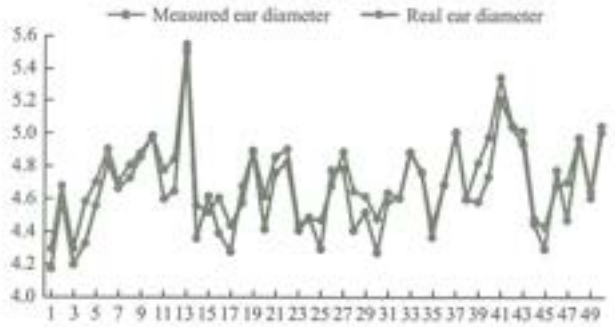

Figure 15 Error analysis for ear diameter

In order to verify the measurement precision of 3D phenotypic traits calculated by the second level detection module, 20 maize ears are selected to do precision test with ear row number and row grains. The test methods are as follows:

1. Randomly select 10 maize ears as the test samples.

2. Acquire images of three views at the same time and extract the ear center of gravity.

3. Substitute into the positive triangulation model to calculate the center of the ear from the three camera shooting center distance.

4. Measure real distance by tape measure.

5. Substitute into the calculation model of ear row number and row grains, and do error analysis.

The error analysis for ear row number and row grains is shown in Table 2, Figure 16 and Figure 17.

The measurement error of row number is multiple of 2 because row number is even. The true value of row number is accurate, so zero error rate should be used to measure accuracy error rate in place. After the test, the zero error rate of row number is 94%. And the grain number per row is less two grains. This pipelining platform can support high precise and efficient maize ear analysis as a practical tool.

Table 2 Error analysis for ear row number and row grains

Serial number	Measured ear row number	Real ear row number	Measured row grains	Real row grains
1	16	16	-28.56	27.67
2	18	18	27.44	28.33
3	18	18	33.13	31.67
4	14	14	31.76	30.33
5	16	16	30.99	29.00
6	16	16	28.38	30.33
7	18	18	32.54	33.33
8	16	16	29.17	30.67
9	18	18	28.66	29.33
10	16	16	31.73	30.00

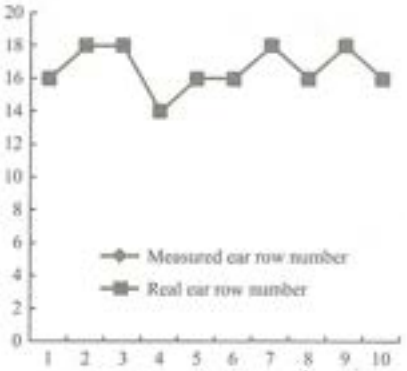

Figure 16 Error analysis for ear row number

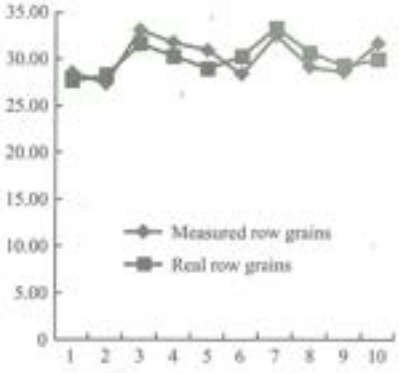

Figure 17 Error analysis for row grains

4 Conclusion

Aiming at these practical problems of high cost, complex computation, long time consuming in modern maize variety test, the high-throughput maize ear analysis platform was constructed in this paper. The pipelining platform realized structure large batch ears to single ear

vertically aligned, the 2D phenotypic information (ear length, ear dimeter, bare tip, etc.) measurements and the 3D phenotypic information (ear row number, row grains, lack of grain yield, etc.) measurements. And on the basis of this, the feasibility of the design scheme of the high-throughput maize ear analysis platform was discussed by means of the prototype. In the experiment, the 2D phenotypic traits computed from the first level measurement module were brought into the second level measurement module as the prior knowledge parameters with the hybrid maize as the test object. So the 3D depth information of maize ear was computed under the absence of additional fixed points. The pipelining platform didn't need to carry out multiple images continuous scanning and stitching and reduced the computational complexity greatly. And the single channel measurement speed can reach 40 spike per minute, the accuracy of the two-dimensional measurement of the platform was above 97.5%, basically meet the expected requirements of this article. This pipelining platform provides a new method for realizing high-throughput maize ear analysis. And this paper provides a reference for the automatic, pipelined and intelligent maize ear analysis.

Acknowledgements

We would like to thank to the reviewers for their helpful comments. This work was financially supported by the Special Fund for supported by Chinese Universities Scientific Fund (2017XD002) and Agro-scientific Research in the Public Interest, China (No. 201203026).

[References]

[1] Alley, S. E., N. J. Hausmann, C. R. Homan, J. J. Kelsick, and M. L. Parlett. 2012. System and method for presentation of ears of corn for image acquisition and evaluation. US20120260618A1 (In USA).

[2] Bi, K., C. Wang., D. Zhu, J. Wang, and Y. Zhang. 2011. A corn testing device based on machine vision. CN101933417A (In China).

[3] Brumback, T. B., S. J. Corak, J. L. Hunter, and Y. G. Lee. 2016. System and method for sensor-based feedback control of a seed conditioning and production process. US9278377B2 (In USA).

[4] Chang, S. 2009. The design and research of automatic feeding device up and down. *Applied Computer Knowledge and Technology*, 5(28): 8076–8078.

[5] Chen, C. 2012. Effects of plant density on grain yield and relative physiological characteristics of maize elite inbred lines and its derived lines. M. S. thesis, Taian, Shandong: Shandong Agricultural University.

[6] Davis, C. M. 2016. Optical robotic sorting apparatus. US9492848B1 (In USA).

[7] Hausmann, N. J., T. E. Abadie, M. Cooper, H. R. Lafitte, and J. R. Schussler. 2009. Method and system for digital image analysis of maize. WO2009023110A1 (In USA).

[8] Huang, G. P. 2010. Identification of quantitative trait locus and heterosis analysis based on single segment substitution lines of yield trait in maize. M. A. thesis. Zhengzhou, Henan: Henan Agricultural University.

[9] Li, H., G. Liu, and P. Liu. 2014. A detection device of maize varieties test. CN103004322B (In China).

[10] Li, X., M. Cheng, Y. Wang and M. Guo. 2010. Study on maize yield and its ear characters under water-limited conditions. *Journal of China Agricultural University*, 15(4): 8–12.

[11] Lie, T., and F. T. Lei. 2008. Real-time crop row image reconstruction for automatic emerged corn plant spacing measurement. *Applied Transactions of the ASABE*, 51(3): 1079–1087.

[12] Liu, C., and B. Chen. 2014. Method of image detection for ear of corn based on computer vision. *Transactions of the Chinese Society of Agricultural Engineering*, 30(06): 131–138.

[13] Liu, G., X. Yang, M. Bai, W. Wei, S. Zhang, and H. Li. 2013. Detecting techniques of maize ear characters based on line scan image. *Transactions of the Chinese Society for Agricultural Machinery*, 44(11): 276–280.

[14] Liu, S, K. Niu, Q. Shi, S. Wang, Q. Yuan, and K. Zhang. 2013. Performance experiment of friction conveying device for maize ears. *Transactions of the Chinese Society of Agricultural Engineering*, 29(12): 9–16.

[15] Ma, Q., J. Jiang, D. Zhu, S. Li, S. Mei, and Y. Lv. 2012. Rapid measurement for 3D geometric features of maize ear based on image processing. *Transactions of the Chinese Society of Agricultural Engineering*, 28(1): 208–212.

[16] Okopnik, D. L., and R Falate. 2014. Usage of the DFRobot RB-DFR-49 infrared sensor to detect maize seed passage on a conveyor belt. *Applied Computers and Electronics in Agriculture*, 102(1): 106–111.

[17] Panigrahi. S., M. K. Misra, C. Bern, and S. Marley. 1995. Background segmentation and dimensional measurement of corn germ plasm. *Applied Transactions of the ASAE*, 38(1):

291–297.

[18] Pearson, T. 2009. Hardware-based image processing for high-speed inspection of grains. *Applied Computers and Electronics in Agriculture*, 69(1): 12–18.

[19] Qi, J., S. Zhang, X. Niu, W. Wang, and Y. Xu. 2011. Design and application of yield monitor system for corn ear. *Transactions of the Chinese Society for Agricultural Machinery*, 42(1): 181–185.

[20] Wang, C., X. Guo, S. Wu, B. Xiao, and J. Du. 2013. Investigate maize ear traits using machine vision with panoramic photography. *Transactions of the Chinese Society of Agricultural Engineering*, 29(24): 155–161.

[21] Wang, C., X. Guo, S. Wu, B. Xiao, and J. Du. 2015. Three dimensional reconstruction of maize ear based on computer vision. *Transactions of the Chinese Society for Agricultural Machinery*, 45(9): 274–279.

[22] Wiendahl, H. P., and A. Rybarczyk. 2003. Using air streams for part feeding systems—innovative and reliable solutions for orientation and transport. *Journal of Materials Processing Technology*, 138(1): 189–195.

[23] Xu, L., and Y. Zhao. 2010. Automated strawberry grading system based on image processing. *Applied Computers and Electronics in Agriculture*, 71(1): 32–39.

[24] Yang, J., H. Zhang, J. Hao, T. Du, F. Cui, N. Li, and G. Liang. 2010. Identifying maize cultivars by single characteristics of ears using image analysis. *Applied Transactions of the Chinese Society of Agricultural Engineering*, 27(1): 196–200.

[25] Zhou, J., Q. Ma, D. Zhu, H. Guo, Y. Wang, X. Zhang, S. Li, and Z. liu. 2015. Measurement method for yield component traits of maize based on machine vision. *Transactions of the Chinese Society of Agricultural Engineering*, 31(3): 221–227.

Design and implementation of IoT-based beef cattle breeding system

Hao Shangbo, Cai Saihua, Sun Ruizhi*, Li Jiayao, and Cheng Chunming

(College of Information and Electrical Engineering, China Agriculture University, Beijing 100083, China)

Abstract: Beef cattle breeding industry plays an important role in animal husbandry, however, the obsolete breeding ideas and imperfect management system make the traditional breeding mode unable to meet the growing demand of beef. In order to deal with the existing problems of beef cattle breeding industry in China, a IoT-based beef cattle breeding system that take RFID (Radio Frequency Identification) technology applied into beef cattle breeding industry was designed and implemented combined with B/S and C/S structures. The system provides the support of collecting and managing to the cowshed and cattle information, feeding information, disease treatment information, epidemic prevention information, weight information and user information. At the same time, the fixed RFID reader is used with the electronic scale to realize the accurate record of weight change during the process of beef cattle breeding. The designed IoT-based beef cattle breeding system has been applied in Lincang, Yunnan Province, China for several years. The running results showed that it is stable and reliable, and the actual needs also can be met by each function. Overall, the system is suitable for fine beef cattle breeding and can help the cattle farm realizing the digital and traceable scientific breeding method.

Keywords: beef cattle breeding system, IoT (Internet of Things), RFID

Citation: Hao, S B., S. H. Cai, R. Z. Sun, J. Y. Li, and C. M. Cheng. 2017. Design and implementation of IoT-based beef cattle breeding system. International Agricultural Engineering Journal, 26(3): 302–309.

1 Introduction

In recent years, beef cattle breeding industry is springing up in China's animal husbandry, accompanied with more and more large-scale beef cattle farms have been built and put into use, it is turning into an economic pillar industry in some places (Kang et al., 2010). However, the increased production of beef in China is still difficult to meet the consumers' demand (Liu et al., 2014), therefore, the scientific and efficient methods of beef cattle culture are urgently needed.

Nowadays, the production management model of beef cattle farms in China is still using traditional way, which is lack of complete breeding information, epidemic prevention information, disease treatment information and etc. Therefore, it is difficult to realize the accurate identification of individual beef cattle, it is difficult to weigh for each beef cattle at regular intervals, and it is difficult to reach the current international requirements for safe and high quality (Zan et al., 2006; Shi et al., 2010).

The emergence and rapid development of Internet of Things (IoT) technology provides a great convenience for human life, and it has been widely used in the smart home, medical industry, commercial and other fields (Zhang et al., 2017; Gomes et al., 2016; Guijarro et al., 2017; Lee et al., 2017; Shirehjini et al., 2016). As the core technology of IoT technology, the characteristic of light and high recognition rate makes RFID suitable for solving the problems that are difficult to identify for beef cattle in beef cattle breeding. Connecting the weighing equipment to the server through network can simplify the weighing process and provide the basis for feed in beef cattle breeding process.

IoT technology has been widely used in agriculture

Received date: 2017-07-08 **Accepted date:** 2017-09-12

***Corresponding author: Sun Ruizhi,** Ph.D., Professor of College of Information and Electrical Engineering, China Agriculture University, Beijing 100083, China. Email: sunruizhi@cau.edu.cn. Tel: 13811435352.

(Ge et al., 2014; Qin et al., 2014; Li et al., 2015) in recent years. Voulodimos (2010) and Lin (2016) used RFID-based mobile devices to manage animal husbandry platform. Karlsen et al. (2012) applied RFID technology into specific identification of animals in seafood supply chain. Abhijith et al. (2013) solved the redundancy problem of sensor data while using WSN technology, they also proposed a multi-level data aggregation technology to effectively monitor and control agricultural products. Balachander et al. (2013) measured and analyzed the received RSS (Received Signal Strength) and then planed and deployed the wireless sensors, they used these sensors into the management applications of precision agriculture and planting. Memon (2016) and Pingzeng (2011) realized the intelligent animal farm by monitoring the farm with various kinds of wireless sensors and IoT technology. Samad (2010), Jayaraman (2016), Wang et al. (2011) realized intelligent farm management system to save farm data records based on RFID technology, the system could regularly collect performance records and operate veterinary services to improve production and management services of farmers and management efficiency of farm. Zhou (2012) and Verdouw (2013) used RFID technology to trace and collect data, and then realized automatic identification and synchronization between devices and servers.

In view of the existing problems of beef cattle breeding industry in China, combined with the B/S structure of browser application and C/S structure of handheld equipment, an IoT-based beef cattle breeding system that applied RFID technology into beef cattle breeding industry was proposed. The proposed system could help people to construct a digital and traceable scientific breeding method.

The other main contents are as follows: The design on IoT-based beef cattle breeding system is introduced. The key equipment and methods on the system are detailed. The deployment and realization of the system are presented, and the conclusion and prospect are discussed.

2 Design on IoT-based beef cattle breeding system

The proposed system is a combination of ASP.NET MVC-based B/S architecture for browser and WinCE-based C/S architecture for handheld equipment. Through the RFID ear tag wearing in the cattle, the system realizes the management of cowshed and cattle information, feeding information, disease treatment information, epidemic prevention information, weight information and user information. The system also can manage and trace the individual information, disease and epidemic prevention information, weight change and so on of beef cattle in the whole process from breeding to sale. Through the communication with breeders and demand analysis method, we design a better database to integrate the weight data from electronic scales and the ear tag data from ear tag reader.

2.1 Overall architecture of the system

The main task of system architecture is to plan the composition of the system according to the identified requirements, and determine the organization between various parts of the system. It is the decisive factor for better realizing the whole system.

In order to realize the substantive functions of the system, the architecture is designed according to the actual requirements. In the stage of data collection, the identification of beef cattle is through RFID ear tag, the data can be input into the system on site using handheld equipment except for conventional manual input, the combination use of electronic scales and fixed RFID readers also can provide the support for gaining weight data of beef cattle. After collecting the data, they are transferred into database to store using wired network or wireless network. Users can query and manage all types of data through front pages and handheld equipment.

The system makes beef cattle breeding process much more digital and informationalized, which can promote the growth of beef cattle and realize the traceable breeding process. The overall architecture of the system is shown in Figure 1.

2.2 Design on system module

The IoT-based beef cattle breeding system can be divided into six modules, they are cowshed and beef cattle information management module, feeding information management module, disease treatment information management module, epidemic prevention information management module, weight information management module and user information management

module. The design schemes of the system modules are shown in Figure 2. The system can provide the record and management in the whole breeding progress of beef cattle, provide the informative feeding data for breeders, improve the feeding quality and provide traceable means for the feeding process. The detailed design of system modules is described as below.

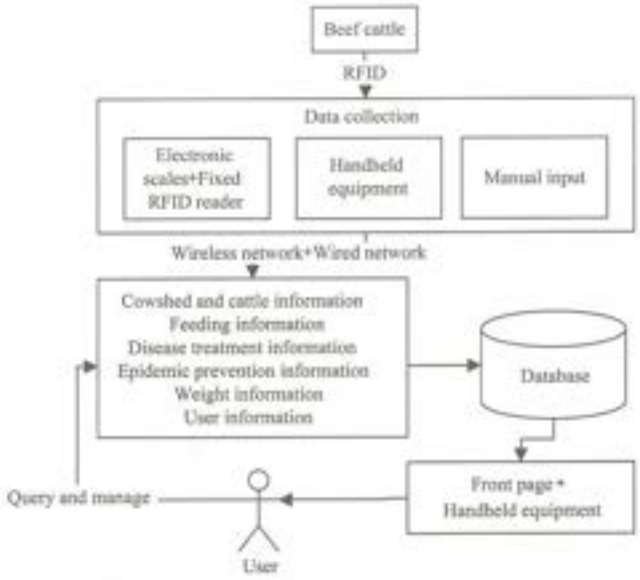

Figure 1 Overall architecture diagram of the system

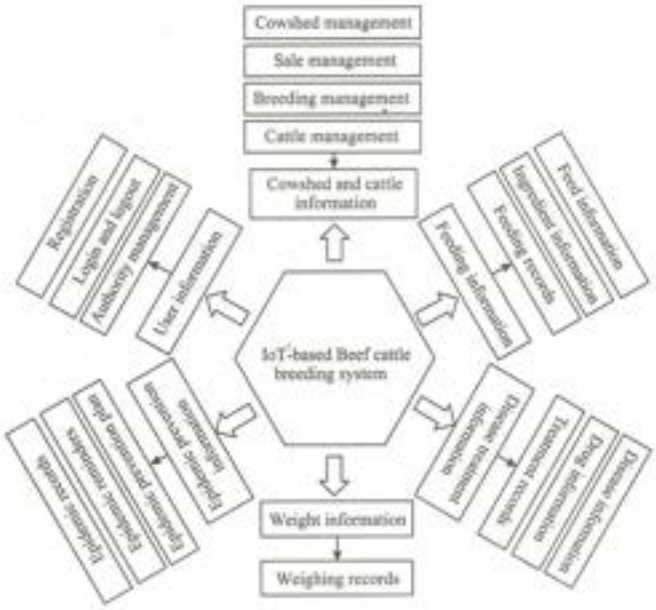

Figure 2 Design schemes of the system modules

Cowshed and beef cattle information management module: this module realizes the management of cowshed information and beef cattle information. Users can query the information through browser and manage the breeding and sale information of beef cattle by reading and writing RFID tags operated by handheld equipment.

Feeding information management module: this module realizes the management of feed information and ingredients information, including the ratios of every ingredient in various feed. Users can query the information through browser, and record the feeding information using handheld equipment.

Disease treatment information management module: this module realizes the management of common disease and common drugs of beef cattle, and records the disease treatment information. Users can query through browser based on ear tag, and record the disease treatment information using handheld equipment.

Epidemic prevention information management module: this module realizes the management of epidemic prevention plan and epidemic prevention record of beef cattle. Users can make the epidemic prevention plan through browser and record the epidemic prevention information using handheld equipment, and the system can remind the users do epidemic prevention before the plan is implemented.

Weight information management module: this module realizes the record and management of weight information. The system records the weight using electronic scales and fixed RFID reader, and users can query the weight change from browser and record the weight information using handheld equipment.

User information management module: this module realizes the management of user information, including user registration, login and other functions, and the system can provide different users interfaces and functions for different users.

Administrator can directly add or delete the data of these functions provided by system to maintain and update the database.

2.3 Design on database

The database of this system is designed according to the requirements of users, the functions and relationships between various entities in beef cattle farms are analyzed. The entities of this system are cowshed, beef cattle, breeder, weighing equipment, feed, ingredient, epidemic prevention plan, disease and drugs. Some links are existing between various entities, such as each breeder can manage multiple cowshed; each cowshed has a set of weighing equipment; each cowshed can feed a variety of

feeds, and vice versa. The E-R diagram of this system is shown in Figure 3, we can realize the corresponding data table to support the realization of the system through the design of database.

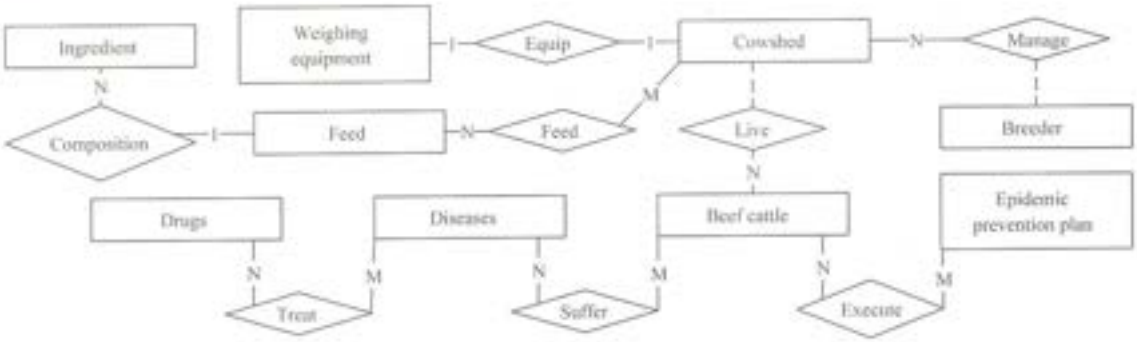

Figure 3 E-R diagram of the system

3 Key equipment and methods on the system

In this system, in addition to general B/S structure of the information management system and front browser page, some key equipment and data processing methods are also used to support the whole beef cattle breeding process.

3.1 Handheld equipment

The handheld equipment is an important part of this system, the time of data input is often after completing the work due to the single input mode of traditional IoT-based system data. In some IoT-based systems, phones are treated as the terminal equipment and data are collected based on two-dimensional code, it is often limited by the environmental brightness and other factors although the data can be collected on-site.

The handheld equipment can read RFID ear tag and it is used in our proposed system, meanwhile, the wireless network is set up in the farm and the handheld terminal is also developed, therefore, the efficiency of data collection and input on-site is much improved.

In this system, the handheld equipment is mainly used by breeders in cowshed to input the data identified from RFID ear tag. In cowshed and beef cattle information management modules, the main functions of handheld equipment are input the information of breeding and sale, modifying the information of cowshed and querying the basic information of beef cattle. In disease treatment information management module, the function is recording the diagnosis and treatment information. In epidemic prevention information management module, the main functions are querying the epidemic prevention plan and recording epidemic prevention information. In weight information management module, the function is input the weight information. The functions of handheld equipment are shown in Figure 4.

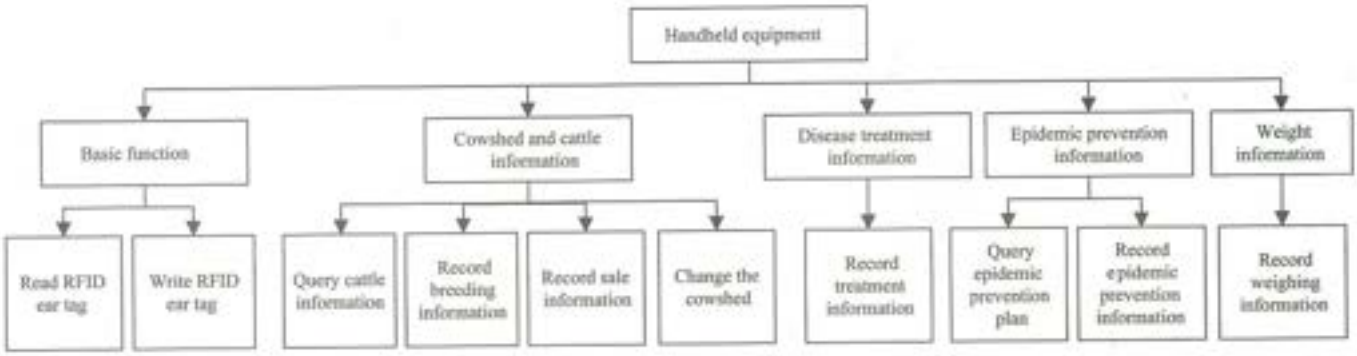

Figure 4 Functions of handheld equipment

3.2 Weighing equipment

The weight change of beef cattle is an important parameter for beef cattle feeding. It is difficult to regular weigh due to the large weight of beef cattle, especially in large beef cattle farms.

The weighing equipment in our system can solve the problem of weighing the beef cattle which was difficult. The weighing equipment is composed of electronic scale,

dash board, fixed RFID reader, antenna, scale railing and sliding door. In these components, the electronic scale is connected with dash board to display and transfer the weight information, the fixed RFID reader is connected with antenna to read and transfer the ear tag data, the scale railing and sliding door are used to secure beef cattle on electronic scale to obtain the accurate weight values. The dash board and fixed RFID reader are connected to LAN, and then, the collected data can be sent and stored in database, and the complete weight data can be obtained after processing. The connection of weighing equipment is shown in Figure 5.

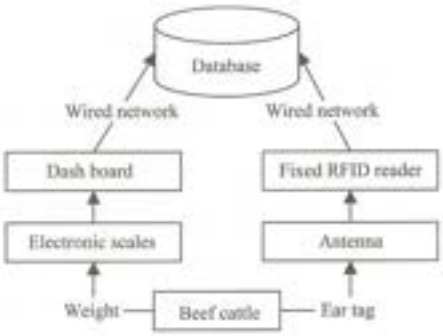

Figure 5 Connection of weighing equipment

3.3 Processing method of weighing data

As mentioned in 3.2, the dash board and fixed RFID reader are connected to LAN to transfer the weight data. The specific steps are listed as follows, the breeder can click the send button in dash board to send the weight data of beef cattle to server database after dash board value is stable. The fixed RFID reader collects the ear tag data from the electronic scale in the fixed time through antenna, and then transfers the data into database.

The separately storing of weight data and ear tag data, and the different time for transferring data into database make the time field of weight data and ear tag data not same, in this case, the weight data can't be obtained directly. Therefore, a method is needed to integrate the weight data and ear tag data to obtain the complete weighing data.

The processing of weighing data method is: to select the unprocessed weight data in time order first, the ear tag data before this data time parameter are intercepted, and then counted the occurrence number of the same ear tag, the highest reading number of ear tag and weight data is recorded as a weighing record. The pseudo code of weighing data method is shown in algorithm 1.

The complete weighing records are obtained after the alignment operation of weight data and ear tag data. It realizes the collecting of the weight information during breeding process, which is helpful for fine beef cattle breeding.

Algorithm 1 Weighing data method

Input: Data set of weight record (DWR), Data set of ear tag record (DER)

Output: Weighing record(WR)

```
1. for weight data (WD) in DWR do
2. for ear tag data (ED) in DER do
3. if ED.time < WD.time then
   4. num[ED.ed]++  // the value of num[ED.ed] is the
      cumulation of the same ear tag, ED.ed is the ear tag
5. end if
6. end for
7. WR.time←WD.time  // assign the WD.time to WR.time
8. WR.weight←WD.weight
9. WR.ed←ED.ed  // ED.ed is the key of maximal num[ED.ed]
10. end for
11. return WR
```

4 Deployment and realization of the system

4.1 The realization of browser pages

The server side of this system is completed using the framework of ASP.NET MVC, and the language of the browser is Razor, the homepage of browser is shown in Figure 6. In browser side, users can use different functions by clicking the different buttons, such as the traceability function of beef cattle, users can view the information of weight change, the situations of disease treatment and the information of epidemic prevention; Breeder can view the information of cowshed through remote connection of the system and the monitor in cowshed; Administrator can modify the information, make the epidemic prevention plan and maintain the database through the system.

The permissions of users are assigned by administrator in this system, different roles can be set to different users and the different pages can be seen for each function after login.

4.2 Realization of handheld application

The operating system of handheld side in this system

is WinCE, the applications of handheld are completed by C# under .NET FrameWork, the page of handheld side is shown in Figure 7.

Figure 7a is the homepage of handheld application, the main functions are listed in the homepage, including the reading and writing functions for the basic RFID ear tag, the management function of beef cattle information, the recording functions of disease treatment and epidemic prevention information, and the recording function of beef cattle weight.

Figure 7b is the breeding page of beef cattle for handheld equipment, breeders mark the ear tags for beef cattle breeding by the writing function of RFID ear tag. 16 bit encoding are composed in the tags, which includes 8 bit breeding time code, 2 bit cowshed code, 4 bit breeder code and 2 bit sequence code, the sequence code is sequentially accumulated in the situation that encoding is existing. After generating the code, the data of beef cattle are input into system and stored in database, and the whole breeding operation is complete.

Figure 7c is the epidemic prevention page for handheld applications. The breeders can query the epidemic prevention plan through scanning RFID ear tag, and then do epidemic prevention after determining it is needed by beef cattle. After epidemic prevention operation, the finish button of handheld equipment is clicked to record the epidemic prevention information.

Figure 7d is the weighing page for the handheld application. The breeders can manual input the weight information and scan the RFID ear tag information of beef cattle in the special situation that weighing operation can't be completed in weighing equipment.

Figure 6 Homepage of browser side

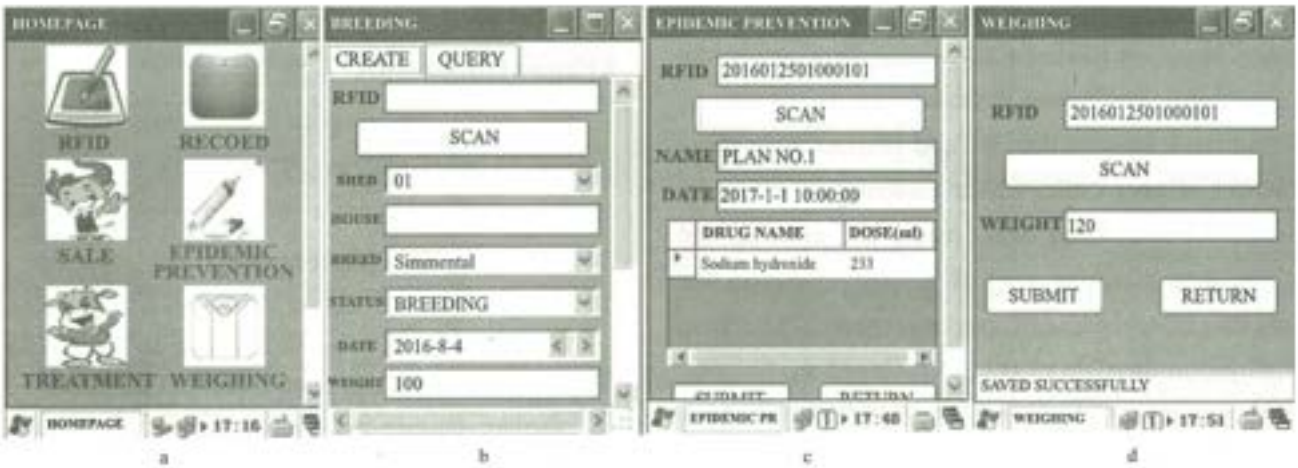

a b c d

Figure 7 Exhibition of handheld page

4.3 Hardware devices and deployments

The system is deployed in beef cattle breeding farm in Lincang, Yunnan Province, China. The software is deployed on Windows Server 2012, the database is Microsoft SQL Server 2012, and the Web server is Microsoft IIS7. Figure 8 shows the hardware composition and on-site deployment.

Figure 8a is the handheld equipment and RFID ear tag. The handheld equipment is equipped with RFID scanning head and can be connected to wireless network. It is also designed for anti-fall, therefore, it is suitable to use in cowshed for breeders.

Figure 8b is the fixed RFID reader and antenna. In deployment of the system, the fixed RFID reader is set up next to the electronic scale and the antenna is set up next to the scale railing of electronic scale. The RFID ear tag data of beef cattle in the electronic scale can be collected by antenna continuously when the fixed RFID reader is opening, and the data is transferred into database through fixed RFID reader.

Figure 8c is the deployment diagram of weighing equipment. The cattle channel is set in the deployment field, and the electronic scale and other hardware devices are placed into the cattle channel, therefore, it is convenient to weigh the weight after driving beef cattle to the cattle channel.

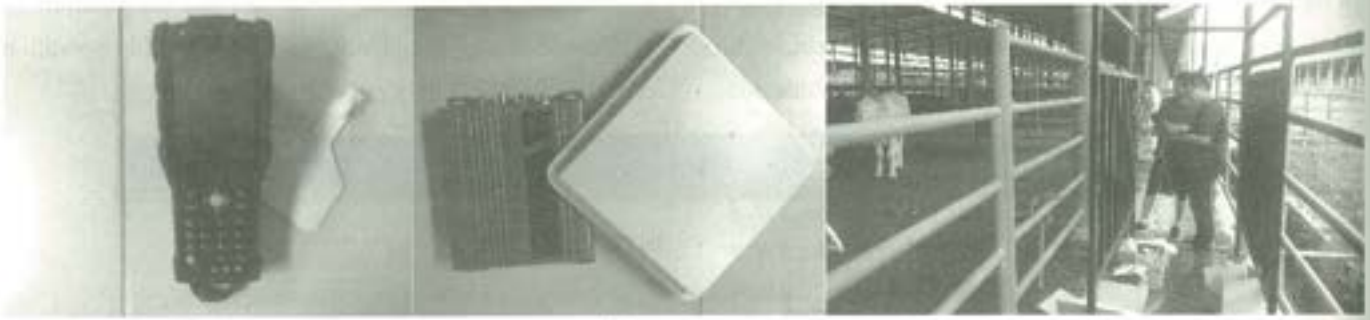

a b c

Figure 8 Hardware composition and on-site deployment

5 Conclusion and prospect

With the fast development of IoT, the using of IoT technology in beef cattle breeding can effectively reduce the labor force spent on individual records of cattle identification, improve the quality management ability, realize the safe breeding mode and help the cattle farm realizing the digital and traceable scientific breeding method. Combined with B/S and C/S structures, this paper realizes a traceable IoT-based system for beef cattle breeding based on RFID ear tag, this system can ensure the availability and realize the data input and storage of breeding farm. Besides that, we also propose a weighing equipment of beef cattle, which combines of electronic scale, dash board, fixed RFID reader and antenna, and then the data matching method is used to collect the weight data of beef cattle in breeding process. The system is deployed in the field of beef cattle breeding, Lincang, Yunnan province, China, the operation of the system is stable and the effect is perfect.

In addition, some records of the system also can be further used to effectively support breeding decisions, such as through the analysis of feeding record and weight change, the evaluation of breeding effect can be realized in breeding process. After confirming the feed amount and proportion of various ingredients in a period of time, the feeding quality can be determined according to the weight change. Meanwhile, the feeding quality can be used to provide advice on breeding, feed types and feeding volume.

Acknowledgements

This work was supported by Chinese Universities Scientific Fund (Grant No. 2017XD001).

[References]

[1] Abhijith, H. V., and M. Dakshayini. 2013. Efficient multilevel data aggregation technique for wireless sensor networks. *August 10-11, 2013: International Conference on Circuits, Controls and Communications*. IEEE. Barcelona, Spain.

[2] Balachander, D., T. R. Rao, and G. Mahesh. 2013. RF

propagation investigations in agricultural fields and gardens for wireless sensor communications. *Information & Communication Technologies*, 755–759.

[3] Ge, W. J., and C. J. Zhao. 2014. State-of-the-art and developing strategies of agricultural internet of things. *Transactions of the Chinese Society for Agricultural Machinery*, 45(7): 222–230. (in Chinese with English abstract)

[4] Gomes, B. D. T. P., L. C. M. Muniz, F. J. Silva e Silva, L. E. T. Ríos , and M. Endler. 2016. A comprehensive and scalable middleware for Ambient Assisted Living based on cloud computing and Internet of Things. *Concurrency and Computation Practice and Experience*.

[5] Guijarro, L., V. Pla, J. R. Vidal, M. Naldi, and T. Mahmoodi. 2017. Wireless sensor network-based service provisioning by a brokering platform. *Sensors*, 17(5): 1115.

[6] Jayaraman, P. P., A. Yavari, D. Georgakopoulos, A. Morshed, and A. Zaslavsky. 2016. Internet of Things platform for smart farming: experiences and lessons learnt. *Sensors*, 16(11): 1884.

[7] Kang, R. J., X. S. Zhang, Z. T. Fu, and W. S. Mu. 2010. Method of traceability information acquisition and transmission for beef cattle sector based on PDA and FSM. *Transactions of the Chinese Society of Agricultural Engineering*, 26(1): 227–231. (in Chinese with English abstract)

[8] Karlsen, K. M., B. Dreyer, P. Olsen, and E. O. Elvevoll. 2012. Granularity and its role in implementation of seafood traceability. *Journal of Food Engineering*, 112(1): 78–85.

[9] Lee, J. S., S. Choi, and O. Kwon. 2017. Identifying multiuser activity with overlapping acoustic data for mobile decision making in smart home environments. *Expert Systems with Applications*, 81: 299–308.

[10] Li, J., M. R. Guo, and L. L. Gao. 2015. Application and innovation strategy of agricultural Internet of Things. *Transactions of the Chinese Society of Agricultural Engineering*, 31: 200–209. (in Chinese with English abstract)

[11] Lin, D. P., C. K. M. Lee, and K.W. Lin. 2016. Research on effect factors evaluation of internet of things (IOT) adoption in Chinese agricultural supply chain. *December 4-7, 2016: IEEE International Conference on Industrial Engineering and Engineering Management*. Bali, Indonesia.

[12] Liu, P. Z., S. S. Bi, X. Y. Xue, Z. M. Deng, G. S. Zang, and Y. S. Gao. 2011. Study on Intelligent Control System for agricultural production based on Internet of Things. *Computer Measurement & Control*, 19(02): 187–200. (In Chinese with English abstract)

[13] Liu, Y. F., C. Yang, and M. L. Wang. 2014. Present situation and prospect of beef cattle industry in China. *Agricultural Outlook*, 4: 10. (in Chinese with English abstract)

[14] Memon, M. H., W. Kumar, A. Memon, B. S. Chowdhry, M. Aamir, and P. Kumar. 2016. Internet of Things (IoT) enabled smart animal farm. *March 16-18, 2016: International Conference on Computing for Sustainable Global Development*, 2067–2072. New Delhi, India. Institute of Electrical and Electronics Engineers (IEEE)

[15] Qin, H. B., D. L. Li, and L. Guo. 2014. Recent advances in development and key technologies of Internet of Things in agriculture. *Journal of Agricultural Mechanization Research*, 4: 246–248. (in Chinese with English abstract)

[16] Samad, A., P. Murdeshwar, and Z. Hameed. 2010. High-credibility RFID-based animal data recording system suitable for small-holding rural dairy farmers. *Computers and Electronics in Agriculture*, 73(2): 213–218.

[17] Shi, L., Z. T Fu, and L. X Zhang. 2010. On RFID-based traceable system for quality insurance of beef cattle breeding. *Computer Applications and Software*, 1: 40–43. (in Chinese with English abstract)

[18] Shirehjini, A. A. N., and A. Semsar. 2016. Human interaction with IoT-based smart environments. *Multimedia Tools and Applications*, 1–23.

[19] Verdouw, C. N., A. J. M. Beulens, and J. Van Der Vorst. 2013. Virtualisation of floricultural supply chains: A review from an Internet of Things perspective. *Computers and Electronics in Agriculture*, 99(6): 160–175.

[20] Voulodimos, A. S., C. Z. Patrikakis, A. B. Sideridis, and E. C. Xylouri. 2010. A complete farm management system based on animal identification using RFID technology. *Computers and Electronics in Agriculture*, 70(2): 380–388.

[21] Wang, K. Q., and K. Cai. 2011. On design of sensor nodes in the rice planthopper monitoring system based on the internet of things. *November 27-28, 2010: International Conference on Photonics and Image in Agricultural Engineering* (PIAGENG 2010). 77520B-77520B-8. Wuhan, China.

[22] Zan, L. S., T. C. Zheng, G. L. Shen, L. G. Wang, and X. H. Zeng. 2006. Design and development of quality traceability information management system and safety of the beef production's entire processes. *Scientia Agricultura Sinica*, 10: 20. (in Chinese with English abstract)

[23] Zhang, Y., and J. T. Wen. 2017. The IoT electric business model: Using blockchain technology for the internet of things. *Peer-to-Peer Networking and Applications*, 10(4): 983–994.

[24] Zhou, Z. W., and Z. Y. Zhou. 2012. Application of internet of things in agriculture products supply chain management. *December 7-9, 2012: International Conference on Control Engineering and Communication Technology* (ICCECT). 259–261. Shenyang, Liaoning. IEEE.

Design and implementation of a selenium-rich grape disease diagnosis expert system

Li Hui[1,2], Zhou Jing[1], Zhang Biao[3], Zhang Lingxian[1,2*]

(1. *College of Information and Electrical Engineering, China Agricultural University, Beijing 100083, China;*
2. *Key Laboratory of Agricultural Informationization Standardization, Ministry of Agriculture, Beijing 100083, China;*
3. *College of Engineering, China Agricultural University, Beijing 100083, China*)

Abstract: In order to solve the problem of disease in the process of grape growing in facilities, a web-based expert system for diagnosis of selenium-rich grape disease was designed. The system took the common grape diseases as the research object, and the traditional experience and the expert knowledge transformation was used as the diagnosis rules. It provided remote support and services to the grape farmers through the Internet by using the ADO technology as the object-oriented interface, the ASP.NET for web design and the HTML language for the system development. This study adopted the method of artificial acquisition to collect and collate the knowledge and adopted the method of combining forward and reverse reasoning to solve the problem that may be a conflict in the process of disease and symptoms matching. By adding, modifying, deleting and querying the data in the knowledge base, the grape disease diagnosis was achieved. The system has the features of safe, simple and practical.

Keywords: selenium-rich grape, disease diagnosis, expert system

Citation: Li, H., J. Zhou, B. Zhang, and L. X. Zhang. 2017. Design and implementation of a selenium-rich grape disease diagnosis expert system. International Agricultural Engineering Journal, 26(3): 310–319.

1 Introduction

With the improvement of living standards, people also have higher demand for daily intake of nutrients in food. The selenium-rich grapes have achieved a lot of attention in recent years because it is rich in selenium elements and a variety of other nutrient elements as well, which can be a supplement to the daily needs of people (Chen et al., 2013). Therefore, it will have broad market prospects to vigorously develop the facility selenium-rich grape cultivation and improve its production.

The selenium-enriched grape facilities are based on the full use of natural environmental conditions, including the greenhouse, plastic sheds and shelters and other protection facilities, to improve or control the environmental factors within the facilities and provide appropriate environmental conditions for the growth and development of selenium-rich grapes (Li et al., 2010; Yan et al., 2013; Wang et al., 2009). As the temperature and humidity in the facilities are obviously higher than those in the open field, the plant growth is relatively dense and young. The occurrence of the disease to the selenium-enriched grapes in the facilities is often earlier and sudden, even more complex, which brings some difficulties in identification, prevention and control of the disease (Li et al., 2015; Zhao et al., 2014). Therefore, it is of great practical significance to understand the characteristics of the selenium-rich grape diseases in the facilities and to diagnose them in time to minimize the damage.

In recent years, with the rapid development of computer technology, agricultural expert system has also made great progress, and is widely used in many aspects of agricultural production management with huge economic and social benefits.

The study of agricultural expert systems originated in the late 1970s, with the earliest in the United States (Ge et al., 2008; Wu et al., 2008). China's agricultural expert system research began in the 1980s. Zhejiang University

Received date: 2017-07-07 **Accepted date:** 2017-08-21

* **Corresponding author: Zhang Lingxian,** Ph.D., Professor of College of Information and Electrical Engineering, China Agricultural University, Beijing, China. Email: zhanglx@cau.edu.cn. Tel: +86-10-62737653.

and the Institute of Sericulture of the Chinese Academy of Agricultural Sciences cooperated to study the expert system of silkworm breeding in 1980. The Institute of Intelligent Machinery of the Chinese Academy of Sciences and the Soil and Fertilizer Institute of Anhui Academy of Agricultural Sciences worked together to develop a mortar black soil wheat fertilization expert system, which had a large scale of application in more than ten counties in the city of Huaibei, and Anhui Province in 1983 (Ma et al., 2005; Yu et al., 2015). Li et al. (2002) developed a web-based diagnosis system for fish disease in 2002. The system used 300 rules, 400 images and charts to construct a web-based expert system to identify fish disorders, which could identify 126 diseases of 9 species of freshwater fish. Duan et al. (2003) had further developed a web-based remote diagnosis system for fish diseases, including synchronous and asynchronous diagnostic systems in 2003. Xu et al. (2006) designed and developed a web-based citrus production expert system, using the forward reasoning on the citrus' diagnosis of 183 kinds of nutrient and pests and diseases, and putting forward corresponding preventive measures and methods in 2006. Chen et al. (2006) designed and developed a web-based tobacco expert system to collect and compile 121 kinds of tobacco nutrition diagnosis and pest diseases with more than 1,000 pictures and video clips. Then the tobacco experts summarized out more than 100 kinds of tobacco pests and weeds, and the relationships the concepts were described in a regular form (Chen et al., 2006). Jin et al. (2009) designed and developed an expert system of grape disease diagnosis based on artificial neural network, and analyzed the symptoms in five infestation sites including grape roots, dendrites, leaves, inflorescence and ears, which could diagnose 18 diseases of grapes. Liu et al. (2011) studied and designed an artificial neural network based diagnosis system for apple disease in 2011. Pertot et al. (2012) designed a web-based plant disease identification system. Sun et al. (2013) used a three-layered B/S architecture to design a crop pest diagnosis system, which was queryable, diagnosable and consultable in 2013. Tan et al. (2014) used computer vision technology combined with BP Artificial Neural Network (ANN) to identify the soybeans with gray leaf spot, mothy soybeans, moldy soybeans and damaged soybeans in 2014. Xu et al. (2014) focused on the three common diseases in sunflower leaves including bacterial leaf spot, black spot and downy mildew disease and developed a sunflower leaf disease diagnosis system based on image recognition in 2014. Xue et al. (2015) designed and developed an Android-based identification of new potato pest's diagnostic system in 2015. Liu et al. (2016) designed a WebGIS-based tobacco pest diagnosis and prediction system in 2016.

At present, it is no longer a vision for the computers entering into the rural areas for the majority of farmers to provide a variety of advisory services. Therefore, it is a feasible and meaningful thing to study how to effectively use the computer to spread the knowledge of agricultural experts to millions of households and to guide farmers to perform scientific diagnosis. This paper mainly includes two parts. Firstly, in the process of system construction, knowledge of a wide range of selenium-rich grape in facilities was collected from a large number of channels for the construction of a database. Secondly, a web-based selenium-rich grape disease diagnosis system was established to provide remote support and services for the grape growers through the internet, helping them to get accurate and objective disease diagnosis results.

2 Knowledge acquisition and presentation

2.1 knowledge acquisition

Knowledge acquisition is a very important part in the process of building a selenium-rich grape disease diagnosis expert system. The basic task of knowledge acquisition is to acquire knowledge for the expert system and establish a sound, perfect and effective knowledge base to meet the needs of solving the problems in the field. In the construction process of the system, knowledge of a wide range of selenium-rich grape in facilities was collected from a large number of channels for the construction of a database. Knowledge was collected and acquired from the knowledge sources, basically in the following three ways:

• Manual acquisition. That is, the knowledge engineers discuss with the domain experts to collect, organize and summarize the relevant knowledge, and

build up a knowledge base after reorganizing the knowledge in a manual way.

• Semi-automatic access. The computer deals with the experts through an intelligent editor tool, organizes and arranges the knowledge base in accordance with the requirements of human-computer interaction.

• Automatic access. The computer directly obtains the knowledge from the experts, books, examples and data, and continuously improves the performance of the knowledge in the acquisition process, for example, using the machine learning.

As the basic information of disease diagnosis mainly comes from the field of knowledge and expert experience, this study has taken the way of artificial acquisition of knowledge collection and finishing in order to ensure the accuracy and applicability of knowledge expression. And in the system operation, the administrator can continuously add, delete and modify knowledge through the management Interface. As the diseases features and prevention approaches of the selenium-rich grape in facilities are different from that of the common grapes cultivated in open field, in order to ensure the accuracy and applicability of the expert system and to facilitate the practical application and operation of the grassroots users, this study has collected nine of the most common grape diseases in facilities.

2.2 Knowledge representation

Because of the empirical and causal characteristics of the knowledge of the selenium-rich grape disease, this study applied the most widely used productive method to express the knowledge of the grape disease diagnosis. The term "productive" was first proposed by American mathematician E. Post in 1943, and its basic form is:

IF <condition 1>, <condition 2>, ..., <condition N> THEN <expression>

Where <condition 1>, <condition 2>, ..., <condition N> are the prerequisites for indicating whether the production is available, and each condition is a compound condition connected with "and" or "or", and the <expression> is a set of conclusions or operations that indicate the conclusions that should be drawn or the operations that should be performed when the prerequisites are met. The meaning of the whole production is that if the premise is satisfied, the action specified by the expression <expression> or the execution of <expression> can be introduced.

The disease knowledge base system has got nine common grape diseases in facilities. The diagnosis and control of diseases in the process of grape growing should be on the basis of the known information such as the site of the diseases and the symptoms to determine the types of diseases in order to make the right disease prevention or treatment decisions and control the development of the disease. The grape growth evidence obtained here uses "I" to represent a record in the disease signature, that is, a primary characteristic attribute that determines the disease. Then it can be expressed as follows.

IF I1 (disease site) AND I2 (disease symptom) $\in \alpha$, THEN D (disease name),

Where, α is the disease knowledge base, D is the disease name based on the above conditions. Some diseases have symptoms in the incidence of multiple parts such as leaves, fruits and others, which need to meet multiple symptoms at the same time to diagnose the disease results. Some typical disease diagnosis method is relatively simple, just a symptom to determine the disease name.

For example, in the grape disease diagnosis rule base, there is a production type:

IF onset site = flower AND symptoms = large amount of rot

THEN disease name = gray mold

3 System design

3.1 Design goals

The expert system tries to combine the knowledge of the planters, experts and the computer technology to establish a web-based selenium-rich in-facility grape disease diagnosis system. This system will provide remote support and services to the grape farmers, so that the experts' knowledge, experience and problem-solving methods can be promoted and inherited, so as to help grape growers to have accurate and objective diagnosis of the diseases.

3.2 Structure and function design

The functional modules of the system include: the

overview module of selenium-rich grapes in the facilities, the prevention and control modules of the selenium-enriched grape diseases, and the diagnosis and system management module of the selenium-rich grape disease. Each functional module is composed of several sub-modules as shown in Figure 1.

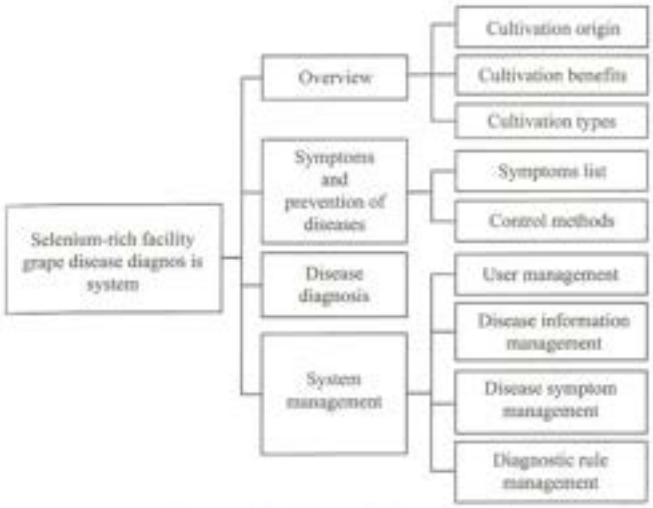

Figure 1 System function module structure diagram

The main functions of the system modules are as follows:

- In-facility grapes overview module. It introduces the basic information of the origin, cultivation benefit and cultivation type of the grapes in facilities.
- Grape disease symptoms and prevention module. It introduces the common symptoms of typical grape diseases, and the control methods of several typical grape diseases in facilities.
- Grape disease diagnosis module. It selects the disease symptoms in the fruit, leaves, flowers and spike, etc., and thus determines the type of grape diseases.
- System management module. It mainly takes management of the grape disease information database, disease symptom database, diagnostic rule base and user information database, including data addition, modification, deletion and etc.

3.3 Database and knowledge base construction

The selenium-rich grape disease diagnosis expert system is using SQL server 2000 to build the system database, and the main contents of the database include:

- The selenium-rich grape disease symptoms table

This table stores the symptoms of grape diseases, as shown in Table 1, and the symptoms set is shown in Table 2.

Table 1 Disease symptom

Field name	Data type	Length	Field description
id	int	4	Automatic identification
symptom	varchar	200	Symptom description
part	varchar	10	Disease part
image	varchar	50	Symptom image file name

Table 2 Symptoms set

id	Symptom	Part	Image
1	Rotten a lot	flower	pic1.jpg
2	White powder	fruit	pic2.jpg
3	Water-stained brown spots with expansion of depression	fruit	pic3.jpg
4	Small black spot on the lesion	fruit	pic4.jpg
5	Rust red conidia	fruit	pic5.jpg
6	Round dark brown spot with diameter of 2 mm on the surface of young fruit epidermis. As the fruit is constantly expanding, the lesion has scab-like surface. When the fruit grows into medium size, the scab falls off.	fruit	pic6.jpg
7	Black coal-like small particles	fruit	pic7.jpg
8	Hardened flesh	fruit	pic8.jpg
9	Cracked fruit	fruit	pic9.jpg
10	Stop growing	fruit	pic10.jpg
11	Mouse gray mold	fruit	pic11.jpg
12	Light brown rounded small spot	fruit	pic12.jpg
13	The middle of the spots gradually become white, depression, with the reddish-brown edge, like "bird" shape	fruit	pic13.jpg
14	Black lesions, hardening cracks	fruit	pic14.jpg
15	Brown spot	leave	pic15.jpg
16	Sporadic small yellow spots appear on the leaves, surrounded by water-like shape	leave	pic16.jpg
17	Translucent, water-like small spots with the edge not clear	leave	pic17.jpg
18	Withered	leave	pic18.jpg
19	Early fall off	leave	pic19.jpg
20	The lesion is dry and may form perforations.	leave	pic20.jpg
21	The veins are rhombic or fusiform.	leave	pic21.jpg
22	Yellow round spot with dark brown margin and light brown or gray center.	leave	pic22.jpg
23	Pale yellow lesions	leave	pic23.jpg
24	Yellow brown spot	leave	pic24.jpg
25	Yellow-green lesions	leave	pic25.jpg
26	White powder	leave	pic26.jpg
27	The back of the lesion produces white mold.	leave	pic27.jpg
28	A large number of orange-yellow powdery spores cover the leaves.	leave	pic28.jpg
29	The back of the diseased leaves has orange summer spores heap, gradually expanded along the veins.	leave	pic29.jpg
30	Crisp spike ear	fringe	pic30.jpg
31	Ear deformed, withered	fringe	pic31.jpg
32	The ear branches of the young ear produce brown water-like small spots, and quickly spread to the surroundings. The entire branch of the spike is dead in serious situation.	fringe	pic32.jpg
33	The surface has black mold and the ear has atrophy and falls off.	fringe	pic33.jpg

• Selenium-rich grape disease basic information table

This table stores the basic information of the grape disease, details the symptoms of each disease and the prevention and treatment methods, and the number of features corresponding to each disease varies. For example, there are three symptoms for the disease of gray mold. See Table 3 and Table 4 for details.

Table 3 Grape disease basic information data

Field name	Date type	Length	Field description
id	int	4	Automatic identification
Disease name	varchar	20	Disease name
symptoms	varchar	50	Basic symptom
prevention	text	16	Prevention method

Table 4 Collection of disease information

id	Disease name	Symptoms	Prevention
1	Powdery mildew	2|10|15|18|26|30|31|	Completely clear the garden. The cut diseased branches and residual leaves should be completely burned each winter. Five-degree stone sulfur mixture is spayed on the plant before germination for the eradication of winter disease. The 800 times 70% methyl thiophanate or 1500 times 15% pink rust wet powder or 400 times sulfur suspension, should be applied in the early onset of the disease and again half a month later so as to guarantee a good control effect.
2	Gray mold	1|11|15|	It is necessary to strengthen the cultivation management in the facilities and reasonably regulate water, fertilizer, temperature and water conditions, to prevent sharp steep branches, and pay attention to timely topping, fixing so as to improve the ventilation and light conditions in the facilities. Drugs should be timely applied before and after flowering. The commonly used drugs include 800 times 40% Exhale leaching agent, 50% Sumilex 200 times liquid and 1000 times 50% iprodione wettable powder. The soil moisture and air humidity within the facility should be reasonably controlled, so as to control high humidity and prevent disease induced conditions.
3	Blackpox disease	9|12|13|14|20|21|22|	Carefully clear the garden. The cut branches, leaves and weeds should be completely burned and removed in winter to reduce the source of infection in the coming year. In the two or three leaves stage, 800 times 70% carbendazim solution or 600 times 78% Kobo WP or 200 times cuproxat, etc. should be sprayed once. And then 200 times Bordeaux with half amount of lime should be applied every 15 days to effectively prevent disease. It is necessary to strengthen the cultivation and management within the facilities, increase application of phosphorus, potash fertilizer, and timely prune the tied vine so as to improve the ventilation and light conditions within the facility and promote the robust branches. Pay attention to the disinfection of seedlings, and apply 10% ferrous sulfate solution plus 1% crude sulfuric acid, or the Bome 3 degrees stone sulfur mixture to dip the seedlings for 1-2 seconds or fully spray, and then dry for planting or cutting.
4	Downy mildew	15|17|19|20|23|24|27|	The diseased branches and fallen leaves should be completely burned and removed before and after pruning in autumn to reduce the source of infection in coming winter. The five-degree stone sulfur mixture should be sprayed on the grape dendrites before germination to kill the winter pathogens. From the beginning of two or three leaves stage, the following drugs should be applied once every 7-10 days including 240 times half amount Bordeaux or 600 times 78% Kobo liquid. At the beginning of the incident, the drugs should be immediately sprayed including 300 times 40% phosphorus aluminum, 2000 times 69% enoylmorpholine or 800 times 72% Klu, 1000 times 58% Biomedium manganese zinc, etc., once every 15 days.
5	anthrax	3|4|5|	Carefully clear the garden. The diseased branches and residual branches should be thoroughly removed. The eradication agent like stone sulfur mixture should be spayed on the mother branch with fruits before sprouting. In the two or three leaves stage, full and careful spraying of 600 times 78% Kobo or 500 times 50% anthrax Ami should be done to prevent the invasion of bacteria. In the fruit coloring or early onset stage, 2000-3000 times 45% amide cream should be applied rapidly. The ear bagging should be implemented in the facilities.
6	Rust	16|18|19|25|28|29|	It is necessary to do a good clearing and overwintering control. The 3-5 degrees Be stone sulfur mixture should be sprayed before sprouting. The management with enough fertilizer to maintain a good growth potential should be strengthened, and the diseased leaves should be timely removed. The drugs should be immediately sprayed in the onset of disease, laying the emphasis on the leaves and leaves back in lower part of the plant. The main reagent includes 0.2-0.3 degrees Be stone sulfur mixture, or 15% rust wet powder 1500 times spray, or the polysulfide suspension 300-500 times, once every 15-20 days.
7	Roots of leaf b light	6|32|33|	In the inflorescence interval and one week after flowering, the following drugs should be applied once including 600 times 50% carbendazim WP or 50% thalidomide wettable powder 1000 times solution, or 800 times 50% methyl thiophanate solution.

• Selenium-rich grape disease diagnosis rules

The rules used in the diagnosis of the grape disease are stored in the table. The diagnostic rules are created and maintained by dynamically adding and deleting columns in the symptom table.

The words that add columns to the symptoms table are as follows:

alter table symptoms add 'powdery mildew 3' bit

This statement indicates that a column named "Powdery mildew 3" is added, that is, the third diagnostic rule for powdery mildew, with the data type bit.

The words that delete columns from the symptoms table are as follows:

alter table symptoms drop column 'Powdery mildew 2'

This statement means that the column named "Powdery mildew 2" is deleted, that is, the second diagnostic rule for powdery mildew removed.

Part of the collection of diagnostic rules are as shown in Table 5, with the columns of symptom, part and image

omitted. As shown in the table, when the id is 2 and 6, the value of powdery mildew 2 is TRUE and the rest is FALSE. This means that the second rule of powdery mildew is for that the disease type of the grape can be judged as powdery mildew when the symptoms of the grapes in the facility are with the id of 2 and 6.

Table 5 Part of the set of diagnostic rules

id	Powdery mildew 1	Gray mold 1	Blackpox disease 1	Downy mildew 1	Downy mildew 2	Anthrax 1	Rust 1	Rust 2	Root 1
1	FALSE	TRUE	FALSE	FALSE	FALSE	FALSE	FALSE	FALSE	FALSE
2	TRUE	FALSE	FALSE	FALSE	FALSE	FALSE	FALSE	FALSE	FALSE
3	FALSE	FALSE	FALSE	FALSE	FALSE	TRUE	FALSE	FALSE	FALSE
4	FALSE	FALSE	FALSE	FALSE	FALSE	TRUE	FALSE	FALSE	FALSE
5	FALSE	FALSE	FALSE	FALSE	FALSE	TRUE	FALSE	FALSE	FALSE
6	FALSE	FALSE	FALSE	FALSE	FALSE	FALSE	FALSE	FALSE	TRUE
7	FALSE	FALSE	FALSE	FALSE	FALSE	FALSE	FALSE	FALSE	FALSE
8	FALSE	FALSE	FALSE	FALSE	FALSE	FALSE	FALSE	FALSE	FALSE
9	FALSE	FALSE	TRUE	FALSE	FALSE	FALSE	FALSE	FALSE	FALSE
10	TRUE	FALSE	FALSE	FALSE	FALSE	FALSE	FALSE	FALSE	FALSE

3.4 Reasoning machine design

3.4.1 Selenium-rich grape disease diagnosis reasoning process

The reasoning process shown in Figure 2 is used in the process of grapefruit disease diagnosis according to the human thinking of disease diagnosis, combined with the experience of experts in the fields.

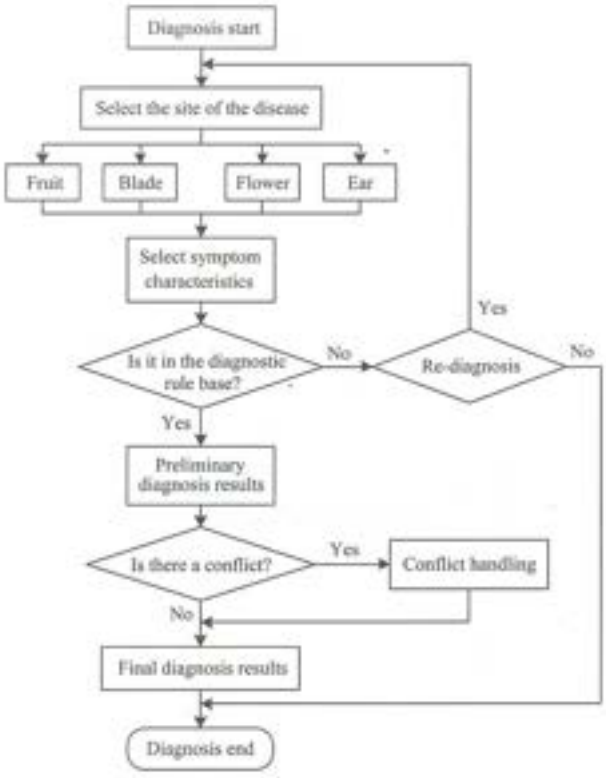

Figure 2 Reasoning process

In this study, both of the positive and negative reasoning methods are adopted according to the traditional production rules system, in which from the beginning of diagnosis to determine the possible occurrence of the disease stage, and from the onset of disease symptoms to determine the specific type of disease, it is a positive reasoning process. Using the following reasoning process to achieve positive reasoning, the rule sets are defined as follows:

Rule 1: IF P1 THEN P2

Rule 2: IF P2 THEN P3

Rule 3: IF P3 THEN q3

Where P1, P2, P3, q3 in the rules are predicate formulas. Suppose the total database has the fact P1, then these three rules are applied for forward reasoning, which is the process that is derived from P1 to infer q3. The forward reasoning link process diagram is shown in Figure 3.

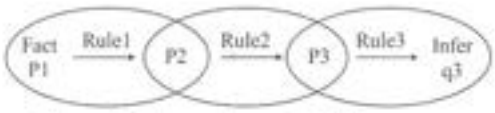

Figure 3 Forward reasoning link process

It is the reverse reasoning process that from the control of possible diseases to the selection of typical symptoms, disease period, the site of the test process, and from the disease name to the disease symptoms, with the detailed symptoms of the disease compared with the user input disease symptoms. Taking the above-mentioned three rules for example, the reverse reasoning method is applied, starting from P1 to infer q3, it is shown in Figure 4.

Firstly, it is assumed that the target q3 is true. With the rule 3 (P3→q3), it is necessary to verify that P3 is true. However, the total database does not have the fact

P3, so the sub-target P3 is assumed to be established. Then with the rule 2 (P3→P3), the P2 should be verified. Similarly, since there is no fact P2 in the database, it is assumed that the sub-target P2 is true. With the rule 1 (P1→P2) to verify P2 is true, P1 should be verified first. Because there is a fact P1 in the database, the assumed target P2 is true, and thus P3 is true, and finally the conclusion q3 is true.

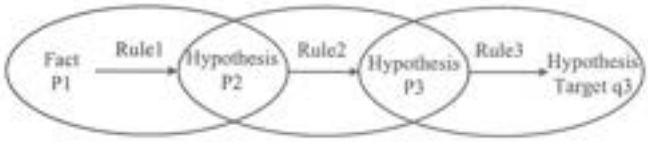

Figure 4 Reverse reasoning link process

Only after the combination of positive and negative reasoning does the final diagnosis results seem more realistic, and the effectiveness and practicality of the expert system can be increased.

3.4.2 Conflict resolution

The so-called conflict refers that in the current input of the disease information, the system infers more than one disease name, causing the phenomenon of conflict. When the user's input is complete, the system has no conflict because each disease is different from the other diseases with different symptoms. However, when the information entered by the user is the common characteristics of several diseases, the conflict may occur, so the process of the conflict is the inevitable phenomenon when the user is using the system. In the case of reasoning, this must be dealt with to ensure the effectiveness of the diagnostic results.

The system firstly uses automatic determination when it tries to resolve the conflict, and then resolves the conflict through the conflict resolution method, and finally outputs the diagnostic results. The conflict resolution rules can be expressed as:

IF <Condition> THEN <Resolution method>

where, <Condition> is the summary of the conflict, and <Resolution method> is the corresponding conflict resolution strategy, which the domain experts often used in the long-term practice and is proved to be effective conflict resolution method. The algorithm is described as follows:

Repeat

Select a conflict resolution rule R from the rule set;

Match R;

If conflict type matches successfully

Then implement the rules to resolve the conflict

Else continues

If the conflict is resolved

Then stop rule-based reasoning

Else continues to expand the rules used

If there is no rule available

Then stop rule-based reasoning

Until there is no matching conflict resolution rule

If the conflict has not been revolved at this time, the system will judge the conflict based on the information in the new rules database of the grape disease diagnosis and the information in the historical records.

If there is no relevant record in the new rules database, or if the information still fails to eliminate the conflict, the system will prompt the user to attach additional disease features as a basis for further reasoning. At this time, relying on human-computer interaction, the conflict can get a reasonable solution.

4 System implementations

The system is developed by using Visual Studio 2005 and SQL server 2000 as the development tools, ADO as the interface of the database, ASP.NET for web design, and HTML as system development language. The main interface of the system is as follows (Figures 5 to 9).

Figure 5 Grape cultivation overview interface

Figure 6 Grape diseases description interface

Figure 7 Grape diseases diagnostic interface

No.	Disease Name	Prevention	Operation
1	Powdery mildew	Completely clear the garden. The cut diseased branches and residual leaves should be completely burned each winter. Five-degree stone sulfur mixture is sprayed on the plant before germination for the eradication of winter disease. The 800 times 70% methyl thiophanate or 1500 times 15% pink rust wet powder or 400 times sulfur suspension, should be applied in the early onset of the disease and again half a month later so as to guarantee a good control effect.	Modify Delete
2	Gray mold	It is necessary to strengthen the cultivation management in the facilities and reasonably regulate water, fertilizer, temperature and water conditions, to prevent sharp steep branches, and pay attention to timely topping, fixing so as to improve the ventilation and light conditions in the facilities. Drugs should be timely applied before and after flowering. The commonly used drugs include 800 times 40% Exhale leaching agent, 50% Sumilex 200 times liquid and 1000 times 50% iprodione wettable powder. It should reasonably control the soil moisture and air humidity within the facility, so as to control high humidity and prevent disease induced conditions.	Modify Delete
3	Blackpox disease	Carefully clear the garden. The cut branches, leaves and weeds should be completely burned and removed each winter to reduce the source of infection in the coming year. In the two or three leaves stage, 800 times 70% carbendazim solution or 600 times 72% Kobo WP or 200 times cuprosat, etc. should be sprayed once. And then 200 times Bordeaux with half amount of lime should be applied every 15 days to effectively prevent diseases. It is necessary to strengthen the cultivation and management within the facilities, increase application of phosphorus, potash fertilizer, and timely prune the tied vine so as to improve the ventilation and light conditions within the facility and promote the robust branches. Pay attention to the disinfection of seedlings, and apply 10% ferrous sulfate solution plus 1% crude sulfuric acid, or the Baume 3 degrees stone sulfur mixture to dip the seedlings 1-2 seconds or fully spray, and then dry for planting or cutting.	Modify Delete
4	Downy mildew	The diseased branches and fallen leaves should be completely burned and removed before and after pruning each autumn to reduce the source of infection in the winter. The five-degree stone sulfur mixture should be sprayed on the grape dendrites before germination to kill the winter pathogens. From the beginning of two or three leaves stage, the following drugs should be applied once every 7-10 days including 240 times half amount Bordeaux or 600 times 70% Kobo liquid. At the beginning of the incident, the drugs should be immediately sprayed including 300 times 40% phosphorus aluminum, 2000 times 69% anoylamarpaline or 800 times 72% Kiu, 1000 times 58% Dimedium manganese zinc, etc., once every 15 days.	Modify Delete
5	Anthrax	Carefully clear the garden. The diseased branches and residual branches should be thoroughly removed. The eradication agent like stone sulfur mixture should be sprayed on the mother branch with fruits before sprouting. In the two or three leaves stage, full and careful spraying of 600 times 70% Kobo or 500 times 50% anthrax Ami should be done to prevent the invasion of bacteria. In the fruit coloring or early onset stage, 2000-3000 times 40% oxide cream should be applied rapidly. The ear bagging should be implemented in the facilities.	Modify Delete
6	Rust	It is necessary to do a good clearing and overwintering control. The 3-5 degrees Be stone sulfur mixture should be sprayed before sprouting. It should strengthen the management with enough fertilizer to maintain a good growth potential, and timely remove the diseased leaves. The drugs should be immediately sprayed in the onset of disease, laying the emphasis on the leaves and leaves back in lower part of the plant. The main reagent includes 0.2-0.3 degrees Be stone sulfur mixture, or 15% rust wet powder 1500 times spray, or the polysulfide suspension 300-500 times, once every 15-20 days.	Modify Delete
7	Roots of leaf blight	In the inflorescence interval and one week after flowering, the following drugs should be applied once including 600 times 50% carbendazim WP or 50% thalidomide wettable powder 1000 times solution, or 800 times 50% methyl thiophanate solution.	Modify Delete

Figure 8 Grape disease information management interface

Grape diseases diagnostic rules management

Disease Name: Powdery mildew

Add Modify

No.	Symptom Descriptions	Diseasedparts	Powdery mildew 1	Powdery mildew 2	Powdery mildew 3
2	White powder	fruit	☑	☑	☑
3	Water-stained brown spots with expansion of depression	fruit	☐	☐	☐
4	Small black spot on the lesion	fruit	☐	☐	☐
5	Rust red conidia	fruit	☐	☐	☐
6	Round dark brown spot with diameter of 2 mm on the surface of young fruit epidermis. As the fruit is constantly expanding, the lesion has scab-like surface. When the fruit grows into medium size, the scab falls off	fruit	☐	☐	☐
7	Black coal-like small particles	fruit	☐	☐	☐
8	Hardened flesh	fruit	☐	☐	☐
9	Cracked fruit	fruit	☐	☐	☐
10	Stop growing	fruit	☑	☐	☐
11	Mouse gray mold	fruit	☐	☐	☐
12	Mouse gray mold	fruit	☐	☐	☐
12	Light brown rounded small spot	fruit	☐	☐	☐
13	The middle of the spots gradually become white, depression, with the reddish-brown edge, like "bird" shape	fruit	☐	☐	☐
14	Black lesions, hardening cracks	fruit	☐	☐	☐
1	Rotten a lot	flower	☐	☐	☐
30	Crisp spike ear	fringe	☑	☐	☑
31	Ear deformed, withered	fringe	☑	☐	☑
32	The ear branches of the young ear produce brown water-like small spots, and quickly spread to the surroundings. The entire branch of the spike is dead in serious situation.	fringe	☐	☐	☐
33	The surface has black mold and the ear has atrophy and falls off	fringe	☐	☐	☐
29	The back of the diseased leaves has orange summer spores heap, gradually expanded along the veins	leaf	☐	☐	☐
25	Yellow-green lesions	leaf	☐	☐	☐
26	White powder	leaf	☑	☑	☑
27	The back of the lesion produces white mold	leaf	☐	☐	☐
28	A large number of orange-yellow powdery spores cover the leaves	leaf	☐	☐	☐
17	Translucent, water-like small spots with the edge not clear	leaf	☐	☐	☐
18	Withered	leaf	☑	☑	☐
19	Early fall off	leaf	☐	☐	☐
20	The lesion is dry and may form perforations	leaf	☐	☐	☐
21	The veins are rhombic or fusiform	leaf	☐	☐	☐
22	Yellow round spot with dark brown margin and light brown or gray center	leaf	☐	☐	☐
23	Pale yellow lesions	leaf	☐	☐	☐
24	Yellow brown spot	leaf	☐	☐	☐
15	Brown spot	leaf	☑	☑	☐
16	Sporadic small yellow spots appear on the leaves, surrounded by water-like shape	leaf	☐	☐	☐

Figure 9 Grape diseases diagnostic rules management interface

5 Conclusions

In view of the most important knowledge acquisition part of the expert system of selenium-rich grape disease diagnosis system, this study adopts the method of artificial acquisition to collect and collate the knowledge, which can guarantee the accuracy and applicability of knowledge acquisition.

Since there may be conflict problems in the disease and symptoms matching search process, a special inference engine is designed by combining positive and negative reasoning methods, so as to make the final diagnostic results more realistic, thereby increasing the effectiveness and practicality of the expert system.

The system uses the Visual Studio 2005 and SQL server 2000 as the development tools. With the help of ADO technology, database technology and expert system theory, the selenium-rich grape disease diagnosis system is achieved through the operation of adding, modification, deletion and query in the knowledge database. The system has the characteristics of safety, simplicity and practicality, which reduced the conflict of disease retrieval and has a good application prospect.

Acknowledgments

This research work has been supported by the Special Fund for Agro-scientific Research in the Public Interest (201303106).

[References]

[1] Chen, J., L. Y. He, S. X. Xu, W. Huang, and W. J. Ma. 2006. Design and implementation of web-based tobacco planting expert system. *Computer Engineering*, 32(4): 280–282.

[2] Chen, J. X., B. Z. Yang, L. H. Fan, C. C. Lai, and J. P. Zheng. 2013. A research on the selenium limit in the selenium-rich grape. *Fujian Analysis & Testing*, 22(4): 31 –33.

[3] Duan, Y. Q., Z. T. Fu, and D. L. Li. 2003. Toward developing and using web-based tele-diagnosis in aquaculture. *Expert Systems with Applications*, 25(2): 247–254.

[4] Ge, Z. Y. 2008. Agricultural expert system application and development. *Journal of Shandong Normal University* (Natural Science Edition), 4: 150–153.

[5] Jin, Y. 2009. The neural network and machine vision based South grape expert system research. Ph.D thesis. Horticulture and Landscape Architecture. Hunan Agricultural University, Changsha.

[6] Li, D. L., Z. T. Fu, and Y. Q. Duan. 2002. Fish-Expert: a web-based expert system for fish disease diagnosis. *Expert Systems with Applications*, 23(3): 311–320.

[7] Li, L. 2010. China's fruit trees production status analysis. *Shanxi Fruit Trees*, 6: 41–43.

[8] Liu, Q. R., D. J. He, H. M. Zhang, S. N. Zhu, and Y. Z. Guo. 2011. Research and design in apple intelligent diagnosis system. *Journal of Agricultural Mechanization Research*, 33(4): 76–78.

[9] Li, X. H. 2015. Several grape fruit disease occurrence characteristics and control technology. *Yantai Fruit Trees*, 3: 28–29.

[10] Liu, X. H. 2016. Design of the diagnosis and prediction system of tobacco diseases and pests based on web GIS. *Journal of Agricultural Catastrophe*, 5: 4–6.

[11] Ma, W. J., and L. Y. He. 2005. The application development of agricultural expert system in China. *Journal of Mountain Agriculture and Biology*, 4: 343–346.

[12] Pertot, I., T. Kuflik, I. Gordon, S. Freeman, and Y. Elad. 2012. Identificator: A web-based tool for visual plant disease identification, a proof of concept with a case study on strawberry. *Computers & Electronics in Agriculture*, 84(84): 144–154.

[13] Sun, J., W. Zhao, R. Wen, and N. Jiang. 2013. A crop pests and disease diagnostic system. *Journal of Changchun University of Technology*, 5: 574–579.

[14] Tan, K. Z., Y. H. Chai, W. X. Song, and X. D Cao. 2014. Identification of diseases for soybean seeds by computer vision applying BP neural network. *International Journal of Agricultural & Biological Engineering*, 3: 43–50.

[15] Wu, X. L., J. L. Gao, Y. D. Zhao, X. C. Pei, and C. F. Zhang. 2008. Agriculture expert system research progress and development direction. *Journal of Agricultural Mechanization Research*, 1: 235–238.

[16] Wang, H. B., X. D. Wang, B. L. Wang, J. X. He, W. C. Liu, and F. Z. Liu. 2009. China's facilities grape industry status and development countermeasures. *Chinese and Foreign Grapes and Wine*, 9: 61–65.

[17] Xu, S. X, L. Y. He, W. Huang, and J. Chen. 2006. The design of web-based orange planting expert system. *Computer Engineering and Applications*, 42(1): 212–215.

[18] Xu, H., F. Lv, and X. M. Yue. 2014. Study of sunflower leaf disease diagnosis method based on image recognition. *Electronic Test*, s1: 6–7.

[19] Xue, L. N., and S. Wu. 2015. Potato pest identification system based on android. *Journal of Anhui Agricultural Sciences*, 28: 346–348.

[20] Yan, G. Z., G Yan, S. H. Yang, W. J. Li, J. J. Li, and L. M. Wang. 2013. Study on soil environmental regulation technology of greenhouse grape promoting and delayed cultivation. *Northern Fruit Tree*, 1: 14–16.

[21] Yu, H., H. B. Zhang, and S. J. Lin. 2015. China's agricultural expert system research progress. *Modern Agriculture*, 7: 59–61.

[22] Zhao, H. L. 2014. Grape common pests and diseases of the occurrence and prevention. *Farmers Friends*, 21: 62–62.

Design and realization of agricultural intelligent inspection robot

Chen Zhichang[1,2], Gao Wanlin[1,2*]

(1. *College of Information and Electrical Engineering, China Agriculture University, Beijing 100083, China*;
2. *Key Laboratory of Agricultural Informationization Standardization, Ministry of Agriculture, Beijing 100083, China*)

Abstract: In view of the agricultural production process, many scenes require human monitoring, an agricultural intelligent inspection robot was put forward. The robot can detect and track pedestrians around the production site and transfer real-time monitoring information to the host computer for storage. Robot consists of three parts: the hardware platform, software systems and intelligent algorithms. They help the robot to achieve common intelligent inspection tasks. The hardware platform is mainly composed of sensors, actuators, mechanical structures and electronic systems. Like human body, the hardware platform configuration is the basis of robot design. The software system is mainly composed of ROS system, like human brain to deal with coordination of various kinds of information. ROS as an open source system, has multi-platform support, multi-language support, toolkit and other advantages. Intelligent algorithm is the robot's "soul", from the intelligent algorithm, we can see the robot targeted feedback to the operator. In this paper, the robot obtained the color image, then the pedestrian detection was carried out by combining the channel characteristic and the faster R-CNN algorithm, and the pedestrian was distinguished from the background and positioned accurately. Then, the pedestrian location information was detected to be transmitted to the depth channel Boosting pedestrian tracking algorithm to track pedestrians. Meanwhile, robot sent back the monitored pedestrian information to the master computer to save through WiFi.

Keywords: robot, pedestrian detection, pedestrian tracking, ROS composed

Citation: Chen, Z. C., and W. L. Gao. 2017. Design and realization of agricultural intelligent inspection robot. International Agricultural Engineering Journal, 26(3): 320–326.

1 Introduction

With the continuous development of computer science and technology, people's way of life has undergone enormous changes, more and more tasks that have been done by people who spend a lot of manpower replaced by the computers in nowadays. With the rapid development of robot technology, artificial intelligence and robot combination of intelligent robots in more and more areas have very good applications.

In the agricultural sector, there are many aspects in agricultural production and processing of agricultural products need human to handle. Such as some food quality requirements of the strict cultivation of agricultural products need to be monitored to prevent agricultural products from damaging and ensure the quality and safety; keeping the idlers away from the important experimental fields to prevent damages to the tests; seed bank and pesticide library should be protected to prevent theft; keeping idlers out of the flour mills to prevent the occurrence of danger etc. Briefly speaking, using pedestrian tracking detection technology and robot technology, designing agricultural intelligent inspection robots can replace manpower in the above-mentioned areas, and will have better results and benefits. It is the direction of future development.

2 Materials and method

2.1 Pedestrian detection

Pedestrian detection is the image or video appear in the pedestrian from the background area and precision positioning. From the time of the issue put forward to the present, pedestrian detection, both detection accuracy and detection speed have been greatly improved, especially in

Received date: 2017-06-27 **Accepted date:** 2017-08-17

* **Corresponding author: Gao Wanlin,** PhD, Professor, Research interests: agricultural informationization and application specific chip. Address: College of Information and Electrical Engineering, China Agriculture University, Beijing 100083 P. R. China. Tel: +86-010-62736755, Email: cau_szmtyjs@163.com.

the past ten years. Machine learning-based pedestrian detection improved the detection performance to a very high level. However, in solving practical problems, the current study is subject to the influence of the environment and pedestrians, and in some cases, cannot achieve the desired results.

Pedestrian detection, from the method, can be divided into the moving object detection method and feature matching method. In the early study of pedestrian detection, the method is mainly based on moving object detection. There are background elimination method (Jain, 1979), frame difference method (Meier and Nagank, 1998) and optical flow method (Lipton et al., 1998). But these methods have great limitations, cannot detect the object in the static image or detect an object that does not move in the video

In recent years, the pedestrian detection algorithm has been developed rapidly. In this paper, the pedestrian detection algorithm, based on machine learning, is used to extract the pedestrian characteristics, and the classification model is constructed according to the characteristics. Then, the pedestrian image data are trained and identified. The At present, the successful features of Haar (Papageorgiou et al., 1998) wavelet feature, LBP (Ojala et al., 1996), HOG (Dalal and Triggs, 2005), and edgelet (Bo and Nevatia R, 2005) are used in pedestrian detection. The general detection framework is to extract features and SVM, adaboost Combine.

Based on deep learning, from the beginning of 2012, pedestrian detection research gradually entered into the people's vision, a variety of pedestrian detections for the deep learning methods and deep learning network structures have been put forward, and it greatly improved the effect of pedestrian detection. Especially in the past three years, the deep learning in the object detection has made great progress, led the pedestrian detection performance and speeded up its upgrading. The great development of object detection was the beginning of the R-CNN (Girshick et al., 2014) method for object detection and segmentation published by Girshick et al. in 2014, followed by a large number of the same series of algorithms, this pedestrian detection method has achieved very good results, and this paper also used this method and channel characteristics to achieve pedestrian detection.

2.2 Object tracking

The goal of the object tracking is to estimate the position and motion parameters of the object after the initial position of the object in the first frame of the image and it is given in the image sequence. The typical object tracking system consists of three parts: object visual model, dynamic model and search strategy (Wang et al., 2011). The objective model of the goal is the most important part of the object tracking, which determines which objective function is used to search for the object of interest in the frame. The dynamic model is pre-defined or obtained through training data learning in order to reduce the object search space and calculate the load. The common dynamic model method has linear regression (Seber and Lee, 2003), particle filter (Ali et al., 2014), Kalman filter (Chang and Ansari, 2005), Mean shift (Comaniciu et al., 2000), the hidden Markov model (Chen et al., 2003) and so on. Finally, the apparent model and the dynamic model are combined, and then the optimal search strategy is used to obtain the most possible position of the object, and the positioning of the tracking object is realized.

In order to deal with the change of the object appearance, the object tracking algorithm in recent years mostly uses the adaptive representation model based on the generated or discriminant formula. The generation method is based on the objective detection, the background of the object after the modeling, according to a certain tracking strategy to track the optimal location of the object tracking. The tracking process and the detection process are independent, and the object is tested and then tracked. The discriminant tracking method is to obtain the object state by the object detection of each frame image, and to see the classification problem of the object and the background. By training the classifier, the object region is selected in the current frame and the background is the largest, detection and tracking will be done at the same time. The discriminant method has better tracking performance than the generating method, and the method of using the incremental learning to distinguish the object and the background is less costly and the tracking effect is better.

2.3 Robot

The robot is a programmable and versatile machine, or a specialized system with computer changes and programmable actions for performing different tasks. It is generally composed by the implementing agencies, drive devices, detection devices and control systems, complex machinery and other components. The future direction of the robot is to research the intelligent systems. At present, the mainstream robot operating systems on the market are ROS, Android and Ubuntu, providing some methods for writing robot navigation and limb procedures. These methods do not need to consider the specific hardware, and they even provide a higher level of command. When the robot operating system started on the robot's computer, it will get robot attribute data, such as the robot's limb length and motion data, and then pass the data to a higher-level algorithm. The data are then processed by these algorithms and returned to the motion instructions of the robot.

3 Hardware platform construction

Intelligent robot mainly consists of two parts: the hardware platform and software system. The "hardware platform" in the intelligent robot component refers to a robot entity, like a human body. Hardware platform mainly involves two major areas of mechanical and electronic technologies, including sensors, actuators, mechanical structure, electronic systems and other components. The hardware platform is the basis of the software system. It provides real-time feedback information to software and receives system information to complete the corresponding action.

3.1 Agricultural intelligent inspection robot hardware platform

The components of intelligent robot hardware platform are mainly four categories: sensors, actuators, mechanical structure and electronic systems. The configuration and performance of hardware platform are directly related to the possibility of a robot application, therefore, a robot project to carry out the first step is based on the project objectives, the appropriate robot hardware platform should be selected. This paper started with the configuration of sensors and actuators in hardware, and the hardware platform of agricultural intelligent inspection robots was designed.

3.2 Sensor configuration

The sensor is a sensing device of the robot, which is the main way for the robot to get the information of the external environment. Whether the sensor type is rich in configuration and the performance or not, its accuracy and reliability are directly related to the appropriate environment data the robot obtained and also the data processing the robot handled.

Sensors, such as accelerometer, angular speedometer, encoder, pressure, temperature, displacement, ultrasonic (infrared) ranging, visible light, microphone and so on, can be obtained from the environment, and detection of information can be regarded as sensors. A variety of sensors of microelectronics miniaturization, integration, high precision, high reliability, high stability and other direction are endless new sensors, appeared in recent years.

Intelligent robot sensor configuration should meet the robot's intelligent needs, and use intelligent technology data sources. The sensor configuration of the agricultural intelligent inspection robot mainly includes the following categories: RGB-D sensor, wide-angle HD RGB sensor, laser radar sensor and infrared distance measurement sensor.

RGB-D sensors are visual sensors that are widely used as somatosensory game devices and as research tools for computer vision. It is mainly used for collecting depth information of near depth images, and is used for robot obstacle avoidance and following tasks. Wide angle HD RGB sensor is used to collect high-definition images, and these high-definition images are used to achieve long-distance pedestrian tracking detection, thus to expand the scope of robot surveillance. Laser radar sensors are used for real-time map establishment and robot position information acquisition, and it is an essential tool to realize path navigation in the process of robot patrolling. The infrared ranging sensor is used to acquire the distance information of the near obstacle, and is used for obstacle detection of moving robot.

3.3 Actuator configuration

The implementing agency has the ability of the

robot to act and react physically to the outside world. Such as robots and mobile robotic chassis drive mechanism are the robot's actuator. The performance indicators of the implementing agency are directly related to whether the expected directive can be carried out smoothly.

In this paper, the agricultural intelligent inspection robot mainly means the mobile chassis, does not involve the implementation of mechanical arm and other institutions. The mobile chassis is not a pure actuator, but a complete robot system that contains sensors, mechanical structures and electronic systems, used as an actuator. The main body of the mobile chassis has a three-wheeled structure, and the first two driving wheels. The last one as a driven wheel is to ensure the accuracy of its turning angle. The response of the mobile chassis to the instruction is guaranteed by the system of the chassis itself, and the mobile chassis can also provide the position and attitude information to the system through its own sensor.

3.4 Hardware platform architecture

The intelligent platform design of the agricultural intelligent inspection robot mainly includes the sensor configuration and the actuator configuration. The sensor is used to obtain the information of the external environment. The actuator provides the mobile ability, the position and attitude information to the system through its own sensor. It is foreseeable that the robot needs a powerful host to process all kinds of information in real time to ensure that the robot can respond to the command in a timely manner. The hardware platform of agricultural intelligent inspection robot has simple interactive function and autonomous navigation function. The hardware platform adopts a distributed architecture, which consists of two hosts, one is an airborne host, the other is a master host, and two hosts are connected directly with WiFi, and all the Ubuntu systems based on ROS are running. The on-board host is used to process information of sensors and actuator, feedback the information to the host computer, and receive commands from the host computer. The host receives the feedback information from the airborne host and issues commands to the on-board host.

4 Software system

The software system in the intelligent robot component is the robot's data processing system, just like a human brain, which is used to collect and process various information. Software system is the bridge between hardware platform and intelligent algorithm, which provides a good foundation for the intelligent robot. The coordinated control of the hardware platform provides information interaction for the upper level intelligent algorithm, and is an integral part of the intelligent robot design.

4.1 Software system selection

With the robot becoming more and more intelligent, robot software system is more and more huge, including the underlying hardware drivers, environmental awareness, motion planning, machine vision, logical reasoning and behavior decision making. For the realization and management of these functions are more and more complex. In order to effectively shorten the development cycle of the robot, reduce the R & D cost and improve the development efficiency, many companies and university research institutions have developed a unified robot software development platform; there is special software to achieve the simulation function. In addition, there is mature algorithm software. These software platforms have their own characteristics, covering all aspects of the field of robots.

ROS is an open source robot software platform, its purpose is to integrate different research results, achieve the algorithm release and code reuse robot software platform. It provides functions like operating systems, including hardware abstraction, underlying driver management, inter-process messaging, and program release management. Applications based on ROS development are currently up to 2000, covering hardware drivers, simulation, motion planning, motion control, environmental awareness and other aspects. As these features meet the needs of the majority of developers, ROS has been widely used. Therefore, this paper will use ROS system as a software system, and it can greatly speed up the robot design and development speed.

4.2 Operating mechanism

ROS processing data is a point-to-point network structure, so the program is running through the following: node, message, topic to achieve indoor autonomous mobile robot function.

A node is a process that executes a task in the ROS operating system and is an executable file in each function package. The modularity of the code in the ROS helps the richness of the intelligent function. The indoor autonomous mobile robot operating system is composed of many nodes. The function packs related to these nodes can be called software modules.

The communication between nodes is carried out through a message mechanism, and each message has its own data structure. The message can contain any array of nested structures, similar to the structure. The node announces a message to a specific topic, and the other node can subscribe to the subject by subscribing to the subject.

The publish/subscribe model in the main body is a very flexible communication paradigm, but this broadcast mode is not suitable for simplifying the node design synchronization mode. ROS, with a pair of more stringent message definition paradigm: request/response. This is similar to the operation of a web server, just like a remote call. The service call is bidirectional: a node sends a request to another node and waits for a response. Each service is initiated by a node, and the response to this service returns the same node, so that the differences between the message and the message can be seen.

A service is a paired message that occurs when a node requests information and another node needs to respond. The service can be used to send message between nodes. A providing ROS node offers a service under a string name, and a client calls the service by sending the request message and awaiting the reply.

ROS has a lot of nodes, messages, services, library files, development tools, and need the effective mechanisms to manage the code, such package, stack to play a role. ROS functional modules are organized in packages. There are nodes in the package, depending on the library, configuration files, etc. and the package provides a convenient portability and reusable software structure.

4.3 Automatic navigation

Robot autonomous navigation is mainly composed of two steps, the real-time positioning and map construction. The use of environmental information after the processing of the data to create and locate the map, it will create a good map to calculate the probability of the map, and get the global and local weight map. Global path planning to accept the weight of the map generated by the global weight map planning from the starting point to the target point of the path as a local path planning reference. Local path planning uses local weight map which is generated by weight map to plan robot's movement information. Then use the package to convert the data obtained by the sensor into real-time environmental information.

Map-based navigation: the built map information and real-time environmental information obtained by the sensor are transmitted to the server, and then refer to the global path to the robot real path for local planning to achieve the purpose of autonomous navigation.

5 Implementation of pedestrian tracking detection algorithm

Artificial intelligence algorithm, is the robot's soul, can make the robot behave more like people. The realization of the intelligent algorithm can give the machine owner some of the ability to replace the human to complete certain tasks. The pedestrian tracking algorithm used in this paper is to use robots to obtain images, first pedestrian detection. If there are pedestrians with a rectangular box circle, and for each pedestrian to create a tracker to track.

5.1 Pedestrian detection algorithm

In recent years, the R-CNN method for target detection and segmentation has been initiated by R Girshick et al., 2014, for the first time using the selective search (Uijlings et al., 2013) and the convolution neural network to combine the target detection. Subsequently, Kaiming He et al. can only read the fixed size of the problem, put forward the SPP-NET (He et al., 2014) method to further improve the detection results. After that, fast R-CNN (Girshick, 2015) and faster R-CNN (Ren et

al., 2015) have also been proposed to achieve end-to-end detection.

In this paper, a pedestrian detection method combining channel characteristics with faster-RCNN was used. Firstly, the VGG16 network pre-trained on ImageNet was used as the main network to extract the original image. After convolution, the original image generated a feature map (Conv4_3) with 256 channels.

Secondly, the channel feature of the image is extracted. The channel feature is preprocessed for the input image. A series of linear and non-linear transformations of the original image are carried out in the pretreatment stage. Each image is transformed into a channel by different transformations. In pedestrian detection, the LUV channel, the gradient intensity channel, and the gradient histogram channel are all very efficient channels.

Then, the channel feature is input into a two-layer convolution neural network. The convolution kernel size is 3, the step size is 1, the maximum pooling layer is 2, the step size is 2, and the output is a 128 channel of the activation map, the size of the input channel characteristics of 1/8.

And then all the obtained channel feature maps are in series, input to the RPN model, RPN model relative to the original version of some improvements, each anchors used a fixed aspect ratio of 0.41, and then from 40 pixels to 1.3 times the steps to generate 9 different sizes of anchors. The RPN model outputed the candidate target area.

The generated candidate target area is put into the Fast R-CNN model. The Fast R-CNN model has two full connection layers, a softmax classifier and a Bbox regressor. The softmax classifier output pedestrian detection results and the Bbox regressor output location information of pedestrian.

5.2 Pedestrian tracking algorithm

In recent years, the target tracking algorithm mostly uses the adaptive representation model based on the generated or discriminant formula. The discriminant method has better tracking performance than the generating method, and the method of using the incremental learning to distinguish the target and the background is less costly and tracking better. In this paper, we chose the online boosting algorithm and pedestrian detection process to extract the depth of channel features to achieve pedestrian tracking.

The tracking method uses a detection-based tracking strategy, that is, uses a sliding window to obtain a candidate region, and calculates the visual feature only once in the search area, and then extracts the features in each sliding window. And, this method uses a coarse to fine search strategy, you can quickly achieve tracking. First, at the beginning of the trace, the initial position is obtained by means of a detector or manually annotated, and then a number of positive and negative samples are collected and the boosting classifier is trained. In each frame of the subsequent sequence, the tracking area is a candidate region with the highest classification scoring. Some positive and negative samples are then collected after the end of the tracking and the classifier has been updated until the end of the tracking.

The tracking method uses the depth channel feature, and the depth channel feature is a feature of the channel feature combined with the faster RCNN method. The network structure and training mode are the same as in the previous section, but need to combine the network output before the full connection layer of the faster-RCNN network with the underlying channel characteristics as the depth channel feature. And then put it into the boosting classifier for training.

6 Conclusion

In this paper, for agricultural production process, many scenes need to monitor the situation, design an agricultural intelligent inspection robot. The hardware platform is mainly composed of three parts: hardware platform, software system and intelligent algorithm. The hardware platform is mainly composed of sensors, actuators, mechanical structures and electronic systems. It is the foundation of robot design. The software system is mainly composed of ROS system. The intelligent algorithm is mainly the pedestrian tracking detection algorithm, use the robot to obtain the image, make the first pedestrian detection, and then the pedestrian has been detected to the tracker for pedestrian tracking.

Finally, the monitored pedestrian information is transmitted back to the master computer through WiFi. Agricultural intelligent inspection robot has high practical value.

[References]

[1] Ali, N. H., and G. M. Hassan. 2014. Kalman filter tracking. *International Journal of Computer Applications*, 89(9): 15–18.

[2] Bo, W., and R. Nevatia. 2005. Detection of multiple, partially occluded humans in a single image by Bayesian combination of edgelet part detectors. *Proceedings of the IEEE International Conference on Computer Vision*, Beijing.

[3] Chang, C., and R. Ansari. 2005. Kernel particle filter for visual tracking. *IEEE Signal Processing Letters*, 12(3): 242–245.

[4] Chen, F. S., C. M. Fu, and C. L. Huang. 2003. Hand gesture recognition using a real-time tracking method and hidden Markov models. *Image and Vision Computing*, 21(8): 745–758.

[5] Comaniciu, D., V. Ramesh, and P. Meer. 2000. Real-time tracking of non-rigid objects using mean shift. *In Proceedings of the 2000 IEEE Conference on Computer Vision and Pattern Recognition*. Hilton Head, SC, USA: IEEE, 142–149.

[6] Dalal, N., and B. Triggs. 2005. Histogams of oriented gradients for human detection. *Proceedings of the IEEE Computer Society Conference on Computer Vision and Pattern Recognition*, San Diego, CA, USA, IEEE.

[7] Girshick, R. 2015. Fast r-cnn. *Proceedings of the IEEE International Conference on Computer Vision*, 1440–1448.

[8] Girshick, R., J. Donahue, T. Darrell, and J. Malik. 2014. Rich feature hierarchies for accurate object detection and semantic segmentation. June 24-27, 2014: *Proceedings of the IEEE Conference on Computer Vision and Pattern Recognition*, 580–587. Ohio, USA.

[9] He, K., X. Zhang, S. Ren, and J. Sun. 2014. Spatial pyramid pooling in deep convolutional networks for visual recognition. *IEEE Transactions on Pattern Analysis and Machine Intelligence*, 37(9): 1904–1916.

[10] Jain, R., and H. Nagel. 1979. On the analysis of accumulative difference pictures from image sequences of real world scenes. *IEEE Trans. Pattern Analysis and Machine Intelligence*, 1(2): 20–214.

[11] Lipton, A., H. Fujiyoshi, and R. Patil. 1998. Moving target classification and tracking from real-time video. *Proc. Fourth IEEE Workshop Applications of Computer*, Princeton, NJ, pp.8–14.

[12] Meier, T., and K. Nagank. 1998. Automatic segmentation of moving objects for video object plane generation. *IEEE Trans. Circuits and Systems for Video Technology*, 8(6): 525–538.

[13] Ojala, T., M. Pietikainen, and D. Harwood. 1996. A comparative study of texture measures with classification based on featured distributions. *Pattern Recognition*, 29(1): 51–59.

[14] Papageorgiou, C., M. Oren, and T. Poggio. 1998. A general framework for object detection. *Proceedings of the International Conference on Computer Vision*, Bombay, India, IEEE.

[15] Ren, S., K. He, R. Girshick, and J. Sun. 2015. Faster r-cnn: Towards real-time object detection with region proposal networks. *IEEE Transactions on Pattern Analysis and Machine Intelligence*, 39(6): 1137–1149.

[16] Seber, G. A. F., and A. J. Lee. 2003. Linear regression analysis (Second Edition). New York: *John Wiley & Sons*.

[17] Uijlings, J. R. R., K. E. A.V. D. Sande, T. Gevers, and A.W.M. Smeulders. 2013. Selective search for object recognition. *International Journal of Computer Vision*, 104(2): 154–171.

[18] Wang, Q., F. Chen, W. Xu, and M. H. Yang. 2011. An experimental comparison of online object-tracking algorithms. SPIE Optical Engineering+ Applications. *International Society for Optics and Photonics*, 8138(3): 815–822.

Design of an automatic pipettor for ISE based on soil nutrient detection

Zheng Jie[1], Zhang Miao[1,2*], Wang Maohua[1], Pan Linpei[1], Li Yanhua[1], Yang Qingliang[1], Chen Ming[1]

(1. *Key Laboratory on Modern Precision Agriculture System Integration Research, Ministry of Education, China Agricultural University, Beijing 100083, China;*
2. *Key Laboratory of Agricultural Information Acquisition Technology, Ministry of Agriculture, China Agricultural University, Beijing 100083, China*)

Abstract: An automatic parallel pipettor was developed to achieve the programmable solution transportation for ion-selective electrode based on soil nutrient detection. A self-designed iterative model, involving variables of sample volume and residual volume, was designed to replace the cleaning operation. 140 soil samples were used for the system evaluation. Five soil nutrients contents, including nitrate-nitrogen, available potassium, calcium, chloride and pH, were simultaneously measured with the automatic pipettor in parallel. The iterative compensation effectively improved the detection accuracy. The average liquid transfer error was less than 0.1 mL. The total testing time was reduced 70% than the manual operation. The research could provide a balanced approach for the enhancement of automation, accuracy and efficiency for soil nutrient detection conducted by ISE.

Keywords: automatic pipettor, soil nutrient detection, ion-selective electrode, cross-contamination

Citation: Zheng, J., M. Zhang, M. H. Wang, L. P. Pan, Y. H. Li, Q. L. Yang, and M. Chen. 2017. Design of an automatic pipettor for ISE based on soil nutrient detection. International Agricultural Engineering Journal, 26(3): 327–332.

1 Introduction

Soil nutrient detection is the basis of site-specific fertilization. Traditional soil test was consisted of 3 steps, including field sampling, soil pretreatment and soil detection (Bai et al., 2006).

Ion-selective electrode (ISE) possessed advantages on cost, detection range and robustness (Heinen et al., 1991). Plenty studies were conducted by ISE for nutrient detection of soil and hydroponic solutions (Wang and Scott, 2010; Tully and Weil, 2014; Jung et al., 2015; Vardar et al., 2015). Kim et al. (2007) developed an ISE nutrient detection platform. The correlation coefficient of nitrate-nitrogen was found to be 0.98 between ISE and FIA automated analyzer in 37 sets of soil detection. Kim et al. (2013) further modified the previous platform to fit the requirement of hydroponic nutrient detection of nitrate-nitrogen (NO_3^--N) and available (K^+). The ISE measurements were strongly related to those determined using standard laboratory instruments with the correlation coefficient of no less than 0.85. But, on-line soil nutrient detection was still a challenge issue, which expected breakthroughs on sensor design, system automation and integration (Yildirim et al., 2006; Ji et al., 2015).

Manual pipettor was commonly used in soil extractant injection and extracts transfer before the detection operation. Commercial high throughput pipettor was recently manufactured to achieve parallel solution delivery in biological and life science studies (American RAININ Liquidator 96). Considering about improvements on detection efficiency, programmable liquid transportation could be employed for soil sample preparation. However, most of the automatic fluidic

Received date: 2017-06-27 **Accepted date:** 2017-08-16

* **Corresponding author: Zhang Miao,** Associate Prof., Ph.D., Key Laboratory on Modern Precision Agriculture System Integration Research of Ministry of Education, China Agricultural University, 100083 China. Email: zhangmiao@cau.edu.cn.

control faced the problem of cross-contamination, which was usually caused by sample residue. Additional rinsing procedure should be considered. Detection time was unavoidable extended (Eacute et al., 2006; Petrek et al., 2008; Su et al., 2014).

In order to verify the feasibility of free-cleaning operation for soil test, a cross-contamination compensation model and a multi-channel automatic pipettor were designed. The testing accuracy and efficiency were analyzed with laboratory experiments.

2 Material and method

2.1 Theoretical basis

The linear relationship between the potential produced by ISE and the logarithm molar content of target ion could be described by the Nernst equation. The concentration of the target ion was calculated by Equations (1) and (2).

$$c_i = 10^{\frac{E_i - E_0}{S}} \quad (1)$$

$$c_{iw} = 1000 N A_r \times c_i \quad (2)$$

where, E_i was the potential of ISE, mV; E_0 was related to the ion-selective membrane and detection environment, mV; c_i was molar concentration of the target, mol L^{-1}; S was response slope, mV $decade^{-1}$. The ideal S for monovalent/bivalent ions were 59.16/28.58 mV $decade^{-1}$ at 25°C. Decade was defined as 10 times variation of molar concentration; c_{iw} was the mass concentration of the component, mg kg^{-1}; N is the ratio of soil and extractant solution. The ratio was selected according the national recommendation with 10 g soil: 25 mL extractant (Zhang et al., 2013); A_r was relative atomic mass. The values were 14.0 and 39.0 for NO_3^- and K^+, respectively; i was the sample number. S and E_0 were usually derived from standard calibration experiments prior the sample detection with artificial solution.

2.2 Cross-contamination compensation

The cross-contamination was defined as the prediction deviation caused by the solution residue. It could be inferred that the current tested sample was formed with 2 parts. One was a unit volume of the real soil sample extract. The other was an uncertain amount of the previous sample residue. Based on the performance test (Kong et al., 2015; Ren et al., 2016), a simplified compensation model was assumed as iterative Equation (3). Equation (4) was its equational transformation.

$$C_{i,T} \times (V + \Delta V) = C_{i,C} \times V + C_{i-1,T} \times \Delta V \quad (3)$$

$$C_{i,C} = C_{i,T} \times \frac{(V + \Delta V)}{V} - C_{i-1,T} \times \frac{\Delta V}{V} \quad (4)$$

where, $C_{i,T}$ was the content calculated according to the ISE tested potential by Equation (1); $C_{i,C}$ was the content derived after compensation; V was the sample volume; ΔV was the volume of the sample residue; the lower case mark of i was the sample number; $(i-1)$ represented for the number of the previous sample.

In this study, the compensation concentration of $C_{i,C}$ was regarded as the expected result produced by ISE. V was chosen of 12.5 mL, which was almost the maximum volume of soil extracts after filtration process; ΔV was determined as 0.8 mL by experiments introduced in 3.1.

2.3 Apparatus and reagent

The NO_3^- ISE (No. 9707BNWP, Thermo, USA), K^+ ISE (No. 9719BNWP, Thermo, USA), Ca^{2+} ISE (No. 9720BNWP, Thermo, USA), Cl^- ISE (No. 9617BNWP, Thermo, USA), and pH ISE (SC200, pHoenix, USA) were employed to predict the soil nutrient status, respectively. The K^+ and Ca^{2+} were extracted by Kelowna (0.25M CH_3COOH + 0.015M NH_4F) (Kim et al., 2007). Other elements were extracted by DDW (distilled de-ionized water), respectively (Adamchuk et al., 2003 and 2005; Sethuramasamyraja et al., 2008). All chemicals purchased from Beijing Lanyi Chemical Products Company were of analytical grade.

The ultraviolet spectrophotometer (UV-2450, Shimadzu, Japan) and Flame photometer (M410, Sherwood, US) were employed as standard analytical methods to measure soil NO_3^--N, K^+ and Ca^{2+} concentrations, respectively.

2.4 Automatic pipettor

The automatic pipettor system was mainly composed of the horizontal/vertical manipulator, 4 peristaltic pumps, 2 stepper motors and 6 proximity sensors, as is shown in Figure 1. The mechanical structure received the programmable commands from a pipettor controller. The horizontal displacement range was 0-50 cm. The vertical displacement range was 0-12 cm. The displacement speed

was 2 cm/s. The flow rate of the peristaltic pump was 50 mL/min. The proximity sensors, located on the horizontal/vertical manipulator, acted as the limit switch of maximum displacement. The prototype system was demonstrated in Figure 2.

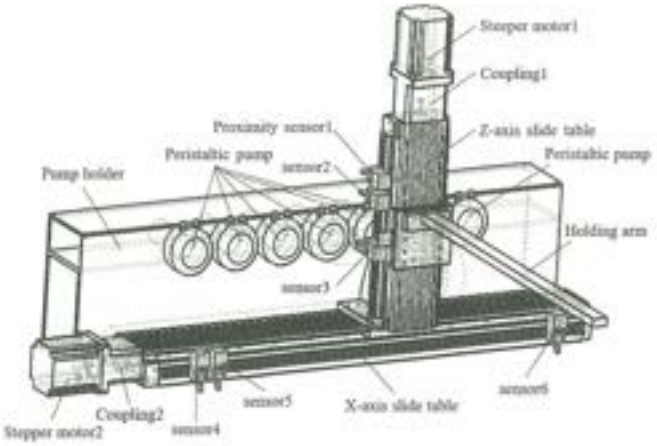

Figure 1 Mechanical structure of the multi-channel automatic pipettor

Figure 2 Prototype of the automatic pipettor

2.5 Soil information

140 soil samples were collected from 20 fields of summer maize, which were located at the northwest suburbs of Beijing. Samples covered 7 growth stages, including non-fertilization, fertilization, V3, V7, VT, maturation and harvest period. The reference information of the 140 soil samples were provided by the soil testing and formula fertilization center, as listed in Table 1.

Table 1 Basic information of 140 soil samples

Samples	Total-nitrogen, g/kg	Ammonium-nitrogen, mg/kg	Organic matter, g/kg	Moisture, %
1-140	0.59-2.33	4.33-120.57	2.41-21.20	12.75-23.46

Soil nutrients test was conducted in laboratory. Samples were processed under recommended pretreatment operation (Bai et al., 2007). After that, each sample was divided into two parts. The first part was detected by recommended spectrometric method. The test results were regarded as the standard reference value. The other one was detected by ISE with the sample pretreated with the self-designed automatic soil pipettor. The oscillator and the centrifuge was applied for sample shaking and filtration.

3 Results and discussion

3.1 Performance of the automatic pipettor

In order to test the precision and stability of the pipettor, solution transportation experiments were carried out. Seven channels of the pipettor were tested simultaneously. In the injection test, the pipettor was controlled to transfer the pre-designated volume of DDW from the sample container to a cylinder. The injection volume could be easily recognized in the cylinder. In the second test, certain amount of DDW was filled into the testing chamber of the detection platform prior to the test. Pumps were programmed on the opposite direction. DDW was delivered from the chamber to the cylinder. The pump out volume left in the cylinder could be easily obtained. The residue was calculated by the injection and the pumped out. Pre-designated volumes of 5, 10 and 12.5 mL were evaluated. Each test was conducted 3 times. Results were summarized in Table 2.

Table 2 Performances of solution transportation by the automatic pipettor

Vol, mL	Test		Test volume, mL							Mean, mL	SD, mL
	Operation		ch 1	ch 2	ch 3	ch 4	ch 5	ch 6	ch 7		
5.0	Injection	1	4.9	4.9	5	5.1	5	5	4.9	4.97	0.07
	Pump out	2	4.1	4.2	4.2	4.2	4.2	4.3	4.2	4.20	0.05
	Residue		0.8	0.7	0.8	0.9	0.8	0.7	0.7	0.77	0.07
10.0	Injection	1	10.1	10	10	9.9	10	9.9	10.1	10	0.08
	Pump out	2	9.4	9.3	9.2	9.2	9.2	9.1	9.2	9.23	0.09
	Residue		0.7	0.7	0.8	0.7	0.8	0.8	0.9	0.77	0.07
12.5	Injection	1	12.4	12.5	12.5	12.5	12.5	12.4	12.5	12.47	0.05
	Pump out	2	11.7	11.7	11.7	11.7	11.7	11.6	11.7	11.69	0.03
	Residue		0.7	0.8	0.8	0.8	0.8	0.8	0.8	0.79	0.03

As concluded from Table 2, the standard deviation of the liquid transportation was less than 0.1 mL. The accuracy was satisfactory for the extractant injection for soil pretreatment. The required ratio of soil to extractant could be accomplished by the pipettor.

Obvious errors were occurred in the pump out operation. An average amount of 0.77-0.79 mL DDW was left in the testing chamber, which would place ineligible influences on the detection precision. Therefore, the ΔV value of the iterative compensation model was determined as 0.8 mL according to the residue volume.

According to Equation (4), a larger volume of sample would reduce the cross-contamination interference. For the purpose of minimizing the residue error, the sample volume was chosen as 12.5 mL, which was also the guaranteed ultimate capacity of soil extract.

3.2 Evaluation of the compensation model

Evaluation experiment was conducted after obtaining the basic parameters of ΔV and V in Equations (3) and (4). Four sets of artificial potassium nitrate with known concentrations of 2.5, 5, 25, 100 and 250 mg/kg were employed as the testing solution. Solution of each concentration was pumped into 7 chambers through the automatic pipettor simultaneously. Four sample sets were detected continuously from the dilute to the dense in sequence. No rinse process was made during the experiment.

Results of NO_3^- ISE were recorded, as shown in Figure 3. The X-axis represented for the standard content of the solution. The Y-axis represented for the predicted concentration by ISE. The direct measurement was recorded in black. The iterative compensation model, discussed in 2.2, was applied to the average value of direct detection. The compensation result was illustrated in red.

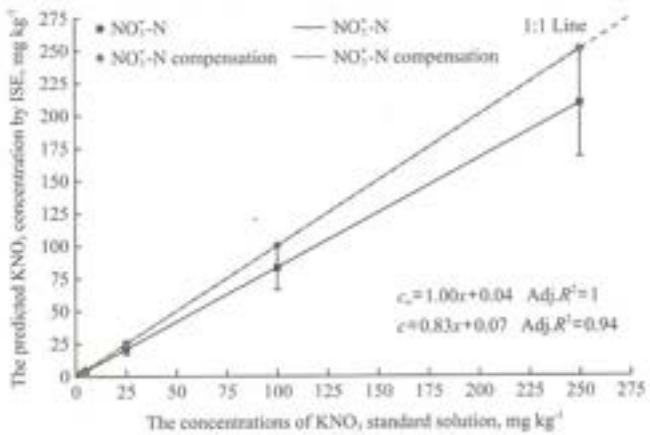

Figure 3 Comparison between the direct measurement and the compensation of standard nitrate solution

As seen from Figure 3, the direct measurement demonstrated obvious deviation with the absolution error of 0.91 - 41.04 mg/kg. The relative error was 0.97% - 18.26%. The compensation data were almost equal to the standard value. The absolute error was obtained of 0.02 - 1.33 mg/kg. The relative error was found to be 0.32% - 1.66%. In case of continuous measurement without effective cleaning, the cross-contamination compensation model could effectively improve the prediction accuracy of nitrate detection.

3.3 Soil test

Soil samples were collected from 20 sites during the 7 growth stages of corn, including non-fertilization, fertilization, V3, V7, VT, maturation and harvest period. The nutrient contents, including nitrate nitrogen, available potassium, calcium, chloride and pH of 140 soil samples were measured. Each sample was separated into 2 parts. The first part was treated with the traditional operation of manually sample preparation and optics detection. The second part was detected with the prototype system illustrated in Figure 2. Operation of the soil solution delivery was carried out by the 7-channel automatic pipettor. The performance comparison between the manual operation and the automatic pipettor was tabulated in Table 3.

Table 3 Efficiency comparison between manual detections and the automatic pipettor

Items	Manual operation	Automatic pipettor
Sample amount	140	
Test elements	nitrate nitrogen, available potassium, calcium, chloride and pH	
Pretreatment, h	8.6	1.4
Detection, h	20	7
Detection Items	Discrete device 1 element/time	Integrated device Maximum 7 elements/time
Total time, h	30.6	8.4
Labor intensity	Intensive	Low

As illustrated in Table 3, conventional manual operation was time-consuming and labor intensive. The automatic system could achieve the programmable batch process of extractant injection, extract transfer and sample detection. It demonstrated apparent superiority on efficiency. Compared with the manual method, the pretreatment rate was reduced from 6 h/100 sample to 1 h/100 sample. The detection rate was speeded up from 8-9 min/ (sample of five elements) to 1 min/ (sample of maximum 7 elements). The total time of soil nutrient testing could reduce more than 70% under low labor intensity.

Soil test results were shown in Figure 4. The X-axis represented the sample number. Each field site was collected seven times. For example, samples of No.1, 21,

41, 61, 81, 101 and 121 were taken from the same place. The Y-axis represented the nutrients status of 5 target ions. As seen from Figure 4, the maize field was in alkalescency condition with soil pH higher than 7.0. Soil macronutrients of nitrate nitrogen, available potassium and calcium varied from 1.24-181.15, 27.23-183.14 and 5.11-886.26 (majority below 300) mg/kg, respectively. Contents of these 3 macronutrients were at a low level in the first stage of the non-fertilization period, as seen in sample 1-20. In periods of fertilization and V3, macronutrients started increasing, as illustrated in samples 21-40 and 41-60. The contents of macronutrients kept decreasing during the rest four growth periods, which would be caused by the nutrient absorption of the maize plant. The pH exhibited greatly fluctuation.

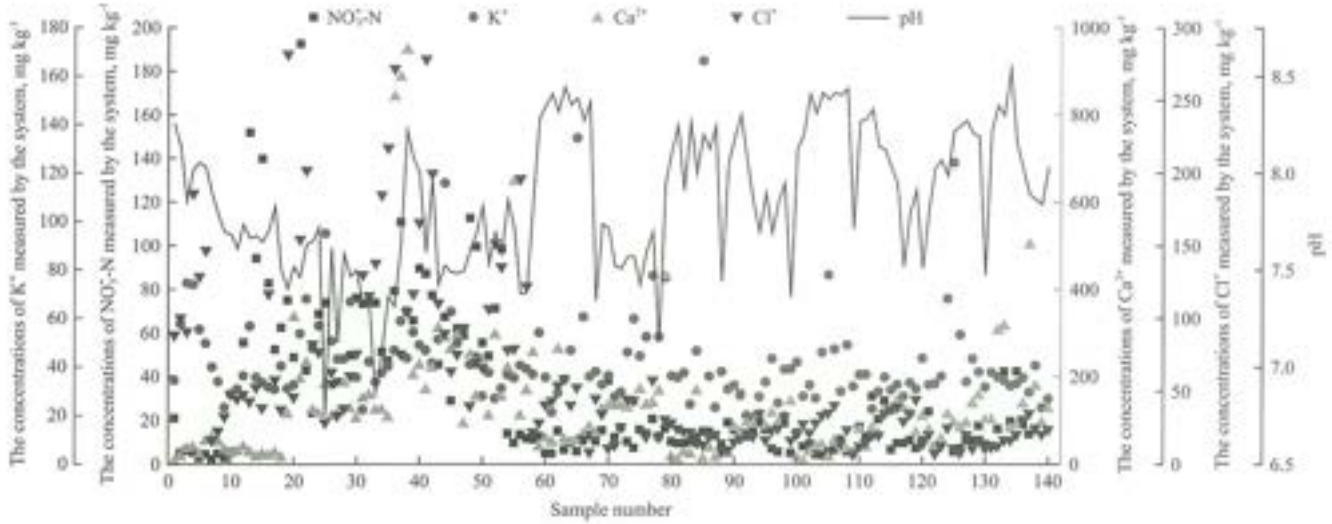

Figure 4 Nutrients variations of summer maize conducted by the automatic pipettor

4 Conclusion

In this study, a cross-contamination compensation model was designed for a self-developed automatic pipettor. Experiments were conducted to verify the feasibility of the system. Following conclusions could be made:

(1) The automatic pipettor could realize precisely liquid sample delivery with the accuracy of 0.1 mL, which could fit the operation standard of soil extractant injection.

(2) The cross-contamination compensation model could reduce the interference of samples residue. The absolute error of predicted nitrate-nitrogen was less than 1.33 mg/kg in standard solution detections carried out by ISE. The automatic pipettor would perform continuous detection without gap time of cleaning.

(3) The self-design automatic pipettor could greatly improve the detection efficiency and labor intensity. The batch measurement process reduced the test duration to less than 1/3 of the manual method.

Acknowledgements

This research was supported by the National Key Research and Development Program (Grant No. 2016YFD0700304 and 2016YFD0800907), Open Fund Project of Key Laboratory of Technology Integration and Application in Agricultural Internet of Things, Ministry of Agriculture (No. 2016KL03), and Yunnan Academician Expert Workstation (Wang Maohua, Grant No. 2015IC16).

[References]

[1] Adamchuk, V. I., E. D. Lund, A. Dobermann, M.T. Morgan, and J. Stafford. 2003. On-the-go mapping of soil properties using ion-selective electrodes. In Stafford JV, Werner A (eds) Precision agriculture. Wageningen Academic, Wageningen, pp 27–33.

[2] Adamchuk, V. I., E. D. Lund, B. Sethuramasamyraja, M. T. Morgan, A. Dobermann, and D. B. Marx. 2005. Direct measurement of soil chemical properties on-the-go using ion-selective electrodes. *Computers and Electronics in Agriculture*, 48 (3): 272–294.

[3] Bai, Y. L., and L. P. Yang. 2006. Soil testing and fertilizer recommendation in Chinese agriculture. *Soil and Fertilizers*

Sciences in China, (2006)2: 3–7.

[4] Eacute, J., R. Ocire, M. D. Eacute, and V. Eacute. 2006. High-throughput pipetting with the programmable pipetman concept®. *Nature Methods*, 2006(3).

[5] Heinen, M, and K. Harmanny. 1992. Evaluation of the performance of ion-selective electrodes in an automated NFT system. *Acta Horticulturae*.

[6] Ji, W., V. I. Adamchuk, A. Biswas, A. M. Su, and Z. Shi. 2015. Simultaneous measurement of multiple soil properties through proximal sensors fusion. *May 12-15, 2015: Global Workshop of Proximal Soil Sensing*. Hangzhou, China.

[7] Jung, D. H., H. J. Kim, G. L. Choi, T. I. Ahn, J. E. Son, and K. A. Sudduth. 2015. Automated lettuce nutrient solution management using an array of ion-selective electrodes. *Transactions of the ASABE*, 58(5): 1309–1319.

[8] Kim, H. J., J. W. Hummel, K. A. Sudduth, and P. P. Motavalli. 2007. Simultaneous analysis of soil macronutrients using ion-selective electrodes. *Soil Science Society of America Journal*, 71(6): 1867–1877.

[9] Kim, H. J., W. K. Kim, M. Y. Roh, C. I. Kang, J. M. Park, and K. A. Sudduth. 2013. Automated sensing of hydroponic macronutrients using a computer-controlled system with an array of ion-selective electrodes. *Computers and Electronics in Agriculture*, 93(2013): 46–54.

[10] Kim, H. J., K. A. Sudduth, J. W. Hummel, and S. T. Drummond. 2013. Validation testing of a soil macronutrient sensing system. *Transactions of the ASABE*, 56(1): 23–31.

[11] Kong, P., M. Zhang, H. Y. Ren, Y. H. Li, and P. Pan. 2015. Rapid pretreatment method for soil nitrate nitrogen detection based on ion-selective electrode. *Transactions of The Chinese Society for Agricultural Machinery*, S1: 102–107. (in Chinese with English abstract)

[12] Petrek, J., and M. Anderson. 2008. Liquidator 96 ready-to-use manual benchtop system. *Nature Methods*, 5(6).

[13] Ren, H. Y. 2016. Research on improvement of multi-channel nutrients detection system based on the ion-selective electrodes. M.S. thesis. China Agricultural University, Beijing.

[14] Sethuramasamyraja, B., V. I. Adamchuk, A. Dobermann, D. B. Marx, D. D. Jones, and G. E. Meyer. 2008. Agitated soil measurement method for integrated on-the-go mapping of soil pH, potassium and nitrate contents. *Computers & Electronics in Agriculture*, 60(2): 212–225.

[15] Su, E. C., J. Kim, Y. O. Dong, Y. Song, S. H. Lee, S. Min, and S. Kwon. 2014. One-step pipetting and assembly of encoded chemical-laden microparticles for high-throughput multiplexed bioassays. *Nature Communications*, 5(3): 3468.

[16] Vardar, G., M. Altıkatoglu, D. Ortac, M. Cemek, and I. Isldak. 2015. Measuring calcium, potassium, and nitrate in plant nutrient solutions using ion-selective electrodes in hydroponic greenhouse of some vegetables. *Biotechnology and Applied Biochemistry*, 62(5): 663–668.

[17] Yildirim, S., S. J. Birrell, and J. W. Hummel. 2006. Laboratory evaluation of an electro-pneumatic sampling method for real-time soil sensing. *Transactions of the ASABE*, 49(4): 845–850.

[18] Zhang, L.N., M. Zhang, M. Sheng, L. Li, and Y. Zhang. 2013. Optimization of pretreatment parameters for ISE-based soil NO3--N detection. *International Agricultural Engineering Journal*, 22(1): 61–69.

Diseases warning system for spinach based on genetic-BP network algorithm

Zhang Lingxian[1,2], Gu Dongyue[1], Liu Chundi[1], Zou Chunyu[1], Li Xinxing[1,2*]

(1. *China Agricultural University, Beijing 100083, China*;
2. *Key Laboratory of Agricultural Informationization Standardization, Ministry of Agriculture, Beijing 100083, China*)

Abstract: A diseases warning model of forecasting spinach common diseases was designed, which could provide a low-cost solution to inform users before plants getting disease. Through systematic learning on a lot of spinach diseases knowledge, the environmental parameters of lowest temperature, highest temperature, average temperature, lowest humidity, highest humidity and average humidity are defined as input parameters. Besides, downy mildew index, leaf spot index, black spot index, blight index and anthracnose index are defined as output parameters of BP network. The BP network's number of hidden layer nodes was determined by genetic algorithm. The improved model has better accuracy and faster convergence speed. A complete system has been developed, consisting of user subsystem, data management subsystem, query subsystem and forecasting subsystem. After training, the system can provide index number of each common disease according to the input environmental parameters.

Keywords: genetic-BP network algorithm, spinach, diseases warning system

Citation: Zhang, L. X., D. Y. Gu, C. D. Liu, C. Y. Zou, and X. X. Li. 2017. Diseases warning system for spinach based on genetic-BP network algorithm. International Agricultural Engineering Journal, 26(3): 333–339.

1 Introduction

Spinaches have a vast market in China and spinaches are grown very widely. With the demand for spinaches consumption increasing, more and more farmers grow spinaches in greenhouses. Diseases of spinaches have become the main factors that obstacle the spinaches productions. Moreover, diseases control activity is an important research problem of agricultural experts.

Nowadays, the major method to control spinach diseases is pesticide spraying while excess pesticide may cause problems of damaging humans' health and ecological balance. Diseases control should base on preventive methods, so it is of great importance to accurately predict diseases, and fairly use pesticide to achieve diseases control effectively. ANN (Artificial Neural Network) is a kind of intelligent algorithm which is suite to describe nonlinear phenomena and resolve complex problems (Worner et al., 2012), so more and more scientists built models to predict crop disease by ANN (Francl et al., 2004).

De-Wolf (1997) classified infect period of wheat tan spot by neural networks in last 1990s (Liu et al., 2008). Morbidity, temperature, relative humidity, precipitation, and leaf wetness duration were defined as input variables. They compared the results of different methods of BP networks, generalized regression neural networks and logistic regression. Results indicated that BP networks could provide more accurate forecast. Liu (2012) used neural networks and principal components analysis to evaluate the severity of rice rhizoctonia. Yong (2016) constructed a dynamic predict model, based on BP neural networks to predict forest disease and insect and rat pest. Shivling (2011) developed an artificial neural network based on system for predicting the risk of powdery mildew in Picrorhiza kurrooa, by putting temperature and wetness duration so as to predict the level of risk at that particular value of the input. Shi (2008) presented a new prediction model by principal components analysis (PCA) and back propagation artificial neural network (BP-ANN)

Received date: 2017-06-27 **Accepted date:** 2017-08-17

* **Corresponding author: Li Xinxing,** Ph.D., Associate Professor, China Agricultural University, Beijing 100083, China. Email: lxxcau@cau.edu.cn.

methods to forecast wheat sharp eyespot. Lankinvega (2008) predicted the fall of barley yellow dwarf virus based on the theory of artificial neural network model, and compared with the results of the multiple regression analysis model. The error of artificial neural network is better than that of multivariate regression analysis. Based on the fusion of RBF neural network and WebGIS, Li (2005) established apple pest disease forecasting system, which can be used to predict diseases and pests, and spread the information network geographic with information system.

Aiming at forecasting different kinds of spinaches diseases, an improved method was chosen which based on the genetic and BP network algorithm and defined environmental parameters as input variables.

2 System design

2.1 Overall design

2.1.1 Work flow

Agricultural plants diseases knowledges were integrated first to determine the primary factors that cause spinaches diseases. Then BP network was chosen to establish a warning model which can be improved by genetic algorithm. The improved algorithm has faster convergence and better accuracy, and it is more suited to establish warning system. After data training, warning system can be used to forecast spinach diseases. The complete work flow is shown in Figure 1.

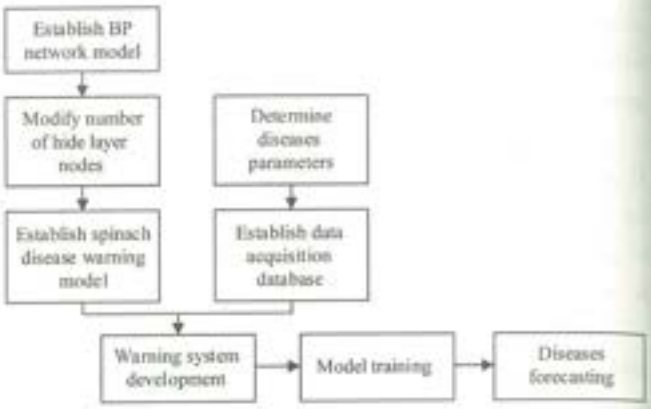

Figure 1 Work flow

2.1.2 System structure and functions

Warning system is composed of user subsystem, data management subsystem, query subsystem and forecasting subsystem. The structure shows in Figure 2.

2.2 Database design

The input and output data are stored in SQL Server 2008 database. And the main two tables were shown in Figure 3 and Figure 4. The data in table sample are used to train network. Table real Time Data is jointly maintained by data acquisition system and diseases warning system.

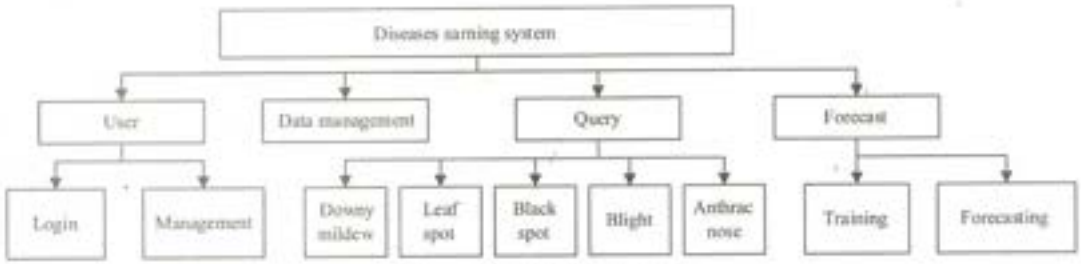

Figure 2 System structure

	field	data type	allow null
▶	sid	int	
	lowestTemperature	float	
	highestTemperature	float	
	averageTemperature	float	
	lowestHumidity	float	
	highestHumidity	float	
	averageHumidity	float	
	downyMildewIndex	float	
	leafSpotIndex	float	
	blackSpotIndex	float	
	blightIndex	float	
	anthracnoseIndex	float	

Figure 3 Example table

	field	data type	allow null
▶	rid	int	
	lowestTemperature	float	
	highestTemperature	float	
	averageTemperature	float	
	lowestHumidity	float	
	highestHumidity	float	
	averageHumidity	float	
	downyMildewIndex	float	☑
	leafSpotIndex	float	☑
	blackSpotIndex	float	☑
	blightIndex	float	☑
	anthracnoseIndex	float	☑
	forecastValidity	bit	☑
	inputTime	datetime	☑
	forcastTime	datetime	☑

Figure 4 Table real Time Data

2.3 Common diseases of spinach

2.3.1 Downy mildew

(1) Symptoms and signs

In the early stages of downy mildew (Yong, 2006), leaf appears small spots without obvious edge, and then they spread out into big amorphous spots. Then the surface of the leaves back appears gray and white layers of mold which become purple gray at last stage. Downy mildew often causes diseased leaves yellow and rot.

(2) Pathogenic regularity

This disease is caused by fungi. Moreover, plants are more likely infected in the environment in which temperature is 10°C and relative humidity is more than 90%. Besides, poor ventilation and excess irrigation both can aggravate state of disease (Yu et al., 2008).

2.3.2 Leaf spot

(1) Symptoms and signs

This disease damages leaves, and the lower leaves infect earlier. In the initial stage, infected parts lost their green color and the edge of these parts change to light brown. Then the spots whose shapes are nearly round spread out and become white and their edges are quite obvious. The diameters are 0.5-3.5 millimeters. Gray and brown mold can be found when air humidity is high.

(2) Pathogenic regularity

This disease is caused by fungi. Moreover, plants are more likely infected in the environment of high temperature and humidity. In addition, the seriously diseased spinaches often can be found in depression and wind scoop land.

2.3.3 Black spot

(1) Symptoms and signs

This disease mainly damaged leaves. Spots appear round or nearly round whose color is light brown to brow. Their diameters are in 2-6 millimeters range. Black molds attach on it.

(2) Pathogenic regularity

Black spot disease is mostly caused by fungi. Spinaches are more likely infected in the high precipitation year and high humidity environment.

2.3.4 Blight

(1) Symptoms and signs

If the spinach were infected blight, their leaves would lose their sheen. Then their mesophyll changes to yellow and root wither. Moreover, infected plans are obviously dwarfed and will appear chlorotic quickly in high temperature.

(2) Pathogenic regularity

The pathogen can attach on infected plant remains to survive summers and winters. And pathogens are disseminated by rain and irrigation water. Spinaches are more likely infected in warm and wet soil.

2.3.5 Anthracnose

(1) Symptoms and signs

Infected leaves appear light yellow spots that spread out into gray and amorphous spots. There are wheeled stripes and black small dots on them.

(2) Pathogenic regularity

Anthracnose disease is mostly caused by fungi. Mycelium can attach on infected plant remains or seeds to survive winters and be disseminated by rain and insects. Spinaches are more likely infected in rainy and high planting density environment.

2.4 Warning model based on genetic algorithm and BP neural network

2.4.1 BP neural network

BP network is a structure based on gradient descent optimization. It is with an algorithm of supervised learning (Yuan, 1999). The learning process of BP network contains the following two phases: In the first phase, the neurons transmit signals forwards. Neutrons in each layer influence only the structures of neurons in the next layer. When the expected output is different from the actual output, namely no expected value is reached, the system will enter the second phase and the neurons transmit signals backwards.

The BP algorithm transmits error signals backwards exactly along the original route and adjusts the weights and thresholds of each layer under the principle of gradient descent of error. Through adjusting the thresholds of neurons in each layer, the modified output will approach the expectations. After being adjusted, the thresholds will be transmitted forwards. Then the expected output will be compared with the actual output.

As described above, the process continues ad infinitum until the output and the expected values reach

an acceptable range or training times exceeds a preset value. The structure of BP neural algorithm is shown in Figure 5.

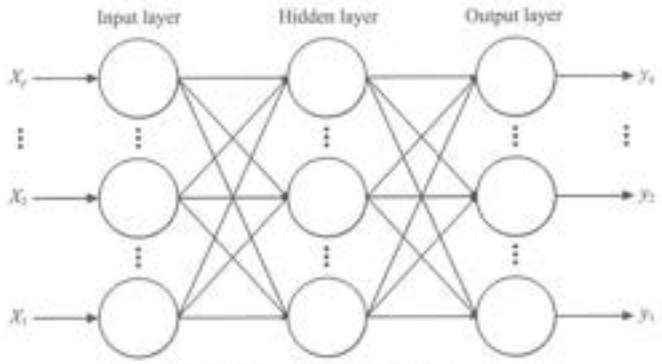

Figure 5 BP network structure

According to the research at this stage, a BP neural network, which contains two hidden layers, can approximate to any continuous function and each arbitrary order derivatives in arbitrary precision. Besides, a neural network, which also possesses multi-layer, can better approximate to the nonlinear function, yet with more computation and it has the possibility to be unstable. For BP neural network, if the settings of the number of hidden layer nodes are reasonable, single hidden layer can achieve the same effect. To reduce the complexity of model calculation, we use the BP neural network with 3 hidden layers here.

A calculate process of BP neural network is below. Let p neurons be in the input layer and h neurons be in the hidden layer nodes, and q neurons be in the output layer. Also let the input value of sample be $(x_1, x_2, \ldots, x_q)$, the output value of sample be $(S_1, S_2, \ldots, S_q)$, the output value of hidden layer nodes be $(O_1, O_2, \ldots, O_h)$, the output value of BP network $(y_1, y_2, \ldots, y_q)$, the weighting between input layer and hidden layer nodes be, the weighting between hidden layer and output layer nodes be w_{ij} (i=1, 2, …, p; j=1, 2, …, h), and the threshold of hidden layer and output layer neurons be v_{jk} (i=1, 2, …, h; j=1, 2, …, q), and we choose Sigmoid function as activation function, calculate the output value of hidden layer nodes:

$$H_j = \sum_{i=1}^{p} w_{ij} x_i + \theta_j, j = 1,2,\ldots,h \quad (1)$$

$$O_j = f(H_j) = \frac{1}{1+e^{-H_j}} \quad (2)$$

Similarly, use the output value of hidden layer nodes as the input value of output layers nodes, and figure out the output value of BP neural network according to the following Equations (3) and (4):

$$I_k = \sum_{j=1}^{h} f(H_j) v_{ij} + \phi_k, \; k = 1,2,\ldots,q \quad (3)$$

$$y_k = f(I_k) = \frac{1}{1+e^{-I_k}} \quad (4)$$

Calculate the actual output y_k according to the samples in sample set one by one, also the error metric E. Then figure out the error metric about the r sample of the network according to the following Equations (5) and (6), and the error metric about the whole sample set of the network:

$$E_p = \frac{1}{2} \sum_{k=1}^{q} (y_{rk} - S_{rk})^2 \quad (5)$$

$$E = \sum_{p=1}^{m} E_p \quad (6)$$

Use the error metric of the output layer to adjust the weight matrix of output layer, also to estimate the error of the hidden layer. Then use the error of the hidden layer to estimate the error of the input layer. All the layers' error estimates come out in this way too, and the estimation can be used to modify the weight matrix, and then form the process of letting the error showed in the output port transfer to the input port stepwise through the direction which is opposite to the direction input signal goes. According to δ earning and control way, adjust the weighting. Below are the weighting adjusting formulas. In the formulas, η is the learning factor, t is the training number, w_{ij} and v_{ij} represent the weightings which are modified after the end of this training, and δ is the error variety between input and output.

$$w_{ij}(t+1) = w_{ij}(t) + \eta \delta_{ri} O_j \quad (7)$$

$$v_{jk}(t+1) = v_{jk}(t) + \eta \delta_{rk} x_i \quad (8)$$

Verify the error between sample output and network output, if it is less than ε(ε<0.001), then BP neural network training process is over, otherwise continue to adjust the weighting or threshold, and then calculate the error again until it becomes less than ε (ε<0.001).

To enhance the training accuracy of the neural network, using the method of increase the neuron

numbers is much easier than the method of adding hidden layers. Thus, network design selected the best neuron numbers, on the premise of as less layers as possible. Theoretically, there is no definite rule for best hidden layer nodes. Yet if there are few hidden layer neurons, fault tolerance will be worse, therefore it cannot recognize the sample which is exclude from training sample sets. Too many neurons in hidden layer will not only cause the learning time stay too long, but also lower the learning ability in learning the new sample. The whole network performance becomes bad. Thus, it is very crucial to confirm the hidden layer nodes of BP network (Li et al, 2008).

2.4.2 Genetic algorithm and BP network

After the introduction of the genetic algorithm, genetic-BP neural network takes advantages of strong global search capability of genetic algorithms. Preliminary study the network nodes of hidden layer, weights and thresholds for global rough precision through genetic algorithms, then position the optimal solution area and determine the optimal number of hidden layer nodes, like weights and thresholds population gathered in the solution space of a few parameters, and then use the BP neural network algorithm to search the smaller fine gradient solution space, finally get the optimal solution.

Genetic algorithm is a probabilistic search algorithm based on the basic idea of simulating the evolution of binary groups and composing the real strings. Specific operation is from all strings by a number of groups consisting of an initial starting of the current population of individuals cyclically selection, crossover and mutation process until the optimal solution can be received. Genetic algorithm flowchart program runs as follows:

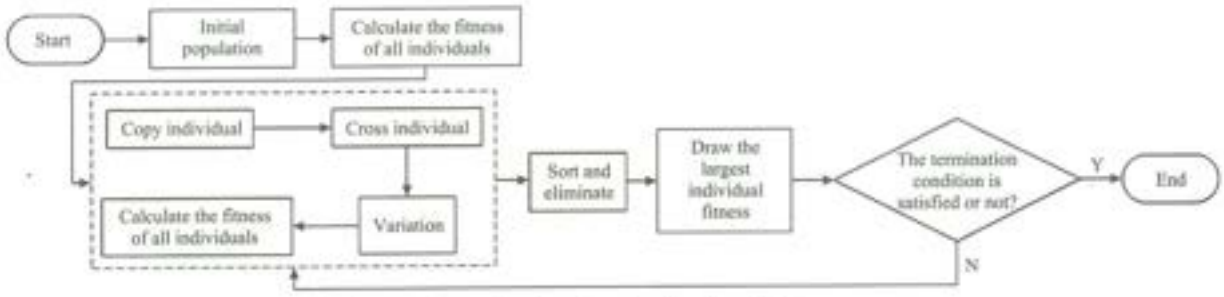

Figure 6 Genetic algorithm flowchart

Genetic algorithm can optimize BP neural network algorithm, including: encoding, decoding, determine the fitness function, genetic manipulating (natural selection, crossover, mutation, etc.). The specific description of this process is as below.

BP neural network weights and thresholds by using real-coded for hidden layer nodes with binary numbers, 0 represents the hidden layer node is invalid, and 1 represents effectiveness. According to the Kolmogorov theorem, the maximum empirical formula can be determined from the hidden layer nodes, where L is the maximum number of hidden layer nodes, n is the number of input layer nodes, o is the number of output layer nodes, and a is in the range of integers from 1 to 10.

To replicate the parent population first, thus creating the same part of the parent offspring. Then conduct crossover and mutation operations on the copied parent. Cross plays in the evolution is a very important role, which is an essential step to optimize the search, while the population is to avoid premature convergence, and mutation is also necessary. Crossover and mutation operations are carried out, the need for real-coded and binary coded should be considered separately.

For binary encodings, only during the operation to produce a cross-cross point immediately before the boundary to the cross-point exchanges chromosome segment. Similarly, generate a random mutation point mutation during the course of the operation. n this variation of a certain mutation rate variation points, change 0 to 1 or change 1 to 0 (Wang et al., 2008).

For real-coded, the cross-based method uses a convex set theory to do crossover operation according to the Equation (9):

$$\begin{cases} y_i^{(1)} = a \times x_i^{(1)} + (1-a) \times x_i^{(2)} \\ y_i^{(2)} = a \times x_i^{(2)} + (1-a) \times x_i^{(2)} \end{cases} \quad (9)$$

Where in $x_i^{(1)}, x_i^{(2)}, y_i^{(1)}, y_i^{(2)}$ respectively adjacent two adjacent i-parent and offspring chromosomes variable, a is the cross ratio of each chromosome, can take a random number in the range 0-1.

Variability is in Equation (10):

$$\begin{cases} y_i = y_i + \beta \times (a_i - y_i),\ 0.5 \le \beta \le P_m \\ y_i = y_i + \beta \times (b_i - y_i),\ \beta < 0.5,\ \beta \le P_m \end{cases} \tag{10}$$

y_i is variable i of variation in chromosomes; β is the random number in 0-1 range, it decides variation in direction; P_m is the mutation rate of the variable i; a_i, b_i respectively are the upper and lower weights and threshold value, the value of +1 and -1.

Fitness of the population through the computer all the chromosomes, chromosome number from the total number of people choose to 1/2 the evolution to the next generation, because the parent has copied before crossover and mutation, so eliminated after 1/2, the population does not vary of change.

After eliminating a new generation of populations by optimizing, returning to the second step, re-replication, crossover and mutation, select options. The cycle of generations knows the best fitness function difference is small or it reaches preset evolution algebra when the program ends. The type of fitness function is below:

$$F = a \times f_1 + b \times f_2 \tag{11}$$

And in which $0<a, b<1$ and $a + b=1$, we select $a = 0.8$, $b=0.2$, $f_1=1/(E+1)$, where E is the BP neural network error metric, $f_2=L/q$, L is hidden layer node maximum number, q is the current number of hidden layer nodes.

2.4.3 Diagnosis warning model based on genetic algorithm and BP network

In this paper, the lowest temperature, highest temperature, average temperature, lowest humidity, highest humidity and average humidity are defined as input parameters. Besides, downy mildew index, leaf spot index, black spot index, blight index and anthracnose index are defined as output parameters of BP network. However, the experimental data are different in different groups, so it is necessary to normalize the experimental data, which contribute to network training speed. Normalization formulas are as follows:

$$X = \begin{pmatrix} x_{11}, x_{12}, x_{13}, x_{14}, x_{15}, x_{16} \\ x_{21}, x_{22}, x_{23}, x_{24}, x_{25}, x_{26} \\ \vdots \\ x_{n1}, x_{n2}, x_{n3}, x_{n4}, x_{n5}, x_{n6} \end{pmatrix} \tag{12}$$

$$Y = \begin{pmatrix} y_{11}, y_{12}, y_{13}, y_{14}, y_{15} \\ y_{21}, y_{22}, y_{23}, y_{24}, y_{25} \\ \vdots \\ y_{n1}, y_{n2}, y_{n3}, y_{n4}, y_{n5} \end{pmatrix} \tag{13}$$

$$\begin{cases} x_{\min j} = \min(x_{1j}, x_{2j}, \cdots, x_{nj}), \\ x_{\max j} = \max(x_{1j}, x_{2j}, \cdots, x_{nj}),\ j = 1,2,\cdots,6; \\ y_{\min k} = \min(y_{1k}, x_{2k}, \cdots, y_{nk}), \\ y_{\max k} = \min(x_{1k}, x_{2k}, \cdots, y_{nk}),\ k = 1,2,\cdots,5; \\ x_{inj} = \dfrac{x_{ij} - x_{\min j}}{x_{\max j} - x_{\min j}} \\ y_{ouj} = \dfrac{y_{ik} - y_{\min k}}{y_{\max k} - y_{\min k}},\ i = 1,2,\cdots,n \end{cases} \tag{14}$$

The normalized data can be used to train network according to the aforementioned method. The trained genetic-BP network can finally warn spinach diseases and forecast the disease type.

3 System implementation

This system is developed with C# and Matlab combined programming techniques. Mixed programming techniques are implemented by calling matlab dynamic-link libraries in C#.

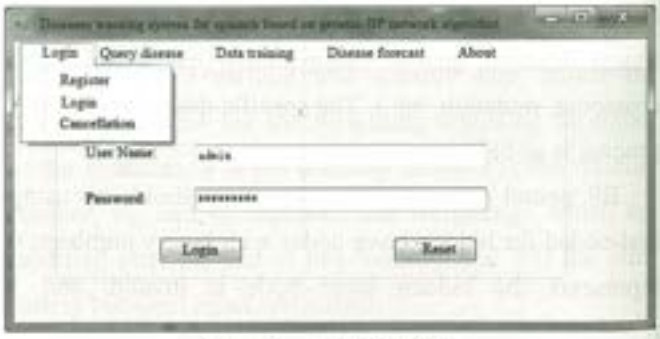

Figure 7 Login interface

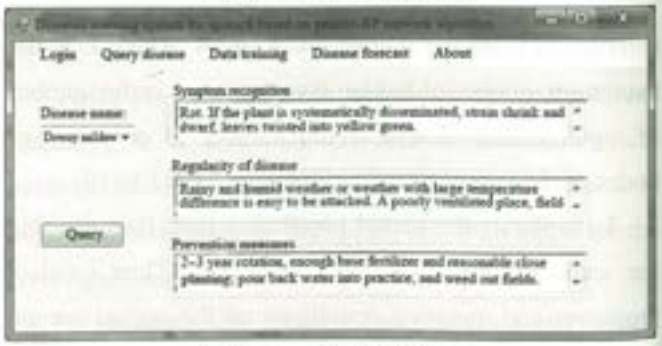

Figure 8 Query interface

Figure 9 Train interface

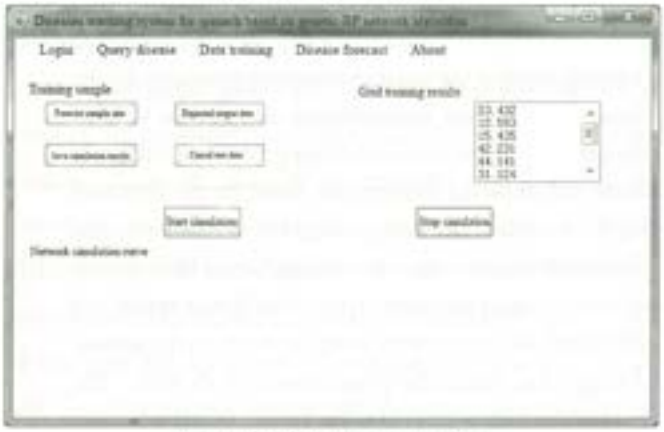

Figure 10 Simulation interface

4 Conclusion

This paper introduces a design of diseases forecasting model based on genetic-BP network algorithm. By way of sample data training, the model can forecast different kinds of diseases quickly and accurately. Basing on this model, the warning system provides a possible solution to ensure spinaches production in a low-costs way. Moreover, this method can be used in other agricultural plants diseases warning.

Acknowledgments

Authors would like to acknowledge the financial support from the earmarked fund for Beijing Innovation Consortium of Agriculture Research System (BAIC07-2017).

[References]

[1] Dalla, M. A., R. D. Magarey, and S. Orlandini. 2005. Modeling leaf wetness duration and downy mildew Simulation on grapevine in Italy. *Agricultural and Forest Meteorology*, 132(1-2): 84–95.

[2] Francl, L. J. 2004. Squeezing the turnip with artificial neural nets. *Phytopathology*, 94(9): 1007–12.

[3] De-Wolf, E. D., and L. J. Francl. 1997. Neural networks that distinguish infection periods of wheat tan spot in an outdoor environment. *Phytopathology*, 87(1): 83–87.

[4] Lankinvega, G., S. P. Worner, and T. Daj. 2008. An ensemble model for predicting Rhopalosiphumpadi abundance. *Entomologia Experimentalis Et Applicata*, 129(3): 308–315.

[5] Li, L., D. Li, Z. Zhou, Y. Zhang, and Z. Fu. 2008. Forecast of disease and pest in apple orchards based on fusion of radial basis function neural network and WebGIS. *Transactions of the Chinese Society for Agricultural Machinery*, 39(3): 116–117. (In Chinese with English abstract)

[6] Li, P. C., and S. Y. Li. 2008. Learning algorithm and application of quantum BP neural networks based on universal quantum gates. *Journal of Systems Engineering and Electronics*, 19(1): 167–174.

[7] Liu, Z. Y., J. F. Huang, and R. X. Tao. 2008. Estimating rice brown spot disease severity based on principal component analysis and radial basis function neural network. *Spectroscopic and Spectral Analysis*, 28(9): 2156–2160.

[8] Michael, J., W. Susan, and P. Worner. 2012. Using artificial neural networks to predict the distribution of bacterial crop diseases from biotic and abiotic factors. *Computational Ecology & Software*, 2(1).

[9] Shi, M. W. 2011. Application of BP neural network and PCA in prediction of plant diseases control. *Advanced Materials Research*, 219(220): 742–745.

[10] Shivling, V. D., C. Ghanshyam, R. Kumar, S. Kumar, and R. Sharma. 2016. Prediction model for predicting powdery mildew using ANN for medicinal plant - Picrorhiza kurrooa. *Journal of the Institution of Engineers*, 1–5.

[11] Wang, X., M. Zhang, J. Zhu, and S. Geng. 2008. Spectral prediction of Phytophthora infestans infection on tomatoes using artificial neural network (ANN). *International Journal of Remote Sensing*, 29(6): 1693–1706.

[12] Wang, Y., W. Gang, and S. Feng. 2012. The dynamic model prediction study of the forest disease, insect pest and rat based on BP neural networks. *Journal of Agricultural Science (1916-9752)*, 4(3).

[13] Yang, X. Q. 2006. The prevention and occurrence of spinach downy mildew. *Northern Horticulture*, 01: 82.

[14] Yu, S., K. Zhu, and F. Diao. 2008. A dynamic all parameters adaptive BP neural networks model and its application on oil reservoir prediction. *Applied Mathematics and Computation*, 95(1): 66–75.

[15] Yuan, Z. R. 1999. Artificial neural network and applications. Beijing: *Tsinghua University Press*, 68–80.

Evaluation model for water environment of Eriocheir sinensis ponds based on AdaBoost classifier

Liu Yiran, Duan Qingling*, Zhang Lu

(College of Information and Electric Engineering, China Agricultural University, Beijing 100083, China)

Abstract: In the industry of pond culturing of Eriocheir sinensis, water environment has been exerting great impact on the survival and growth ability of crabs, so it is of great significance to evaluate whether the water environment is suitable for the growth of crabs in every culturing stage. In this paper, we associated the vast water environmental data and the yield of Eriocheir sinensis pond culturing, and proposed evaluation models for water environment in crab farming based on AdaBoost classifier. We started by extracting the features of water temperature and dissolved oxygen data based on the improved support function. Then the classification model was established using the recapture rate, average weight of the captured crabs and per mu yield as the labels based on AdaBoost algorithm, and the feature dimension was reduced using Linear Discriminant Analysis to simplify the model. Finally, the pond water environment was evaluated according to the classification results and the results of the classifiers were compared. The models were verified with the experiments using the water environmental data and the corresponding yield data that have been gathered in Yixing City, Jiangsu Province from 2014 to 2016. The results showed that the models could well evaluate whether the aquatic environment is adapted to the growth of crabs in every culturing stage and provide the basis for making decisions during the culturing process of Eriocheir sinensis.

Keywords: culturing of Eriocheir sinensis, evaluation, water environment, yield, AdaBoost algorithm

Citation: Liu, Y. R., Q. L. Duan, and L. Zhang. 2017. Evaluation model for water environment of Eriocheir sinensis ponds based on AdaBoost classifier. International Agricultural Engineering Journal, 26(3): 340–348.

1 Introduction

The Chinese mitten crab Eriocheir sinensis has good nutritional and economic values and is very much welcome by people in Chinese aquatic product market. In 2016, more than 10 million mu of Eriocheir sinensis were raised in China, with an annual output of more than 800 thousand tons (Cheng, 2016). However, with the development of crab industry, there are still some problems such as high breeding costs, great disease risks, and low culturing profits. Water environment is the basic condition for the survival of Eriocheir sinensis and influences their growth (Yuan et al., 2017), so it is of significance to evaluate whether the water environment is suitable for the growth of crabs in every stage of Eriocheir sinensis culturing cycle. The existing methods of constructing water environment evaluation model are mainly expert interviews, questionnaire surveys, on-site investigations and so on (Liu et al., 2011; Shi et al., 2013), but lack of joint analysis of the data from production process and yield. In this paper, we associated parameters of water environment that had been collected by Internet of Things (IOT) in crab pond farming with yield data such as the recapture rate, average weight and per mu yield and constructed the evaluation models for water environment of crab pond, which can evaluate the water environment in each stage of crab culturing, provide assistant information for making production decisions, and benefit for production improvement.

Nowadays, domestic and foreign researches have been carried out on many aspects of the water environment of crab farming. The environmental parameters of aquaculture have some influences on the physiology of Eriocheir sinensis. Fialho et al. (2016) conducted a controlled trial and concluded that in suitable

Received date: 2017-07-06 **Accepted date:** 2017-08-24

* **Corresponding author: Duan Qingling**, Ph.D., Professor of College of Information and Electric Engineering, China Agricultural University, Beijing 100083, China. Email: dqling@cau.edu.cn

temperature range, the higher the temperature comes, the more numbers of times the crabs molt, the more quickly the crabs grow. Gu et al. (2015) demonstrated that the linear correlation coefficients between the average weight of crabs and the water temperature are more than 0.9. Qiu et al. (2011) found that the dissolved oxygen content of water environment affects the reproduction, feeding rate and weight gain rate of crabs. Liu et al. (2011) used expert survey, DELPHI, field research and other methods to analyze the factors influencing water quality of fresh water aquaculture pond and selected five key factors as indexes to establish the water quality evaluation index system. Zhou et al. (2013) detected six crab ponds' breeding condition, carrying capacity and yield in different periods and obtained the non-linear relationship among carrying capacity, yield, feeding quantity and total nitrogen of the water using multiple regression. Li et al. (2015) analyzed and compared the water plants density, water temperature, pH-value, dissolved oxygen, recapture rate, average weight and per mu yield of four farmers' pond, drawing the conclusion that the coverage rate of aquatic plants should be controlled from 50% to 70%.

AdaBoost is a popular ensemble learning algorithm, which trains multiple weak classifiers with different training sets, and then combines these classifiers to form a final strong classifier. The advantages of multiple classifiers combination are that of lowering the requirement and simplifying construction difficulty of a single classifier (Zhou et al., 2016; Kim et al., 2008; Natesan et al., 2012). Some researchers have applied the AdaBoost algorithm to aquaculture, for instance, Liu et al. (2017) took the Penaeus vannamei as the research object, and proposed a recognition method for moving larval shrimp based on the improved PCA (Principal Component Analysis) and AdaBoost algorithm. Hao et al. (2015) quantified the behavioral parameters of young crabs under normal and abnormal salinity using image processing technology and established a salinity prediction model using support vector machine and BP-AdaBoost algorithm.

From the analysis above, it is an important measure for improving the production efficiency of crabs that evaluating whether the aquatic environment of each culturing stage is suitable for the growth of crabs, however, the research of the joint analysis and modeling of the data from actual production process of crab culturing and the data of yield is limited because of lacking of data. In order to describe the features of the water environment in each culturing stage, we made the feature extraction from the water temperature and dissolved oxygen data to establish an evaluation model for water environment more quickly and accurately. AdaBoost algorithm was used to construct the model to classify pond water temperature and dissolved oxygen. This paper made the following contributions: (1) the features of water environment parameters in Eriocheir sinensis ponds was extracted using weighted average method based on improved support function; (2) we associated the vast water environment data collected by the IOT with the yield data and constructed evaluation models for Eriocheir sinensis ponds according to the water environmental features, recapture rate, average weight and per mu yield.

2 Construction of evaluation model

2.1 Overall process

We proposed evaluation models for aquaculture environment of Eriocheir sinensis pond based on the existing research results of water environment of crab culture. Figure 1 shows the overall process.

Figure 1 Overall process of evaluation model construction

Data acquisition and preprocessing: Water environmental parameters and the data of yield were collected. The water environmental parameters of culturing process, mainly include water temperature and dissolved oxygen, were collected through IOT. The data were cleaned using a detection method based on sliding window and support vector regression (Duan et al., 2017). Moreover, the abnormal values were eliminated and the missing values were filled. Yield data refer to the recapture rate, average weight and per mu yield of the crabs were also collected.

Feature extraction: Daily, multi-day and abnormal

water environment features were extracted and the feature vectors were constructed.

Model construction: The feature vectors constructed above were used as an input and the yield data were used as labels to construct the classification models. Then the water environmental features were reduced to low dimensions to simplify the models.

Water environment evaluation: Water environment was evaluated according to the water environmental classification results

2.2 Feature extraction

The sampling period of IOT for aquatic product is usually 5 minutes or 10 minutes. The water environmental data are of large amount and change in a smooth range in a relatively short period of time. Therefore, it is reasonable to find values to represent the features of water environment during a period of time. In this paper, we extracted daily, multi-day and abnormal water environment features to describe the water environment.

2.2.1 Feature extraction based on improved support function

The daily water environment features are mainly used to describe the features of water environment in a certain day. We find out the periods of time of maximum values and minimum values of water temperature and dissolved oxygen usually appearing by means of statistical tools, and employ the average values of the water temperature and dissolved oxygen in those periods as the daily water environmental features respectively.

Multi-day water environmental features mainly used the weighted average method to describe the features of water environment for several days. The Eriocheir sinensis usually molt five times during a culturing cycle: the first molt is in March to April, the second is in May, the third is in June, the forth is in July to August and the last is in September approximately (Ai et al., 2014). The first and the fourth molt experienced a long time. In order to describe the features of long time water environment more accurately, we separated the two stages by month, thus the culturing cycle of Eriocheir sinensis is divided into 7 stages, each of which is about one month. Water environmental parameters may change greatly in a long period of time and if there are extreme values in a period of time, the average value will be affected by these values, which can't reflect the long-term features of water environmental parameters. The weighted average value of daily water environmental features of several days can reflect the water environmental parameters of continuous days with the relatively close values accounting for larger weights and a few extreme values accounting for smaller weights. The improved support function is employed to calculate the weights.

The support function (Yager et al., 2001; Yager et al., 2010) sup (m, n) indicates the degree of mutual support of two values n and m, that is, the degree of proximity. The following 3 requirements are necessary to be met:

① $\sup(m,n) \in [0,1]$;

② $\sup(m,n) = \sup(n,m)$;

③ if $|m-n|<|x-y|$, then $\sup(m,n)>\sup(x,y)$, $m,n,x,y>0$.

Weights for water temperature and dissolved oxygen data are calculated based on improved support function. The improved support function is calculated as follows (Duan et al., 2017):

$$\sup(m,n) = \mathrm{SN}(m,n,K,\beta) = K \times (1+\beta(m-n)^6)^{-1} \quad (1)$$
$$K \in [0,1],\ \beta \geq 0$$

where, $\sup(m,n)$ represents the support function; K indicates the worth of support, which is generally set to 1. β indicates the attenuation rate of support, and the greater the value of β reaches, the faster the degree of support declines.

2.2.2 Feature extraction of abnormal water environment

The abnormal water environmental features refer to the features of the water environment which are not suitable for the growth of Eriocheir sinensis. The optimum water temperature range for the growth of crab is between 15°C and 28°C. The crabs grow slowly when the water temperature is below 10°C and they are under stress when the water temperature is above 35°C (Gu et al., 2015). As for dissolved oxygen, the water environment is considered to be bad when it is lower than 3 mg/L, and worse when it is lower than 1 mg/L (Liu et al., 2011). In this paper, the total duration of water temperature below 10°C, the total duration of water temperature above 35°C, the total duration of dissolved oxygen below 3 mg/L and the total duration of dissolved oxygen below 1 mg/L are considered as the features of abnormal water environment.

The features of abnormal water environment mentioned above are calculated as follows.

$$sum = \begin{cases} sum + \frac{1}{2}I & x_i > \in S \wedge x_{i+1} \in S \\ sum + I & x_i > \in S \wedge x_{i+1} \in S \end{cases} \quad (2)$$

$$I = t_{i+1} - t_i,\ i = 1,2,\ldots,n \quad (3)$$

where, *sum* is the total duration; I is the time interval; x_i represents the sensor data; T represents time; S is the set of the sensor data which match the requirements, and n is the number of samples collected by the sensors.

2.2.3 Feature vector construction

In this paper, the water temperature features and the dissolved oxygen features were extracted to construct the water temperature feature vectors and the dissolved oxygen feature vectors respectively. In order to facilitate the description, the names and symbols of the features of water temperature and dissolved oxygen are defined in Table 1.

Table 1 Definitions of water temperature and dissolved oxygen features

Feature name	Symbol definition
The total duration of water temperature below 10°C	*Temp_Low_10*
The total duration of water temperature above 35°C	*Temp_High_35*
High temperature of multi-day water environmental features in stage *i*	*TH_i*
Low temperature of multi-day water environmental features in stage *i*	*TL_i*
The total duration of dissolved oxygen below 3 mg/L	*DO_Low_3*
The total duration of dissolved oxygen below 1 mg/L	*DO_Low_1*
High dissolved oxygen of multi-day water environmental features in stage *i*	*DH_i*
Low dissolved oxygen of multi-day water environmental features in stage *i*	*DL_i*

The water temperature feature vector and dissolved oxygen feature vector are shown in the following Equations (4) and (5).

$$\mathbf{t} = (Temp_Low_10, Temp_High_35, TH_i, TL_i) \quad i = 1,2,\ldots,7 \quad (4)$$

$$\mathbf{d} = (DO_Low_3, DO_Low_1, DH_i, DL_i) \quad i = 1,2,\ldots,7 \quad (5)$$

where, $\mathbf{t}$ represents the feature vectors of water temperature, and $\mathbf{d}$ represents the feature vectors of dissolved oxygen and i is the serial number of the culturing stages.

2.3 Water environmental evaluation model

Evaluation model for aquaculture environment of Eriocheir sinensis ponds was established using classification algorithm, in which the feature vectors were used as inputs, and the data of yield were employed as class labels. The water environment was divided into two categories and the output of the classification model is the evaluation result of it.

2.3.1 Establishment of water environmental classification model

In order to improve the classification accuracy and simplify the difficulty of single classifier construction, the AdaBoost algorithm was used to classify the water environment. The two core ideas of the AdaBoost algorithm are as follows (Cao et al., 2013):

(1) It adjusts the sample distribution on each iteration and forces the next sub classifier to focus on the samples that difficult to be classified.

(2) It adopts weighted voting strategy.

The AdaBoost algorithm introduces the idea of the dynamic allocation algorithm, and does not require any prior knowledge of the weak learning algorithm (Cheng et al., 2013). The training process of AdaBoost classifier is: First, a base classifier was trained using the initial training set; then the weight of current classifier was determined and the sample distribution was adjusted according to the performance of the classifier; thirdly, the next classifier was trained on the updated sample distribution; finally, when a specified number of iteration was reached, all classifiers were integrated together based on weighted voting strategy. The construction process is shown in Figure 2.

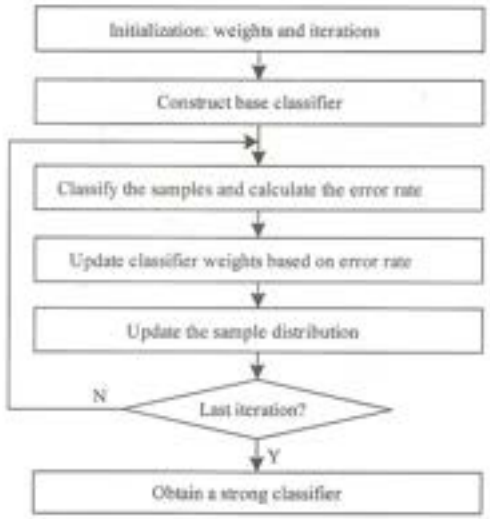

Figure 2 Flow chart of training strong classifier based on AdaBoost algorithm

The weak classifier used in this paper is the decision tree. The principle of decision tree is simple. Moreover, it is not only easy to construct, but also easy to interpret (Liu et al., 1998; Su et al., 2015).

The recapture rate, average weight and per mu yield are three main parameters for evaluating yield in crab farming. The recapture rate refers to the ratio of the number of crabs at the end harvest to the number of crabs at the very start. In this paper, the class of the recapture rate, the average weight and the per mu yield were defined as follows (Wang et al., 2000; Chen et al., 2016).

Table 2 Definitions of the labels of the classification model

Indicators\Labels	Good	Bad
Recapture rate	>70%	≤70%
Average weight	>140 g	≤140 g
Per mu yield	>100 kg	≤100 kg

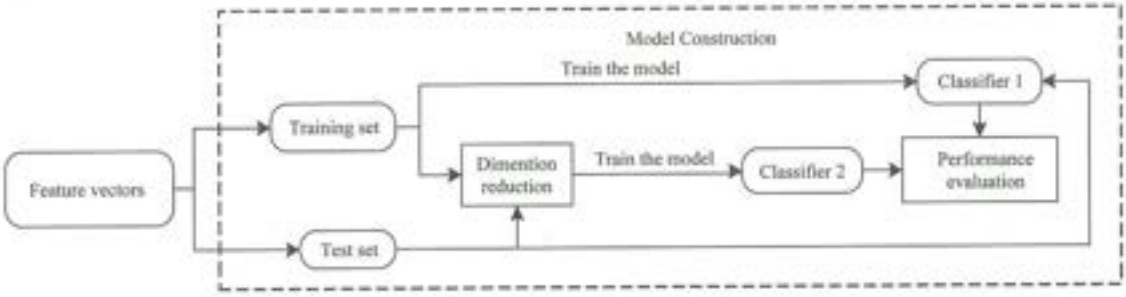

Figure 3 Flow chart of water environmental classification model construction

2.3.2 Water environmental evaluation

We evaluated the water environment in each culturing stage and the complete cycle of culturing using the models constructed above. When evaluating the water environment of a culturing stage, the feature vectors of water environment could not be obtained completely because the culturing cycle is not over. We used historical data to fill up the missing values of the sample feature vectors.

2.3.3 Model simplification

In order to simplify the model structure when the culturing cycle completed, we reduced the dimension of the water environmental feature vectors using linear discriminant analysis method. LDA is a statistical analysis method used to determine a class of a sample, whose basic idea is to project high-dimensional pattern samples into the best discriminant dimension that making the distance between the groups as large as possible (Sharma et al., 2015; Xie et al., 2015). The main difference between LDA and principal component analysis (PCA) is that LDA is a supervised learning method, which takes full consideration of classification performance in projection (Chiu et al., 2015; Elsayed et al., 2015).

3 Experiments

3.1 Datasets

In this experiment, the water environmental data were adopted from the Eriocheir sinensis pond in three towns in Yixing City, Jiangsu Province from 2014 to 2016. The sensors were installed at the direction that wind came, 20 cm of the distance from the bottom of water, and the acquisition period is 10 min. The culture benefit data, such as the recapture rate, average weight of the captured crabs and yield per mu, were obtained by referring the crab farmers' ledgers and the questionnaires filled by the farmers.

The average area of the experimental pond is about 30 mu, and the average water depth is 1 m. The amount of crabs that input at the very start is 1500 to 2000 per mu and the weight of the juvenile Eriocheir sinensis is 6 g approximately. The main feeds are synthetic diet, ice fish and living snails.

3.2 Experimental results and analysis

In this study, the precision, recall and F1-score were used as evaluation criteria for classification model, and their formulas are as follows:

$$Precision = \frac{TP}{TP + FP} \tag{6}$$

$$Recall = \frac{TP}{TP + FN} \tag{7}$$

$$F1 - score = \frac{2 \times Precision \times Recall}{Precision + Recall} \tag{8}$$

where, TP represents the number of true positive instances; FP represents the number of false positive

instances, and *FN* represents the number of false negative instance.

In this paper, we used the Matlab 2014 for data preprocessing, sklearn toolbox for model construction. The experimental data were divided into training set and the test set according to the ratio of 3:1. Learning rate of AdaBoost algorithm was set to 1, and the number of iteration steps was set to 400.

3.2.1 Data statistics results

We analyzed three consecutive years' water temperature and dissolved oxygen data that collected by the sensors of 20 farmers. The periods of time of maximum values and minimum values of water temperature and dissolved oxygen usually appearing are listed in the following table.

Table 3 The time of maximum values and minimum values of water temperature and dissolved oxygen appearing

	Maximum values	Minimum values
Water temperature	16:00-18:00	6:00-8:00
Dissolved oxygen	16:00-18:00	6:00-8:00

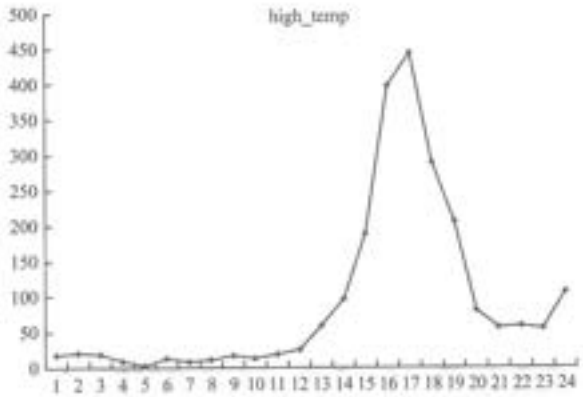

a. Time distribution of maximum values of water temperature

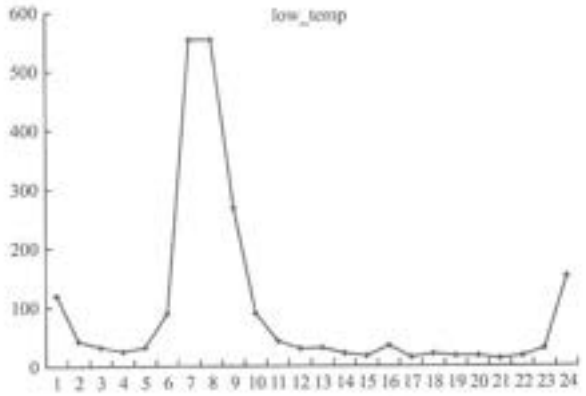

b. Time distribution of minimum values of water temperature

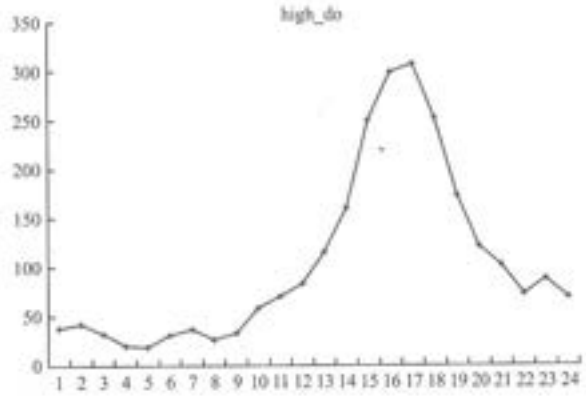

c. Time distribution of maximum values of dissolved oxygen

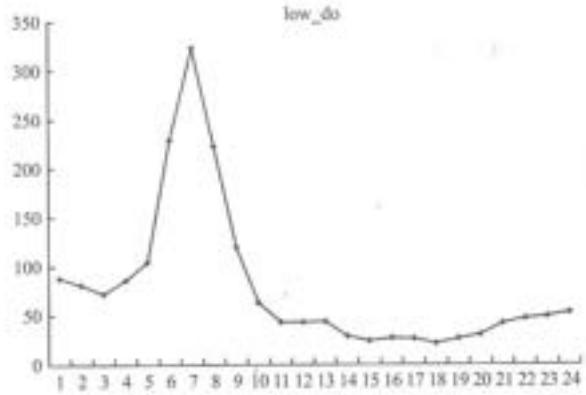

d. Time distribution of minimum values of dissolved oxygen

Figure 4 Time distribution of maximum and minimum values of water environmental parameters

3.2.2 Classification results and analysis

The classification models were trained by the feature vectors constructed from the water temperature features and dissolved oxygen features respectively. The models' performance on the test sets are shown in Table 4 and Table 5.

Table 4 Classification results of water temperature

Labels	Precision	Recall	F1-score
Recapture rate	0.720	0.800	0.755
Average weight	0.688	0.560	0.538
Per mu yield	0.808	0.760	0.772
Average value	0.739	0.707	0.688

Table 5 Classification results of dissolved oxygen

Labels	Precision	Recall	F1-score
Recapture rate	0.910	0.800	0.835
Average weight	0.833	0.767	0.758
Per mu yield	0.847	0.867	0.843
Average value	0.863	0.811	0.812

It can be seen from Table 4 that the average precision, recall and F1-score of water environmental classification according to the water temperature are 0.739, 0.707 and 0.688. All the evaluation criteria values are low. It indicates that the effects of water temperature on the recapture rate, average weight and per mu yield of

Eriocheir sinensis pond culturing are indirect or too much information is lost during features extraction. However, when the mu yield is used as a label to classify the water temperature, it can achieve a higher precision (0.808), and its recall ratio and F1-score ratio are also higher than the recapture rate and average weight as the labels.

It can be seen from Table 5 that the average precision, recall and F1-score of water environmental classification according to the dissolved oxygen are 0.863, 0.811 and 0.812. All the evaluation criteria values are higher than the classification according to the water temperature. It indicates that the effects of dissolved oxygen on the recapture rate, average weight and per mu yield of Eriocheir sinensis pond farming are direct.

3.2.3 Feature reduction results and analysis

The results of feature dimension reduction are shown in Table 6 and Table 7.

Table 6 Results of dimension reduction of water temperature feature vectors

Recapture rate	Average weight	Per mu yield
Temp_High_35	TH_4	Temp_High_35
TH_3	TL_4	TH_4
TH_4	TH_5	TL_4
TL_4		
TH_5		

As is shown in Table 6, the numbers of water temperature features are reduced from 3 to 5, after reducing the dimension using LDA. The multi-day water environmental features of high and low temperature in culturing stage 4 are both reserved when using the recapture rate, average weight and per mu yield as labels. The results show that these 2 features have great influence on classification results of the three models.

Table 7 Results of dimension reduction of dissolved oxygen feature vectors

Recapture rate	Average weight	Yield per mu
DO_Low_1	DO_Low_1	DO_Low_3
DH_3	DH_3	DO_Low_1
DL_3	DL_3	DH_3
DL_4	DL_4	DL_3

As is shown in Table 7, the numbers of dissolved oxygen features are all reduced to 4, after reducing the feature dimension using LDA. The multi-day water environmental features of high and low dissolved oxygen in culturing stage 3 and the total duration of dissolved oxygen below 1 mg/L are all reserved when using the recapture rate, average weight and per mu yield as labels, which are the factors having great influence on classification results of the three models.

3.2.4 Validation of feature dimension reduction

When the culturing cycle completed, the classification models were trained by the feature vectors after dimension reduction, and the model's performance on the test set is shown in Table 8 and Table 9.

Table 8 Classification result of water temperature after dimension reduction

Labels	Precision	Recall	F1-score
Recapture rate	0.720	0.800	0.755
Average weight	0.688	0.560	0.538
Per mu yield	0.808	0.760	0.772
Average value	0.739	0.707	0.688

It is seen from the comparison of Table 4 and Table 8, the average precision of water temperature classification was reduced by 1.4% after using LDA to reduce feature dimension, while recall and F1-score were raised by 5.7% and 5.5% respectively. The precision, recall, and F1-scores were raised by 2.4%, 9.3% and 7.0%, respectively, when using per mu yield as label.

Table 9 Classification results of dissolved oxygen after dimension reduction

Labels	Precision	Recall	F1-score
Recapture rate	0.910	0.800	0.835
Average weight	0.833	0.767	0.758
Yield per mu	0.847	0.867	0.843
Average value	0.863	0.811	0.812

It is seen from the comparison of Table 5 and Table 9, the average precision, recall and F1-score of dissolved oxygen classification was reduced by 0.4%, 6.7% and 4.2% respectively after using LDA to reduce feature dimension.

It is seen from the comparison of Tables 5, 6, 8, and 9, the average precision of classification according to water temperature and dissolved oxygen are 0.739 and 0.863 respectively, and became 0.728 and 0.859 after feature dimension reduction. Although there is a decline, but it is not large.

From the analysis above, we drew the following conclusions. (1) In the case of non-extreme weather, the daily highest values of water temperature and dissolved oxygen appear between 16:00 and 18:00 and the daily

lowest values appear between 6:00 and 8:00. (2) The evaluation models for water environment proposed in this paper has better performance in classifying the dissolved oxygen features. (3) LDA is suitable for the feature dimension reduction for water environmental classification models because precision decreased slightly.

4 Conclusion

(1) In this paper, we proposed evaluation models for water environment of Eriocheir sinensis ponds based on AdaBoost classifier, associated the water environment data that had been collected from the IOT, as well as the recovery rate, average weight and per mu yield jointly. The models made stage evaluations and overall evaluations of the water environment. With an average precision of 0.863 and 0.739, the models have a good performance in classifying dissolved oxygen and water temperature features, which propose a solution to evaluate the water environment in crab farming. The results of the evaluations provided basis for regulation of the water environment, and are helpful to improve the yield.

(2) An extraction method for water environmental features based on the improved support function was designed, helping the classifiers achieving a good performance in classifying the dissolved oxygen features.

(3) The LDA method has a good performance in reducing the feature dimensions under the condition that the precision loss of the classification is less than 2%.

Acknowledgements

This work is supported by the National Public Welfare Industry (Agriculture) Scientific Research Projects (201303107) and also supported by the Program of Science and Technology of Beijing (Z171100001517016).

[References]

[1] Ai, T. S. 2014. Pond culturing technology of large-scale crab. Wuhan: *Hubei Science and Technology Press*

[2] Cheng, C. M. 2016. An annual output of 800 thousand tons of crab industry: These problems will touch your pain. *Modern Fisheries*, (12): 72–73.

[3] Cao, Y., Q. G. Miao, J. C. Liu, and L. Gao. 2013. Advance and prospects of AdaBoost algorithm. *Acta Automatica Sinica*, 39(6):745–758.

[4] Cheng, W. C., and D. M. Jhan. 2013. Triaxial accelerometer-based fall detection method using a self-constructing cascade-AdaBoost-SVM classifier. *IEEE Journal of Biomedical & Health Informatics*, 17(2): 411–419.

[5] Chen, L. J. 2016. Analysis on growth performance and breeding efficiency of Eriocheir sinensis ponds in Xinghua area. M.S. thesis, School of Biology&Basic Medical Science, Soochow University, China.

[6] Chiu, C. Y., C. Y. Chen, Y. Y. Lin, S. A. Chen, and C. T. Lin. 2015. Using a novel LDA-ensemble framework to classification of motor imagery tasks for brain-computer interface applications. *Frontiers in Artificial Intelligence & Applications*, 274: 150–156.

[7] Duan, Q. L., X. Y. Xiao, Y. R. Liu, L. Zhang, and K. Wang. 2017. Data fusion method of livestock and poultry breeding internet of things based on improved support function. *Transactions of the Chinese Society of Agricultural Engineering* 33(Supp.1): 239–245. (In Chinese with English abstract)

[8] Elsayed, M. A., and K. Hamed. 2015. Study of similarity measures with linear discriminant analysis for face recognition. *Journal of Software Engineering & Applications*, 8(1): 478–488.

[9] Fialho, C., F. Banha, and P. M. Anastácio. 2016. Factors determining active dispersal capacity of adult Chinese mitten crab Eriocheir sinensis. *Hydrobiologia*, 767(1): 321–331

[10] Gu, X. Q., and G. Z. Jiang. 2015. Researches on ecological and meteorological factors affecting crab breeding. *Acta Agriculturae Jiangxi*, 4: 88–93.

[11] Hao, M. Z. 2015. Portunus Triberculatus Zoeas growth visualization and abnormal forecasting. M.S. thesis, Electrical Engineering and Computer Science Dept., Ningbo University, China.

[12] Kim, J. H., B. G. Kwon, J. Y. Kim, and D. J. Kang. 2008. Method to improve the performance of the AdaBoost algorithm by combining weak classifiers. *June, 18-20: International Workshop on Content-Based Multimedia Indexing. IEEE*: 357–364. London, UK.

[13] Li, D. G., Y. H. Wang, H. C. Wang, J. Chen, G. L. Luo, and K. L. Chen. 2015. Effect of plant density on crab pond water quality and breeding efficiency. *Journal of Aquaculture*, 36(12): 11–15.

[14] Liu, M. H., H. X. Yu, Q. G. Liu, and R. M. Wang. 2011. Water quality evaluation index system for freshwater aquaculture pond. *Journal of Anhui Agricultural Sciences*, 12(7): 2015–1028

[15] Liu, S., S. Wang, J. Chen, X. Liu, and H. Zhou. 2017. Moving larval shrimps' recognition based on improved principal component analysis and AdaBoost. *Transactions of the Chinese Society of Agricultural Engineering*, 33(1): 212–218. (in Chinese with English abstract).

[16] Liu, X. H., and S. Li. 1998. An optimized algorithm of decision tree. *Journal of Software*, 9(10): 797–800.

[17] Natesan, P., P. Balasubramanie, and G. Gowrison. 2012. Improving attack detection rate in network intrusion detection using AdaBoost algorithm with multiple weak classifiers. *Journal of Information & Computational Science*, 9(8): 2239–2251.

[18] Qiu, R. J., Y. X. Cheng, X. X. Huang, X. G. Wu, X. Z. Yang, and R. Tong. 2011. Effect of hypoxia on immunological, physiological response, and hepatopancreatic metabolism of juvenile Chinese mitten crab Eriocheir sinensis. *Aquaculture International*, 19(2): 283–299

[19] Su, W., F. F. Jiang, D. H. Zhu, J. G. Zhan, H. Y. Ma, and X. D. Zhang. 2015. Extraction of maize planting area based on decision tree and mixed-pixel unmixing methods. *Transactions of the Chinese Society of Agricultural Machinery*, 46(9): 289–295, 301. (in Chinese with English abstract).

[20] Shi, B. 2013. Research on the key techniques of intelligent support system for crab breeding in ponds. Ph.D. diss. Electronic and Information Engineering Dept., Jiangsu University, China.

[21] Sharma, A., and K. K. Paliwal. 2015. A deterministic approach to regularized linear discriminant analysis. *Neurocomputing*, 151(1): 207–214.

[22] Wang, L. Q., W. Hu, and Z. Y. Deng. 2000. Studies on the stocking density, yield and size of the Chinese crab in Ponds. *Reservoir Fisheries*, 20(6): 16–17

[23] Xie, Y., and T. Zhang. 2015. A fault diagnosis approach using SVM with data dimension reduction by PCA and LDA method. *November 27-29, 2015: Chinese Automation Congress. IEEE*: 869–874. Wuhan, China.

[24] Yager, R. R. 2001. The power average operator. IEEE Transactions on Systems, *Man and Cybernetics* 31(6): 724–731.

[25] Yager, R. R. 2010. The Power average operator for information fusion. *June 28 to July 2, 2010: Information Processing and Management of Uncertainty in Knowledge-Based Systems. Applications. International Conference*: 208–220. Dortmund, Germany.

[26] Yuan, Q., Q. D. Wang, T. L. Zhang, Z. J. Li, and J. S. Liu. 2017. Effects of water temperature on growth, feeding and molting of juvenile Chinese mitten crab Eriocheir sinensis. *Aquaculture*, 468: 169–174.

[27] Zhou, L. H., X. H. Gu, Q. F. Zeng, Z. G. Mao, and H. M. Gao. 2013. Environmental effects and structural optimization of crab culture in ponds in reclamation zones of Gucheng Lake. *Journal of Ecology & Rural Environment*, 29(1): 36–42.

[28] Zhou, Z. H. 2016. Machine Learning. Beijing: *Tsinghua University Press*.

Farmer skill training system based on motion sensing technology and user behavior analysis

Cai Yifeng, Ma Qin*, Wang Qing, Chen Hong, Lu Yi, Feng Tianwei, Zhang Ya

(*College of Information and Electrical Engineering, 100083, Beijing, China*)

Abstract: The difficulty in receiving and understanding agricultural technology knowledge has always been a bottleneck restricting the effect of agricultural information service. However, most multimedia teaching system for farmers is lack of man-machine interaction. Rural intelligent experiential information service is an effective way to solve the problem. The farmer skill training system has been designed based on user behavior analysis and motion sensing technology. The system includes body movement interactive module, resource acquisition processing module, multimedia player module, and user behavior analysis module. Based on motion sensing technology and DTW algorithm, users can control the completion of the system through the motion sensing interaction. The system can provide users with training video data while reducing operational complexity. The accuracy of the action can provide users with a convenient experience. Using the fuzzy evaluation algorithm model, by way of making statistics and analyzing the farmers' action in the use of the operation process, rules of the user and accurate positioning of user preferences can be found. The interested training content can be recommended for users according to user preferences and tendencies. Based on motion sensing technology and user behavior analysis method, the multimedia training system provided farmer users with strong interaction and deep sense of immersion. It can realize the new learning mode of multi-dimensional interactive experience and multimedia teaching, and reduce the dependency and complexity operation of traditional mouse and keyboard, and provide an effective method for training the farmers.

Keywords: motion sensing technology, farmer skill training, user behavior analysis, multimedia teaching

Citation: Cai, Y. F., Q. Ma, Q. Wang, H. Chen, Y. Lu, T. W. Feng, and Y. Zhang. 2017. Farmer skill training system based on motion sensing technology and user behavior analysis. International Agricultural Engineering Journal, 26(3): 349–355.

1 Introduction

The difficulty of accepting and understanding the agricultural science and technology information has always been the bottleneck, restricting the effect of rural information service. It is also an important factor affecting the enthusiasm of farmers to use the training information. Rural intelligent experiential information service is an effective way to solve this problem. Agricultural and rural technical information is always more complex, the farmers low educational characteristics make them difficult to understand the highly conceptualized scientific and technological information. The professional science and technology information is hardly accepted by less educated farmers while the information simply pushed to the front of farmers' faces.

The typical training modes and effects of the new professional farmers and the various factors influencing the training effect have become the hotspot of the current domestic and foreign scholars. Research pointed out that the popularization and application of modern distance education in rural areas can avoid the control of the audience's quality level, so that rural informatization can benefit more farmers (Gong et al., 2009). Based on the web, Zhao J. C. (2016) has developed a platform for farmers' personalized learning and education based on neural network, so that farmers can use the network to obtain the knowledge of what they are concerned. Niu J.B. et al. (2010) developed a comprehensive training system

Received date: 2017-06-29 **Accepted date:** 2017-08-17

* **Corresponding Author: Ma Qin**, Ph.D., Associate Professor of College of Information and Electrical Engineering, China Agricultural University, Beijing, China. Email: sockline@163.com.

for farmers based on virtual reality. After analyzing the characteristics of farmer training, this system built a comprehensive training system by virtual reality technology embedding virtual animal and plant model, but the individual training for farmers still lacks. Yoo H. S. et al. (2014) has developed an agricultural training game containing simulators such as crops, livestock, weather, pests, fertilizers and so on, through the historical simulation combined with the game elements, to achieve the purpose of modern agricultural training and entertainment functions. Chen H. et al. (2011) developed a virtual experiential pig disease training system, and farmers have a more intuitive way to understand the pig in the breeding process of common diseases. Torrens F. et al. (2017) developed a welding technology lab based on virtual reality, the trainees can improve the welding method according to the advice made by the system and reduce the damage caused by improper operation.

1.1 User behavior analysis and recommendation system

In the context of big data, a new information filtering technology - personalized behavior based on user behavior has become a popular research direction in recent years (Zhu et al., 2017). It is through the record and analysis of the user's historical behavior data to obtain the user's interest preferences, and then learning the level of information users interested in, the relevant information will be presented in front of the customers. At present, there are many examples of user-based recommendation system at home and abroad. In China, Chen H. C. et al. (2005) proposed a music recommendation system based on music and users' grouping, which builds a method based on content, collaboration and statistics through the user's favorite degree of music group and their group of users. Cheng S. et al. (1977) proposed a document recommendation model based on the integration of time perception and user interest importance. It not only summarizes the user's interest based on behavior analysis, but also assigns the time decay function to allocate a higher time weight for the most recent browsing document, accurately lock user interest and recommended information. While abroad, Abdullah N. et al. (2011) proposed a recommendation system which shows occasionally-purchasing products based on user behavior and opinions in e-commerce sites, and better satisfying the needs of buyers. Out of the traditional way of recommendation, more and more scholars are committed to seeking more innovative, more accurate and more efficient recommendation methods.

In the training system introduced in this paper, the user behavior analysis module is included. It can judge the user's interest based on the user's click history and click frequency in the system. The same type of training video is automatically recommended in the search interface, and it can be recommended to users by video with the same interest. It greatly improved the user experience of the system.

1.2 Motion sensing technology and Kinect

Motion sensing technology can capture the physical movement of objects and change in the environment. It can interact with motion sensing hardware through body movement. When the motion sensing hardware reads the user's actions and translates them into commands, the user can achieve the motion sensing manipulation. In 2014, Microsoft Corp released the Kinect v2 somatosensory device, which is equipped with a depth sensor. Based on the infrared technology, Kinect's infrared lens can diffuse the infrared light. The infrared receiver can be used to capture the reflected light and calculate the distance of objects. The somatosensory technology provided by Kinect has a wide range of applications in many fields such as plant growth measurement (Yu et al., 2016), animal growth monitoring (Stavrakakis et al., 2015), training and education. At present, some studies and achievements have been made on the application of Kinect somatosensory technology in teaching. Based on Kinect v2, Scherer M. et al. (2016) developed residential rehabilitation training system. The system consists of two components, one is for the therapist of the clinical institution and the other is for the patient at home. The application algorithm saves the patient's reference data. The personal motion algorithm compares the current motion data with the recorded motion data, and provides real-time feedback, showing the correctness of the implementation. Palacios-Navarro G. et al. (2015) used Kinect for limb recovery in patients

treated with Parkinson's disease. Wang et al. (2017) has developed an interactive display system of cultural relics by using Kinect. Sasaki Y. and his partners realized the farmer daily operation record system by Kinect (Sasaki et al., 2013). Jamie I. M. et al. (2011) bind Kinect to the electronic whiteboard to realize the application of Kinect in university chemistry education, materialized the abstract molecules to improve the immersion of learning, and to make students more receptive to knowledge. Trajkova M. et al. (2015) used Kinect in ballet teaching to enable students to learn more intuitively and to adjust their actions based on the scores, so that each user can receive top-level training.

In the multimedia teaching for the farmers, the effect of the traditional listening mode, which is dominated by the teachers in the traditional video form, and the learner passively listens to the class, is not satisfactory. But with the emergence of Kinect, we can use its somatosensory technology to analyze the operator's action and understand the intention of the operator based on user behavior analysis. By the farmer skill training system based on motion sensing technology and user behavior analysis, we not only improve the interactive and fun learning, but also enhance the intuition of learning.

2 Construction of user behavior analysis and recommendation model

2.1 Training video scoring model based on fuzzy evaluation

In this paper, the fuzzy evaluation comprehensive evaluation method was used to establish the preference index model for evaluating the farmer skill training video resources.

S1: Establish the evaluation indicators of the farmer skill training video.

$U = \{U_1, U_2\}$ = {video information, user operation};

$U_1 = \{U_{11}, U_{12}, U_{13}, U_{14}\}$ = {users, classification, degree of difficulty, time};

$U_2 = \{U_{21}, U_{22}, U_{23}\}$ = {classification of highest viewing frequency, difficulty level of highest viewing frequency, time of highest viewing frequency}.

S2: Establish the preference evaluation effect set.

$V = \{V_1, V_2, V_3, V_4, V_5\}$ = {very strong, strong, general, poor, very poor};

$V_1 = 100, V_2 = 75, V_3 = 50, V_4 = 25, V_5 = 0$.

S3: Set the weight value for the video resource preferences by collecting user actions.

Take the user operation as an example:

a. Determine user occupation U_{21}, classification of highest viewing frequency U_{22}, difficulty level of highest viewing frequency U_{23}, and time of highest viewing frequency U_{24}.

b. By recording the user operation process, score the above four indicators. For example, operate n_i on $U_{1j}S_j(i)$, i = 1, 2, …, n, j = 1, 2, 3, 4. Constitute the matrix S:

$$\begin{bmatrix} S_1(1) & \cdots & S_1(i) \\ S_2(1) & \cdots & S_2(i) \\ \cdots & \cdots & \cdots \\ S_j(1) & \cdots & S_j(i) \end{bmatrix}$$

c. Determine the weight matrix M for each scoring.

d. Calculate the weight of the evaluation index N = S M.

e. N is normalized to obtain the weight value of the evaluation index.

The weight value of the indicator can reflect the final preference for all operations.

2.2 Training video priority ordering method based on fuzzy evaluation

The training video priority ordering method is as follows, the steps are shown in Figure 1.

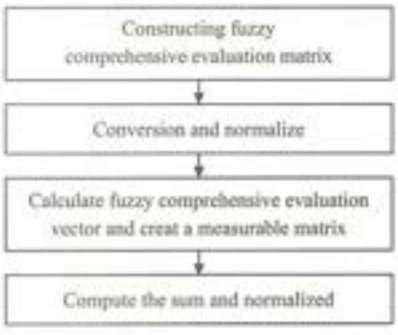

Figure 1 Steps of fuzzy evaluation

S1: $U=|u_1, u_2, \ldots, u_n|$ is the index set of program measures and $\omega=|\omega_1, \omega_2, \ldots, \omega_n|$ is the weight vector. For program X, in accordance with the j-th u_j indices measure, obtain measure value $r_{ij} = [r_{ij-}, r_{ij+}]$ from X_i obtained on the u_j, and form a row vector $R_i=(r_{i1}, r_{i2}, \ldots, r_{in})$, which constituting the fuzzy comprehensive evaluation matrix:

$$R=[R_1,R_2,\ldots,R_m]^T=\begin{bmatrix} r_{11} & \cdots & r_{1n} \\ \vdots & \ddots & \vdots \\ r_{m1} & \cdots & r_{mn} \end{bmatrix} = \begin{bmatrix} [r_{11}^-,r_{11}^+] & \cdots & [r_{1n}^-,r_{1n}^+] \\ \vdots & \ddots & \vdots \\ [r_{m1}^-,r_{m1}^+] & \cdots & [r_{mn}^-,r_{mn}^+] \end{bmatrix} \quad (1)$$

where, R is the interval number decision matrix.

S2: Through the following conversion:

$$a_{ij}=\frac{r_{ij}}{\max r_{ij}},\ i\in I_1,\ j\in N \quad (2)$$

$$a_{ij}=\frac{r_{ij}}{\min r_{ij}},\ i\in I_2,\ j\in N \quad (3)$$

Mentioned above,

$$\min r_{ij}=[\min_{ij}^-,\min_{ij}^+],\ \max r_{ij}=[\max_{ij}^-,\max_{ij}^+] \quad (4)$$

The above decision matrix is normalized to obtain a normalized decision matrix.

Among,

$$a_{ij}=[a_{11}^-,a_{11}^+] \quad (5)$$

S3: Calculate the fuzzy comprehensive evaluation vector and compare the interval number $b_i (i = 1, 2, \ldots, n)$ to create a measurable matrix.

$$b=\omega^*A=(b_1,b_2,b_3,\ldots,b_n) \quad (6)$$

$$P=\begin{bmatrix} p_{11} & \cdots & p_{1n} \\ \vdots & \ddots & \vdots \\ p_{m1} & \cdots & p_{mn} \end{bmatrix} \quad (7)$$

S4: Compute the sum of each row of matrix p, and normalize the sum to obtain the order of decision making.

We proposed a new method of ranking the decision-making scheme based on fuzzy evaluation, gave a concrete way to standardize the decision matrix, and provided a reasonable way to get the order of the scheme from the probability matrix. So that the sorting results are more objective and stable, the evaluation results are more comprehensive, more truly reflect the farmer users tend to the actual situation of video resources, and to achieve human video priority ranking recommended.

3 Farmer skill training system architecture based on motion sensing technology

The system is mainly composed of body movement interactive module, resource acquisition processing module, multimedia player module, and user behavior analysis module, as shown in Figure 2. The user can complete the somatosensory interaction through the simple movement under the control of the system, and achieve providing video data while reducing the complexity of the operation, and providing the users with a convenient experience. The body movement processing and interaction module, the resource acquisition processing module, the multimedia module and the user behavior analysis module are integrated in the host. It is connected to the tracking device, the display and the audio equipment respectively. The resource acquisition and processing module are used to asynchronously acquire information of a video resource and provide it to the system. With the aid of body sensor, complex operation can be simplified into simple body movements, lowering the use threshold, and improving the participation and motivation of farmers users.

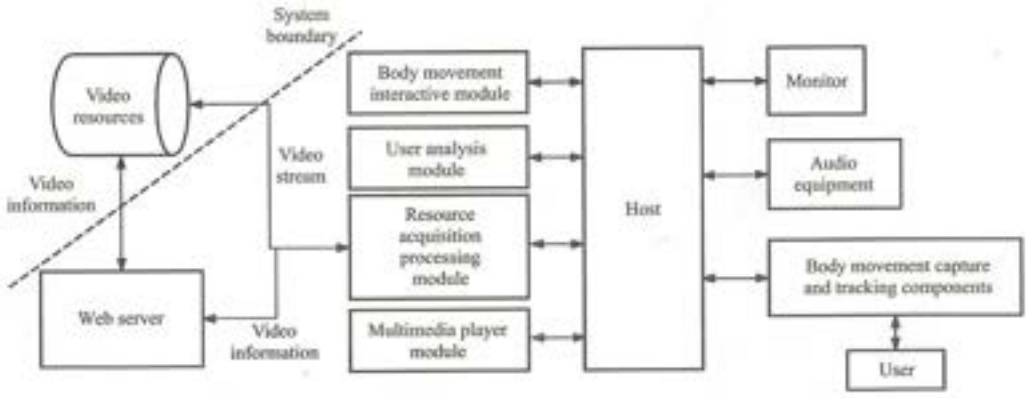

Figure 2 System structure diagram

3.1 Depth image and bone node acquisition

Kinect v2 has the 1920×1080 color camera, and 512×424 depth camera. The depth sensor is loaded, and the depth information is obtained by returning time from

the projected infrared reflection. With a depth camera, the Kinect allows the depth values of everywhere to be sorted into a depth matrix, and the current depth image can be obtained through proper transformation. The depth image captured by the Kinect can be represented by the coordinates (x, y, z), where (x, y) represent the coordinates of the pixel points in the image, and z represents the vertical distance between the coordinate point and the depth camera. The user's bone node data also can be obtained through the depth image, and refresh at 30 frames per second. The acquired 20 bone node data contains three attributes, including the skeletal point type, the position information and the tracking status capturing bone nodes, as shown in Figure 3.

Figure 3 Capture of human skeletal nodes

After the system identifying, the user will see the hand cursor in the screen, which corresponds to the user's hand movement. The user will press the screen to trigger the click effect, or move the cursor through moving hand and move the cursor to achieve drag and drop. The corresponding mapping relationships between specific body movement and operation refer to the Table 1.

Table 1 Mapping table of motion sensing

Operation	The result of motion sensing
Move hand right	The cursor moves to the right in the screen
Move hand left	The cursor moves to the left in the screen
Move hand up	The cursor moves to the up in the screen
Move hand down	The cursor moves to the down in the screen
Hand push	Select
Fisting drag	Drag and move the content as the hand's movements

However, Kinect cannot directly identify more complex actions, such as the user makes waving action or draws circular, Kinect cannot capture the complete action. So, we introduced the Dynamic Time Warping algorithm to solve such problems.

3.2 Dynamic Time Warping algorithm

Dynamic Time Warping (Berndt et al., 1994) refers to the use of Dynamic Time Warping to calculate the two unequal time actions, to not completely equal time sequence of the optimal matching, thus the influence of the time can be ignored, and two sequences of distance measurement can be defined. It is a better way to solve the problem that Kinect cannot accurately identify continuous action. The concrete implementation is: given two time sequences (the movement of the bone nodes) $A=a_1,a_2,a_3,\ldots,a_n$ and $B=b_1,b_2,b_3,\ldots,b_m$, find its best match: $\varphi=(\varphi_A, \varphi_B)$, then

$$\varphi_A = (\varphi_A^1,\varphi_A^2,\varphi_A^3,\ldots\varphi_A^K)\ (1 \le \varphi_A^i \le n,\ 1 \le i \le K) \quad (8)$$

$$\varphi_B = (\varphi_B^1,\varphi_B^2,\varphi_B^3,\ldots\varphi_B^K)\ (1 \le \varphi_B^i \le m,\ 1 \le i \le K) \quad (9)$$

The time series A and B are defined as follows Dynamic Time Warping

$$DTW(A,B) = \min_{\varphi}\{\sum_{i=1}^{K} dtw(\varphi_A^i,\varphi_B^i)\} \quad (10)$$

$dtw(\varphi_A^i,\varphi_B^i)$ equals to the distance between the i-th element in A and the j-th element in B.

In this paper, $dtw(i,j)=|a_i-b_j|$.

To find the optimal matching of A and B can be converted to a two-dimensional matrix S of n by m, $S[i,j]$ is the DTW distance between

submatrix $A'=a_1,a_2,a_3,\ldots,a_i$ and submatrix $B'=b_1,b_2,b_3,\ldots,b_j$,

which can be remember to δ_{ij}. So, the algorithm can be converted to calculate the δ_{nm}, which are calculated from top to bottom, left to right all of the possible matches, by the principle of the Dynamic Time Warping

$$\delta_{ij} = dtw(i,j) + \min\{\delta_{i-1j-1},\delta_{i-1j},\delta_{ij-1}\} \quad (11)$$

can reduce the complexity of the algorithm, which calculate the optimal matching results of the two-time series (Ding et al., 2016). Fifty groups of the experiments showed that the movement which have been processed by Dynamic Time Warping have better recognition rate than the unprocessed ones. The details are shown in Table 2.

Table 2 Matching rate of Dynamic Time Warping

Action	Normal matching rate	DTW matching rate
Move hand left or right	90%	96%
Push hand	90%	92%
Draw circle with hand	78%	92%
Continuous hand movement (such as wave hands)	28%	90%

3.3 Farmer skill training system implementation

Based on the somatosensory technology and user behavior analysis method, the system in this paper can capture the network training resources and provide a more comprehensive skills training system for farmers. The main interface as shown in Figure 4.

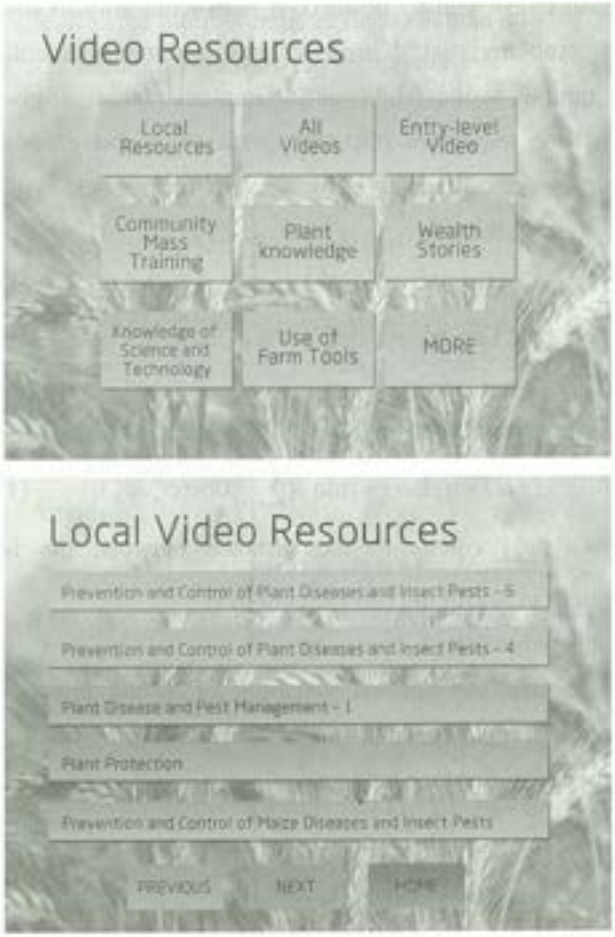

Figure 4 Interface of training system

Where the order of the training resources is rearranged according to the calculation and evaluation of the user behavior analysis and recommendation system, and it recommends higher quality, with more suitable resources for users. Users can learn the video resources through the corresponding motion sensing actions which is mentioned in the table above, through the control of the hand to complete the corresponding button click easily. The farmer training system can make the farmer easy to understand the highly conceptualized scientific and technological information.

4 Conclusion

Compared with the other training methods for farmers, the study based on motion sensing technology achieved the multimedia training system and put forward the user behavior statistical analysis method. The system not only provided training video data for users through a very convenient way, but also made farmers use motion sensing action to control the system easily. The multi-dimensional interactive multimedia training and learning system provided a new way of learning and training for farmers. Specific conclusions are as follows:

• The system provides the farmers with video data. The resource acquisition and processing module can achieve video information asynchronously.

• The system uses the fuzzy evaluation comprehensive evaluation method to establish the preference index system for evaluating the video resources through building the evaluation index system, establishing the preference evaluation effect set, setting the preference weight value and matrix normalization.

• The system uses the motion sensing device to capture the user's skeletal node data with the depth image captured by Kinect, and uses the dynamic programming algorithm to handle the action, which greatly improves the action recognition rate.

Acknowledgements

We would like to thank to the reviewers for their helpful comments. This work was financially supported by the Special Fund from National Science and Technology Support Program (2015BAK04B04).

[References]

[1] Abdullah, N., Y. Xu, S. Geva, and J. Chen. 2011. Infrequent purchased product recommendation making based on user behavior and opinions in E-commerce sites. *2010 IEEE International Conference on Data Mining Workshops*, 1084-1091. Sydney, NSW, Australia, 13–13 Dec.

[2] Berndt, D., and J. Clifford. 1994. Using dynamic time warping to find patterns in sequences. AAAIWS'94 Proceedings of the 3rd International Conference on Knowledge Discovery and Data Mining, 359–370. Seattle, WA, USA, 31 Jul-01 Aug.

[3] Chen, H. C., and A. L. P. Chen. 2005. A music recommendation system based on music and user grouping. *Journal of Intelligent Information Systems*, 24(2-3): 113–132.

[4] Chen, H., Q. Wang, D. H. Zhu, M. X. Meng, and S. S. Tang. 2011. Virtual experiential pig disease training system. *Chinese Journal of Veterinary Medicine*, 47(10): 86–89.

[5] Cheng, S., and Y. Liu. 1977. Document recommendation based on fusion of time-awareness and user interests' importance degree. *Nature*, 267(267): 450–2. 9.

[6] Ding, I. J., and C. W. Chang. 2016. Feature design scheme for Kinect-based DTW human gesture recognition. *Multimedia Tools & Applications*, 75(16): 9669–9684.

[7] Gong, J, and H. Y. Liu. 2009. Modern distance education: digital gap or digital opportunity? *Distance Education in China*, 13(1): 49–52.

[8] Jamie, I. M., and C. R. Mcrae. 2011. Manipulating molecules: using Kinect for immersive learning in chemistry. *Annual UniServe Science Conference (17th: 2011)*, 22. Melbourne, VIC, Australia, 28–30 Sep.

[9] Niu, J. B., Q. Wang, H. Chen, H. Zhu, C. Zhao, and D. H. Zhu. 2010. Design and implementation of farmer training system framework based on virtual reality technology. *Journal of Computer Applications*, 30(s1): 251–253.

[10] Palaciosnavarro, G., I. Garciamagarino, and P. Ramoslorente. 2015. A Kinect-based system for lower limb rehabilitation in parkinson's disease patients: A pilot study. Journal of Medical Systems, 39: 103.

[11] Sasaki, Y., S. Shibusawa, H. Negishi, Y. Tokui, and A. Takemoto. 2013. Development of agricultural work automatic record system by using Kinect for tacit knowledge extraction. *IFAC Proceedings Volumes*, 46(4): 378–383.

[12] Scherer, M., A. Unterbrunner, B. Rieß, and P. Kafka. 2016. Development of a system for supervised training at home with Kinect v2 . *Procedia Engineering*, 147: 466–471.

[13] Stavrakakis, S., W. Li, J. H. Guy, G. Morgan, G. Ushaw, G. R. Johnson, S. A. Edwards. 2015. Validity of the Microsoft Kinect sensor for assessment of normal walking patterns in pigs. *Computers & Electronics in Agriculture*, 117(C): 1–7.

[14] Torres, F., T. Neira, A. Leticia, and S. Marta. 2017. A learning evaluation for an immersive virtual laboratory for technical training applied into a welding workshop. *Eurasia Journal of Mathematics Science & Technology Education*: 13.

[15] Trajkova, M., and M. Ferati. 2015. Usability evaluation of Kinect-based system for ballet movements. Design, User Experience, and Usability: Users and Interactions: 4th International Conference, 464–472. Los Angeles, CA, USA, 2-7 August.

[16] Wang, X. Q., J. Huang, and Y. Z. Zhang. 2017. Design and implementation of virtual interactive display system based on Kinect. *Microcomputer & its Applications*, 36(2): 41–43.

[17] Yoo, H. S., and S. W. Kim. 2014. Virtual farmers training: realistic simulation with amusements using historic simulation and game storyline. *International Journal of Multimedia & Ubiquitous Engineering*, 9(5): 121–130.

[18] Yu, X., H. Song, and S. Wang. 2016. Capture of multi-view point clouds and registration of plants based on Kinect. *International Agricultural Engineering Journal*, 25(1): 74–84.

[19] Zhao, J. C. 2016. Research on key technologies of personalized learning for farmers modern distance education. Ph.D. diss., Chinese Academy of Agricultural Sciences, Beijing.

[20] Zhu, Z. J., and S. Q. Liu. 2017. Research on recommendation system based on user tag. *Modern Computer*, 30(4): 7–10.

High throughput measurement algorithm of maize ear 3D phenotype based on multi-view stereo vision

Ma Qin[1,2*], Zhang Qinchuan[1], Zhu Dehai[1,2], Guo Hao[1,2], Yang Ling[1]

(1. *College of Information and Electrical Engineering, China Agricultural University, Beijing 100083, China;*
2. *Key Laboratory of Agricultural Information Acquisition Technology (Beijing), Ministry of Agriculture, Beijing 100083, China*)

Abstract: As the manual measurement of maize ears in maize precision breeding is low-efficiency, labor-intensive, big-error and difficult to measure 3D indexes (such as row number, kernel number per row, rate of kernel loss, rate of kernel mold), a multi-view stereo vision algorithm for high throughput measurement of maize ear 3D phenotype was proposed. Considering the shape of maize ear is a solid of revolution, we analyzed several methods that acquire images of maize ear in 360 degrees, such as rotating scanner method, plain mirror imaging method and transparent board method. According to our analysis, we used a drop-and-shot method (three CCD cameras crossed 120 degrees mutually) to acquire images of maize ear in all degrees. For optimizing both speed of high throughput maize ear test (reduce full image scan) and accuracy of 3D measurement, we have done the followings: 1) Constructed the regular triangle measurement model based on triangulation, epipolar geometry and a few prior knowledges and solved contradictory equations using least square method. Hence, we can acquire depth information from three cameras that crossed 120 degrees mutually, calculate the 3D coordinates of maize ears according to parallax of three views and recover the 3D phenotype information of maize ears. 2) As the surface of maize ear is curved and the edge of maize ear region is difficult to recognize, we proposed a maize ear spatial overlap model based on regular triangle measurement model to calculate the overlap parts of three views of maize ear without laser mark. The new algorithm does not need to do a lot of image scan, image fusion and image transformation, thus, it can greatly speed up the 3D measurement process. Experiments showed that the average accuracy of maize ear 3D phenotype measurement is 93.96%. Our proposed algorithm provided significant technical and methodological base for high throughput maize ear test which is of great importance for maize ear test efficiency.

Keywords: maize ear, high throughput maize ear test, 3D phenotype, multi-view stereo vision

Citation: Ma, Q., Q. C. Zhang, D. H. Zhu, H. Guo, and L. Yang. 2017. High throughput measurement algorithm of maize ear 3D phenotype based on multi-view stereo vision. International Agricultural Engineering Journal, 26(3): 356–366.

1 Introduction

Maize ear analysis is an important part of maize new varieties breeding and it has great significance for maize production and scientific research. For the maize ear's irregular shape (solid of revolution) and uneven growth, the phenotypic trait (row number, kernel number per row, bare tip rate, lack of kernels, rate of mold kernels, etc.) acquisition device of ear needs to meet the high-throughput and all-dimensional requirements. As the large-scale precision varieties breeding of maize is developing, the shortness of manual maize ear test, such as low-efficiency, labor intensive and big error, becomes more and more serious. Therefore, it is of great importance to investigate the precise measurement algorithm of maize ear 3D phenotype.

Recently, researchers investigated both measurement algorithms and measurement devices for maize ear 3D phenotype.

Hausmann et al. (2009) developed a high-throughput system for image analysis of maize which can measure the width, height, row number and kernel number per row etc. of maize ears. Pearson (2009) developed an image-based hardware using FPGA to separate grains with slight color differences which is high-speed and

Received date: 2017-06-15 **Accepted date:** 2017-09-12

* **Corresponding author: Ma Qin,** Ph.D., Associate Professor, Major in pattern recognition and image processing, College of Information and Electrical Engineering, China Agricultural University, Beijing, 100083, China. Email: sockline@163.com.

low-cost. Zhao et al. (2015) used a modified OTSU method which combines multi-threshold segmentation and RGBM gradient descent to count the kernel number with accuracy of 96.8%. Miller et al. (2017) used sliding-window Fourier transform analysis of image intensity features and Bayesian analysis of contour points to measure the traits of maize ears and kernels on them, further they validated the method by comparing it with the typical manual method. Su et al. (2017) proposed a 3D reconstruction method of potatoes based on machine vision, and used the method to measure the length, width and thickness of potatoes with a relative accuracy of 95% and an absolute error of 3 mm. Gong et al. (2015) modeled the leaves of pakchoi and then accurately measured the leaves area of pakchoi using a stereo vision system. Shao et al. (2016-1; 2016-2) proposed a PSO (particle swarm optimization) based 3D point cloud simplification algorithm and a discrete wavelet threshold based point cloud data denoising algorithm to reconstruct stored bulk grain and estimate its volume. Gage et al. (2017) developed a tassel image-based phenotyping system (TIPS) and validated the proposed system with manual measurement, further their system could measure some characteristics that cannot be measured manually, such as curvature, fractal dimension, skeleton length and perimeter.

Wang et al. (2013; 2014) proposed a three-dimensional reconstruction method of maize ear which generates the point cloud of maize ear by binocular vision. Then they validated the method by RANSAC (Random Sample Consensus) and a method of generating panoramic image of maize ear which acquires a sequence of maize ear images in different perspectives first and then stitches these images by SIFT (Scale Invariant Feature Transform) characters. A computer vision based method which measures the area, perimeter, width and height of maize kernels by watershed segmentation was developed by Wang et al. (2011). Measuring the traits of maize ear is of importance (Cao et al., 2011; Qi et al., 2011), but it is not easy for maize ear's irregular shape. Guo et al. (2007) put forward an idea about constructing three-dimensional model of maize by using prior knowledge of maize. Liu et al. (2014) proposed a method to measure the width, length, row number and kernel number per row of maize ear by rotating the maize ear and acquiring a sequence of images. This method processes one maize ear for about 102 seconds with accuracy about 95%. Ma et al. (2012) measured the 3D traits by one single image using HSV histogram segmentation algorithm. Yang et al. (2011) determined the best single character in the selected characters by using those characters to classify maize varieties with linear regression. Liu et al. (2013) generated the panoramic image of maize ear by a line scan camera and then stitched those images by cross correlation of selected template. This method counted the kernels number and kernel rows number with accuracy of 94.6% and 99.1%, respectively. Wu et al. (2013) developed an automatic test instrument for maize. The equipment processes one sample for about 20 seconds with accuracy of 97%. Han et al. (2010) proposed a machine vision based method to count maize ear rows by edge marker and discrete curvature, the absolute error and relative error of this method are 0.103% and 0.66%, respectively. Duan et al. (2014) proposed a camera calibration method for maize measurement based on binomial distribution and least square method. Liang et al. (2016) developed a novel maize kernel scorer to automatically measure 12 maize kernel traits using line-scan imaging and image processing and automatic control technique, the mean relative error of manual and automatic measurement is less than 5% while processing one maize ear for 6 seconds. Du et al. (2016) proposed a maize ear phenotyping method based on distribution map of kernels. The method captured a sequence of maize ear images by rotating the maize ear with a stepper motor and then used distortion correction method to generate a sequence of standard maize ear images. The method measured row number, kernel number, width and length of maize ear with an accuracy of 94%. Wen et al. (2016) proposed a modeling method of maize ear based on 3D point cloud. They used a 3D scanner to obtain the 3D point cloud data of maize ear and generated precise model of maize ear using about 200 seconds per maize ear.

In conclusion, most solutions of automatic maize ear 3D phenotyping used panoramic photography, image mosaic and image fusion which are complex and time-consuming, hence they cannot meet the requirement of high throughput maize ear test. In order to meet the requirement of high throughput maize ear test, we proposed a high throughput measurement algorithm of maize ear 3D phenotype based on triangulation and a few prior knowledges of maize ear, constructed regular triangle measurement model (RTMM) of maize ear, implemented depth measurement of RTMM and restored maize ear 3D phenotype. We further developed a maize ear spatial overlap model (MESOM) based on RTMM to calculate the overlap parts in three views of maize ear without laser mark and eliminate the overlap parts. Our proposed algorithm avoided a lot of images scanning, images transformation and images fusion, used RTMM and MESOM to calculate maize ear 3D phenotype. Hence, we can speed up the 3D measurement process a lot which is significant for improving the efficiency of maize ear test.

2 Materials and method

High throughput maize ear test devices need to obtain all-dimensional information of maize ear and need to be fast and precise enough at the same time. As the shape of maize ear is solid of revolution, we considered rotating scanner method, plain mirror imaging method and transparent board method. Finally, a drop-and-shot method (three CCD cameras crossed 120 degrees mutually) was adopted to acquire images of maize ear in all degrees which is shown in Figure 1. We can see in Figure 1 that our device consisted of a black box, a tube to drop maize ear, several light sources and three CCD cameras (two-megapixel cameras, three cameras crossed 120 degrees mutually to acquire images of maize ear in all degrees). As Figure 2 displayed, we called the camera at the top of Figure 2 the top camera, the camera at the left of Figure 2 the left camera and the camera at the right of Figure 2 the right camera.

Our proposed new algorithm for high throughput maize ear measurement contained the following three steps:

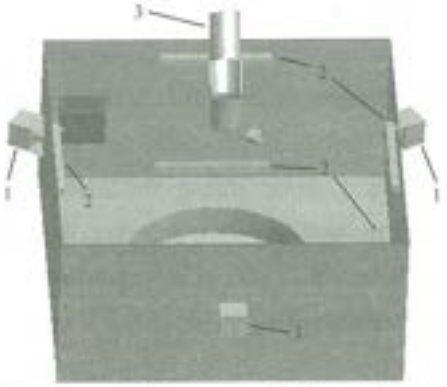

1. CCD cameras 2. Light sources 3. A tube to drop maize ear

Figure 1 Design of image acquisition device

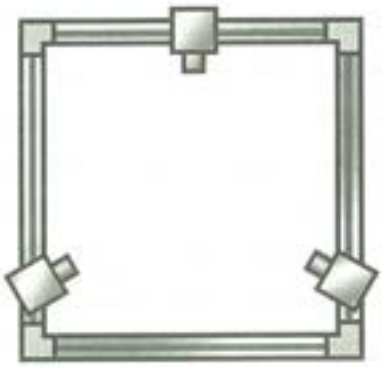

Figure 2 Distribution of cameras

1) Image acquisition and 3D calibration. Due to the non-standard distribution of cameras (three cameras distributed as a regular triangle rather than two cameras placed closely in parallel), we could not use traditional calibration method, such as Hartley algorithm and Bouguet algorithm. Thus, our algorithm calibrated three cameras pairwise and then associated three cameras by a central camera. We firstly obtained the intrinsic matrix of every camera respectively and then calculated the rotation matrix R and translation matrix T pairwise to determine the spatial relationship of three cameras.

2) Construction of RTMM of maize ear. We constructed our RTMM using triangulation and a few prior knowledges, measured depth information of spatial points using epipolar geometry and least square method solving contradictory equations, calculated spatial coordinate of maize ear using parallax of three views of maize ear so that we can measure maize ear 3D phenotype.

3) Construction of MESOM. As the surface of maize ear is curved surface and the edge region of maize ear in every view is difficult to recognition, we constructed MESOM based on RTMM to the overlap parts in three views without laser mark and eliminate the overlap parts.

2.1 Camera 3D calibration

3D calibration needs to correct error brought by manufacturing and installing our device, although three cameras crossed 120 degrees mutually in theory.

We performed 3D calibration by the following three steps.

Step 1: We used a 9*6 white and black chessboard as calibration object and applied Zhengyou Zhang's calibration method to calibrate every single camera. Zhang's calibration method obtained intrinsic and extrinsic parameters of camera by calculating several homography matrices of white and black chessboard in different poses. Figure 3 was the white and black chessboard we used, Figure 4 was the result of corner recognition of the chessboard and Figure 5 displayed the calibration result of single camera.

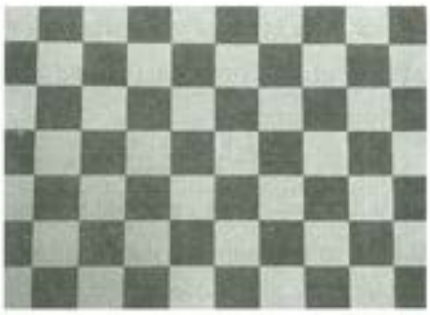

Figure 3 White and black chessboard

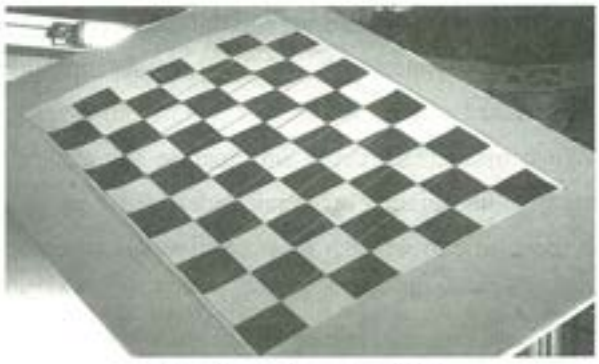

Figure 4 Corner recognition

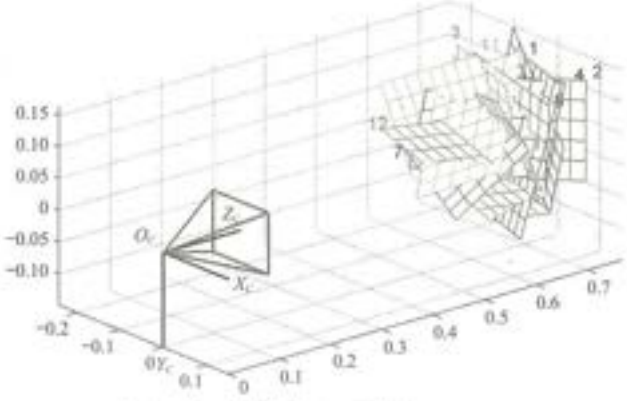

Figure 5 Calibration of single camera

Step 2: In order to calculate the rotation matrix R and translation matrix T between two cameras, we calculated the extrinsic parameters of two cameras respectively as Formula (1), where P_l is the coordinate of point P in left camera system, P_r is the coordinate of point P in right camera system, R_l is the rotation matrix of left camera, R_r is the rotation matrix of right camera, T_l is the translation vector of left camera, T_r is the translation vector of right camera, P is the coordinate of point P in object system.

$$\begin{cases} P_l = R_l P + T_l \\ P_r = R_r P + T_r \end{cases} \tag{1}$$

Two cameras can be associated by a rotation matrix R and a translation vector T as Formula (2) showed.

$$P_l = R^T(P_r - T) \tag{2}$$

Combined formulas (1) and (2), we can reduce Formula (3) to calculate R and T.

$$\begin{cases} R = R_r(R_l)T \\ T = T_r - RT_l \end{cases} \tag{3}$$

Extrinsic parameters of every single camera can be calculated by Zhengyou Zhang's calibration method. And then we can solve R and T by substituting the extrinsic parameters to Formula (3).

Step 3: To make sure that optical axes of two cameras are in parallel and in the same direction, we can decompose rotation matrix R into r_1 and r_2, use these matrices to rotate images of two cameras to one plane. Further, to align the lines in two images, we have to calculate an alignment matrix R_{rect} which maps the polar point of one camera to infinity.

We calibrated three cameras pairwise and associated three cameras by a central camera. Figure 6 displayed two views of the same object captured by two cameras. Figure 7 displayed the simulation result of 3D calibration of two cameras which claimed that the accuracy of our algorithm is reasonably high.

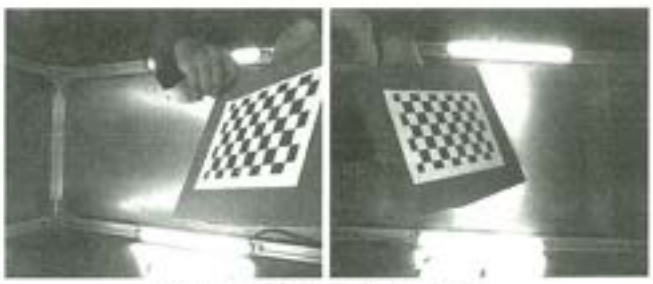

Figure 6 Views of two cameras

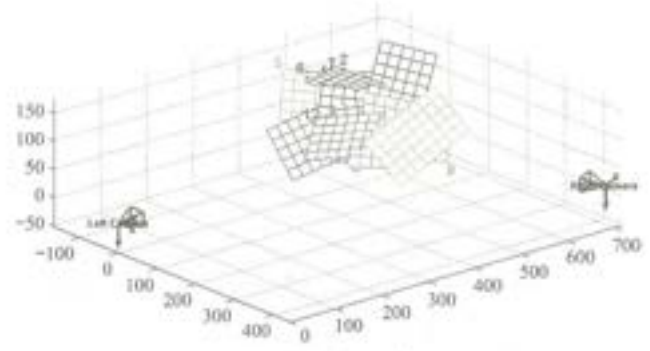

Figure 7 3D calibration of two cameras

2.2 Construction of RTMM of maize ear

We can extract the contour of dropping ear in image by frame difference method. The result is shown in Figure 8.

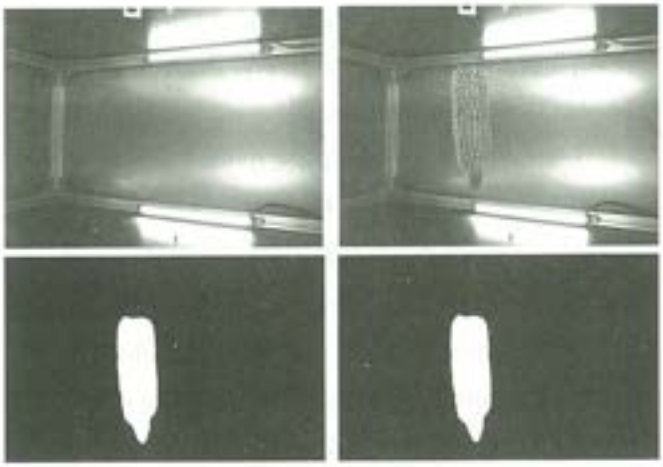

Figure 8 Contour extraction of dropping ear by frame difference method

2.2.1 Epipolar geometry and solve intersection of spatial lines

An observation point in the image plane is corresponded to infinite points in the three-dimensional space. These points are located on the line connecting camera shooting origin and observation point. In this paper, left-camera coordinate system is chosen as world coordinate system, so camera shooting origin O_l is coordinate origin. The task is to calculate Z coordinate value in world coordinate system for three-dimensional space observation point P, which also means the depth information is in front of the camera.

Let the coordinate of P be (X, Y, Z) and let the coordinate of P_l be (x_l, y_l, f_l). P_l is the observation point in left-camera image plane of P. Then, the parametric equation of spatial line is as follows:

$$P = t_l P_l \tag{4}$$

where, t_l is parameter need to calculate, coordinate value of P can be expressed as $(t_l x_l, t_l y_l, t_l f_l)$.

In the same way, set right-camera coordinate system as current coordinate system and give parametric equation of spatial line between P and the observation point in right-camera image plane of P, P_r. But two equations are not in the same coordinate system, it is necessary to convert P_r to world coordinate system firstly. The Formula is expressed as:

$$P'_r = R^T P_r + T \tag{5}$$

where, R and T are the rotation matrix and translation matrix between left-camera and right-camera calculated in 2.1.

Meanwhile, obtain the coordinate value of word coordinate system for the right-camera shooting origin O_r, the value is T. So the parametric equation of spatial line $O_r P_r$ is as follows:

$$P = T + t_r(P'_r - T) = t_r R^T P_r + T \tag{6}$$

Then, according to Formulas (4) and (6), the new Formula is as following:

$$t_l P_l = t_r R^T P_r + T \tag{7}$$

Solve the equations could calculate parameters t_l and t_r, then it is easy to compute the depth information of P. But in the actual measurement process exists camera noise and other measurement errors, it causes that the two spatial lines are non-co-planar and then the equations are contradictory equations. In 2.3.2, use other method to solve the equations.

We can calculate depth information for every two cameras of those three cameras and take advantage of their mean to correct each other so that we can obtain a more accurate result.

2.2.2 Solve contradictory equations

Solve the Equations (7) to calculate the intersection of spatial line, but in actual measurement process the equations are contradictory equations sometimes, that is the two straight lines of actually solving progress may be non-co-planar, the reasons are as follows:

Image noise and accuracy of extract contour, it causes the corresponding points-pairs we selected is not the corresponding points-pairs of actual environment

The errors of calibration progress

The Formula (7) is summarized as:

$$At = T \tag{8}$$

where, A is one 2×3 matrix; t is the 2-dimensional vector needs to solve. The Equations (8) may be contradictory equations because the number of equations are more than variables. Define residual δ of the equations as follow:

$$\delta_i = \sum_{j=1}^{2} a_{ij} t_j - T_i,\ i = 1,2,3 \tag{9}$$

The current task is to solve $t=[t_1, t_2]^T$ and make sure the residual δ is minimum. Define vector $e=[\delta_1, \delta_2, \delta_3]^T$ and judge magnitude of residual by e. This algorithm use minimal 2-norm method

$$\|e\|_2 = \left(\sum_{i=1}^{3} \delta_i^2\right)^{\frac{1}{2}} = \left\{\sum_{i=1}^{3}\left[\sum_{j=1}^{2} a_{ij} t_j - T_i\right]^2\right\}^{\frac{1}{2}} \tag{10}$$

Define two-variables function $Q(t_1,t_2) = \sum_{i=1}^{3} \delta_i^2$, then the problem of solving minimal 2-norm can be converted to the problem of solving the minimum point of the function. For the minimum point of multivariate function, the value of the partial derivative is zero, just like:

$$\begin{bmatrix} \frac{\partial Q}{\partial t_1} \\ \frac{\partial Q}{\partial t_2} \end{bmatrix} = 2\begin{bmatrix} a_{11} & a_{21} & a_{31} \\ a_{12} & a_{22} & a_{32} \end{bmatrix}\begin{bmatrix} \sum_{j=1}^{2} a_{1j} t_j - T_1 \\ \sum_{j=1}^{2} a_{2j} t_j - T_2 \\ \sum_{j=1}^{2} a_{3j} t_j - T_3 \end{bmatrix} = \begin{bmatrix} 0 \\ 0 \end{bmatrix} \tag{11}$$

The Formula (11) can be formed $2A^T(AT-T)=0$. Then form to regular linear equations, the final form is:

$$A^T A t = A^T T \ . \tag{12}$$

The solution of this equation is the least square solution of the original contradictory equations. The solution is the unique solution of the original equations when the value of minimum of residual is zero. So solve Equations (12) to instead of solving the original contradictory equations.

2.2.3 Convert image pixel coordinates to image physical coordinates

Before calculate the depth information of the observation point using Formula (12), it is necessary to convert image pixel coordinates of image coordinate system to image physical coordinates of camera coordinate system.

It is achieved by intrinsic parameter matrix of camera to convent coordinate from camera physical coordinate system to image coordinate system. How can the method convent point from image coordinate system to image physical coordinate system is as the following:

$$p = M^{-1} q \tag{13}$$

where, p is the coordinate of image physical coordinate system; q is coordinate of image coordinate system; M is the intrinsic parameter matrix of camera.

2.3 Maize ear spatial overlap model

Overlapping parts exist when three cameras acquire the dropping maize ears, so it is necessary to remove the overlapping part to prepare for phenotype measurement next step.

2.3.1 Locate position of maize ear

Before calculate the overlap parts of maize ear, we have to locate the maize ear. Hence, we need to select two prior points that are easy to find in three views of maize ear. Our algorithm selected midpoint and quartile as such points. We can calculate the spatial coordinate of midpoint (so is quartile) so that we can locate the maize ear:

Step 1. Calculate the minimum enclosing rectangles of maize ear in three views.

Step 2. Calculate the center points of the minimum enclosing rectangles in three views.

Step 3. Use RTMM to calculate the spatial coordinate of midpoint.

2.3.2 Calculate the overlapping parts

The next task is to calculate the overlapping parts of maize ear when three cameras acquire the image of dropping maize ear, the overlapping parts are only necessary to calculate once.

First some prior facts are as follows:

The angle between optic axis of two cameras is not accurate 120°, this angle needs to calculate by calibration because of the hardware equipment errors.

The center of maize ear is hard to fall the equidistant position of three cameras. The distance from the point to three cameras should be calculated by RTMM in actual environment.

The center of maize ear is not at the center axis of image because of irregular position of ear, so this model could not be established by nature of center axis.

As it is shown in Figure 9, the maize ear is almost dropping vertically because of hardware equipment. The observation plane of maize ear can be considered as a circle approximately. Define O_{top}, O_{left} and O_{right} as the shooting centers of top, left and right camera. Define T_1,

T_2, L_1, L_2, R_1, R_2 as the edge points of maize ear observed by clockwise. It is easy to find arc T_1L_2, arc R_1T_2 and arc L_1R_2 are the overlapping parts of ear.

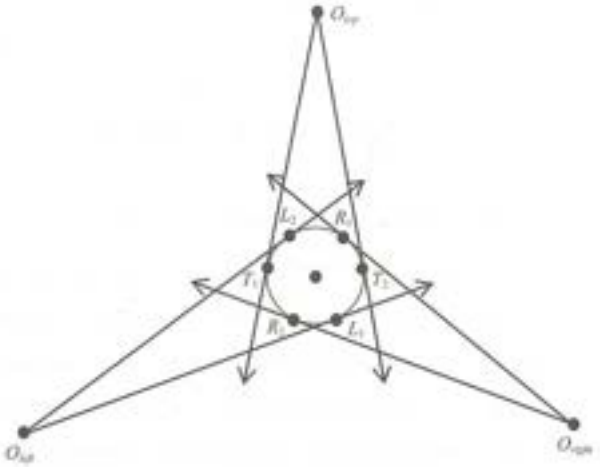

Figure 9 Schematic diagram of spatial overlap region

Then the task is to calculate coordinate of these points. The coordinate calculation method of three cameras is consistent, take the top camera as an example, the calculation model is shown in Figure 10.

Figure 10 Calculation model of tangency for top-camera

where, T_1, T_2 are tangency of circle C, the radius value is half of ear diameter. The coordinate of point C is calculated by RTMM, so it is easy to calculate the length of tangent O_tT_1 and O_tT_2 by Pythagorean theorem.

Set the coordinate of point C as (x_c, y_c, z_c), the length of two tangents as l, the radius of circle as r, then the plane equation of circle C is:

$$(x-x_c)^2+(z-z_c)^2=r^2 \tag{14}$$

At the same time, the distance from O_t to tangency is:

$$x^2+z^2=l^2 \tag{15}$$

The coordinate of T_1 and T_2 can be computed by Formula (14) and Formula (15). Set $a=l^2+x_c^2+z_c^2-r^2$ and the coordinate of T_1 and T_2 can be expressed as:

$$\begin{cases} x_1=\dfrac{3a-\sqrt{a^2+2l^2x_c^2}}{4x_c} \\ z_1=\dfrac{-a+\sqrt{a^2+2l^2x_c^2}}{4z_c} \end{cases}, \quad \begin{cases} x_2=\dfrac{3a+\sqrt{a^2+2l^2x_c^2}}{4x_c} \\ z_2=\dfrac{-a-\sqrt{a^2+2l^2x_c^2}}{4z_c} \end{cases} \tag{16}$$

The coordinate that computed is based on own camera coordinate system, convent the coordinate to corresponding camera coordinate system by Formula $P'=R^TP+T$, the matrix R and T are computed in camera calibration process in the preceding paragraphs.

After these calculation steps for every camera of three, the coordinate of four points about overlapping parts of every camera are calculate achieved. Then remove overlapping parts unnecessary to calculate for three cameras by some rules. In this paper, the rule is only to calculate clockwise direction overlapping parts for every camera, anti-clockwise direction overlapping parts is calculated for the camera anti-clockwise direction to current camera.

2.4 Calculate row number and grain number of maize ear

2.4.1 Choose calculation region of row number

The kernels located at the edge of maize ear image are hardly to observe clearly due to projection deformation, so it is necessary to remove the edge area while calculating row number. For the overlapping parts of three cameras, the row number may be counted twice, so remove these areas to improve precision.

In this paper, cut maize ear image before compute row number, the cutting methods are as follows:

Remove the head and tail of the ear, only left the center area of maize ear (the length half of ear length).

Remove the area that does not need to calculate by Maize ear spatial overlap model.

Choose 80% of residual width region in right align as final counting region.

The schematic diagram of region selection is shown in Figure 11.

2.4.2 Kernel contour extraction

In this paper, use the maize ear contour calculate in the above as mask at first, then separate G color channel of maize ear image and extract kernel contour by OTSU threshold method, as shown in Figure 12.

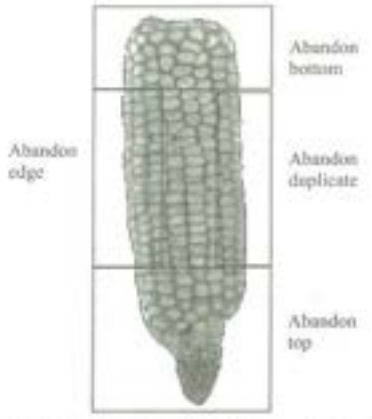

Figure 11 The schematic diagram of row number region selection

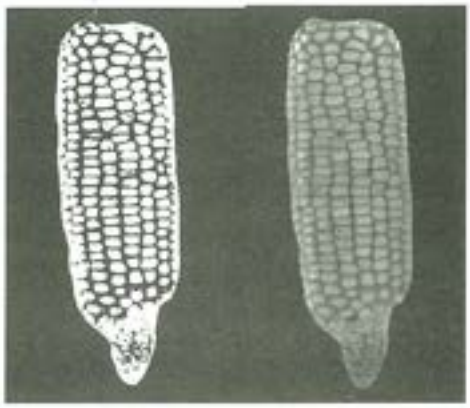

Figure 12 Contour extraction of kernels

2.4.3 Row number calculation of main area

The grains located in middle position of maize ear are regular arrangement relatively, row number at main area is shown in Figure 13. As Figure 13 shows, the image is alternatively composed of the kernel area and the kernel joint area. The kernel area has more white pixel point and the kernel joint area contains more black pixel point. In this paper, use the statistical Formula (17)

$$p_i = \sum_{j=1}^{y} f(i, j),\ i = 1,2,3,\ldots,x \qquad (17)$$

where, $f(i, j)$ is pixel value for the point which located at (i, j) coordinate of the image. The pixel value of white pixel point and black pixel point are 0, 1 respectively. x and y are width and height of main area.

Figure 13 Main area to count row number

Use Formula (17) to count for each column of the image, then a statistical graph is obtained. The statistical graph is shown in Figure 14, it seems like wave line. The wave crest in the graph is kernel area and wave trough is kernel joint area. So the number of wave crest is row number in main area. It is contained 5 wave crests in this image and the row number in actual image is 5.

Figure 14 The statistical graph of row number

2.4.4 Row number calculation of edge region

The errors are big when do row number calculation of edge region, so in this paper, edge region proportion model (ERPM) is established to calculate kernel of edge region. The schematic diagram of ERPM is shown in Figure 15.

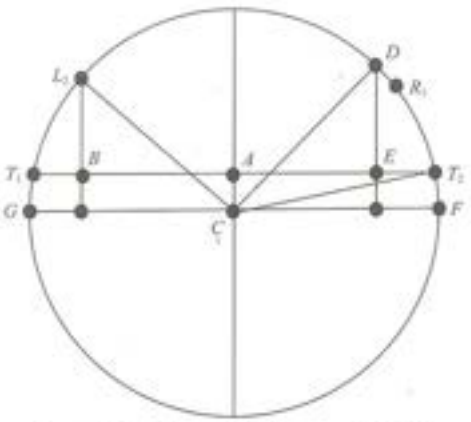

Figure 15 Schematic diagram of ERPM

Set top camera as current camera, T_1T_2 is the maximum width top camera acquired. Arc L_2D is main area and arc DT_2 is the edge region. The coordinate of circle center C is known, so the sinusoidal value of $\angle T_2CF$ is $\frac{r}{l}$, l is the distance between C to origin point. The cosine value of $\angle T_2CF$ is $\frac{AT_2}{r}$. So the length of AT_2 is

$$AT_2 = a = \frac{r}{l}\sqrt{l^2 - r^2} \tag{18}$$

Then the length of AE, ET_2, and AB can be calculated by ration. Set $E=b$, $AB=c$, $\angle T_2CF=\theta$, $\angle T_2CD=\gamma$, $\angle T_2CP=\varphi$, then these formulas can be derived

$$\begin{cases} \theta = \arcsin\dfrac{r}{l} \\ \gamma = \arccos\dfrac{b}{r} - \theta \\ \varphi = \dfrac{\pi}{2} + \arccos\dfrac{c}{r} - \gamma - \theta \end{cases} \tag{19}$$

The ratio between γ and φ is equal to the ratio between main area arc L_2D and edge region arc DT_2. Then the row number of edge region can be calculated by the ratio and the row number of main area.

Each camera can get the number of rows in the area it is in charge of and after which it is calculated after the number of rows in the main area and the number of rows in the edge region. Due to the overlapping area before processing, the information of the number of rows that are processed by the three views will not be repeated, that is to say, the results of the number of rows per row in the final three views should be:

$$r = r_{top} + r_{left} + r_{right} \tag{20}$$

It must be noted that the number of rows here is a floating point number while the actual number of rows should be even, so the statistical results should be even to the nearest integer.

According to the statistical method of row number, the same method can be applied to the number of parameters, statistical calculation of X axis pixel accumulation, which can avoid the interference of a small number of grains or defects effectively.

3 Results and discussion

Take 10 ears of maize, and collect three views of the images at the same time, total 30 data, and the center of gravity for the extraction of ear contour correspondence, which to solve the problem of the RTMM, the distances between maize ear center and three camera centers respectively. Compared with manual measurement, the average accuracy of our proposed algorithm is 93.96% which is shown in Table 1.

We further use our proposed algorithm to calculate the row number and kernel number per row, which can verify that our measurement of row number and kernel number per row is also feasible. The analysis of row number and kernel number per row of the above 10 samples is as shown in Table 2 and Table 3.

Table 1 Table of accuracy analysis of RTMM

Camera	Average error	Minimum error	Maximum error	Standard deviation
Top	6.24%	2.62%	9.51%	0.018
Left	5.96%	2.34%	8.97%	0.021
Right	5.92%	3.94%	7.87%	0.014

Table 2 Results for row number

Index	1	2	3	4	5	6	7	8	9	10
Manual	16	18	18	14	16	18	18	16	18	16
Paper Method	16	18	18	14	16	16	18	16	18	16

Table 3 Results for kernel number per row

Index	1	2	3	4	5	6	7	8	9	10
Manual	27.67	28.33	31.67	30.33	29	30.33	33.33	30.67	29.33	30
Paper Method	28.56	27.44	33.13	31.76	30.99	28.38	32.54	29.17	28.66	31.73

In Table 3, the actual number of rows is measured by the number of lines of the main three rows and then the average number of lines. It can be concluded according to the data from table that, the zero-error rate of the measurement of row number is 100% and the measurement error of the kernel number per row is less than 2.

4 Conclusion

As manual measurement in maize precision breeding is low-efficiency, labor-intensive and difficult to measure 3D phenotype (row number, kernel number per row, rate of kernel loss and rate of kernel mold), we developed a new high throughput measurement algorithm of maize ear 3D phenotype based on multi-view stereo vision. For both high throughput maize test speed and precise 3D measurement, we have done the followings:

1) We analyzed standard structure of binocular vision whose optical axes of cameras are parallel. Then we developed our RTMM of maize ear. We constructed our model using triangulation and a few prior knowledges, measured depth information of spatial points by epipolar geometry and solving contradictory equations using least square method and calculated spatial coordinate of maize ear by parallax.

2) The edge parts of maize ear in every view is difficult to recognize because the surface of maize ear is curved. To solve this problem, we proposed a MESOM model based on RTMM to calculate the overlap parts in three views of maize ear and eliminate the overlap parts without laser mark. We combined RTMM and MESOM to measure maize ear 3D phenotype which avoided a lot of image scanning, image fusion and image transformation and speeded up 3D measurement a lot.

3) Our algorithm had 93.96% average accuracy in 3D measurement, 100% accuracy in maize ear row number measurement and error less than 2 in measuring kernel number per row.

Our algorithm provided important technical and methodological base for high throughput maize ear test which is significant for improving efficiency of maize ear test.

Acknowledgements

We would like to thank to the reviewers for their helpful comments. This work was financially supported by the Chinese Universities Scientific Fund (#2017XD002) and the Special Fund for Agro-scientific Research in the Public Interest (#201203026).

[References]

[1] Cao, J. H., Y. Z. Ran, and J. C. Guo. 2011. The design and realization of corn test system. *Journal of Changchun Normal University*, 30(4): 38–41.

[2] Du, J. J., X. Guo, C. Wang, and B. Xiao. 2016. Computation method of phenotypic parameters based on distribution map of kernels for corn ears. *Transactions of the Chinese Society of Agricultural Engineering*, 32(13): 168–176. (in Chinese with English abstract).

[3] Duan, X. C., J. H. Zhou, and S. J. Wang. 2014. Image calibration method for the ear of corn measurement system. *Journal of Agricultural Mechanization Research*, 36(1): 76–79.

[4] Gage, J. L., N. D. Miller, E. P. Spalding, S. M. Kaeppler, and D. N Leon. 2017. TIPS: a system for automated image-based phenotyping of maize tassels. *Plant Methods*, 13(1): 21.

[5] Gong, L., R. Chen, Y. S. Zhao and C. L. Liu. 2015. Model-based in-situ measurement of pakchoi leaf area. *International Journal of Agricultural and Biological Engineering*, 8(4): 35–42.

[6] Guo, X. Y., C. J. Zhao, Y. Liu, X. Y. Qin, X. Y. Deng, and G.Y.Sun. 2007. Three-dimensional visualization of maize based on growth models. *Transactions of the Chinese Society of Agricultural Engineering*, 23(3): 121–125. (in Chinese with English abstract).

[7] Han, Z. Z., and J. Z. Yang. 2010. Vision research on the machine of counting ear rows in maize. *Journal of Maize Sciences*, 18(2): 146–148, 152.

[8] Hausmann, N. J., T. E. Abdaie, and C, Mark. 2009. Method and system for digital image analysis of maize: US. WO2009023110(A1).

[9] Liang, X. Y., K. Wang, C. L. Huang, X. H. Zhang, J. B. Yan, and W. N. Yang. 2016. A high-throughput maize kernel traits scorer based on line-scan imaging. *Measurement*, 90: 453–460.

[10] Liu, C. Q., and B. Q. Chen. 2014. Method of image detection for ear of corn based on computer vision. *Transactions of the Chinese Society of Agricultural Engineering*, 30(6): 131–138. (in Chinese with English abstract).

[11] Liu, G. Y., X. H. Yang, M. Bai, and H. Li. 2013. Detecting techniques of maize ear characters based on line scan image. *Transactions of the Chinese Society for Agricultural Machinery*, 44(11): 276–280. (in Chinese with English abstract).

[12] Ma, Q., J. T. Jiang, D. H. Zhu, S. M. Li, S. L. Mei, and Y. C. Liu. 2012. Rapid measurement for 3D geometric features of maize ear based on image processing. *Transactions of the Chinese Society of Agricultural Engineering*, 28(Supp.2): 208–212. (in Chinese with English abstract).

[13] Miller, N. D., N. J. Haase, J. Lee, S. M. Kaeppler, N. de Leon, and E. P. Spalding. 2017. A robust, high-throughput method for computing maize ear, cob, and kernel attributes automatically from images. *Plant Journal for Cell and Molecular Biology*, 89(1): 169–178.

[14] Pearson, T. 2009. Hardware-based image processing for high-speed inspection of grains. *Computers and Electronics in Agriculture*, 69(1): 12–18.

[15] Qi, J. T., S. H. Zhang, X. T. Niu, and Y. Xu. 2011. Design and application of yield monitor system for corn ear. *Transactions of the Chinese Society for Agricultural Machinery*, 42(1): 181–185. (in Chinese with English abstract).

[16] Shao, Q., T. Xu, T. Yoshino, Y. J. Zhao, and W. T. Yang. 2016. Point cloud simplification algorithm based on particle swarm optimization for online measurement of stored bulk grain. *International Journal of Agricultural and Biological Engineering*, 9(1): 71–78.

[17] Shao, Q., T. Xu, T. Yoshino, N. Song, and H. Zhu. 2016. Classified denoising method for laser point cloud data of stored grain bulk surface based on discrete wavelet threshold.

International Journal of Agricultural and Biological Engineering, 9(4): 123–131.

[18] Su, Q. H., N. Kondo, M. Li, H. Sun, and D. F. A. Riza. 2017. Potato feature prediction based on machine vision and 3D model rebuilding. *Computers and Electronics in Agriculture*, 137(C): 41–51.

[19] Wang, C. Y., X.Y. Guo, W. L. Wen, and T. Miao. 2011. The measurement of maize kernel shape based on computer vision. *Journal of Agricultural Mechanization Research*, 33(6): 141–144.

[20] Wang, C.Y., X.Y. Guo, S. Wu, B. Xiao, and J. Du. 2013. Investigate maize ear traits using machine vision with panoramic photography. *Transactions of the Chinese Society of Agricultural Engineering*, 29(24): 155–162. (in Chinese with English abstract).

[21] Wang, C. Y., X. Y. Guo, S. Wu, B. Xiao, and J. Du. 2014. Three dimensional reconstruction of maize ear based on computer vision. *Transactions of the Chinese Society of Agricultural Machinery*, 45(9): 274–279. (in Chinese with English abstract).

[22] Wen, W.L., Y. Wang, T. Y. Xu, T. Yang, and X. Guo. 2016. Geometric modeling of maize ear based on three-dimensional point cloud. *Journal of Agricultural Science and Technology*, 18(5): 88–93.

[23] Wu, J. W., X. Y. Guo, and C. Y. Wang. 2013. Automatic test instrument for maize test. *China Seed Industry*, 9: 51–52.

[24] Yang, J. Z., H. S. Zhang, J. P. Hao, T. Q. Du, F. Z. Cui, N. N. Li, and G. M. Liang. 2011. Identifying maize cultivars by single characteristics of ears using image analysis. *Transactions of the Chinese Society of Agricultural Engineering*, 27(1): 196–200. (in Chinese with English abstract).

[25] Zhao, M.M., J. Qin, S. M. Li, Z. Liu, J. Cao, X. H. Yao, S. J. Ye, and L. Li. 2015. An automatic counting method of maize ear grain based on image processing. *Computer and Computing Technologies in Agriculture VIII*, 452: 521–533.

Image segmentation method of adherent corn ears based on improved watershed

Zhang Ya[1], Ma Qin[1,2*], Zhu Dehai[1,2], Liu Zhe[1], Zhang Xiaodong[1], Zhang Fan[1]

(1. *College of Information and Electrical Engineering, China Agricultural University, Beijing 100083, China;*
2. *Key Laboratory of Agricultural Information Acquisition Technology, Ministry of Agriculture, Beijing 100083, China*)

Abstract: Aiming at the problem of corn ears adhering in the process of corn test, the images of adherent corn ears were taken in the whole plot as our research object, and image segmentation method of adherent corn ears based on improved watershed was studied. We mainly proposed an improved watershed segmentation method based on limit corrosion and convex hull detection for common adherent corn ears, such as weak adherent corn ears, ring adherent corn ears, strong adherent corn ears and mixed adherent corn ears. The method can not only divide a variety of common sorts of the adherent corn ears, but also quantitatively calculate the lengths and diameters of the corn ears after the effective correction of the image distortion and the two-dimensional calibration of the image. Experimental results showed that the improved watershed segmentation method could achieve automatic segmentation for common adherent corn ears. The average accuracy rate of the ear length is 97.79%, and the average accuracy rate of the ear diameter is 96.70%. The accuracy rate of the whole system has reached 97.24%. This study provided an important technical basis for the measurement of characteristic parameters of adherent corn ears, and also an important solution to the segmentation problem of class cylinder.

Keywords: corn test, adherent corn ears, improved watershed, image segmentation

Citation: Zhang, Y., Q. Ma, D. H. Zhu, Z. Liu, X. D. Zhang, and F. Zhang. 2017. Image segmentation method of adherent corn ears based on improved watershed. International Agricultural Engineering Journal, 26(3): 367-374.

1 Introduction

Corn test is an important link in the process of genetic breeding of corn crops. It is very important to rapidly and accurately measure the characteristic parameters of corn ears for improving the technology of scientific seed selection and breeding efficiency (Wu et al., 2016). Traditional corn test work mainly relies on manual identification leading to many disadvantages, such as large workload, low efficiency and low precision. Although some of the corn test equipment can automatically collect and identify the characteristic parameters of corn ears, most equipment is multi-channel mode. For the corn ears in the whole plot, high-throughput automated pipeline without artificial adjustment or put the corn ears on the portable object stage arbitrarily or the overall dumping the corn ears cannot avoid the problem of corn ears adhesion. Therefore, in order to realize the high-throughput automatic measurement of the characteristic parameters of the corn ears and improve the measurement precision and efficiency, the problem of automatic segmentation of the adherent corn ears needs to be solved urgently.

In recent years, researchers have applied the machine vision technology to achieve the high-throughput automatic measurement of characteristic parameters of the corn ears (Wang et al., 2014; Li et al., 2016; Liu and Chen, 2014; Liu et al., 2011; Manickavasagan et al., 2008; Pearson, 2009). In order to solve the problem of corn text, researchers have proposed a variety of adhesion image segmentation methods, mainly including corrosion expansion method (Li et al., 2010; Xiao et al., 2015), watershed improvement algorithm (Gao, 2015; Ng et al., 2007; Rao and Srinivas, 2006), shape feature matching method (Zhu et al., 2009; Cai and Pang, 2011), contour

Received date: 2017-06-15 **Accepted date:** 2017-09-12

* **Corresponding author: Ma Q.,** Ph.D., Associate Professor of Department College of Information and Electrical Engineering, China Agricultural University, China. Email: sockline@163.com. Tel: 13391809180.

bump detection method (Wang et al., 2015; Wei and Zhao, 2010) and so on. Weickert et al. (2001) proposed to use the partial differential equation for image denoising and edge enhancement, which combined with the method of watershed segmentation and regional merging, but the segmentation effect for the general noise images is not obvious because of the distortion phenomenon. Xunyi et al. (2010) proposed a method based on the common area and grain contour to find the dividing point, which realized the automatic segmentation of the image of the adhesive maize grains, but the holes of maize grains could easily cause error segmentation and low accuracy. Zhou Jinhui et al. (2015) proposed a method of segmenting the contours of the adherent corn ears according to the freeman chain code tracking the gradient changes of the contours, but only the tandem adhesion of the rules can be segmented and the other types of adhesions cannot be segmented. In this paper, an improved watershed segmentation method based on limit corrosion and convex hull detection was proposed to solve the problem of adherent corn ears which are arbitrarily placed in the process of corn test. The method is fast and efficient and can solve the problem of weak adherent corn ears, ring adherent corn ears, strong adherent corn ears, mixed adherent corn ears and so on, which improves the measurement efficiency of the characteristic parameters of corn ears in the plot.

2 Materials and methods

2.1 Image collection and pretreatment

2.1.1 Definition of adherent corn ears

Weak adherent corn ears: the adhesive part, by the way of head-to-tail connection, is small and do not form an adherent ring.

Ring adherent corn ears: three or more than three corn ears form a ring-shaped adhesive structure through the pattern of weak adhesion.

Strong adherent corn ears: two or over two corn ears adhere through side by side, and the adhesive area is large but no more than the diameter of one corn ear.

Mixed adherent corn ears: the adhesive way combines of weak adhesion, ring adhesion and strong adhesion.

Several common images of adherent corn ears are shown in Figure 1.

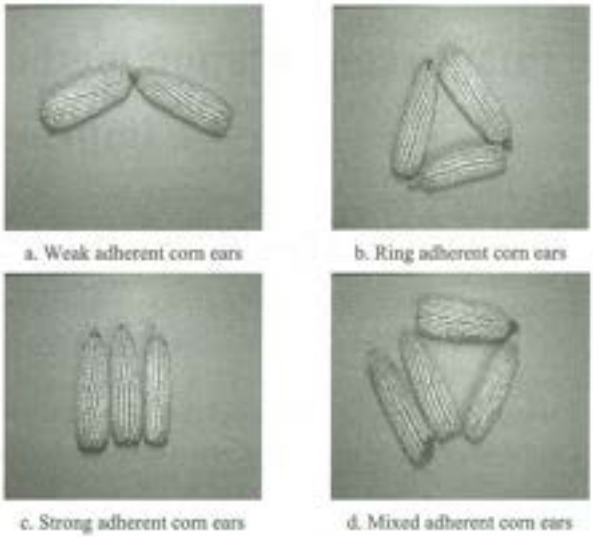

a. Weak adherent corn ears b. Ring adherent corn ears

c. Strong adherent corn ears d. Mixed adherent corn ears

Figure 1 Images of adhesive corn ears

2.1.2 Image collection

The image collection equipment is shown in Figure 2, which consists of a carrier support, an objective table, a camera and light source bracket, a high resolution 4608×3288 CCD camera and a light source. The carrier support is used to support the objective table, and the corn ears are placed in the center of the 1.2 m×0.9 m objective table. The CCD camera and the light source are respectively placed in the top position and the middle position of camera and light source bracket. The images are divided into two categories. One kinds are the small format images including 2-5 adherent corn ears, which are using for the study of segmentation algorithm for a variety of adherent corn ears, and the resolution ratio of the images are 1024×768. The other one kinds are large format images including 40 adherent corn ears, which are served as the study sample for calibration and algorithm validation.

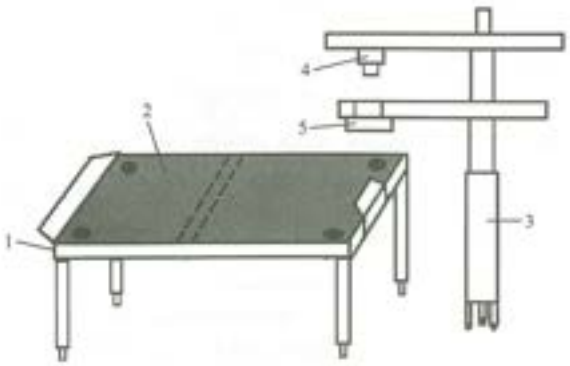

1. Luggage carrier 2. Objective table 3. Camera and light source bracket 4. Camera 5. Light source

Figure 2 Image collection equipment

2.1.3 Two-dimensional image calibration

The purpose of the two-dimensional image calibration is to correspond the distance in the image to the actual distance and find the proportion of the image, in that we can directly measure the real ear length and diameter. Distortion will cause the image loss for the camera perspective. In brief, the object is a straight line, but the image is significantly distorted. In order to accurately calibrate the image, the distortion correction is essential.

This paper regarded the 9×6 black and white grid board as the two-dimensional calibration board, in which the real length p of each small square is 20.0 mm. We found the black and white lattice points on the calibration plate by the sub-pixel level corner detection, and connected and calculated the number of long pixels of all valid square latches according to the set threshold to find the average value L. Get the system calibration parameter a is

$$a = L/p$$

After a large number of calculations, we concluded that in the 1.2 × 0.9 m format, $a = 3.85$, and in the 0.8× 0.6 m format, $a = 5.53$.

2.1.4 Image preprocessing

Image preprocessing includes image denoising and image binarization. In order to eliminate the noise in the image, the method of median filter was used into the image. In order to effectively binarize the image, the RGB histogram of the image floor, the corn ears and the shadow of the corn ears were analyzed, and the image of adherent corn ears was binarized according to feature of the RGB histogram.

2.2 Study on image segmentation algorithm

2.2.1 Convex hull detection method

There must be a convex defect due to the adhesion in the corn ears. According to the convex defect, we can find the points which have the longest distance to the convex hull line and take them as the dividing points. The adherent corn ears are divided by the method of linking the dividing points (Xi, 2013). Draw the contours of the adherent corn ears, as shown in Figure 3, where the red marks are the dividing points. From the analysis of Figure 3, it can be seen that the method of convex hull detection has a good effect on the two adherent corn ears, but it cannot find the dividing points correctly for the three adherent corn ears or over three adherent corn ears. Therefore, the applicability of convex hull detection method is not good enough, and the method will have some damages to the contours of the adherent corn ears.

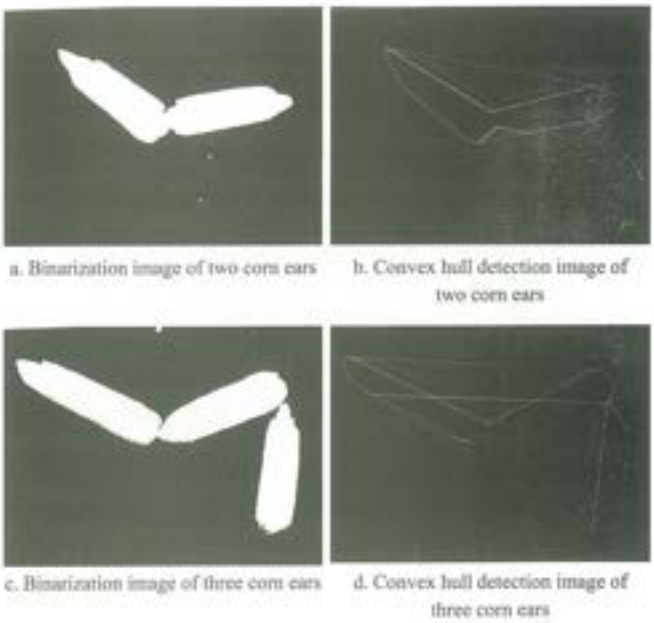

a. Binarization image of two corn ears b. Convex hull detection image of two corn ears

c. Binarization image of three corn ears d. Convex hull detection image of three corn ears

Figure 3 Images of convex packet inspection

2.2.2 Watershed algorithm

The method of watershed algorithm (Yan and Wang, 2012) is a commonly used technique in image segmentation. In the traditional watershed algorithm, each local minimum point corresponds to one segmentation region in the image, which contains both the true target minimum point and the pseudo-local minimum point which is introduced by background noise and texture details. The traditional watershed method easily leads to over-segmentation. The method of improved watershed is to improve the accuracy of watershed algorithm mainly based on the adaptive filter and the marker extraction (Yilihamu, 2013; Yu et al., 2011). However, in the actual process of corn test, the phenomenon of the corn kernels shattering is obvious, which easily causes over-segmentation by marking the location of the corn kernels shattering. Figure 4 is the effect image of the adherent corn ears by using the method of watershed segmentation.

2.3 Watershed segmentation based on limit corrosion and convex hull detection

Firstly, we should remove the disturbance of maize kernels and other impurities by the method of limit

corrosion, and corrode the adherent corn ears all the time without any contours loss until each ear is divided. Secondly, we should detect the image after corrosion by the method of convex hull detection, and find the points which have the longest distance to the convex hull line (dividing points). Finally, we should mark the binarization image by linking the dividing points and invoke the watershed algorithm, so as to achieve the segmentation of the adherent corn ears. Figure 5 is the flow diagram of the algorithm.

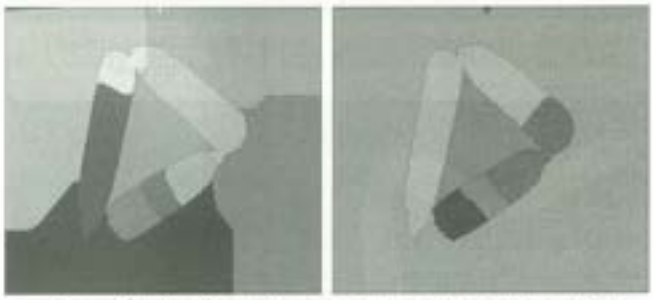

a. Image of traditional watershed algorithm b. Image of improved watershed algorithm

Figure 4 Images of watershed algorithm

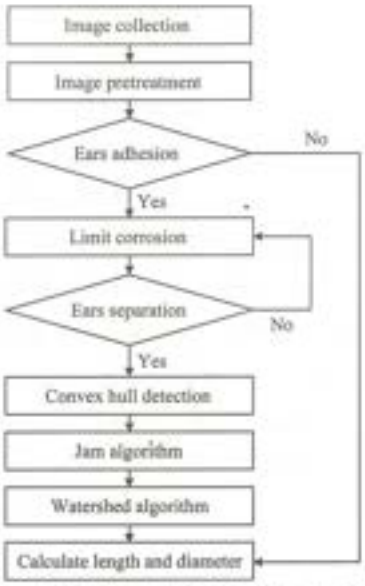

Figure 5 Image of algorithmic process

2.3.1 Judgment of adherent corn ears

Select the shape factor which describes the target boundary as the judge basis of the adherent corn ears (Li et al., 2015). The shape factor SF is defined as:

$$SF = \frac{4(2\lambda + \pi - 2)^2 S}{\lambda \pi L^2}$$

where, S is the area pixel value of a connected region; L is the perimeter pixel value of the connected region; λ is the average value of the ratio of length and diameter of the corn ears.

Measure the area pixel value of the biggest corn ear and mark it as S_{max0}. Corrode the adherent corn ears continually until they are disappeared. Record the number of corrosion as n and the area pixel values of the corn ears after each corrosion as S_{maxi} ($0<i<n$). The specific steps are as follows:

(1) Extract the area pixel value and the perimeter pixel value of each corn ear and calculate the shape factor.

(2) If the shape factor of each contour $SF>SF_0$ and $S<S_{max0}$, it can be judged that there are no adherent corn ears in the image and then the corn ears contour can be extracted. On the contrary, the image of the adherent corn ears should be corroded.

(3) Extract the area pixel value and the perimeter pixel value of each corn after the front corrosion and calculate the shape factor.

(4) If the shape factor of each contour $SF>SF_0$ and $S<S_{maxi}$ ($0<i<n$), it can be judged that the adherent corn ears in the image has been separated. On the contrary, the image of the adherent corn ears should continue be corroded after the front corrosion.

(5) Repeat the steps 3) and 4) until it can meet the condition in 4), or the number of the corrosion times has reachedn.

Figure 6 is the corrosion effect image. The first corrosion can be achieved to remove the impurities such as the kernels shattering, and the final corrosion result can separate the adherent corn ears.

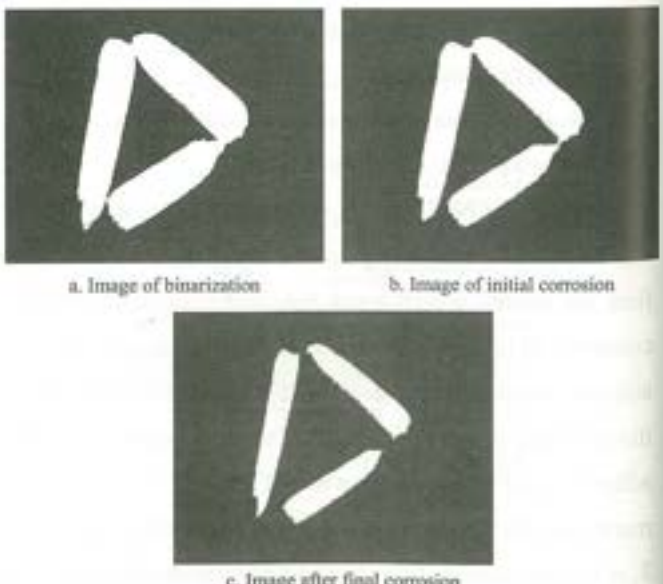

a. Image of binarization b. Image of initial corrosion

c. Image after final corrosion

Figure 6 Effect images of corrosion

2.3.2 Watershed marked with limit corrosion

Firstly, we should separate the adherent corn ears by the method of limit corrosion and detect the edge of the image after the final corrosion. The result of the edge detection is applied to the original binarization image to find the dividing points. Secondly, we should invoke the watershed algorithm which is depicted on the original binary image with black lines. Finally, we can separate the adherent corn ears, and the black lines are formed in the image, as shown in Figure 7.

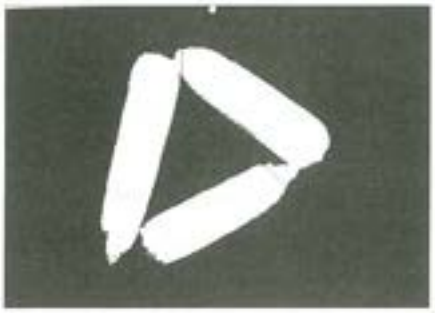

Figure7 Images of watershed marked by ultimate erosion

From the analysis of Figure 7, it can be seen that the contours of the adherent corn ears are separated by the formed black dividing lines in the image. But the position of the dividing lines is somewhat deviated, leading to contour deformation of the corn ears. The reason is that convex hulls can be formed when corrosion occurs from the outer contour of the adherent parts until the adherent parts are separated. The size and position of the convex hulls cause the result deviation after expansion and result in the position deviation of the dividing lines.

2.3.3 Convex hull detection and stuck algorithm

The method of convex hull detection can represent the contours of the adherent corn ears, and the method of stuck algorithm is the way to find the two points whose distance is farthest between the contours. The two points whose distance is farthest must be a pair of points on the convex hull, as shown in Figure 8, q_a and q_b are a pair of points on the convex hull P. L_a and L_b are two parallel lines which are respectively pass the points q_a and q_b. When the two lines L_a and L_b respectively slide along the arc C_a and C_b, they do not touch the other points on the convex hull, which proves that q_a and q_b are a pair of points whose distance are longest on the convex hull. Connect the two points, we can get the longest straight line on the contour.

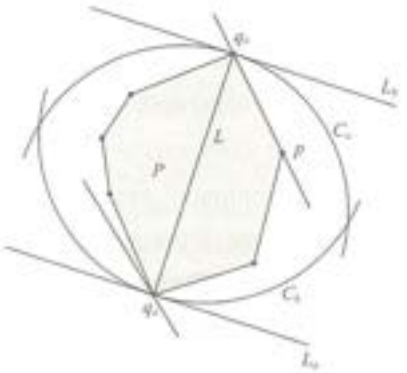

Figure 8 Image of stuck algorithm

For the corn ears after corrosion, straight lines passing through the corn ears are obtained. We should extend the straight lines according to the size of the corrosive element, and the dividing lines passing through the original corn ears are obtained. The accuracy rate of the segmentation method is high and the convexity problem is improved. Figure 9 shows the segmentation effect of adherent corn ears with the method of improved watershed algorithm based on limit corrosion and convex hull detection. The method has good overall effect in contour extraction and no serious deviation of dividing lines, and the watershed segmentation lines can be extracted accurately. Therefore, the improved watershed method based on limit corrosion and convex hull detection can effectively separate the adherent corn ears.

a. Lineation of stuck algorithm b. Watershed marked with stuck algorithm

Figure 9 Images of watershed based on ultimate erosion and convex packet inspection

3 Experiments and results

3.1 Experiment methods

Taking many crossbreed adherent corn ears, which are arbitrarily placed, as our research objects, we collected the image of adherent corn ears and regularized it. The image was calibrated by the method of two-dimensional (2D) and preprocessed as well. We separated the adherent corn ears with the method of improved watershed segmentation algorithm based on the

limit corrosion and convex hull detection and extracted the contours of each corn ear in the binary image after the adherent corn ears were separated. The pixels length and pixels diameter of the corn ears were obtained by the method of creating minimum external rectangle. The actual length and diameter of the corn ears were acquired according to the 2D calibration parameters and the stereoscopic projection correction model (Yang, 2008; Duan et al., 2014).

3.2 Segmentation algorithm accuracy verification

The error of the segmentation algorithm was determined by the length and diameter of the corn ear. In this paper, we measured the length of 40 corn ears in all kinds of adhesion with the segmentation algorithm and the true length of the 40 corn ears. The average error was calculated by comparing the true values with the measured values, as shown in Table 1. The results showed that the average accuracy of weak adherent corn ears is 97.23%, the segmentation accuracy rate of ring adherent corn ears is 96.34%, the segmentation accuracy rate of strong adherent corn ears is 96.98%, and the segmentation accuracy rate of mixed adherent corn ears is 97.13%.

Table 1 Error of segmentation algorithm validation

Adhesion Classification	Adhesion type	Average Error
Weak adhesion	Head-Head	0.03
	Head-Foot	0.04
	Foot-Foot	0.01
	Head-Body	0.03
	Foot-Body	0.03
Ring adhesion	Three Rings	0.04
	Four Rings	0.04
Strong adhesion	Two Ears	0.01
	Three Ears	0.04
	Four Ears	0.04
Mixed adhesion	Strong mixed adhesion	0.03
	Weak ring mixed Adhesion	0.04
	Strong ring mixed Adhesion	0.03

3.3 System accuracy verification

In the actual environment of corn test, the accuracy of the algorithm after the combination of two-dimensional calibration and segmentation algorithm was verified. We measured the length and diameter of 40 adherent corn ears with the method of improved watershed algorithm and the true length and the true diameter of the 40 corn ears. The error was calculated by comparing the true values with the measured values, and the results are shown in Figure 10. From the analysis of the whole system error, it can be seen that the average accuracy of length is 97.79%. The average accuracy rate of diameter reached 96.70%. The accuracy of the whole system can reach 97.24%.

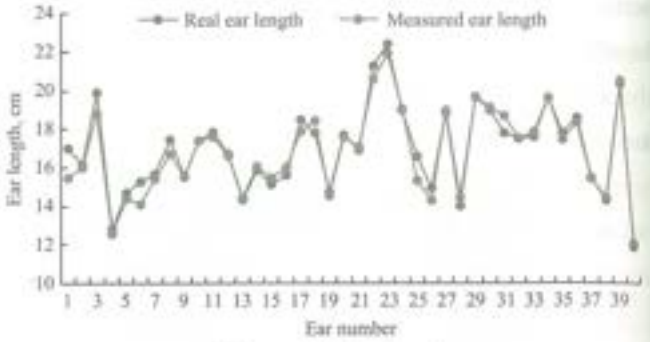

a. Error analysis of ear length

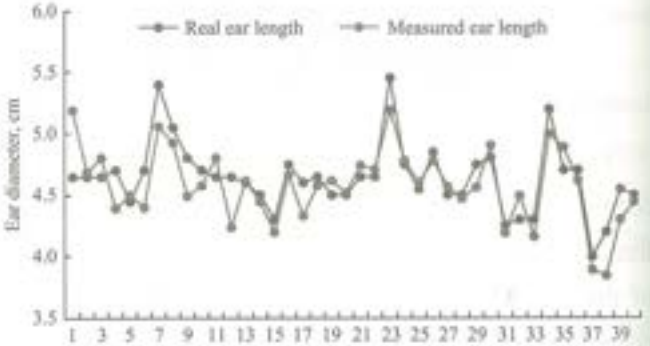

b. Error analysis of ear diameter

Figure 10 Error analysis of the system

The results showed that the accuracy of the system is high, but the errors of partial measuring results are large, mainly because some of the adherent situations are too serious and also because of the rapid expansion of the individual minimum value during the expansion process. In the segmentation results, the diameter error of the corn ears is larger than the length error of the corn ears, which is due to the fact that the actual shape of the corn ears is different, and the measuring position of the diameter is difficult to determine and that is also caused by the projection correction model.

4 Conclusion

Taking many crossbreed adherent corn ears, which are arbitrarily placed, as the research object, we separated the adherent corn ears with the method of improved watershed segmentation algorithm based on the limit corrosion and convex hull detection. The results showed

that the method could effectively divide the adherent corn ears and the length and diameter of the adherent corn ears were calculated quantitatively. The average accuracy of weak adherent corn ears is 97.23%, the segmentation accuracy rate of ring adherent corn ears is 96.34%, the segmentation accuracy rate of strong adherent corn ears is 96.98%, and the accuracy of mixture adherent corn ears is 97.13%. The average accuracy rate of the ear length is 97.79%, and the average accuracy rate of the ear diameter is 96.70%. The accuracy rate of the whole system reached 97.24%, which can meet to the requirement of automatic corn text.

Acknowledgements

This work was supported by Chinese Universities Scientific Fund (2017XD002) and Agro-scientific Research in the Public Interest, China (No. 201203026).

[References]

[1] Cai, J., and Q. Pang. 2011. Image segmentation method and implementation research of strong adhesion cell. *Machine Made*, 49(4): 27–30.

[2] Duan, X. C., J. H. Zhou, and S. J. Wang. 2014. Image calibration method for the ear of corn measurement system. *Journal of Agricultural Mechanization Research*, 36(01): 76–79.

[3] Gao, X. 2015. Study on image segmentation technique of touching rice based on watershed and pits. M.S. thesis., Information Science and Engineering Dept., Henan Industrial Univ., Zhengzhou.

[4] Li, W. J., Y. M. Liu, S. J. Chen, H. Tan, J. Liu, and Z. Tian. 2016. Automatic separating system of maize haploid based on machine vision. *Journal of Agricultural Mechanization Research*, 38(01): 81–85.

[5] Liu, C. Q., and B. Q. Chen. 2014. Method of image detection for ear of corn based on computer vision. *Transactions of the Chinese Society of Agricultural Engineering*, 30(6): 131–138. (in Chinese with English abstract)

[6] Liu, Y., B. Chen, and J. Qiao. 2011. Development of a machine vision algorithm for recognition of peach fruit in natural scene. *Transaction of the ASABE*, 54(2): 694–702.

[7] Li, Y. F., D. X. Zhou, C. Xing, and J. H. Zhang. 2010. Study on rice grain image segmentation based on mathematical morphology. *Agriculture Network Information*, (10): 18–21.

[8] Li, W. Y., M. Li, J. P. Qian, C. H. Sun, S. F. Du, and M. X. Chen. 2015. Segmentation method for touching pest images based on shape factor and separation points location. *Transactions of the Chinese Society of Agricultural Engineering*, 31(05): 175–180. (in Chinese with English abstract)

[9] Manickavasagan, A., G. Sathya, D. S. Jayas, and N. D. G. White. 2008. Wheat class identification using monochrome images. *Journal of Cereal Science*, 47(3): 518–527.

[10] Ng, H. P., S. H. Ong, K. W. C. Foong, P. S. Goh, and W. L. Nowinski. 2007. Masseter segmentation using an improved watersbed algorithm with unsupervised classification. *Computers in Biology and Medicine*, 38(2): 171–184.

[11] Pearson, T. 2009. Hardware-based image processing for high-speed inspection of grains. *Computers and Electronics in Agriculture*, 69(1): 12–18.

[12] Rao, A. R., and V. V. Srinivas. 2006. Regionalization of watersheds by fuzzy cluster analysis. *Journal of Hydrology*, 318: 57-79.

[13] Wu, G., X. L. Chen, and J. Y. Xie. 2016. Design and experiment of automatic variety test system for corn ear. *Transactions of the Chinese Society for Agricultural Machinery*, 47(10): 433–441. (in Chinese with English abstract)

[14] Wang, C. Y., X. Y. Guo, S. Wu, B. Y. Xiao, and J. J. Du. 2014. Three-dimensional reconstruction of maize ear based on computer vision. *Transactions of the Chinese Society for Agricultural Machinery*, 45(9): 274–280. (in Chinese with English abstract)

[15] Wang, Z., G. Jin, and X. W. Sun. 2015. An algorithm of image segmentation for overlapping grain image. *Optics and Precision Engineering*, 13(5): 592–598.

[16] Wei, D. D., and Y. H. Zhao. 2010. An image segment algorithm for overlapped particles based on concave points matching. *Computers and Applied Chemistry*, 27(1): 99–102.

[17] Weicker, T. J. 2001. Efficient image segmentation using partial differential equations and morphology. *Pattern Recognition*, 34(9): 1813–1824.

[18] Xiao, W. Y., Q. Z. Teng, and H. B. He. 2015. Carbide image segmentation algorithm based on morphology. *Journal of Computer Applications*, 35(S2): 277–279.

[19] Xun, Y., G. J. Bao, Q. H. Yang, F. Gao and W. Li. 2010. Automatic segmentation of touching corn kernels in digital image. *Transactions of the Chinese Society for Agricultural Machinery*, 41(04): 163–167. (in Chinese with English abstract)

[20] Xi, Y. Y. 2013. Based on stereo vision fingertips positioning and human computer interaction research. M.S. thesis., Computer Science Dept., Chang An Univ., Xi an.

[21] Yan, Y., and Y. J. Wang. 2012. The research and application of watershed segmentation algorithm based on morphology. *Journal of Changchun Normal University* (Natural Science),

31(12): 20–22.

[22] Yilihamu, Y. 2013. Based on the improved adaptive watershed image segmentation method research. *Computer Simulation*, 30(02): 373–377.

[23] Yu, W. S., Z. Q. Hou, C. Y. Wang, B. Liu, and H. Song. 2011. Watershed algorithm based on modified filter and marked extract. *Journal of Electronics*, 39(04): 825–830.

[24] Yu, W. S., Z. Q. Hou, and J. J. Song. 2011. Color image segmentation based on marked water shed and region merge. *Journal of Electronics*, 39(05): 1007–1012.

[25] Yang, Y. J. 2008. Designation & implementation of camera calibration and distortion image correction algorithm. M.S. thesis., Science Dept., Dongbei Univ., Shenyang.

[26] Zhu, W. X., W. Su, and H. D. Zhang. 2009. Counting of overlapping soybean grain by support vector machine. *Soybean Science*, 28(01): 151–155.

[27] Zhou, J. H., Q. Ma, D. H. Zhu, H. Guo, Y. Wang, X. D. Zhang, S. M. Li, and Z. Liu. 2015. Measurement method for yield component traits of maize based on machine vision. *Transactions of the Chinese Society of Agricultural Engineering*, 31(03): 221–227. (in Chinese with English abstract)

Impacts of fertilization rate on soil quality in Taihu Lake watershed

Xu Wenping, Gao Hongju*

(College of Information and Electrical Engineering, China Agriculture University, 100083 China)

Abstract: The application of chemical fertilizers affects the soil quality greatly. In this paper, data were collected from Taihu Lake watershed area includes soil nutrients and heavy metals in 1477 topsoil samples (PH, OM, N, P, K, AVP, AVK, CEC, Cd, Cr, Cu, Pb, Zn, AVZn, Hg, As and Se), and the grain yield per unit area and fertilization rate per unit area in successive 35 years. Effects of fertilizers on soil quality were investigated using correlation matrix, statistical analysis, PCA (Principal Components Analysis), FCM (Fuzzy c-means clustering analysis) and time series analysis. The fertilization rate of Hangzhou, Zhenjiang etc. was higher through time series analysis. Compared to 1982, the fertilization rate per unit area increased in 2000. However, the partial fertilizer productivity decreased gradually after 1995. Correlation coefficients of PH and P, OM and N are 0.62, 0.90 respectively, which imply that soil acidification and the increase of OM are partly caused by the heavy use of fertilizers. Nevertheless, the average content of OM was increased by only 4.977 g/kg with the continuous application of fertilizers from 1982 to 2000, showing that the fertilizer unabsorbed cannot retain in the topsoil. FCM divided samples into six clusters depending primarily on soil quality attributes, and values of pH are showing the tendency of soils towards acidification for all clusters. Soil quality of clusters which were mainly distributed in Hangzhou, Changzhou and Zhenjiang was bad. Therefore, the heavy use of fertilizers for long term has a negative impact on soil quality and the partial fertilizer productivity.

Keywords: fertilization rate per unit area, soil quality in Taihu Lake, PCA, FCM, time series analysis

Citation: Xu, W. P., and H. J. Gao. 2017. Impacts of fertilization rate on soil quality in Taihu Lake watershed. International Agricultural Engineering Journal, 26(3): 375–384.

1 Introduction

Taihu Lake watershed is an area with integrated economic development in both agriculture and industry. Thus, there is a direct impact of soil quality on the development of local agricultural economy. In recent decades, it has been well documented that ecosystem of Taihu Lake watershed was destroyed (Liu et al., 2017; Zhao et al., 2017; Li et al., 2017), and some thoughts and researches on ecological balance were induced by the explosion of incident of cyanobacteria in Taihu Lake. Fertilization of farmland crops in Taihu Lake watershed was much higher than the crop demand actually, as described in previous study (Xia et al., 2003). Wang et al. (2016) reported that excessive use of chemical fertilizer and massive emissions of livestock excreta were the main reasons for aggravating environmental pollution. They proposed suggestions to relieve the environmental load of nitrogen and promote scientific fertilization. It was also demonstrated that runoff carrying N and P nutrients from chemical fertilizer inputs in agricultural areas is the major contributor to eutrophication in the lake basin (Zhang et al., 2010; Chen et al., 2010; Li et al., 2000). Accordingly, excessive use of fertilizer becomes a common phenomenon, hence, results in water pollution, soil acidification and lower nitrogen use efficiency as researchers have shown in their reviews (Antonangelo et al., 2017; Hu et al., 2017; Liu et al., 2016).

Statistical analysis and correlation analysis were used basically to reveal impacts of fertilization rate on soil

Received date: 2017-07-09 **Accepted date:** 2017-08-27

* **Corresponding author: Gao Hongju,** Associate Professor, College of Information and Electrical Engineering, China Agriculture University, 100083 China. Email: hjgao@cau.edu.cn. Tel: +86-10-62738830.

quality (Yang et al., 2014; Zhang et al., 2010). It was found that more attention has been spent to the sustainable agro-ecosystem and researches are dependent on its practical significance (Stavi et al., 2011; Xia et al., 2010). Fuzzy clustering method was applied into the division of soil management zones, and then the soil can be classified according to the characteristics of soil properties and managed conveniently (Rahul et al., 2015; N. Davatgar et al., 2012; Guo et al., 2013). There are many different algorithms for clustering, fuzzy clustering and fuzzy c-means clustering are applied generally. Two types of clustering methods were used to analyze soil management zones and compare the performance of two methods in the classification management (Hot et al., 2015; Ghosh et al., 2013). There are fewer attributes integrated when studying the soil quality. Followed by it, Bansod et al. (2013) was able to perform fuzzy c-means clustering based on principal component analysis to reduce the number of soil analysis needed. Time series analysis was conducted that account better to explain the changes in attributes (Lopez-Garcia et al., 2017). In conclusion, the degradation of soil fertility is the result of long-term fertilization, and the sustainable development of soil aroused the attention of many researchers. Although, much effort of predecessors contributes to revealing the relationships with fertilization and soil fertility, while not combines the time series for fertilization rate with the soil quality and partial fertilizer productivity together.

The primary goal in this paper is to study the effects of fertilization rate on soil quality by combining these methods, such as statistical analysis, correlation analysis, principal component analysis, fuzzy c-means clustering and time series analysis. Time series analysis was employed to analyze the correlation between the fertilization rate and the partial fertilizer productivity. Effects of fertilization rate on soil quality were analyzed. The rest of paper is as follows: there is a brief introduction to the study area of Taihu Lake. The data collating is presented. Methodologies used in this paper are introduced. The results and discussion about the analysis of each part are illustrated, and conclusions are given at last.

2 Study area and data

2.1 Study area

Taihu Lake watershed (Figure 1) is one of the China's five major freshwater lakes, which is located between latitude 30°55′40″-31°32′58″ and longitude 119°5′32″-120°36′10″, covered an area of 39600 square kilometers. It is dominated by irrigated agriculture, mostly occupied by permanent plain. Taihu Lake watershed belongs to the water network in southern plain with a dense population, rapid development and developed economy.

With the sufficient sunlight resources, it is favorable to develop agriculture in Taihu Lake watershed, and thus its main crops here are rice, wheat and other cash crops.

Figure 1 Boundary map of the study area

2.2 Data set introduction

There are two parts of data mainly involved in the research, they are soil nutrient and heavy metal, fertilization rate and grain yield respectively.

A total of 1477 samples with soil nutrients (N, P, K, PH, CEC, OM, AVP, AVK) and heavy metals (Cd, Cr, Cu, Pb, Zn, AVZn, Hg, As, Se) were collected from Nanjing soil database. Changes of nutrients and heavy metals in soil can be regarded as a criterion for assessing the soil quality.

The data of grain yield and fertilization rate were reorganized using equations which were given as follows before analysis. The grain yield per unit area, the fertilization rate per unit area and the partial fertilizer

productivity were abbreviated as GY, FR and PFP here respectively.

GY (T/Ha)=grain yield/crop area.

FR (T/Ha)=fertilization rate/cultivated area.

PFP (kg/kg)=grain yield/fertilization rate.

Data were collated into the data of fertilization rate per unit area, grain yield per unit area and partial fertilizer productivity with different cities in successive 35 years. These data were prepared for time series analysis.

The detailed sampling sites around Taihu Lake are illustrated in Figure 2. These points are mainly distributed in Wuxi, Changzhou, Suzhou, Zhenjiang, Hangzhou, Jiaxing and Huzhou.

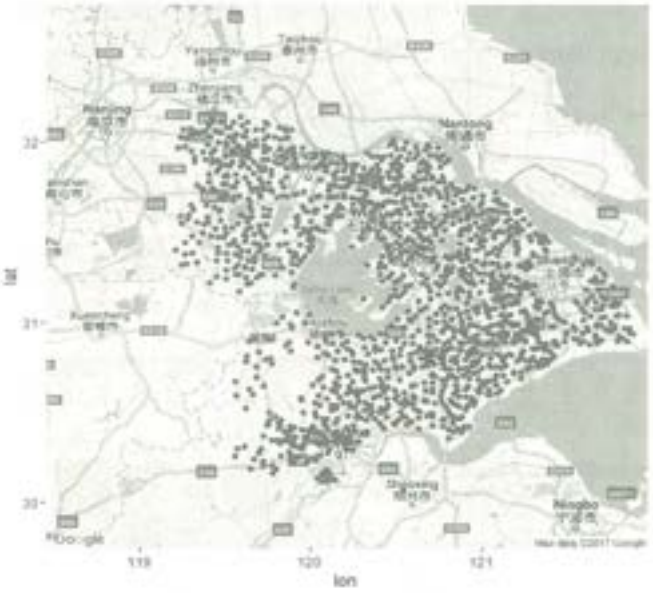

Figure 2 Distribution of sampling sites for analyzing the soil quality

3 Methodologies

3.1 Data preprocessing

3.1.1 Normalization

Because of differences in dimensions, the data should be standardized before analysis. The processed data were conformed to the standard normal distribution and the equation is given as follows:

$$X = \frac{x - \mu}{\sigma} \quad (1)$$

where, the μ means mean, and the σ stands for the standard deviation.

3.1.2 Interpolation

Data were collected manually and then there were some vacant values inevitably which cannot be deleted directly due to the less sample points. Therefore, these missing values were interpolated.

3.2 Multivariate statistical techniques

Multivariate analysis of the soil quality was performed through correlation analysis, descriptive statistical analysis and principal component analysis. Mathematical and statistical computations were performed using Microsoft Office Excel and R (i386 3.3.3).

3.2.1 Correlation analysis

Correlation analysis is a measurement of relationship between two or more variables. To verify possible relations between variables of soil, Pearson's coefficient of linear correlation was calculated between different variables (Jose et al., 2008).

3.2.2 Statistical analysis

Statistical analysis is usually categorized into three parts to analyze the data, such as centralized trend analysis, depending on mean, median and mode to analyze the data mainly. The distribution of these properties was tested using values of skewness and kurtosis. The size and concentration of the data can be observed systematically by statistical analysis.

Data of soil quality were analyzed using this method to obtain characteristics of size and concentration.

3.2.3 Principal component analysis

Principal Component Analysis was abbreviated as PCA in general. PCA is a multivariate method mainly used for reducing data dimensions. The contribution of PCs (principle components) to the preservation of original information is measured by its variance. The complexity of multi-index analysis will be declined greatly and the reliability of system operation will be improved.

The possible origins of nutrients and heavy metals in samples were investigated by PCA. The PCs transformed from the original variables were extracted according to eigenvalues >1.0. Due to different dimensions of each variable, first of all, normalization was done prior to PCA. The data of soil quality were analyzed using PCA to reduce dimensions and prepare for the clustering.

3.3 Fuzzy c-means clustering analysis

Fuzzy c-means was abbreviated as FCM in general. FCM based on PCA was used to classify the selected PCs

and aim at identifying natural clusters.

FCM is completed by R software, and the only shortcoming is that the number of clusters as a parameter which is set in advance. Selecting the appropriate number of clusters plays a key role in the result of clustering analysis. Thus, one critical issue is to find the best NC (number of clusters) based on some indices, which are PE (the partition entropy index), PC (the partition coefficient index), MPC (the modified partition coefficient index), SIL (the silhouette index) and XB (Xie and Beni index) respectively. NC is an optimal value only when XB and PE are minimum values and SIL, PC and MPC are maximum values respectively. The data obtained by PCA were clustered to divide the soil into several parts relying on the characteristics of soil quality, and then analyze each part of soil.

3.4 Time series analysis

Time series analysis is a statistical method of dynamic data processing, and focuses on studying changes of data sequences. The time series diagrams were plotted for analyzing changes of fertilization rate per unit area and partial fertilizer productivity following years.

4 Results and discussion

4.1 Fertilizer based on spatial and temporal analysis

Comparisons of fertilization rates in different cities from 1980 to 2014 were illustrated in Figure 3. It is simply appeared that in Hangzhou, Zhenjiang and Changzhou, the fertilization rates per unit area are higher than those of other cities.

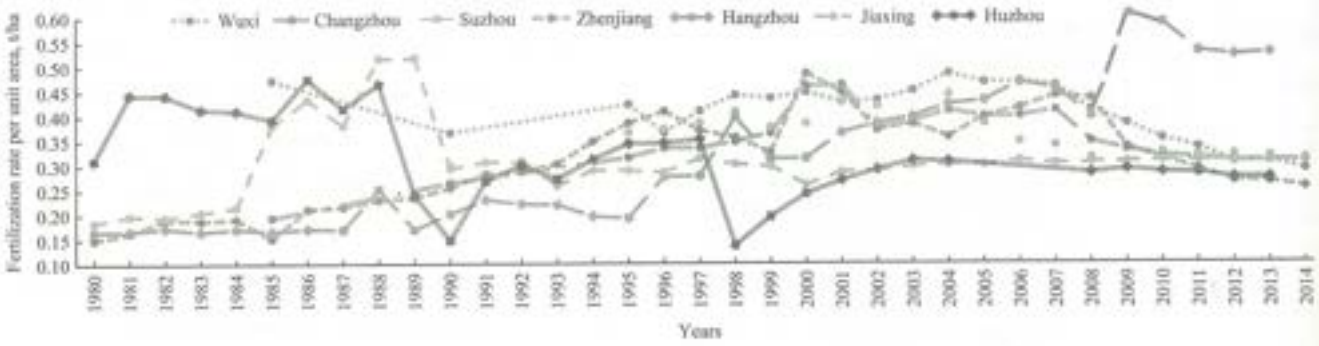

Figure 3 Comparisons of fertilization rates per unit area in different cities

Taking Jiangyin as an example, the time series of fertilization rate per unit area and partial fertilizer productivity were shown in Figures 4 and 5, respectively. Compared to 1982, the fertilization rate per unit area is largely increased in 2000. Furthermore, the trend of partial fertilizer productivity is steeper from 1991 to 1995 corresponding to a remarkably increase, and then began to decline as the fertilization rate increased progressively after 1995.

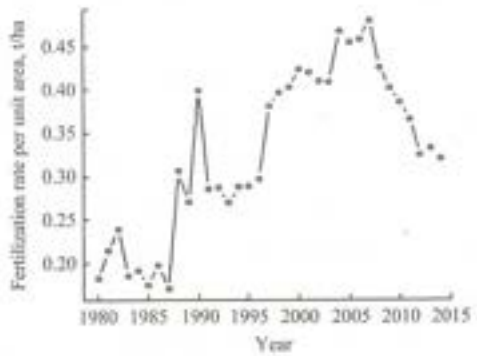

Figure 4 Time series of fertilization rate per unit area

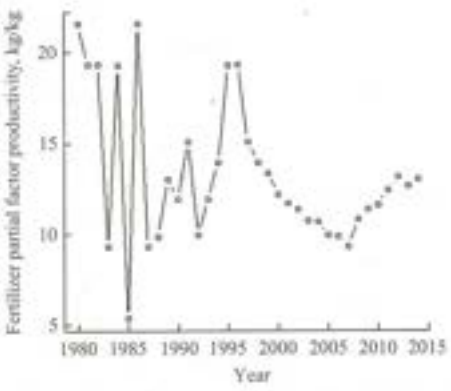

Figure 5 Time series of partial fertilizer productivity

It has been fully proved that the excessive fertilizer was applied in Taihu Lake area, and some parts of unabsorbed fertilizer were washed into the deeper horizons of soil. As observed above, the partial fertilizer productivity decreased after 1995, and the absorbed rate of crops also decreased. In short, there is a negative impact of fertilization rate on agricultural production.

4.2 Results for soil quality

4.2.1 Correlation analysis

For better visualization, correlation coefficient matrices were shown in Figures 6, 7 and 8 respectively. Digits in correlation coefficient matrix represent Pearson correlation coefficient. In addition, different colors in matrix are corresponding to the sizes of coefficient, and the color changes from deep to shallow representing the correlation changes from strong to weak.

Figure 6 Correlation coefficient matrix of soil nutrients

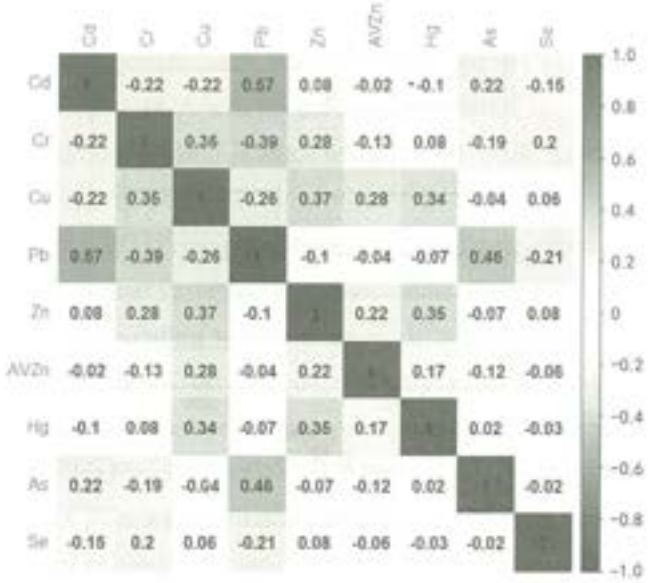

Figure 7 Correlation coefficient matrix of heavy metals

It can be seen that correlation coefficients between PH and P, OM and N are 0.62, 0.9 respectively, with strong correlations. The correlation between other properties is weak, particularly the correlation between AVK and K. A possible explanation is that the increase in OM and the soil acidification are probably caused by the application of fertilizers extensively. Furthermore, the correlation between AVK and K is –0.01, with relatively weak negative correlation, which implies that content of AVK in soil is restricted by the soil fertility instead of the fertilization rate.

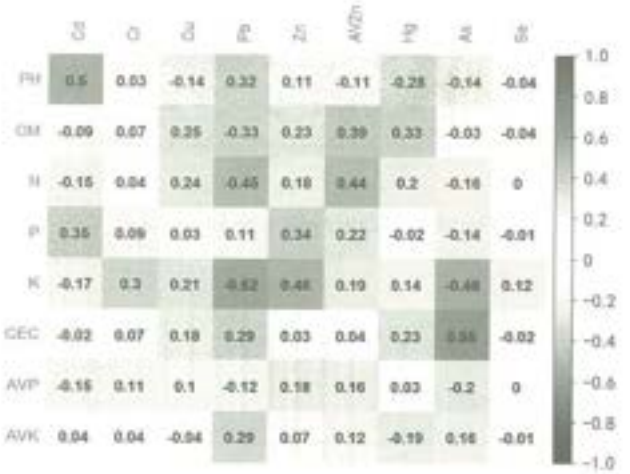

Figure 8 Correlation coefficient matrix between nutrients and heavy metals

As illustrated in Figure 7, correlations between variables in heavy metals are weak generally, indicating the diversity of resources of heavy metals. But correlation coefficients between Pb and As, Pb and Cd are 0.46, 0.57 respectively, with a relatively strong positive correlation. It can be concluded that resource of Pb is similar with As and Cd with a great possibility.

A common belief regarding CEC and As is that their contents in soil can reflect the status of soil fertility. As observed above, there is a strong positive correlation between As and CEC with the correlation coefficient of 0.55. The correlation between Cd and PH is also strong, with a coefficient of 0.5. Accordingly, the content of As affects the soil fertility with the accumulation of As in soil, and the content of Cd tends to favor the soil acidification.

Scatter plots of two variables were shown in Figures 9 and 10. It can be seen that, the regional distribution of some heavy metals presents a trend of polarization. Most of sampling sites have a relatively high content of Pb, with an uneven distribution, while the regional distribution of Cd is more uniform. Soil pollution caused by the use of fertilizers is non-point source pollution, while the soil pollution caused by heavy metals is point source pollution. This means that fertilizer is not the only factor that causes the heavy metal pollution.

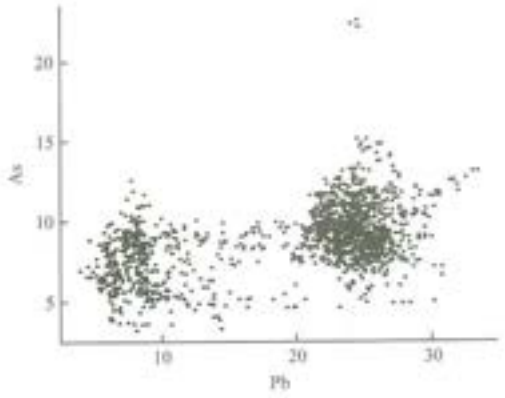

Figure 9 Scatter plot with Pb and As

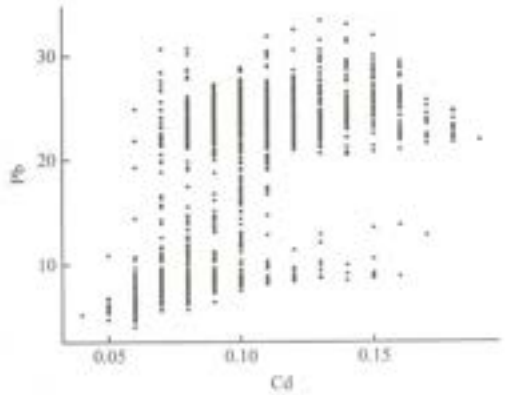

Figure 10 Scatter plot with Pb and Cd

4.2.2 Statistical analysis

The most frequently used parameters (Mean, Min, Max, Var, CV), which can represent the size and concentration of data, were calculated. Where, CV refers to the coefficient of variation. It is well known that OM is a crucial component to maintain the soil fertility and provide nutrients for crops. In brief, the content of OM is regarded as an important factor to assess the soil fertility. Results of statistical analysis were summarized in Tables 1 and 2, and contents of CEC in 1982 are vacant. For analyzing intuitively, Figures 11 and 12 were shown. Compared to 1982, PH has a downward trend in 2000 facing the risk of acidification. As can be seen from Table 1, compared to 1982, OM and N have an upward trend, and this is a general phenomenon with the continuous fertilization year after year. But the average content of OM increases only by 4.977 (g/kg), so that ultimately the small amount of fertilizers was trapped in soil and most of them had been washed into the deep soil. Although acknowledged, fertilization exactly compensates nutrient requirements. Nonetheless, there is a tendency of soil towards acidification likely due to the long-term fertilization.

Table 1 Statistical analysis of nutrients in 1982 and 2000

Nutrients	Year	Mean	Min	Max	Var	CV
PH	1982	6.74	5.44	8.13	0.305	0.082
	2000	6.215	4.96	8.39	0.543	0.119
OM, g/kg	1982	26.242	13.88	45.21	38.447	0.236
	2000	31.219	16.35	42.5	28.318	0.17
N, g/kg	1982	1.555	0.8	2.66	0.107	0.211
	2000	1.769	0.82	2.83	0.132	0.205
P, g/kg	1982	0.704	0.17	1.63	0.074	0.387
	2000	0.654	0.33	1.35	0.024	0.235
AVP, mg/kg	1982	11.382	3.53	88.96	47.451	0.605
	2000	10.677	4.07	31.21	21.779	0.437
AVK, mg/kg	1982	90.134	34.29	178.57	552.823	0.261
	2000	85.701	45.69	152.66	287.892	0.198
CEC, cmol/kg	1982					
	2000	16.271	7.85	23.77	7.974	0.174

Table 2 Statistical analysis of heavy metals in 2000

Heavy metals, g/kg	Mean	Min	Max	var	CV
Cd	0.102	0.04	0.19	0.0007	0.268
Cr	64.028	29.59	113.13	111.874	0.165
Cu	26.307	16.35	93.99	34.745	0.224
Pb	19.602	3.98	33.45	57.546	0.387
Zn	102.993	51.26	200.09	380.748	0.189
AVZn	1.905	0.76	11.31	1.073	0.544
Hg	0.207	0.05	1.2	0.017	0.638
As	8.885	3.19	22.58	4.36	0.235
Se	0.891	0.16	57.26	30.18	6.163

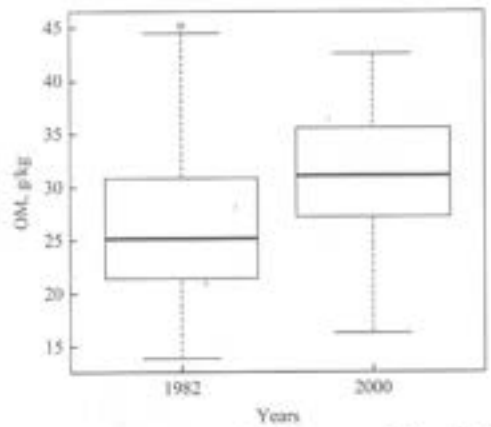

Figure 11 Comparison of OM between 1982 and 2000

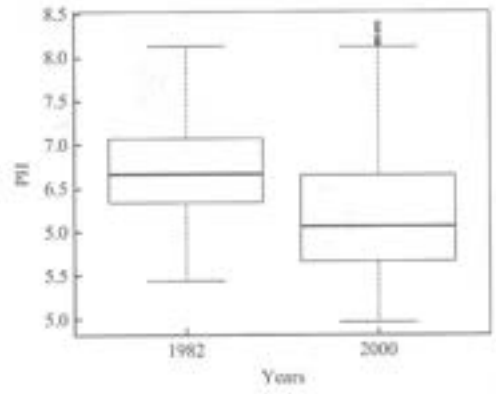

Figure 12 Comparison of PH between 1982 and 2000

Table 2 shows that variances of Cr, Cu and Zn are significantly different from variances of other heavy metals. Variances of Cr, Cu and Zn are much bigger, as this means that distributions of Cr, Cu and Zn are uneven especially. The variance of Cd is lower, and then its distribution is even relatively. The mean of heavy metals varies greatly. For instance, the average content of Cd is 0.102 g/kg; whereas Zn is 102.993 g/kg. It is showed that heavy metals in different areas are uneven and their resources are varied from each other. These results are consistent with the results of correlation coefficient analysis.

In soil science studies, it is a common sense that CV represents the spatial variability of soil properties. CV is usually used for comparing the discrepancy of different dimensions or different scales of measurement. CV of Se has reached 6.163, showing a strong variability, and CV of AVZn and Hg are 0.544, 0.638 respectively, changing obviously. Accordingly, there is an obviously different from each other in different regions with respect to soil characteristics, though they are all around Taihu Lake area.

4.2.3 Results for PCA

PCA was performed to aggregate the variability in these properties and was prepared for FCM. More specifically, PCA was adopted to characterize the type of soil around Taihu Lake, while FCM was used for grouping the soil.

Each PC (Principal Component) is a linear expression of all original variables, and coefficients of the expression are corresponding to eigenvectors. It is possible to infer the variable of original data mainly expressed by PC according to the coefficients of expression which has the larger coefficient.

Six PCs were extracted as listed in Table 3, and the cliff of this analysis was presented in Figure 13. Where, Comp.1 denotes the first PC. As shown in Table 3, the first PC and the sixth PC are accounting for 46.60% and 2.82% respectively, with a large difference. These six PCs are accounting for 93.58% of original information.

4.2.4 Fuzzy c-means clustering

The data, which are organized into PC values after PCA, are used for FCM. FCM based on PCA is completed by R software to analyze characteristics of soil.

Table 3 Information about PCs

PCs	Eigenvalue	Component loading, %	Cumulative loading, %
Comp.1	5.09	46.60	46.60
Comp.2	3.88	24.01	70.60
Comp.3	2.86	9.53	80.14
Comp.4	1.99	5.91	86.05
Comp.5	1.78	4.72	90.76
Comp.6	1.20	2.82	93.58

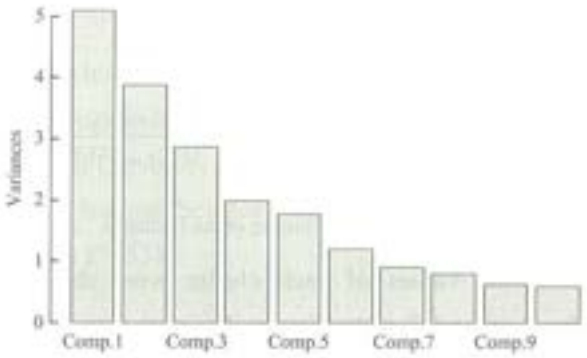

Figure 13 Cliff of the PCA

The first thing to do is selecting the optimal NC (number of clusters). Additionally, different indices followed by different clusters were listed in Table 4, and the line chart was also given in Figure 14 to find the optimal value more intuitively. When NC is six, XB is a minimum value and MPC and SIL are maximum values. Selecting six as the optimal value with comprehensive consideration, despite PE is not a minimum value and PC is not a maximum value. At last, the spatial distribution of each cluster was shown in Figure 15, and different colors represent different clusters.

Table 4 Different indicators followed by different NC

NC	PE	PC	MPC	SIL	XB
2	0.5964639	0.5902092	0.1804183	0.3541781	0.9211374
3	0.9408203	0.4436973	0.1655459	0.393596	0.9293091
4	1.188661	0.3617968	0.1490624	0.3424196	0.876639
5	1.324459	0.3399689	0.1749611	0.3819176	0.5167741
6	1.447187	0.3180616	0.1816739	0.3837727	0.4628576
7	1.55341	0.2983572	0.1814168	0.3641149	0.610551
8	1.690754	0.2656551	0.1607487	0.3232503	0.5451866

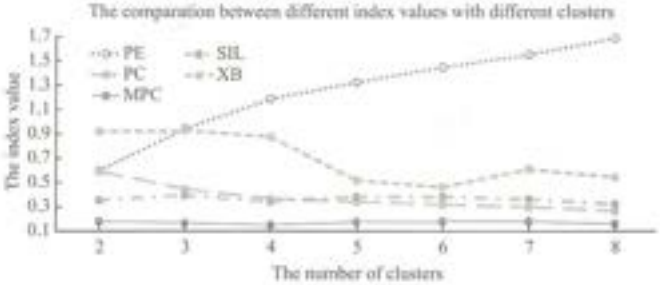

Figure 14 Indicators with different clusters

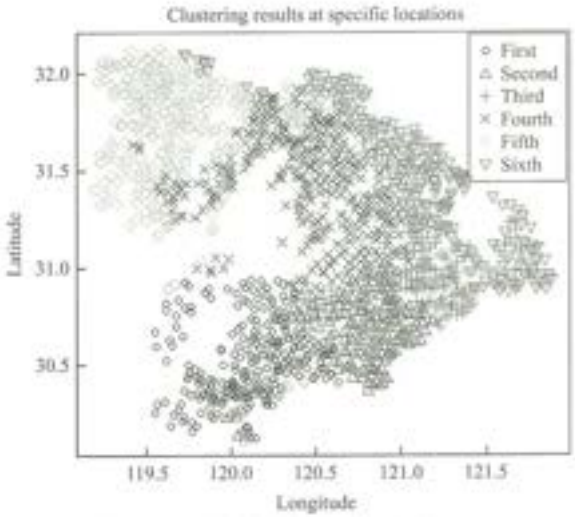

Figure 15 Distribution of each cluster

Attribute values of each cluster were detailed in Tables 5, 6 and 7 respectively. The soil status of each cluster was evaluated in terms of Table 8, which was performed according to the unified system of whole country. Results were given in Table 9. Accordingly, the order of soil quality of six types is 3, 6, 2, 4, 5, and 1, from good to bad. The soil quality of clusters which are mainly distributed in Hangzhou, Changzhou and Zhenjiang is poor. A further scrutiny of Figure 3 shows that the soil quality is poor in areas where more fertilizer has been applied.

As demonstrated above, heavy metals have a strong spatial variability, and their recourses are diverse. The soil acidification and the decrease in partial fertilizer productivity are caused by excessive fertilization around Taihu Lake. In conclusion, there is a serious impact of excessive fertilization on grain yield in the long run.

Table 5 Nutrients for six clusters in 1982

Cluster	PH	OM	N	P	AVP	AVK
first	6.3032	28.3946	1.6052	0.5214	0.0184	0.0718
second	6.5563	31.5525	1.8191	0.7102	0.0104	0.1090
third	6.9904	31.5777	1.8409	0.7778	0.0160	0.1147
fourth	6.5181	27.0051	1.6234	0.7254	0.0079	0.0811
fifth	6.6064	19.7762	1.2597	0.5078	0.0077	0.0836
sixth	7.6555	22.8296	1.3518	1.0557	0.0113	0.0975

Table 6 Nutrients for six clusters in 2000

Class	PH	OM	N	P	K	CEC	AVP	AVK
first	5.8220	33.1322	1.9700	0.5635	19.9481	13.0229	0.0103	0.0680
second	5.7698	35.3835	2.0588	0.6808	19.0957	17.3801	0.0137	0.0870
third	6.6525	34.6310	2.0912	0.8493	18.3840	17.0112	0.0142	0.1080
fourth	5.7865	32.7103	1.7507	0.5987	14.7163	19.1256	0.0084	0.0845
fifth	6.1697	26.1439	1.4273	0.5198	13.7752	15.7302	0.0101	0.0858
sixth	7.3551	27.5836	1.5466	0.8345	18.2631	14.8704	0.0100	0.0894

Table 7 Heavy metals for six clusters in 2000

class	Cd	Cr	Cu	Pb	Zn	AVZn	Hg	As	Se
first	0.0802	62.9400	25.9454	9.9087	104.4396	2.0796	0.2388	6.5982	1.0902
second	0.0776	80.0936	33.5320	8.8556	118.3215	2.0113	0.2907	8.0972	4.1014
third	0.1085	58.6890	25.5779	22.0846	107.1655	3.2326	0.1637	8.4638	0.2355
fourth	0.1037	58.7296	25.9502	24.1195	99.1198	1.7656	0.2547	11.1069	0.2436
fifth	0.1032	62.7426	24.0809	24.3359	86.3377	1.3323	0.1289	9.2283	0.2043
sixth	0.1337	64.5314	24.4299	24.7260	111.9929	1.6265	0.1619	8.6579	0.2259

Table 8 Classification

Classification	OM, g/kg	N, g/kg	AVP, g/kg	AVK, g/kg	AVN, g/kg	PH
1, Extremely high	>40	>2	>0.04	>0.2	>0.15	<4.5
2, Very high	30-40	1.5-2	0.02-0.04	0.15-0.2	0.12-0.15	4.51-5.50
3, High	20-30	1-1.5	0.01-0.02	0.1-0.15	0.09-0.12	5.51-6.50
4, Middle	10-20	0.75-1	0.005-0.01	0.05-0.1	0.06-0.09	6.51-7.50
5, Low	6-10	0.5-0.75	0.003-0.005	0.03-0.05	0.03-0.06	7.51-8.50
6, Very low	<6	<0.5	<0.003	<0.03	<0.03	>8.50

Table 9 Classification of each cluster

Category	PH	OM	N	AVP	AVK
1	Slightly acid	Very high	Very high	High	High
2	Slightly acid	Very high	Extremely high	High	Middle
3	Neutral	Very high	Extremely high	High	High
4	Slightly acid	Very high	Very high	Middle	Middle
5	Slightly acid	High	High	High	Middle
6	Neutral	High	Very high	High	Middle

5 Conclusions

The application of fertilizers for long term has caused serious impacts on soil quality. The fertilization rate around Taihu Lake watershed is considered as a clue, impacts of fertilization rate on soil quality were analyzed through correlation analysis, statistical analysis, fuzzy c-means clustering, time series analysis, etc.

Through time series analysis, it is reported that excessive fertilization rate leads to the decrease in partial fertilizer productivity. This has been a common phenomenon and affects the absorbed rate for crops.

There is a noticeable trend of soil acidification through statistical analysis. The average content of OM increased inconspicuously with the continuous application of fertilizers, showing that the part of fertilizer can remain in the topsoil and most of them can be washed into the deep soil substantially. Correlation coefficients between PH and P, OM and N are 0.62 and 0.9 respectively with the strong positive correlation. It is revealed that soil acidification is caused by the application of fertilizers. After that, FCM was employed to divide the soil into six types, and the lager the fertilization rate is, the worse the soil quality would be.

In conclusion, excessive use of fertilizers for long term causes soil acidification and the decrease in soil fertility. If it is failed to take real-time measures to control the fertilization rate, ecosystem in Taihu Lake will be caught in a vicious circle with respect to the fertilization rate and soil quality. As such, it is imperative to fertilize moderately, which can protect the soil against natural tendency to acidification, guide the agro-production and also maintain the agricultural sustainable development.

Acknowledgments

We acknowledge the sharing of the soil data from China Soil Database, and are grateful for the support from National Natural Science Foundation of China through project 31371531.

[References]

[1] Antonangelo, J. A., J. F. Neto, C. A. C. Crusciol, and L. R. F. Alleoni. 2017. Lime and calcium-magnesium silicate in the ionic speciation of an Oxisol. *Scientia Agricola*, 74(4): 317–333.

[2] Bansod, B. S., and O. P. Pandey. 2013. An application of PCA and fuzzy C-means to delineate management zones and variability analysis of soil. *Eurasian Soil Science*, 46(5): 556–564.

[3] Chen, D. J., J. Lu, and Y. N. Shen. 2010. Artificial neural network modelling of concentrations of nitrogen, phosphorus and dissolved oxygen in a non-point source polluted river in Zhejiang Province, Southeast China. *Hydrological Processes*, 24(3): 290–299.

[4] Davatgar, N., M. R. Neishabouri, and A. R. Sepaskhah. 2012. Delineation of site specific nutrient management zones for a paddy cultivated area based on soil fertility using fuzzy clustering. *Geoderma*, 173-174: 111–118.

[5] Elma, H., and V. P. Bugarin. 2015. Soil data clustering by using K-means and fuzzy K-means algorithm. *23rd Telecommunications forum TELFOR 2015*, 2015, *Belgrade, Serbia. 24-26 Nov.* 890–893.

[6] Ghosh, S., and S. K. Dubey. 2013. Comparative analysis of K-means and fuzzy C-means algorithms. *International Journal of Advanced Computer Science and Application*, 4(4): 35–39.

[7] Guo, Y., Y. F. Tian, H. H. Wu, and Z. Shi. 2013. Study on soil partitioning of farmland based on multi-source data and fuzzy k-means. *Acta Pedologica Sinica*, 50(3): 441–447.

[8] Hu, M., Y. S. Xiang, Z. Zhang, R. H. Cong, F. Y. Huang, J. Q. Zhang, L. L. Shang, and J. W. Lu. 2017. Variation characteristics of farmland soil pH in the past 30 years of Enshi Autonomous Prefecture. *Chinese Journal of Applied*

Ecology, 28(4): 1289–1297.

[9] Janssen, A.B.G., V. C. L. de Jager, J. H. Janse, X. Z. Kong, S. Liu, Q. H. Ye, and W. M. Mooij. 2017. Spatial identification of critical nutrient loads of large shallow lakes: Implications for Lake Taihu (China). *Water Research*, 119: 276–287.

[10] Li, H.B., P. Xing, and Q. L. Wu. 2017. Genus-specific relationships between the phytoplankton and bacterioplankton communities in Lake Taihu, China. Hydrobiologia, 795(1): 1–14.

[11] Lopez-Garcia, P., M. D. Gelado-Caballero, C. Collado-Sanchez, and J. J. Hernandez-Brito. 2017. Solubility of aerosol trace elements: Sources and deposition fluxes in the Canary Region. *Atmospheric Environment*, 148: 167–174.

[12] Liu, X., S. S. Xu, J. W. Zhang, Y. F. Ding, G. H. Li, S. H. Wang, Z. H. Liu, S. Tang, C. Q. Ding, and L. Chen. 2016. Effect of continuous reduction of nitrogen application to a rice-wheat rotation system in the middle-lower Yangtze River region (2013-2015). *Field Crops Research*, 196: 348–356.

[13] Molin, J. P., and C. N. de Castro. 2008. Establishing management zones using soil electrical conductivity and other soil properties by the fuzzy clustering technique. *Sci.Agric.* (Piracicaba, Braz), 65(6): 567–573.

[14] Stavi, I., R. Lal, and L. B. Owens. 2011. On-farm effects of no-till versus occasional tillage on soil quality and crop yields in eastern Ohio. *Agronomy for Sustainable Development*, 31(3): 475–482

[15] Taoufik, G., I. Khouni, and A. Ghrabi. 2017. Assessment of physico-chemical and microbiological surface water quality using multivariate statistical techniques: a case study of the Wadi El-Bey River, Tunisia. *Arabian Journal of Geosciences*, 10(7): 181.

[16] Tripathi, R., A.K. Nayak, M. Shahid, B. Lal, P. Gautama, R. Raja, S. Mohanty, A. Kumar, B. B. Panda, and R. N. Sahoo. 2015. Delineation of soil management zones for a rice cultivated area in eastern India using fuzzy clustering. *Catena*, 133: 128–136.

[17] Wang, D., Y. H. Wang, H. Yang, Z. C. Cai, and X. Y. Yan. 2016. Nitrogen flow features of crop-livestock breeding system in Taihu Lake basin. *Research of Environmental Sciences*, 29(3): 457–464.

[18] Xia, L. Z., and L. Z. Yang. 2003. Research and control of non - point source pollution in Taihu Lake watershed. *Resources and Environment in the Yangtze Basin*, 12(1): 45–49.

[19] Xia, Q. F. 2010. Effects of Chemical Fertilizer Application on Soil Ecosystem and Counter measures. *Journal of Guangdong Agricultural Sciences*, (2010) 9.

[20] Yang., Y. F., T. Shao, M. Y. Lv, S.Y. Sun, J. Y. Zhang, and P. J. Zhang. 2014. Characteristics of soil nutrient and heavy metal pollution in wetlands under different land use patterns in Longwo Lake of Wuhu City, Anhui Province, China. *Chinese Journal of Ecology*, 33(5): 1312–1318.

[21] Zhang, B. Y., T. L. Chen, and B. Wang. 2010. Effects of Long-term uses of chemical fertilizers on soil quality. *Chinese Agricultural Science Bulletin*, 26(11): 182–187.

[22] Zhang, Q. L., Y. X. Chen, G. Jilani, I. H. Shamsi, and Q. G. Yu. 2010. Model AVSWAT apropos of simulating non-point source pollution in Taihu Lake basin. *Journal of Hazardous Materials*, 174(1-3): 824–830.

[23] Zhao, Z. H., Y. Jiang, Q. Y. Li, Y. J. Cai, H. B. Yin, L. Zhang, and J. Zhang. 2017. Spatial correlation analysis of polycyclic aromatic hydrocarbons (PAHs) and organochlorine pesticides (OCPs) in sediments between Taihu Lake and its tributary rivers. *Ecotoxicology and Environmental Safety*, 142: 117–128.

Monitoring spike differentiation stages of winter wheat based on land surface temperature time series and Kalman Filter

Liu Junming[1,2*], Pan Peizhu[1,2], Wang Pengxin[1,2], Cui Zhenzhen[1,2], Hu Xin[3]

(1. *College of Information and Electrical Engineering, China Agricultural University, 100083 Beijing, China;*
2. *Key Laboratory of Remote Sensing for Agri-Hazards, Ministry of Agriculture, 100083 Beijing, China;*
3. *Wheat Research Institute, Shangqiu Academy of Agriculture and Forestry Sciences, 476000 Shangqiu, China*)

Abstract: Spike differentiation is an important reproductive growth process of winter wheat, and monitoring spike differentiation stages is also a significant part of phenology monitoring of winter wheat. By taking Shangqiu, Henan Province as the study area, the paper aims to study the methodology of monitoring spike differentiation stages of winter wheat at regional scale based on assimilation remote sensing LST data with crop growth model. Firstly, the paper established the equation between air temperature at the height of 1.5 m above wheat field and LST after green-turning stage of winter wheat. On this basis, the air temperature was used as assimilated quantity, and Kalman Filter algorithm was applied to assimilate air temperature converted from MODIS LST time series data with air temperature time series data which obtained by Inverse Distance Weighted (IDW) to get the consequent air temperature time series data of wheat field in the whole period of winter wheat. Then, WheatGrow model which can simulate the growth and development of wheat was introduced and calibrated to obtain spike differentiation stages of winter wheat based on the assimilated air temperature time series data. The results showed that: (1) The trend of assimilated air temperature was consistent with the trend of interpolated air temperature, but its spatial variation was close to that of LST. The assimilation effect of daily minimum air temperature was significantly better than daily maximum air temperature, the determination coefficient R^2 of minimum air temperature was 0.94 but only 0.70 for maximum air temperature between assimilation and observation. (2) The study can realize the monitoring of floret differentiation stage, stamen and pistil differentiation stage, anther separation stage, tetrad differentiation stage at regional scale. The validated results showed that the deviation of start date between simulation and observation of spike differentiation stages was less than 5 days, and the deviation of duration was in range of 1 to 4 days.

Keywords: spike differentiation stages, data assimilation, Kalman Filter, WheatGrow model, winter wheat

Citation: Liu, J. M., P. Z. Pan, P. X. Wang, Z. Z. Cui, and X. Hu. 2017. Monitoring spike differentiation stages of winter wheat based on land surface temperature time series and Kalman Filter. International Agricultural Engineering Journal, 26(3): 385–398.

1 Introduction

Spike differentiation is an important reproductive growth process of winter wheat (González et al., 2003; Serrago et al., 2008; Mcmaster et al., 1992), and monitoring spike differentiation stages is also a significant part of phenology monitoring of winter wheat. The traditional method for identifying spike differentiation stages of wheat is mainly estimated by the corresponding relationship between the development of wheat spike and the leaf formation of plant or the elongation of plant stem (Cui et al., 2006; Steinmeyer et al., 2013; Jamieson et al., 2007). However, as the spike differentiation process of wheat is affected by climate conditions, wheat variety characteristics, and cultivation measures, etc, the internal reproductive growth of wheat plant is not completely consistent with the vegetative growth of external organ, so the accuracy of identifying spike differentiation stages of wheat by using such method is relatively low. It is possible to accurately identify the spike differentiation stages by using the method of anatomical observation in the laboratory after field sampling. However, this method is not suitable for

Received date: 2017-06-28 **Accepted date:** 2017-08-19
***Corresponding author: Liu Junming,** Ph.D., Associate Professor of College of Information and Electrical Engineering, China Agricultural University, Beijing 100083,China. Tel: 13910693390, Email: liujunming2000@163.com.

continuous observation of regional spike differentiation process of wheat and it is also destructive to the crop itself.

Along with the in-depth study of basic theory of plant physiology and ecology, CERES-Wheat (Abrecht et al., 1996; Jones et al., 2003; Dettori et al., 2011), APSIM-Wheat (Keating et al., 2003; Balwinder-Singh et al., 2011) and WheatGrow (Cao et al., 1997; Yan et al., 2000; Yan et al., 2000; Zun-Fu et al., 2013) and other wheat growth models based on photosynthesis, respiration, transpiration, nutrition and other mechanism process of wheat have gradually developed, which can accurately simulate the growth and development process of wheat. Among them, WheatGrow model, a growth model based on the mechanism of spike differentiation of wheat established by Cao et, al, can quantitatively provide the identification index of spike differentiation stages, and realize the simulation of winter wheat spike differentiation stages on single point scale and in denomination of "Day". However, as the simulation of spike differentiation stages is developed from single-point studies to regional application, the increase of spatial scale may lead to many difficulties in the acquisition of some macro data and the parameter regionalization (Jin et al., 2012).

Satellite remote sensing technology has the advantages of acquiring surface information extensively, real-timely and periodically. It has a good complementary relationship with the advantages of the crop model featured with strong mechanism and continuous process orientation and time. By coupling the crop model and remote sensing information, the temporal and spatial continuity of crop monitoring can be realized, thus greatly improving the simulation accuracy of crop model. Land surface data assimilation is an effective means to realize the coupling between crop model and remote sensing information (Dorigo et al., 2007; Liu et al., 2013; Xie et al., 2016). The correction of key input parameters in crop model by taking real-time remote sensing information as observational variable and through the adoption of data assimilation method can effectively improve the simulation accuracy of crop model, and enable the single point simulation of crop growth model to develop into regional application (Ren et al., 2011; Li et al., 2015; Xie et al., 2015).

Long-time and continuous air temperature time series data is one of the most important input parameters to drive the operation of WheatGrow model. How to obtain accurate spatio-temporal continuous air temperature time series data sets is the key to extend the WheatGrow model from single point to regional application, and realize the monitoring of spike differentiation stages of winter wheat within a region. At present, the air temperature data is mainly obtained from designated points at long-term observation meteorological stations distributing within the study area. The temperature time series data sets at regional scale is difficult to obtain due to the restrictions on economic and technical conditions, and limited number and uneven distribution of long-term observation meteorological stations within the study area. Although air temperature values at unknown points at regional scale can be estimated by use of the method of spatial interpolation, yet the interpolation results are very uncertain due to the influence of topography, density and distribution of sample points and interpolation method, etc (Noi et al., 2016; Liu et al., 2013; Xu et al., 2011). In addition, in terms of the crop, its growth and yield formation are directly affected by the field microclimate where it exists (Liu et al., 2015), and meteorological stations are usually located at the edge of city or suburban open space. Influenced by urban heat island effect and underlying surface, there are differences between the air temperature of meteorological station and interpolation and farmland. For this reason, the characteristics of air temperature of farmland can't be truly reflected.

In this paper, by basing upon the WheatGrow model, taking winter wheat as the object of study, and regarding air temperature as the assimilated quantity, the author adopts the Kalman Filter Algorithm to assimilated air temperature data time series interpolated and land surface temperature (LST) of remote sensing to obtain the air temperature time series data above the wheat field, and then realizes the monitoring of spike differentiation stages of winter wheat at regional scale.

2 Study area and data

2.1 Study area

Located in the east of Henan Province and the hinterland of Huang-Huai Plain, Shangqiu is one of the main producing area and high yield area within Huang-Huai wheat area (Liu et al., 2016). Located between east longitude 114°49′-116°39′ and northern latitude 33°43′-34°52′, this area belongs to semi-moist continental monsoon climate within the warm temperate zone with annual mean air temperature reaching around 14°C, mean annual sunshine duration 2205-2427 h, annual mean precipitation 623 mm, and annual average frost-free period 211 d. Semi-winterness variety is dominant in the winter wheat plantation. The perennial sowing time of winter wheat is generally during the first 10 days to the second 10 days of October, and the green-turning stage is during the third 10 days of February. The jointing stage is during the second to third 10 days of March, the heading stage is during the second to third 10 days of April, and the maturation stage is during the end of May until the start of June. The study area is as shown in Figure 1.

Figure 1 Map of the study area

2.2 Data

2.2.1 Meteorological data

The meteorological data mainly include the time series of daily maximum air temperature and minimum air temperature at a total of 21 meteorological stations (Figure 1) spreading within and around the municipal district of Shangqiu, Henan Province during the winter wheat growth period from 2015 to 2016. Next, the meteorological data also comprise the daily maximum air temperature, minimum air temperature and phenological data of winter wheat at Shangqiu base station (34°27′N, 115°40′E, elevation: 50.1 m) during the winter wheat growth period from 2005-2006 and 2014-2015. Such data is used for the calibration of WheatGrow model. The above data are derived from China Meteorological Data Network (http://data.cma.cn/).

In addition,2016 agro-meteorological weekly report information published by Shangqiu Meteorological Bureau (http://www.sqqxj.gov.cn/ggqx/nyqxzb/) is also consulted in this study, so as to acquire the green-turning stage, jointing stage, booting stage, heading stage and other critical phenological periods of winter wheat in Shangqiu.

2.2.2 Remote sensing data

The remote sensing data includes: ① Daily surface temperature product of MYD11A1 acquired by MODIS Aqua satellite during the winter wheat growth period in Shangqiu from 2015 to 2016. The spatial resolution is 1km. ② MCD12Q1, three-level land cover product of MODIS with spatial resolution of 500 m. As the study on spike differentiation stages of winter wheat is meaningful only in the winter wheat growing area, it is thus required to extract the winter wheat growing area according to the Land Cover Type5 scheme in MCD12Q1. Remote sensing data are derived from LAADS Web (http://ladsweb.nascom.nasa.gov /data /search.html), and raw data need to be pre-processed by means of embedding, projection, clipping, and etc.

2.2.3 Measured data

Measured data are mainly used to validate the results of spike differentiation stages of winter wheat. The field experiment of spike differentiation stages was conducted at Shuangba testing field of the Test and Demonstration Center under Henan Shangqiu Academy of Agriculture and Forestry Sciences (34°31′55″N, 115°42′37″E, elevation: 50.1 m), the locally common semi-winterness variety of Wenmai 6 was taken as the testing variety, the sowing date was determined at October 15th and the heading stage was generally entered at around April 18th of the next year.

During March 12th to May 31st, 2016, real-time observation and records were conducted with respect to the growth of Wenmai 6 in the experimental field. The procedures mainly comprised ① Air temperature observation of upper underlying surface: Air temperature sensors were arranged at the height of 1.5 m above the wheat field, for the real-time measurement of air temperature above the wheat field. The effective range of sensor measurement is –20°C-60°C, accuracy ±0.5°C, and frequency once per hour. ② Observation of biological indicators: 5-10 wheat plants having uniform and representative growth vigor were taken from the experiment field after washing off mud, so as to determine and record the plant height, tiller number, leaf age of main stem and internodal length of each wheat seedling at every 2-3d. ③ Definition of spike differentiation stages: The main stem of wheat seeding was taken as the object of observation, dissected and placed under the binocular microscope, so as to observe the spike differentiation process and take photos for recording purpose. The descriptions and illustrations for division of spike differentiation stages (compiled by Cui et al., 2006) were taken as the specific reference data for observation of spike differentiation stages, so as to observe and record the specific dates (mainly including the beginning and ending dates of floret differentiation stage, stamen and pistil differentiation stage, anther separation stage, tetrad differentiation stage) emerging from all stages of spike differentiation stages after the green-turning stage of winter wheat. Meanwhile, the beginning date of heading stage in the experiment field was also observed and recorded.

3 Method

3.1 WheatGrow model

In this research, WheatGrow model, i.e. the process-based mechanism wheat growth and development, was taken as a dynamic model which can quantitatively describe the spike differentiation process at the top of wheat stem via PDT (Physiological Development Times). Spike differentiation stages enter into the next stage when PDT has accumulated to a specified value. The PDT threshold values corresponding to floret differentiation stage, stamen and pistil differentiation stage, anther separation stage, tetrad differentiation stage and heading stage are 14.5, 16.1, 17.9, 21.4 and 26.8, respectively (Yan et al., 2000).

In order to simulate the spike differentiation stages of winter wheat, the WheatGrow model needs to be localized and calibrated, and the calibration process is mainly aimed to determine TS (Temperature Sensitivity), PS (Photoperiod Sensitivity), PVT (Physiological Vernalization Time) and IE (Intrinsic Earliness)variety parameters required by the model operation. However, these parameters are difficult to be directly observed. Wenmai 6, a locally common variety of winter wheat, was taken as the standard crop, and the loop iteration for optimization method was adopted to solve the parameter values of calibrated varieties. Specific methods can be described as follows, (1) the average sowing date of winter wheat was determined at October 15th, the average emergence of seedlings date October 21st, the heading date April 17th, and the average duration from emergence of seedlings to heading 178 d according to the phonological observation data of winter wheat during 2005-2006 and 2014-2015 at Shangqiu base station. (2) In the light of the literature (Yan et al., 2000), it is determined that the value ranges for TS, PVT, PS and IE of Wenmai 6 were [1.4, 1.5], [20, 25], [0.004, 0.005] and [0.80, 0.85], respectively. The cycle step sizes for four parameters were separately configured as 0.01, 1, 0.0001 and 0.01. (3) Based on the above parameters, the daily maximum air temperature, minimum air temperature data during the period of 2005-2006 to 2014-2015 at Shangqiu base station, as well as the seeding date, value range of variety parameters and step sizes as determined in No. (1) step, it was possible to run the WheatGrow model on loop iteration basis, calculate the average number of days after extracting the number of days for emergence of seedling until heading obtained from each time of operation, compare the number of days with the standard number of days, and determine the variety parameters combination with minimum difference value as the optimum variety parameter combination. The value ranges for ultimately-determined TS, PS, PVT and IE were 1.5, 0.0048, 25 and 0.85, respectively.

3.2 Spatial interpolation of air temperature

In this paper, in order to obtain the meteorological data of Shangqiu within the growth period of winter wheat, IDW (Inverse Distance Weighted) (Bayazit et al., 2016; Ozelkan et al., 2015) was adopted on account of daily maximum and minimum air temperature data at meteorological stations within and around the municipal district of Shangqiu, so as to generate, via interpretation, the daily maximum and minimum air temperature time series data within the growth period of winter wheat during 2015-2016. The specific calculation formula is described as follows:

$$\lambda_i = \frac{1}{d_i^2} / \sum_{i=1}^{n} \left(\frac{1}{d_i^2}\right) \tag{1}$$

$$Z = \sum_{i=1}^{n} \lambda_i Z_i \tag{2}$$

where, λ_i stands for the weight; n stands for the number of meteorological stations for interpretation purpose; d_i stands for the measured distance between interpolating point and No. i meteorological stations. Z stands for the estimated air temperature value of interpolation. Z_i stands for the measured air temperature value corresponding to No. i (i=1,2,3……n) meteorological stations.

3.3 Establishment of LST and air temperature linear regression model above wheat field

Analysis of the correlation between MODIS LST and the measured air temperature above the wheat field is the key to applying the remote sensing data in the monitoring of winter wheat spike differentiation stages at regional scale. Through the interaction between Terra satellite and Aqua satellite of MODIS, the LST (Land Surface Temperature) data in the same region can be obtained on daily basis. The transit time of Terra satellite is around 10:30 and 22:30, respectively. The transit time of Aqua satellite is around 13:30 and 01:30, respectively. In consideration of the fact that the maxiumum air temperature usually takes place in the afternoon, while the occurrence time of minimum air temperature is relatively close to the transit time at around 01:30, the linear regression was conducted in this paper by respectively extracting LST products (i.e. MYD11A1_Day and MYD11A1_Night) of Aqua satellite within the observed period of field and the daily maximum and minimum air temperature at the height of 1.5m above the wheat field (Figure 2). The regression equations are listed as follows:

$$[AIRT_{max}] = [LST_day] * 1.1805 - 3.6711 \tag{3}$$

$$[AIRT_{min}] = [LST_night] * 0.8931 + 0.9232 \tag{4}$$

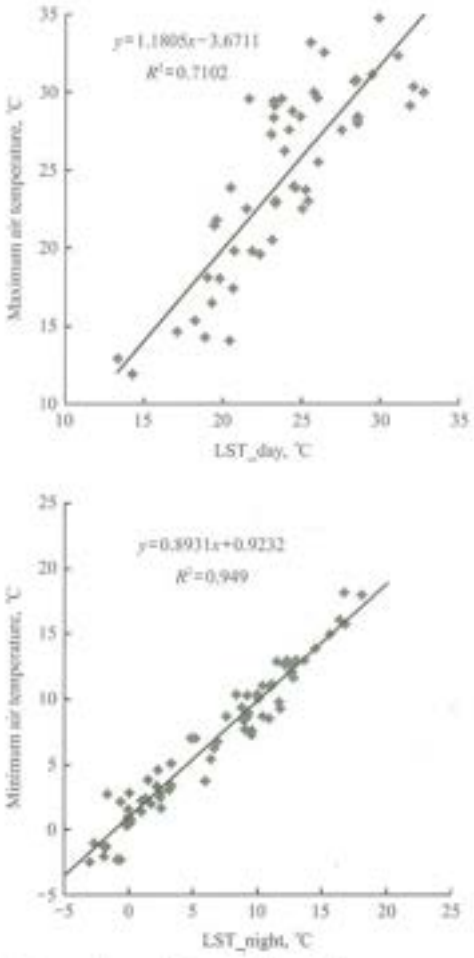

Figure 2 Regression analysis of LST and air temperature of 1.5 m height in wheatfield

3.4 Kalman Filter assimilation algorithm

As a recursive prediction algorithm based on statistical theory, KF (Kalman Filter) algorithm obtains the optimal estimated value of required physical parameters by processing the observational data containing noise and through the adoption of linear unbiased minimum variance estimation method (Peng, 2009; Anadranistakis et al., 2002; Libonati et al., 2008). By combining the model simulation values with the external observation values in the estimation of target parameters, it can effectively reduce the error of estimation process and improve the prediction accuracy. In this study, the continuous air temperature time series above the wheat field was generated at regional scale by

taking land surface temperature products of MODIS as the source of external observation data and by assimilating the air temperature data obtained by interpolation sequentially through the adoption of KF algorithm. The specific recurrence formulas are as follows:

$$Y_t^f = X_t B_{t-1} \tag{5}$$

$$R_t = C_{t-1} + W \tag{6}$$

$$\sigma_t = X_t R_t X_t^T + V \tag{7}$$

$$A_t = R_t X_t^T \sigma_t^{-1} \tag{8}$$

$$B_t = B_{t-1} + A_t (Y_t^o - Y_t^f) \tag{9}$$

$$C_t = R_t - A_t \sigma_t A_t^T \tag{10}$$

where, Y_t^f stands for the estimated value of air temperature, X_t stands for daily maximum and minimum air temperature data at meteorological stations within and around the municipal district of Shangqiu during the winter wheat growth period. B_{t-1} stands for the coefficient vector of interpolation, i.e. weight value λ in the inverse distance weighted of air temperature; R_t stands for the error covariance matrix of extrapolated value B_t, C_{t-1} is the error covariance matrix of B_{t-1}. W stands for the dynamic noise error covariance matrix, σ_t stands for the forecast error covariance matrix; X_t^T stands for the transposed matrix of X_t. V stands for the error covariance matrix of observation noise. A_t stands for the gain matrix, σ_t^{-1} stands for the inverse matrix of σ_t, Y_t^o stands for the "truth-value" of air temperature. That is, the air temperature value at the height of 1.5 m above the wheat field can be obtained from the calculation via formula (3) and (4) by use of MODIS LST product. The recursion of next-step B_t and C_t value can be realized by use of the formula (9) and (10) according to the prediction error.

3.5 Accuracy verification method

MBD (Mean Bias Deviation), MAD (Mean Absolute Deviation) and RMSD (Root Mean Square Deviation) can be selected as indicators for the evaluation of difference between assimilated temperature and measured temperature. Meanwhile, these indicators can also be used as indictors to evaluate the simulation accuracy of spike differentiation stages in WheatGrow model. The specific calculation formulas are as follows:

$$MBD = \frac{1}{N}\sum_1^N (M_i - S_i) \tag{11}$$

$$MAD = \frac{1}{N}\sum_1^N |M_i - S_i| \tag{12}$$

$$RMSD = \sqrt{\frac{1}{N}\sum_1^N (M_i - S_i)^2} \tag{13}$$

where, M_i stands for the simulated value; S_i stands for the measured value; N stands for the number of observation samples. MBD reflects the true deviation, the value of the positive and negative, and the value is closer to zero means the smaller deviation; MAD is used to express the overall prediction accuracy, RMSD is used to express the degree of discretization,and the smaller value of MAD and RMSD the smaller the deviation.

4 Results

4.1 Air temperature assimilation

4.1.1 Air temperature assimilation of single point

Shuangba testing field in Shangqiu was taken as the sample point for the analysis of results of single point air temperature assimilation. The comparison of assimilated air temperature, interpolated and converted air temperature from LST are as shown in Figure 3. It can be found out from Figure 3 that the trend of assimilated air temperature is consistent with the trend of interpolated air temperature, while the values of assimilation are very close to the air temperature converted from LST by linear regression equation. This regular pattern has the same performance at both the maximum and the minimum air temperature. It shows that the air temperature value of assimilation is mainly affected by LST (land surface temperature), the LST level plays the decisive role in the assimilated air temperature, yet the contribution of interpolated air temperature is relatively small. Therefore, subject to the regulation of LST, the maximum air temperature curve of assimilation is above the interpolated maximum air temperature curve, while the minimum air temperature curve of assimilation is below the interpolated minimum air temperature curve.

The deviation between the assimilated air temperature and measured air temperature was further analyzed with MBD, MAD and RMSD. The results are as shown in Figure 4. It can be found out in Figure 4 that R^2 (determination coefficient of assimilated maximum air

temperature and measured maximum air temperature) reached 0.70, the overall deviation was controlled at around 3°C, in which MBD was only 0.8°C. The assimilation effect of the minimum air temperature was better than that of the maximum air temperature, R^2 (determination coefficient of assimilated minimum air temperature and measured minimum air temperature) reached 0.94, MBD, MAD and RMSD were 0.1°C, 1.0°C and 1.3°C, respectively. If compared with maximum air temperature the smaller deviation manifested in the maximum air temperature, the above analysis shows that the air temperature assimilated by KF conforms to the variation characteristics of air temperature of wheat field, and fits for being taken as the input parameter of WheatGrow model for the simulation of spike differentiation stages of winter wheat.

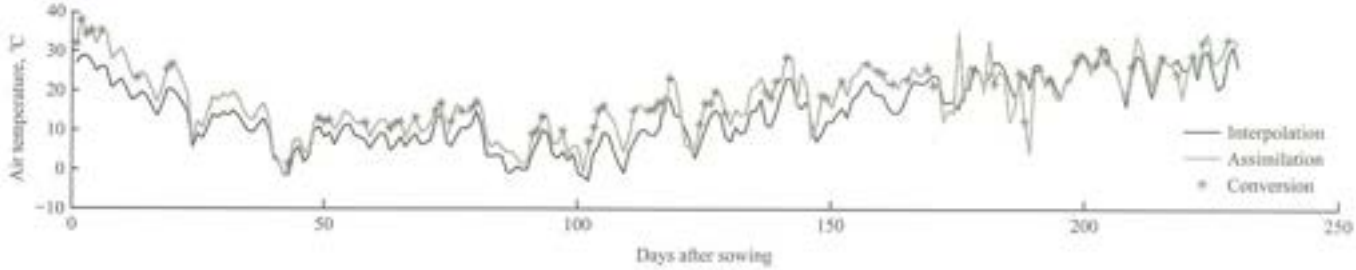

a. Maximum air temperature

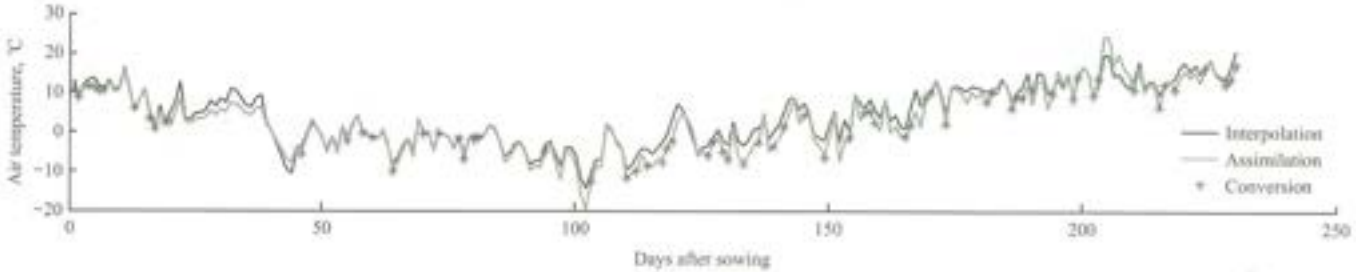

b. Minimum air temperature

Figure 3 Comparison of assimilated air temperature and interpolated and converted air temperature from LST of 2015-2016

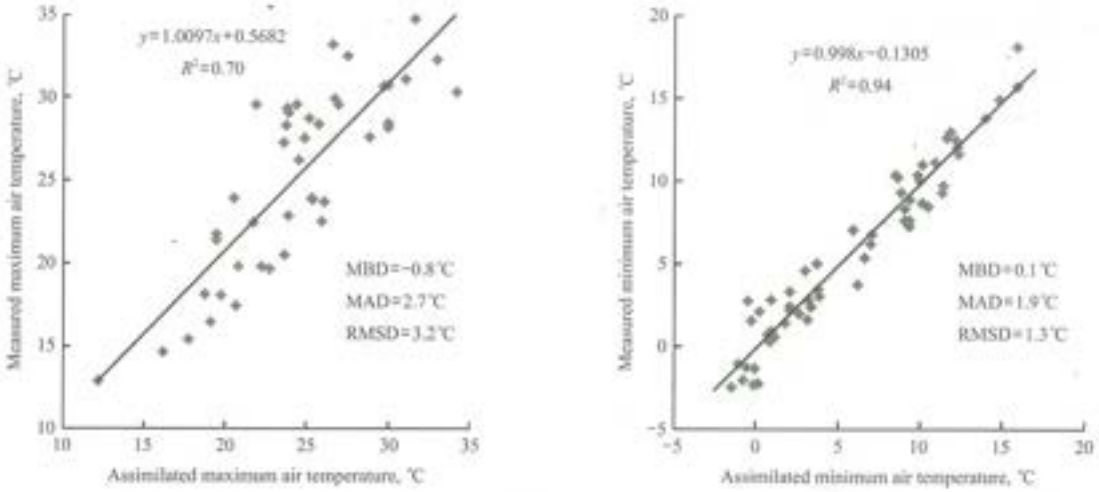

Figure 4 Comparison of air temperature between assimilation and observation

4.1.2 Regional air temperature assimilation

Results of regional air temperature assimilation during the growth period of winter wheat within 2015-2016 were obtained by extending the algorithm to the region scale on the basis of single point air temperature of assimilation. In Figure 5, by taking March 22nd, 2016 as an example, the comparisons between assimilation by KF and MODIS LST products and interpolation by IDW of maximum and minimum air temperatures within the winter wheat planting area of Shangqiu were revealed.

As shown in the figure above, the spatial variability of air temperature of assimilation has kept the variation characteristics of the original MODIS LST remote

sensing images. In the aspect of maximum air temperature, it can be observed from Figure 5a that the maximum air temperature dated March 22nd, 2016 within the north central and northwestern border districts of Shangqiu reached the maximum value of the study area, and the maximum air temperature of assimilation (Figure 5c) also reflected this feature. As shown in the maximum air temperature of interpolation by IDW, the maximum air temperature dated March 22nd, 2016 within the study area ranged between 18°C and 21°C, while the maximum air temperature of assimilation within most areas ranged around 23°C-26°C due to the impact of LST, indicating the obvious effect of LST on assimilated results. Compared with the maximum air temperature, the effect of LST on the assimilated results of minimum air temperature is more obvious. As shown in the comparisons between Figures 5d and 5f, the spatial variation tendency of these two images is almost the same, most of the minimum air temperatures of assimilation are less than 5°C, and the higher minimum air temperature concentrates on the western region. According to the above analysis, it can be observed at the regional scale that the spatial variation of air temperature of assimilation is closer to the variation characteristics of LST, and this regular pattern is more obvious in the assimilated results of minimum air temperature.

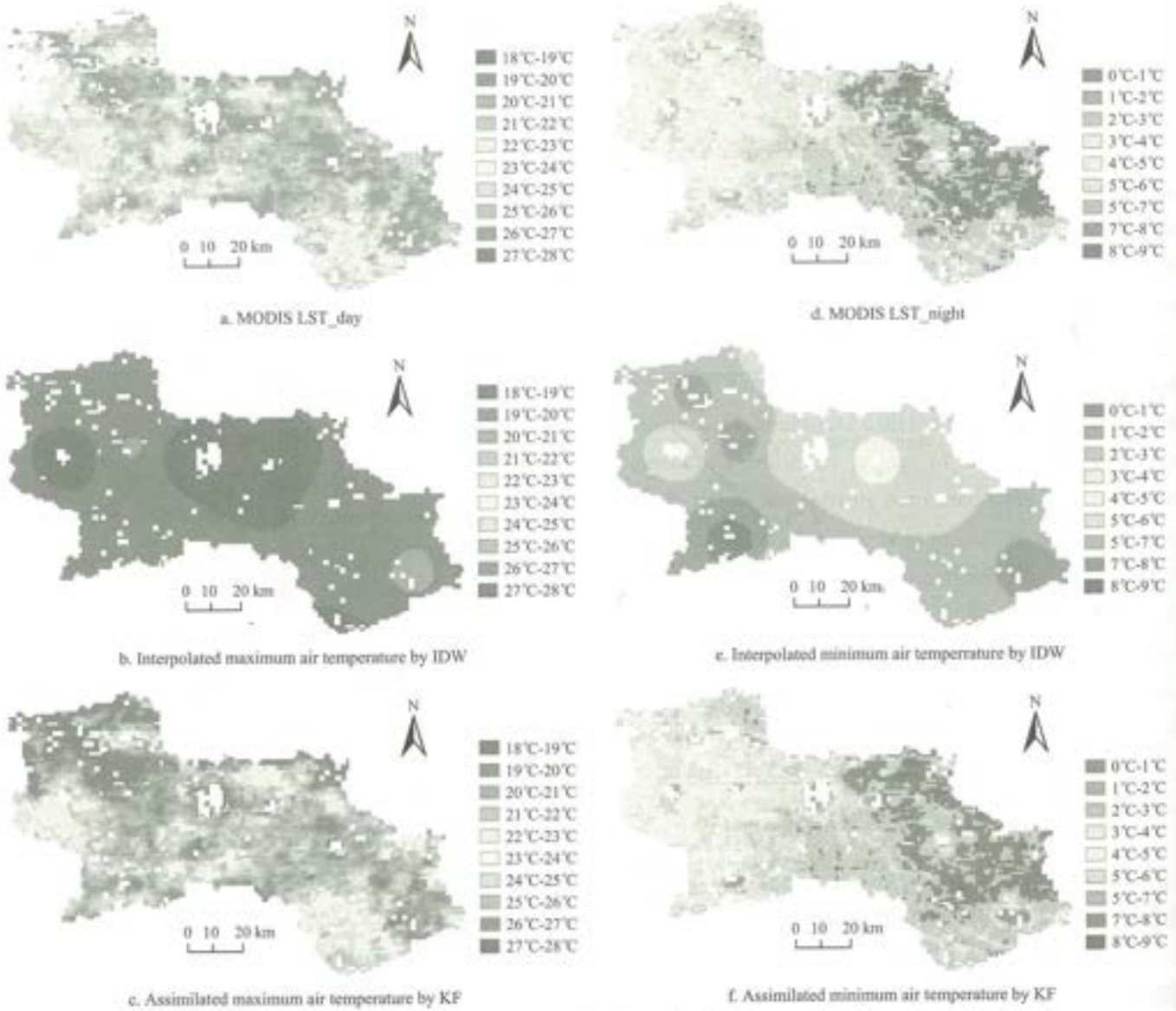

a. MODIS LST_day

d. MODIS LST_night

b. Interpolated maximum air temperature by IDW

e. Interpolated minimum air temperrature by IDW

c. Assimilated maximum air temperature by KF

f. Assimilated minimum air temperature by KF

Figure 5 Comparison of assimilated air temperature of winter wheat planting areas in Shangqiu on March 22nd

4.2 Monitoring of spike differentiation stages

4.2.1 Monitoring of regional spike differentiation stages

According to the above analysis, the distribution chart (Figure 6) of the start dates corresponding to the entry of floret differentiation stage, stamen and pistil differentiation stage, anther separation stage, tetrad

differentiation stage and heading stage after the green-turning stage of winter wheat can be obtained at regional scale by inputting the regional maximum and minimum air temperature time series of assimilation during 2015-2016 into WheatGrow model. In this Figure, the start dates corresponding to each of spike differentiation stage were indicated with the number of days after the emergence of seedlings.

As is shown in Figure 6, the overall spatial distribution of the start dates corresponding to all spike differentiation stages (from floret differentiation stage to heading stage) present the trend of gradual delay from south to north. The start dates of spike differentiation stages was the earliest in Zhecheng and Yongcheng county in the south of Shangqiu, while it was the latest in Minquan county in the north of Shangqiu. In addition, the start dates of spike differentiation stages in the north of Yucheng was also relatively late, the maximum time difference was eight days, and such variation became stable in spike differentiation stages from floret differentiation stage to heading stage.

As is shown in Figure 6a, the start dates corresponding to the floret differentiation stage in Shangqiu during 2015-2016 ranged between 143 d and 151 d after the emergence of seedlings, i.e. March 12th-20th. In the majority of districts, the start dates corresponding to the floret differentiation stage concentrated on about 147-149 d after the emergence of seedlings, the start dates of Zhecheng and Yongcheng in the south concentrated on 143-145 d after the emergence of seedlings, the start dates of floret differentiation stage in Minquan (located in the northwest) and Yucheng (located in the northern region) was the latest.

Following the entry of stamen and pistil differentiation stage, the spatial distribution of start dates still presented the trend of gradual transition from south to north, and the start dates was 149-158d after the emergence of seedlings, i.e. March 18th-27th. As indicated in Shangqiu agricultural meteorological weekly data, jointing stage of winter wheat began to spread during March 21th-28th, 2016, and the start dates of stamen and pistil differentiation stage conformed to the statement as mentioned in the literature (Yan et al., 2000) that there is a good synchronization between the stamen and pistil differentiation stage and phenological jointing stage, showing that the monitoring results of spike differentiation stage was consistent with the actual growth status of winter wheat.

As also indicated in Figure 6b, the start dates of stamen and pistil differentiation stage within the planting area of winter wheat in Suixian, Ningling and Xiayi began about 151-153 d after the emergence of seedlings (March 20-22nd), while the start dates of stamen and pistil differentiation stage of the winter wheat planting area within the municipal district of Shangqiu and Yucheng was relatively late, manifesting the spatial distribution differences distinctly different from those of floret differentiation stage at the start dates. According to the agricultural meteorological information weekly, during March 13th to March 19th, 2016. The average air temperature in Yucheng and the municipal district of Shangqiu was obviously low, if compared with that of Suixian and Ningling, etc. Moreover, the extreme minimum temperature of –3.3°C even appeared at Shangqiu base station. Thus, the start dates of stamen and pistil differentiation stage lagged behind.

The spatial distribution of start dates when the spike differentiation stage entered into anther separation stage and tetrad differentiation stage was shown in Figure 6c and 6d, and it can observed that the start dates of anther separation stage began at 155-163 d after the emergence of seedlings (March 24th - April 1st), while the start dates of tetrad differentiation stage began at 163-171 d after the emergence of seedlings (April 1st-9th). It can be observed from the comparison of these two figures that the start dates of anther separation stage and tetrad differentiation stage maintained almost the same spatial distribution, showing that the temperature fluctuation trends and amplitudes of all regions were relatively consistent within the time period when the spike differentiation of winter wheat entered into the stamen and pistil differentiation stage and tetrad differentiation stage during 2015-2016.

With the advance of spike differentiation of winter wheat, the spatial difference of start dates of spike differentiation stage presented the decreasing trend, especially in Minquan in the northwest. Although the

start dates of floret differentiation stage was later than that of other regions, there was no significant differences between the start dates of heading stage of remaining regions.

As is shown in Figure 6e, until about 173 d after the emergence of seedlings, i.e. during the second ten days of April, the winter wheat in Zhecheng started to enter into the heading stage, and successively heading started in remaining regions during 175-178 d after the emergence of seedlings (April 13th-16th), except that the heading dates in the municipal district of Shangqiu and the northern area of Yucheng were relatively late. The result was basically consistent with the ground monitoring results recorded in Shangqiu agricultural meteorological weekly in 2016.

The spike differentiation of winter wheat is a continuous changing process, and the start date of next spike differentiation stage is the end date of previous spike differentiation stage. Thus, the duration of each spike differentiation stages can be calculated. During 2015-2016, the duration of floret differentiation stage in Shangqiu lasted 6-7 d days,the duration of stamen and pistil differentiation stage lasted 5-6 d, anther separation stage and tetrad differentiation stage lasted 8 d and 10 d, respectively. It was roughly consistent with the variation trend of the duration of actual spike differentiation stages.

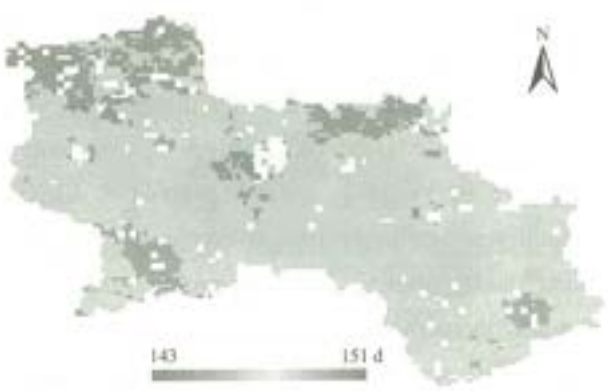

a. Floret differentiation stage

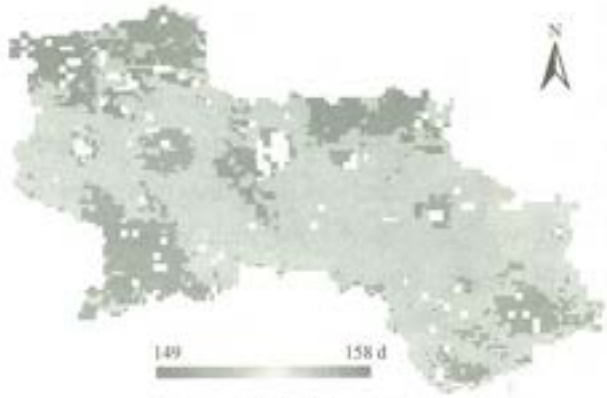

b. Stamen & pistil differentiation stage

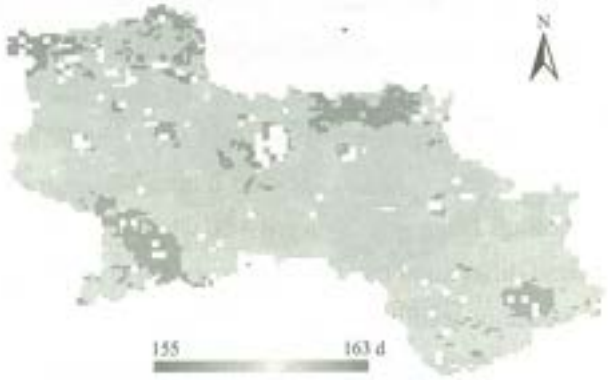

c. Anther separation stage

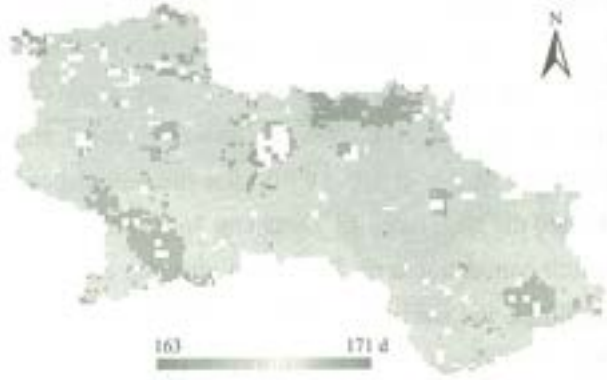

d. Tetrad differentiation stage

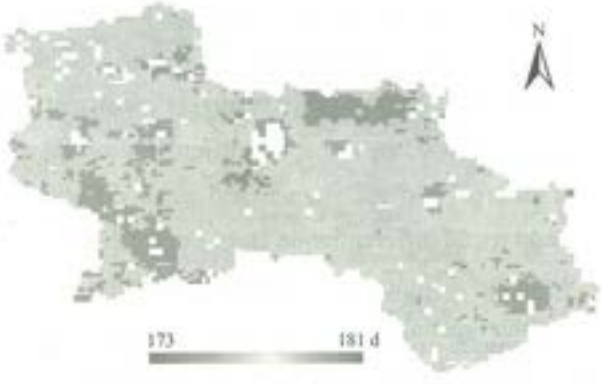

e. Heading stage

Figure 6 Map of the start date of spike differentiation stages in Shangqiu from 2015 to 2016

4.2.2 Verification of spike differentiation stages

According to the above analysis, the start dates of every spike differentiation stage and duration of every stage were obtained through calculation by taking Shuangba Experimental Base as a sample point, and putting the maximum air temperature time series data and minimum air temperature time series data during the winter wheat growth period during 2015-2016 obtained by assimilation, geographic latitude of the experimental field and other parameters into WheatGrow model. Moreover, comparison validation was also conducted by use of the observed results of spike differentiation stages, and the results are shown in Figure 7, Tables 1 and 2.

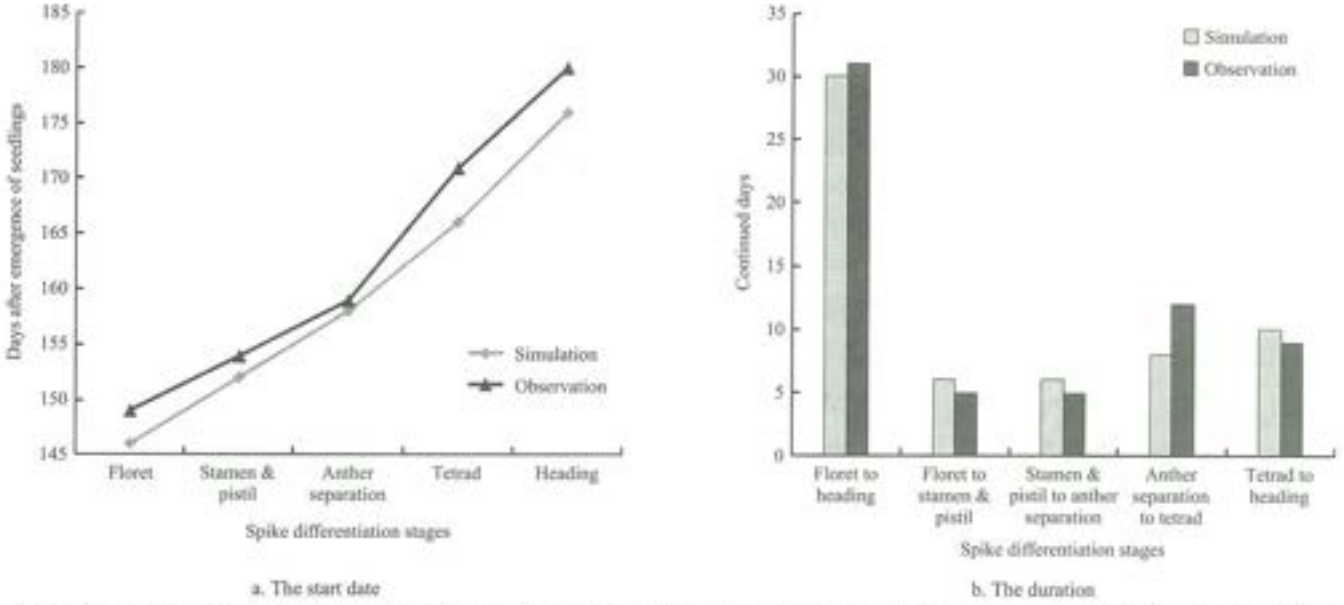

a. The start date

b. The duration

Figure 7 Comparison of start date and duration of spike differentiation stages between simulation and observation from 2015 to 2016

Table 1 Comparison of start date of spike differentiation stages between simulated data and observed data

Category	Floret initiation	Stamen and pistil initiation	Anther separation	Tetrad	Heading	MBD	MAD	RMSD
Simulation	3/15	3/21	3/27	4/4	4/14	-	-	-
Observation	3/18	3/23	3/28	4/9	4/18	-	-	-
ΔD	-3	-2	-1	-5	-4	-3	3	3.3

Note:ΔD represents the deviation between simulated start date and the observed start date of spike differentiation stages.

Table 2 Comparison of duration of spike differentiation stages between simulated data and observed data

Category	Floret to Stamen and pistil	Stamen and pistil to Anther separation	Anther separation to Tetrad	Tetrad to Heading	Floret to Heading	MBD	MAD	RMSD
Simulation	6	6	8	10	30	-	-	-
Observation	5	5	12	9	31	-	-	-
Δd	1	1	-4	1	-1	-0.3	1.8	4.4

Note: Δd represents the deviation of duration of spike differentiation stages between simulated data and observed data, the continued days from Floret to Heading was not used to calculate MBD, MAD and RMSD.

As shown in Figure 7, the overall variation trend of start dates and duration of every spike differentiation stages calculated by WheatGrow model was consistent with the field. As indicated in Table 1 and Table 2, (1) the MBD and MAD between start date of every spike differentiation stage calculated by WheatGrow model and the measured date were all 3 d, RMSD was 3.3 d. Among them, there were relatively large deviations in tetrad differentiation stage (deviation was 5 d). For the rest of every spike differentiation stage, the deviations between simulated date and measured date were less than 5 d, indicating that the validation effect of the start date of every winter wheat spike differentiation stage was good. (2) The deviations of duration between simulation and observation during every spike differentiation stage (calculated by the WheatGrow model) were controlled within 4 d, MBD was 0.3 d, MAD was 1.8 d and RMSD was 4.4 d. Among them, the difference value at the anther

separation-tetrad stage was the largest, i.e. 4 d; The duration of floret-pistil and stamen, stamen and pistil - anther separation, and tetrad-heading was 1 d longer than the measured number of days, while the duration of anther separation-tetrad was shorter than the measured number of days. However, judging from the total number of days of floret-heading, the number of days was very close to the measured number of days under the premise of calculation based on WheatGrow model, i.e. error is only 1 d. It showed that WheatGrow model was ideal for the estimation effect of duration of winter wheat spike differentiation stages.

5 Discussions

In this study, the following several issues still remain to be discussed:

(1) As the air temperature converted by linear regression model with MODIS LST products during assimilation process was taken as "truth-value", thus such value was directly affected by MODIS LST and linear regression equation. For this reason, the precision of assimilation air temperature decreases if MODIS LST extracted is low in accuracy or the effect of linear fitting is poor.

(2) MODIS LST products are the key to realize assimilation by KF. In practice, MODIS LST products may be absent due to cloud pollution. In this paper, the way to deal with this problem can be described as follows, when LST absence appears, it is required to select the LST value when LST was not absent at last moment and take it as the LST at current moment for the continuation of assimilation by KF, which may cause the air temperature of assimilation during the LST-absent time interval to maintain the variation trend of assimilation result at the last moment when LST was not absent. This is obviously out of line with reality, and it is considered to re-conduct assimilation by KF after the reconfiguration of absent LST.

(3) The spike differentiation stages of winter wheat is not only affected by climatic conditions, but also closely related to characteristics of wheat varieties and cultivation measures (Cui et al., 2006; Yang et al., 2007; Steinmeyer et al., 2013; Han et al., 2011). In this paper, only semiwinterness wheat variety was taken as the object of study, for the calibration of WheatGrow model. The parameters calibrated are not entirely suitable for winter and spring wheat varieties.

6 Conclusions

In this paper, under the premise of calibrated WheatGrow model, spatio-temporal continuous air temperature time-series data above the wheat field during the growth period of winter wheat in Shangqiu was obtained by assimilating MODIS LST data and air temperature interpolated by IDW with Kalman Filter. The monitoring of every spike differentiation stage after the green-turning stage of regional winter wheat was realized by the maximum air temperature and minimum air temperature time series of assimilation. The main conclusions are listed as follows:

(1) The continuous air temperature time-series data above the wheat field was obtained by basing upon KF data assimilation algorithm and integrating the advantages of remote sensing technology and crop growth model. The variation trend of assimilated air temperature time-series in wheat field was basically identical to that of the spatial interpolation, yet its spatial variation was closer to that of LST. The determination coefficient R^2 of maximum air temperature was 0.70 and 0.94 for minimum air temperature between assimilation and observation, indicating that the air temperature assimilated by KF complied with the variation characteristics of air temperature in wheat field and fitted as the input parameter of WheatGrow model for the simulation of spike differentiation stages of winter wheat.

(2) Judging from the monitoring results of winter wheat spike differentiation stages, remote sensing technology, geographic information system, spatial interpolation technology and data assimilation technology were integrated in this paper, so as to realize the monitoring of floret differentiation stage, stamen and pistil differentiation stage, anther separation stage, tetrad differentiation stage and heading stage after the green-turning stage of winter wheat. As shown in validated results with single-point, the deviations of start date between simulation and observation during every

spike differentiation stage were within 5 d, and the deviations of duration between simulation and observation during every spike differentiation stage were within 1-4 d. The monitoring result and measured result during the spike differentiation stages were basically identical. The method presented in this paper provides a direction for monitoring spike differentiation stages of winter wheat rapidly, accurately and effectively, and it is of far-reaching significance to the late frost monitoring and yield estimation and relevant researches of winter wheat.

Acknowledgements

This research was supported by the National Natural Science Foundation of China (Grant No.41471342). We thank Shangqiu Academy of Agriculture and Forestry Sciences for the experiment of spike differentiation stages of winter wheat.

[References]

[1] Abrecht, D. G., and S. D. Robinson. 1996. TACT: a tactical decision aid using a CERES based wheat simulation model. *Ecological Modelling*, 86(2-3): 241–244.

[2] Anadranistakis, M., K. Lagouvardos, V. Kotroni, and K. Skouras. 2002. Combination of kalman filter and an empirical method for the correction of near surface temperature forecasts: application over greece. *Geophysical Research Letters*, 29(16): 1776–1779.

[3] Balwinder, S., D. S. Gaydon, E. Humphreys, and P. L. Eberbach. 2011. The effects of mulch and irrigation management on wheat in punjab, india-evaluation of the APSIM model. *Field Crops Research*, 124(1): 1–13.

[4] Bayazit, Y., R. Bakis, and C. Koc. 2016. Mapping distribution of precipitation, temperature and evaporation in seydisuyu basin with the help of distance related estimation methods. *Journal of Geographic Information System*, 08(2): 224–237.

[5] Cao, W., and D. N. 1997. Modelling phasic development in wheat: a conceptual,integration of physiological components. *Journal of Agricultural Science*, 129(2): 163–172.

[6] Cui, J., and T. Guo, 2006. *Spike of Wheat*. Beijing: China Agricultural Press.

[7] Dettori, M., C. Cesaraccio, A. Motroni, D. Spano, and P. Duce. 2011. Using CERES-Wheat to simulate durum wheat production and phenology in Southern Sardinia, Italy . *Field Crops Research*, 120(1): 179–188.

[8] Dorigo, W. A., R. Zurita-Milla, A. J. W. D. Wit, J. Brazile, R. Singh, and M. E. Schaepman. 2007. A review on reflective remote sensing and data assimilation techniques for enhanced agroecosystem modeling. *International Journal of Applied Earth Observation and Geoinformation*, 9(2): 165–193.

[9] González, F. G., G. A. Slafer, and D. J. Miralles. 2003. Floret development and spike growth as affected by photoperiod during stem elongation in wheat. *Field Crops Research*, 81(1): 29–38.

[10] Han, J. L., Q. Yang, W. P. Wang, L. I. Yan-Sheng, and Y. F. Zhou. 2011. Effects of sowing date on the caulis and tillers differentiation of young spike and yield in winter wheat. *Journal of Triticeae Crops*, 32(1): 303–307.

[11] Jamieson, P. D., I. R. Brooking, M. A. Semenov, G. S. Mcmaster, J. W. White, and J. R. Porter. 2007. Reconciling alternative models of phenological development in winter wheat. *Field Crops Research*, 103(1): 36–41.

[12] Jin, H., J. Wang, Y. Bo, G. Chen, and H. Xue. 2012. Estimation on regional maize yield based on assimilation of remote sensing data and crop growth model. *Transactions of the Chinese Society of Agricultural Engineering*, 28(6): 162–173.

[13] Jones, J. W., G. Hoogenboom, C. H. Porter, K. J. Boote, W. D. Batchelor, and L. A. Hunt. 2003. The DSSAT cropping system model. *European Journal of Agronomy*, 18(3-4): 235–265.

[14] Keating, B. A., P. S. Carberry, G. L. Hammer, M. E. Probert, M. J. Robertson, and D. Holzworth. 2003. An overview of APSIM, a model designed for farming systems simulation. *European Journal of Agronomy*, 18(3-4): 267–288.

[15] Li, Z., X. Jin, C. Zhao, J. Wang, X. Xu, G. Yang, and J. Shen. 2015. Estimating wheat yield and quality by coupling the DSSAT-CERES model and proximal remote sensing. *European Journal of Agronomy*, 71: 53–62.

[16] Libonati, R., I. Trigo, and C. C. Dacamara. 2008. Correction of 2m-temperature forecasts using kalman filtering technique. *Atmospheric Research*, 87(2): 183–197.

[17] Liu, C., G. Cao, and M. Zhang. 2013. Influence of temporal and uariablity on estimation of air temperatures from MODIS land surface temperatures. *Remote Sensing Technology and Application*, 28(5): 931–835.

[18] Liu, J., M. Li, P. Wang, and J. Huang. 2013. Monitoring of phenology by reconstructing LAI time series data for winter wheat. *Transactions of the Chinese Society of Agricultural Engineering*, 29(19): 120–129.

[19] Liu, J., N. Wang, P. Wang, X. Hu, and J. Huang. 2015. Simulation of air temperature within winter wheat near-ground layer based on SHAW model. *Transactions of the Chinese Society for Agricultural Machinery*, 46(Supp.): 274–282.

[20] Liu, J., N. Wang, P. Wang, X. Hu, J. Huang, and P. Pan. 2016. Applicability of simultaneous heat and water model for monitoring late frost injury of winter wheat. *Transactions of the Chinese Society for Agricultural Machinery*, 47(6): 265–274.

[21] Mcmaster, G. S., J. A. Morgan, and W. W. Wilhelm. 1992. Simulating winter wheat spike development and growth. *Agricultural and Forest Meteorology*, 60(3-4): 193–220.

[22] Noi, P., M. Kappas, and J. Degener. 2016. Estimating daily maximum and minimum land air surface temperature using modis land surface temperature data and ground truth data in northern Vietnam. *Remote Sensing*, 08(12): 1002.

[23] Ozelkan, E. C. 2015. Spatial interpolation of climatic variables using land surface temperature and modified inverse distance weighting. *International Journal of Remote Sensing*, 36(4): 1000–1025.

[24] Peng, D. 2009. Basic principle and application of Kalman Filter. *Software Guide*, 08(11): 32–34.

[25] Ren, J., Z. Chen, H. Tang, Q. Zhou, and J. Qin. 2011. Regional crop yield simulation based on crop growth model and remote sensing data. *Transactions of the Chinese Society of Agricultural Engineering*, 27(8): 257–264.

[26] Serrago, R. A., D. J. Miralles, and G. A. Slafer. 2008. Floret fertility in wheat as affected by photoperiod during stem elongation and removal of spikelets at booting. *European Journal of Agronomy*, 28(3): 301–308.

[27] Steinmeyer, F. T., M. Lukac, M. P. Reynolds, and H. E. Jones. 2013. Quantifying the relationship between temperature regulation in the ear and floret development stage in wheat (Triticum aestivum L.) under heat and drought stress. *Functional Plant Biology*, 40(7): 700–707.

[28] Xie, Y., P. Wang, and J. Liu. 2015. Winter wheat yield estimation based on assimilation method combined with 4DVAR and EnKF. *Transactions of the Chinese Society of Agricultural Engineering*, 31(1): 187–195.

[29] Xie, Y., P. Wang, H. Sun, S. Zhang, and L. Li. 2016. Assimilation of leaf area index and surface soil moisture with the CERES-Wheat model for winter wheat yield estimation using a particle filter algorithm. *IEEE Journal of Selected Topics in Applied Earth Observations and Remote Sensing*, 10(4): 1303–1316.

[30] Xu, Y., Z. Qin, and Y. Shen. 2011. Estimation of near surface air temperature from modis data in the Yangtze River Delta. *Transactions of the Chinese Society of Agricultural Engineering*, 27(9): 63–68.

[31] Yan, M., W. Cao, W. Luo, and H. Jiang. 2000. A mechanistic model of phasic and phenological development of wheat I. *Assumption and description of the model. Chinese Journal of Applied Ecology*, 11(3): 355–359.

[32] Yan, M. C., W. X. Cao, C. D. Li, and Z. L. Wang. 2000. Validation and evaluation of a mechanistic model of phasic and phenological development of wheat. *Scientia Agricultura Sinica*, 33(2): 43–50.

[33] Yang, Z. Q. 2007. Corresponding relation between leaf and spikelet primordium differentiation of different development type of wheat cultivars. *Journal of Nuclear Agricultural Sciences*, 21(6): 550–556.

[34] Zun-Fu, L., X. J. Liu, L. Tang, L. L. Liu, W. X. Cao, and Y. Zhu. 2013. Regional prediction and evaluation of wheat phenology based on the WheatGrow and CERES Models. *Scientia Agricultura Sinica*, 46(6): 1136–1148.

Remote crop water requirement monitoring system based on multi-sensor

Wang Yongqian[1,2], Fan Lifeng[1,3], Huang Lan[1,3], Zhao Pengfei[1,2], Wang Ziyang[1,3], Wang Zhongyi[1,2,3*]

(1. *College of Information and Electrical Engineering, China Agricultural University, 100083 Beijing, China*; 2. *Modern Precision Agriculture System Integration Research Key Laboratory of Ministry of Education, 100083 Beijing, China*; 3. *Key Laboratory of Agricultural information acquisition technology (Beijing), Ministry of Agriculture, 100083 Beijing, China*)

Abstract: To estimate crop water requirement state accurately, a remote system was built. It makes irrigation decision based on various information when water deficit stress occurs. To meet demand of remote monitoring and automatic control, the system adopted master-slave structure, implemented remote view and control. It integrated crop physiological state and environmental sensors, such as plant electrical signal, stem-flow sensor, et al. In this work, configuration software was used to realize remote interaction between the master and slave. Preliminary results showed that the remote monitoring system is practicable and stable, and it allows us to investigate the relationship between the environmental factors and physiological parameters of crop in the greenhouse. The developed system will be a potential tool for evaluating crop water requirement state and precise irrigation.

Keywords: plant electrical signal, stem-flow sensor, configuration software, physiological state, remote monitoring system

Citation: Wang. Y. Q., L. F. Fan, L. Huang, P. F. Zhao, Z, Y. Wang, and Z. Y. Wang. 2017. Remote crop water requirement monitoring system based on multi-sensor. International Agricultural Engineering Journal, 26(3): 399–409.

1 Introduction

Water stress limits the growth of crop in a short time or even irreversibly. So, estimating crop water requirement accurately and precisely is extremely important. Currently, in most crop cultivation process, crop water requirement state is just determined by the environmental or single physiological state information but rarely monitoring comprehensive physiological state, which is one-sided for decision-making and environmental control. Water stress results in a variety of changes in crops, ranging from altered physiological state to changes in growth rate and plant productivity (Shao et al., 2008; He et al., 2011; Escalona et al., 2015). Therefore, a system monitoring crop physiological states and environmental information simultaneously is significant (Fisher et al., 2010).

In addition to the environmental factors that can reflect crop water state, some previous studies have demonstrated that some physiological state information can be used to predict the crop water requirement state. Chlorophyll is one of the most important pigments related to photosynthesis, and its content determines the efficiency of photosynthesis. Chlorophyll content decreases under water stress and a recovery would be observed following rewatering for maize (Alberte et al., 1977; Efeoğlu et al., 2009; Akhkha et al., 2011). Stem flow of crops is related to soil water content, temperature and radiation, et al, making it to be a suitable and reliable indicator in detecting changes of water state (Ortuno et al., 2005; Conejero et al., 2007; Escalona et al., 2015). Since Tanner C. B. put forward that canopy temperature can be considered as an indicator of crop water deficit (Tanner, 1963), canopy temperature method has become an important means in the diagnosis of crop water

Received date: 2017-07-05 **Accepted date:** 2017-08-22

* **Corresponding author: Wang Zhongyi,** Ph.D., Professor, Department Head of Electronic Engineering, China Agricultural University, Beijing 100083, China. Email: wzyhl@cau.edu.cn. Tel: +86-10-62737778

availability (Jackson et al., 1981; Fisher et al., 2010). Moreover, changes in stem diameter are frequently associated with plant water state (Katerji et al., 1994; Gallardo et al., 2006). Measuring the change in stem diameter of lemon trees, Ortuno et al. (2005) found that the water supply influenced the daily maximum trunk shrinkage directly. Yang et al. (2015) found that the stem base diameter of Populus euphratica seedlings decreased with the drought stress level rose. Furthermore, electrical excitability and signaling are frequently associated with rapid response to environmental stimuli. In our previous work, we have found that plant electrical signal is related to water stress (Wang et al., 2007; He et al., 2011). The characteristic of electrical potential during different light condition could be used as alternative tool to assess early plant stress (Fromm et al., 1998; Wang et al., 2007; Oyarce et al., 2010).

The main objective of this research is to discuss an automatic acquisition technique of crop water comprehensive information, develop sensors that can reflect crop growth and crop water information under water stress and build a remote monitoring system. On the basis of combining physiological state and environmental information, study data fusion technology and apply multifunction regulation devices, to achieve optimal system control and then water saving irrigation.

2 System design

2.1 System architecture design

Because there are many inconveniences during measurements in field, remote monitoring the water requirement of crop is extremely important. Remote crop water requirement monitoring system was designed for accurate monitoring of physiological state and environmental information in greenhouse, and it provided scientific basis for precise irrigation. The system adopted master-slave architecture divided into two parts: the server program and the acquisition-control system.

The acquisition-control system mainly included embedded integrated touch screen (running Monitor and Control Generated System (MCGS), which is a configuration software for rapid constructing monitoring and control system. Model: TPC7062Ti, Beijing Kunlundongtai automation software technology Corporation, China) and sensors. The embedded integrated touch screen has RS485 and Internet interfaces. The sensors included sensor for chlorophyll, stem-flow sensor, leaf temperature sensor, soil temperature and moisture sensor, stem diameter sensor, environmental temperature and moisture sensor, illumination sensor, radiation sensor and plant electrical signal sensor. Sensors could obtain crop physiological state and environmental information, and then the signals would be transmitted to the MCGS through acquisition modules. MCGS stored and managed the data, timely delivered it to the server program for deeper analysis. The embedded integrated touch screen with a network interface make users could browse sensor data, control buttons of irrigation switch, adjust pan-tilt direction of sensor for chlorophyll, and do control operations on the touch screen through the Internet. The acquisition-control system was equipped with an infrared network high-definition camera (DS-2DE7172-A, Hangzhou Hikvision Digital Technology Co., Ltd. China) which could be accessed through Internet, with horizontal direction 360° continuous rotation, vertical –15° to 90°. The camera real-timely monitored crop growth and the sensors in case they dropped from original position.

The server program running on a network server received data from the acquisition-control system. All the data would be uploaded to database and displayed on the program interface. The server program processed the data and then made irrigation judgement. Same to the acquisition-control system, users could control operations on server program, and the commands would be delivered to the acquisition-control system. After configuration, users could check data and do controls on the server program via Internet explorer anytime any place. Remote interaction was realized through Internet between the server program and the acquisition-control system. Architecture of remote monitoring system design is shown in Figure 1.

The system hardware consisted of power supply, signal module, an embedded integrated touch screen, sensors, and router. Power supply consisted of three switching power supply modules, respectively to provide

DC 24V (SA10024, Delixi Group Co., LTD. China), DC12V (SA5012, Delixi Group Co., LTD. China) and DC±12V (NET-50B, Taiwan Ming Wett Electric co., LTD. China) power supply for hardware equipment. Signal module contained acquisition module, output module, signal transducer module and terminal blocks. Modules connected sensors and touch screen. There were 4-20 mA acquisition module (EDA9017, Shandong Lichuang Science and Technology co., LTD. China) and 0-5 V acquisition module (C2000-A1-PAX0200-BX1, Shenzhen Zhonglian Chuangxin Autonomous System co., LTD. China), transmitting signal to the MCGS through RS485 interface. MCGS controlled the solenoid valve through output module. A signal transducer (MIK-502E-1-2-1-1-V2, Hangzhou Meacon Automation Technology Co., LTD. China) changed sensor's voltage output 0-20 mV to current signal 4-20 mA, and then signal would be transmitted to 4-20 mA acquisition module. The sensors are distinguished by address code in the RS485 protocol. All sensors' output and power were connected to terminal block. The hardware board was installed behind the embedded integrated touch screen.

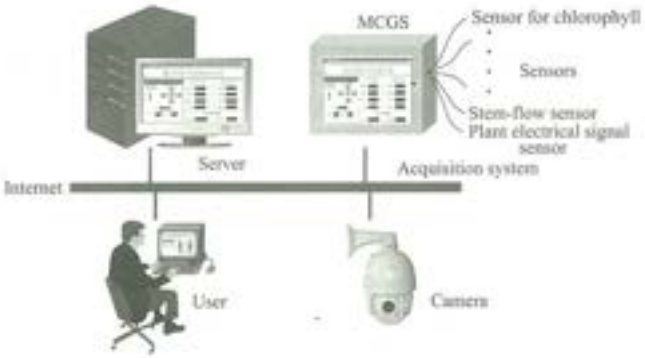

Figure 1 Architecture of the system

2.2 Sensors

2.2.1 Sensor for chlorophyll

The sensor for measuring chlorophyll of plant leaves in a region was designed based on visible-near infrared reflected spectroscopy using a nondestructive method with high accuracy and good repeatability. Researches make clear that the reflectivity of 700 nm light and crop leaf chlorophyll concentration have a significant correlation, which means the higher chlorophyll concentration, the lower reflectivity of 700 nm light. And chlorophyll concentration has no effect on the reflectivity of 840 nm light. In order to eliminate the background interference, we chose 700 nm as the measure wavelength and 840 nm as the reference wavelength. In our previous work, its feasibility and accuracy were verified (Tan et al., 2014).

The sensor had two parts, the detection module and the control module. Detection module included incident and reflected light detection parts. Incident light part contained an astigmatism piece, two optical filters, and two photoelectric sensors. Ensuring the incident light stable and maximum, we placed the incident detection part on the top of system horizontally. Reflected light part contained a quartz glass window, a dispersion prism, two optical filters, two photoelectric sensors. Reflected components were installed in the black opaque lens ensuring undisturbed, and the reflected part was installed on a rotating pan-tilt for the alterable measure scope. Control module installed inside of pan-tilt processed the data received from the detection module, then transmitted it to MCGS through RS485 protocol. The sensor for chlorophyll installation diagram is shown in Figure 2.

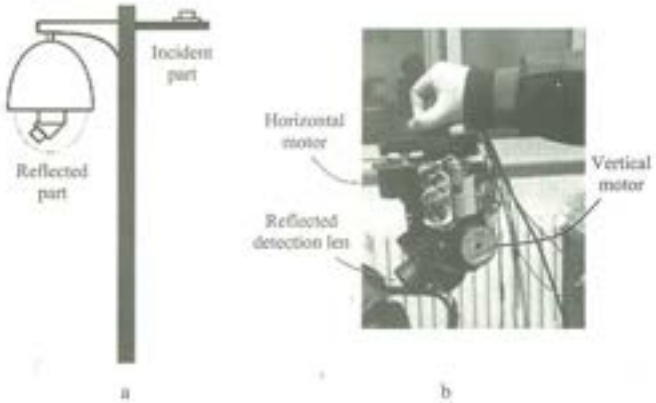

a. Installation diagram of sensor for chlorophyll, the control module was installed inside of pan-tilt above the reflected part b. The reflected part

Figure 2 Sensor for chlorophyll installation diagram

2.2.2 Stem-flow sensor

The stem-flow sensor was designed based on the theory of heat transfer and thermal balance (Kjelgaard et al., 1997). On the basis of this theory, we employed outside package design. And plastic insulation materials were adopted to reduce the external interference. There was a heating element and two sets of thermopile inside. Temperature measuring probe obtained the heat difference produced by the stem-flow movement. The transducer was used for signal excitation and preprocessing. More information about the sensor and

calibration method could be found in our published paper (Liu et al., 2010). Its structure diagram is shown in Figure 3. As a result of the existence of stem flow, the heat generated by the heating element would be delivered to crop top direction, causing temperature difference between two thermopiles. The transducer connected MCGS and the sensor part. This sensor can be used to measure crop which has a small stem diameter of 1-2 cm.

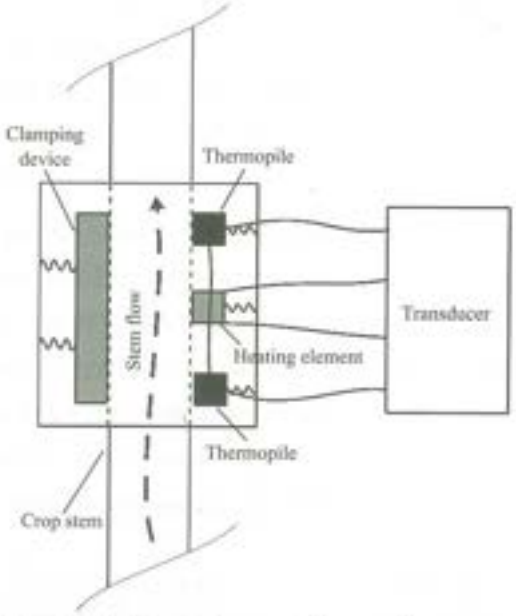

Figure 3 Structure diagram of the stem-flow sensor

2.2.3 Sensor for plant electrical signal

Stimuli give rise to extracellular signal transmission (chemical signal, electrical signal) in plant, and the occurrence and transmission of electrical signal may be the initial response (Huang et al., 2006). We adopted the sensor we used in our previous work for measuring the plant electrical signal, which consisted of two Pt electrodes and a transducer. Considering the environment and signal characteristic, two metal thread electrodes were applied as the measuring electrode. The electrodes were stabbed into the stem of crop. The transducer had high input impedance and low temperature drift (Wang et al., 2009). After the transducer's filter and amplification, the signal would be transmitted to the collecting module then to MCGS.

2.2.4 Other sensors

Monitoring system also integrated other physiological state sensors, leaf temperature sensor (provided by National Engineering Research Center for Information Technology in Agriculture, China), stem diameter sensor (Model: TWZ, accuracy of 0.05% of the full scale, range from 0 to 10 mm, Beijing Taize Science & Technology Development Co., LTD. China) and some other environmental sensors (air temperature and humidity compound sensor, model: DWS-T4,with accuracy of ±0.5°C and ±3% in relative humidity, range from –40°C to 80°C in temperature and 0% to 100% in relative humidity; soil temperature sensor, model: JWB/KP-A, with accuracy of ±0.5°C, range from –20°C to 80°C; soil moisture sensor, model: FDS100, with accuracy of ±2%, range from 0% to 100%; illumination sensor, DZD-T4, with accuracy of ±5% of the full scale, range from 0 to 200000 Lux; radiation sensor, HSTBQ-2, with accuracy of ±2%, measurement wavelength range from 300 to 3000 nm. All these sensors were provided by Beijing ColliHigh Sensing Technology Co., LTD. China). These sensors are supplied by DC 12 V or DC 24 V powers, and their outputs are 4-20 mA or 0-20 mV. They were connected to the signal module.

2.3 Software design

System software was written in MCGS script language. It consisted of embedded program and server program. Embedded program was written in MCGSE configuration environment, running in the embedded integrated touch screen. Server program was written in MCGS online configuration environment, running on server. The architecture of application software written in MCGS configuration soft is shown in Figure 4.

By adding TCP/IP devices, the two MCGS programs established network connections. The interface windows of program were created in user window. All the variables were listed in real-time database window and strategies could be created in operation strategy window.

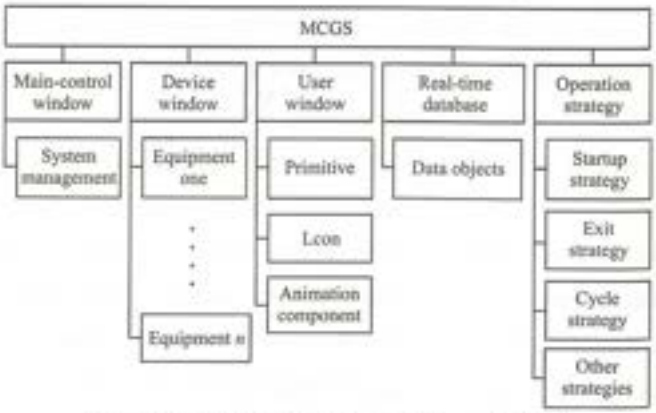

Figure 4 General software architecture of MCGS

2.3.1 Embedded program

Embedded program's functions are as follows: data preprocessing, data transmission to server program, real-time data storage, data copy, information display, irrigation solenoid valve control and control of pan-tilt direction of the sensor for chlorophyll. Embedded program interface is consisted six user windows: main window, system login, historical data, system setting, save setting, and data copy. The main window exhibits the sensors detail data, control buttons and system menu as the Figure 5 shows. Users can do some basic settings on system settings window, such as the time and IP. The setting of start and end time of data copy is in data copy window, and returns state parameter as hints. Data save interval setting is in save setting window.

Signal from collection modules is the standard 4-20 mA type. According to the relationship between signals collected and the actual value they presented, we set data processing function for each signal.

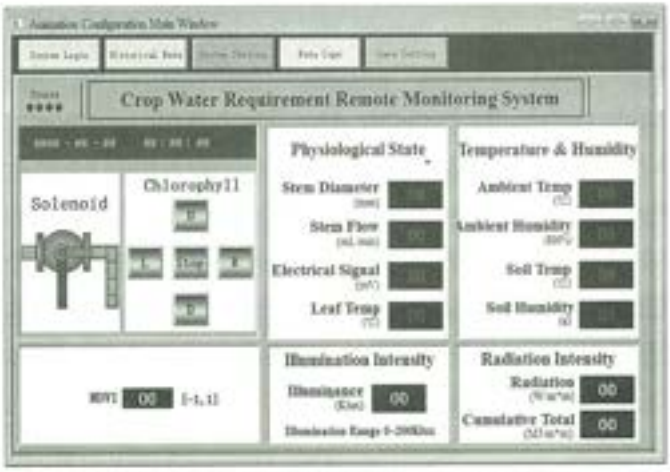

Figure 5 Embedded program running interface

2.3.2 Server program

Server program's functions are as follows: data process, sending data to database, data and control commands display and decision-making. There are two irrigation modes, manual mode and automatic mode. In the automatic mode, the program will perform irrigation operation based on the sensors data. Server program contains two user windows, the main window and calibration window. The main window exhibits the sensors detailed data and control buttons as is shown in Figure 6.

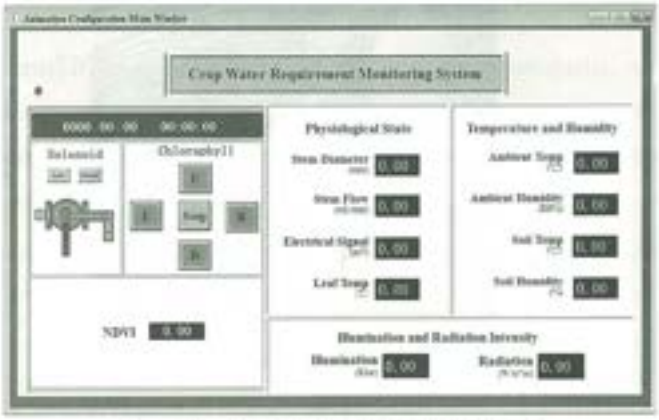

Figure 6 Server program design interface

3 System application

The system was tested with maize (*Zea mays* L.) to verify the feasibility and stability in the greenhouse of China Agriculture University Zhuozhou test site in Hebei province, China. Environmental temperature sensor and leaf temperature sensor were calibrated by precision thermistor. Illumination meter was calibrated by GM technology JTG01 hand-held illumination meter. Users could modify the calibration parameters in the calibration window.

The MCGS acquired data of each sensor regularly, then real-timely displayed and storage. Besides, the server program could also real-timely display, storage data, and upload the data to database. According to the fusion data, system judged whether the crop was currently in the state of water shortage or not. If it was in water shortage, the irrigation operation would be made. The system installation is shown in Figure 7.

System continuously operated months normally without faults. The interface of infrared network high-definition camera is shown in Figure 8, and we can see the chlorophyll sensor. The server program running interface is shown in Figure 9.

The results reveal that: (1) Using MCGS achieved a good automatic remote monitoring system. It is simplicity, good visibility, strong maintainability, stable performance. (2) Acquisition of accurate information about the physiological state of the crop and environmental information was realized. All the sensors operated normally.

1. The acquisition-control system box 2. Reflected light part of sensor for chlorophyll 3. Camera 4. Air temperature and moisture sensor 5. Illumination sensor 6. Radiation sensor 7. Incident part of sensor for chlorophyll

a. Part one of system installation

1. Soil moisture sensor 2. Stem diameter sensor 3. Stem-flow sensor 4. Electrical signal sensor 5. Soil temperature sensor 6. Leaf temperature sensor 7. Drip irrigation equipment

b. Part two of system installation

Figure 7 System installation

1. Camera direction control and zooming control panel 2. Video display area 3. Current time 4. Camera production model and configuration menu

Figure 8 Camera monitoring the sensor for chlorophyll

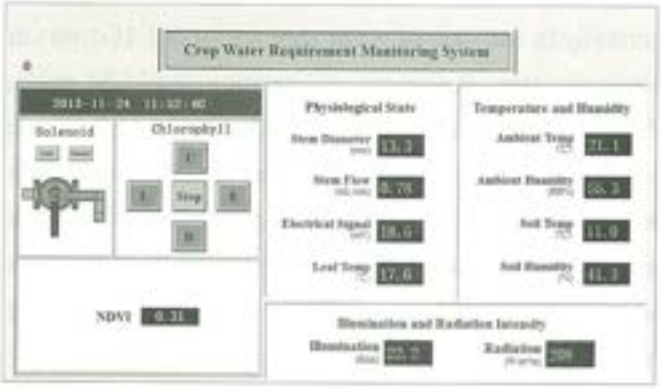

Figure 9 Server program design interface

4 Results and discussion

Plenty of data were obtained in months' operation. Data of sensors in four days is shown in Figures 10-14.

The data in Figure 10 shows the changes of air and leaf sensors in greenhouse. Because of transpiration cooling the leaves, the leaf temperature is lower than air temperature under sufficient water condition. However, when the crop is in water deficit state, transpiration becomes limited which will result in increase of the leaf temperature, even may be higher than air temperature (González-Dugo et al., 2006). After the straw-curtain of the greenhouse is rolled up and ventilation, the air relative humidity begins to decline and reaches its minimum in high noon. In the afternoon, after covering the straw-curtain, the humidity rises. The humidity maintains a high level in the night and reaches its maximum early in the morning. Based on the leaf temperature, judgement can be made whether the crop is in lack of water. And air temperature and humidity as reference show the external environmental conditions.

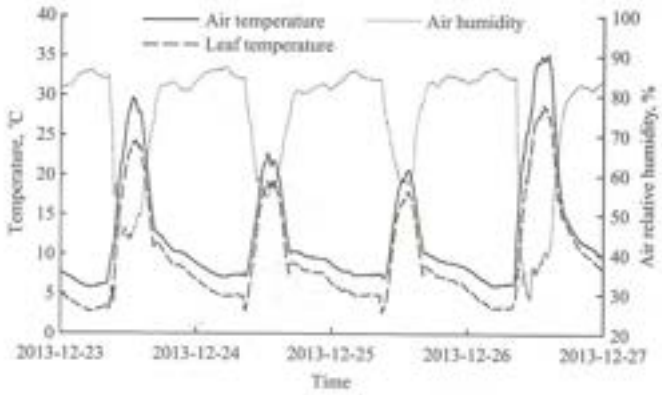

Figure 10 Data of air and leaf sensors

The data of soil moisture and temperature in Figure 11 shows the changes of four days in greenhouse. The soil moisture is the most intuitive factor reflecting if the crop is in water deficit environment. The trend of soil

moisture decreases daily overall, and there are small fluctuations in a day and night. Water migration in soil can accompany with the processes of evaporation, dynamic distribution within the soil and water uptake by roots (Klute, 1973). Soil water moisture exhibits a marked diurnal variation, which occurs in our data shown in Figure12 (Jackson, 1973; Idso et al., 1975). The reason of this is soil water moisture is correlated with soil temperature, atmospheric factors and other movements caused by plants (Jackson, 1973; Idso et al., 1975; Hui-Xing et al., 2007). Meanwhile, soil temperature has a huge effect on crop growth. Higher and lower temperature than certain value will result in biomass decrease (Delucia et al., 1992). The soil temperature sensor goes deep into the underground 30 centimeters and the probe is near the root zone of maize. Because of the soil heat storage capacity, the soil temperature daily changes lags behind the air temperature and manifests periodicity. Relative to air temperature, the soil temperature variation is smaller and slower. And the deeper the sensor goes, the smaller the fluctuation range (Jackson, 1973; Idso et al., 1975). Soil temperature is correlated with soil moisture and a variety of meteorological parameters (season change, radiation intensity, soil texture et al.). Water has a higher specific heat capacity than soil. With the soil moisture decreases, the heat storage capacity of soil weakens, so does the amplitude of fluctuation of soil temperature (Hui et al., 2017).

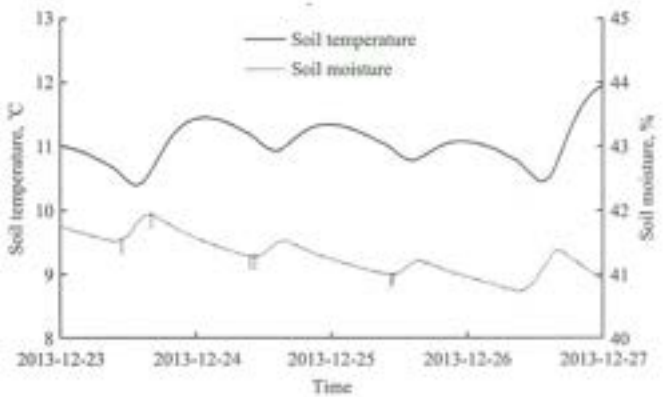

Figure 11 Data of soil sensors

The diurnal fluctuations of radiation and illumination intensity are shown in Figure 12. The tendency of radiation and illumination intensity has high correlation, which precisely illustrates the weather condition of the greenhouse site. The intensity of radiation directly effects many physiological activities such as photosynthesis and transpiration and ambient factors. The necessity of monitoring radiation and illumination intensity is to provide explanation of some data of sensors when the crop is in adequate water state.

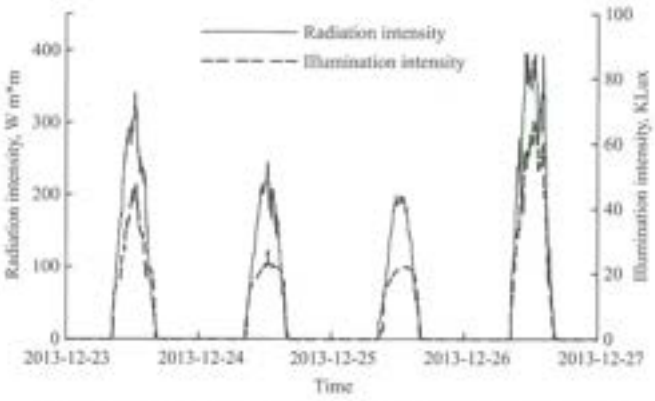

Figure 12 Data of radiation sensor and illumination sensor

The diurnal fluctuations of stem flow are shown in Figure 13. The stem flow is represented in percentage value of maximum diameter shrinkage of four days. Amplitude of stem flow is related to solar radiation, air temperature and soil moisture. (Li et al., 2011). So, the stem flow can reflect crop physiological state information and soil water dynamics. The stem flow data manifests daily periodicity because of existence of transpiration and reaches maximum at noon. As solar radiation intensity in winter is smaller than in summer, the figure just shows the stem flow status of sunny days in winter. And the difference of four day's stem flow simultaneously indicates the difference in radiation intensity. Plants are in water deficit state or sick state, when the stem flow is significantly lower than normal level in sunny days (Gavloski et al., 1992; Ortuño et al., 2006).

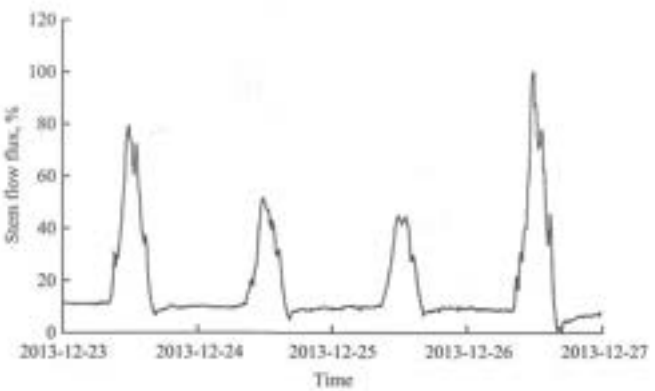

Figure 13 Data of stem flow

Our previously work has elucidated that low environmental temperature induces an obvious change in electrical signals in the cucumber plants and electrical signal can be induced in the leaf tissue by the change in light/dark (Wang et al., 2007). The results reveal the electrical signal decreases from dark to light, and then increases when back to dark. It also can be seen in the Figure 15, when the sun rises, simultaneously causing greenhouse temperature increase, the electrical signal rises and followed by decreases until sunset. The electrical signal plays a role as a switching signal, as we know that electrical signal is always involved in changes of stomatal conductance and CO_2 uptake (Gil et al., 2008; Fromm et al., 2013; Gil et al., 2014). There are fluctuations in day time, which may be effected by the instantaneous change of the ambient factors. Maybe under subsequent lightless conditions at night and lower temperature condition than daytime, the electrical signal starts to rise again (Wang et al., 2009). As we can see in Figure15, with the decrease of the soil moisture, the minimum value of electrical potential per day decreases, which is consistent with published result indicating EP as a good physiological trait is related to soil moisture (Gil et al., 2014). As shown in Figure 14, daily periodic regularity in electrical signal data is evident.

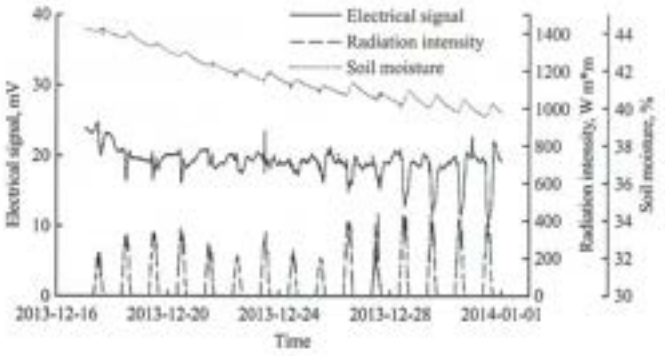

Figure 14 Data of electrical signal sensors and others

Electrical potential (EP) stimulated by external stimuli are various. And previous works indicate that EP behavior depends on plant species and anatomical differences in conductive pathway (Gurovich et al., 2009). Variations in light condition, e.g. dark/ light or light/ dark, will induce EP in plants (Fromm et al., 1998; Gil et al., 2008; Gurovich et al., 2009; Król et al., 2010; Gil et al., 2014), and the EP often manifests a daily rhythm. The explanations of initiation by light-on are divided into many theories. One is that light-induced chloroplast surface charges have an effect on plasma membrane. Another suggests there is a short and transient plasma membrane depolarization induced by light-on and then following a long-running hyperpolarization, which is associated with photosynthesis. As for dark condition, Chloroplastic Ca^{2+} release is possible to change membrane potential (Król et al., 2010). Moreover, the different EP fluctuations in day and-night may be associated with the different stem flow velocities (Gibert et al., 2006).

As a result of sudden drops in temperature, membrane depolarization is evoked and assimilate transport in plants will be strongly reduced even be interrupted (Fromm et al., 2013). In excitable cells of maize, the depolarization will lead to an action potential (Fromm et al., 1994; Król et al., 2010). Similarly, Plieth's result implied that active Ca-channels involved EPs by cold stimuli then resulting in calcium increases (Król et al., 2010). Besides these explanations, H+-ATPase is inhibited to trigger plasma membrane depolarization. The previous work suggested that ambient environmental factors control the whole plant metabolism shaping ATP (Adenosine Triphosphate) availability with action potential generation (Król et al., 2010).

EP may be the primary one in a cascade of physiological response to changes of soil water content (Fromm et al., 1998). With the decrease of soil water content, the concentration of abscisic acid increases in roots, and hormone will be synthesized, simultaneously the EP decreases (Fromm et al., 1998; Gil et al., 2008). After watering, there was an abrupt increase to the original level in EP (Fromm et al., 1998; Sukhov, 2016). The soil and root water content state directly affects stomatal conductance which was associated with EP. Moreover, drought stress can bring about an increase in the apoplastic pH of the leaf causing rapid stomatal closure (Gil et al., 2008).

As light acts like the trigger in electrical potential generating and changes in soil water content may causes EP variation. Correlation analysis was used to analyze the relationship of electrical signal, radiation intensity and

soil moisture. We select the data from 17th December 2013 to 31th December 2013. We take EPmin, Rmax and Soilave respectively for minimum EP in a day, maximum radiation intensity in a day, the average of the whole day data. We found that the Pearson correlation coefficient of EPmin vs Rmax or Soilave respectively are –0.737 and 0.788. The result indicates radiation intensity and soil water content plays an important role in EP's generating and amplitude. To identify whether the soil water content can be inferred from EP, linear-regression analysis was used. The coefficient of determination R^2 of Soilave vs EPmin is 0.622. The result shows it is very important in evaluating crop water requirement state and precise irrigation.

Interestingly, these previous papers have reported that plant electrical signals responding to external stimuli often originate at the roots and travel through the vascular system to the leaves, or vice versa (Król et al., 2010; Gil et al., 2014). These signals are responsible for rapid transmission of information within plant body in order to enable a response of distant organs to abiotic stress (Fromm et al., 2013). Previous works have revealed that stomata should be able to receive information on the soil water status independently from the leaf water potential (Fromm et al., 1998; Gil et al., 2008; Fromm et al., 2013). The rapid response in the leaves as a result of soil water changes suggests that hydraulic or electrical signals involve communication from the root to the leaves (Gil et al., 2008). The EP induced by re-irrigation of drought-stressed in maize and cold systemly propagates via the phloem from roots to leaves to regulate photosynthesis (Fromm et al., 2013).

Furthermore, water stress leads to the loss of chlorophyll. Randall et al. had proved that the majority of chlorophyll lost from maize leaves is lost from the mesophyll cells (Alberte et al., 1977). Randall also explains the reason for this phenomenon is that mesophyll cells get less water resource than bundle sheath cells, for bundle sheath cells is closer to the vascular supply of water, which leads to a greater loss of chlorophyll. Alternatively, it is because they contain more of the light-harvesting chlorophyll a/b-protein which is more susceptible under water stress conditions. Thus, by monitoring leaf chlorophyll content allow us to estimate water requirement of plant. The data of sensor for chlorophyll goes wrong, and will be analyzed after correction.

In addition, for higher plants, stem diameter normally indicates diurnal fluctuations with maximum values before sunrise and minimum values in the afternoon. Plant stem decrease by day is because the stem phloem water drained by transpiration stream, and expansion by night is due to re-hydration of stem phloem and plant growth (Kozlowski, 1972). So, the change of stem diameter lags behind stem flow's change. The stem diameter can reflect soil water content and radiation intensity which can directly affect the stem flow. The data of stem diameter goes wrong as the stem is extremely vulnerable to ambient factors effecting position of stem, and the data will be analyzed after correction.

5 Conclusions

This paper shows that a system based on multi-sensor and physiological state of crop for remote water requirement monitoring system is built and have been tested in greenhouse. Unlike the experiments based on single physiological state, we integrated physiological state sensors, which was important for comprehensive judgement of crop water requirement state. More detailed data, further and deeper data analysis is needed to better understand the law of crop water requirement for guiding the agricultural irrigation. Test results show that the remote monitoring system is practicable and stable, and is a potential tool for evaluating crop water requirement state and precise irrigation.

Acknowledgments

This research was supported by the National Natural Science Foundation of China (61571443), the Specialized Research Fund for the Doctoral Program of Higher Education (20130008110035), the National Key Scientific Instrument and Equipment Development Projects (2011YQ080052), and the China Agricultural University Key Construction Program of the National "985" Project. The authors would like to thank the Key Laboratory of Agricultural Information Acquisition Technology of the Chinese Ministry of Agriculture for their support.

[References]

[1] Akhkha, A., T. Boutraa, and A. Alhejely. 2011. The rates of photosynthesis, chlorophyll content, dark respiration, proline and abscicic acid (ABA) in wheat (Triticum durum) under water deficit conditions. *International Journal of Agriculture and Biology*, 13(2): 215–221.

[2] Alberte, R. S., J. P. Thornber, and E. L. Fiscus. 1977. Water stress effects on the content and organization of chlorophyll in mesophyll and bundle sheath chloroplasts of maize. *Plant Physiology*, 59(3): 351–353.

[3] Conejero, W., J. J. Alarcón, Y. García-Orellana, J. M. Abrisqueta, and A. Torrecillas. 2007. Daily sap flow and maximum daily trunk shrinkage measurements for diagnosing water stress in early maturing peach trees during the post-harvest period. *Tree Physiology*, 27(1): 81–88.

[4] Delucia, E. H., S. A. Heckathorn, and A. D. Thomas. 1992. Effects of soil temperature on growth, biomass allocation and resource acquisition of Andropogon gerardii Vitman. *New Phytologist*, 120(4): 543–549.

[5] Efeoğlu, B., Y. Ekmekci, and N. Cicek. 2009. Physiological responses of three maize cultivars to drought stress and recovery. *South African Journal of Botany*, 75(1): 34–42.

[6] Escalona, J., J. Flexas, and H. Medrano. 2015. Drought effects on water flow, photosynthesis and growth of potted grapevines. *VITIS-Journal of Grapevine Research*, 41(2): 57–62.

[7] Fisher, D. K., and H. Kebede. 2010. A low-cost microcontroller-based system to monitor crop temperature and water status. *Computers and Electronics in Agriculture*, 74(1): 168–173.

[8] Fromm, J., and T. Bauer. 1994. Action potentials in maize sieve tubes change phloem translocation. *Journal of Experimental Botany*, 45(4): 463–469.

[9] Fromm, J., and H. Fei. 1998. Electrical signaling and gas exchange in maize plants of drying soil. *Plant Science*, 132(2): 203–213.

[10] Fromm, J., M. Hajirezaei, V. K. Becker, and S. Lautner. 2013. Electrical signaling along the phloem and its physiological responses in the maize leaf. *Frontiers in Plant Science*, 4(239): 1–7.

[11] Gallardo, M., R. B. Thompson, L. C. Valdez, and M. D. Fernández. 2006. Response of stem diameter variations to water stress in greenhouse-grown vegetable crops. *The Journal of Horticultural Science and Biotechnology*, 81(3): 483–495.

[12] Gavloski, J. E., G. H. Whitfield, and C. R. Ellis. 1992. Effect of restricted watering on sap flow and growth in corn (*Zea mays* L.). *Canadian Journal of Plant Science*, 72(2): 361–368.

[13] Gibert, D., J. L. Mouël, L. Lambs, F. Nicollin, and F. Perrier. 2006. Sap flow and daily electric potential variations in a tree trunk. *Plant Science*, 171(5): 572–584.

[14] Gil, P. M., L. Gurovich, B. Schaffer, J. Alcayaga, S. Rey, and R. Iturriaga. 2008. Root to leaf electrical signaling in avocado in response to light and soil water content. *Journal of plant physiology*, 165(10): 1070–1078.

[15] Gil, P. M., J. Saavedra, B. Schaffer, R. Navarro, C. Fuentealba, and F. Minoletti. 2014. Quantifying effects of irrigation and soil water content on electrical potentials in grapevines (Vitis vinifera) using multivariate statistical methods. *Scientia Horticulturae*, 173(Supplement C): 71–78.

[16] González-Dugo, M. P., M. S. Moran, L. Mateos, and R. Bryant. 2006. Canopy temperature variability as an indicator of crop water stress severity. *Irrigation Science*, 24(4): 233–240.

[17] Gurovich, L. A., and P. Hermosilla. 2009. Electric signalling in fruit trees in response to water applications and light–darkness conditions. *Journal of plant physiology*, 166(3): 290–300.

[18] He, J., Z. Wang, Y. Shi, Y. Qin, D. Zhao, and L. Huang. 2011. A Prototype Portable System for Bioelectrical Impedance Spectroscopy. *Sensor Letters*, 9(3): 1151–1156.

[19] Huang, L., Z. Y. Wang, Z. L. Xu, Z. C. Liu, Y. Zhao, and R. F. Hou. 2006. Design of multi-channel monitoring system for electrical signals in plants. *Modern Scientific Instruments*, 16(4): 45–47.

[20] Hui, L., Z. Xia, and M. Hui. 2007. Effects of water content variation on soil temperature process and water exchange. *Journal of Hohai University*, 35(2): 172–175.

[21] Idso, S. B., J. K. Aase, and R. D. Jackson. 1975. Net radiation-soil heat flux relations as influenced by soil water content variations. *Boundary-Layer Meteorology*, 9(1): 113–122.

[22] Jackson, R. D. 1973. Diurnal Changes in Soil Water Content During Drying, in *Field Soil Water Regime*. ed. R.R. Bruce, ch. 3, 37–55. *Madison, WI: Soil Science Society of America*.

[23] Jackson, R. D., S. B. Idso, R. J. Reginato, and P. J. Pinter. 1981. Canopy temperature as a crop water stress indicator. *Water Resources Research*, 17(4): 1133–1138.

[24] Katerji, N., F. Tardieu, O. Bethenod, and P. Quetin. 1994. Behavior of maize stem diameter during drying cycles: comparison of two methods for detecting water stress. *Crop Science*, 34(1): 165–169.

[25] Kjelgaard, J. F., C. O. Stockle, R. A. Black, and G. S. Campbell. 1997. Measuring sap flow with the heat balance approach using constant and variable heat inputs. *Agricultural and Forest Meteorology*, 85(3): 239–250.

[26] Klute, A., 1973. Soil water flow theory and its application in field situations, in *Field Soil Water Regime*. ed. R.R. Bruce, ch. 2, 9–35. *Madison, WI: Soil Science Society of America*.

[27] Kozlowski, T. T., 1972. Shrinking and Swelling of Plant

Tissues, in *Plant Responses and Control of Water Balance*. ed. T. T. Kozlowski, ch. 1, 1–64. *New York and London: Academic Press*.

[28] Król, E., H. Dziubinska, and K. Trebacz. 2010. What do plants need action potentials for, in *Action potential: biophysical and cellular context, initiation, phases and propagation*. ed. M. L. Dubois, ch. 1, 1–26. *New York: Nova Science Publisher*.

[29] Li, H., Y. Liu, J. Cai, and X. Mao. 2011. Change of sap flow rate and stem diameter microvariation of summer maize and influence factors. *Transactions of the Chinese Society of Agricultural Engineering*, 27(10): 187–191.

[30] Liu, A., X. Liu, L. Huang, X. Wen, Y. Shi, Z. Wang, C. Wang, and R. Hou. 2010. A calibration method for stem-flow sensor based on heat balance. *Transactions of the Chinese Society of Agricultural Engineering*, 26(Supplement 2): 6–10.

[31] Ortuño, M. F., Y. García-Orellana, W. Conejero, M. C. Ruiz-Sánchez, J. J. Alarcón, and A. Torrecillas. 2006. Stem and leaf water potentials, gas exchange, sap flow, and trunk diameter fluctuations for detecting water stress in lemon trees. *Trees*, 20(1): 1–8.

[32] Ortuno, M. F., J. J. Alarcón, E. Nicolás, and A. Torrecillas. 2005. Sap flow and trunk diameter fluctuations of young lemon trees under water stress and rewatering. *Environmental and Experimental Botany*, 54(2): 155–162.

[33] Oyarce, P., and L. Gurovich. 2010. Electrical signals in avocado trees: Responses to light and water availability conditions. *Plant Signaling and Behavior*, 5(1): 34–41.

[34] Shao, H. B., L. Y. Chu, C. A. Jaleel, and C. X. Zhao. 2008. Water-deficit stress-induced anatomical changes in higher plants. *Comptes Rendus Biologies*, 331(3): 215–225.

[35] Sukhov, V., 2016. Electrical signals as mechanism of photosynthesis regulation in plants. *Photosynthesis Research*, 130(1-3): 1–15.

[36] Tan, W. J., Y. Q Wang, P. F. Zhao, L. F. Fan, L. Huang, and Z. Y. Wang. 2014. Development of system for monitoring chlorophyll content of plant population using reflectance spectroscopy. *Transactions of the Chinese Society of Agricultural Engineering*, 30(10): 160–166.

[37] Tanner, C. B., 1963. Plant temperatures. *Agronomy Journal*, 55(2): 210–211.

[38] Wang, C., L. Huang, Z. Y. Wang, and X. J. Qiao. 2007. Monitoring and analysis of electrical signals in water stressed plants. *New Zealand Journal of Agricultural Research*, 50(5): 823–829.

[39] Wang, Z. Y., L. Qiang, L. Huang, L. L. Zhao, Z. L. Xu, R. F. Hou, and C. Wang. 2009. Monitoring system for electrical signals in plants in the greenhouse and its applications. *Biosystems Engineering*, 103(1): 1–11.

[40] Yang, Y. H., Y. N. Chen, W. H. Li, and C. G. Zhu. 2015. Effects of progressive soil water deficit on growth, and physiological and biochemical responses of Populys Euphratica in arid area: a case study in China. *Pakistan Journal of Botany*, 47(6): 2077–2084.

Service modes of agricultural information based on network technology

Hu Hui[1,2], Gao Wanlin[1,2*], Shi Kaite[1,2]

(1. *College of Information and Electrical Engineering, China Agricultural University, 100083, Beijing, China*;
2. *Key Laboratory of Agricultural Informationization Standardization, Ministry of Agriculture, 100083, Beijing, China*)

Abstract: In China, agricultural informatization has been developed, but still confronted by problems because the unitary of the service modes of agricultural information and the information is not being fully utilized. Innovating of the agricultural service information mode is the significant to figure out the problems. From the perspective of network technology, system analysis methods, this paper discusses the agricultural information service modes which are appropriate to China's modern agricultural development. Processes of the real issues were studied by these methods and analyzed the Trading Platform of National Agricultural Science and Technology Achievements Transformation. The research summarizes, how network platform serves in modern agricultural production and the means of information technology that would be implemented in the agriculture, the countryside and farmers, while referring to the meanings of agricultural services, agricultural information distribution and advanced foreign service model.

Keywords: network technology, service mode of agricultural information, trading platform

Citation: Hu, H., W. L. Gao, and K. T. Shi. 2017. Service modes of agricultural information based on network technology. International Agricultural Engineering Journal, 26(3): 410–415.

1 Introduction

Since the China's reform and opening up policy, the country side is the foremost edge for information spread which robust the China's agricultural mechanization and commercialism. But the development of agricultural infrastructure informationization is still deficient. China is facing the challenge of the transmission of information services, moreover the agricultural information resources are also not being used efficiently due to the restraints of rural information network and that the peasantry has less opportunity to acquire related information and guidance. Normally the farmers bank on experience or references of proximity farmers regarding their agricultural activities. At present agriculture informatization in China has a weak basis and delimited by many issues which include overall quality and quantity of information resources which do not accomplish the needs of agricultural production and research. The number of agricultural information services still trails the traditional modes. Modern technologies and Innovations in agriculture-related services would resolve listed problems meritoriously.

The agricultural information service perception is classified into the narrow and broad categories. The narrow category refers to departments, research institutions, agricultural information gathering carried out by commercial companies to meet the service object, processing, transmission, agricultural advisory services, support and research for agricultural information technology and varied productions of agricultural information. The broad category includes the supply chain and technological information, production process, transportation and products sold in agricultural production.

The information dissemination method is pivotal. Agricultural information dissemination pathways should

Received date: 2017-07-08 **Accepted date:** 2017-08-28

* **Corresponding author: Gao Wanlin**, Ph.D., Professor of College of Information and Electrical Engineering China Agriculture University, Beijing 100083 China. Email: cau_szmtyjs@163.com.

have the characteristics of simplicity, richness, smoothness, target consistency, practical implementation, rational layout, fewer intermediate links and other basic requirements. From a practical view, channels and methods of information services should be based on local infrastructure and finical status of the users. Common communication channels used by farmers are mainly television, followed by verbal referrals among vicinity. Computers and networks have arisen and have a massive development potential in various rural areas, but currently are used for learning and entertainment, which doesn't really play a supervisory role in agricultural services.

2 National Agricultural Science and Technology Achievements Transformation Trading Platform

National Agricultural Science and Technology Achievements Transformation Trading Platform (NASTATTP) is a comprehensive service platform consisting of technology, talents, funding, policies and other elements to provide information on China's scientific and technological achievements in agriculture. As Figure 1 depicts, NASTATTP consists of resource integration sub-platforms, science and technology achievement appraisal and assessment sub-platforms, scientific and technological achievements transaction sub-platforms, research cooperation sub-platforms, policy support service sub-platforms, management and technological achievement sub-platforms, testing service sub-platforms and technology investment and financing sub-platforms.

NASTATTP is based on the application of the Internet, primarily being utilized to further enhance the transformation rate of agricultural scientific and technological achievements. It will provide muscular support for the industrial development of agricultural science and technology. The platform purposes the support of policy, supply and demand information, expert services, transaction services, technology investments and financing for both sides of transaction. There is a need of development tools for these applications because they require a complete support system, a large database technology and a large number of dynamic technologies.

NASTATTP's operating system is a Windows Server, uses Visual Basic NET (VB.NET) as a development platform tool and Structured Query Language (SQL) Server 2008 as the database software. Its web page was designed by Active Server Pages.NET (ASP.NET), VB.NET and so on. The database contains large amounts of information and many different data types. NASTATTP will significantly improve the level of transformation of scientific and technological achievements in agriculture, which makes agricultural scientific and technological achievements more user friendly, efficient and standardized. Moreover NASTATTP will explore the idea of China's agricultural information services and will integrate scientific research, technology, capital, products and other factors. It brings the work of government departments, research institutes, agricultural colleges, agricultural enterprises and other units together for the agricultural achievements transformation and trading. NASTATTP is a service integrated agriculture platform.

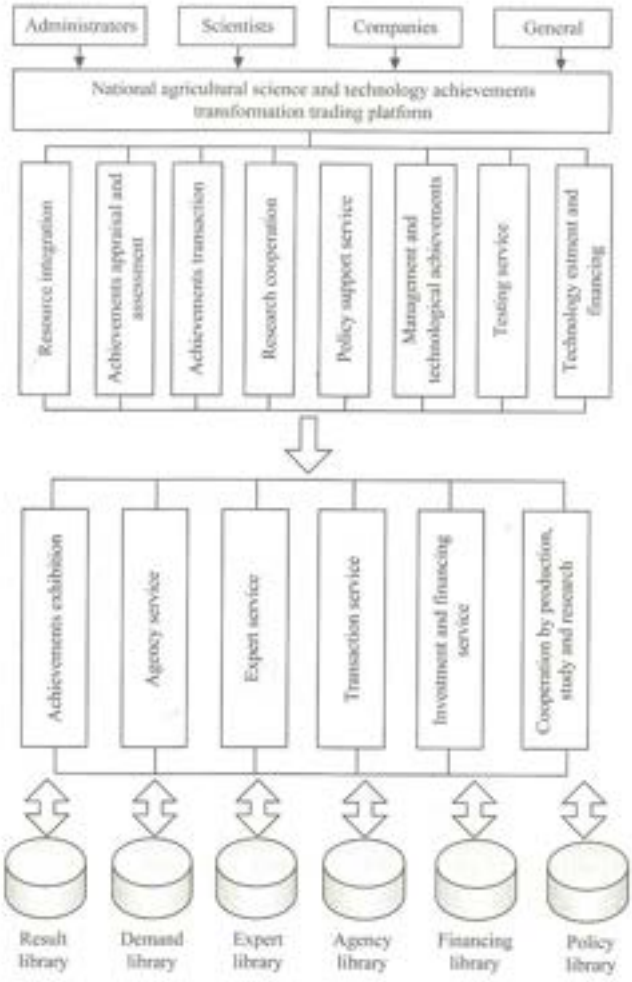

Figure 1 NASTATTP system module

3 Several methods of agricultural information service

3.1 The traditional methods

Traditional information services provided agricultural information to rural areas mainly through television, radio, billboards and other media. Since 2013, national radio broadcast covered 97.79% of the population and television coverage 98.42%. During the 12th "Five Years Plan" period, China has greatly improved the coverage of cable TV and internet in rural areas. Presently, radio and television are moderately trusted way of information dissemination in rural areas. Now internet is gaining huge popularity with the change in technology and the traditional means need to upgrade its services in order to meet the requirements of the industry and field.

3.2 Information service platform based on Internet

The network information service model uses big data of the internet for information processing (collection, selection and processing) and sharing so that it may be useful for the consumers through the information service system, which usually occurs on a network service platform, official micro-blog, professional forums, etc. Farmers often obtain useful information on the Internet because internet has a variety of information resources. The flexible web structure and lack of restrictions are the problematic features of the Internet. In network environment a person simultaneously may have dual role i.e. may be a provider or may also be a user of information services. The conditions of the implementation in this way rely on the Internet and computers. This situation is fairly evident in western part of China. The lack of awareness hinders the farmers from the network information service. However, less use of network resources certainly doesn't mean a lack of demand on the network in rural areas. The news has been reported that piles of oranges or apples cannot be completely sold. This phenomenon takes place because of the relatively backward economy and blocked channels of information in the rural areas. The most efficient way to solve this problem is through the network. From the current situation, the most important functions of providing networks for rural areas are with the latest planting techniques, problem-solving methods and online trading information.

3.3 The role of mobile phones in the agricultural information service

In recent years, mobile communications have been developed rapidly in China, playing an increasingly pivotal role, especially in rural areas. A report said, according to Ericsson, mobile phone ownership rates in rural China rose 90%, and about 50% new subscribers are from the rural market of China. The phone has the advantages of deep penetration rate, mobility, easy to operate and low cost. It should not be underestimated as the potential client's main source of information. Taking the phone as an information tool, there are three main forms: Short Message Service (SMS) group, expert hot-line and landing agricultural information service platform.

During the recent years, China has been establishing agriculture messaging service platforms in many areas. The content of information services includes news, market, practical techniques and meteorological information. In SMS group services, mobile Internet providers upload information to the SMS platform server by the client, after editing short message, and then local farmers will receive the information from the SMS platform. The "12306" SMS platform has carried out, sustained and stabilized the agricultural SMS service for every user in Jiangsu province twice a week, delivering to a total of about 70,000 users, which has widely improved the agricultural information dissemination system in that area. SMS information service's most projecting advantage is its excellent appropriateness and efficient delivery. SMS messaging performance limitations are that its short content and so is not capable to solve practical characteristics in detail. There is still a extensive work for the agricultural authorities to do to close the gap between agricultural information service and mobile operator so that quality of information services would be optimized.

Expert Hot-line information service was one of the first attempts to mobilize rural information dissemination. It aims mainly at farmers' eager to learn about new agricultural technologies and solve their practical

problems that they encounter in the attempt to utilize new agricultural technology. Previously they often relied on radio, television and other traditional media. There has been a typical cooperation between Chinese Agricultural University Graduate Student Union and the Chinese People's Radio "Village Voice" Channel. One of the stations called, "Agricultural Dr. Online", is not only for farmers to solve practical problems, but also to provide the stage for the experts with professional knowledge. With this method, the investment cost is small, operation is simple and the effect is more obvious. It also establishes a direct link between agricultural research and agricultural production. However, this approach has an obvious flaw, namely its fragile to create sustainable service and effective tracking guidance. The hot-line method on the market is limited because questioners cannot explain the problem in detail, so agricultural experts just guide in a general way with their experience and existing knowledge. We need a more open information service platform to bring issues together to discuss and solve the apparent never ending stream of issues. Conditions gradually mature that we should vigorously develop the rural smart phone market with the tendency that more people should choose to use smart phones, the technology should more convenient to buy and telecommunication operators expand their sales channels in the countryside. In fact, the rural mobile phone network has a high proportion of smartphones, some areas have even exceeded over 80%. Operating mobile devices is relatively simple, even if farmers are not first guided by other people. Landing agricultural information service platform as an access to provide agricultural services information by smart phones has the advantage of time and space compared with computers, the application of 3G/4G networks brings a more affluent multimedia experience. Smart phones have network access, decent growth capabilities, more powerful hardware configuration and so on. It is a very decent choice to build technology-based agricultural information relying on the Internet and mobile communications service platform with smart phones as terminals for the agricultural information services.

4 Discussion on agricultural information service

Network media has featured a wide range of products used for information broadcasting, express communication, rich content and expedient access, which collectively signifies a new projection for agricultural information services. Network technology will not only change people's way of life, but also will upgrade the agricultural industry. Network technology utilized in agriculture initiated in the late 1970s, so 40 years development makes this technology applied in agriculture more and more widespread. Agricultural information collection on the network will be used or referred through developed the special agricultural database system. Useful information about crops and agricultural technology will be published on a regular basis through the agriculture information service platform. Factual and effective supervision SMS would be circulated through messaging platforms. The application of different network technologies will exhibit the exceptional advantages of modern information technology. Network technology applications in the field of modern agriculture continue to expand, with the supporting fact that the use of smartphones has become relatively common. Combining network technology with wireless communication technology will further stimulate the development of agriculture network applications.

Xiaoguang Liu described the role of Land-Grant colleges in the development of agricultural service system in the US and its enlightenment to China. They serve as the main agricultural system and expand the scale and scope of services for agriculture and build the basic framework of the organizational system, strengthening agricultural services. China has diverse resources, complex terrain, large regional differences, less arable land per capita. Therefore this approach is not appropriate for China, but there are some researches which would be taken into account for the development China's integrated agricultural services system. In accordance with the concept of organic unity, the land-grant college teaching research and social services come together, and then China has the opportunity to set up an online service

network, which will mainly be reliant on agriculture-related institutions in the development of China's own modern agricultural service system. Thus, this puts great significance on the agricultural cooperation of teaching, research and technology promotion services. In 2013, the new concept of "family farm" first emerged in China. This kind of practice give the impression to encourage and support large contracting land, circulated to the professional and family farms or farmers' cooperatives. Large-scale and intensive agricultural land offers the possibility of combination of production, teaching and research. This is just the preliminary conditions of the combination. Besides, China also needs to narrow the common interests among the agriculture, the countryside and farmers, and achieve an unobstructed communication channel.

The application of the network as an agricultural information service tool will face a serious problem with the recipients' weak ability and awareness about the network. It can be considered that the best combination includes the Internet with the base service effect of village committees, neighborhood committees or farmers' organization. During the period of 12th Five Year Plan (2011-15), the development of agriculture, the countryside and farmers which aimed at promotion of rural agricultural informatization in China, laid a foundation for the application of internet in rural areas in China, therefore, fundamentally realizing the network coverage to each village. At present, it is impractical to let every rural household have the ability of using the internet. There is little difficulty in training the small amount of needed experts with the ability to use the internet through two levels of sections and townships. Some people will be trained to serve for the valuable agricultural information dissemination in villages. Grassroots organizations and local government initiatives should be brought into play and should be an important role in connecting villages with the Internet information service platform as a service terminal to a certain extent, this approach alleviates the contradiction between the rural demand for information services and the shortage of infrastructure.

Network information services also have the potential of deep penetration into the traditional media through the process of network information agricultural dissemination. The main advantage of online media are its rich resources, timeliness and interaction. Traditional media rely on professional editing power, high quality, and the news media credibility. These are key points that network has not yet developed enough to be successful. Therefore traditional media will not be completely withdrawn from the system in the short-run in response to facing the strength of the network. By establishing mutual benefit and complementary advantages, there should be useful link between network and traditional media. Network will primly merge in traditional media. Staffs from television, newspapers, radio and internet media will be rooted through certain channels in the combination of the network and traditional media. The contents from each medium could be reproduced, modified or commented by the other. This is good for using the advantage of traditional media in rural areas, solving the problem of insufficient network in rural areas and allowing them to still play a role. It will also promote traditional media's constructive transformation for the traditional methods to adapt to the modern development.

5 Conclution

Agricultural informatization is the essential characteristics of agricultural modernization in the information economy era, and it is also an inevitable trend of agricultural development. In this paper, we analyzed the National Agricultural Science and Technology Achievements Transformation Trading Platform, and discussed the service modes of agricultural information. With the development of network technology, it will further uplift the development of agriculture network applications and makes better information service.

Acknowledgments

This work was supported by National Key Technology R&D Program of China during the 12th Five-Year Plan Period (Grant #: 2012BAD35B02).

[References]

[1] Gao, L., P. Li, Z. Li, Y. Tao, and H. Hu. 2015. Discussion on the 3X3 Architecture of Agricultural Informationization. *Journal of Agriculture*, 5(4): 97–102.

[2] Lei, W. 2014. Agriculture Informationization in agricultural modernization process. Ph.D. diss., Southwestern University of Finance and Economics., Chengdu.

[3] Lin, Y., J. Zhang, and Y. Xi. 2011. Applications of SMS in Agriculture Information service. *Agriculture Network Information*, 6(03): 124–126.

[4] Liu, G., and C. Dong. 2012. Roles of Land-Grant Colleges in the Development of Agricultural Service System in the US and its Enlightenment to China. *Journal of Nanjing Agricultural University*, 3(03): 133–139.

[5] Chinese Association of Agricultural Science Societies, 2012. National Agricultural Science and Technology Achievements Transformation Services Trading Platform. Available at:http://www.nzhw.org/chengguo/webManager/webManager_getContent.action?id=1. (Accessed 20 August 2017)

[6] Xiao, H., and R. Wan. 2015. Research on Agricultural Information Resource Sharing Models in Big Data Era. *Agriculture Network Information*, 8(04): 33–35.

[7] Yuan, Q. 2015. Study on Model and Method of Agricultural Informatization Level and Benefit Evaluation. Ph.D. diss., College of economics and management, China Agricultural University, Beijing.

[8] Zhang, T., and N. Wu. 2013. Research on Constructing the Policies System of Agricultural Information. *Journal of Intelligence*, 32(3): 159–165.

[9] Zhou, T. 2015. A Review of Research on the Agricultural Informatization Development in China. *Journal of Guangxi University of Finance and Economics*, 139(01): 95–102.

Short-term prediction model for ammonia nitrogen in aquaculture pond water based on optimized LSSVM

Chen Yingyi[1,2,3*], Cheng Yanjun[1,2,3], Cheng Qianqian[1,2,3], Yu Huihui[1,2,3], Li Daoliang[1,2,3]

(1. *College of Information and Electrical Engineering, China Agricultural University, Beijing 100083, China;*
2. *Key Laboratory of Agricultural Information Acquisition Technology, Ministry of Agriculture, Beijing 100083, China;*
3. *Beijing Engineering and Technology Research Center for Internet of Things in Agriculture, Beijing, 100083, China*)

Abstract: Ammonia nitrogen is an important factor in aquaculture; it can poison aquatic nerves and cause economic loss. If the ammonia nitrogen content is too high, it can lead to serious losses in the fish population within a short period of time. However, ammonia nitrogen prediction is inaccurate due to the influence of many factors such as dissolved oxygen, water temperature, and pH. Thus, this paper presents an improved method for ammonia nitrogen prediction in aquaculture ponds. Principle component analysis is utilized to select the key factors from meteorological factors and water quality factors; wavelet threshold de-noising is used to process data; a least squares support vector regression (LSSVR) prediction model is established, and the key parameters are optimized by the adaptive mutation particle swarm optimization algorithm to obtain the optimal least squares support vector regression forecasting model.

Keywords: aquaculture, ammonia nitrogen prediction, least squares support vector regression

Citation: Chen, Y. Y., Y. J. Cheng, Q. Q. Cheng, H. H. Yu, and D. L. Li. 2017. Short-term prediction model for ammonia nitrogen in aquaculture pond water based on optimized LSSVM. International Agricultural Engineering Journal, 26(3): 416–427.

1 Introduction

Aquaculture ponds are a major part of freshwater aquaculture in China, accounting for 43.94% of freshwater aquaculture. Ammonia nitrogen, which is one of the key factors in aquaculture ponds, plays an important role during the process of aquatic growth. Excessive ammonia nitrogen even in a short time will affect aquatic development by poisoning its nerve center, even causing death. This seriously affects aquatic production, resulting in huge economic losses (Zhang and Zhu, 2012). As a result, accurate prediction of ammonia nitrogen in aquaculture ponds is extremely urgent.

The content of ammonia nitrogen in aquaculture ponds is influenced by other factors (e.g., water temperature, dissolved oxygen, and pH). These factors influence each other and are unstable. Thus, it is particularly important to filter out the key factors by optimizing the method. However, it is difficult to determine the representative variables that are independent of each other because of the limited knowledge regarding ammonia nitrogen in aquaculture ponds. Principal component analysis (PCA) is proposed for feature extraction and data dimension reduction (Pearson, 1901). It is effective to select the most representative key factors by using PCA because it considers the relationship among different factors (Singh et al., 2011, Combes and Azema, 2013). Thus, the key factors that affect the change in ammonia nitrogen were identified by adopting PCA in this paper.

The reality and accuracy of original data are interpreted as a condition necessary for further research (Singh et al., 2010). Nevertheless, the data arising from the monitoring stations and experiment might be polluted

Received date: 2017-06-26 **Accepted date:** 2017-08-17

* **Corresponding author: Chen Yingyi,** Ph.D., Associate Professor of College of Information and Electrical Engineering, China Agricultural University, Beijing 100083, China. Email: chenyingyi@cau.edu.cn. Tel: +86 10 62738489, Fax: +86 10 62737741.

by noise signals owing to systematic and random errors. This noisy data often made prediction relatively difficult (Najah et al., 2012). Therefore, it is necessary to remove such noise from the original data. Wavelet theory has been widely applied to signal processing since it was first proposed in the early 1980s by Grossman because of its ability of distinguish noise and useful signals (Grossmann and Morlet, 1984, Kmen and Aslan, 2013). Wavelet analysis is considered a useful tool to analyse detailed temporal patterns of water quality signals over different temporal scales (Liu et al., 2013). Therefore, we adopted wavelet analysis to de-noise and extract features of the original ammonia nitrogen data to improve forecast accuracy in this study.

There are many methods to forecast water quality, such as regression models, artificial neural network (ANN), and support vector machine (Maier et al., 2010, Singh et al., 2011, and Tan et al., 2012). The regression model is the most commonly used due to the rapidity and simplicity of prediction; however, it is difficult to guarantee the accuracy of prediction (Grbić et al., 2013, Wu et al., 2013). The ANN has been applied to many aspects but is not suitable for small sample data (Maier et al. 2010, Almonacid et al., 2013, Ṛouhani and Ravasan, 2013). The support vector machine is considered a better alternative to ANN due to its advantages in solving small samples, nonlinearity, high dimensions, local minimum points and other practical issues (Tan et al., 2012, Cortes and Vapnik, 1995, Dibike et al., 2001, and Chen and Li, 2014). The prediction model based on support vector machine was proved useful for predicting droughts and estimating uncertainty associated with drought predictions (Ganguli and Reddy, 2013). An unscented Kalman filter-based state-space vector regression approach was utilized to predict short-term wind speed and has been proved to have much better performance than ANN (Chen and Yu, 2014). An ASVM has proved to be a promising method for case adaptation in CBD systems (Qi et al., 2015). Thus, the support vector machine method was applied to the prediction of small sample data.

Least squares support vector regression (LSSVR) simplified the model standard SVR to a great extent by applying linear least squares criteria to the loss function instead of a traditional quadratic programming method, which greatly improves the calculation speed and accuracy (Suykens et al., 2002). LSSVR has been successfully applied to many prediction fields. Lin et al. attempted to use an LSSVR technique with monthly fuzzy weighted values to forecast revenue in uncertain economic conditions successfully (Lin et al., 2013). Utterance modelling with i-vectors, which was successfully applied to speaker recognition, has been used in conjunction with a WCCN and LSSVR to address speaker age estimation (Bahari et al., 2014). A PI-adaptive LSSVR controller was applied to a nonlinear inverted pendulum in the presence of disturbance (Naghash-Almasi and Khooban, 2016). Thus, the LSSVR was used to predict changes in ammonia nitrogen in this paper.

However, LSSVR performance heavily depends on the choice of kernel parameters and the regularization parameter, which are necessary to define the optimization problem and the final LSSVR model (Liu et al., 2013, Xie et al., 2013). Therefore, it is necessary to optimize these parameters. Particle Swarm Optimization (PSO) has been successfully applied to optimize the parameters of LSSVR. A PSO–SVM based on the association rules method was presented to diagnose erythemato-squamous diseases and was shown to be promising compared to the previously reported results (Abdi et al., 2013). Liu presented the dissolved oxygen prediction model based on LSSVR optimized by improved PSO and acquired a satisfactory forecasting result (Liu et al., 2013). Geng improved the forecasting precision of port throughput by applying the proposed simulated annealing particle swarm optimization (SAPSO) algorithm to the robust v-support vector regression model (RSVR) (Geng et al., 2015). The PSO was exploited in the SRITCSD method to serve as a multiclassifier for image texture features; meanwhile, the PSO, which can improve the performance of the SRITCSD method, was employed to optimize the LSSVR (Chang et al., 2016). However, PSO has many drawbacks, including premature convergence. The adaptive mutation particle swarm optimization algorithm (AMPSO) was proposed to solve this problem (Lu et al., 2005). Thus, the AMPSO was applied to optimize the

parameters of the LSSVR in this study. The prediction model was tested and compared with other algorithms using the ammonia nitrogen data from a silver cod forming pond. The results show that the accuracy of prediction and the capability of generalization are greatly improved by our proposed approach.

This paper is organized as follows: Section 2 reports the construction of a hybrid forecasting model based on the wavelet analysis approach, least squares support vector regression and principal component analysis. Section 3 describes an application of the hybrid forecasting model. Finally, conclusions and future works are presented in Section 4.

2 Materials and methods

2.1 Data acquisition

The data used in this study were produced from the Tianxiang aquatic products Co., Ltd. in Ninghe County, Tianjin City, China. The experimental pond was approximately one acre, and the average water level was approximately 3 M. Three aerators were installed in the experimental pond. One point was chosen – where the distance from the forming pond was one meter and the depth was one meter – to collect the data (see Figure 1). A water-quality index, which was composed of ammonia nitrogen (AN), water temperature (WT), dissolved oxygen (DO) and pH, and a weather index, which was composed of rainfall (Ra), wind speed (WS), direction of wind (DW), solar radiation (SR), air temperature (AT), air humidity (AH) and atmospheric pressure (AP), were included in the data. The ammonia nitrogen was measured by a DZ-A type aquaculture water quality analyser every 4 hours starting from 0:00. Dissolved oxygen, water temperature and pH were detected by a HQ40d dual input multi-parameter digital analyser every 4 hours starting from 0:00. The weather index acquired from the small weather station was installed next to the silver cod forming pond.

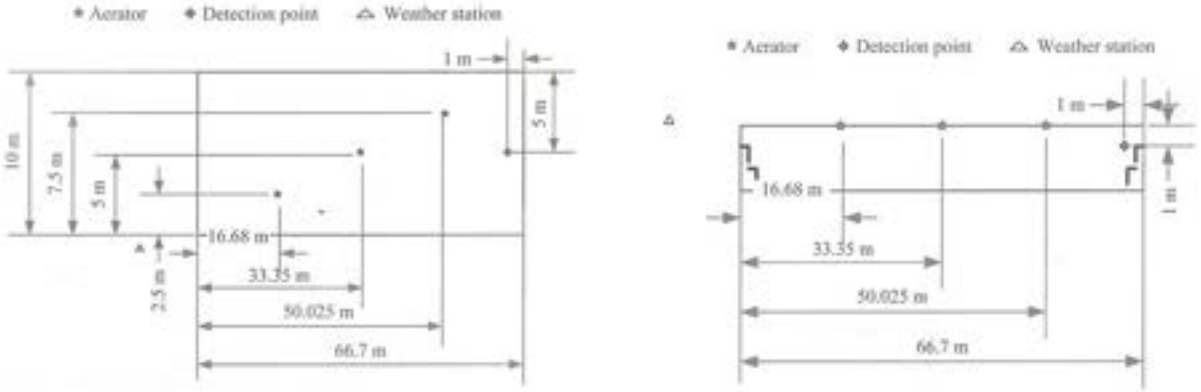

Figure 1 Detection point of water quality data

2.2 Principal component analysis

Principal component analysis (PCA) was proposed for feature extraction and data dimension reduction based on multi-dimensional orthogonal linear transformation of statistical features (Pearson, 1901, Härdle and Simar, 2007). The core idea of PCA is to form several comprehensive indicators (principal component) from a linear combination of primitive variables by studying the original variation of the correlation matrix or covariance matrix of the internal structure of the relationship. The similarity between the variables should be taken into account in the first step. The correlation coefficient was applied to measure the similarity between variables; the formula was as follows Equation (1):

$$r_{jk}=\sum_{i=1}^{n}\frac{\sum_{i=1}^{n}(x_{ij}-\overline{x}_j)(x_{ik}-\overline{x_k})}{\left[\sum_{i=1}^{n}(x_{ij}-\overline{x}_j)^2\sum_{i=1}^{n}(x_{ik}-\overline{x_k})^2\right]^{\frac{1}{2}}}$$
$$(j=1,2,3,\ldots,m) \quad (1)$$

where, x_{ij} is the variable j in data I; x_{ik} is the variable k in data i; $\overline{x}_j$ is the average of variable j; $\overline{x_k}$ is the average of variable k; m is the total number of variables; n is the total number of each variable, and r_{jk} is the correlation coefficient between variable j and variable k.

Contribution rate and cumulative contribution rate are used to evaluate the principal component as follows Equations (2) and (3):

$$\tau_i = \frac{\lambda_i}{\sum_{k=1}^{m}\lambda_k} \quad (i=1,2,..,m) \tag{2}$$

$$\eta_i = \frac{\sum_{k=1}^{i}\lambda_k}{\sum_{k=1}^{m}\lambda_k} \quad (i=1,2,..,m) \tag{3}$$

where, λ_i and λ_k are the matrix eigenvalue; τ_i is the contribution rate of i th principal component, and η_i is the cumulative contribution rate of the first i principal component.

The load matrix of the principal component is used to screen key influencing factors as follows Equation (4):

$$\ell_{ij} = \alpha_{ij}\sqrt{\lambda_i} \tag{4}$$

where, ℓ_{ij} is the correlation degree of principal components between the i th variable and the j th variable.

2.3 Wavelet analysis

Wavelet transform, which treats both the continuous and the discrete-time cases, has proven to be extremely valuable in signal processing (Daubechies, 1990, Rioul and Vetterli 1991). Unlike the Fourier transform, which can be utilized for a multi-scale analysis of a signal through dilation and translation, it can effectively extract the time-frequency features of a signal (Kisi and Cimen, 2011). For a continuous input signal, the time and scale parameters can be continuous, leading to the Continuous Wavelet Transform (Grossmann et al., 1989). Wavelet transform can be defined for discrete-time signals, leading to a Discrete Wavelet Transform (Daubechies, 1988, Rioul and Flandrin, 1992). The Discrete Wavelet Transform requires less computation time and is simpler to develop than the Continuous Wavelet Transform (Smith et al., 1998). Thus, the Discrete Wavelet Transform was applied to de-noise and extract features of the original ammonia nitrogen data.

For a discrete time series $f(t)$, the Discrete Wavelet Transform can be defined as the integration of a signal multiplied by a scaled and translated wavelet function at different time t, written as Equation (5):

$$W_\varphi f(j,k) = \int f(t)\Psi^*_{j,k}(t)dt \tag{5}$$

The original signal $f(t)$ can be obtained by taking the inverse wavelet transform using the following Equation (6):

$$f(t) = \iint W_\varphi f(j,k)\Psi_{j,k}(t)djdk \tag{6}$$

where, j, k are integer numbers; and $\Psi_{j,k}(t)$ is the wavelet basis function (Mallat 1989 Daubechies and Heil 1992), written as Equation (7):

$$\Psi_{j,k}(t) = 2^{\frac{-j}{2}}\Psi(2^{-j}-k) \tag{7}$$

2.4 Least squares Support Vector Regression

Giving a training set $\{x_i, y_i\}_{i=1}^{N}$, least squares support vector regression (Suykens et al. 2002) was defined as follows Equation (8):

$$\min_{w,b,e} J_p(w,e) = \frac{1}{2}w^T w + \gamma\frac{1}{2}\sum_{i=1}^{N}e_i^2 \tag{8}$$

where, w is the normal vector of the hyperplane; $\gamma \in R^+$ is the regularization parameter controlling model complexity and the overfitting phenomenon, $e=[e_1,e_2,\ldots,e_N]^T$, is the learning residual vector; $\varphi(\cdot)$ is the typical nonlinear mapping from the input space into the so-called feature space; and b is the bias.

Introduce the Lagrangian as Equation (9):

$$L(w,b,e;\alpha) = J_p(w,e) + \sum_{i}^{N}\alpha_i(y_i - w^T\varphi(x_i) - b - e_i) \tag{9}$$

where, α_i are the Lagrangian multipliers. The conditions for optimality are Equation (10):

$$\begin{cases} \dfrac{\partial L}{\partial w} = 0 \rightarrow w = \sum_{i=1}^{N}\alpha_i\varphi(x_i) \\ \dfrac{\partial L}{\partial b} = 0 \rightarrow \sum_{i=1}^{N}\alpha_i = 0 \\ \dfrac{\partial L}{\partial e_i} = 0 \rightarrow \alpha_i = \gamma e_i \\ \dfrac{\partial L}{\partial \alpha_i} = 0 \rightarrow y_i - w^T\varphi(x_i) - b - e_i = 0 \end{cases} \tag{10}$$

One obtains a set of linear equations after eliminating w and e in Equation (11)

$$\begin{bmatrix} 0 & 1^T \\ 1 & K \end{bmatrix}\begin{bmatrix} b \\ \alpha \end{bmatrix} = \begin{bmatrix} 0 \\ d \end{bmatrix} \tag{11}$$

where, $1=[1_1,1_2,\ldots,1_N]^T$, $d=[d_1,d_2,\ldots,d_N]^T$, $K_{ij} = k(x_i,x_j) = \varphi(x_i)^T\varphi(x_j) + \dfrac{\delta_{ij}}{\gamma}$ is a Kernel function, $\delta_{ij} = \begin{cases} 1, i=j \\ 0, i\neq j \end{cases}$.

Hence, the regression model is found by solving Equation (9). The resulting least squares support vector regression then becomes Equation (12):

$$f(x)=\sum_{i=1}^{N}\alpha_i k(x_i,x)+B \quad (12)$$

2.5 AMPSO-based optimization of the LSSVR model

Particle swarm optimization algorithm (Eberhart et al., 2001, Trelea, 2003) which is carried out to find the optimal solution by evaluating the position, velocity and fitness of each particle – is a swarm intelligence optimization algorithm. The particle velocity and position update equations for the i th particle and d th dimension can be described as follows:

$$V_{id}^{k+1}=wV_{id}^{k}+c_1r_1(P_{id}^{k}-X_{id}^{k})+c_2r_2(P_{gd}^{k}-X_{id}^{k}) \quad (13)$$

$$X_{id}^{k+1}=X_{id}^{k}+\alpha V_{id}^{k+1} \quad (14)$$

where, w is the inertia weight; k is the iteration number; c_1 is the cognition learning factor; c_2 denotes the social learning factor; r_1 and r_2 are two independent uniformly distributed random variables with range [0,1], P_{id}^{k} denotes the best previous position encountered by the ith particle, and P_{gd}^{k} denotes the global best position of a particle; thus, X_{id} and V_{id} are the position and velocity of the particle, respectively.

An adaptive mutation particle swarm optimization algorithm is proposed in order to overcome the premature convergence of particle swarm optimization algorithm by increasing a random mutation operator (Lu et al., 2005). The particle swarm optimization algorithm can be continued in the case of premature convergence by initializing P_{gd}^{k} with a certain probability in Equations (15)-(17).

$$f_{avg}=\frac{1}{n}\sum_{i=1}^{n}f_i \quad (15)$$

$$f=\max\left\{1,\ \max_{1\le i\le n}|f_i-f_{avg}|\right\} \quad (16)$$

$$\sigma^2=\sum_{i=1}^{n}\left(\frac{f_i-f_{avg}}{f}\right)^2 \quad (17)$$

where, n is the particle swarm size; f_i is the fitness of particle i; f_{avg} is the average fitness of practices; σ^2 is the variance of population fitness, and f is the normalized scaling factor for limiting the size of σ^2.

P_{gd}^{k} is initialized by the following Equation (18) (Chen et al., 2006, Deyi et. al., 2011):

$$P_k=(P_{max}-P_{min})\left(\frac{\sigma_k^2}{n}\right)^2+(P_{min}-P_{max})\left(2\frac{\sigma_k^2}{n}\right)+P_{max} \quad (18)$$

where, P_{max} is the maximum variation probability; P_{min} is the minimum variation probability; P_k is the group global optimization in k iteration, and σ_k^2 is the variance of population fitness in k iteration. Increasing random perturbation was adopted to mutate P_{gd}^{k} as follows Equation (19):

$$P_{gd}^{k}=P_{gd}^{k}(1+0.5\eta) \quad (19)$$

where, η is a random variable subject to Guass (0, 1).

The process of optimizing the LSSVR parameters with AMPSO is presented in Figure 2, which can be described as follows:

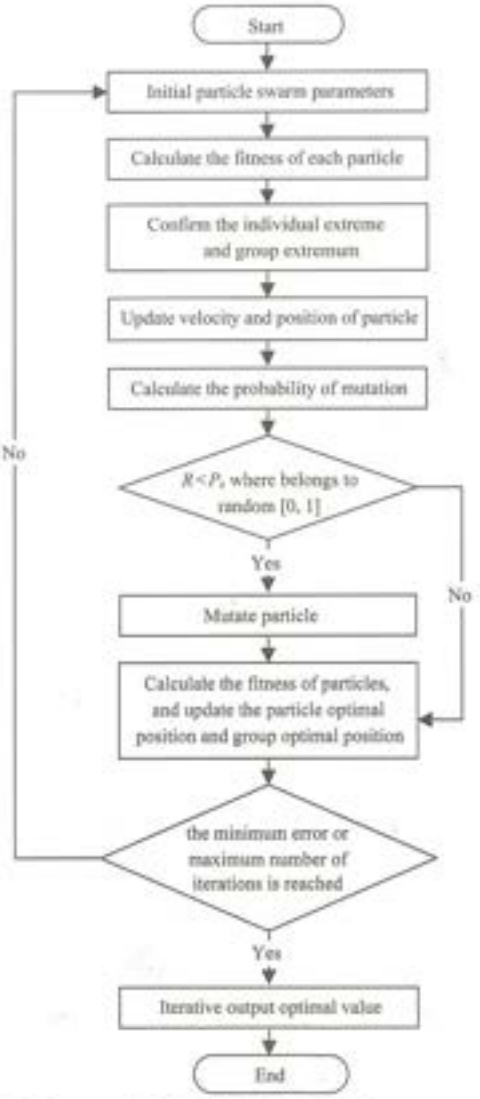

Figure 2 Process of optimizing the LSSVR parameters with AMPSO

Step1: Initial particle swarm parameters: inertia factor, acceleration constant, maximum number of iterations and the minimum allowable error of the

algorithm. And initiate the velocity and position of the particles randomly.

Step2: Calculate the fitness of each particle according to the following formula Equation (20):

$$\text{itness} = \sqrt{\frac{1}{n}\sum_{i=1}^{n}(\bar{y}_i - y_i)^2} \tag{20}$$

where, n is the particle swarm size; y_i is the real value, and $\bar{y}_i$ is the forecast value.

Step3: Confirm the individual extreme and group extremum according to the fitness of each particle.

Step4: Update the velocity and position of the particle by using Equation (12), (13).

Step5: Calculate the probability of mutation by using Equation (14)-(17).

Step6: Mutate the particle by using Equation (18) while $r<P_k$, where r belongs to random [0, 1].

Step7: Calculate the fitness of particles, and update the particle optimal position and group optimal position.

Step8: Iteratively output the optimal value until the minimum error or maximum number of iterations is reached. Otherwise, go to step 4.

2.6 The overall structure of the proposed hybrid algorithm

The process for content prediction of ammonia nitrogen in aquaculture using optimized least square support vector regression is described as follows:

Step1: Collect the data used in this study, and then dispose error data and missing data.

Step2: Filter the key factors for the content prediction of ammonia nitrogen in aquaculture using principal component analysis.

Step3: De-noise and extract features of the key factors data and ammonia nitrogen using wavelet analysis.

Step4: Normalize the data and select the training sample and testing sample.

Step5: Build the model using the AMPSO-LSSVR algorithm.

Step6: Output the results, and evaluate the model.

3 Results and discussions

3.1 Principal component analysis for factors dimension reduction

The data which includes ammonia nitrogen (AN), water temperature (WT), dissolved oxygen (DO), pH, rainfall (Ra), wind speed (WS), direction of wind (DW), solar radiation (SR), air temperature (AT), air humidity (AH) and atmospheric pressure (AP) were acquired once every hour starting from 0:00 during the time period between October 2th and October 10th, 2015. Rainfall was deleted from the data set because there is no rain from October 2th to October 10th. The PCA was chosen to screen the key factors influencing the change of ammonia nitrogen according to the following steps:

Step1: Normalize the original data by the following Equations (21) and (22):

$$x_{ij}^{*} = \begin{cases} \dfrac{x_{ij} - \overline{x_j}}{S_j}, & S_j \neq 0 \\ 0, & S_j = 0 \end{cases} \quad \begin{pmatrix} i = 1,2,\ldots,n \\ j = 1,2,\ldots,m \end{pmatrix} \tag{21}$$

$$S_j = \sqrt{\frac{1}{n-1}\sum_{i=1}^{n}(x_{ij} - \overline{x_j})^2} \tag{22}$$

where, x_{ij} is the variable j in data i; $\overline{x_j}$ is the average of variable j; m is the total number of variables; n is the total number of each variable; S_j is the standard deviation of variable j, and x_{ij}^{*} is the standard data.

Step2: Find the similarity between every pair of variables in the data set using the formula (1), and then list the correlation coefficient matrix.

Step3: Calculate the characteristic value and characteristic vector of the correlation coefficient matrix; the result is shown in Table 1.

Step4: Calculate the contribution rate and cumulative contribution rate using formula (2) and (3); the result is shown in Table 1.

Table 1 Factor the characteristic value and contribution rate of aquaculture

Principal fact	Characteristic value	Contribution rate, %	Cumulative contribution rate, %
1	2.9019	29.02	29.02
2	2.4923	24.92	53.94
3	1.4244	14.24	68.18
4	1.1512	11.51	79.69
5	0.8762	8.76	88.45
6	0.4517	4.52	92.97
7	0.3002	3.00	95.97
8	0.2195	2.20	98.17
9	0.1352	1.35	99.52
10	0.0475	0.48	10.00

5 factors were chosen as the key factors influencing the change in ammonia nitrogen because the cumulative contribution rate of the first five factors is greater than 85%, which we can see from Table 1.

Step5: Calculate the load matrix of the principal fact using Equation (4); the result is listed in Table 2.

Table 2 The load matrix of the principal fact

Fact	Principal fact 1	Principal fact 2	Principal fact 3	Principal fact 4	Principal fact 5
AN	–0.8414	–0.2664	–0.1803	0.1522	–0.0085
WT	0.7663	0.3250	–0.4508	–0.1490	0.1281
DO	–0.2576	0.6340	0.6548	–0.0796	0.0285
pH	0.1168	0.7607	0.5137	–0.1765	0.0112
WS	–0.7012	0.4886	–0.2305	–0.1454	0.0698
DW	0.1236	0.0250	0.1526	0.6828	0.7005
SR	–0.0334	0.5090	–0.2765	0.5948	–0.4280
AT	0.6568	0.6176	–0.3589	–0.0611	0.0795
AH	0.5473	–0.6535	0.2634	–0.2054	0.0354
AP	0.5364	–0.1682	0.3807	0.4258	–0.4153

From Table 2, we can see that the correlation coefficient of AN and WT on the first factor is larger than that of other factors; the contribution of pH to the second factor is the largest, the contribution of DO to the third factor is the largest; the contribution of DW to the fourth and fifth factors is the largest. Thus, the AN, WT, pH, DO and DW were chosen as the principal component index. This also corresponds to the selection of the key factors influencing the change in ammonia nitrogen.

3.2 Wavelet analysis for data de-noising

The Discrete Wavelet Transform was applied to de-noise and extract features of the key factor data selected in section 3.1 and ammonia nitrogen as according to the following steps:

Step1: Decompose the original signal into 3 scales with the appropriate wavelet basis function illustrated in Figure 3.

Step2: Process the wavelet coefficients with the appropriate wavelet thresholding function.

Step3: Obtain the de-noising signal by reconstructing the processed wavelet coefficients with soft thresholding.

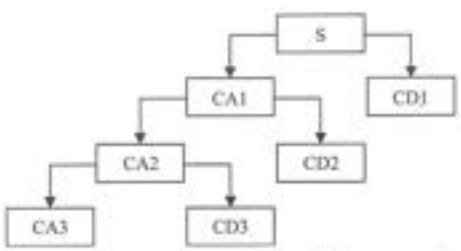

Figure 3 Tree structure of wavelet decomposition

It is difficult to find an ideal wavelet in signal analysis, so a compromise is made between performance and complexity. It is desirable to use few wavelet basis functions and wavelet thresholding functions from different families for the performance evaluation and selecting the wavelet that gives the best performance. The root mean square error (RMSE) and the signal-to-noise ratio (SNR) were used to measure performance. The RMSE and SNR can be illustrated as follows Equations (23) and (24):

$$\mathrm{RMSE} = \sqrt{\frac{1}{n}\sum[f(n)-\hat{f}(n)]^2} \tag{23}$$

$$\mathrm{SNR} = 10\log_{10}\frac{\sum_n f^2(n)}{\sum_n[f(n)-\hat{f}(n)]^2} \tag{24}$$

where, $f(n)$ is the original signal, and $\hat{f}(n)$ is the signal after wavelet threshold de-noising.

The wavelet basis functions haar, dmey, dbN (N=2, 3, …, 10), symN (N=1, 2, … ,10), coifN (N=1, 2, …, 5) and wavelet thresholding function rigrsure were applied to process the ammonia nitrogen; the result is shown in Table 3.

Table 3 The RMSE and SNR of ammonia nitrogen with different wavelet basis functions

Wavelet basis function type	SNR	RMSE
Haar	23.3144	0.0586
dmey	23.0417	0.0605
db2	23.5433	0.0571
db3	23.8969	0.0548
db4	23.8567	0.0551
db5	24.1539	0.0532
db6	24.2507	0.0526
db7	22.9939	0.0608
db8	24.1971	0.053
db9	23.3543	0.0584
db10	23.984	0.0543
sym1	23.3144	0.0586
sym2	23.5433	0.0571
sym3	23.8969	0.0548
sym4	23.7257	0.0559
sym5	23.0542	0.0604
sym6	24.6398	0.0503
sym7	23.7485	0.0558
sym8	23.8564	0.0551
sym9	23.8572	0.0551
sym10	23.5851	0.0568
coif1	23.4919	0.0574
coif2	23.7919	0.0555
coif3	23.1602	0.0597
coif4	23.8815	0.0549
coif5	23.0811	0.0602

The wavelet basis function sym6 was selected as the best wavelet basis function due to the minimum RMSE (0.0503) and the maximum SNR (24.6398). The result of ammonia nitrogen noise reduction is presented in Figure 4. From Figure 4, it can be seen that the change curve of ammonia nitrogen becomes smooth, and the influence of noise and clutter on the ammonia nitrogen was eliminated.

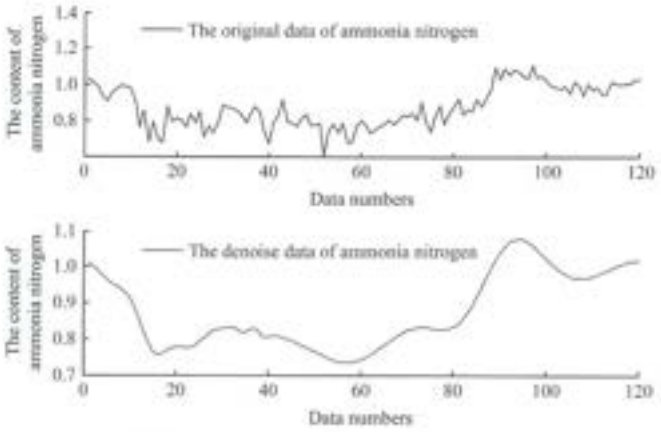

Figure 4 Result of ammonia nitrogen

The wavelet basis functions of water temperature (WT), dissolved oxygen (DO), pH, and direction of wind (DW) were chosen for the same method. Finally, the best wavelet basis function and wavelet thresholding function of each factor were selected as shown in Table 4.

Table 4 Best wavelet basis function of each factor

Factor	Wavelet basis function type	SNR	RMSE
AN	sym6	24.6398	0.0503
WT	coif1	29.9880	0.5977
DO	sym5	27.3846	0.4019
pH	sym3	38.3841	0.1017
DW	db6	47.4163	11.0376

3.3 Results evaluation

The proposed hybrid algorithm was implemented in the Matlab R2012a programming language. We obtained the optimal parameters γ and σ for the prediction model of ammonia nitrogen based on the AMPSO algorithm. The initial parameters of AMPSO were given as follows: the cognition learning factor c_1=1.5, the social learning factor c_2=1.7, the population size of swarm sizepop=30, the iteration number maxgen=300, the inertia weight wmax=1.2 and wmin=0.8; the fitness accuracy of the normalized samples are equal to 0.002. The changing trend of the fitness value is illuminated in Figure 5. From Figure 5, we can see that the fitness value tends to stabilize quickly; the AMPSO converges to the best solution quickly and is more appropriate for seeking the unknown parameters of the LSSVR. The optimal combination parameters were obtained, namely, γ=1000, σ=2.9144.

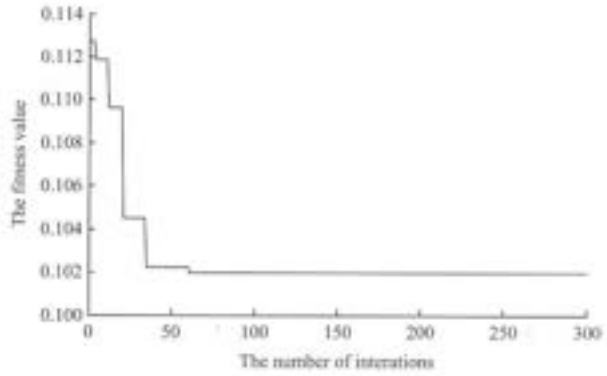

Figure 5 Trend of the fitness value

The optimal combination parameters were adopted to train the ammonia nitrogen prediction model. The training result of the prediction model was shown in Figure 6. From Figure 6, the real values and the predicted training values with AMPSO_LSSVR were not quite different. The test sample set was put into the trained model to predict the change in ammonia nitrogen. The ammonia nitrogen content prediction result is given in Figure 7. From Figure 7, it is shown that the ammonia nitrogen content prediction result is broadly in line with the real values.

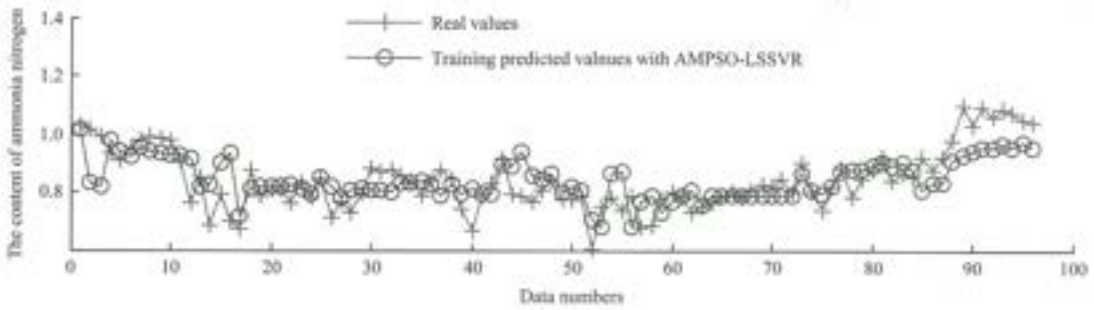

Figure 6 Trained result of the prediction model

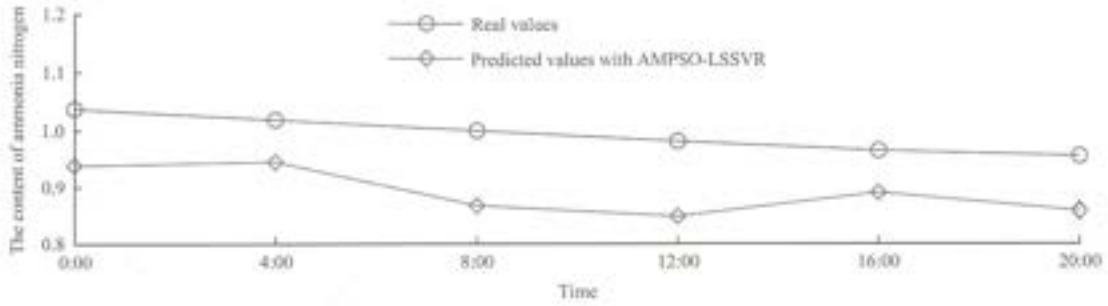

Figure 7 Ammonia nitrogen content prediction result

In addition, the standard least square support vector regression (LSSVR) was compared with the optimized least square support vector regression. The results of different methods are illustrated in Figure 8. The results of the optimized least square support vector regression are closer to the real values. Thus, the accuracy of ammonia nitrogen prediction in the pond aquaculture was improved.

The absolute errors of the standard least square support vector regression and the optimized least square support vector regression are represented in Figure 9. The absolute errors of the optimized least square support are smaller than those of the standard least square support vector regression.

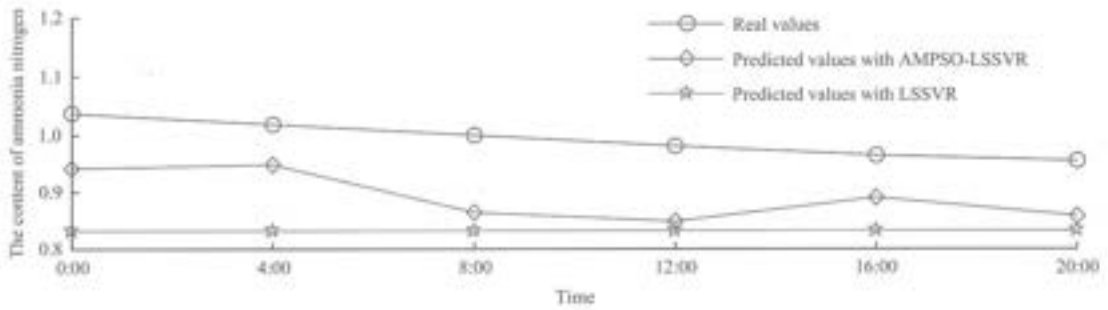

Figure 8 Predicted results of different methods

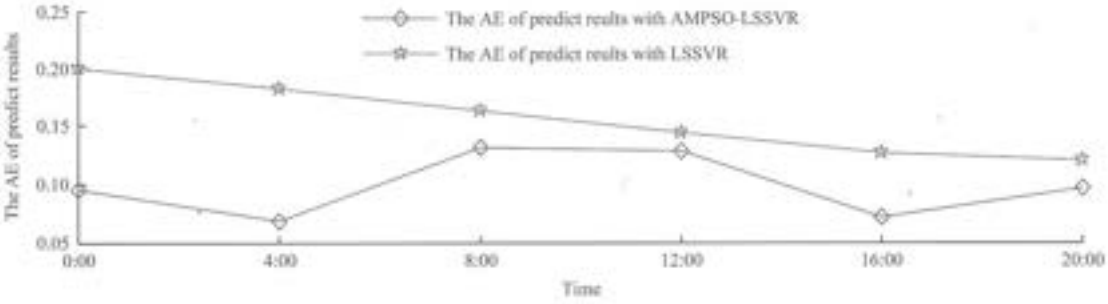

Figure 9 AE of different predicted results with different methods

Different standard statistical performance evaluation criteria, such as root mean square error (RMSE), the mean absolute percentage error (MAPE), the mean absolute error (MAE), the mean relative error (MRE), and the Nash–Sutcliffe efficiency coefficient (NSC), were used to evaluate the performance of various models. The RMSE, MAE and MRE were used to assess the prediction capability of the model proposed in this paper. The MAE and MRE can be illustrated as follows Equations (25) and (26):

$$MAE = \frac{1}{N}\sum_{i=1}^{N}|y_i - \bar{y}_i| \quad (25)$$

$$MRE = \frac{1}{N}\sum_{i=1}^{N}\left|\frac{y_i - \bar{y}_i}{y_i}\right| \quad (26)$$

where, y_i is the real value; $\bar{y}_i$ is the predicted value, and N is the number of samples.

The RMSE, MAE and MRE of different methods are listed in Table 5. The obtained results indicate that the optimized least square support vector regression is far superior to the standard least square support vector

regression. The prediction RMSE of optimized least square support vector regression is reduced by 40.15% compared to that of standard least square support vector regression. The prediction MAE of optimized least square support vector regression is reduced by 41.82% compared to that of standard least square support vector regression. The prediction MRE of optimized least square support vector regression is reduced by 42.29% compared to that of standard least square support vector regression.

Table 5 RMSR and MAE of different methods

Method	RMSE	MAE	MRE
Optimized least square support vector regression	0.0945	0.0903	0.0887
Standard least square support vector regression	0.1579	0.1552	0.1537

The hybrid model proposed in this study is capable of searching for the parameter values of the LSSVR and RBF kernel function. The result of this study demonstrates that the prediction of ammonia nitrogen content is effective and feasible.

4 Conclusions

This paper proposed a hybrid forecasting model that combined principle component analysis, wavelet analysis, and least squares support vector regression and adaptive mutation particle swarm optimization algorithm. The results clearly show that compared with the standard least square support vector regression (LSSVR), the proposed hybrid method of optimized LSSVR has better prediction performance, as measured by RMSE. Further, the optimized LSSVR can effectively consider many dimensions and nonlinearity, non-stationary and finite samples and is a reliable forecasting tool for predicting ammonia nitrogen time series in modern intensive aquaculture.

There is room for further study and development. First, the change in ammonia nitrogen in the aquaculture pond will be different during different farming seasons and different growth periods. In future work, we plan to research the prediction of ammonia nitrogen in aquaculture ponds over longer time periods, taking into consideration different farming seasons and different growth periods to control the ammonia nitrogen in aquaculture ponds. Second, other optimization search algorithms, like genetic algorithm (GA) and ant colony optimization (ACO), can be compared with the adaptive mutation particle swarm optimization algorithm (AMPSO). These are all valuable problems for future research.

Acknowledgements

This paper was supported by the Beijing science and technology plan- Research on intelligent system and equipment for Large-scale freshwater fish breeding (No. Z171100001517016), the EU cooperation projects-Innovative model & demonstration-based water management for resource efficiency in integrated multitrophic aquaculture and horticulture systems (No. 619137), the International Science & Technology Cooperation Program of China - Key technology cooperating research on agricultural internet of things advanced sensors and intelligent processing (No.2013DFA11320), and the Shandong Province Key Research & Development Program - Research on aquaculture management and application platform technology based on big data (No. 2015GGC02066).

[References]

[1] Abdi, M. J., and D. Giveki. 2013. Automatic detection of erythemato-squamous diseases using PSO–SVM based on association rules. *Engineering Applications of Artificial Intelligence*, 26(26): 603–608.

[2] Almonacid, F., E. F. Fernández, P. Rodrigo, P. J. Pérez-Higueras, and C. Rus-Casas. 2013. Estimating the maximum power of a high concentrator photovoltaic (HCPV) module using an artificial neural network. *Energy*, 53(5): 165–172.

[3] Bahari, M. H., M. Mclaren, H. V. Hamme, and D. A. V. Leeuwen. 2014. Speaker age estimation using i-vectors. *Engineering Applications of Artificial Intelligence*, 34(3): 99–108.

[4] Chang, B., H. Tsai, and C. Yen. 2016. SVM-PSO based rotation-invariant image texture classification in SVD and DWT domains. *Engineering Applications of Artificial Intelligence*, 52(C): 96–107.

[5] Chen, G., J. Jia, and H. Qi. 2006. Study on the strategy of decreasing inertia weight in particle swarm optimization algorithm. *Journal of Xian Jiaotong University*, 40(1): 53–56.

[6] Chen, J. L., and G. S. Li. 2014. Evaluation of support vector machine for estimation of solar radiation from measured meteorological variables. *Theoretical & Applied Climatology*,

115(3-4): 627–638.

[7] Chen, K., and J. Yu. 2014. Short-term wind speed prediction using an unscented Kalman filter based state-space support vector regression approach. *Applied Energy*, 113(6): 690–705.

[8] Combes, C., and J. Azema. 2013. Clustering using principal component analysis applied to autonomy-disability of elderly people. *Decision Support Systems*, 55(2): 578–586.

[9] Cortes, C., and V. Vapnik. 1995. Support-vector networks. *Machine learning*, 20(3): 273–297.

[10] Daubechies, I. 1990. The wavelet transform, time-frequency localisation and signal analysis. *IEEE transactions on information theory*, 36(5): 961–1005.

[11] Daubechies, I., and C. Heil. 1993. Ten lectures on wavelets. *The Journal of the Acoustical Society of America*, 93(3): 1671–1671.

[12] Daubechies, I. 1988. Orthonormal bases of compactly supported wavelets. *Communications on Pure and Applied Mathematics*, 41(7): 909–996.

[13] Deyi ,Y. E., H. E. Zhengyou, and T. Zang. 2011. Siting and sizing of distributed generation planning based on adaptive mutation particle swarm optimization algorithm. *Power System Technology*, 35(6): 155–160.

[14] Dibike, Y. B., D. Solomatine, S. Velickov, and M. B. Abbott. 2001. Model induction with support vector machines: introduction and applications. *Journal of Computing in Civil Engineering*, 15(3): 208–216.

[15] Dökmen, F., and Z. Aslan. 2013. Evaluation of the parameters of water quality with wavelet techniques. *Water resources management*, 27(14): 4977–4988.

[16] Eberhart, R. C., Y. Shi, R. C. Eberhart, and Y. Shi. 2001. Particle swarm optimization: developments, applications, and resources. *In IEEE Congress on Evolutionary Computation (CEC 2001)*, 259–263. Seoul, South Korea, 27-30 May.

[17] Ganguli, P., and M. J. Reddy. 2013. Ensemble prediction of regional droughts using climate inputs and the SVM–copula approach. *Hydrological processes*, 28(19): 4989–5009.

[18] Geng, J., M. Li, Z. Dong, and Y. Liao. 2015. Port throughput forecasting by MARS-RSVR with chaotic simulated annealing particle swarm optimization algorithm. *Neurocomputing*, 147(1): 239–250.

[19] Grbić, R., D. Kurtagić, and D. Slišković. 2013. Stream water temperature prediction based on Gaussian process regression. *Expert systems with applications*, 40(18): 7407–7414.

[20] Grossmann, A., and J. Morlet. 1984. Decomposition of Hardy functions into square integrable wavelets of constant shape. *SIAM journal on mathematical analysis*, 15(4): 723–736.

[21] Grossmann, A., R. Kronland-Martinet, and J. Morlet. 1989. Reading and Understanding Continuous Wavelet Transforms. Germany: Springer Berlin Heidelberg.

[22] Härdle, W., and L. Simar. 2012. Applied multivariate statistical analysis. *Technometrics*, 31(2): 265–266.

[23] Kisi, O., and M. Cimen. 2011. A wavelet-support vector machine conjunction model for monthly streamflow forecasting. *Journal of Hydrology*, 399(1): 132–140.

[24] Lin, K., P. Pai, Y. Lu, and P. Chang. 2013. Revenue forecasting using a least-squares support vector regression model in a fuzzy environment. *Information Sciences*, 220(1): 196–209.

[25] Liu, S., L. Xu. Y. Jiang, D. Li, Y. Chen, and Z. Li. 2013. A hybrid WA-CPSO-LSSVR model for dissolved oxygen content prediction in crab culture. *Engineering Applications of Artificial Intelligence*, 29(3): 114–124.

[26] Lu, Z. S., Z. R. Hou, and J. Du. 2005. Particle swarm optimization with adaptive mutation. *Frontiers Engineering in China*, 1(1): 99–104.

[27] Maier, H. R., A. Jain, G. C. Dandy, and K. P. Sudheer. 2010. Methods used for the development of neural networks for the prediction of water resource variables in river systems: current status and future directions. *Environmental Modelling & Software*, 25(8): 891–909.

[28] Mallat, S. G. 1989. A theory for multiresolution signal decomposition: the wavelet representation. *IEEE Transactions on Pattern Analysis and Machine Intelligence*, 11(7): 674–693.

[29] Naghash-Almasi, O., and M. H. Khooban. 2016. PI adaptive LS-SVR control scheme with disturbance rejection for a class of uncertain nonlinear systems. *Engineering Applications of Artificial Intelligence*, 52(C): 135–144.

[30] Najah, A. A., A. El-Shafie, O. A. Karim, and O. Jaafar. 2012. Water quality prediction model utilizing integrated wavelet-ANFIS model with cross-validation. *Neural Computing and Applications*, 21(5): 833–841.

[31] Pearson, K. 1901. On lines and planes of closest fit to systems of points in space. *The London, Edinburgh, and Dublin Philosophical Magazine and Journal of Science*, 2(11): 559–572.

[32] Qi, J., J. Hu, and Y. Peng. 2015. Incorporating adaptability-related knowledge into support vector machine for case-based design adaptation. *Engineering Applications of Artificial Intelligence*, 37(9): 170–180.

[33] Rioul, O., and M. Vetterli. 1991. Wavelets and signal processing. *IEEE signal processing magazine*, 8(4): 14–38.

[34] Rioul, O., and P. Flandrin. 1992. Time-scale energy distributions: a general class extending wavelet transforms. *IEEE Transactions on Signal Processing*, 40(7): 1746–1757.

[35] Rouhani, S., and A. Z. Ravasan. 2013. ERP success prediction: An artificial neural network approach. *Scientia Iranica*, 20(3): 992–1001.

[36] Singh, C. B., R. Choudhary, D. S. Jayas, and J. Paliwal. 2010.

Wavelet analysis of signals in agriculture and food quality inspection. *Food and Bioprocess Technology*, 3(1): 2–12.

[37] Singh, K. P., N. Basant, and S. Gupta. 2011. Support vector machines in water quality management. *Analytica Chimica Acta*, 703(2): 152–162.

[38] Singh, V. H., M. Agrawal, G. C. Joshi, M. Sudershan, and A. K. Sinha. 2011. Elemental profile of agricultural soil by the EDXRF technique and use of the Principal Component Analysis (PCA) method to interpret the complex data. *Applied Radiation and Isotopes*, 69(7): 969–974.

[39] Smith, L. C., D. L. Turcotte, and B. L. Isacks. 1998. Stream flow characterization and feature detection using a discrete wavelet transform. *Hydrological Processes*, 12(2): 233–249.

[40] Suykens, J., T. Van Gestel, J. De Brabanter, B. De Moor, and J. Vandewalle. 2002. *Least Squares Support Vector Machines*. Singapore: World Scientific Publishing.

[41] Tan G., J. Yan, C. Gao, and S. Yang. 2012. Prediction of water quality time series data based on least squares support vector machine. *Procedia Engineering*, 31(16): 1194–1199.

[42] The Ministry of Agriculture, F. F. A., 2016. China fishery statistics yearbook 2016. China Agriculture Press: China.

[43] Trelea, I. C. 2003. The particle swarm optimization algorithm: convergence analysis and parameter selection. *Information Processing Letters*, 85(6): 317–325.

[44] Wu, J., J. Wang, H. Lu, Y. Dong, and X. Lu. 2013. Short term load forecasting technique based on the seasonal exponential adjustment method and the regression model. *Energy Conversion and Management*, 70(70): 1–9.

[45] Xie, G., S. Wang, Y. Zhao, and K. K. Lai. 2013. Hybrid approaches based on LSSVR model for container throughput forecasting: a comparative study. *Applied Soft Computing*, 13(5): 2232–2241.

[46] Zhang, W., and Y. Zhu. 2012. Advances on the research of the hazard of ammonia nitrogen in aquaculture water and its determination method. *Journal of Environmental Hygiene*, 2(6): 324–327.

Detection method of moving object pig based on difference method and energy minimization

Li Yue, Sun Longqing*, Zou Yuanbing, Li Yiyang

(College of Information and Electrical Engineering, China Agricultural University, Beijing 100083, China)

Abstract: In order to improve the real-time and accurate rate of pig detection in monitoring video, a new moving object pig detection algorithm is proposed in static background. Combining the Adaptive Threshold Three-Frame Difference Method and the Background Update Difference Method based on Energy Minimization Theory, do the "and" operation to the difference, do the "or" operation to the background difference of current frame and the result of "and", the complete information of moving object and continuous extraction of the pigs' contours can be obtained. Results of experiments show that the edge continuity index range obtained by this method is 0.7-0.9, while the edge continuity index ranges of the Traditional Three-Frame Difference Method and the Background Difference Method are 0.3-0.5, the detection results are improved remarkably. In this paper, the Background Update Method is combined with the Energy Minimization Segmentation algorithm, the principle is simple and it can help accurately get the contour information of moving objects while the contour extraction results are continuous and complete. This method can adapt to the object detection under complex scenes such as illumination changes, and it can meet the real-time requirements.

Keywords: moving object detection, three-frame difference, background difference, energy minimization

Citation: Li, Y., L. Q. Sun, Y. B. Zou, and Y. Y. Li. 2017. Detection method of moving object pig based on difference method and energy minimization. International Agricultural Engineering Journal, 26(3): 428–438.

1 Introduction

China is a large pig breeding country, according to statistics, statistics such as pig's stock rate, slaughter rate, pork yield are ranked first in the world (Wu et al., 2015). With the development of large scale and intensive farming, the risk of breeding has gradually increased. Real-time health status monitoring and daily activity recording of individual pig (Duan et al., 2015; Xiao et al., 2016) can help quickly find pigs' abnormal behavior and let appropriate measures be timely taken to reduce the occurrence of disease (Zhu et al., 2010; Porto et al., 2013).

Moving object detection is to remove the background content from the video image, detect the moving target and get its movement information. The accuracy and effectiveness of detection algorithm affect the correctness of identification of the moving target. So detection algorithm plays an important role in computer vision (Oczak et al., 2013; Zuriarrain et al., 2013; Ahrendt et al., 2011). Commonly used moving target detection algorithms in static background include Optical Flow Method (Lu et al., 2010), Background Difference Method (Alex et al., 2014), Frame Difference Method (Zhang et al., 2012) and so on. Frame Difference Method and Background Difference Method are widely used in moving object detection because of their simplicity, quickness and real-time. However, slow moving or stationary targets are easy to be missed when Frame Difference Method is used, and one cannot get complete target extraction when the grayscale or the texture of two consecutive frames are close because the "hole" and "double shadow" could appear. To solve this problem, Vieren et al. (1995) proposed a detection method based on three-frame difference, which improved the detection accuracy. Yin et al. (2011) proposed a fast target tracking method based on Mean Shift and Three Frame Difference

Received date: 2017-07-02 **Accepted date:** 2017-08-20

* **Corresponding author: Sun Longqing,** Associate Professor, College of Information and Electrical Engineering, China Agricultural University, Beijing 100083, China. Email: sunlq@cau.edu.cn. Tel: 13910682177, Fax: 86-10-62737482.

Methods, which could effectively overcome the problem of false detection. Pang et al. (2013) put forward a moving object extraction algorithm based on Three Frame Difference and Canny edge detection which can get complete target information with good anti-noise performance. This method could effectively extract the moving object in real-time. Shu et al. (2014) proposed a Five Frame Difference method which reduced the "false detection" to some extent. The establishment and real-time updating of the background model in the Background Difference method is the key to the algorithm. Some researchers have put forward various algorithms for adaptive updating of the background, such as Frame Difference method (Gupte et al., 2002), Kalman Filter method (Messelodi et al., 2005), Single Gaussian Model (Liu et al., 2014), Hybrid Gaussian model (Zhao et al., 2015), etc. Rao et al. (2014) detected moving targets using the Three Frame Difference method and the Calman Filter. Guo et al. (2014) used the Hybrid Gaussian Model and Threshold Segmentation to obtain complete moving pig targets. Li et al. (2013) and Sun et al. (2014) used Adaptive Background Difference method and Three Frame Difference method based on the Kalman Filter Model to achieve real-time tracking of moving target. The above Background Update methods perform better in avoiding the interference of random noise and illumination changes. The shadow and reflection of the moving object will significantly change the shape of the detection target. The contrast between the foreground object and the obscured background area is not enough, the pixels in a frame cannot be clearly distinguished whether they are from foreground or background. Some researchers used Energy Minimization techniques (Boykov et al., 2001) in foreground detection, and this is an effective segmentation method. Malcolm et al. (2007) and Boykov et al. (2001) proposed Graph Cut for video segmentation, which required to specify the object to be detected in the first few frames before the detection, and use its information to detect further. This method achieved real-time and fast segmentation of targets. As time went on, some of the new moving objects in the video image would not be detected. Howe et al. (2004) proposed an automatic detection method based on Graph Cut, the operation time was longer, but the model design was simpler.

In the process of moving target detection, the Three-Frame Difference method is easy to cause the "hole" phenomenon and the Background Difference method is sensitive to the change of scene. This paper presents a detection method of moving target pig which combines Three-Frame Difference method and Background Difference method to extract whole moving area of target, introduces the Energy Minimization theory in Background Difference method, and builds an energy equation to solve the background update problem. The method has strong robustness to the illumination change and it can detect the pig target accurately (Navarrojover et al., 2009, Lind et al., 2005).

2 Algorithm principle

2.1 Improved Three-Frame Difference method

The Traditional Inter Frame Difference or Three-Frame Difference method is real-time, but the motion area extracted is incomplete, the target's contour is not continuous, a lot of holes would appear when detecting slow moving target. In order to improve the real-time and accuracy of pig identification in monitoring video, this paper presents an improved real-time target detection algorithm based on Three-Frame Difference. The algorithm is as follows Equation(1):

(1) Take an image every 3 consecutive frames $f_{i-3}(x,y)$, $f_i(x,y)$, $f_{i+3}(x,y)$ i=4,5,6…;

(2) Transform into grayscale images respectively, and do the Gaussian filtering, median filtering in order to remove the noise of the image. Get the corresponding image $I_{i-3}(x,y)$, $I_i(x,y)$, $I_{i+3}(x,y)$;

(3) Get the difference respectively;

$$\begin{cases} d_{(i-3,i)}(x,y) = |I_i(x,y) - I_{i-3}(x,y)| \\ d_{(i,i+3)}(x,y) = |I_{i+3}(x,y) - I_i(x,y)| \end{cases} \quad (1)$$

where, $d_{(i-3,i)}(x,y)$ represents the difference image between the current frame and the frame before 2 frames, $d_{(i,i+3)}(x,y)$ represents the difference image between the current frame and the frame after 2 frames. If $I_{i-3}(x,y)$, $I_i(x,y)$ have the same frame order as $I_i(x,y)$, $I_{i+3}(x,y)$, then the calculation can be saved, $d_{(i-3,i)}(x,y)$ is same as $d_{(i,i+3)}(x,y)$.

(4) The difference image is binarized in Equation (2):

$$\begin{cases} b_{(i-3,i)}(x,y)=\begin{cases}1 & d_{(i-3,i)}(x,y)\geq T\\ 0 & d_{(i-3,i)}(x,y)<T\end{cases} \\ b_{(i,i+3)}(x,y)=\begin{cases}1 & d_{(i,i+3)}(x,y)\geq T\\ 0 & d_{(i,i+3)}(x,y)<T\end{cases}\end{cases} \quad (2)$$

where, T is the adaptive threshold, $b_{(i-3,i)}(x,y)$ and $b_{(i,i+3)}(x,y)$ are binary images after comparing the difference images and threshold T.

(5) In order to reduce the "hole" phenomenon, process the above binary result morphologically; in order to reduce the "overlap" phenomenon of the target, do the "and" operation to the corresponding pixel (x,y) in 2 binary images; eliminate the small "details" by morphological processing; get the binary image of the target's contour of the current frame. Equation (3):

$$B_i(x,y)=\begin{cases}1 & b_{(i-3,i)}(x,y)\cap b_{(i,i+3)}(x,y)=1\\ 0 & b_{(i-3,i)}(x,y)\cap b_{(i,i+3)}(x,y)\neq 1\end{cases} \quad (3)$$

where, $B_i(x,y)$ is the binary image of "and" operation.

2.2 Background Difference method of Energy Minimization

The basic idea of the Background Difference method is to establish the background model, and divide the current frame from the background image to obtain the moving target area. If the pixel threshold is greater than a certain threshold, it is determined that the pixel in the current frame is the foreground, otherwise is the background. The establishment and updating of background model is the key of background difference method.

2.2.1 Build background model

The background model is built to extract the initial background image, and prepare for the detection of the target. It directly affects the integrity of the moving target (Wang, 2011). This paper uses the method of multi frame image statistics to get the average value, which can greatly avoid the problem of detecting wrong clumps in the background detection when there is moving objects in the first frame. Take N consecutive frames' images in the sequence to calculate the average pixel (Wu et al., 2012) as Equation (4):

$$B_0(x,y)=\frac{1}{N}(K_1(x,y)+K_2(x,y)+...+K_i(x,y)) \quad (4)$$

where, N is the number of sequence frames. N=50 in this paper. $K_i(x,y)$ is the grayscale image of i^{th} frame, $B_0(x,y)$ is the reconstructed background image. The value of each pixel in the background image is its cumulative average grayscale in N frames' images.

2.2.2 Background model update

With the influence of factors like illumination changes and scene changes, the background model should be able to adapt to changes in environment during a certain period of time, so it must be constantly updated. This paper presents an Energy Minimization method to update the background model in real-time so that the background can be updated to the corresponding background of the current video frame when moving objects merge into or move out of the background.

This paper uses manual interaction to specify the approximate region of specific target in the first frame. The Maximum Flow / Minimum Cut theory (Tokmakov et al., 2016, Wang et al., 2012) based on graph theory is adopted, the basic idea is: user forcibly define some "hard constraints", that is, mark some targets' pixels by hand, and set them to be the seed pixels to calculate the grayscale histograms of foreground and background; all the pixels (including the specified foreground, background seed pixels) are nodes of the graph, the adjacent pixels are the edges of the graph, and the difference between the pixels is the weight (grayscale value) of the edge, the network graph is constructed, as shown in Figure 1. By calculating the minimum cut in all segments, other pixels of the video frame are automatically classified into the target or background to complete the detection.

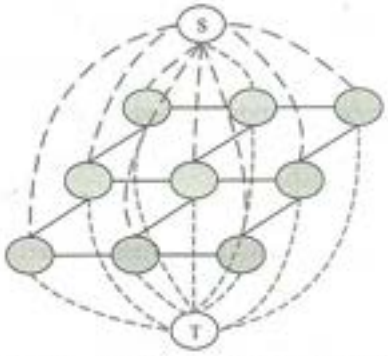

Figure 1 Energy minimization example

The energy function is Equation (5):

$$E(L)=\alpha R(L)+B(L) \quad (5)$$

where, $L=\{l_1, l_2,\ldots l_v\}$ represents the label vector of each pixel in the image, v is the vertex set of the graph, the value of l_i is 0 (background) or 1 (foreground), $\alpha\geq 0$ represents the correlation between the region attribute $R(L)$ and the boundary attribute $B(L)$, $R(L)$ is the intensity of the intensity model (gray histogram) that the pixel belongs to the known foreground or background, $B(L)$ is the weight between the pixel p and the pixel q. The goal is to obtain the L label vector when the $E(L)$ is the minimum.

(1) Calculate region term by Equations (6)-(8):

$$R(L)=\sum_{p\in P} R_p(l_p) \tag{6}$$

$$R_p(1)=-\ln\Pr(l_p \mid \text{'fkg'}) \tag{7}$$

$$R_p(0)=-\ln\Pr(l_p \mid \text{'bkg'}) \tag{8}$$

where, P represents the set of ordinary vertices; $P_p(1)$ represents the weight of the l_p is 1(foreground); $P_p(0)$ represents the weight of the l_p is 0(background); $\ln\Pr(l_p|\text{'fkg'})$ is the probability that the p belongs to the foreground; $\ln\Pr(l_p|\text{'bkg'})$ is the probability that the p belongs to the background.

(2) Calculate boundary term by Equations (9)-(11):

$$B(L)=\sum_{<p,q>\in P} B_{<p,q>}\sigma(l_p,l_q) \tag{9}$$

$$B_{<p,q>}=\frac{\exp\left(-\dfrac{(I_p-I_q)^2}{2\delta^2}\right)}{\mathrm{dist}(p,q)} \tag{10}$$

$$\sigma(l_p,l_q)=\begin{cases}0 & \text{if } l_p=l_q\\ 1 & \text{if } l_p\neq l_q\end{cases} \tag{11}$$

where, p and q represent adjacent vertices; l_p is the tag value of vertex p; l_q is the tag value of vertex q; I_p and I_q respectively represent the gray value of the pixel p and q; δ represents the threshold for p and q brightness difference; $\mathrm{dist}(p,q)$ is the Euclidean distance between p and q; σ is the adjustment factor, if the p and q mark value are the same, then $\sigma=0$, otherwise $\sigma=1$.

2.3 Algorithm implementation

The detailed description of target pig detection algorithm based on the difference method and the energy minimization is as follows:

(1) Input / output image

Input the images in sequence; the detection result of each frame image in binary form is output.

(2) Improve Three-Frame Difference method to detect the contour of moving target pig

Select the interval 3 frames for the difference and set the adaptive threshold to get the binary image.

(3) Improve Background Difference method to detect the area of moving target pig

Background initialization phase: establish a background model of the background difference and specify the foreground pixel in the first frame image.

Background update phase: Update background model based on Maximum Flow / Minimum Cut theory in Energy Minimization.

Calculate the probability of each pixel in the current frame with foreground and background model; each vertex in the graph corresponded to each pixel in the frame, establish the edges between two terminal nodes and these vertices, create the edges between neighbor vertices and construct the network graph; according to the pixel value of each adjacent pixel and the obtained probability density map, the edges are weighted value; the energy minimization algorithm is performed on the corresponding graph to obtain the minimum cut. Calculate the energy value of the next frame, and compare with the previous frame energy value to achieve the background update.

(4) Post-processing phase

Use the mathematical morphological operation to make the movement area continuous, complete, and remove the noise in the background to obtain accurate moving targets.

(5) Contour acquisition phase

Obtain the complete contour image by using the target contour tracking algorithm (Yuan et al., 2010, Chen, et al., 2011), which is only able to track the inner boundary of the target image. In other words, the boundary is within the target, and the "hole" in the image could not be handled. We can accurately obtain the target contour information and it can provide more accurate data for the future behavior identification.

3 Results and discussion

The algorithm program is developed under Microsoft

Visual Studio 2010, Open CV 2.3.1. The hardware operating environment is Intel(R) Core(TM) i7-6700 CPU, running on a 4.00GB memory computer and 64-bit Windows7 system. Image resolution is 192×256, the video frame is 25 frames per second, which basically meets the requirement of real-time.

3.1 Frame interval analysis

For the objects moving fast, smaller intervals are needed. If the selection is not appropriate, when the object in the two consecutive frames there is no overlap, it will be detected as two separate objects. For the objects moving slowly, larger intervals should be chosen. If the time selection is not appropriate, the object will not be detected when the object is almost completely overlapped in the two consecutive frames. According to the activity characteristics of pigs (Hao et al., 2012), this paper uses interval of three frames to make difference. Calculate the difference between the adjacent three frames, and the moving region is detected accurately and effectively. It reduces the background noise and "missed detection" phenomenon, and improves the accuracy of moving target detection. Detection results shown in Figure 2.

a. 19th frame b. Interval 1 frame c. Interval 2 frames d. Interval3 frames e. Interval 4 frames

Figure 2 19th frame threshold segmentation effect

As can be seen from Figure 2, the Traditional Three-Frame Difference method (Figure 2b) and the two-frame interval method (Figure 2c) obtained obscure contours of moving object, in which a lot of "holes" appeared; this paper (Figure 2d) selects three-frame interval method to do the difference, and can obtain a complete target; if four-frame interval (Figure 2e) is used, the moving position of the object is quite different with the expansion of the interval, the target cannot be accurately detected and the detection effect becomes worse.

3.2 Threshold analysis

The grayscale image and the gray histogram of the video image are shown in Figure 3. According to the graph, the gray characteristics of the pig in the video image are obviously different from the background gray scale, the peak and trough of the gray histogram are very obvious. Otsu algorithm (Otsu, 2007, Yang et al., 2009) is simple and has fast processing speed, and it is used to obtain the threshold for the image with obvious double-peak gray histogram. This paper adopts Otsu algorithm to obtain the threshold.

a. Video original image b. Video image grayscale c. Video image gray histogram

Figure 3 Grayscale and gray histogram of video image

Figure 4 shows the color image of moving pig and the threshold image segmentation effect of the Otsu algorithm. From the results of binarization, the threshold obtained by the OTSU algorithm can segment the pig contour more completely, and it provides the basis for the follow-up pig detection.

In Figure 4, three images (Figure 4a, Figure 4b and Figure 4c) are collected by three-frame interval method to make the differential experiment. Figure 4d is the difference result between the 2th frame and the 5th frame, Figure 4e is the difference result between the 5th frame and the 8th frame, and Figure 4f is the two difference

images with "and" operation, and use Otsu method to get binary image. By setting the adaptive threshold, the information in the difference image is more prominent, and the contour of the moving object is clearer. The Otsu method can segment the difference image precisely, and the probability of the background error is greatly reduced.

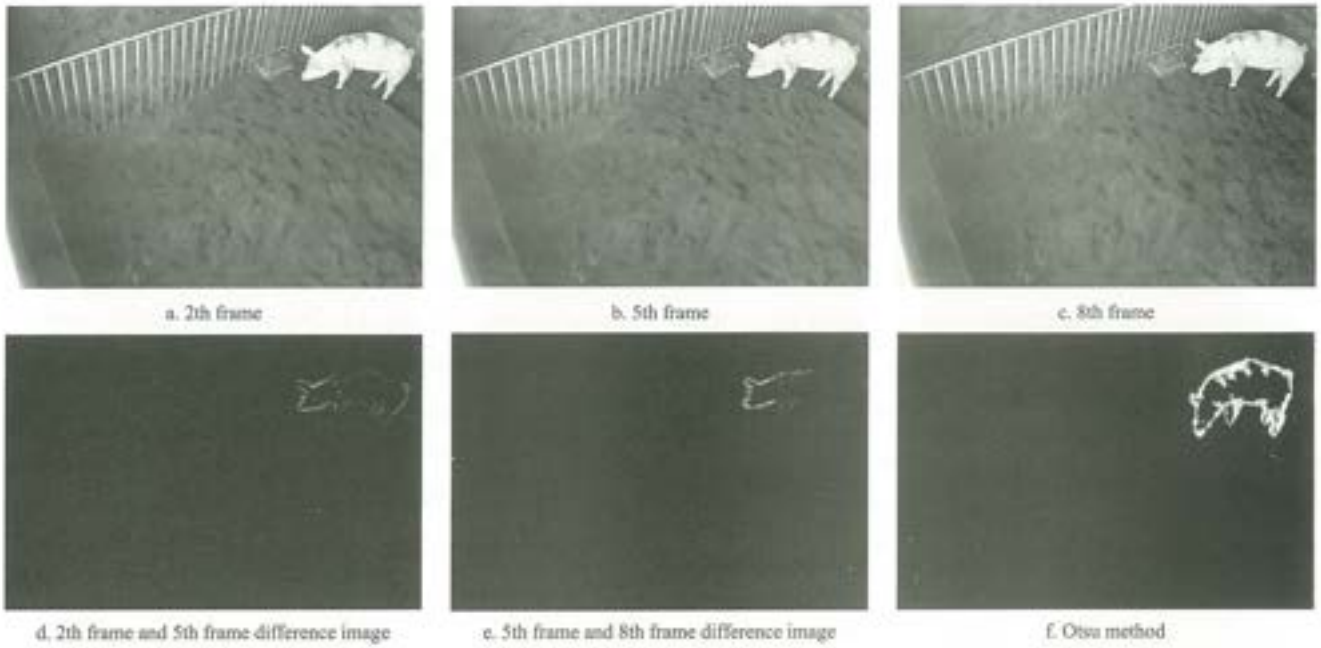

a. 2th frame b. 5th frame c. 8th frame

d. 2th frame and 5th frame difference image e. 5th frame and 8th frame difference image f. Otsu method

Figure 4 Threshold segmentation effect

3.3 Background update analysis

This paper uses the mean method to build initial background, a rapid background extraction can be achieved. It has less computation and can realize object detection more real-time. The initial background is shown in Figure 5.

Figure 5 Initial background

In order to better illustrate the accuracy and effectiveness of the proposed method, the current frame and background image are intercepted in the video, as shown in Figure 6, and the background image is analyzed, as shown in Figure 7.

Figure 6a is a color image in the video sequence, and Figure 6b is the background image obtained by the Traditional Background Difference method. It can be seen from the figure that the Traditional Background Difference method has serious "double shadow" phenomenon, which increases the difficulty of the subsequent target extraction. In this paper, the background updating image based on the energy minimization method can adapt to the changes of light and background, the phenomenon of double shadow is greatly reduced.

a. Original frame b. Background difference method c. New approach

Figure 6 52th frame background update effect

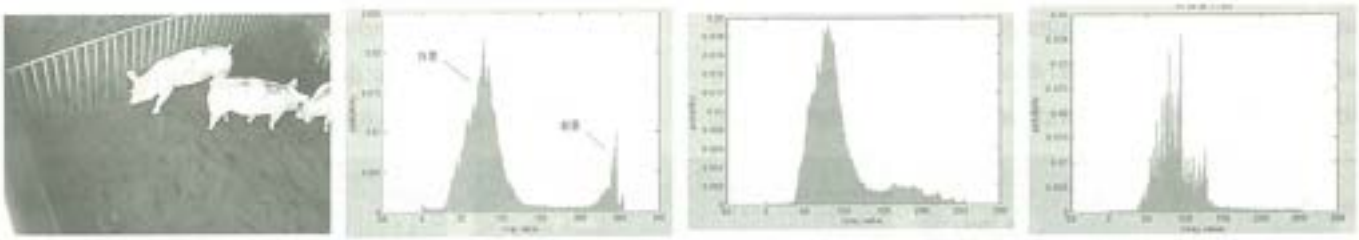

a. Original frame b. Gray histogram of the original frame c. Gray histogram of the background difference method d. Gray histogram of the new approach

Figure 7 364th frame original frame and background gray histogram

Based on the analysis of the video frame and background image in Figure 6, it is concluded as follows: By specifying the target pig in the first frame, the foreground gray value range is obtained, as shown in Figure 7b. The background gray histogram obtained by the Traditional Background Difference method as shown in Figure 7c, the gray histogram is focused on the background pixels and has a large amount of foreground pixels; this paper uses energy minimization idea of graph cut to update background model in real-time. From Figure 7d can be seen that the background gray value range is close to the original video frame gray histogram, and the foreground pixel is less. It shows that the method performs better in updating background.

3.4 Detection results analysis

3.4.1 Intuitive analysis

In order to verify the effectiveness of the improved detection algorithm, the motion objects of surveillance video are detected in real-time, and the algorithm is verified by nearly 80000 frames in the video image. The Three-Frame Difference method, the Background Difference method and the improved method are used to experiment with different video sequences of the same scene. The contrast results are shown in Figures 8-10. Use the contour detection operator for contour detection, the contours of the moving target are shown in Figures 11-13. The sample are 4th, 226th, 465th frame captured in the video.

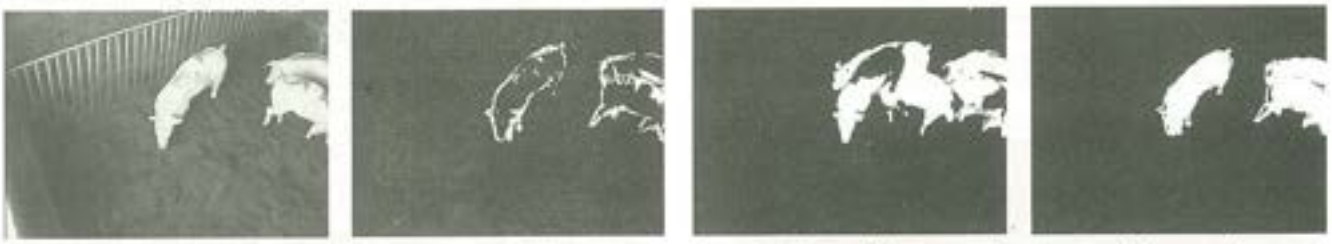

a. Original frame b. Three frame difference c. Background difference d. New approach

Figure 8 4th frame detection effect

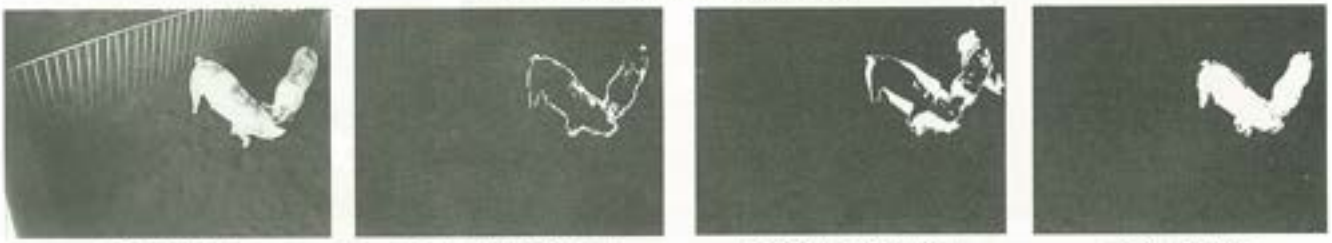

a. Original frame b. Three frame difference c. Background difference d. New approach

Figure 9 226th frame detection effect

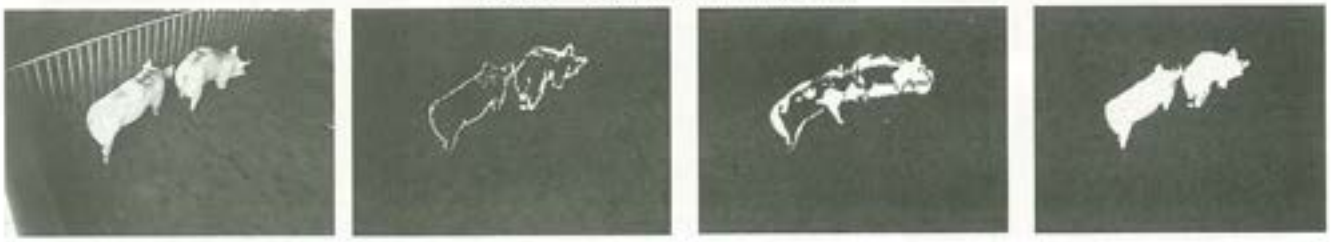

a. Original frame b. Three frame difference c. Background difference d. New approach

Figure 10 465th frame detection effect

a. Three frame difference b. Background difference c. New approach

Figure 11 4th frame contour detection effect

a. Three frame difference b. Background difference c. New approach

Figure 12 226th frame contour detection effect

a. Three frame difference b. Background difference c. New approach

Figure 13 465th frame contour detection effect

From the experimental results, it can be seen that the moving objects based on the Three-Frame Difference method and the Background Difference method have "hole" phenomena and accompanied by noise, as shown in Figure 8b, Figure 9b, Figure 10b and Figure 8c, Figure 9c, Figure 10c. It cannot extract the complete area of the moving target, it is difficult to obtain a complete target contour, and the detection effect is not accurate; this method is more complete to extract the moving target area of pigs, the phenomenon of "hole" and "double shadow" is less, it can describe the contour in detail and reduce the influence of noise.

Edge continuity refers to the continuity of the edge image detected by the edge detection algorithm. If the detection effect is good, each section of the image has a large spatial range, and the continuity is good. If the detection effect is not good, the edge appears fracture or broken, the continuity is bad. As can be seen from Figures 11-13, the Three-Frame Difference Method and the Background Difference Method are used to obtain the contour image discontinuity, as shown in Figure 11a, Figure 12a, Figure 13a and Figure 11b, Figure 12b, Figure 13b; the contour image extracted by this method is more complete and continuous, it is consistent with the target image and has better detection effect.

3.4.2 Quantitative analysis

In order to evaluate the objective performance of the proposed moving object detection algorithm, we use the edge continuity evaluation index (Duan et al., 2016) to analyze different detection algorithms, which is commonly used in literature. Edge continuity refers to existence the edge pixels in the eight neighborhood of the pixel, and the degree of continuity is defined by the number of edge pixels that exist (Zhu, 1996), which directly affects the identification of moving objects.

For the edge binary image W, it is assumed that the

number of consecutive edge segments is m, the i segment is composed of the pixel set $C_i = \{W(x_1^i, y_1^i), W(x_2^i, y_2^i), ...W(x_{s_i}^i, y_{s_i}^i)\}$. The value of the edge segment pixel $W(x_k^i, y_k^i)$ to its edge segment continuity is in Equations (12):

$$c_k^i = \begin{cases} d_k^i / D & d_k^i < D \\ 1 & d_k^i > D \end{cases} \quad (12)$$

where, d_k^i is the distance from the edge pixel $W(x_k^i, y_k^i)$ to the edge space center $(\overline{x_i}, \overline{y_i})$; D is the distance threshold, which can be selected according to the image size and scale.

In order to facilitate the comparison between multiple images, the normalization process is used to satisfy the continuity index range access to [0, 1]. Mo et al. (Mo et al., 2011) constructed the S-function and defined the continuity of the edge segments in Equations (13):

$$SC^i = S(C^i) = 2 \times (\frac{1}{1 + \exp(-C^i / \alpha)} - 0.5) \quad (13)$$

where, C^i is the sum of the continuity of all the pixels in the i segment. After a large number of experimental data testing; α take 2 is the most appropriate.

The continuity index reflects the relationship between the number of edge segments and the length of each edge. Edge detection image continuity index is Equations (14):

$$CIdx = \sum_{i=1}^{m} (n_i \times SC^i) / \sum_{i=1}^{m} n_i \quad (14)$$

where, n_i is the number of pixels in the i edge segment.

Select the first 1000 frames of the video as the display test data, as shown in Figure 14.

The value range of the image continuity index range (CIdx) is [0, 1]. The smaller the value, the worse the continuity of the edge detection image. The bigger the value, the better the continuity of the edge detection image. As can be seen from Figure 14: (1) The Three-Frame Difference method and the Background Difference method are significantly lower than the detection algorithm in this paper, which indicates that the target detection error is large. It cannot get complete and continuous target. (2) According to the continuity index data: The continuity index range of the Traditional Three-Frame Difference method and the Background Difference method are 0.3-0.5. The continuity index range of this method is 0.7-0.9. The contour continuity is improved obviously, and the contour extraction results are accurate, complete and with good robustness.

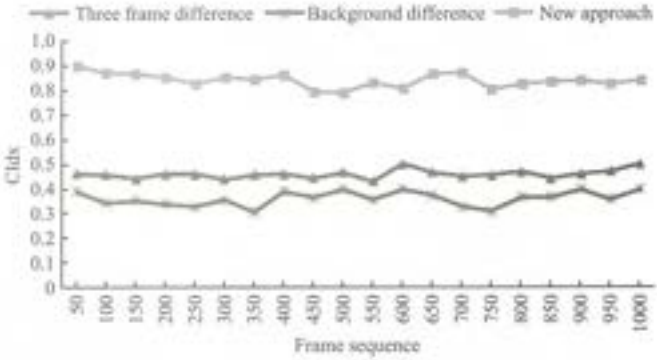

Figure 14 Contrast of Contour Continuity

3.5 Algorithm efficiency analysis

In order to analyze the detection efficiency of different moving object detection algorithms. This paper selected six monitoring videos for experiment, and the average execution time of three different algorithms are shown in Table 1.

Table 1 Different algorithms efficiency comparison results

Video sequence	Frames	Three frame difference	Background difference	New appeoach
		Running time, s Efficiency, fps s^{-1}	Running time, s Efficiency, fps s^{-1}	Running time, s Efficiency, fps s^{-1}
1	74980	3279.97 22.86	3584.13 20.92	3734.06 20.08
2	78502	3408.68 23.03	3729.31 21.05	3901.69 20.12
3	74855	3320.98 22.54	3455.91 21.66	3750.25 19.96
4	84907	3732.18 22.75	4047.04 20.98	4123.70 20.59
5	78510	3575.14 21.96	3682.46 21.32	3877.04 20.25
6	82515	3639.83 22.67	3839.69 21.49	3955.66 20.86
average value		22.64	21.24	20.31

The data in Table 1 shows that the algorithm is stable and effective, the average execution time of different moving object detection algorithms are respectively: The Three-Frame Difference method is 22.64 fps/s, the Background Difference method is 21.24 fps/s, and this method is 20.31 fps/s. In this paper, fusion the Three-Frame Difference method and the background difference method, and transform the background update problem of the Background Difference method into the image segmentation energy minimization. With the single

pixel as processing, the background update time is increased. Compared with the Traditional Background Difference method, this method uses more time and the efficiency is decreased. The segmentation method can detect moving target effectively and meet the requirements of real-time detection.

4 Conclusion

Aiming at the shortcomings of traditional difference method motion target detection algorithm, this paper proposes a three frame difference and energy minimization background difference fusion algorithm. It can be seen from the detection effect that the moving target detection algorithm can detect the complete target pig accurately and extract the continuous contours of the target pig. The main findings of the experiment are summarized as below:

(1) The principle of the algorithm is simple, it can completely detect the moving target of different environment and different speed. The algorithm overcomes the phenomenon that there are empty holes in the Traditional Three-Frame Difference Method, and eliminates the "ghost" and the "drag" phenomenon of the Background Difference Method. The edge continuity index range of this method is 0.7-0.9, the edge continuity index range of the Traditional Three-Frame Difference method and the Background Difference method are 0.3-0.5. The continuity of the contour is improved obviously.

(2) Through the analysis of different video detection efficiency, this method slows down the operation speed compared with the Traditional Three-Frame Difference method and the Traditional Background Difference method, it still satisfies the real-time detection. The findings proposed in this paper provide technical support for the target tracking and the monitoring, and it provides the basis for evaluation, warning.

Acknowledgements

The authors acknowledge that this research was financially supported by the National High Technology Research and Development Program of China (2013AA102306).

[References]

[1] Ahrendt, P., T. Gregersen, and H. Karstoft. 2011. Development of a real-time computer vision system for tracking loose-housed pigs. *Computers & Electronics in Agriculture*, 76(2): 169–174.

[2] Alex, D. S., and A. Wahi. 2014. BSFD: Background subtraction frame difference algorithm for moving object detection and extraction. *Journal of Theoretical & Applied Information Technology*, 60(3): 623–628.

[3] Boykov, Y. Y., and M. P. Jolly. 2001. Interactive graph cuts for optimal boundary & region segmentation of objects in N-D images. *Computer Vision. ICCV 2001. Proceedings. Eighth IEEE International Conference on. IEEE*, 105–112. Vancouver, BC, Canada, 7-14 July.

[4] Boykov, Y., O. Veksler, and R. Zabih. 2001. Fast Approximate Energy Minimization via Graph Cuts. *IEEE Transactions on pattern analysis and machine intelligence*, 23(11): 1222–1239

[5] Chen, Y., W. Li and J. X. Zhang. 2011. Overlapped grapes berry size inspection based on image contour analysis. *Transactions of the Chinese Society for Agricultural Machinery*, 42(8): 168–172.

[6] Duan, Y. B., and J. S. Chen. 2016. A new objective method of evaluation in the image edge detection. *Techniques of Automation and Application*, 35(3): 57–62.

[7] Duan, Y. Y., L. Ma, and G. Liu. 2015. Remote monitoring system of pig motion behavior and piggery environment based on Internet of Things. *Transactions of the Chinese Society of Agricultural Engineering*, (S2): 216–221.

[8] Guo, Y. Z., W. X. Zhu, P. P. Jiao, and J. L. Chen. 2014. Foreground detection of group-housed pigs based on the combination of Mixture of Gaussians using prediction mechanism and threshold segmentation. *Biosystems Engineering*, 125(3): 98–104.

[9] Gupte, S., O. Masoud, R. F. K. Martin, and N. P. Papanikolopoulos. 2002. Detection and classification of vehicles. *IEEE Transactions on Intelligent Transportation Systems*, 3(1): 37–47.

[10] Hao, H. G., and J. Q. Chen. 2012. Moving object detection algorithm based on five frame difference and background difference. *Computer Engineering*, 38(4):146–148.

[11] Howe, N. R., and A. Deschamps. 2004. Better foreground segmentation through graph cuts. *Computer Science*, arXiv:cs/0401017.

[12] Li, Z. Y. 2013. Study on moving object detection and tracking technology in the application of pig behavior monitoring. M.S. thesis., Information and Electrical Engineering Dept., China Agricultural Univ., Beijing, China.

[13] Lind, N. M., M. Vinther, R. P. Hemmingsen, and A. K. Hansen. 2005. Validation of a digital video tracking system for recording pig locomotor behaviour. *Journal of Neuroscience Methods*, 143(2): 123–132.

[14] Liu, L. S., M. X. Shen, G. Y. Bo, B. Zhou, M. Z. Lu, and X. J. Yang. 2014. Sows parturition detection method based on

machine vision. *Transactions of the Chinese Society for Agricultural Machinery,* 45(3): 237–242.

[15] Lu, Z. Y., and W. Liu. 2010. The compensated HS optical flow estimation based on matching harris corner points. *International Conference on Electrical and Control Engineering,* 2279–2282. Wuhan, China, 25-27 June.

[16] Malcolm, J., Y. Rathi, and A. Tannenbaum. 2007. Multi-object tracking through clutter using graph cuts. In *11th IEEE International Conference on Computer Vision*, 1-5. Rio de Janeiro, Brazil, 14-21 October.

[17] Messelodi, S., C. M. Modena, N. Segata, and M. Zanin. 2005. A kalman filter based background updating algorithm robust to sharp illumination changes. In *International Conference on Image Analysis and Processing*, 163–170. Berlin, Heidelberg, 6-8 September.

[18] Mo, S. Q., Z. G. Liu, J. Zhang, and W. X. Wei. 2011. An unsupervised threshold selection method for edge detection based on image self-information. *Journal of Optoelectronics·Laser,* 22(8): 1246–1250.

[19] Navarrojover, J. M., M. Alcañizraya, V. Gómez, S. Balasch, J. R. Moreno, and V. Graucolomer. 2009. An automatic colour-based computer vision algorithm for tracking the position of piglets. *Spanish Journal of Agricultural Research,* 7(3): 535–549.

[20] Oczak, M., G. Ismayilova, A. Costa, S. Viazzi, L. T. Sonoda, and M. Fels. 2013. Analysis of aggressive behaviours of pigs by automatic video recordings. *Computers & Electronics in Agriculture,* 99(C): 209–217.

[21] Otsu, N. 2007. A threshold selection method from gray-level histograms. *IEEE Transactions on Systems Man & Cybernetics,* 9(1): 62–66.

[22] Pang, S. Y., and Y. S. Zhang. 2013. The moving target extraction based on the three frame difference and canny operator. *Journal of Chongqing Technology and Business University (Natural Science Edition),* 30(5): 57–61.

[23] Porto, S. M. C., C. Arcidiacono, U. Anguzza, and G. Cascone. 2013. A computer vision-based system for the automatic detection of lying behaviour of dairy cows in free-stall barns. *Biosystems Engineering,* 115(2): 184–194.

[24] Rao, C. S., and P. Darwin. 2012. Frame difference and kalman filter techniques for detection of moving vehicles in video surveillance. *International Journal of Engineering Research and Applications (IJERA),* 2(6): 1168–1170.

[25] Selsis, M., C. Vieren, and F. Cabestaing. 1995. Automatic tracking and 3D localization of moving objects by active contour models. In *Intelligent Vehicles '95 Symposium. Proceedings of the. IEEE,* 96–100. Detroit, MI, 25-26 September.

[26] Shu, X., D. X. Li, and D. W. Xue. 2014. Five frame difference and edge detection of moving target detection. *Computer Systems & Applications,* 23(1): 124–127.

[27] Sun, L. Q., Z. Y. Li, Q. L. Duan, X. X. Sun, and J. Li. 2014. Automatic monitoring of pig excretory behavior based on motion feature. *Sensor Letters,* 12(3): 673–677.

[28] Tokmakov, P., K. Alahari, and C. Schmid. 2016. Learning semantic segmentation with weakly-annotated videos. *Computer Vision-ECCV,* arXiv: 1603.07188.

[29] Wang, T. Y. 2011.The motion detection based on background difference method and active contour model. In *Information Technology and Artificial Intelligence Conference. IEEE,* 480–483. Chongqing, China, 20-22 August.

[30] Wang, Z. H., J. L. Su, Y. Chen, and S. R. Gong. 2012. Automatic object extraction in nature scene based on visual saliency. *Lecture Notes in Artificial Intelligence and Computational Intelligence,* 547–554. Chengdu, China, 26-28 October.

[31] Wu, L. H., Y. X. Lv, and D. Zhu. 2015. Analysis of pig farmers' attitude towards environmental benefits and its influencing factors: the case of funing county in Jiangsu province. *Journal of Jiangnan University (Humanities & Social Sciences),* 2015(2): 113–121.

[32] Wu, Q. 2012. Detection and tracking technology research of pig behavior based on machine vision. M.S. thesis., Information and Electrical Engineering Dept., China Agricultural Univ., Beijing, China.

[33] Xiao, D. Q., A. J. Feng, Q. M. Yang, J. Liu, and Z. Zhang. 2016. Fast motion detection for pigs based on video tracking. *Transactions of the Chinese Society for Agricultural Machinery,* 47(10): 351–357.

[34] Yang, W. Z., D. L. Li, L. Zhu, Y. G. Kang, and F. T. Li. 2009. A new approach for image processing in foreign fiber detection. *Computers & Electronics in Agriculture,* 68(1): 68–77.

[35] Yin, H. P., Y. Chai, S. X. Yang, and X. Y. Yang. 2011. Fast-moving target tracking based on mean shift and frame-difference methods. *Journal of Systems Engineering and Electronics (S1004-4132),* 22(4): 587–592.

[36] Yuan, W. Q., Q. Dong, and H. F. Sang. 2010. Hand shape contour tracking method based on directional gradient extremum. *Optics and Precision Engineering,* 18(7): 1675–1683.

[37] Zhang, Y. Z., X. Y. Wang, and B. Qu. 2012. Three-frame difference algorithm research based on mathematical morphology. *Procedia Engineering,* 29(4): 2705–2709.

[38] Zhao, Y. C., Z. H. Hu, Y. Bai, and F. Q. Cao. 2015. An accurate segmentation approach for disease and pest based on texture difference guided DRLSE. *Transactions of the Chinese Society for Agricultural Machinery,* 46(2): 14–19.

[39] Zhu, Q. M. 1996. Efficient evaluations of edge connectivity and width uniformity. *Image & Vision Computing,* 14(14): 21–34.

[40] Zhu, W. X., X. F. Pu, X. C. Li, and C. F. Lu. 2010. Automatic identification system of pigs with suspected case based on behavior monitoring. *Transactions of the Chinese Society of Agricultural Engineering,* 26(1): 188–192.

[41] Zuriarrain, I., A. A. Mekonnen, F. Lerasle, and N. Arana. 2013. Tracking-by-detection of multiple persons by a resample-move particle filter. *Machine Vision and Applications,* 24(8): 1751–1765.

MEMBERSHIP APPLICATION FORM

Affix Photo here

ASIAN ASSOCIATION FOR AGRICULTURAL ENGINEERING (AAAE)

I wish to become a member of the AAAE
Membership Categories: (Mark the appropriate box)

☐ LIFE MEMBER	As per the age of a member (minimum US$ 400)
☐ REGULAR MEMBER	US$ 50 per calendar year, and US$ 150 minimum for 3 years*
☐ CORPORATE MEMBER	US$ 400 minimum for 2 years (for industries only)

PERSONAL DETAILS

NAME (Prof./Dr./Mr./Ms.) .....

DATE OF BIRTH: .....

TITLE/POSITION: .....

ORGANIZATION: .....

Mailing Address: .....

.....

Phone: ..... E-mail: .....

Fax: .....

QUALIFICATIONS ATTAINED:

.....

.....

Number of years of professional experience: .....

.....

Special field(s) of interest: .....

Affiliation with other sociefy or association: .....

.....

Please make payment either by bank draft/cheque in favor of "**SINOMACH Academy of Science and Technology Co., Ltd**" and mail to the address below, or ask the AAAE Secretariat for bank information.

AAAE Secretariat
Room 306, College of Food Science and Nutritional Engineering, China Agricultural University
Tel: +86-10-62737401
Fax:+86-10-62737401
Email: aaaese@aliyun.com; iaejeditor@aliyun.com

For Office Use Only Date received: .....

Secretariat Acknowledged ..... Verification of National Affiliation .....
Membership Grade Approved ..... Membership Number .....

Membership Plaque/Certificate/Card issued .....

*Inclusive of US$ 10 for air mailing of journal and other material

JOURNAL SUBSCRIPTION INFORMATION

INTERNATIONAL AGRICULTURAL ENGINEERING JOURNAL (IAEJ)

The *International Agricultural Engineering Journal* (IAEJ) is an International Journal focusing on Research and Development in Agricultural Engineering and is published by the Asian Association for Agricultural Engineering (AAAE). It is a peer-reviewed international journal published only in printed form with 4 issues per year. The official ISSN registration number is 0858-2114. IAEJ is one of the most prestigious international journals in the field of agricultural engineering and has been indexed and abstracted in EI Compendex (Core), Scopus, Elsevier Bibliographic Databases, etc.

Subscriptions to the International Agricultural Engineering Journal (IAEJ) are invited which will enable researchers to get access to the valuable scientific and technological findings of the scientists, engineers, research scholars and professors worldwide working in a diverse range of fields in agricultural engineering.
Subscription rates are as follows:

US$ 280* per annum (four issues)

* Including postage, excluding any bank charges

Please make payment either by bank draft or by cheque:

(1) Payment by check in favor of "**SINOMACH Academy of Science and Technology Co., Ltd**" to the address below:

AAAE Secretariat
Room 306, College of Food Science and Nutritional Engineering, China Agricultural University
Tel: +86-10-62737401
Fax:+86-10-62737401
Email: aaaese@aliyun.com; iaejeditor@aliyun.com

Bank information:

For bank transfer of RMB (人民币转账):

单位名称：国机集团科学技术研究院有限公司
单位地址：北京市海淀区丹棱街 3 号
开户银行：交通银行股份有限公司北京海淀支行
银行账号：110060576018150140601
开户银行代码：301100000099

For bank transfer of US dollars:

Beneficiary Bank: BANK OF COMMUNICATIONS CO. LTD., BEIJING MUNICIPAL BRANCH
SWIFT Code: COMMCNSHBJG
Bank Address:
Beneficiary: SINOMACH Academy of Science and Technology Co., Ltd
Beneficiary A/C No.: 110060576146600001678
Address: No.3 Danling Street, Haidian District,Beijing, P.R.China
Phone No.: +86 10 82606751

Please indicate the volume you intend to subscribe, your shipping address, contact details by email. If you have any other inquiries, please contact AAAE Secretariat by aaaese@aliyun.com.

Call for papers for the International Agricultural Engineering Journal (IAEJ)

Dear All:

The **International Agricultural Engineering Journal (IAEJ)** is an international journal focusing on research and development in agricultural engineering published by the **Asian Association for Agricultural Engineering (AAAE)**.

IAEJ is a peer-reviewed international journal, publishing in four issues per year. The official ISSN registration is 0858-2114. **The scope of *IAEJ* include: soil and water engineering, farm machinery, farm structures, post-harvest technology, biotechnology, food processing and emerging technologies and any other topic related to agricultural engineering.** International Editorial Board was comprises of outstanding scientists and professionals from all other world involved in various agricultural engineering disciplines. *IAEJ* is one of the most prestigious international journals in agricultural engineering and has been indexed and abstracted in *EI Compendex (Core), Scopus, Elsevier Bibliographic Databases*, etc.

IAEJ welcomes high quality research articles from scientists, engineers and academicians worldwide working in a diverse range of fields in agricultural engineering. Authors are solicited to share their valuable scientific and technological findings with this journal by submitting manuscripts on research, projects, survey works, innovative developments and agro-industrial experiences etc.

Manuscripts for review and possible publications should be submitted via e-mails to iaejeditor@aliyun.com. Submission must be original and should not have been published previously or be under consideration for publication elsewhere.

For more information about submission format, please see the *Guidelines for Authors* in IAEJ.

Yours sincerely,

Prof. CHENG Yongqiang

Secretary General of AAAE
Executive Editor-in-Chief
International Agricultural Engineering Journal (IAEJ)

Chinese Society for Agricultural Machinery (CSAM)

SINOMACH | CAAMS

Chinese Academy of Agricultural Mechanization Sciences (CAAMS)

Bird's-eye View of the Campus of CAAMS

National and International Conferences Sponsored by CSAM

MOST-USDA Workshop on Agricultural Products Processing and Food Safety

Hanging Garden Between the Two Main Office Buildings of CAAMS

VIP Guest Room of CAAMS

Academic Conference Room of CAAMS

Conference Hall of CAAMS

Chinese Academy of Agricultural Mechanization Sciences (CAAMS) was established in 1956. It is a large-scale scientific and technological enterprise with the strongest R&D capabilities in modern agriculture machinery, agro-product processing and packaging industry. It also engages in the development of related high-tech industries such as electro-hydraulic system, information, and media, etc. There are over 8,000 staffs, two-thirds of whom are professional researchers and technicians.

CAAMS has remarkably strong R&D platforms and resources including 5 national key laboratories and testing centers, and administration offices of agricultural machinery committees, societies, associations and alliances. It has completed more than 3,000 scientific and technological projects at national and ministerial level, obtained 2,600 important technological achievements and provided over 3,000 new agricultural machines in 9 categories in the past 60 years.

CAAMS has established cooperative relationships with universities, associations, societies, research institutions and government agencies in over 80 countries around the world. The Editorial Office of International Commission of Agricultural and Biosystems Engineering (CIGR) Journal and the Secretariat of the Asian Association for Agricultural Engineering (AAAE) are both located in CAAMS.

While adhering to its enterprise culture of "Manufacture best agro-machinery to benefit agricultural production and processing", CAAMS will continue to focus on its major business and commit to lead China's agricultural equipment industry.

The Chinese Society for Agricultural Machinery (CSAM), whose administrative body is in CAAMS was established in 1963 with a total membership of over 12,500. To help executing China's strategies of sustainable development and vitalizing the country through science and education, CSAM aims at serving agricultural machinery technicians, promoting academic exchanges, increasing international cooperation, and promote agricultural mechanization for the betterment of farmers. It plays an important role in advancing the integration of science and technology with economy for the purpose of speeding up the realization of China's modernization.

The main publications of the CSAM are Transactions of the Chinese Society of Agricultural Machinery, Farm Machinery, and China Agricultural Mechanization. Together with the Chinese Society of Agricultural Engineering(CSAE), CSAM co-sponsors the CIGR Journal.

Address: No.1 Beishatan, Deshengmen Wai, Beijing, 100083, China
Website: http://www.caams.org.cn
http://www.agro-csam.org

International Agricultural Engineering Journal

International Agricultural Engineering Journal (IAEJ) was launched at the Asian Institute of Technology (AIT), Bangkok, Thailand in 1992. Since 1992, IAEJ has been sponsored and published by the Asian Association for Agricultural Engineering (AAAE) with a frequency of four issues per year and it is the official journal of AAAE. It is published only in print copy and over 660 papers in 25 volumes have been published during past 25 years.

IAEJ is an international and multidisciplinary journal. The major goal of this journal is to communicate advances in agricultural engineering, with a particular preference to Asia, to researchers, practicing engineers and decision makers of developing countries. IAEJ publishes peer-reviewed research papers (both theoretical and applied) and state-of-the-art reviews related to agricultural and biosystems engineering. Its scope includes soil and water engineering, farm machinery, ergonomics, farm structures, renewable energy, postharvest technology, food process engineering, agricultural biotechnology, IT in agriculture, and emerging technologies. Subjects of basic engineering and science such as instrumentation, precision agriculture, protected cultivation, global warming, climate change, terramechanics, environment in agriculture, and new materials are also included in the scope of IAEJ.

IAEJ publishes original papers only and the submission of a manuscript will be taken to imply that the contributions are original and that no similar manuscript has been or is being submitted to other journals. Manuscripts are solicited from all areas of specialization in agricultural and biosystems engineering. It is a valuable service provided by AAAE to its members to publish papers in "International Agricultural Engineering Journal" regularly. IAEJ adopts Chicago Style and follows the fIAEJ Guidelines for Authors' strictly.

Through the persistent efforts of the former Editors-in-Chief of IAEJ, Prof. David Gee-Clough, Prof. Vilas M. Salokhe, Prof. Rameshwar S. Kanwar and Dr. Wang Yingkuan and former Executive Editor-in-Chief, Prof.Zhang lanfang, the IAEJ has grown into one of the prestigious international journals in the field of agricultural engineering. We thank all the former Editors-in-Chief and editorial board members for their leadership and generous supports, and special thanks should also go to the current Editor- in-Chief, Prof. Li Shujun, Executive Editor-in-chief, Prof. Cheng yongqiang for their excellent services.

IAEJ is indexed and abstracted in: EI Compendex (Core), Scopus, Elsevier Bibliographic Databases, Agricultural Engineering Abstract by CAB International, Global Health (GH), Chemical Abstracts (CA), Cambridge Scientific Abstracts-Natural Sciences (CSA-Nat Sci), Cambridge Scientific Abstracts-Technology (CSA-T), Pollution Abstracts, Ulriches Periodicals Directory (Ulrich PD), and Applied Mechanics Review.

IAEJ is a quarterly journal, publishing four issues per year. In order to accelerate and streamline the manuscript handling process, an online manuscript submission system, together with the website of IAEJ was set up in 2012. After the launch this journal has provided open access to its contents on the principle that making research findings freely available to the public supports a greater global exchange of knowledge, which in turn can enhance the usefulness and visibility of IAEJ.

Contact Information:
International Agricultural Engineering Journal Room 306, College of Food Science and Nutritional Engineering, China Agricultural University
Tel: +86-10-62737401 Fax:+86-10-62737401
Email: aaaese@aliyun.com iaejeditor@aliyun.com